AD-A270 679

ISAF '92

PROCEEDINGS
of the
Eighth
IEEE

International Symposium on Applications of Ferroelectrics

DTIC
ELECTE
OCT 13 1993
S A D

Editors:
Michael Liu
Ahmad Safari
Angus Kingon
Gene Haertling

This document has been approved for public release and sale; its distribution is unlimited.

Greenville, SC
U S A
August 30 - September 2, 1992

93-23875

IEEE Catalog Number 92CH3080-9

93 10 8 019

Best
Available
Copy

REPORT DOCUMENTATION PAGE

Form Approved
OMB No. 0704-0188

Public reporting burden for this collection of information is estimated to average 1 hour per response, including the time for reviewing instructions, searching existing data sources, gathering and maintaining the data needed, and completing and reviewing the collection of information. Send comments regarding this burden estimate or any other aspect of this collection of information, including suggestions for reducing this burden, to Washington Headquarters Services, Directorate for Information Operations and Reports, 1215 Jefferson Davis Highway, Suite 1204, Arlington, VA 22202-4302, and to the Office of Management and Budget, Paperwork Reduction Project (0704-0188), Washington, DC 20503.

1. AGENCY USE ONLY (Leave blank)	2. REPORT DATE	3. REPORT TYPE AND DATES COVERED
	1 Feb 93	FINAL: 1 Jan 92 - 30 June 93

4. TITLE AND SUBTITLE
1992 International Symposium on Applications of Ferroelectrics

5. FUNDING NUMBERS
G N00014-92-J-1474

6. AUTHOR(S)
M. Liu, A. Safari, A. Kingon and G. Haertling, Editors

7. PERFORMING ORGANIZATION NAME(S) AND ADDRESS(ES)
Clemson University
Clemson, SC 29634-0907

8. PERFORMING ORGANIZATION REPORT NUMBER
92CH3080-9

9. SPONSORING/MONITORING AGENCY NAME(S) AND ADDRESS(ES)
Office of Naval Research

10. SPONSORING/MONITORING AGENCY REPORT NUMBER

11. SUPPLEMENTARY NOTES
Symposium Proceedings

12a. DISTRIBUTION/AVAILABILITY STATEMENT
No restrictions.

12b. DISTRIBUTION CODE

13. ABSTRACT (Maximum 200 words)
The eighth International Symposium on the Applications of Ferroelectrics was held in Greenville, SC, on August 30 to September 2, 1992. It was attended by approximately 260 scientists and engineers who presented nearly 200 oral and poster papers. The three plenary presentations covered ferroelectric materials which are currently moving into commercial exploitation or have strong potential to do so. These were (1) pyroelectric imaging, (2) ferroelectric materials integrated with silicon for use as micromotors and microsensors and (3) research activity in Japan on high permittivity materials for DRAMs. Invited papers covered such subjects as pyroelectric and electrooptic properties of thin films, photorefractive effects, ferroelectric polymers, piezoelectric transducers, processing of ferroelectrics, domain switching in ferroelectrics, thin film memories, thin film vacuum deposition techniques and the fabrication of chemically prepared PZT and PLZT thin films.

The papers continued to reflect the large interest in ferroelectric thin films. It was encouraging that there have been substantial strides made in both the processing and understanding of the films in the last two years. It was equally clear, however, that much still remains to be done before reliable thin film devices will be available in the marketplace.

14. SUBJECT TERMS	15. NUMBER OF PAGES
Ferroelectrics, Piezoelectrics, Pyroelectrics, Thin films, Processing of thin films.	644
	16. PRICE CODE

17. SECURITY CLASSIFICATION OF REPORT	18. SECURITY CLASSIFICATION OF THIS PAGE	19. SECURITY CLASSIFICATION OF ABSTRACT	20. LIMITATION OF ABSTRACT
Unclassified	Unclassified	Unclassified	UL

GENERAL INSTRUCTIONS FOR COMPLETING SF 298

The Report Documentation Page (RDP) is used in announcing and cataloging reports. It is important that this information be consistent with the rest of the report, particularly the cover and title page. Instructions for filling in each block of the form follow. It is important to *stay within the lines* to meet *optical scanning requirements*.

Block 1. Agency Use Only *(Leave blank)*.

Block 2. Report Date. Full publication date including day, month, and year, if available (e.g. 1 Jan 88). Must cite at least the year.

Block 3. Type of Report and Dates Covered. State whether report is interim, final, etc. If applicable, enter inclusive report dates (e.g. 10 Jun 87 - 30 Jun 88).

Block 4. Title and Subtitle. A title is taken from the part of the report that provides the most meaningful and complete information. When a report is prepared in more than one volume, repeat the primary title, add volume number, and include subtitle for the specific volume. On classified documents enter the title classification in parentheses.

Block 5. Funding Numbers. To include contract and grant numbers; may include program element number(s), project number(s), task number(s), and work unit number(s). Use the following labels:

C	- Contract	PR	- Project
G	- Grant	TA	- Task
PE	- Program Element	WU	- Work Unit Accession No.

Block 6. Author(s). Name(s) of person(s) responsible for writing the report, performing the research, or credited with the content of the report. If editor or compiler, this should follow the name(s).

Block 7. Performing Organization Name(s) and Address(es). Self-explanatory.

Block 8. Performing Organization Report Number. Enter the unique alphanumeric report number(s) assigned by the organization performing the report.

Block 9. Sponsoring/Monitoring Agency Name(s) and Address(es). Self-explanatory.

Block 10. Sponsoring/Monitoring Agency Report Number. *(If known)*

Block 11. Supplementary Notes. Enter information not included elsewhere such as: Prepared in cooperation with...; Trans. of...; To be published in.... When a report is revised, include a statement whether the new report supersedes or supplements the older report.

Block 12a. Distribution/Availability Statement. Denotes public availability or limitations. Cite any availability to the public. Enter additional limitations or special markings in all capitals (e.g. NOFORN, REL, ITAR).

- DOD - See DoDD 5230.24, "Distribution Statements on Technical Documents."
- DOE - See authorities.
- NASA - See Handbook NHB 2200.2.
- NTIS - Leave blank.

Block 12b. Distribution Code.

- DOD - Leave blank.
- DOE - Enter DOE distribution categories from the Standard Distribution for Unclassified Scientific and Technical Reports.
- NASA - Leave blank.
- NTIS - Leave blank.

Block 13. Abstract. Include a brief *(Maximum 200 words)* factual summary of the most significant information contained in the report.

Block 14. Subject Terms. Keywords or phrases identifying major subjects in the report.

Block 15. Number of Pages. Enter the total number of pages.

Block 16. Price Code. Enter appropriate price code *(NTIS only)*.

Blocks 17. - 19. Security Classifications. Self-explanatory. Enter U.S. Security Classification in accordance with U.S. Security Regulations (i.e., UNCLASSIFIED). If form contains classified information, stamp classification on the top and bottom of the page.

Block 20. Limitation of Abstract. This block must be completed to assign a limitation to the abstract. Enter either UL (unlimited) or SAR (same as report). An entry in this block is necessary if the abstract is to be limited. If blank, the abstract is assumed to be unlimited.

ISAF '92

PROCEEDINGS
of the
Eighth
IEEE

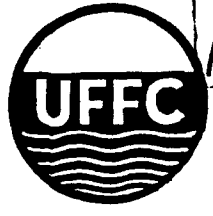
International Symposium on Applications of Ferroelectrics

Editors:

Michael Liu
Ahmad Safari
Angus Kingon
Gene Haertling

Accesion For
NTIS CRA&I
DTIC TAB
Unannounced
Justification
By
Distribution /
Availability Codes
Dist | Avail and / or Special
A-1





DTIC QUALITY INSPECTED 2

Greenville, SC
U S A
August 30 - September 2, 1992

IEEE Catalog Number 92CH3080-9

1992 IEEE 8th International Symposium on Applications of Ferroelectrics

Abstracting is permitted with credit to the source. Libraries are permitted to photocopy beyond the limits of U.S. copyright law for private use of patrons those articles in this volume that carry a code at the bottom of the first page, provided the per-copy fee indicated in the code is paid through the Copyright Clearance Center, 27 Congress Street, Salem, MA 01970. Instructors are permitted to photocopy isolated articles for noncommercial classroom use without fee. For other copying, reprint, or republication permission, write to the IEEE Copyright Manager, IEEE Service Center, 445 Hoes Lane, P.O. Box 1331, Piscataway, NJ 08855-1331. All rights reserved. Copyright © 1992 by The Institute of Electrical and Electronics Engineers, Inc.

IEEE Catalog Number: 90CH3080-9
Softbound: 0-7803-0465-9
Casebound: 0-7803-0466-7
Microfiche: 0-7803-0467-5
Library of Congress Number: 91-58492

Additional copies of this publication are available from

IEEE Service Center
445 Hoes lane
Piscataway, NJ 08854-4150

1-800678-IEEE

EIGHTH INTERNATIONAL SYMPOSIUM ON THE APPLICATIONS OF FERROELECTRICS

August 31-September 2, 1992
Greenville, South Carolina, U. S. A.

PREFACE

The eighth International Symposium on the Applications of Ferroelectrics was held in Greenville, South Carolina on August 30th to September 2nd, 1992. It was attended by approximately 260 scientists and engineers who presented nearly 200 oral and poster papers.

On each day, the technical sessions were led by plenary talks. The three plenary presentations covered ferroelectric materials which are currently moving into commercial exploitation, or have strong potential to do so. These were:

- A review of pyroelectric imaging by Bernie Kulwicki and co-workers of Texas Instruments where arrays of pyroelectric sensors are being successfully produced for infra-red imaging.
- A review of ferroelectric materials integrated with silicon for use as micromotors and microsensors, by Dennis Polla of the University of Minnesota.
- A review of research activity in Japan on high permittivity materials for DRAMs, by Yoichi Miyasaka of NEC. It is believed that future generations of silicon-based microelectronic memories will require high permittivity ferroelectric materials for static capacitors due to the shrinking dimensions of the devices. This will push ferroelectric materials strongly into the microelectronics arena.

Invited papers covered a range of topics, and are listed below:

D. A. Trossell, et al: Pyroelectric and Electro-Optic Properties of Dual Ion Beam Sputtered Lead Titanate Thin Films - GEC Marconi Materials Technology Ltd.
S. R. J. Brueck and A. Mukherjee Electro-Optic and Photorefractive Effects in PLZT Thin Films - Center for High Technology Materials, University of New Mexico
T. R. Shrout and S. L. Swartz: Processing of Ferroelectrics and Related Materials: A Review - Materials Research Laboratory, Pennsylvania State University
V. Ya Shur, et al: Fast Switching in Ferroelectrics: Experimental and Computer Simulation - Ural State University
A. Sternberg, et al: Modified Lead Containing Perovskite Ceramics for Electro-Optic, Electrocaloric, Pyroelectric, and Electrostrictive Applications - Institute of Solid State Physics, University of Latvia
Jan Fousek Domain Investigation: A Select Review - Institute of Physics, Prague
P. K. Larsen, et al: Ultra fast Switching and Fatigue in Lead Zirconate-Titanate (PZT) Thin Films - Philips Research Laboratories
J. Scheinbeim: Piezoelectric and Ferroelectric Polymers - Rutgers State University
T. R. Gururaja: Piezoelectric Transducers for Medical Ultrasonic Imaging - Hewlett Packard
R. Ramesh, et al: Epitaxial Ferroelectric Thin Films for Memory Applications - Bellcore
O. Auciello: A Critical Review of Ferroelectric Thin Film Processing - Microelectronics Center of North Carolina and NCSU
S. Sinharoy, et al: Processing and Characterization of Ferroelectric $BaMgF_4$ and $Bi_4Ti_3O_{12}$ Films for Nonvolatile Memory Field Effect Transistor (FEMFET) Devices - Westinghouse Science and Technology Center
B. Tuttle, et al: Chemically Prepared $Pb(Zr, Ti)O_3$ Thin Films: The Effects of Orientation and Stress - Sandia National Laboratories
J. F. Scott, et al: Microstructure-Induced Schottky-Barrier Effects in Barium Strontium Titanate Thin Films for 16 and 64 Mb DRAM Cells - Department of Physics, University of Colorado

The paper by Shrout and Swartz was unusual because it represented a survey of the community on current and future trends in processing. It generated a great deal of interest and emphasized the fact that much effort

continues to be put into a steady evolutionary improvement in process procedures, particularly through improved synthesis and control of the starting powders.

A somewhat more revolutionary development is that of ferroelectric thin film materials. The papers in Greenville continued to reflect the large interest in these materials which became so apparent at the 7th ISAF held at the University of Illinois in 1990. It was encouraging that there have been substantial strides made in both the processing and the understanding of the thin films during the short intervening period. It was equally clear, however, that much still remains to be done before viable and reliable thin-film devices will be available in quantity in the marketplace. It should also be noted that the growth of activity in ferroelectric thin films has brought researchers with different backgrounds and expertise into the filed. If cross-fertilization is actively encouraged, this can only have a positive impact on the ferroelectrics community. It is with this in mind that we encourage ferroelectric films to be an integral part of the ISAF and IMF meetings, rather than having thin films directed only to the specialist meetings which have evolved (Materials Research Society Symposia, International Symposium on Integrated Ferroelectrics).

As the attendees will well remember, this ISAF meeting came complete with unexpected setbacks with the conference hotel suffering a power outage on two consecutive afternoons. Despite this, the program ran on schedule. Eric Cross entertained guests by flickering candlelight at the conference banquet - giving a personal account some of the people and personalities involved in ferroelectrics over the past 40 years. The Achievement Award was presented to Dr. Wallace A. Smith for his contributions in the filed of composites. It was also announced at the banquet that the next ISF will be held at Pennsylvania State University in 1992, with Professor Amar Bhalla as the general chairman.

A word of thanks to all who participated in this meeting, and all who contributed to making it a success. Special thanks go to Mr. Jamie White of Clemson's Continuing Engineering Education and Mr. Michael Ingram of North Carolina State University for providing organizational support.

Finally, sincere thanks go to the UFFC and IEEE sponsoring organizations and the Office of Naval Research for their financial support of the conference.

Angus I. Kingon
Technical Program Chairman
Department of Materials Science & Engineering
North Carolina State University

Gene Haertling
Symposium General Chairman
Department of Ceramic Engineering
Clemson University

1992 ISAF Organizing Committee And Session Chairs

General Symposium Chair:
Gene Haertling, Clemson University

Technical Program Chair:
Angus I. Kingon, North Carolina State University

Technical Program Committee:
Ahmad Safari, Rutgers, the State University of New Jersey
C. Fred Clark, CeramPhysics, Inc.
S. B. Krupanidhi, The Pennsylvania State University

Publications Committee
S. T. Liu, Honeywell Solid State Electronics Center
Ahmad Safari, Rutgers, the State University of New Jersey

Treasurer:
J. Thomas Cutchen, Sandia National Laboratory

Assistant Treasurer:
Cecil Land, Sandia National Laboratory

Local Arrangements:
Gene Haertling, Clemson University
Jamie White, Clemson University

Session Chairs:
Sidney Lang, Ben-Gurion University
Duane Dimos, Sandia National Laboratory
Andy Bell, Ecole' Polytechnique de Lausanne
David Hall, University of Manchester
Steve Pilgrim, Martin Marietta
Jan Fousek, Institute of Physics, Prague
Gene Haertling, Clemson University
Craig Near, Morgan Matroc
T. R. Gururaja, Hewlett-Packard
Ahmad Safari, Rutgers, the State University of New Jersey
Tom Shrout, The Pennsylvania State University
Jim Scott, University of Colorado, Boulder
Roger Whatmore, GEC-Marconi
Hisao Banno, NGK Spark Plug
Kenji Uchino, The Pennsylvania State University
Joe Dougherty, The Pennsylvania State University
Yoichi Miyasaka, NEC Corporation
Ahmet Erbil, Georgia Institute of Technology
Bruce Tuttle, Sandia National Laboratory
Angus Kingon, North Carolina State University

TABLE OF CONTENTS

Plenary Session 1— Pyroelectric Imaging

Pyroelectric Imaging — *B. M. Kulwicki, A. Amin, H. R. Beratan, and C. M. Hanson* 1

Concurrent Session 1A – Pyroelectrics, Electrooptics

Pyroelectric And Electro-Optic Properties Of Sol-Gel And Dual Ion Beam Sputtered PLZT Thin Films — *D. A. Tossell, J. S. Obhi, N. M. Shorrocks, A. Patel, and R. W. Whatmore* 11
Deposition And Properties Of PLT Thin Films By Magnetron Sputtering From Powder Target — *W.-G. Luo, A.-L. Ding, R.-T. Zhang, Y.-H. Huang, and M. Ge* 19
A Study Of The Properties Of Acetate-Derived PLZT Films On Glass Substrates — *K. D. Preston and G. H. Haertling* 23

Concurrent Session 2A – Pyroelectrics, Electrooptics

Ferroelectric Copolymer And IR Sensor Technology Applied To Obstacle Detection — *F. Bauer, J. J. Simonne, and L. Audaire* 27
The Analytic Representation Of The Effective Nonlinear Coefficients For Biaxial Crystals In The Coordinate Planes — *S. W. Xie, W. Y. Jia, P. J. Wang, and Y. L. Chen* 31
The Concept, Effects and Possible Applications Of Optical And Acoustical Superlattices — N.-B. Ming 35
Lead Calcium Titanate Ceramics And Integrated Optical Filters For Infrared Optical Sensors — *J. de Frutos, F. López, and B. Jiménez* 39
The Relation Between The Mg Concentration Threshold Effect And The Defect Structures Of The Congruent Mg:$LiNbO_3$ — *Q.-R. Zhang and X.-Q. Feng* 43
Optical Associative Memory Using Photorefractive $LiNbO_3$:Fe Hologram, And $LiNbO_3$:Fe And $BaTiO_3$, Phase Conjugate Mirror — *Z. Chen, T. Kasamatsu, M. Shimizu, and T. Shiosaki* 47

Concurrent Session 1B - Dielectrics: Synthesis, Size Effects

The Effect Of Dysprosium On The Microstructure And Dielectric Properties Of $(Ba_{1-x}Sr_x)TiO_3$ Ceramics — *H.-W. Wang and D. A. Hall* 51
Grain Size Effect On The Dielectric Properties Of Strontium Barium Titanate — *U. Kumar, S. F. Wang, S. Varanasi, and J. P. Dougherty* 55
Hydrothermal Synthesis Of Modified Lead Titanate Powders — *C. E. Millar and W. W. Wolny* 59
Sol-Gel Techniques For The Preparation Of Ultrafine $BaTiO_3$ Powders — *Q. Zhang, D. Shen, W. Xue, H. Wang, and M. Zhao* 63

Concurrent Session 2B – Relaxor Dielectrics: Synthesis And Properties

Dielectric Properties And Crystal Structures Of Entire Compositions In The Ternary System $Pb(Mg_{1/2}W_{1/2})O_3$-$Pb(Ni_{1/3}Nb_{2/3})O_3$-$PbTiO_3$ — *A. Ochi, T. Mori, and M. Furuya* 66
Preparation Of Dense Ultra-Fine Grain Barium Titanate-Based Ceramic — *U. Kumar, S. F. Wang, and J. P. Dougherty* 70
High K Low Firing Temperature Capacitors Based On Lead Niobate — *J. E. Day, A. E. Brown, and J. D. Nance* 74
Diffuse Phase Transition And Relaxor Behavior In Perovskites — *H Schmitt, D. Simon, and P. Pitzius* 76

Concurrent Session 1C – Ferroelectrics: Processing, Properties

Processing Of Ferroelectric And Related Materials: A Review — *T. R. Shrout and S. L. Swartz* 80
Preparation And Characterization Of Baruim Titanate Electrolytic Capacitors By Anodic Oxidation Of Porus Titanium Bodies — *S. Venigalla, P. Bendale, R. E. Chodelka, J. H. Adair, and S. A. Costantino* 89
Synthesis Of Ferroelectric $Pb_{1-x}Ca_xTiO_3$ Single Crystals — *N. Ichinose and T. Komachi* 94
Effect Of Grain Size On The Grain Boundary Resistance Of Undoped Barium Titanate Ceramic — *H. Y. Lee and L. C. Burton* 98
Grain Boundary Behaviors Of Ferroelectric Ceramics — *K. Okazaki, H. Maiwa, M. Hagiwara, and S. Sugihara* 103

Electric Fatigue Initiated By Surface Contamination In High Polarization Ceramics — *Q. Jiang, W. Cao, and L. E. Cross* 107

Concurrent Session 2C – Ferroelectrics: Properties, New Materials

Polarization Fatigue In Perovskite Ferroelectric Ceramics And Thin-Films — *J. Chen, M. P. Harmer, and D. M. Smyth* 111
Polarization Switching And Long-Time Relaxation Effects Induced By Off-Center Ions In $KTa_{1-x}Nb_xO_3$ — *L. A. Knauss, C. Jaquays, P. Adhikari, B. E. Vugmeister, and J. Toulouse* 116
Spontaneous Polarization In The Deuterated And Undeuterated Proton Glass $Rb_{1-x}(NH_4)_xH_2AsO_4$ — *N. J. Pinto and V. H. Schmidt* 119
Investigation Of Ferroelectric And Pyroelectric Properties Of Ceramics With Composition $Ba(Li_{2x}Al_{2-2x})O_{4-4x}F_{4x}$ ($0 \le x \le 0.3$) — *S.-Y. Huang, R. Von Der Mühll, J. Ravez, and P. Hagenmuller* 123

Plenary Session 2 — Microsensors And Microactuators

Ferroelectric Microsensors And Microactuators — *D. L. Polla* 127

Concurrent Session 3A – Piezoelectrics And Electrostrictives

Modified Lead Containing Perovskite Ceramics For Electrooptic, Electrocaloric, Pyroelectric and Electrostrictive Applications — *A. Sternberg, L. Shebanov, E. Birks, M. Ozolinsh, V. Dimza, and E. Klotins* 134
Relaxor Ferroelectrics With Lanthanum Perovskites — *T. Takenaka and T. Kanegae* 140
Domain Orientation And Piezoelectric Properties Of Ag Doped PMN-PZT Ceramics — *K. V. R. Murty, S. N. Murty, K. C. Mouli, and A. Bhanumathi* 144
Grain Size Effect On The Induced Piezoelectric Properties Of 0.90PMN-0.10PT Ceramic — *S. F. Wang, U. Kumar, W. Huebner, P. Marsh, H. Kankul, and C. G. Oakley* 148
Effective Electromechanical Properties Of Some $Pb(Mg_{1/3}Nb_{2/3})O_3$-$PbTiO_3$-$(Ba,Sr)TiO_3$ Ceramics — *S. M. Pilgrim, A. E. Bailey, M. Massuda, J. D. Prodey, and A. E. Sutherland* 152

Concurrent Session 4A – Piezoelectrics And Electrostrictives.

The Effect Of Photo-Refractively Induced Periodic Strain Grating On Piezoelectric Vibration In $LiNbO_3$:Fe — *M. Ohki, N. Taniguchi, and T. Shiosaki* 156
Fabrication Of Piezoelectric Ceramic/Polymer Composites By Injection Molding — *L. J. Bowen and K. W. French* 160
Piezoelectric Bimorphs With Quadratic Behavior Using Biased ZnO On Si_3N_4 — *J. G. Smits and W.-S. Choi* 164
Domain Wall Motion In Piezoelectric Materials Under High Stress — *S. Sherrit, D. B. Van Nice, J. T. Graham, B.K. Mukherjee, and H. D. Wiederick* 167
Domain Investigations: A Select Review — *J. Fousek* 171

Concurrent Session 3B – Dielectrics: Properties, Materials And Applications

Non-linear Dielectric Properties Of $KTa_{1-x}Nb_xO_3$ — *X. M. Wang, B. E. Vugmeister and J. Toulouse* 179
Dielectric Behavior Of Ferroelectric Thin Films At High Frequencies — *J. Chen, K. R. Udayakumar, K. G. Brooks, and L. E. Cross* 182
PTC Behavior In Yttria Doped $BaTiO_3$ As Related To Grain Boundary Structure — *R. D. Roseman, J. Kim, and R. C. Buchanan* 185
Nondestructive Evaluation Of Multilayer Capacitors Using Electromechanical Resonance Phenomena — *H.-T. Sun, H.-F. Wang, L.-Y. Zhang, and X. Yao* 189
Destruction Mechanism Of Multilayer Ceramic Actuators — *K. Uchino and A. Furuta* 195

Concurrent Session 4B – Miscellaneous Materials And Applications

Ferroelectric Phase Shifters For Phased Array Radar Applications — *D. C. Collier* 199
Modified Lead Scandium Tantalate For Uncooled LWIR Detection And Thermal Imaging — *R. W. Whatmore, N. M. Shorrocks, P. C. Osbond, S. B. Stringfellow, C. F. Carter, and R. Watton* 202
Low Fire Z5U Ceramic Dielectric For Surface Mount MLC — *S. P. Gupta, C. R. Koripella, and L. A. Mann* 206
Relaxor Studies Of Na, Fe, Mg Doped SBN Ceramics — *S. N. Murty, K. V. R. Murty, G. Padmavathi, K. L. Murty, and A. Bhanumathi* 209

Dielelectric And Ferroelectric Properties In The $Pb(Mg_{1/3}Nb_{2/3})O_3$-$PbTiO_3$-$BaTiO_3$ System — *S. H. Lee, Y. J. Kim, Y. H. Shin, and S. W. Choi* 213

Concurrent Session 3C – Thin Films: Electrical Properties

Ultrafast Polarization Switching Of Lead Zirconate Titanate Thin Films — *P. K. Larsen, G. L. M. Kampschöer, M. B. van der Mark, and M. Klee* 217

Leakage Current Mechanism And Accelerated Unified Test Of Lead Zirconate Titanate Thin Film Capacitors — *I. K. Yoo and S. B. Desu* 225

AC Conductivity And Dielectric Properties Of Sol-Gel PZT Thin Films For Ferroelectric Memory Applications — *X. Chen, A. I. Kingon, and O. Auciello* 229

Concurrent Session 4C – Thin Films: Electrical Properties

Measurement Of Electrooptic Coefficient Of Ferroelectric PLZT Thin Films — *W.-G. Luo, A.-L. Ding, R.-T. Zhang, K. S. Chan, and G. G. Siu* 233

Transverse Electrooptic Properties Of Antiferroelectric Lead Containing Thin Films — *F. Wang, K. K. Li, and G. H. Haertling* 236

Fatigue Effect On The I-V Characteristics Of Sol-Gel Derived PZT Thin Films — *S. C. Lee, G. Teowee, R. D. Schrimpf, D. P. Birnie, III, D. R. Uhlmann, and K. F. Galloway* 240

Defect Structures And Fatigue In Ferroelectric PZT Thin Films — *Z. Wu and M. Sayer* 244

Concurrent Session 5A – Piezoelectrics And Electrostrictives: Composites

New Ferroelectric And Piezoelectric Polymers — *J. I. Scheinbeim, B. A. Newman, B. Z. Mei, and J. W. Lee* 248

Strain Profile And Piezoelectric Performance Of Piezocomposites With 2-2 And 1-3 Connectivities — *Q. M. Zhang, W. Cao, H. Wang and L. E. Cross* 252

An Optimalization Of 1.3.1 PZT-Polymer Composite For Deep Underwater Hydrophone Application — *C. Richard, P. Eyraud, L. Eyraud, D. Audigier and M. Richard* 255

Piezoelectric Transducers For Medical Ultrasonic Imaging — *T. R. Gururaja* 259

Concurrent Session 6A – Piezoelectrics And Electrostrictives: Polymers, Transducers, Processing

Piezoelectric Properties Of "d_{31}-zero", "d_{33}-zero" Or "d_h-zero" Or "d_h-zero" 1-3 Or 2-2 Type Composite Consisting Of 0-3 Subcomposite Of Polymer/$PbTiO_3$ And That Of Polymer/PZT — *H. Banno and K. Ogura* 266

Piezoelectric PZT Tubes And Fibers For Passive Vibrational Damping — *S. Yoshikawa, K. G. Brooks, U. Selvaraj, and U. S. K. Kurtz* 269

Piezoelectric Response Of Precisely Poled PVDF To Shock Compression Greater Than 10 GPa — *F. Bauer, R. A. Graham, M. U. Anderson, H. LeFebvre, L. M. Lee, and R. P. Reed* 273

New Extremely Broadband Ferroelectric Polymer Ultrasound Transducers — *L. F. Brown* 277

PZT-Based Stacked Acoustic Filters — *J. Kosinski, E. Baidy, J. Shannon, A. Safari, and A. Ballato* 281

Concurrent Session 5B – Thin Films: Processing

Reactive Coevaporation Synthesis And Characterization Of $SrTiO_3$-$BaTiO_3$ Thin Films — *H. Yamaguchi, S. Matsubara, K. Takemura and Y. Miyasak* 285

Sol Gel Processing Of Thick PZT Films — *G. Yi and M. Sayer* 289

Lead Titanate Thin Films Deposited By Metallorganic Chemical Vapor Deposition (MOCVD) — *W. C. Hendricks, C. H. Peng, and S. B. Desu* 293

Bulk vs Thin Film PLZT Ferroelectrics — *D. E. Dausch and G. H. Haertling* 297

Highly Oriented (Pb, La)(Zr, Ti)O_3 Thin Films On Amorphous Substrates — *A. Y. Wu, D. M. Hwang, and L. M. Wang* 301

Concurrent Session 6B – Thin Films: Processing

Barium Strontium Titanate Thin Films By Multi-Ion-Beam Reactive Sputtering Technique — *C.-J. Peng, H. Hu, and S. B. Krupanidhi* 305

Controlled Ion Bombardment Induced Modification Of PZT Thin Films — *H. Hu and S. B. Krupanidhi* 309

Microwave Assisted Low Temperature Solid Phase Crystallization Of Ferroelectric Thin Films — *J. Chen, K. R. Udayakumar, and L. E. Cross* 313

Preparation Of Lead-Zirconate-Titanate Thin Films By Reactive RF-Magnetron Cosputtering Using Multi-Element Metallic Targets And Their Evaluations — *T. Yamamoto, T. Imai, and T. Shiozaki* 317

A Critical Review Of Physical Vapor Deposition Techniques For The Synthesis Of Ferroelectric Thin Films — *O. Auciello and A. Kingon* 320

Concurrent Session 5C – Thin Films: Applications And CVD

$LiNbO_3$ Thin Film Capacitor And Transistor Processed By A Novel Method Of Photo-Induced Metallo-Organic Decomposition — *C. H.-J. Huang, H. Lin, and T. A. Rabson* 332

Photo-CVD Of Ferroelectric $Pb(Zr,Ti)O_3$ Thin Films — *T. Katayama, M. Sugiyama, M. Shimizu and T. Shiozaki* 336

MOCVD Growth Of $BaTiO_3$ In An 8" Single-Wafer CVD Reactor — *P. C. Van Buskirk, P. S. Kirlin, R. Gardiner, and S. B. Krupanidhi* 340

Chemically Prepared $Pb(Zr,Ti)O_3$ Thin Films: The Effects Of Orientation And Stress — *B. A. Tuttle, J. A. Voigt, T. J. Garino, D. C. Goodnow, R. W. Schwartz, D. L. Lamppa, T. J. Headley, and M. O. Eatough* 344

Concurrent Session 6C – Thin Films: Applications And Processing

DAAS Technique For Synthesizing Doped PZT And PLZT Thin Films — *C. T. Lin, L. Li and J. S. Webb, R .A. Lipeles, and M. S. Leung* 349

The Study Of PZT Ferroelectric Thin Film And Composite With Amorphous Silicon — *Y. L. Wang, D. H. Wu, H. T. Chen, and D. W. Yu* 353

Microstructure-Induced Schottky Barrier Effects In Barium Strontium Titanate (BST) Thin Films For 16 And 64 Mbit DRAM Cells — *J. F. Scott, M. Azuma, E. Fujii, T. Otsuki, G. Kano, M. C. Scott, C. A. Paz de Araujo, L. D. McMillian, and T. Roberts* 356

POSTER SESSION I: FERROELECTRIC

New Ferroelectric $Ba_{1-x}M_x(Li_{2x}Al_{2-2x})O_{4-4x}F_{4x}$ (M=Pb, Sr) — *S.-Y. Huang, R. Von Der Mühll, J. Ravez, and P. Hagenmuller* 360

Optical Characteristics Of $Pb_5Al_3F_{19}$–Type Crystals — *R. Von Der Mühll, J. Ravez, V. Andriamampianina, J. P. Chaminade, and A. Simon* 364

Poling and Switching Behavior Of Ferroelectric Single Grains Studied By Piezoelectric Resonance — *Y. I. Ryu, J. S. Kim, and I. Yu* 367

The Influence Of La Content In PLZT-x/95/5 Ceramics (x=0.5 to 4%) On The Dielectric, Pyroelectric, Thermally Stimulated Current And Raman Scattering Measurements And Model Interpretation — *J. Handerek, Z. Ujma, D. Dmytrow, C. Carabatos, and I. El-Harrad* 370

Processing And Characterization Of New Members Of Pb-K-Niobate Series — *P. Janna, V. A. Kallur, M. A. Drummond, S. Nigli, and R. K. Pandey* 374

Pyrochlore/Perovskite Phase Transformation In Lead Zinc-Niobate Based Ceramics — *X. Wang and X. Yao* 377

Dielectric Properties Of Bismuth Layer Type Ceramics With Lanthanum And Nickel Co-Substitutions — *B. Huang, X. Wang, and X. Yao* 381

Preparation And Phase Transition Of Nanophase Ferroelectric $PbTiO_3$ Fine Powders — *S. Lu, L. Zhang, and X. Yao* 385

Amorphization Of Bulk And Thin Film PZLT Materials By 1.5 MeV Krypton Ion Irradiation With *in situ* TEM Observation — *L. M. Wang and A. Y. Wu* 389

The Temperature Dependence Of Sound Velocities, Elastic Constants And Acoustic Attenuation Of Lead Lanthanum Zirconate Titanate (Pb, La)(Zr, Ti)O_3 — *A. Y. Wu, G. Nicolaides, and D. M. Hwang* 392

Dielectric, Piezoelectric, And Pyroelectric Properties In The Relaxor Ferroelectric (1-x-y) $Pb(Mg_{1/3}Nb_{2/3})O_3$-$xPbTiO_3$-$yPbZrO_3$ System — *J. S. Ko, Y. J. Kim, Y. H. Shin, and S. W. Choi* 395

Influence Of High Energy Grinding On The Texture, Structure And Electrical Properties Of Barium Titanate — *J. M. Criado, F. J. Gotor, L. Perez-Maqueda, C. Real, M. Mundi, and J. del Cerro* 398

90° - Domain Reversal In $Pb(Zr_xTi_{1-x})O_3$ Ceramics — *S. Li, C.-Y. Huang, A. S. Bhalla, and L. E. Cross* 401

Phenomenological Treatment Of Dielectric Loss of Ferroelectrics Under Hydrostatic Pressure — *S. Fujimoto, Y. Kato, and K. Kanai* 405

POSTER SESSION II: THIN FILMS

Electrode Effects On Electrical Properties Of Ferroelectric Thin Films — *D. P. Vijay, C. K. Kwok, W. Pan, I. K. Yoo, and S. B. Desu* 408

Preparation And Characterization Of Lead Lanthanum Tittanate Thin Films By Metalorganic Decomposition — *A. R. Khan, I. K. You, and S. B. Desu* 412

The Use of Design And Experiments To Evaluate The Reliability Of Ferroelectric Nonvolatile Memories — *T.D. Hadnagy, S. N. Mitra, D. J. Sheldon* 416

Pure And Modified Lead Titanate Thin Films By Sol Gel, — *D. M. Tahan and A. Safari* 420

Effect Of Zr/Ti Stoichiometry Ratio On The Ferroelectric Properties Of Sol-Gel Derived PZT Films — *G. Teowee, J. M. Boulton, E. A. Kneer, M. N. Orr, D. P. Birnie III, D. R. Uhlmann, S. C. Lee, R. F. Galloway, and R. D. Schrimpf* 424

Compositional Control Of Ferroelectric $Pb(Zr,Ti)O_3$ Thin Films Prepared By Reactive Sputtering And MOCVD — *M. Shimizu, K. Hayashi, T. Katayama, and T. Shiosaki* 428

Crystallization And Dielectrical Properties Of PLZT Films Derived From Metallo-Organic Precursors — *P. Sun, L.-Y. Zhang, and X. Yao* 432

Structural Investigation Of Thin Film PLZT Using X-Ray Absoption Spectroscopy — *R. B. Greegor, F. W. Lytle, and A. Y. Wu* 436

Electrical Characterization Of Multi-Ion-Beam Reactive Sputter Deposited PZT Thin Films — *H. Hu and S. B. Krupanidhi* 440

Sol-Gel Lead Zirconate-Titanate Thin Films: Effect Of Solution Concentration — *C. Livage, A. Safari, and L. C. Klein* .. 444

Electrical Characterization Of Sol-Gel Derived PZT Thin Films — *K. R. Bellur, H. N. Al-Shareef, K. D. Gifford, S. H. Rou, O. Auciello, and A. I. Kingon* 448

Control Of Lead Content In PLZT Thin Films Produced Using Cluster Magnetron Sputtering — *K. F. Dexter, K. L. Lewis, and J. E. Chadney* 452

POSTER SESSION III: DIELECTRIC

Effect Of Core Shell Morphology On Dielectric Properties Of Zr Doped $BaTiO_3$ — *T. R. Armstrong R D Roseman, and R. C. Buchanan* 455

High Frequency Dielectric Relaxation In $Pb(Mg_{0.137}Nb_{0.633}Ti_{0.05})O_3$ Ceramics — *C. Elissalde, P. Gaucher, and J. Ravez* 458

Dielectric And Ferroelectric Behaviors Of $Ba(Ti_{1-x}Li_x)(O_{3-3x}F_{3x})$ Ceramics — *C. Elissalde, J. Ravez, and X. Yao* 462

Relaxation In $(Ba_{1-y}Pb_y)TiO_3$ Ceramics — *S. Kazaoui, C. Elissalde, and J. Ravez* 465

A Low-Firing High Properties MLC — *Z. Y. Mao, L. T. Li, and X. Yao* 468

One-Step Low-Temperature Sintering Of $SrTiO_3$ Based Grain Boundary Barrier Layer Capacitor Materials — *Z. W. Yin, B. Xu, and H. Wang* 472

Influence Of Sintering Condition On Microstructure Development Of $BaTiO_3$ Based PTCR Materials — *Z. Z. Huang, H. M. Lu, and Z. W. Yin* 476

Quasi Lumped Parameter Method For Microwave Measurements Of Dielectric Dispersion In Ferroelectric Ceramics — *S. Li, J. Sheen, Q. M. Zhang, S.-J. Jang, A. S. Bhalla, and L. E. Cross* 480

Automated System For Processing Of PLZT Powders Derived From Acetate Precursors — *J. Barrett and E. C. Skaar* 484

PLZT Powders From Acetate Precursors Via Coprecipitation — *C. Lin, B. I. Lee, and G. H. Haertling* 488

Grain Size Effects In Barium Titanate — *K. wa Gachigi, U. Kumar, and J. Dougherty* 492

POSTER SESSION IV: PIEZOELECTRIC, ELECTROSTRICTIVE

The Flexible Composite Ferroelectric Functional Films — *D. Yang* 496

Hysteresis Behavior And Piezoelectric Properties Of Nb Doped PLZT Ceramics — *K. V. R. Murty, K. Umakantham, S. N. Murty, K. C. Mouli, and A. Bhanumathi* 500

Electrical Degradation Process And Mechanical Performance Of Piezoelectric Ceramics For Different Poling Conditions — *T. Tanimoto and K. Okazaki* 504

0-3 Piezoceramic-Polymer Composites Prepared Using Thermoplastics and Elastomers — *M. A. Williams, D. A. Hall, and A. K. Wood* 508

Field Dependence Of The Electromechanical Properties Of Fine Grained Hydrothermally Processed Lead Titanate Ceramics — *L. Pardo, J. Ricote, C. Alemany, B. Jimenez, and C. E. Millar* 512

Processing And Characterization Of Ca, Ce And Na Ion Doped Lead Titanates — *A. Ahmad, T. A. Wheat, J. D. Canaday, A. K. Kuriakose, S. E. Prasad, and S. Varma* 516
Microstructural, Dielectric, Piezoelectric, And Pyroelectric Properties Of Chemically Dervied Modified Lead Titanate — *A. Ahmad and T. A. Wheat, S. Sherrit, and B. K. Mukherjee* 520
Fabrication And Piezoelectric Properties Of PZT Ceramics Prepared By Partial Oxalate Method — *H.-D. Nam and H. Y. Lee* 524
Microstructure And Properties Of Cr_2O_3 Doped Lead Titanate Piezoceramics — *L. Wu, Y.-Y. Lee , and C.-K. Liang* .. 529
Elaboration Process And Study Of Nb-Ni Substituted PZT Ceramics With High d_{33} and e_f Coefficients — *L. Eyraud, P. Eyraud, S. Rey, and M. Troccaz* 533
Piezoelectric Actuators In Rotary Or Linear Motions By Excitation Of Asymmetric Displacement — *Y. Tomikawa, M. Aoyagi, and C. Kuskbabe* 537
High Torque Ultrasonic Motor Using Longitudinal And Torsional Vibrations - Characteristics Of The Motor With A Revolving Torsional Vibrator Used In Common As A Stator And A Rotor — *M Aoyagi, A. Satoh, and Y. Tomikawa* 541
A Study On The Relationship Of Phase Equilibrium And Electromechanical Properties In The Modified $PbTiO_3$-$BiFeO_3$ System — *P. Lu, W. Zhang, D. Shen, W. Xue, and M. Zhao* 545
Large Anisotropy On Electromechanical Properties Of Rare-Earth And Alkaline-Earth Oxides Complex Modified-$PbTiO_3$ Ceramics — *H. Wang, W. R. Xue, P. W. Lu, D. W. Shen, Q. T. Zhang, and M. Y. Zhao* 548
Sol-Gel Techniques For The Preparation Of Ultrafine $PbTiO_3$ Powders — *Q. Zhang, Z. Zhang, D. Shen, H. Wang, W. Xue, and M. Zhao* 551
Development Of Portable DC Voltage Standard Using PZT's — *M. Lal* 554
The Electrical Properties Of Antiferroelectric Lead Zirconate-Ferroelectric Lead Zinc Niobate Ceramics With Lanthanum — *J. S. Yoon, V. S. Srikanth, and A. S. Bhalla* 556
The DC Field Dependence Of The Complex Piezoelectric, Elastic And Dielectric Constants For A Lead Zirconate-Based Ceramic — *E. F. Alberta, D. J. Taylor, A. S. Bhalla, and T. Takenaka* 560
Interfaces Between Electrode Metals And (Pb,La)(Zr,Ti)O_3 In Oxidizing Atmosphere — *S. Sugihara and K. Okazak* .. 565
The Electrostrictive And Related Properties Of $(Pb_{1-x}Ba_x)_{1-3z/2}Bi_z$ $(Zr_{1-y}Ti_y)O_3$ Ceramic System — *G. Li and G. Haertling* 569
Ceramic Actuator With Three-Dimensional Electrode Structure — *Y. Fuda, T. Yoshida, T. Ohno, and S. Yoshikawa* ... 573
Composite Of $BaTiO_3$ And Pb(Zr, Ti)O_3 Fabricated With CO_2 Laser — *S. Sugihara* 577
Anomalous Mechanical And Piezoelectric Coefficients In Piezoceramics Used For Ignition — *P. Gonnard, C. Garabédian, H. Ohanessian, and L. Eyraud* 581
The Mechanism Of Low Temperature Sintering PZT Ceramics With Additives Of Li_2O-Bi_2O_3-CdO — *X. Wang, P. Lu, D. Shen, W. Xue, and M. Zhao* 585
Dielectric, Piezoelectric, and Pyroelectric Properties In The $Pb(Mg_{1/3}Nb_{2/3})O_3$-$PbTiO_3$-$Pb(Zn_{1/3}Nb_{2/3})O_3$ System — *S. H. Lee, Y. J. Kim, K. C. Kim, and S. W. Choi* 588

POSTER SESSION V: ELECTROOPTIC, PYROELECTRIC, PHOTOREFRACTIVE

Influence Of Moisture On Pyroelectric Properties Of Bone — *V. E. Khutorsky and S. B. Lang* 592
A PLZT Optical Phase Modulator And Its Applications — *F. Wang and G. H. Haertling* 596
Model Of Electrooptic Effects By Green Function And Summary Representation: Appllications To Bulk And Thin Film PLZT Displays And Spatial Light Modulators — *A. Y. Wu, T. C. C. Chen, and H. Y. Chen* 600
Field Enhancement And Reduction And Elimination Of Remanent Light Flow In Electrooptic Bulk And Thin Film Displays And Spatial Light Modulators: Theory And Practice — *A. Y. Wu* 604
The Self-Second Harmonic Generation Crystal NYAB Pumped By The Laser Output Of Ti^{3+}:Al_2O_3 — *S. W. Xie, W. Y. Jia, P. J. Wang, T. Liou, and Y. L. Chen* 607
Raman Spectroscopy And Nonlinear Optical Properties Of $PbTiO_3$ Suspension — *Y. Han, Q. Zhou, L. Zhang, and X. Yao* 609
Automatic Ellipsometry Measurement For Anisotropic Materials — *Y. Li, B. You, L. Zhang, and X. Yao* 613
Optical Properties Of $LiNbO_3$, With Ion Implantation And Titanium Thermal Diffusion — *B. You, L. Zhang ,and X. Yao* 617
Optical Properties Of $PbTiO_3$/Epoxy 0-3 Fine Composites — *Q F Zhou, Y. Han, L. Y. Zhang, and X. Yao* 621
Measurement Of Dark Conductivity At Extremely Low Light Levels Using Photorefractive Two Wave Mixing — *A. E. Clement, G. C. Gilbreath, R. McKnight, Jr., J. Reintjes, and J. M. K. Chock* 625
Photorefractive Image Amplification At Extremely Low Light Levels — *G. C. Gilbreath, A. E. Clement, J. Reintjes, and R. A. McKnight, Jr.* 629

Author Index 633

Pyroelectric Imaging

PYROELECTRIC IMAGING

Bernard M. Kulwicki and Ahmed Amin
Texas Instruments Incorporated
34 Forest St., MS 10-13, Attleboro, MA 02703

Howard R. Beratan and Charles M. Hanson
Texas Instruments Incorporated
P.O. Box 655012, MS 37, Dallas, TX 75265

Abstract

Pyroelectric detection represents a significant technology for infrared imaging in the 8-14 μm atmospheric window. Detector materials of interest include $Ba_{1-x}Sr_xTiO_3$, $PbSc_{1/2}Ta_{1/2}O_3$, $PbZr_{1-x}Ti_xO_3$ and $PbTiO_3$. The first two materials typically operate near the phase transition temperature, with dc bias applied. Lead (zirconate) titanates are poled and operate without bias well below their transition temperature. A principal objective of work on pyroelectric imaging has been to produce low-cost infrared cameras which are capable of delivering television quality images and which operate near room temperature without requiring costly cooling systems. Good progress has occurred toward achieving this objective.

Introduction

Infrared imaging, particularly in the wavelength range of 10-14 μm, corresponding to the thermal black body maximum near room temperature and to the atmospheric window, is desirable for a wide range of applications. Some examples include night vision, reconnaissance, target recognition, driving aids, manufacturing controls and security systems [1-2].

Present commercially available systems that provide high resolution and fast response time are based on photon detectors, operating at low temperature (*e.g.* 77 °K) in order to obviate the effects of thermal noise. The majority of such systems utilize photoconductive mercury cadmium telluride (MCT) as the detector material [2-5]. Photovoltaic detectors utilizing MCT [3-6], Si-PtSi Schottky barriers [6-8] and III-V compound superlattices [5,10] are actively being developed. Tradeoffs among the various approaches exist [9,11]. However, all these systems require extensive cooling and thus tend to be costly.

In applications that do not require extremely high resolution or fast response time it is feasible to utilize thermal detectors. The two technologies considered most seriously are thermistor bolometers and pyroelectric detectors. Both offer the possibility to operate near room temperature, without extensive cooling. The greatest effort has been on pyroelectric materials, and the reader is referred to a considerable literature detailing the progress in achieving improved performance over time [12-25].

Approximately ten years ago significant effort was devoted to the development of the pyroelectric vidicon [14-19]. Five years ago activity shifted to hybrid structures with a reticulated thin ceramic detector array, solder bump-bonded, pixel by pixel, to the silicon readout circuitry [17-21]. A device implementation of this type, utilizing a modified PZT ceramic, was described by Shorrocks at the Urbana meeting in 1990 [26]. This effort has continued with the improved performance of phase transition materials such as lead scandium tantalate (PScT) [21,25,47]. The most recent work has explored thin films to minimize thermal mass and further improve responsivity [24-28].

This paper will attempt to review the application of pyroelectric detectors to infrared imaging, emphasizing progress in the last several years. First we shall briefly compare imaging technologies, then discuss the principles of pyroelectricity, proceed to an updated comparison of pyroelectric materials suitable for imaging application, and finally consider the device and system requirements. We will also present the results of some of our own efforts to produce hybrid detectors employing reticulated barium strontium titanate ceramics.

Imaging Technologies

Photon Detectors

The principal means to produce imagery in the 10-14 μm window involves the utilization of cooled small band gap semiconductor arrays in either photoconductive (PC) or photovoltaic (PV) mode [4]. PC devices typically use mercury cadmium telluride as a detector material and are most often employed in scanning mode; *i.e.* a linear detector array mechanically scans the scene, producing very high resolution imagery with extremely short response time [2]. The IR photons absorbed by the semiconductor create electron-hole pairs, and the resulting photo current is proportional to the intensity of the incoming radiation. Shortcomings of this type of detector include the cost and reliability of the scanning and cooling systems, and pixel to pixel variability in the array of PC elements, giving rise to undesirable fixed pattern noise.

Efforts have been underway to produce PV staring arrays (*i.e.* rectangular array of pixels attached to an integrated circuit multiplexer/preamplifier) that eliminate the scanning system and provide improved pixel to pixel uniformity. Substantial activity on PtSi diodes for medium wavelength operation [8] and IrSi for operation out to 10 μm [7-8] have shown promise in achieving high density (648 × 487) pixel arrays with outstanding uniformity. However, till now they appear mainly useful in the shorter wavelength range (up to 5 μm). IrSi diodes require cooling to 45 °K and just then become responsive at 10 μm. Since manufacturing takes advantage of low-cost planar silicon processing technology, it is likely that continued effort will occur to extend the range of operation of these devices. But it is unlikely that the cooling requirement can be eliminated for 10-14 μm operation. Second generation PV MCT devices have also been developed to address the problem of pixel uniformity [6,11].

Research effort is also being devoted to the investigation of GaAs/(Ga,Al)As and other III-V system quantum well superlattices, in order to further extend sensitivity, response and resolution, especially at long wavelength [6,10]. Since these structures can be processed like Si devices, it is hoped that manufacturing cost will be low, but it is likely that cooled systems will continue to be required for acceptable signal to noise levels.

CH3080-0-7803-0465-9/92$3.00 ©IEEE

Thermal Detectors

Thermistor bolometry is a sensitive means to detect infrared radiation [3] and continues to receive attention. In addition to the utilization of conventional semiconductor NTC [29-30] and PTC [31] thermistors, efforts to take advantage of the rapid change in resistivity of high temperature superconductors such as $YBa_2Cu_3O_{7-\delta}$ (YBCO) have shown promise [32-33]. However, the latter approach requires cooling below 125 ^{0}K (below 90 ^{0}K for YBCO).

The utilization of the pyroelectric effect in ferroelectric materials has been of strong interest, since this technology promises elimination of expensive cooling systems (*i.e.* it is relatively low in cost), and has adequate performance for many medium range, human vision limited applications. Recent applications work has emphasized hybrid detector ceramic/IC device structures, using either conventional pyroelectrics operating well below T_c [17-23,26] or phase transition materials operating near the transition temperature under dc bias [19-25]. Additionally, increasing effort is being devoted to the exploration of thin film structures, with the pyroelectric film deposited directly on the IC, taking advantage of surface micro-machining to provide the necessary thermal isolation [28]. This paper will principally consider recent developments in hybrid and thin film pyroelectric detectors.

Pyroelectricity

If the crystal has an electric polarization P_i, then pyroelectricity is defined as the change in electric polarization accompanying a change in temperature. The pyroelectric coefficient p_i relates the change in polarization ΔP_i (a vector) and the temperature change ΔT (a scalar) by:

$$\Delta P_i = p_i \Delta T . \qquad (1)$$

For infinitesimal changes in temperature, equation 1 can be written in a differential form:

$$\partial P_i / \partial T = p_i . \qquad (2)$$

In the mks system of units the polarization P_i (*i.e.* the charge per unit area taken perpendicular to the polarization vector) has the dimension C m^{-2}. Therefore, the pyroelectric coefficient p_i is expressed in C m^{-2} K^{-1} (*e.g.* in the theory we discuss here), or often μC cm^{-2} K^{-1} (*e.g.* in the data we will present later). The pyroelectric coefficient is a polar vector (first rank polar tensor). Thus the maximum number of independent pyroelectric coefficients is three (p_1, p_2, p_3) for the most general triclinic point group 1(C_1).

Symmetry Requirements

Two conditions must exist for the crystal point group to be pyroelectric: the absence of the inversion operation and the existence of a unique polar axis. A unique polar axis is an axis of symmetry for which the two ends are not related by any of the symmetry operations of the point group. Both conditions are necessary. The first condition nulls pyroelectricity in the 11 centrosymmetric (Laue) groups, whereas the second (uniqueness of the polar axis) limits it only to the following point groups: 1(C_1), 2(C_2), 3(C_3), 4(C_4), 6(C_6), m(C_s), mm2(C_{2v}), 3m(C_{3v}), 4mm(C_{4v}), and 6mm(C_{6v}). These are known as the 10 polar groups. In addition, pyroelectricity is allowed in the two limiting Curie groups ∞(C_∞), and ∞mm($C_{\infty v}$) which represent the symmetry of a textured material (*e.g.*, wood) and that of an electrically poled ferroelectric ceramic respectively. If the crystal point group contains a unique polar axis (2, 3, 4, or 6 fold), this will necessarily be the direction of the pyroelectric vector. For point group m(C_s), the polar axis will be anywhere in the mirror plane.

Elastic and Electric Boundaries

Most pyroelectric measurements are made under constant stress, *i.e.* $X_{ij} = 0$ for all values of i,j. The difference between the stress free "unclamped" pyroelectric coefficient p^X and the "clamped" coefficient measured under constant strain p^x could be significant. For triglycine sulfate (TGS) the pyroelectric coefficients measured under constant stress p^X and constant strain p^x are -0.027 and +0.006 μC cm^{-2} K^{-1}, respectively [34].

The relationship between the pyroelectric coefficient measured under constant stress p^X, and that measured under constant strain p^x (the primary coefficient) is given by:

$$p_i^X = p_i^x + \sum_j \sum_k \sum_l \sum_m c_{jklm}^{E,X} d_{ilm}^X \alpha_{jk}^E \quad (i, j, \ldots = 1, 2, 3) \qquad (3)$$

where, $c_{jklm}^{E,X}$ is the elastic stiffness tensor, d_{ilm}^X the piezoelectric tensor and α_{jk}^E the thermal expansion tensor. The superscripts denote the measurement conditions. The second term in the right hand side of equation 3 is known as the secondary pyroelectric effect. It is piezoelectric in origin, and represents the coupling of thermal strain to the polarization vector via the piezoelectric modes of the crystal. The reduced form of equation 3 for the 10 polar groups can be found in [34]. For point groups, 4(C_4), 4mm(C_{4v}), 3(C_3), 3m(C_{3v}), 6(C_6), 6mm(C_{6v}), and the Curie group ∞ mm($C_{\infty v}$), equation 3 takes the form:

$$p_3^X = p_3^x + 2d_{31}^X (c_{11}^{E,X} + c_{12}^{E,x}) \alpha_1^E + 2d_{33}^X c_{13}^{E,X} \alpha_1^E + 2d_{31}^X c_{13}^{E,X} \alpha_3^E + d_{33}^X c_{33}^{E,X} \alpha_3^E . \qquad (4)$$

The effect of dc bias on the pyroelectric voltage will be discussed. The dielectric displacement of the stress free "unclamped" crystal takes the following scalar form:

$$D = \varepsilon E_b + P^{X,E}, \qquad (5)$$

where ε is the dielectric permittivity, E_b the biasing field, and $P^{X,E}$ the polarization vector under constant stress and field. Differentiating with respect to temperature yields,

$$(\partial D/\partial T) = p' = (\partial \varepsilon/\partial T) E_b + (\partial P/\partial T) . \qquad (6)$$

According to equation 6, the ***total*** pyroelectric coefficient p′ consists of a dielectric contribution (the first term on the right hand side) and a spontaneous polarization contribution (the second term). More rigorously, the dielectric contribution in equation 6 should be written as a field integral to account for dielectric nonlinearities. The signal voltage ΔV is given by:

$$\Delta V = \Delta Q / C_X = p' A \Delta T / C_X . \qquad (7)$$

where Q is the charge generated, A the electrode area and C_X the crystal's capacitance. Substituting for p′ from equation 6 in equation 7, noting that $C_X = \varepsilon A/a$ and $V_b = a E_b$, where a is the thickness of the pyroelectric element:

$$\Delta V = \varepsilon^{-1}\,[(\partial\varepsilon/\partial T)\,V_b + a\,(\partial P/\partial T)]\,\Delta T. \qquad (8)$$

The first term in equation 8 is the dielectric contribution (bolometer mode) and the second term is the spontaneous polarization contribution (pyroelectric mode). It must be noted that ΔV is not linear in bias because of the non-linearities of ε. Similarly, the dielectric and thermal properties of the crystal are also functions of the elastic and electric boundaries.

Measurements

The sample is usually prepared in the form of a metallized plate with the surfaces perpendicular to the polar axis (Figure 1). Most pyroelectric measurements are made under constant stress (*i.e.* $\Delta X_{ij} = 0$) in which the sample is allowed to expand freely. It is convenient to measure the pyroelectric current or voltage in a manner that is independent of the sample's impedance, especially near the phase transition where the impedance may vary rapidly. It is also important to keep the pyroelectric voltage ΔV small such that non-linearities in polarization do not become significant [14]. This is achieved by measuring the pyroelectric current under short circuit conditions (*i.e.* at constant field).

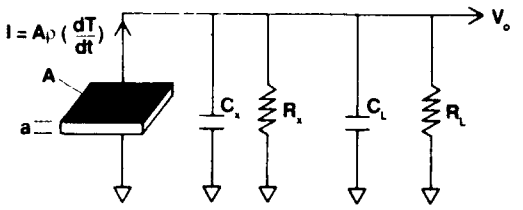


Figure 1. Equivalent circuit of a pyroelectric crystal.

There are two commonly used methods [14] to measure the pyroelectric coefficient: a) measurement of the pyroelectric current or b) measurement of the pyroelectric voltage (charge integration by a capacitor or amplifier). By heating the crystal at a constant heating rate usually 1 or 2 ^{0}C/min and measuring the pyroelectric current [35], the pyroelectric coefficient can be calculated from equation 2 according to $I = -A\,p\,(dT/dt)$. Alternatively, by measuring the pyroelectric voltage ΔV, the pyroelectric coefficient can be calculated from equation 7 according to: $\Delta V = p'A\Delta T/(C_X + C_x)$, where C_x is the shunt capacitor, usually selected $>> C_X$, such that C_X can be ignored. Substituting for $C_X = \varepsilon A/a$ in equation 7 and rewriting in a differential form we obtain:

$$dE/dT = p'/\varepsilon, \qquad (9)$$

i.e., the change of the output voltage per unit thickness (field) of the crystal per unit temperature change is equal to the ratio of the pyroelectric coefficient to the dielectric permittivity. Chopped radiation and other methods for measuring p are listed in [34].

The pyroelectric material figures of merit which describe the current F_i, voltage F_v, and signal to noise F_d are obtained from equation 9 as follows: $F_i = p'/c'$, $F_v = p'/c'\varepsilon$, and $F_d = p'/c'(\varepsilon \tan\delta)^{1/2}$, where c' is the heat capacity per unit volume, and $\tan\delta$ is the dissipation factor. In ferroelectric detectors such as barium strontium titanate (BST), the pyroelectric and the dielectric properties are strong functions of temperature near the phase transition temperature T_c. A technique which we found particularly useful for determining the figures of merit without having to rely upon two separate dielectric and pyroelectric measurements is discussed in [36]. This allows the simultaneous measurements of the pyroelectric and dielectric properties, thereby determining the appropriate figures of merit from one temperature scan.

Thermal Detection

The pyroelectric element can be represented by a current source A p (dT/dt) driving a parallel element-load impedance as shown in Figure 1. Let C_x and R_x be the capacitance and resistance of the pyroelectric element, and R_L and C_L be the load resistance and capacitance (*e.g.* of the preamplifier). Thus, the parallel element - load capacitance C_E and resistance R_E are: $C_E = C_x + C_L$, $R_E^{-1} = G_E = R_x^{-1} + R_L^{-1}$, where G_E is the electrical conductance. The admittance of the circuit is $Y = G_E + i\,\omega\,C_E$.

According to Cooper [37], if the detector thermal capacitance is H and is connected by a thermal conductance G_T to a heat sink, and the incident power is W, the heat balance equation is:

$$\eta\,W = H\,(dT/dt) + G_T T, \qquad (10)$$

where η is the fraction of incident power absorbed by the detector, and T is the temperature difference between the detector and the heat sink. A sinusoidally modulated incident radiation can be expressed by $W = W_o\,e^{i\omega t}$, thus equation 10 has a solution:

$$T = \eta W/(G_T + i\omega H). \qquad (11)$$

The pyroelectric current I and voltage V_o are given by:

$$I = p\,A\,(dT/dt) = i\,\eta\omega\,pAW/(G_T + i\omega H), \qquad (12)$$

$$V_o = I/Y = (i\eta\omega\,pAW)/(G_T + i\omega H)(G_E + i\omega\,C_E) \qquad (13)$$

The current responsivity R_i is defined as the pyroelectric current per unit incident power,

$$R_i = |\,I/W\,| = \eta\omega\,pA/(G_T^2 + \omega^2H^2)^{1/2}. \qquad (14)$$

similarly, the voltage responsivity R_v is,

$$R_v = |\,I/YW\,|$$

$$= \eta\omega\,pA/[G_T G_E(1 + \omega^2\tau_T^2)^{1/2}(1 + \omega^2\tau_E^2)^{1/2}], \qquad (15)$$

where τ_T (= H/G_T) and τ_E (= C_E/G_E) are the thermal and electrical time constants respectively. The voltage responsivity has a maximum R_v (max) at a frequency $\omega = (\tau_T\tau_E)^{-1/2}$ given by:

$$R_v(\max) = \eta\,pA/G_T G_E(\tau_T + \tau_E). \qquad (16)$$

The frequency response of R_v is depicted in Figure 2. The thermal relaxation frequency has been arbitrarily taken smaller than the electrical relaxation frequency. It can be shown that in the region bounded by the thermal and the electrical relaxation frequencies the voltage responsivity is flat within 3 dB of R_v(max).

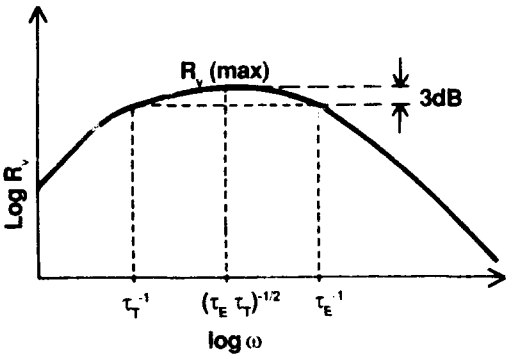


Figure 2. Frequency dependence of voltage responsivity R_v [18].

The current responsivity R_i, however, reaches a steady state value ($= \eta\, p/\sqrt{2}\, c'a$) at the thermal relaxation frequency. For frequencies below the thermal relaxation frequency, R_v is proportional to ω. At frequencies above the thermal and electrical relaxation frequencies, *i.e.* $1/\tau_T << \omega >> 1/\tau_E$, R_v takes the form:

$$R_v = \eta\, p / a\, \omega\, c'\, (C_x + C_L). \qquad (17)$$

The thermal design of the detector is quite important. According to equations 16 and 17, R_v can be increased by decreasing the thermal conductance G_T. This could be achieved by i) thermal insulation and/or ii) using thinner detectors. The preamplifier characteristics determine the detector material figures of merit. For example, if $C_L << C_x$ in equation 17, where $C_x = \varepsilon A/a$, then:

$$R_v = \eta\, p / A\omega\, c'\, \varepsilon, \qquad (18)$$

and $F_v = p/c'\varepsilon$ may be taken as a figure of merit. On the other hand if $C_L >> C_x$, then $F_i = p/c'$ is the appropriate figure of merit.

Pyroelectric Materials

A variety of ferroelectrics have been explored for thermal imaging applications. Some of the more important materials are listed in Table I. It is seen that the majority are perovskites such as PZT, BST, and PScT. Their high polarizability yields large spontaneous polarization and high dielectric permittivity (therefore high induced polarization). Although not a necessary condition for a strong pyroelectric effect, a high polarization is desirable since it often facilitates a substantial change with temperature, particularly in the neighborhood of the Curie point. A high dielectric constant is also useful in many imaging applications where small pixel dimensions constrain the impedance match with the preamplifier.

Table I. Description of Materials for Pyroelectric Imaging

Acronym	Name	Formula
TGS	Triglycine sulfate	$(NH_2CH_2COOH)_3H_2SO_4$
DTGS	Deuterated TGS	$(ND_2CD_2COOD)_3D_2SO_4$
ATGSAs	Alanine+As-doped TGS	$(NH_2CH_2COOH)_3H_2SO_4$: $NH_2CH_2CH_2COOH$:H_3AsO_4
DTGFB	Deuterated triglycine fluoberyllate	$(ND_2CD_2COOD)_3D_2BeF_4$
KTN	Potassium tantalate niobate	$KTa_{1-x}Nb_xO_3$
BST	Barium strontium titanate	$Ba_{1-x}Sr_xTiO_3$
BSCT	Barium strontium calcium titanate	$Ba_{1-x-y}Sr_xCa_yTiO_3$
SBN	Strontium barium niobate	$Sr_{0.5}Ba_{0.5}Nb_2O_6$
PT	Lead titanate	$PbTiO_3$
PCT	Lead calcium titanate	$Pb_{1-x}Ca_xTiO_3$
PLT	Lead lanthanum titanate	$Pb_{1-3x/2}La_xTiO_3$
PLZT	Lead lanthanum zirconate titanate	$Pb_{1-x}La_x(Zr_{1-y}Ti_y)_{1-x/4}O_3$
PZT	Lead zirconate titanate	$PbZr_{1-x}Ti_xO_3$
PZFNTU	Modified PZT	$PbZr_{0.58}Fe_{0.2}Nb_{0.2}Ti_{0.02}O_3$:U
PSZFNTU	Sr-doped modified PZT	$Pb_{1-x}Sr_xZr_{0.58}Fe_{0.2}Nb_{0.2}Ti_{0.02}O_3$:U
PScT	Lead scandium tantalate	$PbSc_{1/2}Ta_{1/2}O_3$
PMN	Lead magnesium niobate	$PbMg_{1/3}Nb_{2/3}O_3$
PZN	Lead zinc niobate	$PbZn_{1/3}Nb_{2/3}O_3$
PZNT	PZT-PZN solid solution	$PbZr_{1-x-y}Zn_{x/3}Nb_{2x/3}Ti_yO_3$
PCoW	Lead cobalt tungstate	$PbCo_{1/2}W_{1/2}O_3$
PGO	Lead germanate	$Pb_5Ge_3O_{11}$
PVDF	Polyvinylidene fluoride	$(CH_2\text{-}CF_2)_n$

Table II compares the performance of a variety of conventional pyroelectrics, *i.e.* poled detectors operating without bias well below the Curie point. In most cases these values represent *typical* properties reported. Significant variation can be expected as a function of differences in processing. The best responsivity (*i.e.* F_d, the detector material noise limited figure of merit) among the single crystals is displayed by alanine/arsenic-doped TGS [38-39] and Ba-doped lead germanate [39]. However, doped crystals are difficult to grow reproducibly, and TGS is sensitive to moisture. Therefore, attention has been given to ceramics, since they tend to be more durable, and complex compositions can be more consistently manufactured.

The PZT family has been extensively studied, and good responsivity has been observed in several compositions [12,16,23, 40]. Considerable effort with PZFNTU (a doped solid solution containing 40 mole% $PbFe_{1/2}Nb_{1/2}O_3$ (sometimes referred to as "modified PZT") has led to the development of an uncooled 10-14 μm camera with a hybrid detector having moderately good performance: 100×100 pixels, NETD = 0.25 °K [26].

Thin films of lead titanate [28] and lead lanthanum titanate [44] have been produced with properties very similar to the best ceramic PZT solid solutions. Combined with surface micromachining to provide adequate thermal isolation of the pixels, thin films promise better performance and simpler processing. Ceramics for hybrid detectors must be thinned, polished, reticulated and metallized, and an array of thermally isolated pixels bonded to the Si. Tens of thousands of pixels must precisely align with the respective circuit elements on the IC.

The technology of producing monolithic IR detectors using ferroelectric thin films is just beginning. Several potential impediments must be overcome in order to be successful, including the development of adequate control of film chemistry, morphology and electrical performance, without deleterious reaction with the silicon. Ultimately, this must be demonstrated in a process that is amenable to volume manufacturing on a consistent basis.

Since conventional ceramic and thin film pyroelectrics are inferior to single crystals, it has been of interest to consider phase transition materials that operate near T_c (or T_t) under dc bias. These detectors are often referred to as "dielectric bolometers," since the induced polarization (either below *or above* T_c) can dominate the pyroelectric response [39]. It is also conceivable to operate in this mode without bias if the polarization direction can be established by preferred orientation, *e.g.* in an epitaxial film. However, most device work to date has taken the former route.

Table III compares materials that have been studied for application in the phase transition region. Values of F_d appear greatly superior to normal pyroelectrics, as one would expect. The very high responsivity promised by KTN appears unattainable on a reliable basis, however, because of the extreme difficulty in obtaining consistent and uniform chemistry [54]. The preponderance of the effort has been devoted to PScT and BST [25,39]. The rhombohedral-rhombohedral transition in PZT and the rhombohedral-tetragonal transition in PZN have also attracted attention, with efforts to enhance the maximum pyroelectric coefficient by means of compositional adjustment [50-52].

It should be mentioned that the measurements given in Table III have been largely obtained by the Byer-Roundy [35] or a related, quasi-static method. For transition materials, it may be more appropriate to characterize them dynamically using chopped black body radiation (Chynoweth method [55]), since this more closely represents the actual condition of application. Well below

Table II. Normal Pyroelectrics ($T < T_c$)

Material	Bias kV/cm	T_c °C	c′ J/cm³K	p μC/cm²K	ε_r	tan δ	F_v cm²/C	F_d (cm³/J)$^{1/2}$	Reference
Single crystals									
TGS	0	49	2.3	0.028	38	0.01	3620	0.066	Herbert [16]
DTGS	0	60	2.4	0.055	43	0.02	6020	0.083	Whatmore (Felix) [25]
ATGSAs	0	51	2.5	0.07	32	0.008	9900	0.19	Bhalla [38]
$LiTaO_3$	0	665	3.2	0.18	43	0.003	1440	0.051	Byer [35]
$LiNbO_3$	0	1210	3.0	0.083	28	0.005	1140	0.025	Byer [35]
SBN 46/54	0	132	2.1	0.043	380	0.003	610	0.065	Byer [35]
PGO:Ba	0	70	2.0	0.032	81	0.001	2200	0.19	Whatmore (Watton) [39]
Ceramics									
PLZT 7/65/35	0	150	2.6	0.13	1900	0.015	300	0.032	Liu [41]
PLZT 8/65/35	0	105	2.6	0.18	4000	0.003	190	0.066	Deb [42]
PZNFTU	0	230	2.7	0.039	290	0.0031	570	0.052	Osbond [23]
PSZNFTU	0	170	2.7	0.049	400	0.0028	520	0.058	Osbond [23]
PGO	0	178	2.6	0.002	25	0.003	350	0.009	Kanduser [43]
Polymerics									
PVDF	0	none	2.4	0.0027	12	0.015	1040	0.009	Whatmore [39]
Thin films									
$PbTiO_3$ sol-gel	0	490	2.9	0.095	200	0.02	1870	0.056	Polla [28]
PLT 90/10 sputtered	0	330	3.2	0.065	200	0.006	1150	0.062	Takayama [44]
PCT 70/30 sputtered	0	270	3.3	0.05	390	0.015	440	0.021	Yamaka [45]
PZT 54/46 sol-gel	0	380	3.1	0.07	950	0.016	260	0.019	Ye [28]

Table III. Phase Transition Materials ($T \cong T_{t(c)}$)

Material	Bias kV/cm	T_t °C	c′ J/cm³K	p'_{max} μC/cm²K	ε_r	tan δ	F_v cm²/C	F_d (cm³/J)$^{1/2}$	Reference
Single crystals									
DTGFB	0	74	2.0	1.4	2400	0.02	3300	0.34	Dougherty [36]
KTN 67/33	2.5	4	3.7	8.0	25000	0.002	1000	0.46	Stafsudd [46]
BST 65/35	5	5	2.5	0.3	20000	0.007	170	0.034	Whatmore [39]
Ceramics									
BST 67/33	1	21	3.2	23.0	31000	0.028	2700	0.84	This work
BST 67/33	2	22	3.2	6.3	33000	0.021	670	0.25	This work
BST 67/33	6	24	3.2	0.70	8800	0.004	280	0.12	This work
BST 65/35	40	29	2.5	0.10	1200	0.0013	380	0.11	Whatmore [39]
PMN:La	90	40	3.0	0.085	1200	0.0008	800	0.10	Whatmore [39]
PScT	53	40	2.7	0.38	2900	0.0027	550	0.17	Shorrocks [47]
PZT 94/6*	0	50	2.6	0.37	300	0.02	5300	0.19	Lian [48]
PZNT 90/8/2*	0	30	2.6	0.185	290	0.019	2800	0.10	Takenaka [49]
PCT 70/30:PCoW 96/4	0	106	3.3	3.0	7400	0.037	1380	0.18	Deb [52]
PLZT 8/60/40 (*sic*)	0	142	3.7	3.2	16200	0.062	600	0.092	Deb [50]
PZN/BT/PT 80/10/10**	0	12	2.7	5.93	4670	0.01	5310	1.08	Deb [51]
PZN/BT/PT 80/10/10	0	85	2.7	2.9	18300	0.018	660	0.20	Deb [51]
Thin films									
PScT sputtered	40	40	2.7	0.52	6000	0.012	360	0.076	Watton [24]
PScT sol-gel	--	40	2.7	0.30	7000	0.002	180	0.10	Shorrocks [20]
PScT MOCVD	20	40	2.7	0.08	1000	0.002	330	0.07	Ainger [53]
KTN metalorganic	30	40	3.7	20.0	1200	0.01	50000	5.0	Schubring [54] "pumped"

* rhombohedral-rhombohedral phase transition
** rhombohedral-tetragonal phase transition

T_c both methods yield the same values, but in the transition region, thermal hysteresis, differences in domain wall motion, or other factors can lead to deviations. Byer-Roundy measurements are performed at constant dT/dt, whereas black body measurements are nearly isothermal. It has been our observation for BST (Table III and Figure 4) that the static F_d decreases with increasing dc bias, but the dynamic responsivity increases (Figure 5). Both measurements tend to saturate at similar levels for sufficiently high bias. It is not clear whether this is true for all materials, although PScT appears to behave similarly [57]. The data presented should therefore be viewed cautiously.

Lead scandium tantalate has been extensively studied both in bulk ceramic form [47] and as thin films made by sol-gel [20], MOCVD [54] and sputtering [24] processes. At bias levels *ca* 40 kV/cm, PScT appears to be an excellent candidate, and µm-thick films have been prepared with F_d approximately 60% of the bulk ceramic value. Strong pyroelectricity associated with the low temperature transitions of PZT [48-49] and PZN [50-52] has also been explored. Behavior of these materials under dc bias or in applications has not yet been reported.

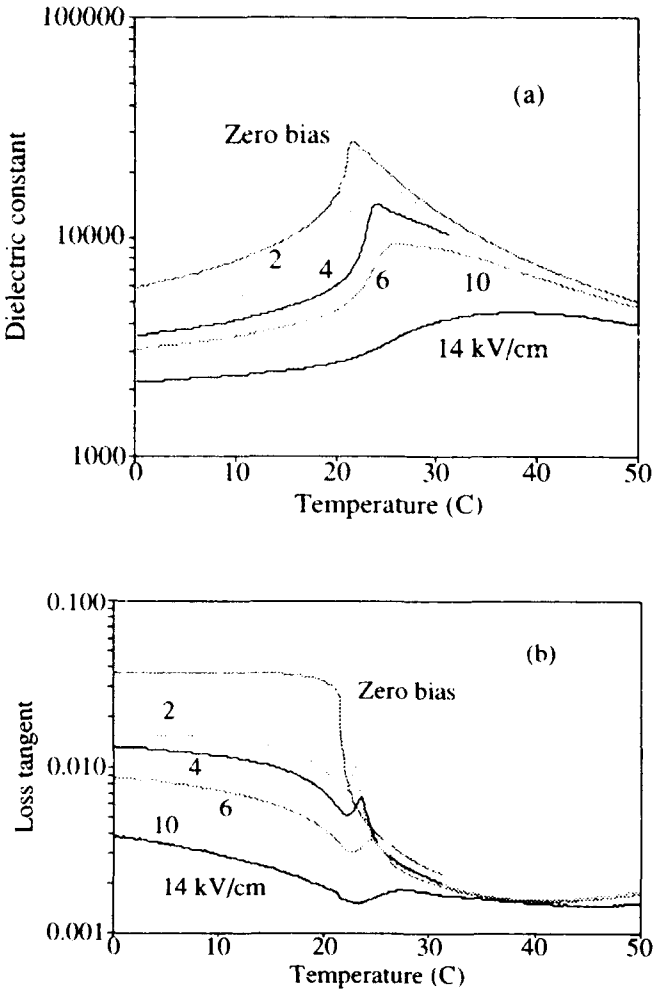


Figure 3. Dielectric constant (a) and loss tangent (b) for BST.

Barium Strontium Titanate

An initial comparison of BST, PMN and PScT [39] demonstrated slightly superior values of F_d for lead scandium tantalate. BST also turns out to have relatively good responsivity under bias, however, and we have devoted significant effort to producing ceramics with acceptable properties for utilization in infrared imaging applications. Some of our results will be discussed here.

Typical dielectric constant and loss tangent, measured at 1 kHz with a 50 mV oscillator level, for 99% dense BST with a Curie point of 21 °C are displayed in Figure 3 as a function of bias field and temperature. The test capacitors were thinned to approximately 250 µm, polished to 1 µm surface finish with alumina powder and contacted with thick film Ag-Pd fired at 750 °C. Good dielectric slope and low loss tangent up to 14 kV/cm suggest that reasonable pyroelectric responsivity might be expected.

Simultaneous Byer-Roundy pyroelectric current/dielectric property measurements yielded the values of F_v and F_d that are presented in Figure 4. In both cases the figures of merit are dominated by the pyroelectric coefficient. They appear high at low bias and decrease (to around 350 cm^2/C for F_v), saturating at 4 kV/cm or so. F_d compares favorably with the values that have been reported for PScT.

The comparable dynamic measurements are displayed in Figure 5. It may be seen that voltage responsivity is initially low, but increases with applied voltage and levels off at approximately the same figure of merit that is measured quasi-statically at high bias. Hybrid detectors and imaging systems built from them have been described by Hanson, *et al* [56]. The balance of this paper is adapted from the latter work.

Array Fabrication and Implementation

The process of manufacturing an uncooled focal plane array (UFPA) begins with a stoichiometric boule of BST doped, compacted and sintered to optimize the microstructure and the electrical properties. Slicing a boule yields UFPA-sized wafers that are ground and polished. After laser reticulation, the wafers are etched to remove the slag, and subsequently annealed in O_2 to restore stoichiometry of the surface. The reticulated pixels are on 48.5 µm centers, and the kerf is approximately 10 µm. Deposition of a parylene backfill, replanarization of the reticulated surface, and application of a common electrode and resonant-cavity IR absorber finishes the processing of the IR-sensitive side of the ferroelectric material. The IR absorber provides better than 90% average absorption over the 7.5 to 13.0 µm spectral region. Mounting the slice to a carrier, optical-side down, facilitates final thinning and polishing. The finished device is about 25 µm thick. Application of contact metal and removal of the parylene backfill completes the pixel array in preparation for hybridization. Meanwhile, fabrication of miniature organic mesas (with over-the-edge metallization) on the readout IC provides the mating part. Mating of the two parts by compression bonding prepares them for packaging and final test. The finished device is an array of 245 × 328 pixels.

The readout IC is a CMOS device fabricated using a process capable of 0.8 µm design rules. The unit cell contains a high-pass filter, a gain stage, a tunable low-pass filter, a buffer, and an address switch. The high-pass filter consists of the capacitance of

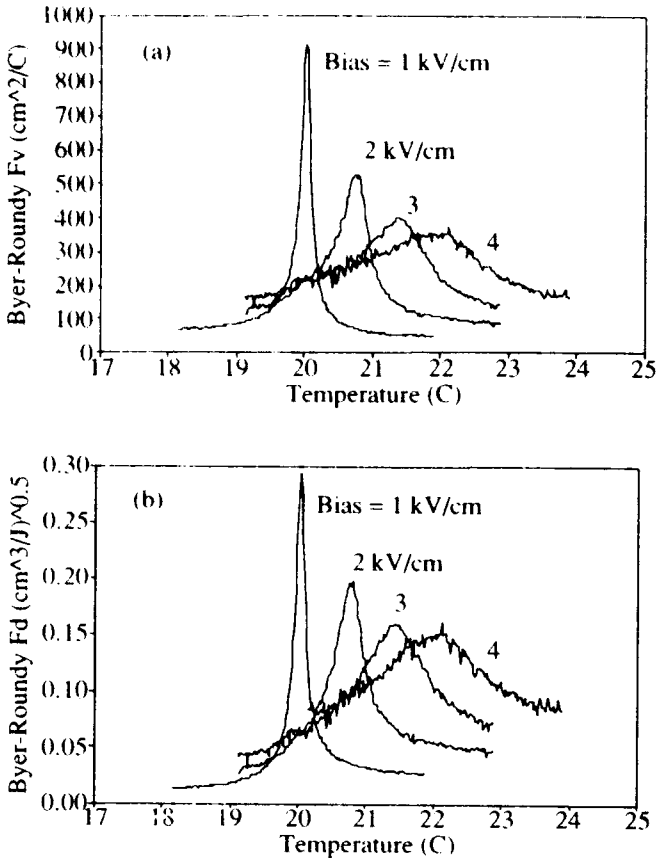


Figure 4. Byer-Roundy Figures of Merit F_v (a) and F_d (b) for BST. The poling voltage is the same as the biasing voltage.

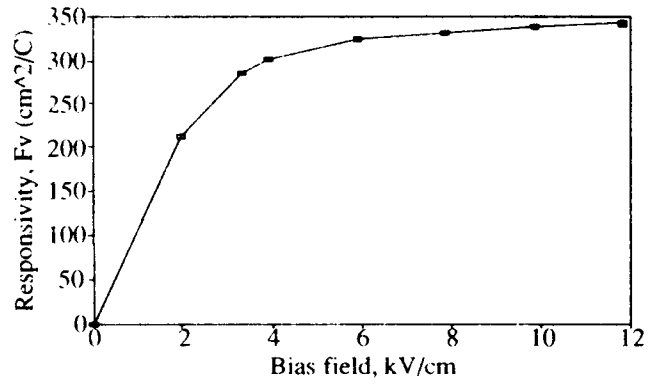


Figure 5. Maximum black body (490 °C) response of a 50 μm thick sample of BST at a chopper frequency of 40 Hz. The poling voltage is the same as the biasing voltage.

the detector itself and a feedback resistor fabricated by deposition of a high sheet resistance material. The feedback resistance is between 10^{11} and 10^{12} Ω which, when attenuated by the Miller effect for an open-loop preamplifier gain of 200, gives a characteristic frequency of about 10 Hz for the high-pass filter. The preamplifier is a simple CMOS inverter. The low-pass filter resistance is actually a diode whose effective impedance is controlled by an in-cell current source. An off-chip voltage determines the current level and hence the resistance, and so the filter is tunable. The high-pass capacitor is actually the gate of an MOS transistor biased to accumulation. The unity-gain output buffer provides the ability to drive the relatively high capacitance load of the column-address lines and column amplifiers.

The array implementation of the unit cells (Figure 6) is standard. A row-address shift register addresses each row sequentially. The addressed row is activated by turning on all the unit-cell switches in that row. This connects the pixel buffer outputs in that row to column-address lines. At the end of the column-address lines are amplifiers, one for each column, having a gain of 1.8. The outputs of the amplifiers feed a multiplexer that provides sequential external access to the outputs. Thus the array output is compatible with standard television formatting. The array mounts onto a single-stage thermoelectric cooler for stabilization near the ferroelectric phase transition. The ceramic DIP array package measures 25 mm × 24 mm × 6 mm thick, and has 40 pins. An anti-reflection coated germanium window covers the packages and allows IR transmission in the 7.5 to 13 μm spectral band.

Any real device implementation includes circuit elements that introduce parasitic capacitance. This results in a responsivity attenuation factor of:

$$A_s = C_d /(C_d + C_p), \tag{19}$$

where C_d is the detector capacitance and C_p is the parasitic capacitance. For this reason it is desirable to select as the pyroelectric material one having a permittivity sufficiently high that the factor A_s does not significantly degrade responsivity. Because the application of an electric field suppresses the permittivity and therefore C_d, the field has the added effect of decreasing A_s as the applied field increases. This effect is especially important when the parasitic capacitance is high, such as for area arrays addressed by only a switch at each pixel site. It is less important if the readout IC contains a preamplifier or buffer at each pixel, thereby reducing line length and parasitic capacitance. If the parasitic capacitance appears mainly as a feedback capacitance in the preamplifier, then the A_s term is less relevant because it multiplies the preamplifier noise as well. A readout IC has been implemented in which this latter condition prevails. In spite of this, the parasitic capacitance places an upper limit on the useful magnitude of the applied field.

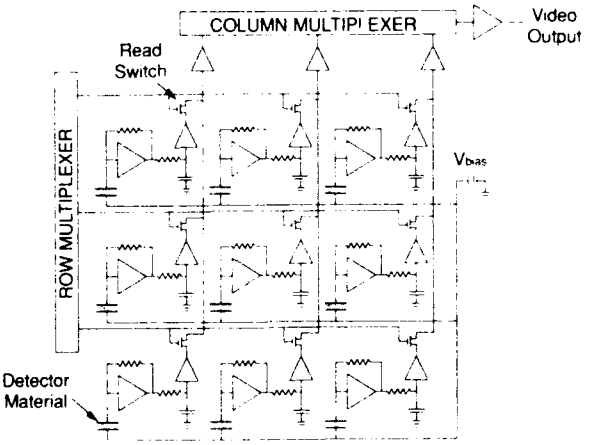


Figure 6. Array implementation of readout IC unit cells [56].

System Operation

Operation of our uncooled sensor is best described in conjunction with the system block diagram in Figure 7. The IR lens, typically $f/1.0$ with a focal length of about 100 mm, forms an IR image on the focal plane array. The chopper periodically interrupts the optical beam. The chopper is an anti-reflection coated germanium wheel (Figure 8) with alternating planar and binary diffractive optic (BDO) regions. The BDO regions diffuse transmitted IR radiation so that the entire array is flooded with approximately the scene-average radiation (actually, local scene average, because the diffuser is not perfectly Lambertian). The planar regions faithfully transmit the image to the array. The shape of the chopper pattern is an Archimedes' spiral designed to best approximate a vertically-traveling chopper. The "open" phase of the chopper occurs for a given pixel when that pixel receives radiation through the planar part of the chopper. the "closed" phase occurs when the image is diffused by the BDO pattern. The chopper rotates at 30 cycles per second, so that the chop rate is 30 Hz for each line.

The action of the chopper modulates the incident radiation between the field-of-view of the pixels and the "scene average." The temperature of each pixel rises and falls accordingly and generates a signal by virtue of its pyroelectric response. The readout IC filters, amplifies, samples and multiplexes the detector signals, one row at a time, and delivers the output at standard RS170 rates. The samples occur immediately prior to opening the chopper in one field and immediately prior to closing the chopper in the next field. The output of each pixel is ac coupled, and so, for a static scene, the fields are identical but of opposite polarity. An off-focal-plane high-pass filter at the multiplexer output removes any distracting artifacts that may result from temperature or bias drift. After a gain stage of between 2× and 4×, a 6-bit analog offset correction removes gross offset non-uniformities.

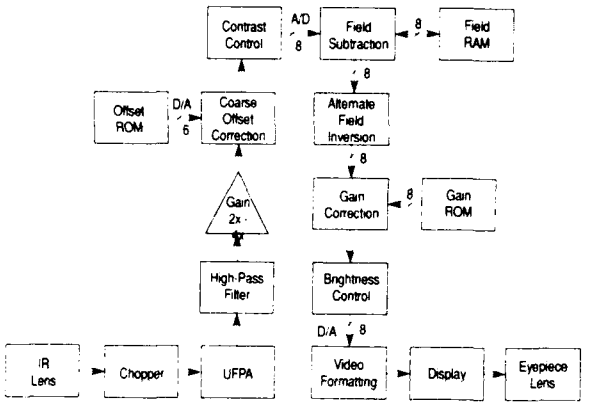


Figure 7. System block diagram [56].

At this point in the processing chain an external contrast setting determines overall gain. As the system converts the video field to 8-bit digital data, the corresponding pixel data stored from the previous field is retrieved, replaced with the present data, and the previous data is subtracted from the present data. Thus, the net output is the difference between samples taken with the chopper open and with the chopper closed. On alternate fields the system changes the sign of the result to maintain consistent polarity from field to field. This field-differencing operation is equivalent to that of a correlated double sampler (CDS), and it adds a filter to the signal and noise data path. The filter transfer function is:

$$H_{CDS}(f) = 2 \sin(\pi f / 2f_c) \qquad (20)$$

where f is the signal frequency and f_c is the chopping frequency. This has the added effect of totally removing offset non-uniformities. Prior to analog conversion and RS170 formatting, a gain word multiplies the value of each pixel to compensate for gain non-uniformities, and a digital adder sets overall brightness. The resulting image is uniform to within about 1.5%. The data is then ready for display and viewing on either an internal or external monitor. An example of an infrared image is shown in Figure 9.

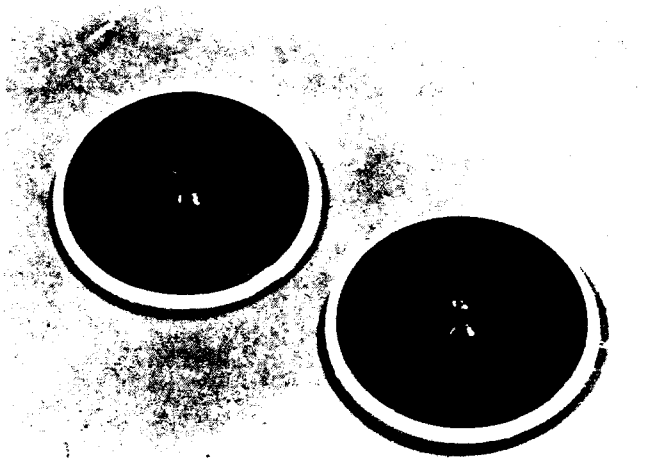


Figure 8. Germanium chopper, showing refractive design (left) and equivalent diffractive (BDO) design [56]

System Performance

These systems have significantly advanced the state of the art in sensitivity and resolution of small, lightweight, uncooled thermal imaging systems. An array-average noise-equivalent temperature difference (NETD) of 0.070 °C with $f/1.0$ optics has been demonstrated. This number improves by about 10% when corrected for vignetting of the test optics. Typical devices have an NETD of about 0.08 °C. Design and fabrication improvements now underway should improve the NETD to about 0.05 °C.

Three independent noise sources combine to limit the present sensitivity. These are temperature fluctuation noise, dielectric loss noise, and preamplifier noise, in order of descending magnitude (although there is not much difference among them). Other noise sources are negligible. All three noise sources are filtered by the preamplifier and the subsequent field-differencing (or CDS) operation. The CDS filter is especially important because it strongly attenuates the low-frequency components of dielectric-loss noise and preamplifier noise, both of which are 1/f in nature. Because the output is the difference between signals from two fields, any noise components that are coherent over the field time interval (*e.g.*, low-frequency noise) are suppressed.

The bandwidth of temperature-fluctuation noise is naturally limited by the detector thermal time constant, but the electric filters provide further attenuation. The effect of the characteristic frequencies of these filters on the signal is minimal. In fact, the CDS filter, as evident from equation 20, doubles the signal while increasing white noise by a factor of only $\sqrt{2}$ and decreasing 1/f noise. Thus it improves the signal to noise ratio by more than a factor of $\sqrt{2}$.



Figure 9. Infrared image obtained using a detector with NETD = 0.2 °K and $f/1.0$ optics.

The modulation transfer function (MTF) for these UFPAs is adequate, but design modifications will provide substantial improvement. Presently, the system MTF at f_0 is about 25%, including all factors. This is limited both by the 63.7% integrated-aperture limit of the pixel itself and by thermal crosstalk via the IR absorber. Simple experiments with the optical coating have shown improvement to 40%. Further planned improvements should increase the overall result to about 60%.

Summary

Recent developments in pyroelectric materials have been reviewed. Transition materials such as BST offer significant advantages, compared with conventional pyroelectrics. Hybrid devices utilizing ferroelectric detector staring arrays are poised for commercial deployment. Research to develop thin film devices with a significant reduction in thermal mass (*i.e.* response time) is proceeding. Monolithic structures also possess a potential advantage in terms of reduced manufacturing cost, since the difficult hybridization operation would not be required. Thin film devices with adequate performance for television quality imaging have not yet been demonstrated.

Uncooled sensors, once relegated to specialty applications, are now prepared to enter the mainstream of thermal imaging applications. Improvements in sensitivity and resolution as well as in weight, size and power have resulted in a technology that opens new applications for thermal imaging and offers the opportunity to address old applications with a new-found flexibility. Near-term improvements in UFPA technology will expand its applicability in the marketplace.

Acknowledgements

The authors wish to thank the many excellent people who have labored long to make this effort successful, particularly Mac Corbin, Dana Dudley, Sam McKenney and Robert Owen. Our appreciation is also accorded to the Balanced Technology Initiative office, the Defense Advanced Research Projects Agency (DARPA), and the U.S. Army Night Vision and Electro-Optics Directorate for their continued support in sponsoring a significant portion of the work.

References

[1] L. A. Berardinis, "Night Vision," *Mach. Des.*, October 24, 1991, pp. 57-61; J. M. Callahan, "Sight at Night," *Automotive Ind.*, October, 1991, pp. 30 ff; J. Haystead, "Thermal Imaging," *Defense Electr.*, April, 1991, pp. 48-52.

[2] S. Borrello, "Focal Planes for Infrared Imaging," *Texas Inst. Tech. J.*, vol. 8, pp. 20-27, 1991.

[3] R. J. Keyes, "Recent Advances in Optical and Infrared Detector Technology," in Topics in Applied Physics, vol. 19: Optical and Infrared Detectors, R. J. Keyes, ed., Springer-Verlag, New York, 1980, pp. 301-319.

[4] D. Long, "Photovoltaic and Photoconductive Infrared Detectors," in Topics in Applied Physics, vol. 19: Optical and Infrared Detectors, R. J. Keyes, editor, Springer-Verlag, New York, 1980, pp. 101-147.

[5] C. T. Elliott, "Future Infrared Detector Technologies," IEE Conf. Publ. 321 (Int. Conf. Adv. IR Detect. Syst., 4th), pp. 61-68, 1990.

[6] CH. Lucas, "Infrared Detection, Some Recent Developments and Future Trends," *Sens. Actuators*, vol. A25-A27, pp. 147-154, 1991.

[7] B.-Y. Tsaur, C. K. Chen and B. A. Nechay, "IrSi Schottky-Barrier Infrared Detectors with Wavelength Response Beyond 12 μm," *IEEE Electron Dev. Lett.*, vol. 11, pp. 415-417, 1990.

[8] W. F. Kosonocky, "Review of Infrared Image Sensors with Shottky-barrier Detectors," *Optoelectron.-Devices Technol.*, vol. 6, pp. 173-203, 1991.

[9] P. Norton and W. Radford, "Responsivity uniformity of infrared detector arrays," *Semicond. Sci. Technol.*, vol. 6, pp. C96-C98, 1991.

[10] A. Zussman, B. F. Levine, J. M. Kuo and J. de Jong, "Extended long-wavelength 11-15 μm GaAs/$Al_xGa_{1-x}As$ quantum-well infrared photodetectors," *J. Appl. Phys.*, vol. 70, pp. 5101-5107, 1991.

[11] C. T. Elliott, "Recent Developments in Infrared Detectors in the United Kingdom," *Nippon Sekigaisen Gakkaishi (J. Jpn. Soc. Infrared Sci. Tech.)*, vol. 1, pp. 2-22, 1991.

[12] R. Lane and K. R. Brown, "The Piezoelectric, Pyroelectric and Dielectric Properties of Thin Ceramic Elements," *Trans. Brit. Ceram. Soc.*, vol. 73, pp. 65-71, 1974; D. Luff, R. Lane, K. R. Brown and H. J. Marshallsay, "Ferroelectric Ceramics with High Pyroelectric Properties," *ibid.*, pp. 251-264.

[13] S. T. Liu, "Critical Assessment of Pyroelectric Detectors," *Ferroelectrics*, vol. 10, pp. 83-89, 1976.

[14] M. E. Lines and A. M. Glass, Principles and Applications of Ferroelectrics and Related Materials, Clarendon Press, Oxford, 1977 pp. 561-578.

[15] E. H. Putley, "Thermal Detectors," in Topics in Applied Physics, vol. 19: Optical and Infrared Detectors, R. J. Keyes, editor, Springer-Verlag, New York, 1980, pp. 71-100.

[16] J. M. Herbert, Ferroelectric Transducers and Sensors, Gordon and Breach Science Publishers Inc., 1982, pp. 266-290.

[17] R. Watton, C. Smith and G. R. Jones, "Pyroelectric Materials: Operation and Performance in the Pyroelectric Camera Tube," *Ferroelectrics*, vol. 14, pp. 719-721, 1976; R. Watton, "Ferroelectrics for Infrared Detection and Imaging," *Proc. 6th Int. Symp. Appl. Ferroelectrics*, IEEE, pp. 172-181, 1986.

[18] R. W. Whatmore, "Pyroelectric devices and materials," *Rep. Prog. Phys.*, vol. 49, pp. 1335-1386, 1986.

[19] R. Watton, "Ferroelectric Materials and Devices in Infrared Detection and Imaging," *Ferroelectrics*, vol. 91, pp. 87-108, 1989; R. Watton and M.A. Todd, "Ferroelectric Ceramics for Infrared Detection," *Brit. Ceram. Proc.*, vol. 41, pp. 205-217, 1989.

[20] N. M. Shorrocks, S. G. Porter, R. W. Whatmore, A. D. Parsons, J. N. Gooding and D. J. Pedder, "Uncooled infrared thermal detector arrays," *Proc. SPIE - Int. Soc. Opt. Eng.*, vol. 1320 Infrared Technology and Applications, pp. 88-94, 1990.

[21] R. W. Whatmore, A. Patel, N. M. Shorrocks, and F. W. Ainger, "Ferroelectric Materials for Thermal IR Sensors, State of the Art and Perspectives," *Ferroelectrics*, vol. 104, pp. 269-283, 1990.

[22] A. Mansingh and A. K. Arora, "Pyroelectric films for infrared applications," *Indian J. Pure Appl. Phys.*, vol. 29, pp. 657-664, 1991.

[23] P. C. Osbond and R. W. Whatmore, "Improvements to Pyroelectric Ceramics via Strontium Doping of the Lead Zirconate-Lead Iron Niobate-Lead Titanate System," *Ferroelectrics*, vol. 118, pp. 93-101, 1991.

[24] R. Watton and M.A. Todd, "Induced Pyroelectricity in Sputtered Lead Scandium Tantalate Films and their Merit for IR Detector Arrays," *Ferroelectrics*, vol. 118, pp. 279-295, 1991.

[25] R. W. Whatmore, "Pyroelectric Ceramics and Devices," in Electron. Ceram., edited by B. C. H. Steele, Elsevier, London, 1991, pp. 169-184; R.W. Whatmore, "Pyroelectric Ceramics and Devices for Thermal Infrared Detection and Imaging," *Ferroelectrics*, vol. 118, pp. 241-259, 1991.

[26] N. M. Shorrocks and I. M. Edwards, "Design and Performance of Thermal Imaging Arrays," *Proc. 7th Int. Symp. Appl. Ferroelectrics*, IEEE, pp. 58-62, 1990.

[27] M. Okuyama and Y. Hamakawa, "$PbTiO_3$ Ferroelectric Thin Films and Their Pyroelectric Application," *Ferroelectrics*, vol. 118, pp. 261-278, 1991.

[28] C. Ye, T. Tamagawa and D. L. Polla, "Experimental studies on primary and secondary pyroelectric effects in $Pb_{1-x}Zr_xTiO_3$, $PbTiO_3$ and ZnO thin films," *J. Appl. Phys.*, vol. 70, pp. 5538-5543, 1991; D. L. Polla, C. Ye and T. Tamagawa, "Surfaced micromachined $PbTiO_3$ pyroelectric detectors," *Appl. Phys. Lett.*, vol. 59, pp. 3539-3541, 1991.

[29] N. Muto, M. Miyayama, H. Yanagida, T. Kajiwara, N. Mori, H. Ichikawa and H. Harada, "Infrared detection by semiconducting fibre," *J. Mater. Sci. Lett.*, vol. 9, pp. 1269-1271, 1990; N. Muto, M. Miyayama, H. Yanagida, N. Mori, T. Kajiwara, Y. Imai, A. Urano and H. Ichikawa, "*IR Detection by Semiconducting Carbon Fiber*," *Sens. and Mater.*, vol. 2, pp. 313-320, 1991.

[30] P. Umadevi, C. L. Nagendra, G. K. M. Thutupalli, K. Mahadevan and G. Yadgiri, "A new thermistor material for thermistor bolometer: material preparation and characterization," *Proc. SPIE - Int. Soc. Opt. Eng.*, vol. 1484 Growth Charact. Mater. Infrared Detect. Nonlinear Opt. Switches, pp. 125-135, 1991.

[31] M. Inaba, M. Miyayama and H. Yanagida, "Infrared sensing properties of positive temperature coefficient thermistors with large temperature coefficients of resistivity," *J. Mater. Sci.*, vol. 27, pp. 127-132, 1992.

[32] V. Bitter, A. Rothwarf and K. Scoles, "High T_c superconductor infrared detectors," *Proc. SPIE - Int. Soc. Opt. Eng.*, vol. 1106 Future Infrared Detector Materials, pp. 142-150, 1989.

[33] S. Verghese, P. L. Richards, K. Char, D. K. Fork, and T. H. Geballe, "Feasibility of infrared imaging arrays using high-T_c superconducting bolometers," *J. Appl. Phys.*, vol. 71, pp. 2491-2498, 1992.

[34] S. T. Liu, in Landolt Bornstein, vol. 11, K-H. Hellwege, ed. in chief, Springer Verlag, New York, 1979, p. 471.

[35] R. L. Byer and C. B. Roundy, "Pyroelectric Coefficient Direct Measurement Technique and Application to a NSEC Response Time Detector," *Ferroelectrics*, vol. 3, pp. 333-338, 1972.

[36] J. P. Dougherty and R. J. Seymour, "Automated simultaneous measurement of electrical properties of pyroelectric materials," *Rev. Sci. Instrum.*, vol. 51, pp. 229-233, 1980.

[37] J. Cooper, "Minimum Detectable Power of a Pyroelectric Thermal Receiver," *Rev. Sci. Instrum.*, vol. 33, pp. 92-95, 1962.

[38] A. S. Bhalla, C. S. Fang and L. E. Cross, "Pyroelectric Properties of Alanine and Deuterium Substituted TGSP and TGSAs Single Crystals," *Mater. Lett.*, vol. 3, pp. 475-477, 1985.

[39] R. W. Whatmore, P. C. Osbond and N. M. Shorrocks, "Ferroelectric Materials for Thermal IR Detectors," *Ferroelectrics*, vol. 76, pp. 351-367, 1987.

[40] S. G. Porter, D. Appleby and E. W. Ainger, "Pyroelectric Ceramics for Thermal Imaging," *Ferroelectrics*, vol. 11, pp. 351-354, 1976.

[41] S. T. Liu, J. D. Heaps and O. N. Tufte, "The Pyroelectric Properties of the Lanthanum-doped Ferroelectric PLZT Ceramics," *Ferroelectrics*, vol. 3, pp. 281-285, 1972.

[42] K. K. Deb, "Investigation of Pyroelectric Characteristics of Modified $PbTiO_3$ Ceramics for Improved IR Detector Performance," *Ferroelectrics*, vol. 88, pp. 167-176, 1988.

[43] A. Kanduser, M. Kosec, A. Levstik and B. B. Lavrencic, "$Pb_5Ge_3O_{11}$ Ceramic Pyroelectric Detector," *Proc. 7th Int. Symp. Appl. Ferroelectrics*, IEEE, pp. 383-386, 1990.

[44] R. Takayama, Y. Tomita, K. Iijima and I. Ueda, "Pyroelectric Properties and Application to Infrared Sensors of $PbTiO_3$, $PbLaTiO_3$ and $PbZrO_3$ Ferroelectric Thin Films," *Ferroelectrics*, vol. 118, pp. 325-342, 1991.

[45] E. Yamaka, H. Watanabe, H. Kimura, H. Kanaya and H. Ohkuma, "Structural, ferroelectric and pyroelectric properties of highly c-oriented $Pb_{1-x}Ca_xTiO_3$ thin film grown by radio-frequency magnetron sputtering," *J. Vac. Sci. Technol.*, vol. A6, pp. 2921-2928, 1988.

[46] O. M. Stafsudd and M. Y. Pines, "Characteristics of KTS Pyroelectric Detectors," *J. Opt. Soc. Am.*, vol. 62, pp. 1153-1155, 1972.

[47] N. M. Shorrocks, R. W. Whatmore and P. C. Osbond, "Lead Scandium Tantalate for Thermal Detector Applications," *Ferroelectrics*, vol. 106, pp. 387-392, 1990; N. M. Shorrocks and R. W. Whatmore, "Ferroelectric Materials," Brit. UK Pat. Appl. GB 2,240,335, July 31, 1991.

[48] J. Lian, N. Okumura, M. Adachi, T. Shiosaki and A. Kawabata, "Mixed Sintering of $PbZrO_3$ Rich PZT Based Ceramics and their Pyroelectric Properties," *Proc. 7th Int. Symp. Appl. Ferroelectrics*, IEEE, pp. 383-386, 1990.

[49] T. Takenaka, H. Komiya and K. Sakata, "$PbZrO_3$ based Composite Pyroelectric Ceramics," *Proc. 7th Int. Symp. Appl. Ferroelectrics*, IEEE, pp. 370-373, 1990.

[50] K. K. Deb, "Pyroelectric characteristics of a hot-pressed lanthanum-doped PZT (PLZT (8/40/60))," *Mater. Lett.*, vol. 5, p. 222-226, 1987; K. K. Deb, M. D. Hill, R. S. Roth and J. F. Kelly, "Dielectric and Pyroelectric Properties of Doped Lead Zinc Niobate (PZN) Ceramic Materials," *Ceram. Bull.*, vol. 71, pp. 349-354, 1992.

[51] K. K. Deb, "Investigation of Pyroelectric Characteristics of 0.8 $Pb(Zn_{1/3}Nb_{2/3})O_3$ - 0.1 $PbTiO_3$ - 0.1 $BaTiO_3$ Ceramics with Special Reference to Uncooled Infrared Detection," *J. Electron. Mat.*, vol. 20, pp. 653-658, 1991.

[52] K. K. Deb, "Pyroelectric Materials," U.S. 4,983,839, January 8, 1991.

[53] F. W. Ainger, C. J. Brierley, M. D. Hudson, C. Trundle and R. W. Whatmore, "Ferroelectric Thin Films by Metal Organic Chemical Vapour Deposition," *Mat. Res. Soc. Symp. Proc.*, vol. 200, pp. 37-47, 1990.

[54] N. W. Schubring, J. V. Mantese, A. L. Micheli, A. B. Catalan and R. J. Lopez, "Charge Pumping and Pseudopyroelectric Effect in Active Ferroelectric Relaxor-Type Films," *Phys. Rev. Lett.*, vol. 68, pp. 1778-1781, 1992.

[55] A. G. Chynoweth, "Dynamic Method for Measuring the Pyroelectric Effect with Special Reference to Barium Titanate," *J. Appl. Phys.*, vol. 27, pp. 78-84, 1956.

[56] C. Hanson, H. Beratan, R. Owen, M. Corbin and S. McKenney, "Uncooled thermal imaging at Texas Instruments," *Proc. SPIE - Int. Soc. Opt. Eng.*, 1992 (in press).

[57] C. Zhili, Y. Xi and L. E. Cross, "Depolarization Behavior and Reversible Pyroelectricity in Lead Scandium Tantalate Ceramics under DC Biases," *Ferroelectrics*, vol. 49, pp. 213-217, 1983.

Pyroelectric, Electrooptics

PYROELECTRIC AND ELECTRO-OPTIC PROPERTIES OF SOL-GEL AND DUAL ION BEAM SPUTTERED PLZT THIN FILMS

D.A. Tossell, J.S. Obhi, N.M. Shorrocks, A. Patel and R.W. Whatmore
GEC-Marconi Materials Technology Ltd
Caswell, Towcester
Northants, NN12 8EQ, UK

Abstract

Thin films of several compositions within the PLZT system have been deposited onto sapphire, MgO, silicon and fused silica substrates using sol-gel and dual ion beam sputtering (DIBS). Using a standard solution preparation route films of composition PLZT (0/50/50) and PLZT (0/30/70) were spin coated onto electroded substrates and fired at temperatures up to 700°C. In addition, a modified solution gave good quality perovskite films at 450°C after only 2 minutes firing time. Pyroelectric coefficients of 100 and 400 $\mu Cm^{-2}K^{-1}$ and figures of merit 1.5-2.2 x $10^{-5}Pa^{-0.5}$ were obtained for the (0/30/70) and (0/50/50) compositions respectively. The DIBS process produced good quality oriented perovskite films for substrate temperatures in the range 550-700°C. The stoichiometry was controlled by sputtering from an adjustable composite metal/ceramic target and by bombarding the growing film with a low energy oxygen ion beam. Transparent films of the cubic paraelectric composition PLZT (28/0/100) were found to have a high reflected-mode quadratic electro-optic coefficient of 2.1 x $10^{-16}m^2/V^2$, although no response could be detected in a transmission mode. Films of the tetragonal ferroelectric compositions PLZT (0/0/100) and (7/0/100) were deposited onto electroded substrates and gave pyroelectric coefficients in the range 50-400 $\mu Cm^{-2}K^{-1}$ and a figure-of-merit of order 2.6 x $10^{-5}Pa^{-0.5}$. The PLZT (28/0/100) films suffered from an intrinsic space charging effect that limited responsivity whereas the ferroelectric compositions suffered only from extrinsic problems such as electrode blistering and pinholing. The results reported here are encouraging with respect to the goal of fully integrated uncooled IR detector elements on silicon readout circuitry.

Introduction

Ferroelectric materials such as lead titanate, lead zirconate titanate (PZT) and lead scandium tantalate (PST) are useful for a wide range of electronic device applications. In particular the quarternary solid solution of PLZT (x, y, z)

$$Pb_{1-3/2x}La_x(Zr_yTi_z)O_3 \qquad (1)$$

is a well known ferroelectric material that exhibits piezoelectric, pyroelectric, linear and quadratic electro-optic properties depending on the composition [1]. The direct integration of these materials in thin film form onto semiconducting substrates would yield significant advantages in terms of increased speed, reduced voltages and enhanced response. Further, circumventing the laborious procedures of bulk ceramic processing and the cutting, polishing and assembly of delicate ceramic wafers into hybrid electronic devices would be a cost effective step. However, the high temperature necessary for the formation of the ferroelectric perovskite phase, coupled with the complex stoichiometry has made this a difficult goal to achieve. At present, a wide variety of thin film synthesis techniques, including MOCVD, sol-gel, RF magnetron and ion beam sputtering, and laser ablation are subject to intensive research [2]. This activity is largely due to the interest in non-volatile radiation hard memories, although there are other important applications for these films in piezoelectric, pyroelectric and electro-optic devices.

At Caswell, there is an established and ongoing effort directed at the commercial development of piezoelectric, electro-optic and pyroelectric [3] devices based on bulk ferroelectric ceramic and composite components. In the area of thin films, sol-gel [4] and dual ion beam sputtering (DIBS) are under active development. In this paper, films of composition PLZT (0/50/50) and (0/30/70) have been deposited by sol-gel, and films of (0/0/100) (ie, pure lead titanate), (7/0/100) and (28/0/100) by DIBS. The primary application of the first two Pb-Zr-Ti-O based compositions is for ferroelectric memories, but good pyroelectric properties have also been reported [5]. Of the Pb-La-Ti-O based materials, (0/0/100) and (7/0/100) have been reported as having favourable properties in thin film form for pyroelectric detection [6] and (28/0/100) similarly for applications requiring a quadratic electro-optic response [7]. The absence of lanthanum or zirconate from these compositions eases the problems associated with stoichiometric control of the films particularly for the complex DIBS process. In addition, the prime ferroelectric memory application of the Pb-Zr-Ti-O films does not benefit greatly from lanthanum doping.

The sol-gel process is a metal organic processing route that can be adapted to give thin films, bulk monoliths or powders by direct precipitation. Simplicity, stoichiometric control and low cost are the primarily advantages of the technique. Due to the wide range of available metallorganic starting materials, it is relatively easy to vary compositions and to obtain complex oxide materials. In a previous paper [4], the application of sol-gel to the fabrication of films of lead scandium tantalate (PST) and lead titanate has been described. This paper details the adaption of the method to films in the Pb-Zr-Ti-O system.

Ion and multiple ion beam deposition techniques have been demonstrated to produce dense films with enhanced optical and mechanical properties [8]. The primary advantage over competing PVD processes lies in the independent control that can be exercised over the energy and flux of the ions used for both sputtering of the target and bombarding of the depositing film. In conventional RF sputtering, and indeed the more complex transient laser ablation methods, little direct control can be exercised over the wide distribution of particle energies in the plasma, which militates against controlled bombardment of the growing film. Controlled bombardment has been shown [9] to increase adatom mobility providing extra energy to supplement thermal energy and reduce the crystallisation temperature. The isolation of the plasma in the ion gun body not only removes a source of uncontrolled bombardment but also allows a lower process pressure since the guns act as gas baffles. These characteristics result in a high degree of process control and flexibility and a number of research groups are now applying ion beam techniques to ferroelectric thin film fabrication [9-11].

Experimental Procedure

DIBS Deposition System

The Nordiko 3450 dual ion beam sputtering (DIBS) system is composed of a cryo and turbomolecular pumped chamber, base pressure 5 x 10^{-8}torr, a target turret, an 800°C rotating heater platen and two 100mm diameter ion guns, Figure 1. The ion gun plasmas are driven by RF (13.56MHz) and represent a significant

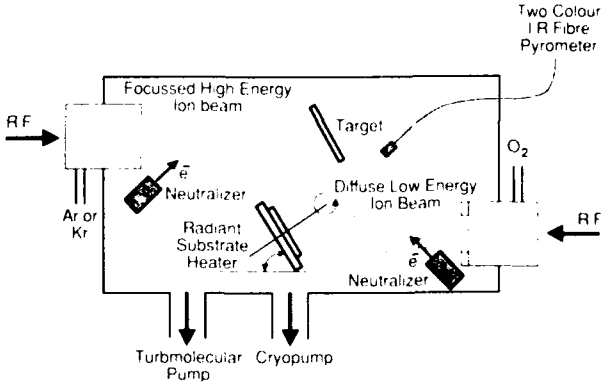


Figure 1 Schematic diagram of Dual Ion Beam Sputtering System.

CH3080-0-7803-0465-9/92$3.00 ©IEEE

step forward from the more common thermal plasma driven Kaufman-type sources. The RF driven guns obviate the need for a hot filament and have been found to run continuously for many hundreds of hours in pure oxygen without attention. In addition, the elimination of the thermal plasma has resulted in much cooler operating conditions within the system as the RF plasmas typically only require 100W input power to sustain the discharge. The chamber is also fitted with two filamentless electron sources for beam neutralisation and two faraday cups for the measurement of beam current density. A two colour IR fibre pyrometer allows accurate measurement of the substrate surface temperature.

Generally, a high energy argon or krypton ion beam in the range 600-700eV, 80-100mA and beam current density (BCD) 1-5mA/cm^2 was used to sputter material from a target while the substrate was immersed in a pure oxygen ion beam of 0-100eV, 0-40mA and BCD 0-0.2mA/cm^2. More energetic ion beams were used to clean the target and substrate prior to film growth. A neutralization level of 110% of the ion beam current ensured stability during the deposition of electrically insulating films. Deposition pressure was typically 10^{-4}torr.

PLZT Film Deposition

DIBS: For PLZT deposition, two adjustable composite target types have been developed as depicted in Figure 2. In the first, pieces of titanium metal and PLZT ceramic were bolted to a copper backing plate through a lead sheet using high purity titanium bolts. Two problems were encountered with this design in that the metallic lead was found to age rapidly making consistent stoichiometric control difficult, Figure 3, and that high energy neutrals reflected from the target impinged damagingly on the depositing film. To overcome this, the second target type, Figure 2(b), composed of lead oxide secured on a titanium plate, was developed and the sputtering gas switched from argon to krypton. The energy of krypton neutrals reflected from the target is reduced since the atomic weights are more closely matched and the absence of metallic lead eliminated target ageing anomalies.

Double polished fused silica and (1102) sapphire were used as substrates for the electro-optic PLZT composition. Single polished (100) silicon, (1102) sapphire and (100) MgO with an e-beam deposited titanium/platinum electrode structure of thicknesses 150Å/2000Å were used for the pyroelectric films. All substrates were cleaned in organic solvents, deionized water and dry nitrogen prior to use. It was found that uniform heating of the substrate was much more difficult for double polished substrates than for single polished. The reasons for this have not been fully determined but it seems likely that the good IR transmission of the double polished substrates, or the difficulty of making good thermal contact onto the heater platen, were to blame. Also, the IR pyrometer revealed a temperature differential of order 100°C between the substrate and the platen, indicating poor thermal contact. To counter this substrates were sealed to the platen by thermally evaporated or sputtered indium and lead films. Ultimately it was found that the films became contaminated by an alien element used for sealing, possibly

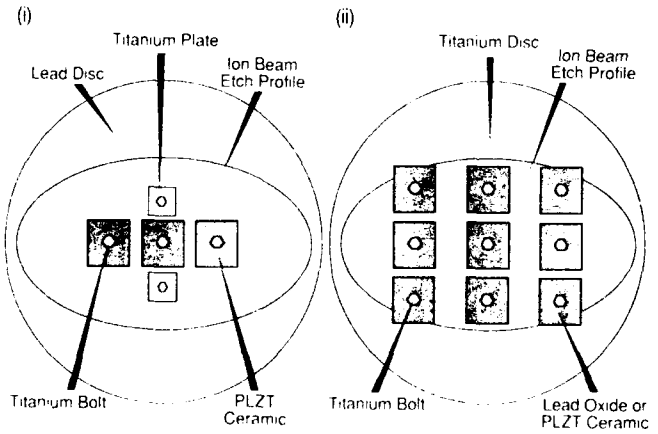


Figure 2 Typical target configurations for (i) metallic lead based target and (ii) lead oxide based target.

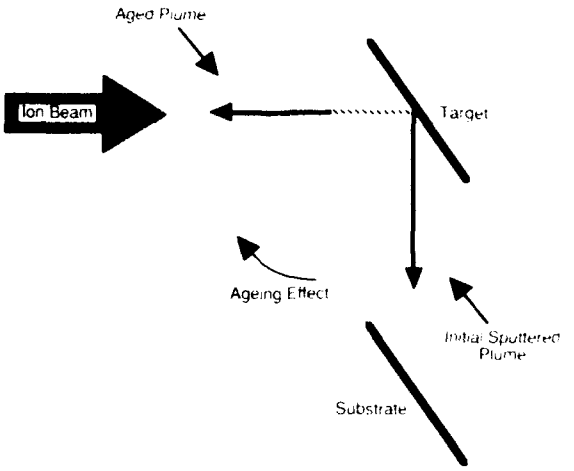
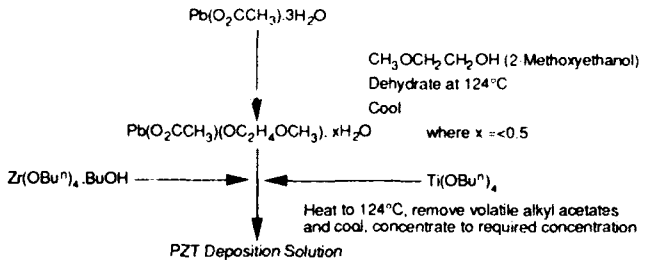


Figure 3 Schematic of target ageing effect.

due to the combination of high temperatures and sputtering by the secondary ion bombardment, so lead constituted an ideal choice. Careful cleaning of the heater platen ensured that the lead film wetted the platen surface at high temperatures. Removal of the lead after deposition was achieved by masking the PLZT film and immersing in a mild HCl/HF acid solution.

Some films were subsequently annealed under varying conditions to induce or improve the perovskite phase.

Sol-Gel: There are a wide variety of metal compounds available for incorporation into the initial stock solution. Of these, the most popular are the metal alkoxides (M-OR), where R = alkyl group. In this study, titanium n-butoxide ($Ti(OBu^n)_4$) and zirconium n-butoxide butanol complex were chosen along with lead (II) acetate ($Pb(O_2CCH_3)_2.3H_20$. Before reaction, all the precursors were tested using a thermogravimetric analyser to determine the oxide yield. A typical solution was then prepared according to the scheme:



Using this basic route, solution compositions of PLZT (0/50/50) and (0/30/70) were prepared. Some solutions were further modified by adding acetylacetone in 2-methoxyethanol; this influenced the solution drying characteristics. Films were deposited by spin coating at 2000rpm for 30 seconds onto sapphire substrates coated with a titanium (100Å)/platinum (1500Å) electrode. After one or two layers the film was baked for two minutes on a hot plate in the range 170-400°C prior to the deposition of further layers. Ultimately, the entire assembly was fired at 450°C on a hotplate for two minutes or at 700°C in a tube furnace for 1-2 hours.

Results

General Structure and Composition of DIBS Films

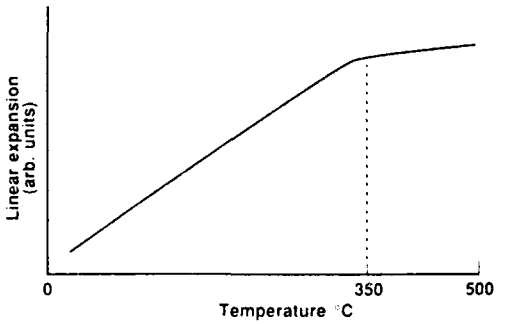
Generally, most PVD deposition processes produce amorphous PLZT films up to 450°C, the pyrochlore phase between 450-500°C, the perovskite phase for the range 500-600°C and the lead deficient films above 650°C; in the 500-550°C regime, there exists a transitional mixed pyrochlore/perovskite structure. In the present study, use of the system in a single ion beam sputter (IBS)

mode with merely molecular oxygen flowing through the secondary ion gun could not produce any perovskite material. Up to 500°C the films remained amorphous and beyond this temperature rapidly became lead deficient. By generating an oxygen plasma in the secondary ion gun whilst keeping all other system parameters identical resulted in complete retention of lead in the films, even in excess of 700°C; under IBS conditions this latter temperature resulted in a purely TiO_2 (rutile structure) film. It is intriguing that the generation of an oxygen plasma seemed to be the critical factor in this effect; drawing an ion beam from the gun so as to bombard the growing film had little further effect on the film for energies up to 100eV. The generation of the ion beam did result in films with a slightly higher refractive index, indicating a higher density, but in all other respects they were identical to those grown with only an oxygen plasma present. Energies in excess of 100eV were detrimental to the film growth rate and gave no discernable advantage in terms of properties. It is apparent that the presence of active oxygen was the key element in enhancing the sticking coefficient of Pb and also, perhaps, that the oxygen plasma to substrate separation was considerably less than the mean free path at the deposition pressure. This implies active species such as O_2^+, O^+ and O reach the substrate unimpeded. Probing of the region between the plasma and the substrate with the faraday cup did not indicate any spontaneous beam generation although this does not rule out a self-neutralising beam. Given these observations a bombarding oxygen ion beam of 100eV and BCD of $0.13mA/cm^2$ was used as standard since this gave the highest refractive index for PLZT (28/0/100) films without limiting the growth rate. In the DIBS mode, the PLZT films were found to be amorphous up to 500°C, above which perovskite peaks began to appear in the X-ray diffraction (XRD) spectra, and were single phase perovskite at or above 600°C. Against expectation, it has not been found that concurrent oxygen ion bombardment lowers the perovskite crystallisation temperature, indeed there is evidence to suggest it is raised by a small increment. However, bombardment does create an extended temperature window within which the perovskite phase dominates, as well as giving denser films.

In addition to the substrate temperature and oxygen ion bombardment, the third dominant parameter controlling the lead content of the films was the target configuration. Even with concurrent oxygen ion bombardment, the volatility of Pb and PbO at elevated temperatures in a vacuum environment is still high. For example, to form stoichiometric lead titanate ($PbTiO_3$) at 600°C required a metallic Pb/Ti target that gave a 9:1 Pb:Ti incident atomic flux on the substrate (as measured cold) was required.

For lanthanum-doped films it was found that an increase in the dopant level occurred between the target and the film. A metallic lead/PLZT (28/0/100) target gave PLZT (35-40/0/100) films. Extra titanium on the target or a lesser La doped target ceramic were used to correct this problem.

Uniformity of film thickness and composition of 2% over 50mm has been achieved for both types of film. The limiting factor was uniformity of heating; films deposited onto cold substrates were uniform to 2% beyond 75mm. In all cases, use of the PLZT/PbO/Ti based target, Figure 2(ii), gave greater uniformity and repeatability from run to run. Growth rates varied from 0.076 to 0.35μm/hour for in-situ grown perovskite films. The use of fully metallic Pb/Ti targets and argon gave the slowest rate, whereas ceramic PLZT/PbO/Ti targets and krypton gave the fastest. This was surprising in view of the known relative sputtering rates of of these elements in their metallic and oxide ceramic states. Amorphous films could be grown at rates in excess of 0.5μm/hour, but this needed to be offset against the required annealing time and final film quality.



Temperature Range C	α x10^{-6}K^{-1}
25 - 350	9.8
350 - 500	6.6
PLZT (8 65 35)	5.2 (Literature[1])

Figure 4 Thermal expansion of PLZT (28/0/100) ceramic.

PLZT (28/0/100) Films

Structure: PLZT (28/0/100) films on fused silica were found to suffer from excessive cracking and delamination in contrast to the results of Mukherjee et al [12]. To investigate this the further thermal expansion coefficient of a 100% dense PLZT (28/0/100) ceramic was determined via dilatometer techniques over the range 25-500°C and is shown in Figure 4. The overall expansion is large compared with fused silica (α typically 0.5 x $10^{-6}K^{-1}$) and other PLZT compositions [1] and displays a distinct change at 350°C of unknown origin. It is likely that the discrepancy in film integrity on fused silica is related to intrinsic growth stress which may offset thermal expansion stresses and can differ widely between deposition techniques (and systems).

The effect of La doping on lead titanate is to reduce the tetragonality at a given temperature and for PLZT (28/0/100) the structure remains cubic at room temperature. Figure 5(i) shows an XRD pattern for randomly orientated polycrystalline PLZT (28/0/100) ceramic. Figure 5(ii), (iii) and (iv) show XRD spectra for (100), (110) and (111) orientated 1μm thick films grown under near identical conditions onto (1102) sapphire. The orientation

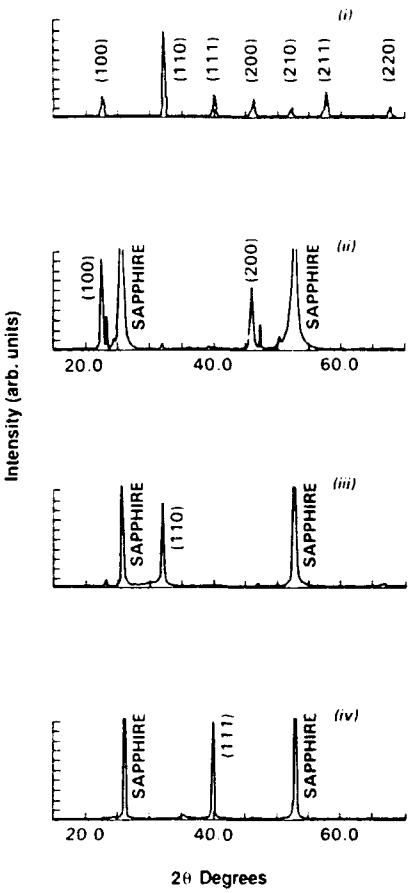


Figure 5 X-ray diffraction traces of (i) PLZT (28/0/100) ceramic and (ii)-(iv) PLZT (28/0/100) films on (1102) sapphire.

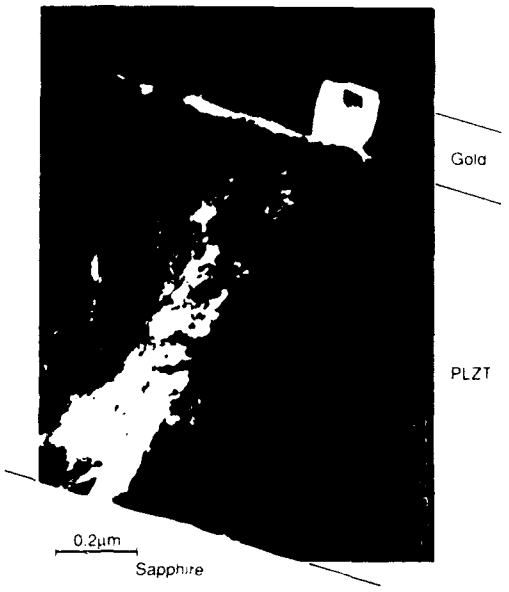


Figure 6 Cross-sectional TEM of PLZT (28/0/100) film.

behaviour is complex; there is some critical process parameter that controls the resultant film orientation which remains to be identified. Figure 6 shows a cross-sectional TEM of a (100) PLZT (28/0/100) film. The grain structure is columnar, of diameter 0.5μm and individual grains traverse the complete 1μm thickness of the film.

Amorphous PLZT (28/0/100) films deposited below 500°C transformed readily to perovskite on annealing above 550°C in a tube furnace in static air or flowing oxygen. However, the orientation was random and the films were prone to suffer from cracking, even for long heating and cooling cycles.

Electrical, Optical and Electro-Optic Film Properties: Figure 7 shows UV/visible transmittance spectra of as-deposited and annealed perovskite PLZT (28/0/100) films, each of thickness 1μm. The in-situ film has superior transmission properties and a refractive index of 2.50. The annealed film is less transparent with an index of 2.45 and a secondary transmittance envelop superimposed onto the interference fringing. Numerical modelling has shown this to be consistent with a decreasing refractive index at the top surface of the film as depicted in Figure 7(ii). This implies incomplete crystallisation and/or stoichiometric deviations during the anneal cycle; extended annealing did not eliminate this phenomenon.

Electrical properties of some films were probed using Cr/Au interdigitated electrodes (IDEs) defined on the top surface using photolithographic techniques. The frequency was varied from 30Hz to 300kHz using a peak field of 9kV/m and dc bias fields up to 5V/μm. A (111) orientated in-situ PLZT (28/0/100) film gave a dielectric constant in excess of 1500 and a loss of 0.16%. Similarly an annealed randomly orientated PLZT (28/0/100) film gave values of 500 and 0.10%. These values remained constant within 1% across the frequency range and also varied little with temperature variations of a few tens of degrees either side of room temperature. This is consistent with a diffuse ferroelectric/paraelectric transition with a Curie temperature of order 25°C [7]. It is likely that the lower values obtained for the annealed films was due to a low dielectric surface layer as evidenced by the optical transmission measurements.

Electro-optic measurements were made in the transverse mode using IDE's to apply the field and viewing between the electrode fingers. Three approaches were used to probe for electro-optic activity:

i) movement of white light interference fringes formed in a transmission mode on the application of an electric field,

ii) variations in transmitted intensity of a He-Ne laser for a film placed between crossed polarizers and under a varying electric field,

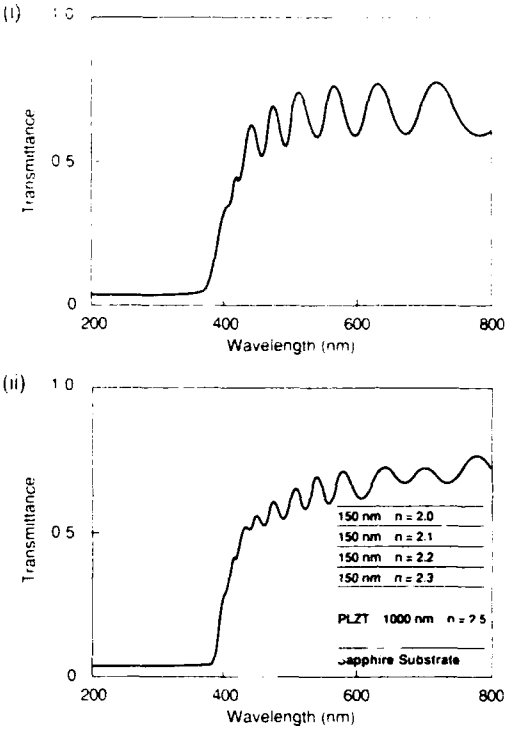


Figure 7 UV/visible transmittance specta of as-deposited and annealed perovskite PLZT (28/0/100) films.

iii) reflected surface changes due to an applied electric field using a white light interferometer (WYKO) instrument.

In all cases, no electro-optic responses were observed from films formed using the annealing approach. For in-situ deposited films large quadratic responses were observed using method (iii) but these could not be duplicated using either of the transmission mode methods. Figure 8 shows the reflected phase response of a 1μm thick 90% (100) orientated PLZT (28/0/100)

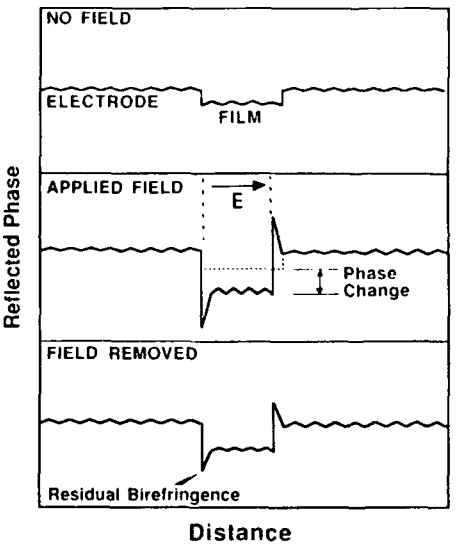


Figure 8 Reflected mode electro-optic response of a PLZT (28/0/100) film.

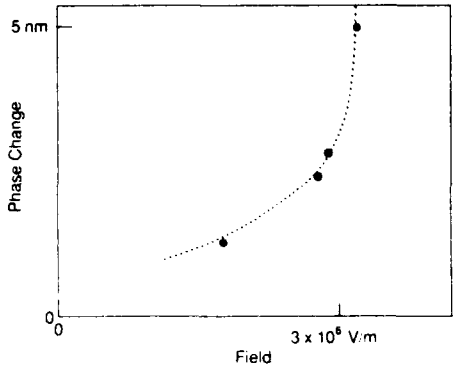


Figure 9 Reflected mode field dependent phase response of a PLZT (28/0/100) film.

film. On application of an electric field, the average relative phase heights of the film and Cr/Au electrode change and large peaks develop adjacent to the electrode edges. On removal of the field the original state was not fully recovered and remanent polarization remains. Reversal of the applied field did not alter the profiles in Figure 8 so the effect did not have a linear component attributable to piezoelectric or linear electro-optic effects. This is confirmed by the quadratic phase to field dependency shown in Figure 9. By attributing the average phase change entirely to a refractive index variation, Δn, a value for the quadratic electro-optic coefficient R could be derived from

$$\Delta n = 0.5 n^3 R E^2 \qquad (2)$$

where n = 2.60. This gives R = 2.10 x $10^{-16} m^2/V^2$ which is large compared to other reported values of 0.6-1.0 x $10^{-16} m^2/V^2$ [7, 12,13]. However, it is likely a significant proportion of the observed phase change is due to a physical electrostrictive surface deformation. Given this value for R a transmitted interference peak shift in excess of 4nm should have been observed in transmission. This was well within the resolution of the optical system. Similarly, a readily detectable intensity change should have occurred for the laser and crossed polarizer method. The cause of this discrepancy is not clear, but it is possible that the electro-optic and electrostrictive responses are working in opposite senses such that Δn and Δt cancel leaving the film with an identical optical thickness.

Also of concern are the peak phase changes adjacent to the electrode edges and the remanent polarization after the removal of the electric field. These are attributed to space charging within the film or at the film/electrode interface. The trapped charge screens the applied electric field and mitigates any electro-active material response. Space charge effects have been regularly observed in bulk ceramic materials at Caswell and are related to structural defects, particularly at the grain boundaries. In a thin film where the crystallisation and stoichiometry may well not be as consistent as in a sintered ceramic, space charge constitutes a serious problem. It is apparent that any thin film deposition process needs to be optimised to produce homogenous films for the device potential to be fully exploited.

PLZT (0/0/100) and (10/0/100) Films

Structure: Figure 10 shows XRD spectra of 1μm thick lead titanate films on silicon, sapphire and MgO substrates. As a general result, it was found that films crystallised more readily on the Pt/Ti electrode than the bare substrate and that the Pt itself took up a highly preferred (111) orientation during PLZT deposition. The orientation of the film was found to be a strong function of the thermal expansion coefficient of the substrate. The low coefficient of silicon (3 x $10^{-6} K^{-1}$) places the film in tension on cooling and at the cubic-tetragonal phase change confines the longer (001) c axis to the plane of the substrate giving a (100) film orientation. For MgO (14 x $10^{-6} K^{-1}$) the opposite occurs giving a (001) film and for sapphire (7.5 x $10^{-6} K^{-1}$) a mixed (100)/(001) orientation results. A (001) orientation would be most beneficial for pyroelectric detection

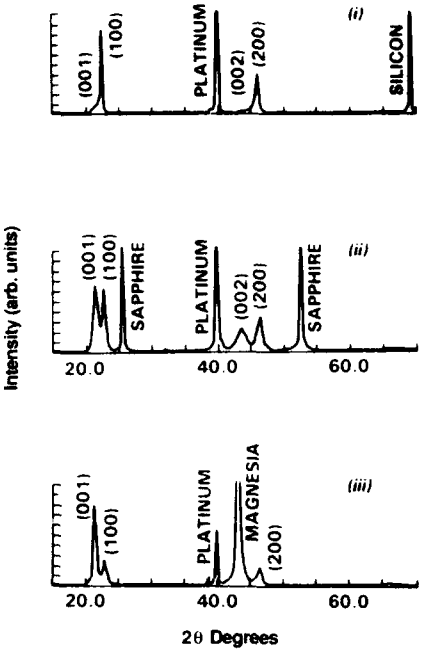


Figure 10 X-ray diffraction traces of lead titanate (PLZT 0/0/100) films on (i) silicon, (ii) sapphire and (iii) MgO substrates.

purposes which implies that for integrated devices on silicon, some method of repoling the film will be necessary. Inserting a barrier layer, such as amorphous alumina, between the silicon and the electrode has been found to force the orientation back towards (001) giving a similar structure to that on sapphire. Work is continuing on barrier layers and also to minimise the deposition temperature thus limiting the thermal mismatch stress that opposes repoling to the (001) state.

Figure 11 shows a SEM image of a lead titanate film on silicon. The grain size is of order 0.75μm and is less columnar than that for PLZT (28/0/100) although single grains do traverse the entire film for thicknesses around 1μm. Also shown in this picture



Figure 11 Normal incidence SEM of a lead titanate film.

is a passage through the film that may penetrate through the electrode. Certainly when top electrodes were applied to films less than 0.75μm thick electrical shorting occurred: for films 1μm thick this was less of a problem. Figure 12 shows bright field plan view TEMs of lead titanate films detached from silicon. The first, Figure 12(i), was grown by argon ion sputtering of a fully metallic Pb/Ti target and shows considerable texture indicating a high level of imperfection and defects in the film. It is probable that much of this disorder has been introduced by low flux high energy bombardment of the film by argon atoms reflected from the target. Comparison to the argon content of films deposited using RF sputtering with RF bias on the substrate places the energy of bombardment at 200-300eV. This is typically half the accelerating potential of the sputtering beam and is consistent with elastic recoil of argon from the target. At these energies, the argon atoms would implant and be capable of damaging the crystal structure of the lead titanate. The second, Figure 12(ii), was grown by krypton sputtering of a ceramic/ metal PbO/ Ti target and shows a greatly reduced level of disorder as well as a larger grain size. Domains and twinning are still visible in some individual grains but the overall film structure and grain texture is similar to that seen by TEM of doped lead titanate bulk ceramics manufactured at Caswell.

A detrimental phenomenon was the appearance of blisters in the Ti/Pt electrode on silicon with a 0.25μm Al_2O_3 barrier layer during PLZT film growth. Figure 13 shows SEM images of the blisters which have a diameter of order 10-15μm. The PLZT film has grown over the blister giving a full coverage (application of top electrodes do not reveal any shorts). The blisters occur under masked regions of the substrate thus eliminating ion bombardment or PLZT as the cause. Replacing the Al_2O_3 layer with 0.36μm of SiO_2 or 0.75μm of BPSG (boron-phosphate-silicate glass) eliminates this effect. The implication is that a chemical interaction occurred between the Ti layer in the electrode and the SiO_2 or

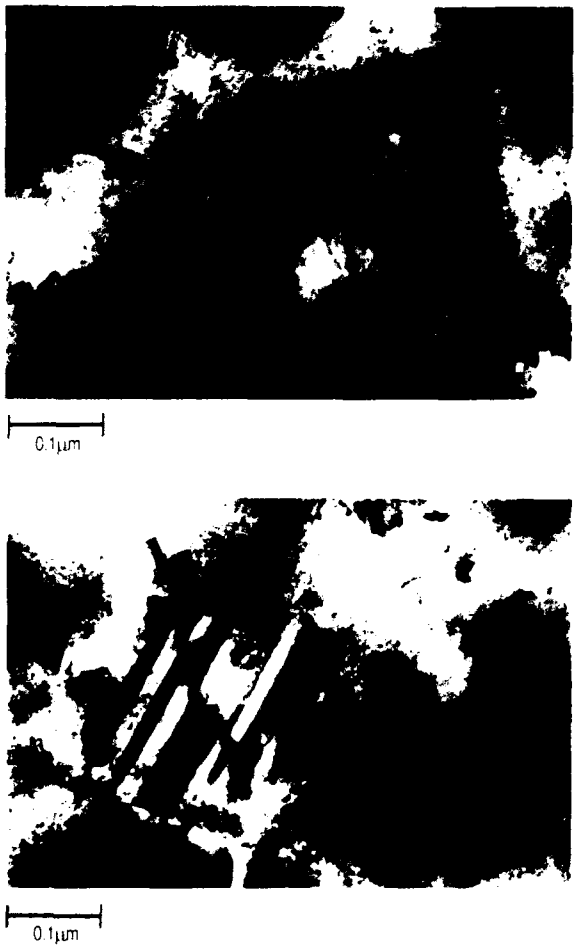


Figure 12 Bright field TEM pictures of detached lead titanate films grown by (i) argon sputtering of a Pb/Ti target, and (ii) krypton sputtering of a PbO/Ti target.

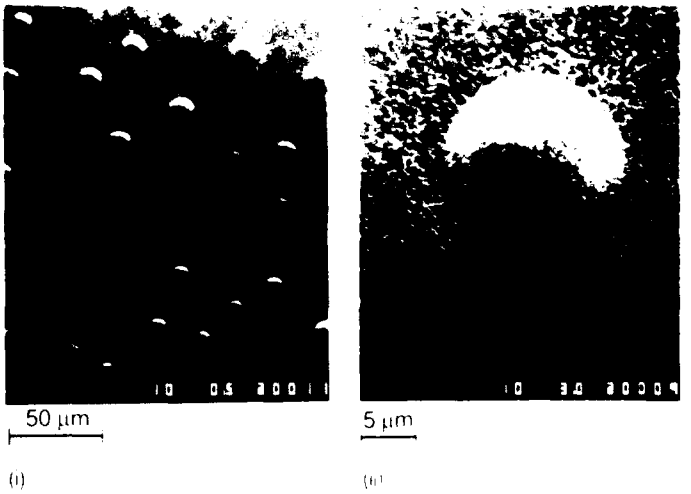


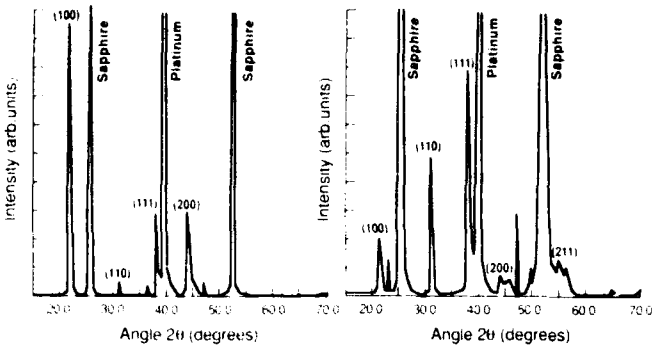
Figure 13 SEM images of blisters in lead titanate/platinum/ titanium/ Al_2O_3/ silicon structure.

BPSG. This gave good adhesion and prevented blistering. For Al_2O_3 which is chemically very stable, poor adhesion resulted and the stresses in the electrode were sufficient to initiate delamination.

Electric and Pyroelectric Film Properties: To examine electric and pyroelectric properties of the films 1mm diameter Cr/Au electrodes were evaporated onto the top surface. For lead titanate, the dielectric constant was 300 and the loss 3.3%; for La doped films, the values were 450 and 1.5%. Limited pyroelectric activity was observed in the as-deposited films, but this was improved by poling at 7kV/mm. Pyroelectric coefficients up to 400μ$Cm^{-2}K^{-1}$ have been observed but more typical average values were 250, 100 and 50μ$Cm^{-2}K^{-1}$ for PLZT (7/0/100) films on MgO, sapphire and silicon respectively; the corresponding figures of merit, F_D, were 2.1, 1.5 and 0.6 x $10^{-5}Pa^{-0.5}$. This illustrates the strong dependence on film orientation and hence substrate. PLZT (0/0/100) films had marginally reduced pyroelectric coefficient but due to their smaller dielectric constant gave F_D similar to those for PLZT (7/0/100). As yet the improved structure of films sputtered from the PbO/Ti target using krypton has not been reflected in their pyroelectric properties. This seems to be related to the difficulty encountered in poling the films and, indeed, in a number of cases the application of poling fields has resulted in a reduction in the pyroelectric response as compared with the pre-poled state. The present F_D compare to 10 x $10^{-5}Pa^{-0.5}$ for sol gel PST [4] and 5-6 x $10^{-5}Pa^{-0.5}$ for PLZT (0/0/100) and PLZT (7/0/100) [6]. In the present work F_D as high as 5.1 x $10^{-5}Pa^{-0.5}$ have been observed but only for isolated regions of particular thin film samples; the problem seems to be that of producing this quality of films reliably over larger areas.

PLZT (0/50/50) and (0/30/70) Sol Gel Films

Structure: Typical XRD spectra for PLZT (0/50/50) and (0/30/70) films are shown in Figure 14. (0/50/50) films tended towards a (100) orientation as the film thickness decreased below 0.5μm; 1μm thick films gave a bulk-like polycrystalline pattern. (0/30/70) films showed similar behaviour except that the preferred orientation was (111). Generally, most films were baked at 170°C for 2 minutes after each spin cycle and then fired at 700°C for 1-2 hours in static air or flowing oxygen. The typical increment in film thickness using unmodified solutions was 0.08μm per layer. Increasing the bake temperature to 400°C between layers gave films with an improved morphology and electrical properties. Modification of the solution with acetylacetone reduced the ultimate film thickness increment per layer to 0.016μm, but gave the highest quality crystalline films for both the (0/50/50) and (0/30/70) compositions at 170°C baking temperature; however, it was found that two spin cycles per bake did not compromise film quality. Further, it was eventually found that six successive layers could be baked to a fully perovskite structure at only 450°C for 2 minutes on a hot plate. Subsequent annealing of this film at 700°C for 2 hours



(i) (ii)

Figure 14 X-ray diffraction traces of (i) PLZT (0/50/50) and (ii) PLZT (0/30/70) films.

did not result in any change in X-ray peak intensities. This is a significant result with respect to processing time and integration onto silicon devices where thermal loading is critical. SEM examination of several films showed a variety of morphologies from the 'rosette type' features, Figure 15(a) to a finer hillock type structure, Figure 15(b). Film morphology is still under investigation and seems to be critically dependent on the structure and history of the electrode as found by other workers [14].

Electric and Pyroelectric Properties: A 0.45μm thick PLZT (0/50/50) film gave a relative permittivity of 800, a loss (at 1kHz) of 3.4% and a pyroelectric coefficient of $100\mu Cm^{-2}K^{-1}$ in an unpoled state. Poling at 5kV/mm improved the permittivity to 910 and the pyroelectric coefficient to $400\mu Cm^{-2}K^{-1}$ giving a figure-of-merit of $2.2 \times 10^{-5}Pa^{-0.5}$. A 0.44μm thick film of PLZT (0/30/70) gave respective prepoling values of 350, 3.6%, $40\mu Cm^{-2}K^{-1}$ and $0.35 \times 10^{-5}Pa^{-0.5}$ but failed on poling. The film manufactured using only a 450°C hotplate bake suffered from a high pinhole density indicating the need to further improve the deposition process.

Discussion

The advantages of ion beam sputtering over the competing PVD techniques of RF magnetron sputtering and laser ablation are well documented for conventional dielectric materials [8]. At present these advantages have not been fully repeated for PLZT film deposition. However the films produced in this work and by other workers [8-10] are now matching those produced by conventional sputtering in which there has been, and still is, considerable activity. However, whereas there now exists limited development potential for RF sputtering there remains considerable scope for improving ion beam methods. Comparison with laser ablation is more difficult since this itself is a new and rapidly developing technique, although it is without dispute that an ion beam process will ultimately offer superior process control. The inherent simplicity and stoichiometry control offered by sol-gel methods make this a serious contender for thin film multicomponent oxides such as PLZT. In particular, the optimisation of a process requiring a maximum temperature of 450°C for short periods of time would be a major advantage for integration onto CMOS silicon. The drawback of the repetitive, tedious nature and slow deposition rate of sol-gel requires automation of the process and this is under active development at Caswell. The potential of sol-gel has been demonstrated by Ye et al [5] who have attained pyroelectric coefficients of $1000\mu Cm^{-2}K^{-1}$ for lead titanate films.

The prospects for the production of integrated pyroelectric IR detectors using PLZT seem brighter than those for thin film electro-optic devices, at least in the short term. The extra constraints imposed by the optical requirements make device quality PLZT films more difficult to produce. Figure 16 shows a schematic of an integrated detector element. The nature of the thermal insulator is a point of discussion. This layer has to allow for the correct orientation of lead titanate, provide a thermal barrier to enhance element responsivity and also perhaps protect the silicon devices

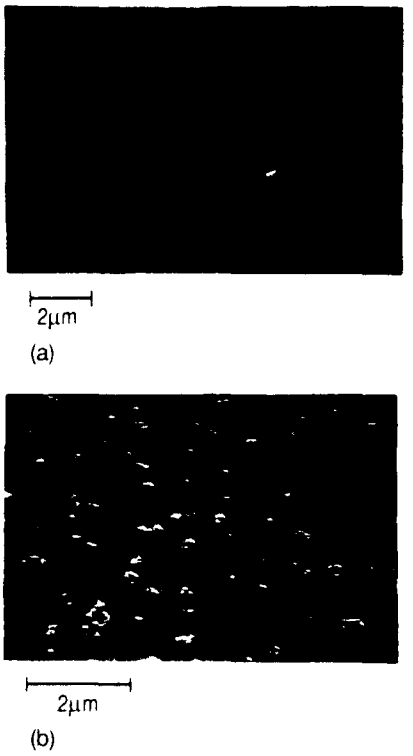


Figure 15 SEM images of (i) 'rosette type structure, and (ii) 'hillock' type structure in PLZT (0/50/50) sol-gel films

during film deposition. The elegant work of Ye et al [6] using polysilicon bridge structures, effectively making the barrier layer air, has demonstrated the remarkable responsivity attainable from an integrated structure. A similar approach is under active investigation at Caswell.

Conclusions

The deposition of ferroelectric films using sol gel and dual ion beam sputtering has been demonstrated. In the DIBS process, the presence of active oxygen has been found to be essential to the formation of perovskite PLZT films. Electro-optic and pyroelectric effects have been observed in these films. A large quadratic electro-optic coefficient of $2.1 \times 10^{-16}m^2/V^2$ was observed in reflection mode for PLZT (28/0/100), but this could not be repeated in a transmission mode, presumably because birefringence and thickness changes work in opposite senses. Peak pyroelectric coefficients of $400\mu Cm^{-2}K^{-1}$ have been observed for PLZT (0/0/100) and (7/0/100) films. Sol-gel has produced PLZT (0/50/50) and (0/30/70) films with similar properties and has shown the potential for film formation at temperatures as low as 450°C.

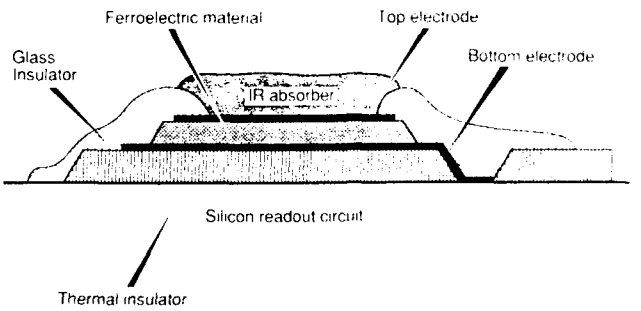


Figure 16 Integrated thermal detector element.

The prospects for fully integrated pyroelectric detector elements on silicon in the near future are good and the DIBS and sol-gel processes have considerable development potential with respect to attaining this goal.

Acknowledgements

Parts of this work have been carried out with the support of the Procurement Executive, Ministry of Defence, DRA, Malvern, and with the support of GEC-Plessey Semiconductors Ltd. The authors thank Dr K Lewis and Mr R Watton for useful discussions.

References

[1] G.H. Haertling, 'PLZT Electro-Optic Materials and Applications - A Review', Ferroelectrics, Vol. 75, pp25-55, 1987.

[2] R.A. Roy, K.F. Etzold and J.J. Cuomo, 'Ferroelectric Film Synthesis, Past and Present: A Select Review', Mat. Res. Soc. Symp. Proc., Vol. 200, pp141-151, 1990.

[3] R.W. Whatmore, 'Pyroelectric Ceramics and Devices for Thermal Infra-Red Detection and Imaging', Ferroelectrics, Vol. 118, pp241-259, 1991.

[4] A. Patel, N.M. Shorrocks and R.W. Whatmore, 'Preparation and Properties of $PbTiO_3$ and $PbSc_{0.5}Ta_{0.5}O_3$ Thin Films by Sol-Gel Processing', IEEE Trans. Ultrason. Ferroelec. Freq. Contr. Vol. 38, pp672-676, 1991.

[5] Chian-pin Ye, T. Tamagawa and D.L. Polla, 'Experimental Studies on Primary and Secondary Pyroelectric Effects in $Pb(ZrTi)_3$, $PbTiO_3$ and ZnO Thin Films', J. Appl. Phys., Vol. 70, pp5538-5543, 1991.

[6] M. Okuyama and Y. Hamakawa, '$PbTiO_3$ Thin Films and their Pyroelectric Application', Ferroelectrics, Vol. 118, pp261-278, 1991.

[7] H. Adachi, T. Misuya, O. Yamazaki and K. Wasa, 'Ferroelectric (PbLa)(ZrTi)O_3 Epitaxial Thin Films on Sapphire Grown by RF-Planar Magnetron Sputtering', J. Appl. Phys., Vol. 60, pp736-741, 1986.

[8] G. Emiliani and S. Scaglione, 'Properties of Silicon and Aluminium Oxide Thin Films Deposited by Dual Ion Beam Sputtering', J. Vac. Sci. Technol., Vol. A5, pp1824-1827, 1987.

[9] S.B. Krupanidhi, H. Hu and V. Kumar, 'Multi Ion Beam Reactive Sputter Deposition of Ferroelectric $Pb(Zr,Ti)O_3$ Thin Films', J. Appl. Phys., Vol. 71, pp376-388, 1992.

[10] A. Kingon, M. Ameen, O. Auciello, K. Gifford, H. Al-Shareef, T. Graettinger, S.H. Ron and P. Hren, 'Processing Structure Relations for Ferroelectric Thin Films Deposited by Ion Beam Sputter Deposition', Ferroelectrics, Vol. 116, pp35-49, 1991.

[11] Guo Hua-cong, Xiao Ding-Quan, Xiao Zhi-Li, Xiu Bi-Zheng, Shao Qu-WQen and Zhu Ju-Mu, 'Multi Ion Beam Reactive Co-Sputtering (MIBRECS) System and Technique for Preparing Complex Oxide Thin Films', Ferroelectrics, Vol. 108, pp65-69, 1990.

[12] A. Mukherjee, S.R.J. Brueck and A.Y. Wu, 'Electro-Optic Effects in Thin Film Lanthanum Doped Lead Zirconate Titanate', Optics Letters, Vol. 15, pp151-153, 1990.

[13] A.Y. Wu, 'Deposition of $PbLaZrTiO_3$, $BaTiO_3$,$SrBaNb_2O_6$, $Ba_2NaNb_5O_{15}$, $KTiOPO_4$ and beta-BaB_2O_4 Thin Films', in 4th Int. SAMPE Electronics Conf., pp722-733, 12-14 June 1990.

[14] G.A.C.M. Spierings, J.B.A. van Zon, M. Klee and P.K. Larsen, 'Influence of Platinum Based Electrodes on the Microstructure of Sol-Gel and MOD Prepared Lead Zirconate Titanate Films', presented at the 4th Int. Symp. on Integrated Ferroelectrics, Monterey, CA, USA, 9-11 March 1992.

DEPOSITION AND PROPERTIES OF PLT THIN FILMS BY MAGNETRON SPUTTERINC FORM POWDER TARGET

Wei-Gen Luo, Ai-Li Ding, Rui-Tao Zhang, Yu-Hong Huang and Min Ge
Shanghai Institute of Ceramics, Chinese Academy of Sciences, Shanghai 200050, China

We have studied the processes, structures and electro-optical properties of lanthanum-modified lead titanate (PLT) thin films prepared by RF magnetron sputtering from sintered powder targets. Highly oriented PLT thin films on glass and (0001) Al_2O_3 substrate, and an epitaxial growth PLT thin films on (100) $SrTiO_3$ have been deposited. The growth mechanism of oriented PLT thin film on amorphous glass was discussed. Electro-optical coefficient ($R\simeq0.6X10^{-16}m^2/v^2$) of PLT films on glass was measured by a new method based on Faraday magneto-optical effect.

Introduction

Many research works have been done about ferroelectric thin films, especially about PLZT material [1]. PLZT film has linear electro-optical (E-O) effect, quadric E-O effect and memory property depending on its composition. It also can be integrated with Si or GaAs semiconducting material. So PLZT is considered a most promise ferroelectric thin film to be used in two-dimensional spatial light modulator [2], nonvolatile optical devices [3]. In all these applications, PLZT thin films are requested to be highly oriented growth or epitaxial growth so as to low working voltage and reduce light scattering.

High quality PLZT thin films are usually prepared by RF magnetron sputtering. The sputtering is a very complicated physical and chemical process, and the sputtering conditions vary with substrate materials and sputtering system. We have studied the sputtering processes of PLZT thin film by magnetron sputtering from a stoichiometric powder target [4]. Highly-oriented or epitaxial PLT thin films have been deposited on different substrates. Especially, highly-oriented PLT thin film can be grown on a glass substrate. As known, glass is an amorphous material mainly consisted of silica, SiO_2. If a PLZT thin film is integrated with Si or GaAs, the PLZT film is usually deposited on SiO_2 film which is used a buffer layer of the Si and GaAs substrate. So it is very meaningful to study growth and its mechanism of PLZT thin film on glass substrate. The results are present in this paper. PLZT (28/0/100) thin film exhibits very good E-O properties, but there are very few reports on measuring method to determine E-O coefficient precisely [5]. The film is usually very thin, about a few thousand angstroms. It is very difficult to measure optical retardation of angstrom order. We use a simple but very accurate method based on Faraday magneto-optical effect to get the quadric electro-optical coefficient of PLT thin film. The PLT films on glass have the quadric electro-optical coefficient in a range from $0.1X10^{-16}$ to $1.0X10^{-16}(m/v)^2$.

Experiment

The PLZT (28/0/100) powder was prepared by mixing high purity PbO, La_2O_3, TiO_2 with a stoichiometry and then sintered at 800°C for four hours. The powders to be used as a sputtering target have to go through the sintering and gronding procedures for two times at least. The particle size of powder is about 5-10 μm. The sintered powder is slight yellow and pressed in a copper dish to be the sputtering target. The thermocouple is put near the backside of the substrate. So the actual temperature of substrate may be 50°C lower than the readout temperatures. Fig. 1 is a schematic picture of sputtering chamber.

The sputtering conditions are summarized in Table 1. X-ray diffraction, TEM and RHEED were employed to examine the structure of PLT thin film. The narrow gap (aout 0.4 mm) electrodes of gold-chromium were evaporated on the surface of PLT film for measuring the E-O properties. Fig. 2 shows the block diagram of the E-O measurement system [6].

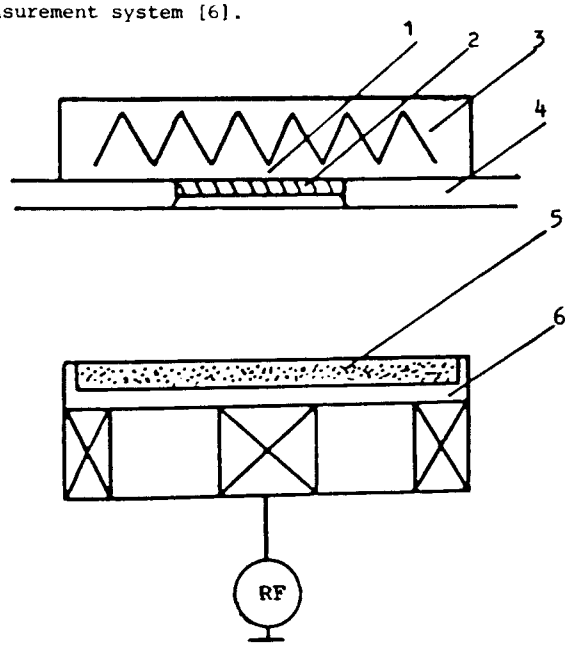


Fig.1. A schematic picture showing the chamber of sputtering. 1. Thermocouple, 2. Substrate, 3. Heater of substrate, 4. Substrate Holder, 5. PLT powder target, 6. Magnetron cathode.

Table 1. SPUTTERING CONDITIONS FOR PLT THIN FILM

Target	(28/0.100) PLT Powder
Target-substrate distance	25--20 mm
Substrate	Glass, $SrTiO_3$, Sapphire
RF power density	1.3--4.0 W/cm^2
Sputtering gas	Ar/O_2=1:1--1:0.5
Total pressure	(2--6)$X10^{-2}$mbar
Substrate temperature	RT--700°C
Deposition Rate	20--60 Å/min

Results and Discussions

1. The relationship of thin film structure and PbO content in sputtering target

In multi-element oxides sputtering, because the evaporative pressure of every element in target is different, this may lead to the content of the deposited film deviation from the target. The deviation is often dependend on the sputtering conditions and systems. In many reports for sputtering PLZT or PLT thin film, the target usually have extra PbO to compensate Pb losing in the sputtering for its high evaporative property. But we found that when the target powder have extra PbO there was always PbO phase existing in as-deposited film and while the powder was stoichiometric the film was pure perovskite structure, as shown in Fig. 3.

The possible reason may be that we sintered the powder at 800°C and the PbO losing was much lower than at 900°C as reported in other literatures. The further

CH3080-0-7803-0465-9/92$3.00 ©IEEE

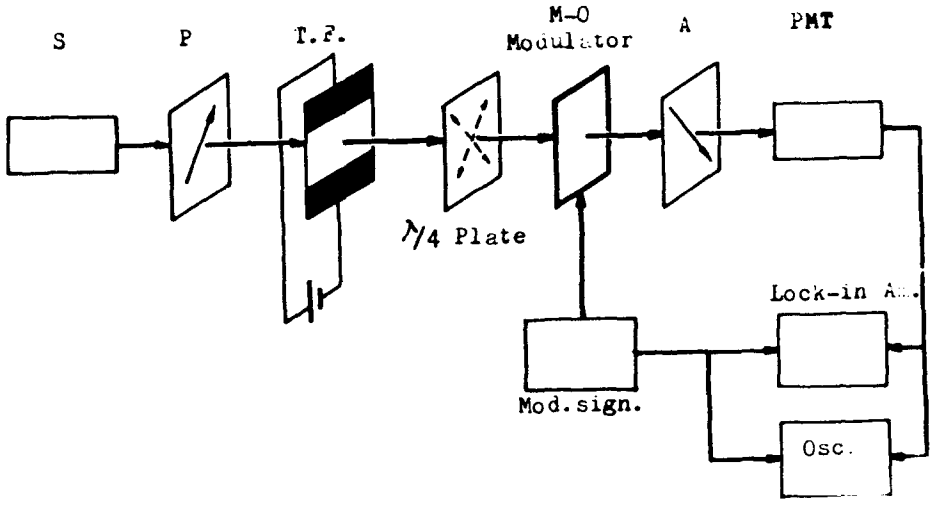


Fig.2. Block diagram of measuring electro-optical coefficient of ferroelectric thin film.

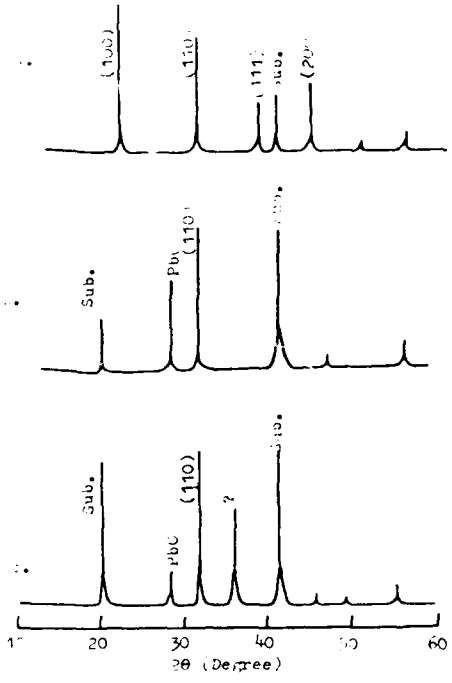


Fig.3. Structures of PLT thin film vs extra PbO in target (a) for no extra PbO, (b) and (c) for extra PbO, and (c) annealed at 600°C/3hr

study is in progress.

2. Oriented growth of PLT thin film on glass substrate

Glass substrate was used to prepare PLT thin film because its heat expansibility is $3.9X10^{-6}K^{-1}$, very close to that of PLZT material. PLT films deposited on the glass substrate were transparent and crack-free. The x-ray diffraction experiments showed that the deposited thin film was amorphous when substrate temperature was lower than 520°C. The film changed to oriented growth alone [100] direction (1=1,2,···) by proper heating treatment. By heating substrate at more higher temperature and proper in-situ heating treatment, the perovskite and highly oriented PLT films were growth on the glass.

As show in Fig. 4, at about 520°C, only amorphous PLT thin film was gotten, and at higher than 550°C, polycrystalline pervoskite PLT film was prepared. It is because the heat energy from substrate provides enough energy for adatoms to nucleate and grow.

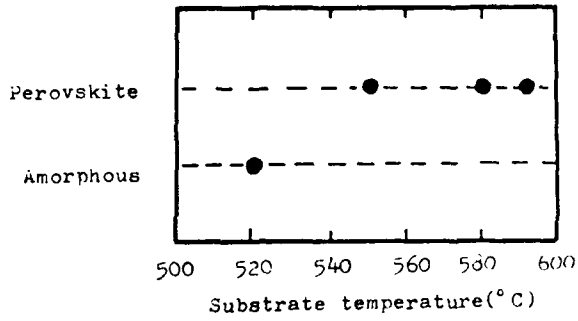


Fig.4. Structure of PLT thin film vs substrate temperature

PLZT (28/0/100) is cubic phase at room temperature. The growth of PLT polycrystalline thin film on glass substrate was obviously oriented in the [100] direction. The degree of film orientation in the [100] direction, α, was determined by measuring the intensities of PLT diffraction peaks and was express as follows:

$$\alpha = 1(100)/[1(100)+1(110)]$$

1(100) and 1(110) are X-ray diffraction intensity of (100) and (110) peak respectively. We showed the preferred orientation degree α of PLT film vs. substrate temperature in Fig. 5. It is clear that the higher the substrate temperature, the easier the growth for oriented PLT thin film. But overheating substrate may lead to decomposition and reevaporating of the deposited film.

In proper sputtering condition, we can get highly oriented PLT thin film (Fig. 6). There is no other diffraction peaks, only (100) peaks (1=1,2). The further TEM analysis (Fig. 7) indicated that the crystallization growth lines were paralleled to each other and the films were preferred (100) oriented. The lattice parameter a was 3.934 Å.

SEM photograph (Fig. 8) suggested that the average diameter of the crystal grains is about 300 Å. They are closely packed and porous-free, and the grain boundaries are very thin.

Why oriented PLT thin film can grow on the amorphous

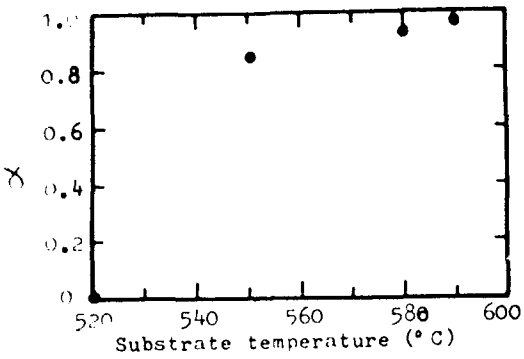


Fig.5. Preferred orientation degree of PLT thin film vs substrate temperature

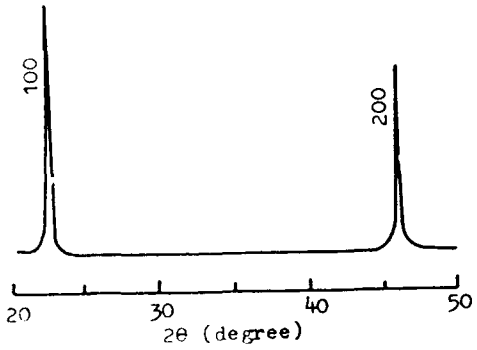


Fig.6. X-ray diffraction spectra for highly-oriented PLT thin film on glass



Fig.7. TEM image for section of PLT thin film



Fig.8. SEM micrograph of PLT thin film on glass (X6000)

glass substrate? We propose it can be explained by the structure of glass. The glass is a very complicated amorphous material. Its main structure is Si-O tetrahedral configuration.According to the crystalliterandom network theory, the structure of glass is similar to the crystal structure in the region of crystallite (about 10 Å) and is random network outside the region. So in the microstructure, the glass substrate is not only a substrate to be used for sputtering without any characteristics but has its own inherent quality which is determined by Si-O tetrahedral configuration. From XRD patterns of glass and fused silica, there was always a diffraction peak at 2θ=22°. It was just like the (100) peak of quartz crystal. So we suggest that it is much easier for PLT (100) to nucleate and grow on glass than other direction for they have similar structure. Its growth may be described by Volmer-Weber mechanism [7].

3. PLT thin film growth on single crystal substrate

Single crystal is good substrate to grow epitaxially and hihgly oriented PLZT thin film. As a promise substrate material, its crystallization parameter and heat expansibility should be matched with the deposited materials. $SrTiO_3$ and R-oriented sapphire are proper substrates on which highly quality PLZT film can be deposited. We have studied the sputtering conditions of PLT film on (100) $SrTiO_3$ substrate. At the substrate temperature of 550°C, epitaxial PLT films were obtained. Fig. 9 showed the x-ray diffraction spectra of PLT on $SrTiO_3$. There are only (100 and (200) diffraction peaks. RHEED image (Fig. 10) further confirmed the epitaxy of PLT film.

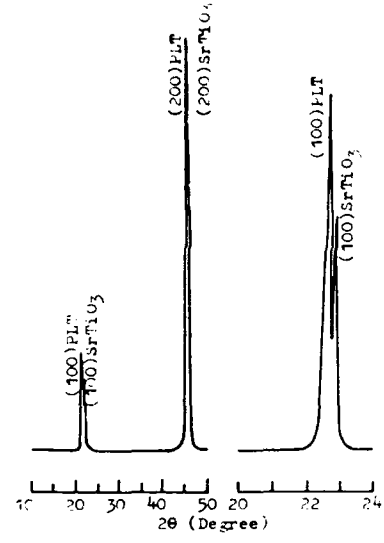


Fig.9. X-ray diffraction spectra of PLT thin film on (100) $SrTiO_3$

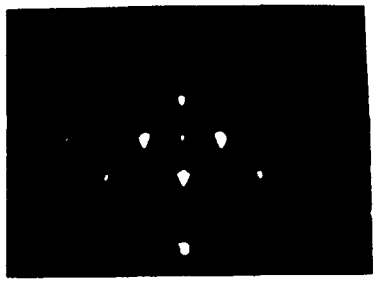


Fig.10. RHEED image for epitaxial PLT thin film

There were two different oriented growth on (0001) sapphire substrate, they were preferred (111) and (100) orientation respectively as shown in Fig. 11. The E-O behavious of the two different kinds of oriented PLT thin films are studied in progress.

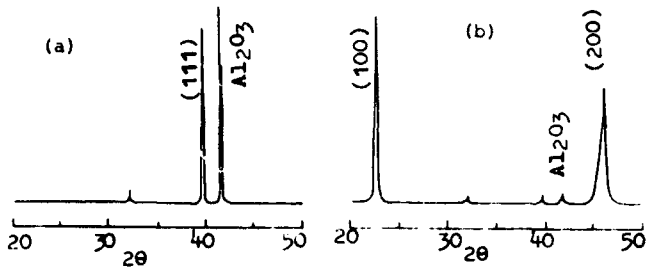


Fig.11. X-ray diffraction spectra for oriented-growth PLT film on (0001) Al_2O_3
(a) (111) orientation, (b) (100) orientation

4. The electro-optical properties of PLT thin film

We have studied the phase transition and dielectric properties of PLZT (28/0/100) hot-pressed ceramics. It is a electric field-induced ferroelectric material. At room temperature, it is cubic perovskite structure, spontaneous polarization is zero. Under electric field, it can be poled. The thin film has the similar properties. The sputtered PLT film was colourless and transparent. Its transmittance was about 80% in visible region. When no electric field applied on the PLT film, the polarized light transmits the PLT thin film without direction change. Under the electric field, the polarization direction of the light emerged from PLT film changed. The film become birefringent. Thebirefringence Δn is quadric relationship to the applying electric field. After removing the electric field, the film turn back to istropy. So the PLT thin film has Kerr E-O effect. The calculated quadric E-O coefficient R is in a range from $0.1X10^{-16}$ to $1.0X10^{-16}$ $(m/v)^2$. Highly oriented PLT thin film has larger R. The relationship of the birefringence Δn vs electric field E for PLT film measured by the Faraday magneto-optical modulating was shown in Fig. 12. How the sputtering conditons effect on the R is discussed in another paper to be published.

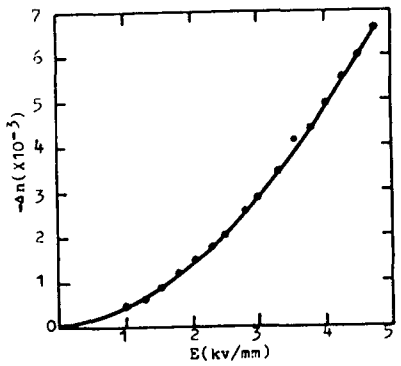


Fig.12. Δn vs E for PLT thin film on glass

From Fig. 13, we found that under lower electric field, Δn of the PLT film is proportional to E^2. Under higher electric field, it deviates from this relationship. There were the similar reports for a (9/65/35) PLZT ceramics [8] and for PLT film [5]. Wang et al [5] contributed thin phenomenon to a high-order E-O effect. We will do further study.

Conclusions

Using powder target, we prepared highly oriented or epitaxial PLZT (28/0/100) thin film on glass or crystal substrate by R.F. magnetron sputtering. The growth mechanism and sputtering conditions are also studied. PLT thin film have good electro-optic properties, and the quadric electro-optic coefficient high as $1.0X10^{-16}$ $(m/v)^2$. Growing highly oriented PLT thin film on glass is valuable to future applications in integrated optics.

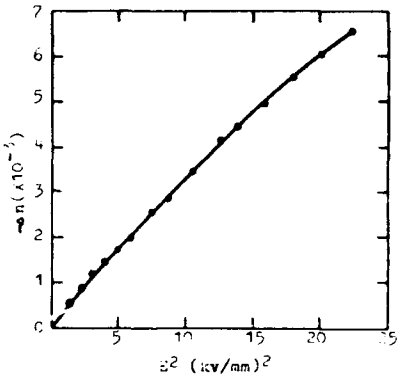


Fig.13. Δn vs E^2 for PLT thin film on glass

Acknowledgement

We gratefully acknowledge the support of this work by National 863 high technology committee.

References

1. For example H. Adachi, it al., "Ferroelectric (Pb, La)$(Zr,Ti)O_3$ epitaxial thin films on sapphire grown by rf-magnetron sputtering" J. Appi. Phys., Vol.60, pp736, 1986
2. S. H. Lee et al., "Two-dimensional Si/PLZT spatial light modulators: design consideration and technology" Opt. Eng., Vol.25, No.2, pp250, 1986.
3. A. Y. Wu, "Deposition of $(Pb,La)(Zr,Ti)O_3$, $BaTiO_3$ $(Sr,Ba)Nb_2O_6$, $Ba_2NaNb_5O_{15}$, $KTiPO_4$ and beta-BaB_2O_4 thin films" Inter. SAMPLE Electronic conf. Series, Vol.4, pp772, 1990.
4. Y. H. Huang, W. G. Luo et al, "Oriented growth PLT thin films on amorphous substrate" Proc. SPIE-Int. Soc. Opt. Eng., Vol.1126, pp36, 1989.
5. F. Wang, "Electro-optic properties of (Pb,La)(Ti,Zr) O_3, $BaTiO_3$, (Sr,Ba) and $Ba_2NaNb_5O_{15}$ thin films by a confocal scanning deferential polarization microscope" ibit, pp712.
6. A. L. Ding, W. G. Luo, R. T. Zhang and K. S. Chen, presented at the IEEE'92 ISAF, Greenville, S. C., Aug. 31-Sep. 2, 1992.
7. R. T. Zhang, M. Ge and W. G. Luo, "The growth mechanism of orientated PLZT thin films sputtered on glass substrate" Proc. SPIE, Vol.1519, pp757, 1991.
8. G. H. Haertling and C. E. Land, "Recent improvements in the optical electro-optic properties of PLZT ceramics" Ferroelectrics, Vol.3, pp269, 1972.

A STUDY OF THE PROPERTIES OF ACETATE-DERIVED PLZT FILMS ON GLASS SUBSTRATES

K. D. Preston and G. H. Haertling
Ceramic Engineering, Clemson University
Clemson, South Carolina 29634

Abstract: Crack-free PZT 0/65/35 films of thicknesses up to 3 μm were deposited onto glass and sapphire substrates using an acetate precursor system at a processing temperature of 500-550° C. Ferroelectric, dielectric and electrooptic properties were measured as a function of excess PbO content from 0 to 4 mol%. Directionally dependent film behavior at high lead content was correlated with the combined effects of tensile strain and domain alignment.

Introduction

The optimum application of ferroelectric films is based on complete characterization of the film properties and processing conditions. The number of influencing factors is as varied as the techniques employed to process the films. However, certain interdependent physical characteristics, such as film thickness and grain size, remain a common consideration regardless of deposition technique[1-5]. Another important feature of film geometry is the development of anisotropic behavior resulting from crystallographic orientation and stress related lattice distortions.

In the course of investigating transverse electrooptic behavior of PZT films, it was found that the addition of excess PbO, a common practice in the processing of lead zirconate-titanate materials, introduced into the films a high level of behavioral anisotropy. The characteristics of the films became dependent upon the direction of measurement. This effect was studied by comparing longitudinal ferroelectric and dielectric properties to transverse electrooptic properties for PZT films on glass and sapphire substrates. A constant film thickness of 3 μm was maintained to reduce the effects of thickness while a PLT buffer layer was used to control grain size.

Experimental Procedure

Film Processing

A thermal decomposition method based on a water-soluble acetate precursor system[4] was used to process PZT 0/65/35 (La/Zr/Ti) films on various substrate materials. The precursor solutions, comprised of stoichiometric combinations of aqueous zirconium acetate (ZrAc), lanthanum acetate (LaAc), titaniumacetylacetonate (TiAcac) and powdered lead subacetate (PbsubAc), were diluted with methanol in a ratio of 5:1 to improve solution stability and avoid film cracking during the heat treatment process. Multilayer films were deposited using an automated dip coating apparatus which allowed for controlled dipping of the substrate into the solution and direct transport of the film/substrate in and out of the heating zone. Through computer interface, precise firing time schedules could be maintained. The completion time of a single firing cycle; i.e., dipping - firing - cooling, varied with substrate, film composition and firing temperature.

From previous experience in processing acetate-derived PLZT and PZT films on sapphire substrates, it was found that without the use of either excess amounts of PbO or the initial application of a buffer layer, significant amounts of pyrochlore were likely to develop[6]. When used as a buffer layer, films in the $(Pb,La)TiO_3$ system provided an improved nucleation surface for PZT film formation[6,7] and have made possible the development of PZT films on glass substrates where lower processing temperatures are required[8].

The substrates used in this study include randomly oriented sapphire and a Corning barium borosilicate glass (#7059) with thermal expansion coefficients of 8.3×10^{-6}/° C and 5.01×10^{-6}/° C, respectively. For ferroelectric and dielectric measurements, thin films (3600Å) of ITO were deposited onto one side of the substrates by magnetron sputtering from a powdered target. The sputtering atmosphere was a 60:40 argon-oxygen mixture at a pressure of 100 mTorr. The substrates were held at a constant temperature of 350° C. The buffer layer composition, PLT 14/0/100, was chosen due to electrooptic compatibility with PZT. Before depositing the films, each substrate was heat treated at 550° C for 2 minutes to remove any remaining organics and improve the conductivity of the ITO. The PZT films were processed by initial deposition of 2 layers (1000Å) of PLT followed by 2 layers of PZT at 550° C, each layer fired for 5 minutes. The remaining layers of PZT were deposited at 500° C, each layer fired for 10 minutes. This process was developed as a compromise between firing the entire film at 500° C, which usually led to film cracking at the grain boundaries where it was suspected an amorphous or poorly crystallized phase was formed, or firing the entire film at 550° C where large deep cracks were formed due to the increase in thermal stress. The more fully developed surface layer processed at 550° C enhanced crystallization of the film processed at 500° C and crack-free films were produced. Without a buffer layer, PZT films could not be processed at such low temperatures even on sapphire. PZT films on sapphire without a buffer layer were fired at 630° C, each layer fired for 2 minutes. Film thicknesses were optically determined from cross sections using a Zeiss image analyzer.

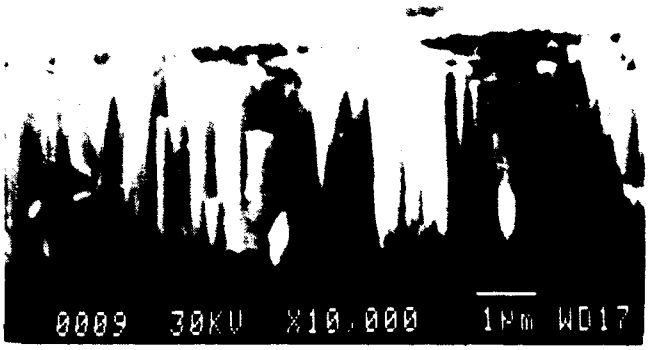


Figure 1. SEM micrograph showing the cross section of a PLT/PZT film on a glass substrate.

X-ray Diffraction

X-ray diffraction patterns were obtained on a Scintag theta-theta powder diffractometer using Cu-Kα radiation at a scan rate of 2°/min. Background subtraction and $K\alpha_2$ stripping were performed using the accompanying software. Line positions were determined by fitting the diffraction peaks with a split Pearson VII profile function.

Ferroelectric and Dielectric Measurements

Film samples with an ITO layer on one side were used to determine ferroelectric and dielectric film properties. It was not always possible to avoid coating the entire surface of the ITO during the dipping process. Access to the ITO layer for use as a bottom electrode was made possible by etching away a portion of the PLT/PZT film with a HCl-HF solution. Aluminum dots, 1mm in diameter, were evaporated onto the film surface as top electrodes. Ferroelectric ac hysteresis loops were obtained using a modified Sawyer-Tower circuit at a frequency of 1 kHz. Small signal dielectric measurements were made on a digital LCR meter.

Electrooptic Measurements

Transverse electrooptic behavior was measured using planar copper electrodes with 50μm gaps. The change in birefringent shift as a function of applied field was measured using a He-Ne laser with a wavelength of 633 nm[8]. A photoelastic modulator was used to modulate the light source while a dc voltage was applied to the film sample. A compensator was used to calibrate the system and to extinguish any contributing birefringence from the glass substrates as a result of thermal cycling.

CH3080-0-7803-0465-9/92$3.00 ©IEEE

Results and Discussion

The PZT films processed using this method were crack free with columnar growth structures typical of that shown in the scanning electron micrograph (SEM) of Figure 1.

From transverse electrooptic measurements of 1μm thick films on PLT/glass substrates it was found that the presence of memory, hysteresis and birefringence were reduced with the addition of excess PbO. To further understand this relationship, ferroelectric and dielectric properties in the longitudinal direction, X_3, were compared to electrooptic properties observed in the planar direction, X_1. Electrode configuration and directional references are shown in Figure 2. The results of this analysis are tabulated in Table I for 3 μm thick PZT films containing 0 and 4 mol% excess PbO deposited onto both PLT/glass and PLT/sapphire substrates. An additional film on sapphire was processed without a buffer layer to compare the effects of grain size. The growth of the PZT films was not significantly influenced by the ITO layer as shown in the XRD pattern of Figure 3. However, low processing temperature and choice of buffer layer composition did promote strong (100) orientations with $I_{(100)}/I_{(110)}$ = 4.5:1 as compared to 0.15:1 for the more randomly oriented film without a buffer layer. Stronger orientation was generally developed on the side without ITO.

The effects of excess PbO were similar for films on both glass and sapphire. Ferroelectric hysteresis loops and their corresponding electrooptic curves are shown in Figures 4 and 5. As mentioned earlier, hysteresis in the ferroelectric loops and electrooptic curves was reduced, along with reductions in coercive field and effective birefringe. At the same time, however, polarization and dielectric permittivity were increased. The only parameter which was not affected was the dissipation factor, tan ∂. The contrasting behavior of increased polarization in the longitudinal direction with limited field-induced birefringence in the transverse direction, indicate a film behavior strongly dependent on direction of measurement.

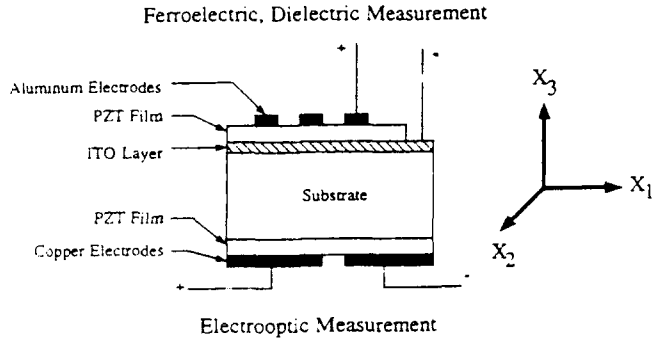


Figure 2. Ferroelectric and dielectric measurements were made in the longitudinal direction, X_3, while electrooptic measurements were made in the transverse direction, X_1.

X-ray diffraction analysis indicates that a phase transformation and tensile strain accompany the incorporation of excess PbO into the PZT perovskite structure. Single phase PZT films containing 0 mol% excess PbO crystallized into a rhombohedral structure as shown in Figure 6. A second phase was observed with the addition of 1 mol% PbO. Based on the location of the peaks at $2\theta \approx 22$ and 29, a likely identification would be the massicot phase of PbO[9] which is the stable form above 489° C. As the excess PbO content was increased to 3 mol% the intensity of the PbO peaks diminished. At 4 mol% these peaks become barely distinguishable with the apparent formation of peaks at $2\theta \approx 21.4$ and 21.8. This transformation can be more clearly seen in the fitted (100) profiles of Figure 7. The triplet peak splitting occurs throughout the diffraction pattern in accordance with the coexistence of a rhombohedral and tetragonal perovskite structure[10,11]. The observed c/a ratio of 1.02 is consistant with that of tetragonal phases in this compositional region. An increase in the interplanar $d_{(100)}$-spacing perpendicular to the films surface shown in Figure 7, is indicative of a planar compressive strain developed in the rhombohedral phase coincident with the accommodation of the excess PbO. The longitudinal tensile strain of $\Delta d/d \approx 3 \times 10^{-3}$, greater than the fracture limit of most crystalline materials, is believed responsible for the anisotropic behavior of the film on a macroscopic level. At this point, there is not enough

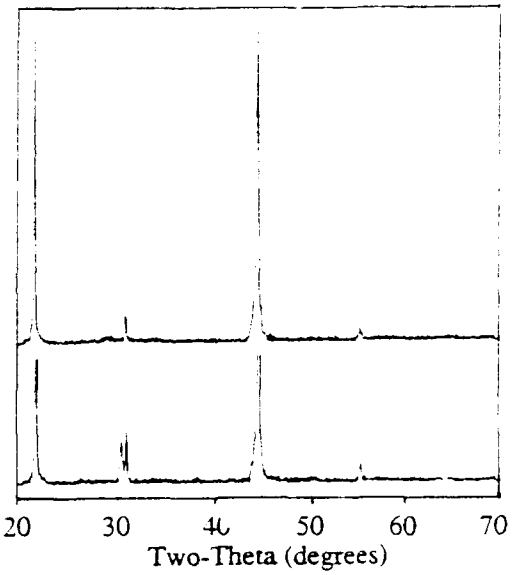


Figure 3. XRD patterns of PLT/PZT films on glass substrates. (top) without ITO, (bottom) with ITO

information to determine if the tetragonal phase has predominately compositional or structural origins. It is conceivable that tensile stresses placed in the (100) direction of a rhombohedral structure could produce tetragonal symmetry. In which case, the preferred (100) orientation could further enhance the anisotropy.

Rhombohedral PLZT ceramics are characterized by their stress sensitivity and ability to withstand large tensile strains through ferroelastic switching[12]. When under the influence of an applied field, either electrical or mechanical, the PLZT ceramics respond through a combination of polarization switching and structural phase changes leading to domain alignment. From electrooptic measurements of thin ceramic plates placed in a strain-biased mode, Maldonado and Meitzer [13] found that the direction of spontaneous polarization was influenced by preferential domain alignment parallel to a tension axis, thereby increasing the value of $\langle P_R^2 \rangle$ as compared to the polarization in a perpendicular direction. In application to the PZT films, strain-induced domain ordering in the X_3 direction depletes the number of domains available for switching in response to an applied field in the X_1 direction. Since the macroscopic birefringence, Δn, is directly proportional to $\langle P_R^2 \rangle$, birefringent shift

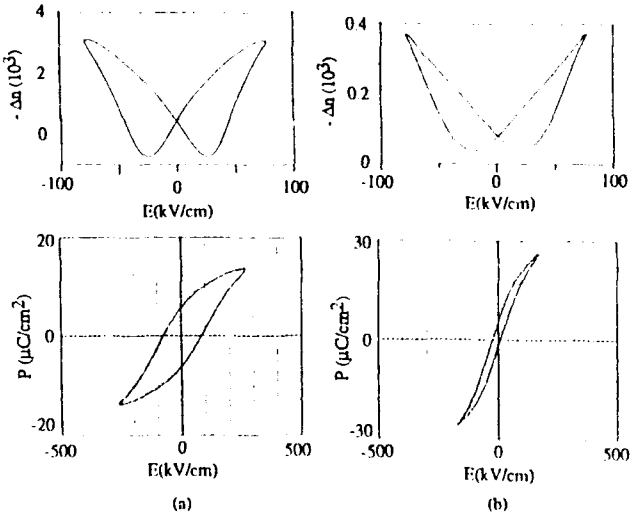


Figure 4. Electrooptic curves and ferroelectric hysteresis loops for PLT/PZT films on glass substrates. (a) 0 mol% excess PbO, (b) 4 mol% excess PbO

Table I. Ferroelectric, dielectric and electrooptic data obtained for PZT films on glass and sapphire substrates.

Substrate	excess PbO (mol%)	E_C (kV/cm)	P_R ($\mu C/cm^2$)	P_S ($\mu C/cm^2$)	tan δ (%)	$-\Delta n$ (10^3) (80 kV/cm)	ε
PLT/sapphire	0	66.5	2.9	3.0	0.089	3.88	112
PLT/sapphire	4	32.0	10.25	20.0	0.086	0.64	224
PLT/glass	0	67.5	5.75	6.0	0.079	3.05	124
PLT/glass	4	14.0	3.5	18.0	0.089	0.37	292
sapphire	4	32.0	14.0	25.0	0.125	5.82	459

in the transverse mode is minimized.

The level of optical transparency in the films varied with excess PbO content. At 0 mol% PbO the films appeared very cloudy. At 4 mol% PbO an average transmission of 60% was observed for films on glass in the wavelength range of 520-800nm. The maximum transmission of the bare substrate was 70%. Microscopic investigation did not reveal any observable reason for the cloudiness. The scattering of light in a polycrystalline material is caused by discontinuities in the index of refraction at grain boundaries and domain walls. When the domains are randomly oriented, the change in refractive index from one domain to another is large and the light is scattered. When the domains are aligned the change in refractive index is smaller and the transmission of light is increased. This could explain why the addition of excess PbO improves the film optical transparency.

The slimmer ferroelectric and electrooptic curves observed for the films with high lead content may be attributable to the coexistence of a rhombohedral and tetragonal phase through improved switching capabilities independent of direction. However, other factors such as grain size could also have an influence. The planar grain size of films processed with a PLT buffer layer was < 1μm compared to 5 μm without a buffer layer. The greater birefringence observed in Figure 8 for the unbuffered film could be attributed to grain size effects since larger grains are less subject to grain boundary pinning allowing for more flexible domain movement. Grain size in the longitudinal direction, X_3, was not determined but should be less dependent on the use of a buffer layer since growth is limited by single layer film thickness and surface effects. Values of coercive field and polarization are very similar for PZT films containing 4 mol% excess PbO on sapphire with and without a buffer layer in support of a similar grain size in the thickness direction. However, without a buffer layer the dielectric constant is larger, approaching the bulk value with a corresponding dissipation factor. This effect could result from microstructural changes occurring with film thickness and is currently under investigation.

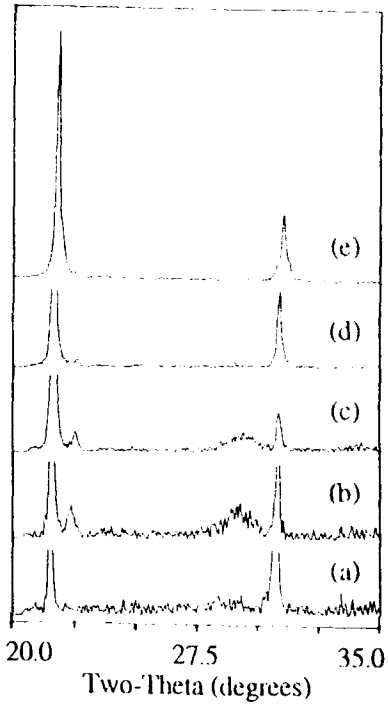


Figure 6. XRD patterns of PLT/PZT films with 0 to 4 mol% excess PbO deposited onto glass substrates. (a) 0 mol%, (b) 1 mol%, (c) 2 mol%, (d) 3 mol%, (e) 4 mol%

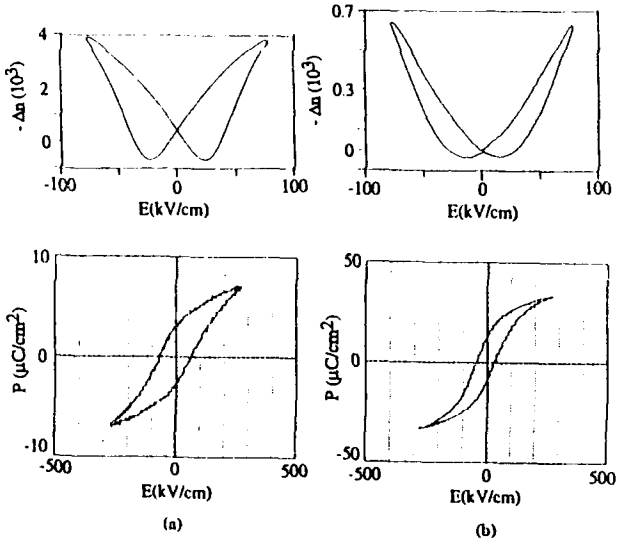


Figure 5. Electrooptic curves and ferroelectric hysteresis loops for PLT/PZT films on sapphire substrates. (a) 0 mol% excess PbO, (b) 4 mol% excess PbO

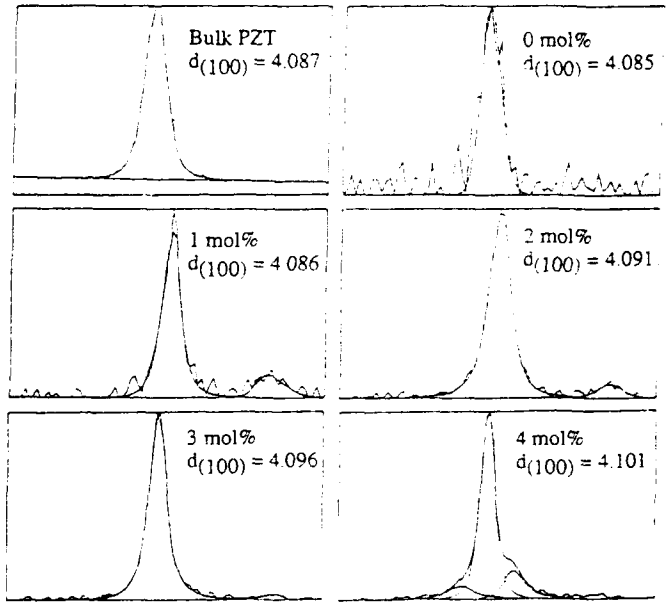


Figure 7. Fitted (100) profiles of bulk PZT and PLT/PZT films deposited onto glass substrates. Interplanar $d_{(100)}$-spacings are given as a function of excess PbO addition.

In general, the film values of remanent polarization, coercive field and dielectric constant differ from the bulk values of P_R = 40 $\mu C/cm^2$, E_C = 13 kV/cm and ϵ = 650. These discrepancies are the result of many influencing factors such as stoichiometry, defect structure, grain size, thermal stess, measurement technique, etc., including the use of ITO as a bottom electrode. Wu and Sayer[3] proposed that a non-ferroelectric (NF) PbO-rich layer is generated at the ITO/film interface through the diffusion of Pb into the glass substrate. The NF phase has a very low dielectric constant which may affect the ferroelectric behavior of the bulk of the film. In this study, an unidentified peak does occur in the XRD patterns for the ITO/glass substrates shown in Figure 3. This peak does not appear in the patterns of ITO/sapphire and could indicate some type of reaction between the glass substrate and film. The extent to which the ITO electrodes may alter the measured film values is uncertain.

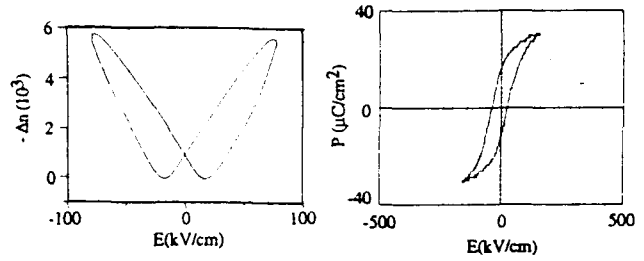


Figure 8. Electrooptic curve and ferroelectric hysteresis loop for PZT film containing 4 mol% excess PbO on a sapphire substrate.

Conclusion

A relationship between the addition of excess PbO and anisotropic film behavior was presented for PZT films on glass and sapphire substrates. Large tensile strains and the formation of a tetragonal phase upon incorporation of PbO into the rhombohedral structure produced directionally dependent properties in the film. The measurement of ferroelectric and dielectric properties in a direction parallel to the tension axis indicated an increase in polarization with PbO content while birefringence in the perpendicular direction was reduced. This effect was attributed to preferential domain alignment and crystallographic orientation. The coexistence of a rhombohedral and tetragonal phase was also thought to be a factor in reducing hysteresis and memory effects.

Acknowledgements

The authors would like to thank Feiling Wang for his assistance in obtaining the electrooptic data and helpful discussions. This work was supported by a grant from Eastman-Kodak.

References

[1] S. B. Desu, C. H. Peng, L. Kammerdiner and P. J. Schuele,"Size Effects in Sputtered PZT Thin Films", Mat. Res. Soc. Symp.Proc., vol. 200, pp. 319-324, 1990.

[2] Y. Y.•Tomashpolski and M. A. Sevostianov, "Size Phenomena in Ferroelectric Vacuum Deposits", Ferroelectrics, vol. 13, pp. 415-417, 1976.

[3] Zheng Wu and Michael Sayer, "Properties of Sol Gel Processed PLZT (2/54/46) Films on Indium Tin Oxide", in Proceedings of the 7th Symp. Appl. Ferroelectrics, Urbana - Champaign, Ill., pp. 677-680, June 6-8 1990.

[4] G. H. Haertling, "Dielectric and Electrooptic Properties of Acetate Derived PLZT X/65/35 Thin Films", (to be published).

[5] K. R. Udayakumar, J. Chen, S. B. Krupanidhi, and L. E. Cross, "Sol-Gel Derived PZT Thin Films for Switching Ferroelectrics, Urbana - Champaign, Ill., pp.741-743, June 6-8 1990.

[6] K. D. Preston and G. H. Haertling, "Microstructural Investigation of Acetate-Derived PLZT Films", Integrated Ferroelectrics, vol.1, no.1, pp. 89-98, 1992.

[7] S. L. Swartz, S. J. Bright, P. J. Melling, and T. R. Shrout, "Sol-Gel Processing of Composite $PbTiO_3$/PLZT Thin Films", Ferroelectrics, vol. 108, no. 71, pp. 1677-1682, 1990.

[8] K. D. Preston and G. H. Haertling, "Comparison of Electro-optic Lead Lanthanum Zirconate Titanate Films on Crystalline and Glass Substrates", Appl. Phys. Lett., vol. 60, no. 23, pp. 2831-2833, June 1992.

[9] JCPDS - International Center for Diffraction Data, 1601 Park Lane, Swathmore, PA 19081-2389, card #38-1477.

[10] P. GR. Lucuta, Fl. Constantinescu, and D. Barb, "Structural Dependence on Sintering Temperature of Lead Zirconate-Titanate Solid Solutions", J. Am. Ceram. Soc., vol. 68, no. 10, pp. 533-537, October 1985.

[11] P. Ari-gur and L. Benguigui, "Direct Determination of the Coexistence Region in the Solid Solutions $Pb(Zr_x Ti_{1-x})O_3$", J. Phys. D: Appl. Phys., vol. 8, pp. 1856-1862, 1975.

[12] A. H. Meitzler and H. M. O'Bryan, Jr., "Ferroelectric Behavior When Subjected to Large Tensile Strains", Appl. Phys. Lett., vol. 19, no. 4, pp. 106-108, August 1971.

[13] Juan R. Maldonado and Allen H. Meitzler, "Strain-Biased Ferroelectric Photoconductor Image Storage and Display Devices", in Proceedings of the IEEE, vol. 59, no. 3, pp. 368-382, March 1971.

Pyroelectric, Electrooptics

FERROELECTRIC COPOLYMER AND IR SENSOR TECHNOLOGY APPLIED TO OBSTACLE DETECTION

F. Bauer*, J.J. Simonne** and L. Audaire***

* Institut de Recherche Franco-Allemand
Saint-Louis F-68301-France
** Laboratoire d'Automatique et d'Analyse des Systèmes du CNRS
du CNRS-Toulouse F-31077-France
*** Laboratoire Infra Rouge du LETI/CENG
Grenoble-F-38041-France

Abstract

The design of an integrated sensing system including a Silicon structure and a P (VDFO.7-TRFEO.3) copolymer is presented.
The monolithic integrated sensor is based on :
- a pyroelectric thermal P(VDF.7-TRFEO.3) copolymer detector,
- a polyimide microelectronic photoresist for thermal insulation,
- a standard process Silicon read-out circuit.
The present paper describes studies undertaken to realize the system. Especially the ISL poling process is presented. Electrical characteristics as well as pyroelectric characteristics are presented.
Intrinsic ferroelectric properties of the copolymer used are given.

1-Introduction

The outstanding piezoelectric properties of polar polymers like PVDF may partly explain the less attention given over the last ten or twenty years to its pyroelectric properties; in addition, its characteristics in this field could appear rather weak with respect to its main challengers : polycrystal ceramics and organic compounds, which present a much higher pyroelectric coefficient. However, this situation has moved recently in favor of PVDF in infrared detection, with the huge impulse given to the world of detectors by the introduction of microelectronics in their technology to imple-ment integrated sensors, and the ability to apply the IC technics to tailor a PVDF sensor coupled with a read out Silicon circuit. In addition, the small magnitude of the infrared signals detected, mixed with a hight level background noise,has imposed the development of matrix arrays rather than unit cells.

These conditions have provided a new interest to PVDF, due to its good chemical characteristics.

In a first step, a 8 x 8 matrix array [1] was elaborated on PVDF, and glued afterwards successfully on a Silicon chip. This procedure, well defined in a laboratory, may impede a low cost-large scale development in industry.

The use of a VDF-TrFE copolymer, which directly crystallizes in a beta phase, appears as a promising substitute to PVDF, as it is available under a liquid form and allows an easier technology to implement the hetero-structure, the other advantage being to present higher pyroelectric performance than PVDF.

The result has been the elaboration of a 32 x 32 focal plane starring array, which is investigated to be used in a multisensing system dedicated to obstacle detection in automotive.

2-The copolymer I.R.Sensor

The infrared sensor is a copolymer starring array associated witch a focal plane, coupled to a signal processing electronic system integrated in a Silicon substrate.

This heterostructure basically includes.

- a copolymer layer P(VDF, 0.7-TrFE, 0.3) allowing the pyroelectric detection after absorption of the I.R. incident radiation; converted into a temperature variation, it will induce a pyroelectric signal between the electrodes deposited above and underneath the copolymer.
- a Silicon substrate which is provided with the readout circuit processed in a 1.2 µm C-MOS technology. The analog electronic signal processing operates at the level of each pixel; integrated into the Silicon chip, it is connected to a serie of address and digital multiplexing elements. The interface between the focal plane and the outer computer, included in the chip, is carried out through gate-arrays analog/digital converters. [2]
- a thermal insulating film, sandwiched between the copolymer and the Silicon support, which is presently made out of polyimide.

The electrical connexion between the copolymer and the Silicon substrate is achieved with a via through the polyimide layer.

3- Technology

The specific Silicon integrated circuit is processed through a standard Full Wafer technology based on deposition, chemical, plasma and reactive ion etching photolithography technics of microelectronic. The different steps of metallization use either Joule evaporation or sputtering, depending on the nature of the metal selected : Aluminum, NickelChromium, Chromium-Gold, or Platinum. Polyimide and copolymer are deposited by spin coating. The thickness of the thermal insulator is 10 µm in our application, while the thickness of the copolymer is adjusted between 4 and 10 µm and depends on the read-out operation frequency (fig.1). The annealing procedure used in the polymerization of the pyroelectric material must avoid thermal shocks to prevent any cracks which should appear by interaction between copolymer and the metal deposited upon it in the following metallization step. This is shown on the next figures where a temperature slope is used to anneal and to cool the VDF-TrFE layer (fig. 2-a), and a temperature step is used instead in the second case (fig. 2-b).
Photolithography is used to elaborate the final step of the copolymer 32 x 32 matrix array. The pixel size is 100 µm x 100 µm.

CH3080-0-7803-0465-9/92$3.00 ©IEEE

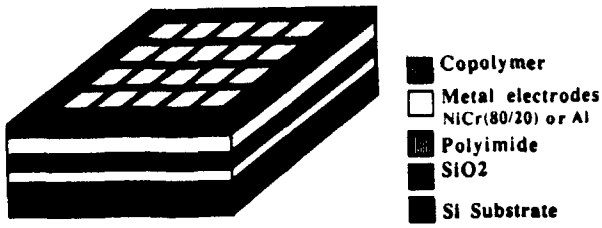


fig.1 Schematic Integrated copolymer/thermal insulator/Silicon heterostructure.

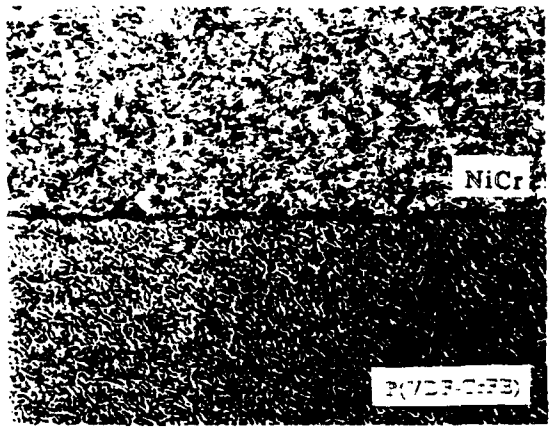


fig.2-a Top view of the copolymer after NiCr deposition when a temperature ramp has been used in the polymerization process. NiCr has been removed from the lower part.

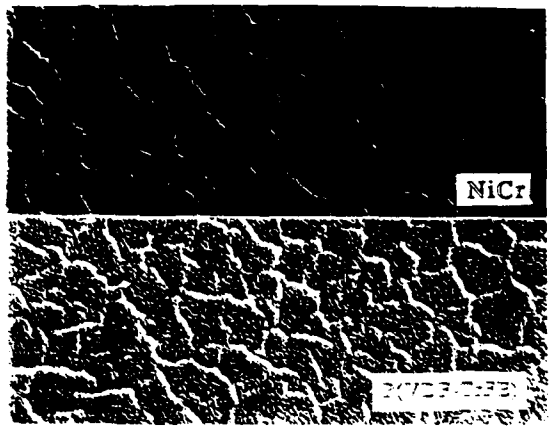


fig.2-b Same view as fig 2-a, when a temperature step is used in the polymerization process of VDF-TrFE.

4- The poling procedure

Any poling method applied to PVDF can be transposed to VDF-TrFE as well. The standard procedures use either the Corona or the plasma effect, or require the application of a d.c. electric field at high temperature (between 50°C to 100°C) applied to the metal electrodes deposited on both surfaces of the pyroelectric material. However, we have much preferred to use the method developed by F. BAUER [3] [4] where a very low frequency electric field (0.1 Hz) is applied to the material at room temperature, allowing to generate many times the hysteresis loop while the magnitude of the field is increased continuously up to a limit slightly under the breakdown condition of the material (10^8 V/m). This operation allows to drain out ions and space charges which might impede the rotation of the dipoles of the crystalline phase, and insures the stability of the polarization and the reproducibility of the procedure.

By substracting the resistive and the capacitives parts from the total current, we perform directly, after integration, the measurement of the polarization. A 6 $\mu C/cm^2$ to 8 $\mu C/cm^2$ remanent polarization has been achieved (fig.3).

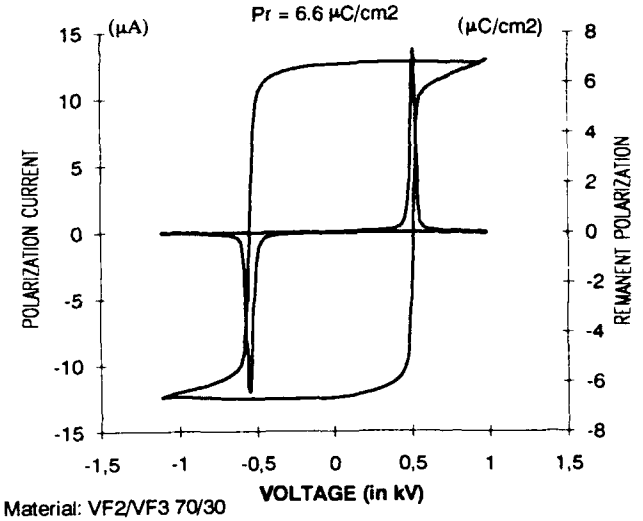


fig.3 Hysteresis and polarization current measurements performed on the array.

It is important to notice that, with PVDF, the polarization is applied before gluing the film on the Silicon chip. With VDF-TrFE, poling of the sample is somewhat more delicate, because it is performed after the elaboration of the whole heterostructure where the read-out and signal processing circuits have been already processed in the Silicon substrate. However, using adequate protective circuits, we have shown that the procedure could be conducted successfully that way.

5-Characterization

Pyroelectric response of a pixel

As the purpose of this paper is more material than system performance oriented, characterization of the matrix presented here will be focused to the copolymer characteristics. The pyroelectric response of a pixel is investigated with a temperature controlled black body, emitting a radiation mechanically chopped at low frequency, using an equipment similar to that used for PVDF array characterization and described in ref. [5]. As shown in fig. 4, a typical curve giving the evolution of the pyroelectric current sensitivity, limited to 700 Hz, exibits a behaviour difference with respect to the reponse of a "free" material, brought about by the heterostructure. In the same way, the unusual voltage response observed in fig. 5, is due to the very low electrical

cut off frequency of the measuring circuit (6 Hz). The effect of temperature on the pyroelectric current (fig. 6) is consistent with the pyroelectric coefficient variation with temperature.

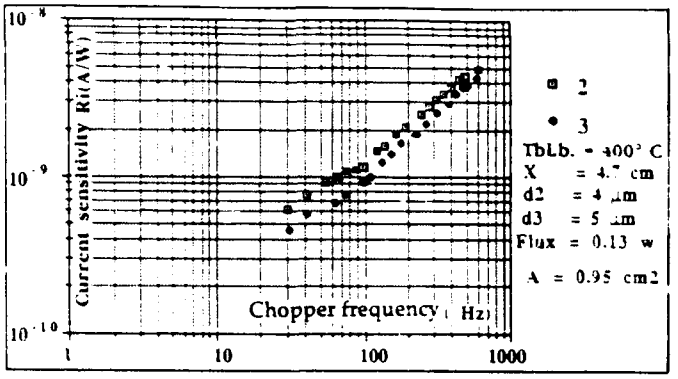


fig. 4 Pyroelectric current sensitivity versus chopper frequency. The distance X between black body and copolymer is 4.7 cm.

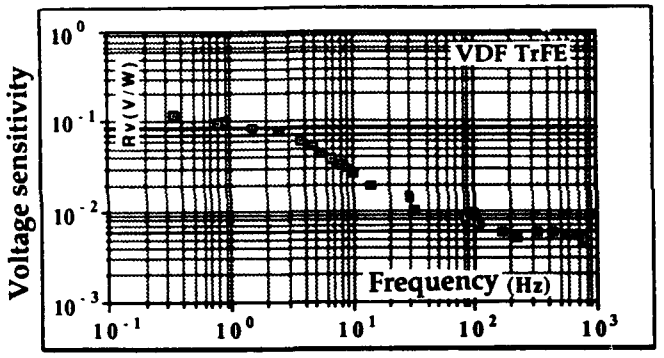


fig.5 Pyroelectric voltage sensitivity versus chopper frequency. Same data as fig.4, except X=7.8 cm.

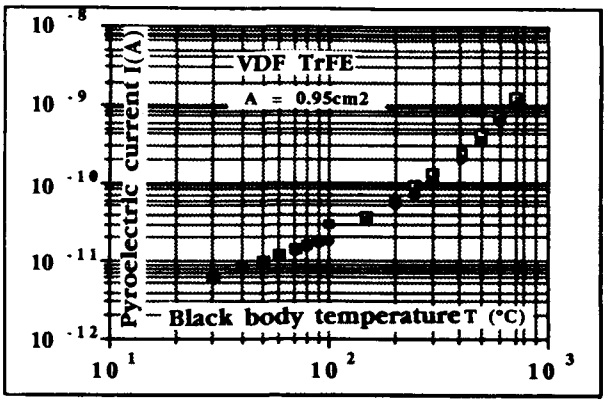


fig.6 Black body temperature effect on the pyroelectric response. X=4 cm, f=217 Hz.

Pyroelectric coefficient

The evaluation of the pyroelectric coefficient p has been achieved by a direct measurement based on dielectric absorption of the material which is heated with a high frequency signal (500 KHz) during a limited period of time (6.5 ms) [6].

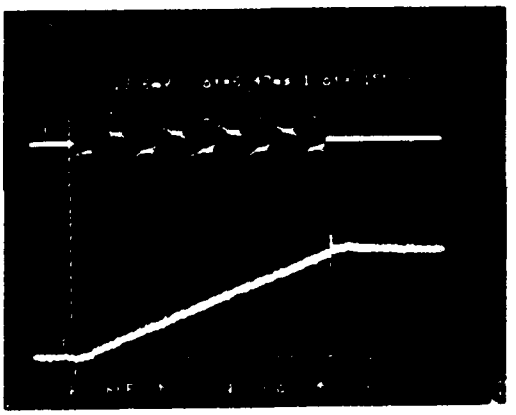
We observe a linearly increase of the pyroelectric voltage V during the heating (fig. 7), p being proportional to his voltage shope according to

$$p = \frac{d \cdot C_v}{U^2 \cdot 2\pi f \cdot tg\delta} \cdot \frac{dV}{dt}$$

Where d is the copolymer thickness, Cv the volumetric specific heat, U and f are respectively the magnitude and the frequency of the voltage applied to the pixel, δ the loss angle.

With d = 5 µm ; Cv = 2.34 J/cm^3. K ; U = 5 v. ; f = 500 KHz ; tg $\delta = 10^{-2}$ and (dV/dt) = 13.6 / 6.47 we get a pyroelectric coefficient p =3.1 nC/cm^2.K.

This value confirms that the pyroelectric performance of VDF-TrFE is not that much weakened by the technology. A possible improvement will relie on a reduction of the stress at the interface with the thermal insulator by a tight selection of this material.



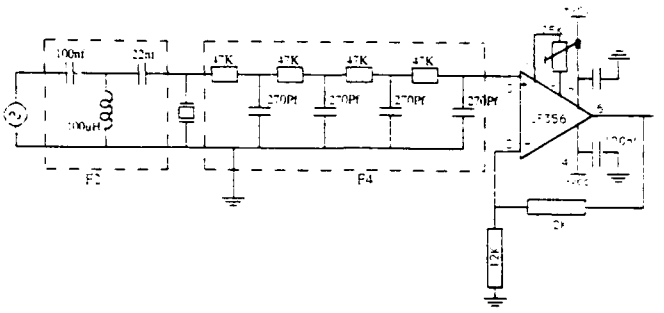


fig. 7 Pyroelectric voltage response due to H.F. heating and corresponding measuring circuit. heating time: 6.47 ms; f= 500 KHz; DV= 13.6 mV.

6- Application

A prototype infra red sensor using a 32 x 32 copolymer focal plane array has been elaborated (fig. 8). After the development of the hybrid technology [7], it marks a new step in the research of a low cost - large scale I.R. sensors applied to civilian applications, with the adaptation of the I.C. technology to polymer materials (reticulation, via), and the feasibility of a poling procedure applied across the whole heterostructure. This investigation is conducted within the European Prometheus-Pro Chip program dedicated to increase the safety in road traffic. It is a part of a multisensing system, used as a passive I.R. obstacle detector and is intended to provide information together with other active I.R. and microwave sensors to an on-board computer in a car.

Thermal imager is another type of application opened to this technology, with an extension of the array to a 128 x 128 elements, already available.

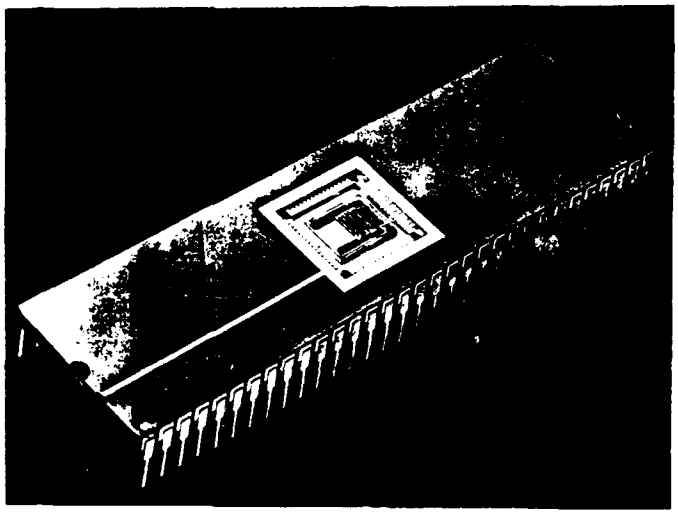


fig.8 View of the I.R. sensor.

7-Acknowledgement

The authors acknowledge the work of their colleagues at LETI/SLIR, ISL and LAAS. They wish to thank J.P. Beconne and A. Mahranne, research workers on the subject for their contribution, and the support given by Prometheus.

8-References

[1] V.V. Pham, D. Estève, E. Bousbiat, J. Farré, R. Leguerre, J.J. Simonne.
"Parameters controlling the design of a pyroelectric PVDF matrix array"
SPIE Vol 1027 Image Processing II, pp. 35-39 (1988).

[2] L. Audaire, J. Cluzel, D. Marion, P. Nicolas, P. Fantigny.
The "random access memory" concept applied to the infrared focal plane. SPIE Vol 865 FPA Technology and Applications, pp. 45-51 (1987).

[3] F. Bauer. French patent 8221025.

[4] F. Bauer. US patent 4611260.

[5] A. Reynes, D. Esteve, J. Farré, V.V. Pham and J.J. Simonne.
"Elaboration and prorerties of a linear pyroelectric PVDF FPA". SPIE Vol 865 FPA Technology and Applications, pp. 40-44 (1987).

[6] NP Hartley, PT Squire, EM Putley
"A new method of measuring pyroelectric coefficients"
J. of Physics E Vol 5 Scientific Instruments, pp. 787-789 (1972).

[7] See for inst . R. Watton.
"Ferroelectric detection and imaging".
Proc. 6 th IEEE-ISAF'86 pp. 172-181 (1986)

THE ANALYTIC REPRESENTATION OF THE EFFECTIVE NONLINEAR COEFFICIENTS FOR BIAXIAL CRYSTALS IN THE COORDINATE PLANES

S.W. XIE, W.Y. JIA, P.J. WANG, Y.L. CHEN

Applied Physics Department, Shanghai Jiao Tong University,
Shanghai 200030, China

Abstract

The paper presents the analytic expressions of the effective second order nonlinear coefficients d_{eff}^{I} and d_{eff}^{II} for five groups of biaxial crystals in the coordinate planes of optical ellipsoid. Using these expressions, the coefficient value can be derived easily without numerical calculation for every point in the phase matching curves.

Keywords: biaxial crystal, analytic expression, effective nonlinear coefficient

Introduction

Recently, with the development of new nonlinear materials, more and more biaxial crystals are used in second order nonlinear optical interactions, such as second harmonic generation(SHG), sum frequency(SF), difference frequency(DF) and optical parametric oscillation(OPO). In order to get the optimum phase matching angles, we have to compute the phase matching curves and calculate the effective nonlinear coefficient for every point in the curves either. Sets of specific computer programs have to be developed, but they are complex to the users. In fact, whenever we use the biaxial crystals, the light propagation directions are usually in optic principal axial planes. For example, in KTP crystal, the optimum phase matching direction of SHG from 1.064μm to 0.532μm is in the plane of xoy, and the optimum phase matching direction of OPO is in the plane of xoz or xoy, etc. . Therefore, we can simplify the effective nonlinear coefficient expressions in optic axial planes. Using brief calculation, the effective nonlinear coefficient value will be obtained immediately.

The Expressions of the Effective Nonlinear Coefficients in the Coordinate Planes of Optical Ellipsoid

From paper[1], it is obvious that in second order nonlinear optical interaction, such as SHG, SF, DF and OPO, the expressions of effective nonlinear coefficients of type I phase matching are all the same, which are

$$d_{eff}^{I}(\theta,\phi,\delta)=(a_i^{e2})^{T}(d_{i\alpha})(a_j^{e1}a_k^{e1}) \tag{1}$$

Same as the expressions of type II phase matching, which are

$$d_{eff}^{II}(\theta,\phi,\delta)=d_{eff}^{IIA}(\theta,\phi,\delta)=d_{eff}^{IIB}(\theta,\phi,\delta)$$
$$=(a_i^{e2})^{T}(d_{i\alpha})(a_j^{e1}a_k^{e2}) \tag{2}$$

where θ, ϕ represent the propagation direction in the principal refractive indices coordinate, δ represents the polarization direction of correspondent electric field, e1 and e2 represent the polarizations of slower light and faster light respectively. Matrixes of $(a_i^{e2}),(a_j^{e1}a_k^{e1}),(a_j^{e1}a_k^{e2})$ are given in paper[2]. Both formula(1) and formula(2) are used in the optical ellipsoid coordinate system, which is same with the principal refractive indices coordinate system o-xyz. Therefore, the nonlinear optical coefficient matrix $(d_{i\alpha})$ must be calculated in this system either. But usually, $(d_{i\alpha})$ is decided by the crystal symmetry. That is, it is related to the crystal physical principal axial coordinate system O-XYZ, which is also different from the crystallography axial coordinate system o-abc. Therefore, the formations of $(d_{i\alpha})$ in the system of physical principal axial coordinate must be transformed into the formations in the system of principal refractive indices coordinate. Considering that, there are 6 possible correlations between the axes of x,y,z and axes of X,Y,Z. For five biaxial crystal groups, 30 different expressions of $(d_{i\alpha})$ are possible. $(d_{i\alpha})$ is a 3×6 matrix. It can be written as a three order tensor, which is

$$\chi'_{ijk}=T_{il}T_{jm}T_{kn}\chi_{lmn} \tag{3}$$

where T represents the transformation matrix between the two coordinate systems. In Table 1, 30 kinds expressions of $(d_{i\alpha})$ are given in detail. In principal refractive indices coordinate plane, the matrixes of $(a_i^{e2}),(a_j^{e1}a_k^{e1}),(a_j^{e1}a_k^{e2})$ can be simplified. So do the effective nonlinear coefficient expressions, which are got from Eq.(1) and Eq.(2) . Following, we will give the results.

1)d_{eff}^{I} for type I phase matching

(1)in xoz plane, $\phi=0$, Ω is the optic axial angle

$\theta<\Omega$, $\delta=\pi/2$,

$$d_{eff}^{I}=(-\cos\theta\ 0\ \sin\theta)(d_{i\alpha})\begin{pmatrix}0\\1\\0\\0\\0\\0\end{pmatrix} \tag{4}$$

$\theta>\Omega$, $\delta=0$,

$$d_{eff}^{I}=(0\quad 1\quad 0)(d_{i\alpha})\begin{pmatrix}\cos^2\theta\\0\\\sin^2\theta\\0\\-\sin2\theta\\0\end{pmatrix} \tag{5}$$

(2)in yoz plane, $\phi=\pi/2$, $\delta=0$

$$d_{eff}^{I}=(-1\quad 0\quad 0)(d_{i\alpha})\begin{pmatrix}0\\\cos^2\theta\\\sin^2\theta\\-\sin2\theta\\0\\0\end{pmatrix} \tag{6}$$

(3)in xoy plane, $\theta=\pi/2$, $\delta=0$

CH3080-0-7803-0465-9/92$3.00 ©IEEE

$$d_{eff}^{I}=(-\sin\phi\ \cos\phi\ 0)\ (d_{1\alpha})\begin{pmatrix}0\\0\\1\\0\\0\\0\end{pmatrix} \quad (7)$$

2)d_{eff} for type II phase matching

(1)in xoz plane, $\phi=0$, Ω is the optic axial angle $\theta<\Omega$, $\delta=\pi/2$,

$$d_{eff}^{II}=(-\cos\theta\ 0\ \sin\theta)\ (d_{1\alpha})\begin{pmatrix}0\\0\\0\\\sin\theta\\0\\-\cos\theta\end{pmatrix} \quad (8)$$

$\theta>\Omega$, $\delta=0$,

$$d_{eff}^{II}=(\ 0\ \ 1\ \ 0\ )\ (d_{1\alpha})\begin{pmatrix}0\\0\\0\\-\sin\theta\\0\\\cos\theta\end{pmatrix} \quad (9)$$

(2)in yoz plane, $\phi=\pi/2$, $\delta=0$

$$d_{eff}^{II}=(\ -1\ \ \ 0\ \ \ 0\ )\ (d_{1\alpha})\begin{pmatrix}0\\0\\0\\0\\\sin\theta\\-\cos\theta\end{pmatrix} \quad (10)$$

(3)in xoy plane, $\theta=\pi/2$, $\delta=0$

$$d_{eff}^{II}=(-\sin\phi\ \cos\phi\ 0)\ (d_{1\alpha})\begin{pmatrix}0\\0\\0\\-\cos\phi\\\sin\phi\\0\end{pmatrix} \quad (11)$$

Putting $(d_{1\alpha})$ matrix of every group and every correlation in Table 1 into Eq.(4)--(11), we will get simple analytic expressions of d_{eff}^{I} and d_{eff}^{II} for five groups of the biaxial crystals in principal refractive indices coordinate planes. Table 2 gives the expressions of d_{eff}^{I} and d_{eff}^{II} for biaxial crystals of orthorhombic group mm2, which are used often. The expressions of biaxial crystals of orthorhombic 222, monoclinic 2, monoclinic m and triclinic 1 can be obtained in similar way. Considering the length of the paper, we'll not provide in detail.

Experiment

The experiment studies of SHG at 1.064μm were performed in two KTP crystals with same thickness. One was cut with a phase matching angle of $\phi=90^{\circ}$, $\theta=67.8^{\circ}$. Another was cut with $\theta=90^{\circ}$, $\phi=21.3^{\circ}$. Their propagation directions were in the yoz plane and xoy plane respectively. And both of them are in the principal refractive indices coordinate planes. From the experiment, we get the conclusion that the SHG efficiency of KTP crystal is higher on the condition that the light direction is in xoy plane.

In theory, KTP crystal is of orthorhombic mm2 group. Its correlations between the axes of x,y,z and axes of X,Y,Z are x=X, y=Y, z=Z. From Table 2, we know that,

in xoy plane $d_{eff}^{II}=-d_{15}\sin^2\phi-d_{24}\cos^2\phi$,

in yoz plane $d_{eff}^{II}=-d_{15}\sin\theta$,

Put $\phi=21.3^{\circ}$, $\theta=67.8^{\circ}$, $d_{15}=6.1\times10^{-12}$(m/v), $d_{24}=7.6\times10^{-12}$(m/v)[5] into equations given above, we will obtain that

in xoy plane $d_{eff}^{II}=-7.402\times10^{-12}$(m/v),

in yoz plane $d_{eff}^{II}=-5.648\times10^{-12}$(m/v).

That is to say, the SHG efficiency in xoy plane is higher. It coincides with the experiment.

Thus, we get the simple analytic expressions of the effective nonlinear coefficients for five groups of biaxial crystals in the optical ellipsoid coordinate planes. They are convenient for the users.

References

[1] S.W.Xie et.al., Acta Optica Sinica, 3,8(1983)697.
[2] S.W Xie et.al., Journal of Shanghai Jiao Tong Univ., 1(1982)37.
[3] G.M.Wang et.al., Acta Optica Sinica, 5,5(1985)416.
[4] M.H.Jiang, Crystal Physics. Shandong Science & Technology Press, (1980).
[5] F.C.Zumsteg et.al., Journal of Applied Physics, 47,11 (1976) 4980.
[6] T.Y.Fan et.al., Applied Optics, 26,12 (1987) 2390.

Table 1. Second Order Nonlinear Optical Coefficient Matrixes for Biaxial Crystals in the Optical Ellipsoid Coordinate System

NUMBER	I	II	III	IV	V	VI
OPTICAL ELLIPSOID AXES &CRYSTAL PHYSICAL AXES	x=X y=Y z=Z	x=Y y=X z=Z	x=Z y=Y z=X	x=Z y=X z=Y	x=X y=Z z=Y	x=Y y=Z z=X
TRANSFORMATION MATRIXES	$\begin{pmatrix}1&0&0\\0&1&0\\0&0&1\end{pmatrix}$	$\begin{pmatrix}0&1&0\\1&0&0\\0&0&-1\end{pmatrix}$	$\begin{pmatrix}0&0&1\\0&1&0\\-1&0&0\end{pmatrix}$	$\begin{pmatrix}0&0&1\\1&0&0\\0&1&0\end{pmatrix}$	$\begin{pmatrix}1&0&0\\0&0&1\\0&-1&0\end{pmatrix}$	$\begin{pmatrix}0&1&0\\0&0&1\\1&0&0\end{pmatrix}$
ORTHORHOMBIC 222 GROUP (X=a, Y=b, Z=c)	$\begin{pmatrix}0&0&0&d_{14}&0&0\\0&0&0&0&d_{25}&0\\0&0&0&0&0&d_{36}\end{pmatrix}$	$\begin{pmatrix}0&0&0&d_{25}&0&0\\0&0&0&0&d_{14}&0\\0&0&0&0&0&d_{36}\end{pmatrix}$	$\begin{pmatrix}0&0&0&d_{36}&0&0\\0&0&0&0&d_{25}&0\\0&0&0&0&0&d_{14}\end{pmatrix}$	$\begin{pmatrix}0&0&0&d_{36}&0&0\\0&0&0&0&d_{14}&0\\0&0&0&0&0&d_{25}\end{pmatrix}$	$\begin{pmatrix}0&0&0&d_{14}&0&0\\0&0&0&0&d_{36}&0\\0&0&0&0&0&d_{25}\end{pmatrix}$	$\begin{pmatrix}0&0&0&d_{25}&0&0\\0&0&0&0&d_{36}&0\\0&0&0&0&0&d_{14}\end{pmatrix}$
	Recognizing Kleinman Symmetry: $d_{14}=d_{25}=d_{36}$					1 independent element
ORTHORHOMBIC *mm2* GROUP (X=a, Y=b, Z=c)	$\begin{pmatrix}0&0&0&0&d_{15}&0\\0&0&0&d_{24}&0&0\\d_{31}&d_{32}&d_{33}&0&0&0\end{pmatrix}$	$\begin{pmatrix}0&0&0&0&d_{24}&0\\0&0&0&d_{15}&0&0\\d_{32}&d_{31}&d_{33}&0&0&0\end{pmatrix}$	$\begin{pmatrix}d_{33}&d_{32}&d_{31}&0&0&0\\0&0&0&0&0&d_{24}\\0&0&0&0&d_{15}&0\end{pmatrix}$	$\begin{pmatrix}d_{33}&d_{31}&d_{32}&0&0&0\\0&0&0&0&0&d_{15}\\0&0&0&0&d_{24}&0\end{pmatrix}$	$\begin{pmatrix}0&0&0&0&0&d_{15}\\d_{31}&d_{33}&d_{32}&0&0&0\\0&0&0&d_{24}&0&0\end{pmatrix}$	$\begin{pmatrix}0&0&0&0&0&d_{24}\\d_{32}&d_{33}&d_{31}&0&0&0\\0&0&0&d_{15}&0&0\end{pmatrix}$
	Recognizing Kleinman Symmetry: $d_{15}=d_{31}$, $d_{24}=d_{32}$					3 independent elements
MONOCLINIC 2 GROUP (Y=b, Z=c)	$\begin{pmatrix}0&0&0&d_{14}&0&d_{16}\\d_{21}&d_{22}&d_{23}&0&d_{25}&0\\0&0&0&d_{34}&0&d_{36}\end{pmatrix}$	$\begin{pmatrix}d_{22}&d_{21}&d_{23}&-d_{25}&0&0\\0&0&0&0&-d_{14}&d_{16}\\0&0&0&0&d_{34}&-d_{36}\end{pmatrix}$	$\begin{pmatrix}0&0&0&-d_{36}&0&d_{34}\\d_{23}&d_{22}&d_{21}&0&-d_{25}&0\\0&0&0&d_{16}&0&-d_{14}\end{pmatrix}$	$\begin{pmatrix}0&0&0&d_{36}&d_{34}&0\\0&0&0&d_{16}&d_{14}&0\\d_{23}&d_{21}&d_{22}&0&0&d_{25}\end{pmatrix}$	$\begin{pmatrix}0&0&0&d_{14}&d_{16}&0\\0&0&0&d_{34}&d_{36}&0\\d_{21}&d_{23}&d_{22}&0&0&d_{25}\end{pmatrix}$	$\begin{pmatrix}d_{22}&d_{23}&d_{21}&d_{25}&0&0\\0&0&0&0&d_{36}&d_{34}\\0&0&0&0&d_{16}&d_{14}\end{pmatrix}$
	Recognizing Kleinman Symmetry: $d_{14}=d_{25}=d_{36}$, $d_{23}=d_{34}$, $d_{16}=d_{21}$					4 independent elements
MONOCLINIC m GROUP (Y=b, Z=c)	$\begin{pmatrix}d_{11}&d_{12}&d_{13}&0&d_{15}&0\\0&0&0&d_{24}&0&d_{26}\\d_{31}&d_{32}&d_{33}&0&d_{35}&0\end{pmatrix}$	$\begin{pmatrix}0&0&0&0&-d_{24}&d_{26}\\d_{12}&d_{11}&d_{13}&-d_{15}&0&0\\-d_{32}&-d_{31}&-d_{33}&d_{35}&0&0\end{pmatrix}$	$\begin{pmatrix}d_{33}&d_{32}&d_{31}&0&-d_{35}&0\\0&0&0&-d_{26}&0&d_{24}\\-d_{13}&-d_{12}&-d_{11}&0&d_{15}&0\end{pmatrix}$	$\begin{pmatrix}d_{33}&d_{31}&d_{32}&0&0&d_{35}\\d_{13}&d_{11}&d_{12}&0&0&d_{15}\\0&0&0&d_{26}&d_{24}&0\end{pmatrix}$	$\begin{pmatrix}d_{11}&d_{13}&d_{12}&0&0&d_{15}\\d_{31}&d_{33}&d_{32}&0&0&d_{35}\\0&0&0&d_{24}&d_{26}&0\end{pmatrix}$	$\begin{pmatrix}0&0&0&0&d_{26}&d_{24}\\d_{32}&d_{33}&d_{31}&d_{35}&0&0\\d_{12}&d_{13}&d_{11}&d_{15}&0&0\end{pmatrix}$
	Recognizing Kleinman Symmetry: $d_{15}=d_{31}$, $d_{24}=d_{32}$ $d_{12}=d_{26}$, $d_{13}=d_{35}$					6 independent elements
TRICLINIC 1 GROUP (Z=c)	$\begin{pmatrix}d_{11}&d_{12}&d_{13}&d_{14}&d_{15}&d_{16}\\d_{21}&d_{22}&d_{23}&d_{24}&d_{25}&d_{26}\\d_{31}&d_{32}&d_{33}&d_{34}&d_{35}&d_{36}\end{pmatrix}$	$\begin{pmatrix}d_{22}&d_{21}&d_{23}&-d_{25}&-d_{24}&d_{26}\\d_{12}&d_{11}&d_{13}&-d_{15}&-d_{14}&d_{16}\\-d_{32}&-d_{31}&-d_{33}&d_{35}&d_{34}&-d_{36}\end{pmatrix}$	$\begin{pmatrix}d_{33}&d_{32}&d_{31}&-d_{36}&-d_{35}&d_{34}\\d_{23}&d_{22}&d_{21}&-d_{26}&-d_{25}&d_{24}\\-d_{13}&-d_{12}&-d_{11}&d_{16}&d_{15}&-d_{14}\end{pmatrix}$	$\begin{pmatrix}d_{33}&d_{31}&d_{32}&d_{36}&d_{34}&d_{35}\\d_{13}&d_{11}&d_{12}&d_{16}&d_{14}&d_{15}\\d_{23}&d_{21}&d_{22}&d_{26}&d_{24}&d_{25}\end{pmatrix}$	$\begin{pmatrix}d_{11}&d_{13}&d_{12}&d_{14}&d_{16}&d_{15}\\d_{31}&d_{33}&d_{32}&d_{34}&d_{36}&d_{35}\\d_{21}&d_{23}&d_{22}&d_{24}&d_{26}&d_{25}\end{pmatrix}$	$\begin{pmatrix}d_{22}&d_{23}&d_{21}&d_{25}&d_{26}&d_{24}\\d_{32}&d_{33}&d_{31}&d_{35}&d_{36}&d_{34}\\d_{12}&d_{13}&d_{11}&d_{15}&d_{16}&d_{14}\end{pmatrix}$
	Recognizing Kleinman Symmetry: $d_{14}=d_{25}=d_{36}$, $d_{15}=d_{31}$, $d_{24}=d_{32}$, $d_{23}=d_{34}$, $d_{16}=d_{21}$, $d_{12}=d_{26}$, $d_{13}=d_{35}$					10 independent elements

Table 2. d_{eff}^{I}, d_{eff}^{II} Formations of Orthorhombic mm2 Group in the Coordinate Planes

CRYSTAL KINDS	KTP LFMH LSFMH $HCOON_a$		KBs mNA	BNN KN	DSS LBO	
NUMBER	I	II	III	IV	V	VI
OPTICAL ELLIPSOID AXES &CRYSTAL PHYSICAL AXES	x=X y=Y z=Z	x=Y y=X z=Z	x=Z y=Y z=X	x=Z y=X z=Y	x=X y=Z z=Y	x=Y y=Z z=X
$(d_{i\alpha})$ FORMATIONS	$\begin{pmatrix} 0 & 0 & 0 & 0 & d_{15} & 0 \\ 0 & 0 & 0 & d_{24} & 0 & 0 \\ d_{31} & d_{32} & d_{33} & 0 & 0 & 0 \end{pmatrix}$	$\begin{pmatrix} 0 & 0 & 0 & 0 & d_{24} & 0 \\ 0 & 0 & 0 & d_{15} & 0 & 0 \\ d_{32} & d_{31} & d_{33} & 0 & 0 & 0 \end{pmatrix}$	$\begin{pmatrix} d_{33} & d_{32} & d_{31} & 0 & 0 & 0 \\ 0 & 0 & 0 & 0 & 0 & d_{24} \\ 0 & 0 & 0 & 0 & d_{15} & 0 \end{pmatrix}$	$\begin{pmatrix} d_{33} & d_{31} & d_{32} & 0 & 0 & 0 \\ 0 & 0 & 0 & 0 & 0 & d_{15} \\ 0 & 0 & 0 & 0 & d_{24} & 0 \end{pmatrix}$	$\begin{pmatrix} 0 & 0 & 0 & 0 & 0 & d_{16} \\ d_{31} & d_{33} & d_{32} & 0 & 0 & 0 \\ 0 & 0 & 0 & d_{24} & 0 & 0 \end{pmatrix}$	$\begin{pmatrix} 0 & 0 & 0 & 0 & 0 & d_{24} \\ d_{32} & d_{33} & d_{31} & 0 & 0 & 0 \\ 0 & 0 & 0 & d_{15} & 0 & 0 \end{pmatrix}$
xoz plane $0<\theta<\Omega$ (ϕ=0) $\Omega<\theta<\pi/2$	$d_{eff}^{I}=d_{32}\sin\theta$ $d_{eff}^{II}=0$ $d_{eff}^{I}=0$ $d_{eff}^{II}=-d_{24}\sin\theta$	$d_{eff}^{I}=d_{31}\sin\theta$ $d_{eff}^{II}=0$ $d_{eff}^{I}=0$ $d_{eff}^{II}=-d_{15}\sin\theta$	$d_{eff}^{I}=-d_{32}\cos\theta$ $d_{eff}^{II}=0$ $d_{eff}^{I}=0$ $d_{eff}^{II}=d_{24}\cos\theta$	$d_{eff}^{I}=-d_{31}\cos\theta$ $d_{eff}^{II}=0$ $d_{eff}^{I}=0$ $d_{eff}^{II}=d_{15}\cos\theta$	$d_{eff}^{I}=0$ $d_{eff}^{II}=d_{15}\cos^2\theta+d_{24}\sin^2\theta$ $d_{eff}^{I}=d_{31}\cos^2\theta+d_{32}\sin^2\theta$ $d_{eff}^{II}=0$	$d_{eff}^{I}=0$ $d_{eff}^{II}=d_{15}\sin^2\theta+d_{24}\cos^2\theta$ $d_{eff}^{I}=d_{31}\sin^2\theta+d_{32}\cos^2\theta$ $d_{eff}^{II}=0$
yoz plane ($\phi=\pi/2$)	$d_{eff}^{I}=0$ $d_{eff}^{II}=-d_{15}\sin\theta$	$d_{eff}^{I}=0$ $d_{eff}^{II}=-d_{24}\sin\theta$	$d_{eff}^{I}=-d_{31}\sin^2\theta-d_{32}\cos^2\theta$ $d_{eff}^{II}=0$	$d_{eff}^{I}=-d_{31}\cos^2\theta-d_{32}\sin^2\theta$ $d_{eff}^{II}=0$	$d_{eff}^{I}=0$ $d_{eff}^{II}=d_{15}\cos\theta$	$d_{eff}^{I}=0$ $d_{eff}^{II}=d_{24}\cos\theta$
xoy plane ($\theta=\pi/2$)	$d_{eff}^{I}=0$ $d_{eff}^{II}=-d_{15}\sin^2\phi-d_{24}\cos^2\phi$	$d_{eff}^{I}=0$ $d_{eff}^{II}=-d_{15}\cos^2\phi-d_{24}\sin^2\phi$	$d_{eff}^{I}=-d_{31}\sin\phi$ $d_{eff}^{II}=0$	$d_{eff}^{I}=-d_{32}\sin\phi$ $d_{eff}^{II}=0$	$d_{eff}^{I}=d_{32}\cos\phi$ $d_{eff}^{II}=0$	$d_{eff}^{I}=d_{31}\cos\phi$ $d_{eff}^{II}=0$
x axis	$d_{eff}^{I}=0$ $d_{eff}^{II}=-d_{24}$	$d_{eff}^{I}=0$ $d_{eff}^{II}=-d_{15}$	$d_{eff}^{I}=0$ $d_{eff}^{II}=0$	$d_{eff}^{I}=0$ $d_{eff}^{II}=0$	$d_{eff}^{I}=d_{32}$ $d_{eff}^{II}=0$	$d_{eff}^{I}=d_{31}$ $d_{eff}^{II}=0$
y axis	$d_{eff}^{I}=0$ $d_{eff}^{II}=-d_{15}$	$d_{eff}^{I}=0$ $d_{eff}^{II}=-d_{24}$	$d_{eff}^{I}=-d_{31}$ $d_{eff}^{II}=0$	$d_{eff}^{I}=-d_{32}$ $d_{eff}^{II}=0$	$d_{eff}^{I}=0$ $d_{eff}^{II}=0$	$d_{eff}^{I}=0$ $d_{eff}^{II}=0$
z axis	$d_{eff}^{I}=0$ $d_{eff}^{II}=0$	$d_{eff}^{I}=0$ $d_{eff}^{II}=0$	$d_{eff}^{I}=-d_{32}$ $d_{eff}^{II}=0$	$d_{eff}^{I}=-d_{31}$ $d_{eff}^{II}=0$	$d_{eff}^{I}=0$ $d_{eff}^{II}=d_{15}$	$d_{eff}^{I}=0$ $d_{eff}^{II}=d_{24}$

The Concept, Effects and Possible Applications of Optical and Acoustical Superlattices

Nai-ben Ming

National Laboratory of Solid State Microstructures, Nanjing University, Nanjing 210008, P. R. China

Abstract

The physical properties, such as nonlinear optic coefficient, electro-optic coefficient and piezoelectric coefficient, in a ferroelectric single crystal with regular laminar domains are not constant but periodic or quasiperiodic function of spatial coordinates, such a crystal may be called an optical or acoustical superlattice. In this paper, an overview will be given of our experimental and theoretical results on the concept, novel effects and new applications of the optic and acoustical superlattices.

Introduction

Early in 1962, Bloembergen et al. showed that with periodic modulation of nonlinear susceptibilities, enhancement of nonlinear optical processes may be achieved with quasi-phase-matching [1]. Inspired by this theoretical consideration, the first sample of the optical superlattice have been realized in $LiNbO_3$ crystals with periodic laminar ferroelectric domains [2-4]. Enhancement of frequency doubled light output is observed verifying theoretical predictions [5]. Recently the experimental and theoretical results show that it is possible to use the optical superlattices to obtain the second-harmonic generation of blue light [6,7], the second-harmonic spectrum [8], the third-harmonic generation directly [9], to design a novel modulatable four-path splitter [10] and to generate blue laser light directly from a diode laser using a waveguide system with superlattice structure [11-14]. On the other hand, the excitation and propagation of elastic wave in an acoustic superlattice has been analyzed and the resonators and transducers with high frequencies up to 1000 MHz have been fabricated by using the acoustic superlattices of $LiNbO_3$ and $Ba_2NaNb_5O_{15}$ crystals [15-19].

Concept of Optical and Acoustical Superlattice

As an example, a ferroelectric single crystal, such as a $LiNbO_3$ (LN) single crystal with periodic laminar ferroelectric domains (PLFDs), is shown in fig. 1(a). The arrows in the figure indicate the directions of the spontaneous polarization of domains. Note that from one domain lamella to the next the spontaneous polarization are opposite which is equivalent to a rotation of 180° of the next lamella around X-axis, as shown in fig. 1 (a). In so doing, or according to the reference [20] and the crystallographic relationship between positive domain and negative domain[21], the physical properties of next lamella associated with the odd-rank tensor, such as nonlinear optic coefficient, electro-optic coefficient and piezoelectric coefficient should change its sign from "+" to "-", as shown in fig. 1(b). In this single crystal, the physical properties are not constant, instead, they are periodic function of spatial coordinates. If the periodicity can compare with optical wavelength and acoustical wavelength, this crystal may be called optical superlattice (OSL)

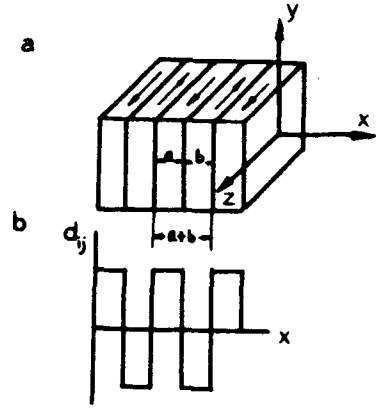


Fig. 1. Schematic diagram of optical and acoustical superlattice. (a) A single $LiNbO_3$ crystal with periodic laminar ferroelectric domains. (b) Corresponding nonlinear optical coefficient as a periodic function of x.

or acoustical superlattice (ASL). As an example, the optical micrograph of OSL of LN revealed by etching is shown in fig. 2. The period of the OSL is 6.8 μm which is two times of the coherent length of the second-harmonic generation in LN crystal for fundamental wavelength of 1.06 μm. Examples of this kind of OSLs and ASls include $LiNbO_3$, $LiTaO_3$ (LT) [22], $Ba_2Na_5NbO_{15}$ (BNN) [17] and $(NH_2CH_2COOH)_3H_2SO_4$ (TGS) [23], have been prepared in my lab. In general, a material, which optic and acoustic properties are a periodic or quasi-periodic function of spatial coordinates and its reciprocal

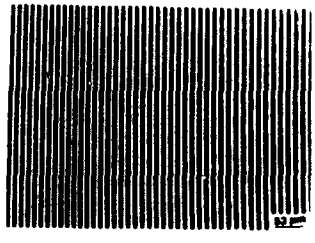


Fig. 2. The optical micrograph of optical superlattice of $LiNbO_3$ revealed etching. The period a+b is 6.8μm.

vectors are comparable with the acoustic or optic wave vectors, can be called OSL and ASL. By periodic or quasiperiodic modulation of microstructures, including the ferroelectric and

CH3080-0-7803-0465-9/92$3.00 ©IEEE

ferroelastic domain structures, the compositions and the crystallographic orientations, OSLs and ASLs can be obtained.

The Enhancement of Second Harmonic Generation in $LiNbO_3$ Optical Superlattices

There are two methods to obtain second harmonic generation (SHG) with high efficiency. One is phase matching (PM) which is commonly used. The other is quasi-phase-matching (QPM) proposed by Bloembergen [1]. The QPM can be realized only in an OSL. In general, the superlattice is described by the reciprocal vector which magnitude is

$$g_n = n\,2\pi/(a+b) \qquad (1)$$

and direction is perpendicular to the domain layer, where a and b are the thicknesses of positive and negative domains, a+b is the period of the OSL, $2\pi/(a+b)$ is a primitive reciprocal vector and n is an integer. In fact, QPM is that the mismatch of wave vectors between second harmonic wave and the fundamental wave is compensated by the reciprocal vector in the OSL. As we known, the nonlinear optical coefficient d_{31} of LN is commonly used and can be phase matched. However, the largest nonlinear optical coefficient d_{33} is 6.2-8.9 times larger than d_{31} [21] and can not be phase matched. If we can utilize d_{33} by quasi-phase-matching (QPM), the enhancement of second harmonic generation (SHG) in an OSL of LN is possible. The SH intensity of LN with superlattice structure fulfilling QPM condition for d_{33} has been compared with single domain crystal fulfilling PM condition for d_{31}. An order of magnitude enhancement predicted theoretically has been realized [5].

The Enhancement of SHG in $LiTaO_3$ Optical Superlattices

$LiTaO_3$ is a positive uniaxial crystal with small birefringence, so it can not fulfil the phase matching (PM) condition with birefringence. Therefore this material has not been utilized as a nonlinear optical crystal, although it has sizable nonlinear optical coefficient. We have utilized OSL of LT to obtain the SHG of 1.06 μm, and the SHG efficiency about 15% has been reached [22].

The SHG of Blue Light in $LiNbO_3$ Optical Superlattices

We have used a OSL of LN with thickness of 0.78 mm to generate 430-435 nm radiation by quasi-phase-matched frequency doubling at room temperature. Blue light output of 0.2 μJ energy has been obtained for input energy of 5 μJ of fundamental wave [7]. From the limited data of SHG of blue light and the systematic studies of fundamentals of OSL, we conclude that, with the OSL, the demands for a miniaturized and compact device of generation of blue light by frequency doubling of a laser diode for a variety of applications including optical data storage can be met.

Enhancement of the Third Harmonic Generation in Quasi-periodic Optical Superlattice (QP-OSL) of LN

Hereafter we shall take $LiNbO_3$ crystals with laminar ferroelectric domain structures as an example. In such a material, the directions of spontaneous polarizations in successive domains are opposite, as are the signs of nonlinear optical coefficients. This structure forms a one-dimensional (1D) superlattice for nonlinear optical effect. On this basis, a quasi-periodic optical superlattice (QP-OSL) can be constructed. It consists of two fundamental blocks of A and B arranged according to the production role $S_j = S_{j-1}:S_{j-2}$, for $j>3$ with $S_1 = A$ and $S_2 = AB$, where : stands for concatenation. Both blocks, A and B, are composed of one positive and one negative ferroelectric domain as shown in fig. 3, where a_A and a_B represent the thicknesses of the positive domains in block A and B, and b_A and b_B represent the thicknesses of the negative ones. Let $a_A = a_B = l$, $b_A = l(1+\delta)$, $b_B = l(1-t\delta)$, where l, δ and t are adjustable structure parameters during the design of a QP-OSL. The sequence of the blocks, ABAABABA..., produces a QP-OSL, see Fig. 3. With the QP-OSL, a series of reciprocal vectors can be provided to compensate the phase mismatches of the optical parametric processes in the material. Unlike the periodic OSL which has reciprocal vector, see eq.(1), a QP-OSL provides reciprocal vectors governed by two integers, which has the form

$$g_{mn} = 2\pi(m+n\tau)/D \qquad (2)$$

where $D = \tau l_A + l_B$, with the golden ratio $\tau = (1+\sqrt{5})/2$; $l_A = a_A + b_A$ and $l_B = a_B + b_B$ are thicknesses of fundamental blocks of A and B, as shown in fig. 3. It is clear that the reciprocal vectors of the QP-OSL can be adjusted by l, δ and t. Because of this property, some coupled optical parametric processes will be likely to occur in the QP-OSL with efficient conversion. The process of the third harmonic generation (THG) discussed here is a coupled parametric process, e.g., the SHG process and the frequency up-conversion process (FUP), which mixes the fundamental frequency with the second harmonic, are coupled in this QP-OSL. As just mentioned above, there are more series of reciprocal vectors in QP-OSL than that in the periodic superlattice and we can adjust the structure parameters l, δ, t during design the superlattice. In this case, it is possible to design

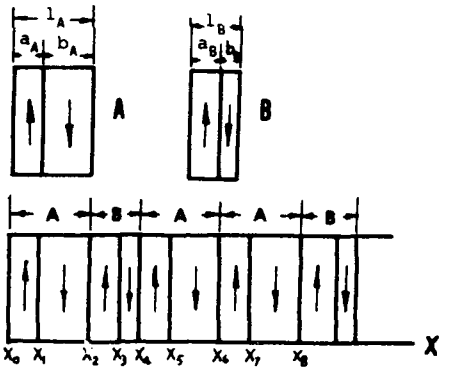


Fig. 3. Quasi-periodic optic superlattice made of a single $LiNbO_3$ crystal (the arrows indicate the directions of the spontaneous polarization). (a) The two building blocks of a QP-OSL, each composed of one positive and one negative ferroelectric domain. (b) Schematic diagram of a QP-OSL.

and prepare a QP-OSL with two special reciprocal vectors. One is used to compensate the mismatch of wave vectors in a SHG process. The other is used to compensate the mismatch of wave vectors in the frequency up-conversion process. By adjusting the parameters properly, the optimum condition has been found, which is $l = 6.08$ μm, $\delta = 0.01$ and $t = 1.90$ with the third harmonic intensity $I(3\omega) \sim 122000$ K; where K is a constant when incident light are given. To obtain an appreciation for the enhancement of the third harmonic available in our case, consider a commonly used two-step process. The second harmonic is generated in the first $LiNbO_3$ crystal using the nonlinear coefficient d_{31} with phase matching; then it mixes with

the fundamental frequency in the second $LiNbO_3$ using the same nonlinear coefficient and PM; and the relative output intensity of THG is $I(3\omega) \sim 11{,}000K$. Compared with it, the enhancement of THG in our case is increased by an order of magnitude, which is favourable to the practical applications. A detailed theoretical analysis of SHG and THG in the QP-OSL has been published in reference [9].

Resonator Made of Acoustical Superlattices of $LiNbO_3$

For a periodic acoustical superlattice (ASL), by using Green's function method to solve the elastic wave equations, the electric impedance of resonator can be derived, then the resonance frequency can be obtained, which is

$$f_n = n\,v/(a+b),\ n = 1,2,3... \qquad (3)$$

where v is the velocity of the longitudinal wave propagating along the z axis. It is worth noting that the resonance frequency are determined only by the periodicity of the ASL, a + b, not by the total thickness of the wafer. As we know, the thickness of a resonator working at several hundred mega-hertz with ordinary materials, such as the single domain $LiNbO_3$ crystal, is too thin to be fabricated by regular processing techniques. However, it is easy to grow the ASL of $LiNbO_3$ crystals with the thickness of each lamellae of several microns [15-17, 24-30]. Therefore, it is possible to fabricate the acoustic devices operating at frequencies of hundreds MHz to several GHz by using the ASL. A set of resonators with working frequencies in the range of 500-1000 MHz has been made of the ASL of $LiNbO_3$ crystals [15]. The measured and calculated resonance frequencies are listed in Table I. It indicates that the experimental values are very close to the theoretical ones.

Table I. Relationship between the Resonance Frequency f_1 and the Periodicity a + b of $LiNbO_3$ Acoustic Superlattice

Resonantor	Periodicity of ASL, a+b (μm)	Frequency of Resonance f_1, MHz cal.	mes.	Error (%)
No.1	7.4	989	975	1.4
No.2	8.2	892	882	1.1
No.3	10.0	732	710	3.0
No.4	11.0	665	686	3.0
No.5	13.2	554	552	0.4
No.6	13.3	550	553	0.5

Resonators Made of Acoustical Superlattices of $Ba_2NaNb_5O_{15}$

$Ba_2NaNb_5O_{15}$ (BNN) possesses not only superior electro-optical [31] and nonlinear optical properties [32] but also good acoustic properties [33,34]. In particular, the z-cut plate of this material has a thickness longitudinal mode coupling factor 0.57 [33] which is about three times large than that of LN. Hence, this material is useful for ultrasonic device applications. As we know, the microtwinning is often appeared in as-grown BNN crystal and the detwinning procedure is complex [35]. After the study of the influence of microtwins on the performance of these materials, that is, by transformation on the component of piezoelectric tensor from the untwined coordinate system to the twinned coordinate system, we conclude that the component of the piezoelectric tensor, h_{33}, keeps constant from one lamella to the next one. Namely, microtwins have no influence on acoustic resonance properties of the ASL arranged along the z axis, and a longitudinal planar wave is excited along the z axis in this case. A set of resonators with working frequencies in the range of 200-400 MHz have been made of the ASL of BNN crystals. The measured resonance frequencies are very close to the theoretical ones. Both experimental and theoretical results show that the resonators of BNN ASL have low acoustic loss [17].

Transducers Made of Acoustical Superlattice of $LiNbO_3$ Crystals

After study of the elastic wave equation, the electrical impedance of a transducer made of ASL has been obtained which is a function of the number of laminar domains N and area of electrode A [16]. For transducers made of regular material, such as a single domain LN crystal, under high frequency operation the static capacitance is the main part of the impedance at resonance frequency. As a result, the insertion loss of transducer is very high. In our case, the real part of the impedance can be equal to or even large than the imaginary part by choosing N and A suitably. The transducers thus will have an insertion loss near 0 dB in a 50Ω measurement system. A set of transducers with working frequencies in the range of 300-800 MHz have been made of the ASL of LN. A typical experimental result shows that an insertion loss of near 0 dB at 555 MHz is achieved, which is in good agreement with the theory, and the 3 dB bandwidth of the transducer is 5.8% [16].

Conclusions

Based on the studies of ferroelectric domain structures and the influence of growth striations on para-ferroelectric phase transitions, a new type of crystals with periodic or quasi-periodic laminar ferroelectric domains has been prepared. It has been demonstrated that this kind of crystals produce significant effects in optical and acoustical wave processes and can be used as new types of devices for a variety of applications in the opto-electric and acousto-electric field. We believe that it is possible to use modern experimental techniques to control the microstructures and thus to develop a new types of synthetic materials with pre-designed microstructures.

Acknowledgement

This work is supported by a grant for key research project from the State Science and Technology Commission of China.

References

1. J. A. Armstrong, N. Bloembergen, J. Ducuing and P. S. Pershan, "Interactions between Light Wave in a Nonlinear Dielectric", Physical Review, 127(1962), 1981-1939.
2. D. Feng, N.-B. Ming, J.-F. Hong, J.-S. Zhu, Z. Yang and Y.-N. Wang, "Enhancement of Second-harmonic Generation in $LiNbO_3$ Crystals with Periodic Laminar Domains", Appl. Phys. Lett., 37(1980), 607-609.
3. D. Feng, N.-B. Ming, J.-F. Hong and W.-S. Wang, "Ferroelectric Crystals with Periodic Laminar Domains", Ferroelectrics, 91(1989), 9-19

4. A. Feisst and P. Koidl, "Current Induced Periodic Ferroelectric Domain Structures in $LiNbO_3$ Applied for Efficient Nonlinear Optical Frequency Mixing", Appl. Phys. Lett. 47(1985), 1125-1127.
5. Y.-H. Xue, N.-B. Ming, J.-S. Zhu and D. Feng, "The Second-harmonic Generation in $LiNbO_3$ Crystals with Periodic Laminar Ferroelectric Domains", Chinese Physics, 4(1984), , 554-564
6. G. A. Magel, M. M. Fojer and R. I. Byer, "Quasi-phase-matched Second-harmonic Generation of Blue Light in Periodically Poled $LiNbO_3$", Appl. Phys. Lett., 56(1990), 108-110.
7. Y.-L. Lu, L. Mao, S.-D. Cheng, N.-B. Ming and Y.-T. Lu, "Second-harmonic Generation of Blue Light in $LiNbO_3$ Crystals with Periodic Ferroelectric Domain Structures", Appl. Phys. Lett., 59(1991), 516-518.
8. Y.-Y Zhu and N.-B Ming, "Second-harmonic Generation in a Fibonacci Optical superlattice and the Dispersive Effect of the Refractive Index", Phys. Rev. B 42(1990), 3676-3679
9. J. Feng, Y. Y. Zhu and N.-B. Ming, "Harmonic Generation in an Optical Fibonacci Superlattice", Phys. Rev. B 41(1990), 5578-5582.
10. J. Feng and N.-B. Ming, "Light Transmission in Two-dimensional Optical Superlattices", Phys. Rev. A 40(1989), 7047-7054.
11. J. Webjorn, F. Laurell and G. Arvidsson, "Fabrication of Periodically Domain Inverted Channel Waveguides in Lithium Niobate for Second Harmonic Generation", J. Lightwave Technology, 7(1989), 1597-1600.
12. E. J. Lim, M. M. Fejer and R. L. Byer, "Second-harmonic Generation of Green Light in Periodically Planer Lithium Niobate Waveguide", Electronics Letters, 25(1989), 174-175.
13. C. J. van der Poel, J. D. Bierlein, J. B. Brown and S. Colak, "Efficient Type I Blue Second-harmonic Generation in Periodically Segmented $KTiOPO_4$ Waveguides", Appl. Phys. Lett., 57(1990), 2074-2076.
14. J. Khurgin, S. Colak, R. Stolzenberger and R. N. Bhargava, "Mechanism for Efficient Blue Second-harmonic Generation in Periodically Segmented Waveguides", Appl. Phys. Lett., 57(1990), 2540-2542.
15. Y.-Y. Zhu, N.-B. Ming, W.-H.Jiang and Y. A. Shui, "High-frequency Resonance in Acoustic Superlattice of $LiNbO_3$ Crystals", Appl. Phys. Lett., 53(1988), 2278-2280.
16. Y.-Y. Zhu, N.-B. Ming, W.-H. Jiang and Y.-A. Shui, "Acoustic Superlattice of $LiNbO_3$ Crystals and its Applications to Bulk-wave Transducers for Ultrasonic Generation and Detection up to 800 MHz", Appl. Phys. Lett. 53(1988), 1381-1383.
17. H.-P. Xu, G.-Z.Jiang, L. Mao, Y.-Y. Zhu, N.-B. Ming, J.-H. Yin and Y.-A. Shui, "High-frequency Resonance in Acoustic Superlattice of Barrium Sodium Niobate Crystals", J. Appl. Phys., 71(1992), 2480-2482.
18. Y.-Y. Zhu and N.-B. Ming, "Ultrasonic Spectrum in Fibonacci Acoustic Superlattices" Phys. Rev. B40(1989), 8536-8540.
19. N.-B. Ming, Y.-Y. Zhu and D. Feng, "Ferroelectric Crystals with Periodic Laminar Domains as the Micron Superlattices for Optic Acoustic Processes", Ferroelectrics, 106(1990), 99-104.
20. "Standards on Piezoelectric Crystal", Proc. IRE, 37(1949), 1378.
21. A. Rauber, "Chemistry and Physics of Lithium Niobate", Current Topics in Materials Science, vol.1, ed. E. Kaldis and H. J. Scheel, (Amsterdam and New York, North-Holland, 1977), 481-601.
22. D. Feng, W.-S. Wang, Q. Zhou and Z.-H. Geng, "Second Harmonic Generation in $LiNbO_3$ Crystals with Modulated Structure", Chinese Phys. Lett., 3(1986), 181-184.
23. W.-H. Wang and M. Qi, "Research on TGS Single Crystal Growth with Modulated Structures", J. Crystal Growth, 79(1986), 758-761.
24. N.-B. Ming, J.-F. Hong, Z.-M. Sun and Y.-S. Yang, "Rotational Striations in Czochralski-grown $LiNbO_3$ Single Crystals", Acta Physica Sinica, 30(1981), 1672-1675.
25. N.-B. Ming, J.-F. Hong and D. Feng, "The Structures of Ferroelectric Domains in Czochralski-grown $LiNbO_3$ Single Crystal", Acta Physica Sinica, 31(1982), 104-108.
26. N.-B. Ming, J.-F. Hong and D. Feng, "The Growth Striations and Ferroelectric Domain Structures in Czochralski-grown $LiNbO_3$ Single Crystals", J. Materials Science, 17(1982), 1663-1670.
27. Z.-M. Sun, N.-B. Ming and D. Feng, "Temperature Fluctuation at Solid-liquid Interface Caused by Rotation of Growing Crystals in Czochralski Method", J. Inorganic Materials, 1(2)(1986), 207-211.
28. J.-F. Hong and Y.-S. Yang, "Preparation of $LiNbO_3$ Crystals with Periodic Laminar Domains by Electric Current Modulation", Acta Optica Sinica, 4(1984), 821-824.
29. J. Chen, Q. Zhou, J.-F. Hong, W.-S.Wang, N.-B. Ming and D. Feng, "Influence of Growth Striations on Paraferroelectric Phase Transitions: Mechanism of the Formation of Periodic Laminar Domains in $LiNbO_3$ and $LiTaO_3$", J. Appl. Phys., 66(1989), 336-341.
30. N.-B. Ming, Physical Fundamentals of Crystal Growth, (Shanghai,Shanghai Science and Technology Press, 1982), 45-67; 415-417.
31. S. Singh, D. A. Draegert and J. E. Geusic, "Optical and Ferroelectric Properties of Barium Sodium Niobate", Phys. Rev. B, 2 (1970), 2709-2724.
32. J. E. Geusic, H. J. Levinstein, S. Singh, J. J. Rubin and L. G. Van Uitert, "The Nonlinear Optical Properties of $Ba_2NaNb_5O_{15}$", Appl. Phys. Lett., 11(1967), 269-271.
33. A. W. Warner, G. A. Coquin and J. L. Fink, "Elastic and Piezoelectric Constants of $Ba_2NaNb_5O_{15}$", J. Appl. Phys., 40(1969) 4353-4356.
34. A. W. Wsasrner, G. A. Coquin, A. H. Meiteler and J. L. Fink, "Piezoelectric Properties of $Ba_2NaNb_5O_{15}$", Appl. Phys. Lett., 14(1969), 34-35.
35. A. W. Vere, J. G. Plant and B. Cockayne, J. Materials Science, 4(1969), 1075.

LEAD CALCIUM TITANATE CERAMICS AND INTEGRATED OPTICAL FILTERS FOR INFRARED OPTICAL SENSORS.

J. de Frutos
Dpto. Física Aplicada. UPM. E.U.I.T.Telecomunicación.
Crta Valencia, Km 7. 28031. Madrid. Spain.

F. López
Dpto. de Ingeniería. Universidad Carlos III. Leganés (Madrid). Spain.

B.Jiménez
Itto de Ciencia de Materiales "Sede A". Serrano 144. 28006. Madrid. Spain

Lead calcium titanate ceramics (PTC) show properties that make them excellent candidates for pyroelectric sensors.

In the present work, a new system to improve greatly the performance of lead calcium titanate ceramics for infrared sensor is proposed. The main characteristic of the system would be its capability to integrate, on same substrate, different thin film optical filters with defined geometries, in order to obtain arrays of optical filters. Each point on the substrate would correspond to a filter with a previously defined wavelength profile

The first achievement of the system proposed is the obtention of a multispectral substrate with different optical filters integrated in the same plane, that correspond to the focal plane of the pyroelectric PTC sensor.

This concept would allow to obtain multispectral integrated sensor or "retinae", by hibridid or monolithic coupling of the filters on the pyroelectric detector in the same or very close substrate (focal plane)

The results of the preliminary experiments carried out have demonstrated the feasibility of the system proposed. Thin film optical filter with appropriate size, position and homogeneity have obtained combining different vacuum evaporated multilayer on the substrate.

At the same time, experimental results of the pyroelectric response of the PTC are shows.

1.- INTRODUCTION

Work on new infrared (IR) sensors is at present centred on the development of focal plane arrays [1] for their use in imaging systems, and in the search for new materials [2,3].

One of such materials is calcium-modified lead titanate in ceramic form [4]. It behaves as a good pyroelectric material because it has a high pyroelectric coefficient, γ, a small dielectric constant, ϵ', and a moderately high Curie temperature. It also happens that it is sensitive to a broad band of wavelengths. In applications such as astronomical measurements, spectroscopic analysis of gases, and IR signature identification, it is necessary to have with wavelength selection capability; and this is generally achieved by putting, before the detectors, a device with one or more optical filter, that are mechanically or manually selected in order to have specific wavelengths.

In this paper a study is made of pyroelectric properties of ceramics of lead titanate modified with different amounts of calcium, and a proposal is put forward to integrate, over a pyroelectric linear array of Ca-modified lead titanate elements, different thin-film interferencial filters which permit the selection of wavelengths. The integration over the pyroelectric array of the interferencial filter will have spatial and spectral resolution, and can therefore be considered as a spectral retina.

2.- THE SPECTRAL RETINA

In a previous paper [5] a discussion was made of the concept of spectral retina, which basically consists on the selection of a certain wavelength by a narrow band-pass filter, and the assignment of one or several pixels from a linear array of sensors. Each detector (pixel) or group of them, can thus produce a signal proportional to the optical power received within the band of wavelengths defined by the filter just on top. This is sketched in Fig. 1.

CH3080-0-7803-0465-9/92$3.00 ©IEEE

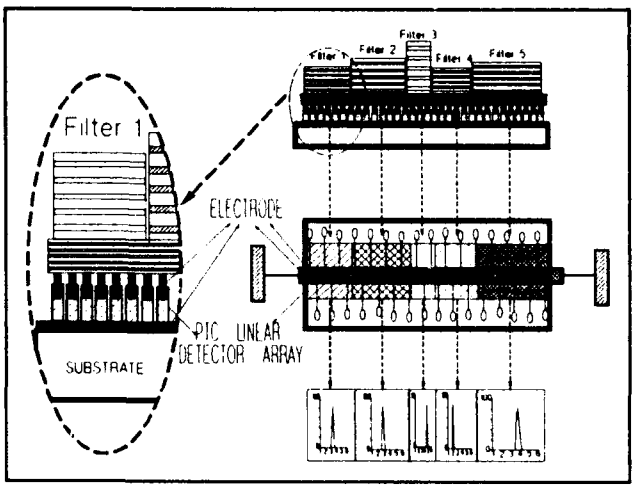


Fig. 1.- FILTER ARRAYS COUPLED TO DETECTOR ARRAYS (SPECTRAL RETINA)

Making use of the concept of spectral retina, it is possible to design many configurations of interferential filters, with specific spectral bands and geometrical distributions over the array of detectors. The number of individual detectors to be covered by a filter will depend on the characteristics of the signal to be detected. The signal/noise ratio can be improved with respect to that of an individual detector by a factor of $N^{1/2}$, N being the number of detectors covered by each filter, because the signal delivered by the detectors adds linearly while noise adds in quadrature [6].

The integration of spectral retinae may be achieved in hybrid form (putting the array of filters, deposited on a substrate, over the detector arrays) or in monolithic form (directly integrating the filters over the detector arrays). In the former, it is necessary to align properly both arrays; in the latter, the detector arrays and the interferential filter films should be compatible in order to have a good adhesion between them.

Two different techniques are required for the manufacture of multispectral arrays of IR filters. On the one hand, optical coating techniques so as to obtain the interferential filters; on the other, photolithographic techniques in order to distribute spatially the filters along the substrate. Optical coating techniques are usually based on vacuum evaporation deposition processes (sputtering or chemical vapour deposition). And photolithographic techniques (masking, etching, stripping, etc.) are borrowed from silicon Microelectronics. The integration capability of filters, prepared with these techniques should, in principle, be similar to that achieved in Microelectronics. But, in practice, this is far from being so, because each interferential filter is a multilayer, formed by 15 or more different layers, and this definitely hinders the process of integration. However, integration levels as required for spectral retinae are easily achieved.

3.- EXPERIMENTAL RESULTS

Ferroelectric ceramics of nominal composition

$$Ca_x\ Pb_{1-x}\ [Ti_{0.96}\ (W_{0.5}\ Co_{0.5}\ )_{0.04}\ ]\ O_3$$

with x=0.24, 0.30 and 0.35, which will be hence be designated as PTC24, PTC30 and PTC35 respectively, were prepared by a reactive method as previously described [7].

These ceramics were mechanized into disks of 12 mm diameter and thickness under 0.5 mm. Which were vacuum coated with silver on their flat surfaces, and polarized by applying fields of 70 (PTC24), 30 (PTC30) and 15 kV/cm (PTC35), at 120 °C, and cooling down to room temperature without withdrawing the field.

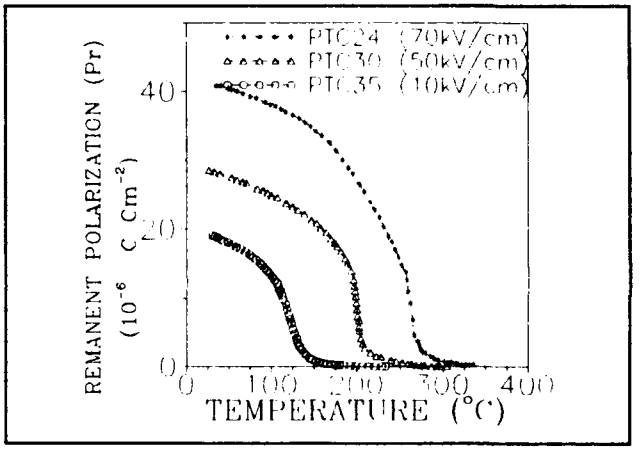


Fig. 2a.- REMANENT POLARIZATION vs TEMPERATURE

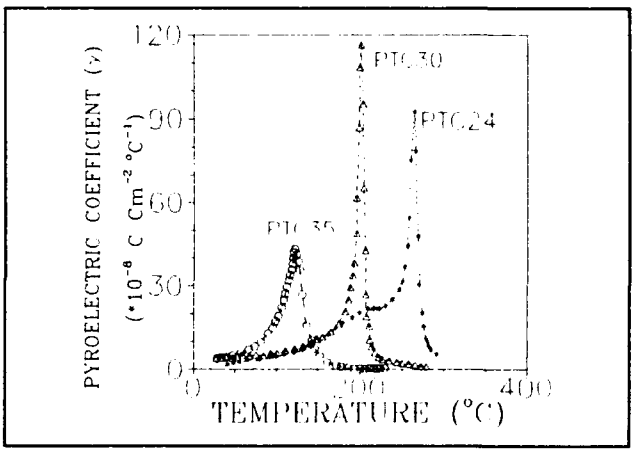


Fig. 2b.- PYROELECTRIC COEFFICIENT vs TEMPERATURE

Making use of the charge integration method, remanent polarization against temperature diagrams have been traced, for each of the compositions (Fig. 2a); and the pyroelectric coefficients have been obtained as derivates of the previous curves (Fig. 2b).

Dielectric permittivities at 1 kHz, ϵ', have been measured with an automatic impedance bridge. Fig. 3 shows values of this quantity as a function of temperature for the different contents in Ca. It is clear that, as [Ca] increases, the maximum value achieved by ϵ' decreases appreciably.

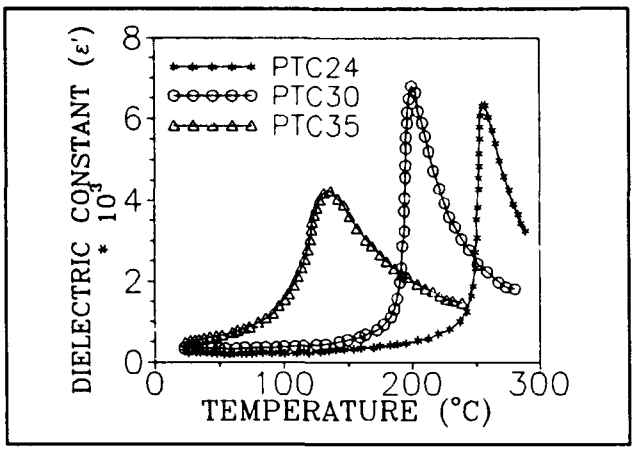


Fig. 3.- DIELECTRIC PERMITTIVITIES AT 1 kHz FOR EACH OF THE COMPOSITION

The remanence value of the piezoelectric coefficient d_{33}, after a heating process, provides some insight into the reversibility of the polarization state of the samples. In order to get this information, samples were heated up to the desired temperature, which was maintained for 30 minutes, and then cooled down to room temperature. Before and after each heating process, the value of d_{33} was measured in a Berlincourt d_{33}-meter.

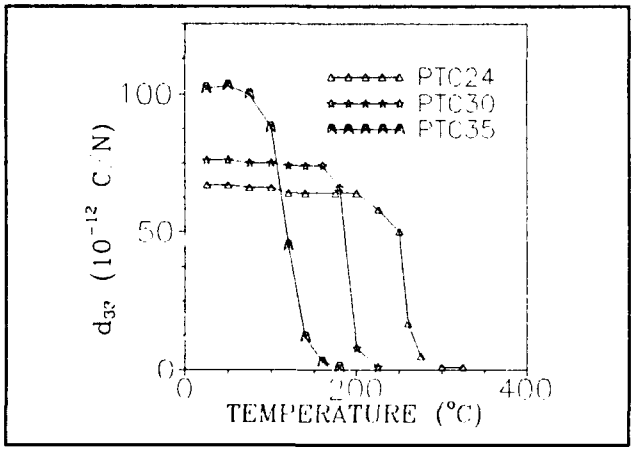


Fig. .- THE REMANENCE VALUE OF THE PIEZOELECTRIC COEFFICIENT D_{33}, AFTER A HEATING PROCESS.

In Fig. 4 remanent values of d_{33} are represented against temperature and it can be seen that the trend is very similar to that of Fig. 2a.

The materials that have been studied can be used to prepare linear arrays sensors [8], over which arrays of interferential filters can be integrated. The response of the pyroelectric array pixels is very similar to that obtained from individual detectors [8].

In order to verify the possibility of obtaining interferential filter arrays, we integrated two narrow band-pass filters on a silicon wafer by lift-off processes. The filters were centred on 1.32 and 1.55 μm and were obtained by alternatively depositing layers of germanium (high refractive index) and of silicon monoxide (low refractive index). The multilayer structure of the former one is

SILICON/ HLH 2L HLH L HLH 2L HLH/ AIR

where H (L) designates a layer of Ge (SiO) with an optical thickness of $\lambda/4$ (at 1.4 μm). The final thickness of the filters is of some 2.5 μm.

The use of lift-off techniques for the manufacture of IR filters was described in a previous paper [5]. In the present case the resin used for the process was Dynachem 50 cps, which was spinner-deposited on a silicon wafer at 2500 rpm, so as to obtain a film of 2.25 μm aprox., and then cured at 90 °C for 1 hour.

After eliminating the resin from the zones selected for the deposition of the filters, the wafer was taken to vacuum chamber so as to deposit the interferential (Fabry-Perot) filter.

The elimination of the resin was carried on with Macdermid S43 stripper. This stage is the most critical of the integration process, because the total etching time of the resin is very long (about 12 hours in an ultrasonic bath) and the filters may get damaged.

Following the previous process we have prepared the two interferential filters of which transmission curves in the infrared are presented in Fig. 5.

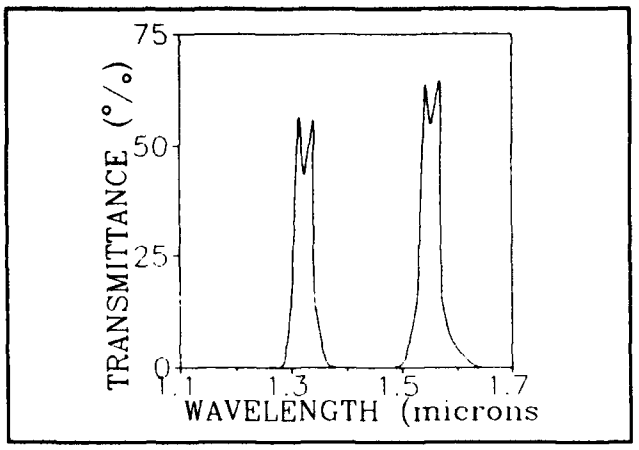


Fig. 5.- SPECTROPHOTOMETRIC TRANSMITTANCE CURVES OF TWO NARROW BAND-PASS FILTERS CENTRED AT 1.32 AND 1.55 μm INTEGRATED ON A SILICON WAFER.

4.- CONCLUSIONS

Values of the pyroelectric coefficient, dielectric constant an remanent-d_{33}, show that Ca-modified lead titanate is an excellent pyroelectric sensor. The choice of the content in Ca will depend on the specific application; e.g., for temperatures under 125 °C the most adequate would be PTC30.

Making use of these materials, it is possible to build linear sensor arrays. The response of pyroelectric array pixels is very similar to that of individual detector [8]. Integrating over them filter arrays, it is possible to obtain spectral retinae, with spectral and spatial resolution.

The possibility of integrating several filters over a substrate has been proved experimentally. This supports the idea of achieving multispectral IR sensors (retinae) consisting of filter arrays coupled to detector arrays.

5.- REFERENCES

[1] J.T. Woolaway, "New sensor technology for the 3 to 5 μm imaging band", Photon. Spectra, (Feb) 113-119, 1991

[2] R. Watton," Ferroelectric materials and devices in infrared detection and imaging" Ferroelectrics 91, 87-108 (1989)

[3] R.W. Wathmore, "Pyroelectric ceramics and devices for thermal infra-red detection and imaging", Ferroelectrics, 118, 241-259 (1991)

[4] J. de Frutos and B. Jiménez, "Lead titante ceramics for infrared sensor" Sensor and Actuators A, 32 393 (1992)

[5] F.López, J.de Frutos, A.M.González, A.Navarro. "Integrated optical filters for infrared electrooptical gas sensors". Sensors and Actuators B, 6 (1992), 170-175

[6] E.L.Dereniak and D.G. Crowe, Optical radiation detectors, New York: Wiley, 1984, ch 9.

[7] L. del Olmo, C. Fandiño, J. L. Pina, J. Mendiola, C. Alemany, L. Pardo, B Jimenez and E. Maurer.Spanish Patent nº 555469 (1980) Spain.

[8] R.Takayama, Y. Tomita, K.iijima, I. ueda. "Pyroelectric properties and application to infrared sensors of $PbTiO_3$, $PbLaTiO_3$ and $PbZrTiO_3$ ferroelectric thin films". Ferroelectrics, Vol 118, 325-342 (1991)

THE RELATION BETWEEN THE Mg CONCENTRATION THRESHOLD EFFECT AND THE DEFECT STRUCTURES OF THE CONGRUENT Mg:$LiNbO_3$

Qi-ren Zhang, Department of Physics, Suznou Railway Teacher's College, Suzhou 215009, P. R. China

Xi-qi Feng, Shanghai Institute of Ceramics, Academia Sinica, Shanghai 200050, P. R. China

Abstract

Congruent Mg:$LiNbO_3$ with Mg concentrations 0, 1.0, 2.7, 5.0 and 6.0 mol% are prepared. A set of defect models as consistent with the density measurement are proposed. When the Mg concentration (Mg) beyonds a critical value $(Mg)_c$, there would be Nb-site Mg in the form of $Mg_{Li}Mg_{Nb(1/3)}{}^{Nb}{}_{Nb(2/3)}O_3$ appeared in the crystal. The $(Mg)_c$ varies as the ratio Li/Nb of the crystal and should be 5.30 mol% for the congruent crystal. We propose that the optical absorptions of the reduced crystals are due to defects comprising both F centers, formed under reduction, and different types of dipolarons. When (Mg) beyonds $(Mg)_c$, there would be $(Mg_{Li}$-$Mg_{Nb})$-F-$(Mg_{Li}$-$Nb_{Nb})$ occured in the reduced crystal. Which causes the abrupt change of the optical absorption of the crystal. It is consistent with our optical absorption measurement.

Introduction

The optical damage due to laser-induced refractive index inhomogeneities is strongly diminished in samples grown from a congruent melt containing MgO above a critical concentration $(Mg)_c$. The optical absorption features and several other properties of the thermal-chemical reduced (TCR) crystal exhibits abrupt changes when (Mg) is raised above the $(Mg)_c$. Which is called the Mg-concentration threshold effect.

The abrupt changes in physical properties of the TCR crystal indicates an abrupt change of defect structure in the crystal when the (Mg) is raised above $(Mg)_c$. The main purpose of this paper is to demonstrate the relation between the (Mg)-threshold effect and the defect structures of the congruent Mg:$LiNbO_3$.

Defect Models

The congruent $LiNbO_3$ has the composition $(Li_2O)_{50-x}(Nb_2O_5)_{50+x}$, where x denotes excess Nb_2O_5 in the crystal and in the present study x=1.4. Each excess Nb_2O_5 may form an intrinsic Li-deficient defect where Nb should occupy Li-site. The equation can be written as

$$(50-x)Li_2O+(50+x)Nb_2O_5=2(50-x)LiNbO_3+(10x/3)(Nb_{Li}{}^{Nb}{}_{Nb(1/5)}{}^{V}{}_{Nb(4/5)}O_3) \quad (1)$$

Let the intrinsic defect be denoted by defect 1. The undoped congruent crystal contains 2(50-x) perfect lattices and 10x/3 defect lattices 1.

Being doped into the crystal, MgO may incorporate with the excess Nb O to form extrinsic impurity contained defects, where Mg May primary occupy Li-site. On the basis of defect chemistry, we may generally write down the equation

$$3(t\,MgO+Nb_2O_5)=(t+5)(Mg_{2t/(t+5)}{}^{Nb}{}_{6/(t+5)}O_3) \quad (2)$$

It looks like that the defect structures are modified by the parameter t, there may be manifold defects in the crystal varying with (Mg) and the process may become very complex.

However, some principles should comply with on the foundations of crystallography: 1, the crystal maintains local electroneutrality; 2, the bonding energy of the crystal tends to minimum, therefor, the doped impurity tends to be evenly distributed; 3, lattice distortion tends to minimum, therefor there would be no large defect cluster gathered in the crystal. So, only several certain types of defect may be formed varying with (Mg) in the crystals.

One possible defect derives from equation

$$MgO+Nb_2O_5=MgO+(5/3)(\text{defect 1})=2(Mg_{Li(1/2)}{}^{Nb}{}_{Li(1/2)}{}^{V}{}_{Nb(1/2)}{}^{Nb}{}_{Nb(1/2)}O_3)$$

Let the new defect be denoted by defect 2, each MgO incorporates with one Nb O transforming 5/3 defect 1 to 2 defect 2. If there are k MgO doped into the crystal, we may obtain the equation

$$(50-x)Li_2O+(50+x)Nb_2O_5+k\,MgO=2(50-x)LiNbO_3+(5/3)(2x-k)(\text{defect 1})+2k(\text{defect 2}) \quad (3)$$

With increasing (Mg), defect 1 decreases and

CH3080-0-7803-0465-9/92$3.00 ©IEEE

defect 2 increases. While the amount of Mg equals to the amount of the excess Nb_2O_5, the crystal contains no defect 1 but perfect lattice and defect 2. When (Mg)=2x/(100+2x),(=2.724 mol%, x=1.4).

Another possible defect with increasing (Mg) can be derived from that the Li-deficiencies in defect 1 are just filled up with Mg

$$2MgO+Nb_2O_5=MgO+2(\text{defect 2})=2(Mg_{Li}Nb_{Nb}O_3+e)+\tfrac{1}{2}O_2$$

where $Mg_{Li}Nb_{Nb}O_3$ is singly electropositive and should trap an additional electron in a certain way to maintain the local electroneutrality. Let it be denoted by defect 3, each additional MgO, on the basis of equation (3), transforms 2 defect 2 into 2 defect 3. The equation can be written as

$$(50-x)Li_2O+(50+x)Nb_2O_5+k\,MgO=2(50-x)LiNbO_3+(8x-2k)(\text{defect 2})+2(k-2x)(\text{defect 3})+\tfrac{1}{2}(k-2x)O_2 \quad (4)$$

As increasing (Mg), defect 2 decreases and defect 3 increases, up to k=4x, the crystal concontains no defect 2 but perfect lattice and defect 3. When (Mg)=x/(25+x), (=5.30 mol%, x=1.4).

If more MgO being doped into the crystal, therefor, there is no Li-vacancy existed in the crystal and Mg may occupy Nb-site. The third possible defect can be derived from equation

$$4\,MgO+Nb_2O_5=3(Mg_{Li}{}^{Mg}{}_{Nb(3/1)}{}^{Nb}{}_{Nb(2/3)}O_3)$$

Let the new defect be denoted by defect 4, each 3 defect 4 forms the compound $Mg_4Nb_2O_9$. The chemical equation can be written as

$$(50-x)Li_2O+(50+x)Nb_2O_5+k\,MgO=2(50-x)LiNbO_3+(8x-k)(\text{defect 3})+\tfrac{1}{2}(8x-k)O_2+(3/2)(k-4x)(\text{defect 4}) \quad (5)$$

As increasing (Mg), defect 3 decreases and defect 4 increases, while k=8x, the crystal contains neither cation vacancy nor excess Nb_2O_5, but perfect lattice and defect 4. When (Mg)=x/(25+2x),(=10.07 mol%, x=1.4).

The defect models discussed are listed in table 1.(ref.1)

Table 1 Defect Models

MgO (mol%)	Defects contained
0	1
0 to 2.72	1 and 2
2.72 to 5.30	2 and 3
5.30 to 10.07	3 and 4

Density Measurement Result

In order to determine the defect models, a group of Mg:$LiNbO_3$ samples with different (Mg) are prepared. Their density are carefully measured. Assuming each lattice has an equal average volume $\bar{v}$, $\bar{v}$ can be obtained by substituting the experimental density of the undoped congruent $LiNbO_3$, d=4.637 g/cm^3 into the density formula $d=148.376/\bar{v}$, then $\bar{v}$=31.998 rel. unit. Therefore, the densities of the crystals varying with (Mg) can be calculated corresponding to equations (3), (4) and (5).

The experimental and calculated results are in good agreement as shown in table 2 and figure 1.(ref.1)

Table 2 Density(in g/cm^3) of Mg:$LiNbO_3$ with different (Mg)

MgO(mol%)	Experiment	Calculation
0	4.637	4.637
1.00	4.634	4.634
2.70	4.631	4.629
5.00	4.642	4.647
5.30	/	4.650
6.00	4.639	4.644
9.00	4.594	4.617
10.07	/	4.607

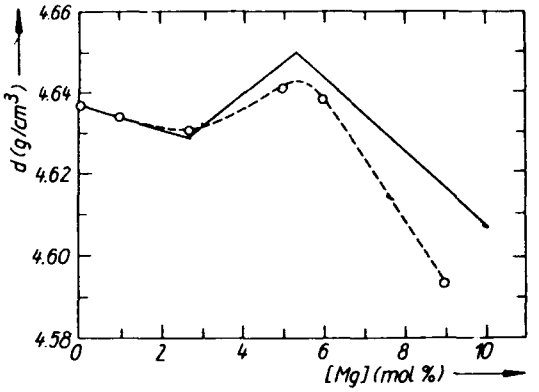


Fig.1. Density of Mg:$LiNbO_3$ with different (Mg)

Optical Absorption Measurements

The thermal-chemical reduced (TCR) Mg:$LiNbO_3$ emerge optical absorptions. TCR was performed by annealing the samples in vacuum (10^{-5} mmHg) under 1000°C for 0.5h. The optical absorption spectra due to TCR were obtained by taking differential spectra between a group of the TCR and the control samples with a Backman 5270 spectrophotometer at RT. The absorption results are shown in table 3.(ref.2)

It can be obviously seen that the samples

Table 3. Absorption data of TCR Crystals

(Mg) (mol%)	Surface//C (nm)	Surface⊥C (nm)
0	514 540 600	325 515
1.0	514 540 595	325 515
2.7	514 530 575	325 515
5.0	514 530 590	325 515
6.0	780 1470	1400

with (Mg) below or equal to 5.0 mol% emerge similar broad visible absorption bands. However the sample with (Mg) raised above 6.0 mol% exhibits an abrupt change of the optical absorption features and emerges infra-red absorption band instead of visible bands. And the critical Mg concentration $(Mg)_c$ occurs in the region 5.0-6.0 mol%.

Existence of Oxygen Vacancy under TCR

There are several arguements against the existence of oxygen vacancy in the crystals under TCR depending on the fact that the density of the crystal increases under TCR.(ref.3 and 4)

Oxygen may escape from their lattice-sites in different ways. If an oxygen escapes from its lattice-site leaving a Schottky defect, the density of the crystal decreases. If it escapes from its site leaving a Frenkel defect, the density of the crystal maintains unchanged. However, if it escapes from its site followed by a lattice contracting under TCR and leaving no lattice vacancy, the density of the crystal increases. In fact, the density variation of the crystal under TCR relies on the ratio of the ways oxygen escaping from their lattice-sites. Therefore, we believe that oxygen vacancies can be formed and yet be attended by an increase of density under TCR.

Origin of the Optical Absorptions

The optical absorptions caused by TCR of undoped and lightly Mg-doped congruent $LiNbO_3$ are characterized by a strong, thermally stable, and broad band peaked near 514 nm with two small shoulders on its longer wavelength side. Its origin was interpreted to F center by Sweeney (ref.5) and Arizmendi (ref.6), and to dipolaron by Schirmer (ref.3), and to complex defects composed by F center with different types of dipolarons by us (ref.2), respectively. The TCR heavily Mg-doped crystal emerges a band near 1470 nm instead of the visible bands of the lightly Mg-doped crystals. Its origin was ascribed to Mg^+ (ref.5) and to the appearance of Mg^{2+} in the Nb^{5+}-site (ref.7).

According to the stacking fault model of congruent $LiNbO_3$, there would be Nb_{Li} adjacent to Nb_{Nb} forming Nb_{Li}-Nb_{Nb} dipolarons. The oxygen adjacent to the dipolarons are more thermally unstable. They may be prior to escape from their lattice-site and form F centers under TCR. Since the bonding of an Nb^{5+} ion to its neighboring O^{2+} ions has a rather covalent behavior, it tends to trap additional electron. Therefore, the two electrons from the F center should be shared with two adjacent Nb^{5+} forming a (Nb_{Li}-F-Nb_{Nb}) defect. This defect has as its main features the F center and a Nb_{Li}-Nb_{Nb} dipolaron. The Nb^{5+} ions adjacent to F centers would share F electrons with the oxygen vacancies and exhibit partly Nb^{4+} behavior. This center is associated with the Nb antisite, so its concentration decreases with increasing Li/Nb ratio in the TCR undoped crystal. We propose that the optical absorptions of the TCR undoped crystal are mainly caused by this center, which is consistent with the observation of Garcia-Cabanes (ref.8) that the optical absorption strongly decreases with increasing Li/Nb ratio.

In lightly Mg-doped $LiNbO_3$ with (Mg) 2.70 mol%, as (Mg) increases, the Nb_{Li}-Nb_{Nb} would progressively replaced by Mg_{Li}-Nb_{Nb} dipolarons. Under TCR, the oxygen adjacent to the dipolarons may also prior to escape from their lattice-sites and form F centers. In this defect, both Mg and Nb have partly covalent behavior and would share F electrons with the oxygen vacancy, resulting in (Mg_{Li}-F-Nb_{Nb}) defect. Since the (Mg_{Li}-F-Nb_{Nb}) and the (Nb_{Li}-F-Nb_{Nb}) are comparable in structure, they should possess similar optical absorption features. And the (Mg_{Li}-F-Nb_{Nb}) defect formed under TCR is associated with defect 2 in the crystal.

The crystals with (Mg) between 2.70 and 5.30 mol% contains defect type 2 and 3. In de-

fect type 3, the monovalent Li-deficient is just filled up by a divalent Mg^{2+} ion and an additional electron is trapped, its neighboring oxygen is thermally more stable against F center formation. Therefore, we believe that the optical absorptions of the TCR lightly Mg-doped crystal are mainly caused by the (Nb_{Li}-F-Nb_{Nb}) and (Mg_{Li}-F-Nb_{Nb}) defects. So the crystals with (Mg) between 0-5.30 mol% have similar optical absorption features.

The heavily Mg-doped crystals, with (Mg) between 5.30-10.01 mol%, contain defect type 3 and 4. The electrically neutral defect cluster formed by three defect 4 is stacked by two cation prism in the C direction with an oxygen at the center of one prism and surrounded by one Nb_{Nb}, one Mg_{Nb}, and two Mg_{Li}. Since both Mg^{2+} and Nb^{5+} have partly covalent behavior, this oxygen is thermally more unstable than all the other oxygens and is easy to escape under TCR, resulting in a (Mg_{Li}-Mg_{Nb})-F-(Mg_{Li}-Nb_{Nb}) defect. This defect has as its main features the F center and both the (Mg_{Li}-Mg_{Nb}) and the (Mg_{Li}-Nb_{Nb}) dipolarons. The two F electrons in this defect are shared by the four partly covalent cations, it raises the ground state of the system and makes the optical absorptions of the center shifting to the infra-red region. Therefore, the TCR heavily Mg-doped crystals with (Mg) raised above 5.30 mol% exhibit an abrupt change on the optical absorption features. The appearance of Mg_{Nb} in the heavily Mg-doped congruent crystals has been confirmed by OH^- infra-red absorption measurements (ref. 9).

The Relation Between (Mg) Threshold Effect and the Defect Structures

The (Mg) threshold effect makes the congruent Mg:$LiNbO_3$ exhibiting abrupt changes on physical properties when (Mg) raised above a critical $(Mg)_c$..It implies an abrupt change of defect structure in the crystals when (Mg) is raised above $(Mg)_c$. We proposed that the (Mg) threshold effect is originated from the appearance of Mg_{Nb}. According to above discussions on defect structures, Mg_{Nb} appears in the crystal when (Mg) exceeds $x/(25+x)$. However this is not a precise formula because of the existence of other types of minor defects, but we may use it to evaluate $(Mg)_c$ approximately. The curve of $(Mg)_c$ varying with the parameter x is approximately a straight line. In the present study x=1.4, for congruent crystal, the $(Mg)_c$ should approximately be $(Mg)_c$=5.30 mol%, in the region 5.0-6.0 mol%. According to our optical absorption measurements and other experiments (ref.7), the $(Mg)_c$ falls in the region 5.0-6.0 mol%. Our theoretical result coincides with the experiments.

Reference:

(1) Qi-ren Zhang and Xi-qi Feng, Phys. Rev.B, 43, pp.12019-12024, 1991.

(2) Qi-ren Zhang and Xi-qi Feng, Phys. Stat. Sol. (a) 121, pp. 429-435, 1990.

(3) O. F. Schirmer, O. Thiemann and M. Wohlecke, J. Phys. Chem. Sol.52, pp. 185 1991.

(4) D. D. Smyth, Ferroelectrics 50, 93, 1983.

(5) K. L. Sweeney and L. E. Halliburton, Appl. Phys. Lett. 43, 336, 1983.

(6) L. Arizmendi, J. M. Cabrera and F. Agullo-Lopez, J. Phys. C, 17, 515, 1984.

(7) Xi-qi Feng, Qi-ren Zhang and Jianchen Liu, Sci. China 33 (1), 108, 1990.

(8) A. García-Cabañes, J. A. Sanz-García, J. M. Cabrera, F. Agulló-López, C.Zaldo, R. Pareja, K. Polgár, K. Rakaśnyi and I. Földvari, Phys. Rev. B 37, 6085, 1988.

(9) Xi-qi Feng and Qi-ren Zhang (unpublished)

OPTICAL ASSOCIATIVE MEMORY USING PHOTOREFRACTIVE $LiNbO_3$:Fe HOLOGRAM, AND $LiNbO_3$:Fe AND $BaTiO_3$ PHASE CONJUGATE MIRROR

Zhiming CHEN, Tadashi KASAMATSU, Masaru SHIMIZU and Tadashi SHIOSAKI

Department of Electronics, Faculty of Engineering,
Kyoto University, Kyoto 606-01, Japan

Abstract

Experimental results were presented for phase conjugate wave generation, and the possibility of an application to an optical associative memory was discussed. Using an iron-doped lithium niobate single crystal, more than 300% reflection efficiency was achieved by the degenerate four-wave mixing method, and it was almost independent of the total incident optical intensity. The generator was then applied as a phase conjugate mirror to an all-optical associative holographic memory to reflect and amplify the diffracted beams. The retrieved output image was formed by using partial input illumination. Using a barium titanate single crystal, about 70% stable phase conjugate reflection was obtained by the self-pumping method. In order to accelerate the speed of the generation, a new method, called accelerated-SPPC, was presented.

Introduction

There have been many reports on the photorefractive (PR) effect in such crystals as $LiNbO_3$, $BaTiO_3$, $Bi_{12}SiO_{20}$, $Bi_{12}TiO_{20}$ and $Ba_xSr_{1-x}Nb_2O_6$.[1-8] The PR effect has been studied for applications to optical amplification, phase conjugate wave generation, optical storage and optical information processing because large optical interactions can be produced in the photorefractive materials using a light source with the lowest possible intensity. The study of phase conjugate wave generation has become one of the most promising research fields since the initial studies began in the early 1970s.[9] Owing to optical distortion correction, whereby all distortions in the wavefront of the incident laser beam are reversed upon reflection from the phase conjugate mirror, a wide variety of potential applications have been demonstrated.[10-13] $LiNbO_3$:Fe and $BaTiO_3$ single crystals are useful materials for phase conjugate generation using degenerate four-wave mixing (DFWM), self-pumping (SP) and mutual pumping (MP) methods, as is well known.[14-18]

However there have been few papers reporting on phase conjugation by DFWM in $LiNbO_3$:Fe and self-pumped phase conjugate generation from $BaTiO_3$ with a stable and high reflectivity. The purpose of this study was to investigate $LiNbO_3$:Fe and $BaTiO_3$ single crystals as phase conjugate generators using the DFWM and SP methods respectively. A high reflectivity was obtained and the generator was then applied to an all-optical associative memory. In this paper, we will describe some of the results obtained concerning the phase conjugate generators and their application to the optical associative memory.

Phase Conjugation by Four-Wave Mixing Using $LiNbO_3$:Fe

A Y-cut $LiNbO_3$:Fe0.09mol% crystal with a thickness of 3.3 mm[19] was used for this study. This crystal showed an absorption coefficient of 1.9 cm^{-1} at a wavelength of 514.5 nm. Figure 1 shows the experimental arrangement for degenerate four-wave mixing. An Ar ion laser operating at 514.5 nm was used and the light polarization was parallel to the incident plane. The external incident angle 2θ was 11° and the internal angle $2\theta_i$ was about 5°. Here, the backward pump beam I_b was adjusted incoherently with probe beam I_p and forward pump beam I_f (the optical path differences were more than 40cm), so only a transmission grating (single grating) was induced by the coherent "writing" beams I_p and I_f. This grating was monitored by the diffraction of I_b (called the "reading" beam) to produce a fourth "output" beam I_c which was phase-conjugated with I_p. The intensity of the created phase conjugate wave increased in the initial stage of the beam-coupling and then decreased after a peak because of optical damage. In our experiment, the maximum intensity was defined as I_c and the rela-

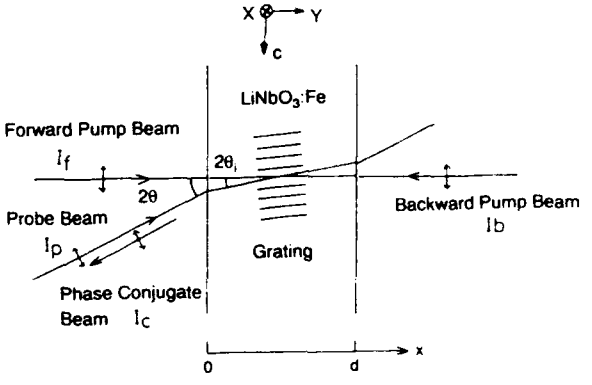


Fig.1. Experimental arrangement for four-wave mixing.

CH3080-0-7803-0465-9/92$3.00 ©IEEE

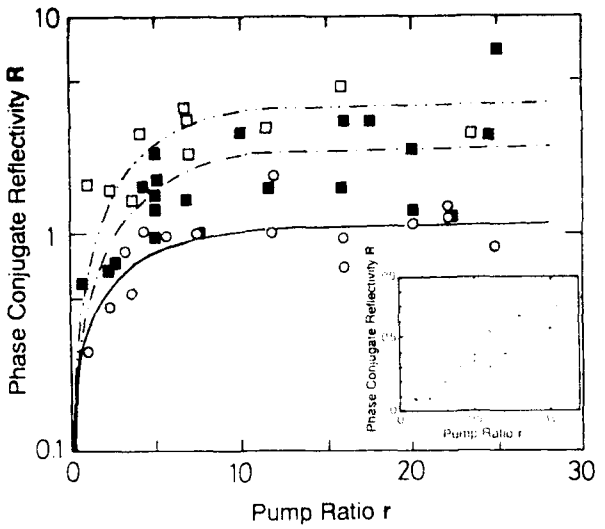


Fig.2. Pump ratio r dependence of phase conjugate reflectivity R with I_b=83mW/cm² and ◘(double dot & dashed curve) for β=0.05; ■(single dot & dashed curve) for β=0.1; ◘(solid curve) for β=0.2. Inset for I_f=1.2mW/cm² and β=0.1.

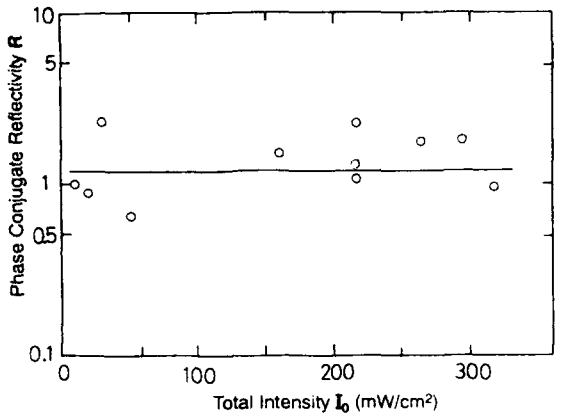


Fig.3. Total intensity I_0 dependence of phase conjugate reflectivity R with β=0.1.

tive time was defined as the response time τ_{max}. The dependence of the reflection efficiency $R=I_c(0)/I_p(0)$ on the pump ratio $r=I_b(d)/I_f(0)$ was measured. The inset of Fig.2 shows the dependence of the reflectivity with I_f=1.2mW/cm² and $\beta=I_p(0)/I_f(0)=0.1$ on the pump ratio of r ranging from 0 to 1. The dependence observed was clearly linear for small r. The dependence of the reflectivity with I_b=83mW/cm² and β=0.05, 0.1 and 0.2 on r with a range of 1 to 25 is shown in Fig.2. Because the real part of the coupling coefficient $\gamma=\Gamma/2+i\Gamma'$ was dependent on β,[20] the reflectivity R with β=0.05 showed a large value of more than 300%, and a amplified I_c beam was created. This demonstrated the material's potential for use in optical associative memories. Figure 3 shows that the phase conjugate reflectivity R with β=0.1 is independent of the total incident light intensity $I_0=I_p+I_f+I_b$. In Fig.4 the dependence of the response time τ_{max} on the incident total intensity I_0 was presented. It can be seen that a total energy of about E_{fwm}=20J/cm² was needed to produce I_c in the crystal.

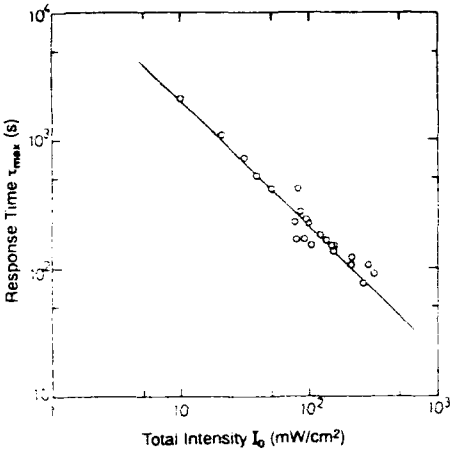


Fig.4. Total intensity I_0 dependence of response time τ_{max}.

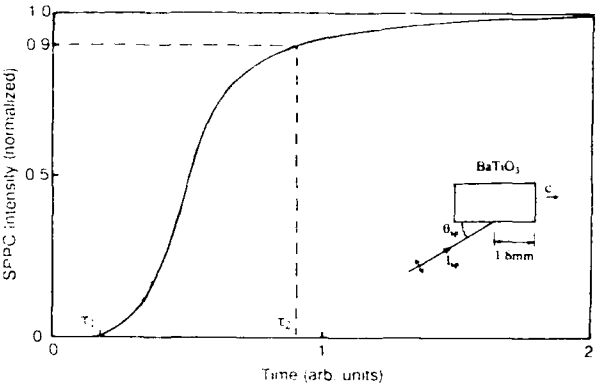


Fig.5. Time dependence of self-pumped phase conjugation wave intensity.

Self-Pumped Phase Conjugation Using $BaTiO_3$

A $BaTiO_3$ single crystal[21] of 2.6mmx2.8mmx3.8mm(c) with an absorption coefficient of 1.5 cm^{-1} at 514.5 nm was used for this study. An extraordinary polarized beam from a 514.5-nm cw Ar ion laser was used to study the response of self-pumped phase conjugation (SPPC). In order to obtain the stable output of SPPC, we changed the incident light position and, the region from 1.6 to 2.0 mm from +c face was found to be the most suitable region to obtain a stable output of SPPC in the crystal. Hence, the incident position was selected at about 1.8 mm from the +c face in this experiment. The diameter of the incident pump beam I_{sp} was focused down to about 0.3 mm by a convex lens. During measurements, the recorded gratings in the crystal were photoerased by a strongly uniform illumination. A stable response of SPPC I_{sc} was observed, as shown in Fig.5. The τ_1 and τ_2 were defined as delay time and response time respectively. The external angle θ_{sp} of incidence of the pump beam to the entrance face was changed from 6° to 38°. The dependence of the reflectivity $R_{sp}=I_{sc}/I_{sp}$ with I_{sp}=0.61mW on the incident angle θ_{sp} is illustrated in Fig.6. The measurement in Fig.6 shows that a high reflectivity of the SPPC of about 70% could be induced within an angle of 16° to 30°. This result shows the possibility that the SPPC could be directly ap-

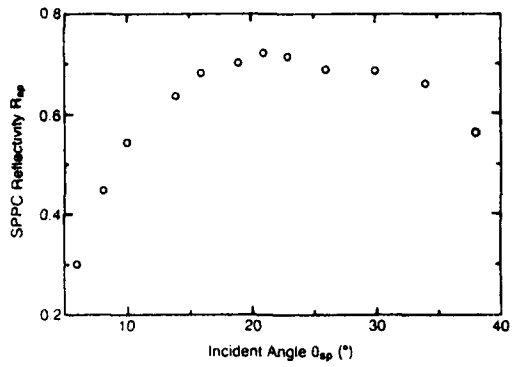


Fig.6. Incident angle θ_{sp} dependence of SP phase conjugate wave reflectivity R_{sp} with incident beam intensity I_{sp}=0.61mW.

plied to an optical associative memory to reflect the diffracted beams if a readout beam with a power of 40 μW was used. In Fig.7 the dependence of the delay time τ_1 and response time τ_2 on the intensity of pump beam is presented. It indicated that a total energy of about 12.5 mJ was needed to create the self-pumped phase conjugate wave and about 54.2 mJ was needed to achieve 90% of the full output. For a low-power I_{sp}, the response time was so long that the application would be limited. For the purpose of solving the problem, we used a new method called accelerated-SPPC. In order to accelerate the generation of I_{sc}, a strong light beam, which was coherent with the weak I_{sp}, was led into the same incident position in the same incident plane with an angle of about 2° to I_{sp}. The result was that the response time of I_{sc} was accelerated more than 100 times and became as quick as that of the strong beam.

Application to Optical Associative Memory

The basic principle of the optical associative memory is as follows. Several (N) images are recorded in a volume hologram by using a separate reference beam for each. In the associative step, a certain input image (or a partial one) is illuminated only with the signal beam. As a result, N diffracted beams centered angularly in the direction of the reference beams are created, with intensities corresponding to the correlation coefficients between the input and the stored images. The diffracted beams are then amplified and

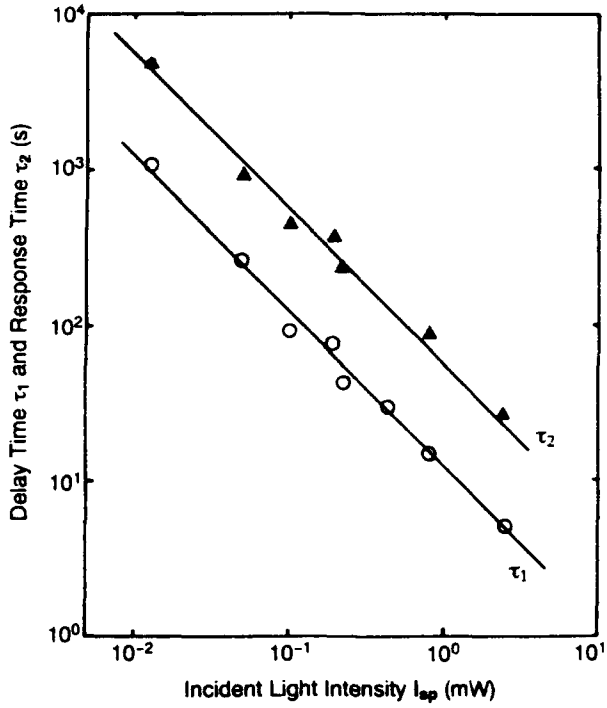


Fig.7. Incident beam intensity I_{sp} dependence of delay time τ_1 (O) and response time τ_2 (▲).

reflected from the phase conjugate mirror. These beams run back to the hologram and illuminate it from the opposite side. This results in an output most closely resembling the input or a retrieval of the stored image on the screen.

An *X-cut $LiNbO_3$:Fe0.10mol% sample with a thickness of 1.8* mm was used for the real-time holograph in the optical associative memory.[3] The configuration of an optical associative memory system is shown in Fig.8. A half-prism and a pinhole were fixed to an X stage. Because the focus of lens L_2 was adjusted into the hologram crystal, by moving the X stage the incident angle of the reference beam I_r could be changed and multiple images were holographically recorded. The signal beam I_s was expanded to 15mm to carry images and was then focused into the crystal by lens L_1. The $LiNbO_3$:Fe0.09mol% crystal mentioned was used as the phase conjugate mirror to amplify and reflect the diffracted beams.

In the writing step, an image s (Fig.9(a)) was placed at the input

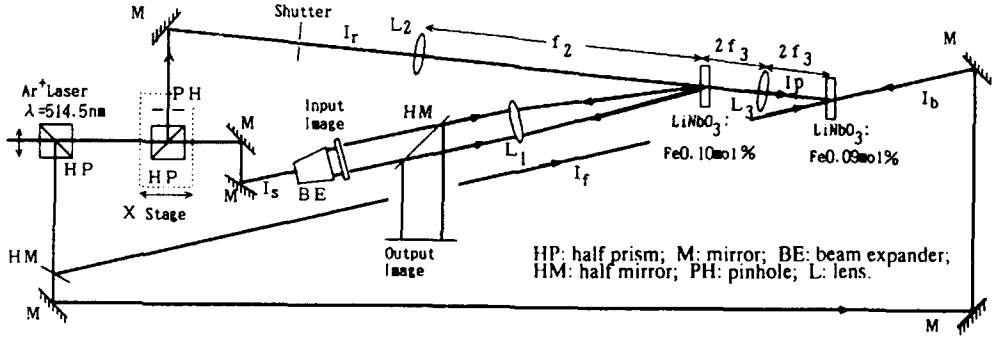


Fig.8. Configuration of optical associative memory system.

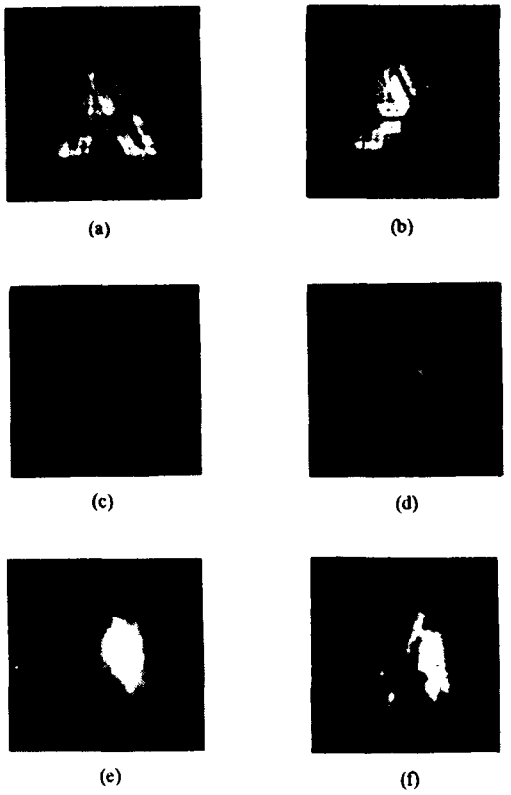


Fig.9. (a) Single-stored image s; (b) partial image input s'; (c) output at 77 seconds; (d) output at 180 seconds; (e) output at 300 seconds; (f) output at 480 seconds.

position and recorded with I_s=6mW/cm^2 and I_r=110mW/cm^2 for 300 seconds to create the holograph, whose diffraction efficiency η was more than 20%. In the associating process, a partial image s' (Fig.9(b)) was used as an input image with I_r=0, I_s=6mW/cm^2, I_f=20mW/cm^2 and I_b=100mW/cm^2. The outputs are shown in Figs.9(c)-9(f). The indistinct and clear s' occurred at 77 seconds (Fig.9(c)) and 180 seconds (Fig.9(d)), respectively. At 300 seconds the retrieved output (Fig.9(e)) was formed on the screen. At 480 seconds the clear completed image s was read out (Fig.9(f)). But after 600 seconds of continuous illumination, the output began to be blurred because of the optical damage created in the crystals. In addition, the effective reflectivity of observed output image can be expressed as

$$R_{obs} \approx R\eta^2 T^4 c,$$

where R is reflectivity of the phase conjugate mirror, η the diffractive efficiency of the holograph, T surface intensity transmissivity of the holograph and c cross-correlation of s' with s. Hence, the requirements for using $LiNbO_3$:Fe as the hologram and phase conjugate mirror are that:

(a) faithfulness of the stored image is high;

(b) diffraction efficiency η is as large as possible;

(c) gain or reflectivity of the phase conjugate mirror is large;

(d) response time of the phase conjugate mirror τ is short;

(e) degradation by readout is as small as possible.

Conclusions

PR crystals $LiNbO_3$:Fe and $BaTiO_3$ were investigated as a phase conjugate generator, and more than 300% and 70% reflection efficiencies were obtained, respectively. Using the former generator in an optical associative memory, we observed retrieval of the stored image by a partial input. However, some problems remained to be solved, in particular, the degradation of the information in the writing and reading steps. The results of the latter generator demonstrated a possibility that the accelerated-SPPC could be directly applied to an optical associative memory to reflect the diffracted beams if a readout beam with a power of 40 μW was used.

Acknowledgements

The authors wish to thank Mr. H. Tominaga and Fujikura Ltd. for providing with the $BaTiO_3$ single crystal. This work was partly supported by a Grant-in-Aid for Developmental Scientific Research (B) (1) (No. 03555060).

References

1) J.Baquedano, M.Carrascosa, L.Arizmendi and J.M.Cabrera: J. Opt. Soc. Am. B **4** (1987) 309.
2) D.Nolte: Condens. Matter News **1** (1992) 17.
3) Y.Tanaka, Z.Chen, T.Kasamatsu and T.Shiosaki: Jpn. J. Appl. Phys. **30** (1991) 2359.
4) T.Suzuki and T.Sato: Appl. Opt. **31** (1992) 606.
5) Y.Owechko: IEEE J. Quantum Electron. **25** (1989) 619.
6) S.I.Stepanov, M.P.Petrov and S.L.Sochava: Ferroelectrics **92** (1989) 199.
7) F.Vachss and T.Y.Chang: J. Opt. Soc. Am. B **6** (1989) 1683.
8) S.R.Montgomery, J.Yarrison-Rice, D.O.Pederson, G.J.Salamo, M.J.Miller, W.W.Clark III, G.L.Wood and E.J.Sharp, R.R.Neurgaonkar: J. Opt. Soc. Am. B **5** (1988) 1775.
9) B.Ya.Zel'dovich, N.F.Pilipetsky and V.V.Shkunov: *Principles of Phase Conjugation*, Springer Series in Optical Sciences (Sprinter-Verlag, Berlin, 1985) Vol.42.
10) D.M.Peppepper, J.AuYeung, D.Fekete and A.Yariv: Opt. Lett. **3** (1978) 7.
11) J.Feinberg and R.W.Hellwarth: Opt. Lett. **5** (1980) 519.
12) G.J.Dunning, E.Marom, Y.Owechko and B.H.Soffer: Opt. Lett. **12** (1987)346.
13) O.Ikeda: J. Opt. Soc. Am. B **4** (1987) 1387.
14) J.Feinberg, D.Heiman, A.R.Tanguay, Jr. and R.W.Hellwarth: J. Appl. Phys. **51** (1980) 1297.
15) J.O.White, M.Cronin-Gollomb, B.Fischer and A.Yariv: Appl. Phys. Lett. **40** (1982) 450.
16) S.Weiss, S.Sternklar and B.Fischer: Opt. Lett. **12** (1987) 114.
17) P.Gunter and J.-P. Huignard: *Photorefractive Materials and Their Application II* (Springer-Verlag, Berlin, Heidelberg, New York, London, Paris, Tokyo, 1989) Chap.6.
18) A.Yariv, S.-K.Kwong and K.Kyuma: Appl. Phys. Lett. **48** (1986) 1114.
19) M.Ohira, Z.Chen, T.Kasamatsu and T.Shiosaki: Jpn. J. Appl. Phys. **30** (1991) 2326.
20) Z.Chen, T.Kasamatsu and T.Shiosaki: to be published in Jpn. J. Appl. Phys. **31** (1992)
21) O.Nakao, K.Tomomatsu, S.Ajimura, A.Kurosaka and H.Tominaga: to be published in Jpn. J. Appl. Phys. **31** (1992).

Dielectrics : Synthesis, Size Effects

THE EFFECT OF DYSPROSIUM ON THE MICROSTRUCTURE AND DIELECTRIC PROPERTIES OF $(Ba_{1-x}Sr_x)TiO_3$ CERAMICS

HONG-WEN WANG and DAVID A. HALL

Materials Science Centre, University of Manchester
Grosvenor Street, Manchester M1 7HS, United Kindom

ABSTRACT

A study was performed on the microstructure and dielectric properties of barium strontium titanate ceramics having compositions $(Ba_{1-x}Sr_x)TiO_3$, and $(Ba_{0.99-x}Sr_xDy_{0.01})TiO_3$, with x in the range from 0 to 0.3. In all cases, the addition of dysprosium resulted in a marked reduction in grain size, from ≈50 μm to ≈1μm, which was accompanied by a substantial increase in dielectric permittivity below the Curie temperature. Furthermore, the peak in permittivity at the Curie point was strongly suppressed by Dy-doping, and the phase transition range became broad and diffuse, particularly at the higher levels of strontium. TEM observations of a high density of dislocations and an inhomogeneous distribution of strontium within the grains suggest that the chemical segregation of strontium is largely responsible for this diffuse phase transition behaviour.

I. INTRODUCTION

Barium titanate ceramics have been used extensively as capacitor dielectrics for the past 40 years[1]. Over this period, numerous studies of the dielectric properties of barium titanate-based ceramics have been carried out. Pure $BaTiO_3$ undergoes a paraelectric to ferroelectric phase transition at 130°C, which is accompanied by a sharp peak ($\epsilon_r \approx 10{,}000$) in the dielectric permittivity. Isovalent dopants, such as strontium or lead, are often employed to lower or raise the Curie point for particular applications. However, coarse-grained ceramics still possess many undesirable characteristics with respect to their use in stable capacitors, notably a strong dependence of permittivity on temperature and electric field[2-3]. As a result, extensive efforts have been made to produce fine-grained ceramics in which these characteristics are less pronounced.

Fine-grained barium titanate ceramics (grain size ≈ 1 μm) possess a high permittivity at room temperature ($\epsilon_r \approx$ 3000-5000) and show relatively stable dielectric properties over fairly wide ranges of electric field and temperature. The mechanism responsible for the high permittivity in fine-grained materials has been discussed by several authors, but a comprehensive and universally-accepted explanation has yet to be presented[4-6].

Yamaji et.al.[7] found that incorporation of 0.8 at% Dy (a donor) on the barium site caused an increase in permittivity ($\epsilon_r \approx 3000$) and a reduced dependence of ϵ_r on temperature and D.C. bias voltage. The materials were said to have a fine-grained (≈1.25 μm) microstructure and a reduced frequency of 90° domains (only 10% of the grains showed 90° domains). The results were interpreted in terms of the model developed by Buessem et al.[4-5], which assumed that the width of ferroelectric 90° domains in $BaTiO_3$ ceramics remains constant at ≈1 μm. The high permittivity of the fine-grained ceramic below the Curie point is then attributed to the internal stress generated from the cubic-tetragonal phase transition on cooling.

In contrast, Arlt et.al.[6] found very fine 90° domains (width ≈0.1μm) in $BaTiO_3$ ceramics with a grain size of 0.5 μm, and suggested that the average width of 90° domains is proportional to the grain size for grain sizes in the range 0.1 to 10 μm. In this case, it was suggested that 90° domain-wall motion might play an important part in the high permittivity of fine-grained $BaTiO_3$ ceramics. Arlt et.al. suggested that the absence of 90° domains in Yamaji's work[7] might be a result of cation vacancies produced by the donor dopant, since it was known that lead vacancies have a strong influence on the formation and mobility of ferroelectric domains in $Pb(Zr,Ti)O_3$.[8]

It seems likely that a treatment incorporating aspects of both of these models (ie. internal stress and the presence of 90° domains) may provide the correct explanation. Recently, Arlt and Pertsev[9] have suggested that the high permittivity is actually due not solely to the increase in domain wall area, since the effective force constant for domain wall displacement is inversely proportional to the domain width, but to an additional increase in domain wall mobility as a result of the reduced tetragonality of fine-grained ceramics.

In $Ba_{0.65}Sr_{0.35}TiO_3$ ceramics, Osbond et.al.[10] found that the permittivity below the Curie temperature for fine-grained (≈1 μm) materials was lower than that for coarse-grained materials, in contrast to the situation for $BaTiO_3$. The present study was carried out in order to provide further information on the grain size-property relationships in barium titanate-based materials, and to clarify the apparently anomalous result for $Ba_{0.65}Sr_{0.35}TiO_3$ ceramic. Barium strontium titanate ceramics were prepared having compositions $(Ba_{1-x}Sr_x)TiO_3$ and $(Ba_{0.99-x}Sr_xDy_{0.01})TiO_3$, with x in the range 0 to 0.3, dysprosium being employed as a grain growth inhibitor.

II. EXPERIMENTAL PROCEDURE

The starting raw chemicals were high purity $BaCO_3$, TiO_2, $SrCO_3$, and Dy_2O_3 (all >99%). Specimens were prepared by the conventional mixed oxide method. The compositions prepared were $(Ba_{1-x}Sr_x)TiO_3$ and $(Ba_{0.99-x}Sr_xDy_{0.01})TiO_3$, with x = 0, 0.1, 0.2, and 0.3, these being referred to as BT, B1ST, B2ST, and B3ST (for the non-Dy-doped materials), and BDYT, B1SDYT, B2SDYT, and B3SDYT (for the Dy-doped materials). Each batch was ball-mixed in a polypropylene bottle with ZrO_2 balls and 99.5% pure ethanol for 4 hours and subsequently calcined at a temperature of 1000°C for 4 hours in a pure alumina crucible. The calcined powders were then ball-milled for 4 hours and dried on a hot plate. The dry powder cakes were pulverized using a mortar and pestle and then pressed in a steel die at 200 MPa to produce 10mm diameter green disks. These disks were then sintered at a temperature of 1400°C for 4 hours.

The sintered samples were polished and electroded using Dupont 7095 silver paste. Dielectric properties were measured by a digital LCR meter (HP4284A) from -20°C to 150°C using a heating rate of 3°C/min and a recording interval of 2°C. Microstructures of polished and subsequently chemically or thermally etched specimens were observed by SEM. TEM specimens were prepared from the bulk materials by mechanical thinning followed by ion bombardment with 5kV accelerating voltage and 14° incident angle. The microscopy was done using a Philips EM400T operating at 120kV. Chemical microanalysis was carried out by nanoprobe energy dispersive X-ray analysis (EDX). Crystalline phases in the bulk materials were identified by XRD using CuKα radiation, the (002) and (200) peaks being used to estimate the tetragonality of each composition.

CH3080-0-7803-0465-9/92$3.00 ©IEEE

III. RESULTS

(1) Sintered density, grain size and tetragonality

The sintered densities, grain sizes and tetragonalities for all specimens investigated are shown in Table 1. It is evident that the Dy-doped materials always have a higher sintered density and finer grain size than the undoped ones. It is well known that dysprosium is an effective grain growth inhibitor in $BaTiO_3$[7] and from these observations it is clear that it functions in a similar manner in barium strontium titanate ceramics.

All compositions studied were pure perovskite phase after calcination. The c/a ratios in sintered bodies show that the tetragonality of the unit cell was reduced as Sr content increased. The further reduction of c/a ratio in the Dy-doped materials may be due to the combined effect of the slight increase in the Sr/Ba ratio and the reduction in grain size[7].

Table 1. Sintered Density, Grain Size and Tetragonality for Each Composition.

Composition I.D.	Density (g/cm^3)	Grain size (μm)	c/a ratio
BT	5.72	20-100	1.0100
B1ST	5.69	20-100	1.0080
B2ST	5.68	20-100	1.0060
B3ST	5.67	20-100	1.0035
BDYT	5.92	0.5-1.5	1.0095
B1SDYT	5.85	0.5-1.5	1.0068
B2SDYT	5.73	0.5-1.5	1.0040
B3SDYT	5.71	0.5-1.5	1.0000

(2) Dielectric properties

Significant variations in dielectric properties were observed as a function of both Sr-and Dy-doping, as shown in Fig.1. The most pronounced effect of the addition of strontium is a reduction in the Curie temperature, with a shift ≈ 3°C/at% Sr, in accord with previous results[1]. The reduction in grain size caused by the addition of dysprosium was accompanied by a depression of the peak in permittivity at the Curie point and a general broadening of the phase transition, which became more pronounced as the level of strontium increased. For the materials containing 30% strontium and 1% dysprosium, the dielectric properties were relatively independent of the cooling rate employed, as shown in Fig.1(b). Unfortunately, it was not possible to obtain a reliable measurement of the dielectric properties of materials quenched directly from the sintering temperature due to their semiconducting nature.

For all compositions, it is evident that the fine-grained, Dy-doped materials always exhibit substantially higher values of permittivity in the ferroelectric region below the Curie point.

(3) Microstructure

Domain patterns for the BT and BDYT specimens are shown in Fig.2. The domain width in pure, coarse-grained $BaTiO_3$ is estimated as 0.5-1 μm. Unfortunately, the domain pattern in fine-grained BDYT was not easily revealed by chemical etching. From the TEM micrograph shown in Fig.2(b), it appears that in this material the laminar domains initiate at grain boundaries and stretch into the grain. The domain width was estimated to be 0.1 μm, which agrees with that reported by Arlt et.al. for pure $BaTiO_3$[6], but the frequency of 90° domains is not consistent with Yamaji's work[7]. To eliminate the artefacts caused by ion-beam bombardment, we also observed the domain structure after heating the TEM specimen up to 200°C for 1 hr then cooling to room temperature. This suggested that fine domains do exist in fine-grained Dy-doped $BaTiO_3$. The

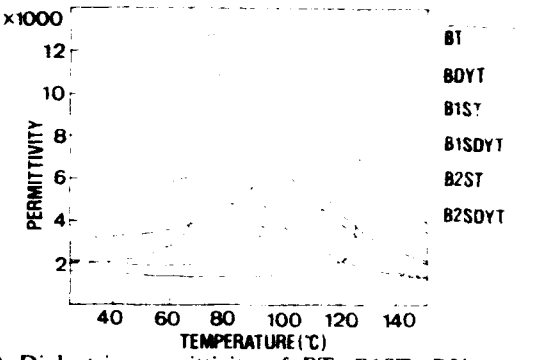


Fig.1(a) Dielectric permittivity of BT, B1ST, B2ST and the corresponding Dy-doped compositions BDYT, B1SDYT, and B2SDYT.

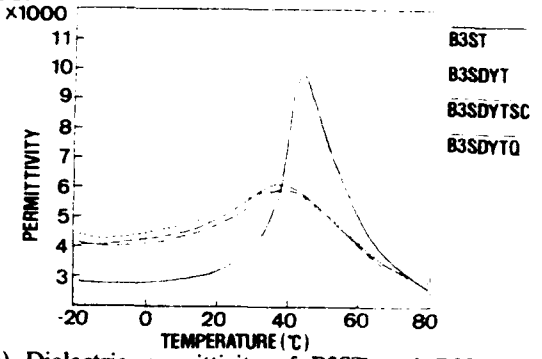


Fig.1(b) Dielectric permittivity of B3ST and B3SDYT. The dielectric permittivity of B3SDYT is relatively independent of the cooling rate after sintering. Similar behaviour is observed for samples subjected to cooling rates of 1°C/min (B3SDYTSC), furnace cooling (≈ 5°C/min, B3SDYT), or air quenching from 1100°C (B3SDYTQ).

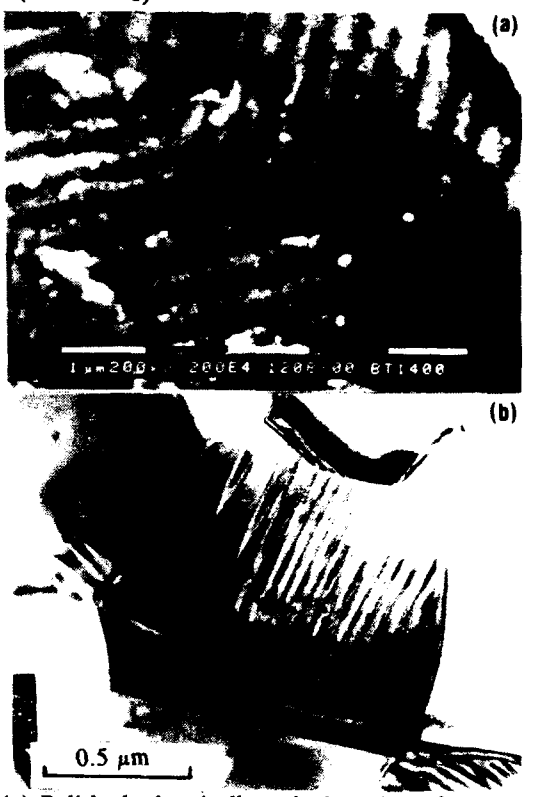


Fig.2 (a) Polished, chemically etched section of coarse-grained $BaTiO_3$ ceramic. The width of the domain is ≈ 0.5-1 μm, depending on the grain orientation. (b) Domain structure in Dy-doped $BaTiO_3$ as observed by TEM. The domain width is ≈ 0.1 μm.

remaining doubt is whether the domain structure in a thin foil is the same as that of the bulk material due to the difference in mechanical constraint.

Clear and well-defined domain structures were not observed in the fine-grained B3SDYT sample at room temperature. Instead, a core-shell like structure was observed, with the core characterized by a high-density of dislocations (Fig.3). In addition, there were many strain spots within the fine grains, which became more evident under electron bombardment during observation. However, when the temperature decreased down to -60°C, the domain structures became clearly evident. Fig.4 shows the domain structures at -20°C and 40°C obtained by heating the thin foil from -60°C to 60°C. When cooling down to -20°C again, these domains reappeared. The domain structures observed at low temperatures suggest that the contribution of domain walls to the permittivity of B3SDYT in the tetragonal phase region may still be important. Nanoprobe EDX analysis indicated that Sr in the shell region (near grain boundaries) is higher than that in the core region, as shown in Fig.5. This might be due to the segregation of Sr to the grain boundary, which resulted in DPT characteristics.

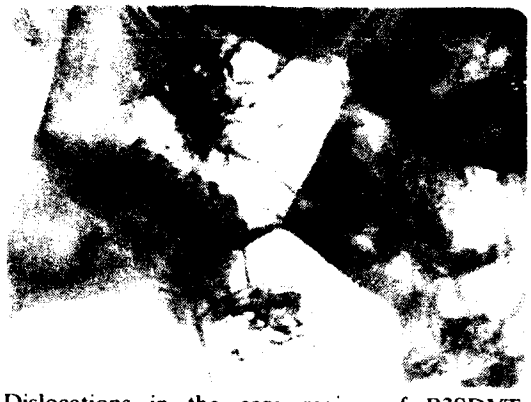


Fig.3 Dislocations in the core region of B3SDYT grain. Observation was performed at room temperature.



Fig.4 (a) Domain structure of B3SDYT at -20°C. (b) Disappearance of the domain structure of B3SDYT at 40°C. The domain structure reappeared when the specimen was cooled down to -20°C again.

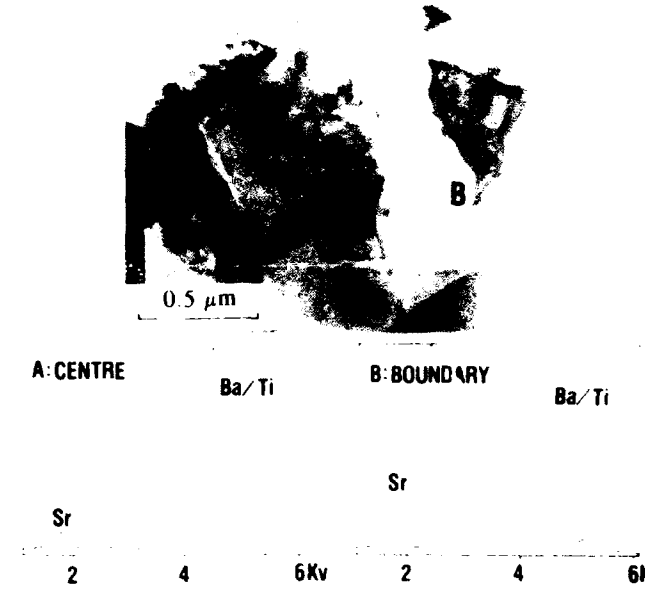


Fig.5 Nanoprobe EDX shows that the Sr content in the grain boundary region was higher than that in the grain centre region.

IV. DISCUSSION

(1) Grain growth inhibition and diffuse phase transition behaviour

It is well known that donor dopants act as effective grain growth inhibitors when present in concentrations greater than a certain threshold level $[D]_c$. For dysprosium, it is found that $[D]_c \approx 0.4$ at% [7]. The transition from coarse to fine-grained coincides with a transition from semiconducting to insulating behaviour as a result of a change in the mechanism of charge compensation, from electronic:

$$Dy_2O_3 + 2TiO_2 \rightarrow 2Dy_{Ba}^{\cdot} + 2Ti_{Ti}^{x} + 6O_o^{x} + \frac{1}{2}O_2 + 2e'$$

to ionic:

$$2Dy_2O_3 + 3TiO_2 \rightarrow 4Dy_{Ba}^{\cdot} + 3Ti_{Ti}^{x} + 12O_o^{x} + V_{Ti}^{////}$$

In the latter case, it is assumed that titanium vacancies will be the dominant cation defect[11]. Recently, Desu and Payne[12] have put forward a comprehensive model which suggests that the donors might segregate to the grain boundaries, and therefore impede grain growth. The inhibition of grain growth results in continuous densification, fine-grained microstructures, and a high sintered density, as observed for all our Dy-doped specimens. It is known that rapid grain growth leads to intra-granular porosity which impedes densification in the final stage of sintering[13], as observed for the non-Dy-doped materials.

The broadened permittivity-temperature characteristic in fine-grained $BaTiO_3$-based ceramics, termed "diffuse phase transition" (DPT), is important for commercial temperature-stable capacitor applications[14]. Additives such as ZrO_2[15], $CdBi_2Nb_2O_9$[16], and $Bi_4Ti_3O_{12}$[17] have been employed to achieve this requirement. The microstructures of these ceramics are often characterized by a core-shell structure, comprising a core of ferroelectric domains and a paraelectric shell. It is believed that this core-shell structure is due to compositional fluctuations during sintering and is the origin of the macroscopic DPT behaviour in $BaTiO_3$-based materials[14-17]. The model given by

Desu and Payne[12] explains the interfacial segregation in $BaTiO_3$ and $SrTiO_3$ ceramics, in which the isovalent dopants segregate to the interfacial regions (grain boundaries), in terms of strain energy considerations. The higher the strain energy, the greater the driving force for segregation. For example, the Ba/Ti ratio observed for 10 at% Ba^{2+} in $PbTiO_3$, $SrTiO_3$ and $CaTiO_3$ ceramics at the interface was 0.162, 0.24, and 0.532, respectively.[12] In the present study, a core-shell like structure was observed in fine-grained Dy-doped barium strontium titanate but not in fine-grained $BaTiO_3$ and non-Dy-doped $(Ba,Sr)TiO_3$. The segregation of Sr near grain boundaries was also observed in the former sample. This could be explained if we take grain boundaries as a segregation sink for isovalent ions. For a fine grain size, such as 1 μm in our case, the grain boundariy region can not be ignored. The segregation of Sr toward the grain boundaries from the grain centre will cause lattice mismatch and internal stress within the grain which will subsequently produce dislocations when the Sr concentration is sufficiently high. The DPT behaviour observed in the Dy-doped barium strontium titanate can thus be attributed partly to an inhomogeneous distribution of strontium. For the coarse-grained, non-Dy-doped $(Ba_{1-x}Sr_x)TiO_3$ materials, the influence of strontium segregation on the dielectric behaviour should be negligible. For example, if we take the effective thickness of the strontium rich layer as 0.25 μm, the proportion of the total volume occupied by the segregation region would be ≈ 75 % for the fine-grained materials (grain size ≈ 1 μm) and only 2 % for the coarse-grained materials (grain size ≈ 50 μm). Hypothetical strontium concentration profiles within fine and coarse-grained materials are presented in Fig.6.

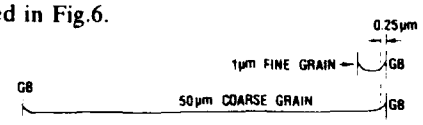


Fig.6 Hypothetical Sr concentration profile near the grain boundary. The proportion of the total volume occupied by the Sr-rich region will be much smaller in coarse-grained materials.

Attempts to produce a more homogeneous distribution of strontium by quenching directly from the sintering temperature resulted in a more homogeneous distribution of the donor, Dy, and produced a dark, semiconducting material, as noted by Desu and Payne[12]. It is likely that the internal stress in the fine-grained materials will also play some part in broadening the phase transition region, since it is well known that the transition temperature of barium titanate-based ceramics is dependent on hydrostatic pressure[10]. The relative contributions of compositional inhomogeneity and internal stress to the DPT behaviour of fine-grained barium strontium titanate ceramics have yet to be established.

(2) High permittivity of Dy-doped materials

The high permittivity of fine-grained $BaTiO_3$ ceramics in the ferroelectric state (below Tc) has been explained in terms of internal stress[4,5] or of an increased domain wall contribution[6]. In the present study, we have observed ferroelectric domain structures in all of the Dy-doped, fine-grained materials, in contrast to previous reports[7]. It could be suggested that this itself does not represent conclusive evidence that fine domains would exist in bulk materials since, as noted above, the mechanical constraint in a thin foil will be different to that of a grain clamped in 3 dimensions. However, Arlt has presented clear evidence of fine 90° domain structures in polished, etched sections of fine-grained $BaTiO_3$ ceramics[18]. Thus, it appears likely that the domain-wall contribution will play a major role. An analysis of the results in terms of the recent model developed by Arlt and Pertsev[9] would not be appropriate at present, since it has not yet been possible to determine the lattice parameters of all the materials in the tetragonal region, and the dielectric behaviour is further complicated by the segregation of strontium.

Further work will be required in order to clarify the effects of strontium segregation, and to quantify the domain wall and volume contributions to the high permittivity of the fine-grained materials. In particular, this will involve the preparation of materials by 'chemical' methods, which should produce a more homogeneous initial distribution of strontium, and the fabrication of fine-grained barium strontium titanate ceramics without the use of a donor dopant.

CONCLUSIONS

The dielectric properties of fine- and coarse-grained $(Ba_{1-x}Sr_x)TiO_3$ were measured and correlated with their microstructures. All of the fine-grained materials exhibited a higher dielectric permittivity below the cubic-tetragonal phase transition than that of the coarse-grained materials. With increasing levels of strontium, the peak in permittivity at the Curie point was suppressed and the phase transition region was broadened. TEM observations suggest that domain-walls may make a substantial contribution to the high permittivity of the fine-grained ceramics, and that the DPT behaviour is due to the combined effects of compositional heterogeneity and internal stress.

ACKNOWLEDGEMENTS

The authors would like to thank Mr. G. Cliff for assistance with the TEM work and the Nuffield Foundation for financial support.

REFERENCES

1. B. Jaffe, W.R. Cook, and H. Jaffe, "Piezoelectric Ceramics" Academic Press (1971)
2. R.J. Brandmayr, Tech. report ECOM-2719, August (1966)
3. H.C. Graham, N.M. Tallan and K.S. Mazdiyasni, J. Amer. Ceram. Soc. 54, [11]548-553(1971)
4. W.R. Buessem, L.E. Cross, and A.K. Goswami, J. Amer. Ceram. Soc. 49, [1]33-36(1966)
5. W.R. Buessem, L.E. Cross, and A.K. Goswami, J. Amer. Ceram. Soc. 49, [1]36-39(1966)
6. G. Arlt, D. Hennings, and G. de With, J. Appl. Phys. 58, [4] 1619-1625(1985)
7. A. Yamaji, Y. Enomoto, K. Kinoshita and T. Murakami, J. Amer. Ceram. Soc. 60, [3-4]97-101(1977)
8. R. Gerson, J. Appl. Phys. 31, 188-194(1960)
9. G. Arlt and N.A. Pertsev, J. Appl. Phys. 70, [4]2283-2289(1991)
10. P.C. Osbond, et.al., ISAF '86, 384-351(1986)
11. H.M. Chan, M.P. Harmer, and D.M. Smyth, J. Amer. Ceram. Soc. 69, 507-510 (1986)
12. S.B. Desu, and D.A. Payne, J. Amer. Ceram. Soc. 73, [11] 3391-3421(1990)
13. J. Zhao, and M.P. Harmer, J. Amer. Ceram. Soc. 71, [7]530-539(1988)
14. D. Hennings, Int. J. High Technol. Ceram. 3, 91-111(1987)
15. H.Y. Lu, J.S. Bow, and W.H. Deng, J. Amer. Ceram. Soc. 73, [12]3562-3568(1990)
16. D. Hennings and R. Rosenstein, J. Amer. Ceram. Soc. 67, [4] 249-254(1984)
17. R.S. Rawal, M. Kahn, and W.R. Buessem, Adv. in Ceram. vol.1 edited by L.M. Levinson. Amer. Ceram. Soc. p.172-188(1981)
18. G. Arlt, J. Mater. Sci. 25, 2655-2666(1990)

GRAIN SIZE EFFECT ON THE DIELECTRIC PROPERTIES OF STRONTIUM BARIUM TITANATE

U. Kumar, S. F. Wang, S. Varanasi, and J. P. Dougherty

Center for Dielectric Studies
Materials Research Laboratory
The Pennsylvania State University
University Park, PA 16802

Abstract: In this paper, the grain size effect observed on the dielectric properties of $Sr_{0.2}Ba_{0.8}TiO_3$ (SBT) ceramic is reported. For this study, SBT powder prepared by a hydrothermal procedure was used. A porous ceramic was prepared by sintering the powder compacts between 1100°C-1350°C/5min.-10h, either by conventional sintering or by 'fast firing'. When the average grain size of the ceramic was between 0.75-1.2 μm, the room temperature dielectric constant peaks to 5500-6000. In porous fine grain ceramic also, classic P vs. E hysteresis behavior is observed.

Introduction

Grain size effects on the dielectric properties of $BaTiO_3$ has been an active area of research over three decades. Ever since, Kniekamp and Heywang[1] reported the observation of anomalously high room temperature dielectric constant in $BaTiO_3$ ceramic with an average grain size of 1 μm, several research articles appeared in the literature. Careful literature review indicate that the observed grain size effect is a strong function of several external and a few internal variables. Effect of chemical purity, preparation procedure, initial particle size distribution of the powder, final grain size distribution, resistivity of the grains and the grain boundaries and the density of the ceramic etc., should be considered as external contributions to the dielectric anomaly. Through careful preparation it is possible to minimize the effect of external variables.

While discussing the intrinsic effect, it is necessary to consider the boundary conditions very carefully. Buessem et al.,[2] prepared high density ceramic with varying grain sizes. SEM analysis of the fine grain ceramic showed fewer ferroelectric domains as compared to coarse grain ceramic. It is well known that in a coarse grain ceramic, the volume change associated with the cubic to tetragonal phase transition is minimized through domain formation. In fine grain ceramic, grains without multi-domains will induce stress of complex nature on other grains. Anomalous increases in the dielectric constant of fine grain ceramic are explained as a direct consequence of the stress.

Arlt et al., [3] on the other hand, observed that the domain size is a strong function of grain size. Through SEM and TEM observations, they observed an increase in the domain density when the average grain size of the ceramic was between 1 μm and 10 μm. Additionally, the domain size reduced as a function of grain size. They proposed that the increase in room temperature dielectric constant is at least partially due to the increase in domain wall density.

Shaikh et al., [4] observed similar anomaly in a porous ceramic. Effect of density on the magnitude of dielectric constant is discussed in a paper by wa Gachigi et al.,[5] in this issue.

In fine grain $BaTiO_3$ ceramic, the tetragonal to orthorhombic transition occurs nearer to 25°C instead of 0-5°C. Some of the observations, such as the difference in domain size, splitting of <200> peak in XRD patterns are expected to be influenced by the presence of the orthorhombic phase.

To minimize the complications due to the orthorhombic phase, it is desirable to investigate the grain size effect in $BaTiO_3$-based solid solutions. Moreover, understanding the size effect in commercially important solid solutions such as $Sr_{1-x}Ba_xTiO_3$, $Ba(Zr_xTi_{1-x})O_3$ etc., is essential to tailor the microstructure of fine grain thin layer MLCs and thin films. In this paper, we describe the grain size effect on the dielectric properties of $Sr_{0.2}Ba_{0.8}TiO_3$ ceramic. We have used conventional and 'fast firing' schedules to prepare ceramics with differing densities. The size effects were studied through microstructure, XRD, dielectric, and P vs. E hysteresis behavior.

Experimental

For this study, $Sr_{0.2}Ba_{0.8}TiO_3$ powder, prepared by hydrothermal procedure, (Cabot Corporation, Boyertown, PA) was used. The B. E. T. surface area of the powder is 14.6 m^2/gm. The SEM micrograph of the powder (Fig. 1) clearly shows the size uniformity.

The powder was blended with appropriate amount of PVA solution and glycerol. Pellet preparation and binder evaporation procedures are elaborated in Ref. [6]. Binder removed pellets were sintered between 1100°C and 1350°C for 5min.-10h in a clean furnace. For conventional firing, heating and cooling rates were maintained as 400°C/h. For 'fast firing', the samples were heated to 950°C at a rate of 400°C/h. and then to the soak temperature at 1000°C/h. They were cooled to room temperature with a similar schedule. Bulk density was measured only when the density of the sintered samples were greater than 90% theoretical. For the rest of the samples, geometrical densities are reported. Procedure for dielectric and P vs. E measurements are elaborated in Ref. [7].

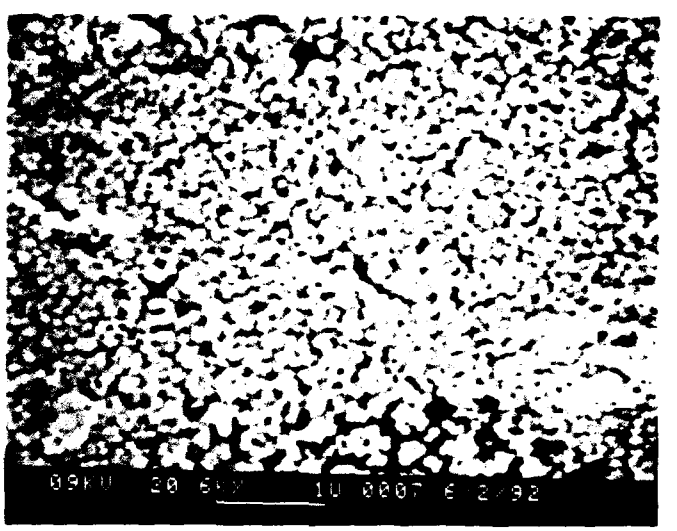
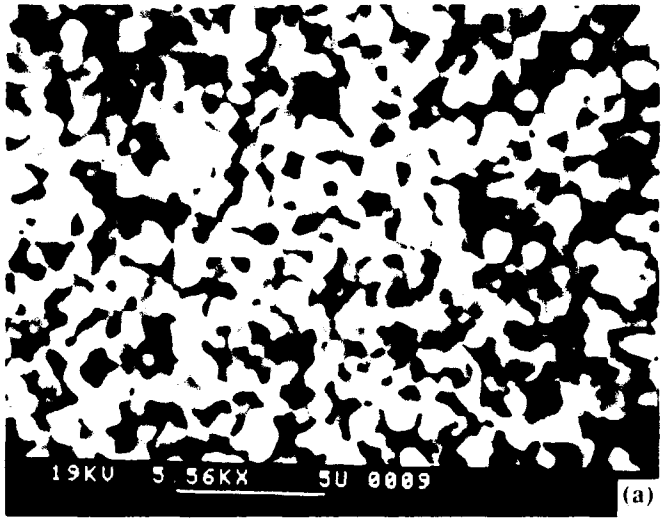


Fig. 1. SEM micrograph of 'as received' SBT powder.

CH3080-0-7803-0465-9/92$3.00 ©IEEE



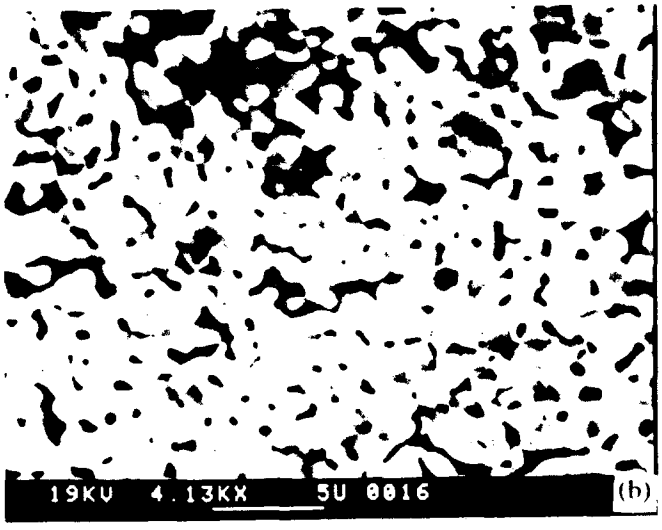


Fig. 2. Typical microstructure of SBT ceramic sintered at (a)1100°C/10h and (b) 1200°C/2h.

Results and Discussions

Densities of the sintered pellets are listed in Table 1. Typical microstructures of the samples sintered below 1250°C are shown in Fig. 2. As the particle size distribution of the starting powder was narrow, the grain size distribution of the sintered ceramic also remained narrow. But when the sintering temperature was raised beyond 1250°C, abnormal grain growth occured. Thus it was not possible to prepare samples with uniform grain size in the range of 3-10 μm.

In Fig. 3., the temperature effect on the dielectric properties are compared. These K vs. T plots are not compensated for porosity. Higher room temperature dielectric constant observed in samples sintered at 1200°C with an average grain size of 0.9 μm, and 87% of theoretical density (Table 1), clearly shows the existence of grain size effect in SBT very similar to that observed in pure $BaTiO_3$. Dielectric constant values at room temperature and at T_c of all the samples are compared in Table 1. To compensate the values for porosity, Botcher's equation was used.

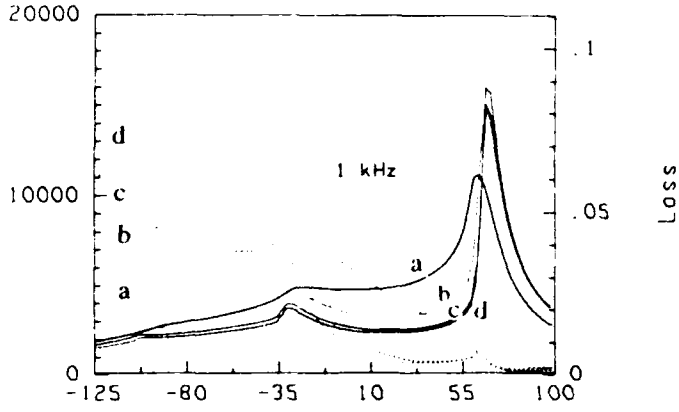


Fig. 3. Dielectric properties of SBT ceramic sintered at (a)1200°C/2h, (b) 1300°C/2h, (c) 1350°C/2h and (d) 1350°C/10h; solid lines are dielectric constant and dotted lines are dielectric loss data measured at 1 kHz.

Table 1. Physical and dielectric properties of SBT ceramic

Sint. Temp (°C/h)	Ave g.s (μm)	Dens (% theo)	K_{RT} (obs.)	K_{RT} (Cal)	$K_{at\ Tc}$ (Obs.)	$K_{at\ Tc}$ (Cal.)	Curie Cons. x10^5 °C	T_{c-t} (°C)	T_{t-o} (°C)	Pr (μC/cm^2)	Ec (KV/cm)
1100/4	0.7	65.87	2360	4840	4480	9180	1.56	61			
1100/6	0.75	68.26	2880	5500	5650	10800	1.73	63			
1100/10	1.25	69.45	3775	6260	7280	12080	1.54	62	-20	2.1	1080
1150/5	0.9	68.87	3095	5800	7720	14475	1.78	65	-24		
1175/0.5		74.64	3700	5970	7190	11600	1.47	61	-22	2.95	1700
1200/0.5	0.7	76.17	3850	5990	9800	13360	1.49	62	-19	1.98	1480
1200/2	0.9	87.17	4810	5970	11160	13800	1.40	63	-24	3.88	1125
1300/2	>8.0	96.34	3200	3390	14750	15600	1.51	67	-26	4.36	590
1350/2	>10.0	97.07	2480	2590	16000	18740	1.50	66	-28	4.70	530
1350/10	>10.0	97.19	2310	2890	15050	15700	1.47				
1255/5m(F)	1.0	72.53	3270	5570	8630	14680	1.70	64	-25		
1275/5m(F)	1.2	78.52	3580	5280	10075	14870	1.49	64	-25	2.44	870
1300/5m(F)	1.2	80.92	3660	5400	11580	16220	1.50	65	-25	3.44	840

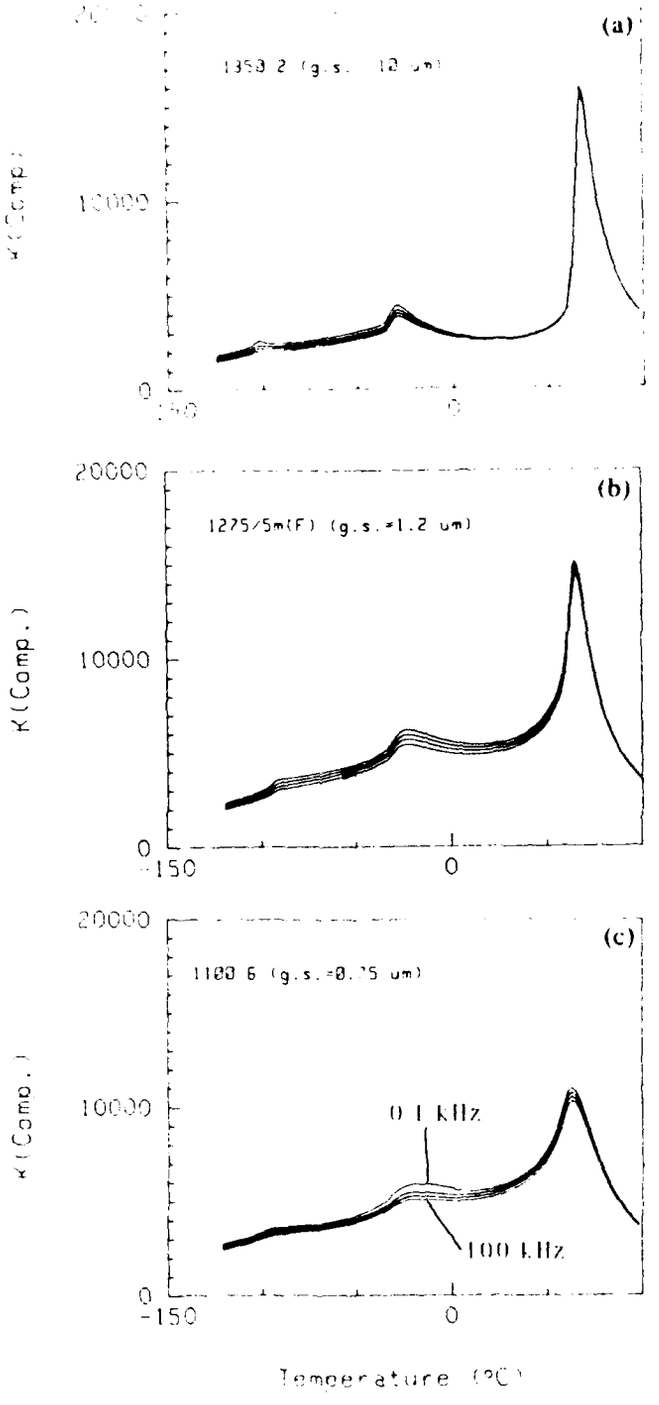


Fig. 4. Effect of measuring frequency on the dielectric properties of SBT ceramic sintered at (a) 1250°C/2h, (b) 1275°C/5min (Fast fired), and (c) 1100°C/6h; measuring frequencies were 0.1, 1, 10, and 100 kHz.

Comparing the porosity corrected values, it is clear that a peak room temperature dielectric constant of 5500-6000 is observed when the average grain size of the ceramic is between 0.75-1.2 μm. In Fig. 4a,b, and c, the frequency effect on the dielectric constant of ceramic with differing grain sizes are plotted. Above T_c, K vs. T behavior is nearly independent of measuring frequency in all the cases. In Table 1, Curie constant of these samples are compared. As seen the magnitude falls within a narrow range of 1.4-1.7 x 10^5(°C). In Fig 4b and c, fine grain ceramic show smearing of dielectric peak at all three transition temperatures. In table 1, two of the transition temperatures are listed. When the average grain size of the ceramic is reduced from 10 μm to 0.7 μm, the cubic to tetragonal transition temperature decreases from 67°C to 62°C, whereas the tetragonal to orthorhombic transition temperature raises from 28°C to 19°C. Since the dielectric peak corresponding to the orthorhombic to rhombohedral transition occurs over a large temperature range in fine grain ceramic, these values are not tabulated.

In Fig 5, the P vs. E behavior of three samples is compared. As seen, in fine grain ceramics, the induced polarization reduces systematically. But, since the density of these samples are not the same, only the general behavior should be considered for comparison. Even in a fine grain porous ceramic, appearance of the classic P vs. E hysteresis is particularly noticeable. In Table 1, P_r and E_c values calculated from the hysteresis curves are listed.

In Fig 6 a and b, the polished and etched microstructures of two of the sintered ceramics are shown. The samples were polished slowly and carefully, so that the surface temperature of the samples are maintained always nearer to room temperature. To get a representative domain structure of the bulk, about 0.1-0.2 mm thick surface layer was removed before polishing. In Fig. 6b, domains in the fine grain ceramic is very clearly seen. Since the density of the samples fired at temperatures below 1300°C were low, it was not possible to polish them properly. At present eventhough the existence of multi domains in fine grain ceramic is clearly demonstrated, it is necessary to prepare dense ceramic to quantify the domain size and the domain density as a function of grain size.

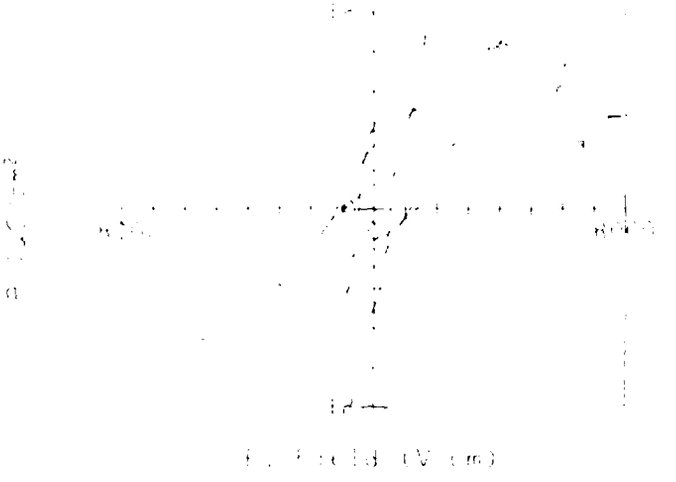


Fig. 5. P vs. E hysteresis behavior of SBT ceramic sintered at (1) 1350°C/10h, (2) 1200°C, and (3) 1100°C/10h.

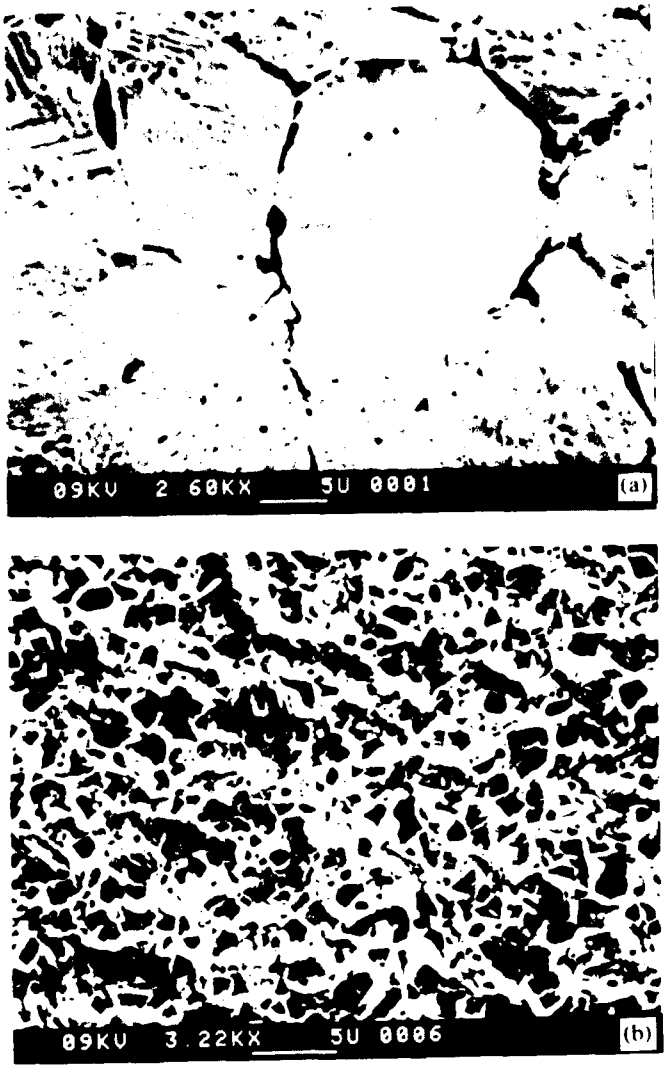


Fig. 6. Polished and etched microstructure of SBT ceramic sintered at (a) 1300°C/10h, and (b) 1300°C/10 min.

Conclusions

Based on the experimental observations, the following conclusions are drawn:

1. When the grain size of the ceramic is between 0.75-1.2 μm, the K_{RT} values peaks to 5500-6000.

2. The Curie constant of the ceramic is relatively independent of the grain size.

3. In fine grain ceramics, suppression of Tc and enhancement of low temperature transitions are clearly seen.

4. Fine grain ceramics also show classic P vs. E hysteresis behavior.

5. Etched and polished microstructure of fine grain porous ceramic show multi-domain characteristics.

To quantify the results, it is necessary to prepare dense ceramics with differing average grain sizes ranging from 0.1μm to 10μm with narrow distribution.

Acknowledgements: Authors gratefully acknowledge the financial support from Cabot Corporation of Boyertown, PA and the Ben Franklin Partnership Program of the Commonwealth of PA. Authors also acknowledges the technical support provided by Mingfong Song.

References

[1] H. Kniekamp, and W. Heywang," Depolarization effects in polycrystalline $BaTiO_3$," Z. Agnew Phys., Vol. 6, p.385-390, (1954).

[2] W. R. Buessem, L. E. Cross, and A. K. Goswami, J. Am. Ceram. Soc., vol. 49, p. 33 (1966).

[3] G. Arlt, D. Hennings, and G. deWith," Dielectric properties of fine grained $BaTiO_3$," J. Appl. Phys., Vol. 58, p.1619-1625 (1984).

[4] A.S. Shaikh, R. W. Vest, and G. M. Vest," Dielectric properties of ultrafine grained ceramic," IEEE Trans. on Ultrasonic, Ferroelectrics and Frequency Control, Vol. 36, no.4, p.407-412 (1989).

[5] K. wa Gachigi, U. Kumar, and J. P. Dougherty," Grain size effects on $BaTiO_3$," this issue.

[6] U. Kumar, S. F. Wang, and J. P. Dougherty," Preparation of dense ultra-fine grain barium titanate -based ceramics," this issue.

[7] S. F. Wang, U. Kumar, W. Huebner, P. Marsh, H. Kunkel, and C. Oakley," Grain size effect on the induced piezoelectric properties of 0.90PMN-0.10PT ceramic," this issue.

And the references in [1]-[7].

HYDROTHERMAL SYNTHESIS OF MODIFIED LEAD TITANATE POWDERS

C. E. Millar, W. W. Wolny.
Ferroperm A/S, Hejreskovvej 6, 3490 Kvistgård, Denmark.

L. Pardo
Instituto de Ciencia de Materiales (Sede A). CSIC,
Serrano,144, 28006 - Madrid, Spain

Abstract

Hydrothermal synthesis has shown promise as a technique for preparing submicron powders of multicomponent oxides. Powders obtained by this technique have been used successfully to achieve fine grained, dense ceramics. Here, the processing of modified lead titanate powders by hydrothermal synthesis and the fabrication of ceramics from the powder produced are described. Results of powder and ceramic characterisation are presented and related to the processing conditions used. The dielectric and piezoelectric properties of the ceramics obtained are compared with those for ceramics prepared by conventional mixed oxides. Finally, the use of hydrothermal synthesis for the preparation of ceramics for high frequency devices will be discussed.

Introduction.

Hydrothermal synthesis has been used by a number of researchers to prepare lead titanate powders [1,2]. The powders obtained are of submicron particle size and are generally realized at temperatures below 300 °C. However, much of the work carried out has concentrated on producing pure lead titanate powders, and little attention has been given to modified compositions or the sintering behavior of the powders.

Here, the aim of the work was to produce hydrothermally synthesized powders and then to manufacture fine grained ceramics for use in high frequency medical transducers. To this end, a simple route based on TiO_2 powders has been developed for the preparation of the precursor for hydrothermal synthesis. Although the precursor obtained is less reactive than those prepared from $TiCl_4$ or Ti-alkoxide, the process is less complicated and entails reduced risk to health, making it more suitable for large scale production. A composition of samarium modified lead titanate was chosen, which has a high k_t and k_t/k_p ratio, suitable for high frequency single element devices. This paper describes the powder preparation and the ceramic fabrication, and relates the processing conditions to the properties obtained. In addition, the material is evaluated for high frequency applications.

Experimental Procedure.

The modified lead titanate with composition, $(Pb_{0.88},Sm_{0.08})(Ti_{0.99},Mn_{0.01})O_3$ (PTS), was prepared as follows. The required quantities of lead, samarium and manganese nitrates were dissolved in de-ionized water and mixed together. The mixed solution was then added to a stirred suspension of fine TiO_2 powder (particle size < 0.2 μm) in de-ionized water. The pH was adjusted to between 8 and 12 using NaOH solution and the volume of water increased to 2 liters, giving a concentration of 0.5 M.

The suspension was then placed into a 4 litre autoclave. The percentage of volume filled (50 %) and the temperature determined the pressure. Hydrothermal synthesis was carried out for 10 hours at a temperatures between 250 and 300 °C (2 - 8 MPa). The resulting powders were washed repeatedly to remove the nitrate and sodium ions. A sample of the powder was reserved for characterisation, which included, X-ray diffraction (XRD) and determination of particle size and morphology by scanning and transmission electron microscopy (SEM & TEM).

At this stage the fabrication of ceramics has not been optimised. Instead the powders were processed by a similar method to that used for mixed oxides. A binder was added to the wet powder and the powder was dried. Discs were dry pressed and sintered at 1100 - 1200 °C for 2 hours. The sintered discs were ground to obtain parallel faces and electroded. The discs then were poled at 100 °C for 10 minutes with an electric field of 8 kV/mm. After ageing for 24 hours, the dielectric and piezoelectric properties were measured. The sintered ceramics were characterised using SEM to determine average grain size and quantitative energy dispersive X-ray analysis (EDX) technique to study composition.

CH3080-0-7803-0465-9/92$3.00 ©IEEE

Results and Discussion.

An XRD pattern for a powder synthesized at 290 °C for 10 h, pH of 8 (PTS-8) is shown in Figure 1. The powder comprised the perovskite phase, along with a small amounts of unreacted TiO_2. A large peak was also observed at 2.64 Å. The

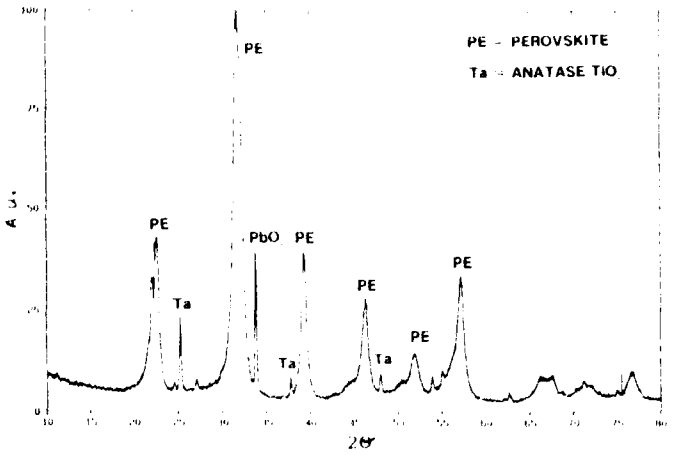


Figure 1 XRD pattern for powder, PTS-8 synthesized at 290 °C, for 10 hours (pH=8).

nature of this peak suggested the presence of a preferentially orientated, well crystallized phase, consisting of particles much larger than those of the perovskite.

The SEM micrograph of the powder, shown in Figure 2, indicates that the perovskite particles are submicron in size.



Figure 2 SEM micrograph of powder, PTS-8, synthesized at 290 °C for 10 h (pH=8).

From TEM, the particle size was determined to be 50 to 200 nm. In addition, SEM examination revealed the presence of a few (approximately 3 volume %) large hexagonal shaped crystals (see Figure 3) which give rise to the diffraction peak at 2.64 Å. EDX analysis of these crystals showed the presence of lead, indicating that they were of a lead oxide composition; the XRD analysis matched PbO_2 [3]. To the authors knowledge, it is the first time that these crystals have been observed in the processing of lead titanate by hydrothermal synthesis. Their presence may be related to the use of lead nitrate as a raw material. However, the crystals are not detrimental to the preparation of lead titanate ceramics as they are removed during sintering.



Figure 3 SEM micrograph of PbO_2 phase in PTS-8 powder.

Attempts were made to eliminate the presence of unreacted TiO_2 after synthesis. These included: increasing the reaction temperature; and/or pH; and sieving or milling the TiO_2 powder to decrease the agglomerate size. Although, a reduction in the quantity of TiO_2 phase was achieved, it was not possible to remove it entirely. However, powders containing the lowest TiO_2 content were obtained by replacing the TiO_2 starting material with an ultra-fine powder (Tioxide, UF12). After synthesis at 290 °C for 10 h (pH=10), the XRD pattern, presented in Figure 4, shows that the powder (PTS-UF) comprised mainly the perovskite phase, with only small quantities of rutile TiO_2 (approximately 4 %) and PbO_2.

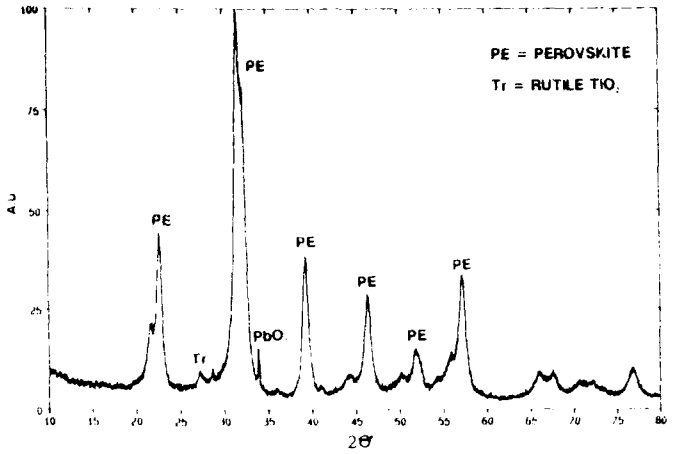


Figure 4 XRD trace of PTS-UF ceramic sintered at 1150 °C for 2 hours

The optimum sintering temperatures for the ceramics were dependant on the hydrothermal conditions used to prepare the powders. For example powders synthesized at 290 °C (pH < 12), ceramics with maximum density were obtained by sintering at 1150 °C for 2 hours. However, powders synthesized at higher temperatures or pH ≥ 12, required a sintering temperature of 1200 °C.

After sintering, XRD analysis showed the ceramics contained both the perovskite phase and a small quantity of rutile TiO_2. The TiO_2 content of the PTS-UF ceramics was estimated at approximately 4 %, Figure 5. PbO_2 was not detected in any of the ceramics.

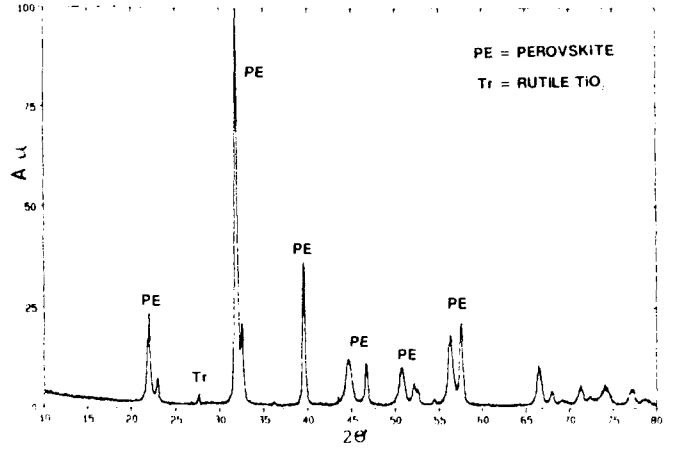


Figure 5 XRD pattern for Powder PT(Sm)-UF synthesized at 290 °C for 10 hours (pH=10)

SEM examination of polished and etched surfaces of ceramics sintered at 1150 °C for 2 hours, revealed the average grain size of the ceramic to be 1 μm, as shown in Figure 6. The pore size ranged from 1 to 4 μm.

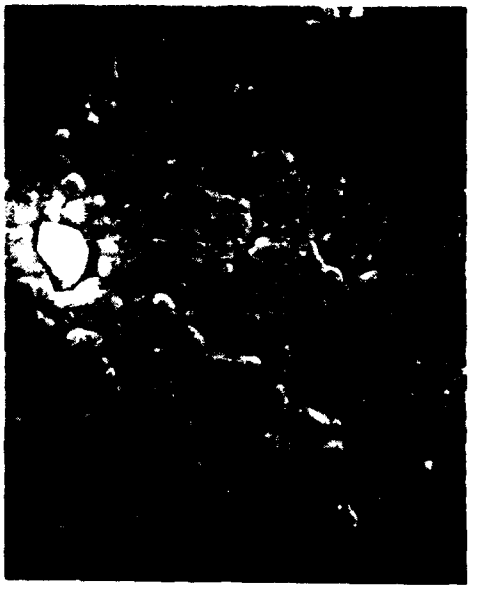


Figure 6 SEM Micrograph of a polished and thermally etched surface of PTS-8.S ceramic sintered at 1150 °C for 2 h.

The EDX results a PTS ceramic is presented in Table I. The measured values obtained are similar to those of the nominal compositions, indicating that good compositional control was achieved.

Table I EDX results for PTS-8.S (S = TiO_2 powder sieved) sintered at 1150 °C for 2 hours.

ratio	nominal	measured
Pb/(Pb+Sm)	0.92	0.90
Sm/(Pb+Sm)	0.08	0.10
Ti/(Ti+Mn)	0.99	0.99
Mn/(Ti+Mn)	0.01	0.01
(Pb+Sm)/(Ti+Mn)	0.96	0.89

From the dielectric and piezoelectric properties for the PTS ceramics presented in Table II, it can be seen that the values obtained are similar to those of Ferroperm's Pz-34 (a similar composition to PTS) prepared by mixed oxides. Comparison of PTS-UF with the other PTS ceramics indicates that the reduction of the TiO_2 second phase had little effect on the dielectric properties, but gives an improvement in both the density and the piezoelectric properties. Thus, PTS-UF offers advantages over Pz-34 of higher piezoelectric properties, lower porosity and finer grain size.

Table II Comparison of Properties of PTS ceramics with Pz-34.

Ceramic	density g/cm³	ε_r	tan δ	kt %	kp %
PTS-8	7.2	190	0.007	43	7
PTS-8.S	7.4	206	0.011	42	7
PTS-12.S	7.4	189	0.011	43	7
PTS-UF	7.7	205	0.011	48	5
Pz-34	7.6	200	0.019	40	3

S= TiO_2 powder, sieved.
8 & 12 refer to the pH used for synthesis

The thickness of some of the PTS-8 discs was reduced to 0.24 mm, resonant frequency 10 MHz, without any appreciable change in properties, and the materials were evaluated for high frequency devices. Their low relative permittivity limits them to single element transducers, used, for example, in intravascular imaging. For these applications, the high k_t/k_p ratio, Figure 7, reduces unwanted resonances, the high k_t value leads to an efficient transducer, and the low dielectric loss gives low noise. The lower porosity of PTS-UF ceramics will allow thinner, higher frequency elements to be manufactured. Finally, ceramics prepared from these hydrothermal powders are especially suitable for single element devices, where the piezoelectric element is very small, often 1 - 2 mm in diameter.

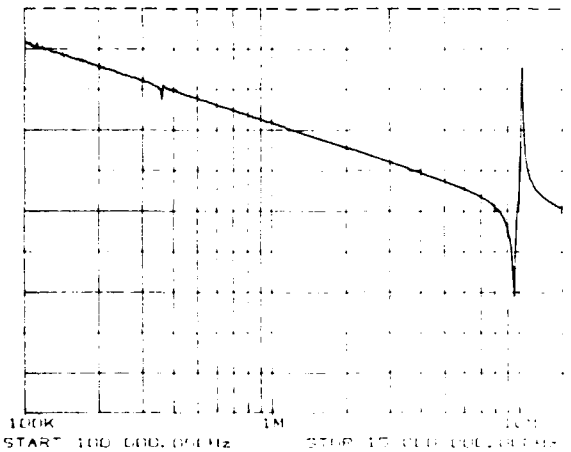


Figure 7 Impedance curve for a 10 MHz PTS-8 ceramic.

Conclusions

A simple route has been developed for the preparation of modified lead titanate powders by hydrothermal synthesis which is suitable for large scale production.

The powders obtained have submicron particle size.

Ceramics fabricated from these powders have higher densities and improved piezoelectric properties than those of a similar composition prepared by the mixed oxides route.

The ceramics offer fine grain size and properties suitable for high frequency single element devices.

REFERENCES

[1] D. J. Watson, C. A. Randall, R. E. Newnham, and J. H. Adair, "Hydrothermal Formation Diagram in the Lead Titanate System," Ceram. Trans: Ceramic Powder Science II vol. I, pp. 154-162, 1988.

[2] M. Suzuki, S. Uedaira, H. Masuya and H. Tamura, "Hydrothermal Synthesis of Lead Titanate Fine Powders," Ceram. Trans: Ceramic Powder Science II vol. I, pp. 163-170, 1988.

[3] P. Rüetschi and B. D. Cahan, "Anodic Corrosion and Hydrothermal and Oxygen Overvoltage on Lead and Lead Antimony Alloys," J. Electrochem. Soc. vol. 104, pp. 406-413, 1957.

ACKNOWLEDGEMENTS

This work was funded by Brite/Euram project, contract number 0504

SOL-GEL TECHNIQUES FOR THE PREPARATION OF ULTRAFINE $BaTiO_3$ POWDERS

* Qitu Zhang, Dawei Shen, Hui Wang, Wanrong Xue and ** Meiyu Zhao

*Department of Silicate Engineering
Nanjing Institute of Chemical Technology
5 Xinmofan Road
Nanjing, Jiangsu 210009, P. R. China
**Shanghai Institute of Ceramics
Chinese Acadamy of Science
Shanghai 200050, P. R. China

In this study the synthesis of $Ba(OC_2H_5)_2$ from $Ba(ClO_4)_2$ and $LiOC_2H_5$ was discussed first, then $Ba(OC_2H_5)_2$ and $Ti(OC_4H_9)_4$ were used as precursors to prepare ultrafine $BaTiO_3$ powders. The result shows that $Ba(OC_2H_5)_2$ can be obtained from $Ba(ClO_4)_2$ and $LiOC_2H_5$. The ethyl alcohol solutions of $Ba(OC_2O_5)_2$ and $Ti(OC_4H_9)_4$ mixed in equal mols were hydrolyzed in refluxing, to form gel. The gel was dried at 90°C and then heat treated at 900°C for 2 hours. The obtained $BaTiO_3$ powders have an average particle size of 0.15μm.

Introduction

With the development and applications of the high performence ceramics, higher and higher demands have been posed upon the purity, particle size and homogeneity of the raw materials. The high purity, small particle size and good homogeneity of the raw materials are the bases of the reliability and stabilty of ceramic products.

Sol-gel processing in forming compounds has attracted much of recent research interest.[1][2] The ultrafine powders prepared by this technique are ultrapure, homogenous and stoichiometical and can meet the high demands of today's high performance ceramics. The repeatablity of these ceramic products can also be improved. Several researchers have prepared $BaTiO_3$ powders through sol-gel processing.[3][4][5] It revealed from their reports that high performance ultrafine $BaTiO_3$ powders can be obtained via hydrolysis from barium and titanium alcoholates.

In this study $Ba(OC_2H_5)_2$ was derived from the reaction of $Ba(ClO_4)_2$ and $LiOC_2H_5$.[6] Then ultrafine $BaTiO_3$ powders was synthesized using $Ba(OC_2H_5)_2$ and $TiO(C_4H_9)_4$ as precursors.

Exprimental Procedure

Raw Materials

$LiOC_2H_5$, $Ba(ClO_4)_2$, $Ti(OC_4H_9)_4$, ethylene glycol and absolute alcohol are the raw materials in this study.

Preparation of $Ba(OC_2H_5)_2$

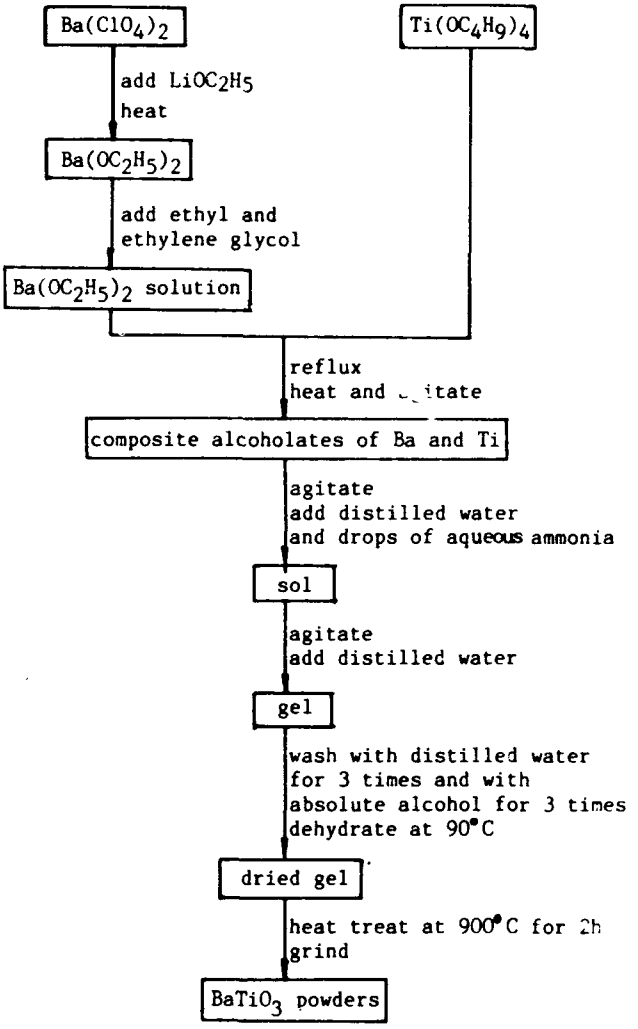
Mix $Ba(ClO_4)_2$ and $LiOC_2H_5$ alcoholic solutions at a 1:2 mole ratio. The mixed solution was then refluxed for 10 hours under heating and agitating condition while following reaction occured

$$Ba(ClO_4)_2 + 2LiOC_2H_5 \longrightarrow Ba(OC_2H_5)_2\downarrow + 2LiClO_4$$

Centrifugate the products after the reaction completed. Wash the precipitate three times with absolute alcohol, and $Ba(OC_2H_5)_2$ is obtained.[6]

Formation of Ultrafine $BaTiO_3$ Powders

Dissolve $Ba(OC_2H_5)_2$ into the solution of ethyl alcohol and ethylene glycol mixed at a 4:1 volume ratio. The solubility of $Ba(OC_2H_5)_2$ in absolute alcohol can be increased due to the presence of ethylene glycol, therefore the overall concentration of $Ba(OC_2H_5)_2$ is also increased. The solubility can be determined through chemical analysis. Mix the solution with tetrabutyl titanate in equal mols and follow sol-gel process to prepare ultrafine BaTiO powders. The technological process is listed as following



Tests and Analyses

Differential thermal and thermal gravity analyses were conducted on the derived gels with a LCT-II thermal analyzer, the temperature ascending rate in the analyses is controlled to be 10°C/min. The phase analysis was performed with a D/max-rA X-ray diffractometer on the dried gels which were heat treated at 300°C, 750°C and 900°C for 2 hours respectively. For the ultrafine $BaTiO_3$ powders derived form the gel which was heated at 900°C, particle size and appearance was observed with a JE-100CX TEM.

Result and Discussion

CH3080-0-7803-0465-9/92$3.00 ©IEEE

Differential Thermal and Thermal Gravity Analyses

TG-DTA results for dried gel were shown in Fig.1. A endothermic peak appears at 95°C accompanied with 40% weight loss according to the curves. This owed to the volatilization of large amount ethanol and water. The heat release peak appears at 285°C along with a 10% weight loss is supposed to be the buring out of organic matter in the gel structure. There is also a heat release peak at 725°C on DTA curve but no significant corresponding TGA effect emerges. This is caused by the transformation from amorphous to cystalline $BaTiO_3$ at this temperature.

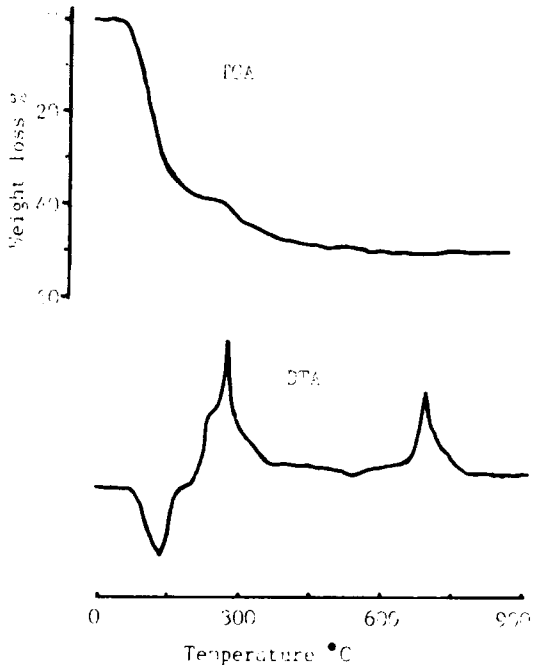


Fig.1 TG-DTA results for dried gel

X-ray Diffraction

Fig.2 shows the X-ray diffraction patterns for the powder samples derived from dried gels heat treated at different temperatures.It has been envinced that the sample existed in amorphous state at 300°C. A large amount $BaTiO_3$ crystal and a few amorphous matter coexisted at 750°C. This shows no difference with TG-DTA results. The samples heat treated at 900°C seems fully crystallized. Formation of crystal at a temperature far below the theoretical solid state reaction temperature is determined by characteristics of gel. Solid state reaction is related to the diffusion process. The diffusion coefficient is rather small at a lower temperature and the reaction occurs too slow to complete. In sol-gel process, with the existence of ethylene glycol, $Ba(OC_2H_5)$ and $Ti(OC_4H_9)_4$ were refluxed to form composite alcoholate of Ba and Ti(alcoholate in the form of ≡Ti-O-Ba- or ≡Ti-O-C_2H_4-O-Ba-). A gel with its components mixed at atomic level was obtained after hydrolysis. Remove the organic matter at around 300°C, the amorphous $BaTiO_3$ forms. The derived powder has small particle size and considerable activity and will crystallize at a relatively low temperature.

Particle Size Analysis

The particle size and appearance of the ultra-

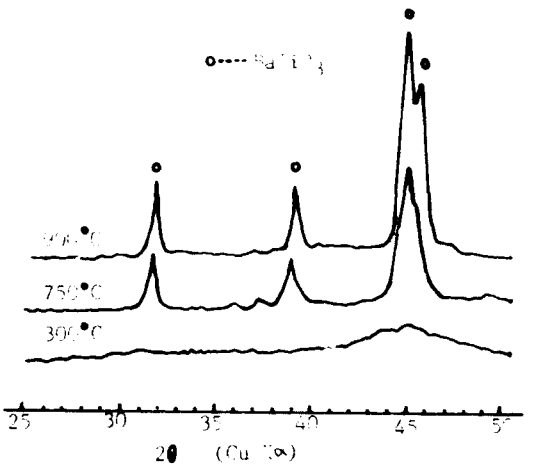


Fig.2 X-ray diffraction patterns for the powder samples derived from gels heated at different temperature

fine $BaTiO_3$ powders heat treated at 900°C for 2 hours were observed with a JF-100CX TEM. The result is shown in Fig.3. The average particle size, according to the TEM photograph, is 0.15μm. It is also shown that the particles are narrowly distributed in size and is spherical or polyhedral in appearance.



Fig.3 Particle appearance observed through TEM for the powder derived from 900°C heat treated gel.

Conclusions

1. $Ba(ClO_4)_2$ and $LiOC_2H_5$ can be used as precursors to form $Ba(OC_2H_5)_2$. And $BaTiO_3$ ultrafine powders can be prepared following sol-gel process from $Ba(OC_2H_5)_2$ and $Ti(OC_4H_9)_4$.

2. Ethylene glycol added to ethyl alcohol can increase the solubility of $Ba(OC_2H_5)_2$ greatly and thus the concentration of $Ba(OC_2H_5)_2$ and $Ti(OC_4H_9)_4$ can be increased. This leads to a fast sol-gel process to form $BaTiO_3$ gel.

3. Sol-gel prepared ultrafine $BaTiO_3$ powders crystallize significantly if heated to 750°C and crystal fully develops at 900°C.

4. Sol-gel prepared $BaTiO_3$ powders are ultrafine, narrowly distributed in size and spherical and polyhedral in appearance.

References

[1] Y. Charbouillot etal., "AMINOSILS: new solid state protonic materials by the sol-gel process," J. Non-Cryst. Solids, vol.103, pp.325-330, 1988.

[2] K. Okada etal., "Characterization of the spinel phase from SiO_2-Al_2O_3 xerogels and the formation process of mullite," J. Am. Ceram. Soc., vol.69[9], pp.652-656, 1988.

[3] Y. Abe etal., "Preparation of polymetalloxanes as a precursor for oxide ceramics," J. Non-Cryst. Solids, vol.121, pp.21-25, 1990.

[4] J. J. Ritter etal., "Alkoxide precursor synthesis and characterization of phases in the Barium-Titanium oxide system," J. Am. Ceram. Soc., vol.69(2), pp.155-161, 1986.

[5] P. P. Phule etal., "Comparison of $Ba(OH)_2$, BaO and Ba as starting materials for the synthesis of Barium-Titanate by the Alkoxi-demethod," J. Am. Ceram. Soc., vol.70(5), pp.C108-C109, 1987.

[6] W. Weng etal., "A study on preparation of $BaTiO_3$ powders through sol-gel process."(in Chinese) in Proceedings of 1st National Symposium on the Sol-gol Techniques, Yangzhou, pp.7-11, April 1990.

Relaxor Dielectrics : Synthesis and Properties

DIELECTRIC PROPERTIES AND CRYSTAL STRUCTURES OF ENTIRE COMPOSITIONS IN THE TERNARY SYSTEM $Pb(Mg_{1/2}W_{1/2})O_3$-$Pb(Ni_{1/3}Nb_{2/3})O_3$-$PbTiO_3$

Atsushi Ochi, Toru Mori and Mitsuru Furuya
Fundamental Res. Labs. NEC Corp.
4-1-1 Miyazaki, Miyamae, Kawasaki, 216 Japan

ABSTRACT

Over the entire range of composition in ternary system $Pb(Mg_{1/2}W_{1/2})O_3$ - $Pb(Ni_{1/3}Nb_{2/3})O_3$ - $PbTiO_3$ (PMW - PNN - PT), crystal structures and dielectric properties were investigated. From the results, a morphotropic phase boundary (MPB) was found on the compositional line with 45 to 50 mol% PT content. Pt rich composition with Tc>100℃ showed steep temperature dependence of dielectric constant. PMW rich composition with Tc around room temperature or below showed diffuse phase transition. Superlattice reflections due to the ordering of Mg and W ions in the perovskite B-site were observed in the X-ray diffraction patterns of PMW rich composition. Frequency dependence of dielectric constant was observed in these composition. D-E hysteresis loops had small coercive electric field. These results indicate that PMW rich compositions were relaxor ferroelectric. Downwards Curie temperature shift according to the PMW content was saturated in the PMW rich compositional region, which suggests PMW rich region is not a simple solid solution but a nanometer-composite of ordered region and disordered region.

INTRODUCTION

Recently, lead-based perovskite compounds have been extensively utilized for multilayer ceramic capacitors (MLCCs), piezoelectric actuators, transducers and so on. Among lead-based perovskite compounds, PMW has been known to form solid solutions with low firing temperature, high resistivity, and wide variety of temperature dependence of dielectric constant. PMW is an antiferroelectrics with Tc=38℃, and Mg and W ions are ordered in the B-site sublattice. Solid-solution systems containing antiferroelectric $Pb(Mg_{1/2}W_{1/2})O_3$ have been widely studied, such as $Pb(Mg_{1/2}W_{1/2})O_3$-$PbTiO_3$,[1] $Pb(Mg_{1/2}W_{1/2})O_3$-$Pb(Mg_{1/3}Nb_{2/3})O_3$,[2] $Pb(Mg_{1/2}W_{1/2})O_3$-$Pb(Fe_{1/2}Ta_{1/2})O_3$,[3] $Pb(Mg_{1/2}W_{1/2})O_3$-$Pb(Fe_{1/2}Nb_{1/2})O_3$,[4] $Pb(Mg_{1/2}W_{1/2})O_3$-$BiFeO_3$[5] and $Pb(Mg_{1/2}W_{1/2})O_3$-$PbZrO_3$[6].

Yonezawa developed dielectric materials for MLCCs in the ternary system $Pb(Mg_{1/2}W_{1/2})O_3$-$Pb(Ni_{1/3}Nb_{2/3})O_3$-$PbTiO_3$ (PMW-PNN-PT).[7] This system has excellent properties for capacitors because the antiferroelectric component, PMW, moderates or weakens the ferroelectricity of PNN and PT. Thus, capacitors with various characteristics, Y5V, Y5U, Y5T of the Electronic Industries Association (EIA) specifications, can be easily designed through the use of this system. Figure 1 shows the temperature variation of dielectric constant in this ternary system.

In the PMW-PNN-PT ternary system, end components have different dielectric phases and different crystal structures to each other; PMW is an antiferroelectric of Tc=38℃ with B-site cations ordered, PNN is a relaxor ferroelectric of Tc=-120℃ with relaxor type B-site cation arrangement, and PT is a normal ferroelectric of Tc=490 ℃ with simple perovskite

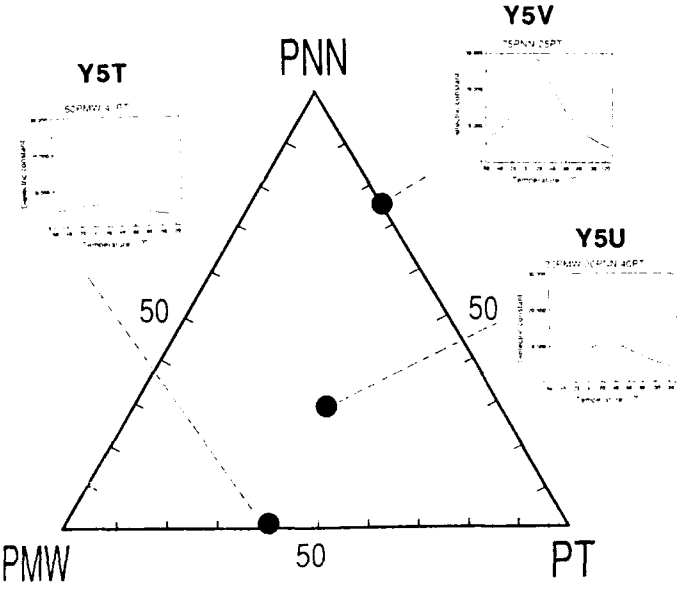


Figure 1. Temperature dependence of dielectric constant for ceramic chip capacitor's practical compositions in PMW - PNN - PT system.

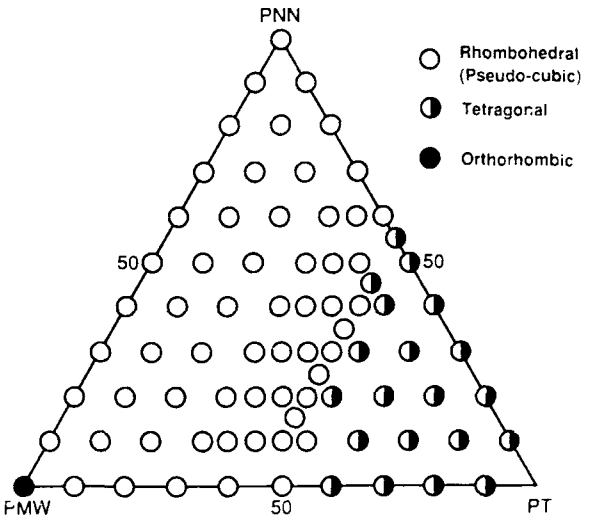


Figure 2. Crystal structures in $Pb(Mg_{1/2}W_{1/2})O_3$ - $Pb(Ni_{1/3}Nb_{2/3})O_3$-$PbTiO_3$ system at room temperature.

CH3080-0/92/0000-0465-9/92$3.00 ©IEEE

structure. Dielectric behavior and crystal structures of this solid solution are therefore very interesting. In this paper, we studied crystal structures and dielectric properties over the entire range of composition in order to understand the effect of PMW component quantitatively. Based on the results obtained, we discuss the relationship between crystal structures and dielectric properties in this system.

EXPERIMENTAL PROCEDURE

Disk samples of all compositions in this ternary system were prepared by the conventional mixed oxide method. Oxide raw materials of PbO and WO_3 with purity>99.9% and MgO, NiO, Nb_2O_5 and TiO_2 with purity>99.5% were weighed in stoichiometric proportions and mixed by ball-milling with deionized water, using resin pots and resin-coated lead balls. The mixtures were calcined at 800 to 850 ℃. The calcined powders were ball-milled again, dried and pressed into pellets of 16mm diameter. Disk samples were fired at 900 to 1250℃.

Crystal structures and lattice constants were determined by X-ray diffraction patterns. Capacitance and dissipation factor were measured over the temperature range -200 to 350℃ at the frequencies 100Hz to 100kHz using a digital LCR meter (YHP4274A).

In order to evaluate the compositional dependence of the dielectric behavior, D-E hysteresis loops were measured by means of a Sawyer-Tower circuit using chip capacitors fabricated with silver-palladium internal electrodes.

RESULTS AND DISCUSSION

Over the entire composition in PMW-PNN-PT system

Figure 2 shows the crystal structures at room temperature in this ternary system. Tetragonal phase is in the compositional region with PT content more than 45 to 50 mol%, orthorhombic phase only in pure PMW and pseud-cubic in the remaining compositional region. A morphotropic phase boundary (MPB) was found on the compositional line with 45 to 50 mol% PT content. Figure 3 shows the compositional dependence of dielectric constants in this system. Comparing Fig.2 with Fig.3, the compositions around MPB are found to exhibit the highest dielectric constants at room temperature. In addition, it should be pointed out that extra peaks from superlattice structures appeared in the PMW-rich compositional region, as shown in Fig.4. Figure 5 indicates the intensity ratio of superlattice extra peak (1/2 1/2 1/2) to perovskite (1 1 1) peak. The superlattice structure appears because some part of Mg and W ions are ordered in 1:1 NaCl-type arrangement at the B-site sub-lattice of perovskite.

Based on the results obtained above, it was thought that the characteristic of this ternary system could be clearly understood by investigating the crystal structures and dielectric properties as a function of PMW/PT ratio. The compositional line of 30mol% PNN content were selected, and with changing PMW/PT compositional ratio dielectric properties and crystal structures were intensively studied.

Crystal structure and dielectric properties

Figure 6 shows the lattice constant at room temperature. Figure 7 shows the temperature dependence of dielectric constant. According to Fig.6 and Fig.7, both side compositions of the MPB (PMW/PNN/PT=25/30/45) had considerably

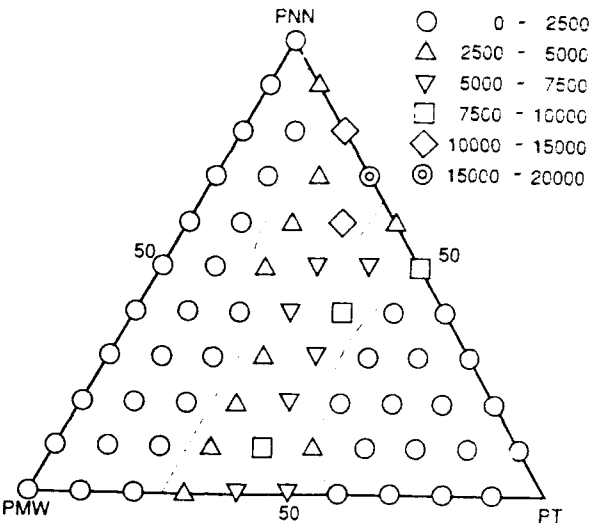


Figure 3. Dielectric constants in $Pb(Mg_{1/2}W_{1/2})O_3$ - $Pb(Ni_{1/3}Nb_{2/3})O_3$ - $PbTiO_3$ system at room temperature.

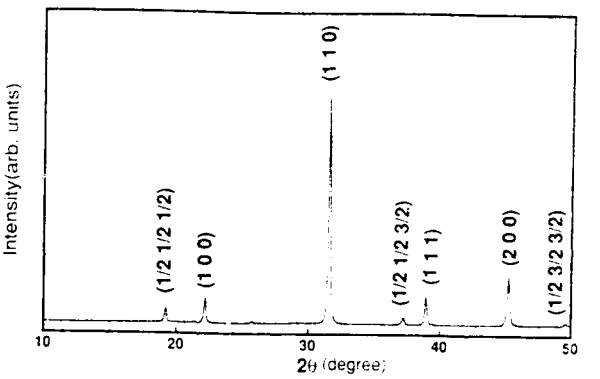


Figure 4. X-ray diffraction pattern for the composition of PMW/PNN/PT=60/30/10 including extra peaks from super lattice.

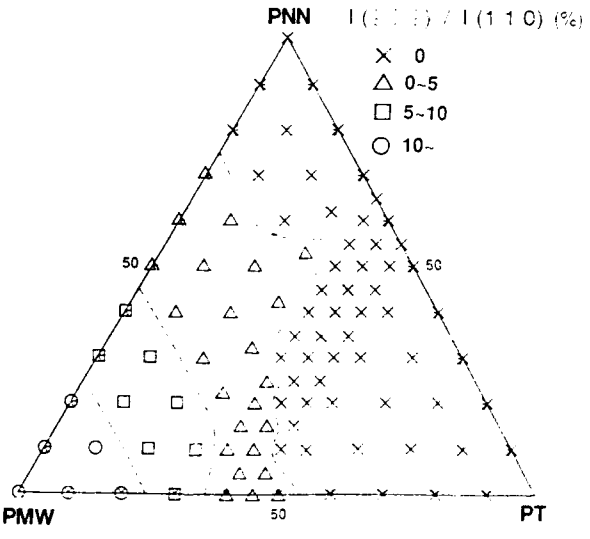


Figure 5. Relative intensity of superlattice reflection (1/2 1/2 1/2) to the fundamental (110) reflection in ternary system $Pb(Mg_{1/2}W_{1/2})O_3$ - $Pb(Ni_{1/3}Nb_{2/3})O_3$ - $PbTiO_3$

different shape of dielectric constant vs. temperature curve. In the tetragonal phase, the curve was sharp and the maximum dielectric constant was high. In the pseud-cubic phase, the curve was broad and the maximum dielectric constant was below 10000. In accordance with the increase of PMW content, the temperature coefficient of dielectric constant decreased and the Curie temperature shifted downward. It is understood that PMW acts strong depressor and shifter in this ternary system.

Curie temperature as a function of PMW content

Figure 8 shows the relationship between Curie temperature and superlattice structure. Within 30mol% PMW, region I, the downwards Curie temperature shift is proportional to the PMW content. Over 30mol% PMW, region II, the downwards shift of Curie temperature becomes weak and showing saturation, while the superlattice peak intensity becomes stronger. From the results, most Mg and W ions on the B-site of perovskite are found to be disordered in region I, and the ferroelectricity is remarkably depressed by Mg and W component. On the other hand, in region II, some of the PMW component forms ordered clusters, and the other Mg and W ions are disordered. The interference of the ferroelectricity therefore has been saturated. It is reported that Mg ions are inactive with regard to ferroelectricity[8,9]. Mg ions arranged randomly in B-site sublattice effectively depress the ferroelectricity, compared with Mg ions in the ordered clusters.

Frequency dependence of Curie temperature

As described above, temperature dependence of dielectric constant is broad in PMW rich compositions, which is characteristic to relaxor ferroelectric. Frequency dependence of temperature variation of dielectric constant, which is the essential phenomena of relaxor ferroelectrics, was also measured. Figure 9 shows the result for 0.3PMW-0.3PNN-0.4PT. Figure 10 indicates the frequency dispersion of Curie temperature as a function of PMW content. A parameter ΔT_c was defined here as the difference between the Curie temperature measured at 100Hz and that measured at 10kHz; which represents the degree of relaxation in phase transition. As for compositions within 20mol% PMW content, the frequency dispersion was not observed (ΔT_c=0). Over 30mol% PMW content, ΔT_c was not zero and the dielectric behavior around transition temperature was the same as that of typical relaxor ferroelectric. The value of ΔT_c increases with the increase of PMW content reaching the maximum at 50 or 60mol% PMW content, and ΔT_c at 70mol% PMW decreased. The decrease in ΔT_c is thought to be related to an appearance of antiferroelectricity from the ordering of Mg and W ions.

D-E hysteresis loops and dielectric phases

D-E hysteresis loops were measured in order to observe the dielectric phase directly. As shown in Figure 11, the D-E hysteresis loops for PMW/PNN/PT=50/30/20 is characteristic of the typical relaxor ferroelectric with small coercive electric field. The D-E hysteresis curve for PMW/PNN/PT=10/30/60 is rectangular with large coercive force. For the composition of PMW/PNN/PT=70/30/0, an antiferroelectric phase is seen at -110 ℃ and moreover, a ferroelectric phase appears at lower temperature of -150 ℃. This type phase transition (ferro - antiferro - para) has been also reported for PMW-PT and PMW-PMN system. [2]

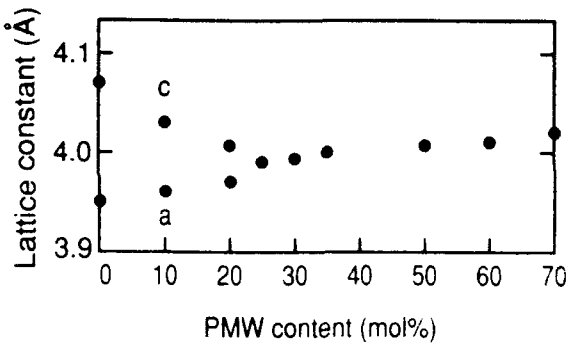


Figure 6. Lattice constant for the dielectric composition; xPMW-0.3PNN (1-x)PT (x=0 -0.7).

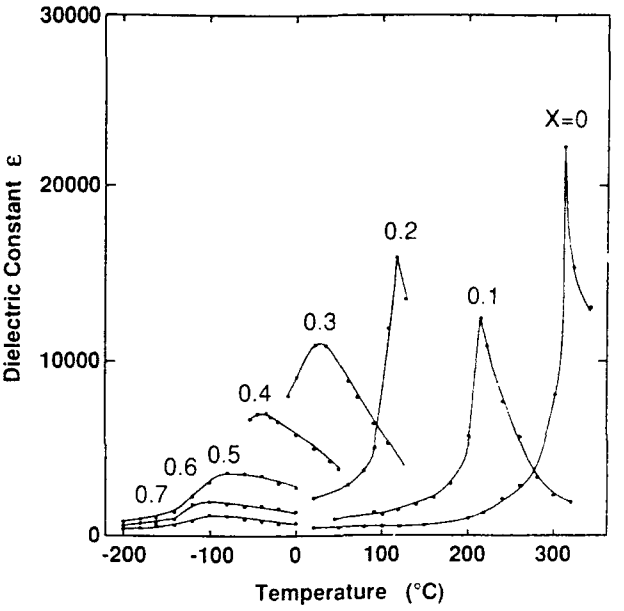


Figure 7. Temperature dependence of dielectric constant for the composition; x PMW - 0.3PNN - (1-x)PT (x=0 - 0.7).

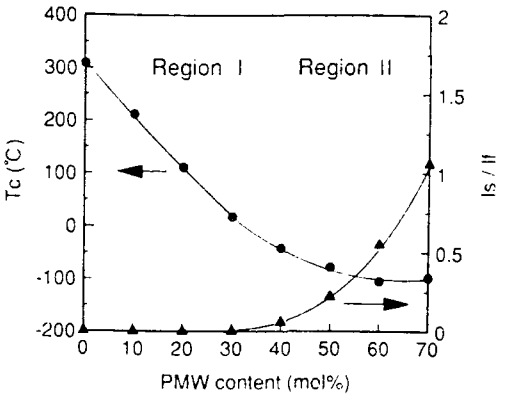


Figure 8. Curie temperature and intensity ratio of superlattice reflection for the composition xPMW-0.3PNN-(1-x)PT, where I_s is the intensity of the superlattice (1/2 1/2 1/2) reflection and I_f, the fundamental (100) reflection.

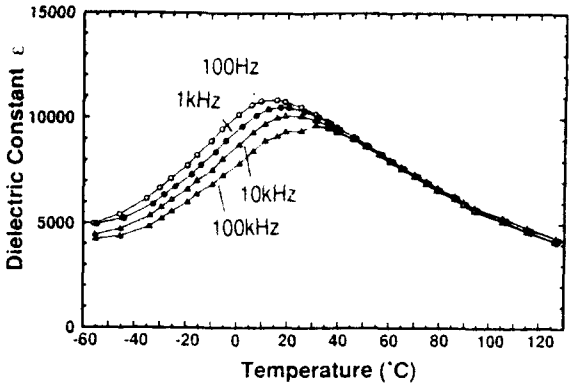


Figure 9. Frequency dispersion of dielectric constant vs temperature curve for the composition of PMW/PNN/PT= 30/30/40 (x=0.3), where measurement frequency range is 100Hz to 100kHz.

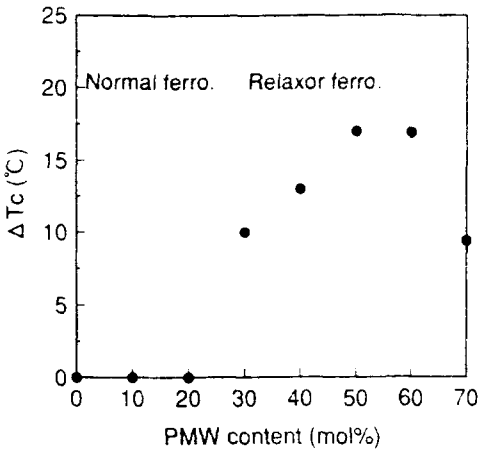


Figure10. Frequency dispersion of Curie temperature as a function of PMW content, where Δ Tc=Tc(10kHz)-Tc(100Hz)

CONCLUSION

Crystal structures and dielectric properties over the entire compositions in the PMW-PNN-PT system were investigated. In this system, a morphotropic phase boundary (MPB) existed around the compositional line of 45 to 50mol% PT content. The compositions around MPB were found to exhibit the highest dielectric constants. On the compositional line of 30mol% PNN content, dielectric properties and crystal structures were investigated in detail. Compositions such as PMW/PNN/PT=50/30/20 showed relaxor ferroelectric behavior of the diffuse phase transition, frequency dispersion of dielectric constant and D-E hysteresis loops with small coercive forces. In the PMW-rich compositional region, Superlattice reflection from B-site cation ordering appeared and downwards Curie temperature shifts saturated. It is considered that some PMW component is incorporated into the clusters with ordered B-site cations ordered, while the other Mg and W ions were disordered.

ACKNOWLEDGEMENT

The authors would like to acknowledge Drs. S. Takahashi, S. Saito, N. Shohata, K. Utsumi, M. Yonezawa and M. Shirakata for useful discussions. They also acknowledge K. Iimori, H. Yokoyama, H. Higuchi, M. Midorikawa and T. Manako for sample preparations and measurements.

REFERENCE

1) A. I. Zaslavskii and M.F. Bryzhina: Kristallografiya 7 (1962) 709. translation : Sov. Phys.-Crystallogr. 7 (1963) 577.
2) G.A.Smolenskii, N.N.Krainik and A.I.Agranovskaya: Fiz. Tverd. Tela 3 (1961) 981. translation: Sov. Phys.-Solid State 3 (1961) 714.
3) K.Uchino and S.Nomura: J.Phys.Soc.Jpn. 41 (1976) 542.
4) M.H.Lee and W.K.Choo: J. Appl. Phys. 52 (1981) 5767.
5) K.Uchino and S.Nomura: Jpn. J. Appl.Phys. 17 (1978) 51.
6) T.Kobayashi, S.Sugiyama and K.Uchino: Ferroelectrics Lett. 7 (1987) 75.
7) M. Yonezawa: Ferroelectrics 68 (1986) 181.
8) N. W. Thomas: Ferroelectrics 100 (1989) 77.
9) N.N.Krainik and A.I.Agranovskaya: Fiz. Tverd. Tela 2 (1960) 70. translation: Sov.Phys.-Solid State 2 (1960)

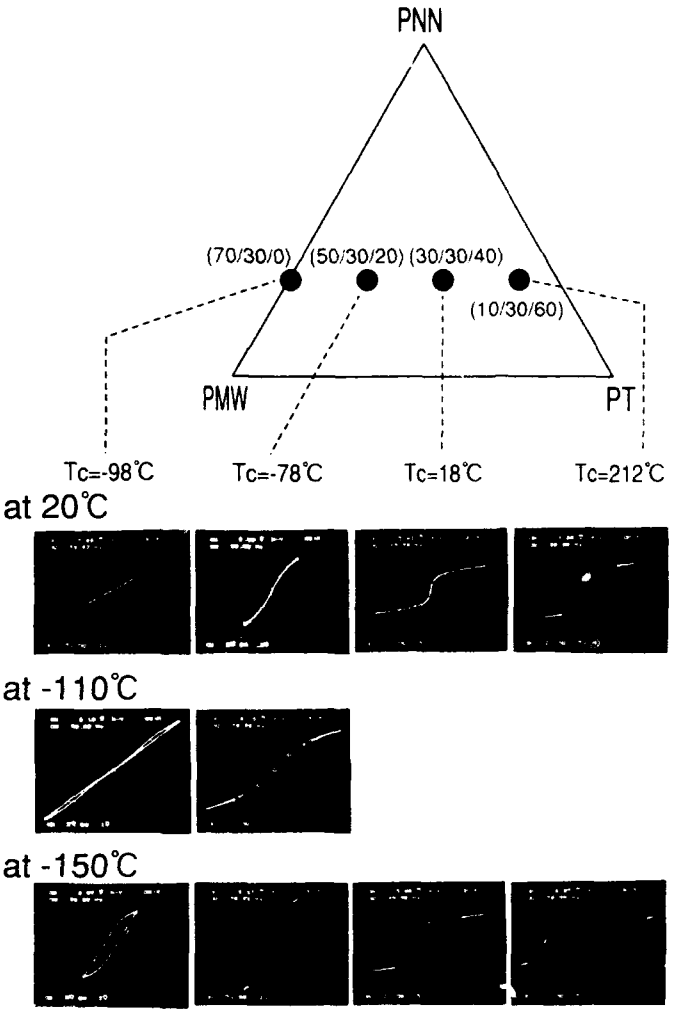


Figure 11. Compositional and temperature dependence of D-E hysteresis loops, where the vertical axes D and the horizontal axes E are in arbitrary units.

PREPARATION OF DENSE ULTRA-FINE GRAIN BARIUM TITANATE-BASED CERAMICS

U. Kumar, S.F. Wang, and J.P. Dougherty

Materials Research Laboratory
The Pennsylvania State University
University Park, PA 16802

Abstract: Recently, we have sintered hydrothermal $BaTiO_3$ with 3-5 wt% Bi_2O_3 to very high densities at 850°C. In this paper, new results on the effect of lower concentrations of Bi_2O_3 on the densification and the dielectric properties of the $BaTiO_3$ ceramic are discussed. As an expansion of this work, hydrothermal $Sr_{0.2}Ba_{0.8}TiO_3$ was sintered with 0-5 wt% Bi_2O_3 between 850-1250°C. When 5 wt% Bi_2O_3 was added, the powder compacts sintered to a bulk density of >5.2 gms/cc, at 950°C. The room temperature dielectric constant of this ceramic was 1500, and K vs. T plot followed the Z5U industrial specification.

Introduction

In a recent paper[1], by comparing the effect of Bi_2O_3 on the sintering behavior of high purity $BaTiO_3$ powders prepared by different procedures, good sinterability of hydrothermal $BaTiO_3$ at temperatures as low as 850°C was demonstrated. By performing XRD and DTA measurements on these mixtures, the following reaction sequence was identified:

$$1\ BaTiO_3 + 10\ Bi_2O_3 \rightarrow 5\ [(Bi_2O_3)_{0.8}(BaO)_{0.2}] + Bi_{12}TiO_{20} \qquad \text{(Eq. 1)}$$

As the reaction products melt at 717°C and 847°C respectively, good densification occurs at low temperatures through liquid phase sintering.

In a different paper[2], the effect of Bi_2O_3 addition on the microstructural development and the dielectric properties of the sintered ceramic was discussed. For this work, hydrothermal $BaTiO_3$ powder compacts with 3, 5, and 7 wt% Bi_2O_3 were sintered between 750°-950°C/2h.

In this paper, the results of the latest studies on the effect of Bi_2O_3 addition on the densification, microstructure development, and the dielectric properties of the hydrothermal $BaTiO_3$ ceramic are explained. The result and discussion section of this paper is divided into four parts. In the first part, some of the physical and electrical characteristics of the ceramic are reviewed. In the second part, the effect of smaller quantities of Bi_2O_3 on the densification and dielectric proprieties of the BT ceramics are discussed. In the third part, the effect of Bi-addition during the hydrothermal process on the microstructural development is discussed. In the final part, the effect of Bi_2O_3 on the properties of $Ba_{0.8}Sr_{0.2}TiO_3$ is analyzed.

Experimental

The surface area of the as received hydrothermal powders (Cabot Corporation, Boyer Town, PA) were measured by BET technique. To prepare the pellets, the hydrothermal powders were mixed with 0-5wt% of Bi_2O_3 (Johnson Matthey, Seabrook, NH) in an agate morter and pestle. Several 1/2" disks were prepared in a steel die, by applying uniaxial pressure (30000-35000 psi) at room temperature. Pellets with about 53% green densities were prepared by using 1.5-1.7 wt% PVA and 1.5-2.0wt% glycerol as binder and plasticizer. After binder evaporation, the green pellets were sintered between 750-1250°C/0.5-2h in a closed crucible. The bulk density of the well sintered disks were measured by noting the weight loss in Xylene. Fractured microstructure of the ceramic was analyzed with an SEM (ISI-SKI 130, Akashi Beam Technology Corp., Tokyo, Japan). The dielectric properties of the ceramic disk samples were measured using a computer controlled LCR bridge (4274A, Hewlett Packard, CO) system.

Results and Discussion

Physical characteristics of the as received powders used for this study are listed in Table 1.

Table 1. The properties of $BaTiO_3$ Powders.

I.D.	Composition	Additions	S.A (m^2/gm)	L.O.I (wt%)
BT1	$BaTiO_3$	--------	8.54	1.8
BT2	$BaTiO_3$	200ppm of Nb	7.96	1.4
BT3	$BaTiO_3$	0.28wt% Bi_2O_3	7.59	--------
BT4	$BaTiO_3$	3wt% Bi_2O_3	8.17	--------
BST20	$Ba_{.8}Sr_{.2}TiO_2$	--------	14.5	0.9

Part 1:

The hydrothermal $BaTiO_3$ sinters to high densities at low temperatures. In Fig. 1., the shrinkage profiles of hydrothermal and non-hydrothermal high purity $BaTiO_3$ powder compacts with 5 wt% Bi_2O_3 are compared. In this figure, good densification of hydrothermal powder compacts is clearly seen to occur at about 750°C. Typical microstructures of the sintered compact are shown in Fig. 2. When the samples were sintered between 750-1250°C with 3, 5, and 7 wt% Bi_2O_3, irrespective of the sintering temperature and the flux concentration, the average grain size of the ceramic remained as 0.15-0.2 μm, which was also the initial particle size of $BaTiO_3$ powder. Typical dielectric properties of the sintered ceramics are given in Fig. 3. A broad transition at around 110°C, and the suppression of other lower temperature transitions are typical of this fine grain ceramic. Though the dielectric peak corresponding to cubic to tetragonal transition is clearly detected, room temperature XRD patterns of these ceramic did not show clear splitting in <200> peaks.

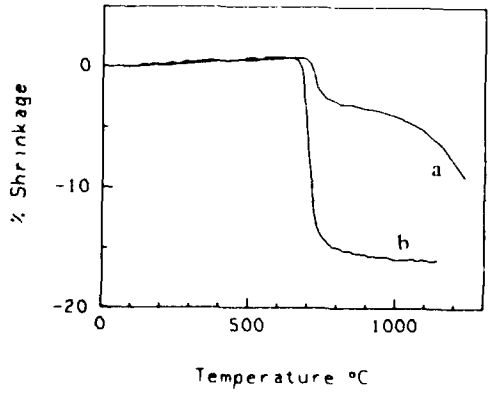


Fig. 1 Shrinkage profiles of (a) high purity $BaTiO_3$ (Transelco) + 5wt% Bi_2O_3 and (b) BT2 + 5wt% Bi_2O_3.

CH3064-0-7803-0465-9/92$3.00 ©IEEE

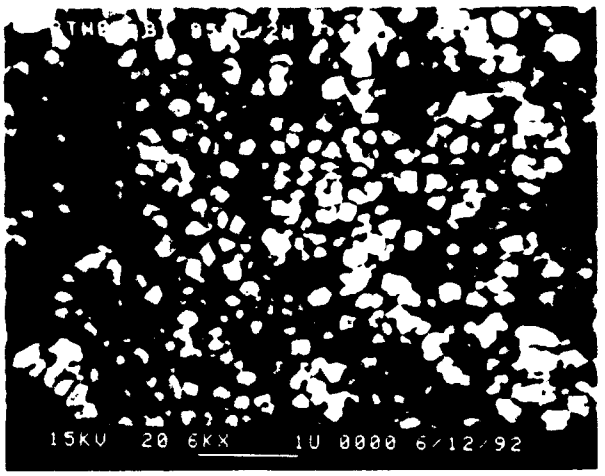


Fig. 2 Typical microstructure of BT sintered with Bi_2O_3. This microstructure represent the fracture surface of BT2 with 7wt%Bi_2O_3 sintered at 850°C/2h.

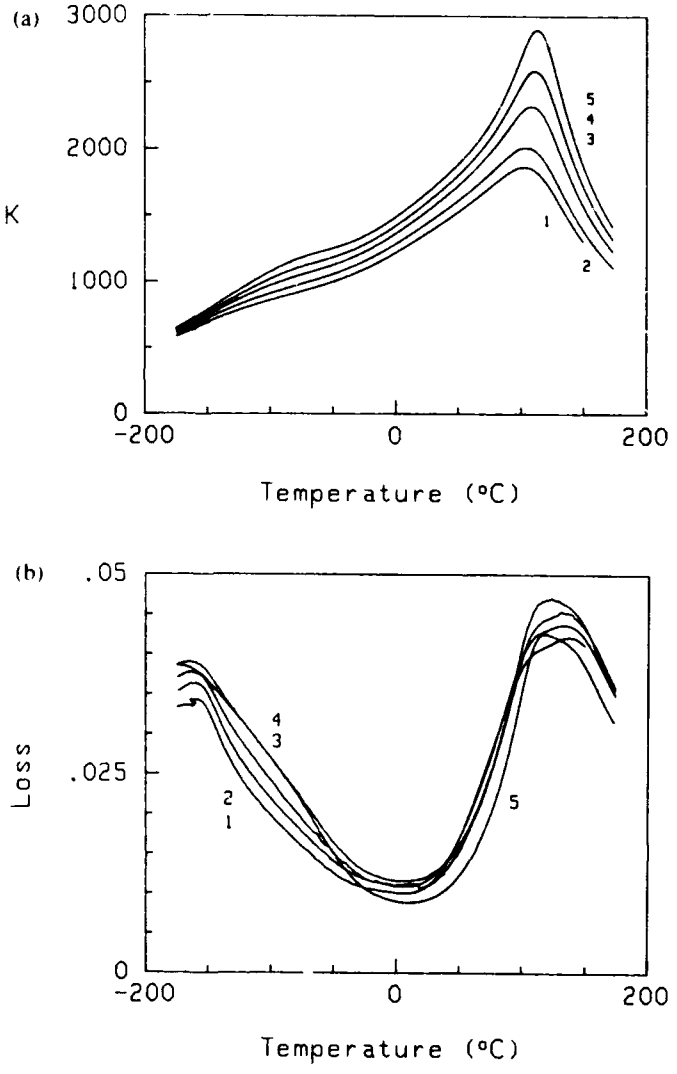


Fig. 3 The dielectric properties of BT2 ceramic with 5wt% Bi_2O_3 sintered at various temperatures; (a) K vs. T and (b) tan δ vs. T; the properties were measured at 1kHz. Sintering temperatures of ceramics are (1) 750°C, (2) 800°C, (3) 850°C, (4) 900°C, and (5) 950°C. The magnitudes are not corrected for porosity.

Part 2.

In this section, the effect of smaller concentrations of Bi_2O_3 on the properties of $BaTiO_3$ ceramic is discussed. To achieve good densities in these ceramics, it was necessary to sinter the compacts at higher temperatures. Even after sintering at 1250°C, the microstructure of the ceramic looked very similar to that shown in Fig. 2. In Table 2, some of the physical and electrical characteristics of the sintered ceramic are listed. The dielectric properties of the ceramic showed qualitatively similar behavior as seen in Fig. 3. Since the liquid phase volume is low, higher T_c and K_{RT} are observed. In these ceramic also, the dielectric peaks corresponding to lower temperatures transitions are also suppressed.

Table 2. Physical and dielectric properties of BT1 and BT2 ceramic with 1 wt% Bi_2O_3

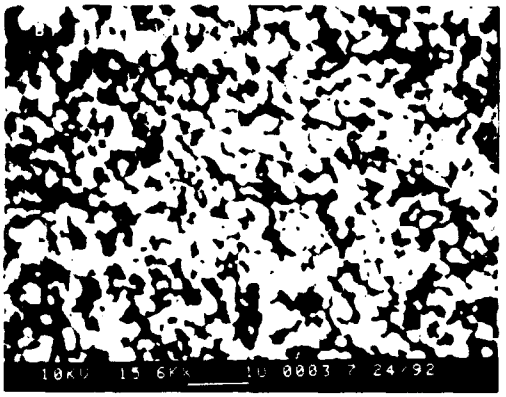
I. D.	Sint. Temp (°C/h)	wt.loss %	Bulk ρ gm/cc ± 2%	K_{max} @ 1kHz	T_{max} (°C)	K_{RT}	Tan δ
BT1	1150/2	1.09	4.99	3185	127	1300	0.017
	1250/1	1.15	5.52	5820	127	2000	0.033
BT2	1150/2	1.43	5.61	5800	121	2340	0.013
	1250/2	1.50	5.79	7075	123	2650	0.019

Part 3:

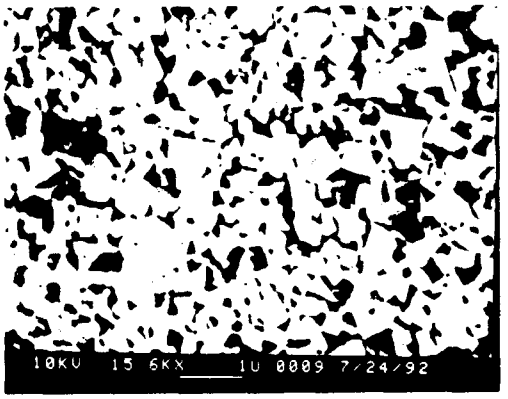
In two batches of $BaTiO_3$, Bi-ions were introduced during the hydrothermal processing. To introduce Bi-ions in the structure, an appropriate amount of Bismuth in the nitrate form was added during the formation of Titanium hydroxide[3]. To this mixture, Ba- solution was added for the $BaTiO_3$ formation. Due to the complexity of the reaction, the nature of Bi^{3+}addition is unknown. In the XRD patterns of the reacted powder, few additional diffraction peaks other than the major $BaTiO_3$ peaks were detected. These peaks with feable intensities could not be matched to any of the Bismuth Titanate or Barium Bismuth Titanium Oxide compounds, unambiguously. The concentration of Bi-ion listed in Table 1, was calculated through atomic absorption spectroscopy. The powder compacts were sintered between 900°-1250°C/0.5-3h. The density and the weight loss data of the sintered compacts are listed in Table 3. It is necessary to increase the sintering temperature above 1000°C to achieve sufficiently good densities. When the samples were sintered over a platinum sheet, comparatively better densities were observed at lower temperatures. But the bottom surface of the ceramic, especially in BT4, was bright yellow in color, indicating the segregation of liquid phase. This observation indicates that the viscosity of the liquid is low.

The microstructure and the dielectric properties of 3 wt% Bi-added samples are very similar to that shown in Fig. 2 and Fig. 3. But the properties of 0.3 wt% Bi- containing samples showed marked differences. The microstructural evaluation as a function of sintering temperature is compared in Fig. 4a, b, c and d. When the samples were sintered beyond 1050°C, the average grain size of the ceramic increased to >10μm. In K vs T plots, dielectric peaks corresponding to three transitions could be detected very clearly. In Table 3, some of the dielectric properties are listed. The dielectric properties of these samples varied as a function of measuring frequencies at all temperatures. Careful analysis of the microstructure, density, and the dielectric properties of the ceramic as a function of sintering temperature and time indicate the grain growth mechanism is dominantly diffusion controlled in nature.

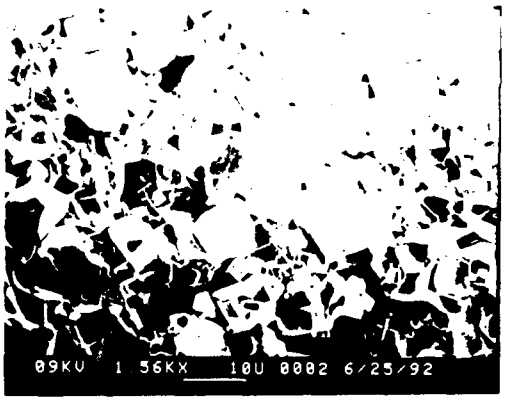
(a)



(b)



(c)



(d)

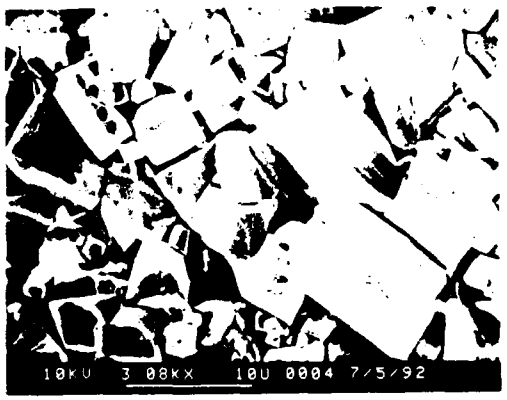


Fig. 4 Fractured microstructures of BT3 ceramics sintered at (a) 1000°C/1h, (b) 1050°C/1h, (c) 1100°C/1h, and (d) 1150°C/2h

Table 3: Physical properties of BT3 and BT4 ceramic.

I. D.	Sint. Temp. °C/h	Setter	Wt. loss %	Bulk ρ gm/cc
BT3	1000/0.5	ZrO_2	0.78	4.40
	1000/1	ZrO_2	0.58	4.54
	1000/2	ZrO_2	0.52	5.30
	1000/3	ZrO_2	0.81	5.28
	1050/1	ZrO_2	0.55	5.28
	1050/1.5	ZrO_2	0.84	5.36
	1050/2	ZrO_2	1.07	5.60
	1100/2	ZrO_2	1.18	
	1150/2	ZrO_2	1.17	5.65
	1200/2	ZrO_2	1.37	5.68
	1250/2	ZrO_2	1.34	5.68
BT4	850/2	Pt	0.6	4.59
	850/2	ZrO_2	0.92	4.76
	900/2	Pt	0.63	4.98
	950/2	Pt	0.66	5.31
	1000/1	ZrO_2	0.92	5.22
	1100/2	ZrO_2	1.36	5.82
	1200/2	ZrO_2	1.76	5.89
	1250/2	ZrO_2	2.03	5.91

Part 4:

In the $Ba_{0.8}Sr_{0.2}TiO_3$ (BST) powder used for this investigation, small amount of carbonates were detected through XRD patterns. In a separate paper presented in this conference, the effect of grain size on the dielectric properties of pure porous ceramic is discussed. In that study, the smallest average grain size achieved through conventional sintering was 0.2 μm, and in this ceramic, dielectric peaks corresponding to three transitions are clearly identified.

The densification behavior of BST as a function of flux concentration and the sintering temperatures are represented in Fig 5. Primarily because of the presence of strontium, it is necessary to sinter the ceramic with higher flux concentrations and at higher temperatures. K vs. T plots of the flux added ceramic are given in Fig. 6 and 7. Suppression of dielectric peaks at the transition temperatures are clearly seen. XRD patterns of these ceramic failed to show splitting in <200> peaks due to tetragonality.

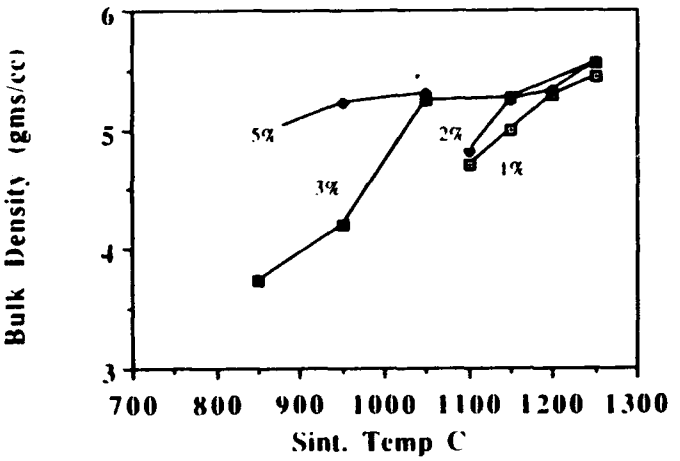


Fig. 5 Effect of flux concentration in the densification behavior of $Sr_{0.2}Ba_{0.8}TiO_3$. These ceramics were sintered for 2hr.

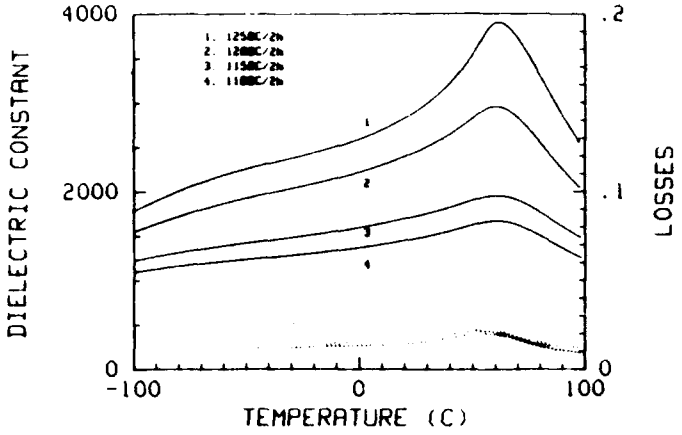


Fig 6 K vs T plots of SBT20 with 2wt% Bi_2O_3, which were measured at 1kHz. These ceramics were sintered at 1. 1250°C, 2. 1200°C, 3. 1150°C, and 4. 1100°C for 2hr.

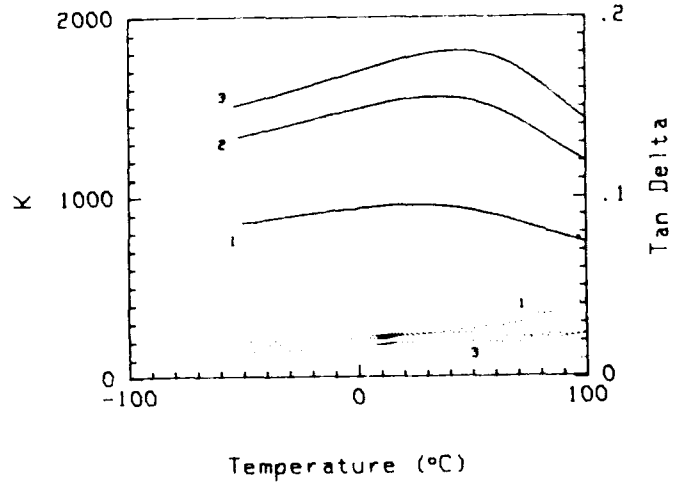


Fig. 7 K vs T plots of SBT20 with 5wt% Bi_2O_3, which were measured at 1kHz. The ceramics were sintered at 1. 850°C, 2. 950fiC and 3. 1050°C.

Conclusions

1. When smaller amount of Bi_2O_3 was added to hydrothermal $BaTiO_3$ to achieve high density, it was necessary to sinter the compact at higher temperatures.

2. Addition of Bi_2O_3 during the hydrothermal preparation of $BaTiO_3$, produced an unidentifiable Bi-based second phase. To achieve high densities, even with 3 wt% Bi_2O_3, it was necessary to sinter the compacts beyond 1000 C. This observation indicates the importance of processing procedure.

3. When the Bi_2O_3 concentration was reduced to 0.28 wt%, good densification, accompanied with grain growth occurs beyond 1000 C. Careful consideration of weight loss observed during sintering, grain growth and the dielectric properties suggest that the densification is accomplished dominantly by grain boundary and bulk diffusion mechanisms.

4. When 5 wt% Bi_2O_3 was added to $Sr_{0.2}Ba_{0.8}TiO_3$ powders, the compacts sinter to bulk densities >5.2 gms/cc at 950°C. Percentage changes in TCC calculated from C vs T plots of this ceramic show Z5U industrial specifications, with a room temperature dielectric constant of 1500. By changing the particle size and the concentration of the Bi_2O_3, it appears that it is possible to reduce the sintering temperature to 850°C, which is the typical thick film processing temperature.

Acknowledgements: Authors gratefully acknowledge the financial support from Cabot Corporation of Boyertown, PA and the Ben Franklin Partnership Program of the Commonwealth of PA. Authors also acknowledges the technical support provided by D Laubscher and Mingfong Song.

References

[1] U. Kumar, and J. P. Dougherty,"Sintering behavior of high purity $BaTiO_3$ in the presence of Bi_2O_3 as the liquid phase", Communicated to J. Am. Cer. Soc.

[2] U. Kumar, and J. P. Dougherty,"Dielectric properties of fine grain hydrothermal $BaTiO_3$ sintered with Bi_2O_3", Communicated to J. Am. Cer. Soc.

[3] Cabot Patent.

HIGH K LOW FIRING TEMPERATURE CAPACITORS BASED ON LEAD NIOBATE

John E. Day
Arthur E. Brown
Joseph D. Nance

Kemet Electronics
P.O. Box 5928
Greenville, S.C. 29606

Abstract

Dielectric formulations based on lead magnesium niobate and lead iron niobate which achieve a Z5U temperature characteristic with a dielectric constant of 12000 have been developed for the manufacture of multilayer ceramic capacitors. A low melting temperature glass frit was added to the formulation to achieve a firing temperature of between 975 °C and 1050 °C, allowing the use of silver electrodes with from 18% to 25% palladium added. The addition of lead iron tungstate and cadmium titanate further reduced the firing temperature to between 850 °C and 900 °C, which allowed the use of pure silver electrodes. An insulation resistance of 10,000 ohm-Farads and a dissipation factor (DF) of 1% were achieved with excellent long term life reliability and an aging rate of less than 2%. High quality capacitors can be manufactured using standard manufacturing techniques and very careful safety and environmental procedures.

Introduction

Multilayer ceramic capacitor technology is continually being improved to reduce chip size by increasing dielectric constant and to reduce cost by reducing firing temperature, which allows the use of less expensive electrode materials. A series of dielectric formulations have been developed based on lead perovskites which have higher dielectric constant and lower firing temperature than has been achieved with traditional barium titanate formulations.

Figure 1 shows typical construction of an axially leaded multilayer ceramic capacitor. Construction is similar whether barium titanate or lead perovskite materials are used. Figure 2 is a summary of typical capacitor materials for NPO, X7R, and Z5U temperature characteristic dielectrics. The new lead perovskite materials have been developed for Z5U characteristic capacitors. A very high dielectric constant (K) can be achieved with lead perovskite materials. These materials permit the use of very high silver content electrodes, leading to low cost and increased volumetric efficiency, as shown graphically in figure 3.

For reference, figure 4 shows the relative temperature stability of the three major dielectric types. Z5U is the least stable, but has the highest volumetric efficiency because it has the highest K. It is important to note that even though Z5U characteristic capacitors are often referred to as general purpose, the reliability of the Z5U dielectric may be, as is the case for this new lead perovskite family, as good as for NPO or X7R characteristic capacitors. Therefore, if a particular circuit does not require highly temperature stable capacitance, then Z5U may be specified to take advantage of the increased volumetric efficiency with no loss of reliability.

Perovskites in general have an ABO_3 structure. Dielectric properties are controlled by substituting secondary materials (to shift and/or depress the shape of the temperature characteristic curve). In barium titanate materials such as calcium and strontium can substitute for barium on the A sites and zirconium or tin on the B sites. In the lead perovskite system substitution occurs primarily on the B site; niobium, magnesium, iron, tungsten, and manganese are all employed to achieve optimum dielectric characteristics. Figure 5 summarizes the structure modifications which are employed.

Figure 1.

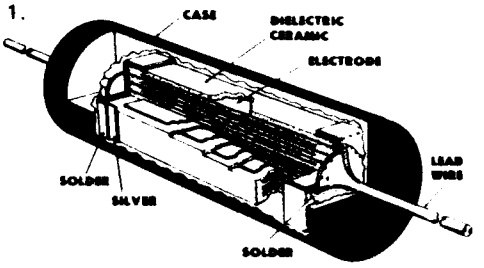


Figure 2. **Multilayer Ceramic Capacitor Materials**

Temperature Characteristic	NPO	X7R	Z5U
Material	Nd_2TiO_5	$BaTiO_3$	$BaTiO_3$
K	50 - 100	1200 - 3000	4000 - 10000
Electrode Material Pd/Ag	30/70	30/70	30/70
K	50 - 60	3000 - 5000	10000 - 15000
Electrode Metal Pd/Ag	70/30	100/0	100/0
Material			PMN - PFN
K			12000
Electrode Metal Pd/Ag			18/82
K			10000
Electrode Metal Pd/Ag			0/100

PMN: $Pb(Mg_{1/3}Nb_{2/3})O_3$

PFN: $Pb(Fe_{1/2}Nb_{1/2})O_3$

Figure 3. K and Electrode System Compared BaTiO3 vs Pb–Nb Dielectrics for Z5U

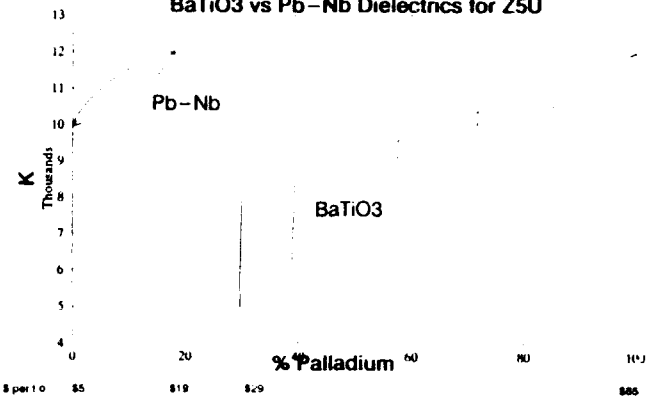
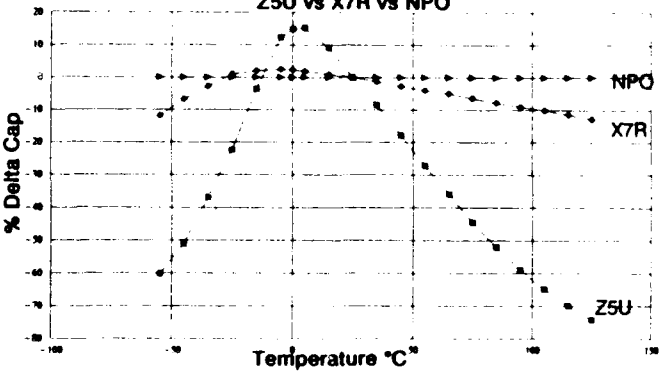


Figure 4. Temperature Coefficient of Capacitance Z5U vs X7R vs NPO



CH3080-0-7803-0465-9/92$3.00 ©IEEE

Dielectric Development

PMN (lead magnesium niobate) is a high dielectric constant material, but it requires a sintering temperature of about 1200 °C. Development focused on reducing the firing temperature and improving K and insulation resistance. The addition of PFN (lead iron niobate) reduced the sintering temperature somewhat. Further reduction was obtained by adding a lead germanate glass frit sintering aid. The ratio of PMN to PFN was adjusted to obtain the highest dielectric constant. Finally a small amount of manganese dioxide was added to improve the insulation resistance. This yielded a K 12000 dielectric which sinters at 1045 °C. At this firing temperature inexpensive electrodes containing 18% palladium and 82% silver can be used. Figure 6 summarizes the formulation [1]. This formulation has been successfully manufactured for several years.

Properties of MLC's manufactured with this formulation are shown in figure 7. Compared to most other Z5U dielectrics the DF and the aging rate are quite low. Modulus of rupture (MOR), a measure of the breaking strength of the capacitor, is unfortunately lower than for most barium titanate based dielectrics.

Further improvements were made to the system to reduce the firing temperature to 900 °C, which allows the use of silver electrodes, at the expense of dielectric constant. Lead iron tungstate was added to reduce the firing temperature further. A lead-zinc-copper-borate frit was developed to replace the lead germanate frit. This, in addition to using cadmium titanate as a sintering aid, enabled capacitors to be fired dense at 900 °C [2]. Capacitor properties are similar, with the exception of the reduced dielectric constant, which means that chips are somewhat larger because more electrode layers are required for a given capacitance.

Dielectric Processing

Processing of these lead perovskite materials is similar to that of other ceramic materials. Figure 8 summarizes the process steps. Initial starting materials are lead oxide, niobium pentoxide, magnesium oxide, iron oxide, tungsten oxide, and manganese dioxide. The appropriate formulation is weighed out, wet milled to homogenize, and dried. The dried powder is then calcined to pre-react the materials. The frits are then added and the batch is wet milled to achieve the target final slurry particle size. Film forming binders are added after milling and this slip is then cast into ceramic green tape. Electrodes are screen printed onto the tape, multiple layers are laminated, and chips are cut apart. The green chips then go through binder bakeout and firing, termination and epoxy coating, and testing and packaging. Effective engineering controls must be implemented in the manufacturing process and great care must be taken to insure worker safety when using lead based materials.

Conclusions

Dielectric formulations based on lead perovskites have been developed which have higher K and lower firing temperature than traditional barium titanate dielectrics. A 100 nf 0805 leaded chip has been manufactured which has excellent DF, IR, and a low aging rate. A relatively low MOR makes utilization of these parts difficult for surface mount applications. Techniques for increasing the MOR were the subject of some additional work. Innovative sintering aids are a key to achieving the properties which were reported.

References

[1] Park, H.D. and Brown, A.E. U.S. Patent # 4,550,089 (1985)

[2] Park, H.D. and Nance, J.D. U.S. Patent # 5,011,803 (1991)

Figure 5.

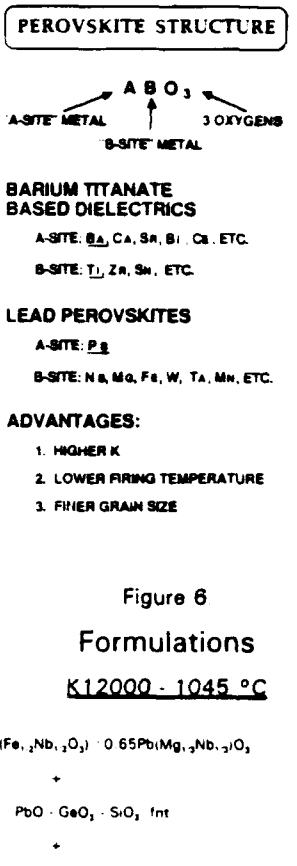


Figure 6

Formulations

K12000 - 1045 °C

$0.35Pb(Fe_{.2}Nb_{.2}O_3) \cdot 0.65Pb(Mg_{.3}Nb_{.3})O_3$

+

$PbO \cdot GeO_2 \cdot SiO_2$ frit

+

MnO_2

K10000 - 900 °C

$0.85Pb(Fe_{.2}Nb_{.2}O_3) \cdot 0.1Pb(Mg_{.3}Nb_{.3})O_3 \cdot 0.05PbFe_{.5}W_{.5}O$

+

$CdO \cdot TiO_2$ sintering aid

+

$PbO \cdot ZnO \cdot CuO \cdot B_2O_3 \cdot SiO_2$ frit

+

MnO_2

Figure 7.

0805 - 100 NF Properties

K 12000

DF 1%

+ 10 TCC 15% 85TCC -50%

IR 10000 ohm-Farads IR@85°C 3000 ohm-farads

Aging Rate 1 6% per decade

MOR 140MPa

Voltage Rating 50 volts

Dielectric Thickness 25 microns
Grain Size 2-3 microns

Breakdown Voltage 600 volts

Life Test 0 failures in 4000 hours at 85°C, 100 volts applied

Firing Temperature 1045°C

Electrode Composition 18/82 Pd/Ag

Figure 8.

Processing of PB - NB Dielectric

- Mix powders
- Mill to reduce particle size
- Calcine to pre-react
- Add frit and mill to disperse
- Add binders and disperse
- Cast slip to form green sheet
- Manufacture green chips with electrodes
- Bakeout binders and fire chips
- Terminate, lead attach, and epoxy coat chips
- Test and package

DIFFUSE PHASE TRANSITION AND RELAXOR BEHAVIOR IN PEROVSKITES

Heinz Schmitt, Doris Simon and Peter Pitzius
Fachbereich Physik, Universität des Saarlandes, D-6600 Saarbrücken, Germany

Abstract: Some of the properties of the materials with diffuse phase transitions and relaxor behavior are common to all. This article attempts to present a number of selected measurements which have been used to explore the different characteristics of the perovskite ABO_3 relaxors such as PLZT, lead scandium tantalate and lead magnesium niobate respectively. Finally, in view of the experimental results, the paper presents two different models. One on the basis of compositional heterogeneities, and the other on the basis of intrinsic instabilities and the broken translation invariance of the lattice. A comparison of the two models shows that it is extremely difficult to distinguish between the two models.

Introduction

Diffuse phase transitions are a more general phenomenon. In perovskites ABO_3 it is found in "pseudo"- quaternary solid solutions with statistical occupation of the A- and the B-position (e.g.: $(PbBa)(ZrTi)O_3$), in materials with a statistical occupation of the B-position with ions of different valency (e.g.: $Pb(ScTa)O_3$ (PST) and $Pb(Mg_{1/3}Nb_{2/3})O_3$ (PMN)) or in the case of doping the ternary solid solutions at the A-position (e.g.: $(Pb_{1-1.5x}La_{x\Delta 5x})(Zr_{1-y}Ti_y)O_3$ (PLZT)).

Some properties of materials with diffuse phase transitions are common to all:
- In the non polar state, even far above the temperature of the maximal value of the dielectric permittivity there exist anomalies which can be ascribed to a local polarization.
- Even below T_C, the material macroscopically show the cubic symmetry.
- The material looks like a polar glass.
- The low frequency dielectric constant shows no Curie-Weiss-Law (CWL), it is not divergent. The permittivity is strongly frequency dependent (relaxor behavior).
- The weak field dielectric permittivity reaches a high peak value typical for a ferroelectric perovskite near T_C, but the dielectric maximum does not mark a phase change into a ferroelectric phase.
- There exist a switchable displacive phase transition.

A first explanation has been offered for the relaxor ferroelectric behaviors by G.A. Smolenskii [1, 2]. He suggested, that in for example $PbMg_{1/3}Nb_{2/3}O_3$ the Mg and Nb ions do not order, so that across any trace in the material there are fluctuations in Mg : Nb concentrations and that these statistical compositional fluctuations lead to large fluctuations in the Curie-temperature. So, over a wide temperature range, there is a mixture of non polar and polar regions, which are growing with decreasing temperature. If the scale of heterogeneity is of the order 10 - 20 nm as proposed, then for measurements with a probing radiation such as x-ray or optical frequency the random array will reflect the cubic symmetry.

Another aspect was discussed by L.E. Cross [3]. If one considers the stability of very small polar micro regions, the energy hill ΔG_D, separating alternative domain states, which is many times kT for domains of macroscopic volume, becomes comparable to kT (k = Boltzmann's constant, T = temperature). That means, the polar regions are unstable against thermal agitation now.

But some additional facets of behavior must also be considered. For some aspects of diffuse phase transitions (DPT), PLZT is a suitable material because of the large solubility of La in the solid solution PZT. Whereas in the case of PST, the ordering or disordering of the B-site cations allow to produce a ferroelectric or a relaxor-type material, which - in principle - may allow a test of the different models [4,5].

Local Polarization

The principal idea of Smolenskii's model was, that in solid solutions, there exist compositional fluctuations. The result are micro domains, "Känzig regions", with different Curie temperatures T_C. A Gaussian distribution in T_C gives the deviation from the Curie-Weiss-Law (CWL) as it is observed at relaxor materials. The micro domains in the model are assumed to be produced by static compositional fluctuations, so the original model is not able to explain all experimental details.

Another aspect may also be of importance. In all multi-component materials one will find compositional fluctuations, but in pure $Pb(ZrTi)O_3$ (PZT), normally no DPT is present, and one finds no DPT in e.g. PLZT x/1-y/y: 10/35/65. But in PLZT 10/65/35 a DPT and relaxor behavior is found, although it can be expected that the compositional fluctuations in both PLZT-compositions are similar. So at least in the upper two points the model has to be completed.

The reasons which are responsible for the deviations from the CWL firstly explained by Smolenskii's model may also influence other properties in a similar way. At a normal phase transition from the paraelectric to the ferroelectric state, there occur anomalies in the susceptibilities, which generally can be described by a lattice susceptibility χ_{ij} and the order parameter p:

$$\chi_{ij} = \chi_{oij} + \sum g_{ijkl} p_k p_l \qquad (1)$$

The coupling constant g_{ijkl} describes the breaking of symmetry by the phase transition. In perovskites with a diffuse phase transition (DPT) there is, below T_C (the temperature of the maximal value of the permittivity-) no deviation from the cubic symmetry of the high temperature phase in such samples, which are cooled down without any applied electric field from the high temperature phase to the thermally depoled state. But even far above T_C not only for the low frequency dielectric susceptibility typical deviations from the classical behavior are found. G. Burns assumed a local polarization with disappearing mean value for the thermally depoled state [6]. Then, the term $p_k p_l$ in relation (1) can be replaced by the mean square deviation P^2_{loc} of this local polarization. The g_{ijkl} are to be replaced by an effective coupling constant:

$$\chi = \chi_o + g^* P^2_{loc} \qquad (2)$$

This formalism consequently can be applied to a series of different measurements. The validity of the relation for the dielectric constant at optical frequencies, related to the electronic polarizability, was confirmed by Burns for PLZT, PMN and PST with measurements of the refractive index [6]. g^* was estimated by the tensor of the quadratic electrooptic effect, and so P^2_{loc} can be determined.

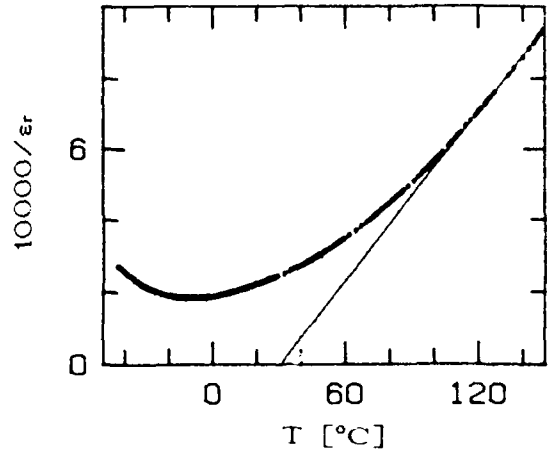


Figure 1: The reciprocal relative dielectric constant of a strongly disordered PST sample (order parameter S=0) as a function of temperature and a CWL fit (straight line) onto the curve for the values measured at higher temperatures.

CH3080-0-7803-0465-9/92$3.00 ©IEEE

In analogy to ideal ferroelectrics, where via electrostriction the properties are influenced by the spontaneous polarization, in DPT materials there exist similar relations for thermal expansion and influence of hydrostatic pressure on the dielectric constant as it was verified by Schmidt [7] and Setter and Cross respectively [5]. Our own results show the influence of the local polarization on the entropy and the static dielectric constant [8]. So P^2_{loc} was determined for PLZT and PPZT, the Praseodym-modification of PLZT [8], which show a strongly similar behavior as PLZT or disordered PST. Figure 1 now shows the reciprocal relative dielectric constant ε_s^{-1} of strongly disordered PST. Far above T_c the local polarization becomes small, and ε_s^{-1} follows a CWL. This is demonstrated by the straight line in Figure 1. In this way, the temperature T_0 can be determined by extrapolating the high temperature curve of ε_s^{-1} to lower temperatures. The Curie constant, then has a value of $C = 3.8 \cdot 10^5$ K. The deviation from the straight line is $\sim P^2_{loc}$, which allows, by use of additional results, e.g. the entropy as a function of temperature, the calculation of P^2_{loc} [8].

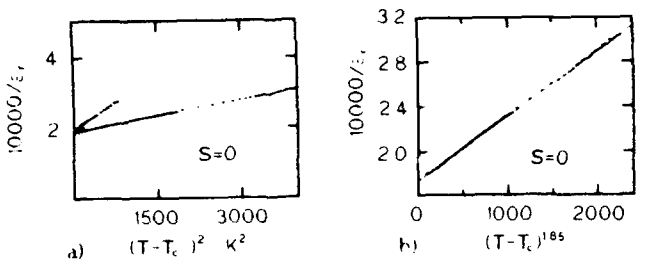


Figure 2: The reciprocal relative dielectric constant of a strongly disordered PST sample (order parameter S=0) represented as a function of $(T-T_c)^2$ (a), and fitted with an critical exponent γ=1.85 (b).

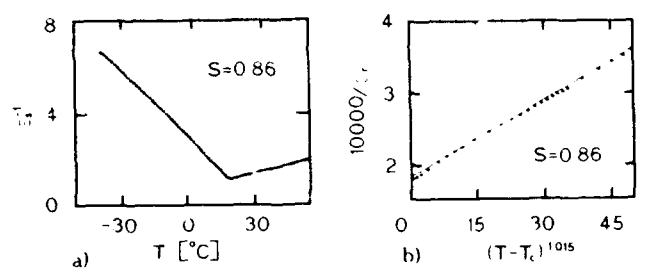


Figure 3: The reciprocal dielectric constant of a well ordered PST sample (S=0.86) represented as a function of $T-T_c$ (a), and fitted with a critical exponent γ=1.015 (b).

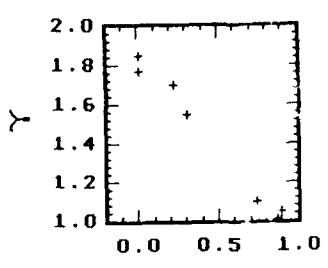


Figure 4: Critical exponent γ as a function of the order parameter.

The deviation from the CWL, caused by the local polarization leads to a minimum for ε_s^{-1} at T_c. As it is demonstrated in Figure 1, ε_s is continuous and shows no divergence. But near the minimum of ε_s^{-1} at the temperature T_c, ε_s^{-1} can be developed:

$$\varepsilon_s^{-1} = \varepsilon_{max}^{-1} + \ldots (T - T_c)^2 + \ldots \qquad (3)$$

Smolenskii designates this as "mean" phase transition temperature [2]. With the exception of the maximum of the dielectric constant there is really no direct effect which marks this temperature. As yet mentioned above, Smolenskii assumed a Gaussian distribution for this mean phase transition temperature produced by Känzig regions which should be responsible for the DPT, but equation (3) describes the behavior of ε_s^{-1} better than a more precice Gaussian distribution. Figure 2a shows the dependence of the reciprocal static dielectric constant ε_s^{-1} as a function of $(T-T_c)^2$, according to equation (3). The nearly quadratic behavior is demonstrated, and also that in accordance to Figure 1, the coefficient A in the free elastic enthalpy

$$= G_0 + \frac{1}{2} AP^2 + \frac{1}{4} BP^4 + \frac{1}{6} CP^6 \qquad (4)$$

remains always positive. Measurements of the coefficients A, B and C were performed on PLZT below T_c [9]. The results were received from the high field ends of the branches of the P(E) curves, which were measured at different temperatures. The result is, that also here, A is always positive, B always negative and C always positive, and all the coefficients are strongly temperature dependent. A more detailed analysis of the potential function shows, that there exist different stable and metastable regions. In the thermally depoled, macroscopically non ferroelectric state, the system is, even cooled down below T_t ... T_c, in a metastable central minimum. If the stability criterion $\partial^2 G / \partial P^2 = 0$ is fulfilled and if the system is in this relative minimum, and if then an electrical field (which is large enough) is switched on, the system is switched from the metastable into a stable minimum. Then the polarization is irreversibly induced, a phase transition happens, if the condition $4B/5 = 4AC$ is reached by decreasing the temperature. In this way P^2_{loc} may influence preferably via A in equation (4) the free elastic enthalpy G.

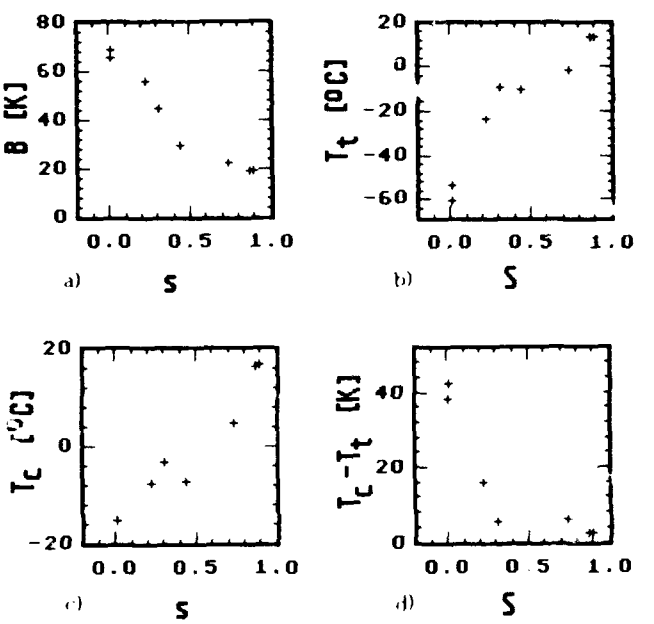


Figure 5: The influence of the order parameter on the broadening of the $\varepsilon(T)$ curve (a), the temperature T_t (b), the temperature T_c (c) and the difference $T_c - T_t$ (d).

For the local polarization with its disappearing mean value but not disappearing mean square deviation P^2_{loc}, micro regions may be responsible. Cross has shown, that there is some evidence for dynamical disorder [3]. ESR investigations of Burggraaf demonstrate, that with decreasing temperature the local anisotropy gradually increases [10]. This increasing of P^2_{loc} with decreasing temperature indicates the dynamical form of the micro regions at high temperatures. Measurements of the sound velocity in PLZT show a small anomaly near T_c [11]. The coupling acoustic

and optical properties indicate a tendency of softening near T_C. With decreasing temperature below T_t, the temperature where the macroscopic polarization P_S of the poled sample vanishes, the fluctuations become slow. In the low temperature region, they are frozen and the relaxor materials show glasslike properties such as a plateau in the thermal conductivity [12].

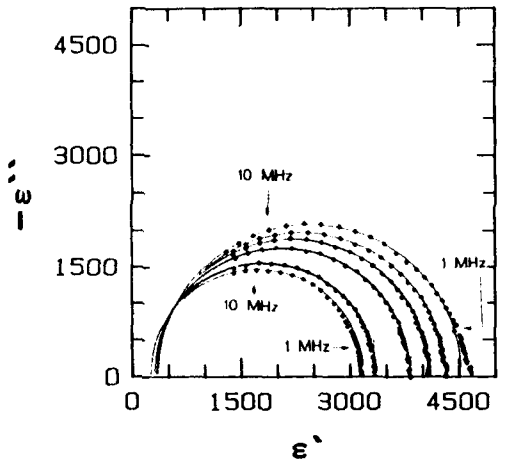


Figure 6: The complex dielectric constant ε^* of strongly disordered PST with the frequency as a parameter, measured in the range from 100 Hz up to 13 MHz for 6 selected temperatures. The radii of the Debye-circles become larger with decreasing temperature (T_i=13.3 °C, 21.4 °C, 27.4 °C, 35.0 °C, 44.0 °C, 50.1 °C).

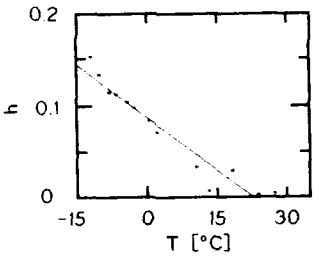


Figure 7: Relaxation-parameter h, taken from Cole-Cole-fits for the relaxation process shown in figure 6 as a function of temperature.

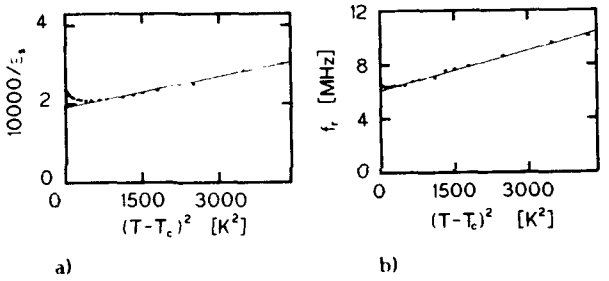


Figure 8: Reciprocal low frequency dielectric constant ε_{rs}^{-1} (a) and relaxation frequency f received from the relaxation process shown in figure 6 as a function of $(T-T_C)^2$. The proportionality is evident.

In PST, a thermal treatment allows ordering or disordering the B-site cations Sc and Ta. The degree of ordering can be controlled by X-ray diffraction [5]. Well ordered samples show the appearence of superlattice sattelite reflections [4,5]. Thus, in relation to the basis reflections, the intensity of the superlattice reflections define the order parameter S. This order parameter was calculated by the Rietveld powder profile and refinement program. In this way, the properties of PST as a function of ordering and disordering can be studied. As it was found by Burggraaf and Setter, strongly disordered PST shows a DPT and relaxor behavior, whereas a well ordered sample looks like a classical ferroelectric. Figure 2a presents the reciprocal dielectric constant ε_s^{-1} as a function of $(T-T_C)^2$ for a strongly disordered PST-sample ($S \approx 0$) and figure 3a shows ε_s^{-1} as a function of $T\ T_C$ for a well ordered material ($S = 0.86$). As it is described in figure 2b and figure 3b, the real exponents are 1.85 and 1.015 respectively. For partially ordered samples exponents between 1.85 and 1.015 are found. Figure 4 shows this critical exponent γ as a function of the order parameter S. In a similar manner, the low frequency dielectric properties are changing not abrupt but gradually with S. This is shown in figure 5a-d. Here the broadening of the ε (T)-curve (a), T_C (b), T_t (c) and T_C-T_t (d) are to be seen as a function of S. Figure 5d demonstrates, that a thermally depoled sample must be cooled at least 40 K below T_C to induce a remanent polarization P_r.

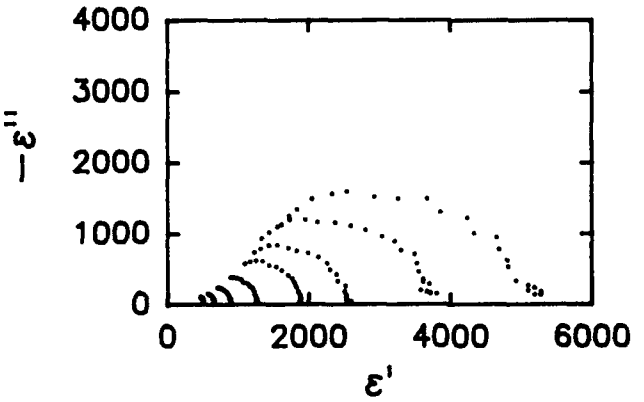


Figure 9: The complex dielectric constant ε^* of PMN with the frequency as a parameter, measured in the range from 100 Hz up to 13 MHz for some selected temperatures in the temperature range from 18 °C up to 210 °C. The radii of the Debye-circles become larger with decreasing temperature (T_i=27.5 °C, 47 °C, 68 °C, 89 °C, 120 °C, 150 °C, 181 °C, 211 °C).

Relaxor behavior

The frequency dependence of the dielectric susceptibility, the relaxor behavior, of materials with a DPT is known since a longer time [13, 14, 15, 16]. By IR-spectroscopy, for PLZT 9/65/35, Lurio found only 3 LO-modes and 2 TO-modes which are nearly temperature independent. The third TO-mode he could not find. He was able to fit the spectrum with a set of 6 damped oscillators [17]. Burns [18] has estimated the frequency of the "lossed" soft mode ω_o to 0 - 50 cm^{-1}.

Experimentally it cannot be distinguished between an overdamped oscillator and a relaxator system. Concluding the contribution of the temperature independent IR-active modes, the overdamped oscillator can be described by:

$$\varepsilon(\omega) = \varepsilon_{\infty} + \frac{A_o}{\omega_1^2 + j\gamma_o\omega} \qquad (5)$$

a form which is equivalent to a Debye relaxation, where $\varepsilon_{rs}^{-1} \sim f_o \sim \omega_o^2$ (f_o: relaxation frequency). This behavior was shown in a previous paper for PLZT [19]. Here, there are presented some results for PST [20] and PMN.

In figure 6, the relaxor behavior of strongly disordered PST is demonstrated. In this figure, the complex dielectric constant with the frequency as a parameter in the range

from 100 Hz up to 13 MHz is plotted for some selected temperatures. In this case, at larger distances from T_C (T_C = - 13 °C) the relaxation is of the Debye-type. Approaching to T_C and below T_C, the relaxation becomes more and more distributed. The relaxation must be fitted with a Cole-Cole formalism, where the distribution-parameter h marks the degree of distribution. In figure 7, the growing up of the distribution, indicated by the distribution-parameter h can be seen. Ordered or partially ordered samples show also relaxations, but they are very small and strongly distributed. The dielectric relaxation shown in figure 6 is typical for disordered PST-samples with a diffuse phase transition. A MLS-fit, applied to the data of the complex dielectric constant ε^* yields ε_∞ and ε_{rs}, the high frequency and the low frequency dielectric constant of the relaxation process. Further, the relaxation frequency f can be calculated. Figure 8a shows ε_{rs}^{-1}, and figure 8b the relaxation frequency f_r as a function of $(T-T_C)^2$. The result is: $f_r \sim \varepsilon_{rs}^{-1} \sim \omega_o^2$.

Measurements which were performed on PMN show similar results. Figure 9 represents the complex dielectric constant ε^* with the frequency as a parameter for different temperatures in the temperature range from 18 °C to 210 °C. For higher temperatures, the relaxation is of the Debye-type, whereas the relaxation shows more and more a distribution when the temperature decreases. The calculation of the characteristical data of the relaxation process yields similar results as one receives for PLZT and PST respectively [19, 20].

At this point it should be mentioned, that the mechanism which changes these linear properties of relaxor materials in comparison with normal ferroelectrics influences the nonlinear properties too [21]. But these effects are not further discussed in this work.

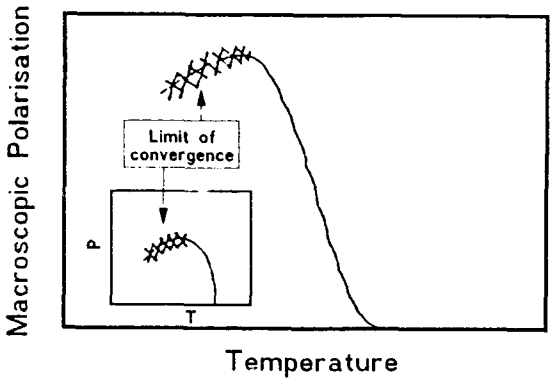


Figure 10: Macroscopic polarization P_r as a function of temperature according to the mean field approximation model on the basis of micro regions with a Gaussian distribution of transition temperatures T_c. (Inlet: P(T)-curve without distribution).

Models

In Smolenskii's model the existence of micro regions with its Gaussian distribution of transition temperatures produced by compositional fluctuations in multi-component systems was the main idea. There is no direct information whether these regions are dynamical cluster. In the original model, the cluster were static regions. But via the Lyddane-Sachs-Teller relation there is also in this case some indirect influence.

On the basis of Smolenskii's model the interaction between the micro regions was calculated with a mean field approximation. The micro regions themselves may show normal ferroelectricity, that means, a CWL-law and also spontaneous polarization p(T) below their individual transition temperatures $T_{c\text{-local}}$. The micro regions with their p(T) are now the interacting parts is the macroscopic system. An important additional assumption is, that the size of the micro regions is dependent on a external electric field. If the dipole-dipole interaction of the micro regions is proportional to P, one can see not only the anomalies in ε, but also the irreversibility of the P(T)-curve (figure 10). Cooling down from higher temperatures, the interacting constant is too small to generate a macroscopic polarization and one gets a polar glass [11].

The second model proposed is made on the basis of a homogeneous system which can be described by a hamiltonian as it is used for normal ferroelectrics [22,23]. This hamiltonian contains a linear term which has the dimension of a local field. This term considers the local defects which derange the invariance of the translation symmetry and which are coupling with the local dipole moments in the relaxor material PLZT, PST and PMN. So it can be considered that all materials with DPT has compositions with an intrinsic instability, e.g. with the tendency to rotate the O-octahedra of elementary cells containing a La and a Zr and to stretch the O-octahedra containing a Pb and a Ti respectively. In PST, the different statistical arrangements of elementary cells with Sc or Ta on the B-positions induce these effects. So manifold different cells are simultaneously present one in the neighbourhood of other types. This should not be confounded with macroscopical compositional fluctuations. If we follow H. Megaw [24], and assume, that the forces which determine the structure are short range forces, these different cells are relatively weak coupled. This intrinsic instability makes it understandable, that some authors did not found the expected third TO-mode for PLZT. A result of Lurio was, that his measurements can be fitted by 6 damped oscillators and the frequency of ω_o, the third TO-mode is relatively low. We suppose, that we have a similar behavior for PST and PMN.

If we have it to do with an overdamped oscillator system according to (5), in the Debye-type like relaxation -neglecting $\varepsilon_\infty \cdot \omega_o^2$ is proportional to ε_{rs}^{-1} the measured relaxation frequency f_r (figure 8). That means, the relaxation can be ascribed to the "lossed" soft mode. These results are also supported by other results, such as the temperature dependence of the distribution of relaxation times and elastic measurements. This model explains microscopically the existence of the local polarisation or of polarization cluster in relaxor materials. It can be concluded, that relaxor materials can be described by this model qualitatively and partially quantitatively although some important simplifications are made: e.g. the mode coupling is not considered, the coupling constants were scalars and the solution of the SCPA used must be improved.

References

[1] G.A. Smolenskii, A.I. Agranovskaya, Sov. Phys. Sol. State 1, 1429 (1959).
[2] G.A. Smolenskii, J. Phys. Soc. Jap., **28**, Suppl., 26 (1970).
[3] L.E. Cross, Ferroelectrics, **76**, 241 (1987).
[4] C.G.F. Stenger, F.L. Scholten, A.J. Burggraaf, Solid State Commun., **32**, 989 (1979).
[5] N. Setter, L.E. Cross, J. Appl. Phys., **51**, 4356 (1980).
[6] G. Burns, B.A. Scott, Solid State Commun., **13**, 423 (1973).
[7] G. Schmidt, Ferroelectrics, **31**, 105 (1981).
[8] B. Kirsch, H. Schmitt, H.E. Müser, Ferroelectrics, **68**, 275 (1986).
[9] H. Schmitt, B. Kirsch, Ferroelectrics,**124**, 225 (1991).
[10] A.J. Burggraaf, C.G.F. Stenger, Ferroelectrics, **20**, 185 (1978).
[11] J. Bamberg, H. Schmitt, Ferroelectrics, **54**, 143 (1984).
[12] E. Fischer, W. Hässler, V.I. Fritsberg, phys. stat. sol. **66**, 169 (1981).
[13] A.M. Glass, J. Appl. Phys., **40**, 4699 (1969).
[14] A.C. Belous, Y.N. Venetzev, E.L. Politova and Y.M. Poplavko, Sov. Phys. Sol. State, **21**, 1803 (1979).
[15] K. Uchino, Phase Transitions, **2**, 591, (1981).
[16] T.L.Reinecke, K.L. Ngai, Ferroelectrics, **20**, 309 (1978).
[17] A. Lurio and G. Burns, J. Appl. Phys., **45**, 1986 (1974).
[18] G. Burns, Phys. Rev. B, **13**, 215 (1975).
[19] H. Schmitt, A. Dörr, Ferroelectrics, **93**, 309 (1989).
[20] P. Pitzius, H. Schmitt, A. Dörr, Ferroelectrics, **106**, 155 (1990).
[21] M. Bogs, H. Beige, P. Pitzius, H. Schmitt, Ferroelectrics, **126**, 197 (1992).
[22] B. Kirsch, Thesis, Saarbrücken, 1983.
[23] B. Kirsch, K.H. Weyrich, H. Schmitt, to be published.
[24] H. Megaw, C.N.W. Darlington, Acta cryst., **A31**, 161 (1975).

Ferroelectrics: Processing, Properties

Processing of Ferroelectric and Related Materials: A Review

Thomas R. Shrout† and Scott L. Swartz*

†Materials Research Laboratory
The Pennsylvania State University
University Park, PA 16802
*Battelle Memorial Institute
Columbus, OH 43201

ABSTRACT

The objective of this article is to present a synopsis of recent, ongoing, and future evolutionary developments pertaining to the fabrication/processing of ferroelectric materials, with an emphasis on polycrystalline ceramics. The basis for the review was derived from relevant literature over the last dozen years, including the responses from a worldwide questionnaire. This survey addressed issues such as chemical synthesis methods vs. conventional processes and anticipated future developments in processing and their impact on new applications, if any. The survey participants were scientists and engineers, both academic and industrial, involved in research and development of ferroelectrics and related materials. The primary conclusion of this survey revealed that evolutionary advancements in the processing of ferroelectric ceramics will continue to impact commercial production over the next ten years.

I. INTRODUCTION

Ferroelectric and related materials continue to be exploited for numerous applications, including recent concepts of "smart" or intelligent systems, whereby multifunctional components are required.[1-4] In recent years, substantial research and development has been devoted to ferroelectric materials in the form of single crystals, polymers, composites, and especially, thin films. References are provided for these important topics, but the primary focus of this paper pertains to polycrystalline materials. The most widely used and researched ferroelectric structural types, compositions, applications, and their state of development are presented in Table 1. Although the materials and ceramic fabrication methods for the ferroelectric materials described had their origin decades ago, this paper attempts to review evolutionary advances in the processing and fabrication of ferroelectric ceramics. The data presented is based on the compilation of responses to a questionnaire from more than 100 international scientists and engineers, of both academic and industrial backgrounds. In addition, recent processing developments and novel fabrication schemes, their future impact on new applications, if any, are discussed.

I. MATERIALS AND APPLICATIONS

As presented in Table I, the most widely used ferroelectrics are found in the perovskite family general formula ABO_3, which includes hundreds of compositional modifications (e.g., solid solution substitutions and/or dopants). In addition to ceramic materials, ferroelectric polymers, including PVF_2 and other co-polymers, are well established in the market place. Perhaps the most significant development comes not from monolithic materials but in the tailoring of physical properties using the nature of composites. Through the concept of phase connectivity[5-7], properties can be engineered to give orders of magnitude performance enhancement. Specifically, piezoelectric composites are finding increasing use in applications such as ultrasonic transducers for bio-medical imaging[8-9] and towed-array hydrophones.[10]

The ability to fabricate known ferroelectric materials in thin-film form offers applications such as non-volatile memories and DRAMs, both soon to be commercial realities. Furthermore, thin-film offers the potential of engineered crystallographic technology, thus allowing the exploitation of non-centrosymmetric materials such as ZnO and AlN, which in polycrystalline form cannot be made piezoelectrically active.[11,12]

Overall, however, in the field of ferroelectric polycrystalline ceramics, No new materials are foreseen that will provide revolutionary impact to new applications. Instead, evolutionary advances in the processing of ferroelectric ceramics will lead to improvements in existing commercial applications and to a gradual implementation of existing materials in new applications. For example, although ceramic materials such as relaxor ferroelectrics have been known for some forty years, progress in their commercialization for MLC capacitors and actuators has resulted from recent enhancements in their processing and fabrication.[13-16]

III. FABRICATION/PROCESSING OF FERROELECTRIC CERAMICS

Fabrication technologies for all electronic ceramic materials have the same basic process steps as presented in Figure 1, regardless of the application: **powder preparation, powder processing, green forming, and densification.**

A. Powder Preparation

The goal in the preparation of ferroelectric powders is to achieve a ceramic powder which, after consolidation, yields a product satisfying specified performance standards. A secondary goal is to produce a powder that can be consolidated/densified at lower temperatures. The most important commercialized powder preparation methods for ferroelectric ceramics include: mixing/calcination, coprecipitation from solvents, metal organic decomposition and hydrothermal processing. The trend in powder preparation is towards powders having particle sizes less than 1 μm and little or no agglomerates for enhanced reactivity and uniformity. Such powder qualities allow for the development of fine-grained microstructures with enhanced mechanical and electrical properties. Most importantly, fine particulates are critical for the continuing miniaturization of electro-ceramic devices. Examples of the four basic methods are presented in Table 2 for the preparation of $BaTiO_3$ powder. References relevant to processing advancements, particularly in regard to multilayer capacitor applications, including review articles[18,43], are given at the end of this paper.

Specific examples of significant developments in *mixing/calcination* processes are given for the PbO-based relaxor-based materials $Pb(Mg_{1/3}Nb_{2/3})O_3$ [PMN] in Table 3. The primary limitation for the development of ferroelectric relaxors has been in the consistent synthesis of phase-pure perovskite powders and ceramics. However, this problem has been successfully addressed through an improved understanding of the surface properties of the constituent oxides, crystal chemistry of PMN, and overall kinetics of the synthesis reaction. Specifically, the "B-site precursor method, whereby the B-site oxides are prereacted to form a columbite phase, allows enhanced dispersion and favors formation of the perovskite phase in contrast to lead-niobate pyrochlores.

Note, many of the advances in mixing/calcination have come through the better understanding of process-structure-property relationships. For example, knowledge of the underlying physiochemical behavior of Pb-based perovskites, also including pyrochlores and Bi-layer structures, allows for controlled morphological developments during calcination or "soft agglomeration," whereupon high reactive materials can be readily prepared.

CH3080-0-7803-0465-9/92$3.00 ©IEEE

Coprecipitation is a chemical method whereby insoluble compounds (e.g., hydroxides or oxalates, etc.) are precipitated from a solution of metal salts (e.g., chlorides), and the precipitated product is calcined to form the desired oxide powder. The advantage of this technique over calcination of mixed oxides is that intimate mixing of the precursors (in the solution phase) leads to lower calcination temperatures and the preparation of high-purity and fine-particle-size powders, see Table 3. Limitations are that the calcination step may once again result in agglomeration of fine particulates and the need for milling. An additional problem is that contaminants from the coprecipitation process (e.g., chlorides, carbonates, etc.) may linger in the powder after calcination. For example, commercially available, high-purity $BaTiO_3$ powder prepared by the well-known oxalate process, whereby a Ba-Ti chloride solution is precipitated by oxalic acid and the resulting precipitate is calcined. However, the sintering performance of these high-purity $BaTiO_3$ powders is hindered by the presence of $BaCO_3$, which is formed during calcination.

Metal organic decomposition (MOD), often referred to as sol-gel processing, in which metal-containing organic chemicals (e.g. alkoxides) react with water in a non-aqueous solvent to produce a metal hydroxide or hydrous oxide, or in special cases, an anhydrous metal oxide. Powders typically require calcination to obtain the desired phase. A major advantage of the MOD method is the control over purity and stoichiometry that can be achieved with powder crystallite size on the order of 5-50 nm. However, powder processing methods for nano-sized particulates have not been developed to take full advantage of such fine powders.

The advantage of this technique over mixing/calcination is exemplified by multilayer capacitors fabricated using alkoxide-derived relaxor based dielectrics. Capacitors produced with this powder have lower sintering temperatures and submicron grain sizes, thus allowing thinner layers and enhanced dielectric breakdown strength. Such benefits, however, are contrasted by expensive chemicals and processing methods.

Hydrothermal synthesize uses hot (above 100°C) water under pressure to produce crystalline oxides[62] and is widely used in the formation of Al_2O_3 (Bayer Process). The major advantage of the hydrothermal technique is that crystalline powders of the desired stoichiometry and phases can be prepared at temperatures significantly below those required for calcination. Another advantage is that the solution phase can be used to keep the particles separated and thus minimize agglomeration. The major limitation of hydrothermal processing is the need for the feedstocks to react in a closed system to maintain pressure and prevent boiling of the solution. Currently, Sakai Chemical and Cabot Corporation offer commercially available $BaTiO_3$-based powders, with PZT materials from Morgan Matroc in the late stages of development.

Laboratory research has shown the considerable benefits of hydrothermally-synthesized powders, e.g. Ba:Ti homogeneity, lower sintering temperatures, etc. However, these powders perform dramatically differently in post processing and sintering behavior requiring further developments for successful commercialization. As an example of their unique behavior, the intrinsic nature of OH-bonding in hydrothermally derived $BaTiO_3$ powders is thought to greatly influence densification[63], particularly when accompanied by a Bi_2O_3-based flux, whereby densification could be achieved at temperatures less than 800°C.[64]

Hybrid Synthesis

A wide spectrum of ferroelectric ceramic powders may also be produced by the hybrid process involving both chemical synthesis and conventional powder processing steps. For example, promising results have been reported for PZT ceramics derived from powders prepared from the conventional processing of a mixture of PbO and a hydrothermal zirconium titanate precursor.[60,65] The use of chemical synthesis methods to

Table 1. Ferroelectric Materials and Applications[17-23]

Structural Family	Composition	Application	Development Stage
Perovskite	$BaTiO_3$	Capacitors	Commercialized
	$(Ba,Sr)TiO_3$	IR Detectors	Development[24]
	$(Ba,Sr)TiO_3$ (doped)	PTCR Thermistors	Commercialization
	$Pb(Zr,Ti)O_3$ (PZT)	Transducers	Commercialization
		Actuators	Development[25]
	$Pb,La(Zr,Ti)O_3$ (PLZT)	Electro-optics	Commercialization
	Ca-doped $PbTiO_3$ Sm-doped $PbTiO_3$	Transducers (hydrophones)	Development/Commercialization[26,27]
	$Pb(Sc,Ta)O_3$	IR Detectors	Development[28]
	$(Na,Bi)TiO_3$	Transducers (Pb-free)	Research[29]
	$Pb(Mg,Nb)O_3$ (Relaxors)	Capacitors	Commercialization[30,31]
		Actuators	Development[32,33]
		Electro-optics	Research[34,35]
	$Ba(Zn,Ta)O_3$	Microwave Resonators	Commercialization
Tungsten-Bronze	$PbNb_2O_6$	Transducers (hydrophones)	Commercialization
	$(Sr,Ba)Nb_2O_6$	Electro-optics	Research/Development[36]
Bismuth-Layer Structure	$Bi_4Ti_3O_{12}$, Bi_2WO_6	Transducers (accelerometers)	Commercialization
Perovskite-Layer Structure	$Sr_2Nb_2O_7$ $La_2Ti_2O_7$	Transducers (high-temperature)	Research[37]
	$Bi_2(Zn,Ni,Nb)O_2$	Capacitors	Development[38]/Commercialzation[39]
Composites	PZT/Polymer	Transducers	Development[9,10]
Polymers	PVF2,Co-polymers	Transducers	Development/Commercialization[40-42]
Miscellaneous	$Li_2B_4O_7$ and $AlPO_4$ (Crystals)	Transducers	Development
	ZnO films	(high-frequency)	Commercialized
	AlN films		Research[11]

Note: Development stage may refer to limited commercial introduction specific to certain geographical regions.

uniformly distribute dopants to conventionally prepared powders of $BaTiO_3$ for capacitors is another way to combine the performance advantages of chemical synthesis and cost effectiveness of conventional processing.(61)

B. Powder Processing

A basic guideline of powder manufacturing is to do as little processing as possible to achieve the targeted performance standards. Ceramic powder fabrication is an iterative process during which undesirable contaminants and defects can enter into the materials at any stage. Therefore, it is best to keep the powder processing scheme as simple as possible to maintain flexibility. Uncontrollable factors such as changes in characteristics of as-received powders must be accommodated to achieve reproducibility in the processing from batch to batch of material. Keeping the processing simple is not always possible for ferroelectric ceramics, based simply on their complex nature, e.g. the need for precise stoichiometry control and dopants.

A fundamental requirement in powder processing and perhaps key to the continued performance enhancement is characterization of the as-received or synthesized powders.(66) Information on tap and pour density, particle size distribution, specific surface areas, and chemical and phase analysis are critical. Uniaxial compaction behavior, in particular, is easily measured and provides data on the nature of the agglomerates in a powder.

Milling is required for most powders, either to reduce particle size or to aid in the mixing of component powders. Commonly employed types of comminution include ball milling, vibratory, attrition, and jet milling, each possessing its own advantages and disadvantages. For example, ball milling is well suited for mixing, but not for comminution, unless varying media sizes and long milling times are used. Vibratory milling is well suited for comminution, but extreme care in dispersion/rheological behavior must be considered, whereas attrition milling, though very effective, is generally more expensive. Example of advances in terms of powder processing are given in Table 4. As presented, attrition milling allows for the preparation of extremely fine particulates, generally are achievable by chemical synthesis methods. Along with the introduction of high performance milling media, e.g. partially stabilized zirconia (PSZ), minimizing contamination, attrition milling is finding growing usage for the processing of electronic ceramics.

Figure 1. Schematic of iterative processing of ferroelectric ceramics and key characterization methods. "Key to performance and reliability lies in the understanding of precursor-process-structure property relationships."

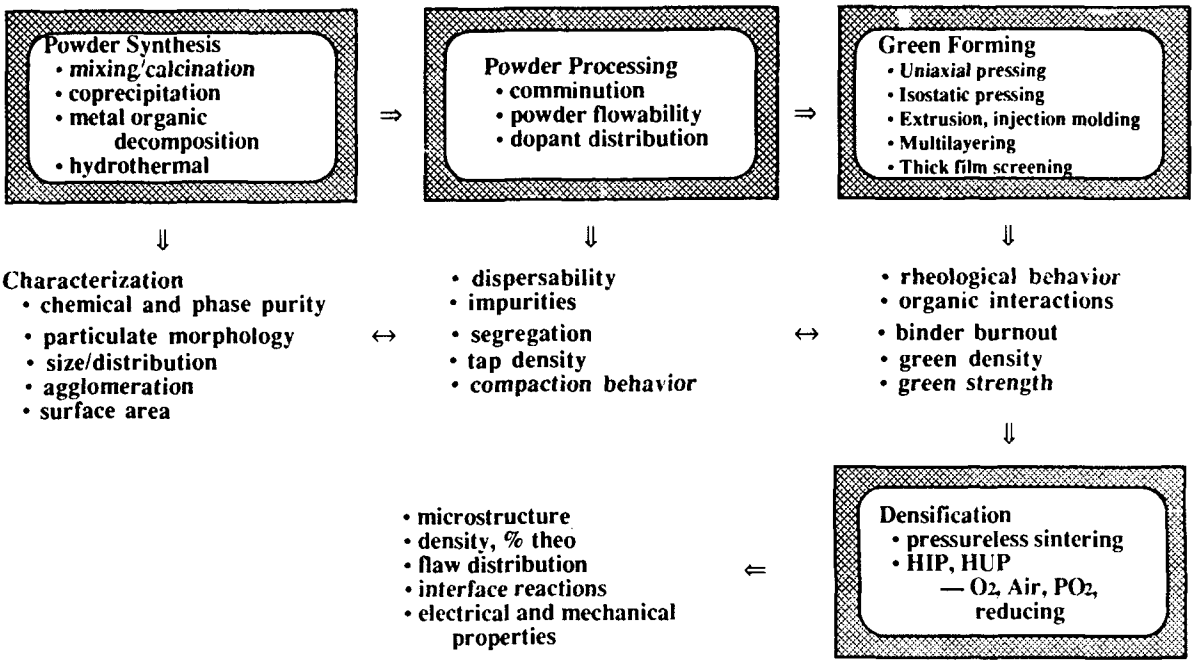


Table 2. Methods Used to Prepare $BaTiO_3$ Electronic Ceramic Powders

Method	Reaction	Particle Size
Mixing/calcination	$BaCO_3 + TiO_2 \xrightarrow{\Delta T} BaTiO_3 + CO_2\uparrow$	1 μm to 100 μm
Coprecipitation	$Ba^{2+} + TiO^{2+} + 2\,C_2O \xrightarrow[4]{2-} \xrightarrow{H_2O} BaTi(C_2O_4)_2 4H_2) \xrightarrow{\Delta T}$	0.5 μm (after calcining and milling)
Hydrothermal	$Ba(OH)_2 + Ti(OH)_4 + \xrightarrow[\Delta T,P]{H_2O\ pH} BaTiO_3 + 2H_2O$	Nanosize to 5 μm
Metal organic (Alkoxide)	$Ba(OR)_2 + Ti(OR)_4 + \xrightarrow[solvent]{H_2O\ \Delta T} BaTi(OR) \xrightarrow{\Delta T} BaTiO_3 + 6R$	5.0-50.0 nm, (crystallite size) [agglomerate size larger]

Progress in understanding the surface chemistry of con ponent and reacted materials has allowed the wide spread usage of aqueous processing as well as the ability to disperse fine particulates through surface passivation.[67] With growing environmental concerns related to the use and/or disposal of hazardous solvents, aqueous processing will continue to become important in the future.

"With the advances presented above and the overall control of incoming raw materials, e.g. morphology, purity, etc., high performance ceramics are generally achievable without the implementation of expensive chemical methodologies, making the mixing/calcination process the method of choice for most ferroelectric materials well into the future." However, continued development of powder processing methods for fine-particle size powders will allow future commercialization of chemical methods if the cost of their advanced powders can be reduced.

C. Green Forming

Green forming is one of the most critical steps in the fabrication of ferroelectric ceramics. The choice of green forming technique depends on the ultimate geometry required for a specific application. There are many different ways to form green ceramics, several of which are summarized in Table 5. Perhaps, of all the methods, the most significant advances in processing have been in the realm of multilayer fabrication, which includes: piezoelectric/electrostrictive capacitors (>50 billion units/year), piezoelectric/electrostrictive actuators, and varistors, as well as several in non-ferroelectric applications (e.g. ceramic packaging).[69,70]

Table 6 summarizes recent developments in MLC fabrication. Naturally, the enhanced performance arises from the corresponding development in binders, dispersants, and overall organics and their role in sheet formation. In addition, ultra-thin MLCs have led to the need for correspondingly thin metallization. Of particular significance in the fabrication of MLCs is that based on magnetic tape fabrication technology, whereupon thin sheets can be formed >600 ft./min., while being simultaneously electroded.[71]

Recent developments in the fabrication of piezoelectric-polymer composites, primarily for bio-medical ultrasound and towed array transducers, are given in Table 7. In addition to achieving fine-scale composites, current emphasis lies in the ability to economically fabricate large areas (>meter-square).

D. Densification

Densification of ferroelectric materials generally requires high temperature and atmosphere control (O_2, PbO, vacuum, etc.) to minimize the porosity in consolidated ceramics. Heat-controlled cycles are critical to microstructural development and grain size control. Techniques such as fast firing and rate controlled sinte[illegible] have been utilized to inhibit or eliminate undesirable sinte[illegible] mechanisms. Hot isostatic pressing (HIP), which [illegible] gaseous pressure at high temperature, has found m[illegible] commercialization in contrast to hot uniaxial pressing, whic[illegible] limited to relatively simple shapes. The HIP process has bee[illegible] shown to greatly enhance the dielectric breakdown strength (DBS) of multilayer ceramics and actuators and can be used to prepare transparent materials, including PLZTs and PMN. Advancements in HIP processing of PbO-based ferroelectrics have also been made with the introduction of oxygen atmosphere compatible systems (see Table 8).

Work continues to find economical densification proce[illegible]ses by which macro-defect free ceramics with near theoretical densities can be achieved, allowing one to approach the maximum properties allowable in ferroelectric ceramics. Much of the progress in this direction, however, will be made through advances in the powder synthesis, processing, and forming methods.

Table 3. Advances in Synthesis of Ferroelectric Materials

Advancement	Material	Demonstrated Benefits
Conventional (Mixing/Calcination) Powder Synthesis		
Pre-reaction of B-site precursors (Columbite method)	$Pb(Mg,Nb)O_3$	Improved perovskite phase purity[44]
Modification of surface chemistry (pH control) to optimize dispersion	$Pb(Mg,Nb)O_3$	Improved perovskite phase purity[14]
Crystal chemical engineering (doping with $BaTiO_3$, $SrTiO_3$)	$Pb(Zn,Nb)O_3$	Improved perovskite phase purity[45,46]
Reactive calcination (optimization of calcination conditions	PMN, PZT	Improved sintering reactivity[47]
Advanced Powder Synthesis Methods		
Alkoxide Synthesis	Pb-based relaxors	Fine-particle-size powders[31,49] Thin-layer MLCs
Pechiney Method (Citrate decomposition)	$BaTiO_3$ Ba,$SrTiO_3$,PZT	Fine-particle-size powders[50,51,52] High purity
Oxalate Coprecipitation	$BaTiO_3$	Fine-particle-size powders[53,54] High purity, stoichiometry
Hydrothermal Synthesis	$BaTiO_3$, PZT	Fine-particle-size powders[55,56,57,58,59] Lower sintering temperatures
Hybrid Methods		
PbO + hydrothermal $(Zr,Ti)O_4$	PZT	Improved compositional uniformity[60] Fine grain size
Chemical methods for dopant addition "nanoheterogeneity"	$BaTiO_3$	Uniform dopant incorporation[61] (X7R dielectrics)

Table 4. Advances in Powder Processing

Concept	Benefit
• High energy milling e.g. attrition $PbO+MgO+Nb_2O_5 \rightarrow PMN$	• Submicron powders[47,68] • Dispersion[14]
• PSZ media	• Minimal contamination
• Aqueous processing	• Non-toxic solvent • Low cost
• Surface powder chemistry understanding e.g. "Passivation - $BaTiO_3$"	• Rheological control (dispersability)

IV. SUMMARY

The primary conclusion of this review is that the fabrication of ferroelectric ceramic materials will continue to see evolutionary advances, primarily in the areas of synthesis and processing. The implementation of recent improvements in processing methods for conventional powders (e.g. attrition milling, dispersion, etc.) will extend the performance of ferroelectric ceramics. However, there will be a need for advanced powder synthesis methods and associated handling and consolidation procedures for the high-performance end of certain applications, e.g. cryogenic actuators for space. Without revolutionary advances, the primary focus of development will be on reducing cost of advanced powder synthesis methods, such as hydrothermal synthesis and coprecipitation. If these cost issues can be addressed, advanced synthesis methods will significantly enhance existing materials (e.g., $BaTiO_3$-based dielectric ceramics and PZT-based piezoelectric ceramics). Although the discovery of new ferroelectric materials is not anticipated, continued improvements in the processing of emerging ferroelectric ceramics, such as PbO-based relaxors, will lead to their increased use in existing applications (capacitors and actuators), and enable their development for emerging applications (e.g., E-field tunable transducers for sonar and bio-medical ultrasound).[97]

Table 5. Green Forming Procedures for Ferroelectric Ceramics

Green Forming Method	Geometries	Applications
Uniaxial Pressing	Disks, toroids, plates	Disk capacitors, piezo transducers, igniters, inch-worm actuators
Cold Isostatic Pressing	Complex and simple	High-frequency ultrasonic transducers
Colloidal Casting	Complex shapes	Transducers
Extrusion	Thin sheets (>80 μm) rods, tubes, honeycombs, substrates	Igniters PTC thermister heaters
Injection Molding	Complex shapes	PZT-composites
Multilayer Fabrication	Thin sheets/multicomponent	Capacitors, actuators Varistors

Table 6. Advances in MLC Manufacturing

Advances	Benefits	Development Stage
Ultra-thin MLCs • ≤10μ	• Cap. Vol. Eff. • High energy storage[73] (replace tantalum & electrolytics)	Commercialized[31,72]
• ≤ 6μ		Research/Development[74]
• Fine Metallization		Development[75]
• High Speed Fabrication	• Low cost (>600 ft/min.)	Development[71]
• Low-Fire — Ag:Pd electrodes	• Low cost	Commercialized
• Material/Dielectrics —High K >5000 X7R	• Cap. Vol. Eff.	Development[76]/Commercialized
—Relaxors, e.g. PMN-based	• Cap. Vol. Eff.	Commercialized
—Varistors (ZnO)	• Surface Mount Chip Integration	Commercialized
—PZTs, PMN	• Actuators	Commercialized

V. SURVEY RESULTS

Prior to conducting this review, a worldwide survey was conducted of scientists and engineers involved in ferroelectric materials research, from both academic and industrial organizations. This survey addressed significant recent and anticipated developments of ferroelectric materials, and the question of whether conventional fabrication methods for ferroelectric materials will be sufficient for future applications requirements. Responses were categorized by geographical region (North America, Europe, and the Far East). Results of this survey are summarized below:

- The field of ferroelectric films, although outside the scope of this review, was recognized as an area where significant recent developments were achieved, and where an even larger number of future developments and applications were anticipated. The importance of ferroelectric films was recognized by the largest percentage of respondents, regardless of geographical region.
- Multilayer ceramics, both actuators and capacitors, were identified as an application area where significant recent developments, particularly in terms of ultra-thin layers and the incorporation of relaxor ferroelectrics, have been made, especially by respondents from the Far East
- Advances in conventional processing was cited as an area of significant recent achievement, although there was little confidence that conventional processing would see additional advances in the future. Chemical synthesis of ceramic powders, by sol-gel and coprecipitation methods, was recognized as important to future development of existing and emerging applications, but strives must be made to achieve economical feasibility, perhaps being achievable through combined methodologies, i.e. hybrid processes.

Areas identified as seeing significant recent developments included hot-pressing and HIP techniques and piezoelectric composites, whereas research topics identified as important to future applications include thick film processing for multicomponent packaging, assemblage of nano-composites for electro-optics and ferro-fluids, relaxor ferroelectrics, smart materials, and optoelectronic materials.

ACKNOWLEDGEMENTS

The authors wish to thank all those who took time out from their busy schedules to answer our questionnaire. The following is a partial list of industries, universities, and government laboratories from which the responses came:

Companies

Toshiba, Sakai Chemical, Denka, NEC, Sumitomo Metals, Matsushita Electric, Murata, Nippon Soda, Mitsubishi Mining and Cement (Materials), Kyocera, Hitachi, TDK, AT&T, DuPont, Battelle, Martin Marietta, BM Hi-Tech, Piezo Systems, Alcoa, MRA Laboratories, Centre Engineering, Acoustic Imaging, Krautkramer Branson, Hewlett Packard, Alliant Ceramics, Cleveland Crystals, ITEK Optical, IBM, Vitramon, Army (Fort Monmouth), Siemens, Philips, GEC Marconi, Ferroperm, CNET/France Telecom, ISMRA Lab CRTSMAT, Toshiba Tungalloy, Morgan Matroc

Shonan Institute of Tech, National Defense Academy, Science University at Tokyo, Nagoya, Kyushu Institute of Tokyo, Penn State, Texas A&M, Office of Naval Research, Florida University, Montana State, Naval Research Lab, Institute of Physics-Rostov, Ben-Curion University, University des Saarlandes, Ecole Polytechnique de Lausanne, National Institute in Inorganic Materials, Hachinohe Institute of Technology, Institute of Crystallography (Moscow), Indian Institute of Science, Osaka University

A special thanks to JoAnn Mantz for her help in putting together the questionnaire and this manuscript.

Table 7. Advances in the Fabrication of PiezoPolymer Composites

Advances	Benefits	Development Stage
Extrusion	≤100 micron PZT rods ≤10 micron	Development[77] Research[78]
Pick and Place (Weaving)	Large Area (> meter-squared)	Development[79]
Lost Mould Method	10 μ -100 scale	Development[80,82]
Injection Molding	Low cost	Development[83]
Fill and Dice	Simplistic	Commercialized

Table 8. Advances in the Densification of Ferroelectric Materials

Advances	Benefit	Development Stage
• Pressureless sintering —Vacuum/atmosphere control —Rate-controlled densification	• Transparent PLZT • Lower Firing Temp PZTs	Development[84,84] Research[86]
• Hot uniaxial pressing (HUP)	• PZTs (pyroelectric ~10 μ wafers • Transparent PMN, SBN,	Commercialized Research[87,88]
• Hot isostatic pressing (HIP)	• Complex shapes • Multilayer capacitors — fatigue reduction • Multilayer actuators • Transparent PMN, PLZT	Research/Development[89,91] Commercialized[88-91]
• Hot forging	• Grain orientation e.g. $Bi_4Ti_3O_{12}$	Research[29,37,92]
• Mixed sintering	• Flat †T.C.C. MLCs	Research[93,94]
• Fluxes (liquid phase) e.g. lithium oxide & fluorides	• Low firing temps	Research/Development[95,96]

†Temperature coefficient of capacitors.

REFERENCES

1. R.E. Newnham and G. R. Ruschau, "Smart Electroceramics," J. Amer. Cer. Soc., **74**, pp. 463-479 (1991).

2. R.E. Newnham, "The Golden Age of Electroceramics," Adv. Ceram. Mater., **3**, 12-16 (1988).

3. H. Yanagida, "Intelligent Materials--A New Frontier," Angew. Chem., **100**, 1443-46 (1988).

4. C.A. Rogers, "From the Editor," Journal of Intelligent Material Systems and Structures, **1**,3 (1990).

5. R.E. Newnham, "Composite Electroceramics," J. Mater. Educ., **7**, 605-51 (1985).

6. R.E. Newnham, et al., "Connectivity and Piezoelectric-Pyroelectric Composites," Mater. Res. Bull., Vol. **13**, No. 5, pp. 525-536, 1978.

7. H. Banno and S. Saito, "Piezoelectric and Dielectric Properties of Composites of Synthetic Rubber and $PbTiO_3$ or PZT," Jpn. J. Appl. Phys., Vol. **22**, Suppl. 22-2, pp. 67-69 (1983).

8. H. Masuzawa, Y. Ito, . Nakaya, et al., "Electrostrictive Materials for Ultrasonic Probes in the $Pb(Mg_{1/3}Nb_{2/3})O_3$-$PbTiO_3$ System," Japanese Journal of Applied Physics, Vol. **28**, Supplement 28-2, pp. 101-104 (1989).

9. Wallace A. Smith, "New Opportunities in Ultrasonic Transducers Emerging From Innovations in Piezoelectric Materials," Proc. 1992 SPIE Int'l Symp. New Developments in Ultrasonic Transducers and Transducer Systems, July 1992.

10. R.Y. Ting, "Evaluation of New Piezoelectric composite Materials for Hydrophone Applications," Ferroelectrics, Vol. **67**, pp. 143-157 (1986).

11. N.D. Patel and P.S. Nicholson, "High Frequency, High Temperature Ultrasonic Transducers," NDT International **23** [5] pp. 262-266 (1990).

12. Y. Ito, K. Kushida, H. Kanda, H. Takeuchi, and K. Sugawara, "Thin-Film AlN Ultrasonic Transducer Arrays for Operation at 100 MHz," Ferroelectrics in press (1992). Presented at the Second European Conference on the Application of Polar Dielectrics, London, United Kingdom, 12-15 April 1992.

13. T.R. Shrout and A. Halliyal, "Preparation of Lead-Based Ferroelectric Relaxors for Capacitors," Am. Ceram. Soc. Bull., Vol. **66**, No. 4, pp. 704-711 (1987).

14. T.R. Shrout, et al., "Enhanced Processing of Perovskite $Pb(Mg_{1/3}Nb_{2/3})O_3$ Relaxors through Understanding of the Surface Chemistry of the Component Powders," in Ceramic Powder Science, Ceramic Transactions, Vol. **1**, ed. by G.L. Messing, et al., American Ceramic Society, Westerville, OH, pp. 519-527 (1988).

15. M. Lejeune and J.P. Boilot, "Low-Firing Dielectrics Based on Lead Magnesium Niobate," Mat. Res. Bull., Vol. **20**, pp. 493-499 (1985).

16. Joseph P. Dougherty, "Fifth U.S.: Japan Workshop on Dielectric and Piezoelectric Materials," Office of Naval Research Report, N66005 (1990).

17. T. Shiosaki, "Recent Developments in Piezoelectric Materials," Ferroelectrics, **91**, pp. 39-51 (1989).

18. S.I Swartz, "Topics in Electronic Ceramics," IEEE Trans. Elect. Insul. Digest on Dielectrics **25**, 935-987 (Oct. 1990).

19. L.L. Hench and J.K. West (Eds.), Principles of Electronic Ceramics, John Wiley & Sons, Inc., New York, 1990.

20. J.M. Herbert, Ferroelectric Transducers and Sensors, Gordon and Breach Science Publishers, Inc., New York (1982).

21. G.H. Haertling, "Piezoelectric and Electrooptic Ceramics," in Ceramic Materials for Electronics: Processing, Properties, and Applications, ed. by R.C. Buchanan, Marcel-Dekker, Inc., New York, pp. 139-225 (1986).

22. R.C. Pohanka,P.L. Smith, and G.H. Haertling, "Recent Advances in Piezoelectric Ceramics," in Electronic Ceramics: Properties, Devices, and Applications, ed. by L.M. Levinson, Marcel Dekker, Inc., New York, pp. 45-145 (1988).

23. Helmut Thomann, "Piezoelectric Ceramics," Advanced Materials, **2**, pp. 458-463 (1990).

24. B.M. Kulwicki, A. Amin, H.R. Beratan and C.M. Hanscon, "Pyroelectric Imaging," (to be published, Proc. 8th Int'l Symp. on Application of Ferroelectrics (1992).

25. S. Takahashi, "Recent Developments in Multilayer Piezoelectric Ceramic Actuators and Their Applications," Ferroelectrics, **91**, 293 (1989).

26. Y. Yamashita, et al., "$(Pb,Ca)((Co_{1/2}W_{1/2})_x Ti_{1-x})O_3$ Piezoelectric Ceramics and Their Applications," Jpn. J. Appl. Phys., Vol. **20**, Suppl. 20-4, pp. 183-187 (1981).

27. H. Takeuchi, et al., "Electromechanical Properties of $(Pb,Ln)(Ti,Mn)O_3$ Ceramics," J. Acoustic Soc. Amer., Vol. **72**, No. 4, pp. 1114-1120 (1982).

28. R.W. Whatmore, P.C. Osbond, N.M. Shorrocks, "Ferroelectric Materials for Thermal IR Detectors," Ferroelectrics, Vol. **76**, pp. 351 (1987).

29. T. Takenaka and K. Sakata, "Grain Oriented and Mn Doped $(NaBi)_{(1-x)/2}Ca_xBi_4Ti_4O_{15}$ Ceramics for Piezo- and Pyrosensor Materials," Sensors and Materials **1** pp. 35-46 (1988).

30. T.R Shrout and J.P. Dougherty, "A World Review on Lead Based $(Pb(B_1B_2)O_3)$ Relaxors Versus $BaTiO_3$ Dielectrics for Multilayer Ceramic Capacitors," Proc. Symp. on Ceramic Dielectrics, H.C. Ling (ed.), Am. Ceram. Soc. (1989).

31. Masatomo Yonezawa, Kazuaki Utsumi, Atsushi Ochi, and Toru Mori, "Research and Development of Relaxor Ceramics at NEC, Procs. 7th IEEE Int'l Symp. on Applications of Ferroelectrics, pp. 159-164 (1990).

32. R. Aldrich, "Requirements for Piezoelectric Materials for Deformable Mirrors," Ferroelectrics **27**, 19-25 (1986).

33. K. Uchino, "Electrostrictive Actuators: Materials and Applications," Am. Ceram. Soc. Bull., Vol. **65**, No. 4, pp. 647-652 (1986).

34. N.C. Kim, D.A. McHenry, S.J. Jang, and T.R. Shrout, "Fabrication of Optically Transparent Lanthanum Modified $Pb(Mg_{1/3}Nb_{2/3})O_3$ Using Hot Isostatic Pressing," J. Amer. Ceram. Soc., **73**, 923-928 (1990).

35. D.A. McHenry, J.R. Giniewicz, S.J. Jang, T.R. Shrout, and A.S. Bhalla, "Optical and Electro-Optical Properties of Lead Magnesium Niobate-Lead Titanate," Ferroelectrics **107**, 45-46 (1990).

36. S. Musikant, Optical Materials, An Introduction to Selection and Applications, Marcel-Dekker, Inc., New York, 1985.

37. P.A. Fuierer and R.E. Newnham, "$La_2Ti_2O_7$ Ceramics," J. Am. Ceram. Soc. **75** [11] pp. 2876-81 (1991).

38. M.F. Yan, H.C. Ling, and W.W. Rhodes," Low-Firing, Temperature-stable Dielectric Compositions Based on Bismuth Nickel Zinc Niobates," J. Am. Ceram. Soc., **73**, 1106-117 (1990).

39. Xao Yi: private communication.

40. T.T. Wang, J.M. Herbert, and A.M. Glass, editors, The Applications of Ferroelectric Polymers, Blackie, Glasgow, United Kingdom (1987).

41. H. Ohigashi, K. Koga, M. Suzuki, T. Nakanishi, K. Kimura, and N. Hashimoto, "Piezoelectric and Ferroelectric Properties of P(VDF-TrFE) Copolymers and Their Application to Ultrasonic Transducers," Ferroelectrics **60**, 263-276 (1984).

42. T. Furukawa, "Piezoelectricity and Pyroelectricity in Polymers," IEEE Transactions on Electrical Insulation **24**, 375-394 (1989).

43. J.H. Adair, et al., "A Review of the Processing of Electronic Ceramics with an Emphasis on Multilayer Capacitor Fabrication," J. Mater. Ed., Vol. **9**, No. 1-2, pp. 71-118 (1987).

4. S.L. Swartz and T.R. Shrout, "Fabrication of Perovskite Lead Magnesium Niobate," Mat. Res. Bull. **17**, 1245-50 (1982).

5. A. Halliyal, et al., "Stabilization of Perovskite Phase and Dielectric Properties of Ceramics in the $Pb(Zn_{1/3}Nb_{2/3})O_3$-$BaTiO_3$ System," Am. Ceram. Soc. Bull. Vol. **66**, pp. 671-676 (1987).

6. O. Furukawa, Y. Yamashita, M. Harata, T. Takahashi, and K. Inagaki, "Dielectric Properties of Modified Lead Zinc Niobate Ceramic," Jpn. J. Appl. Phys., **24**, 96-99 (1985).

7. T.R. Shrout, P. Papet, S. Kim, and G.S. Lee, "Conventionally Prepared Submicron Lead-Based Perovskite by Reactive Calcination," Journal of the American Ceramic Society **73**, 1862-1867 (1990).

8. S. Kim, G.S. Lee, S. Venkataramani, and T.R. Shrout, "Fabrication of Fine Grain Piezoelectric Ceramics Using Reactive Calcination and Milling," Journal of Materials Science **26**, 1141 (1991).

9. F. Chaput and J.P. Boilot, "Alkoxide Hydroxide Route to Synthesize Barium Titanate Based Powders," J. Am. Ceram. Soc., **73** p. 942 (1990).

50. B.J. Mulder, "Preparation of $BaTiO_3$ and Other Ceramic Powder by Coprecipitation of Citrates from Alcohol," Am. Cer. Soc. Bull., **49** [11], 990-993 (1970).

51. P.C. Osbond, N.J. Payne, N.M. Shorrocks, R.W. Whatmore, and R.W. Ainger, "Dielectric and Microstructural Properties of Barium Strontium Titanate Ceramics Prepared form Citrate Precursors," Sixth IEEE Int'l Symp. on Applications of Ferroelectrics, pp. 748-51 (1986).

52. Maria A. Zaghete, Carlos O. Paiva Santos, José A. Varela, Elson Longo, and Yvonne P. Mascarenhas, "Phase Characterization of Lead Zirconate Titanate Obtained from Organic Solutions of Citrates," J. Amer. Ceram. Soc., **75** [8] 2088-93 (1992).

53. K. Osseo-Asare, F.J. Arriagada, and J.H. Adair, "Solubility Relationships in the Coprecipitation Synthesis of Barium Titanate: Heterogeneous Equilibria in the Ba^{+2}-$C_2O_4^{-2}$-H_2O System," in G. L. Messing, E.R. Fuller, Jr., and Hans Hausin, eds., Ceramic Powder Science, Vol. 2, 1987, pp. 47-53.

54. J.M. Criado, F.J. Gotor, C. Real, F. Jimenez, S. Ramos, and J. Del Cerro, "Application of the Constant Rate Thermal Analysis Technique to the Microstructure Control of $BaTiO_3$ Yielded From Coprecipitated Oxalate," Ferroelectrics, **115**, pp. 43-48 (1991).

55. W.J. Dawson and S.L. Swartz, "Process for Producing Sub-Micron Ceramic Powders of Perovskite Compounds with Controlled Stoichiometry and Particle Size," U.S. Patent 5,112,433, 12 May 1992.

56. W.J. Dawson, "Hydrothermal Synthesis of Advanced Ceramic Powders," Am. Ceram. Soc. Bull., Vol. **67**, No. 10, pp. 1673-1678 (1988).

57. K. Abe, et al., "Process for Producing a Composition which Includes Perovskite Compounds," U.S. Patent #4,643,984 (1987).

58. J. Menashi, et al., "Barium Titanate Based Dielectric Compositions," U.S. Patent #4,832,939 (1989).

59. K. Fukai, K. Hidaka, M. Aoko, and K. Abe, "Preparation and Properties of Uniform Fine Perovskite Powders by Hydrothermal Synthesis," Ceramics International, **16** pp. 285-290 (1990).

60. Takashi Yamamoto, "Optimum Preparation Methods for Piezoelectric Ceramics and Their Evaluation," Ceramic Bull., **71**, pp. 978-985 (1992).

61. D.Swanson, S.A. Bruno, I. Burn, K. Sasaki, and H.E. Sorgna, "Advanced Dielectric Powders for Improved Capacitor Reliability," Proc. Multilayer Ceramic Reliability, 68-86, The Pennsylvania State University (1991).

62. E.P. Stambaugh and J.F. Miller, "Hydrothermal Precipitation of High Quality Inorganic Oxides," in S. Somiya, ed., Proceedings of First International Symposium on Hydrothermal Reactions, Gakujutsu Bunken Fukyu-kai (c/o Tokyo Institute of Technology), Tokyo, Japan, pp. 859-872 (1983).

63. D. Hennings and S. Schreinemacher, "Characterization of Hydrothermal Barium Titanate," J. Euro. Ceram. Soc., **9**, 41-46 (1992).

64. U. Kumar, S.F. Wang, and J.P. Dougherty, "Preparation of Dense Ultra-Fine Grain Barium Titanate-Based Ceramics," (to be published).

65. T. Takagi, K. Anetani, and K. Shimizo, "Lead-containing Oxide Powder," U.S. Patent #4,812,426 (1989).

66. K.K. Verna and A. Roberts in G.Y. Onoda, Jr., and L.L. Hench, eds., Ceramic Processing Before Firing, John Wiley & Sons, Inc., New York, pp. 391-407 (1978).

67. James H. Adair and Thomas R. Shrout, "Surface Passivation of Perovskite Compounds in Aqueous Suspension," (to be patented).

68. P. Papet, J.P. Dougherty, and T.R. Shrout, "Particle and Grain Size Effects on the Dielectric Behavior of the Relaxor Ferroelectric $Pb(Mg_{1/3}Nb_{2/3})O_3$," J. Mat. Res., **5**, 1-8 (1990).

69. K. Utsumi, Y. Shimada, and H. Takamizawa, "Monolithic Multicomponent Ceramic (MMC) Substrate," in K.A. Jackson, R.C. Pohanka, D.R. Uhlmann, and D.R. Ulrich, eds., Electronic Packaging Materials Science, Materials Research Society, Pittsburgh, PA, pp. 15-26 (1986).

70. H.T. Sawhill and co-workers, "Low Temperature Co-Firable Ceramics with Co-Fired Resistors," International Society of Hybrid Microelectronics Proceedings, p. 473-480 (1986).

71. Joe Rainwater, Vistatech Corporation, Dallas, Texas (private communication).

72. Detlev Hennings, Mareike Klee, and Rainer Waser, "Advanced Dielectrics: Bulk Ceramics and Thin Films," Advanced Materials, **3** p. 334-340 (1990).

73. G.R. Love, "Energy Storage in Ceramic Dielectrics," J. Am. Ceram. Soc., **73** 323-328 (1989).

74. G.H. Maher, "MLC Capacitors with 6 Microns Active Dielectric and X7R Electrical Characteristics," presented at the 91st Am. Cer. Soc. Meeting, Indianapolis, IN (1988).

75. A. Burer, BMC Tech. Co. (private communication).

76. T.T. Srinivasan, Ferro Corp. (private communication).

77. H. Park, CPS, Inc. (private communication).

78. Shoko Yoshikawa, The Pennsylvania State University (private communication).

79. Dean Bathol, Fiber Materials, Inc. (private communication).

80. K. Lubitz, A. Wolff, G. Preu, R. Stoll, and B. Schulmeyer, "New Piezoelectric Composites for Ultrasonic Transducers," Ferroelectrics in press (1992). Presented at the Second European Conference of the Application of Polar Dielectrics, London, United Kingdom, 12-15 April 1992.

81. Ulrich Bast, Dieter Cramer, and Andreas Wolff, "A New Technique for the Production of Piezoelectric Composites with 1-3 Connectivity," Ceramics Today-Tomorrow's Ceramics: Materials Science Monographs, 66C, Ed., P. Vincenzini, Elsevier Publishing, Proc. of the 7th Int'l Meeting on Modern Ceramics Tech., Montecatini Fermi, Italy, 2 June (1990).

82. G. Preu, A. Wolff, D.Creamer, and U. Bast, "Microstructuring of Piezoelectric Ceramic," ECERS (European Ceramic Soc.), Augsburg, Germany (Sept. 1991).

83. L. Bowen, Materials Systems, Inc. (private communication).

84. K. Nagata, et al., "Vacuum Sintering of Transparent Piezo-Ceramics," Ceram. Int., Vol. 3, No. 2, pp. 53-56 (1977).

85. G.S. Snow, "Fabrication of Transparent Electrooptic PLZT Ceramics by Atmosphere Sintering," J. Am. Ceram. Soc., Vol. **56**, No. 2, pp. 91-96 (1973).

86. K. Lubitz, H. Hellebrand, D. Cramer, and I. Probst, "Low Sintering PZT for Multilayer Actuators," Proc. ECERS, Augsburg, Germany (Sept. 1991).

Nobuko, S. Van Damme, Audrey E. Sutherland, Lori Jones, Keith **Bridges, and Stephen** R. Winzer, "Fabrication of Optically Transparent and Electrooptic Strontium Barium Niobate Ceramics," J. Amer. Ceram. Soc., **74**, pp. 1785-1792 (1991).

J.R. Giniewicz, D.A. McHenry, S.J. Jang, T.R. Shrout, A.Bhalla, and F.Ainger, "Characterization of (1-x) $Pb(Mg_{1/3}Nb_{2/3})O_3$-(x)$PbTiO_3$ and $Pb(Sc_{1/2}Ta_{1/2})O_3$ Transparent Ceramics by Uniaxial Hot-Pressing," Ferroelectrics, **109**, 167-172 (1990).

L.J. Bowen, W.A. Schulze, and J.V. Biggers. "Hot Isostatic Pressing of PZT," Powder Metallurgy Int., **12** [2], 42-96 (1980).

M. Takata, S. Kawahara, K. Kayeyama, and S.Toyota, "The HIP Treatment of Magnetic and Piezoelectric Ceramics," Proc. of Int'l Conf. Hot Isostatic Pressing/Lulea, **11**, 399-401, 15-17 June (1987).

Mituhiro Takata and Keisuki Koyeyama, "The High Frequency Transducer of HIP-Densified Piezoelectric Ceramics," Jap. J. of Appl. Physics, **22** Supplement 22-2, pp. 148-149 (1983).

H. Watanabe, T. Kimura, and T. Yamaguchi, "Particle Orientation During Tape Casting in the Fabrication of Grain-Oriented Bismuth Titanate," J. Am. Ceram. Soc., **72** [2] pp. 289-93 (1989).

J. Belsick, Y. Yamashita, and M. Harata, "Ceramic/Ceramic Composite for Multilayer Capacitor Application," Proc. IEEE 7th Int'l Symp.Application of Ferroelectrics, 44-47 (1990)

Brahim Boufrou, Filbert Desgardin, and Bernard Raveau, "Tetragonal Tungsten Bronze Niobate, $K_{0.2}Sr_{0.4}NbO_3$: A New Material for Capacitors with Flat Dielectric Curves," J. Am. Ceram. Soc., **74**, pp. 2804-2814 (1991).

J.M. Haussanne, O. Regreng, J. Lostec, G. Desgardin, M. Halmi, and B Raveau, "Sintering of Various Perovskites with Lithium Salts," Proc. 6th CIMTEC, Milan, Italy (1986).

G. Desgardin, I. Meg, and B. Raveau, "$BaLiF_3$-A New Sintering Agent for $BaTiO_3$-Based Capacitors," Ceramic Bulletin, **64**, pp. 564-570 (1985).

T.R. Shrout and J. Fielding, Jr., "Relaxor Ferroelectric Materials," Proceedings of the 1990 IEEE Ultrasonics Symposium 711-720 (1990).

PREPARATION AND CHARACTERIZATION OF BARIUM TITANATE ELECTROLYTIC CAPACITORS BY ANODIC OXIDATION OF POROUS TITANIUM BODIES

S. Venigalla, P. Bendale, R.E. Chodelka, J.H. Adair
Department of Materials Science and Engineering,
University of Florida, Gainesville, FL 32611
and
S.A. Costantino
Cabot Performance Materials,
Boyertown, PA 19512

ABSTRACT

Low temperature (50-60°C) anodic oxidation of porous titanium bodies in an aqueous electrolyte containing Ba^{2+} in solution has been employed to infiltrate $BaTiO_3$ onto a large surface area. Microstructural and dielectric characterization indicates the possibility of achieving extremely high capacitance values by further improving the porosity of the Ti bodies and electroding the $BaTiO_3$ surface using electroless plating techniques.

INTRODUCTION

Several recent reports have indicated that $BaTiO_3$ may be electrolytically deposited onto Ti metal substrates at temperatures as low as 55°C (1-6). The anodically deposited $BaTiO_3$ films usually have cracks and fissures as discussed by Basca et.al (6). However, $BaTiO_3$ films that are electrically insulating have been prepared in our laboratories by reducing the temperature and current at which the films are deposited (1,2). We have also controlled the oxidation potential of the electrolytic solution by purging the system with oxygen during the anodic deposition. By careful handling in air, we have also developed the capability to reduce the formation of $BaCO_3$ on the surface of the thin films.

The objective of the current paper is to report the preparation of the first generation of electrolytic $BaTiO_3$ capacitors based on anodic deposition techniques reported in several earlier papers for $BaTiO_3$ and using technology reported for electrolytic capacitors composed of more conventional materials, but lower dielectric constant such as γAl_2O_3 and Ta_2O_5 (1,2,7). The general processing steps and resulting dielectric properties of this first generation of electrolytic $BaTiO_3$ capacitors are presented followed by a discussion on how to improve dielectric performance in future generations. The $BaTiO_3$ electrolytic capacitors have the potential to serve as components in applications requiring high capacitance at relatively low working voltages of 1 to 2V.

MATERIALS AND METHODS

Preparation of Porous Titanium Bodies

Porous titanium pellets (12 mm diameter and 2 mm thick) having approximately 50% theoretical density were prepared from 99.4% pure, -100 mesh titanium powder (Johnson Matthey, Ward Hill, MA) employing an uniaxial hydraulic press. The green pellets were subsequently sintered at 1000°C in argon atmosphere for 4 hours to improve the mechanical strength while retaining most of the porosity. The sintered pellets were estimated to be of about 60% theoretical density.

The sintered titanium pellets were welded to a 0.5 mm dia. titanium wire to provide an electrical contact during further processing and fabrication.

Electrochemical Deposition of $BaTiO_3$

Figure 1 shows a schematic diagram of the electrochemical apparatus for the deposition of barium titanate by anodic oxidation of the porous titanium bodies. The theoretical background for the formation and phase stability of barium titanate under aqueous electrochemical conditions was described in detail elsewhere[2,8,9]. The deposition was performed for 24 hours under potentiostatic conditions (10-20V) at temperatures as low as 50-60°C. The electrolyte contained Ba^{2+} in 0.5M concentration as $Ba(CH_3COO)_2$ and NaOH in 2M concentration to provide highly alkaline conditions necessary for the formation of $BaTiO_3$. The solution was purged with high purity oxygen throughout the deposition period to promote the oxidation process.

The deposited samples were immediately washed in ammoniated water to avoid the formation of $BaCO_3$ on surface and subsequently dried in a vacuum desiccator. Samples 2 and 3 were heat treated at 180°C in vacuum to further eliminate the moisture and slowly cooled to room temperature.

Fabrication of the Capacitor

A schematic diagram of the capacitor is shown in Figure 2. The titanium wire welded to the porous titanium body serves as the internal electrode whereas an aluminum disc of equal diameter attached to the body with carbon paint serves as the external electrode. An aluminum wire soldered to the disc acts as the lead. The rest of the porous body is covered with carbon paint to achieve the maximum contact area of the external electrode. For Sample 3 only, electroless deposition of copper onto the surface of the porous body was carried out in an attempt to further increase the contact area by a possible infiltration of copper into the body.

CH3080-0-7803-0465-9/92$3.00 ©IEEE

Electroless deposition of Cu was carried out under highly alkaline conditions to avoid dissolution of barium titanate. The sample was washed in deionized water and then in ethanol before drying. After electroding, all capacitors were hermetically sealed in a hard polymer envelope and characterized for dielectric properties.

Characterization

Microstructural and dielectric characterization of the capacitors was performed in the Major Analytical Instrumentation Center (MAIC) at the University of Florida. X-ray diffractometry (XRD) (Philips APD3720, Cu-Kα, 40kV-20mA), and scanning electron microscopy (SEM) (Jeol JSM6400) were used to characterize the microstructural and compositional features. An LF impedence analyzer (HP 4192A) was employed to measure dielectric parameters such as resistance (Z), dissipation factor (d), and capacitance (C) at frequencies ranging from 5 Hz to 13 MHz, under series equivalent circuit mode.

RESULTS AND DISCUSSION

Constituent Phases:

As shown in Figure 3, the X-ray diffraction data for the electrochemically treated porous titanium pellet (Sample 1) confirms the formation of $BaTiO_3$ on titanium surface. However, the data also reveals the presence of substantial amount of $BaCO_3$, despite rigorous precautions taken during the deposition process to avoid its formation. Since the X-ray analysis is restricted to the outer surface of the pellet, it is at present believed that $BaCO_3$ might have precipitated from the electrolyte solution in contact with the pellet at the time of its removal from the reaction vessel. Future experiments will focus on modifying the washing procedures to facilitate the removal of $BaCO_3$ from surface.

Microstructure:

Scanning electron micrographs from different regions of the fracture surface of Sample 1 are shown in Figure 4. As indicated there, electrochemical infiltration of $BaTiO_3$ is limited to a few hundred micron depth into the porous Ti pellet, while the inner regions remain entirely free of deposition. This implies the insufficient porosity of the sintered Ti pellet to allow complete penetration of the electrolyte during the deposition process. Further experiments are being performed to achieve complete penetration of the electrolyte by improving the sintered porosity of the Ti bodies and also by applying vacuum during the initial stage of the deposition process. In the region close to the surface, the needle-like morphology of the deposition product indicates the presence of $BaCO_3$ on surface, which is also confirmed by the X-ray diffraction data.

Dielectric Properties:

The dielectric characterization data for various samples (after fabricated into capacitors as described earlier) is summarized in Table 1. The variation of capacitance and dissipation factor (tan δ) with applied frequency is graphically illustrated in Figures 5 and 6 respectively.

Capacitance values are in the range of 1-5 mF at low frequencies (upto 50 Hz) and 50-100 nF at higher frequencies (upto 1 MHz). The dissipation factor varied from about 15 at low frequencies to about 0.5 at higher frequencies. Very high capacitances at low frequencies associated with extremely large dissipation factors are likely from the presence of alkali ions and moisture in the treated samples. Heat-treatment at 180°C in the case of Samples 2 and 3 has resulted only in a slight decrease in tan δ. Further experiments are being performed to evaluate the feasibility of using alkali-free electrolytes in the deposition process. Use of high temperature heat-treatments (in the range of 500-600°C) may help remove the chemically adsorbed water.

Calculated volumetric efficiencies are in the range of 1000-5000 $\mu F.V/in^3$, taking the entire volume of the sample into account. These values, as such, fall between those corresponding to Ta_2O_5 electrolytic and conventional ceramic capacitors[7]. However, it is expected that the volumetric efficiency can be substantially higher if complete infiltration of $BaTiO_3$ is achieved.

External electroding by electroless plating of Cu (Sample 3) has resulted in a small increase in capacitance both at low and high frequencies.

Preliminary studies on the polarization characteristics of the samples indicated the paraelectric behavior with large leakage currents, confirming the necessity for high temperature heat treatments. Break down strength measurements on these samples are currently being performed.

REFERENCES

1. S. Venigalla, P. Bendale, E.D. Verink, Jr., J.R. Ambrose, and J.H. Adair, "Preparation of Barium Titanate Thin Films at Ultra-Low Temperatures," accepted for publication in Proceedings of the Materials Research Society, Volume 143, 1992.
2. P. Bendale, S. Venigalla, J.R. Ambrose, E.Verink, and J.H. Adair, "Preparation of Barium Titanate Films at 55°C by an Electrochemical Method," Manuscript Number 195586 P, Submitted to the Journal of American Ceramic Society.
3. M. Yoshimura, S.-E. Yoo, M. Hayashi, and N. Ishizawa, "Preparation of BaTiO3 Thin Film by Hydrothermal-Electrochemical Method," *Jpn. J. Appl. Phys.*, **28** [11] L2007-09 (1989).
4. N. Ishizawa, H. Banno, M. Hayashi, S.-E. Yoo, and M. Yoshimura, "Preparation of BaTiO3 and SrTiO3 Polycrystalline Thin Films on Flexible Polymer Film Substrate by Hydrothermal Method," *Jpn. J. Appl. Phys.*, **29** [11] 2467-72 (1990).
5. K. Kajiyoshi, N. Ishizawa, and M. Yoshimura, "Preparation of Tetragonal Barium Titanate Thin Film on Metal Substrate by Hydrothermal Method," *J. Am. Ceram. Soc.*, **74** [2] 369-74 (1991).
6. R. Basca, P. Ravindranathan, and J.P. Dougherty, "Electrochemical, Hydrothermal, and Electrochemical-Hydrothermal Synthesis of Barium Titanate Thin Films on Titanium Substrates," J. Mater. Res., 7[2] 423-428 (1992).
7. E.L. Hierholzer, H.B. Drexler, H.T. Cates, J.F. Rhodes, and S.D. Das, "Capacitors," Chapter 8 in Handbook of Components for Electronics, C.A. Harper (ed.), McGraw-Hill Book Co., New York, NY, 1977, pp.8-1 - 8-155.

8. A.R. Prusi and Lj.D. Arsov, "The Growth Kinetics and Optical Properties of Films Formed Under Open Circuit Conditions on a Titanium Surface in Potassium Hydroxide Solutions," *Corros. Sci.*, **33** [1] 153-164 (1992).
9. J.H. Adair, B.L. Utech, K. Osseo-Asare, and J.P. Dougherty, "Solubility and Phase Stability of Barium Titanate in Aqueous Suspension," presented at the Fifth US-Japan Seminar on Dielectric and Piezo Electric Ceramics, held in Kyoto, Japan, December 11-14, 1990.

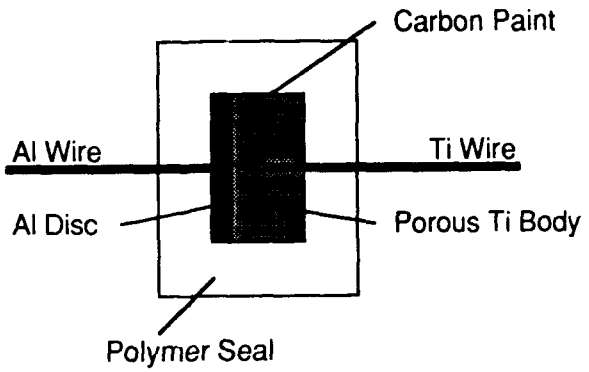


Figure 2. Schematic diagram illustrating the fabrication of porous $BaTiO_3$ electrolytic capacitor.

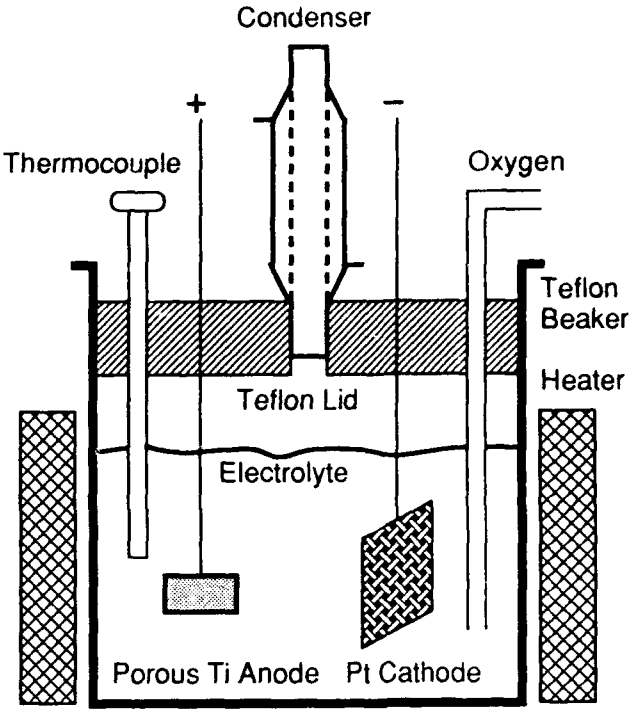


Figure 1. Electrochemical apparatus for the low-temperature deposition of $BaTiO_3$ on titanium.

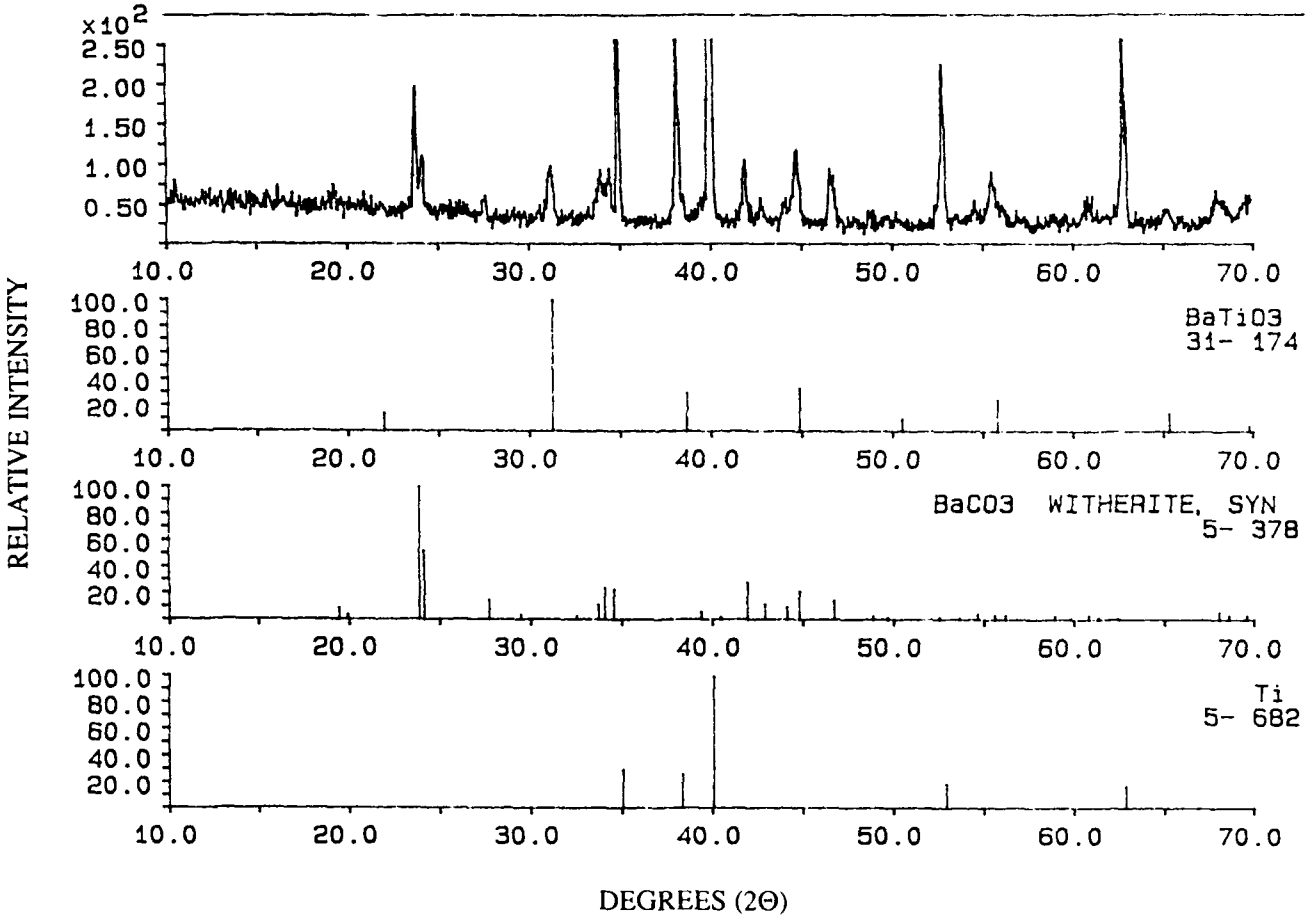


Figure 3. X-ray diffraction analysis data for Sample 1 after elctrochemical deposition, shown with standard JCPDS reference patterns for $BaTiO_3$, $BaCO_3$, and Ti.

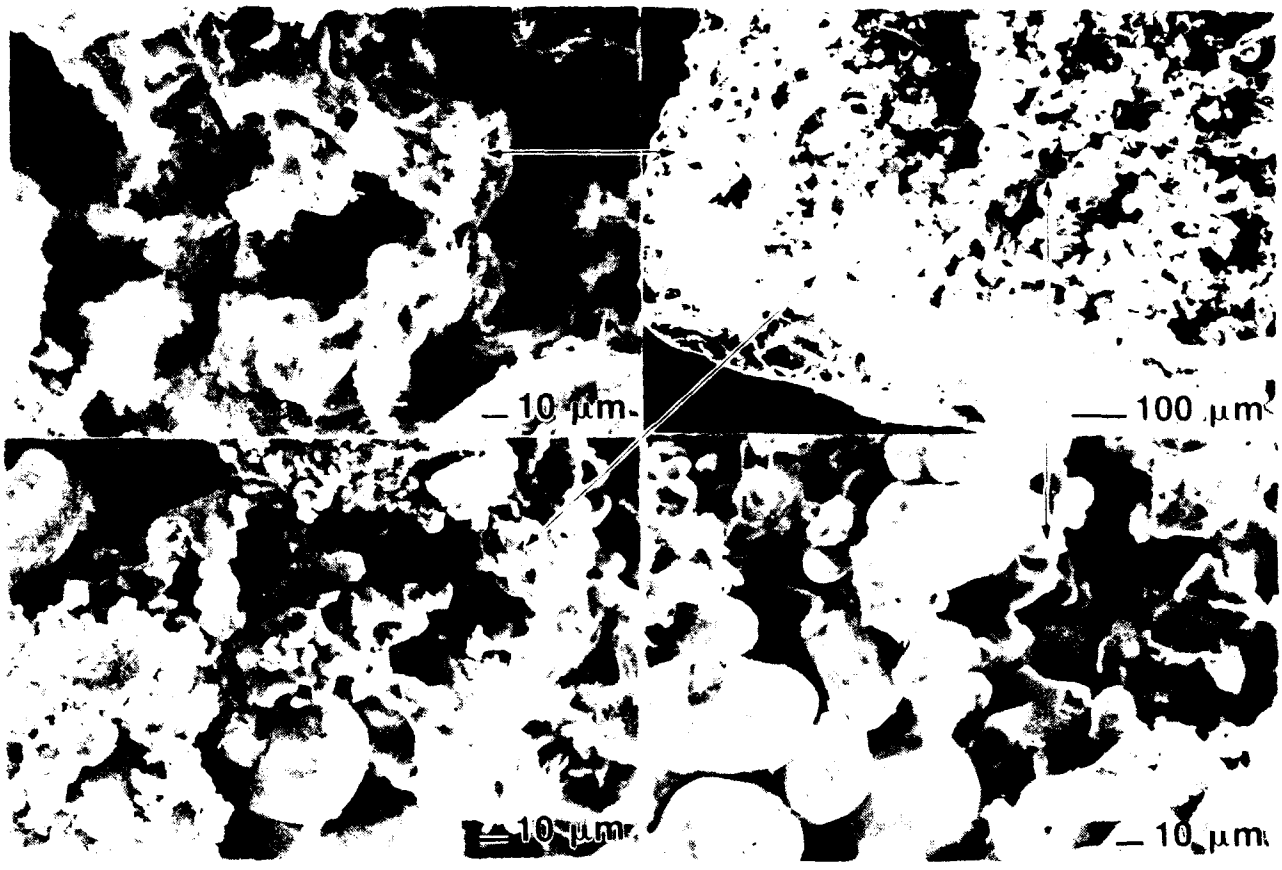


Figure 3 Secondary electron images obtained from the SEM analysis of the fracture surface of Sample 1 after electrophoretic deposition, showing only a partial infiltration of $BaTiO_3$ into the pellet.

Table 3 Dielectric characterization data

Sample 1				Sample 2				Sample 3			
f	Z	d	C	f	Z	d	C	f	Z	d	C
5 Hz			5.1mF	5 Hz	565 Ω		2.0mF	5 Hz	194 Ω		5.4mF
10			2.0	10	549		0.9	10	195		2.2
25			0.8	25	377		0.5	25	193	16	0.6
50			0.3	50	380	16	0.2	50	170	14	0.3
75			0.1	75	381	12	0.1	75	168	11	0.2
100			69 nF	100	381	10	41 nF	100	167	9	95 nF
250			12	250	373	5	8.0	250	165	7	66
500			3.5	500	339	3	2.8	500	143	4	26
1kHz	83 Ω	2.3	1.3	1kHz	279	1.9	1.3	1kHz	139	3	5.0
10			0.3	10	107	0.9	0.2	10	88	1	0.3
50			60 nF	50	43	0.8	96 nF	50	44	0.8	98 nF
100			29	100	29	0.8	72	100	26	0.8	72
1MHz	27	0.9	6.1	1MHz	7	0.9	30	1MHz	7	0.9	32
5			3.7	5	2	4.0	58	5	3	6.1	92
10	5	3.3	1.7	10	4	0.4	3.9	10	4	0.5	4.6
13			0.3	13	6	0.2	2.1	13	6	0.3	2.4

f = Frequency, Z = Impedance, d = Dissipation Factor (tan δ), C = Capacitance

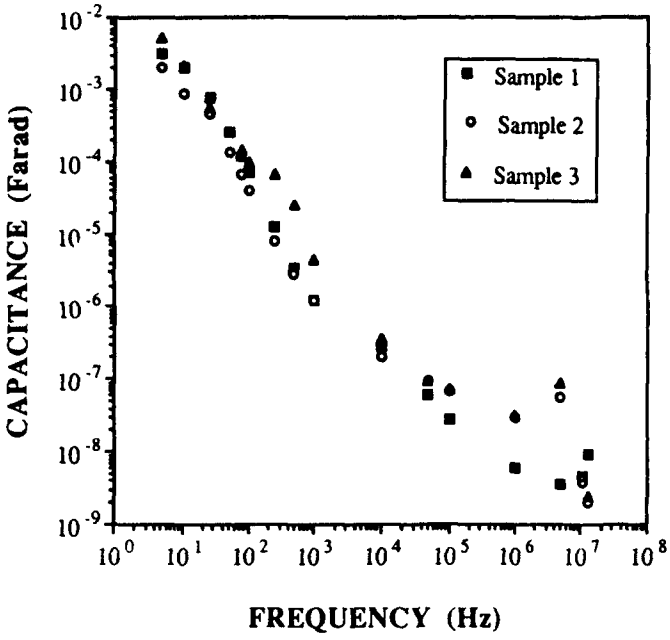


Figure 5. Variation of capacitance with frequency.

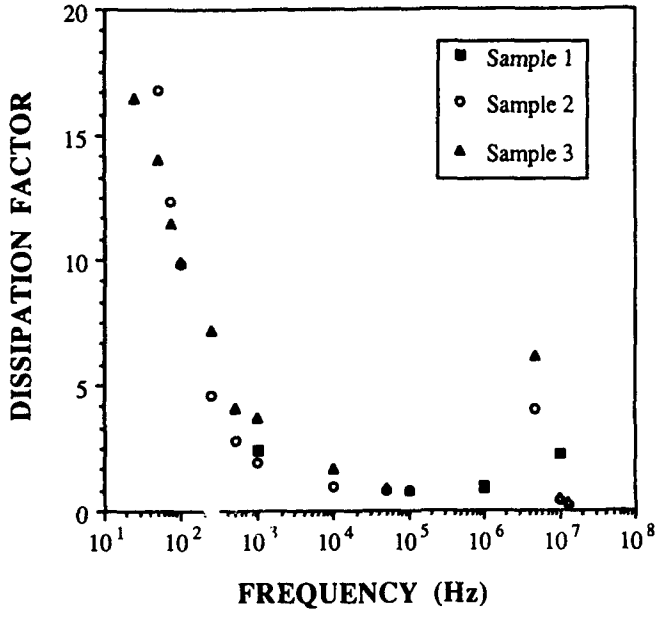


Figure 6. Variation of dissipation factor (tan δ) with frequency.

SYNTHESIS OF FERROELECTRIC $Pb_{1-x}Ca_xTiO_3$ SINGLE CRYSTALS

Noboru Ichinose and Tomonori Komachi
School of Science and Engineering
Waseda University
3-4-1 Ohkubo, Shinjuku-ku, Tokyo 169 Japan

Ferroelectric single crystals in the $Pb_{1-x}Ca_xTiO_3$ system have been successfully grown by using PbO flux method. Maximum volume of crystals is a function of the Ca concentration and decreases with increase of x from about $60mm^3$ at x=0 to $0.05mm^3$ at x=0.3. Lattice constants of a and c axes are decreasing with increase of x. Curie points are also linearly decreasing from 487℃ at x=0 to 478℃ at x=0.1, depending on the Ca concentration.

Introduction

It is well known that lead titanate ($PbTiO_3$) is a very useful piezoelectric material because of its high Curie temperature (Tc=490℃) and low dielectric constant (~200). However, pure lead titanate ceramic is very difficult to sinter because of its large tetragonality (c/a=1.064). On cooling the strong anisotropy of ceramic material creates many internal stresses at the cubic-tetragonal transition and, as a consequence, the ceramic becomes fragile. However, dense modified $PbTiO_3$ ceramic bodies were obtained by the addition of small amount of additives such as Nb_2O_5.[1] Furthermore, large piezoelectric anisotropy has been reported in ceramics modified with Ca or Sm.[2,3] Especially, concerned with the piezoelectric properties, Kp is very low (1.1%) at a Ca concentration of 24mol% in the $(Pb_{1-x},Ca_x)[(Co_{1/2}W_{1/2})_{0.04}Ti_{0.96}]O_3$ system. Anisotropy in the coupling constant leads this material to wide applications, such as ultrasonic devices, medical electronic devices and a variety of sensors. However, the physical reason for this large piezoelectric anisotropy has been remained unclear.

Here, we have attempted to grow the ferroelectric single crystals in the $Pb_{1-x}Ca_xTiO_3$ ($0.30 \geq x \geq 0$) system in order to elucidate its origin.

Experimental

Crystal Growth Procedure

The crystals of pure $PbTiO_3$ were grown using various kinds of flux by many researchers.[4,5] These methods are useful for the growth of large polydomain crystals which are usually thick and opaque. Kobayashi[6] reported the growth of single crystals of $PbTiO_3$ using the well known Remeika[7] technique. He used a mixture of $PbTiO_3$, KF and PbO. Even in this method it has been found that the crystals are heavily twinned are not suitable for studying domains.

We have applied the PbO method to the case of the $Pb_{1-x}Ca_xTiO_3$ in order to prepare crystals suitable for several measurements. Figure 1 shows the flow chart of manufacturing process. The molar ratio of the starting materials, $Pb_{1-x}Ca_xTiO_3$ ($x = 0 \sim 0.3$) and PbO is 1:4 (for example, in the case of x 0.20, 10.429g of $PbTiO_3$, 1.170g of $CaTiO_3$ and 38.4g of PbO). A mixture of $PbTiO_3$, $CaTiO_3$ and PbO powder is placed in a platinum crucible (volume 75ml).

Furnace arrangement for growth of $Pb_{1-x}Ca_xTiO_3$ single crystals is shown in Fig.2. In the case of x=0, the eutectic point of the mixture is about 850℃, which was determined by a thermal differential method. However, as the melting point of $CaTiO_3$ (1915℃) is higher than that of $PbTiO_3$ (1285℃), the holding temperature for the $Pb_{1-x}Ca_xTiO_3$ system is higher depending on the Ca concentration. Tentative phase diagram is shown in Fig.4. The holding temperature is chosen from 1000 to 1200℃ as shown in Fig.3, depending on the Ca concentration. In this figure, a slower cooling rate between 600 and 400℃ is necessary for preventing crystals from thermal stress at the Curie point of about 490℃.

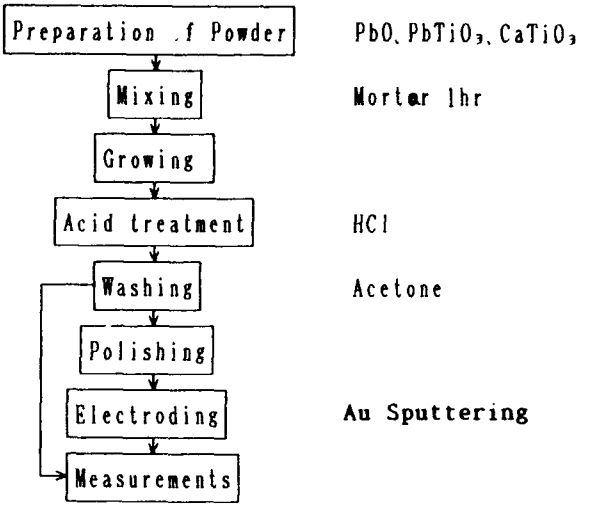
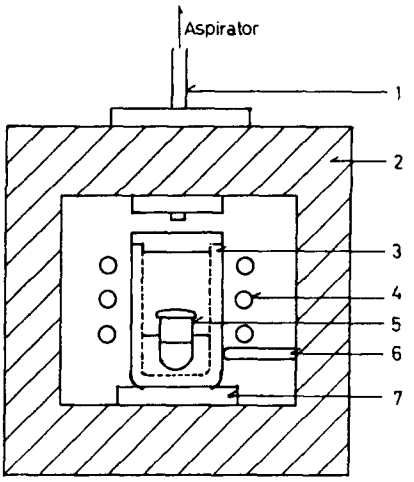


Fig.1 Flow chart of manufacturing process



1 Al_2O_3 tube
2 Firebrick
3 Al_2O_3 crucible
4 SiC heater
5 Pt crucible
6 Thermocouple
7 Firebrick

Fig.2 Furnace arrangement for growth of $Pb_{1-x}Ca_xTiO_3$ single crystals

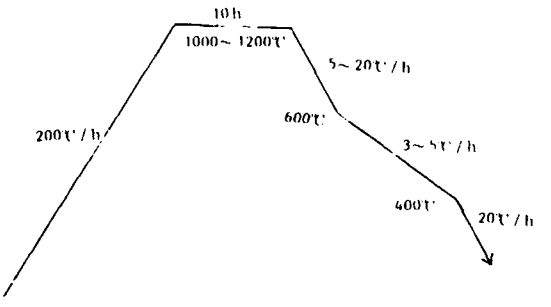


Fig.3 Heat diagram for $Pb_{1-x}Ca_xTiO_3$ single crystal growth

CH3080-0-7803-0465-9/92$3.00 ©IEEE

Measurements

Domains were determined by the intercept method in scanning electron microscope (SEM) photographs. The final products were examined by X-ray diffraction using CuK_α radiation. The compositions of crystals were decided by Energy Dispersive X-ray (EDX) analysis and Inductive Coupled Plasma (ICP) method. Relative dielectric constants were measured by LCR meter (YHP-4194A) at 1kHz.

Results and Discussion

Grown crystal

Figure 5 represents maximum volume of grown crystals as a function of the Ca concentration x. In the case of x=0, reddish single crystals are found in the product with size of about 5.8×5.7×1.8mm. They are almost polydomain crystals. The volume of grown crystals is exponentially decreasing with increase of x in the $Pb_{1-x}Ca_xTiO_3$ system as shown in Fig.4. The crystal size for x=0.3 is 0.39×0.37×0.31mm. It shows metallic grey-silver in color.

These crystals etched by HCl show domain structure. In the case of x=0.10, maximum width is about 21μm and minimum one is about 3μm. It is found that the domain are almost 180° domain. This domain may be due to no strain because of slow cooling between 600℃ and 400℃.

Energy dispersive X-ray analysis shows the 3 peaks corresponding to Pb, Ti and Ca in Ca modified $PbTiO_3$ crystals as shown in Fig.6. Figure 7 shows the actual composition of Ca versus nominal composition of Ca in the $Pb_{1-x}Ca_xTiO_3$ single crystals. It is found in Fig.6 that coincidence is fairly good at above X=0.15.

The X-ray diffraction techniques have shown that these crystals are single ones having tetragonal lattice c=4.152Å and a=3.903Å for x=0, and c=4.115Å and a=3.885Å for x=0.25, respectively. Figure 8, 9 and 10 represent X-ray diffraction patterns for x=0, x=0.1 and x=0.2 in the $Pb_{1-x}Ca_xTiO_3$ system, respectively. In these figures, powders are crushed using single crystals. In the case of x=0, the powder is including the impurity of PbO which is coming from the flux. Lattice parameters for these crystals are shown in Fig.8.

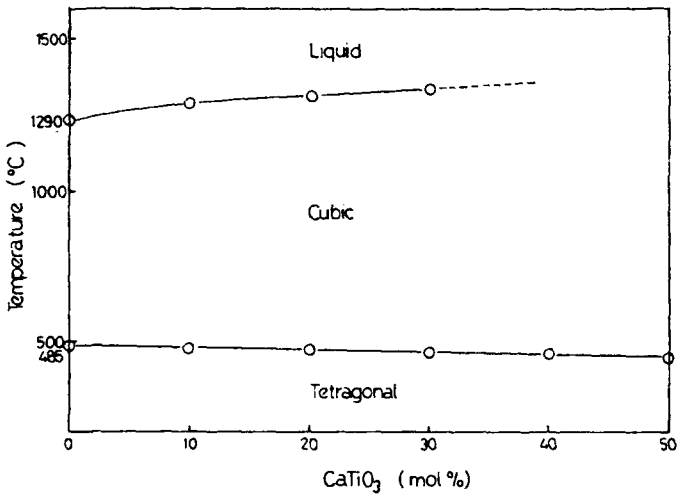


Fig.4 Phase diagram of $PbTiO_3$-$CaTiO_3$ system

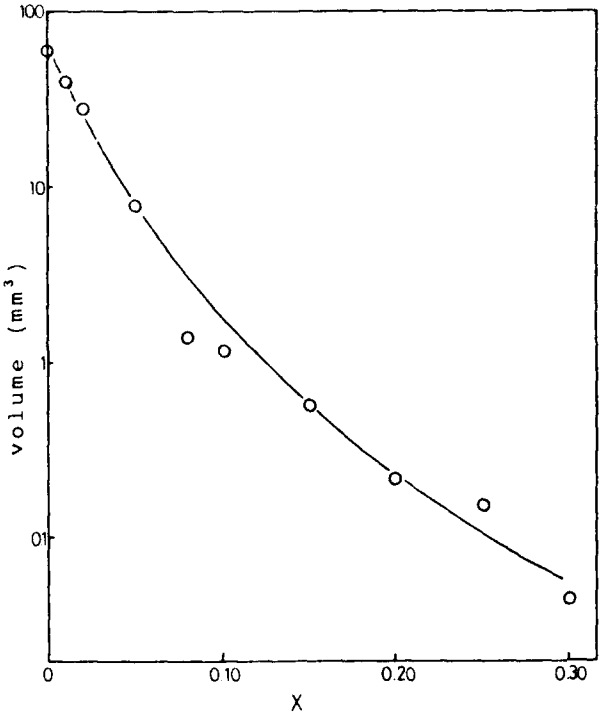


Fig.5 Maximum volume of crystals as a function of the Ca concentration X

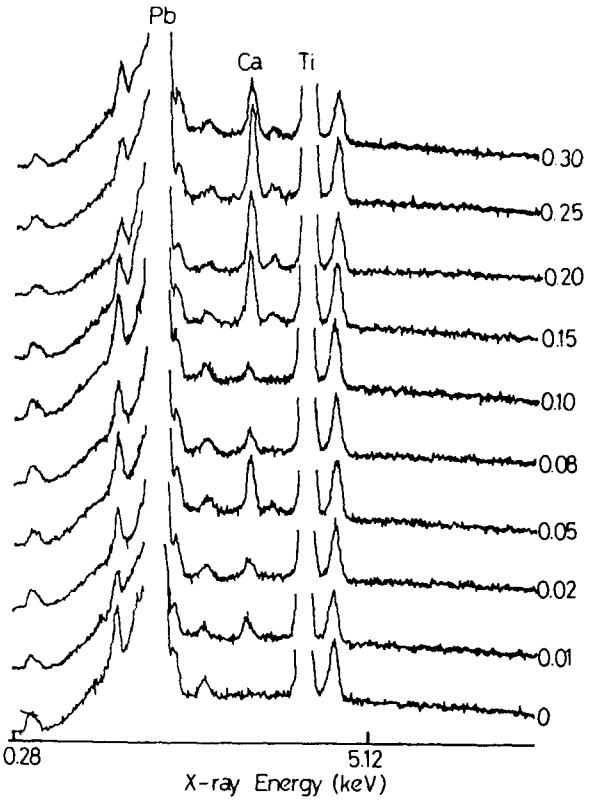


Fig.6 Energy Dispersive X-ray diffraction patterns of $Pb_{1-x}Ca_xTiO_3$ single crystal

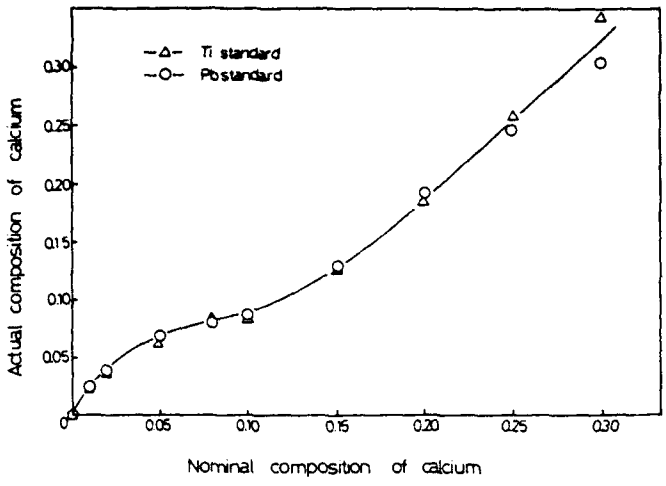


Fig.7 Quantative analysis of calcium in $Pb_{1-x}Ca_xTiO_3$ single crystal

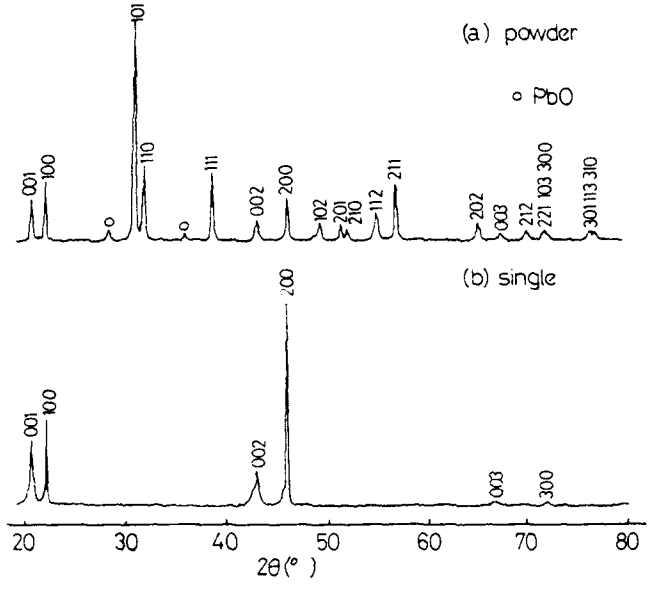


Fig.8 X-ray diffraction pattern of $PbTiO_3$

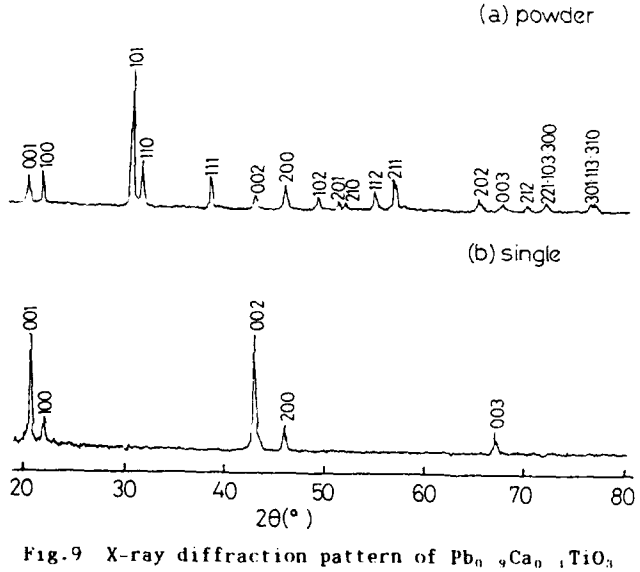


Fig.9 X-ray diffraction pattern of $Pb_{0.9}Ca_{0.1}TiO_3$

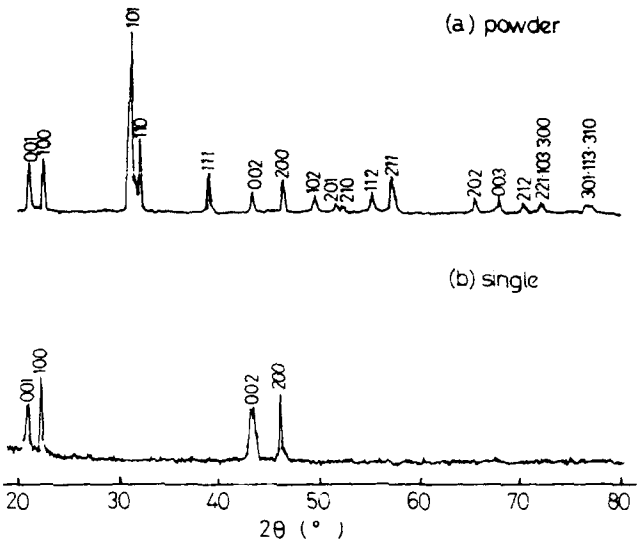


Fig.10 X-ray diffraction pattern of $Pb_{0.8}Ca_{0.2}TiO_3$

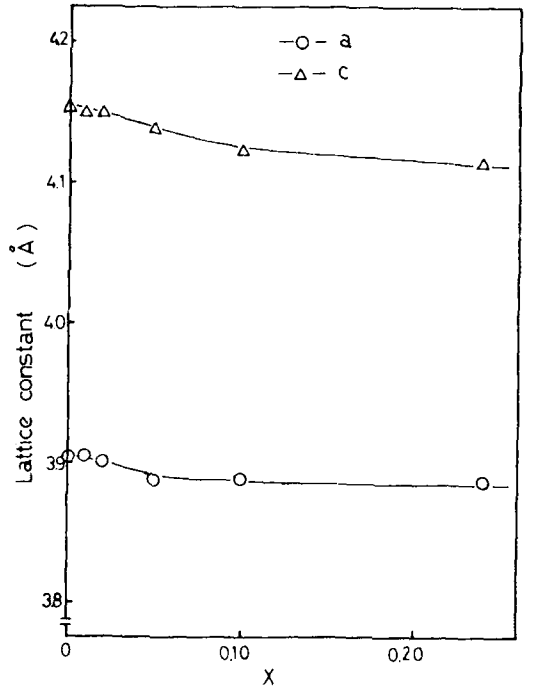


Fig.11 Lattice constant as a function of the Ca concentration X

Ferroelectric properties

Figure 12 and 13 show the variation of permittivity as a function of temperature at 1kHz for x=0 and x=0.10, respectively. It is seen that at room temperature the dielectric constant is of the order of 30. It rises very steeply to a maximum of 1×10^4 in the neighbourhood of Curie point Tc. It is found in Fig.14 that Curie points are linearly decreasing from 487℃ at x=0 to 478℃ at x=0.1, depending on the Ca concentration. Maximum permittivity is also decreasing in the following; 1.44×10^4 for x=0, 1.21×10^4 for x=0.01 and 0.87×10^4 for x=0.05.

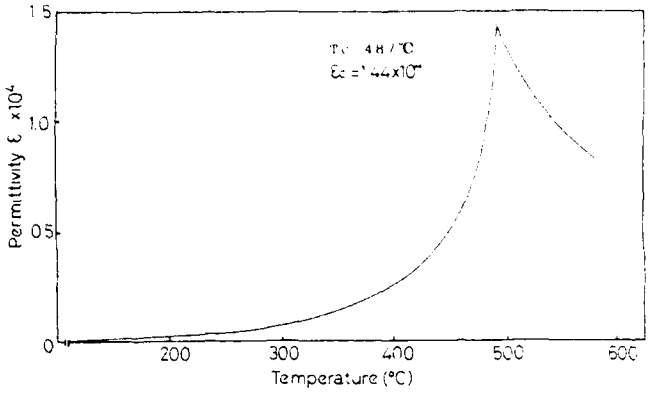


Fig.12 Permittivity of $PbTiO_3$ as a function of temperature

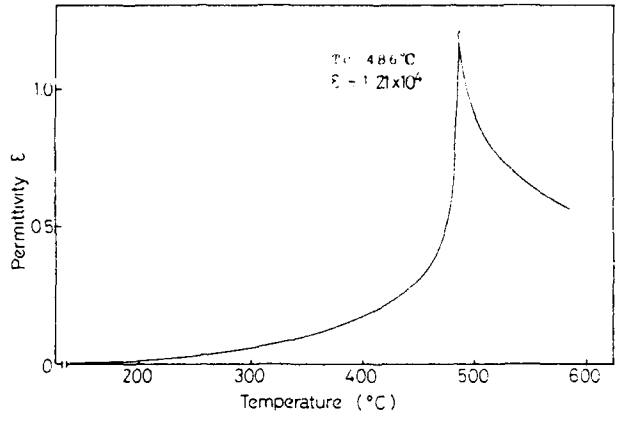


Fig.13 Permittivity of $Pb_{0.99}Ca_{0.01}TiO_3$ as a function of temperature

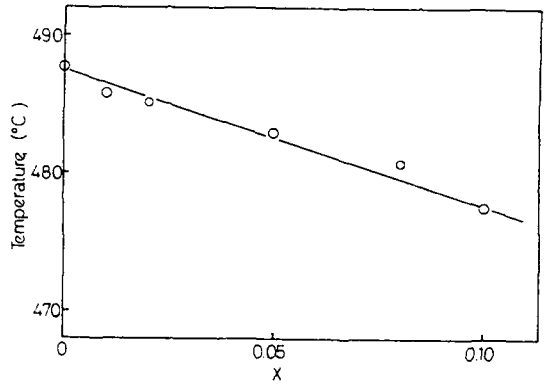


Fig.14 Curie Point Tc as a function of the Ca concentration X

Conclusions

In conclusion, we have successfully grown the ferroelectric single crystals in the $Pb_{1-x}Ca_xTiO_3$ system. However, at higher concentration of Ca, the crystal size is very small for dielectric and piezoelectric measurements. So, we are aming to prepare higher quality crystals with large size by using another flux.

References

[1] S.Ikegami, I.Ueda and T.Nagata, "Electromechanical properties of $PbTiO_3$ ceramics containing La and Mn," J. Acoust.Soc.Am.50, 4 (part 1) p1060 1066, 1971

[2] Y.Yamashita, K.Yokoyama, H.Honda and T.Takahashi, "(Pb,Ca)[(Co, W,)Ti]O, Piezoelectric Ceramics and Their Applications," Proceedings of the 3rd Meeting on Ferroelectric and Their Application, 20, Suppl.20~4, pp.183~187, 1981

[3] H.Takeuchi, S.Jyomura, E.Yamamoto and Y.Ito, "Electromechanical properties of (Pb,Ln)(Ti,Mn)O, ceramics (Ln=rare earths)," J. Acoust. Soc. Am., vol.72, pp. 1114-1120, 1982

[4] E. G. Fesenko, O. P. Kramarov, A. L. Khodakov and M. I. Sholokhovich, "Properties of Single Crystals of Lead Titanate and Single Crystals of Solid Solutions $(Ba,Pb)TiO_3$," Izv. Akad., Nauk SSSR, Ser, Fiz. 21, 305 10, 1957

[5] V. G. Bhide, K. G. Deshmakh and M. S. Hegde, "Ferroelectric Properties of Lead Titanate," Physica. 28, 871-76, 1962

[6] J.Kobayashi,"Growing Ferroelectric $PbTiO_3$ Crystals," J. Appl. Phys., 29 [5] 866-67, 1958

[7] J. P. Remeika, "Method for Growing Barium Titanate Single Crystals," J. Am. Chem. Soc.,76 [3] 940 41, 1954

EFFECT OF GRAIN SIZE ON THE GRAIN BOUNDARY RESISTANCE OF UNDOPED BARIUM TITANATE CERAMICS

Hee Young Lee* and Larry C. Burton*

*Dept. of Materials Science and Engineering, Yeungnam University, Kyongsan, 712-749, Korea.

*Dept. of Electrical and Computer Engineering, The Pennsylvania State University, University Park, PA 16802, U.S.A.

Abstract

Effect of grain size on the grain boundary resistance of undoped $BaTiO_3$ ceramics fired at 1270 ~ 1410℃ was investigated assuming cubic grains sharing their faces with adjacent grains. Two-step firing technique was used to produce samples of different grain sizes ranging from about 1 to over 40 μm. Grain boundary resistance values were estimated from the complex impedance plots of samples measured at about 455℃. It was found that the grain boundary resistivity is approximately constant and is in the range of $2.7 \times 10^{-3} \sim 2.8 \times 10^{-2}$ Ω·m², if the average grain size is larger than 1 μm. It was also found that the grain resistivity is in the range of 37 ~ 180 Ω·m at 455℃, when the grain is partially depleted of mobile charge. When the grain was smaller than about 1 μm, the grain was totally depleted of mobile charge, and as a result, the grain boundary would control the overall resistance. In such case, grain boundary layer extended to the center of the grain, and the situation might be viewed as the disappearance of the grain. Thus, there would be single semicircle in the complex impedance plot. Such a case was observed in this study, indicating the feasibility of the grain boundary model we had proposed.

1. INTRODUCTION

Many electronic conductors can be viewed as grain boundary-controlled devices, in that their electrical characteristics are largely influenced by the presence of grain boundaries. Examples include PTC thermistors, varistors, and grain boundary barrier layer capacitors. Electrical properties of these materials may not be provided by other classes of materials, and consequently they found wide and unique applications in electronic components, including self-regulated heater, degausser, surge arrester, line conditioner, etc. For this reason, semiconducting ceramics have been investigated by numerous researchers and the role of grain boundaries in dc resistivity is well understood. [1,2] Many quantitative models which are in good agreement with measured data have been proposed. However, the role of grain boundaries of high resistivity ceramics in electrical resistance and capacitance is not still clear.

Recently, it has been reported that certain high K capacitors based on $BaTiO_3$ show relatively fast degradation rate. [3] Although degradation due to defects from non-optimized processing can be improved by the ever-improving manufacturing technologies, intrinsic degradation resulting from the inherent physical and chemical properties of materials cannot be avoided unless the careful selection of chemical composition and processing technique is made. Intrinsic degradation behavior of various MLC capacitors were studied in detail by Burton et al. [3] According to them, generic intrinsic degradation curve can be schematically represented as the one in Figure 1. As seen in the figure, there are three distinct regions, of which the second is the most important. In that region, the exponential increase of leakage current with time occurs. Two possible models to explain this observed behavior have been proposed, and one of them is related to the gradual decrease of grain boundary barrier height due to cation migration toward the grain boundary. Therefore, it is quite appropriate to try to understand the degradation behavior in terms of grain boundary resistance. As a rough but initial approach of a series of systematic research, the grain boundary resistivity of undoped $BaTiO_3$ ceramics with different grain sizes is being presented in this paper.

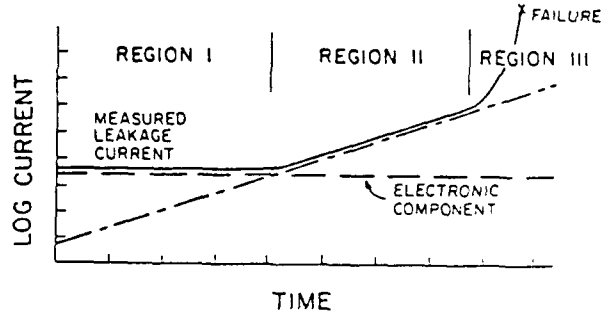


Figure 1. Generic plot of leakage current versus time for intrinsic degradation mechanisms. [3]

2. GRAIN BOUNDARY RESISTANCE IN HIGH K CERAMIC

The origin of grain boundary resistance to charge transfer is the potential barrier present along the boundary. The potential barrier is developed by the

CH3080-0-7803-0465-9/92$3.00 ©IEEE

majority charge carriers trapped at the grain boundary states and by the compensating opposite space charge distributed toward the inside of the grain. For n-type electronic conductors, these are electrons and positive space charge. Additional charge can arise from electrons trapped while traversing the grain boundary under voltage bias, from a discontinuity in the normal component of polarization, and trapped ions at the grain boundary. The latter two sources of charge can be compensating as well, reducing the net charge at the grain boundary. If the material is in the non-ferroelectric state, grain boundary resistance can be modelled simply in terms of the formation of double Schottky barrier at the grain boundary. The assumptions for the model included homogeneous grain and grain boundary, no polarization discontinuity at the grain boundary, and no second phases along the boundary. For n-type materials, grain boundary potential under thermal equlibrium without voltage bias is expressed as

$$\Phi_o = \frac{q^2 N_D W^2}{2 K \varepsilon_o} = \frac{q^2 N_{GB}^2}{8 K \varepsilon_o N_D} \qquad (1)$$

where N_D is the donor impurity concentration in the grain, N_{GB} the occupied grain boundary state concentration by electrons, W the half-width of space charge layer, and K the relative dielectric constant.

Assuming the composition of samples is constant and the firing condition does not change donor impurity concentrations, grain size dependence of equilibrium potential barrier can be sketched as Figure 2. [4] Although the graph was drawn for values of parameters assumed in the figure, the same shape will be obtained with different threshold grain size and saturated potential barrier height. Below the threshold value, grains are totally depleted of mobile charge, and the potential barrier increases in proportion to the square of the grain size. At the threshold, total number of charge carriers is exactly equal to the number of grain boundary states. Moreover, according to the model, the grain boundary barrier saturates so that the resistance of the grain boundary per unit area should be the same. Under small voltage bias, electrons in the conduction band move to the next grain by thermal activation, so that the resistance of single grain boundary may be expressed as follows.

$$R_{gb} = R_o \exp(\Phi_o / k T) \qquad (2)$$

where R_o is the constant related to the resistance of the grain.

If we further assume all the grains are of cube having the same sizes and sharing their faces with adjacent grains, the grain boundary resistance per unit grain boundary area may be expressed by the following equation.

$$\rho_{gb} = R_{GB} (A d / t) \qquad (3)$$

where R_{GB} is the total grain boundary resistance, A the area of electrode, t the thickness of a sample, and d the average grain size.

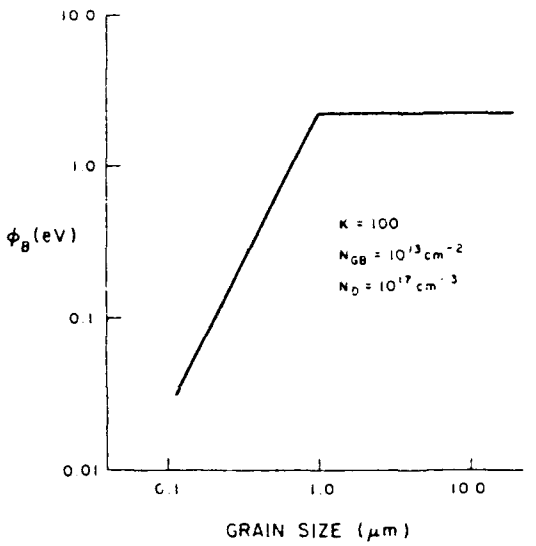


Figure 2. Dependence of calculated barrier height on grain size under suitable assumptions (values of parameters indicated). [4]

3. EXPERIMENTAL PROCEDURE

$BaTiO_3$ powder used in this study was the highest purity commercial powder with cation sublattice A/B ratio of 1.000.* In order to control the microstructure of otherwise undoped $BaTiO_3$ ceramics, powder compacts in disc shape were fired at 1270°C for 30 minutes using a fast heating rate of 10°C/min. This yielded sintered ceramics with about 87% theoretical density and less than 1 μm grain sizes. 2 mol% barium nitrate was added to stoichiometric barium titanate to avoid discontinuous grain growth during the primary firing process. Secondary firing was performed in the temperature range 1310°C ~ 1410°C for 30 minutes in order for uniform grain growth to occur.

Analysis of complex impedance can be used to obtain valuable information about grain boundary resistance in polycrystalline materials. [5] Impedance measurements were made for disc samples with a Hewlett-Packard 4192A Impedance Analyzer. Typically resistance and reactance values are measured across a frequency range usually up to 1 MHz, in order to minimize an error from lead inductance. Two probe dc resistance was measured with Keithley 617 Electrometer during impedance measurement, while 4 probe dc resistivity was measured for bar-shaped samples cut from discs of the same lot. This was necessary to identify grain, grain boundary, and contact contributions to the total impedance.

Sample temperatures were maintained at values in the 350°C to 600°C range. This is because the resistance

* TICON HPB powder, TAM Ceramics, Inc.

limit of the bridge is only about 1.3 MΩ, and elevated temperatures are required to bring sample resistances below this value. This is somewhat objectionable, since our ultimate goal is to learn more about capacitor ceramics near room temperature. However, we may still gain some useful information, since the role of grain boundary may actually be enhanced at elevated temperatures due to the decrease in dielectric constant.

4. RESULTS AND DISCUSSION

Apparent densities and average grain sizes of sintered ceramics were determined. Results showed 87 ~ 95 % density increasing with secondary firing temperature, and increasing grain sizes with temperature as well. Average grain sizes determined by the line intercept method are summarized in Table 1.

Table 1. Average grain diameters of undoped $BaTiO_3$ ceramics calcined and fired at various temperatures (Ba/Ti ratio = 1.02).

Firing Temperature (℃)	Calcining Temperature (℃)	Average Grain Diameter (μm)
1270	1100	1.0
1270	1200	3.4
1310	1100	8.2
1330	1100	12
1365	1100	13
1390	1100	20
1410	1100	25
1400	1200	40

Complex impedance plots for undoped $BaTiO_3$ ceramics with different grain sizes are illustrated in Figure 3. As seen in the figures, single semicircle appears when the average grain size is smaller than 1 μm, while two clearly discernible semicircles do when the average grain size is larger than 1 μm. This result is consistent with the previously reported result by Lee et al. [6], and can be explained by the following.

When the grain size is smaller than some critical value, the grain will lose all of its electrons to the grain boundary states, and the electrical resistivity of the grain will be increased since charge carrier concentration in the grain vanishes. In this case modified grain boundary layer extends to the center of the grain, and the difference between grain and grain boundary no longer exists. In fact, we may view the situation as the disappearance of the grain. This concept is supported by the fact that the single relaxation in 1 μm sample in Figure 3 occurs at about the same frequency for the grain boundary relaxation in the samples of larger grain sizes (Figure 4).

On the other hand, as grain size increases, total number of mobile charge carriers present in the grains

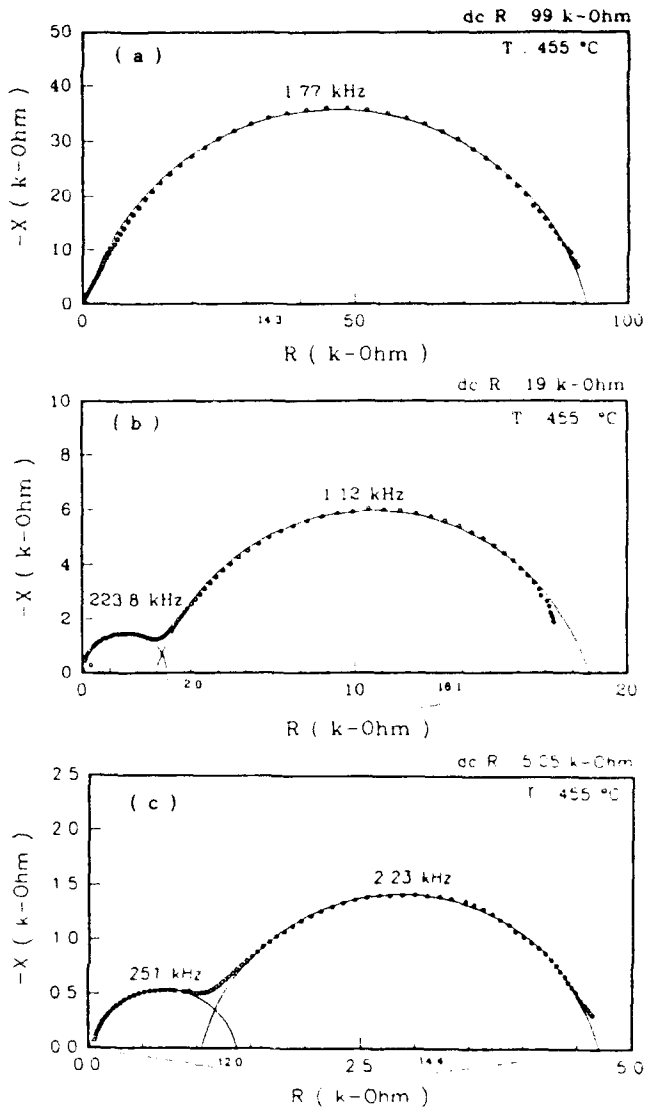


Figure 3. Complex impedance diagrams of undoped $BaTiO_3$ ceramics with various average grain sizes at 455℃ : (a) 1.0 μm, (b) 8.2 μm, and (c) 20 μm.

begins to exceed total number of grain boundary states, i.e. the grain will be partially depleted of mobile charge. Therefore, the resistance of the grain will become smaller than that of the grain boundary due to the presence of free carriers. At the same time, the resistance of unit area of the grain boundary is expected to stay at about the same values according to Figure 2 and equation (2).

For undoped $BaTiO_3$ ceramics, partial depletion may occur for the ceramic of grain sizes larger than 1 μm at 450℃. Two semicircles observed for ceramics with grain sizes larger than 1 μm should be assigned to grain and grain boundary contributions, with the high frequency arc being assigned to grain contribution. Contact resistance is negligibly small for high resistivity ceramics as verified by four point probe dc resistivity measurements.

In general, the threshold grain diameter for partial

depletion may change since the charge carrier concentration can be a strong function of temperature, whereas the grain boundary state density is not. This statement can even be applied to ceramics of the same compositions. If the composition is allowed to change, the threshold value will, of course, vary as well.

In our experiments, threshold grain sizes for partial depletion do not seem to change in the temperature range of 400 ~ 550°C. Therefore, it may be reasonable to assume that the charge carrier concentration is about constant or changes little in this temperature range for undoped $BaTiO_3$ ceramics.

Incidentally, relaxation time constants, τ, for two different relaxation mechanisms are expected to vary exponentially with inverse temperature according to the following equation.

$$\tau = \tau_0 \exp (E_r / k T) \qquad (4)$$

where E_r is an activation energy for relaxation. This relationship is illustrated in Figure 4 for two typical cases. When the grain is totally depleted, only grain boundary relaxation mechanism is evident.

Since time constant is defined by the RC product, the above exponential dependence is almost contained in the exponential dependence of resistance. Capacitance values in the temperature range we have studied are given by the Curie-Weiss law, and not a strong function of temperature. Thus, the activation energy for electrical resistivity is expected to be about the same with activation energy for relaxation, especially if single relaxation mechanism exists. The important thing one can recognize immediately in the figure is that the activation energies for grain boundary and grain mechanisms are different with the former having a higher energy. The similar activation energies are observed in the inverse temperature dependence of logarithmic bulk resistivity measured by four-point probe dc technique shown in Figure 5. From the figure, it is evident that two linear regions appear for 20 μm ceramic which has partially depleted grains, i.e. mobile charge carriers in the grains. As expected by the grain boundary model we proposed, dc resistivity of samples with partial depletion is much lower than samples with total depletion. Especially at the lower temperature region below 440°C for 20 μm ceramic, the resistivity increases much more moderately with lower activation energy than 1 μm ceramic as temperature is lowered. It is interesting to note that the activation energy in this region is very close to that of the relaxation mechanism of grain, whereas the activation energy in high temperature region is about the same with that of the relaxation mechanism of grain boundary.

We have previously reported that the activation energy and the logarithm of resistivity are approximately linearly correlated for a class of commercial X7R capacitors. [7] The same trend seems to

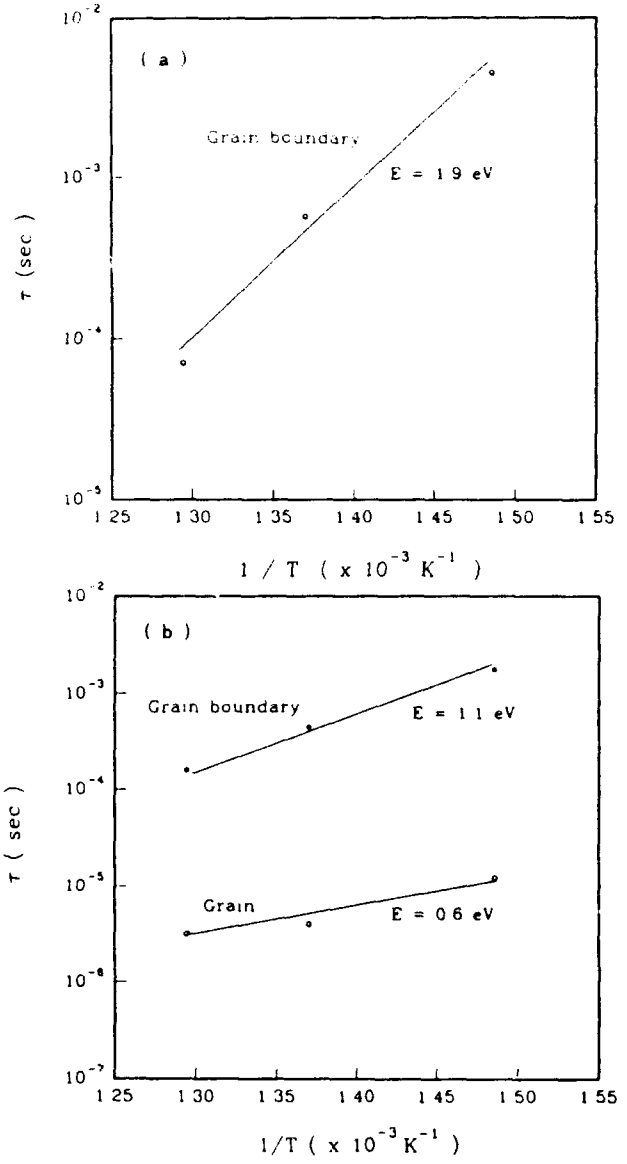


Figure 4. Logarithmic relaxation time versus inverse temperature for $BaTiO_3$ with average grain sizes of (a) 1 μm and (b) 20 μm.

be true for undoped $BaTiO_3$ ceramics whose electrical properties we are reporting in this communication. The only difference is that, even for samples with low resistivity such as 20 μm ceramic, at sufficiently high temperature the activation energy increases to that of high resistivity ceramic. We may assign the high activation energy in the range of 1.2 ~ 1.5 eV to the thermal activation energy required for grain boundary transmission. The low activation energy at temperatures below 440°C for 20 μm ceramic may be due to hopping potential in the grain. In this case, the charge carrier density may be constant as reported previously for a X7R material, and thus the activation energy is controlled by the mobility of carriers. The possibile intrinsic carrier generation above 440°C for 20 μm ceramic may be responsible for the increased activation energy.

According to the model described in section 2, the

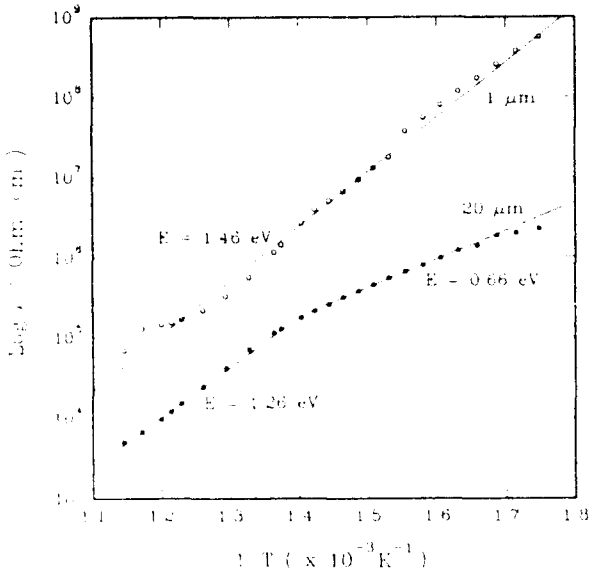


Figure 5. Four-point resistivity of undoped $BaTiO_3$ ceramics with different average grain sizes as a function of inverse temperature.

resistivity of unit area of grain boundary should be the same for all samples exhibiting partial depletion of mobile charge. In addition, if we assume the thickness of the grain boundary layer including space charge region is negligibly thin compared to the grain diameter, the resistivity of the grain should also be the same for materials with fixed compositions. The data calculated from equation (3) are tabulized below.

Table 2. Calculated resistivity of grain and grain boundary of undoped $BaTiO_3$ ceramics at 455°C.

Average Grain Diameter(μm)	ρ_g (Ω m)	ρ_{gb} (Ω m²)
1.0	-	5.7×10^{-3}
8.2	160	6.9×10^{-3}
12	37	3.1×10^{-3}
13	42	2.7×10^{-3}
20	63	3.7×10^{-3}
25	180	2.8×10^{-2}

Although the model we proposed is simple and based on several assumptions, one may find out the relatively good agreement between the model and the experimental data from this table.

5. SUMMARY AND CONCLUSIONS

For undoped $BaTiO_3$ ceramics with different average grain sizes, we can conclude the following.

When the average grain size was smaller than 1 μm, single semicircle appeared in the complex impedance plots in the temperature range 400 ~ 550°C, while two clearly discernible semicircles appeared when the average grain size was larger than 1 μm. Since threshold grain sizes for partial depletion do not seem to change in the above temperature range, it may be reasonable to assume that the charge carrier concentration is about constant or changes little in this temperature range.

From the analysis of relaxational time constants, the single semicircle observed for 1 μm sample was attributed to the grain boundary contribution. Two semicircles appeared for samples with grains larger than 1 μm were attributed to grain and grain boundary contributions. Contact resistance was negligibly small, which was confirmed by four-point dc resistivity measurement. Activation energies for grain boundary and grain mechanisms are different with the former having a higher energy. Thermal activation energy values obtained from the Arrhenius plot of four-point resistivity seemed to be related to those from time constants. Possible explanation for two linear regions resulting in two different activation energies for 20 μm sample was presented.

From the calculation under cubic grain assumption, It was found that the grain boundary resistivity was approximately constant and was in the range of $2.7 \times 10^{-3} \sim 2.8 \times 10^{-2}$ Ω m², and that the grain resistivity was in the range of 37 ~ 180 Ω·m at 455°C, if the average grain size was larger than 1 μm.

6. REFERENCES

[1] L. M. Levinson (ed.), "Grain Boundary Phenomena in Electronic Ceramics", *Advances in Ceramics*, Vol. 1, Am. Ceram. Soc. (1981).

[2] M. F. Yan and A. H. Heuer (eds.), "Character of Grain Boundaries", *Advances in Ceramics*, Vol. 6, Am. Ceram. Soc. (1983).

[3] L. C. Burton et al., "Intrinsic Mechanisms of Multilayer Ceramic Capacitor Failure", Annual Report, ONR Contract No. N00014-83-K-0168 (1986).

[4] H. Y. Lee, S. S. Villamil, and L. C. Burton, "Grain Boundary Impedance in Ferroelectric Ceramic", *Proceedings, 6th IEEE International Symposium on Applications of Ferroelectrics*, 361-366 (1986).

[5] J. E. Bauerle, "Study of Solid Electrolyte Polarization by a Complex Admittance Method", *J. Phys. Chem. Solids*, Vol. 30, 2657 (1969).

[6] H. Y. Lee, X. Qiu, and M. A. Watts, "Effect of Grain Size on the Electrical Properties of Capacitor Ceramics", presented at *the 91st Ann. Meet. of the Am. Ceram. Soc.*, Apr. 23 ~ 27, Indiannapolis, IN, U.S.A. (1989).

[7] L. C. Burton et al., "Intrinsic Mechanisms of Multilayer Ceramic Capacitor Failure", Annual Report, ONR Contract No. N00014-83-K-0168 (1984).

Grain Boundary Behaviors of Ferroelectric Ceramics above Curie Point

Kiyoshi Okazaki, Hiroshi Maiwa, M. Hagiwara and Suna Suginara
Department of Materials Science and Ceramic Technology
Shonan Institute of Technology,
1-1-25, Tsujido Nishikaigan, Fujisawa, 251, Japan

Instead of the famous Maxwell Wagner double layer theory for the anomalous dielectric absorption current, a new space charge model is proposed based on the experimental results of $BaTiO_3$ ceramics when an electric field is applied above the Curie point. This model can explain the very big charge more than 1000 $\mu C\ cm^{-2}$ stored during the charging by dc field application above the Curie point and the time dependence of discharging absorption current. When dc field is applied at room temperature to $(Sr,Ba)TiO_3$ ceramics with a Curie point of 50 °C, the behaviors corresponds to those of $BaTiO_3$ when a dc field is applied above the Curie point. The sample can have a giant space charge polarization. The apparent pyroelectric current was measured with discussion on the role of grain boundaries.

Keywords: space charge effect, high poling, ferroelectric ceramics, $BaTiO_3$, $(Sr,Ba)TiO_3$, anomalous absorption cerrent, pyroelectric current

1. Introduction

In 1960, Okazaki proposed two types of space charge models for $BaTiO_3$ ceramics in order to explain very complicated phenomena occuring when an electric field is applied at various temperatures below and above the Curie point.[1] One of the space charge effects is produced by electric field application above the Curie point (P_2 effect).[1][2][3] Other is generated during the aging process after normal poling (P_3 effect).[3][4][5] In this report, the P_2 effect of $(Sr,Ba)TiO_3$ ceramics with a Curie point below room temperature was examined and the role of grain boundaries such as a storage battery was discussed.

2. Experimental

Based on the anomalous dielectric absorption currents above the Curie point of $BaTiO_3$ (BT) ceramics[2], the effects of giant space charge of $(Sr,Ba)TiO_3$ (SBT) ceramic samples with a Curie point of 50 °C were measured. The phenomena of charging and discharging process of SBT above room temperature should correspond to those of BT above T_c. The treatment of poling at a temperature above T_c named as "high pole or high poling". High poled ferroelectric ceramics have a giant space charge polarization more than 1000 $\mu C\ cm^{-2}$. The pyro electric current of SBT was measured using a galvanomer with observation of the grain boundary using a SEM.

3. Results and Discussion

3. 1 Anomalous dielectric absorption currents of ferroelectric ceramics above Curie point

As is well known, when an electric field, V, is applied to R C series circuit, the charging and discharging current is expressed as

$$i_c = V \cdot R^{-1} \cdot \exp(-t \cdot RC) \quad i_d \qquad (1)$$

and the total stored charge, Q, by the flowing current should be

$$Q = f(C,V) \quad C \cdot V \ (C). \qquad (2)$$

However, when V is applied to $BaTiO_3$(BT) ceramics above the Curie point, T_c, the charging and discharging currents should not expressed by eq.(1). Namely, the logarithm of currnt, i_d, and the logarithm of discharging time, t_d, have a good linear relationship. This means that the phenomena cannot be explained by the well known Maxwell Wagner double layer theory. The anomalous dielectric absorption dielectric is experimentally expressed as

$$i_d = i_1 t^{-n}. \qquad (3)$$

where i_1 is the discharging current at t_d 1 min.

CH3080-0-7803-0465-9/92$3.00 ©IEEE

Table 1. Experimental ε values of $BaTiO_3$ ceramics above T_c and the total amount of stored space charge

$T_p=T_d$ (℃)	E_p (kV/cm)	t_p (s)	i_1 ($\times10^{-10}$ A/cm²)	ε	Q_d (μC/cm²)
130	2	100		0.946	
〃	8	〃		0.867	
〃	20	〃		0.837	
〃	〃	1000		0.635	
〃	〃	3000		0.562	
〃	〃	10000		0.468	
160	20	100	600	0.890	94
〃	〃	300	703	0.700	273
〃	〃	1000	712	0.562	898
〃	〃	3000	720	0.526	2685
190	2			0.923	
〃	6			0.732	
〃	20			0.678	

The i_d in BT ceramics above T_c is dependent on the field application temperature, T_p, the applied field, E_p, the field application time, t_p and the discharging temperature, T_d. Then, in the ferroelectric ceramics above T_c,

$$Q = f(C, V, E_p, T_p, t_p, T_d). \quad (4)$$

When only ε = 1, eq.(3) = eq(1). Table 1 illustrates the experimental ε values of BT ceramics above T_c and the total amount of stored spsce charge under various high poling conditions. For example, when E_p = 2 kV/mm, T_p = 130 ℃ and t_p = 3000 s for BT,

$$\varepsilon = 0.526 < 1. \quad (5)$$

When ε < 1, the total charge of the anomalous discharge current should be infinite,

$$Q = \int I \cdot dt \to \infty. \quad (6)$$

As is well known, the spontaneous polarization, P_s, of BT single crystal at room tempetature is about 25 μC/cm². The P_s of BT ceramics at room temperarure is on the order of about 7-10 μC/cm². However, the total charge to be stored in BT above T_c during the charging and discharging process is possibly more than 1000 μC/cm². Yamanaka also reported the giant polarization.[7] Galvanometric measurement shows that the Log I-Log t linear relationship held true even after one week. The charging and discharging process is very similar to that of a storage battery. For the storage of electric charge in BT ceramics, a barrier layer is necessary in the ceramics. It can be considered that the barrier in BT ceramics above T_c seems to be the grain boundaries. This is because there is no domain wall above T_c. This result apparently cannot be explained by the principle of conservation of energy. Okazaki has proposed a new space charge model for anomalous dielectric absorption current as shown in Fig. 1. Followings are the basic idea;

a. inside every grain, a space charge with a very long relaxation time exists.
b the space charge migrates according to diffusion equation corresponding to R-C distrubuted circuit.
c the migration of the space charge is limitted at the grain boundaries.

The model of the space charge inside grain, the simulated equivalent circuit and the calculated results of normalized Log I - Log t relatinship are shown in Fig. 1(a), (b), (c) and (d).[6]

The space charge model of Okazaki for dielectric absorption model can explain;

(1) the experimental results of eq.(3) in the first charging and discharging process, and (2) the total charge cannot approach infinite.

3.2 Microstructure and properties of SBT samples

The SBT sample used in this experiment is a disk 10 mm in diameter and 0.5 mm in thick which was cut from a high voltage commercial capacitor. Figure 2 shows the dielectric properties. Grain boundary structures of SBT are shown in Fig.3. The grain size is 1 ~ 3 μm. Samples include a small amount of Bi_2O_3 in order to improve the break down voltage. Phenomena at room temperature of SBT samples when a dc electric field is applied should correspond to those of high poled BT ceramics.

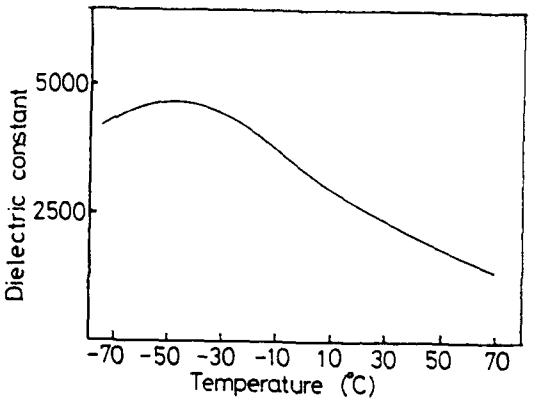


Fig. 2. Dielectric properties of SBT sample

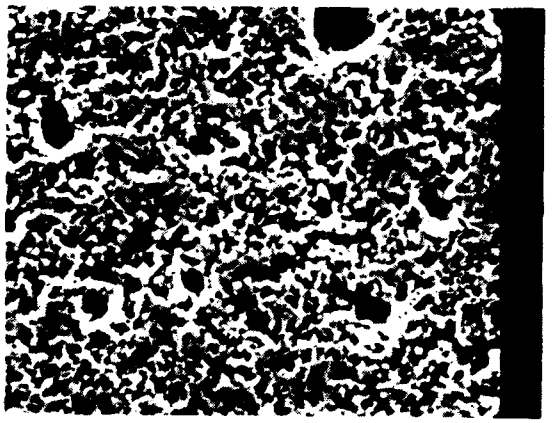
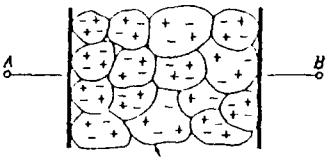
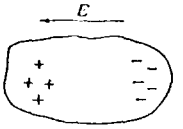


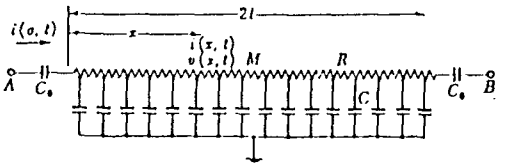
Fig. 3. SEM photograph of SBT sample



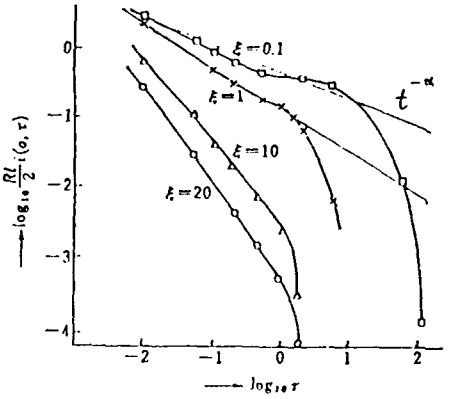
(a) inside every grain, a space charge with a very longe relaxation time exists.



(b) the migration of the space charge is limitted at the grain boundary.



(c) the space charge migrates according to diffusin equation corresponding to RC distrubuted circuit.



(d) Normalized Log I — Log t relationship

Fig. 1. Space charge model for dielectric absorption current

3.3 Pyroelectric current of high poled SBT

Figure 4 shows a pyroelectric current of SBT sample high poled at 140 ℃ under 5 kV/mm for 3000 s at a heating rate of 1 ℃/min from 25 ℃ to 180 ℃. The pyroelectric current is gradually increased with increasing temperature. If the sample is kept at a constant temperature, it should be slowly decreased with time with a very long relaxation time. The measurement was made for 30000 s, but the pyroelectric current is still alive at a value of 1×10^{-9} A/cm^2.

Figure 5 shows the pyroelectric pulse current observed at repeated temperature change of 25 ℃ and 60 ℃ oil bath. This result predict a possibility of pyroelectric application of high poled ferroelectric materials.

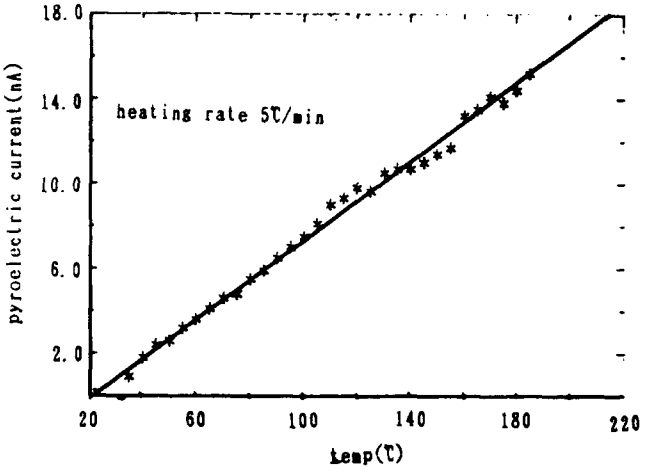


Fig. 4 Pyroelectric current of a high poled SBT sample.

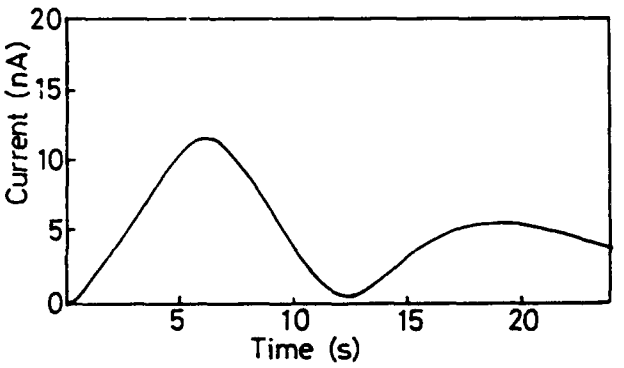


Fig. 5 Interrrupted pyroelectric current of SBT sample

Summary

Space charge model proposed for the anomalous dielectric absorption current current of ferroelectric ceramics above Curie point. The pyroelectric current of $(Sr,Ba)TiO_3$ ceramics above the Curie point was measured and discussed.

References

1) K. Okazaki: Denki gakkaishi 79 (1959) 905. [in Japanese]
2) K. Okazaki: Seramiku yuudentai kougaku, (Ceramic Engineering for Dielectrics [in Japanese]) (Gakkensha, 1968) translated into Russian (Energy Pubrishing Office, in Moscow),
3) K. Okazaki and H. Maiwa; 1992 10 JJAP in press
4) S. Takahashi: Jpn. J. Appl. Phys. 20 (1981) 95.
5) K. Okazaki and T. Tanimotp; Ferroelectrics, Vol. 131. (1992) 25.
6) K. Okazaki: Denkizairyo kougaku enshyu (Exercise of Electrical Enginnering Materials) (Gakkensha, Tokyo, 1967) p. 93. [in Japanese]
7) S. Yamanaka: Denki Gakkakaishi 77 (1957) 1294. [in Japanese]

ELECTRIC FATIGUE INITIATED BY SURFACE CONTAMINATION IN HIGH POLARIZATION CERAMICS

Qiyue Jiang, Wenwu Cao and L. E. Cross
Materials Research Laboratory
The Pennsylvania State University
University Park, PA 16802

ABSTRACT

Recently electric fatigue phenomenon in high polarization ceramics has attracted more and more attention because of the development of high strain actuators and ferroelectric memory devices. We report a study on fatigue behaviors of hot pressed PLZT with composition 7/68/32 under different surface conditions. It is found that the fatigue occurred at a few thousand of cycles is mainly caused by contaminated surface instead of intrinsic structure deterioration. For the same gold electrodes, samples with conventionally cleaned surface showed significant fatigue within 10^5 switching cycles while samples with surfaces cleaned by an improved procedure did not fatigue even after 10^8 switching cycles. The mechanism of fatigue introduced by surface contamination is explained by interface degradation between ceramic and electrode.

INTRODUCTION

Many applications of high polarization ceramics, such as high strain actuators and ferroelectric memory devices, involve repeated reversals of the polarization. One critical limitation on the performances of these devices is the fatigue associated with repeated electrical cycling.

In 1953, McQuarrie [1] first reported the time dependence of the P-E hysteresis loop in a $BaTiO_3$ ceramic. He found that after several weeks of switching at 60 Hz, the square shaped hysteresis loop was changed to a distinct propeller shape with some obvious decrease in both the maximum polarization and the remnant polarization. Merz and Anderson [2] studied fatigue behavior in a single $BaTiO_3$ crystal, a gradual reduction of polarization after a few million switching cycles was observed and the fatigue behavior was related to the patterns of the electric field (sine wave or pulse train wave). The ambient atmosphere was also reported to affect on the switching stability of $BaTiO_3$ single crystal [3]. A more detailed study of fatigue was carried out by Stewart and Cosentino on La or Bi doped PZT ceramics [4], they showed that the polarization decreased rapidly and was reduced to half of its original value after $5x10^6$ switching cycles. They concluded that the patterns of electric field, the types of electrodes, and the ambient conditions had no significant effects on the fatigue behavior. Fraser and Maldonado [5] also studied the same La doped PZT ceramics and reported significant effects of the electrodes. They found that when indium was used as electrode material instead of gold or silver, there was still 85% of the original remnant polarization left after 10^9 switching cycles, but fatigue occurred much faster when using lead, aluminum, gallium, silver and gold as electrode material. Carl [6] observed significant degradation in the La or Mn doped $PbTiO_3$ ceramics, after only a few thousand switching cycles the polarization dropped to 30% of its original value together with some increase of the coercive field, and some cracks were also observed on the surfaces of the samples under SEM.

Despite the fact that the fatigue effect is the major factor which prevents some potential applications of ferroelectrics, only a limited number of papers have been published on this subject. In addition, these published results by different investigators are often in contradiction, and there are no satisfactory explanations for these discrepancies. Therefore a systematic study on this subject is needed in order to understand the origin and mechanism of fatigue behavior. We report here the first part of an extensive study of the fatigue behavior on La doped lead zirconate titanate(PLZT) ceramic system. The reason for choosing PLZT ceramic system is because its relatively low coercive field, large polarization and square shaped hysteresis loop. Moreover, hot pressed PLZT ceramics are transparent, therefore have potential applications in non-volatile memory, electro-optical, and elctrostrictive devices. In this paper, the focus will be on the effect of surface contamination on the fatigue behavior. We believe that different surface conditions was one of the main reasons for the inconsistencies of those reported experimental results.

EXPERIMENT PROCEDURES

Lanthanum doped lead zirconate titanate ceramic specimens were fabricated from mixed oxides by hot pressing technique. The composition used in this study is $Pb_{0.93}La_{0.07}(Zr_{0.68}Ti_{0.32})_{0.9825}O_3$. Conventionally, this formula is simplified to a form 7/68/32 according to the mole ratio of La/Zr/Ti. The average grain size is about 5μm. At room temperature 7/68/32 is in rhombohedral phase. Samples were first cut into platelets with the areas of about 10 mm^2 and thicknesses in the range of 150-300μm, then annealed at 600 °C for 1 hour to release the mechanical stress generated during cutting and grinding processes.

In conventional cleaning procedure, organic solvents (alcohol or acetone) were used to rinse the samples and then the samples were dried in air at room temperature. An improved cleaning method used in our experiments is described as follows: first the samples are cleaned by conventional procedure, then they are further cleaned ultrasonically in solvent, and finally the samples are heated in a furnace for 1 hour at 500-600°C. Gold electrodes were sputtered onto the sample surfaces.

The properties studied here are the remnant polarization P_r, the maximum polarization P_m, coercive field E_c, and the dielectric constant in depoled state. High voltage sine wave AC field was used to switch the polarization, and the hysteresis loops were measured though a conventional Sawyer-Tower circuit and a Nicolet 214 digital oscilloscope.

RESULTS AND DISCUSSION

Fatigue in PLZT Specimens Cleaned by Conventional Procedure

Fig.1 shows a typical result obtained at 10 Hz from a specimen cleaned by conventional procedure. One can see that the fatigue started at about 10^3 switching cycles, and proceeded very rapidly between 10^5 - 10^6 cycles. The polarization P_r dropped to a value below 30% of the initial values after 10^6 switching cycles. The changes of the saturated polarization which was not show here have similar behavior as that of the remnant polarization P_r. Fig.2(a) and 2(b) are typical hysteresis loops before and after the fatigue test. The coercive field E_c also increased with switching cycles. We found that the polarization decrease is always accompanied by the increase of the coercive field E_c, which is consistent with the results obtained by other researchers [4][5][7]. Measurements made at the frequencies of 100 Hz and 200 Hz did not show apparent difference.

Fatigue in PLZT Specimens Cleaned by Improved Procedure

Fig.3 shows the changes of the polarization and coercive field with switching cycles for samples cleaned by improved procedure. The experiment was carried out at a frequency of 100 Hz. No fatigue was observed even after 10^8 switching cycles. We can see this more clearly from the two hysteresis loops in Fig.4, which were recorded at 10^3 and $2x10^8$ switching cycles, respectively. We can conclude from these experimental results that the fatigue shown in Fig.1 is purely extrinsic, i.e., caused by dirty surfaces. The actual lifetime of PLZT 7/68/32 ceramics with average grain size 5 μm is much longer than that shown in Fig.1. For improperly cleaned samples, the organic contaminants are trapped at the ceramic-electrode interfaces. During switching, a large electric field(15-40 kv/cm) was continuously applied on the sample, the trapped contaminates will cause large field concentrations resulting a failure of the electrode bonding.

CH3080-0-7803-0465-9/92$3.00 ©IEEE

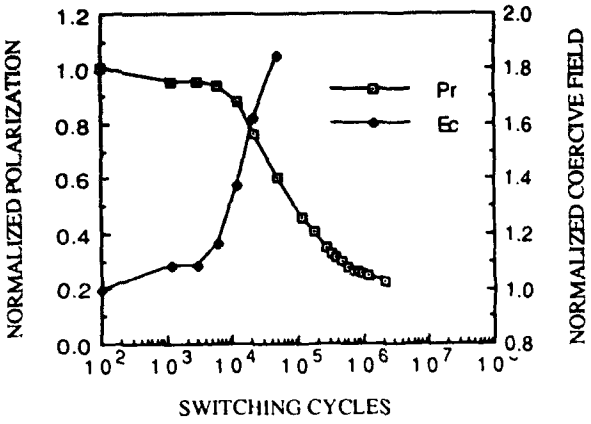


Fig.1 The changes of the normalized remnant polarization P_r and coercive field E_c with switching cycles for a conventionally cleaned PLZT 7/68/32 specimen.

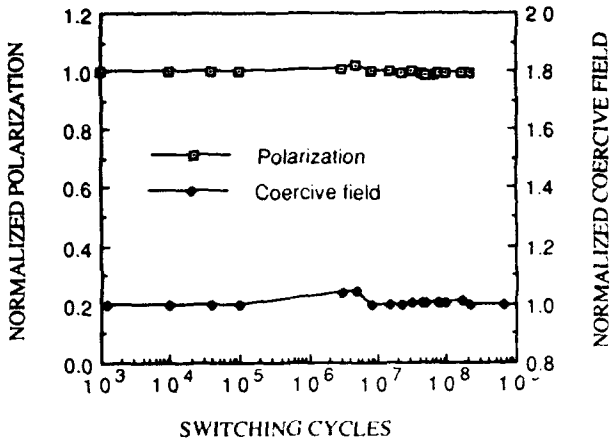


Fig.3 The normalized polarization and coercive field as functions of the switching cycles for a specimen cleaned by the improved procedure.

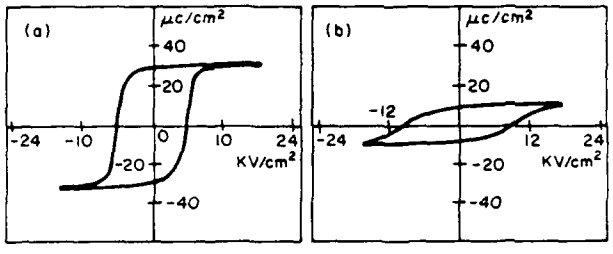


Fig.2 Typical hysteresis loops at 10^3 (a) and $3x10^6$ (b) switching cycles for a conventionally cleaned PLZT 7/68/32 sample at a frequency of 10 Hz.

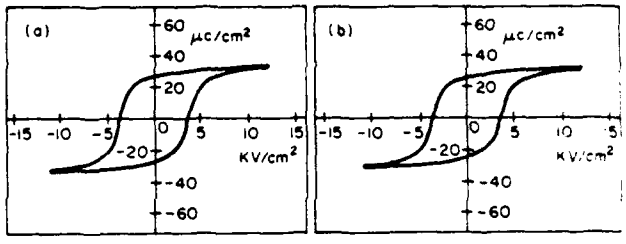


Fig.4 Typical hysteresis loops of a sample cleaned by improved procedure at a frequency of 100 Hz. (a) at 10^3 switching cycles, and (b) at $2*10^8$ cycles.

Although these experimental results may not be used as a proof to discredit the validity of other previous explanations on fatigue in terms of internal domain behavior, we can at least conclude that the fatigue in fine grain hot pressed PLZT 7/68/32 is caused by the improper ceramic-electrode interface, may be eliminated through an improved cleaning procedure described above. This finding is encouraging for many prospective applications of ferroelectrics.

Fatigue Originated from Surface Contamination

A. Deterioration of Ceramic-Electrode Interface under High AC Field

In fatigue experiments the possible sources of contaminants are: abrasive residue from grinding process; residue of solvents(water, alcohol or acetone); water in the air; residue of the bonding glue from cutting process; skin grease from finger touch. Without further cleaning these contaminants are left on the surfaces of specimens, and being sandwiched between the sample surface and the electrode, producing a poor interface contact. The effects of solvents and skin grease were further examined in the following experiments. First, the samples were etched by H_3PO_4 acid to remove the abrasive residues and skin grease, then the following surface treatments were given to three different samples:

a) sample 1 was washed by water and acetone, then rubbed both surfaces by fingers;

b) sample 2 was washed by water and acetone, then let it dry in the air;

c) sample 3 was washed by water and acetone, then heat treated in a furnace at 500 °C for 1 hour (free from contamination).

Fig.5 shows the results from the fatigue tests on these samples using a 100 Hz sine wave AC field. The remnant polarization of sample 3 did not decrease at all after 10^8 switching cycles, only E_c increased slightly. The P_r of sample 2 fatigued to 85% of its initial value after 10^8 switching cycles and E_c increased about 18%. Sample 1 was the worst among the three samples, its P_r reduced to 30% of the initial value, and E_c increased 50% after only $2x10^6$ cycles. Since the three samples only differ in surface treatments, these discrepancies in fatigue results can only be explained in terms of the different degree of surface contamination.

Although the experiments clearly indicate that the fatigue is initialized at the interface between the surface and electrode. The reactions of organic contaminants under high AC field at the interface are very complicated. A few possible explanations for what might have happened at the interface are: [8][9] 1) electrochemical reaction, such as ionization of contaminants, reduction of the chemical composition near the sample surface; 2) corona, high voltage can ionize water and organics, causing partial discharge which leads to a time related continuous degradation of the dielectric property; 3) contact deterioration effect, residue of solvents and skin grease prohibit a direct contact of the metal electrode with the sample surface, resulting a poor contact. When a poor contact occurs, a large field is applied to the contaminant layer which has much smaller dielectric constant than the sample, causing electrochemical reaction, resulting in a partial failure of the contact.

The electrode surface of a fatigued sample (which was cleaned by conventional method) was examined under SEM, and many regions were found where the electrode has been separated from the ceramic as shown in Fig.6. We believe from our experimental observations that the explanation 3) above may be the most appropriate one.

B. The nature of the fatigue by surface contamination

In order to find the nature and degree of damage produced during fatigue, different heat treatments were given to a fatigued sample. Table 1 listed the remnant polarization P_r and the coercive field E_c measured after the fatigued sample went through a heat treatment at 300 °C for 3 hours. Only partial recovery of P_r was

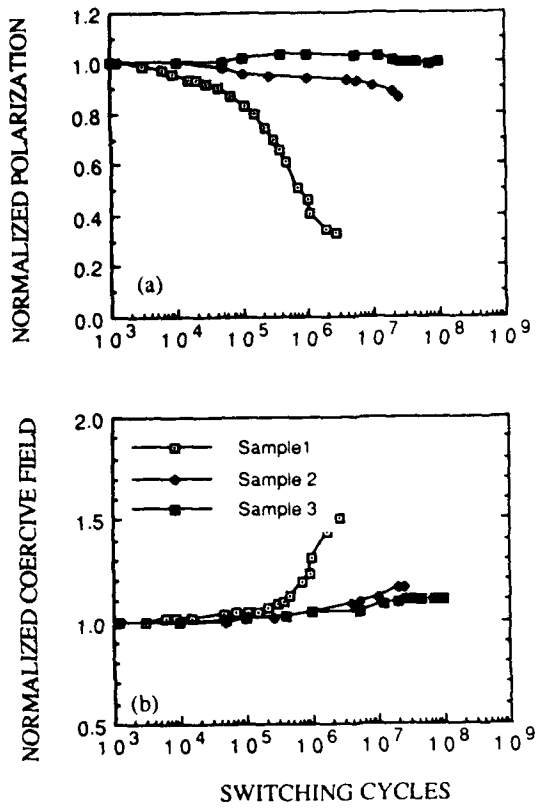


Fig.5 The normalized remnant polarization (a) and coercive field (b) as functions of switching cycles.Sample 1 was contaminated by solvent and skin grease; sample 2 was contaminated by solvent; sample 3 was cleaned by the improved procedure.

Table 4.1 Comparison of the remnant polarization (P_r) and the coercive field (E_c) for a PLZT 7/68/32 sample under different treatments

	P_r (μc/cm^2)	E_c (kv/cm)
Before fatigue	27.0	5.0
After fatigue	6.0	6.8
After 300°C heating	19.2	10.4
After 600 °C heating	22.4	7.3
After removal of 30μm	22.5	7.2

achieved and E_c became even larger. The sample then experienced further heat treatment at 600 °C for 1 hour, further improvements were observed as shown in Table 1. However, the P_r and E_c still could not recover to their initial values, which means that part of the damage in the fatigued sample is permanent. In order to investigate the depth of the damage from surface initiated fatigue, the sample was then ground off a 15 μm thick layer from each surface and re-electroded. The measured results (table 1) show no further improvement, which indicates that the damage has propagated to the interior of the sample.

Previously, fatigue in ferroelectrics was explained as due to the stabilization of domain walls [1][4][10]. Fatigue caused by domain pinning usually can be recovered by heating the samples to paraelectric phase[4][10]. In our experiments, total recovery did not occur even after the fatigued sample has been heated to as high as 600



Fig.6 SEM photograph taken from the electroded surface of a fatigued sample.

°C which is 470 °C higher than the dielectric maximum temperature. Therefore, the fatigue we have observed could not be due to the domain wall pinning, instead, we believe that the intergranular microcracking is responsible for the non-recoverable fatigue initiated by surface contamination. Scanning Electron Microscopy was performed on a fatigued sample(Fig.7 a) and non-fatigued sample(Fig.7 b) with ground surfaces. The samples were etched using H_3PO_4 acid to remove gold electrodes. On the micrographs in Fig.7, we can see some of the grinding damages and etch-pits for the non-fatigued sample, while for the fatigued sample we see a lot of grains without grinding damages and etch-pits. This means that a whole layer over these grains was pulled out during etching, which indicates that the bonding between grains was weakened during fatigue test. In addition, some cracks around grain boundaries are clearly visible, but no large cracks were observed either on the surfaces or on the cross section of the fatigued sample.

Fig.8 is an optical micrograph which was taken from a fatigued sample after the electrode being carefully removed. Many regions in the original transparent sample become opaque, which indicates that the nonuniform damage in the fatigued sample. This non-uniform damage is due to the partial failure of the electrode caused by the trapped contaminates.

SUMMARY AND CONCLUSIONS

A systematic study has been carried out on the influence of surface conditions on the fatigue behavior of hot pressed PLZT 7/68/32 ceramics with an average grain size of 5μm. It is found that the observed fatigue which occurred within 10^5 switching cycles is actually caused by surface contamination. These surface contaminates cause deterioration of the contact between the ferroelectric ceramic and the electrode, resulting an inhomogeneous field distribution in the specimen. Microcrackings are generated at the grain boundaries due to high electric field concentration. As a result, the applied field then will be concentrated across those cracks parallel to the electrode, which effectively raise the coercive field and lower the polarization. The conventional cleaning method is proved to be inappropriate for specimens used under high AC field. This surface contamination initiated fatigue can be eliminated though an improved surface cleaning procedure. Our results show that the ferroelectric properties of PLZT 7/68/32, such as the polarization and the coercive field, can be preserved for more than 10^8 switching cycles if the surface contaminates are removed.

Contrary to some reported results [4][10], We found that part of the fatigue damages are permanent and are throughout the entire sample. The fatigued properties i.e., the reduced polarization and the increased coercive field can be partially recovered though heat treatment, however, a complete recovery is not possible.

It should be pointed out that the results obtained here are applicable only for small grain ceramics, the fatigue mechanism in large grain systems is different [11].

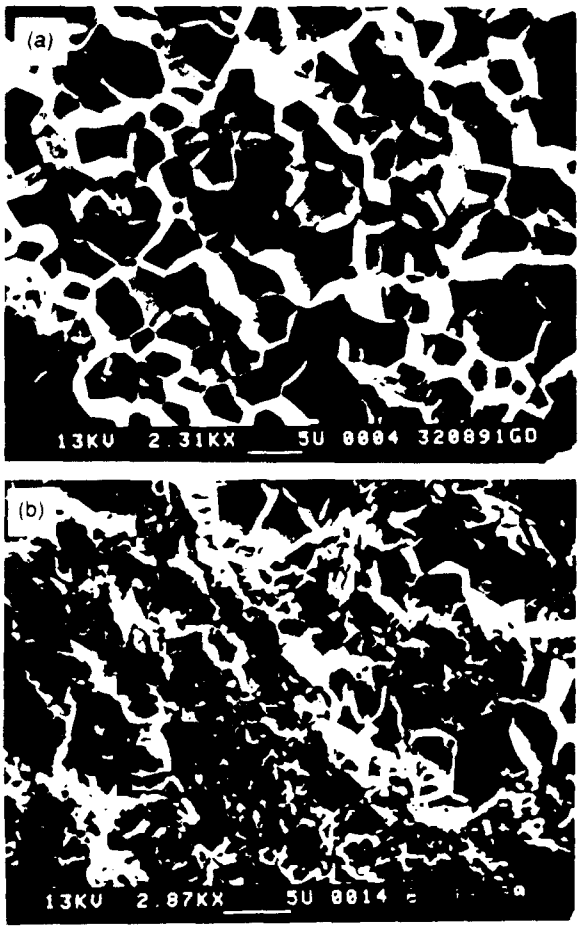


Fig.7 SEM photograph taken from a non-fatigued sample (a) and fatigued sample (b) after chemical etching.

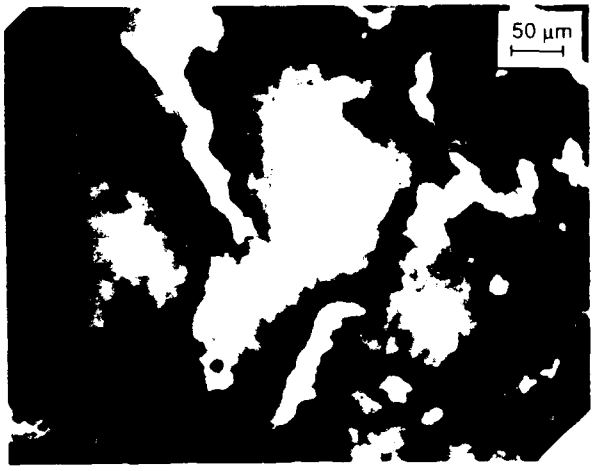


Fig.8 Transmission optical micrograph taken from a fatigued sample.

REFERENCES

[1] Malcolm McQuarrie. "Time Effects in the Hysteresis Loop of Polycrystalline Barium Titanate", J. Appl. Phys., **24**, pp. 1334-1335, 1953.

[2] W. J. Merz and J. R. Anderson. "Ferroelectric Storage Device", Bell Lab. Record, **33**, pp. 335-342, 1955.

[3] J. R. Anderson, G. W. Brady, W. J. Merz and J. P. Remeika. "Effects of Ambient Atmosphere on the Stability of Barium Titanate", J. Appl. Phys., **26**, pp. 1387-1388, 1955.

[4] W. C. Stewart and L. S. Cosentino. "Some Optical and Electrical Switching Characteristics of a Lead Zirconate Titanate Ferroelectric Ceramics", Ferroelectrics, **1**, pp. 149-167, 1970.

[5] D. B. Fraser and J. R. Maldonado. "Improved Aging and Switching of Lead Zircanate-lead Titanate Ceramics with Indium Electrodes", J. Appl. Phys., **41**, pp. 2172-2176, 1970.

[6] K. Carl. "Ferroelectric Properties and Fatigue Effects of Modified $PbTiO_3$ Ceramics", Ferroelectrics, **9**, pp. 23-32, 1975.

[7] W. R. Salaneck. "Some Fatigue Effects in 8/65/35 PLZT Fine Grained Ferroelectric Ceramics", Ferroelectrics, **4**, pp. 97-101, 1972.

[8] Carl J. Tautscher, pp. 4-5 in Contamination Effects on Electronic Products, Marcel Dekker, INC., New York. Basel. Hong Kong, 1991.

[9] K. L. Mittal, Morton Antler," Effect of Surface Contamination on Electric Contact Performance"; pp.179-182 in Treatise on Clean Surface Technology, Vol **1**, Edited by K.L.Mittal. Plenum Press, New York and London, 1987.

[10] Ennio Fatuzzio and W. J. Merz, pp.102-104 in Ferroelectricity, North-Holland Publishing Company, INC New York, 1967.

[11] Hun-Taeg Chung, Byoung-Chul Shin, and Ho-Gi Kim. "Grain Size Dependence of Electrically Induced Microcracking in Ferroelectric Ceramics", J. Am. Ceram. Soc., **72**(2), pp. 327-329, 1989.

Ferroelectrics: Properties, New Materials

Polarization Fatigue in Perovskite Ferroelectric Ceramics and Thin-Films

Jie Chen, M. P. Harmer, and D. M. Smyth
Department of Materials Science & Engineering
Lehigh University, Bethlehem, PA 18015

Abstract

Ferroelectric polarization fatigue (loss of polarization with cycling) of donor and acceptor doped $BaTiO_3$ ceramics and PZT thin-films has been investigated. Donor-doped $BaTiO_3$ ceramics showed significantly improved fatigue characteristics when compared with acceptor-doped materials. Enhanced fatigue properties were also observed in donor-doped PZT thin-films. The electric field assisted migration of charged species within ferroelectric materials may be responsible for the degradation/fatigue behavior. Results confirm the expectation that oxygen vacancies play an important role in degradation/fatigue under the electric switching.

Introduction

Many applications of both ferroelectric thin-films and bulk ceramics utilize polarization switching in their operations. Some of these include ferroelectric memory devices [1-3], electro-optical devices [4], and actuators [5]. A major problem for commercial applications is the long term stability of these devices. During fatiguing, the polarization decreases with increasing switching cycles. There are several possibilities for fatigue in thin-films and bulk materials, and a number of papers have been published in the past thirty years to study this problem [6-13]. The high field required for rapid switching is adequate to cause ionic migration in ferroelectric materials, particularly in thin-films due to the extremely high applied field (>105V/cm). Thus, it is important to investigate the interrelations between the charged species and the fatigue properties to further understand the degradation mechanism. Due to the lack of defect chemistry information and the difficulty in controling the chemical composition in Pb-based systems, $BaTiO_3$ was used as a standard material to study the fatigue behavior (the defect structure and transport properties are well understood in $BaTiO_3$). For comparison of the results, fatigue properties of undoped and donor-doped PZT thin-films were also conducted in this study.

Experimental Procedure

The compositions of undoped, acceptor, and donor-doped $BaTiO_3$ ceramics examined in this study are as follows:

$BaTiO_3$	A/B=0.995
$BaTi_{0.999}Al_{0.001}O_3$	0.1mol% of Al in Ti-site
$BaTi_{0.98}Ca_{0.02}O_3$	2mol% of Ca in Ti-site
$BaTi_{0.97}Nb_{0.03}O_3$	3mol% of Nb in Ti-site

The specimens were prepared using a liquid mix method [14]. This technique has been shown to make homogeneous specimens with highly accurate atomic ratios. The powders were pressed into pellets and sintered at 1400°C for 2hrs in air. The pellets were ground and polished to a thickness of 150~250μm. The finished surfaces were ultrasonically cleaned and heated on a hot plate for 10min at 200°C. Gold electrodes were evaporated onto the surfaces under high vacuum; and to improve the electrical contact, a room temperature drying Ag paste was also applied on the top of the Au electrode.

Ferroelectric thin-films of $Pb(Zr_{0.5}Ti_{0.5})O_3$ (PZT) and $Pb(Zr_{0.5}Ti_{0.5})_{0.95}Nb_{0.05}O_3$ (PNZT) with 5mol% excess Pb were prepared by a sol-gel method [15]. Pb, Zr, Ti, and Nb precursors were prepared separately by distillation of Pb acetate, Zr n-propoxide, Ti iso-propoxide and Nb ethoxide in 2-methoxyethanol. The stock solutions were prepared by combining the precursors in the required stoichiometric ratio and distilling them at 124°C. The stock solutions were hydrolyzed using 2-methoxyethanol solution containing water and HNO_3, and then spin-cast three layers on $Pt/Ti/SiO_2/Si(100)$ substrates. The films were dried at 150°C on a hot plate between each layer, then annealed at 300°C, and finally crystallized at 650°C for 1hr in flowing O_2.

Microstructure examinations and crystalline phase identification of the thin-films were conducted by Scanning Electron Microscopy (SEM), Transmission Electron Microscopy (TEM), and X-Ray Diffraction (XRD), respectively.

CH3080-0-7803-0465-9/92$3.00 ©IEEE

Top electrodes (30mil diameter or 100x100μm²) were evaporated on the film surfaces through a shadow mask. P-E hysteresis measurements were conducted using a modified Sawyer-Tower Circuit on both $BaTiO_3$ ceramics and PZT thin-films. The polarization degradation study was conducted by cycling the specimens at 20~30KV/cm, 100~800Hz for $BaTiO_3$ ceramics and 5~10V (215~430KV/cm), 50K~200KHz for thin-films, followed by measuring remanent polarization at 100Hz.

Results and Discussion

(1) Bulk $BaTiO_3$ Ceramics

In the acceptor doped $BaTiO_3$, acceptor ions represent a negative charge, and the charge compensation is achieved by oxygen vacancies [14,16]. For example:

$$2BaO + Al_2O_3 \longrightarrow 2Ba_{Ba} + 2Al_{Ti}' + 5O_O + V_O^{\cdot\cdot}$$
$$BaO + CaO \longrightarrow Ba_{Ba} + Ca_{Ti}'' + 2O_O + V_O^{\cdot\cdot}$$

Under high fields, these defects or defect complexes can migrate during the switching cycles. Oxygen vacancies are the most mobile ionic defects in the perovskite structure, so it is expected that acceptor doping will increase the degradation during the electrical switching.

In donor doped materials, donor charges are compensated by electron or cation vacancies [17] (in Pb-based perovskite, they are compensated by cation vacancies only) depending on the doping levels. For example:

$$2BaO + Nb_2O_5 \longrightarrow 2Ba_{Ba} + 2Nb_{Ti}^{\cdot} + 6O_O + 1/2O_2 + 2e' \quad (<0.5mol\%)$$

$$5BaO + 2Nb_2O_5 \longrightarrow 5Ba_{Ba} + 4Nb_{Ti}^{\cdot} + V_{Ti}'''' + 15O_O \quad (>0.5mol\%)$$

For ionic compensation, the concentration of oxygen vacancies is strongly reduced, and it is expected that donor-doped materials will have a high stability through the switching cycles.

The acceptor and donor-doped $BaTiO_3$ show typical "hard" and "soft" ferroelectric behavior as observed in PZT ceramics. Fig.1 shows the hysteresis loops of Ca-doped and Nb-doped $BaTiO_3$ before and after 10^8 and $5x10^8$ switching cycles at 30KV/cm electric field. Ca-doped sample shows a clear fatigue characteristic. The remanent polarization drops to 35% of its original value after 10^8 switching cycles. But Nb-doped specimen shows an excellent fatiguing resistance up to $5x10^8$ switching cycles. The normalized remanent polarization as a function of switching cycles is shown in Fig.2 for a variety of doped and undoped samples. All the samples are cycled using unipolar stress at 30KV/cm. Different materials show a significant difference in the fatigue behavior. Pure $BaTiO_3$ (A/B=0.995, naturally acceptor doped) shows a continuous decrease of remanent polarization through the entire cycling range, but the total degree of degradation is relatively low (up to $3x10^8$ cycles compared with all acceptor doped materials). For Ca-doped $BaTiO_3$ ($BaTi_{0.98}Ca_{0.02}O_3$, heavily acceptor doped), the remanent polarization falls off catastrophically after $2x10^6$ cycles, which demonstrates a strong degradation behavior due to the high concentration of oxygen vacancies. The degradation behavior of 0.1mol% Al-doped $BaTiO_3$ ($BaTi_{0.999}Al_{0.001}O_3$, slightly acceptor doped), falls in between undoped and heavily Ca-doped samples. The donor-doped sample, with 3mol% Nb ($BaTi_{0.97}Nb_{0.03}O_3$, heavily donor-doped), shows a striking improvement in stability, with almost no degradation out to 10^9 cycles. This result clearly demonstrates that oxygen vacancies play an important role in degradation.

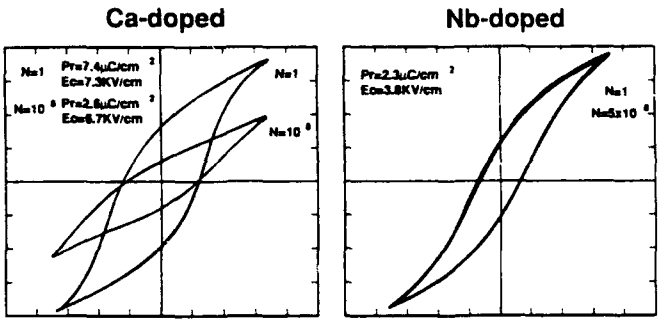


Fig.1 Hysteresis loops of Ca-doped $BaTiO_3$ before and after 10^8 and $5x10^8$ switching cycles.

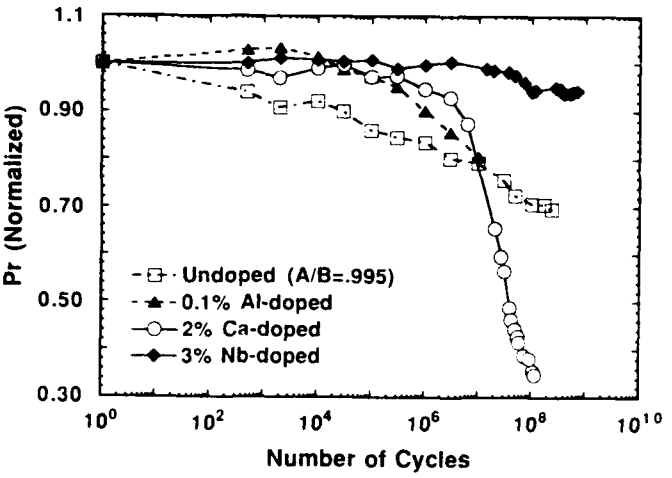


Fig.2 Normalized remanent polarization of $BaTiO_3$ as a function of the number of switching cycles, switching field 30KV/cm.

It is not clear why undoped $BaTiO_3$ (A/B=0.995) shows an early stage of degradation (see Figure 2). There are two possibilities for this early stage fatigue: (1)Undoped $BaTiO_3$ contains a large grain structure and defect migration may be easier in this material. (2)The large amount of porosity within the materials could cause a nonuniform distribution of the electric field, so that the local areas may degrade in the early stages.

(2) PZT Thin-Films

Fig.3 shows the XRD patterns of sol-gel derived PZT and PNZT thin-films, which were annealed at 650°C for 1 hr. Near-pure perovskite phase was obtained in both films. SEM micrographs of both cross section and plane views of PZT thin-films are shown in Fig.4 (a, b). A uniform thickness of ~2300Å was obtained from 0.4M stock solution by three coating layers. The grain size is approximately 0.1μm. A small amount of pyrochlore phase was identified by TEM techniques in both PZT and PNZT thin-fi! ns (see Fig.5 (a,b)). This second phase is in the form of crystallized agglomerates with a particle size of 100Å. The Nb-doped film contains a larger amount of pyrochlore than undoped PZT, which indicates that pyrochlore formation is easier in Nb-doped material.

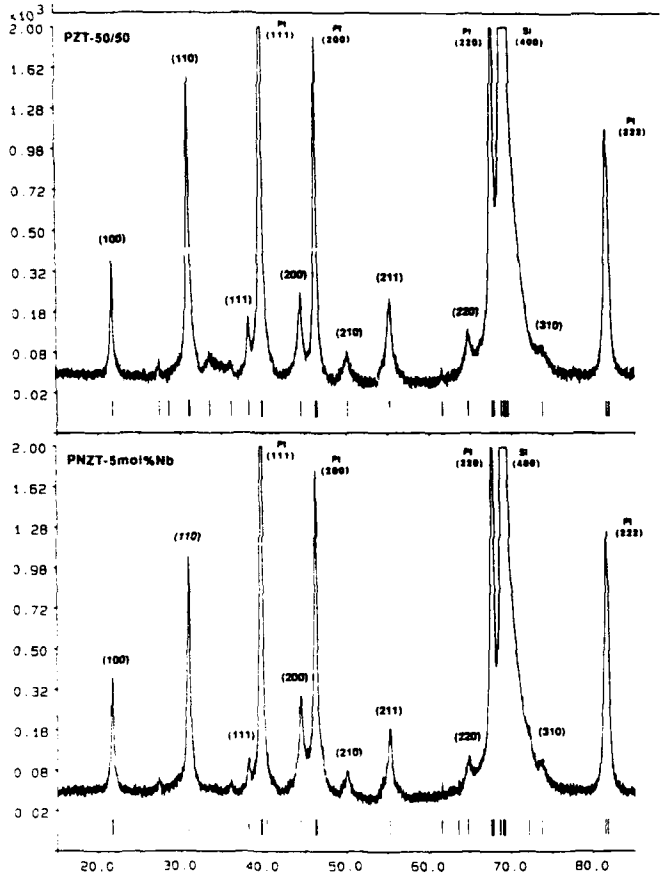


Fig.3 X-ray diffraction patterns of PZT and PNZT thin-films.

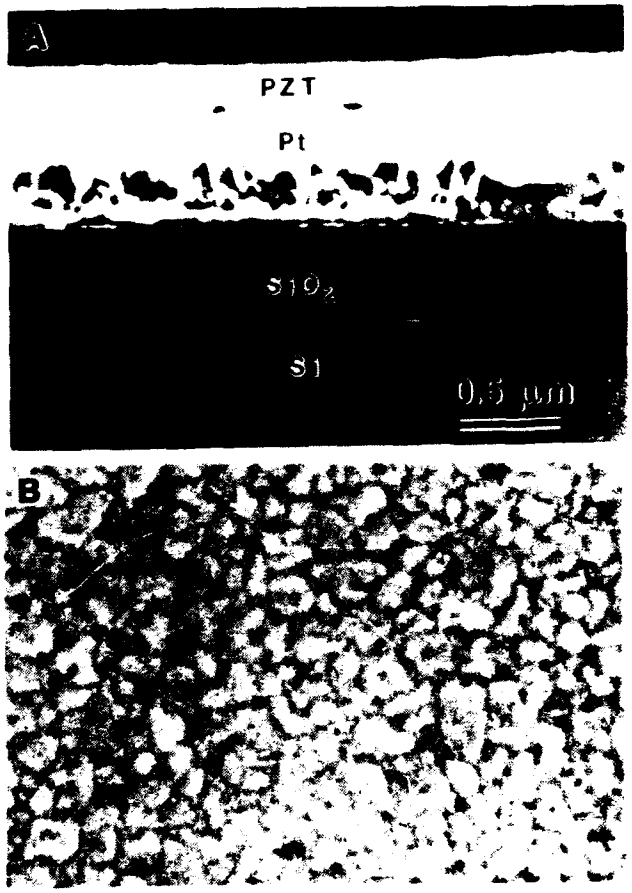


Fig.4 SEM images of (a) cross section and (b) plane view of PZT thin-films.

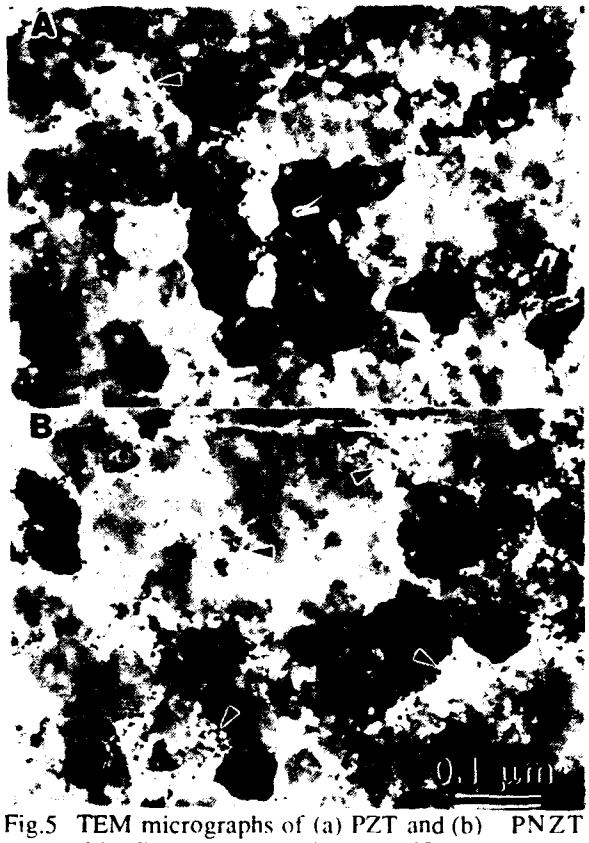


Fig.5 TEM micrographs of (a) PZT and (b) PNZT thin-films annealed at 650°C/1hr. The pyrochlore phase is indicated by the arrows.

Fig. 6 shows the ferroelectric hysteresis loops of PZT thin-films before and after switching cycles (bipolar stress, applied voltage 10V, ~430KV/cm). After $3x10^{10}$ cycles, the field induced remanent polarization dropped from $13\mu C/cm^2$ to $4.6\mu C/cm^2$. Fig.7 shows the remanent polarization and coercive field as a function of the number of switching cycles. Under such high fields, polarization starts to degrade after $5x10^7$ cycles. With increasing switching cycles, the remanent polarization decreases continuously. It was also observed that the capacitance of the film decayed concurrently with the polarization degradation. The normalized remanent polarization of both PZT and PNZT thin-films is plotted in Fig.8 as a function of switching cycles. Nb-doped PZT films show a clear improvement in fatigue properties compared with undoped PZT (improved by an order of magnitude). However, the enhanced fatigue properties in donor-doped PZT films are much less than in bulk $BaTiO_3$ ceramics.

A possible cause of this phenomenon is the lack of accurate chemistry control in Pb-based systems. During high temperature annealing, lead-loss can result in the formation of lead and oxygen vacancies.

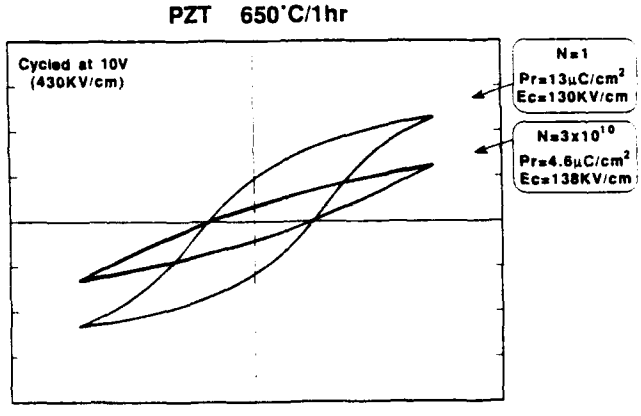


Fig.6 Hysteresis loops of PZT thin-films before and after $3x10^{10}$switching cycles.

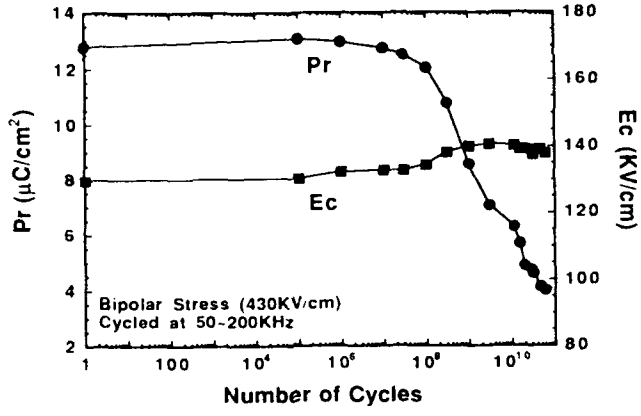


Fig.7 Remanent polarization and coecive field of PZT thin-films as a function of switching cycles.

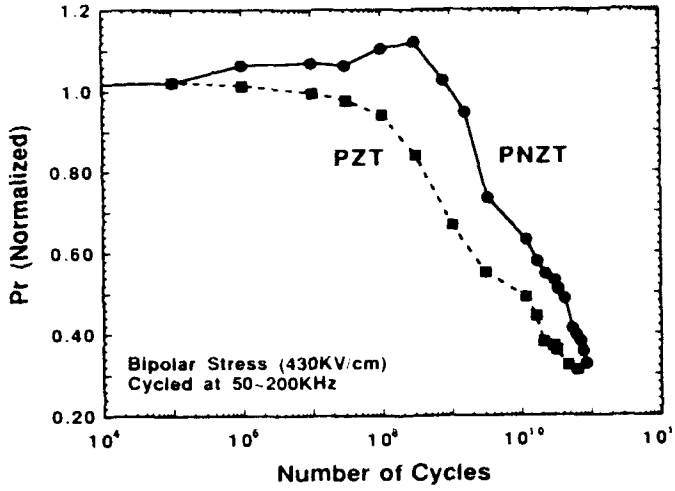


Fig.8 Normalized remanent polarization of undoped and Nb-doped PZT thin-films as a function of switching cycles

$$Pb_{Pb} + O_O \longrightarrow PbO + V_{Pb}'' + V_O''$$

Lead and oxygen vacancies can combine to form defect complexes (V_{Pb}''-V_O'') at low temperatures. These defects or defect complexes (especially the unassociated oxygen vacancies) can migrate or contribute to charge motion under high field which causes increased degradation.

Another reason why donor doping is not as effective in PZT films as it is in bulk $BaTiO_3$ is due to the formation of a second phase. A small amount of pyrochlore phase was observed in these films by TEM techniques, particularly in PNZT thin-films. The formation of pyrochlore phase may alter the stoichiometric ratio of the original composition. Nb is likely to segregate within the pyrochlore phase, since lead niobate prefers to form pyrochlore structure instead of perovskite structure. If some of the Nb is not incorporated into the perovskite structure, less of a doping effect is expected.

These experiments clearly demonstrate that the defect species play an important role in polarization degradation for both bulk $BaTiO_3$ ceramics and PZT thin-films. The possible mechanism of polarization fatigue is the electric field induced migration of charge species, especially the oxygen vacancies. One possibility is that the gradual motion of charge species will cause a redistribution of these defects and result in a non-uniform distribution of applied field. This may cause local dielectric breakdown or incomplete switching. Another possibility is that the charged species can interact with domain walls or spontaneous polarizations. When domains form through the paraelectric-ferroelectric transition, they try to align to minimize the free energy of the system. Under the high field, the migration or redistribution of charged species occurs. The possible segregation of charged

species and the interaction between the defects and domain walls or spontaneous polarization can establish a new equilibrium state assisted by the cycling field. Due to this pinning effect, domain or polarization switching becomes difficult. In-situ TEM observation of ferroelectric domain switching is in progress, and we believe that the detailed study of polarization reversal and the domain pinning effects would be very useful to further understand the fatigue mechanism in ferroelectric materials.

Summary

Donor-doped $BaTiO_3$ ceramics show a significant improvement in polarization fatigue compared with undoped and acceptor-doped materials. The improved fatigue behavior is also observed in Nb-doped PZT thin-films, but the magnitude is smaller than in bulk $BaTiO_3$. Results confirm the expectation that oxygen vacancies play an important role in polarization degradation. The possible causes of degradation are the electric field induced defect migration (particularly the oxygen vacancies) and the interactions between charged species and domain walls or spontaneous polarization. To improve the long term stability of ferroelectric thin-films, it is required to carefully consider the processing conditions, the defect chemistry and the doping effects.

* This research was supported by DARPA/ONR and McDonnell Douglas Electronic Systems Co.

References

[1] C. A. Araujo, L. D. McMillan, B. M. Melnick, J. D. Cuchiaro, and J. F. Scott, "Ferroelectric Memories," Ferroelectrics, 104, 241 (1990).
[2] S. K. Dey and R. Zuleeg, "Processing and Parameters of Sol-Gel PZT Thin Films for GaAs Memory Applications," Proceeding of the 1st Symposium on Integrated Ferroelectrics, Colorado Springs, 1989.
[3] D. Bondurant, "Ferroelectric RAM Memory Family for Critical Data Storage," Ferroelectrics, 112, 273 (1990).
[4] G. H. Heartling, "Piezoelectric and Electrooptic Ceramics," Ceramic Materials for Electronics, pp139, Ed. by R. C. Buchanan, Marcel Dekker, New York, 1986.
[5] K. Uchino, L. E. Cross, and R. E. Newnham, "Electrostrictive Effects in Paraelectric-Ferroelectric-Antiferroelectric Phase Transition," Jpn. J. Appl. Phys., 19, L425 (1980).
[6] D. M. Smyth, "Charge Motion in Ferroelectric Thin Films," Ferroelectrics, 116, 117 (1991).
[7] H. M. Duiker, P. D. Beale, J. F. Scott, C. A. Arajo, B. M. Melnick, and J. D. Cuchiaro, "Fatigue and switching in Ferroelectric Memories: Theory and Experiment," J. Appl. Phys. 68[11], 1 (1990).
[8] W. Pan, C. Yue, and O. Tosyali, "Fatigue of Ferroelectric Polarization and the Electric Field Induced Strain in Lead Lanthanum Zirconate Titanate Ceramics," J. Am. Ceram. Soc., 75[6], 1534 (1992).
[9] W. H. Shepherd, "Fatigue and Aging in Sol-Gel Derived PZT Thin Films," MRS Symp. Proc. vol.200, 277, 1990.
[10] K. Cal, "Ferroelectric Properties and Fatiguing Effect of Modified $PbTiO_3$ Ceramics," Ferroelectrics 9, 23 (1975).
[11] W. R. Salaneck, "Some Fatigie Effects in 8/65/35 PLZT Fine Grained Ferroelectric Ceramics," Ferroelectrics, 4, 97 (1972).
[12] C. F. Pulvari and J. R. Sprouri, "A New Graded Electrode for Forming Intimate Contact with Ferroelectrics," IEEE Trans. on Electron Devices, vol.ED-16, 532 (1969).
[13] D. B. Fraser and J. R. Maldonado, "Improved Aging and Switching of Lead Zirconate Titanate Ceramics with Indium Electrode," J. Appl. Phys., 41, 2172 (1970).
[14] N. H. Chan, R. K. Sharma, and D. M. Smyth, "Nonstoichiometry in $SrTiO_3$," J. Electrochem. Soc., 128, 1762 (1981), "Nonstoichiometry in Acceptor-Doped $BaTiO_3$," J. Am. Ceram. Soc., 65[3], 167 (1982).
[15] K. D. Budd, S. K. Dey, and D. A. Payne, "Sol-Gel Processing of $PbTiO_3$, $PbZrO_3$, PZT and PLZT Thin Films," Brit. Ceram. Proc., vol.36, 107 (1985). K. D. Budd, Ph.D. Thesis, University of Illinois at Urbana-Champaign, 1986.
[16] Y. H. Han, J. B. Appleby, and D. M. Smyth, "Calcium as an Acceptor Impurity in $BaTiO_3$," J. Am. Ceram. Soc., 70[2], 96 (1987).
[17] H. M. Chan, M. P. Harmer, and D. M. Smyth, "Compensating Defects in Highly Donor-Doped $BaTiO_3$," J. Am. Ceram. Soc., 69[6], 507 (1986).

POLARIZATION SWITCHING AND LONG-TIME RELAXATION EFFECTS INDUCED BY OFF-CENTER IONS IN $KTa_{1-x}Nb_xO_3$

L.A. Knauss, C. Jaquays, P. Adhikari, B.E. Vugmeister and J. Toulouse
Physics Department, Lehigh University, Bethlehem, PA 18015

Abstract

A most striking anomaly is observed in the behavior of KTN. It is the appearance of a remnant polarization well above T_c. We have measured hysteresis loops at different frequencies in a 3% KTN crystal. The shape of the loop changes significantly with frequency, a behavior that is due to the slow relaxation of randomly distributed off-center Nb ions interacting in clusters. We have developed a model of this relaxation and can calculate the hysteresis loops which are in good agreement with experiment.

Introduction

The appearance of a spontaneous or remnant polarization usually marks the onset of ferroelectricity. It is in fact the very existence of a switchable polarization that is used to define ferroelectricity. Recently it has been shown that mixed ferroelectrics can present very anomalous features such as a remnant polarization above the transition temperature, T_c.[1] This result comes from the observation of hysteresis loops in $KTa_{1-x}Nb_xO_3$ (KTN) above T_c.

In KTN, the Nb ions have been shown, by EXAFS,[2] to reside in one of eight (111) off-center positions. At high temperature, they can presumably jump between their 8 equivalent positions. The appearance of a polarization must then correspond to the preferential occupation of 4 of these 8 positions. Above the transition, this can only come about because of the existence of metastable states, as it is the case near a first-order transition. In KTN, however, a remnant polarization has been observed as far as 25K above the transition, revealing strongly enhanced slow relaxation effects. In the present article, we have investigated these effects by studying the frequency dependence of the hysteresis loops and of the remnant polarization. We have also developed a theory which shows this polarization to be related to the slow relaxation of randomly distributed off-center ions interacting in clusters.

Experimental Results

The polarization measurements have been made using a modified version of the Sawyer-Tower circuit. In particular, a variable resistor (50-100kΩ) was added in parallel with the reference capacitor (5μF) in order to avoid the building of excess charge on the reference capacitor due to conduction in the sample. Acquisition of hysteresis loops was done using a LeCroy digital oscilloscope from which the data was transferred to the computer. The maximum field applied was 2kV/cm. The measurements reported below were obtained on a 3% Nb sample with dimensions 1 x 0.7 x 0.08 cm, coated with evaporated Aℓ electrodes.

Two hysteresis loops are presented in Fig. 1. The narrow one was obtained at 10Hz and the wider one at 2 kHz, both at T = 69.8K, i.e. clearly above the transition at T_c = 64K. Besides the decrease in the loop size or remnant polarization, we also note an increase in the maximum polarization with decreasing frequency. These two characteristic features are indeed predicted by the theory below and can also be given a rather simple physical explanation.

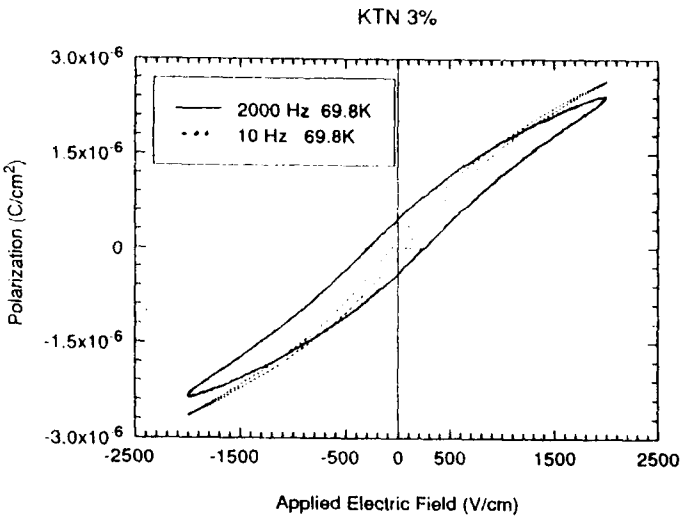


Fig. 1. Experimental hysteresis loops measured at •••, 10Hz and, — 2kHz, with E_{max}=2kV/cm at T=69.8K, on KTN 3% Nb (T_c=64K)

In a previous publication,[3] we have clearly shown that polar microregions, 20 to 100 Å in size, form significantly above T_c. The formation of these regions, or clusters, is due to the strong interaction that exists between closely spaced dipoles, mediated by the highly polarizable lattice. The frequency dependence of the shape of the loop suggests, as T_c is approached from above, a slowing down of the relaxation of nearby dipoles forming a cluster, due to the presence of other clusters.

Theoretical Model

We have considered here the smallest possible cluster, i.e. a pair of dipoles. The interaction between pairs is treated in the framework of a random molecular field theory developed earlier by one of us.[4] Such an approach is a generalization of the well-known Bethe-Peierls cluster theory to systems with configurational disorder.

In order to simplify the approach, we consider an Ising system or one in which the dipoles can only have two orientations. The Hamiltonian of a pair of dipoles can then be written in the form:

$$H = - K_{12}\ell_1\ell_2 \qquad (1)$$

where $K_{12} \equiv K(r_{12})$ is the interaction energy between the two dipoles separated by a distance r_{12} and $\vec{\ell}_i = \vec{d}_i^*/|\vec{d}_i^*|$ is the unit vector along the direction of the dipole on site i, d^* being the effective dipole moment in the highly polarizable lattice. The energy levels of a pair are presented in Fig. 2 below.

CH3080-0-7803-0465-9/92$3.00 ©IEEE

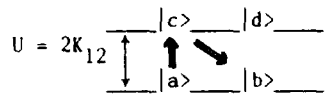


Fig. 2. Energy levels of a dipole pair (cluster) $|a\rangle = |{+}{+}\rangle$, $|b\rangle = |{-}{-}\rangle$, $|c\rangle = |{+}{-}\rangle$, $|d\rangle = |{-}{+}\rangle$

If we assume that the Hamiltonian describing the dipole lattice interaction can be written as a sum of one-particle Hamiltonians, then, the relaxation or flip of two dipoles (clusters) cannot be the result of a single process; it must involve successive flips of each dipole as shown by the arrows in Fig. 2. The transition probabilities, W, for the relaxation of a cluster of two dipoles can then be written:

$$W_{ac} = W_{ad} = W_{bc} = W_{bd} = W_o\, e^{-U/T}$$
$$W_{ca} = W_{da} = W_{cb} = W_{db} \equiv W_o \qquad (2)$$

The relaxation law for the average dipole moment of a pair can then be obtained from the kinetic balance equations for the population, P, of the energy levels:

$$\frac{dP_a}{dt} = -2W_{ac}P_a + W_{ca}(P_c + P_d)$$
$$\frac{dP_b}{dt} = -2W_{ac}P_b + W_{ca}(P_c + P_d) \qquad (3)$$

with $P_a + P_b + P_c + P_d = 1$ and $P_c = P_d$

From (3), we get:

$$\frac{d}{dt}\langle \ell_{12}\rangle_U = -2W_o\, e^{-U/T}\, \langle \ell_{12}\rangle_U \qquad (4)$$

with $\langle \ell_{12}\rangle_U \equiv (P_a - P_b)$

In order to take into account the interaction of a given dipole pair with other dipole pairs and with the external field, we make the commonly used assumption that the average value of the dipole moment approaches its quasiequilibrium value for a given internal E_{int} and external E field. The relaxation of ℓ_{12} can then be described by:

$$\frac{d}{dt}\langle \ell_{12}\rangle_{E_{int},U} = -2W_o e^{-U/T}\left[\langle \ell_{12}\rangle_{E_{int},U} - \langle \ell_{12}\rangle^{eq}_{E_{int}+E,U}\right] \qquad (5)$$

$$\text{where } \langle \ell_{12}\rangle^{eq}_{E_{int},U} = \frac{\mathrm{Tr}\,\ell_{12}\exp[-\frac{1}{T}(\frac{U}{2}\ell_{12}^2 + 2E_{int}\ell_{12})]}{\mathrm{Tr}\,\exp[-\frac{1}{T}(\frac{U}{2}\ell_{12}^2 + 2E_{int}\ell_{12})]} \qquad (6)$$

We now need to average Eq. (5) over the internal field distribution and over the distribution of potential barriers U. To do so, we rewrite it in the integral form and consider only the steady state regime in the oscillating external field, $E = E_o \cos \omega t$. We thus obtain an equation for the average dipole moment L(t) (or equivalently for the field induced polarization, $P = nd^*L$)[4]:

$$L(t) = -\int_o^\infty dt' \frac{\partial Q(t')}{\partial t'}\, L_{12}(t-t') \qquad (7)$$

$$\text{with } L_{12}(t) = \int dU \Phi(U) \int dE_{int} f[E_{int}+E(t), L(t)] \langle \ell_{12}\rangle^{eq}_{E_{int},U} \qquad (8)$$

and $f(E_{int})$, the distribution function of internal molecular fields,

$$Q(t) = \int dU \Phi(U) \exp(-2W_o t e^{-U/T}) \qquad (9)$$

$$\Phi(U) = \int d\vec{r}\,\delta[U - 2K_{12}(r)] \exp(-\frac{4\pi}{3} nr^3) \qquad (10)$$

Eq. (7) is the self-consistent integral equation for the polarization induced by an external field E(t). As can be seen, the solution of this equation depends on the magnitude as well as on the frequency of the external field, and on temperature. We have solved Eq. (7) numerically above the transition temperature and have also found that the numerical results can be approximated reasonably well by a 3-parameter function:

$$L(t) = A \tanh[\, a \cos \omega t + b \sin \omega t] \qquad (11)$$

in which the parameters A, a and b depend on E_o, ω/W_o, T and the ratio T_c/T_c^{MF} where T_c^{MF} is the transition temperature predicted by mean field theory. The value of T_c^{MF} is of the order of the average value of the potential barrier U. For that reason, the smaller the ratio T_c/T_c^{MF}, the more pronounced will the freezing effects be and the larger the hysteresis loop. As can be seen from Eq. (11), the width of the hysteresis loop is proportional to Ab while Aa determines the maximum value of the polarization. Calculated hysteresis loops are shown in Fig. 3 for two different frequencies in the ratio of 1/100. Comparing Figs. 1 and 3, we find qualitative agreement between the experimental and the theoretical results. For the lower frequency the area inside the loop, and the remnant polarization, is smaller than for high frequency. In contrast, the maximum polarization is greater for the lower frequency.

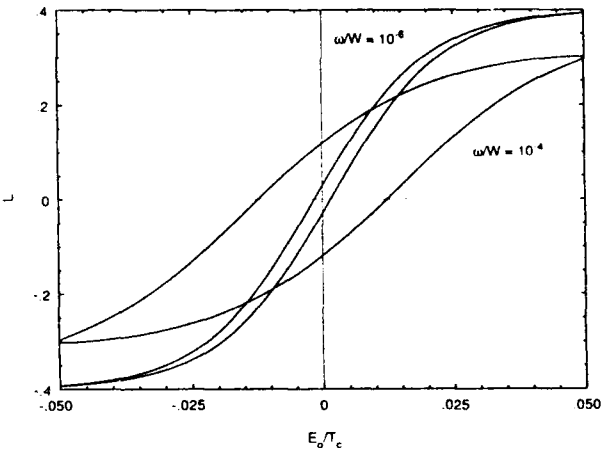


Fig. 3. Calculated hysteresis loops, plot of $L \equiv P/nd^*$ vs E_o/T_c for two frequencies normalized by the spontaneous transition rate, W_o.

These two features can in fact be understood rather intuitively. At a lower frequency, ω, of the external field, the dipole system has more time to respond and, for a given distribution function of the relaxation times, a greater fraction of the dipole pairs are able to contribute to the maximum polarization. Conversely, upon removing the field, more of them have time to relax to their random state giving a smaller remnant polarization. One slight discrepancy can be noticed between the calculated and experimental hysteresis loops. The latter do not approach a zero slope at high field. This is due to the existence of an intrinsic dielectric constant, different from 1, in the high polarization state. Such a dielectric contribution was not included in the calculated loops which only contain the dipole contribution.

Conclusion

The present polarization results show that, in KTN, the strong interaction that exists between pairs or clusters of closely spaced dipoles is responsible for long time relaxation effects. These effects include the observation of hysteresis loops or a remnant polarization above T_c and, as we shall show in a forthcoming publication, dielectric dispersion.

Acknowledgments

This work was partially supported by grant No. N00014-90-J-4098 from the Office of Naval Research.

References

1. J. Toulouse, X.M. Wang, L.A. Knauss and L.A. Boatner, Phys. Rev. B43, 8297 (1991).

2. O. Hanske-Petitpierre, Y. Yacoby, J. Mustre de Leon, E.A. Stern and J.J. Rehr, Phys. Rev. B44, 6700 (1991).

3. J. Toulouse, P. DiAntonio, B.E. Vugmeister, X.M. Wang and L.A. Knauss, Phys. Rev. Lett. 68, 232 (1992).

4. B.E. Vugmeister and M.D. Glinchuk, Rev. Mod. Phys. 62, 993 (1990).

SPONTANEOUS POLARIZATION IN THE DEUTERATED AND UNDEUTERATED PROTON GLASS $Rb_{1-x}(NH_4)_xH_2AsO_4$

Nicholas J. Pinto and V. Hugo Schmidt
Department of Physics, Montana State University, Bozeman, Montana 59717

Spontaneous polarization of mixed single crystals of Rubidium Ammonium Dihydrogen Arsenate (RADA) and its deuterated counterpart (DRADA) are presented together with the pure ferroelectric Rubidium Dihydrogen Arsenate (RDA) and its deuterated counterpart (DRDA). There is a sharp rise in the spontaneous polarization at the ferroelectric transition temperature T_c for the pure crystals as this transition is first order. The change in the spontaneous polarization in the mixed (x=0.08) crystals below T_c is gradual however, indicating the presence of acid hydrogens and ammonium cations that are still mobile and in the paraelectric phase. These mixed crystals show coexistence of paraelectric/proton glass and ferroelectric order below the glass "transition" temperature T_g. The maximum values of the spontaneous polarization in the deuterated samples are greater than in the undeuterated samples. Also, the maximum value of the spontaneous polarization in the mixed crystals below T_c at the lowest temperatures reported is found to be slightly lower than the corresponding value in the pure crystals.

Proton glass behavior was discovered by Courtens[1] in 1982 in a mixture of RbH_2PO_4 (RDP) and $(NH_4)H_2PO_4$ (ADP). Here RDP is a pure ferroelectric and ADP is a pure antiferroelectric. In a mixture of the form $(RDP)_{1-x}(ADP)_x$, (RADP), for a certain range of x values, proton glass behavior appears below the "freezing" temperature T_g due to frustration between ferroelectric and antiferroelectric ordering. In this range the system makes a smooth transition to the glass regime from the paraelectric regime as temperature is reduced below the glass "transition" temperature. If a spontaneous polarization were present in these mixed crystals it could be measured by conventional means like a Sawyer-Tower[2] circuit, and its value would depend on the amount of ferroelectric material present. For pure proton glasses the equilibrium spontaneous polarization is zero. In such crystals a quasi-equilibrium polarization can be generated by field-cooling[3,4] the sample down into the nonergodic region.

The crystal structure of these mixed systems is of the KH_2PO_4 (KDP) type. A variety of mixed systems of the KDP type can be prepared by substituting Rb for K and As for P. In addition, these systems can be deuterated by growing the crystals from deuterated materials. In this work we have substituted As for P, thereby obtaining $Rb_{1-x}(NH_4)_xH_2AsO_4$ (RADA) mixed crystals. While the spontaneous polarization in pure ferroelectrics of the KDP type has been studied,[5-9] few experiments[10-12] have been performed on spontaneous polarization in mixed crystals. Dielectric measurements[13] in mixed RADA crystals for $0.04<x<0.10$ show coexistence of paraelectric/proton glass and ferroelectric order below the ferroelectric transition temperature. In this paper we extend previous results[14] on spontaneous polarization of RADA and its deuterated counterpart and compare them to RDA and DRDA. Spontaneous polarization has also been calculated from the dielectric measurements along the a axis of mixed crystals and compared to that obtained from saturated hysteresis loops.

Mixed crystals were obtained by slow evaporation of aqueous solutions of RbH_2AsO_4 (RDA) and $(NH_4)H_2AsO_4$ (ADA) mixed in the proper molar ratios. The deuterated crystals were grown under an atmosphere of argon to maintain a high percentage of deuteration. The ferroelectric transition temperature T_c depends on the percent of deuteration in the crystal. The x values in the mixed crystals are determined from our measured T_c's with the aid of phase diagrams published for deuterated[15] and undeuterated[16] RADA. Small platelets perpendicular to the c tetragonal axis were cut from single crystals. Silver electrodes were evaporated in vacuum after polishing the surfaces to ensure that the faces were parallel. Polarization measurements were obtained from saturated dielectric hysteresis loops using the Sawyer-Tower circuit with a 60 Hz voltage source.

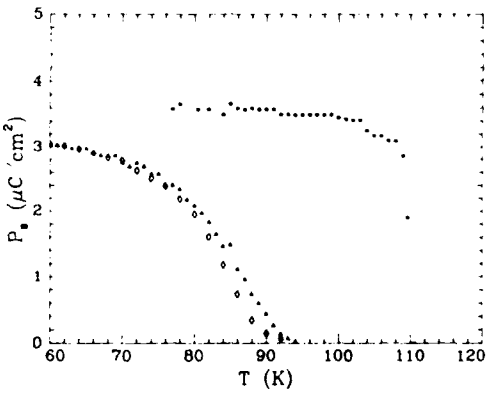


Figure 1 Spontaneous polarization obtained from saturated hysteresis loops in RDA (x=0; •) and RADA (x=0.08; ▲) as a function of temperature. The open diamond symbol represents spontaneous polarization obtained from Eq. (3) and Fig. 3 for RADA x=0.08.

Figure 1 shows the spontaneous polarization of the undeuterated RADA sample. The ferroelectric transition for x=0 is first order[9,17] and the transition temperature T_c is found to be 110 K. This is evidenced by the sharp rise in spontaneous polarization at T_c. The spontaneous polarization reaches a value of (3.6±0.5) μCcm^{-2} at temperatures far below T_c. The large error bars in the spontaneous polarization results from the uncertainty in computing the surface area of the sample due to its small size. Within the limits of our experimental

CH3080-0-7803-0465-9/92$3.00 ©IEEE

Table 1: Tabulated values of β and γ defined in Eq. (1) for RDA and DRDA together with fitting parameters defined in the text.

Ref.	Sample	C(K)	T_o(K)	ΔP_s $\mu C\,cm^{-2}$	β c.g.s.	γ c.g.s.
8	RDA	--	108.5	3.7	-20×10^{-11}	12×10^{19}
9	RDA	3100	108.5	3.6	-6.9×10^{-11}	4.4×10^{19}
This work	RDA	2200	104	3.0	-16.7×10^{-10}	15.4×10^{-18}
This work	DRDA	3500	156	4.5	-9.4×10^{-10}	3.8×10^{18}

error this value agrees with that reported by Kamysheva et al.[9] who have obtained a maximum value of (4.2±0.2) μCcm^{-2} from specific heat measurements.

From the expression of the free energy (G) as a function of polarization (P):

$$G(P,T) = G_0(T) + \frac{\alpha}{2}P^2 + \frac{\beta}{4}P^4 + \frac{\gamma}{6}P^6 + \ldots \qquad (1)$$

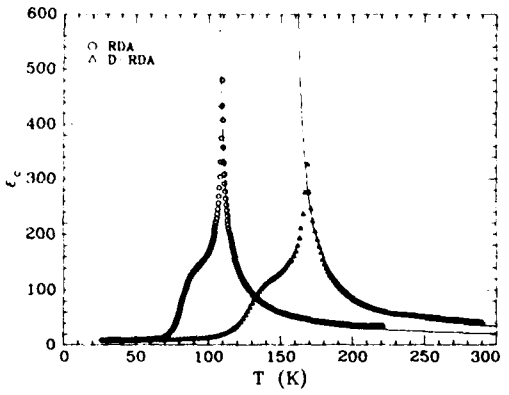


Figure 2: Real part of the dielectric permittivity ϵ_c' at 1 kHz as a function of temperature along the c axis, (○) for RDA and (△) for DRDA. Solid line represents a fit to the Curie-Weiss law of Eq. (2).

where $\alpha = \alpha_o(T-T_o) = 4\pi(T-T_o)/C$, C is the Curie-Weiss constant and T_o is the Curie-Weiss temperature, we have calculated the thermodynamic coefficients β and γ for the pure crystals. In Fig. 2 we show the dielectric constant as a function of temperature measured along the c axis at 1 kHz and very low applied electric field (10 V/cm) for the pure crystals. The solid line is a fit to the Curie-Weiss law:

$$\epsilon_c' - \epsilon_{c\infty} = C/(T-T_o) \qquad (2)$$

This fit gives a value of C=2200±20 K and T_o=104 K for RDA; we have assumed a value of 10 for the "infinite frequency" dielectric response $\epsilon_{c\infty}$. Using this value for C we calculate β=-16.7×10^{-10} c.g.s. and γ=15.4×10^{-18} c.g.s. from the expression $(\Delta P_s)^2 = -3\beta/4\gamma$ and $(\Delta P_s)^2 = -4\alpha/\beta$ where ΔP_s=3.0 μCcm^{-2} is the jump in the spontaneous polarization at T_c. It must be pointed out that Eq. 1 truncated at the P^6 term cannot be expected to fit such a big P_s [$\Delta P_s \approx P_s(0\ K)$] very well. Table 1 shows the corresponding values obtained from saturated hysteresis loops[8] and from specific heat measurements[9]. The difference in our values arises from the low T_o and C values obtained from fitting Eq. 2 to Fig. 2.

The spontaneous polarization for x=0.08 RADA is also shown in Fig. 1, and can be compared to that for the pure ferroelectric. The spontaneous polarization rises gradually in this case due to the presence of the ammonium cation centers, many of which are still in the paraelectric phase for some temperature range below T_c. However, at temperatures below 55 K the applied electric field needed to obtain saturated hysteresis loops exceeds the dielectric breakdown field of the sample, hence saturation polarization could not be computed below this temperature. The value of the spontaneous polarization measured at the lowest temperature reported is (3.0±0.5) μCcm^{-2}. We note that this value of the saturation polarization is less than that for the pure sample. We also performed dielectric measurements along the a axis for the same mixed crystal to verify the variation in spontaneous polarization obtained from hysteresis loops as a function of temperature below T_c. The glass transition is not seen in this sample at the temperatures covered in this experiment but is seen at lower temperatures.[13] The spontaneous polarization in this case can be obtained from:

$$P_{sd} = P_{so}\left(\frac{\epsilon_1'}{\epsilon_1' + \epsilon_2'}\right) \qquad (3)$$

where P_{sd} is the spontaneous polarization obtained from the dielectric data, P_{so} is the maximum spontaneous polarization of the pure crystal well below T_c, and ϵ_1' and ϵ_2' are defined in Fig. 3. Here ϵ_2' represents the contribution to the dielectric constant from the paraelectric portion of the x=0.08 sample and $(\epsilon_1' + \epsilon_2')$ would represent the contribution to the dielectric constant from the same sample in the absence of the ferroelectric phase transition. Dielectric data for RADA x=0.4 has been included to help extrapolate qualitatively the Curie-Weiss behavior in the x=0.08 crystal to temperatures below T_c.

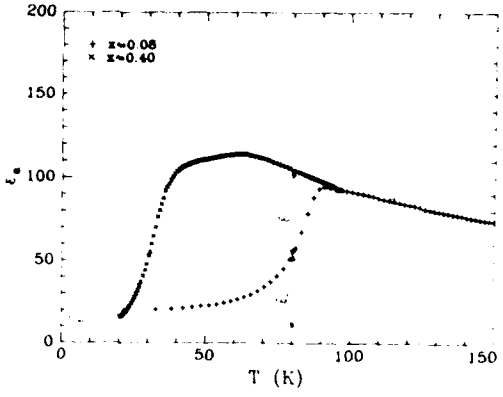


Figure 3: Real part of the dielectric permittivity ϵ_a' for the undeuterated mixed crystals at 1 kHz as a function of temperature along the a axis. ϵ_∞' is assumed to be 10.

In Fig. 1 we show the variation in P_{sd} as a function of temperature below T_c and compare it to that obtained for the same sample from saturated hysteresis loops. The agreement is good within the limits of experimental error. Here we have used P_{so}=3.6 μCcm^{-2} from Fig. 1.

In the case of mixed RADP samples, however, the spontaneous polarization is found to approach the value of the pure ferroelectric RDP[11] at low temperatures. It must be pointed out that coexistence of ferroelectric/proton glass phase has not been reported in RADP mixed crystals below the ferroelectric transition temperature.

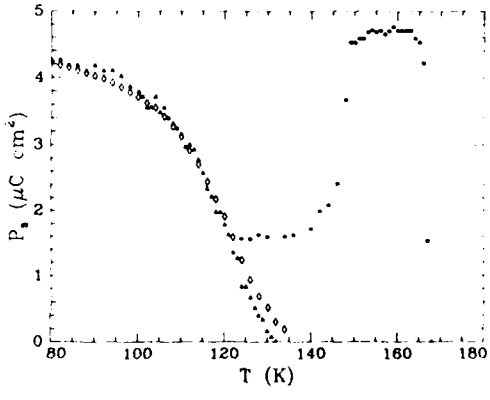


Figure 4: Spontaneous polarization obtained from saturated hysteresis loops in DRDA (x=0; •) and DRADA (x=0.08; ▲) as a function of temperature. The open diamond symbol represents spontaneous polarization obtained from Eq. (3) and Fig. 5 for DRADA x=0.08.

Fig. 4 shows the spontaneous polarization in the case of the deuterated samples. Here, deuteration effects raise the transition temperatures and the values of the spontaneous polarization as compared to the undeuterated counterpart. Similar effects of deuteration are seen in the phosphates.[5,6] The transition in the pure sample is sharp when compared to the mixed sample. The value of the spontaneous polarization below T_c for the pure sample is (4.7±0.2) μCcm^{-2}. The variation in the spontaneous polarization in the x=0.08 sample is gradual as in the case of the undeuterated sample and approaches a value of (4.2±0.2) μCcm^{-2} at the lowest temperatures measured. From Fig. 2, the Curie-Weiss fit for DRDA yields C=3500±50 K and T_o=156 K. T_c for DRDA is found to be 168 K. This increase of about 1000 K for the Curie-Weiss constant in the deuterated sample is consistent with that observed in KDP[6] and RDP[7] upon deuteration. Using this value for C we obtain for DRDA, β=-9.4x10^{-10} c.g.s. and γ=3.8x10^{-18} c.g.s. where we have used ΔP_s=4.5 μCcm^{-2} as the jump in the spontaneous polarization at T_c. These values are tabulated in Table 1. We have calculated P_{sd} for the deuterated case from Fig. 5 and Eq. 3 by a method analogous to that used to calculate the spontaneous polarization from the dielectric data in the undeuterated crystals. From Fig. 4 we have used P_{so}=(4.7 μCcm^{-2}. In Fig. 5 the glass transition for the x=0.08 crystal is seen around 43 K where the dielectric constant begins dropping faster with decreasing temperature. Here too, dielectric data for x=0.28 have been included to help extrapolate the Curie-Weiss behavior of the x=0.08 crystal below T_c. The result is plotted in Fig. 4 and can be compared to that obtained for the same sample from saturated hysteresis loops.

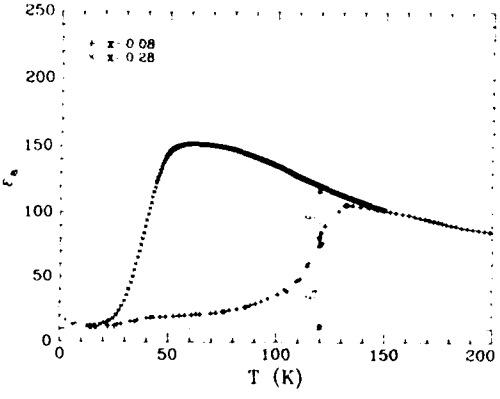


Figure 5: Real part of the dielectric permittivity ϵ_a' for the deuterated mixed crystals at 1 kHz as a function of temperature along the a axis. ϵ_∞' is assumed to be 10.

In Fig. 4 we notice a drop in the spontaneous polarization for the pure sample below 153 K. This effect was seen in two separate samples. Below 120 K the hysteresis loops could not be saturated because the necessary electric field would exceed the dielectric breakdown field of the crystal. However, saturated loops appeared above 120 K with increasing polarization as temperature was increased. This effect could indicate pinning of ferroelectric domains due to crystal defects or impurities at lower temperatures, thus giving a reduced value of spontaneous polarization. Further investigation of this effect is planned.

The experimental results show that deuteration increases the maximum value of the spontaneous polarization in the pure crystals. Also, the maximum value of the spontaneous polarization in the mixed crystals is lower than that of the pure crystal. This indicates that at the lowest temperatures recorded

there are still paraelectric clusters intimately interlocked with the ferroelectric clusters. This type of coexistence is also seen[13] down to 5 K from dielectric permittivity in these RADA mixed crystals. The gradual increase in spontaneous polarization below T_c in the mixed crystals follows the gradual decrease in the dielectric constant of the corresponding crystals below T_c.

The authors would like to thank Dr. S. Waplak for his encouragement in getting this project started and Dr. S.L. Hutton for automating the dielectric permittivity apparatus. This work was supported by National Science Foundation Grant DMR-9017429 and Department of Energy Equipment Grant DOE-FG05-91ER79046.

References

[1] E. Courtens, "Competing structural orderings and transitions to glass in mixed crystals of $Rb_{1-x}(NH_4)_xH_2PO_4$," J. Phys. Lett. **43**, L-199 (1982).

[2] C.B. Sawyer and C.H. Tower, "Rochelle Salt As A Dielectric," Phys. Rev. **35**, 269 (1930).

[3] A. Levstik, C. Filipič, Z. Kutnjak, I. Levstik, R. Pirc, B. Tadič and R. Blinc, "Field-Cooled and Zero-Field-Cooled Dielectric Susceptibility in Deuteron Glasses," Phys. Rev. Lett. **66**, 2368 (1991).

[4] N.J. Pinto, K. Ravindran, V.H. Schmidt and S.L. Hutton, "Field-cooled and Zero-field-cooled Static Susceptibility of DRADA," Bull. Am. Phys. Soc. **37**, 236 (1992).

[5] G.A. Samara, "The Effects of Deuteration on the Static Ferroelectric Properties of KH_2PO_4 (KDP)," Ferroelectrics **5**, 25 (1973).

[6] B.A. Strukov, A. Baddur, V.N. Zinenko, A.V. Mishchenko and V.A. Koptsik, "Isotopic Effect in RbH_2PO_4 crystals," Sov. Phys. Solid State **15**, 939 (1973).

[7] C.W. Fairall and W. Reese, "Thermodynamic Properties of KH_2AsO_4 and KD_2AsO_4," Phys. Rev. B **6**, 193 (1972).

[8] I.S. Zheludev, V.V. Gladkii, E.V. Sidnenko and V.K. Magataev, "Dielectric Nonlinearity and Phase Transition in KH_2PO_4-Type Crystals," Ferroelectrics **8**, 567 (1974).

[9] L.N. Kamysheva, Yu.S. Zolototrubov and S.A. Gridnev, "Dielectric Properties of RbH_2AsO_4," Ferroelectrics **8**, 559 (1974).

[10] S.A. Gridnev, L.N. Korotkov, L.A. Shuvalov and R.M. Fedosyuk, "Dielectric and Polarization Properties of Single Crystals of Solid Solutions of KDP-ADP in the vicinity of the Phase Transitions," Sov. Phys. Solid State **36**, 522 (1991).

[11] E. Courtens, "Structural Glasses and $Rb_{1-x}(NH_4)_xH_2PO_4$," Helv. Phys. Acta, **56**, 705 (1983).

[12] Y. Ono, T. Hikita and T. Ikeda, "Glassy Dielectric Behavior in the Mixed Crystal System $K_{1-x}(NH_4)_xH_2PO_4$," Ferroelectrics **79**, 327 (1988).

[13] F.L. Howell, N.J. Pinto and V.H. Schmidt, "Complex Permittivity of the Deuterated and Undeuterated Proton Glass $Rb_{1-x}(NH_4)_xH_2AsO_4$," to appear in Phys. Rev. B **46** (1992).

[14] N.J. Pinto, S. Waplak, S.L. Hutton, F.L. Howell and V.H. Schmidt, "Spontaneous Polarization in the Proton Glass $Rb_{1-x}(NH_4)_xH_2AsO_4$," Bull. Am. Phys. Soc. **37**, 287 (1992).

[15] J.P. DeLooze, B. MacG. Campbell, N.S. Dalal and R. Blinc, "Isotope Effects in the Phase Diagram of the $(NH_4)_xRb_{1-x}H_2AsO_4$ Proton Glass," Physica B **162**, 1 (1990).

[16] Z. Trybula, V.H. Schmidt and J.E. Drumheller, "Coexistence of Proton Glass and Ferroelectric order in $Rb_{1-x}(NH_4)_xH_2AsO_4$," Phys. Rev. B **43**, 1287 (1991).

[17] R. Blinc, M. Burgar and A. Levstik, "On The Order Of The Phase Transition In KDA Type Ferroelectric Crystals," Solid State Commun. **12**, 573 (1973).

INVESTIGATION OF FERROELECTRIC AND PYROELECTRIC PROPERTIES OF CERAMICS WITH COMPOSITION $Ba(Li_{2x}Al_{2-2x})O_{4-4x}F_{4x}(0\leq x\leq 0.3)$

Sui-Yang HUANG, R.VON DER MÜHLL, J.RAVEZ and P.HAGENMULLER
Laboratoire de Chimie du Solide du CNRS, Université Bordeaux I, 351 cours de la Libération, 33405 Talence Cedex, France.

ABSTRACT

Structural, ferroelectric, pyroelectric and dielectric relaxation properties of ceramics with composition $Ba(Li_{2x}Al_{2-2x})O_{4-4x}F_{4x}(0\leq x\leq 0.3)$ have been investigated. XRD patterns show a lattice close to that of $BaAl_2O_4$. The parameters increase with rising x up to x=0.1 and then remain constant. The Curie temperature T_C decreases regularly from T_C=396K(x=0) down to T_C=324K(x=0.1) and then increases again with x up to T_C=460K(x=0.3). The values of the spontaneous polarization P_s are in the range 1-22 $nC.cm^{-2}$. The solid solutions seem to be of weak ferroelectric type with a maximum of P_s around 200K and low values of ε_r', the pyroelectric coefficient p and P_s. A dielectric relaxation is detected for $Ba(Li_{0.4}Al_{1.6})O_{3.2}F_{0.8}$ with a relaxation frequency from 10^2 to 10^4Hz between 300 and 520K. A model accounting for weak ferroelectricity is proposed.

1.INTRODUCTION

Single crystals of composition $BaLi_{2x}Al_{2-2x}O_{4-4x}F_{4x}$ ($0.15\leq x\leq 0.3$) have been prepared by Dunne and Stemple and the XRD patterns are very close to that of hexagonal $BaAl_2O_4$[1]. The crystals have been claimed to be ferroelectric with a Curie point T_C=400-426K. Hysteresis loop has been observed for a crystal with composition x=0.2 at 300K and the spontaneous polarizations P_s for the solid solutions are in the range 80-140 $nC.cm^{-2}$. However, the experimental error reported on ε_r' was about 100% and that for P_s about 30%. The Curie temperature T_C seems not to be related to the composition. No further investigation for the compound has been reported since this first study.

The purpose of the present work is to determine the composition limits of the solid solution domain and to investigate the dielectric, pyroelectric and relaxation properties of the corresponding ceramics. A model for explaining the ferroelectricity in the materials is suggested.

2.EXPERIMENT

$BaAl_2O_4$ powder is first prepared by firing in air at 1573K for 30h a stoichiometric mixture of $BaCO_3$ (Merck 99%) and $Al(OH)_3$ (Prolabo 99.0%):

$$2BaCO_3 + 4Al(OH)_3 \rightarrow 2BaAl_2O_4 + 6H_2O + 2CO_2$$

The XRD patterns may be indexed with the hexagonal unit cell parameters a=10.449(1)Å and c=8.793(1)Å. The solid solution ceramics were then synthesized by solid state reaction:

$$(1-x)BaAl_2O_4 + x(BaF_2 + 2LiF) \rightarrow Ba(Li_{2x}Al_{2-2x})O_{4-4x}F_{4x}$$

The starting materials BaF_2(Merck 99.0%), LiF(Merck 99.0%) and previously prepared $BaAl_2O_4$ were ground and then pressed with an uniaxial pressure of 390MPa. The pellets obtained (8mm in diameter and about 2mm thickness) have been sintered in platinum sealed tubes under oxygen atmosphere at 1613-1773K for 2h. The XRD patterns of the ceramics showed that solid solutions appear between x=0 and 0.3.

3.RESULTS AND DISCUSSION

3.1.X-ray diffraction and microstructure

The XRD patterns of the ceramic surface and ground ceramic powders were recorded at room temperature by 0.02° step counting and a time counting of 12 seconds. The solid solutions crystallize with hexagonal symmetry. The parameters determined by a least-square method are reported in Fig.1. The variation of a and c for ceramic surface differ from that

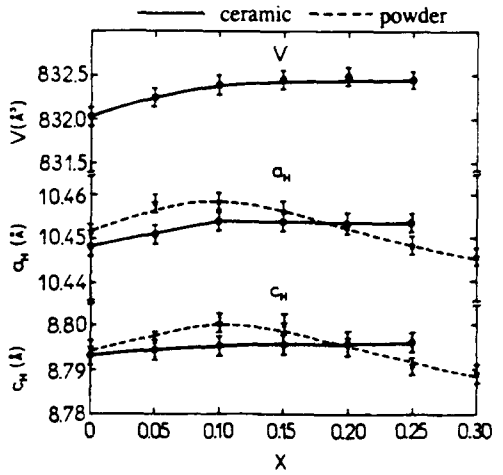


Fig.1 Variation of the lattice parameters a,c and unit cell volume V with x.

of powders of the bulk. This phenomenon results probably either from stresses developed within the grains or from the deformation of the grains during sintering, it had been previously observed by Ye and al.[2] in ceramics of $LiTaO_3$-type.

For a ground ceramic powder the lattice parameter a rises first with substitution rate x up to 0.1, and then remains constant. The c-parameter increases slowly with rising x in the whole homogeneity range. The unit cell volume V

CH3080-0-7803-0465-9/92$3.00 ©IEEE

increases between x=0 and 0.1 and becomes then practically constant for x>0.1. The substitution of Li^+(r_{Li^+}(IV)=0.59Å) for Al^{3+}($r_{Al^{3+}}$(IV)= 0.39Å) involves a unit cell dilatation for 0≤x≤0.1. For x>0.1 we can only suppose that the increase of the F/O ratio gives a tendency to an ordering of F^- around Li^+ and O^{2-} around Al^{3+}. Slight modifications in the structure can then occur and allow a constant value for cell volume.

The solid solution is isostructural with $BaAl_2O_4$ related to the β-tridymite[3]. The [AlO_4] tetrahedra are linked by corners to form layers perpendicular to the c-axis. The layers are connected to build up a three-dimensional framework. The asymmetric unit encloses three crystallographically independent cavities. These cavities are filled by the large 9-coordinated Ba atoms. We have drawed $BaAl_2O_4$ lattice by the computer program "STRUPLO 84"[4] using Hörkner's data[3]. Fig.2 shows the projections along (0001) and (10$\bar{1}$0). After coupled substitution of Li for Al and F for O, Li atoms occupy the tetrahedral sites and F replaces O.

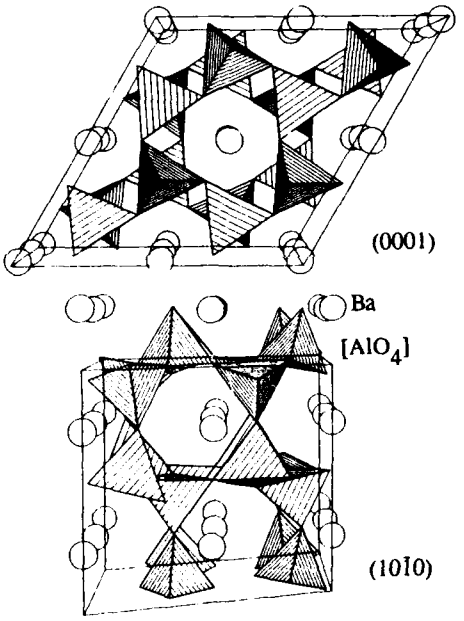


Fig.2 Projection of $BaAl_2O_4$ along (0001) and (10$\bar{1}$0).

3.2.Ferroelectric properties

The capacitance and dielectric losses of pellets measured using gold electrodes have been recorded between 120 and 800K in a 20-300kHz frequency range . The temperature evolution of the permittivity ε_r' and tanδ are reported in Fig.3 for $BaAl_2O_4$. A maximum of ε_r' corresponds to a decrease of tanδ at T_C=396K. This value is in good agreement with that reported for a single crystal with composition $Ba_{0.98}(Al_{0.999}Cu_{0.001})_2O_{4-\delta}$[5]. Fig.4 shows the frequency and temperature dependence of permittivities ε_r' and ε_r'' for the solid solution $BaLi_{0.4}Al_{1.6}O_{3.2}F_{0.8}$. The frequency dispersion both in ε_r' and ε_r'' is obvious. The variation of T_C vs x is given in Fig.5. T_C

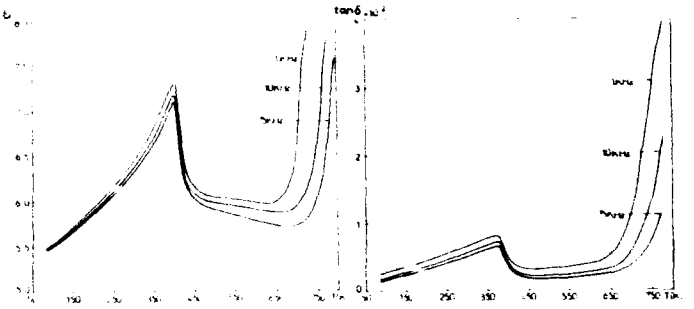


Fig.3 Temperature dependences of ε_r' and tanδ for a $BaAl_2O_4$ ceramic.

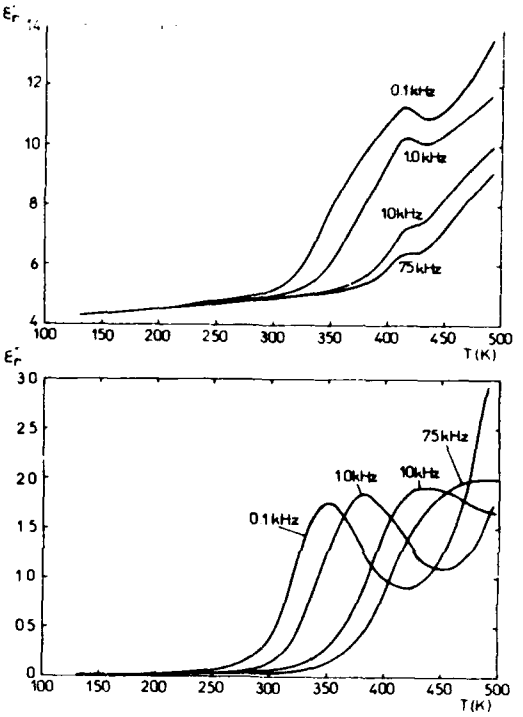


Fig.4 Temperature evolution of ε_r' and ε_r'' for a $BaLi_{0.4}Al_{1.6}O_{3.2}F_{0.8}$ ceramic.

decreases first with rising x up to 0.1 and then increases. The spontaneous polarization results from the atomic displacement Δz of the central atom Al(Li) in the tetrahedra along the polar axis from its position in the paraelectric phase. The substitution of a bigger Li^+ cation

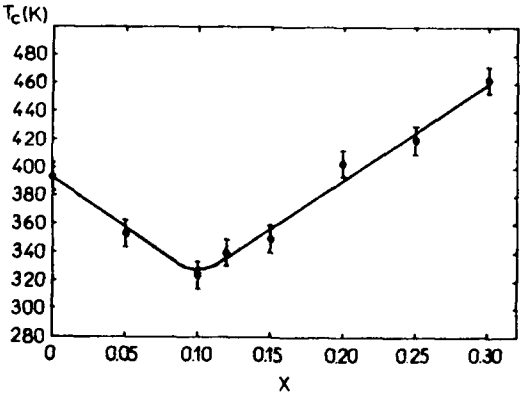


Fig.5 Evolution of the Curie point T_C vs x for $BaLi_{2x}Al_{2-2x}O_{4-4x}F_{4x}$.

for Al^{3+} leads to decrease of T_C, the increase in size of the central atom limiting its shift in the tetrahedral site. For $x>0.1$, the increase T_C-value implies certainly a small structural change which did not appear in the XRD patterns.

3.3.Pyroelectric properties

Pyroelectric measurements have been performed on ceramic samples by a thermal depolarization method[6]. They were first poled by heating at the temperature $T_p=T_C-30K$ with a dc field of 10-14kV/cm for 3 mn. The samples are short-circuited after polarization at the same temperature for 10h to eliminate the space charges. The measurements were performed with a heating rate of 6K/min. The thermal variation of the pyroelectric coefficient p calculated from the pyrocurrent is reported in Fig.6 and that of spontaneous polarization P_s in Fig.7. P_s increases first with temperature, it reaches a maximum at

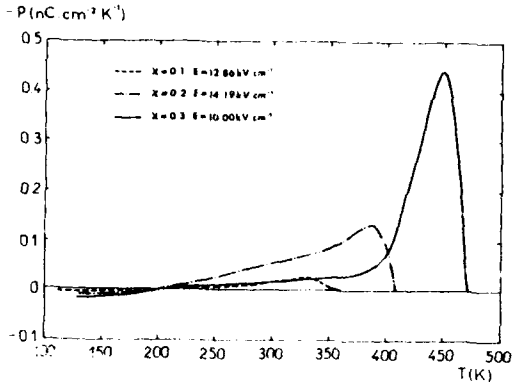


Fig.6 Thermal variation of the pyroelectric coefficient p for ceramics corresponding to x=0.1, 0.2 and 0.3.

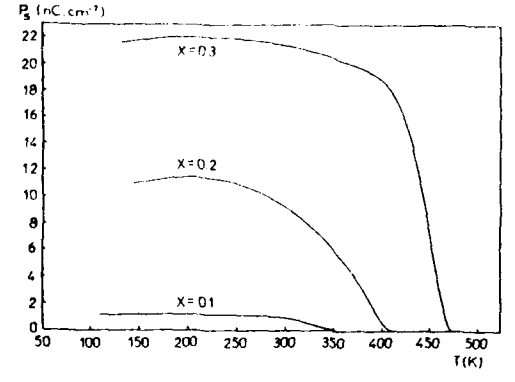


Fig.7 Temperature dependence of the spontaneous P_S for 0.1,0.2 and 0.3.

T_m=200K and then decreases down to zero at the Curie point. This unusual behavior was previously found for the single crystal $Ba_{0.98}(Al_{0.999}Cu_{0.001})_2O_{4-\delta}$ [5] for the ceramic $BaAl_2O_4$ and also for some other materials, e.g. $Li_2Ge_7O_{15}$[7] and $CsCoPO_4$[8]. These ferroelectrics have weak a permittivity ε_r' and a Curie constant C at T_C and they present an unsual behavior of the thermal dependence of the spontaneous polarization. By comparison with proper ferroelectrics, e.g. $BaTiO_3$, they are called "weak ferroelectrics" by Tagantsev[9]. Some models have been proposed to explain the "weak ferroelectricity" since the 70's, between both most important ones the first is the two nonequivalent sublattice (TNS) model[9,10] and the second is the pseudoinherent-ferroelectric model[11,12]. We suggest an "imperfect antiferroelectric" model by modifing the TNS model. In the average structure (Fig.2) there are two types of $[AlO_4]$ tetrahedra, their spontaneous polarization vectors are opposite. The situation is similar to that of the antiferroelectrics, the spontaneous polarizations in $BaAl_2O_4$ are opposite, but nonequivalent, so that they don't fully compensate. A strong coupling between sublattice polarizations drastically reduces the values of the Curie constant and the permittivity and gives a maximum in the temperature variation of spontaneous polarization P_S.

3.4.Dielectric relaxation

The frequency dependence of the real ε_r' and imaginary part ε_r'' of the permittivity is shown in Fig.8 at various temperatures for the composition $Ba(Li_{0.4}Al_{1.6})O_{3.2}F_{0.8}$. A dielectric relaxation is detected in both ferroelectric and paraelectric phases. The temperature dependence of the relaxation frequency f_r is reported in Fig.9. Log f_r varies linearly vs 1/T in both ferroelectric and paraelectric states, even around T_C, following an Arrhenius law. The activation

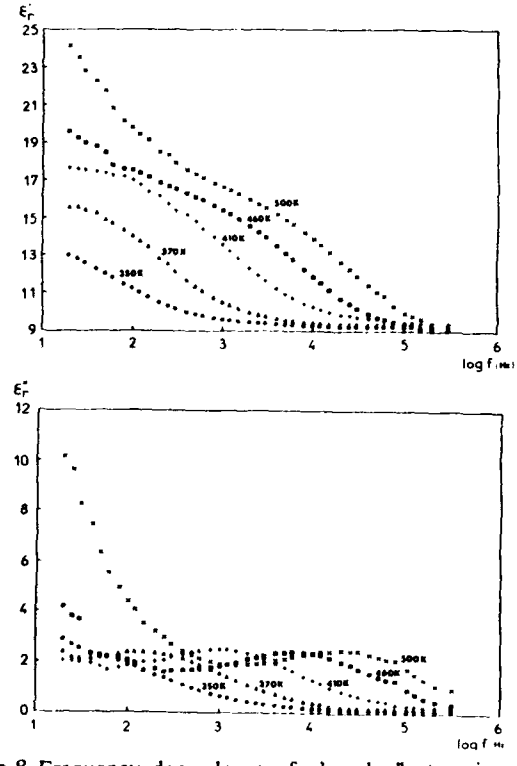


Fig.8 Frequency dependence of ε_r' and ε_r'' at various temperatures for a $BaLi_{0.4}Al_{1.6}O_{3.2}F_{0.8}$ ceramic.

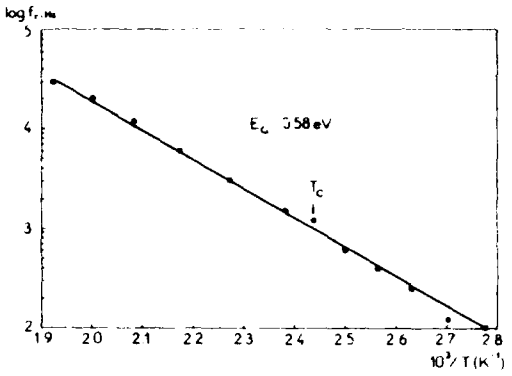


Fig.9 Temperature dependence of the relaxation frequency f_r for $BaLi_{0.4}Al_{1.6}O_{3.2}F_{0.8}$.

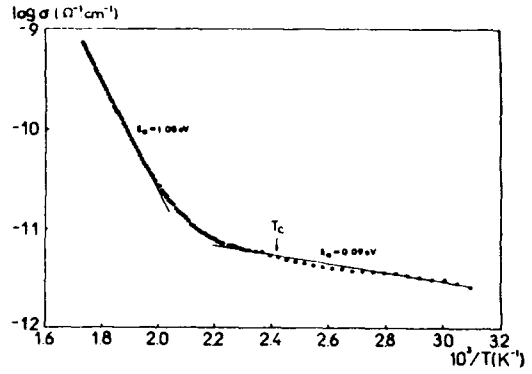


Fig.10 Variation of the dc conductivity vs 1/T for $BaLi_{0.4}Al_{1.6}O_{3.2}F_{0.8}$.

energy E_a=0.58eV is relatively small. These results let us suppose that the relaxation is not related to intrinsic polarization but may be caused by charge carrier displacement. Fig.10 gives the variation of the dc conductivity vs 1/T for the same sample. The curve slope below T_C is different from that above T_C. It shows two mechanisms of dc conductivity. In the solid solution $Ba(Li_{0.4}Al_{1.6})O_{3.2}F_{0.8}$, Li^+ and F^- ions are smaller and their charges are weak. Below T_C, the dc conductivity results likely from free charges due to ceramic defaults. In the high temperature phase $T>T_C$, the mobility of the Li^+ and F^- ions increases the dc conductivity. We may think that mixed Li^+/F^- ions give rise to the relaxation.

4.CONCLUSIONS

The ferroelectric and pyroelectric properties and the dielectric relaxation have been investigated. A relation between the Curie point T_C and the compositon rate x seems to exist. The Curie point T_C decreases first with rising x and then increases linearly. The results show that the material is a weak ferroelectric. An "imperfect antiferroelectric" model modified from a previous TNS model has been proposed to account for the unusual ferroelectric and pyroelectric properties. The measurement of temperature dependences of ε_r' and ε_r'' vs frequency in the range 20-300kHz shows a dielectric relaxation phenomenon with a relaxation frequency $f_r=10^2$-10^4Hz between 360 and 520K with appearance of an Arrhenius law. The relaxation is related to Li^+ and F^- ion.

REFERENCES

[1]T.G.Dunne and N.R.Stemple,"Ferroelectric Properties of $BaLi_{2x}Al_{2-2x}F_{4x}O_{4-4x}$," Physical Review, Vol.120, n.6, pp.1949-1950, December 1960.

[2]Zuo-Guang Ye, R.Von Der Mühll, J. Ravez et P.Hagenmuller, "Etudes Physico-chimiques d'une Nouvelle Phase Hydroxofluoree Ferroélectrique de Type $LiTaO_3$," J.Phys.Chem.Solids, Vol.49, n.10,pp. 1153-1158, 1988.

[3]W.Hörkner and Hk.Müller-Buschbaum, "Zur Kristall- struktur von $BaAl_2O_4$," Z.anorg.allg.Chem. Vol.451, pp.40-44, 1979.

[4]R.X.Fischer, "STRUPLO84, a Fortran plot program for crystal structure illustrations in polyhedral representation," J.Appl.Cryst., Vol.18, pp.258-262, 1985.

[5]A.A.Bush and A.G.Laptev, "Dielectric and pyroelectric properties of $BaAl_2O_4$ single crystals," Fiz.Tverd.Tela, Vol.31, pp.317-318, March 1989.

[6]R.L.Byer and C.B.Roundy, "Pyroelectric coefficient direct measurement technique and application to a NSEC response time detector," Ferroelectrics, Vol.3. pp.333-338, 1972.

[7]A.A.Bush and Yu.N.Venevtsev, "Pyroelectric properties of $Li_2Ge_7O_{15}$ ferroelectric single crystals," Fiz.Tverd.Tela,Vol.28, pp.1970-1975, July 1986.

[8]D.Blum, J.C.Peuzin and J.Y.Henry, "MM'PO_4, A new family of ferroic compounds," Ferroelectrics, Vol.61, pp.265-279, 1984.

[9]A.K.Tagantsev, I.G.Sini and S.D.Prokhorova, "Weak ferroelectrics," Izvestva Akademii.Nauk SSSR, Ser.Fiz., Vol.51, n.12, pp.2082-2089, 1987.

[10]V.Dvorak and Y.Ishibashi, "Two-Sublattice Model of Ferroelectric Phase Transitions," J.Phys.Soc.Japan, Vol.41, n.2, August 1976.

[11]J.Kobayashi, Y.Enomoto and Y.Sato, "A Phenomenological Theory of Dielectric and Mechanical Properties of Iinproper Ferroelectric Crystals," Phys.Stat.Sol.(b), Vol.50, pp.335-343, 1972.

[12]K.Gesi, ""Improper" Ferroelectric Properties of $NaNO_2$ and $AgNa(NO_2)_2$," Phys.Stat.Sol.(a), Vol.15, pp.653-658, 1973.

Microsensors and Microactuators

FERROELECTRIC MICROSENSORS AND MICROACTUATORS

Dennis L. Polla
Center for Microelectromechanical Systems
Department of Electrical Engineering
200 Union Street S.E. (4-178)
University of Minnesota
Minneapolis, Minnesota 55455
(612) 625-4873

ABSTRACT

Ferroelectric thin films have been integrated with silicon micromachined structures to form micromechanical pressure sensors and infrared detectors. These devices are based on the piezoelectric and pyroelectric effects in $Pb(Zr_xTi_{1-x})O_3$ and $PbTiO_3$ thin films, respectively. Surface-micromachining techniques have been used to form structures which are easily deformable for mechanical force sensing or exhibit a low thermal mass and low thermal conductivity to the substrate for infrared detection applications. The ferroelectric and surface-micromachining technologies presented have furthermore been shown to be compatible with a 3-μm CMOS technology. Both microsensors and microactuators have been fabricated using ferroelectric thin film technology. Representative examples in this work are 1) a pyroelectric infrared detector array, 2) acoustic pressure sensors, 3) micromechanical linear positioner, and 4) piezoelectric microactuator.

INTRODUCTION

Ferroelectric thin films have recently been shown to be promising materials for microsensor applications.[1-4] They are particularly attractive in that can be incorporated into sensor structures in a wide variety of configurations and can be operated by using either direct charge detection or wave/resonance type phenomena. Ferroelectric materials offer the possibility of enhanced performance in these applications due to the extremely high electromechanical coupling coefficients (~200 pC/N for lead zirconate titanate). We have integrated sol-gel deposition methods for lead zirconate titanate (PZT) and lead titanate ($PbTiO_3$) with surface micromachining techniques to produce microsensor structures on silicon-based micromechanical structures, i.e., thin mechanical membranes of polycrystalline silicon or silicon nitride. These include piezoelectric pressure sensors and pyroelectric infrared detector arrays.

A basic cross section of a typical micromechanical structure used in both the pressure sensor and infrared detector structures of this paper is shown in Fig. 1. For the pressure sensor we specifically design the membrane to easily deform in response to an applied force such as that associated with acoustic energy. For the pyroelectric detector we specifically design useful thermal properties into the detector pixel. These are low thermal mass, low thermal conductance from the detector element to the substrate, and low thermal cross talk between pixels.

MATERIALS

The ferroelectric thin films (PZT and $PbTiO_3$) used in the device structures of this work were deposited by sol-gel spin casting. The films were dispensed in successive 800-900 Å spin-coatings and fired at 650 °C for 30 minutes. The selection of these materials is based on the ability to achieve extremely high piezoelectric and pyroelectric coefficients through simple chemical modifications of the starting materials.

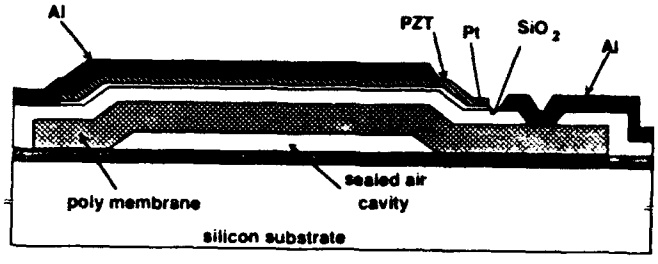


Fig. 1. Cross section of a micromachined sensor structure with ferroelectric active thin films. The piezoelectric material is PZT for mechanical microsensor applications and $PbTiO_3$ for pyroelectric detector applications. Solid-state micromachining is used to form air gaps to allow either mechanical deformation or low thermal conductivity in pressure sensor and infrared detection applications, respectively.

Sol-gel processing of piezoelectric materials has the advantage of greater compositional control over sputter-deposition, and therefore the flexibility in optimizing film properties for a particular microsensor or microactuator application. Sol-gel derived films must be deposited by spin or dip coating. Several sol-gel deposition techniques have been previously reported.[5-7] To date, only sol-gel deposition techniques using alkoxide precursors have been used for microsensor[8] and microactuator applications.[9,10]

PZT films with various ratios of zirconate to titanate have been prepared by sol-gel methods in our laboratory. The device work discussed below used films of 54% zirconate to 46% titanate. This ratio lies near the morphotropic phase boundary and can be expected to exhibit strong piezoelectric properties, although the validity of the bulk material phase picture for these thin film samples still remains an open question. These films have exhibited excellent microstructure[10] and good ferroelectric properties (Table I), although some variation with deposited film thickness has been observed. The ability to achieve proper crystallization of the piezoelectric films is critical and is aided by the use of a platinum nucleation electrode formed by sputter deposition prior to sol-gel deposition.

Considerable study has been carried out in our laboratory on the dependence of film microstructure on the sol-gel precursors[12] and on optimizing the sol-gels to obtain dense films. Films between 0.2 and 1.0 μm have been deposited on platinum substrates, and this thickness range is adequate for sensor applications. Thicker films are however susceptible to cracking and further study of the coating process is necessary.

Test samples of the 54/46 PZT were fabricated using a platinum lower electrode and gold upper electrode. Some representative results are shown in Table 1. Piezoelectric properties (see Fig. 2) were measured by a load cell technique on film samples without the top electrode. Pyroelectric properties

CH3080-0-7803-0465-9/92$3.00 ©IEEE

were measured on test structures utilizing bulk micromachining techniques, where the substrate underneath the film test area was etched away. A plot of the pyroelectric coefficient vs. temperature is shown in Fig. 3. These values demonstrate the viability of thin film forms of PZT for sensing schemes based on charge detection.

The piezoelectric voltage developed across the film thickness is directly proportional to the piezoelectric coefficients, with contributions from both the d_{33} and d_{31} coefficients. The actual voltage developed is inversely proportional to the capacitance per unit area of the film. This suggests that, particularly for the case of pyroelectric detection, sensor performance could be improved by encapsulation of the PZT with a low dielectric constant insulator. A high quality insulator would also alleviate the problem of charge leakage through the ferroelectric film.

Table 1 Summary of measured ferroelectric thin film electrical and mechanical properties.

Parameter	PZT(54/46)	$PbTiO_3$	$PbZrO_3$	La-$PbTiO_3$
Piezoelectric Coefficient d_{33} (pC/N)	190-250	20	240	200
Pyroelectric Coefficient (nC/cm^{2}K)	50 - 70	75 - 96	---	65
Dielectric Constant	800 - 1100	80-120	100	110
Resistivity (Ω-cm)	10^7-10^8	10^7-10^8	10^8	10^8
Loss Tangent (tan δ) ($x10^{-3}$)	10-20	18-30	20	4

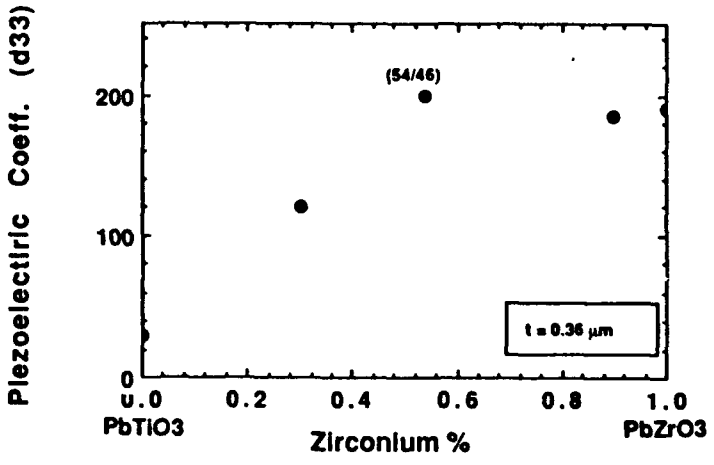


Fig. 2. Measured piezoelectric coefficient d_{33} in PZT (54/46) thin films.

Prior knowledge of the mechanical properties of the constituent materials are also important to the design of microsensors and microactuators. In particular, the internal stress and Young's modulus of the composite membrane is important in determining the mechanical properties of the device and its associated electrical response. Fig. 4 shows a plot of the measured effective Young's modulus in PZT thin films of varying thickness.

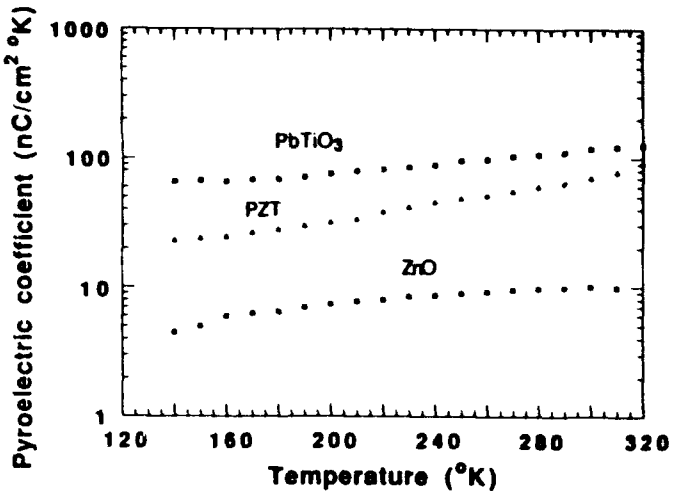


Fig. 3. Measured pyroelectric coefficient in ferroelectric thin films PZT and $PbTiO_3$ and non-ferroelectric ZnO.

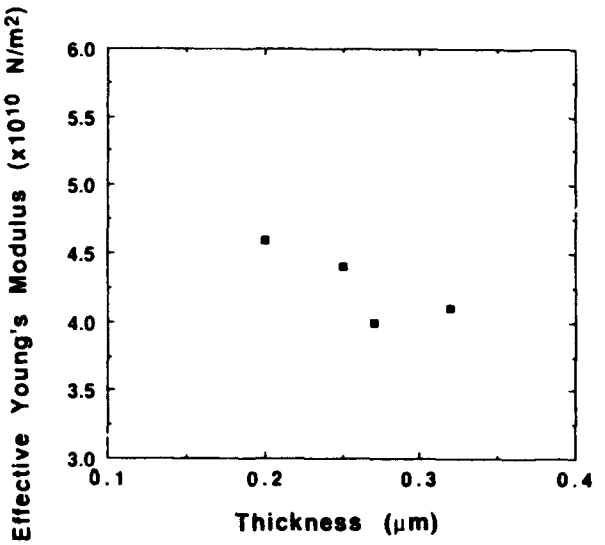


Fig. 4. Measured effective Young's modulus E/(1-v) for sol-gel deposited PZT thin films.

MICROMACHINING

Micromachining refers to the materials processing techniques used to form useful micromechanical structures. Two general forms are used: bulk-micromachining and surface-micromachining. The major difference lies in the removal of the backside substrate or a sacrificial layer from the surface of the wafer. Of the two approaches, we believe surface-micromachining holds more promise for smart sensor systems for the following reasons: 1) no two-sided photolithography is required, 2) no non-standard chemicals are used, 3) precise dimensional control can be achieved, and 4) the mechanical integrity of the substrate is not weakened.

Ferroelectric fabrication begins with either MOS circuits processed up to the point of source-drain contact opening if integrated microsensor structures are to be made or with Si_3N_4/SiO_2 covered silicon substrates if off-chip electronics are to be used. A 0.3 μm-thick layer of low-pressure-chemical-vapor-deposited (LPCVD) silicon nitride and a 0.8 μm-thick layer of phosphosilicate glass (PSG) are first deposited at 800 °C

and 450 °C, respectively. The silicon nitride layer forms an encapsulation layer to protect the almost finished CMOS circuitry from subsequent processing of the on-chip sensors and the PSG serves as the sacrificial oxide spacer used in the formation of sensor membrane structures. The PSG is patterned and chemically etched to form anchor regions for a subsequent phosphorus-doped polysilicon microstructure membrane deposition (by LPCVD). Sensor membrane regions are defined and anisotropically patterned in a SF_6/CCL_2F_2 plasma by reactive-ion-etching (RIE). A high-temperature anneal at 1050 °C for one hour is performed in a nitrogen ambient to improve polysilicon stress properties. A 500-1000 Å-thick lower platinum electrode is then sputtered over the entire wafer. The platinum serves the dual purpose of providing an adhesion/nucleation surface for the subsequently deposited PZT of $PbTiO_3$ thin film and serves as the lower electrode for piezoelectric and pyroelectric microsensors.

Sol-gel spin-casting of ferroelectric PZT or $PbTiO_3$ is then carried out as previously described. The ferroelectric films are then patterned by either chemical etching or ion beam sputter etching. Photolithography is then used to protect the ferroelectric thin films in carrying out a lateral sacrificial etching step of the PSG layer. This step is commonly called surface-micromachining. Doubly-supported, suspended, structures are released using 48 wt% hydrofluoric acid to undercut the PSG spacer layer. The polysilicon membrane therefore forms an easily deformable structure desirable for force sensing or a low thermal mass structure necessary for pyroelectric detection. For pressure sensors, the open side walls of the microbridge are sealed by the directional sputtering of silicon dioxide.

A top electrode to the ferroelectric thin film is then deposited by Ti/Au evaporation. Contact openings to both the CMOS transistors and sensor bottom polysilicon electrode are then chemically etched. This is followed by sputtering aluminum (2% Si) to form interconnects and bonding pads.

A representative fabrication outline is described in Fig. 5.

MICROSTRUCTURE AND CIRCUIT INTEGRATION

Integrating ferroelectric thin films with silicon-based micromechanical structures requires several process considerations. First, the micromechanical structures used in this work are based on the surface-machining of thin film polycrystalline silicon membranes formed 0.7-1.5 µm above the surface of a silicon wafer. The polycrystalline silicon membrane forms the mechanical support of the microstructure and implements desirable properties such as a compliant membrane or low thermal mass structure. Although we have also used tungsten and silicon nitride as micromechanical support materials, polycrystalline silicon represents a material which can be easily tailored to have a wide range of mechanical and/or electrical properties through simple adjustments in device geometry, thickness, and process deposition conditions. Second, Ti-Pt is used as the lower electrode for $Pb(Zr_xTi_{1-x})O_3$ thin films. This serves as a nucleation surface and prevents the chemical interaction of the $Pb(Zr_xTi_{1-x})O_3$ thin film with the polycrystalline silicon membrane. Third, step coverage issues are important in the spinning of the solution over the elevated micromechanical structure. Fourth, cracking of the $Pb(Zr_xTi_{1-x})O_3$ material is observed for film thicknesses greater than 1.0 µm. Fifth, electrical fatigue characteristics are believed to be dependent on the top electrode material. In our work both gold and platinum have been used. Finally, the resulting composite membrane structure must exhibit sufficient mechanical strength to undergo typical deformations encountered in both microsensing and microactuation.

There are several key sensor-circuit integration challenges: 1) realization of highly oriented ferroelectric thin films on micromechanical membranes, 2) compatible merging of ferroelectric thin film deposition techniques with a high performance analog circuit processes, and 3) the ability to carry out necessary micromachining techniques while ensuring the integrity of both microsensors and circuits.

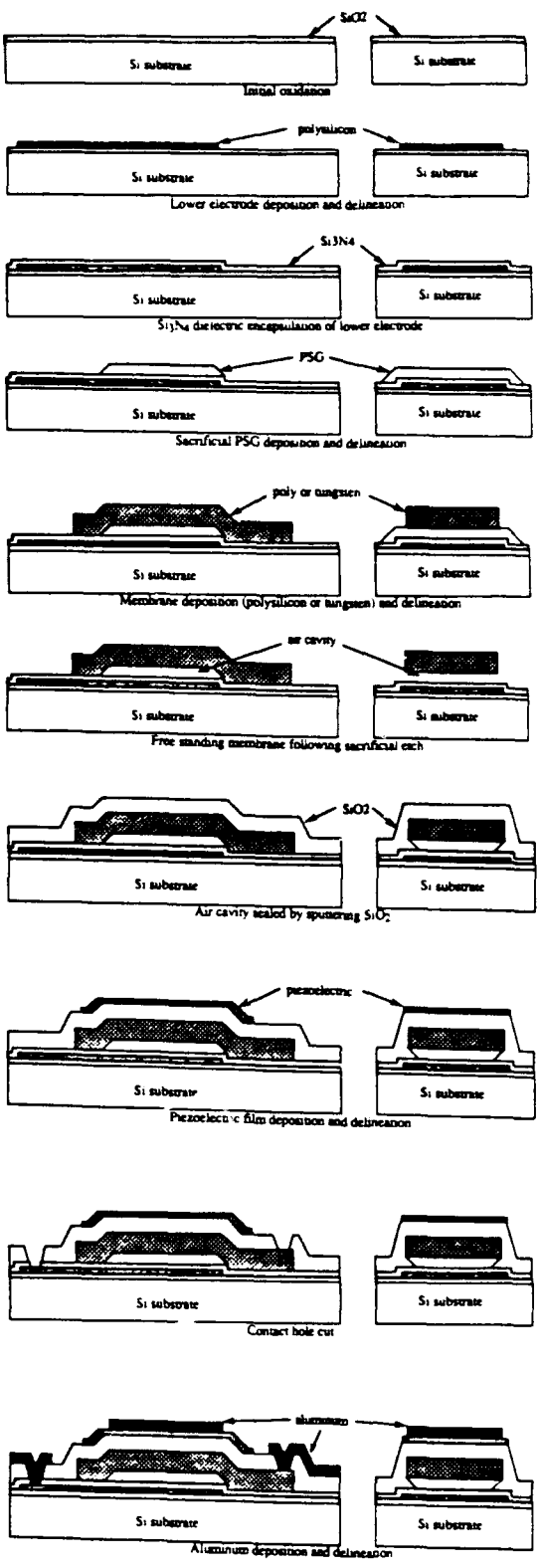


Fig. 5. Representative surface-micromachining steps involved in the fabrication of ferroelectric thin film sensors.

A representative current-voltage characteristic for an on-chip depletion mode NMOS transistor is shown in Fig. 6. A custom high-voltage NMOS process has been developed to allow integration of ferroelectric thin films with microactuator structures. For the PZT thin films prepared in our laboratory, typical breakdown voltages are 6 to 9 x 10^5 V/cm. This implies maximum operating voltages of 20 to 100 V for most devices applications.

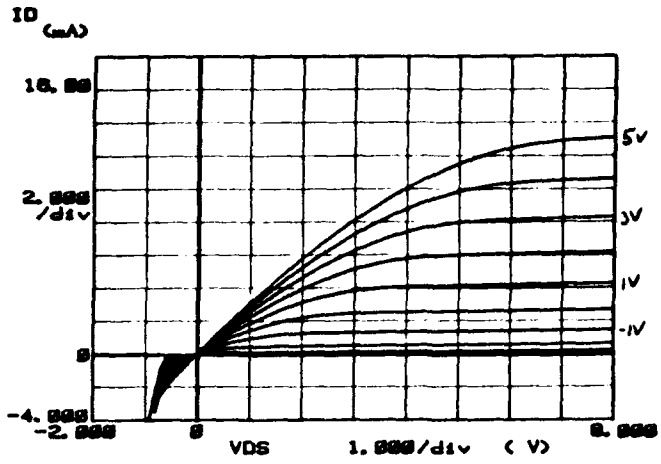


Fig. 6. Current-voltage characteristic of an integrated circuit fabricated with on-chip PZT piezoelectric microactuators (microvalves).

PYROELECTRIC INFRARED DETECTORS

Pyroelectric detectors have long been used for room-temperature infrared sensing applications. These detectors are usually limited by thermal losses to an ambient heat sink and parasitic interconnection losses when integrated with hybrid circuitry[13-15]. This paper uses solid-state micromachining techniques to minimize conductive heat losses to achieve thermal isolation between detector elements. Polysilicon is used as a microbridge to form pyroelectric infrared detector structures with an extremely low frequency operation due to conductive heat losses.

Pyroelectric materials are well known in their application as room-temperature infrared detector elements. In this work the integration of sol-gel deposited lead titanate ($PbTiO_3$) thin films on 1.0 μm-thick polycrystalline silicon micromachined membranes for pyroelectric sensing. While other $PbTiO_3$ infrared detector structures have been previously reported the unique aspects of this work are 1) the sol-gel deposition of $PbTiO_3$ thin films for infrared detector applications, 2) the integration of $PbTiO_3$ thin films on low thermal mass polycrystalline silicon membranes through the use of solid-state micromachining techniques, and 3) demonstration of fabrication compatibility with silicon MOS electronics.

Devices incorporating micromachined components and integrated circuits reported in the past have been implemented in such a way that microsensors and integrated circuits occupy separate areas on the chip or involve bump interconnection of two substrates. Chips implemented in this manner often have long interconnections from the sensors to the signal processing circuits especially in applications involving two-dimensional arrays and complex signal processing circuits. This often degrades sensor performance due to parasitic losses.

This paper describes a vertical integration approach to alleviate these problems. In this approach the sensors are fabricated on top of the integrated circuits and the interconnections between the sensors and the signal processing circuits are formed via contact openings. This implementation saves chip area since the sensor array, integrated circuits, and routing circuits virtually occupy the same area.

Each microsensor generates charge through pyroelectric effect which is the result of the alteration of the internal dipole moment of the capacitor film through a change in temperature. This change in temperature produces a displacement current parallel to the polar axis given by

$$I = Ap(T)\frac{dT}{dt} \qquad (1)$$

where p(T) is the pyroelectric coefficient evaluated at temperature T and A is the surface area normal to the polar axis. For response times greater than the thermal time constant the responsivity, r, of the pyroelectric element is described by [14]

$$r = \frac{V}{W(\omega)} = \frac{p(T)R_L}{\rho c_p d(1 + [\omega R_L(C_a + C_c)]^2)^{\frac{1}{2}}} \qquad (2)$$

where R_L is the equivalent parallel resistance of the detector and load resistor, ρ is the density, c_p is the heat capacity, d is the thickness of the detector element, C_a is the amplifier capacitance, and C_c is the capacitance of the detector element.

Diagnostic 64 x 64 element pyroelectric infrared imager chips have been fabricated as a demonstration vehicle for the three-dimensional integrated microsensor concept. Fig. 7 shows the three-dimensional cross section of a cell. A standard 3-μm NMOS process is first carried out through the point of first contact openings. A 0.5 μm-thick LPCVD silicon nitride film is then blanket-deposited to protect the circuits. Back-end polysilicon microstructure machining [6] and microsensor fabrication processes are then carried out. Surface-micromachined 1.2 μm thick polysilicon thin membranes are formed 0.8 μm above the surface of a silicon wafer. Each of the 4096 polysilicon microbridges measure 50 x 50 μm^2 with 75 μm pitch has its own simple preamplifier fabricated directly beneath an air gap. Sol gel deposition of $PbTiO_3$ on the heavily-doped polysilicon membrane was used to form each pyroelectric element [7]. Each 0.36 μm-thick $PbTiO_3$ thin film sensor measures 30 x 30 μm^2 and generates charge through the pyroelectric effect (p = 90±5 $nC/cm^2\text{-}^oK$ for $PbTiO_3$). The fabrication process requires five sensor masking steps in addition to the standard NMOS process. An optical photograph of a finished die is shown in Fig. 8.

Sensor and circuit characterization were carried out in atmosphere at room temperature. The circuits in the diagnostic chips were completely functional with no observable shift in threshold voltages or degradation of mobility due to the back end micromachining and microsensor fabrication steps.

Fig. 9 shows the performance characteristics of a $PbTiO_3$ pyroelectric element. The measured blackbody voltage responsivity for a $PbTiO_3$ pyroelectric element at 297 K and a chopping frequency of 50 Hz is 4.0×10^4 V/W. The measured normalized detectivity D^* at 297 K and 30 Hz is 4×10^8 $cm\text{-}Hz^{1/2}/W$.

The infrared imaging chip was operated in a serially scanned mode. All elements were functional. No adjacent element responsivity has observed under single element infrared exposure. The voltage gain for the on chip circuitry is approximately 48 dB and demonstrates the functionality of the imager. Further systems work is required to make this a practical imaging device.

We have selected $PbTiO_3$ as the pyroelectric thin film material. The fact that this material is easy to process by sol-gel deposition directly on heavily-doped polysilicon membranes greatly simplifies fabrication. Further work underway suggests that the responsivity of this device can be improved through intentional lanthanum doping of the $PbTiO_3$.

Device and circuit characterization were carried out prior to and after microsensor processing. No significant degradation was apparent. In addition, it appears that the chip area per sensor can be significantly reduced by use of surface micromachining rather than bulk-machining methods. The ability to fabricate these microsensors in VLSI NMOS processes suggests further integration of ferroelectric sensors with high-density standard cell analog and digital building blocks.

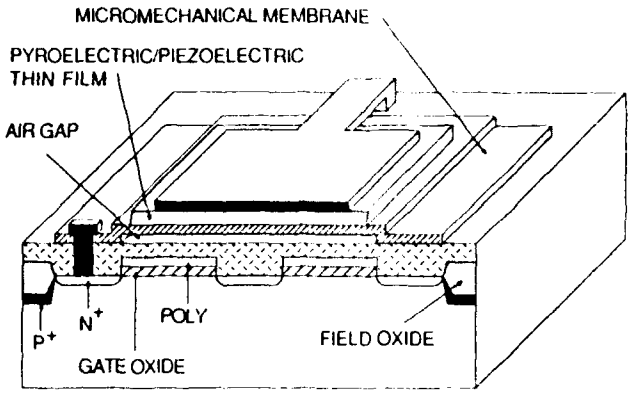


Fig. 7. Cross section of vertical integrated microsensor concept. Solid-state micromachining is used to form an air bridge immediately above the preamplifier circuit.

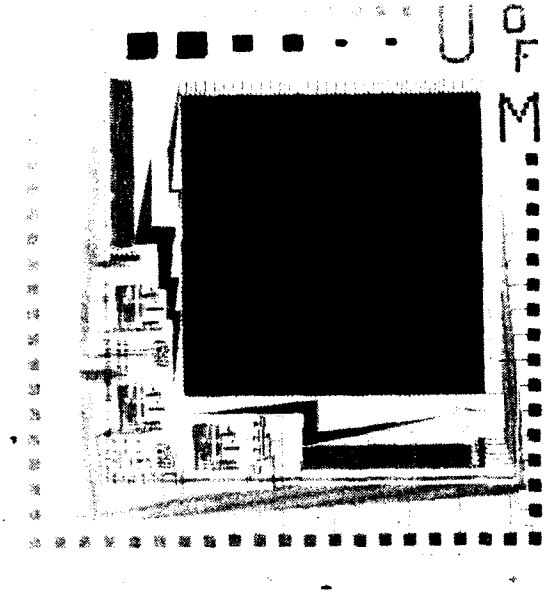


Fig. 8. 64 x 64 element infrared imager fabricated using NMOS circuits, $PbTiO_3$ ferroelectric thin films, and polysilicon microbridge technologies.

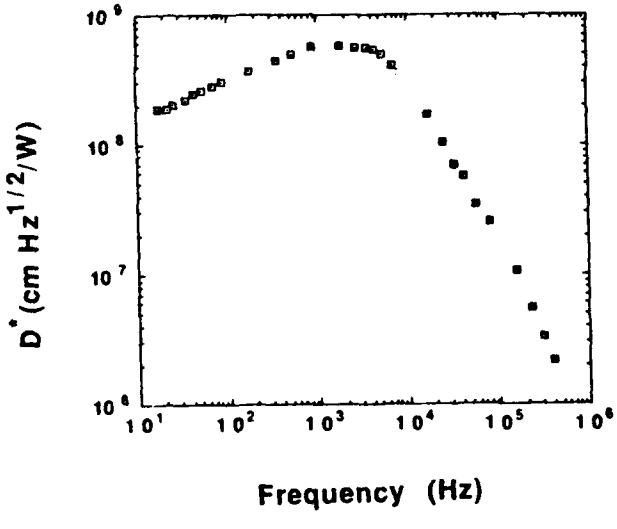


Fig. 9. Detector performance measured in a $PbTiO_3$ infrared detector element.

MICROMACHINED PRESSURE SENSORS

Modeling of the piezoelectric sensor is done using the basic theory of mechanical beams. The beam is a layered structure of support material (polycrystalline silicon), bottom electrode (Ti/Pt), piezoelectric material (PZT), and top electrode (Pt). The thin film mechanical properties of the materials involved, with the exception of PZT have been previously studied. Some preliminary data has been obtained on PZT by our group.[16] A closed form solution can be obtained assuming that the deflections are small relative to the sensor dimensions and assuming a simple set of boundary conditions at the edges of the beam. It has been shown by Choi[17] that for the materials involved, assuming typical beam dimensions of between 10 and 100 μm on a side, the vertical deflection even under a pressure excitation of 1 mbar is only on the order of 10 nm. Thus, the assumption of small deflections is justified and the sensor would not be expected to bottom out. Piezoelectric charge is induced normal to the piezoelectric film surface. The contribution of charge directly due to the normal pressure component (proportional to the d_{33} coefficient) is relatively insignificant compared to that due to the transverse strain of the beam as it deforms (proportional to the d_{31} coefficient) under the excitation. The induced charge then produces a voltage signal inversely proportional to the capacitance/unit area of the piezoelectric film. The induced charge/unit area at each point on the sensor varies greatly over the sensor area, as it is proportional to the induced stress. However, the voltage across the film is constrained to a single value due to the presence of the top and bottom electrodes. To find this voltage, the induced charge/unit area can be integrated over the sensor area and this total charge divided by the capacitance of the electrode bounded piezoelectric film. Alternatively, an average stress component (σ_{xy}) can be calculated and this quantity then divided by the capacitance per unit area. The relationship of the key quantities in the sensitivity figure (S) are as follows:

$$S \sim \frac{d_{31}\sigma_{xy}}{\epsilon / t} \qquad (2)$$

where ϵ is the thin film dielectric constant with thickness t.

The voltage sensitivity of ferroelectric film sensors with their very large d_{31} coefficients is therefore not necessarily greatly enhanced over that of sensors made with non-ferroelectric piezoelectric films. However, the signal charge/unit area is enhanced by two orders of magnitude over such non-ferroelectric materials as ZnO and AlN. This allows voltage amplification by using composite dielectric structures and also greatly improves the signal-to-noise situation.

Piezoelectric pressure sensors based on $Pb(Zr_xTi_{1-x})O_3$ thin films have been fabricated in a silicon IC-compatible process using surface micromachining techniques. The diagnostic pressure sensors fabricated in this work have dimensions ranging from 20 x 20 μm^2 to 250 x 250 μm^2 and make use of 0.45 μm-thick $Pb(Zr_xTi_{1-x})O_3$ piezoelectric capacitors supported 0.8 μm above the silicon substrate on 1.6 μm-thick deformable polycrystalline silicon membranes. Fig. 10 shows the unamplified voltage of a $Pb(Zr_xTi_{1-x})O_3$ pressure sensor as a function of acoustic pressure.

MICROACTUATORS

Novel micropositioning actuators has been fabricated based on the inverse piezoelectric effect. The basic device shown in Fig. 11 is implemented in a geometry of N piezoelectric bars connected in a meander line configuration which are mechanically in series and electrically in parallel[10]. Each bar is electroded on two opposing faces parallel to the length of the bar with electrical connection made to the terminals of a dc variable power supply. The piezoelectric polarity between bars is alternated to achieve linear expansion and linear contraction in adjacent bars. Because both

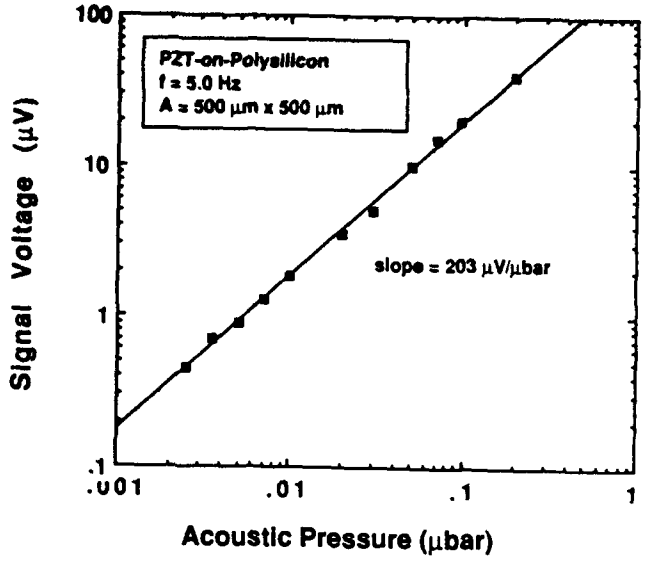


Fig. 10. Acoustic pressure sensor responsivity using a PZT thin film on a surface-micromachined membrane.

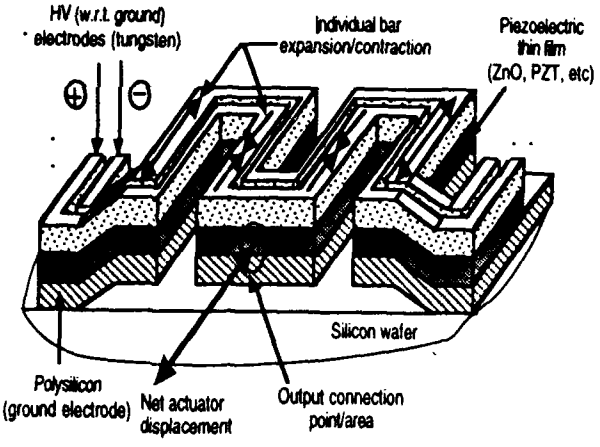


Fig. 11. Schematic of micromeanderline positioner.

ends of the meanderline are anchored to a silicon substrate, the center of the meander line experiences a forward displacement equal to N times the change in length of a single piezoelectric bar. An additive displacement is therefore obtained. The folded geometry allows substantially large displacement to be obtained on a microfabricated chip.

The positioning force obtained from the meanderline has been derived by Robbins[10]. The force F_{pz} is given by

$$F_{pz} \approx 2 E d_{31} w V \qquad (3)$$

where V is the applied voltage, w is the width of the piezoelectric bar, d_{31} is the piezoelectric coupling constant, and E is Young's modulus.

Initial results obtained for this device are currently encouraging. Linear displacements have been achieved in the range of 0 - 4 μm as shown in Fig. 12. Problems have been encountered in the the fabrication of this device due to the long effective length over which mechanical integrity of the structure is to be maintained.

Diagnostic microvalves have also been fabricated using PZT thin film technology and polycrystalline silicon cantilever membranes. These device structures are similar to the generic device shown in Fig. 1 but are singly supported in the form of a cantilever. These device have been actuated to achieve vertical deflection of the tip. Tip deflections measured using an optical microscope are approximately 4 μm. Further details of this work will be presented elsewhere as this work progresses.

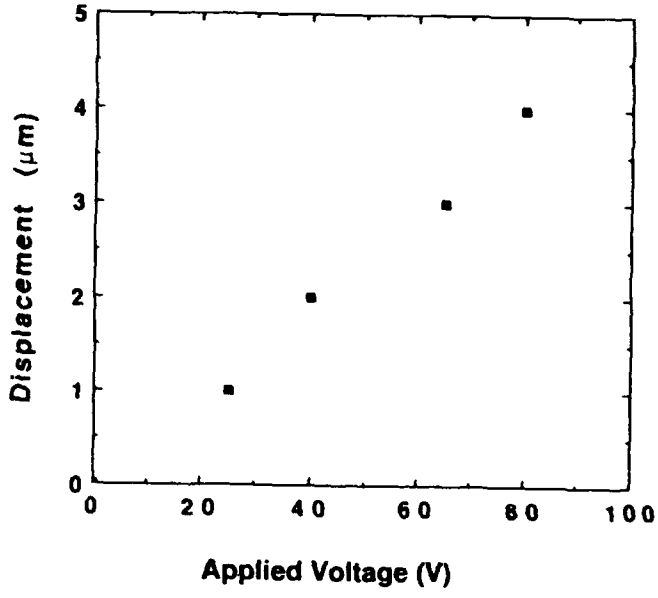


Fig. 12. Measured displacement of microfabricated PZT meanderline positioner. The device consists of 16 piezoelectric expander bars.

CONCLUSIONS

In conclusion, we have demonstrated the integration of sol-gel ferroelectric films into micromachined sensor structures. The primary advantage of PZT over other piezoelectric thin films is its large piezoelectric effect. The primary advantage of $PbTiO_3$ lies in its extremely high pyroelectric coefficient. The nature of the sol-gel deposition process and micromachining techniques is compatible with conventional integrated circuit technologies and may offer a high performance, low-weight, solution to future smart guidance and navigation applications.

For the pyroelectric infrared detectors described in this work, sol-gel deposited $PbTiO_3$ thin films have been integrated with polycrystalline silicon microstructures and analog CMOS circuits. Solid-state micromachining techniques have been applied in the formation of a thin film polycrystalline silicon membranes for reduced thermal mass and air gaps for thermal isolation purposes. Sol-gel deposited $PbTiO_3$ offers a significantly higher pyroelectric coefficient than other IC-compatible thin film materials and is compatible with CMOS integrated circuit processing technologies. The extremely high pyroelectric coefficient attainable in $PbTiO_3$ thin films deposited on polycrystalline silicon micro-bridges suggests further pyroelectric or deformable membrane piezoelectric microsensing applications.

For the piezoelectric pressure sensor and microactuators presented, surface-micromachining techniques have been used to form deformable polysilicon membranes. Deformation strains are transduced to an overlaying PZT piezoelectric thin film in sensing and generated during actuation. The advantages of piezoelectric sensing include the high signal-to-noise ratio and low power consumption. The strong advantage of piezoelectric microactuators lies in their ability to generate extremely large forces when compared to other actuation methods operating at equivalent voltages and low currents.

ACKNOWLEDGEMENTS

This work was supported by the National Science Foundation Presidential Young Investigator program. The author would like to acknowledge contributions from his students and the following colleagues: Professor William P. Robbins, Dr. Takashi Tamagawa, and Dr. Chian ping Ye.

REFERENCES

1. T. Tamagawa, D. L. Polla, and C.-C. Hsueh, *IEEE International Electron Devices Meeting*, San Francisco, Technical Digest, p. 617, Dec. 1990.
2. D. L. Polla, C. Ye, and T. Tamagawa, "Surface-Micromachining of $PbTiO_3$ Pyroelectric Detectors," *Appl. Phys. Lett.* 59, p. 3539, 1991.
3. M. Sayer, "Integrated Piezoelectric and Pyroelectric Devices from Thin Film Ferroelectrics," *Mat. Res. Soc.* 1991 Fall Meeting, Boston, MA, Dec. 1991.
4. P. Schiller C. Ye, T. Tamagawa, and D. L. Polla, "Design and Process Considerations for Ferroelectric Film-Based Piezoelectric Pressure Sensors," *4th International Symposium on Integrated Ferroelectrics*, Monterey, CA, Mar. 1992.
5. R. W. Vest and J. Xu, "$PbTiO_3$ Films for Metalloorganic Precursors," *IEEE Trans. on Ultrasonics, Ferroelectrics, and Frequency Control*, 35, p. 711 1988.
6. G. Yi, Z. Wu, and M. Sayer, "Preparation of $Pb(Zr,Ti)O_3$ Thin Films by Sol Gel Processing: Electrical, Optical, and Electro-Optic Properties, *J. Appl. Phys.*, 64, p. 2717 1988.
7. S. K. Dey and R. Zuleeg, "Integrated Sol-Gel PZT Thin-Films on Pt, Si, and GaAs for Non-Volatile Memory Applications," *Ferroelectrics*, 108, p. 37 , 1990.
8. T. Tamagawa, C. Ye, C.-C. Hsueh, and D.L. Polla, "Sol-gel Derived Lead Zirconate Titanate (PZT) Films,"*3rd International Symposium on Integrated Ferroelectrics*, Colorado Springs, CO, Mar. 1991.
9. K. R. Udayakumar, S. F. Bart, A. M. Flynn, J. Chen, L. S. Tavrow, L. E. Cross, R. A. Brooks, D. J. Ehrlich, *IEEE Micro Electro Mechanical Systems*, Nara, Japan, Proceedings, p. 109, 1991.
10. W. P. Robbins, *IEEE Trans. on Ultrasonics, Ferroelectrics, and Frequency Control*, UFFC-38, p. 461 1991.
11. D. L. Polla, C. Ye, P. Schiller, and T. Tamagawa, "Application of PZT and Related Thin Films in Piezoelectric Microsensors," *Mat. Res. Soc.* 1991 Fall Meeting, Boston, MA, Dec. 1991.
12. C. Ye, T. Tamagawa, Y. Lin, and D. L. Polla, "Pyroelectric Microsensors by Sol-Gel Derived $PbTiO_3$ and La-$PbTiO_3$ Thin Films," (I 1.9), *Mater. Res. Soc.*, 1991 Fall Meeting, Boston, MA, 1991.
13. S. T. Liu and D. Long, "Pyroelectric Detectors and Materials," *Proc. of the IEEE* 66, pp. 14-26, 1978.
14. E. H. Putley, "The Pyroelectric Detector," *Semiconductors and Semimetals*, Vol. 5, R. K. Willardson and A. C. Beer (eds.), Academic Press, New York, 1970.
15. R. L. Byer and C. B. Roundy, "Pyroelectric Coefficient by Direct Measurement Technique and Application to a nsec Response Time Detector," *IEEE Trans. Sonics & Ultrasonics*, 3, p. 333, 1972.
16. E. L. Dereniak and D. G. Crowe, Optical Radiation Detectors, Wiley, New York, 1984.
17. W. Tjhen, C.-P. Ye, P. Schiller, T. Tamagawa, and D. L. Polla, "Properties of Piezoelectric Thin Films for Micromechanical Devices and Systems," *3rd IEEE Workshop on Micro Electro Mechanical Systems*, Nara, Japan, Jan. 1991.
18. J. Choi, "GaAs Microsensors," Ph.D. thesis, University of Minnesota, 1991.

Piezoelectrics and Electrostrictives

MODIFIED LEAD CONTAINING PEROVSKITE CERAMICS FOR ELECTROOPTIC, ELECTROCALORIC, PYROELECTRIC AND ELECTROSTRICTIVE APPLICATIONS

A.Sternberg, L.Shebanov, E.Birks, M.Ozolinsh, V.Dimza, and E.Klotins

Institute of Solid State Physics, University of Latvia, 8 Kengaraga St., LV-1063 Riga, LATVIA

Abstract: The authors discuss the physical background of the feasible diversity of modified lead-containing perovskite ceramic compositions with field-induced first order and diffused phase transitions, a number of particular model devices being considered. Specific changes of structure and properties of the PLZT ceramics doped with 3d-elements and radiation efects in some of the compositions are examined.

Introduction

The present report is an attempt to represent from a common point of view the most recent results and trends in possible applications and studies of modified lead-containing perovskite ceramics. The nature of the phase transition and the state of polarization are important for the efficiency of any special application.

Electrocaloric effect

Considerable interest has been recently paid [1-3] to electrocaloric effect (ECE) - a general property of dielectric substances to change their temperature under electric field applied under adiabatic conditions (ΔT_{ECE}). A large ECE is expected at field-induced first order phase transition (PT) in ferroelectrics (FE). Potential applications - energy conversion (the absolutely higher values of ΔT_{ECE} obtained so far equal to 2.6 K and belong to ceramic composition $Pb_{0.99}Nb_{0.02}(Zr_{0.75}Sn_{0.20}Ti_{0.05})_{0.98}O_3$ [4], of the three-component solid solution series which is referred once more hereafter concerning the large field-induced deformation), cascade microcryogenic devices.

The $PbSc_{0.5}Ti_{0.5}O_3$ (PST) solid solutions are found to be a useful material for active elements for the last [2]. A temperature difference of ΔT_{ECE}=1.0-1.8 K at field intensities 20-30 kV/cm in the interval of 210-310 K can be achieved by simultaneous or separate isomorphic substitution of Sb and Co ions in B-sites of the lattice (the greatest value in the temperature range now). This is due to structure rearrangement at the PT (a large volume jump ΔV=0.078 Å^3) and a high degree of the Sc and Ta ion ordering (Ω=0.85-0.90) at field-induced paraelectric (PE) - ferroelectric (FE) phase transition Fm3m - R3m.

To maintain a high ECE in modified PST solid solution it is necessary to satisfy the following requirements:

- to keep a high ordering of trivalent and pentavalent ions in the B-sites;
- the substituting ions must have a high electronic polarizability;
- stability of the initial structure should not be lost by overtension of A-O and B-O bonds.

Characteristics of the structure , PT and ECE of some doped PST solutions are given in Table 1.

Table 1

Characteristics of structure and ECE of doped lead-scandium tantalate solid solutions

Dopant	Shift ΔT_m,K	ECE ΔT_{ECE},K	Amount of pyrochlore, % vol.	Nature of PT
In	-20	0.80	8	diffused
Ga	-14	0.75	7.6	sharp
Mn	-38	0.25	3.8	strongly diffused
Ni	-32	0.50	0	diffused
Fe	-12	0.85	1.9	sharp
Co	**-10**	**1.30**	**0**	**sharp**
Zn	-12	0.75	1.18	diffused
Y	-18	1.40	0	sharp
V	+4	0.70	0	diffused
Sb	**-19**	**1.50**	**1**	**sharp**
Nb	+7	1.10	0	sharp
Ti	+11	1.25	2	sharp
Zr	+10	0.85	3	diffused
Hf	+8	0.60	5	diffused
Sn	-17	0.70	4.4	diffused

Note. Applied field intensity ~ 25 kV/cm. Amount of dopant - 10 mole %. Shift of ECE maximum temperature ΔT_m is given with respect to the temperature of ECE maximum T_m=295 K in undoped PST.

The highest value of ΔT_{ECE} obtained by optimization of technology has reached 2.3 deg at 50 kV/cm and +7°C temperature (2 deg at standard field of 25 kV/cm).

Introduction of the film (e.g.,tape casting) techniques to reduce operating voltage of the active ECE element as well as fabricating of MLC's to achieve higher electric field strengths (Dr.W.Lawless - private communication) seem to be next step in ECE active elements technology.

PST solutions (black coated, e.g., by matrix electrodes, ceramics plates) in the range of a strong dependence of the ECE on applied field intensity, and fast response ($\sim 10^{-6}$ sec) may find application of high sensitivity and high resolution (~0,1 K) thermal image modelling and IR detector testing.

Electrostriction

High values of longitudinal strain (~0.87%) have been observed [5] in the $Pb_{0.97}La_{0.02}(Zr_{0.66}Ti_{0.11}Sn_{0.23})O_3$ composition of $Pb(Zr,Sn,Ti)O_3$ tripple solid solution system, mentioned hereabove, at room temperature at the field-enforced PT from antiferroelectric (AFE) to FE state. A switching time of <1 μs was detected (under field >30 kV/cm).

By optimization of the technological cycle (hot pressing, thermal treatment) improving ceramics microstructure and phase homogeneity we have obtained

CH3080-0-7803-0465-9/92$3.00 ©IEEE

the value of relative deformation in the composition about ~1.4% at the field of ~40 kV/cm. A field-enforced transition from tetragonal AFE to rhombohedric FE phase has been observed by X-ray studies at 20°C (obtained unit cell parameter values: a_T=4.119±0.001 Å; c_T=4.095±0.001 Å; V_T=69.48±0.04 Å^3 in the AFE phase and a_R=4.1181±0.0006 Å; α_R=89.80±0.02 deg; V_R=69.83±0.02 Å^3 in the FE phase. A small change of entropy at the AFE to FE phase transition (opposite to the case of ECE where a large entropy jump at the FE to PE phase transition is utilized) explains the weak dependence of the critical field on temperature. It is worth to notice that pronounced first order PT properties including double hysteresis loops amongst oxygen perovskite ceramics are observed only if the FE and PE phases transfer to AFE phase. It may be related to supposedly exclusive first order character of the AFE-PE transitions, explaining extremely high parameter values characteristic to the Pb(Zr, Sn, Ti)O_3 solid solution series and related to field-induced first order PT: field-enforced strain and ECE.

However, there is a number of problems like hysteresis, nonanalytic deformation-field dependence, and fatigue effect, regardless to the extremely high values of electric field-controlled strain considerably exceeding the ones of the relevant parameters of classic electrostrictive materials and "giant electrostriction" in FE relaxors, (e.g., in PMN-PT, PMN-PSN and PLZT X/65/35 compositions the value of Q_{11} is more than 0.02 m^4/C^2). In FE relaxor materials in the region of the strongly diffused PT at the field-induced change from macroscopically nonpolarized to FE state the growth, orientation and merging of polar microregions is followed by high mechanical strains proportional to polarization P square ($s_{11}=Q_{11}P_1^2$). Material returns to its nonpolarized state upon removal of the applied field. The longitudinal electrooptic (EO) effect and electrostriction (providing the most essential contribution, about 60%, to the optical path variation) are used in the electrically-controlled Fabry-Perot near IR interferometer without polarizers [6]. ITO electrodes are applied to opposite faces of PLZT ceramics plane parallel plate of thickness ~1 mm. The quarter-wave voltage $U_{\lambda/4}$ at λ=3.39 μm has been 510 V and 2100 V for PLZT 8.5/65/35 and 10/65/35, respectively (contrast ratio - 9:1).

Pyroelectric effect

The lead-containing perovskite ceramics including modified PZT are distinguished by a relatively high values of the pyroelectric coefficients and used in pyroelectric IR detectors. We have developed a design for light switches and alarm devices. The concentrator of radiation is shaped as a cone (instead of mirrors or lenses) simplifying its production. Sensitivity of the device having the form of cylinder is easily varied within wide limits by the size of the latter. The radiation can be detected from a narrow spatial angle. At the length of 150 mm and diameter of 50 mm the operating distance is up to 15 m.

Electrooptic effect.

The most familiar transparent ferroelectric ceramics (TFC) system PLZT is a typical FE relaxor material and a diffused PT model, maintainig a high value of the quadratic EO-coefficients (R~5.10^{-16} m^2/V^2) in a rather wide temperature range [7]. The optical axis in TFC can be induced and controlled by applied electric field (mechanic tension, temperature, irradiation) and a ceramic microstructure allow for reversion of local microregions without the change of polarization in surrounding matrix. TFC has a number of applications in optoelectronic devices, some of them being developed at the University of Latvia:

- wide aperture modulators [7] ("Pulsar" series), using parallel plate of interdigital type (engraved) electrodes of rise-time in microsecond region; apperture up to 70 mm;
- a PLZT frequency shifter [8] (20 kHz) as well as a voltage-controlled PLZT $\lambda/4$ phase plate have been introduced in the laser heterodyne interferometer for automatic displacement measurements with the accurracy ±10 nm and 1 Hz display update rate (see optical arrangement of interferometer in the Fig.1).

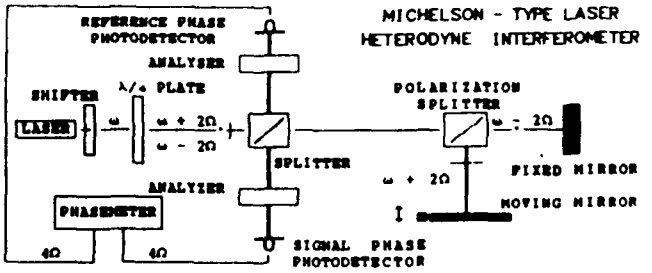


FIGURE 1. Optical arrangement of a PLZT Michelson type laser heterodyne interferometer.

- a commercial version of low voltage PLZT ceramics Kerr cell with computer controlled DC and AC voltage sources for didactic use, classroom demonstrations, and transfer of information by laser beam [9-10] (see experimental set-up on Fig.2). Such modulators can also be successful as choppers in lock-in amplifier techniques.

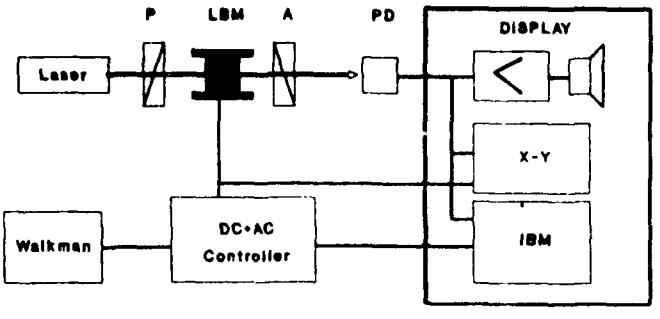


FIGURE 2. Experimental set-up of Kerr cell demonstrations.

- a PLZT modulator for computer-controlled CW laser beam (He-Ne, λ=0.633; 1.15 μm, YAG:Nd) intensity manipulation for biological and medical purposes. To avoid the effects due to some instability of the values of PLZT EO-coefficients with temperature and time as well as to obtain a linear input-output EO-conversion the modulator is provided with a voltage controller using a photoelectric feedback. The controller can be drived by an analog or digital (8 bit) periodical or chaotic electric signal, providing optical output with no less than 20 gray scale levels; duration of pulse step - less than 0.5 msec; rise and decay time - <0.2 msec.
- an intracavity matrix adressed (30x30 programmable scanning elements of 0.45x0.45 mm^2 clear aperture) PLZT spatial-time modulator is demonstrated with a pulse YAG:Nd laser [11]. A diffraction limited beam quality and 10 μsec direction exchange time have been achieved; optical threshold energy up to 11 J/cm^2 (a schematic picture of the device is given in Fig.3). The losses caused by PLZT here are compensated by additional pumping of the output radiation intensity. Laser pointing, location and projection are possible applications.

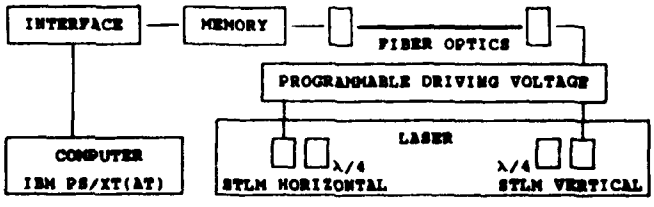


FIGURE 3. A schematic picture of the integrated duplex mode electrode laser switching arrangement.

Doping with 3-d elements

A series of experiments have been made [12-15] to study the effects of 3d-dopants on the structure, the optical, dielectric and mechanical properties of PLZT 8/65/35 ceramics. On the other hand, introducing of small amounts of admixture has allowed to obtain more information about a number of fundamental phenomena in solids: relaxor FE phase transitions, Jahn-Teller effect, ordering etc. in perovskite structures.
Examination of Mn and Fe dopant effects has shown that Mn^{3+} and Fe^{4+} are the dominating forms of admixture ions in the perovskite lattice which means that Jahn-Teller (d^4) configurations are most preferred. A small fraction (no more than 1%) of Mn ions are introduced as Mn^{2+} ions. The J-T ($Fe^{4+}Mn^{3+}$) centres are activators while the other ones (Fe^{3+}, Mn^{2+}) may be used for EPR sounding of the lattice environment.
The J-T centres interacting with soft mode vibrations promote the shift of FE phase transition to higher temperature, represent elementary dipoles (at medium temperature) and cause the polar distortion of the elementary cell (at low temperature).
The processes observed at doping provide some suggestions concerning the properties of PLZT material. The Raman spectra of PLZT show bands characteristic to disordered solids (Fig.4, bands I, II) which correlate with EPR signal with g_{eff}~4.3 and with the $\mathcal{E}^*$ dispersion at 10^4 -10^7 Hz (Fig.5, region II). La^{3+} ions obviously are responsible for the distortion of oxygen octahedra and "relaxing" Ti ions in the off-site positions inside the octahedra. Thus, La^{3+} ions are responsible for localized distortions of the lattice (O_6^{2-} octahedra) and the increase of the concentration of additional elementary dipoles, on the one hand, and prevents the long-range ordering of the A-sublattice, on the other.
The manifestations of the lattice interaction with the J-T centres of modified PLZT are seen in:
- optical absorption [12];
- $\mathcal{E}^*(\nu,T,t)$, P(E) (Fig.5) [15] and $\Delta 1/1(F)$ behaviour [12];
- Raman spectra (central plate broadening) (Fig.4) [13];
- electromechanic and elastic properties [12];
- X-ray diffraction [12];
- EPR dependence on admixture concentration [14].

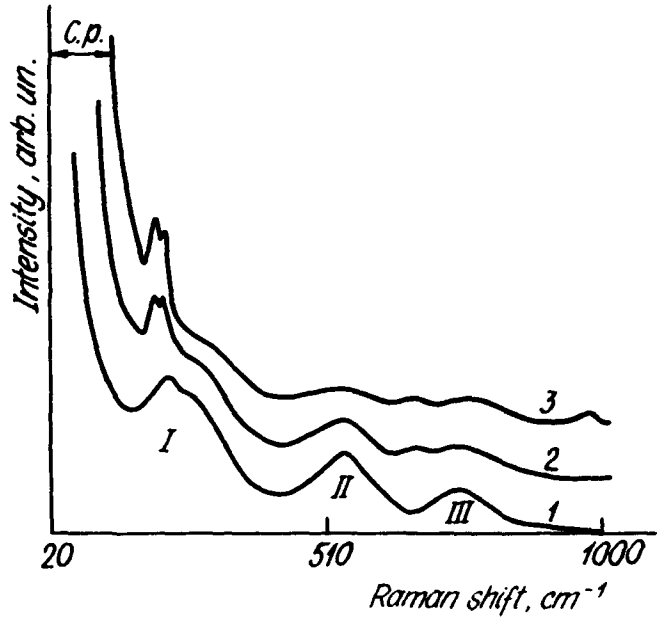


FIGURE 4. Raman spectra of pure (curve 1), doped with 1 wt.% Fe (2) and Mn (3) PLZT 8/65/35. I, II, III - "amorphous" bands; C.p. - central peak demonstrating a critical behaviour.

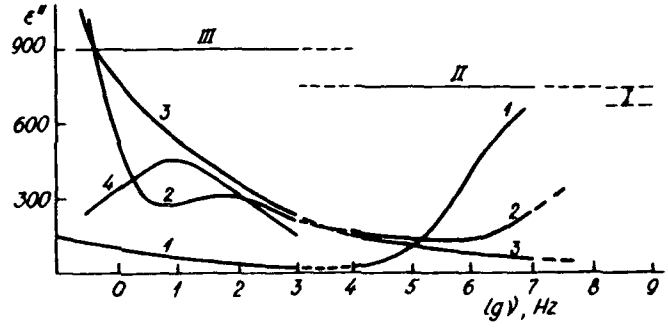


FIGURE 5. $\mathcal{E}''(\nu)$ of pure (curve 1), doped with 1 wt.% Fe (2) and Mn (3), γ-irradiated (dose 3.10^9 rad) (curve 4) PLZT 8/65/35. $T_{measur}=T_M$ +10 deg; T_M - temperature $\mathcal{E}(T)$ maximum at 10^3 Hz, $E_{\sim}$<1 V/cm;

Radiation effects

Different kind of irradiation (γ-rays, electrons, neutrons) may be used to introduce defects control defect concentration and obtain information about the defect processes in materials studied under different conditions (e.g., state of polarization, sample geometry). There is some interest to investigate radiation damage with regard to application.

Experiments were made on ceramic specimens of PLZT X.65/35 (X=4.5-11 at/%La) and PSN [15], detecting significant alterations of the optical and dielectric properties. Most recently electron-irradiated PST, PSN and PSN-Ba ceramics have been investigated (fluences up to 3.10^{17} electr/cm^2 as well as neutron-irradiation studies of the effects with respect to the dose (5.10^{17}; 10^{18} n/cm^2) (to be published).

All the optical (absorption difference ΔD) and dielectric (hysteresis loops, ε, tgδ) measurements were made at room temperature. Annealing as well as aging were studied.

The change of optical properties of PLZT 8-11/65/35 ceramics is mainly observed near the absorption edge - a characteristic maximum in ΔD appearing 370-390 nm irrespective to the type of radiation employed (Fig.6,a). Intensity of coloring (the value of ΔD) depends on the type of irradiation, fluence, as well as of thickness of the sample. Defects can be annealed at temperatures between 400-700 ^{o}C (Fig.6,b).

In the case of electron- and neutron- irradiated PSN and PSN+Ba ceramics without changes at the absorption edge (360-370 nm) supplementary ΔD maximum at ~490 nm appears, however completely annealed at temperatures about 250^{o}C. (Fig.6,c).

The maximum of ΔD in PMN ceramics is shifted to longer waves of 510 nm. The change of ion charge, redistribution of genetic defects, appearance of true radiation defects as a result of ion displacement aparently are associated with the observed color centers of the broad absorption band.

PSN, PST and PMN compounds are more resistant to irradiation as compared to PLZT in what concerns the change of dielectric parameters caused by irradiation. (It has to be noticed that some activity is observed in compounds of the first group for which reason they cannot used in experiments immediatly after irradiation). The most pronounced change occurs in the shape of the hysteresis loops in the "hard" FE samples (e.g., PLZT 4.5-6/65/35) (Fig.7). This may be explained by classic mechanisms leading to the appearance of intrinsic radiation-induced bias fields in FE substances. The state of polarization of the sample - thermally depolarized (TD), polarized by electric field (EP) during its irradiation is important (Fig.8). The upper symmetric loop is observed in TD-samples while identical samples polarized before irradiation show pronounced asymmetric hysteresis. Fig.8 also demonstrates observed build-up process of the loop size under repeated cycling conditions related to rearrangement and relaxation of radiation-induced defects. Regarding loop-formation the following is observed. Starting with symmetric loops upon increasing the temperature to the next annealing stage, the loop becames assymmetric which can be explained by redistribution (diffusion, drift) of radiation - induced defects in samples polarized during a previous measurement. Long-time aging (~8 months) leads to a similar result, as annealing in the same kind of samples. Measurements of the complex dielectric permeability of γ-irradiated samples suggest there is a decay of the most probable relaxation frequency of the dielectric polarization with aging [15] (Fig 5, curve 4).

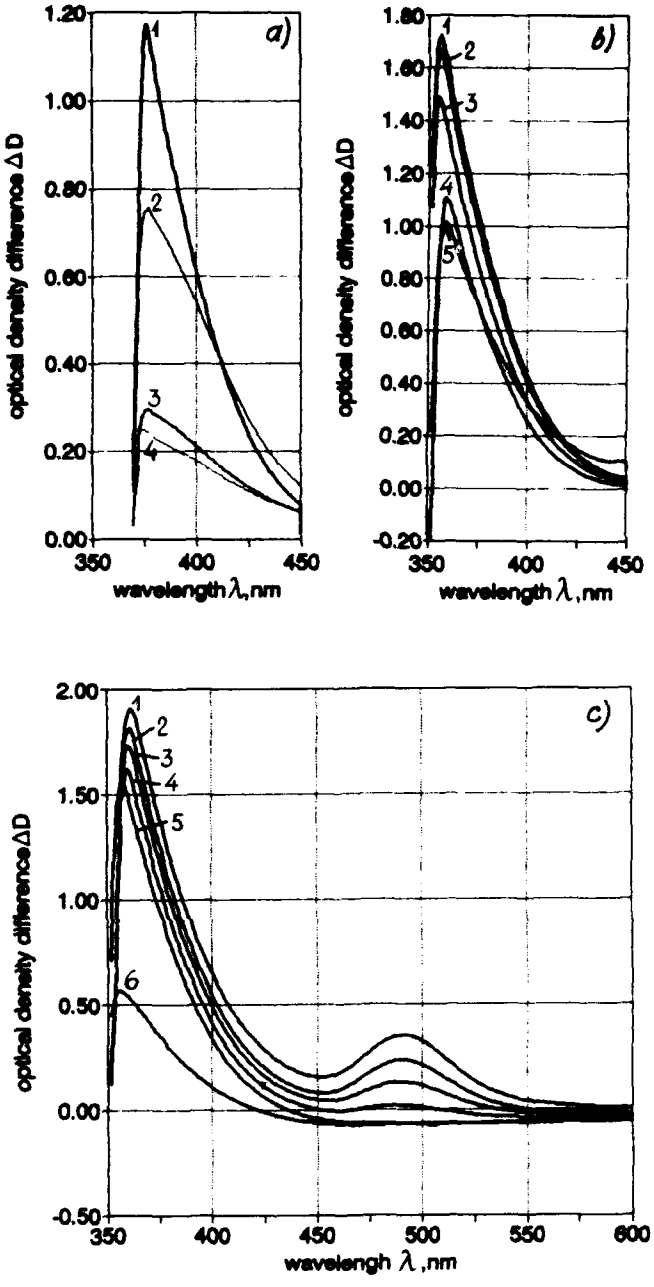


FIGURE 6. Optical density difference ΔD vs. wavelength: a) of PLZT 10/65/35 irradiated by: 1 - neutrons (2.10^{18} n/cm^2); 2 - electrons ($8,4.10^{17}$ electr./cm^2); 3 - γ-rays and neutrons (5.10^{3} rad; 2.10^{16} n/cm^2); 4 - γ-rays (9.10^{8} rad.); sample thickness d=0,3 mm;
b) of PLZT 9,75/65/35 irradiated by neutrons (fluence 10^{18} n/cm^2 (1) and annealed up to: 2 - 165^{o}C; 3 - 192^{o}C ; 4 - 220^{o}C; 5 - 274^{o}C (2 deg/min); d=0.25 mm;
c) of PSN, irradiated by neutrons (fluence 5.10^{17} n/cm^2)(1) and annealed up to: 2 - 165^{o}C; 3 - 192^{o}C; 4 - 220^{o}C; 5 - 274^{o}C (2 deg/min); d = 0.25 mm.

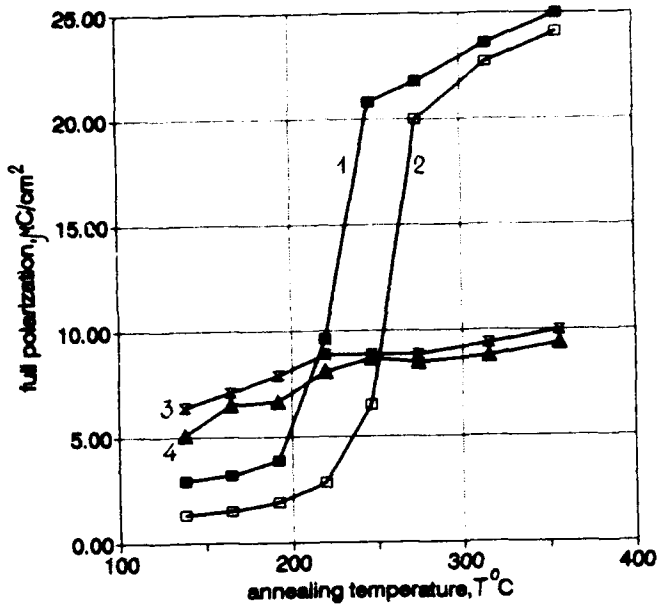


FIGURE 7. Dependence of the change of full polarization in neutron-irradiated samples of PLZT 4.5/65/35 at E=15 kV/cm (1,2) and PLZT 9,75/65/35 at E=13 kV/cm (3,4) on annealing temperature (2 deg/min) for doses of 5.10^{17} n/cm^2 (1,3) and 10^{18} n/cm^2 (2,4); d=1 mm.

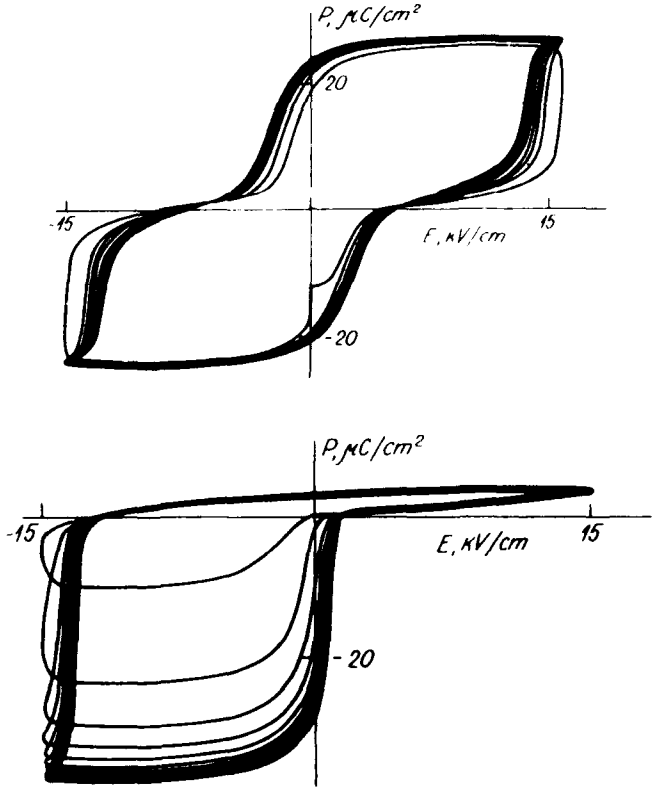


FIGURE 8. Formation of hysteresis loops in PLZT 6/65/35 ceramics, irradiated by neutrons (fluence 5.10^{17} n/cm^2) at repeated switching of the applied field E = 15 kV/cm; T=20°C. Samples: thermally depolarized - upper curve; electrically polarized - lower curve during its irradiation; d = 1 mm.

Conclusion

In the applications considered above the modified lead-containing perovskite compounds are used in the form of plates (thick films) about 0.3 mm thick cut from bulk ceramic bulbs. Some of them holding a strong position in the field as they are, the knowledge obtained in search for modified compositions and comprehensive studies of their structure and properties are regarded as a good basis for thin film product development being of current interest and more attractive in many of applications.

References

[1] L.Shebanov and K.Borman, "On lead-scandium tantalate solid solution with high electrocaloric effect", Ferroelectrics, vol.127, pp.143-148, 1992.

[2] V.Sinyavsky, N.D.Pashkov, Y.M.Gorovoy and L.Shebanov, "The optical ferroelectric ceramic as working body for electrocaloric refrigerators", Ferroelectrics, vol.90, pp.213-217, 1989.

[3] E.Corcoran, "Memorable Revival", Scientific American, pp.109-110, July 1991.

[4] A.B.Tuttle and D.A.Payne, "The effects of microstructure on the electrocaloric properties of $Pb(ZrSnTi)O_3$ Ceramics", Ferroelectrics, vol.37, pp.603-606, 1981.

[5] W.Y.Pan, C.Q.Dam, Q.M.Zhang and L.E.Cross, "Large displacement transducers based on electric field forced phase transitions in the tetragonal $(Pb_{0.97}La_{0.02})(Ti,Zr,Sn)O_3$ family of ceramics", J.Appl.Phys., vol.66, pp.6014-6023, 1989.

[6] M. Knite, M.Ozolinsh, and A.Sternberg, "Electrooptical and electrostrictive PLZT ceramics light modulators for infrared",Ferroelectrics, vol.94, pp.67-72, 1989.

[7] A.Sternberg, "Transparent ferroelectric ceramics: properties and applications", Ferroelectrics, vol.91, pp.53-67, 1989. A.Sternberg, "Transparent ferroelectric ceramics - recent trends and *status quo*", Ferroelectrics, vol.131, 1992, to be published.

[8] E.Klotins, P.Kreicbergs, J.Kotleris, and A.Kapenieks, "Laser heterodyne displacement measuring using PLZT frequency shifter", Sensors and Actuators, A, vol.25-27, pp.271-275, 1991.

[9] M.Ozolinsh, P.Paulins, A.Viesturs, M.Kundzins, K.Kundzins and A.Krumins, "PLZT laser beam modulator", Ferroelectrics, vol.128, pp.73-78, 1992.

[10] H.Kammer, "Electrooptics in educational physics: basic demonstration-experiments with a TFC-device", Ferroelectrics, vol.131, 1992, to be published.

[11] V.Alekseev, V.Liber, A.Starikov, A.Anspoks, E.Auzins, E.Klotins, and J.Kotleris, "High efficiency angular deflection of the laser beam: PLZT/intracavity array", Ferroelectrics, vol.131, 1992, to be published.

[12] V.I.Dimza, A.A.Sprogis, A.E.Kapenieks, L.A.Shebanov, A.V.Plaude, R.Stumpe and M.Books, "Structure and dielectric and optical properties of (Mn, Fe, Co, Eu)-doped PLZT ceramics", Ferroelectrics, vol.90, pp.45-55, 1989.

[13] V.Dimza, P.Paulins, M.E.Zhang, Q.Chen and Z.Lin, "Studies of Raman scattering spectra (RSS) of PLZT and PST doped with 3d-elements", Ferroelectrics, vol.131, 1992, to be published.
[14] V.Dimza, I.P.Bikov, M.D.Glinchuk and J.T.Cheng, "EPR studies of manganese-doped PLZT 8/65/35 ceramics", Phys.Stat.Sol.(a), vol.132, N.2, 1992, to be published.
[15] A.I.Burkhanov, A.V.Shilnikov, M.Shuvaev, V.Dimza and A.Sternberg, "Dielectric relaxation in alloyed and γ-irradiated ferroceramics PLZT 8/65/35", Ferroelectrics, to be published.
[16] A.Sternberg, A.Krumina, A.Sprogis, A.Rubulis, G.Grinvalds, L.Shebanov, H.W.Weber, H.Klima, H.Schwabl, S.Dindun, and U.Ulmanis "Radiation effects on physical properties of PLZT ceramics", Ferroelectrics, vol.126, pp.233-238, 1992. A.Sternberg, A.Krumina, A.Sprogis, H.W.Weber, H.Klima, H.Schwabl, S.Dindun and U.Ulmanis, "Radiation effects in PLZT and PSN ceramics", Ferroelectrics, vol.131, 1992, to be published.

RELAXOR FERROELECTRICS WITH LANTHANUM PEROVSKITES

Tadashi Takenaka and Toshio Kanegae

Faculty of Science and Technology, Science University of Tokyo,
Noda, Chiba-ken, 278 JAPAN

Lanthanum perovskite compounds, $La(B^{I}_{1/2}B^{II}_{1/2})O_3$ (B^{I}=Ni, Co, Mg; B^{II}=Ti), are studied as a candidate for stabilizers to form perovskite-type $Pb(Zn_{1/3}Nb_{2/3})O_3$ (PZN)-based ceramics. A conventional sintering technique is utilized to prepare the ceramic samples with PZN-based solid solution. The ratios of the perovskite phase to the pyrochlore phase were more than 90 % at 10 mol%-modification of $La(Ni_{1/2}Ti_{1/2})O_3$ (LNT), $La(Mg_{1/2}Ti_{1/2})O_3$ (LMT) or $La(Co_{1/2}Ti_{1/2})O_3$ (LCT). Effects on suppression of the pyrochlore phase in these ceramics are evaluated for the dielectric and electrostrictive properties.

The transverse electrostrictive strain, $S_1 \sim -0.75 \times 10^{-4}$, is induced by electric field of 30 kV/cm in the thickness direction in the 5 mol%-LNT modified PZN-based ceramics. The magnitude of strain is a little small but the strain hysteresis is very small as compared with those of piezoelectric ceramics.

1. Introduction

Relaxor ferroelectrics which consist of lead-based complex compounds show indistinct Curie points at the phase transition between the ferroelectric and paraelectric phases, *i.e.*, they exhibit a diffuse phase transition. Among a lot of relaxor ferroelectrics, lead zinc niobate,[1] $Pb(Zn_{1/3}Nb_{2/3})O_3$ (abbreviated to PZN), with perovskite structure displays the highest[2] Curie temperature, T_C, of 140 °C. The crystal structure is a rhombohedral symmetry with lattice constants of a=4.061 Å and α=89°55' at room temperature. The PZN system is promising[2,3] for various dielectric, piezoelectric and electrostrictive applications, because PZN shows a large maximum dielectric constant at T_C, and exhibits excellent dielectric and piezoelectric properties. However, the ceramics of PZN compounds prepared by the usual sintering process have a pyrochlore structure in which applications to dielectric and piezoelectric materials are inactive.

Various modified sintering methods have been proposed to form perovskite PZN ceramics. In one of them, many kinds of metallic ions are substituted for part of the Pb^{2+} and Zn^{2+} ions in PZN to introduce a strong ionic bond. A single-phase perovskite structure can be produced by substituting, for example, 6 mol%-$BaTiO_3$-modified[4] or 10 mol%-$KNbO_3$-modified[5,6] PZN.

In this paper, several lanthanum perovskite compounds,[7] $La(B^{I}_{1/2}B^{II}_{1/2})O_3$ (B^{I}=Ni, Co, Mg; B^{II}=Ti), are studied to stabilize the perovskite-type $Pb(Zn_{1/3}Nb_{2/3})O_3$ (PZN)-based ceramics which were prepared by modification of the lanthanum perovskites as follows:

$(1-x)Pb(Zn_{1/3}Nb_{2/3})O_3 - xLa(Ni_{1/2}Ti_{1/2})O_3$ [LNT100x],[8]

$(1-x)Pb(Zn_{1/3}Nb_{2/3})O_3 - xLa(Mg_{1/2}Ti_{1/2})O_3$ [LMT100x] and

$(1-x)Pb(Zn_{1/3}Nb_{2/3})O_3 - xLa(Co_{1/2}Ti_{1/2})O_3$ [LCT100x],

where the brackets [ ] show the respective abbreviations of the solid solutions. The effects on suppression of the pyrochlore phase were studied on the dielectric and electrostrictive properties.

2. Sample Preparation and Experiments

PZN-based ceramic samples were prepared by a conventional sintering technique. Reagent-grade (> 99 %) oxide powders of PbO, ZnO, Nb_2O_5, La_2O_3, NiO, MgO, CoO and TiO_2 were used as the starting materials. The constituents were dried prior to weighing. Weighed raw materials were mixed in a polyethylene pot with agate balls or zirconia balls and acetone for 10 hours. After drying, the mixture was calcined at 800 °C for 1~2 hour. The calcined material was ground and ball-milled again for 20 hours. The dried powder was granulated with polyvinyl alcohol solution as a binder, and then pressed into disks 20 mm in diameter and about 1~1.5 mm in thickness. The disks were sintered in a capped MgO crucible to prevent evaporation of PbO during the sintering process at 1050 °C for 2 hours in air after burning out the binder at 500 °C for 3 hours.

The crystalline structure was examined by an X-ray powder diffraction technique using CuKα radiation. After cutting and polishing of 0.2~0.5 mm in thickness, fired-on silver paste was used as the electrodes for electrical measurements.

The temperature dependence of the dielectric constant, ε_s, and dielectric loss tangent, tanδ, were measured at 10 kHz, 100 kHz and 1 MHz using an automated dielectric measurement system with a multifrequency LCR meter (YHP 4275A) in the temperature range of -80~200 °C. The D-E hysteresis loop was observed using a standard Sawyer-Tower circuit at 50 Hz.

Electrostrictive measurements, that is, strains under the applied electric field, were measured by a standard strain gauge method. Variation of resistance was measured using a Wheatstone bridge because resistance of the strain gauge attached to the sample varies in proportion to the strain ($\Delta l/l$) induced by an applied electric field in the sample.

3. Results and Discussion

3.1 *Suppression of pyrochlore phase*

Figure 1 shows the X-ray powder diffraction patterns of $La(Ni_{1/2}Ti_{1/2})O_3$ (LNT), $La(Mg_{1/2}Ti_{1/2})O_3$ (LMT) and $La(Co_{1/2}Ti_{1/2})O_3$ (LCT) ceramics, which all have a single phase of perovskite structure. The Galasso's book[7] includes the data on LNT and LMT, but no data on LCT.

Figure 2 shows the X-ray diffraction patterns for the solid solution of the $(1-x)Pb(Zn_{1/3}Nb_{2/3})O_3$ (PZN)-x·$La(Ni_{1/2}Ti_{1/2})O_3$ (LNT) [LNT100x]. The pattern of PZN(LNT0) indicates a pyrochlore structure, however, the intensity of the perovskite phase in the system [LNT100x] increases as the LNT content (x) increases. The intensities of X-ray diffraction patterns were used to determine the amount of perovskite phase present in each composition. The ratio of relative intensities, I_{PERO} and I_{PYRO}, of the (110) perovskite peak and the (222) pyrochlore peak,

CH3080-0-7803-0465-9/92$3.00 ©IEEE

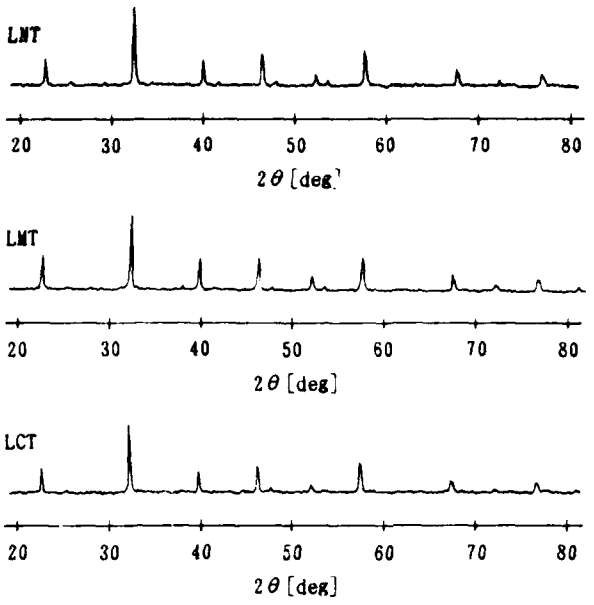


Fig. 1 X-ray diffraction patterns of $La(Ni_{1/2}Ti_{1/2})O_3$ (LNT), $La(Mg_{1/2}Ti_{1/2})O_3$ (LMT) and $La(Co_{1/2}Ti_{1/2})O_3$ (LCT) ceramics.

respectively, was used to yield the volume percentage of the perovskite phase as follows:

Perovskite phase [%] = I_{PERO} x 100 / (I_{PERO}+I_{PYRO}).

Figure 3 shows the volume percentage of the perovskite phase in PZN-LNT, PZN-LMT and PZN-LCT systems as a function of the mole percentage of modified LNT, LMT or LCT. The ratio of the perovskite phase to the pyrochlore phase continuously increases as the mole percentage up to 15 mol% of LNT, LMT or LCT increases. For example, the perovskite ratio of LNT5 (x=0.05 in the PZN-LNT system), with measured density ratios above 90 % to the X-ray theoretical density, reaches 75 %. The rate of increase of the perovskite phase was small for the amount of x over 0.05, and finally reached 96 % at x=0.15 with a saturated trend.

The reason why the perovskite phases increase as the increasing of the lanthanum perovskites is that elecrtonegativity differences, $\Delta\chi=(\chi_{A\text{-}O}+\chi_{B\text{-}O})/2$, of lanthanum perovskites are larger than that of PZN, where $\chi_{A\text{-}O}$ is the elecrtonegativity difference between the A-site cation and oxygen, and $\chi_{B\text{-}O}$ the elecrtonegativity difference between the B-site cations and oxygen, while tolerance factors, $t=(r_A+r_O)/((r_B+r_O)\sqrt{2})$, of them are smaller than that of PZN, where r_A, r_B and r_O are the respective ionic radii. Both $\Delta\chi$ and t are necessary to be larger for the perovskite structure. The lattice constants determined by X-ray diffraction patterns decreased as the La content increased, because the ion radius of La^{3+} was smaller than that of Pb^{2+}.

3.2 *Dielectric properties*

Figure 4 shows the temperature dependence of ε_S and tanδ of LNT4, LNT5, LNT6, LNT7 and LNT10 at 10 kHz. The temperature, T_0, of maximum ε_S for the respective LNT100x were 50 °C, 33 °C, -5 °C,-11 °C and -44 °C, respectively. The temperature of the ε_S peak depends on the amount of modified La ions. Similarly, the temperature of increasing-up-tanδ shifted to lower temperature as La ions increased.

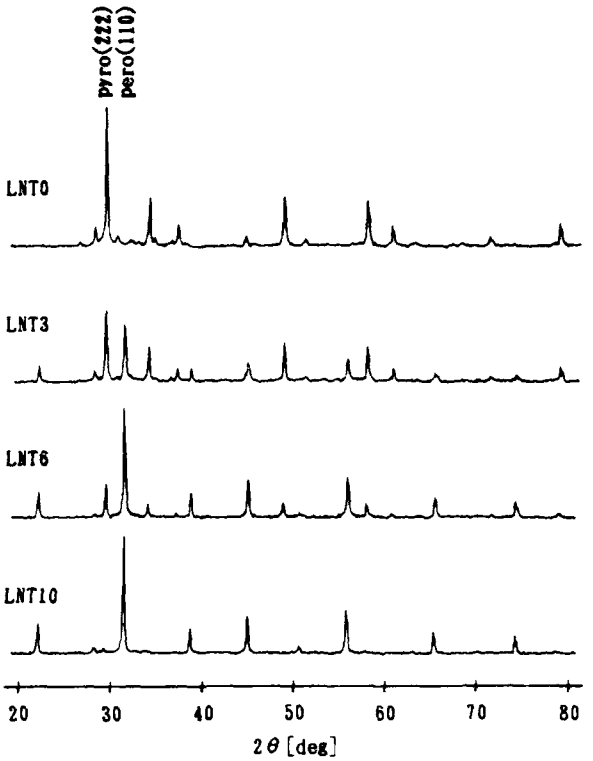


Fig. 2 X-ray diffraction patterns of $(1\text{-}x)Pb(Zn_{1/3}Nb_{2/3})O_3$ (PZN) -x·$La(Ni_{1/2}Ti_{1/2})O_3$ (LNT) [LNT100x] (LNT0, LNT3, LNT6 and LNT10).

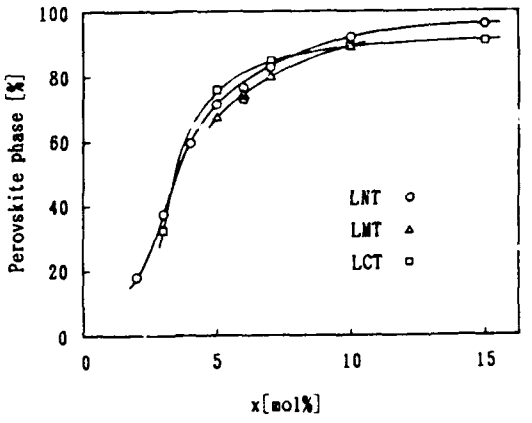


Fig. 3 Volume ratio of perovskite phase as a function of the amount (x) of modified LNT, LMT or LCT.

Temperature dependence of the reciprocal dielectric constant, $1/\varepsilon_S$, of relaxor ferroelectrics usually obeys a special quadratic law

$$1/\varepsilon_S \propto (T\text{-}T_0)^2,$$

where T_0 is the temperature of maximum ε_S, instead of the normal ferroelectric Curie-Weiss law. Figure 5 shows temperature dependence of the $1/\varepsilon_S$ on the square of temperature in LNT4, LNT5, LNT6, LNT7 and LNT10 ceramics measured at 10kHz, indicating to obey the temperature-square's law.

Figure 6 shows temperature dependence of the ε_S and tanδ in LNT5 measured at 10kHz, 100kHz and 1MHz. The maximum of ε_S was shifted to higher temperature as the measured frequency

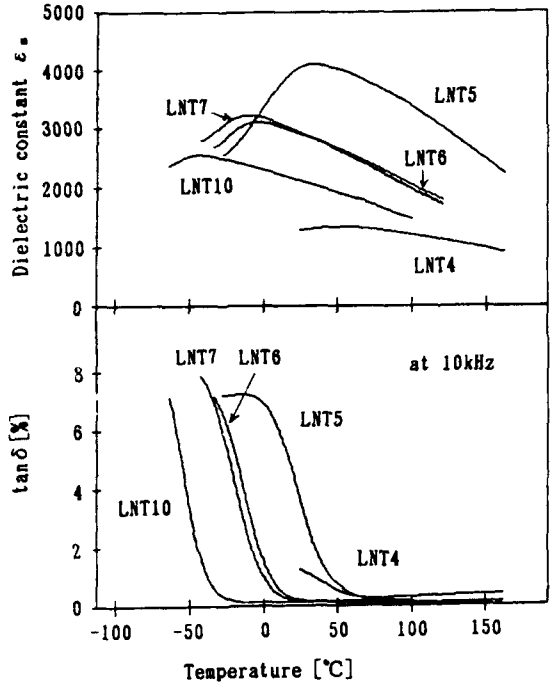


Fig. 4 Temperature dependence of dielectric constant, ε_S, and loss tangent, tanδ, in the (1-x)PZN-x·LNT [LNT100x] (LNT4, LNT5, LNT6, LNT7 and LNT10) measured at 10kHz.

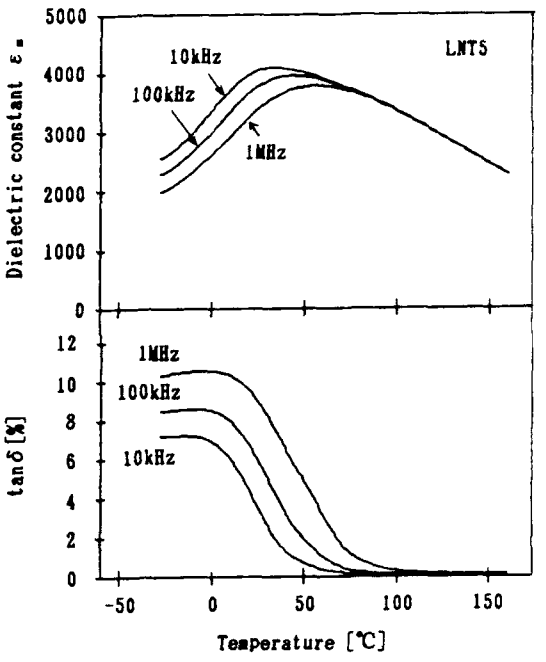


Fig. 6 Temperature dependence of ε_S and tanδ at 10kHz, 100kHz and 1MHz in 0.95PZN-0.05LNT [LNT5] ceramics.

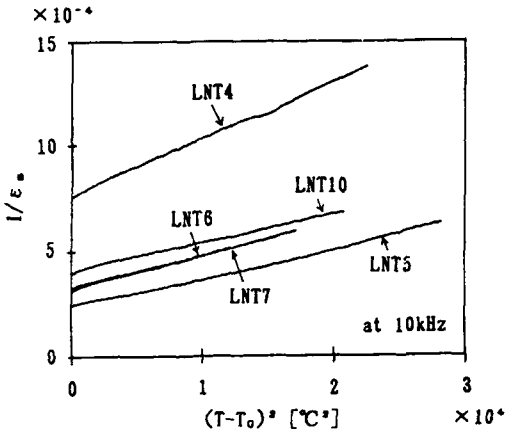


Fig. 5 Temperature dependence of reciprocal dielectric constant, $1/\varepsilon_S$, on the square of temperature in LNT4, LNT5, LNT6, LNT7 and LNT10 at 10kHz .

increased. An increase in frequency by one order of magnitude leads to a shift in the maxima by about 10 °C. These solid solutions which consist of PZN and lanthanum perovskites as the end members seem to be a ferroelectric with disordered perovskite structure because of a typical case with a diffuse phase transition characterized by a broad peak and a remarkable frequency dispersion in the temperature dependence of the ε_S.

3.3 *D-E hysteresis loop*

Weak D-E hysteresis loops could be observed at room temperature in some LNT100x system while the ε_S peak is seen below room temperature. Figure 7 shows D-E hysteresis loops of LNT4, LNT5, LNT6, LNT7 and LNT10 at 10 °C, respectively. The spontaneous polarization of LNT5 did not fall to zero over the temperature range of the ε_S peak. The coercive force, E_C, and remanent polarization, P_r, were 3.4 kV/cm and 2.5 μC/cm^2 at room temperature in LNT5, respectively, whose values were smaller as compared with those of piezoelectric PZT ceramics.

3.4 *Electrostrictive properties*

The transverse strain, S_1, induced by an applied electric field in the thickness direction, was measured at room temperature under a driving frequency of about 0.07 Hz. The strains of LNT5, LNT6, LNT7 and LNT10, as a function of the applied electric field are shown in Fig. 8. Negative values of the strain signify the direction of shrink. The strain value, S_1=-0.30 and -0.75 x 10^{-4}, in PZN-LNT5 was obtained under the applied electric field, E_3, of 20 and 30 kV/cm, respectively. The calculated effective piezoelectric coefficient, d_{31}, theoretically defined as $\delta S_1/\delta E_3$, was -45 x 10^{-12} m/V at the applied electric field of 20~30 kV/cm. The magnitude of strain in LNT10 was small but the strain hysteresis was very small as compared with that of LNT5 and LNT6, whose strain hysteresis corresponded to the respective D-E hysteresis loops.

Figure 9 shows temperature dependence of the strain, S_1, at 18 and 30 kV/cm in LNT5 and LNT6. The temperature coefficient of strain, $\Delta S_1/\Delta T$, were less than -1 %/°C.

4. Conclusions

Lanthanum perovskites, La($B^I_{1/2}B^{II}_{1/2}$)O_3 (B^I=Ni, Co, Mg; B^{II}=Ti) are used for the stabilizations to Pb($Zn_{1/3}Nb_{2/3}$)O_3 (PZN) ceramics resulting in the perovskite structure. The modification of around 10 mol% La($Ni_{1/2}Ti_{1/2}$)O_3 (LNT), La($Mg_{1/2}Ti_{1/2}$)O_3 (LMT) or La($Co_{1/2}Ti_{1/2}$)O_3 (LCT) are more effective. The ratios of the perovskite phase to the pyrochlore phase of the PZN ceramics with

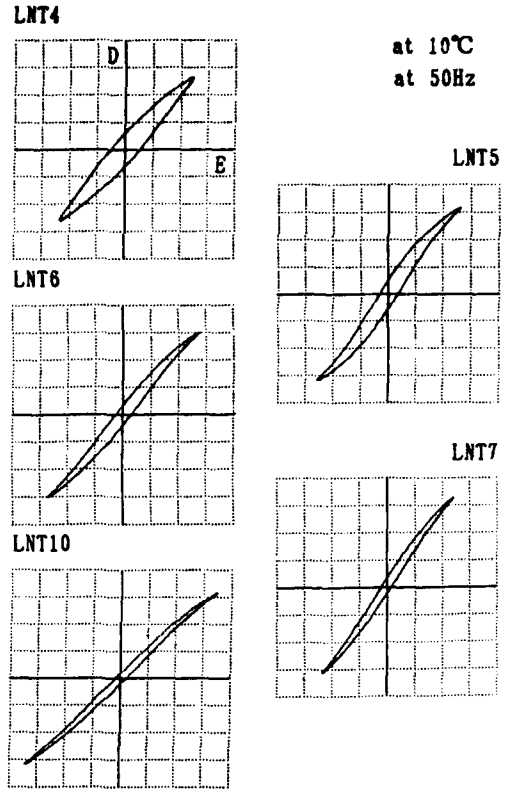


Fig. 7 D-E hysteresis loops of LNT4, LNT5, LNT6, LNT7 and LNT10 at 10 °C (50Hz).

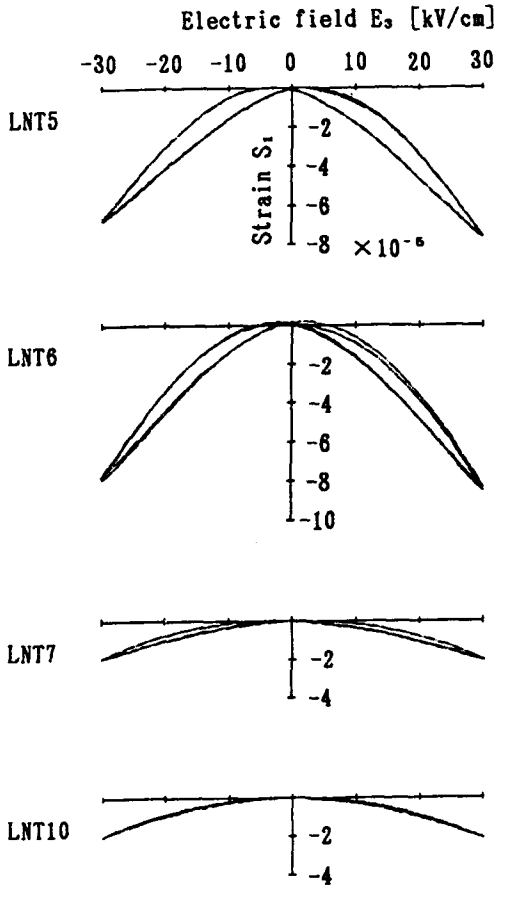


Fig. 8 The transverse strain, S_1, induced by electric field in the thickness directions of LNT5, LNT6, LNT7 and LNT10.

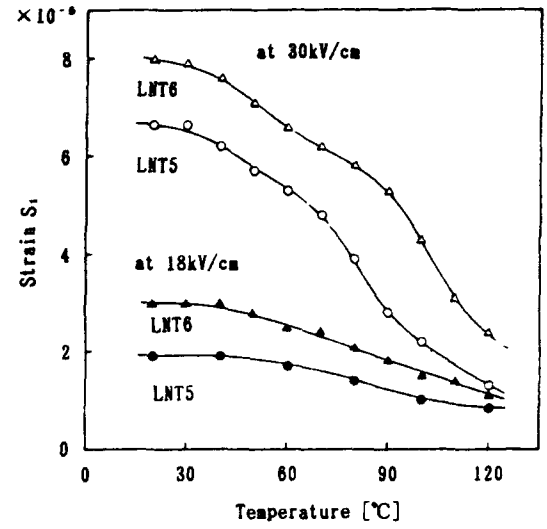


Fig. 9 Temperature dependence of strain, S_1, of LNT5 and LNT6 at 18 kV/cm and 30 kV/cm, respectively.

10 mol% LNT, LMT or LCT modification were more than 90 %.

PZN-based ceramics with LNT, LMT or LCT modification appear to be applicable for use as electrostrictive materials with little strain hysteresis and high temperature stability in the vicinity of room temperature.

A part of this work was supported by the Ogasawara Science and Technology Foundation.

References

[1] Y. Yokomizo, T. Takahashi and S. Nomura, "Ferroelectric Properties of $Pb(Zn_{1/3}Nb_{2/3})O_3$", *J. Phys. Soc. Jpn.*, vol.**28**, pp.1278-1284, May 1970.

[2] T. R. Shrout and J. P. Dougherty, "Lead Based $Pb(B1B2)O_3$ Relaxors vs $BaTiO_3$ Dielectrics for Multilayer Capacitors", in *Ceramic Dielectrics: Composition, Processing and Properties*, Ceramic Transactions Vol.**8**, The American Ceramic Society, Inc., 1990, ch.1, pp.3-19.

[3] J. Kuwata, K. Uchino and S. Nomura, "Phase Transitions in the $Pb(Zn_{1/3}Nb_{2/3})O_3$-$PbTiO_3$ System", *Ferroelectrics*, vol.**37**, pp.579-582, 1981.

[4] A. Halliyal, U. Kumar, R. E. Newnham and L. E. Cross, "Stabilization of the Perovskite Phase and Dielectric Properties of Ceramics in the $Pb(Zn_{1/3}Nb_{2/3})O_3$-$BaTiO_3$ System", *Am. Ceram. Soc. Bull.*, vol.**66**, pp.671-676, April 1987.

[5] T. Takenaka and K. Sakata, "Control of Crystal Structure in the Ceramics of $Pb(Zn_{1/3}Nb_{2/3})O_3$ by a Composition-Modification", *Annual Report of Study Group on Applied Ferroelectrics in Japan*, vol.**24**, pp.50-53, 1977 [*in Japanese*].

[6] T. Takenaka, M. Satou, K. Nakata and K. Sakata, "Piezoelectric Properties of $Pb(Zn_{1/3}Nb_{2/3})O_3$-$KNbO_3$-PZT Solid Solution", *Ferroelectrics*, vol.**128**, pp. 67-72, 1992.

[7] F. S. Galasso, *Structure, Properties and Preparation of Perovskite-type Compounds*, London: Pergamon Press, 1969, ch.2, p.38.

[8] T. Kanegae, K. Sakata and T. Takenaka, "Piezoelectric and Electrostrictive Properties of $Pb(Zn_{1/3}Nb_{2/3})O_3$-based Relaxors", *Jpn. J. Appl. Phys.*, vol.**30**, Part 1, No.9B, pp. 2232-2235, September 1991.

DOMAIN ORIENTATION AND PIEZOELECTRIC PROPERTIES OF Ag DOPED PMN - PZT CERAMICS

K. V. Ramana Murty, S. Narayana Murty, K. Chandra Mouli and A. Bhanumathi
Solid State Laboratories, Department of Physics
Andhra University, Waltair-530 003 **INDIA**

ABSTRACT

The hysteresis, dielectric and piezoelectric properties of the ternary 0.5 PMN - 0.5 PZT ceramics with Ag substitution are described. These ceramics show good square hysteresis loops and hence are promising for thin film memory applications At high Ag concentrations the dielectric loss decreased indicating an increase in the ordering of the structure. There is remarkable increase in the piezoelectric properties particularly the thickness coupling factor K_t and the piezoelectric charge coefficient, d_{33}.

INTRODUCTION

The solid solution of the system PZT (Lead Zirconate Titanate) near the morphotropic phase boundary are widely used in electronic devices (1,2) because of its excellent piezoelectric properties. The ternary compound $Pb(Mg_{1/3}b_{2/3})O_3$ - $Pb(zr_{1-x}Ti_x)O_3$ near the morphotropic phase boundary (3) form a solid solution of the perovskite structure and has high dielectric constant and planar coupling coefficients. The addition of transition metal oxides promotes densification. Higher planer ccupling coefficients are reported (4) with the addition of NiO. The morphotropic phase boundary shifts (5) towards the higher $PbTiO_3$ content when Ba or Sr is added to the composition.

The hysteresis behaviour, dielectric and piezoelectric properties of the 0.5 PMN-0.5 PZT modified with Ag near the morphotropic phase boundary are presented in this paper.

EXPERIMENTAL PROCEDURE

Sample preparation:

The ceramic compositions were prepared from the high purity PbO, MgO, Nb_2O_5, TiO_2, ZrO_2 and Ag_2O of reagent grade. The preparation of these ceramics is very difficult due to the narrow sintering temperature range of PMN and the formation of pyrochlore phase of $Pb_2Nb_2O_7$. To avoid the pyrochlore phase formation, a method is developed (6) in which the coulombite precursor of $(MgNb_2)O_6$ is prepared first and then the precursor is mixed with PbO to prepare $Pb(Mg_{1/3}Nb_{2/3})O_3$. Hence the constituent materials are taken and the precursor is prepared first by calcining at 700°C for 4 hrs. Then the other materials are mixed with this precursor and the usual procedure of calcination and sintering is followed. The calcination and sintering condition for preparing the PMN - PZT ceramics are 950°C for 3 hrs and 1225 - 1250°C for 4 hrs respectively.

The sintered pellets were polished and as fired silver paint was applied on both the faces of the pellets for electrical contacts and fired at 500°C for 1 hr.

Poling: For piezoelectric measurements and hysteresis behaviour the sintered pellets were poled by applying high electric fields of 20 KV/cm for 1 hr at elevated temperatures in silicon oil.

Hysteresis behaviour and microscopy:

The hysteresis behaviour of the ceramic compositions is studied by using the modified Sawyer - Tower circuit (7). The values of remanent and saturation polarisation and coercive field are obtained from the hysteresis loops. The microscopy studies of the prepared ceramic compositions is done by using Philips SEM model 520M. The grain size of the ceramic compositions is determined by linear intercept method.

Piezoelectric measurements:

The piezoelectric coupling coefficients of the ceramics samples are

CH3080-0-7803-0465-9/92$3.00 ©IEEE

determined by the resonance - antiresonance technique (8) using HP impedence analyser model 4192A. The piezoelectric coefficients measured are K_p, K_t, d_{33}, d_{31} and g_{31}. The coefficient d_{33} is measured by using the Berlincourt d_{33} meter.

The Curie temperature of the ceramic compositions is determined from the peak of dielectric constant vs temeperature curve.

RESULTS AND DISCUSSION

Because of the volatilization of PbO at high tenperatures and the narrow sintering range of PMN, it is very difficult to obtain good ceramics in the PMN - PZT system. Using the coulombite precursor method the following ceramic composition were prepared and studied.

$$Pb_{1-x}Ag_{2x}(Mg_{1/3}Nb_{2/3})_{0.5}(Zr_{0.55}Ti_{0.45})_{0.5}O_3$$

Where x = 0, 0.005, 0.010 and 0.015.

The density of the PMN - PZT ceramics increases with the introduction of Ag^+ in the A sites of the perovskite type ternary system. But with increase in Ag the density remains almost the same.

The SEMs of the ceramic compositions revealed liquid phase at the grain boundaries. Monovalent Ag substitution in PMN - PZT ceramics promotes the grain growth. The grain size increases slightly in 0.5 PMN - 0.5 PZT with the introduction of 1 mole % Ag and then decreases.

The hysteresis behaviour in the ternary PMN - PZT system is being reported for the first time. In 0.4 PMN - 0.6 PZT compositions hysteresis loop attains (9) saturation only for the 1 mole % Ag added composition. But for 0.5 PMN - 0.5 PZT, saturation is attained for the undoped composition also. In this compositions P_r and P_s increase with increasing Ag content. There is a slight increase in the coercive field E_c. The variation of P_r, P_s and E_c with Ag content in 0.5 PMN - 0.5 PZT ceramics is shown in Fig.1. The composition with 3 mole % Ag exhibits maximum P_r and P_s and minimum dielectric loss. P_s attains a maximum value of 42 C/cm^2. This indicates that the orientation of domains increases with increasing Ag content.

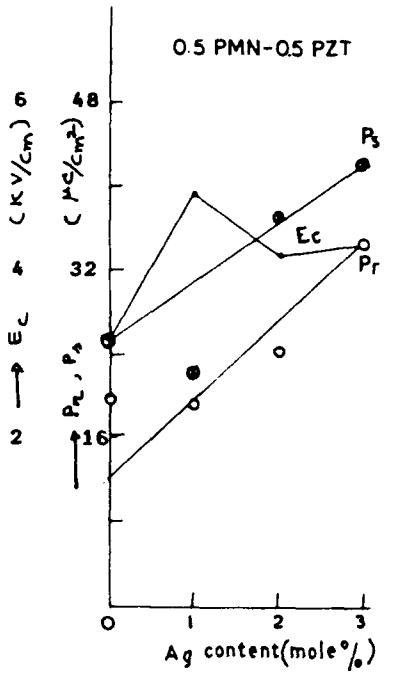


Fig. 1 Variation of P_r, P_s and E_c with Ag content in 0.5 PMN - 0.5 PZT ceramics

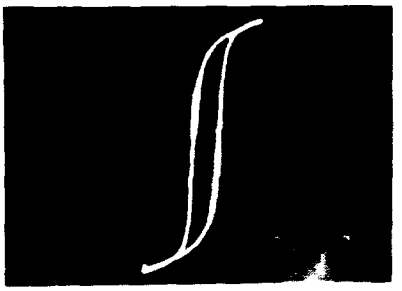


Fig. 2. Hysteresis loop of Ag added 0.5 PMN-0.5 PZT.

Most of this compositions show excellent square hysteresis loops (Fig.2), smaller coercive field and large remanent polarisation. As such, these will be promising for thin film memory applications.

With the introduction of Ag in 0.5 PMN-0.5 PZT ceramics the room temperature dielectric constant increases and the ferroelectric Curie temperatures decreases and

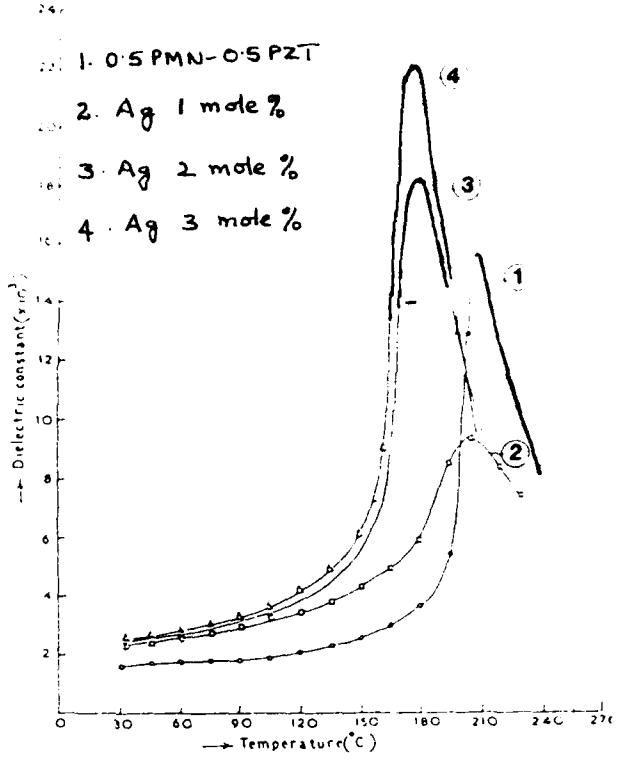


Fig. 3. Variation of dielectric constant of Ag doped 0.5 PMN - 0.5 PZT ceramics

the peak dielectric constant decreases. But as the Ag concentration is increased Tc increased. The dielectric constant vs temperature curves (Fig. 3) shows diffusiveness only for the 1 mole % Ag added composition. Surprisingly with increasing Ag, the dielectric constant curves become sharper indicating an increase in the degree of ordering in the structure. In other PMN - PZT systems also (9) only 1 mole % Ag composition exhibits diffusive nature. The dielectric loss is also considerably lowered with Ag content. Similar behaviour was reported (10) in La doped PMN - PT.

Maximu values of K_p, K_t, d_{31}, d_{33} and g_{31} are obtained in the 0.5 PMN-0.5PZT composition with Ag substitution than in other series (9). The variation of these coefficients with Ag content in the base 0.5 PMN - 0.5 PZT is shown in Fig. 4. Both the coupling factors K_p and K_t reaches maximum values of 42.6 % and 32.5 % respectively for the 1 mole % Ag substituted composition. The thickness coupling factors K_t is almost doubled with introduction of Ag in PMN-PZT. Probably Ag componsates for Pb losses at

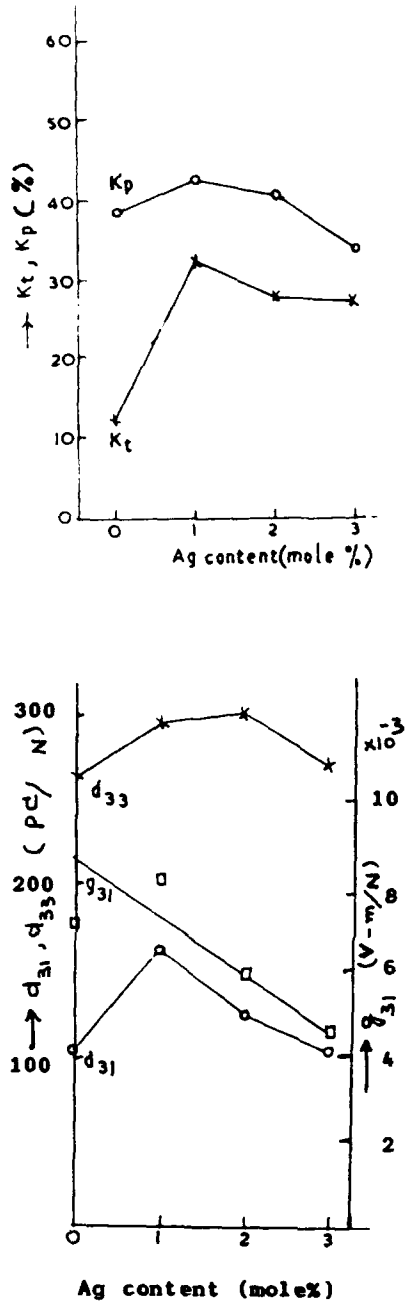


Fig. 4. Variation of piezoelectric properties of Ag doped 0.5 PMN-0.5 PZT ceramics

higher temperatures. Maximum piezoelectric coupling coefficients d_{33} of 162.0 pC/N and g_{31} of 8.17 V - m/N are obtained for the 1 mole % Ag added compositions. But d_{33} coefficients shows an optimum value of 302 pC/N for the 2 mole % Ag added composition. This indicates that the Ag addition facilitates increase of non 180° domains in the 0.5 PMN - 0.5 PZT compositions.

CONCLUSIONS

1. Ag may be compenseting for the Pb losses at higher temperatures. This is reflected in the very low dielectric losses in Ag substituted compositions.
2. P_r and P_s are maximised with Ag introduction in 0.5 PMN - 0.5 PZT ceramics.
3. Dielectric constant curves exhibit diffusive nature only for 1 mole % Ag substituted composition. The curves for other concentrations are sharp, indicating increased ordering in the structure.
4. Introduction of Ag in PMN - PZT ceramics leads to peak K_p, K_t and d_{33} values.

Acknowledgements:

One of the authors (KVR) wishes to thank CSIR, New Delhi for the financial assistance.

REFERENCES

1. B. Jaffe, R.S. Roth and S. Marzullo
J. Res. Natl. Bur. Stand. (U.S) 55(5) 239 (1955)
2. D.A. Berlincourt, C.Cmolik and H. Jaffe
Proc. IRE. (February) 220 (1960)
3. H. Ouchi, K. Nagalo and S. Hayakawa
J. Am. Ceram. Soc. 48(12) 630 (1965)
4. H. Ouchi, M. Nishikawa and S. Hayakawa
J. Am. Ceram. Soc. 49 (11) 577 (1966)
5. H. Ouchi
J. Am. Ceram. Soc. 51(3) 169 (1969)
6. S.L. Swartz and T.R. Shrout
Mater. Res. Bull. 17 1245 (1982)
7. J.K.Sinha
J. Sci. Inst. 42 696 (1965)
8. IRE Standards Piezoelectric crystals
Proc. IRE. 46 764 (1958)
9. K.V. Ramana Murty
Ph.D thesis, Andhra University,INDIA(1991)
10. M.T. Lanagan, N. Yang, D.C. Dube and Jang
J. Am. Ceram. Soc. 72(3) 481 (1989).

GRAIN SIZE EFFECT ON THE INDUCED PIEZOELECTRIC PROPERTIES OF 0.9PMN-0.1PT CERAMIC

S.F. Wang, U. Kumar, W. Huebner[$], P. Marsh[$$], H. Kankul[$$] and C.G. Oakley[$$$]

Materials Research Laboratory, The Pennsylvania State University, University Park, PA 16802
[$] Department of Ceramic Engineering, University of Mossouri-Rolla, MO 65401
[$$] Echo Ultrasound, R. D. 2, Box 118, Reedsville, PA 17084
[$$$] Tetrad Corporation, 12741 E. Caley Ave., Engelwood, CO 80111

Abstract: Lead magnesium niobate ($Pb(Mg_{1/3}Nb_{2/3})O_3$-PMN)-lead titanate ($PbTiO_3$-PT) solid solutions are widely researched to produce devices that can be used in low and high electric field applications. For some applications, such as medical ultrasonic transducers, it is necessary to prepare the ceramic with high density and small average grain size. This paper describes the effect of grain size on the low and high field properties of 0.90PMN-0.10PT ceramics. To prepare highly dense ceramic, vibratory and attrition milled powders were sintered between 1000-1250°C. The average grain sizes of the sintered ceramics varied from 0.7 to 3.5 μm. To understand the grain size effect, dielectric, pyroelectric, electrostrictive, and induced piezoelectric properties were studied.

Introduction

Relaxor ferroelectric materials are widely studied for their dielectric, electrostrictive and induced piezoelectric properties. In the past decade, these materials were used in a variety of applications ranging from multi-layer capacitors to ultrasonic transducers[1,2]. Takeuchi et al.,[2] investigated the effect of 0.90PMN-0.10PT ceramic for the medical imaging in the 1-3 configuration. Because of the high operating frequency, the dimensions of the 'cylindrical' ceramic posts are restricted to only a few tens of microns in all directions. To manufacture such posts reliably and reproducibly, it is necessary to use high density ceramic with small grain size.

The grain size effect on the low and high field properties of PMN-based ceramics has been investigated by several researchers[3-6]. In general, the properties degrade as the grain size is reduced. For example, in 0.93PMN-0.07PT ceramic, the peak dielectric constant drops from 25,000 to 5000 when the average grain size is reduced from 5 μm to 0.3 μm[5]. The size effects observed in these ceramics were attributed to the extrinsic and intrinsic effects such as pore volume, low-K grain boundary phase, and micropolar domain densities. From the literature survey, it appears that the properties of the fine grain ceramic can be improved by minimizing the effect of extrinsic variables and by improving the homogeneity.

In this paper, the effect of average grain size on the low and high electric field properties of 0.90PMN-0.10PT ceramic is reported. Ceramics with average grain sizes ranging from 0.7 to 3.5 μm were prepared from vibratory and attrition milled powders. Low field properties such as dielectric constant and high field properties such as P-E hysteresis, pyroelectric, electrostrictive and a few of the electric field induced resonance properties were investigated as a function of grain size.

Experimental

Preparation

To prepare the ceramic powder, a coulumbite precursor technique was adopted[7]. The magnesium niobate precursor was prepared by calcining the appropriate mixture of MgO(J.T. Baker, Phillipsburg, NJ) and Nb_2O_5(Transelco, NJ) at 1000°C/5h and then at 1100°C/5h. The completion of reaction and the phase purity were checked by comparing the XRD pattern with the JCPDS standard. The PMN-PT batches were prepared by calcining the appropriate mixture of PbO(Hammond, Pottstown, PA), $MgNb_2O_6$, and TiO_2 (Whittake, Clark, and Daniel, South Plainfield, NJ) powders at 900°C/5h.in a closed alumina crucible. To vary the initial average particle size, the calcined powder was subjected to the following grinding schedule. First, the powder was wet ball milled in alcohol in a nalgene bottle with ZrO_2 grinding media for 24h. After drying, a portion of the powder was vibratory milled(Sweco) for 24h. For vibratory milling, a 30 vol% slurry was prepared with water and a few drops of Tamol 901 was used as a dispersant. To minimize contamination, small yittria stabilized ZrO_2 spheres were used as milling media. To increase the surface area further, a small portion of the vibratory milled slurry was attrition milled(Reliance) for an additional 24h. The ball milled, vibratory milled, and attrition milled powders were named as batch A, B, and C, respectively. The ZrO_2 contamination level, and the B.E.T. surface area of these powders are listed in Table 1.

The dried powder was granulated with 5 wt% of Dupont 5200 binder in acetone media. After passing the mixture through a 100 mesh sieve, 1/2" dia. disks were cold pressed in a steel die with 30,000-35,000 psi uniaxial pressure. The binder from the disks was removed by a two stage heat treatment at 300°C/3h and then at 500°C/5h. These pellets were sintered in a closed alumina crucible at 1000-1250°C/1-5h. A small amount of PbO-ZrO_2 mixture was heated along with the pellets to control the lead oxide atmosphere inside the crucible. All the sintered samples were annealed at 950°C/2h. to evaporate excess PbO. The weight losses during these preparation stages were monitored accurately.

Characterization

The bulk densities of the sintered specimens were calculated by measuring the weight change in Xylene. The grain size distribution was analyzed from the microstructures of fractured and polished surfaces. The microstructures were recorded using ISI-DS130 Secondary electron microscope.

Detailed experimental descriptions of dielectric, pyroelectric, P-E hysteresis, and electrostrictive measurements can be found in Ref.8. Dielectric measurements were made on gold sputtered discs

Table 1. Properties of Powder:

	A	B	C
ZrO_2 impurity (wt%)	0.67	0.71	1.03
B. E. T.(m^2/gm) Surface Area	1.29	3.17	15.46

CH3080-0-7803-0465-9/92$3.00 ©IEEE

while cooling from 100°C to -100°C at a rate of 2°C/min. For pyroelectric measurements, the electroded samples were cooled from 50°C to -75°C with an electric field of 10 KV/cm. After neutralizing the surface charge, the pyroelectric current was measured by heating the specimen to 50°C at 4°C/min. For P-E hysteresis and transverse electrostrictive measurements, an a. c. triangular field of ± 10 kV/cm was applied at a frequency of 0.1 Hz. The transverse strain measurements were made with a strain gauge technique. By differentiating E vs. s_2 plots, $-d_{31}$* values as a function of electric field were calculated.

AC impedance measurements were performed on circular disk samples of t < 0.3 mm with sputtered silver electrodes. Resonance curves of conductance G, and resistance R of the samples at various biases were recorded with an HP 4194A impedance analyzer at 25°C. Series and parallel resonance frequencies f_s and f_p of thickness resonance mode were used to calculate k_t with the equation given in Ref.9.

Results and Discussion

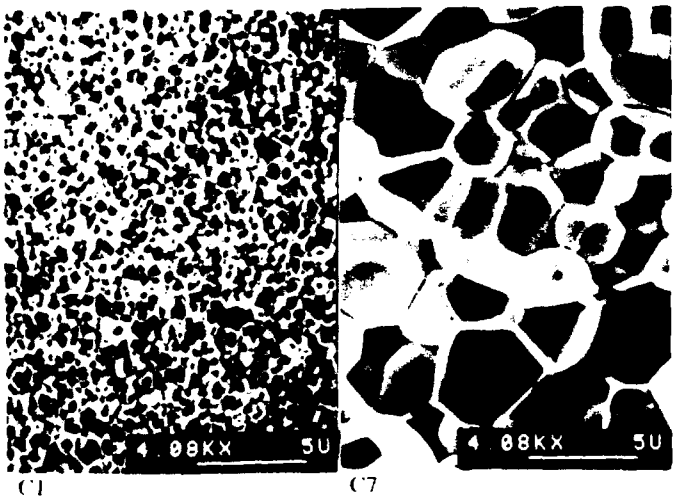
Physical Properties

The density and weight loss data of batch B and batch C samples are listed in Table 2. In general, samples sintered at lower temperatures show slightly higher density due to limited grain growth. Among the two batches, as the initial average particle size of C was lower, it sintered to comparatively higher densities. At higher sintering temperatures, as the grain growth mechanisms dominate, both batches sintered to similar densities. While batching the powders for calcination, to ensure the completion of reaction, 0.5 wt% excess PbO was added. But after sintering and annealing, higher weight losses were observed (Table 2). As reported by Wang and Scultz[6], our sample surfaces also showed a small number of pyrochlore grains. Since the pyrochlore is lead deficient in nature, excess PbO is evaporated while annealing.

The polished and fractured microstructures of a few of the sintered samples are reproduced in Fig. 1. The mean average grain sizes for all the samples are listed with standard deviation in Table 2.

Table 2. Physical Properties of the ceramic.

	Si. Tem. °C/h	wt. loss %	Density gm/cc	% Theo.	Ave. g.s. (μm)
B1	1000/1		7.28±0.04	89.24	
B2	1050/1	1.10	8.00±0.02	98.06	1.1±0.2
B3	1100/1	1.10	7.99±0.01	97.94	1.2±0.3
B4	1150/1	1.11	7.98±0.02	97.84	1.3±0.3
B5	1200/1	1.16	7.96±0.03	97.57	1.7±0.5
B6	1250/1	1.20	7.90±0.02	96.84	2.2±0.8
B7	1250/5	1.32	7.83±0.03	95.98	3.3±1.3
C1	1000/1	0.85	7.92±0.03	97.08	0.7±0.2
C2	1050/1	0.99	8.00±0.03	98.08	1.0±0.3
C3	1100/1	1.03	7.99±0.02	97.94	1.4±0.4
C4	1150/1	1.06	7.98±0.02	97.82	1.5±0.5
C5	1200/1	1.02	7.94±0.02	97.33	1.9±0.6
C6	1250/1	1.13	7.88±0.03	96.59	2.4±0.8
C7	1250/5	1.29	7.80±0.03	96.51	3.6±1.8



C1 C7

Fig 1. Fractured surfaces of C1 and C7

Table3. Dielectric Properties of the ceramic

	g.s. μm	Kmax	Tmax °C	Tan δ at 25°C	δ (°C)
B2	1.1	17800±470	48	0.0582	40
B3	1.2	22250±050	46	0.0686	38
B4	1.3	23750±720	46	0.0718	34
B5	1.7	25300±600	45	0.0765	31
B6	2.2	28850±790	43	0.0829	27
B7	3.3	33000±550	42	0.0922	
C1	0.7	13900±300	48	0.0474	
C2	1.0	20800±360	43	0.0725	33
C3	1.4	23350±510	42	0.0792	32
C4	1.5	24700±420	42	0.0803	32
C5	1.9	25450±810	41	0.0795	30
C6	2.4	25800±720	41	0.0850	29
C7	3.6	27450±300	40	0.0891	

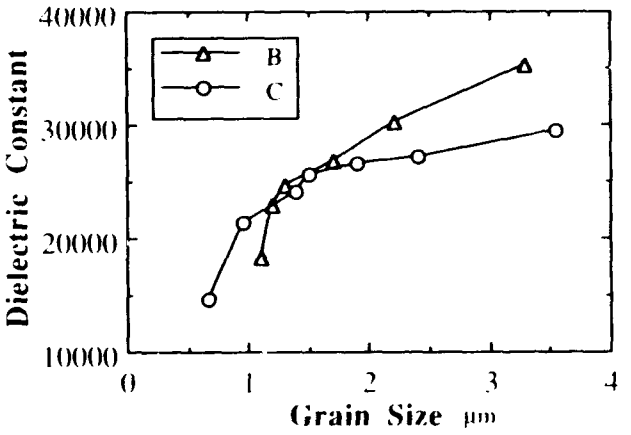


Fig.2. Effect of average grain size on K_{max}. The dielectric constant was compensated for porosity with Weiner's rule.

Low Electric Field Properties

The relevant dielectric properties are compared in Table 3. At least four samples were used to calculate the percentage change in the dielectric constant. The maximum dielectric constant (K_{max}), after compensating for porosity with Weiner's equation[10], is ploted in Fig.2, as a function of average grain size. Comparatively, the K_{max} of the samples from series B, changes as a strong function of grain size. In both batches, K_{max} reduces drastically when the grain size is <1μm.

High Electric Field Properties

The effect of grain size on the P vs. T behavior is compared in Fig. 3 and 4. To plot these figures, the polarization was calculated from the pyroelectric current. In relaxor ferroelectric materials, P vs. T behavior below the pyroelectric depolarization temperature, T_d, reflects the degree of cohesiveness among macrodomains. Below T_d, if the macrodomains are highly stable, ΔP with respect to ΔT will be small. When the material is heated, the stable macrodomains will convert into microdomains, over a narrow temperature interval around T_d. In our investigation, the samples sintered at higher temperatures show these behaviors very clearly. When the sintering temperature is reduced, increasingly large changes in P with respect to temperature is observed below T_d. More over, in these samples the macrodomains transform into microdomains over a wider temperature around T_d. Careful analysis of P vs. T behavior points out the importance of proper processing. In series C samples, as the grains were grown from finer particles, the grain size effect is minimized.

The induced polarization and the transverse strain characteristics of the fine grain samples from both batches show degradation of properties. This observation is clearly demonstrated by plotting $-d_{31}$* vs. E field, as a function of grain size (Fig. 5 and 6). These measurements were made at 25°C. When the grain size is above 3 μm, a maximum $-d_{31}$* of about 500 pC/N is observed. When the grain size is reduced, the magnitude of maximum $-d_{31}$* reduces with an increase in the corresponding electric field.

The piezoelectric thickness coupling coefficients calculated from the resonance curves observed at different d.c. biases are plotted in Fig. 7 and 8. These measurements were made at 25°C with increasing bias voltages. In both batches, coarse grained samples showed increased coupling at lower electric fields. The absolute values of coupling coefficients also increased as the grain size is increased.

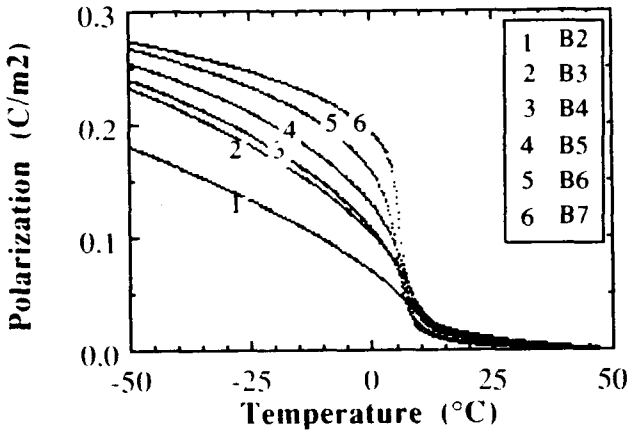


Fig.3. Polarization vs. Temperature behavior of batch B samples.

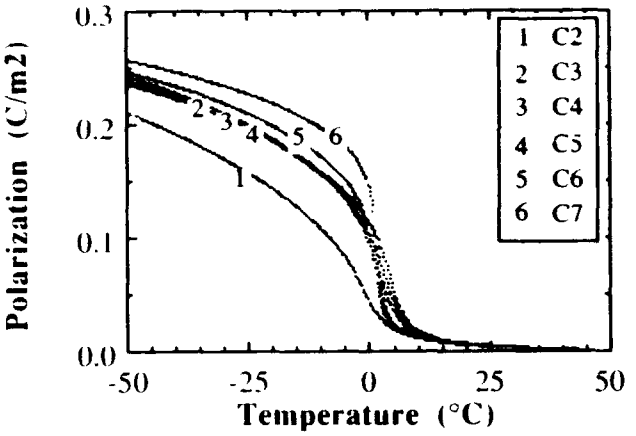


Fig.4. Polarization vs. Temperature behavior of batch C samples.

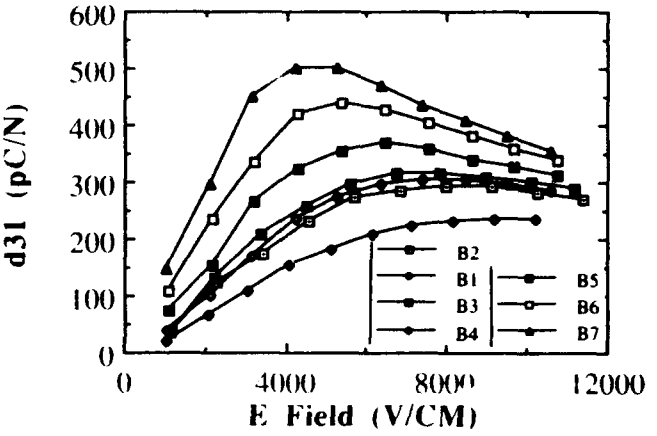


Fig.5. Effective transverse piezoelectric d coefficients of batch B samples; calculated from electrostriction data.

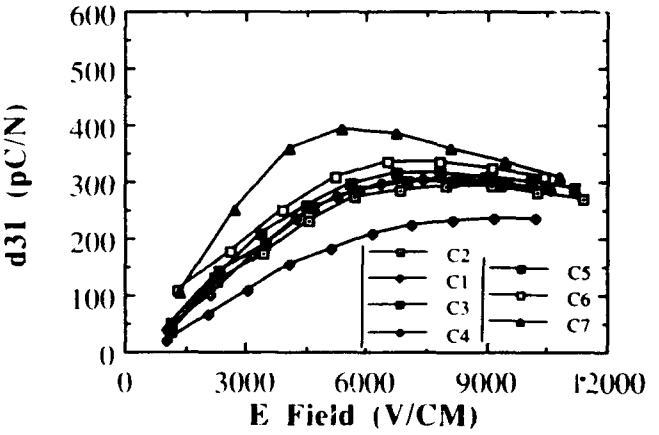


Fig.6. Effective transverse piezoelectric d coefficients of batch C samples; calculated from electrostriction data.

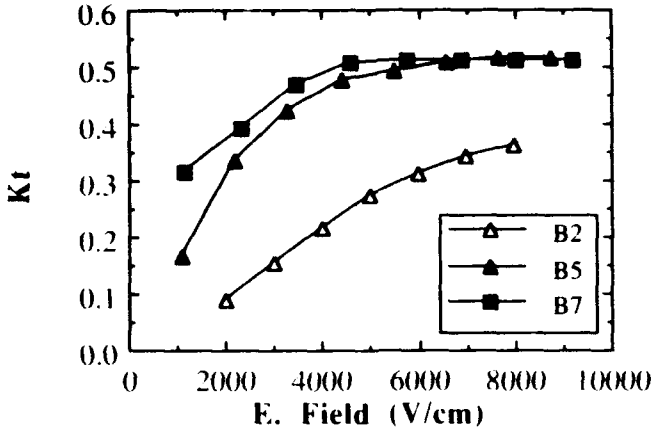


Fig.7. Thickness coupling coefficients of batch B samples at different d. c. bias fields; calculated from resonance curves.

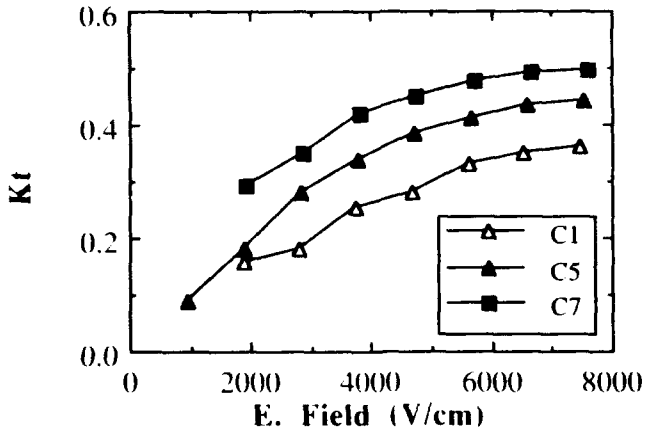


Fig.8. Thickness coupling coefficients of batch C samples at different d. c. bias fields; calculated from resonance curves.

Discussion

As mentioned in the introduction section, the grain size effect on the properties may be attributed to extrinsic and intrinsic variables. In the present samples, through careful annealing the effect of extrinsic variables are minimized. For example, B2, B3, B4 and C2, C3, C4 samples with similar weight losses and therefore with similar second phase volume at the grain boundary, show noticeable differences in the low and high electric field properties. As observed in all the properties, large grain samples with lower density show better properties as compared to fine grain samples with higher densities.

Careful analysis of the the low and high electric field properties show clear distinction between the properties of series B and series C samples. Slight depression of T_{max} and T_d in series C samples may be attributed to the higher concentration of Zr^{4+} ions as dopant[11]. Considering the average grain sizes of all these samples, ranging from approximately 0.7 μm to only 3.5 μm, it appears that the sintering temperature also influences the properties. From the surface area of the milled powders, the equivalent spherical diameter of the series B and series C powders are calculated as 0.23 μm, and 0.047 μm, respectively. Comparing the grain sizes, it is clear that the series C samples show at least 15 times growth during sintering. Because of this growth, it is hypothised that these samples are more homogeneous as compared to series B samples. Hence, the lesser influence of the average grain size on the low and high field properties of series C samples may be attributed to higher degree of homogeneity.

Conclusion

In this paper, the dielectric, pyroelectric, electrostrictive, and the induced piezoelectric properties of 0.90PMN-0.10PT ceramic are compared as a function of grain size. Comparatively, samples prepared from coarse particle compact show higher grain size dependance. When the average grain size is around 3.5 μm, irrespective of the initial powder characteristics, the ceramic show similar high electric field properties. Through transverse strain measurements, a high $-d_{31}^*$ of 500 pC/N at a d.c. bias of 4300 V/cm is observed. When the samples were prepared from very fine powders, the magnitudes of K_{max}, d_{31}^*, and k_t reduces only moderately as the grain size is reduced to 1.5 μm. Since the effect of extrinsic variables such as density and the grain boundary phase are minimized through careful preparation, the observed grain size

Acknowledgements: Financial support from Echo Ultrasound of Reedsville, PA and The Ben Franklin Partnership Program of the commonwealth of PA and technical support from Mingtong Song are gratefully acknowledged.

References

[1] W. Y. Pan, W. Y. Gu, D. J. Taylor and L. E. Cross, "Large Piezoelectric effect induced by Direct Current Bias in PMN:PT Relaxor Ferroelectric," Jpn. J. Appl. Phys., 4, p653 (1989).

[2] H. Takeuchi, H. Masuzawa, C. Nakaya, and Y. Ito, "Relaxor Ferroelectric Transducers," 1990 IEEE Ultrasonic Symposium, Aomanic, p697-705 (1990).

[3] K. Uchino, M. Tatsumi, I. Hagashi, and H. Hayashi,Jpn J. Appl. Phys., 24, 733-735 (1985).

[4] T. R. Shrout, U. Kumar, M. Megheri, N. Yang, and S. J. Jang," Grain Size Dependance of Dielectric and Electrostriction of $Pb(Mg_{1/3}Nb_{2/3})O_3$ -based ceramic," Ferroelectrics, 76, 479-85 (1987).

[5] P. Peppet, J.P. Dougherty and T.R. Shrout,"Particle and Grain Size Effects on the Dielectric Behavior of the Relaxor Ferroelectric $Pb(Mg_{1/3}Nb_{2/3})O_3$," J. Mater. Res., 5[12], 2902-2909 (1990) (and the references there of).

[6] H. C. Wang, and W. A. Schultze," The role of excess magnesium oxide and lead oxide in determining the microstructure and the properties of lead magnesium niobate," J. Am. Cer. Soc., 73[4] 825-32 (1990) (and the references there of).

[7] S. Swartz and T. R. Shrout, "Fabrication of Perovskite Lead Magnesia Niobate," Mat. Res. Bull., 17, 1245-1250 (1982).

[8] U. Kumar, L. E. cross, and A. Halliyal," Pyroelectric and electrostrictive properties of (1-x-y)PZN.xBT.yPT ceramic solid solution system," J. Am. Ceram. Soc., 75[8], p-2155-64 (1992).

[9] "IRE standards on piezoelectric crystals: Measurements of piezoelectric ceramic,1961", Proc. IRE, 49, p-1161-1169 (1961)

[10] D. F. Rushman, and M. A. Strivens," The effective permittivity of two-phase systems," Proc. Phys. Soc. 59, p-1011-1016 (1947).

[11] D. J. Voss, S. L. Swartz and T. R. Shrout," Pyroelectric and Electrostrictive properties of B-site modifications on dielectric and electrostrictive properties of lead magnesium niobate ceramics," Ferroelectrics, 50, p-203-208 (1983).

EFFECTIVE ELECTROMECHANICAL PROPERTIES OF SOME $Pb(Mg_{1/3}Nb_{2/3})O_3$-$PbTiO_3$-$(Ba,Sr)TiO_3$ CERAMICS

S. M. Pilgrim, A. E. Bailey, M. Massuda, J. D. Prodey, and A. E. Sutherland
Martin Marietta Laboratories, 1450 South Rolling Road, Baltimore, MD 21227

Abstract-- A number of $Pb(Mg_{1/3}Nb_{2/3})O_3$-based materials were characterized to determine the effects of temperature on their induced strain and hysteresis properties. Simultaneous determination of the transverse and longitudinal properties allows the calculation of both an effective Poisson ratio and an effective hydrostatic d coefficient. One composition showed significant variation in the effective Poisson ratio (0.28 to 0.40) across the temperature interval 0 to 40°C. The large, effective hydrostatic coefficients (up to 300 pC/N) combined with the high permittivity of the materials provide potential for use as a hydrostatic sensor.

I. Introduction

This paper addresses the effective piezoelectric properties of PMN-X (*lead magnesium niobate solid* solutions with lead titanate (PT) and either barium titanate (BT) or strontium titanate (ST)) as an enabling material for various electromechanical applications. In essence, the PMN-X materials are electrostrictors that provide higher output from a given volume or given output from a smaller volume than conventional piezoelectrics. Like all electrostrictors, the PMN-X materials show a quadratic dependence of strain on electric field and have "Curie" temperatures (T_{max}) below the use temperature, where T_{max} is defined as the temperature of maximum relative permittivity, K_{max}. They have minimal remanent polarization and therefore do not exhibit piezoelectric creep, long-term depoling, or permanent property change from temperature excursions (<~600°C). The electrostrictive ceramics described in this report are chemically and physically similar to the Pb-based materials which are in commercial use for multilayer capacitors and to the conventional lead zirconate-titanate, lead titanate, and piezoelectric PMN ceramics in use by the Navy [1,2,3,4]. They are dense (ρ=~8.0 g/cm^3), but prone to mechanical failure in tension. However, they combine the modulus of conventional ceramics with a very large induced strain (usable values of >600 microstrain) and low hysteresis [5,6].

Although such desirable properties have been reported in the literature for a wide variety of Pb-based systems [7,8], the materials have not been put to widespread, practical use. Practical application is complicated by the relaxor nature (frequency dependence) of the materials and the field dependence of their properties. Applications have generally been limited by the lack of a) an engineering database, b) commercial production, c) fundamental understanding of process/property relationships, and d) predictive capability [9].

Previous work demonstrated the promise and initial potential of the materials [10,11], and highlighted the importance of the relationship between the induced transverse and longitudinal strains as the material goes through its phase transition.

II. Experimental Procedure

Physical and Weak-field Properties

Three compositions (Table I) were processed using a columbite precursor synthesis method [6,12,13]. Specifically, the method uses CFC-113 as the milling agent, ball milling as the mixing and grinding method, and commercially available raw materials (AVX Corp.). *All starting powders, pressing steps, calcining and* sintering schedules were as previously described [11].

TABLE I
SAMPLE NAMES AND COMPOSITIONS

Name	Composition
S250075	0.975(0.925PMN-0.075PT)-0.025ST
B250075	0.975(0.925PMN-0.075PT)-0.025BT
B500100	0.95(0.90PMN-0.10PT)-0.05BT

The compositions were prepared in 50-g batches and, after both calcining and sintering, were assessed for perovskite phase purity by x-ray diffractometry (XRD). Pellets, nominally 11 mm in diameter and 2-mm thick, of each composition were uniaxially pressed (20 MPa), isopressed (200 MPa), and sintered (3 h at 1185°C with a sacrificial Pb source). All samples were 100% perovskite within the detection limits -- primary pyrochlore peak at 29.25° entirely absent. The sample dimensions were measured before sintering, after sintering, and after polishing with 1000 grit SiC paper to determine weight loss, volume shrinkage and density (see Table II).

CH3080-0-7803-0465-9/92$3.00 ©IEEE

TABLE II
PHYSICAL PROPERTIES OF COMPOSITIONS

Sample	Weight Loss (%)	Shrinkage Volume (%)	Density (g/cm^3)
S250075	1.2±0.04	36.8±1.6	7.77±0.09
B250075	0.7±0.0	35.5±0.7	7.83±0.21
B500100	0.9±0.1	31.2±0.4	7.67±0.03

The weight loss and the volume shrinkage are typical for these materials. The densities of the materials are high -- approximately 95% of the basic theoretical density of 8.15 g/cm^3.

After the physical measurements were taken, the samples were electroded with sputtered gold and fire-on silver. Weak-field measurements of dielectric loss and permittivity at 1 kHz (Table III) were used as an initial screening of the material over a temperature range from -50°C to 100°C and frequencies of: 0.1, 1, 10 and 100 kHz [11]. These measurements, for both increasing and decreasing temperature ramps, showed no dielectric aging and typical relaxor frequency dispersion [1,11].

TABLE III
WEAK-FIELD ELECTRICAL PROPERTIES

Sample	T_{max} (°C)	K_{max} @ T_{max}	Loss tangent @ T_{max}
S250075	11.1	22678	0.0438
B250075	12.6	22249	0.0464
B500100	20.5	18164	0.0455

All data from the decreasing temperature ramps.

Temperature Dependence of Effective Piezoelectric d_{31} and d_{33} at Large AC Amplitude

Basic high-field properties, transverse strain and induced polarization, were collected under AC drive fields of 0-1.0 MV/m (DC bias of 0.5 MV/m), at frequencies between 1 and 300 Hz across the temperature interval -25 to 60°C. All measurements were done using an integrating capacitor or piezoresistive strain gages [10,11]. These measurements served as a baseline for the more innovative measurements of induced transverse and longitudinal strains as functions of temperature. As listed in Table IV and illustrated in Fig. 1, the compositions were primarily electrostrictive across the entire temperature range of measurement. Figure 1 also shows the effect of frequency and temperature on the induced transverse strain and hysteresis as a function of temperature for selected frequencies.

TABLE IV
HIGH-FIELD ELECTROMECHANICAL PROPERTIES

Composition	T_{max} (°C)	Transverse Microstrain	Polarization (mC/m^2)
S250075	11.1	96	148
B250075	12.6	117	157
B500100	20.1	116	143

T_{max} @ 1 kHz, transverse strain and peak polarization @ 100 Hz with a drive field of 0 to 1.0 MV/m taken at 25°C.

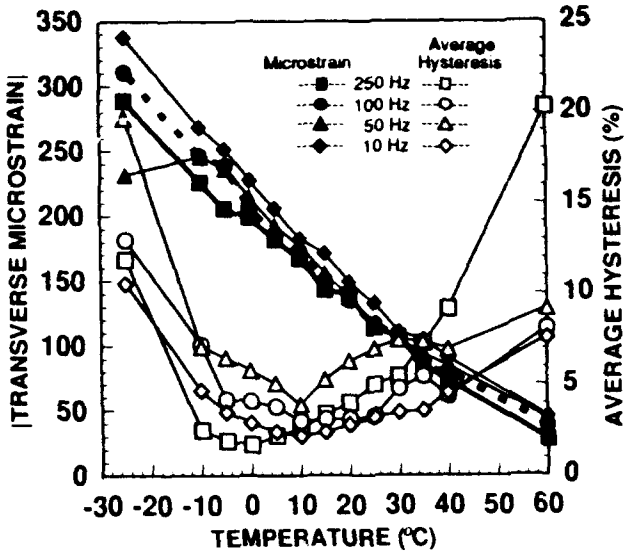


Fig. 1. Typical induced transverse strain and hysteresis curves for the B250075 material at 1 MV/m as a function of temperature.

Since electromechanical materials are used in both the transverse (d_{31}) and longitudinal (d_{33}) strain modes, induced strain and hysteresis for both modes are needed to fully characterize the material behavior. Simultaneous testing allows measurement or calculation of the:

- Ratio between transverse and longitudinal strain (effective d_{31}/d_{33}, the effective Poisson ratio) across each material's transition temperature, under identical environmental conditions, as a function of AC field
- Relation of electrical loss (hysteresis) in the transverse and longitudinal modes
- Effective hydrostatic d coefficients for prediction of passive performance in real environments.

The test set-up is shown schematically in Fig. 2. Pellets of each material were bonded to insulating Macor blocks using Humiseal insulating varnish. Strain gages were mounted to the ground surface for measurement of transverse strain (effective d_{31}). An aluminum button was mounted over the strain gage as a target for the longitudinal strain measurement. A Kaman displacement sensor (Kaman Instruments) was mounted a small distance from the aluminum target. The sensor determines longitudinal displacement (effective d_{33}) by measuring eddy currents in the button induced by a small constant magnetic field from the sensor. The magnitude of the eddy current changes as a function of the distance between the target and the sensor, which varies as the pellet expands. Measurements were done at various temperatures in a Delta Design environmental chamber in order to characterize each material as a function of temperature.

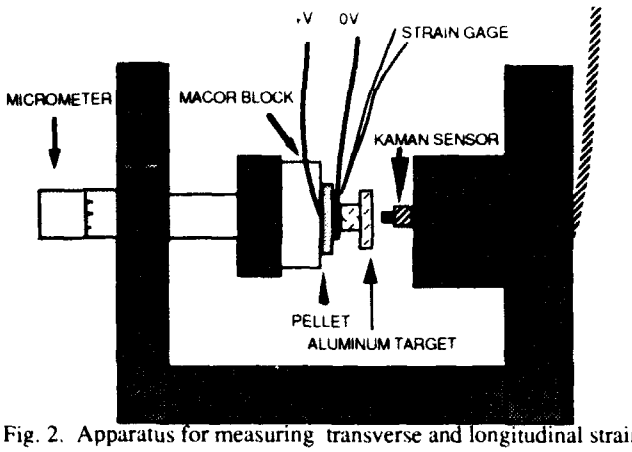


Fig. 2. Apparatus for measuring transverse and longitudinal strains.

The peak strains and average hysteresis for 1.0 MV/m cycles are shown as functions of temperature in Figs. 3 through 5 for representative pellets from each composition. The increase in strain and hysteresis as the temperature is lowered is ascribed to increased piezoelectric contributions to the total strain [8,11].

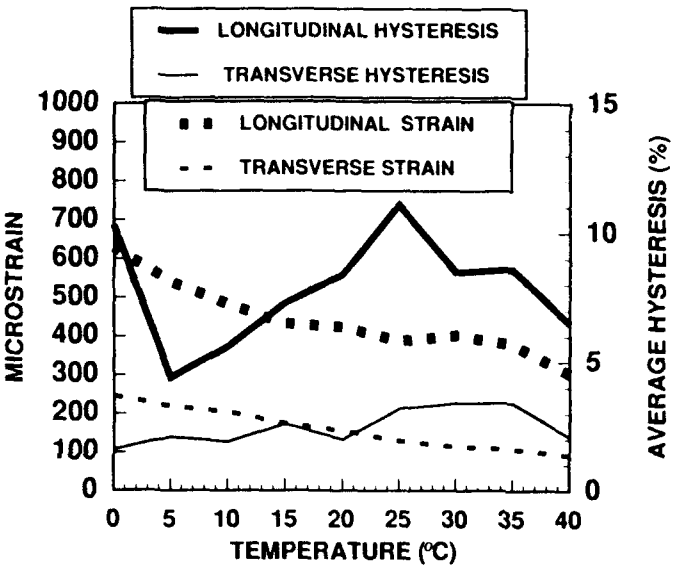


Fig. 3. Induced strain and hysteresis for the S250075 composition.

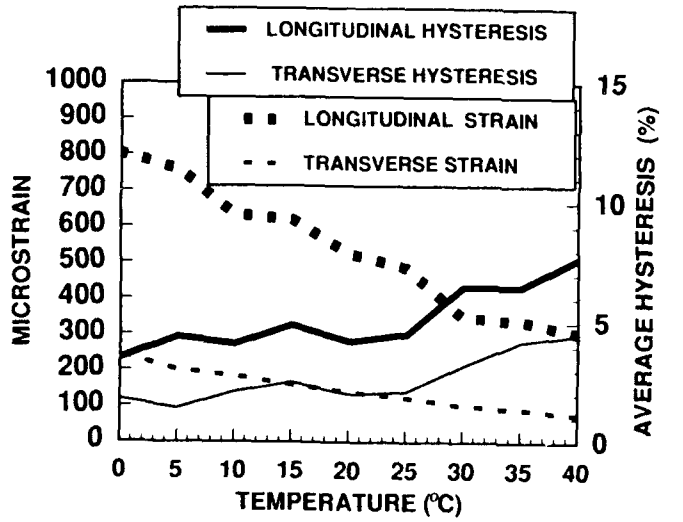


Fig. 4. Induced strain and hysteresis for the B250075 composition.

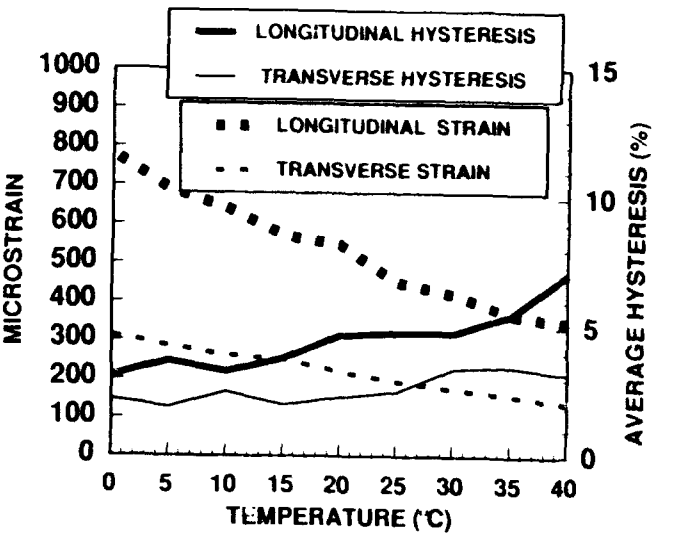


Fig. 5. Induced strain and hysteresis for the B500100 composition.

As expected, the materials with the lower transition temperatures, S250075 and B250075, yielded lower transverse strains for a given temperature. Each composition maintained a low hysteresis; however, the S250075 showed no clear trend with temperature. The minimum hysteresis level (~ 2%) is attributed to noise during data acquisition. The S250075 and B250075 materials yielded nearly identical transverse strains across the given temperature range, but the BT-doped material yielded higher longitudinal strains as the temperature decreased. The B500100 material yielded similar longitudinal strains and hysteresis as the B250075 material, but with higher transverse strains.

Calculation of the ratio of peak transverse to longitudinal strain gives an indication of the effective Poisson ratio of the material (Fig. 6). NB this can be >0.5 since the strains are large and the volume is not necessarily constant across the entire temperature range. The d_{31}/d_{33} ratio was relatively constant for the BT-doped material and the lowest of the compositions (~0.28). However, the ratio increased to values over 0.4 at lower temperatures for the ST-doped material. This change in ratio is not correlated with the high-field transition [14]; however, similar behavior has been noted previously in another ST-doped PMN [15]. The B500100 material had the largest d_{31}/d_{33} ratio.

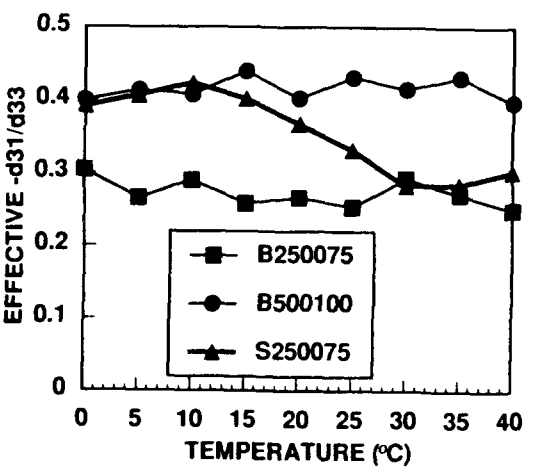


Fig. 6. Ratio of transverse to longitudinal induced strain.

Material performance under real, hydrostatic, conditions was estimated from strain values for possible sensor applications. The effective hydrostatic d coefficients shown in Figure 9 were calculated from the large AC-field transverse and longitudinal strains using the equation

$$d_h = d_{33} - 2d_{31} \qquad \text{Eqn 1.}$$

In general, d_h values increase somewhat at lower temperatures except for the S250075 material. Note the hydrostatic d values are much greater than those commonly found in conventional piezoelectric materials and are accompanied by larger permittivities [2,3,4].

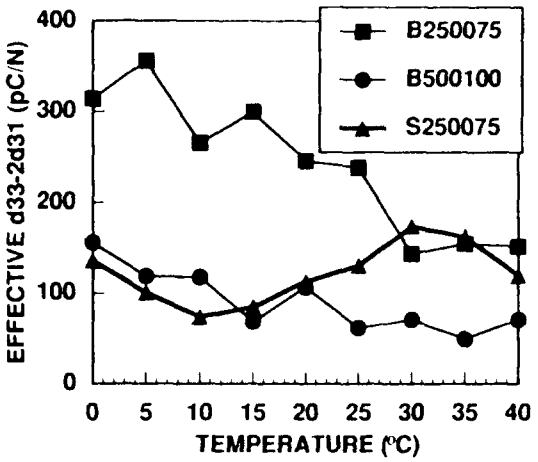


Fig. 7. Effective hydrostatic piezoelectric coefficients.

III. Conclusion

All compositions showed high-field properties consistent with weak-field properties reported previously for relaxor ferroelectrics. In particular, the frequency dependence of the electromechanical properties was typical--both strain and polarization decreased with increasing frequency. The induced transverse and longitudinal strains tracked with one another across the temperature interval as did the associated hystereses. The ratio of the induced strains was different for each composition and showed temperature dependence in the S250075 composition. Calculation of the effective hydrostatic d coefficient of the materials suggested that PMN-X materials have application as high-sensitivity hydrostatic sensors.

Acknowledgement

The authors gratefully acknowledge funding of this work by the Navy via contract N66001-91-C-6012.

References

[1] L. E. Cross, "Ferroelectric Ceramics--Tailoring Properties for Specific Applications," in Final Report for N00014-89-J-1689 covering February 1991 to January 1992. The Materials Research Laboratory, The Pennsylvania State University, 1992.

[2] Piezoelectric Ceramics, EDO Corp., Western Division, EWC 02742 8806 10M, Salt Lake City, UT.

[3] Piezoelectric Ceramic for Sonar Transducers (Hydrophones and Projectors), MIL-STD 1376A(SH), 20 December 1988.

[4] B. Jaffe, W.R. Cook Jr., and H. Jaffe, Piezoelectric Ceramics, New York, NY: Academic Press, 1971.

[5] L. E. Cross, "Relaxor Ferroelectrics," Ferroelectrics, vol. 76, pp. 241-267, 1987.

[6] S. M. Pilgrim, M. Massuda, and A. P. Ritter, "Electrostrictors for Active Sonar - Final Report covering October 1989 to January 1991 N00014-89-C-2357," Martin Marietta Laboratories MML TR 91-7c, January 1991.

[7] Landolt-Bornstein Group III: Crystal and Solid State Physics, Volume 16a: Oxides, Eds. K.-H. Hellwege and A. M. Hellwege, New York, NY: Springer-Verlag, 1981.

[8] K. Uchino, "Electrostrictive Actuators: Materials and Applications," Ceramics Bulletin, vol. 65, pp. 647-656, 1986.

[9] "Deformable Mirror Actuators for Rapid Retargeting, WL-TR-89-20 DTIC," Alexandria, VA: Defense Technical Information Center, 1989.

[10] S. M. Pilgrim, M. Massuda, and A. E. Sutherland, "Development of Advanced Active Sonar Materials and Their Microstructure-Property Relations N62190-91-M-0322," Martin Marietta Laboratories MML TR 91-33c, June 1991.

[11] S. M. Pilgrim, A. E. Bailey, M. Massuda, J. D. Prodey, and A. E. Sutherland, "Development of Advanced Active Sonar Materials and Their Microstructure-Property Relations N66001-91-C-6012," Martin Marietta Laboratories MML TR 92-2c, January 1992.

[12] A. E. Sutherland, S. M. Pilgrim, A. E. Bailey, and S. R. Winzer, "Dielectric Aging of Doped PMN-PT Ceramics," in Ceramic Transactions Vol. 15, American Ceramic Society: Westerville, OH, 1990, pp. 105-27.

[13] S. L. Swartz and T. S. Shrout, "Fabrication of Perovskite Lead Magnesium Niobate," Materials Research Bulletin, vol. 17, pp. 1245-50, 1982.

[14] S. M. Pilgrim, M. Massuda, and A. E. Sutherland, "Electromechanical Determination of the High-field Phase Transition of $Pb(Mg_{1/3}Nb_{2/3})O_3$-$PbTiO_3$-$(Ba,Sr)TiO_3$ Relaxor Ferroelectrics," Journal of the American Ceramics Society, vol. 71, 1992.

[15] Private communication, K. A. Rittenmeyer, NRL/USRD, Orlando, FL.

Piezoelectrics and Electrostrictives

THE EFFECT OF PHOTO-REFRACTIVELY INDUCED PERIODIC STRAIN GRATING ON PIEZOELECTRIC VIBRATION IN $LiNbO_3$:Fe

Michio OHKI, Nobuyuki TANIGUCHI and Tadashi SHIOSAKI
Department of Electronics, Faculty of Engineering,
Kyoto University, Sakyo-ku Kyoto, 606

Abstract

Strong nonlinear behavior was observed in a $LiNbO_3$:Fe piezoelectric resonator with a photorefractive periodic grating. The resonator is a y-cut plate with Au electrodes totally or partially deposited on both faces. The current-voltage and the admittance-frequency characteristics show nonlinear behavior such as hysteresis only near the resonance frequency. In some conditions, the current changes negatively with the voltage. These characteristics depend on the Q-value of the resonator. The present nonlinear phenomena do not occur when the Q-value is too large, while they occur at larger values of Q in usual resonators. We found that the Q-value of the resonator with the photorefractive grating varied when the resonator was annealed or when the period of the grating was changed.

Introduction

The application of the photorefractive (PR) effect to holography and optical processing has developed in recent years.[1] This effect is the phenomenon in which the refractive index of an electrooptic crystal varies according to the incidence of visible rays. Interference of two coherent optical waves yields fringes which cause excitation and diffusion of carriers that form a spatial charge distribution. The variation of the refractive index is caused by the internal electric field from the charge distribution through the Pockels effect. The application to acoustics has also developed; an acoustic wave is filtered by the periodic variation of the acoustic velocity that is caused by the periodic internal electric field.[2] In this paper, we describe the influence of the PR effect on acoustic vibration, especially piezoelectric vibration, from a new point of view. A piezoelectric resonator made of $LiNbO_3$:Fe with the PR grating is examined as the sample. We view electromechanical characteristics near the resonance frequencies of the modes of vibration.

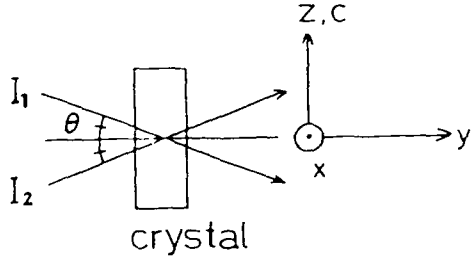


Fig.1. The configuration of the sample to which two coherent light waves are incident and for which the PR grating is written in the c-direction.

Experimental Methods

A y-cut plate of $LiNbO_3$:Fe is used as the sample. Two coherent light waves are incident into the sample, as illustrated in Fig.1. Interference of two coherent optical waves yields fringes which cause excitation and diffusion of carriers that form a spatial charge distribution, so the PR grating is written in the c-direction of the crystal, as illustrated in Fig.2. The sample is rectangular, 7.185mm (x)x 1.511mm(y)x 4.029mm(z). The length of the sample in the x-direction is larger than the width in the z-direction. The light wave is s-polarization, that is, the electric field is in the x-direction, of an Ar^+ laser whose wavelength λis 514.4nm. The ratio of I_1 to I_2 is 1:1, and the diameter of the beam is about 20mm, larger than the sample. The period of the PR grating Λ can be changed by changing the angle θ in Fig.1. In our experiment, the value of Λ is selected to be about 1μm and 3.9μm. After the PR grating is written, whole Au electrodes are deposited on the y-planes, and 1) the frequency characteristics of admittance, 2) the current-voltage (I-V) characteristics, and 3) the spectral analysis of harmonic generation are respectively measured near the resonance frequencies of the following mn modes where m denotes the direction of electric field and n denotes the strain S_n: 1) the 21-coupling, length-extensional mode, 2) the 24-coupling, thickness-shear mode, and 3) the 22-coupling, thickness-extensional mode,as illustrated in Fig.3. In the vibration of 21-mode, the displacement not only in the x-direction but also in the z-direction exists in the case of this sample. Concerning the 21-mode, the measurement is made in the case of not only whole electrodes but also partial ones, 2mm(x) x1mm(z).

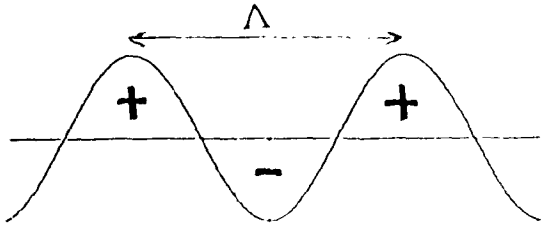


Fig.2. The sinusoidal charge distribution written in the c-direcrion.

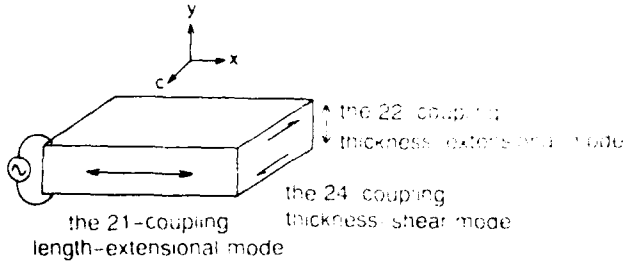


Fig.3. The modes of piezoelectric vibration in y-cut plate of $LiNbO_3$.

CH3080-0 7803-0865-9/92$3.00 ©IEEE

The optical diffractive grating can be erased after annealing at 200°C for 1h. This is well known in the field of optics. Therfore, we perform the similar measurement as above after annealing to compare with the characteristics before annealing. A virgin y-cut plate, on which the PR grating has not been written, is prepared to examine the intrinsic characteristics of $LiNbO_3$:Fe.

In measuring the frequency characteristics of admittance, we also note the variation of 1) the Q-value of the resonance, 2) the resonance frequency ω_R, and 3) the existence of the nonlinear jump phenomena, due to annealing.

Results and Discussion

Table I shows the variation of Q and ω_R after the annealing in the 21-mode for two values of Λ and two kinds of electrodes. We find that the rate of the variation is larger when the electrodes are partial or when the value of Λ is larger.

When the Q-value is very small, for example, about 2000 in the sample before annealing with the partial electrodes and the grating of Λ= 3.9μm, we observe the nonlinear jump phenomenon of an admittance circle, as shown in Fig.4. Although the $LiNbO_3$: Fe resonator without the PR grating shows an intrinsically weak nonlinear jump phenomenon, the sample with the PR grating shows the phenomenon at phase angles other than that of the former. After annealing of the sample, the Q-value increased tenfold to about 20000, and the nonlinear jump phenomenon disappeared. The usual nonlinear effect, intrinsic to the $LiNbO_3$:Fe resonator, must be enhanced when the Q-value increases because the higher orders of strain become more effective. Therefore, the nonlinear phenomena observed here for the sample with the PR grating are unusual and due to a completely different mechanism.

On the other hand, in the case of the sample with the whole electrodes and the grating of Λ=3.9μm, although the nonlinear jump phenomenon did not appear before annealing, the phenomenon appeared and the Q-value decreased after annealing. This suggests the existence of the PR grating after annealing. On the other hand, the optical Bragg diffraction did not occur after annealing, so the PR grating is considered to disappear. These two facts are seemingly not consistent with each other. The grating seems to partially remain even after annealing. The thermal energy seems too low to erase the PR grating completely. The nonlinear phenomena are confirmed by the I-V characteristics or the harmonic generation, as well as by the admittance characteristics. Figure 5(a) shows the I-V characteristics of the sample with the whole elec-

Table I. The variation of the Q-value and the resonance frequency ω_R of the 21-mode after annealing. The simbols "N", "I" and "D" denote no significant change, an increase and decrease, respectively. The value in parentheses shows the variation numerically.

Λ Electrodes		1μm	3.9μm
Whole	ω_R	N	I(0.05%)
	Q	N(10000~15000)	D(20000 → 5600)
Partial	ω_R	I(0.025%)	I(0.05%)
	Q	I(2600 → 17000)	I(2000 → 20000)

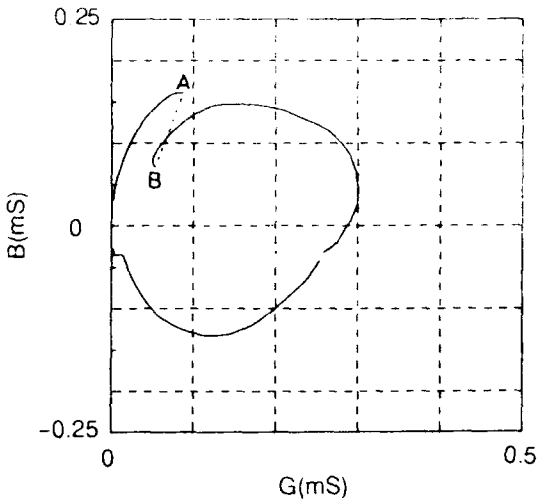


Fig.4. Nonlinear jump phenomenon observed in the admittance circle near the resonance frequency of the 21-mode.

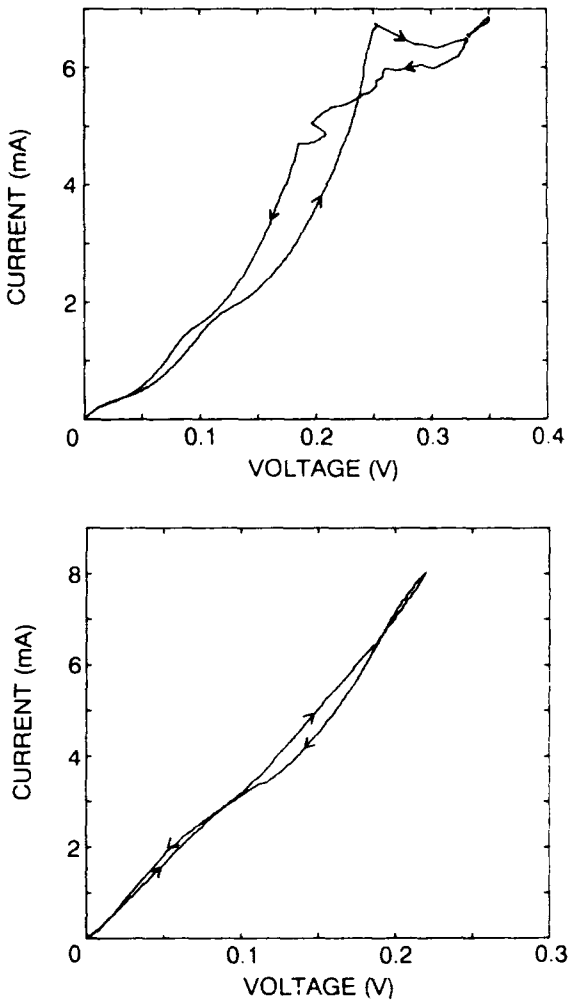


Fig.5. (a) The I-V characteristics of the sample with the PR grating at the resonance frequency of the 21-mode. (b) The intrinsic I-V characteristics at the resonance frequency of the 21-mode.

trodes and the grating of Λ=1μm after annealing, and Fig.5(b) shows the intrinsic characteristics of $LiNbO_3$:Fe for comparison. In Fig.5(a), we observe hysteresis and the marked variation of the gradient dI/dV. The gradient becomes negative in some range of the voltage. On the other hand, the weak nonlinearity in Fig.5(b) is caused by the large Q-value of the resonator, and is the usual effect. The harmonic generation was also observed in both samples. Not only odd harmonics but also even ones were observed.

Table II shows the variation of Q and ω_R after the annealing in the 24- and 22-modes. Only the whole electrodes are used. The value of ω_R in the 22-mode shows a tendency to decrease after annealing. This feature is different from the results in other modes. Another influence of the PR grating on the piezoelectric vibration is greater in the 22-mode than in other modes. The nonlinear jump phenomenon from the PR grating was observed in the 24-mode as well as in the 21-mode, but not in the 22-mode.

The $I-V$ characteristics in the 24-mode for the sample with the grating of Λ=1μm before annealing, in Fig.6, show marked hysteresis and a negative gradient, as in the 21-mode. On the other hand, the intrinsic characteristics in the 24-mode show little hysteresis and no negative gradient.

The $I-V$ characteristics in the 22-mode for the sample with the grating of Λ=1μm before annealing, in Fig.7(a), show hysteresis, but similar hysteresis is also observed in the intrinsic characteristics in the 22-mode, as in Fig.7(b). Hence, we cannot conclude at present the influence of the PR grating on the nonlinear phenomena in the 22-mode, even though the Q-value in the 22-mode was influenced by the PR grating. On the other hand, in the 21- and 24-modes, we can conclude the influence of the PR grating on the nonlinear phenomena, involving the low Q-value.

We also find that the variation of ω_R after annealing has nothing to do with that of Q. The variation of ω_R probably has to do with that of the stiffness of the nonlinear spring.

Finally, we consider the mechanism of the generation of the nonlinearity. The PR grating is made of a sinusoidal charge distribution as in Fig.2. If the charges at a distance of Λ/2 vibrate in an in-phase state as in Fig.8(a), the vibration is still linear. But, if they vibrate in an antiphase state as in Fig.8(b) for some reason, the nonlinearity could be caused by Coulomb's force between the neighboring charges. The inherent nonlinearity could be also enhanced by the antiphase vibration. The antiphase vibration could be caused by the interaction between the periodic internal electric field caused by the periodic charge distribution and the polarization that resulted from the piezoelectric effect when the external electric field was applied, that is, the polarized charges accompanied with the piezoelectric vibration could be strained periodically by the

Table II. The variation of the Q-value and the resonance frequency ω_R of the 24- and 22-mode after annealing.
The notations used are the same as in Table I.

Modes \ Λ		1μm	3.9μm
24	ω_R	N	I(0.08%)
	Q	N(4000 → 3000)	N(1300 → 2100)
22	ω_R	N	D(0.15%)
	Q	N(4800~5500)	I(300 → 3400)

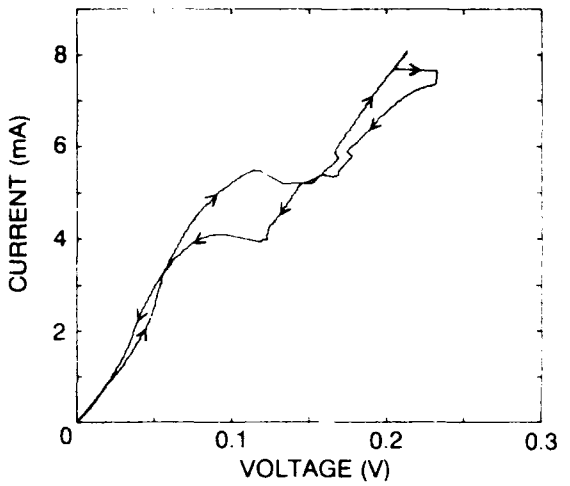
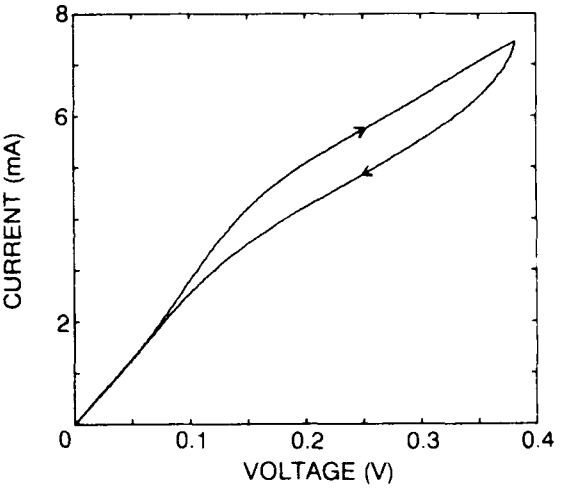


Fig.6. The $I-V$ characteristics of the sample with the PR grating at the resonance frequency of the 24-mode.



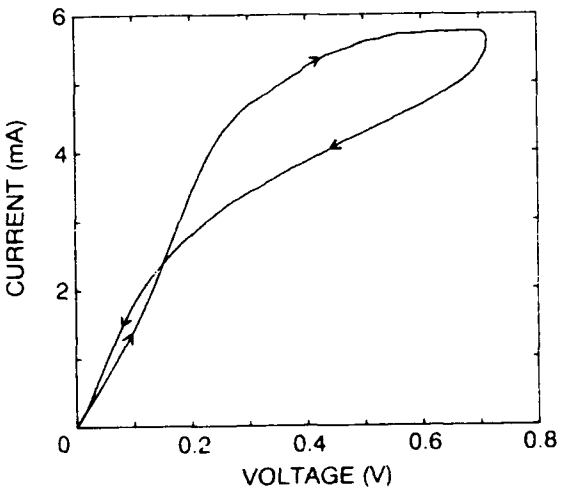


Fig.7. (a) The $I-V$ characteristics of the sample with the PR grating at the resonance frequency of the 22-mode. (b) The intrinsic $I-V$ characteristics at the resonance frequency of the 22-mode.

internal electric field accompanied with the PR grating. The decrease of Q-value and the negative dI/dV could be caused by a shift of energy from the in-phase vibration to the antiphase one. If the displacement become larger, involving the increase of the Q-value or the external electric field, the in-phase vibration inherent in the piezoelectric one could predominate, so the nonlinearity could disappear.

The difference of the characteristics in the 22-mode from those in the 21- and 24-modes could be explained by this model. In the 21- and 24-modes, the displacement exists in the z-direction, the direction of the PR grating. On the other hand, in the 22-mode, a clamp exists in the z-direction, so the mechanism mentioned above is not be applied, because the nonlinearity explained by this model requires the displacement in the direction that has both the piezoelectricity and the PR grating, the z-direction, in this case.

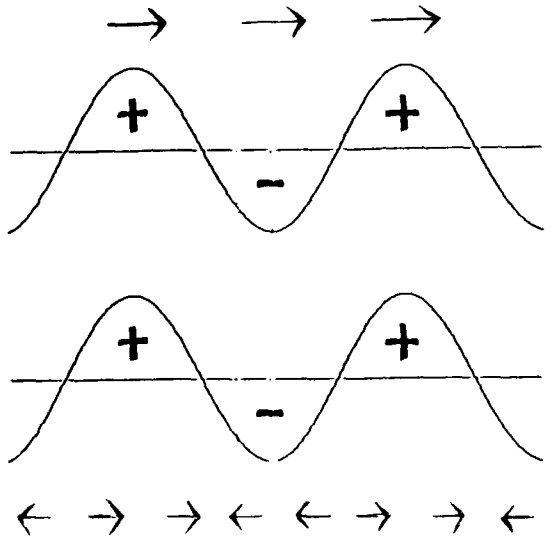


Fig.8. (a) Charges at a distance of $\Lambda/2$ vibrate in an in-phase state. (b) Charges at a distance of $\Lambda/2$ vibrate in an antiphase state.

The influence of the type of electrodes on the experimental results might be explained as follows. Charges on the electrodes involved with the piezoelectric vibration may influence the vibration state of the positive and the negative charges in the crystal directly, so the charasteristics could change according to the type of electrodes.

Conclusion

1) The PR grating written in the piezoelectric resonator ($LiNbO_3$:Fe) causes the nonlinear acoustic vibration.
2) This phenomenon disappears when the Q-value is too large. The mechanism is different from that of the usual nonlinear vibration.
3) This phenomenon is marked in the case of the 21- and 24-coupling, while it is not clear in the case of the 22-coupling.
4) The PR grating seems to partially remain even after annealing.

References

1) A.Yariv: *Optical Electronics* (Holt,Rinehart and Winston Inc.,Orlando,1991) 4th ed.,Chaps.17 and 18
2) D.E.Oates and J.Y.Pan: Ferroelectronics **92** (1989) 253.

FABRICATION OF PIEZOELECTRIC CERAMIC/POLYMER COMPOSITES BY INJECTION MOLDING.

Leslie J. Bowen and Kenneth W. French,
Materials Systems Inc.
53 Hillcrest Road, Concord, MA 01742

Abstract

Research at the Materials Research Laboratory, Pennsylvania State University has demonstrated the potential for improving hydrophone performance using piezoelectric ceramic/polymer composites. As part of an ONR-funded initiative to develop cost-effective manufacturing technology for these composites, Materials Systems is pursuing an injection molding ceramic fabrication approach. This paper briefly overviews key features of the ceramic injection molding process, then describes the approach and methodology being used to fabricate PZT ceramic/polymer composites. Properties and applications of injection molded PZT ceramics are compared with conventionally processed material.

Introduction

Piezoelectric ceramic/polymer composites offer design versatility and performance advantages over both single phase ceramic and polymer piezoelectric materials in both sensing and actuating applications. These composites have found use in high resolution medical ultrasound as well as developmental Navy applications. Many composite configurations have been constructed and evaluated on a laboratory scale over the past thirteen years. One of the most successful combinations, designated 1-3 composite in Newnham's notation [1], has a one-dimensionally connected ceramic phase (PZT fibers) contained within a three-dimensionally connected organic polymer phase. Hydrophone figures of merit for this composite can be made over 10,000 times greater than those of solid PZT ceramic by appropriately selecting the phase characteristics and composite structure.

The Penn State composites were fabricated [1] by hand-aligning extruded PZT ceramic rods in a jig and encapsulating in epoxy resin, followed by slicing to the appropriate thickness and poling the ceramic. Aside from demonstrating the performance advantages of this material, the Penn State work highlighted the difficulties involved in fabricating 1-3 composites on a large scale, or even for prototype purposes. These are:

1) The requirement to align and support large numbers of PZT fibers during encapsulation by the polymer.

2) The high incidence of dielectric breakdown during poling arising from the significant probability of encountering one or more defective fibers in a typical large array.

Over the past five years several attempts have been made to simplify the assembly process for 1-3 transducers with the intention of improving manufacturing viability and lowering the material cost. Early attempts involved dicing solid blocks of PZT ceramic into the desired configuration and back-filling the spaces with a polymer phase. This technique has found wide acceptance in the medical ultrasound industry for manufacturing high frequency transducers [2]. More recently, Fiber Materials Corp. has demonstrated the applicability of its weaving technology for fiber-reinforced composites to the assembly of piezoelectric composites [3]. Another exploratory technique involves replicating porous fabrics having the appropriate connectivity [4].

For extremely fine scale composites, fibers having diameters in the order of 25 to 100 μm and aspect ratios in excess of five are required to meet device performance objectives. As a result, these difficulties are compounded by the additional challenge of forming and handling extremely fine fibers in large quantities without defects. Recently, researchers at Siemens Corp. have shown that very fine scale composites can be produced by a fugitive mold technique. However, this method requires fabricating a new mold for every part [5].

This paper describes a new approach to piezoelectric composite fabrication, viz: Ceramic injection molding. Ceramic injection molding is a cost-effective fabrication approach for both Navy piezoelectric ceramic/polymer composites and for the fabrication of ultrafine scale piezoelectric composites, such as those required for high frequency medical ultrasound and nondestructive evaluation. The injection molding process overcomes the difficulty of assembling oriented ceramic fibers into composite transducers by net-shape preforming ceramic fiber arrays. Aside from this advantage, the process makes possible the construction of composite transducers having more complex ceramic element geometries than those previously envisioned, leading to greater design flexibility for improved acoustic impedance matching and lateral mode cancellation.

Process Description

Injection molding is widely used in the plastics industry as a means for rapid mass production of complex shapes at low cost. Its application to ceramics has been most successful for small cross-section shapes, e.g. thread guides, and large, complex shapes which do not require sintering to high density, such as turbine blade casting inserts. More recently, the process has been investigated as a production technology for heat-engine turbine components [6,7].

The injection molding process used for PZT molding is shown schematically in Figure 1. By injecting a hot thermoplastic mixture of ceramic powder and organic binder into a cooled mold, complex shapes can be formed with the ease and rapidity normally associated with plastics molding. Precautions, such as hard-facing the metal contact surfaces, are important to minimize metallic contamination from the compounding and molding machinery. For ceramics, the binder must be removed nondestructively, necessitating high solids loading, careful control of the binder removal

CH3080-0-7803-0465-9/92$3.00 ©IEEE

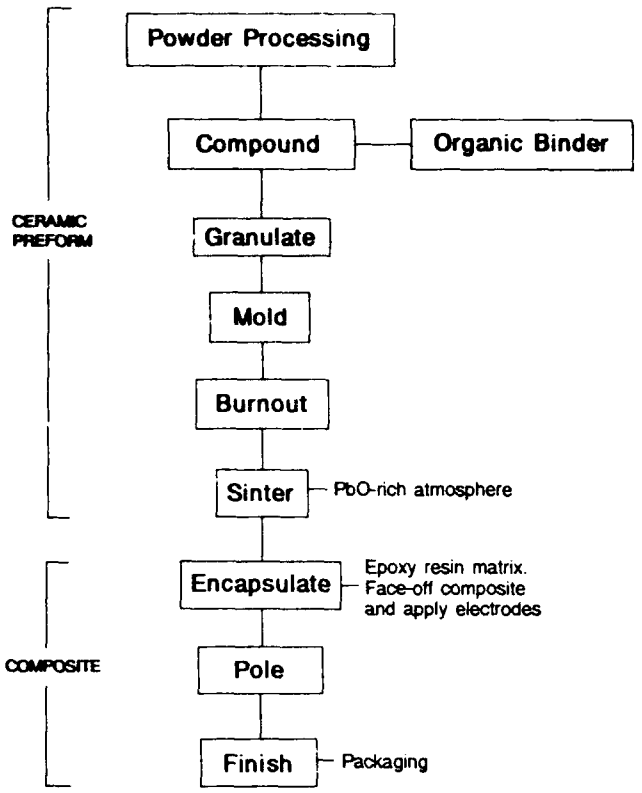


Figure 1: Injection Molding Process Route.

process, and proper fixturing. Once the binder is removed, the subsequent firing, poling and epoxy encapsulation processes are similar to those used for conventional PZT/polymer composites [1]. Thus, the process offers the following advantages over alternative fabrication routes: Complex, near net-shape capability for handling many fibers simultaneously; rapid throughput (typically seconds per part); compatibility with statistical process control; low material waste; flexibility with respect to transducer design (allows variation in PZT element spacing and shape); and low cost in moderate to high volumes. In general, because of the high initial tooling cost, the ceramics injection molding process is best applied to complex-shaped components which require low cost in high volumes.

Composite Fabrication and Evaluation

The approach taken to fabricate 1-3 piezoelectric composites is shown in Figure 2a, which illustrates a PZT ceramic preform concept in which fiber positioning is achieved using a co-molded integral ceramic base. After polymer encapsulation the ceramic base is removed by grinding. Aside from easing the handling of many fibers, this preform approach allows broad latitude in the selection of piezoelectric ceramic element geometry for composite performance optimization. Tool design is important for successful injection molding of piezoelectric composites. The approach shown in Figure 2b uses shaped tool inserts to allow changes in part design without incurring excessive retooling costs. Figure 2c shows how individual preforms are configured to form larger arrays.

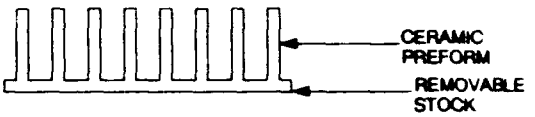


Figure 2a: Preform Configuration (Approx. 400 ceramic elements)

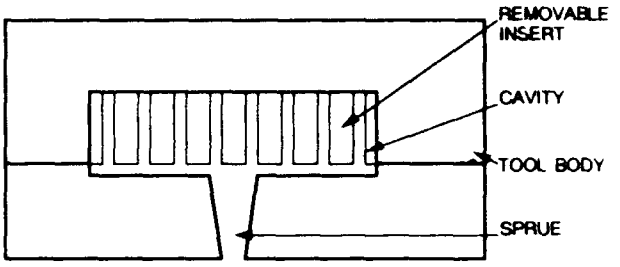


Figure 2b: Injection Molding Tool Configuration

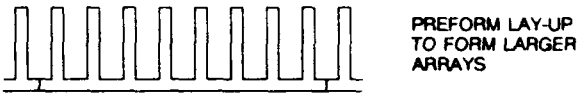


Figure 2c: Large Area Composite Arrays made from Preforms

Figure 2: Preform Approach to Composite Fabrication.

In practice, material and molding parameters must be optimized and integrated with injection molding tool design to realize intact preform ejection after molding. Key parameters include: PZT/binder ratio, PZT element diameter and taper, PZT base thickness, tool surface finish, and the molded part ejection mechanism design. In order to evaluate these process parameters without incurring excessive tool cost, a tool design having only two rows of 19 PZT elements each has been adopted for experimental purposes. Each row contains elements having three taper angles (0, 1 and 2 degrees) and two diameters (0.5 and 1mm). To accommodate molding shrinkage, the size of the preform is maintained at 50x50mm to minimize the possibility of shearing off the outermost fibers during the cooling portion of the molding cycle.

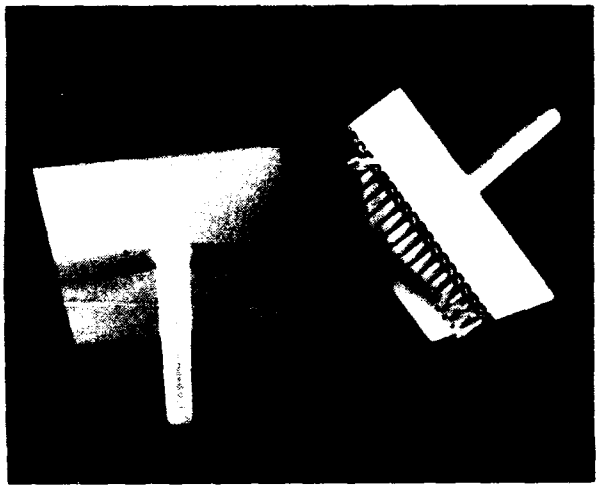


Figure 3: Injection Molded 1-3 Composite Preforms.

Figure 3 shows green ceramic preforms fabricated using this tool configuration. Note that all of the PZT elements ejected intact after molding, including those having no longitudinal tapering to facilitate ejection. Slow heating in air has been found to be a suitable method for organic binder removal. Finally, the burned-out preforms are sintered in a PbO-rich atmosphere to 97-98% of the theoretical density. No problems have been encountered with controlling the weight loss during sintering of these composite preforms, even for those fine-scale, high-surface area preforms which are intended for high frequency ultrasound.

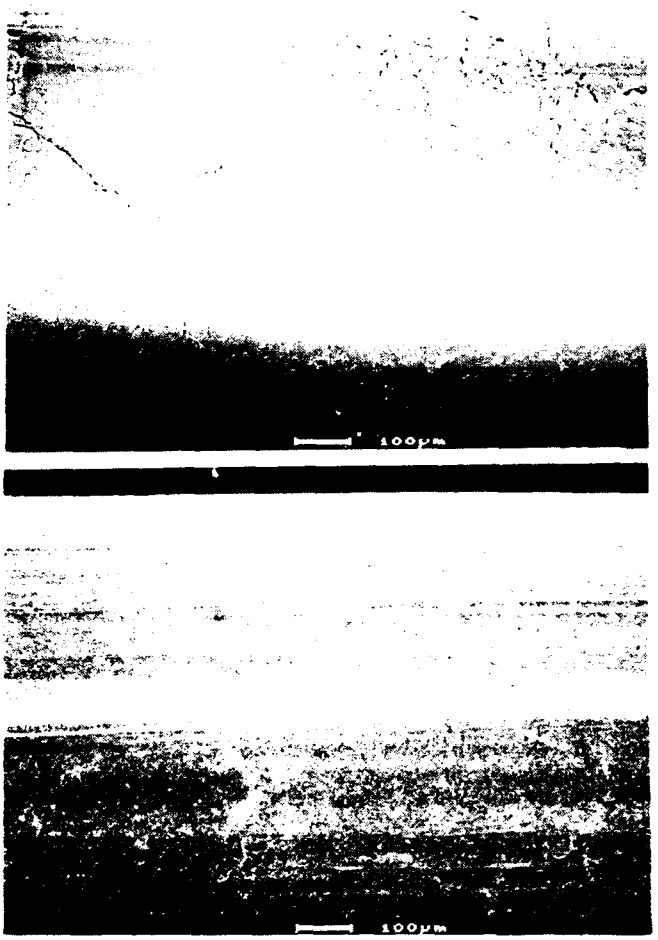


Figure 4: Scanning Electron Micrographs of As-molded (Upper) and As-sintered (Lower) Surfaces of PZT Fibers.

Figure 4 illustrates the surfaces of as-molded and as-sintered fibers, showing the presence of shallow fold lines approximately 10μm wide, which are characteristic of the injection molding process. The fibers exhibit minor grooving along their length due to ejection from the tool. Figure 5 shows the capability of near net-shape molding for fabricating very fine scale preforms; PZT element dimensions only 30μm wide have been demonstrated. The as-sintered surface of these elements indicates that the PZT ceramic microstructure is dense and uniform, consisting of equiaxed grains 2-3μm in diameter.

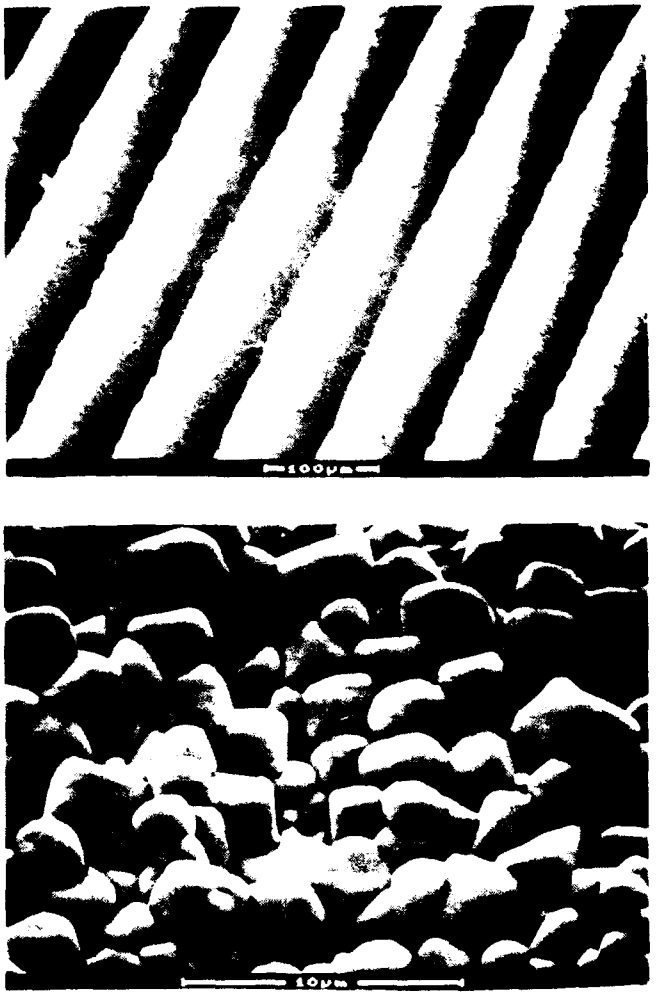


Figure 5: Fine-scale 2-2 Composite formed by Near Net-shape Molding (Upper Micrograph). As sintered Surface (Lower Micrograph).

In order to demonstrate the lay-up approach for composite fabrication, composites of approximately 10 volume percent PZT-5H* fibers and Spurrs epoxy resin were fabricated by epoxy encapsulating laid-up pairs of injection molded and sintered fiber rows followed by grinding away the PZT ceramic stock used to mold the composite preform. Figure 6 shows composite samples made from freshly-compounded PZT/binder mixture and from reused material. Recycling of the compounded and molded material appears to be entirely feasible and results in greatly enhanced material utilization.

Table 1 compares the piezoelectric and dielectric properties of injection molded PZT ceramic specimens with those reported for pressed PZT-5H samples prepared by the powder manufacturer. When the sintering conditions are optimized for the PZT-5H formulation, the piezoelectric and dielectric properties are comparable for both materials. Since the donor-doped PZT-5H formulation is expected to be particularly sensitive to iron contamination from the injection molding equipment, the implication of these measurements is that such contamination is negligible in this injection molded PZT material.

*Powder supplied by Morgan Matroc, Inc., Bedford, Ohio; Lot 105A.

Table 1: Properties of Injection Molded Piezoelectric Ceramics.*

Specimen Type	Relative Permittivity	Dielectric Loss (1kHz)	d33 (pC/N)
Die-Pressed	3584	0.018	745
Inj. Molded**	3588	0.018	755

*Aged 24 hours before measurement.
**Poling conditions: 2.4kV/mm, 60°C, 2 minutes.

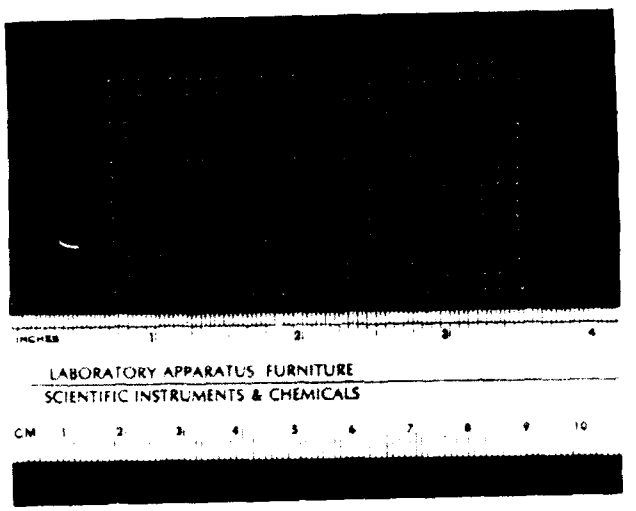


Figure 6: Injection Molded PZT Fiber/Epoxy Resin Composites prepared by the Preform Lay-up Method.

Summary

Ceramic injection molding has been shown to be a viable process for fabricating both PZT ceramics and piezoelectric ceramic/polymer transducers. The electrical properties of injection molded PZT ceramics are comparable with those prepared by conventional powder pressing, with no evidence of deleterious effects from metallic contamination arising from contact with the compounding and molding equipment. By using ceramic injection molding to fabricate composite preforms, and then laying up the preforms to form larger composite arrays, an approach has been demonstrated for net-shape manufacturing of piezoelectric composite transducers in large quantities.

Acknowledgements

This work was funded by the Office of Naval Research under the direction of Mr. Stephen E. Newfield. The authors wish to thank Ms. Hong Pham for technical assistance, and Dr. Thomas Shrout of the Materials Research Laboratory, Penn. State University for electrical measurements.

References

[1] R. E. Newnham et al, "Composite Piezoelectric Transducers," Materials in Engineering, Vol. 2, pp. 93-106, Dec. 1980.

[2] C. Nakaya et al, IEEE Ultrasonics Symposium Proc., Oct. 16-18, 1985, p 634.

[3] S. D. Darrah et al, "Large Area Piezoelectric Composites," Proc. of the ADPA Conference on Active Materials and Structures, Alexandria, Virginia, Nov. 4-8, 1991, Ed. G. Knowles, Institute of Physics Publishing, pp 139-142.

[4] A. Safari and D. J. Waller, "Fine Scale PZT Fiber/Polymer Composites," presented at the ADPA Conference on Active Materials and Structures, Alexandria, Virginia, Nov. 4-8, 1991.

[5] U. Bast, D. Cramer and A. Wolff, "A New Technique for the Production of Piezoelectric Composites with 1-3 Connectivity," Proc. of the 7th CIMTEC, Montecatini, Italy, June 24-30, 1990, Ed. P. Vincenzini, Elsevier, pp 2005-2015.

[6] G. Bandyopadhyay and K. W. French, "Fabrication of Near-net Shape Silicon Nitride Parts for Engine Application," J. Eng. for Gas Turbines And Power, 108, pp 536-539, 1986.

[7] J. Greim et al, "Injection Molded Sintered Turbocharger Rotors," Proc. 3rd. Int. Symp. on Ceramic Materials and Components for Heat Engines, Las Vegas, Nev., pp. 1365-1375, Amer. Cer. Soc. 1989.

PIEZOELECTRIC BIMORPHS WITH QUADRATIC BEHAVIOR USING BIASED ZnO ON Si_3N_4

Jan G. Smits and Wai-shing Choi
Department of Electrical Engineering, Boston University
44 Cummington Street, Boston MA,02215

ABSTRACT

Piezoelectric bimorphs have been made by sputtering ZnO on Si_3N_4 . The ZnO was sandwiched between Cr/Au electrodes. Bimorphs of 1688 and 2980 μm long were produced.

INTRODUCTION

Piezoelectric bimorphs are useful tools in many instruments; a listing of many of their applications has been given in [1]. Currently the most useful bimorphs are the ones made of PZT ceramics, because of the large values of d_{31}. A drawback of these devices is that the minimum thickness is quite large, around 250 to 300 microns, which makes it unsuitable for use in integrated circuit techniques, as it is impossible to grind the thickness of the PZT down to a few microns. For this reason it is imperative that we look for thin deposited films which are piesoelectric. Quite a number of researchers have shown considerable progress toward making thin film PZT material, but there still are problems with the d_{31} value, [2,3,4]. We have been working on ZnO on Si or Si_3N_4 cantilevers, and although the d_{31} is much lower than that of PZT, it may still be a quite interesting combination, because some other effects are showing up, which create a large deflection at even modest voltages. Other authors have made almost similar devices, not completely identical, but do not report large deflections, [5].

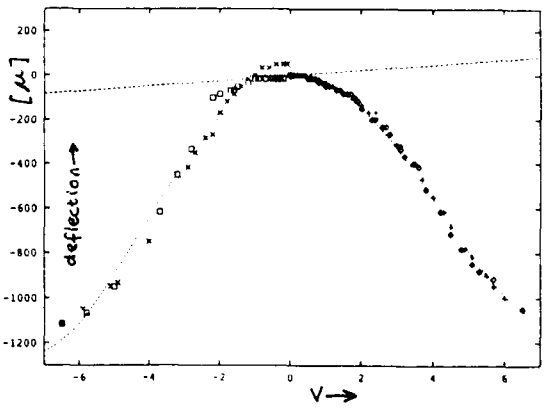
FABRICATION OF THE DEVICES

We started with cleaned 3 inch diameter (100) wafers. They were oxidised to a thickness of 0.5μm. Windows with dimensions of 500 by 2000 μ were patterned in the oxide by etching in HF. On top of the oxide we sputtered ZnO which was to be used later as a sacrificial layer. The ZnO was patterned to fit in the oxide windows. Then Si_3N_4 film was sputtered over the entire wafer, Cr-Au electrodes were evaporated and positioned in a lift-off process; ZnO was sputtered again on the wafer and patterned in ZnO etch, and then we deposited Cr-Au on top of the ZnO. After this the wafer was covered with photoresist and a window in the resist was made to open a moat around the cantilever beam. This moat was used to etch through the Si_3N_4 in HF and stop at the sacrificial ZnO. Then the wafer was immersed in a ZnO etchbath and the sacrificial layer was etched. At that moment we had a cantilever beam which was 1860μ long and 300μ wide.

EXPERIMENTAL RESULTS

We have measured the deflection of the bimorphs by applying voltages on their electrodes and found that it is described mostly by a large quadratic term and a small linear term, which is the piesoelectric effect. The deflections are quite large; 6 V on the bimorph gives deflections of the tip of around 1 mm. Considering that the whole length of the bimorph is only 2 mm, we conclude that these deflections are very large indeed.

Three effects are known to produce a quadratic behavior: 1) Electrostriction 2) Joule heating 3) Maxwell Stress compression.



CH3080-0-7803-0465-9/92$3.00 ©IEEE

Of these we can eliminate the electrostriction, because the sign of effect is wrong. The beams should bend up with any voltage, while ours bend down.

The Maxwell Stress compression is due to the force exerted by the electrodes on each other, which squeeses the material from underneath the electrodes. However, this effect is around 4 orders of magnitude too small to cause these large deflections.

The only explanation for the large deflections remains in the thermal expansion of some of the materials due to Joule heating of the film.

In order to verify the deflection of the bimorph when it actually behaves as a bimetallic, we set up the equations governing a bimetallic, and used these to expand the equations of heterogeneous bimorphs , which we have published elsewhere. [6]. Using M, F, p, V as generalised forces $\mathcal{F}$ (they are the moment on a beam, the force on the beam, the pressure on the beam, and the voltage on the electrodes) and $\alpha, \delta, \mathcal{V}, Q$ as generalised displacements $\mathcal{D}$, (the rotation at the tip, the deflection, the volume displacement, and the charge on the electrodes,) we can write the matrix equation connecting them as

$$\mathcal{D} = E\mathcal{F} \tag{1}$$

The matrix E is a four by four matrix containing the material constants and dimensions of the elements that make up the bimorph . If we allow the temperature to play a role in the deflection of the bimorph , we must create a fifth column in the matrix, while we also need a fifth row in the matrix to account for the dependence of the entropy as a function of all of the mentioned variables. We use the following variables: σ is entropy, θ is temperature, α is the thermal expansion coefficient, $\Delta\alpha$ is the difference between the expansions of top and bottom.(not to be confused with the tip rotation for which we also use α), π_3 is the pyroelectric coefficient, ρ and c are specific mass and specific heat, $C = \rho_p c_p + \rho_{Si} c_{Si}$. $G = Lwh_{Si}h_p$.

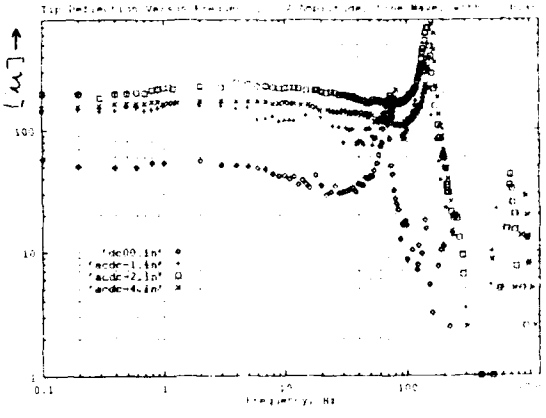
Now with this we can write the fifth column (to save space) of the constitutive equations when the device is stress free assembled at zero Kelvin, (a factor A is assumed as is indicated in [7]:

$$\begin{pmatrix} \alpha \\ \delta \\ \mathcal{V} \\ Q \\ \Delta\sigma \end{pmatrix} = \begin{pmatrix} \frac{-6\Delta\alpha BL}{K} \\ \frac{-3\Delta\alpha BL^2}{K} \\ \frac{-\Delta\alpha BL^2}{K} \\ \pi_3 Lw \\ C + G\frac{e_{11}^{Si}h_p^2 + e_p h_{Si}^2}{K}(\Delta\alpha)^2\theta \end{pmatrix} \begin{pmatrix} M \\ F \\ p \\ V \\ \Delta\theta \end{pmatrix} \tag{2}$$

As can be seen from equation (2) the deflection is proportional to the temperature. For comparison, the term E_{14} is the piesoelectric term, and the comparable part is the piesoelectric contribution $d_{31}V$, which can be compared with the thermal contribution $\Delta\alpha\Delta\theta$. With a voltage difference of 1 Volt and a piesoelectric coefficient of 5×10^{-12}, the piesoelectric term is 5×10^{-12}. With a difference between the expansion coefficients ZnO and Si_3N_4 of 3×10^{-6} and a temperature change of 1°C, the thermal contribution is 3×10^{-6}. Hence the thermal contribution is 6 orders of magnitude larger than the piesoelectric contribution. Because the thermal conduction to the environment is not completely known, we don't know what the temperature is , but a few degrees change is very likely during a cycle and this could easily take care of this large deflection.

FREQUENCY DEPENDENCE

We have measured the frequency dependence of the tip deflection of the bimorphs, as shown in figure 2, in which the deflection is plotted for various biasing voltages. It is observed that the deflection increases with biasing voltage, as was to be expected from the static deflection measurements.



It is also observed that the deflection curve starts to bend down at around 10 Hz, which we attribute to air damping; this occurs long before the resonance peaks of first resonance. Further, it is observed that without bias, the "true" resonance occurs at 142 Hz, but due to the quadratic behavior of the bimorph the first subharmonic is also observed at half of "true" resonance, 71 Hz. Another interesting observation is that the resonance frequencies are subject to the bias voltage. The bimorph seems to stiffen under increasing bias voltage. A plot of the resonance frequency versus bias voltage is given in figure 3. This effect poses a problem, for which we have no direct answer. If the large deflections are partially due to Joule heating, then the effect of heating the material would be to soften all elastic constants which would lead to a lowerng of the resonance frequencies. Here we see the opposite. The phenomenological treatment of this effect would be to include a field dependent term in the elastic constant. This would change the normal elastic part of the piezoelectric equations to :

$$S_1 = s_{11}^E(1 + \gamma E_3)T_1 + d_{31}E_3 \qquad (3)$$

This requires the presence of a term $\frac{1}{2}s_{11}^E\gamma E_3 T_1^2$ in the thermodynamic potential of which S_1 is the derivative with respect to T_1. The thermodynamic potential is not known *a priori*, it is not the Gibbs function because that is only valid with constant temperature. Let us call it X. From (3) we can conclude that the elastic part of X, X_{el} should be:

$$X_{el} = \frac{1}{2}s_{11}^E T_1^2 + \frac{1}{2}s_{11}^E\gamma E_3 T_1^2 + d_{31}E_3 T_1 \qquad (4)$$

The dielectric part of X, X_{di} has no unusual features, so it will just be:

$$X_{di} = \frac{1}{2}\epsilon_{33}^T E_3^2 \qquad (5)$$

For the total thermodynamic potential we find that it should be:

$$X = X_{el} + X_{di} =$$

$$\frac{1}{2}s_{11}^E T_1^2 + \frac{1}{2}s_{11}^E\gamma E_3 T_1^2 + d_{31}E_3 T_1 + \frac{1}{2}\epsilon_{33}^T E_3^2 \qquad (6)$$

The dielectric part of the constitutive equations will now be $\frac{\partial X}{\partial E_3}$ or :

$$D_3 = \frac{1}{2}s_{11}^E\gamma T_1^2 + d_{31}T_1 + \epsilon_{33}^T E_3 \qquad (7)$$

The term containing γ describes the elastostriction effect [6].

REFERENCES

1 J.G.Smits, Susan I. Dalke, Thomas K. Cooney. The Constituent Equations of Piezoelectric Bimorphs. Sensors and Actuators, Vol. 28 1991 pp.41-61.

2 M. Okyuyama, Y. Hamakawa, Ferroelectric $PbTiO_3$ Thin films and their application. Int. J. Engng. Sci. Vol 29, pp391-400 1991.

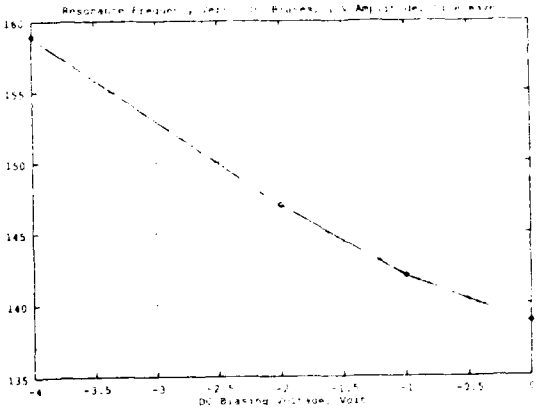
3 M.Okyama, Y. Hamakawa, Si- Monolithic Miniature Ultrasonic Sensor Using $PbTiO_3$ Thin Film Prepared on a Si or SiO_2 Cantilever. Sensors and Materials, Vol 1 (1988) pp. 15-24.

4 M.Sayer, Piezoelectric Thin Films Devices, Presented at the IEEE Ultrasonics '91 Symposium. December 8-11,1991.

5 F.R.Blom, D.J.Yntema, F.C.M.Van De Pol, M.Elwenspoek, J.H.J.Fluitman, and J.A.Popma, Thin-Film ZnO as Micromechanical Actuator at Low Frequencies. Abstract of Transducers '89. 5th International Conference on Solid-State Sensors and Actuators and Eurosensors III, June 25-30, 1989, Montreux, Switzerland, p.121.

6 Shiv R. Joshi, Nonlinear Constitutive Relations for Piezoelectric Materials. Abstracts Active Materials and Adaptive Structures Symposium, page 87, November 4-8 1991, Alexandria, VA.

7 Jan G.Smits and Wai-shing Choi, The Constituent Equations of Piezoelectric Heterogeneous Bimorphs. IEEE Transactions on Ultrasonics, Ferroelectrics and Frequency Control, Vol. 38, 1991, pp 256 - 270.



DOMAIN WALL MOTION IN PIEZOELECTRIC MATERIALS UNDER HIGH STRESS

S. Sherrit, D.B. Van Nice, J.T. Graham,
B.K. Mukherjee, H.D. Wiederick

Royal Military College of Canada, Kingston, Ontario,CANADA

ABSTRACT

We have investigated the time dependence of PZT (Navy I and III) to a high stress applied parallel to the poling axis. The time dependence was found to be linear in ln(t), with slope activated in temperature with an activation energy of 0.29 eV- 0.32eV for the the Navy I material and 0.62 eV- 0.80 eV for the Navy III material. The slope was also found to be linear in stress. We have postulated that this time dependence is due to reorientation of the 90° domains in the sample.

INTRODUCTION

The increase in use of ferroelectric actuators for stable microposition and high stress applications[1,2,3,4] has led to renewed interest in ferroelectric hysteresis and domain wall effects.[5,6] Typically for an ideal actuator material one would like a response that is rate independent and linear in the electric or stress fields. However, for most common materials the piezoelectric response is not linear at high fields[7] and the response of the material is found to be dependent on the rate of application of the field[8]. In this paper we describe an apparatus we have developed to test the piezoelectric response of Navy I and Navy III PZT at high stress.

EXPERIMENTAL

The apparatus is shown in Figure 1. A piezoelectric voltage is induced across a 0.5 μF capacitor (General Radio, $R_{DC} \cong 10^{12}\Omega$) in parallel with the sample by compressing (T up to 50 MPa) a disk shaped sampleof PZT in a Monsanto tensometer converted to allow for compression. The voltage across the sample and shunt capacitor is

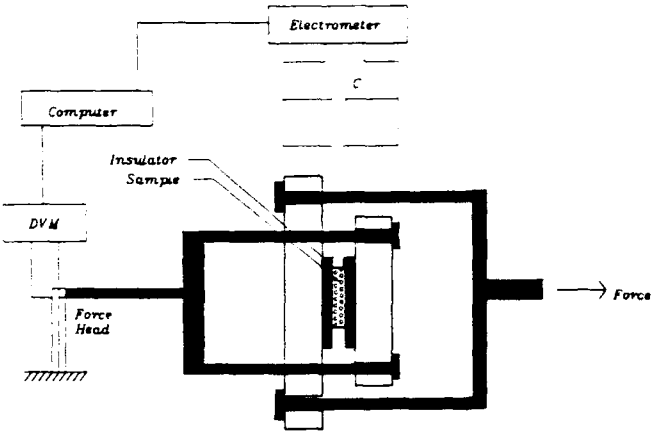


Figure 1. Schematic of the apparatus used to measure voltage, stress curves.

measured using a Keithly 619 electrometer which has a 200 TΩ input impedance. The sample is isolated from the apparatus using two 2 cm thick lucite disks. The force (Y output on tensometer) is monitored using a Keithly 199 Digital Multimeter/ Scanner. The sample temperature is set using a heat lamp and the temperature is measured using a chromel-alumel thermocouple. The rate of application of the stress is controlled by a series of Belleville washers mechanically in series with the sample. In order to produce a step function in stress the Belleville washers are removed.

It is important to note that this experimental setup has a time constant of the order of a 10^4- 10^5 seconds and that surface contamination of the insulating lucite blocks can affect the measurement by reducing the time constant and care should be taken to counter this. It should also be noted that although the stress is applied parallel to the direction of poling the strain field in the 1 and 2 directions can be produce substantial stress in the plan due to traction at the surface of the disk.

CH3080-0-7803-0465-9/92$3.00 ©IEEE

RESULTS

The initial impetus for this research was to measure d_{33} as a function of the ramped stress T by noting that

$$d_{33} = \frac{dD}{dT} = \frac{dQ}{dF} = C\frac{dV}{dF}. \quad (1)$$

where D,Q,C,V are the dielectric displacement, charge, total capacitance of the sample and shunt capacitor and voltage respectively. The Force F is equal to the product of the disk area and stress.

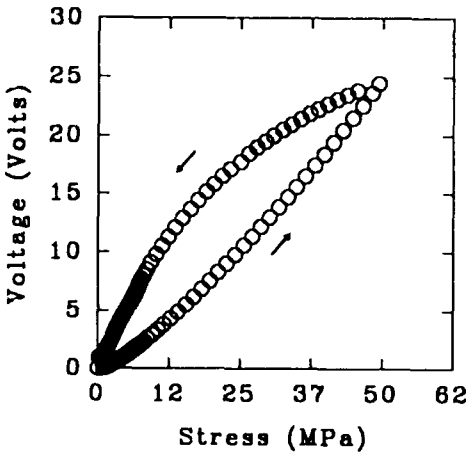


Figure 2. Voltage stress curve for a Navy I sample.

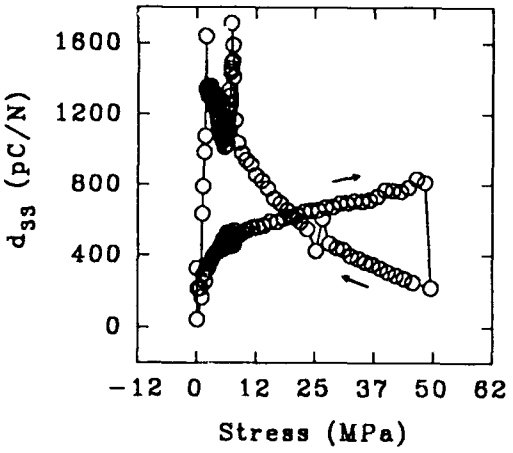


Figure 3. $d_{33} = C\frac{dV}{dF}$ as a function of the compressive stress.

The curve in Figure 2 shows the voltage as a function of the stress as the stress is increased to 51 MPa and then decreased back to the starting stress for a Navy I PZT sample produced by B.M Hi-Tech of Collingwood,Ont. A force of 20 kN corresponds to a stress of about 51 MPa for this sample. The ramp rate in stress at low stress (T < 10 MPa) is about 0.2 MPa/s. At higher force the ramp rate is 2.0 MPa/s. This was accomplished by putting two Belleville washers with different spring constants in series and straining the combination at a constant rate. As can be seen in Figure 2 there exists both a time dependent and nonlinear behavior. The time dependence is seen in the hysteresis and change in slope of the V vs T curve as the ramp rate in force changes at 10 MPa. The time dependence is accentuated in the plot of d_{33} vs stress shown in Figure 3. As can be seen an abrupt change occurs as the stress ramp rate changes. If the hysteresis were due to leakage current in the electrometer or shunt capacitor one would expect that the voltage ramping down in stress would be lower than the voltage ramping up in stress; however the opposite is true, which suggests that the ramp rate in stress was too fast to allow the piezoelectric to respond.

In order to investigate the time response the Belleville washers were removed and a 51 MPa step was applied to the sample in a few seconds. The piezoelectric voltage was monitored as a function of time for up to 10^4 seconds. The results are shown in Figure 4. As can be seen in the figure the voltage response of the PZT sample is linear in logarithmic time at low times and as the time approaches 1000 seconds the RC decay of the apparatus begins to dominate. The data were found to fit a function of the form

$$V = [V_o + m\ln(t)]e^{(-t/RC)} \quad (2)$$

where V_o is the intercept of the voltage axis, RC is the time constant of the apparatus, and m is the slope of the curve at t < 500 s. It should be noted that the maximum voltage is smaller for the data in Figure 4 compared to Figure 2 even though this is

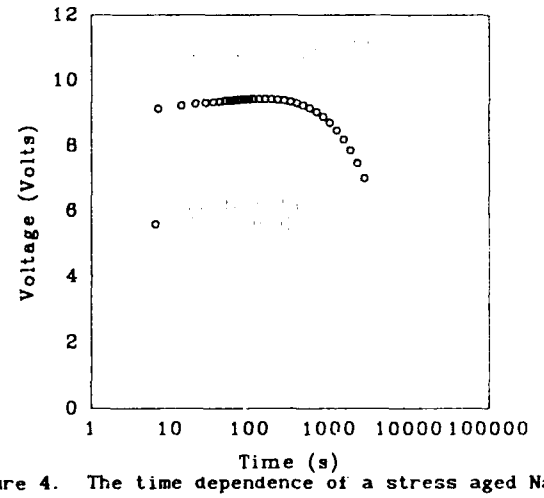


Figure 4. The time dependence of a stress aged Navy I sample at high stress.

the same sample and the same force was applied.

The decrease in voltage is due to stress aging. If the sample was left at high stress (50 Mpa) for sufficient time ($>10^5$ seconds) a significant decrease in the voltage occurred, which stabilized at about 45% its initial value. It was also noted that the aging time decreased as the temperature was increased. Samples that initially showed clean radial resonances displayed many sideband resonances after stress aging.

The voltage time plots at three different temperatures are shown in Figure 5. As can be seen from the curves the slope m is seen to increase with

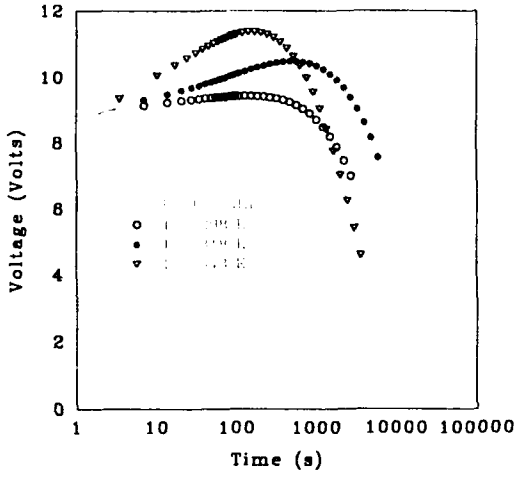


Figure 5. The time dependence of a stress aged Navy I sample at various temperatures.

increasing temperature which suggested that the domain wall motion causing this time dependence was thermally activated. We fit the data using an Arrhenius equation of the form

$$m = \frac{m_0}{T} e^{(-E_a/KT)} \qquad (3)$$

where E_a is the activation energy and m_0 is a pre-exponential factor. The data and fit to the data using equation (3) are shown in Figure 6 for a Navy I and Navy III sample. As can be seen from the figure the fit is good at least over the limited temperature range between 25° C and 70° C. The activation energy of the Navy I sample was determined to be 0.29 eV The experiment was repeated for another Navy I sample from a different batch and the activation energy was found to be 0.32 eV The activation energy for the Navy III sample was determined to be 0.62 eV, however we have measured activation energies as high as 0.80 eV for other Navy III samples.

The slope of the ln(t) time response is plotted as a function of the applied stress in Figure 7 for a Navy I sample. The slope is found to be linear in stress up to 42 MPa. We have monitored the stress relaxation of the apparatus with and without the sample present and found that when the PZT sample is present the stress relaxation is increased. This result and the slow time response that we have measured suggests that the time dependent piezoelectric response is associated with the domain motion of 90° domains. The slow response and activation with temperature is thought to be associated with the rearrangement of the atoms as the domains flip 90 degrees.

It is interesting to note that this logarithmic time response is responsible for the dispersion in the piezoelectric constant at low frequencies. If

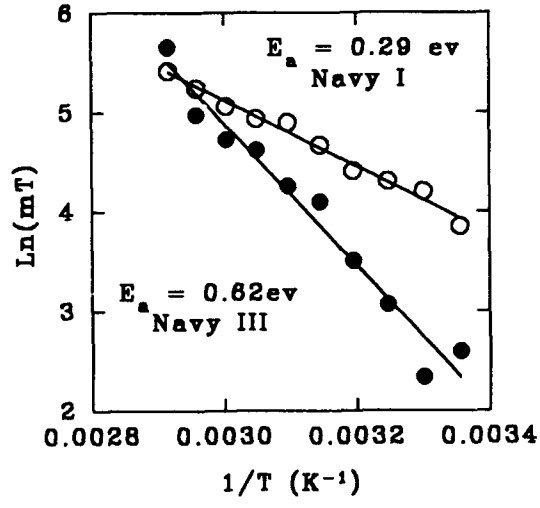


Figure 6. An arrhenius plot of ln(mT) vs 1/T for Navy I and III materials. The quantity mT is in VK.

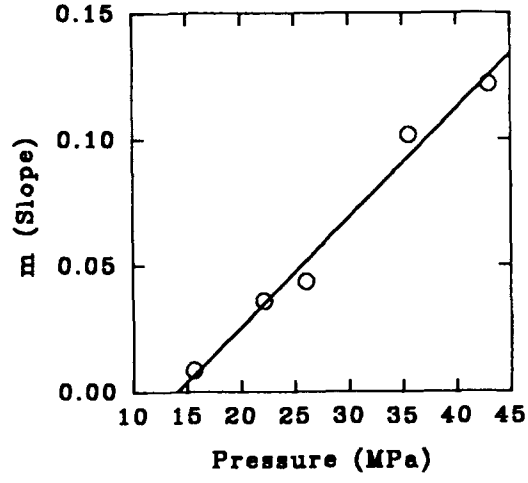


Figure 7. The slope m as a function of the applied stress for a Navy I sample.

a slowly varying AC stress is applied to the sample at about 0.10 Hz only domain wall motion that can keep pace with the changing stress will contribute to the measured signal. As the frequency is decreased more domains have time to re-align and the response is larger. This suggests that when making direct measurements of the piezoelectric response at high fields the time dependence can become significant and the measurement is likely to display dispersion.

The time dependence is also found in the dielectric constant, as is shown in Figure 8. The curves show the measured capacitance of a Navy I sample; a) prior to stressing the sample, b) stressed at 50 MPa for periods greater than an hour, c) immediately after releasing the stress. The measurement frequency for the capacitance was 1 kHz. The result is a consistent decrease in capacitance at high stress and an increase in capacitance as the stress is released regardless of the temperature. The decrease in capacitance is not responsible for the increased voltage as a function of time since the standard capacitor is 200 times greater than that of the sample and a fractional change in the sample capacitance would be too small to account for the change in voltage with time.

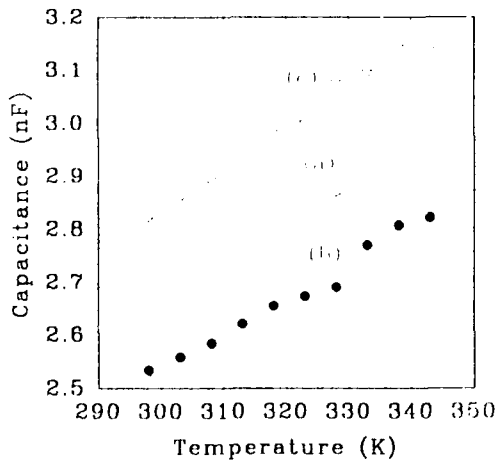


Figure 8. The capacitance of the sample at 1 kHz as a function of temperature. The various curves are; a) prior to stress, b) stressed at 50 MPa, and c) immediately after stress is released.

These results also suggest that part of the ferroelectric hysteresis found in D-E curves can be attributed to the time responce of the piezoelectric ceramic under high field and experiments are currently being set up to investigate the time dependence at high electric field.

ACKNOWLEDGEMENTS

The authors gratefully acknowledge the financial assistance of an ARP grant awarded by CRAD, Department of National Defence, CANADA.

REFERENCES

[1]K. Nakamura, H. Shimizu, "Hysteresis-Free Piezoelectric Actuators using LiNbO Plates with a Ferroelectric Inversion Layer", Ferroelectrics, Vol. 93, pp. 211-216, 1989

[2]C. Richard, P. Eyraud, L. Eyraud, M. Richard, G. Grange, "1.3.1 PZT Polymer Composites for High Pressure Hydrophone Application", Proceeding of European Conference on the Application of Polar Dielectrics, To be Published in Ferroelectrics

[3]S. Sherrit, H.D. Wiederick, B.K. Mukherjee, S.E. Prasad, "Stress Isolation PZT Air Composites", Ferroelectrics, To be published.

[4]Q. C. Yu, S. Yoshikawa, J.R. Belsick, R.E. Newnham,"Piezoelectric Composites with High Sensitivity and High Capacitance for Use at High Pressures", IEEE Trans. on Ultrasonics, Ferroelectrics and Frequency Control, Vol. 38, pp 634-639, 1991

[5]G. Arlt, " The Role of Domain Walls on the Dielectric, Elastic and Piezoelectric Properties of Ferroelectric Ceramics", Ferroelectrics, Vol. 76, pp. 451-458, 1987

[6]G. Arlt, "Microstructure and Domain Effects in Ferroelectric Ceramics" Ferroelectrics, Vol. 91, pp. 3-7, 1989

[7]R.F. Brown, G. W. McMahon, " Properties of Transducer Ceramics under Maintained Planar Stress", J. Acout. Soc. Am., Vol. 38, pp. 570-575, 1965

[8]Don Berlincourt and Helmut H.A Krueger, "Domain Processes in Lead Titanate Zirconate and Barium Titanate Ceramics", Journal of Appl. Phys, vol. 30, pp. 1804-1810, November, 1959

DOMAIN INVESTIGATIONS: A SELECT REVIEW

Jan Fousek
Institute of Physics, Czechoslovak Acad.Sci., Na Slovance 2,
18040 Prague 8

Abstract. Practically all macroscopic properties of ferroelectrics are extensively influenced by their domain structures though the mechanisms involved vary. First we survey the role of domains, whether of advantage or detrimental, in practical devices. Following is a brief review of recent progress in selected areas of research: role of ferroelasticity in the formation of domain structures (2D and 3D constraints), domain wall conditioned permittivity, high field dielectric response of ferroelectric lock-in phases. Finally several topical subjects promising interesting prospects are mentioned.

1. Introduction. Domain phenomena in applications

The investigations of domains in ferroelectric, ferroelastic and in ferroic materials in general have become an extensive field of research. A series of specialized conferences has been established to provide a forum for researchers in this area: the first International Symposium on Domains in Ferroelectric and Related Materials was held in 1989 at Volgograd, the second took recently place at Nantes. The Proceedings /1,2/ as well as previous special issues of Ferroelectrics on domain structures /3/ give a good insight into the manifold activities in the studies of domains and domain-conditioned phenomena. In the Soviet Union, another series of meetings was originated on ferroelastic materials. A good deal of phenomena in ferroelastics are connected with domains and thus the Proceedings serve as an invaluable source of information /4/. Some aspects are treated in the recently published book of Salje /5/.

Consider a standars (poly)crystalline dielectric sample such as TiO_2 forming the heart of a device. External forces such as electric field and mechanical stress (whether static or in form of a wave) result in modifications of its properties which may be directly measured e.g. by its dielectric response or sensed by probes, e.g. by a laser beam. These modifications are described by tensorial properties (electromechanical, photoelastic, etc.) which are tabulated in textbooks of crystal physics. All one needs to know is the symmetry of the sample and the geometry of the setup. If, however, in the black box there is a ferroelectric material, it may be divided into domains which make the device to exhibit a much wider variety of phenomena. Its overall response to external forces involves (cf. fig. 1)

- tensorial properties of domains, depending on their volume and orientation,
- enhanced susceptibilities (such as electric, mechanical, piezoelectric) due to domain walls,
- domain volume redistribution (switching),
- phenomena resulting from impedance jumps on the walls which influence wave propagation (such as light scattering or waveguiding).

To describe the overall response is a rather complex task. In contrast to the previous case more entry information will be required about the content of the "black box".

Studying domain phenomena offers, for basic research, a rewarding subject; often by relatively simple means we obtain surprising and interesting results. Still, it was and is the quest for applications that provides the most effective impetus for further domain research. It was soon realized that it was the domain phenomena which were responsible for the effectivity of poling process in barium titanate ceramics and for its possible subsequent time changes. A concentrated hunt for ferroelectric memories terminated around 1960, though with little success. Optically addressed memories based on domain processes in bismuth titanate and PLZT came next. Discovery of coupled ferroelectricity and ferroelasticity in gadolinium molybdate led to constructing ingenious devices based on single domain wall behaviour rather than on statistical processes. The recent wave of interest originates in the development of thin film memories and perhaps also in several other practical aspects to be mentioned later.

Table 1 gives a simplified overview surveying major application efforts. Letters in the 1st column specify the role of domains. In A domains reduce figures of merit or result in increased noise of the device. In contrast, in the B category the device function relies completely on the presence of static domain structure or on domain switching. In the case C domains may improve the function (enhanced SHG in periodic domain textures, domain fixing of holograms). It is rather interesting that in the area where ferroelectrics became unbeatable, i.e. in piezoelectric ceramics, domains play a two-fold contravening role: we desperately need them for poling and after that they become highly unwanted; this is the box D. In the last column, + indicates commercial availability of the device. For domain-oriented researchers, its presence at switching elements is a new and stimulating fact.

All these categories put specific requirements on domain behaviour. They range from mastering poling processes and stability oof single domain states (A), over wall motion with well defined threshold and no time degradation (part of B), formation of retunable regular textures (parts of B and C) up to blocking domain walls to reduce their linear response (D). In what follows we give a short review of recent progress

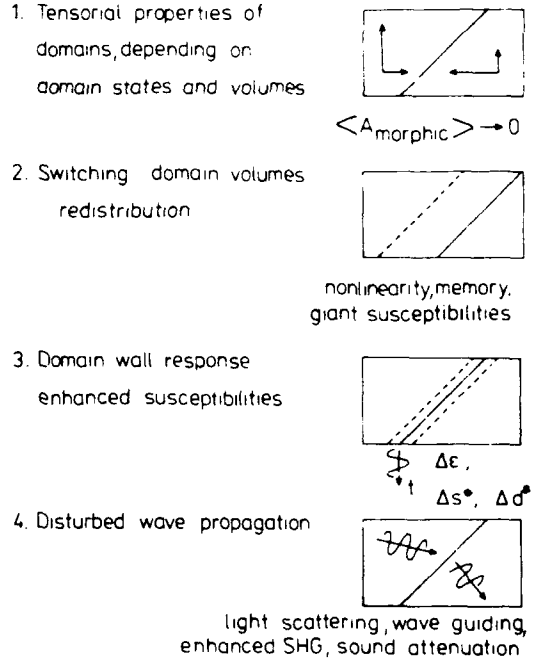


Fig. 1 Types of response of the ferroelectric sample in a device

CH2880-6/7802-0165 $01.00 ©IEEE

Table 1. SURVEY OF APPLICATIONS OF FERROELECTRICS

	physical property	example of device	
A	permittivity	capacitors, thermometers	+
		microwave resonators	+
	pyroelectricity	IR detectors, imaging	+
	electro-optics	lumped modulators	+
		spatial light modulators	+
		directional couplers	-
	nonlinear optics	frequency multipliers	+
		parametric oscilators	+
		phase conjugators	-
	photorefraction	optical memories	-
		image processors	-
B	electric bistability	switching elements	+
		analog memories	-
	switchable birefringence	light valves	+
		displays	-
		optical memories	-
		image processors	-
		diffraction gratings	-
	diel. nonlinearity	variable capacitors	-
	electro-optics	diffraction gratings	-
	piezoelectricity	hypersonic transducers	-
C	nonlinear optics	second harm. generators	-
	photorefraction	optical memories	-
D	piezoelectricity	transducers, motors	+
		sensors, positioners	+
		resonators, filters	+

A - domains unwanted. B - device based on domain structure or switching. C - domains may improve device function. D - domains in ceramics play a two-fold role.

in a few selected areas. In the 2nd section we present a brief discussion of the formation of ferroelastic domains due to mechanical boundary conditions. Next, we review domain wall contribution to susceptibilities. Some emphasis will be put on the properties of lock-in phases originating in incommensurate phases. Their specific high-field nonlinear behaviour will be shortly dealt with in the 4th section. Finally, we point out some topical interesting problems.

2. Domain formation. Ferroelastic approaches

In recent years a considerable progress has been achieved in understanding the role of ferroelasticity in the formation of domains. A pair of domains 1, 2 is called ferroelastic if the two constituents differ in spontaneous strain tensor u_s^1, u_s^2, measured with respect to the paraelastic phase. For mechanically free conditions, the u_s tensor determines the change of shape of a finite sample and the change $\Delta V(T_{tr})$ of the unit cell volume at the transition temperature T_{tr}. The latter is given by the trace of the u_s determinant. Let us recall that, but for the domains with antiparallel polarization and for antiphase pairs, all other domain pairs in common ferroelectric ceramic materials are ferroelastic.

Clearly, ferroelastic domain pattern can be influenced by mechanical stress. Methods of engineering regular domain patterns by external applied stress or by built-in defects have been surveyed in ref./6/. Here we shall briefly review some results concerning the role of boundary conditions. Having in mind the situation during the domain formation, i.e. at the phase transformation, two cases A and B can be treated separately. In A, the transformation process in a sample proceeds in restricted volume. This is particularly relevant to ceramics where a grain is in contact with neighbouring matter and can be considered as clamped (3D clamping). In B, it is taken into account that during the transformation of the 1st order or during the 2nd order transition in a temperature gradient the paraelastic and ferroelastic phases must coexist, meeting along a phase boundary, which limits the development of strain (2D clamping). In either case, there is a close similarity to problems treated in theory of martensitic transformations in metals.

A) Transitions in restricted volume have been considered in a number of papers by Roitburd (see /7,8/ and for ferroelectrics in particular the problem was discussed by Arlt /9,10/. Consider a hypothetical compound transforming into any of two single domain states characterized by strains u_s^1 and u_s^2 and schematically represented in fig. 2a; we assume for the components $u_{11s}=-u_{22s}=u_s$. Should the transition proceed under clamped conditions, the elastic energy develops extending over the sample, with the density

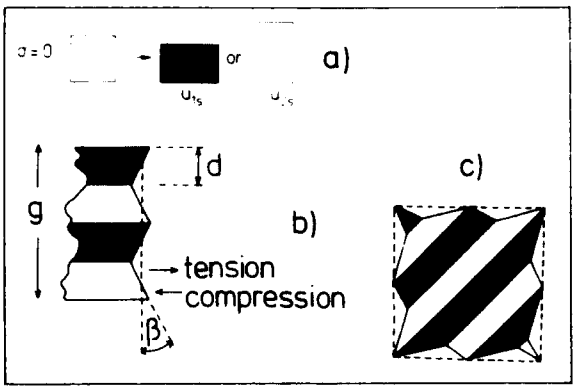


Fig. 2 Domains in restricted volume: stress relief in 2D. See text

$$U_{elast}(\text{long.r.})=(c_{11}-c_{12})(u_s)^2 \qquad (1)$$

in which c_{ii} denote elastic moduli and which may reach appreeciable values compared to energy gain due to the change of phase: this may lead to suppressing the transition. However, if a polydomain state is formed such as in fig. 2b, the average strain is

$$\langle u_s \rangle = (1-\alpha)u_s^1 + \alpha u_s^2 \qquad (2)$$

where the volume fraction of domain 2 is α. For $\alpha=1/2$ we have $U_{elast}(\text{long r.})=0$. Still, the matching with the surroundings is not perfect (fig. 2c) and it has beeen shown that the misfit elastic energy extending over a thin layer at the surface has the approximate form /10/

$$U_{elast}(\text{short r.})=Kc_{11}\beta^2 d/g. \qquad (3)$$

Here K is a numerical factor, the angle β is defined in fig. 2c, d stands for the domain slab thickness and g for the sample linear dimension. The occurence of domain walls in the sample (grain) is connected with the energy density per unit volume

$$U_{wall}= \sigma/d \qquad (4)$$

where σ denotes the surface wall energy density. By minimizing the sum of the last two energies we obtain for the equilibrium domain width /10/

$$d=(\sigma/Kc_{11}\beta)^{1/2}g^{1/2}. \qquad (5)$$

This is the example of a stress-relieving domain mechanism in two dimensions (in fig. 2b,c) walls are assumed perpendicular to paper). Since with decreasing grain size g the wall energy decreases as g^2 while the

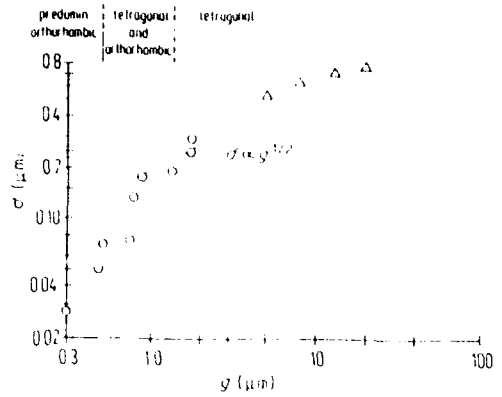


Fig. 3 Domain width vs. grain size.
After /10/

elastic energy as g^3, there exists a critical size g_{crit} below which the grain remains single domain. Fig. 3 taken from ref. 10 shows that for $BaTiO_3$ ceramics the proportionality (5) is well satisfied within some interval. The model leads to the estimation g_{crit}=40nm.

If the material allows, by symmetry, for more than one ferroelastic domain pair (e.g. tetragonal $BaTiO_3$), the stress relief requirement may lead to more complicated 3D domain textures. The most often occuring pattern in coarse-grain ceramics of barium titanate is reproduced in fig. 4 /11/ (arrows indicate direction of polarization). Its remarkable feature /11/ is that it can be polarized without appreciable change in averaged strain. It appears that similar studies of stress relieving domain configurations for orthorhombic and rhombohedral phases of perovskites such as PZT have not yet been performed.

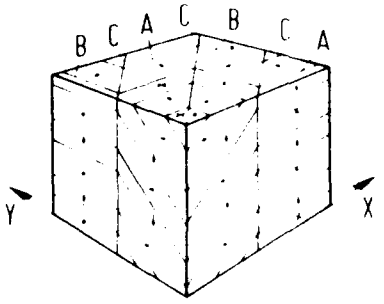


Fig. 4 Domain configuration in $BaTiO_3$ ceramics: stress relief in 3D

B) For a mechanically free sample, i.e. when all applied stress components vanish, the ground state of the ferroelastic phase is single domain and the above considerations do not apply. However, during the 1st order transition process the two phases are in mechanical contact and this results in 2D elastic constraints. The problem of phase coexistence and its consequences for the formation of ferroelastic domains has been treated by a number of authors (e.g. refs. 12 to 15). The basic question is: can a planar phase boundary (PB) exist with a single domain state on one side? This may call for some general deformation of lattices on both sides connected with the elastic energy ΔU. To keep ΔU=0 we require that the strain additional to u_s (on the ferroelastic side) is zero. A PB perpendicular to the vector $\underline{n}$ which fulfils this requirement may be referred to as permissible PB; it exists when the following conditions are satisfied:

$$u_{ij,s}=(1/2)(s_i n_j + n_i s_j) \qquad (5a)$$

$$\omega_{ij}=(1/2)(s_i n_j - n_i s_j). \qquad (5b)$$

Here $\underline{s}$ is the displacement vector. The last equation defines mutual rotation of the two lattices. The first one puts some restrictions on the u_s tensor. For transitions at which $\Delta V(T_{tr})$=0 the problem of PB existence was discussed in refs. 12, 13. All ferroelastic transitions are classified into two groups: permissible PB (1) does or (2) does not exist. Understandably, approximate solutions are also possible /13/. It is obvious that if a PB exists between the parent phase and a particular domain state (a), another PB is permissible between the parent phase and the domain state (b): both are related by appropriate symmetry elements.

Two practical results emerge from these considerations. First, suppose that a permissible PB between the paraelastic phase and the domain state (a) does exist, having the orientation (hkl). If the transformation proceeds in a temperature gradient gradT oriented perpendicularly to (hkl), the probability that the crystal goes over into a single domain state is greatly enhanced. Thus cooling in an oven with controlled sample rotation provides a method for obtaining single domain samples. This has been demonstrated for $PbZrO_3$ where a "sharp" PB leading to single domain is the (130) plane /14/ and also for $NaNbO_3$ crystals /15/, The same trick is being used for poling $BaTiO_3$ crystals for optical applications.

In the alternative case, a permissible PB does not exist simply because the spontaneous strain components do not allow for a solution of eq. (5). As shown above by eq. (2), a domain texture consisting of properly chosen domain states with relative occupancy α makes it possible to control the average spontaneous strain $\langle u_s \rangle$. Even in this case eqs. (5) can be used to determine (hkl) of the PB between the paraelastic phase and **twinned** ferroelastic phase such that the elastic energy is minimized and at the same time we obtain the volume fraction α. Thus the simple theory predicts the PB for multidomain states as well as the domain wall density. The cubic to tetragonal transition in $NaNbO_3$ /15/ with spontaneous strain components u_a, u_c provides one of known examples. We obtain $h=(u_a/u_c)^{1/2}$, l = 0, $k=[(u_a+u_c)/u_c]^{1/2}$, $\alpha/(1-\alpha)=-u_c/u_a$. For the last factor this calculation gives 2.12 and the observed value of 2 is close. The calculated values of angles which $\underline{n}$ makes with the crystallographic axes agre well with observations, within a 1 degree accuracy.

In both 3D and 2D constraint cases, the resulting domain structure is formed at the transition temperature. Below it, therefore, it has to be considered as metastable. Still, the relaxation times can be expected to be very long, especially for 3D constraints which survive at lower temperatures, though quantitatively modified.

The two mechanisms A, B illustrate model situations in which the effect of stresses has been at least approximately accounted for by theory. Some observations accentuate even further their role. In a boracite crystal /16/ a new orthorhombic transient phase occurs in the vicinity of a non-permissible cubic/tetragonal PB which is believed to be induced by the stress around the PB. In lead orthovanadate, complicated star-like domain patterns are formed in the ferroelastic phase containing regions in which, due to the high stress concentration, the paraelastic phase is stabilized /17/. Phenomena like these may seriously influence macroscopic properties of multidomain samples.

We may mention that the 2D constraint along the phase boundary resembles a kind of epitaxy. The present interest in epitaxial ferroelectric layers will inevitably lead to investigating 2D constraint conditions

along the layers, taking into account elasticity of the substrate and splitting of the layer into ferroelastic domains, and to formulation of simple models which may use the results already known for PBs.

3. Domain-wall attributed susceptibilities

It is accepted generally that domain walls may increase the permittivity by a contribution $\Delta\varepsilon$. Despite of that for no material a satisfactory set of data is available that would lead to a model convincingly explaining this behaviour. ig. 5 shows schematically basic mechanisms of $\Delta\varepsilon$. In a), the crystal lattice **within** the wall responds by permittivity differing by with respect to the bulk. In b), the wall (now represented by a single line) shifts retaining its planarity while in c) it reacts as a membrane, being pinned at discrete points. In d) a nucleus (cluster) with opposite polarization is formed on (at) the wall.

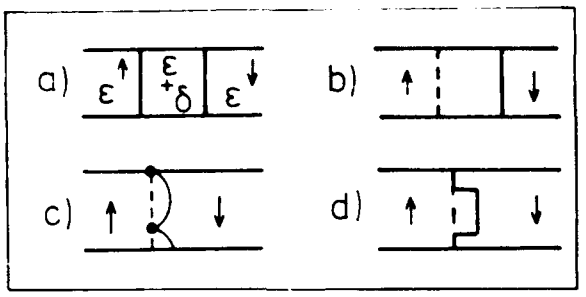


Fig. 5 Mechanisms of $\Delta\varepsilon$, schematically

Dispersion behaviour for a) depends on the microscopic details: here $\Delta\varepsilon$ may relax in the radiofrequency region (reversal of permanent dipoles) or up to the infrared. In the wall-shift mechanisms b,c,d we expect that $\Delta\varepsilon(\omega)$ will be governed by the equation of motion

$$m(d^2x/dt^2)+\beta(dx/dt)+kx=2P_oE \qquad (6)$$

The very existence of $\Delta\varepsilon > 0$ depends on the restoring force coefficient k and to elucidate its origin is the main task. Basic mechanisms considered are: pinning to local defects /18,19,20/, pinning to surface /21/, interaction between close walls /19/.

Coupling to strain may also be essential. Two simple cases are schematically shown in fig. 6. In a),

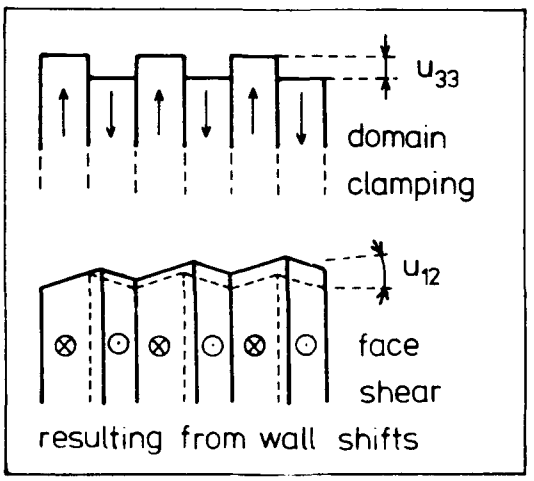


Fig. 6 Two simple cases od domain coupling to induced strain

domains differ in sign of the piezoelectric coefficient d_{33} and thus applied field tends to create the surface profile shown which is difficult to realize: the higher density of domains the more effective is the domain clamping. Thus at frequencies below the thickness resonance domains decrease the magnitude of oermittivity from free to clamped value and when wall shifts are small we have effectively $\Delta\varepsilon<0$. This effect was indeed observed for $BaTiO_3$ /22/.

In b), spontaneous shear u_{12} exists due to piezoelectric coupling in the paraelectric phase. In a multidomain sample the overall $\langle u_{12}\rangle=0$. Field induced wall shifts /23/ lead to macroscopic shear deformation which would be suppressed above the face shear mode resonance frequency

$$\omega_r=(\pi/l)\sqrt{c^E_{66}/\rho} \qquad (7)$$

In this and similare cases, when damping would be low, wall shifts are accompanied by a transfer of huge mass of the whole sample and this would be the source of m in eq. (6). By contrast, forbidding the macroscopic deformation (e.g. clamped grains, cf. section 2) provides a source of k /24/.

It seems that the emergence of fast broad band impedance analyzers (such as HP 4192A and 4191A) that make it possible to follow dielectric relaxation properties as the system undergoes spontaneous or induced changes has recently boosted targeted investigations of $\Delta\varepsilon$. Here we briefly survey results for two very different kinds of ferroelectrics: ferroelastic KH_2PO_4 and nonferroelastic Rb_2ZnCl_4.

In KDP and isomorphous crystals the "tail" of $\Delta\varepsilon$ extends some 40 K below T_{tr} /25/ where around the temperature T_F it disappears. T_F is often called domain freezing temperature. Fig. 7 shows this effect, together with the influence of biasing field and frequency /26/. Recently dispersion studies /23,26/ were performed on pure KDP as well as on crystals with excess KOH ions and some isomorphs. Accompanying $\Delta\varepsilon$ is a domain-induced increase in elastic compliance /26/ (fig. 8) which also freezes out at T_F and is analogical to plasticity of metals connected with twinning mechanism. When ω_r is reached a great part of $\Delta\varepsilon$ diappears. Thus most of $\Delta\varepsilon$ at low frequencies is connected with wall shifts mimicking the face shear mode (fig. 6b). On further increasing frequency the remaining $\Delta\varepsilon$ shows

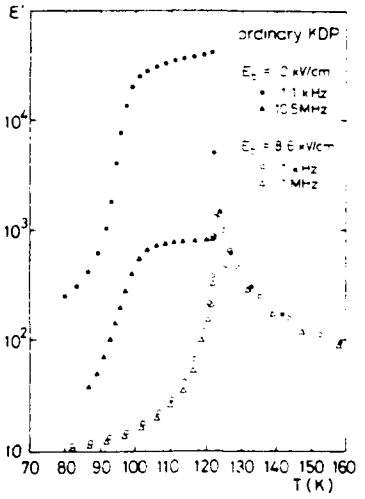


Fig. 7 $\Delta\varepsilon$ and its freezing out in KDP. After /26/

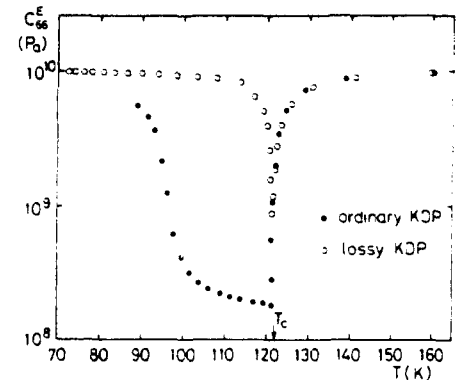


Fig. 8 Domain enhancement of s^E_{66} in KDP and its freezing out. After /26/

a relaxational decrease with a distribution of relaxation times centered around $\tau_m=1/\omega_m$. The latter was found to satisfy the Vogel-Fulcher law

$$\tau_m=\tau_o \exp[E/(T-T_o)] \qquad (9)$$

where T_o is very close to T_F. Thus the domain freezing effect is in fact a phenomenon of anomalous increase of the relaxation time: at T_F the measuring frequency exceeds ω_m and thus $\Delta\varepsilon$ falls. Since ω_r can be controlled by sample dimensions and ω_m by temperature, we may have both cases $\omega_r \lessgtr \omega_m$. The analysis of the results led to the following model /23,26/. The applied electric field causes dipole reversal (connected with protonic motion) in two-dimensional clusters along and within domain walls. If the crystal is free to deform ($\omega<\omega_r$), cluster formation is unsymmetrical and causes the wall to shift. This results in shear deformation (fig. 6b). When ω surpasses ω_r, the shear is forbidden (clamped conditions). However, dipole reversal along the wall continues till its own relaxation frequency ω_m is reached. The latter is determined by the configurational entropy of the dipolar reorientation which decreases with decreasing T since spontaneous polarization in the domains adjacent to the wall approaches its saturated value. At the Vogel-Fulcher temperature T_o the configurational entropy reaches its limiting value and the dipole reversal stops.

It thus appears that KDP offers an interesting combination of two $\Delta\varepsilon$ mechanisms mentioned above: response of the lattice inside the wall itself (here represented by dipolar reorientation in 2D clusters along the wall) and shifts of wall as a whole under mechanically stress-free condition. From a microscopic point of view the dipolar reorientation in the KDP domain wall has been treated in ref. /27/.

Recently much attention has been received by crystals in which between the ferroelectric (C) and normal (N) paraelectric phase there exists another so-called modulated or incommensurate (IC) phase. In it the crystal lattice is distorted with respect to N by a frozen-in wave of atomic displacements whose wavelength $2\pi/k_i$ is not commensurate with the lattice spacing. In what follows we shall have in mind crystals of the A_2BX_4 family, represented by compounds like Rb_2ZnCl_4 (abbr.RZC) or K_2SeO_4. In their "lock-in" phase C these are improper uniaxial ferroelectrics, with 6 domain states differing in the value of phase φ of the order parameter. Above the C-IC transition temperature T_L the modulation takes the shape of perfectly regular quasi-domain structure /28/ with alternating local pokarization. Domain walls are perpendicular to the modulation axis x. In the free energy function the so-called Lifshitz term is essential, linear in the spatial derivative:

$$\Lambda\, r^2(d\varphi/dx) \qquad (9)$$

where r is the order parameter modulus. Since the sign of Λ is given, also the sequence of domain states ...6,1,2,3,4,5,6,1,... when one goes along x, is fixed /28/. Permittivity grows when T_L is approached from above. The accepted model is that the wall response is described by eq. (6). The relaxation is nearly Debye type /29/ (thus m=0), with f_o in the region of 10^8 to 10^9 Hz. The origin of the restoring force is the repulsive interaction of walls. Eq. (6) leads to /30/

$$\Delta\varepsilon\,(\omega=0)=(2\pi P_s^2 w^2/b)(1/x_o)\exp(x_o/w) \qquad (10)$$

$$f_o=k/2\pi\beta. \qquad (11)$$

Here x_o is the distance between walls, w and b are constants.

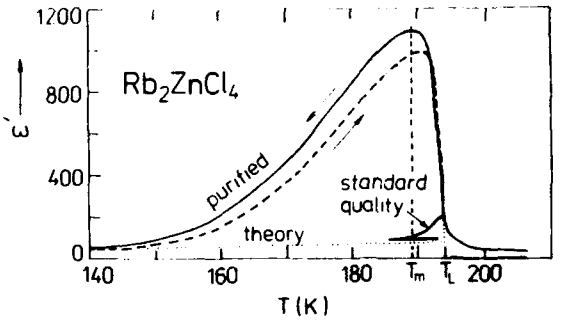


Fig. 6 Permittivity of Rb_2ZnCl_4 measured along its polar axis in the ferroelectric phase. After /30,31/

As in any ferroelectric, the ground state is single domain and thus at T_L permittivity ε is expected to drop, on cooling, to its small background value (cf. fig.9, dotted curve). Instead a tail of $\Delta\varepsilon$ is observed (full curve, for standard quality RZC crystal) which received considerable attention of theoreticians. It has been connected with the response of remnant domain walls pinned to defects /19,20/. Recent data /30/ showed that in specially purified crystals this effect is by far more pronounced in value of $\Delta\varepsilon$ and in temperature width, as shown in fig. 9. The most striking features of this behaviour are: i) temperature T_m of permittivity maximum does not coincide with the phase transition which proceeds svereal K above, as shown by optical and dispersion data. ii) $\Delta\varepsilon$ is roughly the same for cooling and heating run. iii) between T_L and about 175 K we have relaxation spectra with average characteristic frequency shown in fig.10 while at lower temperature a "diffusive" dispersion mechanism dominates shown in fig. 11.

The discussion of some of these data /30,31/ may be based on eq. (6) assuming m=0. This gives Debye equations corresponding to relaxation spectra observed in the upper temperature interval. The origin of the restoring force may be twofold: repulsive wall interaction potential U(n) depending on domain wall density n and trapping of walls by local defects. Both mechanisms can combine, giving /20/

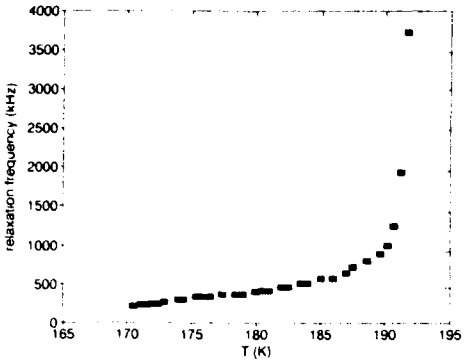


Fig. 10 Relaxation frequency of ε in the upper part of the C phase. Purified RZC /30/

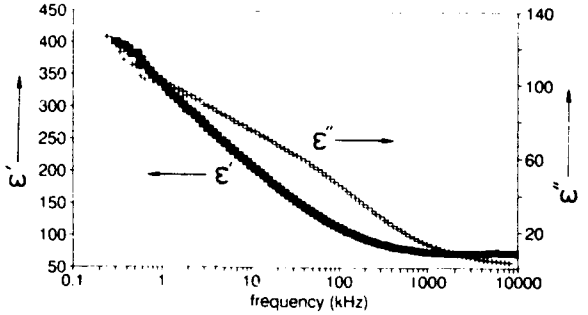


Fig. 11 Diffusive dispersion in the lower part of the C phase (T=150 K). Purified RZC

$$k = U''(n) + gN^{2/3}/4 \qquad (12)$$

where g stands for the effective elastic modulus hindering wall curvature (model of fig. 5c) and N is defect concentration. Close below T_L where wall distance is small, the term U"(n) dominates. It can be speculated that below T_m the role of pinning to defects grows (second term in eq. 12). For static permittivity the eq. (6) with m=0 leads to

$$\Delta\varepsilon = 16\pi P_s^2\, n/k. \qquad (13)$$

Since P_s changes but little, the origin of the $\Delta\varepsilon(T)$ curve below T_m must be sought in k(T) or n(T). On cooling $\Delta\varepsilon$ decreases, which would rewuire, by eq. (13), an increase in k. However, fig. 10 and eq. (11) indicate that k decreases. This leaves the wall density n(T) as the responsible factor for the $\Delta\varepsilon(T)$ behaviour. We might accept that domain wall density decreases on cooling but since $\Delta\varepsilon(T)$ is roughly reversible this would call for reappearance of walls on heating, an unlikely process since no physical reasons seem to exist for it and also since special nucleation of groups of six walls (stripples, see sec. 4) would be required /6,28,30/.

Thus the model of oscillating walls leads to yet unsolved difficulties and it could only be substantiated by direct data on temperature dependence of wall density n(T), at present not available.

Alternatively, the model of lattice response **within** the wall (fig. 5a) could explain $\Delta\varepsilon(T)$ without calling for unexpected function n(T). Theoretical background for such a wall response in this kind of materials is, however, missing. In fact the oscillating walls model is generally believed to be suitable for describing dielectric properties in the IC phase.

It is interesting to note that two types of dispersion behaviour (Debye or diffusive) of $\Delta\varepsilon$ is not uncommon in ferroelectrics. Despite some general theoretical attempts (e.g. /32/), a model for the diffusive mechanism is missing.

4. Ferroelectric lock-in phases in high fields

In a good sample of classical uniaxial ferroelectric (TGS, $BaTiO_3$ free of 90° walls), hysteresis loops are well rectangular. Polarization reversal process proceeds by the following mechanisms: formation of nuclei of the opposite domain, their forward and lateral growth, coalescence of domains. Switching times in constant fields are determined by nucleation probability and domain wall mobility. In the latter, mutual interaction of walls has not been considered an important factor.

Data on switching in ferroelectric lock-in phases of A_2BX_4s are not numerous. Most measurements of ac hysteresis loops point to a rather special form: the loop is swan-neck shaped with small remanent polarization compared to the saturated value and with small coercive field compared to the field at which P saturates. Fig. 12 shows an example, taken for standard RZC crystal 2.3 K below T_m /33/. For highly purified crystals we have observed even lower coercivity, in an interval of several K on both sides of T_m.

An alternative way to represent high field dielectric nonlinearity is to measure permittivity ε as a function of biasing field. For standard quality RZC ε was shown to be independent of E up to the threshold field E_o = 30 V/cm while for $E > E_o$ ε changes linearly with 1/E /34/. Such a dependence can be explained by the model of oscillating walls which led to eq. (10). Biasing field brings pairs of walls together (cf. left part of fig. 14) so that the distance x_o which dominates in the interactive repulsion decreases. This results in decreasing in proportion to 1/E.

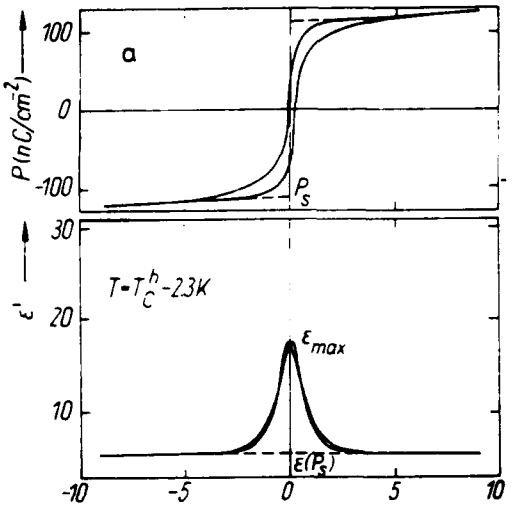


Fig. 12 Hysteresis loop and $\varepsilon(E)$ of standard quality RZC in the C phase /33/

It was found that for highly purified sample of RZC the dependence $\varepsilon(E)$ is practically without hysteresis. Fig. 13 shows an example of such measurement /31/ taken at about 4 K below T_L: curves for rising and decreasing E are practically identical, in contrast to common behaviour of uniaxial ferroelectrics.

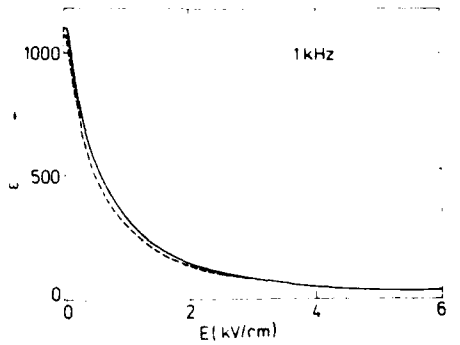


Fig. 13 Permittivity vs. bias in the C phase of purified RZC /31/

It thus appears that nonlinear dielectric properties of lock-in ferroelectric phases of A_2BX_4 crystals differ from those observed for usual ferroelectrics. It can be suggested that mechanisms responsible for the former are as follows. In a defect-free crystal, domain walls can freely move under applied field, feeling only the interaction potential of neighbouring walls. There is therefore no threshold and no hysteresis. As domains with unfavourable orientation narrow (fig. 14, left) walls coming close create pairs and repulse each other. This interaction is responsible for signs of saturation in form of swan-neck-shaped P(E) dependence. It is now essential that the pair of walls in this case cannot coalesce. This would create instead an antiphase boundary which may be energetically unfavourable. The only process which would make the sample single domain is the formation of complicated nuclei, so-called stripples /29,31/ consisting of six walls and terminating in a line defect (see right part of fig. 14). Their formation seems however, improbable since in the C phase the average distance of walls is large.

But not even formation of a classical nucleus, such as that of domain state 1 embedded in the region of domain state 6 is very probable. Such a nucleus would be partly dressed into the domain wall 1-6, in contrast to the natural sequence 6-1 (cf. sec. 3). On the basis of the free energy function including the term given by eq. (9) we obtain for the difference in wall energy densities, in some approximation,

$$\sigma(1\text{-}6) - \sigma(6\text{-}1) = \Delta\pi r^2 > 0, \qquad (14)$$

Thus the 1-6 wall is unfavourable in the whole range of the phase C and the formation of simple nuclei may be therefore suppressed.

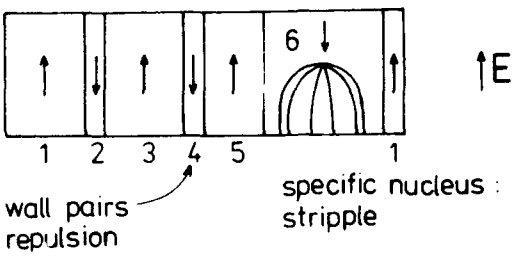


Fig. 14 Schematical representation of the lock-in phase, see text

We thus may have a material which exhibits novel features not uninteresting from the point of view of practice: very strong dielectric nonlinearity in a not too narrow temperature interval, with small hysteresis which can be, by controlled purity, reduced to vanishing values. The same kind of effects can be expected in other members of the A_2BX_4 family in different temperature regions.

5. Concluding remarks

Some of the problems discussed above delineate interesting topics for further research. In connection with sec. 3 we may mention domain structures in lock-in ferroelastic phases, in particular studies of wall densities developing through T_L and below in the C phase, possible direct observation of stripple mechanisms, studies of domain wall conditioned elastic compliances. Highly purified $(TMA)_2CuCl_4$ might be a good candidate for a model material. Much more detailed studies along the lines indicated in sec. 4 are needed to throw sufficient light on the high field processes in lock-in ferroelectric phases, possibility of nucleation, frequency dependence of nonlinearities due to walls gliding freely but for their interaction.

However, we left untouched many exciting problems that wait for concentrated experimental and theoretical effort. Their list contains domain formation in nonferroelastics, particularly the existence of dynamical clusters above T_c, their possible connection with the birth of well defined domains below T_c but also the existence and role of microdomains in the ordered phase. It is felt that the area of photoinduced domain effects, addressed in connection with optical properties of PLZT and with hologram fixing years ago, was left in an unsatisfactory state of affairs and is worth of further investigations. Perhaps the hottest topic are domain structures and their properties in 2D and 1D systems, i.e. in thin films and in fibers. In all mentioned cases we believe that the essential condition of success is the choice of a model material, meeting basic physical requirements such as suitable crystal symmetry, location of transition point, bandgap width etc., but at the same time capable of technological processing aimed at obtaining well defined samples with known and controlled quality.

References

/1/ Ferroelectrics, vol. 111, Part B, 1990.

/2/ Proc. 2nd International Symposium on Domain Structure of Ferroelectrics and Related Materials, Nantes 1992. To appear in Ferroelectrics.

/3/ Ferroelectrics, vols. 97 and 98, 1989.

/4/ Izvestiya Akad. Nauk. SSSR, ser. fiz., vol. 43, No.8, 1979; vol. 47, No.3, 1983; vol. 50, No.2, 1986; vol. 51, No.2, 1989; vol. 53, No.7, 1989;

/5/ E. K. H. Salje, Phase transitions in ferroelastic and co-elastic crystals. Cambridge University Press, 1990.

/6/ J. Fousek, "Ferroelectric domains: recent progress in understanding their static and dynamic properties", in Ferroelectric Ceramics, ed. N. Setter, Birkhäuser Verlag, Basel. To appear.

/7/ A. L. Roitburd, "Theory of formation of heterophase structure in phase transformations in solids", Soviet Physics - Uspekhi, vol. 17, p. 326, 1974.

/8/ A. L. Roytburd, "Elastic domains and polydomain phases in solids", to appear in ref. 2.

/9/ G. Arlt, "The role of domain walls in the dielectric, elastic and piezoelectric properties of ferroelectric ceramics", Ferroelectrics, vol. 76, pp. 451-458, 1976.

/10/ G. Arlt, "Twinning in ferroelectric and ferroelastic ceramics: stress relief", J. Material Science, vol. 25, pp. 2655-2666, 1990.

/11/ G. Arlt and P. Sasko, "Domain configuration and equilibrium size of domains in $BaTiO_3$ ceramics", J. Appl. Phys., vol. 51, pp. 4956-4960, 1980.

/12/ L. A. Shuvalov, E. F. Dudnik, V. A. Nepochatenko and S. V. Vagin, "Phase boundaries in ferroelastics", Izvestiya Akad. Nauk SSSR, ser. fiz., vol. 49, pp. 297-300, 1985. (In Russian.)

/13/ C. Boulesteix, B. Yangui, M. Ben Salem, C. Manolikas and S. Amelinckx, "The orientation of interfaces between a prototype phase and its ferroelastic derivative: theoretical and experimental study", J. Physique, vol. 47, pp. 461-471, 1986.

/14/ J. Dec, "Monodomain state formation in antiferroelectric $NaNbO_3$ and $PbZrO_3$ crystals", Ferroelectrics, vol. 97, pp. 197-200, 1989.

/15/ J. Dec and J. Kwapulinski, "Phase boundaries in $NaNbO_3$ single crystals", Phase Transitions, vol. 18, pp. 1-9, 1989.

/16/ Z. G. Ye and H. Schmid, "Domain studies of the electric field or stress-induced phase transitions in ferroic crystals of $Cr_3B_7O_{13}Cl$, $Cd_2Nb_2O_7$ and $Pb(Mg_{1/3}Nb_{2/3})O_3$", in ref. 2.

/17/ C. Manolikas and S. Amelinckx, "Phase transitions in ferroelastic lead orthovanadate as observed by means of electron microscopy and electron diffraction", phys. stat. sol. (a), vol. 60, pp. 607-618, 1980.

/18/ J. Fousek and V. Janoušek, "The contribution of domain wall oscillations to the small-signal permittivity of triglycine sulphate", phys. stat. sol., vol. 13, pp. 195-206, 1966.

/19/ P. Prelovšek and R. Blinc, "Defect and fluctuation effects at the incommensurate-commensurate phase transition in Rb_2ZnCl_4", J. Phys. C: Solid State Phys., vol. 17, pp. 577-588, 1984.

/20/ T. Nattermann, "Dielectric tails in K_2ZnCl_4: no evidence for an intrinsic chaotic state", phys. stat. sol. (b), vol. 133, pp. 65-70, 1986.

/21/ M. E. Drougard and R. Landauer, "On the dependence of the switching time of barium titanate crystals on their thickness", J. Appl. Phys., vol. 30, pp. 1663-1668, 1959.

/22/ J. Fousek, "The contribution of domain walls to the small-signal complex permittivity of $BaTiO_3$", Czech. J. Phys., vol. B 15, pp. 412-417, 1985.

/23/ K. Kuramoto, "Dielectric dispersion accompanied with the domain freezing in KH_2PO_4 single crystal", J. Phys. Soc. Jpn., vol. 56, pp. 1859-1867, 1987.

/24/ G. Arlt and N. A. Pertsev, "Force constant and effective mass of 90° domain walls in ferroelectric ceramics", J. Appl. Phys., vol. 70, pp. 2283-2289, 1991.

/25/ A. Fousková, P. Guyon and J. Lajzerowicz, "Mesures diélectriques et observations optiques des domaines du dihydrogene phosphate de potassium", C. R. Acad. Sc. Paris, vol. 262, pp. 907-910, 1966.

/26/ E. Nakamura and K. Kuramoto, "Resonance and relaxational dispersions around the domain freezing temperature in KH_2PO_4", J. Phys. Soc. Jpn., vol. 57, pp. 2182-2190, 1988.

/27/ J.-Y. Koo and J.-J. Kim, "Thermodynamic theory of domain wall freezing in KDP-type crystals", to appear in ref. 2.

/28/ V. Janovec and V. Dvořák, "Perfect domain textures in incommensurate phases", Ferroelectrics, vol. 66, pp. 169-187, 1986.

/29/ K. Hamano, H. Sakata, H. Izumi, K. Yoneda and K. Ema, "Effect of purification on dielectric properties near the commensurate-incommensurate transition point in Rb_2ZnCl_4", Phase Transitions, vol. 11, pp. 279-296, 1988.

/30/ V. Novotná, H. Kabelka, J. Fousek, M. Havránková and H. Warhanek, "Dielectric properties of Rb_2ZnCl_4 crystals in the commensurate phase" submitted.

/31/ J. Fousek and V. Novotná, "Manifestation of domains in the dielectric properties of ferroelectric lock-in phases", to appear in ref. 2.

/32/ N. M. Galiyarova, "Dielectric properties and dynamic behaviour of domain walls in the weak low-frequency electric fields from thermodynamics view", to appear in ref. 2.

/33/ G. Sorge, H. Maack and L. A. Shuvalov, "Low frequency dielectric properties of Rb_2ZnCl_4", phys. stat. sol. (a), vol. 93, pp. 315-320, 1986.

/34/ A. Levstik, H.G. Unruh and P. Prelovšek, "Direct measurement of the interaction potential between discommensurations in Rb_2ZnCl_4", Phys. Rev. Letters, vol. 58, pp. 1953-1955, 1987.

Dielectrics: Properties, Materials, and Applications

NON-LINEAR DIELECTRIC PROPERTIES OF $KTa_{1-x}Nb_xO_3$

X.M. [illegible]ang, B.E. Vugmeister and [illegible]. Toulouse
Physics Department, Lehigh University, Bethlehem, PA 18015

Abstract

We have measured the field dependence of the dielectric constant in two crystals of $KTa_{1-x}Nb_xO_3$ with x=1.2% and 15.7%. For both concentrations we fit $\epsilon(E)$ with an expansion in powers of the applied DC field E to find the first non-linear coefficient, $\epsilon^{(2)}$. $\epsilon^{(2)}$ exhibits two distinct temperature dependences, first, at high temperature a strong divergence as $(T-T_c)^{-\alpha}$, then a crossover to a much weaker dependence. This crossover is interpreted as being from a dynamic to a static regime. An outline of the corresponding theoretical modeling in progress is also presented.

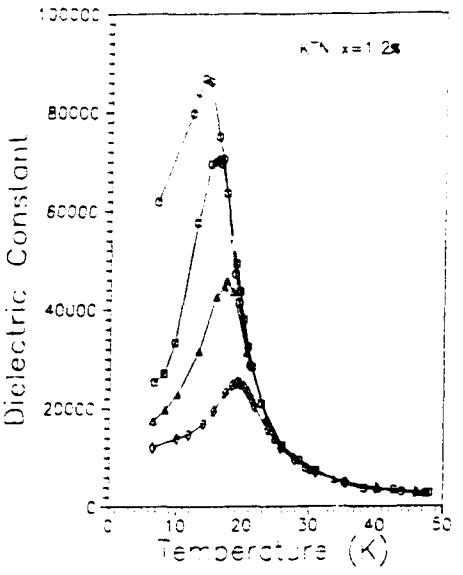
Introduction

The two mixed systems $KTa_{1-x}Nb_xO_3$ (KTN) and $K_{1-y}Li_yTaO_3$ (KLT) both undergo unusual ferroelectric transitions induced by the presence of off-center impurity ions forming dipoles. These transitions are preceded by the appearance, many degrees above T_c, of precursor polar microregions[1] and exhibit atypical features such as early deviations from a Curie-Weiss law, a cusp shape of the dielectric constant peak at T_c, the observation of a corresponding dielectric loss peak on the low temperature side of the dielectric constant peak as well as a small dispersion near the transition and, finally, differences between the dielectric peaks measured in the field cooled (FC) or zero-field cooled (ZFC) conditions.[2] Because several of these features are typical of spin glass-forming systems,[3] and because spin glass transitions are characterized by the divergence of the non-linear susceptibilities,[4] we have measured the dielectric constant of KTN as a function of field.

Experiments

Measurements of the dielectric constants were performed with a general radio capacitance bridge (Model 1615) at 1 kHz and for different DC bias fields. For each value of the bias field, measurements were made as a function of decreasing temperature (FC condition). At each point, the temperature was stabilized for approximately 15mn before the measurement was actually recorded.

The results for two KTN crystals with x=1.2% and 15.7% are shown in Fig. 1a and 1b. Both sets are very similar, showing a strong decrease in the peak height with increasing DC field. However, it is important to note that the magnitude of this DC field is very different for the two crystals, between 0 and 250V/cm for the 1.2% crystal and between 0 and 2.5kV/cm for the 15.7% crystal or a factor of 10 between the two crystals. Thus, in the lower concentration crystal, a much smaller DC field is required in order to depress the strong susceptibility. In the above, we assume that the single dielectric peak observed in the 1.2% crystal corresponds to the high peak in the 15.7% crystal. This is contrary to a previous assignment[5] which was based on a combination of dielectric and Raman measurements unfortunately made on two different crystals with similar but not equal concentrations of niobium. The present assignment is based on new Raman measurements directly made on the dielectric crystal.[6]



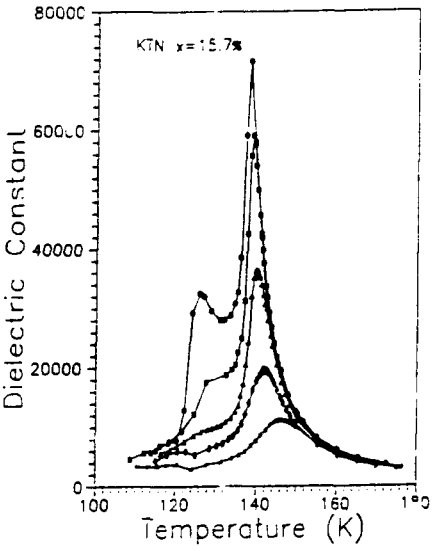


Figure 1a) Dielectric constant vs. temperature under various dc bias for the 1.2% Nb sample o 0 kV/cm; 0.05 kV/cm; 0.10 kV/cm; 0.25 kV/cm; and 1b) for the 15.7% Nb sample, o 0 kV/cm; 0.25 kV/cm; 0.5 kV/cm; 1 kV/cm; * 2 kV/cm.

The above results for the 15.7% crystal are presented in a different form in Fig. 2 where we have plotted the field dependence of the dielectric constant

CH3080-0-7803-0465-9/92$3.00©IEEE

at several temperatures close to T_c. The range of temperatures corresponds to that in which we have noted earlier a deviation from a Curie-Weiss law and other anomalous features. The curves in Fig. 2 clearly reveal the non-linearities of the dielectric constant. They can be fitted to an expansion of the form:

$$\varepsilon = \varepsilon^{(0)} + \varepsilon^{(2)} E^2 + \varepsilon^{(4)} E^4$$

in which $\varepsilon^{(2)}$ and $\varepsilon^{(4)}$ represent the first two non-linear coefficients. Only even terms are expected in the expansion because of the symmetry of the dielectric tensor.

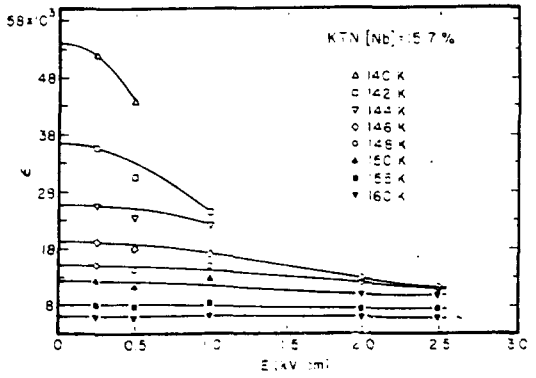
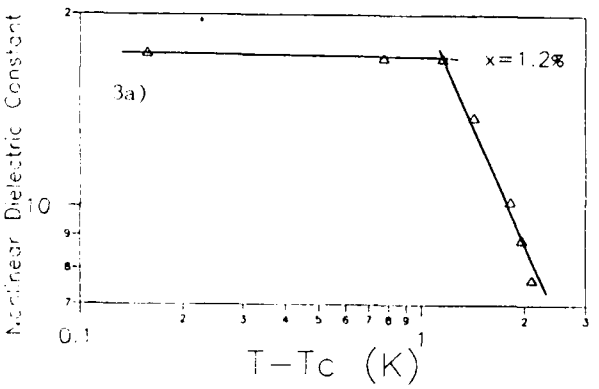


Figure 2. Dielectric constant of KTN (15.7%) vs. dc bias at various temperatures. The solid lines are fitting results.

The values obtained from the fit for the two coefficients are plotted on a log-log scale in Fig. 3a and 3b for the two crystals respectively as a function of $(T-T_c)$. For both crystals we note the existence of two ranges. At higher temperatures $\varepsilon^{(2)}$ increases very rapidly with a steep slope approximately equal to 9 (±0.4) in both cases. Closer to T_c the slope becomes almost null for the 1.2% and equal to about 2 for the 15.7%. More important than the difference in the low temperature slope are the very different temperature ranges in which the two regimes are observed. In the 1.2% crystal, the steep slope extends down to almost T_c + 2K while in the 15.7% crystal the crossover occurs as far as T_c + 16K.



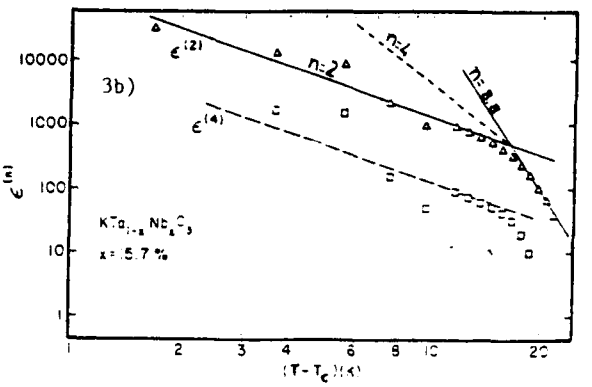


Figure 3. Log-log plot of $\varepsilon_{NL}^{(2)}$ and $\varepsilon_{NL}^{(4)}$, coefficients of the first and second non-linear terms of the $\varepsilon(E)$ expansion vs $\ln(T-T_c)$ a) for x = 1.2% Nb, T_c = 13.8K b) for x = 15.7% Nb, T_c = 138.6K

Interpretation

In a previous publication[1], we reported hysteresis loop measurements which showed that the departure from a Curie-Weiss law corresponded to the appearance of polar microregions (20 - 100 Å). This also corresponds here to the present observation of dielectric non-linearities. We are thus led to the conclusion that the dielectric non-linearities are due to the presence of the polar microregions.

An explanation remains to be given for the existence of two ranges with a steep slope in the higher temperature range, and for the differences between the two concentrations. It is reasonable to suppose that, at first, the polar microregions are dynamical, i.e. they either persist for a certain lifetime or they are permanently present but can reorient as a unit. In the second and lower temperature range, the interactions between dipoles becoming increasingly strong and more distant dipoles beginning to lock-in, the polar regions grow in size and become static at the same time. This interpretation can also account for the concentration dependence observed.

For low concentrations, the average distance between impurity dipoles will be large or the number of near neighbor dipoles will be small, and the distribution function of inter-dipole distances will be relatively narrow. One then expects that the dynamical regime will extend close to the transition. On the contrary, for high concentrations, the average distance between impurity dipoles will be small and the distribution function of distances relatively broad. Then, it appears that the cross-over of close dipole pairs from the dynamical to the static regime will occur farther away from the transition.

With regard to the field strength required to lower the dielectric peak, or equivalently the value of the non-linear coefficient $\varepsilon^{(2)}$, it is clear that if the average distance between impurity dipoles is large, the average interaction energy will be small. Consequently, for low concentrations, a small field will be sufficient to decouple the dipoles from one another or to overcome their mutual internal random fields and align them.

One of us has recently proposed a random field

theory[7] in order to explain dipole-induced transitions in highly polarizable crystals. In this theory, the order parameter is chosen to be:

$$L = \overline{\langle \ell_i \rangle}$$

where the moment of each dipole is $\vec{d}_i = d\hat{\ell}_i$ and the two brackets and the upper bar represent orientational and configurational averages respectively. Each dipole d_i finds itself in the field E_{int} of all the surrounding dipoles. Because these are randomly distributed, the resulting internal fields are themselves random, with a distribution function $f(E_{int},L)$ which clearly also depends on the order parameter L. The value of L can be obtained by solving the following self-consistent equation:

$$L = \int_0^\infty f(E_{int},L)\ \langle \ell_i \rangle_{E_{int}}\ dE_{int}$$

The same theory can be applied to calculate the dielectric constant and its non-linear coefficient: $\varepsilon(E) = nd^*L/E$ where n is the dipole concentration, and d^* the effective dipole moment in the highly polarizable crystal. Instead of the moment ℓ_i of a single dipole, we shall use the average moment of a pair of dipoles, $\langle \ell_{ij} \rangle_{E_{int},E}$, now a function of the applied field as well as the local field. Such a calculation is in progress and resembles that pertaining to long time relaxation effects and the observation of hysteresis loops above T_c, which is presented in this volume.

References

1. J. Toulouse, P. DiAntonio, B.E. Vugmeister, X.M. Wang and L.A. Knauss, Phys. Rev. Lett. 68, 232 (1992).

2. J. Toulouse, X.M. Wang, L.A. Knauss and L.A. Boatner, Phys. Rev. B43, 8297 (1991).

3. D. Chowdhury, "Spin Glasses and Other Frustrated Systems", (Princeton University Press, Princeton, N.J., (1988) p. 1.

4. R. Omari, J.J. Prejean and J. Souletie, J.Physique 44, 1069 (1983).

5. P. DiAntonio, X.M. Wang, J. Toulouse and L.A. Boatner, Ferroelectrics, 120, 107 (1991).

6. P. DiAntonio and J. Toulouse (unpublished).

7. B.E. Vugmeister and M.D. Glinchuk, Rev. Mod. Phys. 62, 993 (1990).

Acknowledgments

This work was partially supported by the Division of Materials Sciences, US Department of Energy under contract No. DE-FG02-86ER 45258.

DIELECTRIC BEHAVIOR OF FERROELECTRIC THIN FILMS AT HIGH FREQUENCIES

J. Chen, K. R. Udayakumar, K. G. Brooks, and L. E. Cross
Materials Research Laboratory
Pennsylvania State University
University Park, PA 16802

Abstract

The high frequency dielectric response of sol-gel derived lead zirconate titanate (PZT) thin films has been investigated. Conceptualizing the presence of interface layers was critical in explaining the dielectric measurements. By a careful control of the processing parameters, aided by rapid thermal annealing, the low frequency dielectric charactersistics could be sustained upto a GHz range. $Ba_{0.5}Sr_{0.5}TiO_3$ which is paraelectric at room temperature appears to be a potential candidate material for high frequency applications.

Introduction

In these modern times, many and varied are the applications of high frequency dielectrics; in high resolution/ digital communication devices encompassing cellular phone and satellite communications, in microelectronics and packaging for high speed switching mode power supply, in frequency sensors for microwave detection, to plainly list but a few. Dielectrics qualifying for such applications must possess high dielectric permittivity, low dissipation loss, and low temperature coefficient of electrophysical properties. Ferroelectric materials, which constitute a unique subclass of dielectrics, while very promising in satisfying these general attributes, suffer from a drop in the dielectric constant at a characteristic frequency, ascribed to the piezoelectric resonance of the crystallites as well as the inertia of the domain boundaries; other plausible explanations advanced for the phenomenon include the existence of interface layers at the film-electrode boundary, impurities in the film, and grain imperfections as also grain boundaries. At still higher frequencies, an additional drop in the relative permittivity may occur, assigned generally to dielectric relaxation. In paraelectric materials, no piezoelectric resonance can occur if the phase is centrosymmetric: the clamped and free dielectric constant, which refer to the dielectric constant at frequencies above and below piezoelectric resonance respectively, are equal to one another. At a given high frequency, dielectric relaxation can still cause a fall in the dielectric permittivity in this non-polar phase.

Shifting the focus from the confines of the bulk materials to the dielectric behavior of ferroelectric thin films at low-amplitude a.c. field of high frequencies, as in the present study, the dominant factors that influence relaxation appear to be connected to the presence of interface layers, and grain imperfections. For, first, these films have been characterized by very small grain sizes, in the 0.1-0.2 μm range [1,2], that has the effect of displacing the threshold frequency due to the piezoelectric clamping of grains or domains to higher levels; and second, fabrication of the films through the sol-gel process ensures maximal chemical purity. This study will, consequently, argue that the dielectric dispersion in the 1 MHz to several GHz range stems from the presence of barrier layers and grain imperfections, both of which can be squarely linked to the film processing.

Results and Discussion

The PZT films used in the study were of the morphotropic phase boundary composition (with a Zr/Ti mole ratio of 52/48), fabricated by the sol-gel spin-on technique. The details of the film fabrication as well as the structural and electrophysical characterization of these films have been outlined in Refs. 1 and 2; the dielectric and ferroelectric property measurements were limited to the radio frequency range in these earlier studies. For dielectric measurements in this study, a high frequency impedance analyser (HP 4191A) was used. All the films were rapid thermally annealed at temperatures and times as specified.

Fig. 1 is a plot of the dielectric permittivity as a function of frequency for a 0.385 μm thick PZT film, rapid thermally annealed in the temperature range of 600-800°C for 60 seconds. It is patent from the figure that with increasing annealing temperature, the relaxation frequency decreases systematically; of greater import is the precipitous tumble in permittivity to almost a cipher at this frequency. While this latter point is seemingly baffling at first glance, the frequency response of the measured dielectric constant and the corresponding impedance spectrum from the equivalent circuit model, based on properties of the

CH3080-0-7803-0465-9/92$3.00 ©IEEE

film core, the electrode, and a series resistance [3], lends a modicum of understanding to the anomalous dielectric behavior. Sayer et al. [3] postulated the formation of an interface layer at the top electrode-film boundary and the film-substrate boundary; by varying the internal barrier layer thickness from 0.01 μm to 0.5 μm (the disturbed layer at both the interfaces are lumped) on a film of 1 μm total thickness, the dielectric constant was computed, which has been reproduced here as Figure 2. Scrutiny of this figure, and its juxtaposition with Fig. 1, reveals a striking similarity, tempting the speculation of the presence of interface layers of increasing thickness with increasing severity of annealing of the films. As observed by the authors [3], the calculated higher dielectric constant for films with thicker barrier layers might be related to the assumption of the full thickness of the film in the computations, when in

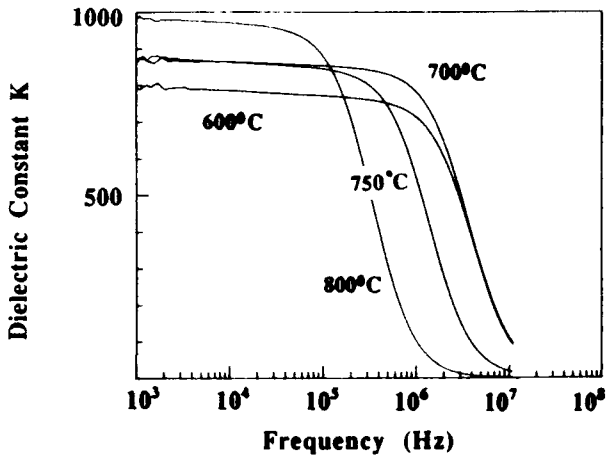


Fig. 1 High frequency dielectric response of PZT thin films, annealed 600-800°C at a constant dwell time of 60 seconds. Note the systematic change in the relaxation frequency with annealing temperature.

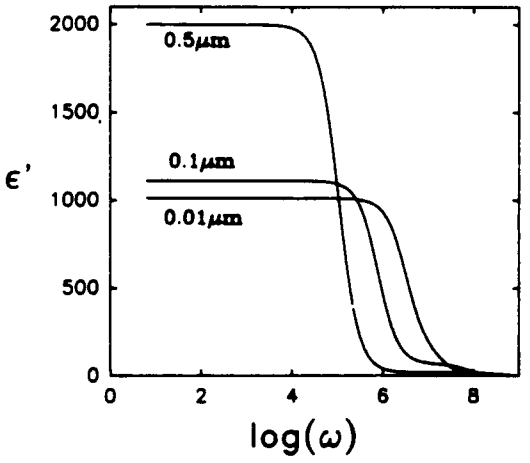


Fig. 2 Computed dielectric constant of a 1 μm film with varying internal barrier thickness; the true value of ε'=1000 (reproduced from Sayer et al. [3])

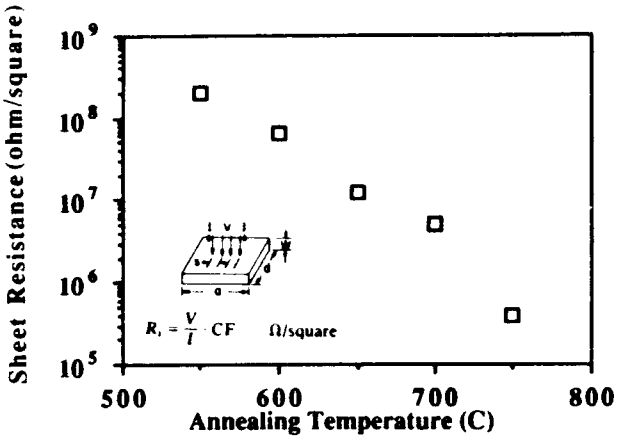


Fig. 3 Resistivity plotted as a function of annealing temperature.

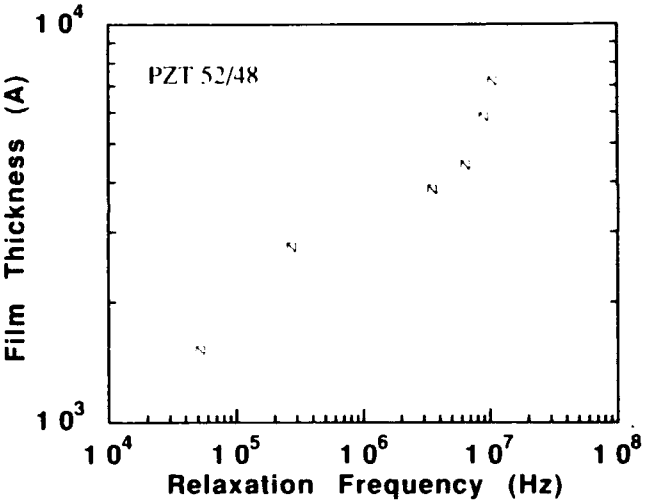


Fig. 4 Relaxation frequencies determined for films of varying thickness shows a drop for thinner films.

reality, it should be smaller by a thickness equal to that of the disturbed layers. In our earlier study [1], the high frequency dielectric relaxation was alluded to the formation of low resistivity surface layers whose resistivity changes with the annealing conditions; from Fig. 3, it is apparent that higher annealing temperature results in lower resistivity of this anomalous layer. Maintaining the same processing parameters, dielectric relaxation frequencies of films varying in thickness from 0.15 μm to 0.75 μm were determined (Fig. 4); thinner films are privy to lower relaxation frequencies, indicating heightened sensitivity to the interface layer formation. When the thermal budget was reduced during annealing by lowering the dwell time from 60 seconds to 10 seconds, there was no

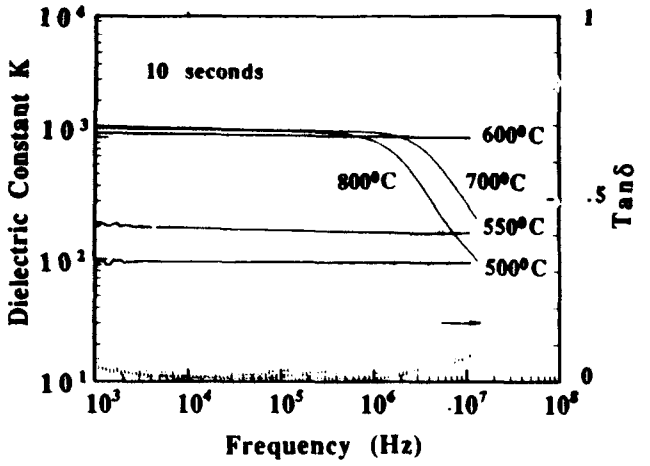


Fig. 5 Dielectric permittivity plotted as a function of frequency for various annealing temperatures but with a reduced dwell time of 10 seconds.

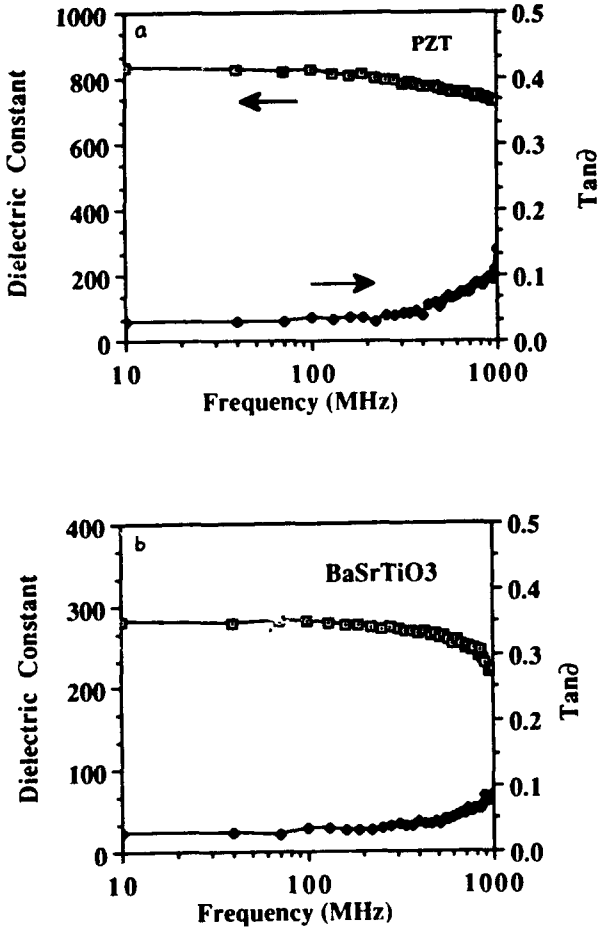


Fig. 6 The frequency characteristics of ferroelectric PZT films (a), and paraelectric BST films (b); note the non-dispersive behavior upto the measured frequency of 1 GHz by a careful control of the growth of the interface layer.

evidence of relaxation in films annealed at 500 to 600°C (Fig. 5); interface layer growth may thus be controlled to eliminate low frequency dielectric dispersion. Extending this theme, by manipulating the processing parameters, the low frequency dielectric permittivity and loss of the PZT films could be sustained upto a GHz, as shown in Fig. 6a. A solid solution system embracing compositions that is paraelectric at room temperature is the (Ba, Sr)TiO_3 (BST) system; specifically, thin films in the BST system, of composition corresponding to a Ba/Sr mole ratio of 50/50, fabricated by the sol-gel chemical technique, revealed dispersion-free dielectric charactersistics (Fig. 6b) for measurements upto a GHz.

Summary

Earlier studies of both bulk ceramics and thin films has shown that the utility of ferroelectrics for high frequency applications is limited on account of the dielectric dispersion at 1 MHz to a few hundred MHz depending on the specific material. The present endeavor has shown that by a deliberate interplay of the processing parameters, dielectric relaxation in the PZT films can be prevented upto a GHz. Films that are ferroelectric at room temperature are *intrinsically* subjected to relaxation due to the piezoelectric clamping of grains or domains, and the inertial response of domain wall movement. It would therefore appear prudent to examine the feasibility of films that are paraelectric at room temperature for high frequency applications; $Ba_{0.5}Sr_{0.5}TiO_3$ falls in this category, and the first results are indeed promising.

References:

[1] J. Chen, K. R. Udayakumar, K. G. Brooks, and L. E. Cross, "Rapid thermal annealing of sol-gel derived PZT thin films", J. Appl. Phys., pp. 4465-69, May 1992

[2] K. R. Udayakumar, J. Chen, S. B. Krupanidhi, and L. E. Cross, "Sol-gel derived PZT thin films for switching applications", Proc. Seventh Intl. Symp. Appl. Ferroelectrics, 1990, pp. 741-43

[3] M. Sayer, A. Mansingh, A. K. Arora, and A. Lo, "Dielectric response of ferroelectric thin films on non-metallic electrodes", Integrated Ferroelectrics, vol. 1, pp. 129-146, 1992.

PTC BEHAVIOR IN YTTRIA DOPED $BaTiO_3$ AS RELATED TO GRAIN BOUNDARY STRUCTURE

R. D. Roseman, J. Kim and R. C. Buchanan, Dept. of Materials Science and Engineering, University of Illinois at Urbana-Champaign, Urbana, IL 61801

Abstract

Lattice structure and phase distribution along the grain boundaries in Y_2O_3 doped $BaTiO_3$, with Zr^{4+} as a counterdopant, were investigated with respect to their impact on PTC behavior. This doping, related to A and B-site occupancy, creates ionic defect states which segregate during annealing to different morphological regions along the grain boundaries, identified as non-domain and domain regions. TEM high resolution imaging, HOLZ pattern and EDS analysis of these regions showed differences in composition, lattice parameters and lattice plane coherency across the grain boundaries. Optimum doping in light of these structural changes resulted in lower resistivity and enhanced PTC effects, the stress release being the driving force for sharp PTC transitions.

Introduction

Ferroelectric barium titanate, $BaTiO_3$, is typically used as the base material for non-linear positive-temperature-coefficient (PTC) resistors. $BaTiO_3$ exhibits high intrinsic resistivity, $>10^{10}$ Ω·cm, when prepared in an oxidizing atmosphere. Through controlled A-site doping using ions such as La^{3+},Y^{3+}, Nd^{3+}, or B-site doping using Nb^{5+} or Ta^{5+}, semiconducting properties can be obtained [1]. Within a very narrow dopant concentration range (0.1-0.3 m/o), electronic compensation and n-type conduction result from the formation of Ti^{3+} donor ions [1,3-6]. This is accompanied by local distortion of the Ti-O octahedron and a change in the local polarization field. The increased conduction in these materials is due to overlap of these polarization fields, resulting in small polaron conduction [2]. The associated positive temperature coefficient of resistance (PTCR) characteristics, manifested as a large increase in resistance (by several orders of magnitude) over a narrow temperature range near the phase transition, corresponds to a disappearance of the spontaneous polarization and a change in the lattice structure [1,3-6].

In the grain boundary region oxygen is adsorbed during annealing, reducing the Ti^{3+} concentration within this region [3]. Vacancies and defects can, likewise, diffuse to the grain boundary regions, becoming electron or acceptor trap sites [1,7-10]. Theories on the PTC effect suggest that a space charge or barrier layer is produced as electrons move toward the grain boundary, which acts to repel the electron flow. At temperatures below the critical ferroelectric phase transition, low resistivity is found due to (+) spontaneous polarization charges neutralizing (-) grain boundary charges in crystallographically coherent areas along the grain boundaries, creating a low resistance path [3,4].

The domain structure and dimensions in doped (PTC) $BaTiO_3$, are comparable to the ferroelectric domain patterns typically observed by TEM in undoped $BaTiO_3$ [11]. Across a grain boundary, 90°domains can be found, but this domain pattern is not common because a favorable crystal orientation is required in both neighboring grains [11,12]. Within the PTC material, electron motion is encumbered by a spectrum of potential barriers at the grain boundaries. The heights of these barriers depend on the charge compensation at the junctions of matching domains and on the corresponding dielectric constants. The lowest barriers will govern the low temperature resistivity [11].

The lattice, domain and microstructures should, therefore, all play a prominent role in PTC materials. However, the structure of the grain boundary region and its exact contribution to the development of the PTC effect are not fully understood. In this study, lattice, domain structure and resultant strains in Y_2O_3 doped PTC $BaTiO_3$ were investigated, and related to these microstructural features as well as to bulk PTC behavior.

Experimental

The materials used in this study were high purity $BaTiO_3$* with a Ba/Ti atomic ratio of 0.997, Yttria Nitrate pentahydrate and Zirconyl Nitrate hydrate.** The $BaTiO_3$ was ball milled with 0.0-3.5m/o of the nitrates for 12 hrs. using ZrO_2 balls in a 60vol% isopropyl alcohol-40vol% deionized water solution. An addition of 1 w/o Menhaden fish oil was used as dispersant. A binder mixture of PVA and Carbowax, 1 w/o each, were then added and the slurry ball milled an additional 1.5 hrs. Each slurry was spray dried and the powders uniaxially pressed at 20 ksi into discs, 1.6 cm diameter by 0.2 cm thick. All samples were fired on ZrO_2 setters in air at a sintering temperature of 1350°C/2 h. A heating rate of 10°C/min was used up to 550°C/30 min to facilitate binder and nitrate burnoff. After sintering the samples were cooled at 100°C/hr to 1220°C and annealed in air for 6 hours. A cooling rate of 100°C/hr. was then used to 800°C followed by furnace cooling to room temperature.

Structural characterization of the materials was accomplished using: High resolution TEM (Hitachi 9000 at 300 keV) (Phillips CM-12, 420 at 120keV) techniques for determination of grain boundary and domain lattice structures. Phase distribution, uniformity and elemental analysis was carried out using EDS (beam size 100-250 A). An SEM (Hitachi S-800 at 20 keV) was used for grain size analysis. Measurements for the dielectric and resistivity responses were carried out within the temperature range of 25 °-250°C at a heating rate of 5°C/min. Resistance measurements were made using a constant voltage source at 0.01 volts, in series with the sample and a picoscale ammeter. Computer simulation of the high resolution HOLZ patterns using an EMS program was carried out in order to determine lattice parameter of the grain boundary phases.

* Ticon-HPB,TAM Ceramics, Inc., Niagara Falls, NY

** Aldrich Chemical Company, Inc. Milwaukee, WI

Results and Discussion

Samples made by doping the $BaTiO_3$ lattice with Y_2O_3 (<0.25 m/o) and with Y_2O_3 plus ZrO_2 (2.0 m/o) produced microstructures with similar average grain size, 24 μm, as shown in Figure 1. Comparison of the permittivity and resistivity behaviors versus temperature for the modified samples are shown in Figure 2. As seen, the yttria plus

CH3080-0-7803-0465-9/92$3.00 ©IEEE

zirconia doped samples showed enhanced conductivity and PTC behavior. The dielectric permittivity of this sample, likewise, correlated to the resistivity behavior, showing a more pronounced and sharper phase transition.

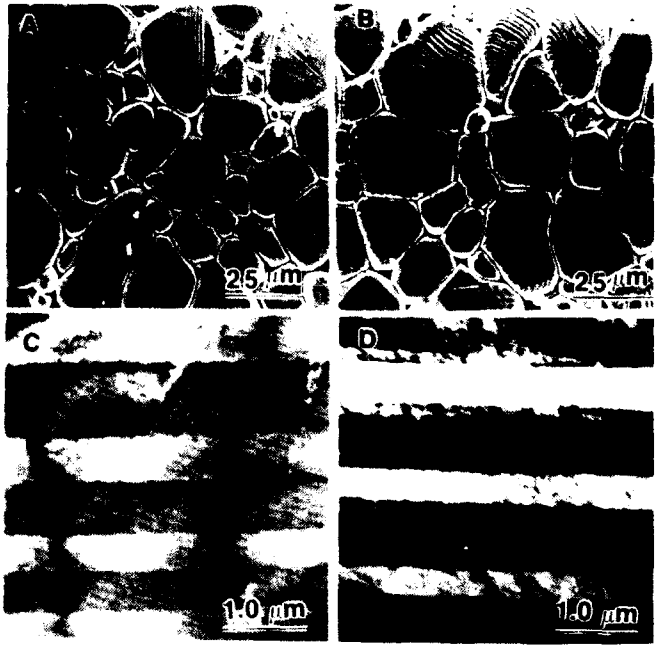


Fig. 1 SEM micrographs comparing grain size for PTC, $BaTiO_3$ doped with: A) Y_2O_3 B) Y_2O_3 + ZrO_2. TEM images of each sample showing domain structure of grain interior: C) Y_2O_3 D) Y_2O_3 + ZrO_2.

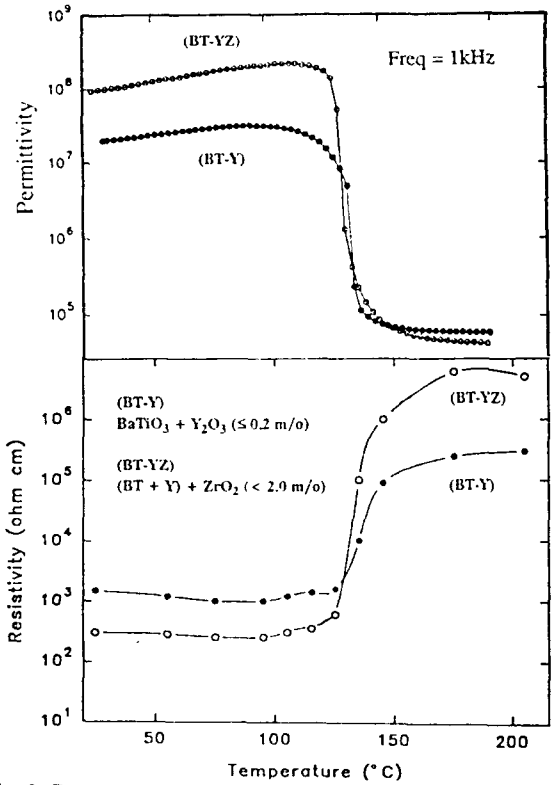


Fig. 2 Permittivity and resistivity responses to temperature, comparing effects of ZrO_2 on Y_2O_3 doped samples.

TEM images of the interior domain structure of these materials are also shown in Figure 1. As seen, both the yttria and yttria plus zirconia samples show similar wide banded domains within the grain interiors. Comparison of the grain boundary regions of the two PTC materials are given in the TEM images of Figure 3. Regions with no domain structure, which extended up to 1 μm into the grains, were found to be common near the grain boundaries within each sample, but were randomly distributed. These typical TEM images show that only relatively small regions of continuous domain structure form across the grain boundaries in the yttria doped samples. Comparison of domain width between the interior and grain boundary region of this sample (Figures 1D and 3A) shows a much smaller domain width in the grain boundary. In the yttria plus zirconia doped material larger areas of a fine domain structure formed across the grain boundaries as illustrated in the TEM of Figure 3B, in marked contrast to the wide domain patterns in the grain interior (Figure 1C).

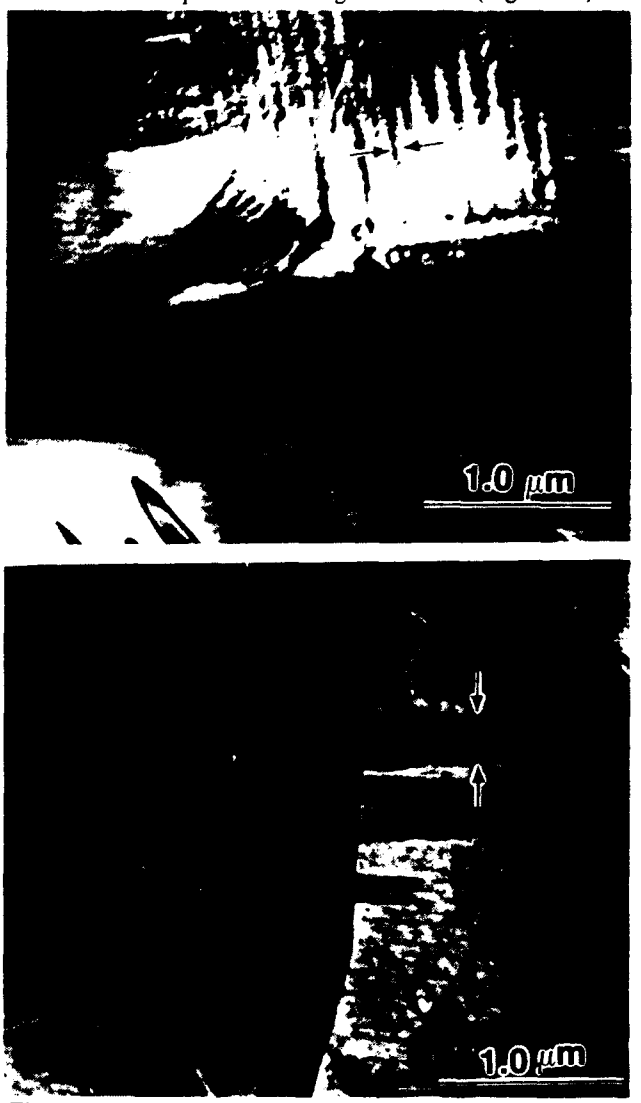


Fig. 3 TEM micrographs comparing domain structures near the grain boundary for $BaTiO_3$ samples doped with (A) Y_2O_3 (B) Y_2O_3 + ZrO_2.

Through the use of CBED and HOLZ pattern analysis, lattice parameter data as well as volume percent strain were calculated for the different regions. Results are given in Table 1. For the Y_2O_3 doped samples, a non-domain region is observed near the grain boundaries. This phase tended

towards cubic, with expanded lattice parameters. In contrast, both the interior and domain regions along the grain boundary featured tetragonal, reduced a-axis lattice structures. The volume expansion mismatch (4.0%) between the regions create, therefore, an overall stressed condition along the grain boundaries. The EDS data also shows a slight deficiency of yttrium in the non-domain areas.

With ZrO_2 additions, the grain boundary and interior domain regions both featured expanded lattice parameters with a similar degree of tetragonality. In contrast, the non-domain regions along the grain boundaries were highly pseudocubic, resulting in significant volume strains being developed (9.0%). The result is a finer domain structure near the grain boundaries in the ZrO_2 doped samples although, within the domain regions the degree of tetragonality was similar to that of pure $BaTiO_3$ (1.011). As shown by the EDS data, the fine domain regions also exhibit a higher concentration of Y and lower concentration of Zr than the interior domain regions. In contrast, non-domain areas near the grain boundary indicate little Y, but larger concentrations of Zr. These segregation effects, therefore, are consistent with ionic defect regions.

Table 1
Lattice Parameters and EDAX Analysis Using TEM, CBED and HOLZ

$BaTiO_3$ + (mol %)	c-axis (A ±.002)	a-axis	c/a	G.B. Strain (%)	EDAX (Y%)	(Zr%)
0.24 m/o Y_2O_3						
G.B. Domain	4.028	3.991	1.009	4	0.3	
Non-Domain	4.026	4.003	1.005		0.2	
Interior	4.035	3.993	1.011		0.3	
0.24 m/o Y_2O_3 + ZrO_2						
G.B. Domain	4.037	3.994	1.011	9	0.8	0.4
Non-Domain	4.019	4.008	1.002		----	1.0
Interior	4.034	3.997	1.009		0.3	1.3

As previously discussed, Y substitution onto the A-sites in $BaTiO_3$ at low concentration results in some Ti^{4+} reduction to Ti^{3+}. The presence of the larger Ti^{3+} ions should cause a lattice distortion to a more tetragonal structure, a condition confirmed by the TEM and HOLZ pattern data, where a high degree of tetragonality is observed even in the fine domain, stressed regions. Conversely, the lower tetragonality in the non-domain regions indicate an essential absence of Ti^{3+} ions, which, therefore, would be non-conducting. Preferential A-site Y^{3+} ion occupancy in these samples is also inferred from the low resistivities obtained, as seen in Figure 2. Here, ZrO_2 additions ($\leq$2.0 m/o) to the Y_2O_3 doped $BaTiO_3$ samples cause also a significant decrease in resistivity. The lower resistivity can be attributed to greater (Ti^{3+})electronic compensation in the Zr-doped PTC samples. In terms of the TEM data, this condition corresponds to a higher concentration of domains crossing the grain boundaries and smaller non-domain regions along these boundaries.

The fact that the effects with added Zr are observed at even low concentrations of Y_2O_3, indicate that the Y^{3+} partitions to the Ti^{4+} site at all Y_2O_3 concentrations within the PTC range. These results can be modeled by the following shortened defect equations.

$$(x)\,Y^{3+} \xrightarrow{BaTiO_3} (x-y)\,Y_{Ba}^{\cdot} + (x)\,Ti_{Ti}^{'} + (y)\,Y_{Ti}^{'} + (y/2)\,V_{O}^{\cdot\cdot} \qquad (1)$$

Equation (1) holds for low dopant concentrations, and under conditions where: ($x >> y$) for Ti rich samples. Here the substitution of Y^{3+} on Ba^{2+} sites result in small polaron electronic compensation (Ti_{Ti}), which yields n-type conduction. Concurrent ionic defects formed are shown as some Y^{3+} partitions to Ti^{4+} sites with oxygen vacancy compensation. The above TEM data indicate these ionic defects segregate to non-domain regions along the grain boundaries. With Zr added, the defect equation becomes:

$$(x)\,Y^{3+} + (z)\,Zr^{4+} \xrightarrow{BaTiO_3} [x-y+z]\,(Y_{Ba}^{\cdot}) + z(Zr_{Ti}) + [y-z]\,(Y_{Ti}^{'}) + [x-y+z]\,(Ti_{Ti}^{'}) + [y-z]/2\,(V_{O}^{\cdot\cdot}) \qquad (2)$$

Equation (2) shows that the role of Zr^{4+} is to displace Y^{3+} from the B (Ti^{4+}) sites onto the A sites, a condition which would increase conductivity. Excess Zr also occupies Ti^{4+} sites, the effect being an expanded lattice parameter in the Zr modified material. The Ti^{4+} ions displaced to the grain boundary enhance sintering through formation of a liquid phase.

Detailed high Resolution TEM imaging of the grain boundary regions were carried out. One prominent type features no domains on either side of the grain boundary and was much more prevalent in the Y^{3+} doped samples. Figure 4 shows a detail of this type region, indicated as a narrow, incoherent region along the grain boundary and occurring only over a few lattice cells, as seen by the distortion from the regular lattice pattern. In this region, no dislocations are found to relieve the strain. Instead, there is observed a regular array of lattice distortion, seen as white spots, along the grain boundary. Through computer simulation techniques, these lattice distortions were calculated to be O vacancies. As indicated, these areas of no domain region have also a pseudocubic structure with a low concentration of Y^{3+} (and Ti^{3+}) ions, and are, therefore, non-conducting. These incoherent grain boundaries, which are permanent, therefore, would present an effective barrier to electron transport.

The second type structure is found where a non-domain region is adjacent to a domain region across the grain boundary. For this condition, a similar incoherent grain boundary is formed, but with fewer or no oxygen vacancies along the boundary. As indicated, the domain regions exhibit greater tetragonality with high Ti^{3+} concentration, relating to regions of high conductivity. As conduction electrons encounter the barrier region, therefore, low conductivity between grains might expected in thin regions where polarization effects might dominate.

Figure 5 shows the third type grain boundary structure where a domain region is continuous across two grains. In these regions, a coherent grain boundary is formed, indicated by the modulated, lattice structure, in which there is little difference between the domain lattice on either side of the

grain boundary. In these regions, low resistance paths develop, easily overcoming any grain-grain boundary potential.

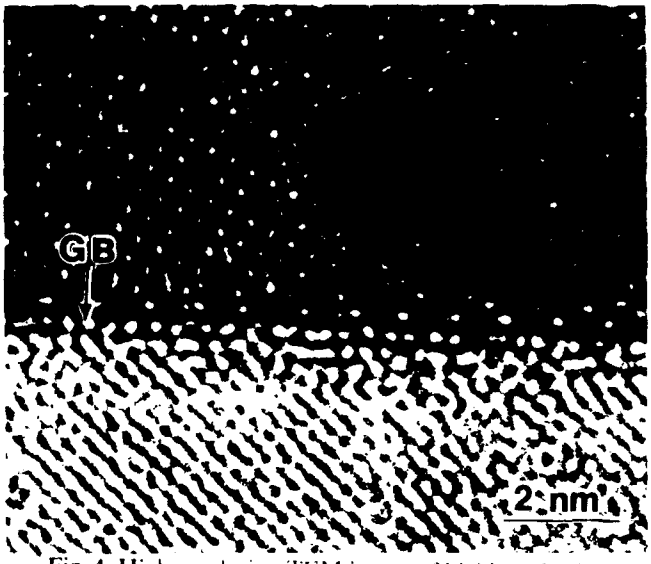


Fig. 4 High resolution TEM image of highly defective, incoherent grain boundary region between areas of non-domain structure across grain boundary.

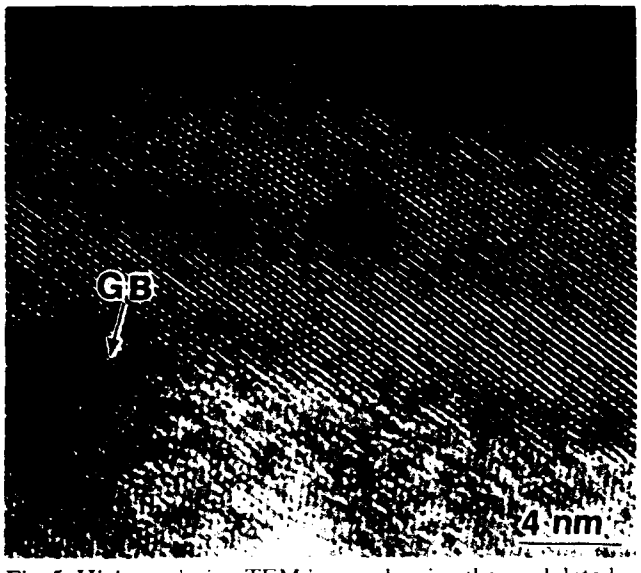


Fig. 5 High resolution TEM image showing the modulated, coherent grain boundary region between domains across the grain boundary.

The three regions described develop from segregation of the dopants and oxygen defects non-uniformly along the grain boundaries. The PTC effect in $BaTiO_3$ is, therefore, highly dependent upon these grain boundary structures which also affect the ferroelectric phase transition. In the cubic phase, $BaTiO_3$ is not polar and small polaron conduction likewise decreases. Samples with a high lattice strain, i.e. large tetragonality differences between non-domain and domain regions, have been shown to exhibit a sharp and large PTC transition. This can be attributed to a fast phase transformation throughout the sample, with release of stress as the driving force. A sharp change in the permittivity and spontaneous polarization are also associated with the fast ferroelectric transition near T_c. Conversely, lower strained samples show diffuse transformations and poor PTC response. These factors all relate to the grain boundary structure and resultant strains which develop and must, therefore, be considered an essential part of the PTC response mechanism.

Conclusions

- Stresses in Y-doped $BaTiO_3$ PTC ceramics arise from the coexistence of non-domain and domain phase regions, of differing volumetric expansions, along the grain boundaries.
- With Y-doped samples the strain differential was ~4% compared to 9% for the Y+Zr-doped samples. This resulted in higher tetragonality and finer domains in the grain boundaries, and also a sharper ferroelectric phase transition, driven by release of the stress.
- The non-domain regions have been correlated to ionic defects (Y'_{Ti} and $V_{\ddot{O}}$) which segregate to regions in the grain boundary during annealing.
- The PTC effect in $BaTiO_3$ has been shown to be highly dependent upon the existence of these structural regions along the grain boundaries and the stress condition which they generate.

Acknowledgements

This work was supported by ONR DARPA contract N00014-88-K-0317 and in part by NSF under contract number NSF-DMR89-20538. Microanalysis was carried out in the Center for Microanalysis of Materials at the University of Illinois, which is supported by the U.S. Department of Energy under contract number DE-AC-02-76ER-01198.

References

1. B. Kulwicki "PTC Materials Technology, 1955-1980," Grain Boundary Phenomena in Electronic Ceramics, Edited by L. Levinson, Advances in Ceramics, Vol. 1, pp. 138-154 (1981).
2. I. Bunget and M. Popescu, "Physics of Solid Dielectrics," in Materials Science Monographs, 19, ed., C. Laird, (1978), Elsevier, Amsterdam, Translation, V. Vasilescu (1984).
3. R. W. Newnham, "Structure-Property Relations in Electronic Ceramics," Journal of Materials Education, Vol. 6, No. 5, pp. 806-839 (1984).
4. G. H. Jonker, "Some Aspects of Semiconducting Barium Titanate," Solid State Electronics, Vol. 7, pp. 895-903 (1964).
5. W. Heywang, "Resistivity Anomaly in Doped Barium Titanate," Solid-State Electron, 3, 51 (1961).
6. G. H. Jonker, "Equilibrium Barriers in PTC Thermistors," Grain Boundary Phenomena in Electronic Ceramics, Edited by L. Levinson, Advances in Ceramics, Vol. 1, pp. 155-166 (1981).
7. J. Daniels and R. Wernicke, "Part V. New Aspects of an Improved PTC Model," Philips Research Report, 31, 544-559 (1976).
8. R. Wernicke, "Part IV. The Kinetics of Equilibrium Restoration in Barium Titanate Ceramics," Philips Research Report, 31, 526-543 (1976).
9. Y. Chiang and T. Takagi, "Grain-Boundary Chemistry of Barium Titanate and Strontium Titanate: 1, High Temperature Equilibrium Space Charge," J. Am. Ceram. Soc., 73 [11] 3278-85 (1990).
10. B. M. Kulwicki, A. J. Purdes, "Diffusion Potentials in $BaTiO_3$ and the Theory of PTC Materials," Ferroelectrics, 1, 253-63 (1970); 2, 176 (1971).
11. H. B. Haanstra and H. Ihrig, "Transmission Electron Microscopy at Grain Boundaries of PTC-Type $BaTiO_3$ Ceramics," J. Am. Ceram. Soc., Vol.63, No. 5-6, 288-291, (1980).
12. T. Malis and H. Gleiter, "Investigation of the Structure of Ferroelectric Domain Boundaries by Transmission Electron Microscopy," J. Appl. Phys., Vol.47, No.12, 5195-5200, Dec. (1976).

NONDESTRUCTIVE EVALUATION OF MULTILAYER CAPACITORS USING ELECTROMECHANICAL RESONANCE PHENOMENA

SUN Hong-Tao, WANG Hong-Fang, ZHANG Liang-Ying and YAO Xi
Electronic Materials Research Laboratory
Xi'an Jiaotong University
Xi'an 710049, P.R.China

Under the mechanically free and clamped boundary conditions, electromechanical resonances of ceramic multilayer capacitors are calculated using vibration and piezoelectric equations. $BaTiO_3$- and $Pb(Mg_{1/3}Nb_{2/3})O_3$-based multilayer capacitors have been used to examine the theoretical calculation. Frequency spectra of impedance and phase angle, capacitance and loss tangent of the capacitors under dc bias fields are carefully measured. A sudden change around the resonant frequency is observed in these spectra. A damped resonance indicates a defective capacitor while an undamped resonance is corresponding to defect free. Experimental results suggest that it is possible to use the spectra as a real time nondestructive evaluation method.

Introduction

Reliability of electronic components becomes more and more important for complicated electronic equipments and systems [1]. Ceramic multilayer capacitor (MLC) has been extensively used in the field of electronics for its advantages of large capacitance and small volume. MLC is a composite structure made from alternating layers of metal (electrode) and ceramic (dielectric material). It is crucial to MLC production that metal and ceramic materials should be well matched in sintering over 1000 ℃ [2]. In order to guarantee the product quality, the capacitance of every MLC is tested before selling. However, the passed MLC probably still has some defects which affect the reliability of the capacitor while hardly change the capacitance. A delamination between electrode and dielectric material is one of the most frequent and harmful defects in MLC. Currently, the delamination is detected using destructive physical analysis (DPA) [3]. DPA only represents the quality of a batch of MLC, and is strongly dependent on sampling, sectioning and inspecting.

Nondestructive evaluation (NDE) of macro-defects of MLC is of great importance for quality control in mass production. In recent years, most researchers are paying main attention to NDE, especially to rapid testing of individual capacitor. Various methods have proposed for screening defective MLC, for example, electrically excited acoustic emission [4], scanning laser acoustic microscopy [5], corona current [6] and electromechanical resonance spectra [7]. Among these methods, the resonance spectra are very attractive because of their potentiality of application. It has not yet been achieved to identify the exact relationships between defects and resonance spectra. Obviously, it is necessary to extend both theoretical and experimental research.

Calculation

MLC from ferroelectric materials, under a bias field, exhibits electromechanical resonances similar to the ones observed in piezoelectric transducers. Based on mechanical vibration equation and piezoelectric equations, the electromechanical resonances around resonant frequency could be calculated. Because no permanent polarization is built up within the dielectric, only induced polarization is parallel to the bias field and the signal field, MLC structure is favorable to expansion vibration while exerts high damping to shear vibration. Therefore, expansion waves are only considered in the following. The pronounced resonance depends on the dimension of MLC construction. The thickness resonance is damped by the electrode-dielectric interfaces. The length resonance is also damped by the terminations at either end of the capacitor. Only the width resonance is relatively undamped. Fig.1 is a schematic drawing of MLC in a given vertical coordinate. To simplify the calculation, it is assumed that MLC without delamination has a free boundary while MLC with delamination has a clamped boundary. All tensors are labeled according to Voigt convention [8].

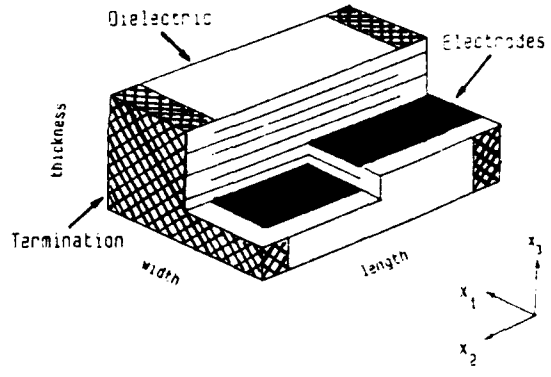


Fig.1 Schematic drawing of a multilayer ceramic capacitor.

The mechanical vibration equation of a contineous elastic medium is

$$\rho \frac{d^2 \xi_1}{dx_1^2} = \frac{\partial T_1}{\partial x_1} \tag{1}$$

where ρ is density of the material, ξ is displacement, T is stress applied on the material. No heat exchange occured in the material around the resonance frequency. The piezoelectric equations under an adiabatic condition are used.

$$S_1 = s_{11} T_1 + d_{31} E_3 \tag{2}$$

$$D_3 = d_{31} T_1 + \varepsilon_{33} E_3 \tag{3}$$

where d and ε are piezoelectric modulus and dielectric constant, s and S are elastic compliance coefficient and strain, D and E are electric displacement and electric field, respectively.

The strain is the partial derivation of ξ with respect to x, i.e.

CH3080-0-7803-0465-9/92$3.00 ©IEEE

$$S_1 = \frac{\partial \xi_1}{\partial x_1} \tag{4}$$

In this case, the vibration equation associated with electromechanical resonances becomes

$$\rho \frac{d^2 \xi_1}{dx_1^2} = \frac{1}{s_{11}} \frac{\partial^2 \xi_1}{\partial x_1^2} \tag{5}$$

This equation determines the mechanical and electric parameters in the resonant region.

In the resonant region, a simple harmonic vibration satisfies the vibration equation (5).

$$\xi_1 = \xi e^{j\omega t} \tag{6}$$

where j is imaginary, ω $(=2\pi f)$ is angular frequency and t is time. The amplitude of the vibration ξ is

$$\xi = A \cos(\frac{\omega}{v} x_1) + B \sin(\frac{\omega}{v} x_1) \tag{7}$$

where A and B are constants to be determined from a boundary condition. The sound velocity is as follows.

$$v = \sqrt{\frac{1}{\rho s_{11}}} \tag{8}$$

Two extreme cases of free and clamped boundaries are used to determine A and B . The boundary condition is $T_1 = 0$ when $x_1 = 0$ or w (MLC width) for a free boundary, and $S_1 = 0$ when $x_1 = 0$ or w for a clamped boundary. After simple methematic derivations, dielectric constant ε $(= D_3 / E_3)$ can be obtained.

For the free boundary, dielectric constant is

$$\varepsilon = \varepsilon_{33} + \frac{d_{31}^2}{s_{11}} \frac{2v}{\omega w} tg\frac{\omega w}{2v} \tag{9}$$

For the clamped boundary, dielectric constant is

$$\varepsilon = \varepsilon_{33} \tag{10}$$

Table 1 lists some physical data of BT– and PMN–based ceramics. Using the data given in Table 1, the electromechanical resonances under the two extreme boundary conditions are calculated from equations (9) and (10), as plotted in Fig.2. It is confirmed that the clamped boundary results in disappearence of the electromechanical resonances.

Table 1 Some related physical data of BT– and PMN–based ceramics.

Materials	BT	PMN
$\rho(10^3\ kg/m^3)$	5.7	7.7
$\varepsilon_{33}/\varepsilon_0$	1700	8000
d_{31} $(10^{-12}\ C/N)$	−78	−200
s_{11} $(10^{-12}\ m^2/N)$	7.0	11.2
v (m / s)	5000	3400

Actually, the electromechanical resonance of piezoelectric MLC is between the two extreme cases in which no delamination condition is close to a free boundary while delamination condition can be represented as a clamped boundary. In addition, the piezoelectric modulus is unknown, which is dependent on the induced polarization of MLC under a dc bias. It is difficult to calculate the exact data of the MLC resonances. Based on $\omega w/(2v) = \pi/2$, however, it is easy to determine the resonant frequency f_r from the physical data of MLC listed in Table 1. For BT– and PMN–based MLC, the frequency constants $f_r w$ (MHz.mm) are equals to 2.5 and 1.7 respectively.

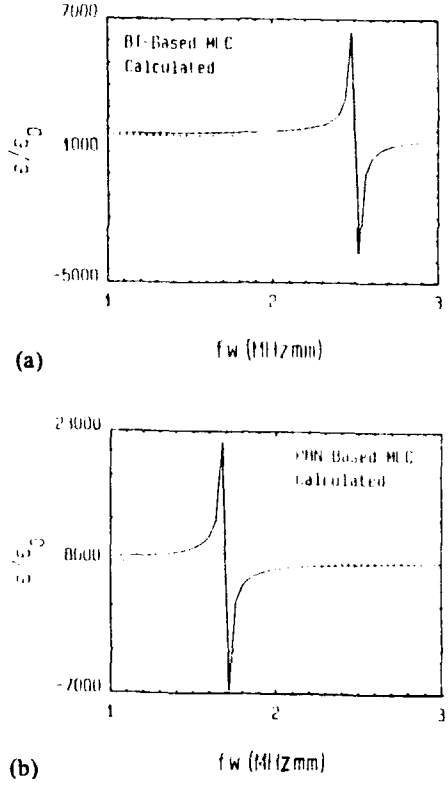


Fig.2 Calculated dielectric frequency spectra under the conditions of free and clamped boundaries for (a) BT– and (b) PMN–based MLC.

Measurements

Generally, the resonant frequency is in the range of several MHz for most of MLCs, since their width is always in the mm range. In order to exite the piezoelectricity of the dielectric, a dc bias should be applied on MLC during the measurement. A computerized low–frequency impedance analyzer is used to measure the resonance behaviors of MLC. The analyzer has a frequency range from 5 Hz to 13 MHz and a dc bias of up to 35 V.

Fig.3 shows the frequency spectra of capacitance of PMN–based MLC under 0V, 20V and 35V dc bias. From this figure, it can be concluded that the measured resonances are due to the induced piezoelectricity. No resonances of inductance and capacitance of the electric circuit and the capacitor are take place in our measurements.

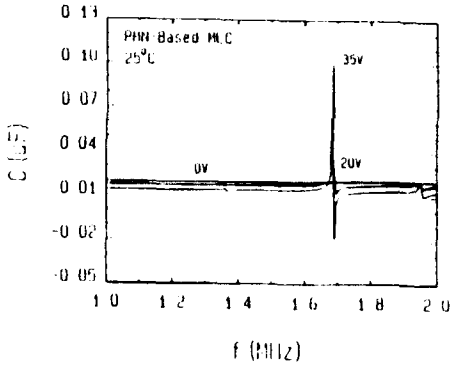


Fig.3 Frequency spectra of capacitance of PMN–based MLC under 0V, 20V and 35V dc bias.

The electromechanical resonance phenomena of MLC are observed in the frequency spectra of impedance Z and phase angle θ, capacitance C and loss tangent tgδ. Which is the best candidate for the nondestructive evaluation? The contrast and repeatability of the spectra are most important for the application of NDE. The contrast or the hight of resonance peak (hereinafter, the subscript r) indicates the sensitivity to a delamination of MLC. The repeatability or reproducibility means the stability of the resonances measured from time to time. In addition, a low dc bias is very convenient for a rapid real time testing. Two types of MLCs from BT– and PMN–based materials are chosen for this examination.

Because most MLCs are used around room temperature, it is preferable that the evaluation is carried out at room temperature. But it may be asked how wide is the temperature range for the evaluation. Fig.4 shows a temperature dependence of C_r (capacitance at resonant frequency) for PMN–based MLC. It can be seen that the suitable temperature is from 0 ℃ to 50 ℃ which is in agreement with the operation temperature. Similar phenomena are also observed in the other spectra of PMN–based MLC. The temperature effect of the resonances of BT–based MLC is the same as that of PMN–based MLC. All measurements in this paper are performed at room temperature except indicated.

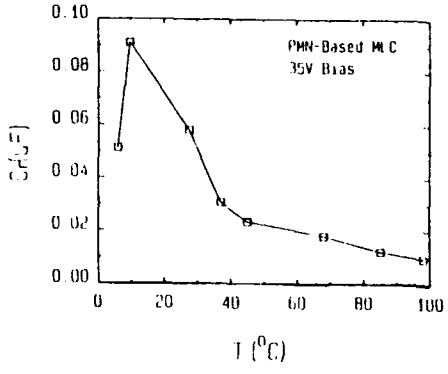


Fig.4 Temperature dependence of the electromechanical resonance of PMN–based MLC.

Because the piezoelectricity of MLC is not polarized permanently, the electromechanical resonances take place only in case of a applied bias V_b. It has no doubt that, the stronger a dc bias, the stronger the resonances are. It is very interesting that the bias effect on the contrast, under 35V dc bias, obeys the same experimental relation ($\sim V_b^2$) for Z_r, θ_r, C_r and tgδ_r, i.e. impedance, phase angle, capacitance and loss tangent at resonant frequency. This means that the piezoelectric modulus is proportional to the applied bias. Fig.5 illustrates the bias dependence of the C_r contrast of PMN–based MLC. From this figure, it is concluded that a large bias enhances the contrast.

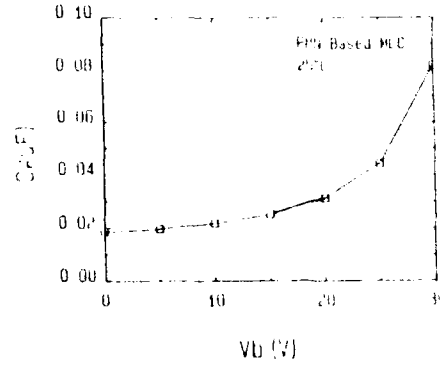


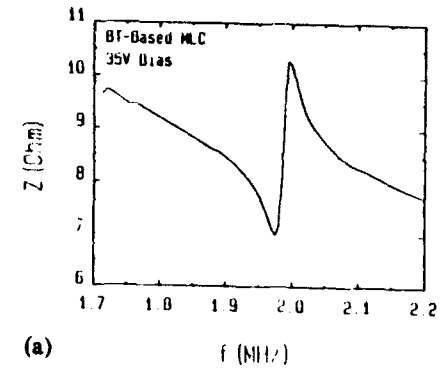
Fig.5 Bias effect of PMN–based MLC on the electromechanical resonance.

Results and Discussion

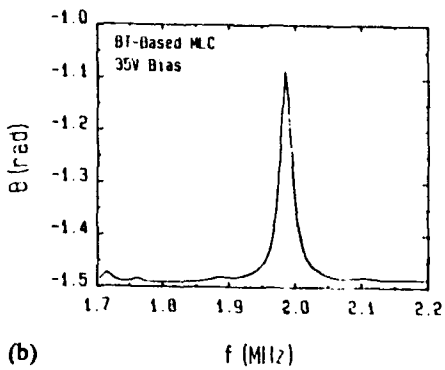
To demonstrate the difference among these four spectra, the electromechanical resonances of capacitors were measured at the same condition. Fig.6 and 7 show measured results of BT– and PMN–based MLC respectively. For PMN–based MLC, it can be found that the contrast is the best for θ and tgδ, good for C and bad for Z. The constrast of tgδ is the highest in the four spectra for BT–based MLC. If a higher bias is applied on BT–based capacitor, the constrast of C is better. Several batches of MLCs over hundreds of samples were carefully examined at different conditions and times. The results indicate that the Z spectra of PMN–based capacitor have the highest repeatability, C is the second, and θ and tgδ are the last. The four spectra of BT–based capacitor is all good. These conclusions are summaried in Table 2. In overall, the C spectra of PMN–based capacitor are the best way for the evaluation of PMN while the tgδ spectra are best for BT–based MLC test. In addition, all MLCs tested have the smallest fluctuation of capacitance and dielectric loss under no dc bias. This is beneficial to the rapid testing in mass production. It is not difficult to understand this phenomenon from the above calculation. The capcitance resonance is a direct effect while the others are indirective for relating to real part of impedance.

Table 2 The contrast and repeatability of the electromechanical resonances.

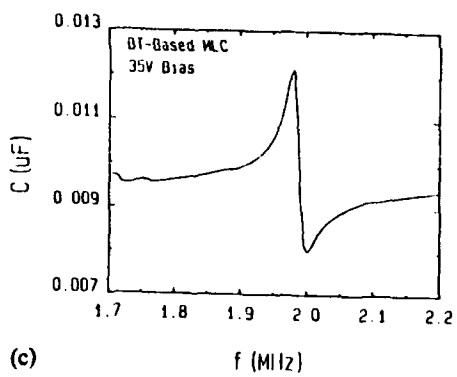
	Spectrum	Z	θ	C	tgδ
BT	Contrast	Poor	Good	Poor	Excellent
	Repeatability	Good	Good	Good	Good
PMN	Contrast	Poor	Excellent	Good	Excellent
	Repeatability	Excellent	Poor	Good	Poor



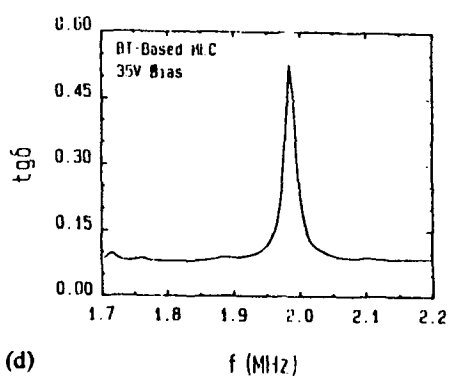
(a)



(b)

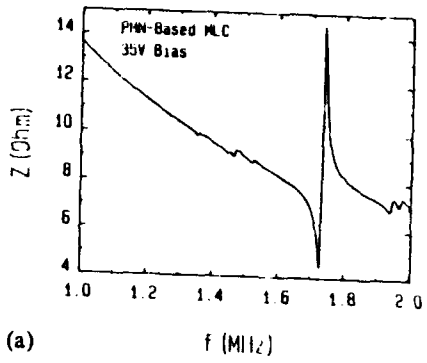


(c)

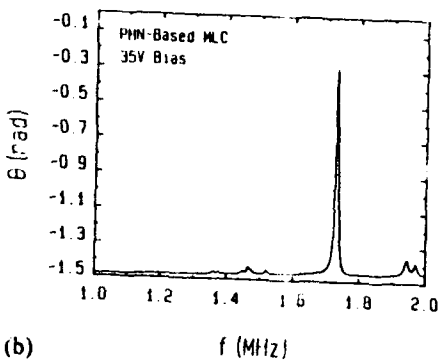


(d)

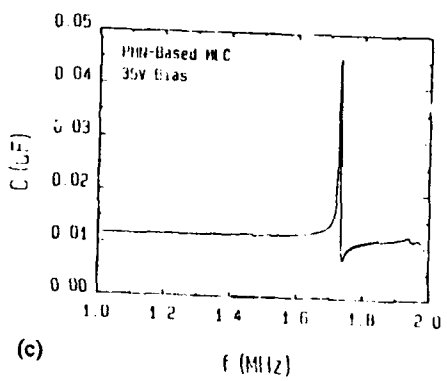
Fig.6 Frequency spectra of (a) Z, (b) θ, (c) C, and (d) tgδ for BT–based MLC.



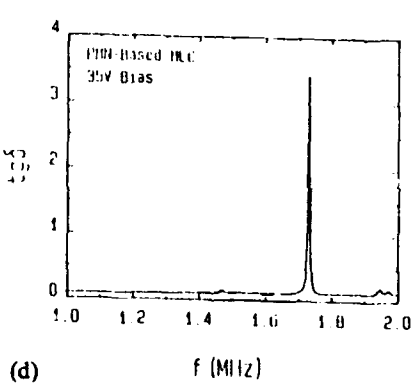
(a)



(b)



(c)



(d)

Fig.7 Frequency spectra of (a) Z, (b) θ, (c) C, and (d) tgδ for PMN–based MLC.

Using the computerized impedance analyser, many capacitors were tested. The statistical distributions of $tg\delta_r$ and C_r of a batch of BT- and PMN-based MLCs are given in Fig.8 and 9 respectively. A damping resonance suggests that the MLC has a delamination. On the contrary, an undamping resonance means that the MLC is without delamination. In these figures, delaminated MLC is located in the left while good MLC in the right. The quality of MLC located in the middle depends on the screening criterion.

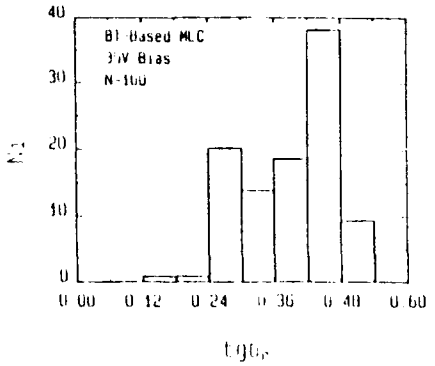


Fig.8 Statistical distribution of the resonant loss tangent $tg\delta_r$ for 100 BT-based MLCs.

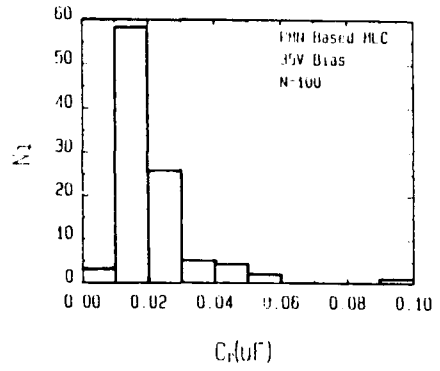


Fig.9 Statistical distribution of the resonant capacitance C_r for 100 PMN-based MLCs.

Two batches of PMN-based MLCs were detected by DPA [9]. One has about 10% defective capacitors and the other includs over 40% defective capacitors. The two batches are examined by the electromechanical resonance under 20V bias. The statistical results are quite different between the two batches of capacitors, as shown in Fig.10. If the critical capacitance is 0.015 μF, the two batches of capacitors have about 4% and 52% defective MLC respectively. The confirmation from accelerated life test is going on.

Conclusion

The calculation indicates that width expansion waves are pronounced in the electromechanical resonances. Delaminations can be approximated as a clamped boundary and can lead to a damped resonance. The expermental results suggest that the capacitance is one of the best candidates for a real time testing of the quality control of MLC both in contrast and repeatability.

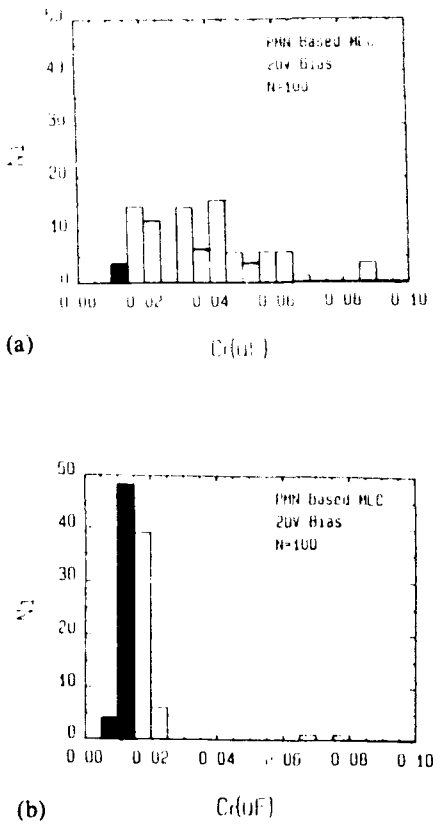


Fig.10 Statistical results of the resonant capacitance C_r for two batches of PMN-based MLCs including (a) 10% and (b) 40% defects by statistics of DPA.

Acknowledgements

This project is supported by the National Advanced Materials Committee of China. The authors would like to acknowledge Mr.Z.Y.Mao and Mr.Z.P.Wang both of Hongming Electronic Component Factory for providing the capacitors used in this study.

References

(1) G.O.Dayton, "First Symposium for Reliability in Multilayer Ceramic Capacitors," J. Am. Ceram. Soc., 72, pp.2221-2222, December 1989.

(2) M.Kahn, D.P.Burk, I.Burn and W.A.Schulze, "Ceramic Capacitors," in Electronic Ceramics: Properties, Devices and Applications, edited by L.M.Levinson, Marcel Dekker Inc., New York, 1988, pp.191-274.

(3) American National Standard (ANS)/ Electronic Industies Association (EIA), "Standard of Destructive Physical Anaysis for Multilayer Ceramic Capacitors," RS-469-1980, Washington DC, 1980.

(4) L.W.Kessler and J.E.Semmens, "Characterization of the Microstructure of Ceramics Used in Multilayer Ceramic Capacitors by Means of the Scanning Laser Acoustic Microscope," J. Am. Ceram. Soc., 72, pp.2271-2275, December 1989.

(5) N.H.Chan and B.S.Rawal, "An Electrically Excited Acoustic Emission Test Technique for Screening Multilayer Ceramic Capacitors," IEEE Trans. Compon. Hybrids. Manuf. Technol., 11, pp.358–362, April 1988.
(6) S.Sumita, M.Ikeda, Y.Nakano, K.Nishiyama and T.Nomura, "Degradation of Multilayer Ceramic Capacitors with Nickel Electrodes," J. Am. Ceram. Soc., 74, pp.2739–2746, November 1991.
(7) O.Boser, P.Kellawon and R.Geyer, "Electromechanical Resonances in Ceramic Capacitors and Their Use for Rapid Nondestructive Testing," J. Am. Ceram. Soc., 72, pp.2282–2286, December 1989.
(8) J.F.Nye, Pysical Properties of Crystals, Oxford University, London, 1956, Chapter 5, pp.110–130.
(9) Z.P.Wang, Private Communication, June 1992.

Destruction Mechanism of Multilayer Ceramic Actuators

Kenji Uchino
Materials Research Laboratory
The Pennsylvania State University
University Park, PA 16802 USA

and

Atsushi Furuta
Tokyo Research Laboratory
Tokin Corporation
Shiboguchi, Takatsu-ku
Kawasaki 213, Japan

Destruction mechanism in multilayer ceramic actuators has been investigated under cyclic electric fields. Crack propagation has been observed dynamically using CCD microscopy, and the accompanying characteristics of the induced displacement and acoustic emission were measured simultaneously. The piezoelectric $Pb(Ni_{1/3}Nb_{2/3})O_3$ - $PbTiO_3$ and the phase-transition-related actuator material (antiferroelectric) $PbZrO_3$ - $PbSnO_3$ - $PbTiO_3$ exhibit a remarkable difference in the destruction manner probably due to the strain induction mechanism. The effect of layer thickness on the destruction process has also been studied.

Introduction

In these several years piezoelectric/electrostrictive ceramic actuators have become very popular for micro-positioning in optical and precision machinery fields and active vibration suppression in mechanical structures.[1] The expanding number of applications of ceramic actuators has made the endurance of the devices very important.

This paper describes the destruction mechanism of multilayer-type ceramic actuators observed by optical microscopy, induced displacement and acoustic emission measurements, and proposes a safety system which can stop the actuator before its troublesome sudden complete collapse.

Experiments

Multilayer model actuators were prepared by tape casting method. The samples simulating the interdigital electrode configuration [Fig. 1(a)] used in this experiment have only one internal ceramic layer with a thickness of 100 μm, 200 μm or 300 μm, as shown in Fig. 1(b).

The piezoelectric $Pb(Ni_{1/3}Nb_{2/3})_{0.6}Ti_{0.4}O_3$ (PNNT) and the phase-transition-related actuator material $Pb_{0.99}Nb_{0.02}[(Zr_{0.7}Sn_{0.3})_{0.955}Ti_{0.045}]_{0.98}O_3$ (PNZST) were prepared, and the average grain size of the device was roughly the same (~5 μm), independent of the composition and the layer thickness. The PNZST is initially antiferroelectric, but changes into ferroelectric under an applied electric field.[2] Rather isotropic expansive strains are associated with this phase transition, and the magnitude of the strain ($\sim 1.5 \times 10^{-3}$) is twice larger than that of the piezoelectric PNNT. The longitudinally and transversely induced strains in the piezoelectric PNNT are 0.8×10^{-3} and -0.3×10^{-3}, respectively, with opposite sign.[3]

Note that the multilayer model actuator used in this experiment exhibits an exaggeratedly large internal stress concentrated around the electrode edge so as to accelerate the failure of multilayer actuators.

Figure 2 show the measuring system composed of a CCD microscope (Toshiba, IK-C40), a displacement sensor (Millitron, Nr. 1301) and an acoustic emission sensor (NF Circuit Design Block, AE-905). The sample was driven by a triangular electric field of E_{max} = 2-4 kV/mm at 0.1 Hz.

Results

Crack Propagation: Crack generation and propagation resulting from the internal stress was observed and recorded dynamically using a CCD microscope and a VCR. Figures 3(a) and 3(b) show typical crack propagation processes observed for the PNNT and PNZST samples (200 μm in layer thickness). The crack initiates at the internal electrode edge in the PNNT sample and propagates to another electrode obliquely, also outward of the electrode and along the ceramic-metal electrode interface. On the contrary, the crack starts between the pair electrodes slightly inside the electrode edge in the PNZST, then propagates along the center area, finally branching around the electrode edge. It is noteworthy that the crack opens wide under the electric field and closes at zero field.

This difference is probably due to the difference in internal stress distribution. The sign of the longitudinally - or transversely-induced strain is opposite in the piezoelectrics, while in antiferroelectrics undergoing a phase change, rather isotropic expansive strains are induced in both directions. Therefore, the internal stress distribution in antiferroelectrics differs from that of piezoelectrics.

Similar crack propagation processes were observed in the different layer-thickness samples, however, significant differences were recognized in the fracture toughness. Figures 4(a) and 4(b) plot the layer thickness dependence of the critical deformation cycles required for the initial crack generation and of the crack propagation speed per drive cycle (measured in PNZST). A dramatic improvement in the fracture toughness is obtained in the thinner layer sample, even though the driving electric field is the same of all samples. The reason is not clear, but it may be related to the ratio between the grain size and the layer thickness.

Displacement Changes during Failure: The destruction of the device brings a change in the induced displacement. Figures 5(a) and 5(b) show the variation of the induced displacement during the crack propagation process for the model actuators of PNNT and PNZST, respectively, with a layer thickness of 200 μm. The displacement is enhanced remarkably at the initial stage; this can probably be attributed to the bending deformation associated with the crack opening and closing process. Further increase in the number of deformation cycles leads to a decrease in the magnitude of the displacement. The effective electric field in the ceramics decreases because the narrow air gap is associated with complete crack formation.

Variation of Acoustic Emission: Acoustic emission (AE) events were counted during the destruction process of the PNZST sample with a layer thickness of 200 mm (Fig. 6). The AE count increases remarkably after the crack initiation, reaching a maximum at 60 cycles, where the crack propagation speed is maximum, and the largest displacement is observed. Later, the AE count leveled off after the crack was completed.

CH3080-0-7803-0465-9/92$3.00 ©IEEE

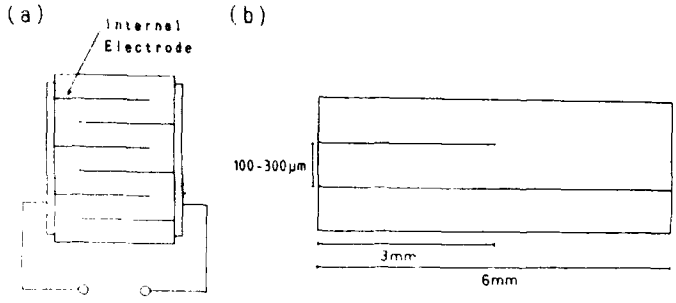


Fig. 1 Structure of (a) conventional multilayer actuator with an interdigital electrode, and (b) electrode configuration of a model actuator used in this study.

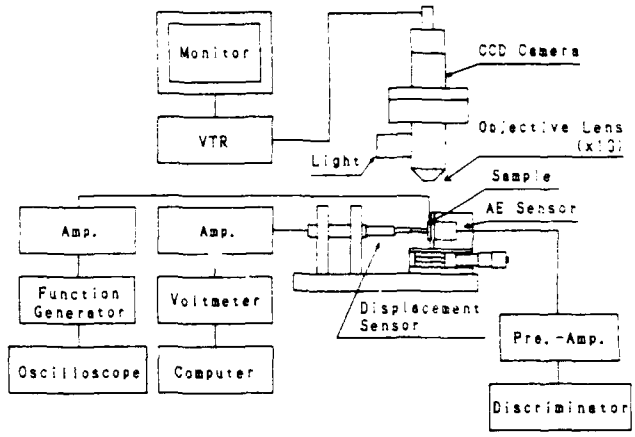


Fig. 2 Measuring system for the crack propagation experiments.

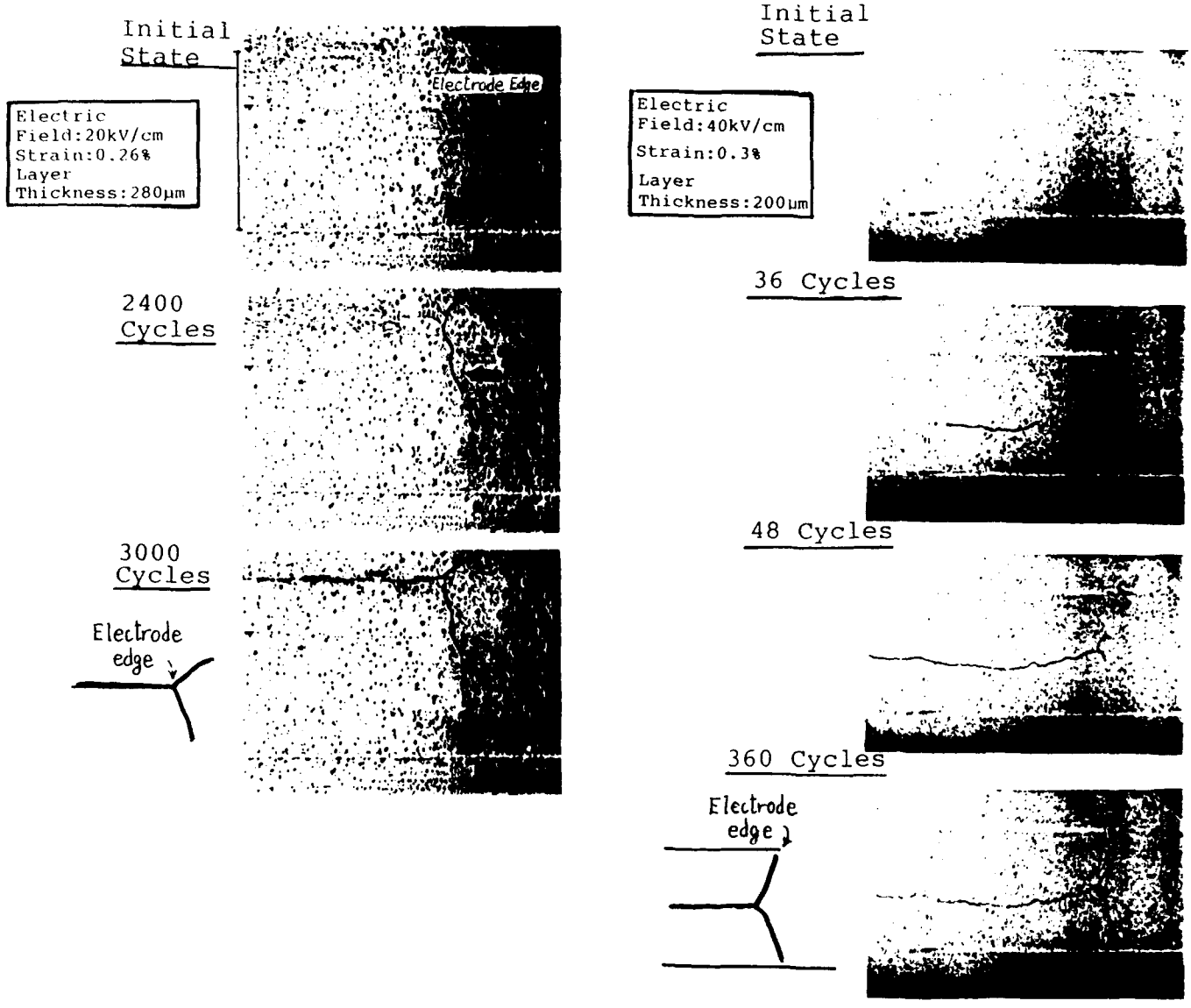


Fig. 3 Crack generation and propagation process in the multilayer model actuator. (a) Piezoelectric PNNT, and (b) antiferroelectric PNZST.

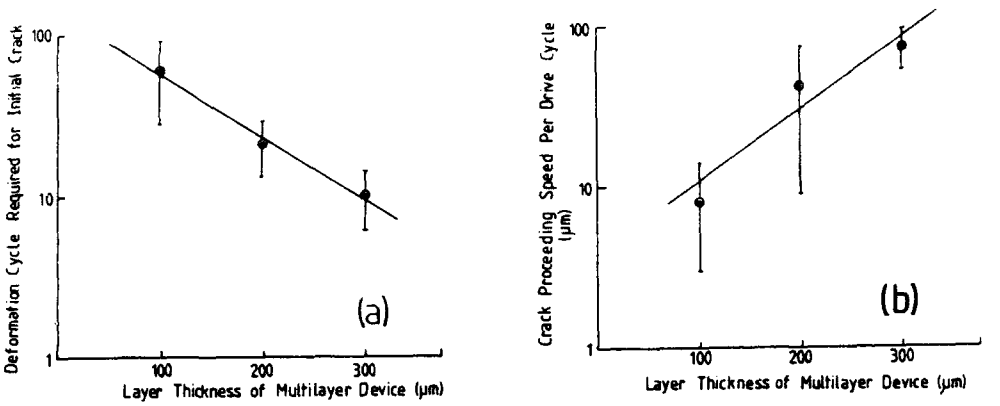


Fig. 4 Layer thickness dependence of the critical deformation cycle required for the initial crack generation (a), and of the crack propagation speed per drive cycle (b).

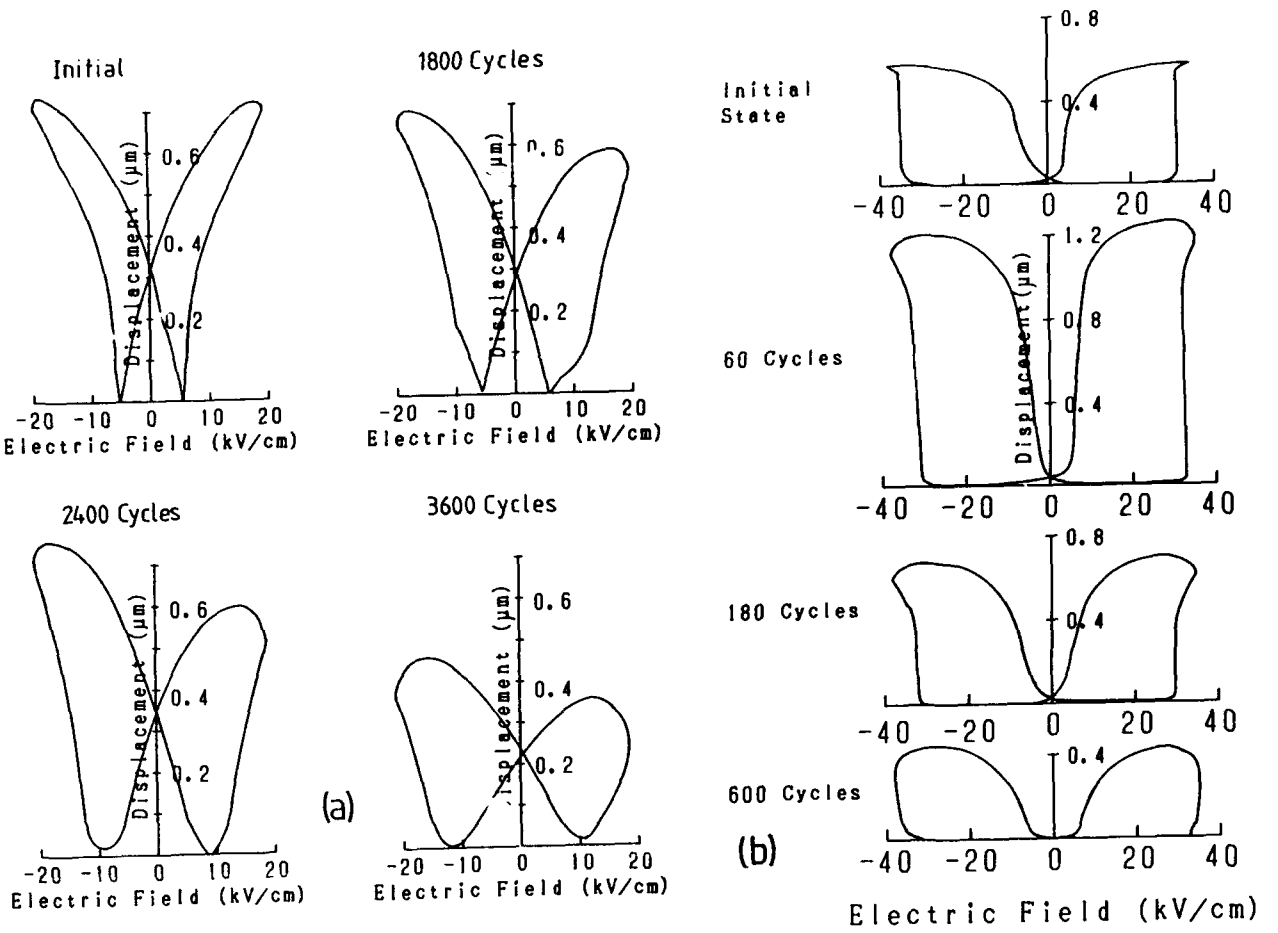


Fig. 5 Variation of the displacement during the destruction. (a) PNNT and (b) PNZST.

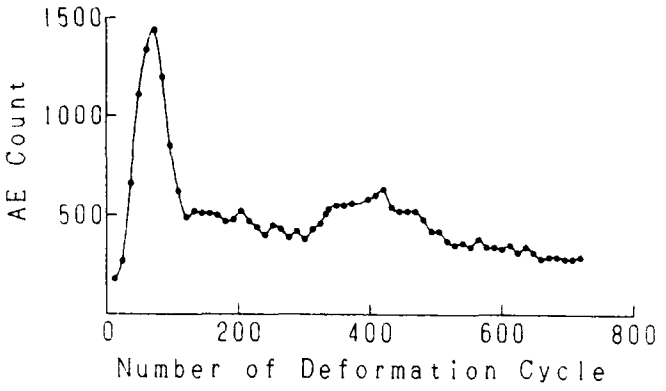


Fig. 6 Changes in acoustic emission count during the fracture process measured in a model actuator of PNZST.

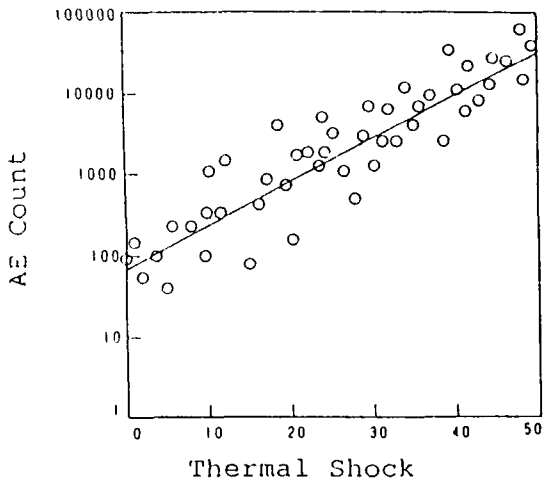


Fig. 7 AE count change monitored in a 200-layers sample of PNNT with aging time. The accelerated aging was performed by a thermal shock treatment.

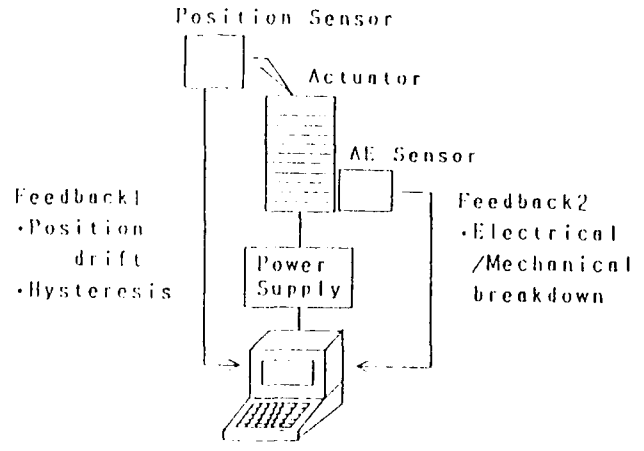


Fig. 8 Very smart actuator system with a reliability test function as well as position sensor.

The AE count change was also monitored for a 200-layers sample of PNNT ($10 \times 10 \times 20$ mm^3) with aging time.[4] An accelerated aging test was performed by a rapid-heat treatment up to 100°C in a second. Figure 7 shows that the AE count increases by three orders of magnitude at the final failure of the device in comparison with the virgin state. The monotonous increase of AE may be attributed to successive accumulation of cracks generated in the actuator device.

Summary and Discussions

The crack generation and propagation in multilayer ceramic actuators was observed dynamically during cyclical electric fields. In piezoelectrics, the crack initiated near the edge of the internal electrode and propagated basically in three directions: two cracks moved toward the outside electrostrictively inactive region forming an angle of 100° with each other, while the third moved along the ceramic-electrode interface. This behavior can be explained theoretically based on finite element calculations.[5]

On the contrary, in antiferroelectrics, the crack begins slightly inside the edge of the internal electrode and propagates along the center area between the pair electrodes. Later crack branches are generated around the electrode edge. Theoretical calculations are now in progress.

In both cases the apparent displacement becomes slightly larger than that of the virgin state, and the AE count increases drastically associated with the crack propagation.

Finally we propose a very smart actuator system containing a safety feedback function (Fig. 8), which can stop an actuator drive safely without causing any serious damages on to the work, e.g. in a precision lathe machine. The AE might be one of good predictors for actuator failure. A certain level of the AE count will indicate a timing to replace the ceramic actuator.

References

[1] K. Uchino, Piezoelectric/Electrostrictive Actuators. Tokyo: Morikita Publ. Co., 1986.

[2] K. Uchino, "Shape Memory Ceramics," in Proceedings MRS Int'l Mtg. on Advanced Materials, vol. 9, pp. 489, 1989.

[3] Tokin Technical Catalogue, Multilayer Piezoelectric Actuator Series. Tokin Corp., 1986.

[4] T. Hirose and K. Uchino, "Acoustic Emission in Ceramic Actuators," Ferroelectrics, vol. 87, pp. 295, 1988.

[5] S. Takahashi, A. Ochi, M. Yonezawa, T. Yano, T. Hamatsuki and I. Fukui, "Internal Electrode Piezoelectric Ceramic Actuator," Jpn. J. Appl. Phys., vol. 22, Suppl. 22-2, pp. 157, 1983.

Miscellaneous Materials and Applications

FERROELECTRIC PHASE SHIFTERS FOR PHASED ARRAY RADAR APPLICATIONS

Donald C. Collier

Norden Systems, Inc.
P.O. Box 5300
Norwalk, CT 06856

ABSTRACT

The traditional rotating reflector antenna associated with airport traffic control systems is being replaced in some applications by a new design concept called the phased array. Generally planar in shape, it is made up of thousands of closely spaced, individual radiators whose composite beam can be shaped and spacially directed in microseconds, enabling it to track a multitude of targets at one time. This is accomplished electronically by RF phase shifters associated with each individual radiating element. No moving parts are required.

State of the art, passive phased array antennas are limited in their application by cost, more than any other factor. Even utilizing the latest technology and fabricating techniques, the required phase shifters are not cheap, and with a typical array requiring thousands of individual antenna elements, each with its own phase shifter, the price of the total system quickly becomes prohibitive.

INTRODUCTION

This paper proposes the use of ferroelectric materials in the design of phase shifters for RF applications as a means of overcoming the limitations of current technology. A simple and novel design will be outlined, and test results presented. (Refer to Figure 1.)

Numerous attempts have been made to lower the cost of phased array elements. Investigations into the use of PIN diodes were carried out in the 1960's and '70's, since they lent themselves to a cheap phase shifter design, but no way was found to avoid the high insertion losses that their utilization entailed especially at Ku band and above. Ferrite phase shifters have gained popularity in recent years, as initial problems of weight, size and operational speed have been overcome. but their unit cost and complexity have prevented them from becoming the building block that array designers are searching for. As a result, phased array antennas are still for the most part an expensive luxury in the defense industry arsenal, limited to specialized applications in which antenna cost and complexity are outweighed by unusual mission requirements.

THE FERROELECTRIC PHASE SHIFTER

The ferroelectric phase shifter design is based on a material whose dielectric permittivity can be made to vary by application of a DC electric field, parallel to the polarization of the RF energy, and normal to its direction of propagation. Variations in permittivity alter the RF propagation velocity, and if placed inside a waveguide structure, will change the cutoff wavelength and dispersion of the waveguide itself; the two effects translate into propagation phase variation. A short waveguide section containing ferroelectric material would constitute the key element for accomplishing electronic scanning of an economical array antenna configuration. Such a section is the waveguide flange illustrated in Figure 2, a phase shifter developed at Norden Systems with the assistance of United Technologies Research Center (UTRC) in Hartford, CT.

It consists of a material sample placed in a Ku-band flange whose b-dimension is decreased from 0.311 inches to 0.100 inches by means of a gradual taper section on either side of the phase shifter flange. See the photo of Figure 3. The height taper allows lower voltages to be applied across the sample to achieve a given electric field.

The voltage requirement is lowered further by splitting the sample in half along the a-dimension of the flange and depositing a thin conductive layer between the two halves. A voltage is then applied to the center conductor, creating a vertical E-field to the grounded flange. Matching layers are placed on either side of the sample to couple the RF energy in and out of the material. These rectangular layers of dielectric are needed in the design of the phase shifter because of the impedance mismatch between air and the high permittivity ferroelectric. If not dealt with, most impinging radiation would simply be reflected off the front face of the material. The energy can be coupled efficiently, however, by the appropriate use of matching layers.

One barrier to the application of ferroelectrics to device designs has been the unavailability of a low-loss voltage-tunable material. Recently, a material developed by Penn State Materials Research Labs was reported to exhibit a permittivity of 3000-4000 with a loss tangent less than 0.01 in the centimeter wavelength region. The material is a member of the Perovskite family, a

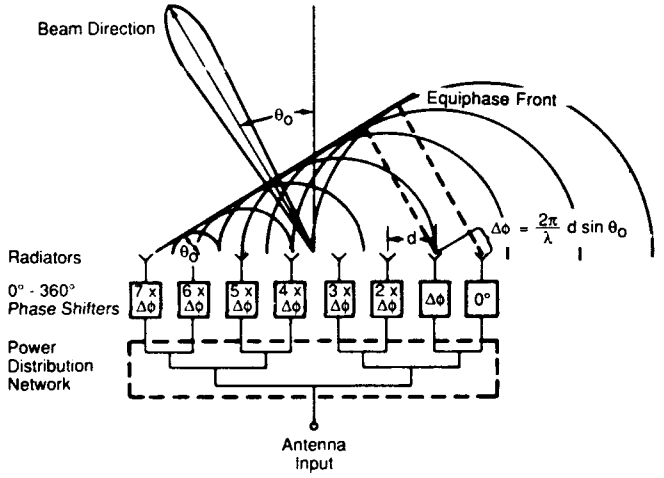


Figure 1. Beam-Steering Concept Using Phase Shifters at each Radiating Element

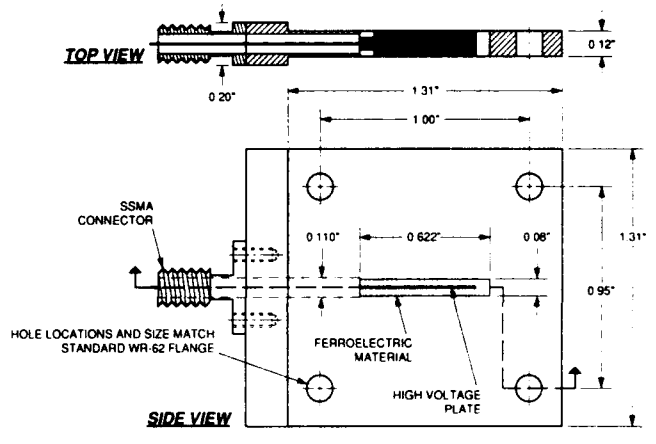


Figure 2. Waveguide Flange with Coaxial High Voltage Attachment

CH3080-0-7803-0465-9/92$3.00 ©IEEE

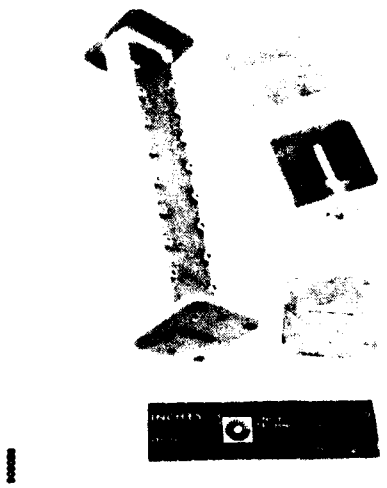


Figure 3. Photo of Phase Shifter

ceramic consisting of a combination of barium and strontium titanate (BST). The BST family of ferroelectrics has long been advocated for use in RF applications.

With the assistance of technicians at UTRC, the Penn State ferroelectric material was inserted in the waveguide flange and coupled to the waveguide taper sections via the dielectric matching layers. The test fixture consisting of the flange and waveguide tapers was connected to a Hewlett Packard 8510 Network Analyzer and to a source of DC voltage. As the voltage was incrementally increased, the change in phase of the RF signal was recorded. A chart showing the superimposed phase curves vs. frequency, as viewed on the network analyzer screen, is illustrated in Figure 4. Each curve represents the phase of the RF signal at a given DC voltage excitation.

The test results are plotted as a single curve in Figure 5.

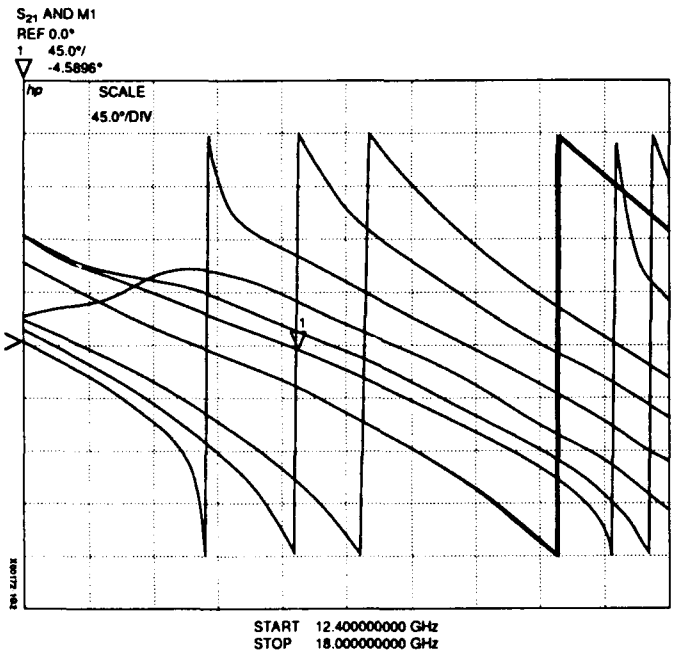


Figure 4. Network Analyzer Graph of Superimposed Phase Curves vs. Frequency

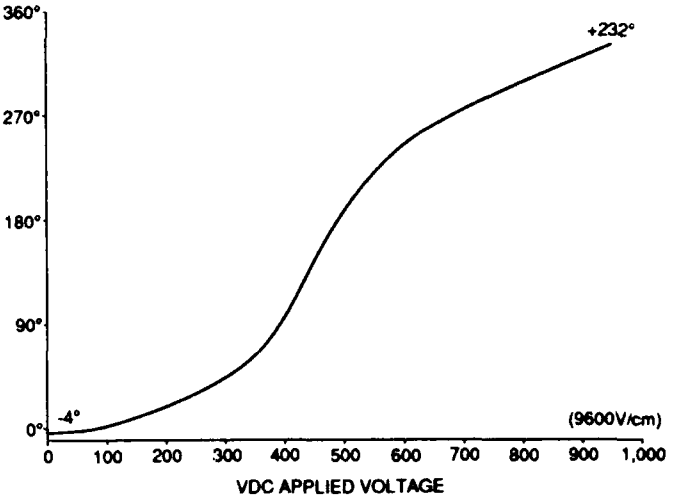


Figure 5. RF Phase Shift vs. DC Applied Voltage

The insertion loss was measured in the same test setup. Its value, -13.4 dB at 16 GHz, was for too great to consider the waveguide flange a serious competitor in the phase shifter marketplace. The reasons for this large insertion loss were then examined.

Norden Systems uses the EEsof RF simulation software called Touchstone. With this design aid, the waveguide flange with ferroelectric material, adhesive and matching layers was simulated. When the graphs of the insertion loss and RF phase in simulation matched the plots obtained from the HP 8510 (see Figure 6), it was discovered that the ferroelectric material, instead of measuring a loss tangent on the order of 0.01 had in reality a loss tangent of 0.147.

Clearly, this particular sample of BST was not suitable for commercial applications. It was next postulated what the behavior of the phase shifter would have been had the loss tangent been as advertised, or approximately an order of magnitude less. Figure 7 shows the effect on the insertion loss. Such a sample of ferroelectric would have held promise.

A future low-cost, two-dimensional, beam-agile planar array utilizing ferroelectric phase shifting technology would be attainable, depending on several factors:

a. The material loss tangent goal of <.01 must be reached. Loss tangent translates into insertion loss, and one-way losses on the order of 1-2 dB would be competitive in today's market..

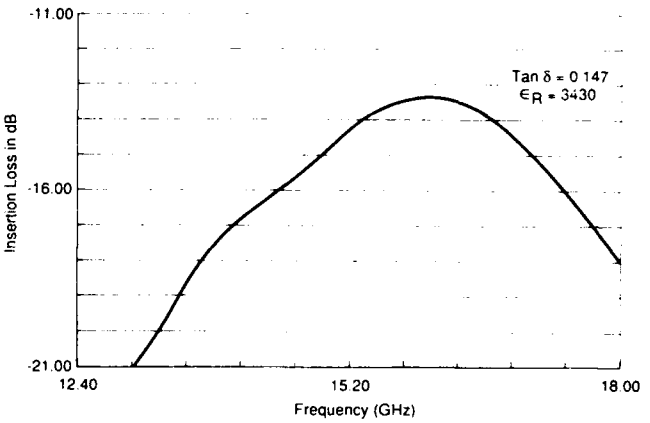


Figure 6. EESOF - Touchstone Software Simulation

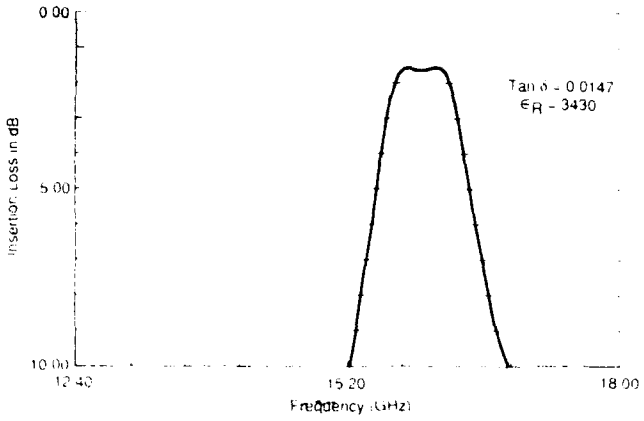


Figure 7. EESOF - Touchstone Software Simulation

b. The DC driver requirements imposed on the ferroelectric phase shifter by a specific antenna design must be realizable; that is, the driver circuit must be simple, cheap, and the driving potential must not be excessive. The presence of high voltages in an antenna array would constitute a serious design problem.

c. The permittivity must change at least 50% with application of the DC bias field.

d. The material must be structurally rugged enough to withstand the temperature and vibration environments encountered in many radar applications.

REFERENCES

1. Cecil E. Land and Richard Holland, "Electro-optic Effects in Ferroelectric Ceramics," *IEEE Spectrum*, pp. 71-78, February 1970

2. United States Patent No. 4,636,799, "Poled Domain Beam Scanner"
   Inventor: Frederick Kubick
   Assignee: United Technologies Corp.
   Filed: May 3, 1985

3. United States Patent No. 4,706,094, "Electro-optic Beam Scanner"
   Inventor: Frederick Kubick
   Assignee: United Technologies Corp.
   Filed: May 3, 1985

4. Dr. Frank J. Elmer and Dr. Sei Joo Jang, "Development of a Voltage Controlled Ceramic Phase Shifter," *Army Science Conference Proceedings*, Assistant Secretary of the Army, Research Development and Acquisition, Department of the Army, 25 October 1988.

5. "Ferroelectric-Scanned Phased Array Antenna," Patent Pending
   Inventors: Donald C. Collier, Britt Kustom, and Kevin Krug
   Assignee: United Technologies Corp.
   Filed: 6 March, 1991

6. "An R.F. Phase Shifting Device in a Waveguide Flange," Patent Pending, Inventors: Donald C. Collier, Britt Kustom and Kevin Krug
   Assignee: United Technologies Corp.
   Filed: 25 June 1991

Modified Lead Scandium Tantalate for Uncooled LWIR Detection and Thermal Imaging

R.W. Whatmore[1], N.M. Shorrocks[1], P.C. Osbond[1], S.B. Stringfellow[1], C.F. Carter[1] and R. Watton[2]
(1) GEC-Marconi Materials Technology Ltd, Caswell, Towcester, Northants, NN12 8EQ, UK
(2) Defence Research Agency (Malvern), St Andrew's Road, Malvern, Worcs, WR14 3PS, UK

Lead scandium tantalate (PST) has been shown to have exceptionally good pyroelectric figures of merit, especially for small detectors of the type involved in the large arrays needed for uncooled solid state thermal imaging. This paper will review the properties of PST in relation to those of other materials which have been considered for use in this role and discuss how dopants, including K/Bi, Nb, Ti and Zr can be used to modify the properties of the material in a way which would be beneficial to certain modes of detector operation, particularly with respect to the elimination of the requirement for cooling. F_D figures-of-merit of over 20 x $10^{-5}Pa^{-1/2}$ are reported. A concern for the user of devices under electrical bias is the possible change in the properties of the active material with time. This is particularly so in the case of dielectric bolometers where they are subject to high bias fields (up to 5V/μm) for extended periods. The results of measurements of the properties of PST after ageing under such fields are presented. The major observed change is in the dielectric loss which increases gradually due to a thermally activated process, showing an increase in loss of about 20% after 5000 hours at 100°C, corresponding to >5 years at or below 70°C. These changes are acceptable for device applications. Single element detectors have been made using PST and their properties assessed in comparison with conventional pyroelectric ceramics. It has been shown that detectivities (D^*) of 2.5x10^8 cmHz$^{1/2}$W^{-1} can be obtained for 1 mm^2 detectors. These are 40% greater than for a detector of the same design made with a standard pyroelectric material (a modified lead zirconate). Decreasing the area of the detector to 0.1mm^2 gives a D^* of 7x10^8 cmHz$^{1/2}$W^{-1}.

Introduction

The prime drive for infra-red detection and the associated thermal imaging equipments over the past twenty years has been for military night vision, target acquisition and missile guidance. In recent years, requirements in this field have turned increasingly towards technologies with the potential to deliver lightweight compact and low power imaging heads. The non-military applications of such heads in thermal imaging are also very wide, including product inspection for fault isolation and quality assurance[1], fire detection and prevention (eg, in aircraft[2] and around spacecraft[3]), remote temperature measurement (eg, in aeromechanics[4] or in laser heat treatment of materials[5]), medical diagnosis[6], monitoring of burns patients[7] and automotive vision enhancement[8]. The most important move to make such applications practical is the development of uncooled thermal imaging, recognising its significant advantages in the above aspects in comparison with the cooled photon detector technologies with the implications of bulky and expensive cryogenics. The result has been the development of uncooled thermal detectors, particularly based on the use of pyroelectric ceramic materials.

The applications of the pyroelectric effect in infra-red detection and thermal imaging have been extensively reviewed[9-12]. Pyroelectric detectors generally consist of thin flakes of a ferroelectric material, electroded on the major faces and connected to a high impedance FET buffer amplifier. The temperature change generated by the absorption of the IR energy releases charge which appears as a voltage across the detector element. Pyroelectric ceramics have many advantages over alternative materials, amongst which they offer electrical properties which are easily modified by doping combined with low potential manufacturing costs and the provision of large areas which make device production very economic. A particularly promising system has been developed which modifies $PbZrO_3$ by solid solution with Pb_2FeNbO_6 and $PbTiO_3$, with the inclusion of UO_3 as a conductivity controlling dopant[13,14]. Further improvements to this system can be engendered[15] by using substitution of Sr^{2+} for Pb^{2+}.

In the last few years, there has been considerable interest in using ferroelectrics close to their Curie temperatures and under an applied electrical bias field. This so-called 'dielectric bolometer' mode of operation has been shown to give higher performance figures-of-merit than can be achieved in conventional pyroelectric materials, particularly for large arrays of small detectors for solid state pyroelectric thermal imaging[16]. The advantages which are generally achieved by operation in this mode are very high pyroelectric coefficients (typically an order-of-magnitude higher than conventional pyroelectrics) and low dielectric losses. The high dielectric constant which might seem to be a disadvantage of operating near T_c in fact serves to give good matching of a small element's capacitance to the capacitance of the amplifier.

This paper discusses the optimisation of the material for use in pyroelectric thermal imaging arrays and some examples of devices using these materials.

Material Choice and Optimisation

In the discussion which follows, the materials figure-of-merit[10] which most closely describes signal-to-noise ratio will be used to compare materials. This is $F_D = p/(c'[\varepsilon\varepsilon_0\tan\delta]^{1/2})$ (where p = pyroelectric coefficient, ε = dielectric permittivity, tanδ = dielectric loss and c' = volume specific heat). The voltage figure-of-merit $F_V = p/c'\varepsilon\varepsilon_0$ will also be used. It should be noted that p and ε (and thus F_D) are strongly dependent upon applied field and temperature and must be measured over a range of conditions when dielectric bolometer operation is being considered. ε and tanδ should also be measured at the frequency of interest (usually 50 to 200Hz for thermal imaging applications).

The development of an optimised pyroelectric ceramic based on modified lead zirconate has been extensively discussed elsewhere[13,14,17] and will not be repeated here. Table 1 gives the properties of a hot-pressed ceramic with composition $Pb[(Zr_{0.58}Fe_{0.20}Nb_{0.20}Ti_{0.02})_{0.995}U_{0.005}]O_3$. This is referred to as Mod.PZ. The room temperature F_D for this material is typically ~2.85 x $10^{-5}Pa^{-1/2}$.

Table 1
Electrical Properties of Mod.PZ Pyroelectric Ceramic

p(20°C)	=	4.1 x $10^{-4}Cm^2K^{-1}$
ε (80Hz)	=	350
tanδ (80Hz)	=	0.0094
c'	=	2.67 x $10^6Jm^{-3}K^{-1}$
F_D	=	2.85 x $10^{-5}Pa^{-1/2}$

The ferroelectric $PbSc_{1/2}Ta_{1/2}O_3$ (PST)[21,22] has been shown to give excellent figures-of-merit when compared with other materials such as $KTa_xNb_{1-x}O_3$ (KTN)[18], $Ba_{0.65}Sr_{0.35}TiO_3$ (BST65/35)[19] and $(Pb_{0.99}La_{0.01})(Mg_{1/3}Nb_{2/3})O_3$ (PLa01MN)[20]. It is also relatively easy to fabricate as a fully dense, stable ceramic by hot-pressing. Figure 1 shows the temperature dependence of F_D under a field of 5V/μm when compared with BST65/35 and PLa01MN under similar field conditions and Mod.PZ at zero bias (ie, in pyroelectric mode). It can be seen that the F_D for PST is 3.5 times the value for Mod.PZ at 25°C. The PST ceramic F_D peaks at a value 80% greater than its nearest dielectric bolometer rival (BST65/35).

CH3080-0-7803-0465-9/92$3.00©IEEE

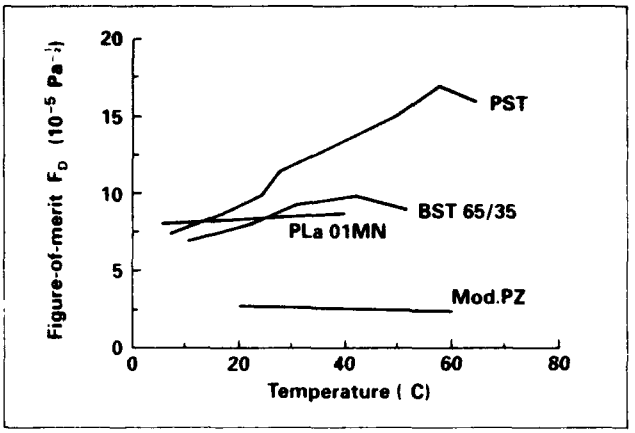


Fig. 1. Variation of F_D with temperature for several dielectric bolometer materials compared with Mod.PZ.

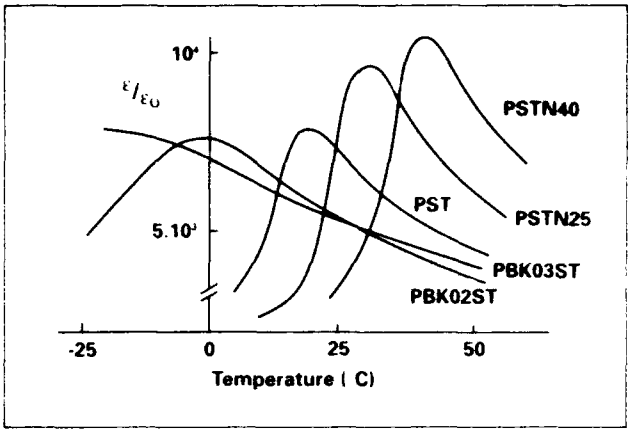


Fig. 2. Variation with temperature of the dielectric permittivity of several modified PST ceramics (a) PSTN25, (b) PSTN40, (c) PBK02ST, (d) PBK03ST, (e) PST.

Doped PST Ceramics

The use of ferroelectric ceramics in dielectric bolometer mode has the slight disadvantage in relation to conventional pyroelectric mode that the material must be temperature stabilised in the region of (usually just above) T_C to gain optimum performance. If external operational temperatures can range from -40 to +70°C and T_C is chosen in the region of 25°C, this will entail heating the material from the low external temperature end and cooling it from the high. While thermoelectric coolers are readily available, the task of providing up to 30°C of cooling while coping with an array dissipation of a few hundred milliwatts can take cooling powers of a few watts. Generally, it is much easier to provide heating than cooling. Hence, a T_C towards the upper end of the external temperature range is desirable.

Several dopants have been explored to assess their effects on T_C and electrical properties in the PST system. These include:

a. K^+, Bi^{3+} as a balanced A site substituent for Pb^{2+}, formulated as $[Pb_{1-x}(K_{0.5}Bi_{0.5})_x](Sc_{1/2}Ta_{1/2})O_3$ and coded here as PKB(x.100)ST.

b. Solid solution between $(Pb(Sc_{1/2}Ta_{1/2})O_3)_{1-x}(Pb(Sc_{1/2}Nb_{1/2})O_3)_x$ coded here as PSTN(x.100).

c. Solid solution between $(Pb(Sc_{1/2}Ta_{1/2})O_3)_{1-x}(PbZrO_3)_x$ coded here as PSTT(x.100).

d. Solid solution between $(Pb(Sc_{1/2}Ta_{1/2})O_3)_{1-x}(PbZrO_3)_x$ coded here as PSTZ(x.100).

The dielectric and pyroelectric properties of hot-pressed ceramics in all these series have been explored in detail. The effect of K^+,Bi^{3+} substitution as in (a) is to reduce T_C, while making the phase transition more diffuse. The substitution of 2% of K^+, Bi^{3+} for Pb reduces the zero bias T_C from 25°C in undoped PST to around 0°C. Conversely, the solid solution with lead scandium niobate tends to increase T_C (as would be expected as PSN has a T_C of about 110°C when well ordered with respect to Sc/Nb[23]). The variation of dielectric constant with temperature for both types of dopant are shown in Figure 2. The upward shift in T_C given by the Niobium substitution did not, interestingly, follow Vergard's law and while a Nb:Ta ratio of 1:3 was expected to give an upward shift in T_C of about 15°C, the observed behaviour was non-linear and a 2:3 ratio was needed. Figure 3a shows the F_D values (at 5V/μm) for some of these ceramics when compared with undoped PST. It can be seen from Figure 3a that PBK03ST has a very much broader dielectric peak than either PBK02ST or undoped PST. The PBK03ST shows pronounced relaxor behaviour associated with low B-site ordering[23]. X-ray diffractometry[24] suggested about 25% ordering, compared with 65% for PBK02ST or undoped PST. The peak value of F_D obtained from PBK02ST compared well with that from undoped PST, but shifted downwards by about 25°C. The PBK03ST was interesting in that F_D was almost independent of temperature over the range assessed. In this sense, it was similar to PLa01MN[20] (see Figure 1) but PBK03ST has an F_D about 21% higher for the same applied field. This material would be expected to give very useful performance over a wide range of temperature, in a situation where temperature stabilisation is impractical. The two curves for PSTN25 correspond to before and after annealing at 1150°C for 100 hours, which gave a large decrease in dielectric loss and a corresponding increase in F_D. The annealed material would allow the optimum operating range of a detector to be increased by about +20°C with no degradation in detector sensitivity.

The dielectric properties of solid solutions with $PbTiO_3$ and $PbZrO_3$ of the types c and d above are reported elsewhere[25]. Figure 3b shows the variation of F_D for PSTT10 and PSTZ12.5 in comparison with undoped PST. It can be seen that here again, significant increases in optimum operating temperature have been obtained at quite modest doping levels. The peak value of F_D obtained for the $PbTiO_3$ doped material is quite comparable with that for undoped PST, while the $PbZrO_3$ doped material shows significant improvements at high temperature, peaking at over 20 x $10^{-5}Pa^{-1/2}$.

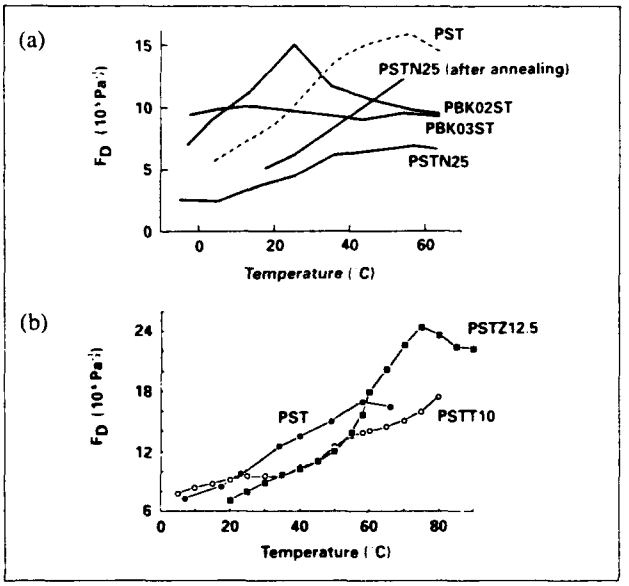


Fig. 3. Comparison of F_D/temperature for several modified PST ceramics (a) PSTN25, (b) as (a) after annealing, (c) PBKO2ST, (d) PBKO3ST, (e) PST, (f) PSTT10, (g) PSTZ12.5.

Ageing of PST Ceramics

It is a matter of some concern that the use of bias fields in dielectric bolometer detectors should not cause long term degradation of the relevant properties of the material or lead to dielectric breakdown. For the study of ageing in PST, single element detectors 1.5mm square and 31μm thick were assembled in Ge-windowed cans with dry N_2. These were aged in batches of 10 under 155V (5V/μm field) at temperatures ranging from -20°C to +125°C. Periodically, their properties were assessed at 20°C and 5V/μm bias field. Control batches were stored at room temperature and +70°C with no bias field. The pyroelectric voltage response was measured at 80Hz, referred to a $LiTaO_3$ standard and using a 500K black body. ε and tanδ were measured at 1kHz using a GR bridge at 0.5Vrms. Loss was measured 90s after applying the bias. The observed loss decreased with time, taking about 30 minutes to stabilize. The 90s data was consistently 10% higher than the stable value. As relative changes are analysed, the basic conclusions are unaffected by this.

In general, the dielectric loss, capacitance and pyroelectric voltage response tend to increase with time stored under bias, very approximately linearly with log (time) see Figures 4a, b and c. The changes in dielectric loss were most significant. Several null results have been observed. There were no significant changes at -20°C, 155V (1900 hours), at 20°C, 0V (two years), and at 70°C, 0V (4700 hours). The increase in loss was independent of frequency (60-10000Hz). The process of assessment involved applying and removing a strong electric field many times. One sample was switched like this 1000 times (20°C, ~0.5Hz) with no effect on capacitance and loss.

Figure 4 shows that storage under bias in the paraelectric phase gradually increases the dielectric loss under bias in the ferroelectric phase of PST, doubling after 3500 hours at 100°C. The process is thermally activated, the rate increasing by about an order of magnitude every 25°C. This corresponds to an activation energy of 1eV. The change in capacitance, Figure 4b, is slower. The rate tends to increase with temperature, though it is not a good match to a simple activation energy. The pyroelectric voltage response data, Figure 4c, is subject to the largest measurement error. There is no evidence of any decrease in response and an indication of a slight increase. The F_D material figure of merit is proportional to the product of the pyro voltage response with the square root of the ratio of capacitance to loss. This is dominated by the dielectric loss, and is reduced by about 20% after 5000 hours at 100°C (probably equivalent to over 5 years at or below 70°C). This ageing is unlikely to affect performance during long term operation.

During this sequence of experiments, two de-ageing techniques were attempted. After 1050 hours, five samples from the 100°C/155V batch were selected and subsequently aged open circuit. Similarly after 1090 hours at 70°C/155V, five samples were aged with a reversed bias field, but measured with the original field sense. The results are also shown on Figure 4a, b and c. The former set showed no change in pyro response and slow but complete de-ageing of capacitance. About half the loss increase was reversed after 100 hours, but there was no change after the next 3500 hours. Reversing the ageing field had the most dramatic effect. In both capacitance and loss, it appears as if this reversal has started a new ageing process that is both additive with and similar to the original process.

In summary, it has been observed that elevated temperatures alone do not degrade the electrical properties and that bias fields applied below ~30°C have little effect. Bias fields applied in the paraelectric phase result in thermally activated ageing. The major changes which occur do so in the dielectric loss and reversing the ageing field adds to the original changes.

To assess the reasons for the observed changes, measurements of dielectric constant/temperature were performed on both unaged and aged specimens. The ageing caused both an increase in peak value and a decrease in peak width. These changes match those expected and observed for PST first order transitions under a small dc bias field. Observations on

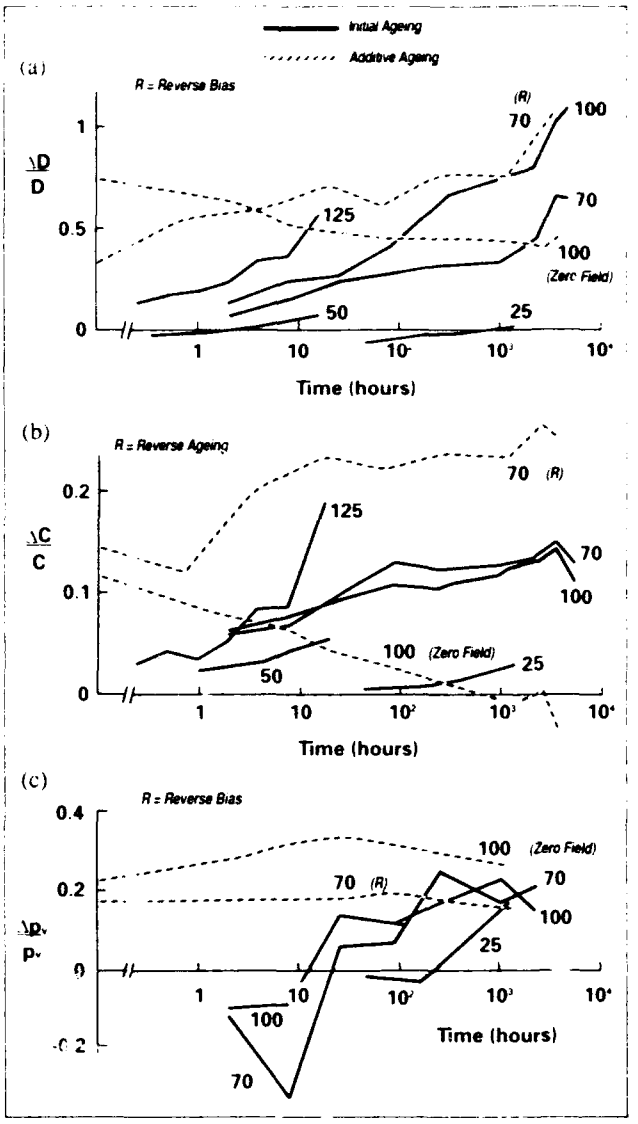


Fig. 4. Relative changes in (a) dielectric loss (Δtanδ/tanδ), (b) capacitance (ΔC/C) and (c) pyroelectric voltage response ($\Delta p_V/p_V$) during ageing under bias at various temperatures. Dashed lines show the cumulative effect of a second ageing period with modified conditions.

ferroelectric hysteresis loops also suggest the existence of an internal bias field, produced by the ageing and opposing the external bias. The hysteresis loop shift suggests its magnitude is about 0.5V/μm, 10% of the external field. This is consistent with the observed zero bias dielectric peak shift. A possible cause[26] is the moving of charged defects, such as oxygen vacancies, through the ceramic grains, building up at a blocking interface. The limited effectiveness of thermal annealing suggests that many of these defects move into deep traps. The ageing of 70μm thick samples gave a significantly lower ageing rate. This suggests that if the underlying cause of ageing is the motion and accumulation of charged defects, it is the sample surface, not the grain boundaries, which provide the significant blocking interfaces. The behaviour on ageing field reversal is not understood.

This conclusion has been supported by further studies on PST doped with 0.5% uranium as a B-site substituent. In this case the uranium, acts as an electron donor, reducing the room temperature resistivity to $10^{10}\Omega m$ from $10^{12}\Omega m$ in undoped PST. No significant changes in loss were seen after 12 hours ageing at 100°C. As uranium acts as an electron donor[14], it would be expected to reduce the oxygen vacancy concentration and thus reduce this mechanism as a source of ageing. (This material possesses too low a resistivity for a low noise detector).

Device Evaluation

PST has been evaluated as an active material in a variety of devices including single element detectors, linear and two dimensional arrays. Figures 5a, b and c show the responsivity, noise and detectivity (D*) as functions of field at 25°C for 1mm^2 PST detectors. The F_V for PST at 4V/μm and 25°C is ~0.06m^{2}C^{-1} (cf 0.05 for Mod.PZ)[21]. This is reflected in their similar responsivities under these conditions. The much higher ε of PST, however, gives very low noise and a detectivity which is 40% higher. At 1mm^2 the PST element is not ideally matched to the amplifier noise, and much greater advantage can be obtained by operating with smaller detector elements. Figure 6 shows the variation of D* with element area for single element detectors. Values of up to 7 x 10^{8}cmHz$^{1/2}$W^{-1} can be obtained at 0.1mm^2.

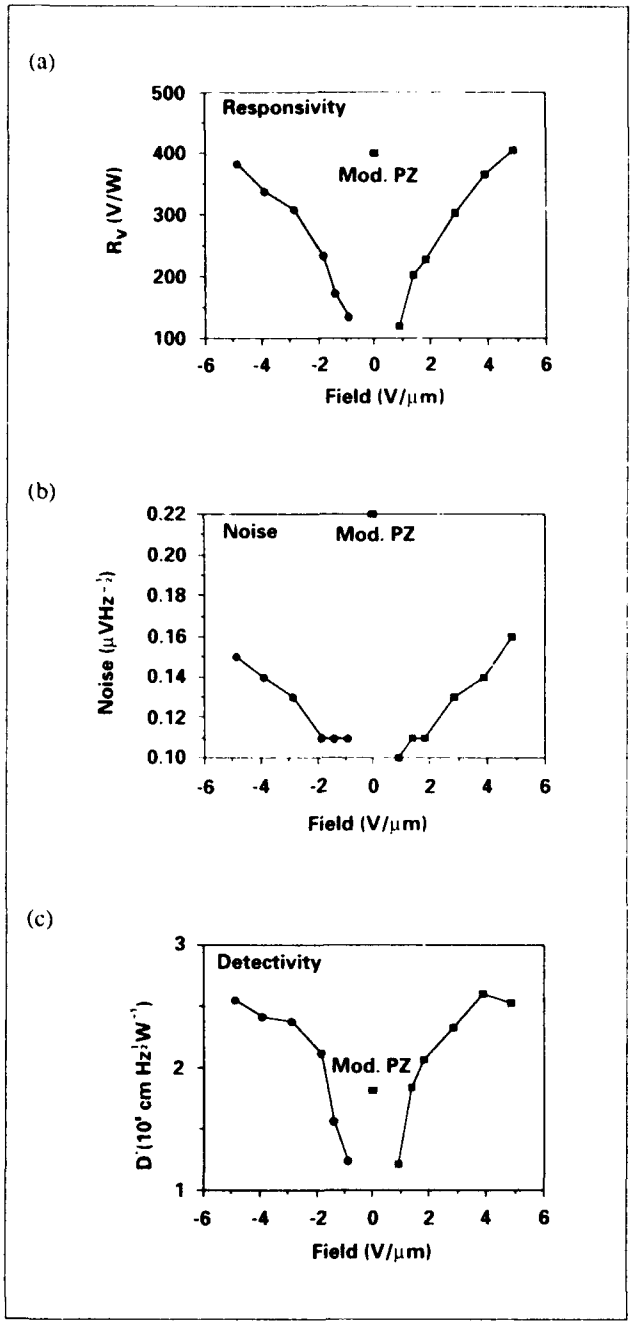


Fig. 5. (a) responsivity, (b) noise, and (c) detectivity, measured at 10Hz on 1 x 1mm PST single element detectors at 4V/μm bias and 25°C, when compared with Mod.PZ detectors of similar construction.

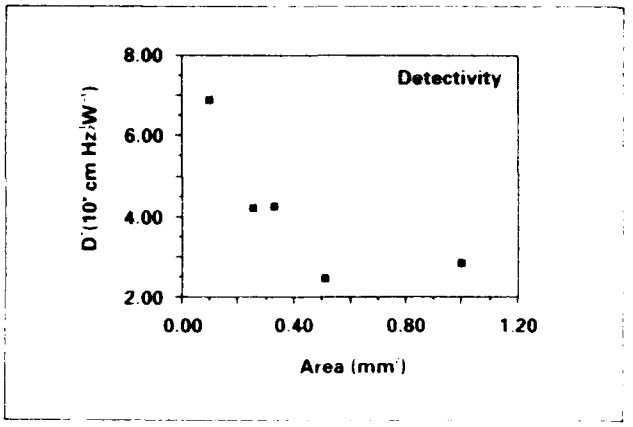


Fig. 6. Detectivity measured at 10Hz as a function of element area for single element detectors using PST at 4V/μm, 25°C.

Acknowledgement

This work has been carried out with the support of the Defence Research Agency, Malvern.

References

[1] N Zuech, Test and Measurement World pp73-83, Oct 1990.
[2] M L Parsons, P Hutchins and V Y Tseng, Proc SPIE 1308, pp312- 324, 1990.
[3] B M Harper, T D Normal and D R Exley, Proc SPIE 1313, pp309-320, 1990.
[4] V M Lutovinov, A A Poskachey und V I Sukharev, Fluid Mechanics - Soviet Research 19, 2, pp82-91, 1990.
[5] A R Rosenthal, Laser und Optoelecktronik 22, 5, pp44-49, 1990.
[6] C M Black, R P Clark, K Darton, M G Goff, T D Norman and H A Spikes, J Biomed. Eng 12, pp281-6, 1990.
[7] J C Ferguson, C J Martin, G C Cameron, I Gow, M V Mansi and T J Liddicoat, J. Phot Sci 37, pp181-4, 1989.
[8] J M Callahan, Automotive Industries, p31, 1991.
[9] S G Porter, Ferroelectrics 33, pp193-206, 1981.
[10] R W Whatmore, Rep Prog Phys 49, 1335-86, 1986.
[11] R Watton, Ferroelectrics 91, pp87-108, 1989.
[12] R W Whatmore, Ferroelectrics 118, pp241-259, 1991.
[13] R W Whatmore and A J Bell, Ferroelectrics 35, pp155-60, 1981.
[14] R W Whatmore, Ferroelectrics 49, pp201-10, 1983.
[15] P C Osbond and R W Whatmore, Ferroelectrics 118, pp93-101, 1991.
[16] R W Whatmore, A Patel, N M Shorrocks and F W Ainger, Ferroelectrics 104, pp269-283, 1990.
[17] R W Whatmore and F W Ainger, Proc SPIE 395, pp261-6, 1983.
[18] O M Stafsud and M Y Pines, J Opt Soc Am 6, pp1153-5, 1971.
[19] P C Osbond, N I Payne, N M Shorrocks, R W Whatmore and F W Ainger, Proc 6th IEEE ISAF, pp348-351. (CH2358-0/86/0000-348), 1986.
[20] R W Whatmore, P C Osbond and N M Shorrocks, Ferroelectrics 76, pp351-367, 1986.
[21] N M Shorrocks, R W Whatmore and P C Osbond, Ferroelectrics 106, pp387-392, 1990.
[22] N M Shorrocks and R W Whatmore, Ferroelectrics, to be published, 1992.
[23] C G F Stenger and A J Burgraaf, Phys Stat Sol (a), 61, pp653-664, 1980.
[24] C G F Stenger and A J Burgraaf, Phys Stat Sol (a) 61, pp275-285, 1980.
[25] P C Osbond and R W Whatmore, J Mat Sci, in press, 1992.
[26] T Baiatu, R Waser and K Hardtl, J Am Ceram Soc, 73, pp1663-1673, 1990.

Low Fire Z5U Ceramic Dielectric for Surface Mount MLC

S.P. Gupta, C.R. Konpella, and L.A. Mann
KEMET Electronics Corporation
PO Box 5928
Greenville, SC 29606

Abstract

A method for simultaneously lowering the sintering temperature and increasing the mechanical strength of barium titanate dielectrics has been developed. The method also results in high dielectric constant. This technique is useful in designing ceramic dielectrics for use in the manufacture of multilayer ceramic capacitors for applications in surface mount circuit assemblies. The low sintering temperature makes it possible to utilize low cost silver/palladium electrodes, and the mechanical strength makes surface mount capacitors less susceptible to damage due to mechanical or thermal stresses during the assembly process. The electrical and mechanical properties of a Z5U dielectric developed using this method are discussed and compared to commercially available Z5U materials.

Introduction

The demand for miniaturized surface mount multilayer ceramic capacitors (MLC) has impelled manufacturers to develop ceramic materials that offer both volumetric efficiency and mechanical robustness. In the US, the 0805 (0.080 x 0.050 inches) chip size is rapidly replacing the 1206 chip (0.120 x 0.060 inches) as the most popular in the industry, 0603 chips (0.060 x 0.030 inches) are being widely used, and 0402 chips (0.040 x 0.020 inches) are now available. This transformation has been made possible by the development of materials that possess both high dielectric constant and sufficient mechanical strength to withstand the various mechanically and thermally induced stresses associated with the manufacture of surface mount circuit assemblies. The development of a family of low-fire barium titanate materials that meet the Electronics Industries Association (EIA) specifications for Z5U dielectrics is discussed below.

Background

A key characteristic of an MLC is the interleaving of the dielectric and electrode materials, which are co-fired into a monolithic structure as shown in Figure 1.

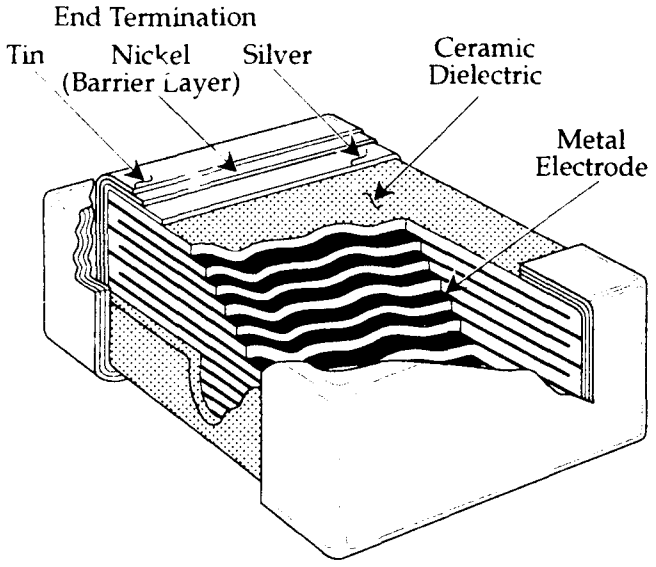


Figure 1. Construction of an Multilayer Ceramic Capacitor

Barium titanate continues to be the backbone of most ceramic dielectrics used in the manufacture of ceramic capacitors. Historically, two approaches have been taken in modifying barium titanate to get the right combination of dielectric and physical properties for producing capacitors. The first approach is to add dopants to barium titanate in order to adjust its dielectric properties so that they meet the temperature coefficient of capacitance (TC), dissipation factor (DF) and insulation resistance (IR) requirements set forth by the EIA. In this case, palladium is commonly used as the electrode material due to the relatively high sintering temperature of barium titanate (1300°C or greater).

An alternate approach is to utilize additional additives to lower the sintering temperature to less than 1150°C so that less costly silver/palladium alloys can be used as electrodes. This usually results in slightly lower dielectric constants as compared to similar high-fire materials. It will be demonstrated that properly chosen sintering aids can also enhance the mechanical strength of the ceramic. This is an important consideration in developing dielectrics for use in surface mount ceramic capacitors.

Experimental

Two types of sintering aids were studied. The first, a non-reactive glass frit designated as Type A, consisted of a glass former with a melting point of about 450°C. The second, designated as Type B, was a reactive glass frit with a melting temperature of about 1000°C. The terms "reactive" and "non-reactive" are used to describe the interaction of the sintering aid with the barium titanate. A reactive frit is one that is largely incorporated into the barium titanate lattice during firing, whereas a non-reactive frit remains for the most part at the boundaries of the barium titanate grains.

The sintering aids were milled along with commercial $BaTiO_3$ and various additives using a Sweco vibratory mill. The milled slurry was then mixed with an aqueous binder system and cast into green ceramic tape. Green chips were manufactured from the tape using a process that involves screen printing electrode patterns with 30% Pd/70% Ag ink, stacking and laminating the printed layers, and then dicing the resultant pads into individual chips. The green chips then went through a binder bakeout process and were bisqued at approximately 880°C. The chips were fired using a batch kiln in a layer of zirconia sand at temperatures ranging from 1115°C to 1145°C.

The capacitance, DF, TC, Curie temperature, and IR of the fired chips were measured according to the procedures outlined in ANSI/EIA RS-198. Modulus of rupture (MOR) was measured using a three-point bend test with a sample size of 30 chips.

Results and Discussion

Initial studies compared the effects of the two types of sintering aids on the electrical and physical characteristics of a barium titanate dielectric. A summary of the properties of 0805 capacitors made using the two types of glass frits is given in Table 1, and fractured cross sections of the two samples are shown in Figures 2 and 3. In both cases, 36 electrodes were used and the dielectric thickness was approximately 13 microns. Other than the type of glass frit used, the dielectric formulations were identical.

CH3080-0/93/0000-0206$03.00 © IEEE

Table 1. Summary of Electrical and Physical Properties of MLC made with Two Different Types of Sintering Aids

Property		Type A	Type B
Capacitance (nF)		105	115
DF		2.5%	1.7%
TC	10°C	+ 2%	+ 9%
	85°C	- 61%	- 54%
IR (Ω-F)	25°C	10,000	15,000
	85°C	1,500	3,000
Dielectric Constant		7,000	7,500
Breakdown Voltage (v/mil)		600	1,000
Curie Temperature		10°C	10°C
MOR (MPa)		170	490

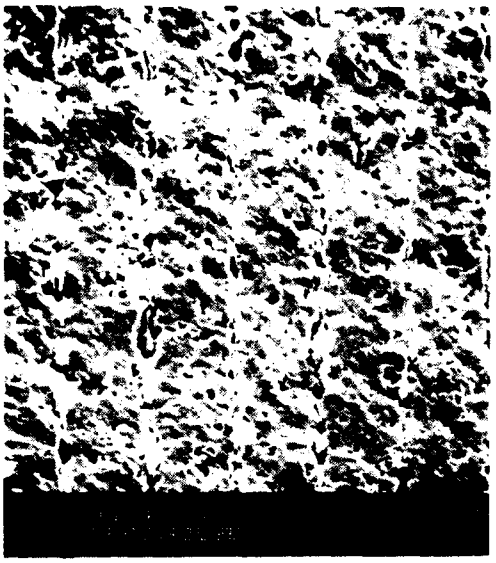


Figure 2. Photomicrograph of Fractured Cross-Section of Dielectric with Type A Glass Frit

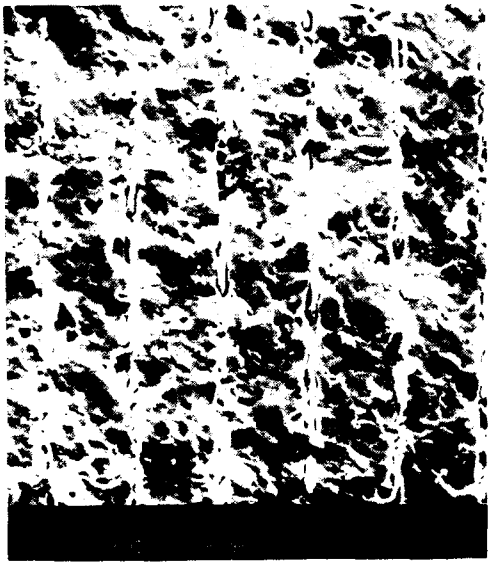


Figure 3. Photomicrograph of Fractured Cross-Section of Dielectric with Type B Glass Frit

It is evident from the photomicrographs of the fractured cross sections that the Type A non-reactive glass frit resulted in a more porous dielectric than obtained with the Type B reactive glass frit. This porosity was responsible for the inferior breakdown strength and modulus of rupture of capacitors made with the Type A sintering aid. Only minor differences were observed between the two samples in regard to capacitance, DF, and IR.

The high porosity, low breakdown strength, and low modulus of rupture obtained when the non-reactive Type A frit was used as a sintering aid rendered the resulting ceramic undesirable for use in the manufacture of surface mount MLC. The reactive glass frit, however, resulted in a ceramic with good dielectric properties and excellent mechanical strength.

Further studies were carried out using different amounts of the reactive glass frit to better understand its impact on the properties of the dielectric. Table 2 summarizes the effect of glass frit content when the reactive frit (Type B) was used. Except for the amount of glass that was added, the dielectric formulations were identical. The effect of glass content on dielectric constant as a function of temperature is shown in Figure 4.

Table 2. Summary of Electrical Properties of MLC made with Three Different Glass Frit Levels

Property		Glass Content 4%	5%	6%
Cap (nF)		115	119	126
DF		1.6%	1.6%	2.1%
TC	10°C	+ 2%	+ 5%	+12%
	85°C	-53%	-54%	-56%
IR (Ω-F)	25°C	10,000	11,000	12,000
	85°C	4,000	4,500	5,000
Dielectric Constant	(25°C)	7,300	7,800	8,200
Curie Temperature		10°C	5°C	0°C

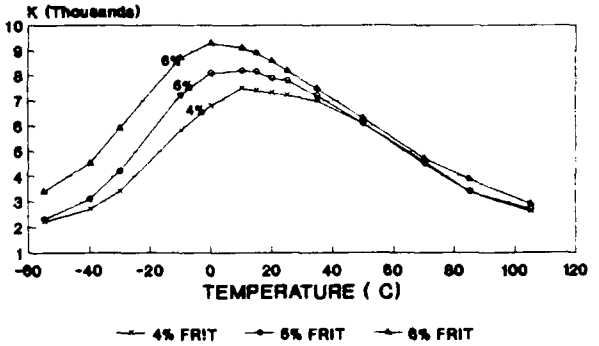


Figure 4. Temperature Coefficient of Capacitance vs Frit Content

It is evident that adding more glass lowered the Curie temperature of the dielectric, and increased the dielectric constant at the Curie point. This phenomenon is a result of the reactive nature of the glass being used. When a non-reactive glass is used, the opposite effect is observed. This is due to the dilution effect of the relatively low K glass phase at the grain boundaries of the higher K barium titanate grains.

Using 5% reactive glass resulted in dielectric properties that satisfy the EIA Z5U specifications (DF less than 4%, TC of -56% to +22% between 10°C and 85°C, and insulation resistance greater than 1,000 Ω-F at 25°C).

Comparison of Proprietary Z5U Dielectric with Other Z5U Materials

Table 3 compares the properties of the proprietary Z5U dielectric with two barium titanate Z5U dielectrics available from commercial sources.

Table 3. Comparison of Proprietary Z5U Dielectric with Commercial Low-Fire Z5U Dielectrics

Property	Commercial Dielectrics Z5U-1	Z5U-2	Proprietary Dielectric
K (25°C)	5,000	8,500	7,500
DF	1%	2%	2%
TC 10°C	-11%	- 3%	+ 9%
85°C	-51%	-48%	-54%
IR 25°C	10,000	15,000	15,000
(Ω-F) 85°C	3,000	3,000	3,000
Breakdown Voltage (V/mil)	800	800	1,000
MOR (MPa) 1206 Size Chips	170	180	400

The commercial Z5U products are typical of Z5U materials on the market. The outstanding characteristics of the proprietary Z5U dielectric are its unusually high mechanical strength, as characterized by its modulus of rupture (>400 MPa for a 1206 size chip), and high dielectric strength (>1,000 volts/mil). These properties are especially significant in light of it's relatively large grains (3-5 microns). The modulus of rupture is higher than that of most X7R dielectrics, which range from 200 MPa to 400 MPa. These characteristics make it an ideal material for manufacturing surface mount ceramic capacitors.

Summary

A high K, low-fire Z5U barium titanate dielectric with excellent mechanical strength has been developed. A reactive glass frit was used to lower the sintering temperature to below 1150°C without compromising the dielectric constant. The mechanical strength of this dielectric is equivalent or superior to that of most X7R dielectrics. This, combined with its high breakdown strength, make it an ideal material for the manufacture of surface mount multilayer ceramic capacitors.

RELAXOR STUDIES OF Na, Fe and Mg DOPED SBN CERAMICS

S.Narayana Murty, K.V.Ramana Murthy, G.Padmavathi, A.Bhanumathi
Solid State Physics Laboratories, Department of Physics,
Andhra University, Visakhapatnam-530 003, **INDIA**.
And
K.Linga Murty
Depts. of Nuclear Engg. and Materials Science Engg.
North Corolina State University, Raleigh NC 27695 **USA**

Abstract

Sodium doped Strontium Barium Niobate ceramics with tetragonal tungsten bronze structure were prepared by the powder metallurgical technique. The effect of various dopants on the properties of SBN ceramics have been investigated. Relaxor characteristics have been studied. The dielectric loss is very low in all the compositions. Curie temperature increases slightly and the dielectric constant decreases with increasing frequency. The dielectric constant vs temperature curves indicate a broad maximum which is a characteristic of diffuse phase transition.

Introduction

Strontium Barium Niobate ($Sr_x Ba_{1-x}Nb_2O_6$) is ferroelectric solid solution with tetragonal tungsten bronze structure (1,2). It has a high electro-optic coeffiecient and high pyroelectric coeffiecient (3,4). Piezoelectric and SAW properties of these materials have been extensively studied by various researchers (5) in single crystal form. The tungsten bronze structure ferroelectrics are a large class of technically important materials. In many of these meterials diffuse phase transition has been reported. The important characteristics of tetragonal tungsten bronze ferroelectrics are: they exhibit excessively large values of permittivity compared to those predicted by Lyddane Sachs Teller relation; they do not confirm to the usual soft phonon mechanism; they are associated with lattice instabilities evidenced by the large Raman cross sections observed for one or more of the low frequency lattice modes.

Although there is a vast literature on ferroelectric properties of single crystals of SBN, work on ceramics is meagre. This is because it is difficult to obtain high density ceramics of this material useful for device application. In pure SBN (6) T_c is of the order of 94°C by doping with alkali elements T_c is greatly increased. Hence, in this work by doping with suitable cations we have tried to enhance T_c and decrease the dielectric loss. When the interstitial vacancies are filled partially or fully with alkali elements T_c is raised. The purpose in introducing **Na** is to increase the density and raise T_c. Role of sodium in sintering process is to cause **A** position vacancies because it is volatile. Volatility of **Na** causes **A** position vacancies. It is well known that these vacancies aid sintering by diffusion process. Also, by filling the structure with **Na** ions, there is an improvement in ferrolectric properties as reflected by an increase in T_c. The effect of different cations such as **Na**, **Fe** and **Mg** on the lattice parameters and ferroelectric properties of Sr Ba Nb_2O_6 ceramics have been reported in this communication.

Experimental

Solid solutions of the following compositions were prepared by the conventional ceramic technique.

$(Sr_x Ba_{1-x})_{0.8} Na_{0.4} Nb_2O_6$
where x = 0.3 to 0.6

$(Sr_{0.6}Ba_{0.4})_{0.8} R_y Na_{0.4} Nb_2O_6$
where R = Fe, Mg, Cr, Mn, Li, Ni, Zn, Y & Ca

High purity reagent grade oxides of the constituent materials, weighed according to their stoichiometric proportions were dry ground into fine powder and calcined in platinum crucibles and pressed into discs. The firing temperatures are the same reported earlier (6,7). X-ray diffraction patterns of all the compositions were obtained on a Reich-Seifert, FRG, X-ray diffractometer using Cu K_α radiation with Ni filter. The lattice parameters were computed using a computer programme by the least squares fitting (LSQ) procedure of the high - angle X-ray diffraction lines. The dielectric dispersion was measured with a Hewlett-Packard LF impedance analyser model 4192A with 16095A as probe fixture. The dielectric constant was studied at different frequencies viz. 1KHz, 100KHz, 500KHz and 1MHz. The dielectric loss factor was also measured in the tenperature range 30-400°C.

Results and Discussion

Dielectric Studies:

The variation of dielectric constant with temperature for different compositions are shown in figures (1-3). A broad transition is observed in all the compositions which is a characteristic of diffuse phase transition. The broadness decreases gradually with the increase of **Sr** content. The dielectric loss (ε'') decreases with increase of **Sr** content and attains a minimum value of 0.009 for Sr = 0.6 composition. The dielectric data is presented in the Table. As **Sr** content increases T_c decreases from 353°C to 230°C while the dielectric constant increases to nearly five times of its value. As Sr/Ba ratio changes gradually, the room temperature dielectric constant increases from 163 to 595 and peak dielectric constant increases from 239 to 3360 with **Na** held

CH3080-0-7803-0465-9/92$3.00 ©IEEE

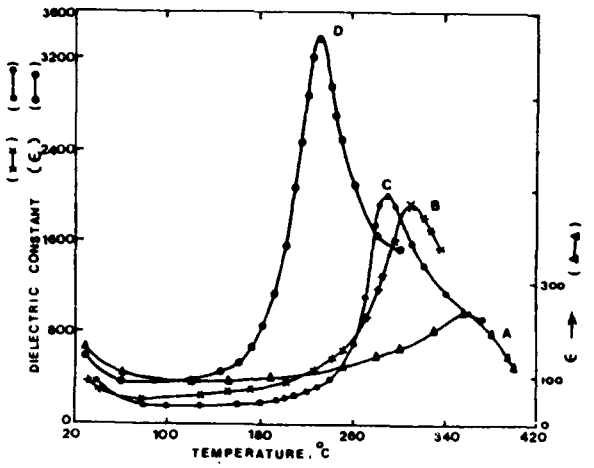


Fig. 1: Dielectric constant plotted against temperature for Sr/Ba ratio variation compositions.

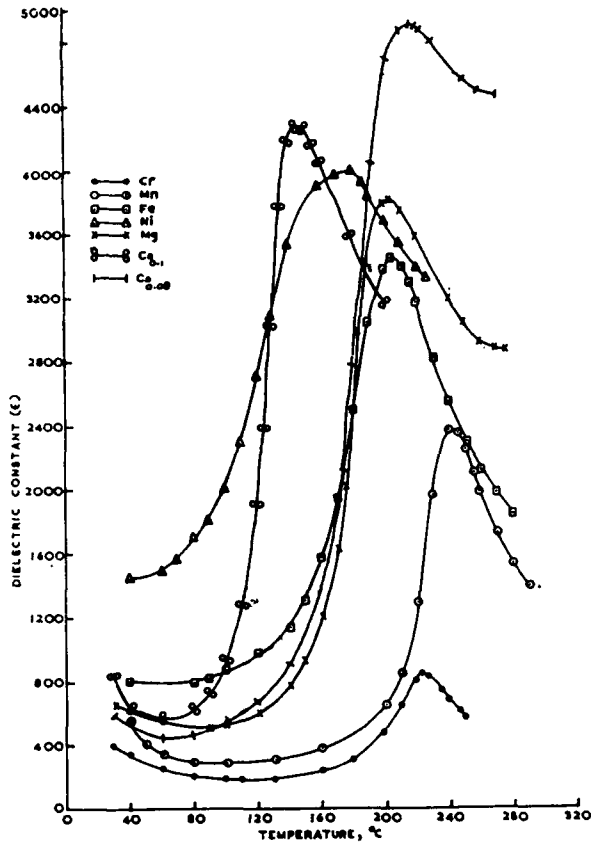


Fig. 2. Variation of dielectric constant with temperature for SBN - Na ceramics at 1KHz.

constant. It is evident from Fig. 1 that the peak becomes more sharper as Sr content increases. The ferroelectric transition temperature is considerably lowered with the introduction of different valency cations. Curie temperature decreases from 245°C to 145°C with the increase of the ionic radius of the additives. But in Li composition T_C rises to 245°C and the dielectric

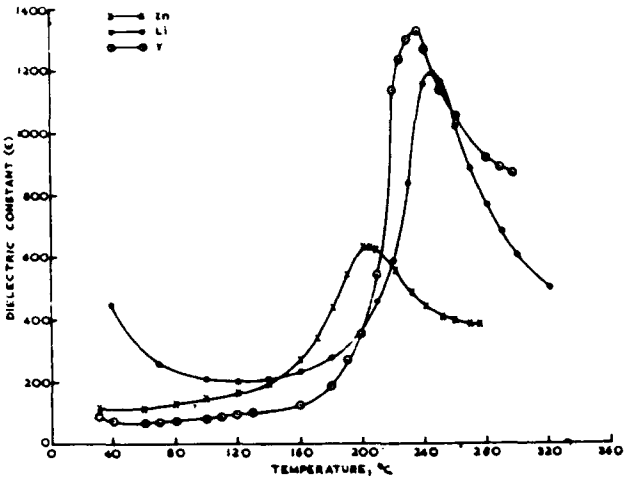


Fig. 3: Plot of dielectric constant Vs temperature for SBN - Na ceramics at 1 KHz.

constants are relatively low. The substituted ionic sizes and the site occupancy play an important role in determining the dielectric constant. Na^+ occupies A_1, A_2 sites and Li^+ enters the smaller C site.[7] Moreover, Li composition is a filled structure and the others are unfilled structures. The dielectric loss is very low for Ca, Na, Fe and Mg doped compositions. Maximum loss was observed in Mn composition. Changes in temperature should be related with some disorder in the Sr and Ba relations, because it is possible for Fe^{3+} to enter into B - sites and A sites in some particular conditions as per the Hennings (8) report. The EPR spectrum indicates that Iron enters as Fe^{3+} in B - sites. In Jimenez's (9) work on SBN ceramics a large decrease in curie temperature of nearly 50°C was reported when doped with Fe, Mn, Cr and La.

Relaxor characteristics:

In the tungsten bronze structure ferroelectric ordering studies have shown that compositional heterogeneity leading to

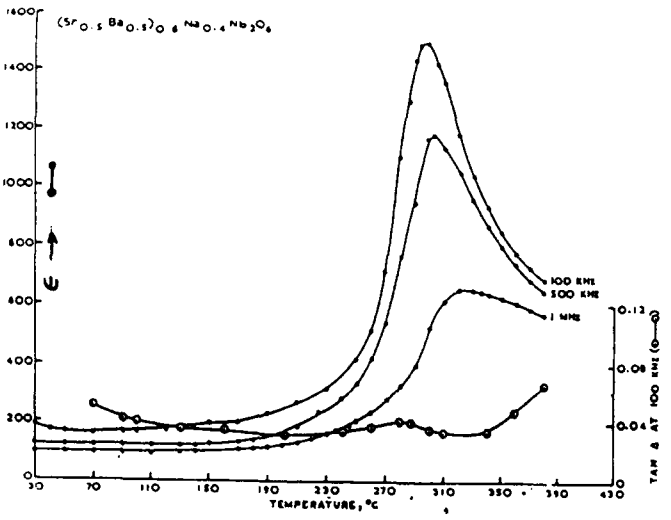


Fig. 4: Temperature dependence of the dielectric constant and Tan δ at different frequencies for SBN - Na composition.

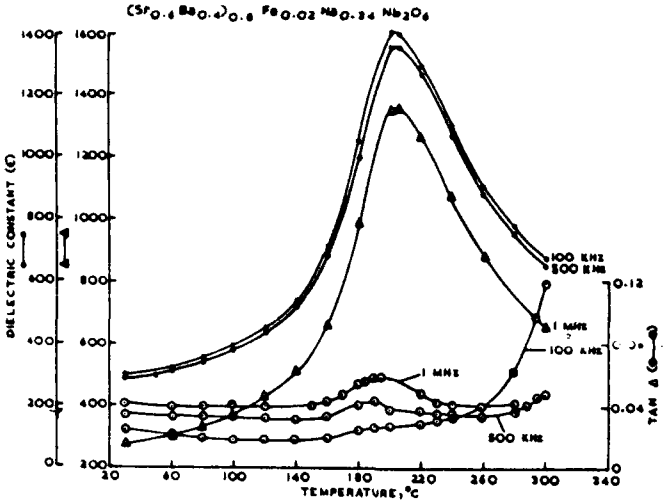


Fig. 5 : Temperature dependence of the dielectric constant and Tan δ at different frequencies for **Fe** doped sample.

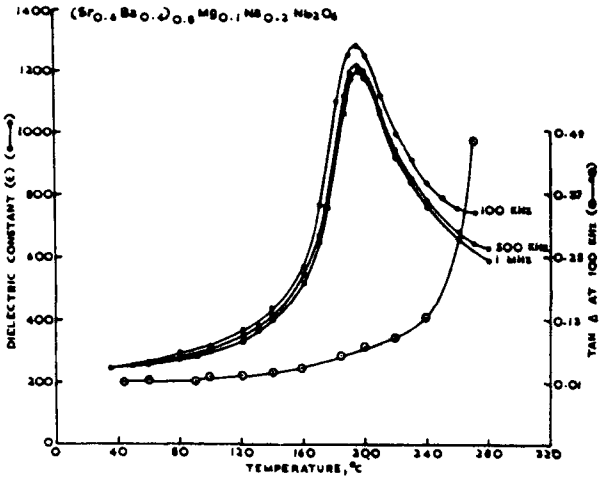


Fig. 6: Temperature dependence of dielectric constant and dielectric loss at different frequencies for Mg doped composition.

a breakdown of translational symmetry is responsible for relaxor character. The termprature dependence of dielectric constant for Na, Fe, Mg doped compositions at different frequencies are shown in figures (4-6). The results are shown in the Table. The peak dielectric constant decreases with the increase of frequency as well as Sr/Ba ratio. The frequency dependence of the dielectric constant curves are all similar ie; almost all the curves are close to each other. But for Sr = 0.5 composition the response is quite different. There is a large difference in the peak dielectric constants spread over a vide temperature range. The site occupancy and the distribution of equal number of Sr and Ba ions may be the reason for this difference of behaviour. Increase in frequency broadens the dielectric curve.

The common feature of all the relaxor materials is that one or more of the available cation sites in occupied by more than one kind of ion. In ferroelectric relaxors, the dielectric properties within the transition region become strongly dispersive at low radio frequency ie; 1 KHz to 1 MHz. The characteristic behaviour of ferroelectric relaxors is the strong frequency dependence of the dielectric properties in the high frequency range. Increasing the frequency shifts the dielectric constant peak to a higher temperature. The dielectric loss curves decreases slightly in the beginning and increases to peak maximum and again decreases slowly with increase of temperature. The dielectric loss peak is shifted to higher temperatures with increase of frequency. But in certain compositions Mg and Ca the loss peak was not observed upto 300°C and the curve is in increasing trend. Probably the dielectric loss peak may be in still higher temperatures. Smolenskii (10) and Cross (11) have also observed the similar diffuse phase transitions in **PMN** and **PST**.

Acknowledgements

Thanks are due to Department of Science and Technology, New Delhi for the award research grant. One of the authors (SNM) in is grateful to Council of Scientific and Industrial Research, New Delhi for providing the financial assistance in the form of Research Associateship.

References

(1) P.B. Jamieson, S.C. Abrahams and J.L. Berusteen, **J. Chem. Phys.** 48,5048 (1968)

(2) M.H. Framcombe and B. Lewis, **Acta.Cryst.**, 11, 696 (1958)

(3) P.V. Lenzo, E.G. Spences and A.A.Ballman **Appl. Phys. Lett.**, 11, 23 (1967)

(4) A.M. Glass, **J. Appl. Phys.**, 40, 4699, (1969)

(5) R.R. Neurgaonkar, M.H. Kalisher,T.C.Lim, E.J. Staples and K.L. Kester, **Mat. Res. Bull.**, 15, 1235 (1980)

(6) K.Umakantham, S.Narayana Murty, K.S.Rao, A.Bhanumathi, **J.Mater.Sci.Lett.**, 6, 565 (1987)

(7) S.Narayana Murty, G.Padmavathi, A.Bhanumathi and K.Linga Murty, **Phys. Stat. Soli.** (a), 128, K 47 (1991)

(8) D.Hennings and H.Pomplum, **Ferroelectrics** 7, 345 (1974)

TABLE

Frequency dependence of dielectric data of modified SBN ceramics

Sample	Ionic Radii	ε''	ε_{RT}				ε_{Tc}				T_c °C			
			1KHz	100K	500K	1MHz	1KHz	100K	500K	1MHz	1K	100K	500K	1MHz
0.3/0.7	-	.168	163	237	209	201	239	769	748	740	353	355	355	355
.4/.6	—	.015	353	192	191	190	1932	1175	1144	1113	310	290	290	290
.5/.5	—	.270	575	202	133	113	2000	1495	1173	650	290	297	302	330
.6/.4	—	.009	595	355	353	336	3360	2667	2613	2587	230	244	244	244
Cr-SBNNa	.52	.037	398	143	140	139	841	605	584	574	222	225	225	225
Mn	.60	.403	711	345	307	294	2367	1574	846	675	242	245	280	245
Fe	.64	.026	998	302	293	289	3440	1403	1368	1353	205	200	200	205
Mg	.66	.014	645	255	253	251	3787	1282	1217	1199	202	195	195	195
Li	.68	.042	719	191	189	188	1190	855	841	836	245	267	267	267
Ni	.69	.024	1458	997	975	962	3962	3330	3283	3213	180	160	165	165
Zn	.74	.043	111	201	194	190	627	1202	1110	986	205	200	205	207
Y	.89	. 116	98	92	85	82	1330	283	273	261	235	205	210	215
Ca	.99	.016	592	351	349	346	4892	1911	1845	1830	217	205	200	205
Ce o.1	.99	.024	842	354	349	346	4271	1122	1013	990	145	185	182	182

(9) B. Jimenez, R.G.Polledo, C.Alemany, J. Mendiola and E.Maurer, **Ferroelectrics**, 14, 687 (1976)

(10)G.A.Smolenskii,V.A.Isupov, A.I.Agranovskaya and S.N. Popov, **Soviet Physics - Solid State**, 2, 2584 (1961)

(11)L.E. Cross, **Ferroelectrics**, 76, 241 (1987)

DIELECTRIC AND FERROELECTRIC PROPERTIES IN THE $Pb(Mg_{1/3}Nb_{2/3})O_3$-$PbTiO_3$-$BaTiO_3$ SYSTEM

S.H.Lee, Y.J.Kim, Y.H.Shin*, and S.W.Choi
Department of Physics, Dankook University,
29 Anseodong, Cheonan, Chungnam, Korea
* Cheonan National Junior Technical College

Absract

Dielectric, pyroelectric and piezoelectric properties in the (1-x-y)PMN-xPT-yBT solid solution series have been investigated. About 85% of the theoretical density was achieved for pellets sintered at 1250°C for 2 hr. The dielectric constant and pyroelectric coefficient increased with increasing grain size of the samples at various compositions. Further addition of $BaTiO_3$ affects the electrical properties of PMN-PT and the phase transition temperature is continuously shifted to lower temperature with increase of a small amount of $BaTiO_3$.

Introduction

The dielectric, pyroelectric and piezoelectric properties of $Pb(Mg_{1/3}Nb_{2/3})O_3$-$PbTiO_3$(PMN-PT)system have been widely studied in both single crystal and solid solution forms[1,2]. PMN-PT solid solutions exhibit a range of relaxor ferroelectric properties dependent on composition. At about 35 mol% PT the PMN-PT phase diagram exhibits a morphotropic phase boundary (MPB). PMN-PT compositions near the MPB are both of technical and scientific interest since anomalously high electrostrictive coefficients are known to exist in such compositions[3].

Present study was carried out with the system $xPb(Mg_{1/3}Nb_{2/3})O_3$-$yPbTiO_3$-$zBaTiO_3$ (x+y+z=1)to obtain a lower Curie temperature and higher dielectric properties at room temperature.

Experimental procedure

Ceramic samples were prepared by conventional sintering technique.[4] Reagent grade oxide powders $PbCO_3$, $BaCO_3$, TiO_2, Nb_2O_5 and MgO with purity better than 99% were used as starting materials. The calcined powders were mixed with a binder (3%wt,PVA) using the mortor. Pellets which are 10mm in diameter and 0.5mm thick were pressed at 700 kg/cm^2. The binder burned out by heating process at 500°C. The pellets were sintered at various temperatures i.e., 1100, 1150, 1200 and 1250°C for 2hr. The pellet were placed on platinum foil in an enclosed alumina crucible. The sintering was done in a lead rich atmosphere by placing a small amount of an equimolecular mixture in the same crucible. A heating rate of 300°C/hr was to further avoid PbO loss.

The grain size was determined of fracture surfaces of the pellets using scanning electron microscopy (SEM). Weight loss and apparent density were measured for all the samples sintered at various temperatures by using Archimedes' water displacement method.

Dielectric measurements were measured of 0.1-100 kHz at the temperature rate of 4 C/min, with a multi-frequency LCR meter. Pyroelectric measurements were measured by the static Byer-Roundy method[5]as the samples were heated, again at a rate of 4°C/min. Prior to the dielectric, pyroelectric and piezoelectric measurements, the samples were poled by appling a DC field of about 15 kV/cm. The electromechanical coupling factor of the samples were measured at room temperature by using resonance-antiresonance method[6].

Results and discussion

Sintering and grain size

Figure 1 shows the dielectric constant and pyroelectric coefficient of 0.65PMN-0.30PT-0.05BT ceramics at various sintering temperatures. The effect of sintering temperature on the dielectric and pyroelectric properties was pronounced and cosistent over the entire set of compositions investigated. An increase in sintering temperature resulted in an increase in maximum dielectric and pyroelectric coefficient. The effect of sintering temperature was most pronounced for the 0.65PMN-0.30PT-0.05BT ceramics which maximum dielectric constant increased from 3100 to 5000 and 6100 as the sintering temperature was increased from 1150 to 1200 and 1250°C.

Scanning electron micrographs of the fracture surface of the composition 0.65PMN-0.30PT-0.05BT sintered at various temperatures are shown in Figure 2 and show increasing grain size with increasing sintering temperature. The sample sintered at 1100°C showed smaller grain size ($<1.5\,\mu$) where as large grain sizes of about 5-7μ were observed for the samples sintered at 1250°C as shown in Figure 2. It is clearly evident from the Figure 1, that dielectric constant and pyroelectric coefficient increase with increasing grain size.

Dielectric properties

Figure 3 shows the temperature dependencies of dielectric constant and dissipation factor at various frequencies (0.1 - 100 kHz) for composition 0.60PMN-0.35PT-0.05BT. The composition showed a broad maxima of dielectric constant and an increase in transition temperature with increasing frequency, characteristic of relaxor ferroelectrics. Corresponding frequency dispersion of the dissipation factor was also observed.

The temperature dependence of dielectric constant (at 1 kHz) for a ragne of compositions are shown in Figures 4 and 5. The variation of transition temperature with composition is shown in Figure 6. The transition temperature decreases almost linearly with the addition of $BaTiO_3$, their rates of decrease are about 8-10°C/mol%.

Pyroelectric and piezoelectric properties

Figures 7 and 8 show the temperature dependence of pyroelectric coefficient for the compositions 0.60

CH3080-0-7803-0465-9/92$3.00 ©IEEE

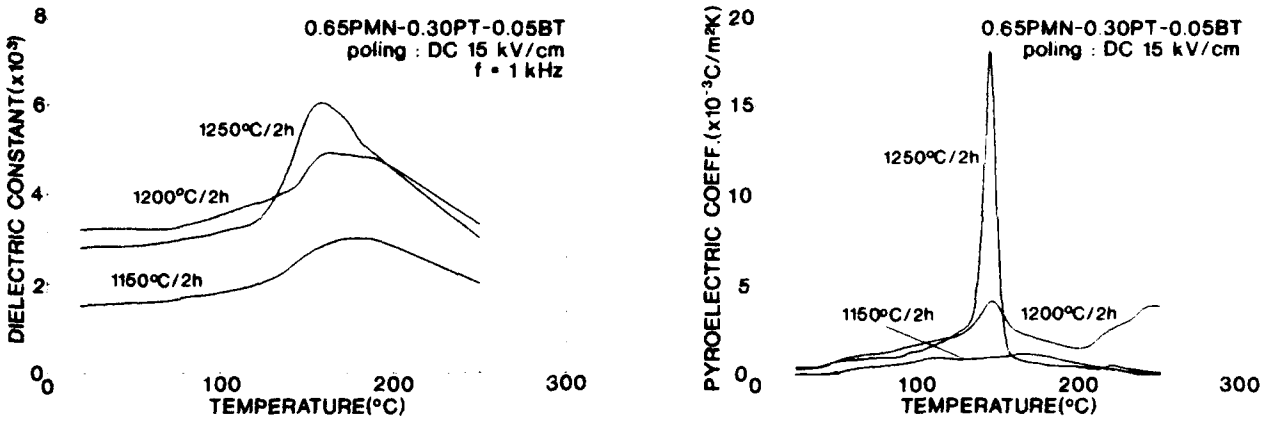


Figure 1. Dielectric constant and pyroelectric coefficient of 0.65PMN-0.30PT-0.05BT ceramics at various sintering temperature.



Figure 2. SEM micrographs of the fracture surface of the composition of 0.65PMN-0.30PT-0.05BT at various sintering temperature.

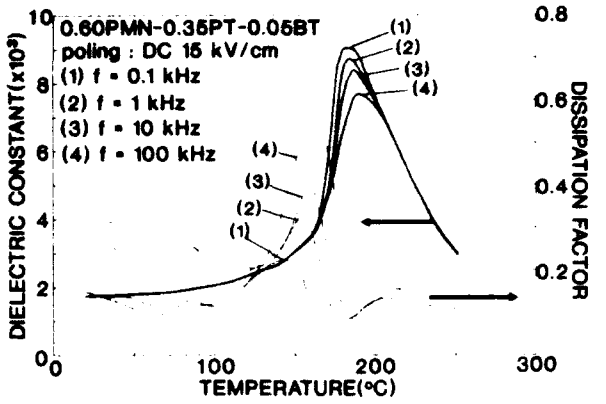


Figure 3. Temperature dependence of dielectric constant and dissipation factor at various frequencies for 0.60PMN-0.35PT-0.05BT system.

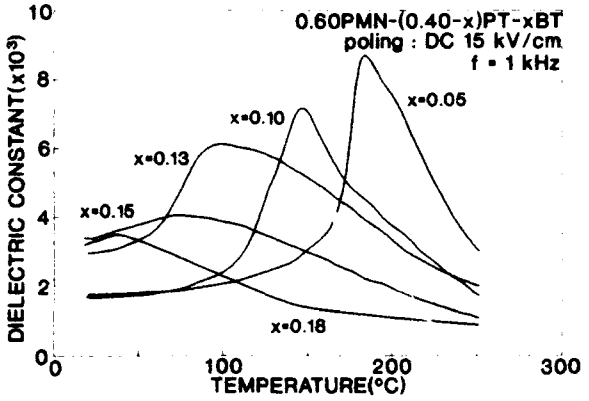


Figure 4. Dielectric constant vs. temperature in the 0.60PMN-(0.40-x)PT-xBT system.

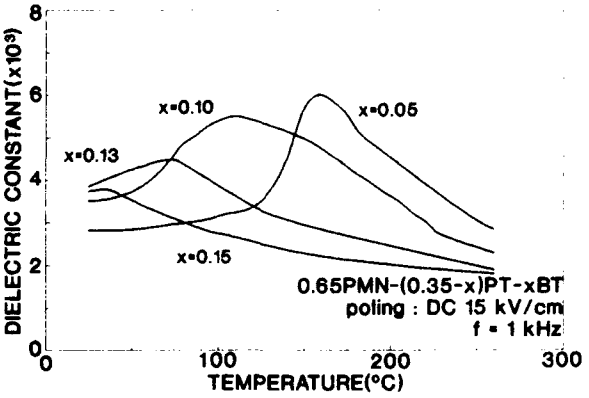


Figure 5. Dielectric constant vs. temperature in the 0.65PMN-(0.35-x)PT-xBT system

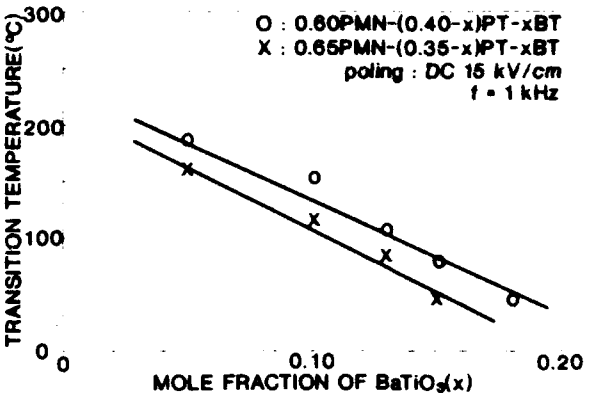


Figure 6. Variation of the transition temperature as a function of the mole fraction of $BaTiO_3$

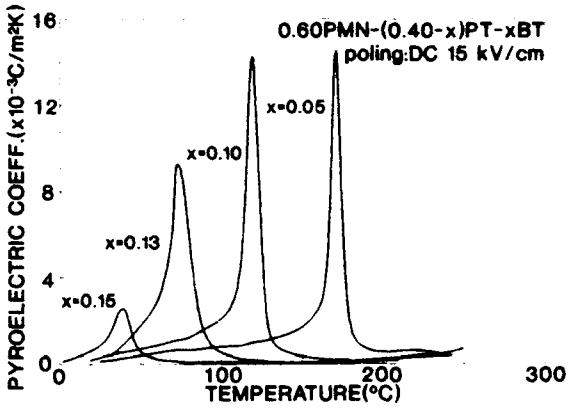


Figure 7. Pyroelectric coefficient vs. temperature in the 0.60PMN-(0.40-x)PT-xBT system.

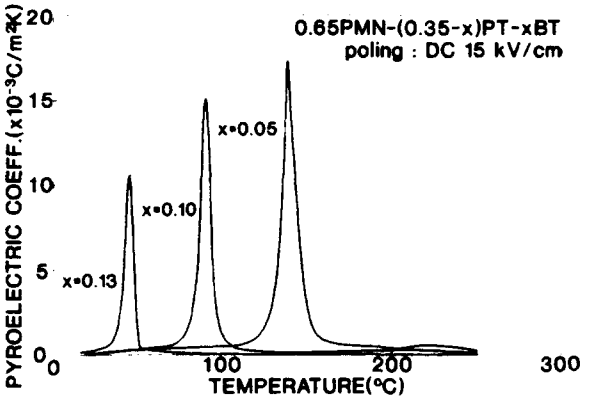


Figure 8. Pyroelectric coefficient vs. temperature in the 0.65PMN-(0.35-x)PT-xBT system.

PMN-(0.40-x)PT-xBT and 0.65PMN-(0.35-x)PT-xBT, respectively. The peak temperature of pyroelectric coefficient with compositions might be similar to that observed in dielectric constant vs. temperature studies. In each series the maximum pyroeletric coefficient is observed for the compositions 0.60PMN-0.35PT -0.05BT and 0.65PMN-0.30PT-0.05BT, respectively. The addition of $BaTiO_3$ affects the dielectric and pyroel-

ectric properties of PMN-PT and the phase transition temperature is continuously shifted to lower temperature with increase of an amount of $BaTiO_3$. But the magnitude of the maximum pyroelectric coefficient decreases with increasing $BaTiO_3$ as shown in Figures 7 and 8.

Figure 9 shows the room temperature value of electromechanical coupling factor(kp) of the composition (1-x-y)PMN-xPT-yBT series as a function of mole fraction of $BaTiO_3$. In each series the maximum electromechanical coupling factor is obtained near the maximum dielectric and pyroelectric coefficient.

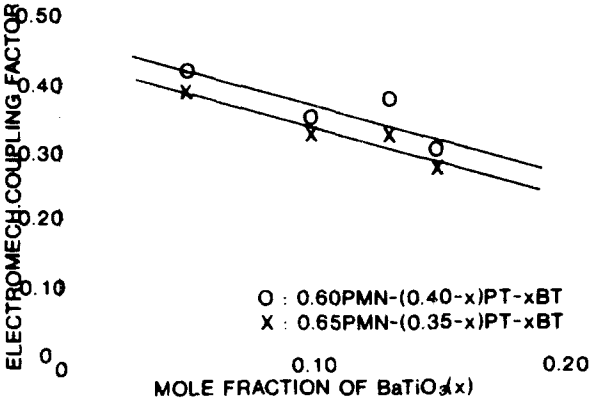


Figure 9. Electromechanical coupling factor as a function of mole fraction of BT at the room temperature.

Conclusions

About 85% of the theoretical density was achieved for pellets sintered at 1250°C for 2hr. An increase in sintering temperature resulted in an increase in grain size. The dielectric constant and pyroelectric coefficient increased with increasing grain size of the samples sintered at various temperatures. The addition of $BaTiO_3$ to the PMN-PT system resulted in the reduced dielectric constant and the phase transition temperature decreases almost linearly with the addition of $BaTiO_3$ without significantly changing the dielectric and pyroelectric behavior. The maximum electromechanical coupling factor occurs in the compositions 0.60PMN-0.35PT-0.05BT(0.4).

Acknowledgement

This work was supported by the Korea Science and Engineering Foundation (KOSEF) through the Science Research Center(SRC) of Excellecne Program.

References

(1) P, Ravindranathan, S. Komarneni, A.S.Bhalla and R. Roy, " Synthesis and Dielctric Properties of Solution Sol-Gel Derived 0.9PMN-0.1PT Ceramics" J.Am.Ceram. Soc.,vol.74, pp.2996-2999, 1991.

(2) S.W.Choi, T.R.Shrout, S.J.Jang and A.S.Bhalla, "Dielectric and Pyroelectric Properties in the Pb($Mg_{1/3}Nb_{2/3}$)O_3-$PbTiO_3$ System," Ferroelectrics, vol.100 pp.29-38, 1989.

(3) S.W.Choi, T.R.Shrout, S.J.Jang and A.S.Bhalla, "Morphotropic Phase Boundary in Pb($Mg_{1/3}Nb_{2/3}$)O_3-PbTiO_3System," Materials Letters, vol.8, pp.253-255, July 1989.

(4) T.Takenaka, Y.Soma and K.Sakada, "$PbZrO_3$-Based Piezoelectric Ceramics Containing Pb($Zn_{1/3}Nb_{2/3}$)O_3" Trans.Inst. Electron. Ceram. Eng. Japan vol.E69, pp.468-470,1986.

(5) R.L.Byer and C.B.Roundy, "Pyroelectric Coefficient Direct Measurement Technique and Application to a NSEC Response Time Detector." Ferroelectrics, vol.3, pp.333-338, 1972.

(6) IRE Standands on Piezoelectric Crystal: Measurement of Piezoelectric Ceramics, Proc. 1961," IRE(Inst. Radio Engrs.) vol. 49(7), pp.1161-1169, 1961.

Thin Films: Electrical Properties

ULTRAFAST POLARIZATION SWITCHING OF LEAD ZIRCONATE TITANATE THIN FILMS

P.K. Larsen, G.L.M. Kampschoer, M.B. van der Mark and M. Klee*
Philips Research Laboratories,
P.O. Box 80.000, 5600 JA Eindhoven, Netherlands
*Philips Forschungslaboratorium Aachen, 5100 Aachen, Germany

Abstract

The switching behaviour of thin Lead Zirconate Titanate (PZT) thin films prepared by different spin-coating techniques was investigated. Some films show switching times as short as 360 ps, others show a wide time distribution. These results can be explained in terms of the morphology of the films, and suggestions are given for the possible domain structure and switching mechanisms involved.
To obtain the necessary sub-nanosecond experimental resolution, both the rise time of the switching pulse and the current limiting effect of the LRC network have to meet high specifications. How this was done is described in some detail.

Introduction

The application of ferroelectric thin films in non-volatile ferroelectric random access memories (FERAMs) is based on their reversable remanent electric polarization. The reversal of the polarization can be carried out by applying a voltage pulse of proper polarity and amplitude across the ferroelectric film, situated between two electrodes (in a capacitor geometry). The switching of the ferroelectric capacitor has to fulfil a number of requirements. The pulse voltages should be compatible with VLSI voltages which at the moment are 5 V but dropping towards 3 V in the near future. A switching polarization larger than 10 $fC/\mu m^2$ ($1\mu C/cm^2$) is needed for reliable detection and this level has to be reached within a short time ($\leq$ 10 ns). The number of allowed reversal operations has to be large (10^{14}-10^{15}) and the stability of the poled layers has to be very good (10 years without applied voltage).

It is clear from the above mentioned requirements that the switching process in ferroelectric thin films is of critical importance for FERAM applications. It is related to material properties such as composition and morphology of the ferroelectric film and of the electrodes as well. It depends on the temperature and on switching parameters such as pulse amplitude and pulse duration. These topics needs to be investigated and understood. So far studies of switching have mainly been application motivated although the area is of basic scientific interest as well.

Early studies of switching in single crystal layers of $BaTiO_3$, having thicknesses (d) of the order of 0.1 mm, demonstrated values of the switching time t_s ranging from approximately 10 nanoseconds to minutes, depending on the electrical (switching) field (E) [1-3]. Investigations of the dependence of switching time on the thickness gave some conflicting results showing both a linear dependence [1] and an independence on the thickness in the high field range [3]. The lower limit of the high field range was of the order 1-10 kV/cm, depending on the thickness.

The linear dependence found by Merz [1] was ascribed to domain walls propagating across the film with a field dependent speed v_s ($= \mu E$). If the nucleation rate is very high, the switching speed is only determined by v_s giving $t_s = d/v_s$. If these results ($\mu \approx 2.4\ 10^{-4}$ m^2/Vs) are supposed valid for a submicron thick film, e.g. d = 0.5 µm, one finds $t_s \approx 0.14$ ns at E = 150 kV/cm.

Results by Stadler [2,3] demonstrated the possibility that the switching time does not depend on the sample thickness but only on the electric field, $t_s = 9\ E^{-1.4\pm0.1}$ (E in kV/cm, t_s in µs). In some cases it was found that d/t_s was larger than the speed of an elastic wave. This observation together with the independence on sample thickness led to a suggestion that the reversal of polarization is caused by a simultaneous reversal in all the cells rather than it is related to domain wall movements. In this case the switching time at a field of 150 kV/cm would be in the range 5-13 ns, independent on the film thickness.

Investigations of single crystals of $PbTiO_3$ (PT) [4] showed at high fields a linear relationship between $1/t_s$ and the applied field in samples with a high concentration of domains. The mobilities ($\mu = d/t_s E$) were found to vary from $2\ 10^{-7}$ to $3.7 \cdot 10^{-6}$ m^2/Vs. For a 0.4 µm film and a field of 150 kV/cm this would correspond to switching times in the range from 100 ns down to 5 ns. For samples with a low concentration of domains the lateral motion of domain boundaries were determined. A linear dependence on the electric field was also found in this case with mobilities ranging from 10^{-8} to 10^{-7} m^2/Vs.

More recent work on the kinetics of switching has been carried out on submicron polycrystalline films of KNO_3 [5] and $PbZr_xTi_{1-x}O_3$ (PZT) [6-9]. The switching results by Scott et al. on polycrystalline sub-micron thick PZT (x=0.54) films [6,7] were interpreted with a two-dimensional domain growth kinetics and a switching time satisfying an activation field dependence. The films were prepared by sputtering and the reported switching times were in the range of 10-100 ns [6]. Recent experiments by different groups on sol-gel prepared sub-micron PZT films of similar composition (x=0.52-0.53) showed much smaller switching times [8,9]. It was found that the switching time decreased with the capacitor area down to a limiting value which was determined by the response time of the experimental set-up. In both cases this value was of the order of 2 ns. Consequently, the intrinsic switching time in PZT for these sol-gel films must be smaller than 2 ns.

In this paper an analysis of the conditions necessary to perform switching measurements in the sub-nanosecond range will be given together with a description of the test set-up on which measurements were carried out on different samples. The results will be discussed on the basis of possible domain structures and switching models.

Experimental Details

Conditions for fast switching

Figure 1 shows the schematic lay-out of the electrical circuit for switching measurements in the nanosecond range. The three main elements are the pulse generator, the probing circuit and the signal analyzer which are connected with coaxial transmission lines.In the insert two configurations of the probing circuit are shown. In circuit (a) [8] the resistor R_1 ($=Z_0$) serves as impedance match to the transmission line coming from the pulse generator. This ensures that reflection from the probe circuit back towards the generator only occurs during times where

CH3080-0-7803-0465-9/92$3.00 ©IEEE

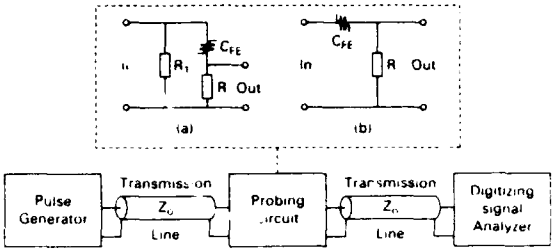


Fig. 1 Schematic lay-out of the circuit for fast pulse switching measurements. The inset shows two configurations of the probe circuit.

the ferroelectric capacitor (C_{FE}) is being charged or discharged. Such reflection can be minimalized by maximizing the impedance consisting of C_{FE} and R, i.e. by making C_{FE} as small as possible. The output signal (Out) is being transmitted into a *impedance matched transmission line and signal analyser.* Therefore there will be no reflection back to the probing circuit. The effective load resistance R' is the parallel impedance of R and Z_0, where Z_0 (= 50Ω) is the impedance of the transmission line/signal analyzer. Turning to circuit (b) [9], this is the same as circuit (a) but without the matching resistor R_1. Consequently, since there will never be an impedance match there will always be reflection towards the signal generator, i.e also when the charge on C_{FE} is constant.

The relative advantages and disadvantages of the two probe circuits depend on factors such as the time scale of the switching experiments, the desired pulse amplitudes and the sensitivity of the signal generator to reflected power. The instrumental time resolution τ_i, is given by the pulse risetime, τ_r, and the bandwidth of the analysing system, τ_a, according to:

$$\tau_i = \sqrt{(\tau_r^2 + \tau_a^2)}. \qquad (1)$$

Our standard equipment (HP 8161 pulse generators, a summing pulse amplifier, Tektronix 602 digitizing signal analyser) yields a smallest time resolution of $\tau_i \approx 2$ ns [8].

A simplified equivalent scheme for the probe circuits is shown in Fig. 2a. Here R_g is the impedance of the pulse generator and L is the circuit inductance. The ferroelectric thin film capacitor can be considered as composed of a strongly non-linear switching capacitor C_{FE} (having a square hysteresis loop) parallel with a (non-switching) dielectric capacitor C_{diel}. In addition there will always be some parasitic capacitance C_p. This results in the equivalent diagram of the ferroelectric capacitor shown in Fig. 2b.

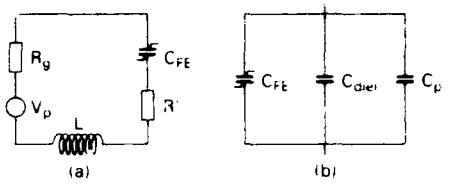


Fig. 2 a) Equivalent diagram of the probe circuit shown in Fig. 1. b) Equivalent diagram of a ferroelectric capacitor with parasitic capacitance.

The diagram of Fig. 2a is in fact a series LRC circuit but with an non-linear capacitor. It allows for an estimation of the minimum charging time when the switched polarization charge, ΔQ, is replaced by a corresponding capacitance

$$C_s = \Delta Q / V_p. \qquad (2)$$

Here $\Delta Q = \Delta P^* A_{FE}$, where ΔP is the polarization change for an applied pulse of amplitude V_p and A_{FE} is the area of the ferroelectric capacitor. The inductance L of our test circuit with test probes is in the range of 10-20 nH. The series resistance R_s (= R_g + R') is approximately 60 Ω (R_g=50 Ω, R'=8.33Ω). Neglecting the system risetime, the circuit current can be calculated as a function of time from the analytical solutions given in standard textbooks. In the quasi static range ($(2L/R_s)^2 < LC_s$) calculations for capacitor values of 200 and 40 pF and an pulse amplitude of 15 V give a time dependent voltage over the load resistor R' shown in the left hand panel of Fig. 3. It should be noted that for a linear capacitive load the current shape is independent of the pulse amplitude. In the inset the time from the onset of the pulse until the voltage has decreased to 10% of the maximum is displayed as function of the capacitance. This time is approximately equal to $2.3R_sC_s$ and in the following it is

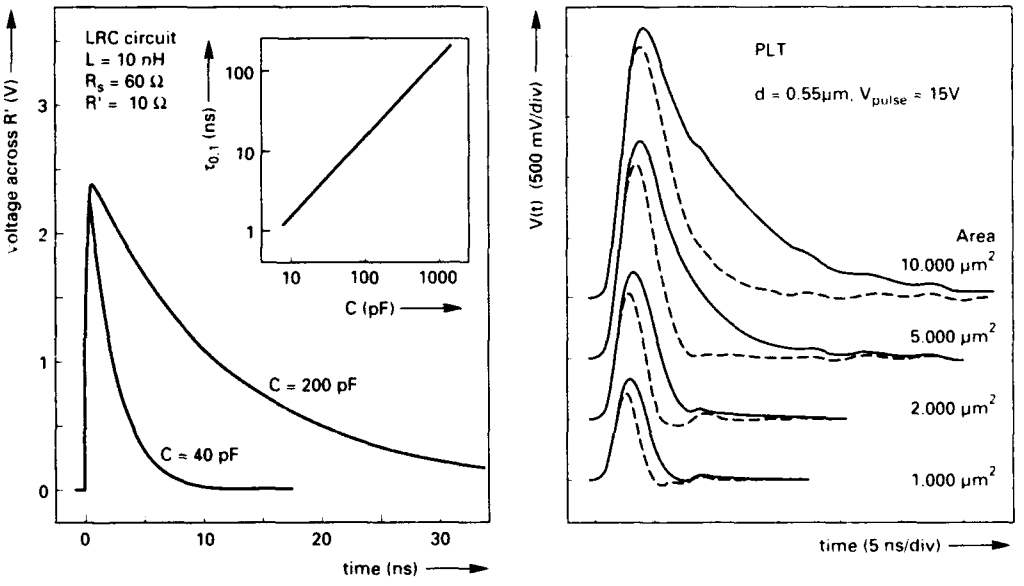


Fig. 3 Left hand panel shows for an LRC circuit the voltage across a 10 Ω load versus time after onset of a 15 V pulse. The inset gives the time from the onset to the time where the signal is reduced to 10% of its maximum. The right hand panel shows experimental switching results (from ref. 8).

denoted as τ_{RC}.

In the right hand panel of Fig. 3 experimental switching curves for a thin film of La doped $PbTiO_3$ (see ref. 8) are shown. The full line curves represent the cases where the polarization is reversed by the application of the 15 V amplitude pulse. Here the change in polarization is about 300 fC μm^{-2}. Using Eq. (2) one calculates for the capacitor areas A_{FE} = 10 000 and 2 000 μm^2 the equivalent capacitances of 200 and 40 pf, respectively. A comparison between the corresponding curves of the left and the right hand sides of Fig. 3 shows a good agreement in line shape and switching time. The exception is the initial behaviour since no signal rise and response times have been included in the calculations. The difference in the switching speed between the switching and the nonswitching curves (there is no polarization reversal by application of a second voltage pulse of the same polarity) is only caused by the different charges involved. An interesting consequence is that if the same charge is switched for different voltages (i.e. in the range where the polarization is saturated) the switching speed will depend reversely on the voltage in this range (see Eq. (2)). This might erroneously be explained as a real physical effect caused by an increase of the speed of polarization reversal with increasing field, but actually it is only caused by the current limiting effects of the network.

These results confirm the experimental results of Ref. (8) that the measured response times are limited by τ_r. Therefore, the true (physical) switching time t_s is smaller than 2 ns. A requirement obviously needed for studies of switching kinetics is that the experimental time resolution τ_{exp} be smaller than the physical switching time. Here τ_{exp} is determined by the instrumental time resolution as well as the time needed to deliver the polarization charge.

$$\tau_{exp} = \sqrt{(\tau_r^2 + \tau_{RC}^2)} \qquad (3)$$

τ_{RC} can be calculated from the polarization change, the pulse amplitude and the circuit characteristics by

$$\tau_{RC} = 2.3 R_s \Delta P A_{FE} / V_p \qquad (4)$$

This time can in principle be minimized by reducing R_s and the capacitor area A_{FE}. However, with standard instrumental impedances of 50 Ω, the lower limit of R_s is of the order of 50Ω. In practice A_{FE} must be reduced. For instance, if ΔP = 300 fC μm^{-2} and V_p = 10 V a value of $\tau_{RC} < 0.2$ ns requires $A_{FE} < 60$ μm^2 (C_s = 1.74 pF).

A further complication arises by reducing the RC time because the oscillatory range of the LRC circuit is reached when $(2L/R_s)^2 > LC_s$. This behaviour is likely met in the sub-nanosecond range. It will be treated below in the discussion of the experimental results.

Experimental set up for sub nanosecond pulse switching

A determination of the switching kinetics requires at least a comparison and better a subtraction of the time dependences of the switched and the nonswitched polarizations. These measurements have to be carried out on a proper timescale ($\tau_{exp} < t_s$). In this subsection an experimental set-up having a limiting value of τ_r = 0.1 ns is briefly described. A more complete description will be published elsewhere [10].

A usual pulse sequence for measuring switching transients consists of double bipolar pulses. The first of two consecutive pulses of the same polarity reverses the polarization and is a switching pulse while the second one is nonswitching. If only switching transients of one polarity are studied, a pulse sequence (defined by w_1, w_2 and w_3) as that shown in Fig. 4 can be used. Here the switching from negative to positive polarity can be investigated. The rise time of the two positive pulses is one of the instrumental speed determining factors, while the negative pulse just serves to reverse the polarization. A very short risetime is therefore not required for this pulse. The width of the negative pulse is equal to the sum of the widths of the two positive pulses to avoid any DC bias effects.

A schematic diagram of the experimental set-up is shown in Fig. 5. The outputs from a very fast (τ_r = 45 ps) and fast pulse generator (Models 4050 and 2600 from Picosecond Pulse Labs., Inc., respectively) are added and led to the input of the probing circuit (see inset, Fig. 1). The response time of the

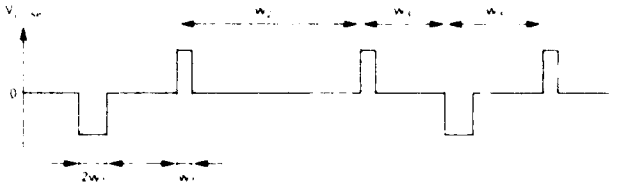


Fig. 4 A pulse sequence for switching measurements

adding circuit is about 90 ps. The output from the probing circuit is being measured by a Tektronix model 7704 sampling scope ($\tau_a \leq$ 30 ps). Its output is being averaged by a digitizing signal analyser (Tektronix DSA 602) yielding the final switching and nonswitching time dependence. The time sequence of the positive and negative pulses are being determined by a triggering and delay circuit based on HP model 8161 pulse generators. The maximum frequency is determined by the fast pulse generator (f_{max} = 100 kHz, PSPL model 2600). In order to obtain the necessary time resolution the switching and the nonswitching response are measured sequentially. For this there is a pulse selector to directly trigger the input of the sampling scope to either the first or the second of the two positive pulses. It should be noted that the period (w_2) of 5 μs is about $2 \cdot 10^5$ times the desired jitter level (≤ 20 ps) and that an exact triggering of the

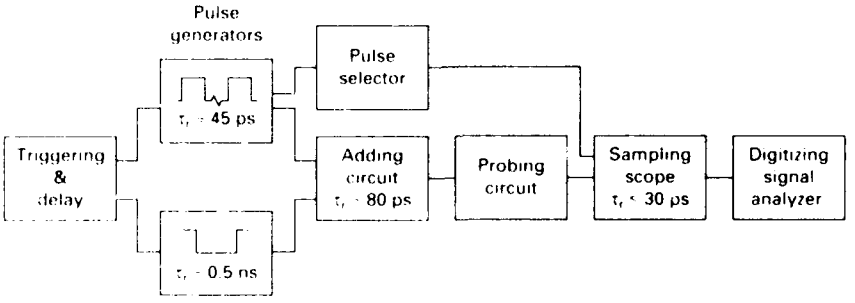


Fig. 5 Schematic lay out of experimental set-up for sub nanosecond measurements

sampling scope is required. The instrumental time resolution for the overall set-up is estimated to be 90-100 ps. The parameters of the pulse sequence for measurements carried out with this set-up are w_1 = 10 ns, w_2 = 5 µs and w_3 = 2.5 µs.

The probing circuit consists of a capacitor test structure with capacitor areas ranging from 50.000 μm^2 down to 9 μm^2 and two probes. The test structure was prepared on a 10 cm diameter oxidized Si wafer provided with a common Ti/Pt bottom electrode, a ferroelectric or dielectric layer and a top electrode (details are given below). The latter two types of layers were etched to the desired areas. No bonding pads were used because they lead to additional parasitic capacitances. The probes were coaxially shielded with the resistors (R = 10 Ω and R_1 = 50 Ω) mounted between the shield and the tip. The shields of the two probes were connected with a broad metal strip to make a good common ground and to decrease induction.

Testing of the experimental set-up

In order to investigate the performance of the experimental set-up a capacitor structure using SiO_2 as a purely dielectric layer was made. In Fig. 6 the response to an applied voltage pulse, measured across the resistor R (see Fig. 1, inset (b)), are shown for two capacitors. It is seen that the signal has an oscillatory behaviour and that the initial peak is the dominating part of the signal. Some part of the curves, e.g the minimum observed at about 600 ps after the signal onset, is common for the different curves and is caused by variations in the waveform of the applied pulse. However, the initial oscillations demonstrate a charging behaviour. This can be related to the LRC circuit parameters. The oscillation period T_{osc} is given by

$$T_{osc} = 2\pi\sqrt{(1/LC - (R/2L)^2)}. \quad (5)$$

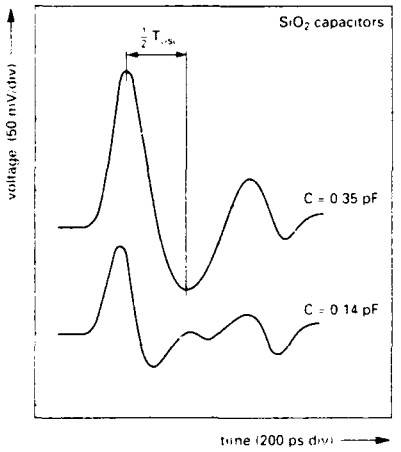


Fig. 6 Signal response to a voltage pulse for two SiO_2 capacitors on a Si wafer.

The half period $1/2T_{osc}$, measured as indicated in Fig.6, is shown in Fig. 7 as a function of capacitance for the different capacitors. It is seen that the measured period in a large range is proportional to $\sqrt{C}$. In this range the second term of Eq.(5) can be neglected. From this the circuit inductance L can be determined to be 10 nH. For small values of capacitance $1/2T_{osc}$ is essentially constant with a value of 80 to 90 ps. This value is slightly smaller than the estimated instrumental resolution.

For a ferroelectric capacitor one can discuss its behaviour on the basis of the equivalent diagram of Fig. 2b. The

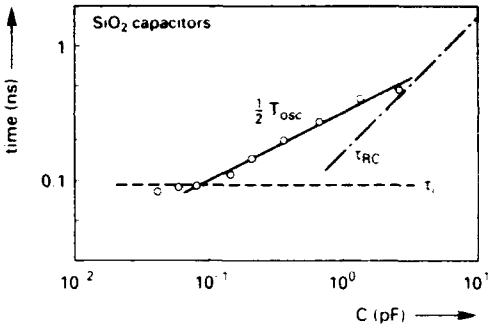


Fig. 7 The measured period 1/2 T_{osc} as a function of capacitance measured for SiO2 capacitors on a Si wafer

dielectric response (C_{diel} + C_p) will give rise to the same type of oscillations as just discussed. This limits the time resolution. Here we take $1/2T_{osc}$ as an appropriate circuit depending response time, denoted τ_{LC}. This is approximately given by

$$\tau_{LC} \approx \pi\sqrt{(LC)}. \quad (6)$$

The capacitance is determined as described above, using the nonswitching polarization change to determine C_{diel}.

For the non-linear polarization reversal response caused by C_{FE} (see Fig. 2b) there can be no oscillations since the charge is fixed after the reversal of polarization (until a pulse of opposite polarity and sufficient amplitude is applied). The charging time in this case is therefore given by Eq.(4). In order to allow a comparison of the two circuit dependent response times, the calculated time τ_{RC} is also shown as function of C in Fig. 7.

Preparation of PZT test structures

Ferroelectric PZT films of compositions x = 0.53 and 0.35 were grown on oxidized Si(100) substrates provided by a bottom electrode consisting of a thin Ti adhesion layer and a Pt layer. The top electrode deposited on the PZT film was Pt as well. Details about the electrodes have been given in Ref.(11). Five PZT thin film samples (A-E) were prepared by spin-coating techniques using different precursor routes. In all cases the films were prepared by repeating a spin-coating step followed by an intermediate heat treatment step until the desired film thickness was obtained. Subsequently the films were annealed at 650-700°C. Sample A with composition x = 0.53 was prepared by decomposition of organometallic compounds (MOD process) using a furnace pretreatment at 500 C after each coating. Details of the precursors etc. have been given in Ref.(12). Samples B-E were prepared by modified sol-gel techniques [12,13]. Samples B and C had the Ti-rich composition (x = 0.35). Sample B was given a high temperature pretreatment at 600°C after each coating, whereas sample C was pretreated at 300 C. The samples D and E had, similar to sample A, a composition located at the morphotropic phase boundary (x = 0.53). Both films (D, E) were given low temperature pretreatments at 300-350°C either by hot-plate heating (D) or by furnace treatment (E). The thickness of all five films after the final anneal (650-700 C) were in the range 0.40-0.45 µm.

Ferroelectric capacitors were prepared by etching away the top electrode and the PZT film outside the capacitor area. In this way there is access to both the bottom and top electrode within a short distance and the parasitic capacitance is minimized.

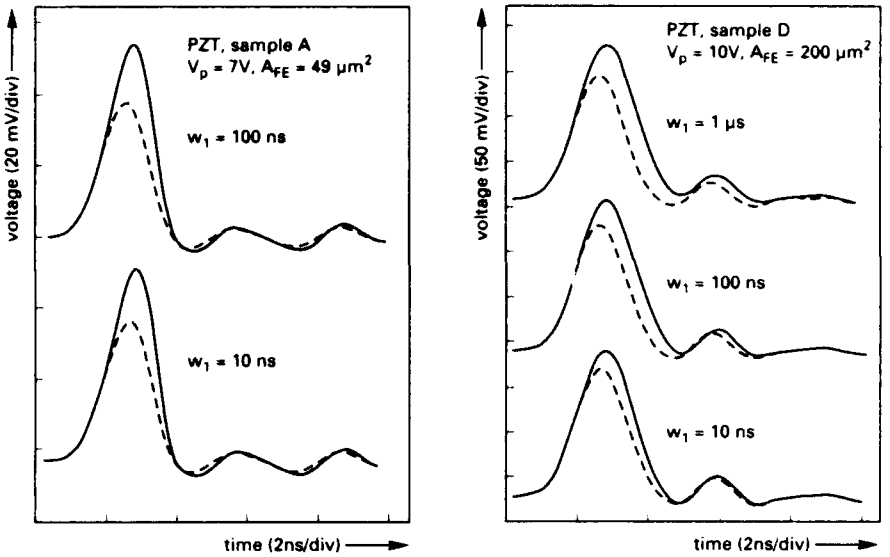


Fig.8 Measurements for samples A and D of the voltage across R for the first and the second pulse (solid and broken line, resp.) of a double pulse following upon a double pulse with opposite polarity.

Results

Influence of pulse width

It was discussed in the preceeding section that in order to assure that the experimental response time is small the ferroelectric charge to be switched also must be small. This of course leads to a decrease in the signal. If we compare 'fast' versus 'slow' switching of the same charge, the current will be larger in the former than in the latter case. Fast switching is therefore more readily detectable than slow switching. Obviously, there is a problem if the switching is distributed in time containing both fast and slow switching components. One way of investigating such effects is to measure the influence of the pulse width.

These measurements were made with a set-up which already was described in Ref.(8) and which has an instrumental time resolution of 2 ns. The pulse sequence in this case has double bipolar pulses. The delay (w_2) between the leading edge of two consecutive pulses of the same polarity was 10 μs, the delay between pulses of the opposite polarity (w_3) was 5 ms and the pulse width was variable between 10 ns and 2 μs.

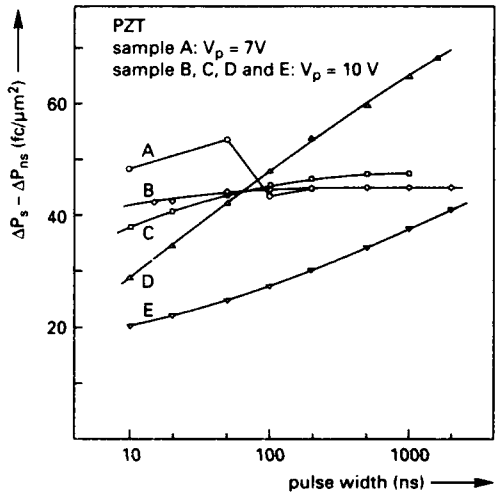


Fig. 9 The difference between the switched and nonswitched polarizations as a function of the pulse width for samples A, B, C and D. The lines are drawn to guide the eye.

Figure 8 shows for samples A and D the time dependence of the signal across R (see inset (a), Fig.1) for a switching and a nonswitching pulse using different pulse widths (the same for both polarities). For sample A, both curves are independent of the pulse width while for sample D the switching curve is reduced in amplitude with decreasing pulse width.

By integrating the signals the switched (ΔP_s) and nonswitched (ΔP_{ns}) polarizations can be determined. The difference, $\Delta P_s - \Delta P_{ns}$, between these two quantities corresponds to the difference between the positive and negative remanent polarizations. In Fig. 9, this difference is plotted versus the pulse width for all five samples. For samples C, D and E the polarization markedly decreases with the pulse width whereas for sample B the polarization is independent of the pulse width. The apparent increase in polarization for sample A is merely experimentally caused (e.g. due to measurements on different capacitors).

The increase in polarization with increasing pulse width for samples C, D and E can be ascribed to a distribution of switching times. For a short pulse width only a small part of the polarization can be reversed and consequently the state of the sample is less changed than it is after a longer pulse. For sample A and B the switching is faster than the minimum pulse width of 10 ns and consequently a greater width of the switching pulse does not increase the polarization.

For memory applications it is undesirable that the polarization depends on the pulse width and only samples A and B seem to have an appropriate behaviour. Clearly for a distinction between fast and slow switching behaviour, measurements are needed on a sufficiently small (fast) timescale. An evaluation on basis of 'low-frequency' hysteresis measurements is obviously improper. A further discussion of the results and the possible causes of the differences is given below.

Sub-nanosecond switching of PZT

In this subsection we describe measurements on sample A with the experimental set-up having sub-nanosecond resolution. Fig. 10 displays in the left hand panel the time dependence of the voltage across R for the switching and the nonswitching pulses for ferroelectric capacitors of different areas. In the right

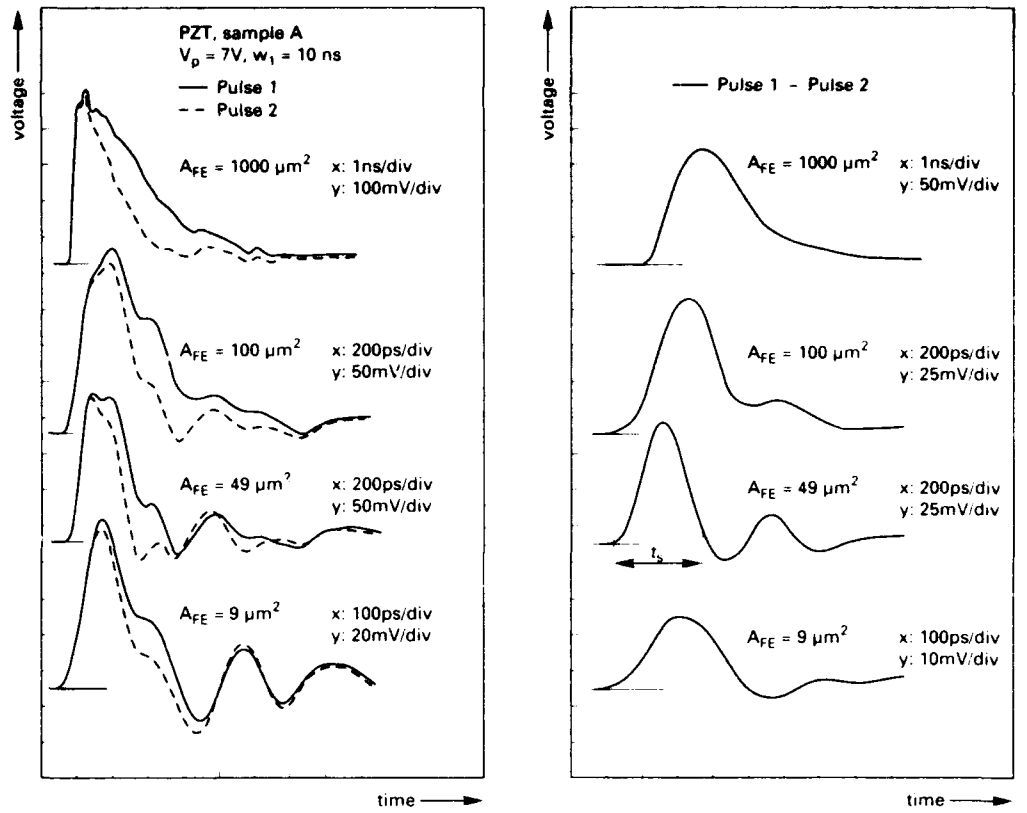


Fig. 10 Measurements on sample A. Left hand panel: Measurements of the voltage across R for the first and the second pulse (solid and broken curve, resp.) following upon a pulse of opposite polarity for ferroelectric capacitors having different electrode areas. Right hand panel: Curves of the difference between the voltages for the first and the second pulse.

hand panel the corresponding difference curves are shown. The curves show one main peak and a series of minor oscillations. These are largely caused by a non-ideal pulseform and were observed as well in the measurements of the SiO_2 capacitors described above. Here they are apparent if the curves for the capacitors of areas 100 and 49 µm² are compared (left hand panel). With decreasing area of the ferroelectric capacitors the response time of the signals decreases and switching times as short as 300-400 ps are observed.

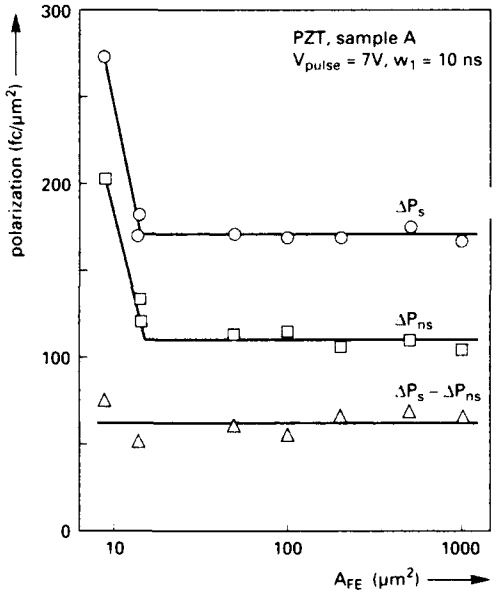


Fig. 11 The dependence of the polarization of sample A on the area of the ferroelectric capacitor.

From integration of the time dependent voltages the switched and non-switched polarization and their difference has been determined as function of the capacitor area A_{FE}. The results are shown in Fig. 11. For small areas there is an apparent increase in the polarization. This is caused by a parasitic capacitance and is not present in the difference curves. It should be noted that the polarization values determined in these measurements agree with those determined above using the other set-up.

After this verification of the measurements we turn back to Fig. 10. As a measure for the switching time we take the time from the onset of the difference pulse until the signal has decreased to 10% of the peak value. This time t_s is indicated in Fig. 10 (right hand panel, 49 µm²). In some cases the non-ideal pulseform has to be taken into account when measuring t_s. On the basis of two different measuring series, t_s has been determined as a function of the capacitor area and is plotted in the upper panel of Fig. 12. For $A_{FE} \geq 100$ µm² there is a marked increase of t_s with area while there is a levelling off for the smallest areas. This could mean that we are reaching either the intrinsic switching time for the ferroelectric film or a limit which is given by the experimental resolution. We have therefore calculated the time resolutions τ_{LC} (with $C = \Delta P_{ns} A_{FE}/V_p$) and τ_{RC} (with $C = \Delta P_s A_{FE}/V_p$) and these are shown in Fig. 12, upper panel, together with the instrumental resolution τ_i. Clearly, the experimental resolution is considerably smaller than t_s for the smallest capacitors but it cannot be neglected. If one corrects the switching time for the experimental broadening the true switching time t_s' should be obtained. This time is calculated by

$$t_s' = \sqrt{(t_s^2 - \tau_{LC}^2 - \tau_{RC}^2 - \tau_i^2)}. \quad (7)$$

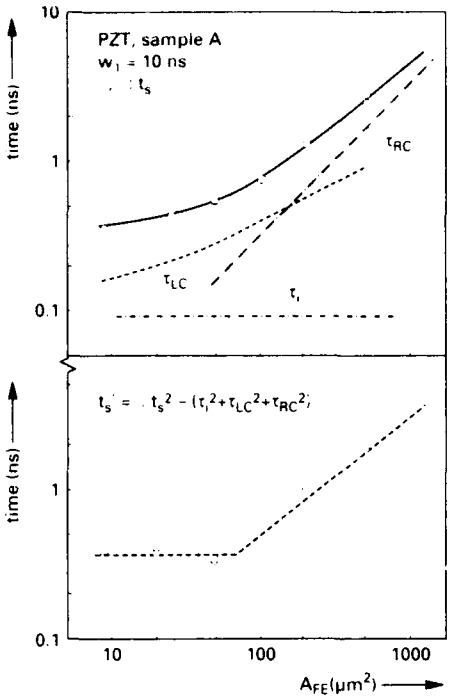


Fig. 12 Upper panel: The switching time ts measured for sample A as a function of the capacitor area. The circle and the squares represent two sets of measurements. The instrumental response time τ_i and the calculated times τ_{LC} and τ_{RC} are also shown. Lower panel: The switching time t_s' after correcting t_s for experimental broadening.

In Fig. 12, lower panel, t_s' is plotted as function of A_{FE}. For small areas it is constant within the experimental spreading and has a value of about 360 ps. Above 100 μm^2 t_s' increases with the area. Here the experimental resolution becomes larger than the true switching time and consequently a larger accuracy in determining both t_s' and the resolutions are needed to obtain reliable values in this range.

We have here experimentally determined a switching time of 360 ps for one sample at an electric field of 16 V/μm (V_p = 7V, d = 0.43μm). Other (preliminary) results indicate an increase in switching time for decreasing field but they will not be included here.

Discussion

There are two main points which we will address here. One is the explanation of why in some cases one finds that the switching has a wide time distribution while in other cases the switching is very fast. The second point is the discussion of possible causes of the very short switching time of 360 ps measured for an applied field of 16 V/μm for sample A.

Concerning the first point we note that samples C, D and E were prepared with a low temperature pretreatment step after each spin-coating, whereas sample A and B were prepared with a higher temperature furnace pretreatment. In the latter cases the temperature was high enough to produce crystalline PZT [12], while in the former cases only amorphous phases were formed (i.e. after each coating treatment). A recent investigation by Klee et al. [14] in which thin PZT films were prepared by different spin-coating techniques and investigated by transmission electron microscopy (TEM) has shown that in the case of high temperature heating steps after each spin-coating the film has a columnar morphology with an epitaxial relationship of the grains across the film. For the low temperature heating steps the film is

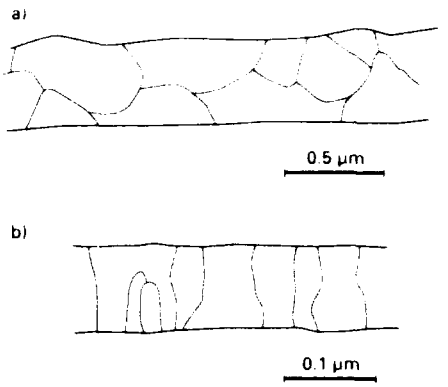


Fig. 13 Film morphology for a) a coarse grained PZT film and b) a fine grained film with columnar structure and an epitaxial relationship within the column For

ceramic-like with at least two grains across the film. These grains do not have any epitaxial relationship. In Fig. 13 the two structures are indicated with their typical dimensions (the bars indicate the lateral dimensions only).

The switching in the situation with a columnar, epitaxial structure is similar to that of a single crystal, while for the other case the situation is similar to a ceramic. The ferroelectric domains are limited within each grain and in the last case switching means at least a redistribution of charge within the film at the domain walls (at the grain boundaries). Since PZT is a good insulator this process needs time. With a distribution of grain sizes and crystallographic orientations one therefore expects a distribution of switching times, with each sample giving its own characteristiscs. This explains the observations for samples C, D and E and perhaps also the measurements described in Refs.(6,7). For the case of the columnar, epitaxial structure, domains can proceed across the film from one to the other electrode. Switching in which only charge redistribution occurs at the electrodes will not be limited by any internal charge redistribution and can therefore be fast. This is most probably the case for the switching in samples A and B.

In Fig. 14, we show two possible domain configurations allowing fast switching. In both cases the charge at the film/electrode interfaces changes in sign at switching. For the 180° domains there is no charge at the domain walls. For the 90° domains these domain interfaces are charged but with the same charge independent of the direction of the electric field. Therefore no charge redistribution at the domain walls is needed in this case.

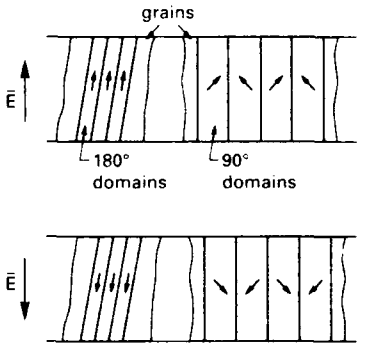


Fig. 14 A 180° and a 90° domain configuration in a film with a columnar structure with an epitaxial relationship across the film.

Finally, we will shortly comment on the actual switching mechanism. We exclude the case of two-dimensional domain growth because the lateral mobilities are very small [4]. Then

there seems to be two possibilities. One is the mechanism described by Merz [1] in which a high nucleation rate is supposed. The switching time is then determined by the speed of domain walls propagating across the film. With our results (t_s = 360 ps and d = 0.43 μm) one finds v_s = 1 km/s. This is still considerable smaller than the propagation speed of an elastic wave and might well be possible. However, the results obtained for single crystal $PbTiO_3$ indicated much smaller speeds at the actual field of = 15 V/μm. The second possibility is that described by Stadler [2]. In this case the switching is a bulk effect and is not caused by movements of domain walls. This means that all the dipoles in a domain are almost simultanously reoriented by the electric field. This behaviour has recently been treated by Cabezuelo et al. [15] and by Messenger [16]. In each unit cell the ions will change between equivalent configurations, separated by potential barrier(s).

Obviously, a further discussion of the details of switching requires further experimental information. The dependence of the switching time on thickness, field and temperature have to be studied. Knowledge about the relation between the actual domain structure and the switching time is needed. This can be obtained by carrying out switching measurements and TEM investigations on the same sample.

Summary

In this paper we have described an experimental set-up for ultrafast switching measurements. The instrumental time resolution was measured to be ≤ 100 picoseconds. An analysis of the test circuit showed that this could be considered as a LRC network having an non-linear ferroelectric capacitor. The switching and the nonswitching ferroelectric charges were shown to determine the RC and LC network time constants, respectively, and the overall experimental resolution. Experiments on PZT films demonstrated switching within 360 picoseconds as well as switching time distributions extending to more than 2 microseconds. It was argued that the extended switching times can be related to a ceramic-like morphology of the films and that they are caused by the time needed for charge redistribution within the films. The fast switching is observed in films with an epitaxial relationship within columnar grains. It can be explained by 180 and 90 domain configurations needing only charge redistribution at the film-electrode interphases during switching. Two switching mechanisms might explain the fast switching. One is based on a high nucleation rate and propagation of domains across the film thickness. The other one assumes a simultanous reorientation of the ferroelectric dipoles (bulk switching).

Acknowledgements

The authors wish to thank W. Brand and M. Ulenaers for their technical assistance in preparing and structuring the PZT films. A. de Veirman is gratefully acknowledged for discussions of her TEM work and G. Arlt for discussions of domain structures.

References

[1] W.J. Merz, "Switching Time in Ferroelectric $BaTiO_3$ and its Dependence on Crystal Thickness", J. Appl. Phys., vol. 27, pp. 938-943, 1954.

[2] H.L. Stadler, "Ferroelectric Switching Time of $BaTiO_3$ Crystals at High Voltages", J. Appl. Phys., vol. 29, pp. 1485-1487, 1958.

[3] H.L. Stadler, "Thickness Dependence of $BaTiO_3$ Switching Time", J. Appl. Phys., vol. 33, pp. 3487-3490, 1962.

[4] E.G. Fesenko, A.F. Semenchev and V.G. Gavrilyatchenko, "The Switching of $PbTiO_3$ Crystals", Ferroelectrics, vol. 13, pp. 471-473, 1976.

[5] J.F. Scott, B. Pouligny, K. Dimmler, M. Parris, D. Butler and S. Eaton, "Activation Field, Fatigue, and Waiting-Time Effects in KNO_3 Thin-Film Memories", J. Appl. Phys., vol. 62, pp. 4510-4513, 1987.

[6] J.F. Scott, L. Kammerdiner, M. Parris, S. Traynor, V. Ottenbacher, A. Shawabkeh and W.F. Oliver, "Switching Kinetics of Lead Zirconate Titanate Submicron Thin-Film Memories", J. Appl. Phys., vol. 64, pp. 787-792, 1988.

[7] H.M. Duiker, P.D. Beale, J.F. Scott, C.A. Paz de Araujo, B.M. Melnick, J.D. Cuchiaro and L.D. McMillan, "Fatigue and Switching in Ferroelectric Memories: Theory and Experiment", J. Appl. Phys., vol. 68, pp. 5783-5791, (1990).

[8] P.K. Larsen, G.L.M. Kampschöer, M.J.E. Ulenaers, G.A.C.M. Spierings and R. Cuppens, "Nanosecond Switching of Thin Ferroelectric Films", Appl. Phys. Lett., vol. 59, pp. 611-613, 1991.

[9] S.K.Dey, C.K. Barlingay, J.J.Lee, T.K. Gloerstad and C.T.A. Suchicital, "Advances in Processing and Properties of Perovskite Thin-Films for FRAMs, DRAMs, and Decoupling Capacitors", Proceedings 3rd Intern. Symp. Int. Ferroelectrics, Colorado Springs, pp.30-43, 1991.

[10] M.B. van der Mark, G.L.M. Kampschöer and P.K. Larsen, (in preparation).

[11] G.A.C.M. Spierings, J.B.A. van Zon, M. Klee and P.K. Larsen, "Influence of Platinum-Based Electrodes on the Microstructure of Sol-Gel and MOD Prepared Lead Zirconate Titanate Films", Proc. 4th Int. Symp. Integrated Ferroelectrics, Monterey, March 9-11, 1992.

[12] M. Klee and P.K. Larsen, "Ferroelectric Thin Films for Memory Applications: Sol-Gel Processing and Decomposition of Organo-Metallic Compounds", Proc. 25th Aniversary Meeting Dielectric Society, London, April 13-15, 1992.

[13] G. Yi, Z. Wu and M. Sayer, " Preparation of $Pb(Zr,Ti)O_3$ Thin Films by Sol Gel Processing: Electrical, Optical, and Electro-Optic Properties", J. Appl. Phys., Vol. 64, pp. 2717-2724, 1988.

[14] M. Klee, U. Mackens and A. de Veirman, " $Pb(Zr_xTi_{1-x})O_3$ Films Produced by a Modified Sol-Gel Technique: Thin Film Growth and Electrical Properties", Proc. 2nd Int. Symp.on Domain Structure of Ferroelectrics & Related materials, Nantes, July 7-10, 1992.

[15] M.J. Cabezuelo, J.E. Lorenzo and J.A. Gonzalo, "Ferroelectric Switching Revisited", Ferroelectrics, Vol. 87, pp. 353-359, 1988.

[16] G.C. Messinger, "Ferroelectric Memories: A Possible Answer to the Hardened Nonvolatile Question", IEEE Trans. Nucl. Sci., vol. 36, pp. 1461-1466, 1988.

LEAKAGE CURRENT MECHANISM AND ACCELERATED UNIFIED TEST OF LEAD ZIRCONATE TITANATE THIN FILM CAPACITORS

In K. Yoo and Seshu B. Desu
Department of Materials Science and Engineering
Virginia Polytechnic Institute and State University
Blacksburg, VA 24061

Leakage current was investigated for lead zirconate titanate (PZT) thin films on platinum (Pt) and ruthenium oxide (RuO_x) electrodes. Schottky emission was observed for both PZT capacitors. An accelerated unified test technique was also suggested which can measure fatigue and time dependent dielectric breakdown (TDDB) simultaneously in a short period of time. PZT films on RuO_x electrodes show longer breakdown lifetime than those on Pt electrodes under alternating voltage stresses.

Introduction

There have been many attempts to develop non-volatile memories using ferroelectric materials. It is well known that the main limitations for such commercial applications are degradation properties such as fatigue, aging, and electrical degradation including low voltage breakdown. With recent development of ceramic electrodes for ferroelectric capacitors[1-4], the fatigue problem has been overcome and it has been reported that no significant fatigue was observed up to 10^{11} test cycles for lead zirconate titanate (PZT) thin films using RuO_x electrodes[3,4]. However, it has also been pointed out that PZT films with such ceramic electrodes show higher leakage current than those with conventional metal electrodes, with long pre-breakdown range under DC electric fields[1]. In order to improve leakage current and breakdown properties for such films, the mechanisms for these phenomena should be understood extensively. Leakage current and TDDB of PZT films on Pt electrodes have been reported by some authors[5,6]. In this paper, the source of such conduction was investigated for PZT films on both Pt and RuO_x electrodes.

In our earlier studies on degradation properties, we have shown that oxygen vacancy is a common source of degradation properties and it is expected that reliability can be improved simultaneously by controlling oxygen vacancy behavior. This leads us to the realization of the importance of correlation studies among fatigue, aging, and leakage current/TDDB. The correlation studies also bring about the issue of necessity of simultaneous reliability test techniques. So far, each degradation test has been performed separately for qualification of a device. For example, fatigue was mainly tested under alternating pulses or square waves and time dependent dielectric breakdown (TDDB) test was carried out under DC electric fields. But , eventually, the device should be qualified under real service conditions. Hence, a unified test technique is required for simultaneous evaluation under the same service condition. It is also desirable to accelerate the unified test in order to evaluate devices in a short period of time. Therefore, breakdown of PZT films with both Pt and RuO_x was investigated in this paper in conjunction with fatigue for both correlation studies and development of unified test.

Leakage current

Current-voltage characteristic curves (I-V curve) for PZT films with Pt and RuO_x electrodes are shown in Fig. 1 where "instant" breakdown fields (the minimum electric field at which devices break down as soon as it is applied to the sample) are also shown. It was observed that PZT films with Pt electrodes show frequent fuse effect (momentary increase of leakage current during test) with low electrical degradation before breakdown. For RuO_x electrodes, electrical degradation (with a smaller scale of fuse effects that Pt electrodes) occurs earlier and lasts longer than Pt electrodes before breakdown. When polarity is reversed, I-V characteristic becomes asymmetric.

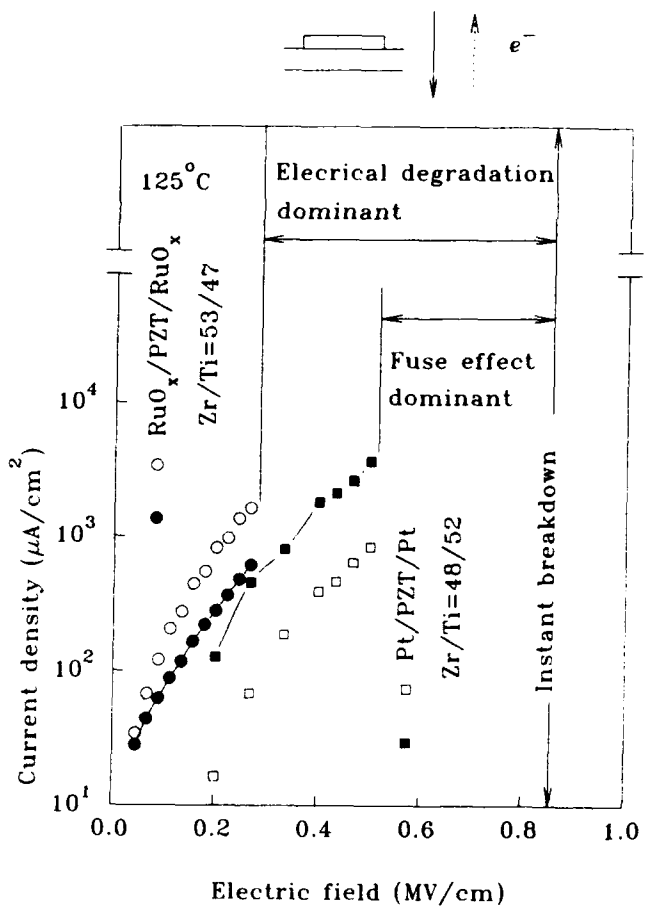


Fig. 1 Current-Voltage Characteristics

CH3080-0-7803-0465-9/92$3.00 ©IEEE

There are several types of leakage current mechanisms[7]. Ohmic behavior is observed at low fields. Under high electric fields, where devices exhibit non-ohmic current, electrical behavior is governed by oxygen vacancy diffusion, space charge limited current (SCLC) injection, grain boundary potential barrier, tunneling, Schottky emission, or Poole-Frenkel emission. SCLC injection occurs under fields on the order of 1-10kV/cm, and Schottky emission, under fields on the order of 0.1MV/cm. Tunneling is observed under fields on the order of 100MV/cm. I-V characteristics of PZT capacitors did not show ionic type conduction at temperatures lower than 150°C. It is hard to believe that leakage current of PZT thin films is controlled by grain boundary potential barrier because there exists little chance for the thin film to form grains across electrodes as long as film thickens is of the order of 1000Å. Therefore, the likely leakage current mechanism may be Schottky emission or Poole-Frenkel emission. Schottky emission occurs at the insulator-electrode contact and Poole-Frenkel, in the bulk. Then, the asymmetric I-V curve in Fig. 1, which is due to opposite polarity, highly supports the Schottky emission as a pertinent leakage current mechanism for PZT thin films, because the I-V curve should be symmetric for Pool-Frenkel emission as long as such emission occurs in the bulk.

The Schottky emission is analogous to thermionic emission of electrons from metal into vacuum. For metal-insulator junction, the emission is governed by the equation:

$$J = A^{**}T^2\exp[(-\phi_B + a\sqrt{E})/kT] \qquad (1)$$

where J is the current density, A^{**} is the effective Richardson constant, ϕ_B is the effective Schottky barrier height, a is a constant, and E is electric field. When the Schottky emission occurs in linear dielectrics, a plot of $\ln J$ versus $E^{1/2}$ (voltage dependence) or $\ln(J/T^2)$ versus $1/T$ (temperature dependence) would be linear. However, for ferroelectrics, there exists polarization under external electric fields and the polarization gives rise to an internal field. Thus, the net (effective) electric field is expressed as a local field and the electric field term should be replaced as follows:

$$E = E_A - \eta P \qquad (2)$$

where E_A is the applied external field, η is the depolarization factor, and P the polarization induced by external field E_A. Since polarization P is measurable at each electric field, when J versus $(E_A-\eta P)^{1/2}$ is plotted, it gives good curve fitting for PZT films as shown in Fig. 2. Temperature dependence of leakage current of PZT films are shown in Fig. 3. Electrical degradation starts as soon as electric field is applied at high temperature showing high current level. These currents are excluded when calculating activation energy of stabilized leakage current. PZT films with Pt electrodes show essentially the same Richardson constant for each polarity with dissimilar activation energies. The potential barrier difference may come from difference in PZT-Pt interface conditions between top and bottom electrodes which may be due to the effect of processing conditions. As for RuO_x electrodes, Richardson constant of the top electrode is different from that of the bottom electrode, which implies contact structures are different from each other. In the light of the fact that PZT films were annealed at 650°C after deposition on the bottom electrode, and the top electrode was deposited on PZT with no annealing, it is highly possible that an interlayer forms between PZT and bottom electrode only. Even though PZT/bottom electrode forms higher potential barrier than top electrode, it gives higher Richardson constant, which results in higher electron emission from bottom to PZT than from top to PZT.

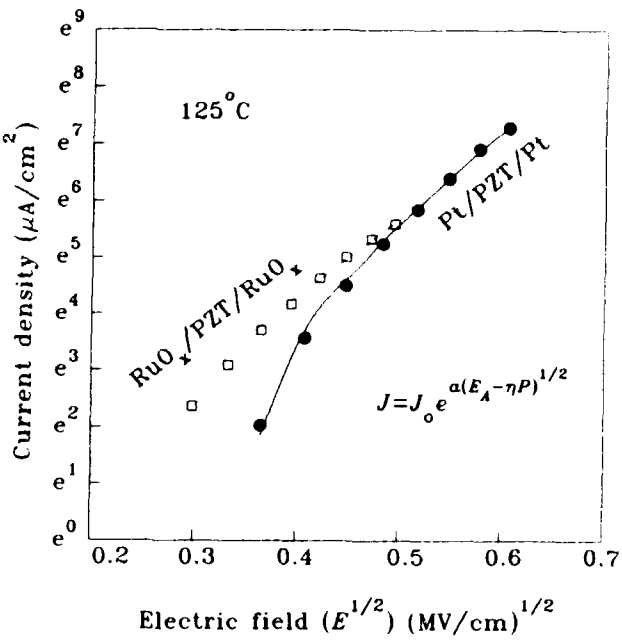


Fig. 2. Internal Field Effect on I-V Characteristics

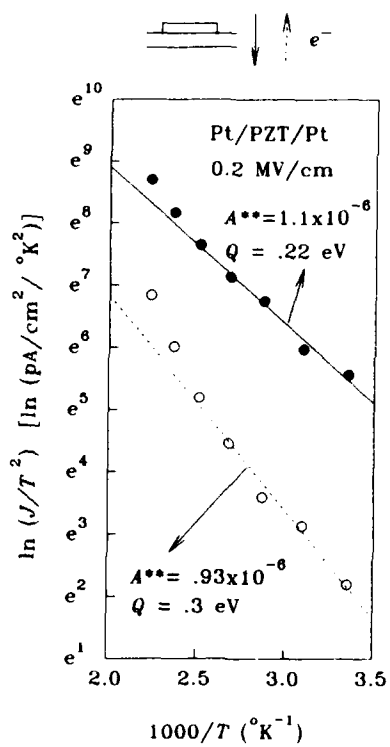


Fig.3.a Temperature Dependence of Leakage Current (Pt).

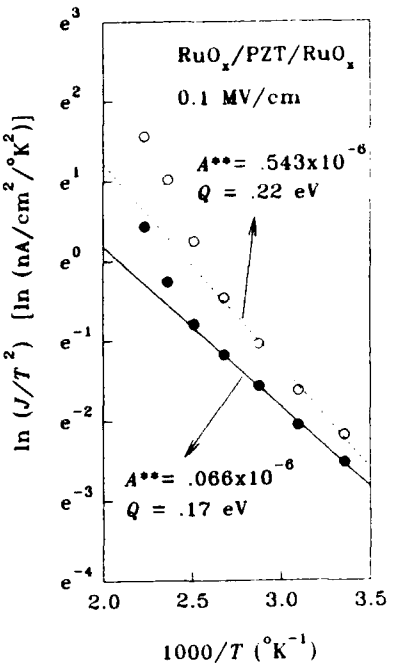


Fig.3.b Temperature Dependence of Leakage Current (RuO_x).

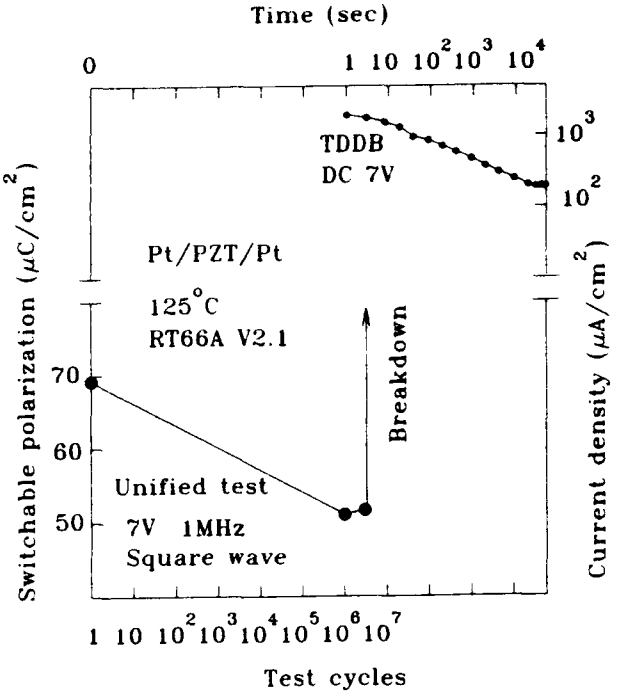


Fig. 4 Breakdown Test under DC and AC Field.

Accelerated unified test

The conventional breakdown test of a device is carried out under DC electric field at a certain temperature. But in ferroelectric memory applications, alternating pulses are applied to devices in order to switch their polarization state. In this case, the actual breakdown occurring under AC pulses may show different TDDB results from those under DC bias. Since breakdown test under such AC field is close to real service conditions, it is desirable for reliability testing to run fatigue test until breakdown occurs. In general, however, fatigue test takes a long time with much more delayed breakdown under normal conditions such as at room temperature up to 10^{11} cycles, so that the test needs to be accelerated controlling frequency, voltage, temperature, etc. in order to save testing time. An example of accelerated unified test for PZT films is shown in Fig. 4, where TDDB under DC voltage is evaluated by testing time and unified fatigue/breakdown, by test cycles. Comparison of the unified test between Pt and RuO_x electrodes is illustrated in Fig. 5, where PZT films with Pt electrodes show fast fatigue with sudden breakdown when samples are tested by 1MHz square wave at 200°C and ±7V. On the other hand, RuO_x shows no breakdown up to 10^9 cycles. This may result from long range of pre-breakdown of PZT films on RuO_x electrodes. Even though electrical degradation occurs earlier in PZT films on RuO_x, it does not affect polarization as long as the current level is still low compared to the polarization. As for Pt electrodes, it may show longer lifetime than RuO_x because it has lower electrical degradation rate; however, fuse effect might affect polarization during operation even if it is not the real dielectric breakdown. In general , it has been observed that once PZT with Pt electrode break down after fatigue/breakdown test, it shows permanent failure, which means that the sudden increase of polarization in unified test for PZT with Pt electrodes is caused by real breakdown. It is possible that breakdown has been accelerated by alternating electrical shock.

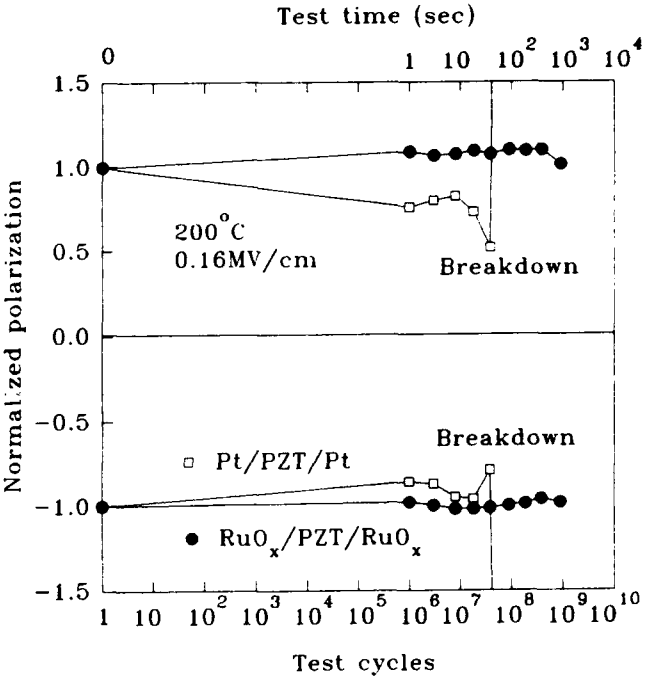


Fig. 5 Unified Test for PZT Capacitors

As pointed out in fatigue mechanism[1,2], PZT-electrode interface tends to trap vacancies such as oxygen vacancy because of mismatch in lattice structures between PZT and the electrodes. Then vacancies are continuously trapped at the interface for the Pt electrode even under AC field because of abrupt transition of chemical potential from PZT to Pt. On the RuO_x forms smoother chemical potential transition in that sense and therefore the vacancies can move back and forth under alternating voltage stresses. Vacancies will move more freely from PZT to RuO_x under DC field and gives higher electrical degradation which might be related to the ionic conduction; however, this degradation can be partially healed by opposite vacancy movement from RuO_x to the PZT bulk, which can delay the breakdown. Similar "healing effect" by vacancy movement has been reported by some authors[8].

Conclusions

Following results are obtained from this research.

1) Leakage current of PZT capacitors shows Schottky emission behavior.

2) Schottky barrier heights are asymmetric between top and bottom electrodes probably because of different electrode processing conditions during capacitor fabrication.

3) PZT capacitors with RuO_x show earlier electrical degradation than those with Pt electrodes under DC electric field. However, films on RuO_x show better breakdown properties under AC field because of healing effect due to better lattice match between PZT and electrodes.

References

[1] S.B. Desu and I.K. Yoo, "Electrochemical Models of Failure in Oxide Perovskites," ISIF 92 Proceedings, 1992.

[2] I.K. Yoo and S.B. Desu, "Mechanism of Fatigue in Ferroelectric Thin Films, " Physica Status Solidi(a), vol. 133, no. 2, 1992

[3] D. Vijay, W. Pen, C.K. Kwok, I.K. Yoo, and S.B. Desu, "Electrode Effects on Electrical Properties of PZT Thin Films, " ISAF 92 Proceedings, 1992.

[4] S.D. Bernstein, T.Y. Wong, Yanina Kisler, and R.W. Tustison, "Reactively Sputtered RuO_x Electrodes for Ferroelectric PZT Capacitors.

[5] J. Carrano, C. Sudhama, and J. Lee, "Electrical and Reliability Characteristics of Lead Zirconate Titanate (PZT) Ferroelectric Thin Films for DRAM Applications," IEEE IEDM, pp.255-256, 1989.

[6] C. Sudhama , J.C. Carrano, L.H. Parker, V. Chikarmane, J.C. Lee, A.F. Tasch, W. Miller, N. Abt, and W.H. Shepherd, "Scaling Properties in the Electrical and Reliability Characteristics of Lead Zirconate Titanate (PZT) Ferroelectric Thin Film Capacitors," MRS Sym. Proc. vol. 200, pp.331-336, 1990.

[7] H.Y. Lee, K.C. Lee, J.N. Schunke and L.C. Burton, "Leakage Current in Multilayer Ceramic Capacitors," IEEE Trans. , vol. CHMT-7, no. 4, pp. 443, 1984.

[8] I.K. Yoo, L.C. Burton, and F.W. Stephenson, "Instability of Insulation Resistance for Thick Film Capacitors," ISHM Proc., pp.83-87, 1985.

AC CONDUCTIVITY AND DIELECTRIC PROPERTIES OF SOL-GEL PZT THIN FILMS FOR FERROELECTRIC MEMORY APPLICATIONS

Xiaohua Chen, Angus I. Kingon and Orlando Auciello*
Department of Materials Science and Engineering,
North Carolina State University, Raleigh, NC27695-7907, U.S.A.
*Also Microelectronic Center of North Carolina

Abstract

Dielectric properties and a.c. conductivity of sol-gel PZT thin films are measured at frequencies between 10 and 10^6 Hz and temperatures between 25 °C and 500 °C. At high frequencies, e.g. > 2 kHz, a maximum is observed in the real part of the complex dielectric constant, which corresponds to the Curie point. However, at low frequencies, e.g. 200 Hz, the dielectric constant increases monotonically with temperature. A space charge blocking model and an electric charge hopping model are discussed in order to explain this phenomenon. Further experimental results on the frequency dependence of dielectric constant and a.c. conductivity provide additional support for the charge hopping model. The activation energy of a.c. conductance at high (Q1) and low (Q2) temperature ranges are obtained by fitting the data with formula $G_{ac}=G_{10}e^{-Q_1/kT}+G_{20}e^{-Q_2/kT}+G_{er}$. These values are about 1.3 ev and 0.34 ev, respectively, and have the relation $Q_2=(1-n)Q_1$. Implications are discussed.

Introduction

The ability to fabricate ferroelectric thin films has brought about extensive research on macroscopic electric and ferroelectric behavior, such as fatigue, retention and leakage current. These macroscopic properties directly determine the performance of the ferroelectric device. It is commonly believed the properties are related not only to the lattice structure of the film material, but also to other microscopic factors, such as, electrode/ferroelectric thin film interface, grain and/or domain boundaries, space charges, donor or *acceptor dopants, etc.*. To improve the performance of the devices, it is very important to understand the effects of the microscopic features mentioned above on the macroscopic system properties. In this paper, we concentrate on the small signal (low applied voltage) properties. While the device operate at high applied field, they are commonly exposed continuously to low fields. In addition, the low field properties may be correlated directly to the microscopic features mentioned above.

For an ideal ferroelectric bulk material, the real dielectric constant usually shows a peak around the ferroelectric/paraelectric phase transformation temperature, and obeys the Curie-Weiss law on the higher temperature side of the peak [1]. This peak is an indication of the phase transformation. However, our experimental results of sol-gel $PbZr_xTi_{1-x}O_3$ (PZT) thin films showed that sometimes, especially at low frequencies, the peak might not appear, instead, the real dielectric constant monotonically increased with temperature. The monotonic increase has been observed in many dielectrics, and was attributed to space charge blocking effect [2]. The question which arises is whether, for the PZT thin films, the phenomenon can also be explained with the space charge blocking effect ,or whether an alternative mechanism must be invoked. In the present paper, we will show that for PZT thin films, there is difficulty in utilizing the space charge blocking model to explain the experimental results. An alternative model will be discussed.

Experimental

The sol-gel PZT thin films (Zr/Ti =53/47) analyzed in this paper were provided by Raytheon Corporation. They were deposited onto oxidized silicon substrates with about 1000 Å films of Ti and Pt serving as the bottom electrode. The PZT film thickness is about 1700Å. Top contacts of $100x100(\mu m)^2$ area were deposited by a plasma sputter deposition technique with lift-off photolithography. Ferroelectric hysteresis loop measurement revealed good ferroelectric behavior.

The a.c. conductance and complex capacitance were measured by an HP4192A Impedance Analyzer. The temperature of the film during the measurements was controlled by an OMEGA mode CN2010 temperature controller. The whole experimental system was controlled by an HP9000/PC305 computer. For the a.c. measurements, the signal level was set at 0.1 V, and the parallel circuit mode was used.

Results and Discussions

Since dielectric constant and conductivity are directly proportional to the capacitance and conductance of specimen capacitor, respectively, for simplicity, we will just show capacitance and conductance data without converting to the corresponding dielectric constant and conductivity. Figure 1 shows the real part (C') of the complex capacitance of PZT thin film vs. temperature for various frequencies. At high frequencies, the capacitance shows a wide peak around the Curie temperature of PZT, which indicates the ferroelectric/paraelectric phase transformation as mentioned before. However, at low frequencies, the capacitance increases monotonically with temperature, without showing the phase transformation peak. The increase of the dielectric constant with temperature at low frequencies has been observed in many dielectric bulk materials and has been attributed to space charge blocking at electrodes [2]. It has been suggested that high signal frequencies be used to avoid this space charge blocking effect . For the PZT thin films, from Fig.1, it seems initially that the observed phenomena can be explained by the phase transformation dominating the dielectric behavior at high frequencies, but with the space charge effect masking the peak at *low frequencies*. However further experiments discussed below will show that the space charge effect can not fully account for all the experimental results. Another mechanism must be invoked to explain the results.

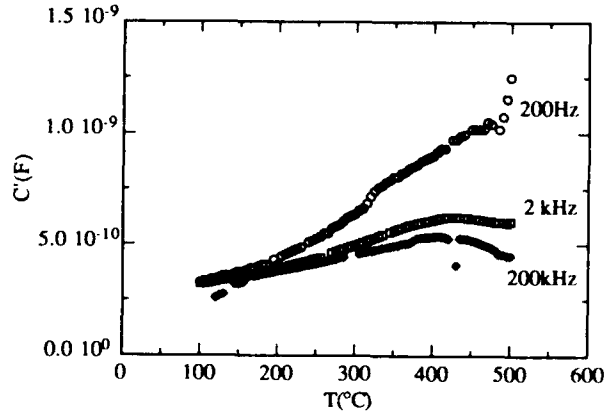


Fig.1 Real part of complex capacitance as functions of temperature at various frequencies for sol-gel PZT thin film.

Before proceeding with the discussion, it is relevant to clarify the term "space charge " in insulators.

Space charge usually appears in insulators, semiinsulators and semiconductors. Since PZT is an insulator, we will just restrict the discussion to insulators in the present paper. The general term " space charge " has often been used in literature without specifying *the nature*. However, it can have several different meanings based on the origin of the charge. It can be roughly classified into the following categories:

1) The charge resulting from carriers which are injected from electrode into the insulator under a strong electrical field[3].

CH3080-0-7803-0465-9/92$3.00©IEEE

These charge carriers are usually electronic. The charge carriers distribute in the insulator nonuniformly. If the electrical current is controlled by this type of space charge, it follows the Langmuir-Child law, i.e. $I = b V^2$, where I and V are d.c. electric current and applied voltage, respectively, b is a constant [3].

2) The charge within the depletion region which results from the mismatch of the Fermi level of the electrode and the insulator, or from the surface states of the insulator. This kind of charge is nonmobile. This is the case of the so called Schottky contact in the semiconductor field [4].
3) The charge accumulated around grain boundaries in some ionic ceramic materials without any external electric voltage applied. Since the energy to form a negatively charged cation vacancy differs from that of positively charged anion vacancy on grain boundary, there exists an excess of one type of charge which must be neutralized by opposite charges. These opposite charges distribute around the grain boundary, forming the space charge cloud [2].
4) The charge resulting from the carriers which pile up in the front of blocking electrodes or other blocking interfaces, e.g. grain boundaries, after application of an electric field. This effect is also known as interfacial polarization. The charges were compensated by each other or by other charges in the insulator before the electrical voltage is applied. After an electrical voltage is applied, the carriers with positive and negative charges migrate in opposite directions until they are stopped by the blocks mentioned above, forming the space charge zone. The space charge blocking effect can lead to the dispersion of the real dielectric constant at low frequencies, and particularly at higher temperatures because of the higher mobility of the charge carriers [2,5]. This type of space charge is what is referred to in the space charge blocking model mentioned in the proceeding sections. In the following sections, when we mention space charge, it will always mean this type of space charge.

The space charge blocking effect on a.c. conductivity and dielectric properties has been intensively studyed theoretically and experimentally [6,7]. The basic results are that both real dielectric constant ε' and a.c. conductivity σ_{ac} exhibit a step like change, similar to a Debye relaxation behavior as depicted in Fig.2. The log-log plot of ε' vs. $\omega\tau$ reveals a straight line with a slope of -2 in the transient frequency range [7]. These behavior are the characteristics of a Debye relaxation. As a matter of fact, the interfacial polarization can be simulated by a capacitor with or without leakage. This capacitor is connected in series with the ferroelectric film layer which is usually represented by a parallel capacitor - resistor unit [5,6] . The process of charging to this system is virtually of a Debye relaxation. Figure 2 depicts theoretical curves of the real (ε') and imaginary (ε'') parts of the complex dielectric constant and a.c. conductivity (σ_{ac}) vs. frequency ($\omega\tau$) of an ideal Debye relaxation. Here ω is angular frequency, τ is the relaxation time. In real cases, the curve may change somewhat, e.g., the peak may be widen. However, the relaxation characteristics , i.e., the step changes of σ_{ac}, ε' vs. $\omega\tau$ and the peak of ε'' vs. $\omega\tau$ remain unchanged [5-7].

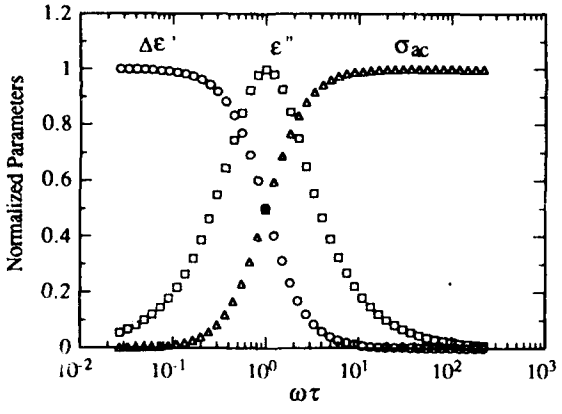


Fig.2 Normalized a.c. conductivity σ_{ac}, real (ε') and imaginary (ε'') parts of complex dielectric constant of an ideal Debye relaxation as functions of frequency. $\Delta\varepsilon' = \varepsilon' - \varepsilon$. τ is relaxation time.

For the case of PZT thin films, the dielectric properties (complex capacitance) and the a.c. conductance G_{ac} were measured as functions of frequency and temperature . The real part C' of the complex capacitance vs. frequency at various film temperatures are shown in Fig.3. Being consistent with Fig.1, the real capacitance at high temperatures in Fig.3 show a strong dispersion at low frequencies. However, the characteristic of the space charge blocking effect, i.e., a step change as shown in Fig.2 was not observed. Figure 4 shows a plot of a.c. conductance vs. frequency at various temperatures for the same specimen analyzed in Figs.1 and 3. No step change like that shown in Fig.2 was observed , either. On another sol-gel PZT thin film from an alternative source, we once measured C' and G_{ac} as functions of frequency at up to 600 °C and at down to 5 Hz , and no sign of the step change of C' and G_{ac} were observed. The phenomena described above have also been observed in laser ablated PZT thin films [8]. These experimental results could not be explained by the space charge blocking effect alone.

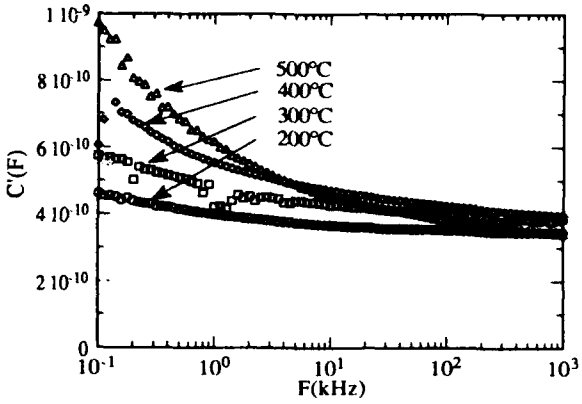


Fig.3 Real capacitance vs. frequency at various temperatures for sol-gel PZT thin film. The dispersion at high temperatures are obvious. No shoulder as shown in Fig.2 was observed down to 5 Hz at up to 500 °C.

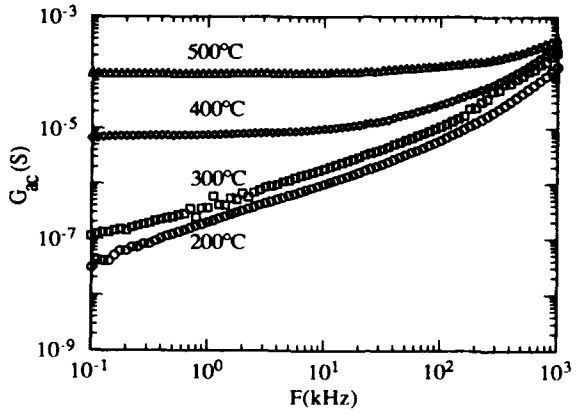


Fig.4 AC conductance of a sol-gel PZT thin film as functions of frequency at various temperatures. At lower temperatures (< 200 °C), Gac~ω^n at frequencies between 10 Hz and 100kHz. The slope n is about 0.7 .

By further inspection of Fig.4, some interesting features can be observed. At low temperatures (< 300°C), the log-log plot of a.c. conductance exhibits a linear behavior in 10^{-1}-10^{-2} kHz frequency range. At high temperatures (>350°C), a component which is independent of frequency, a characteristic of d.c conduction , becomes dominant at low frequencies. Generally, a.c. conductance is composed of two parts, i.e.,

$$G_{ac}=G_0+G(\omega) \quad (1)$$

where G_0 is the frequency independent component which predominets at high temperatures and low frequencies, and $G(\omega)$ is frequency dependent component which is proportional to ω^n and predominant at low temperatures and high frequencies. The exponent n is equal to the slope of the log-log plot , and was found to be about 0.6~0.8 in our sol-gel PZT thin films. Comparing Fig.3 with Fig.4, it appears that the strong low frequency dispersion of real capacitance is related to the frequency independent component G_0 . This implies that the G_0 is not simply due to the normal d.c. conduction because a normal d.c. conduction does not contribute to any polarization, hence to the dielectric constant .

In order to get a better insight into the mechanism governing the real capacitance and conductance behavior analyzed above, imaginary part (C") of the complex capacitance was calculated from the a.c. conductance by using the formula $C''=\omega G_{ac}$ [2]. A log-log plot of C" vs. F for various film temperatures are shown in Fig.5. The first noticeable feature is that there is no peak which is one of the characteristics of the space charge blocking effect. Secondly, the slope of the straight line of logC"~log F at high temperatures and low frequencies equals -1 which is the natural result of the frequency independent conduction.

The above-described behavior has been widely observed in so-called charge carrier systems [9-11]. Jonscher performed extensive analysis of a great deal of dielectric data for a large number of materials, and suggested dividing those materials into two types [11]. The first type includes the materials in which dipoles play a major role in the polarizing process. In this type of dipole systems, dielectric loss peak can be observed in the frequency spectrum. This peak is due to the dipole reorientation under the applied electric fields. The second includes the materials in which hopping charge carriers, electrons or electronic holes, ions etc., dominate the polarizing process. For this type of charge carrier systems, no dielectric loss peak could be observed even at the lowest frequencies. Instead, a strong low frequency dispersion of real dielectric constant was commonly observed [11]. Our PZT thin films clearly belong to the second type.

Moreover, Jonscher also recognized that the dielectric behavior of the charge carrier systems usually obey a "universal" power law of the form: [10]

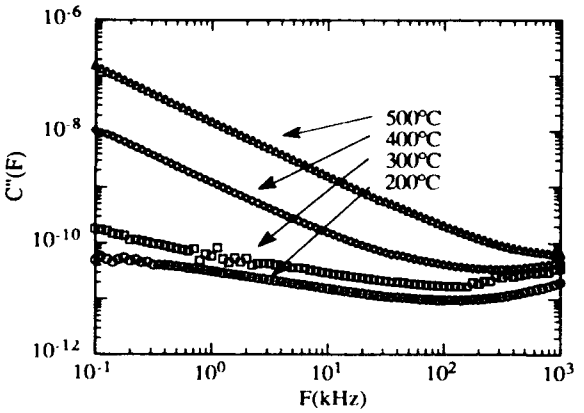


Fig.5 Imaginary part of the complex capacitance of a sol-gel PZT thin film vs. frequency at various temperatures. The slope at 500 °C and 400°C at low frequency range are -1.

$$C''(\omega) \sim (\omega/\omega_c)^{n_1-1}+(\omega/\omega_c)^{n_2-1} \quad (2)$$

where both exponents n_1 and n_2 are in the range of 0 to 1. ω_c is thermally activated and determined by hopping distance, activation energy, temperature and other parameters [12,13]. It has the form:

$$\omega_c=\omega_e e^{-E_a/kT} \quad (3)$$

where ω_e is a characteristic frequency and E_a is hopping activation energy. By using the relation between a.c. conductance G_{ac} and imaginary capacitance C", Eq.(1) can be easily derived from Eq.2, i.e.,

$$G_{ac}=\omega C'' \sim \omega((\omega/\omega_c)^{n_1-1}+(\omega/\omega_c)^{n_2-1}) \quad (4)$$

In the special case, $n_1=0$, $n_2=n$, Eq.(4) becomes

$$G_{ac}=p\omega_c + p(\omega_c)^{1-n}\omega^n = G_0+G(\omega) \quad (5)$$

where p is a constant, $G_0=p\omega_c=p\omega_e e^{-E_a/kT}$, which is frequency independent component with an activation energy of E_a; $G(\omega)=A\omega^n$, which is frequency dependent component. Here A is independent of frequency, but dependent on temperature in the form

$$A=p(\omega_c)^{1-n}=p\omega_e^{1-n}e^{-(1-n)Ea/kT} \quad (6)$$

Obviously, the *apparent* activation energy $(1-n)E_a$ of $G(\omega)$ is much smaller than the activation energy of G_0.

In order to confirm the validity of Eq.(5) to our PZT thin films, the activation energy of the frequency dependent and independent components were measured by fitting the curve of the a.c. conductance vs. reciprocal of temperature using the equation :

$$G_{ac}=G_{10}e^{-Q_1/kT}+G_{20}e^{-Q_2/kT}+G_{er} \quad (7)$$

where the first and second terms correspond to G_0 and $G(\omega)$ in Eq.(1) or Eq.(5), respectively. Q_1 and Q_2 are the corresponding activation energy. G_{er} is a temperature independent but frequency dependent parameter which needs to be introduced to get a good fitting. It is not clear at this time whether G_{er} has any physical meaning , e.g. a representation of some temperature insensitive conduction processes, or not at all. In any case, the first two terms are the main object of the discussion here.

Figure 6 shows the a.c. conductance vs. reciprocal of the film temperature for three different frequencies. The data was obtained on cooling. In the later period of measurements, i.e., at lower temperatures, good contact between the electrical probe tip and the top Pt contact on the PZT film could be broken due to a thermally induced contraction of the probe tip. Therefore, the probe tip needed to be relocated on the Pt contact whenever a break occurred. The relocation of the electrical probe tip may be responsible for the abnormal abrupt changes observed in Fig.6, especially on the curve of 0.2 kHz. In the figure, the solid lines are the fitting curves. The fitting is very good at 20 kHz and 2 kHz. At 0.2 kHz, because the conductance value is in the vicinity of the sensitivity of instrument, and also because of the above-mentioned probe tip relocation, the data deviates from the fitting curve. It is relevant to notice that the curve section in the high temperature range and low frequencies is the frequency independent component, while the less temperature sensitive part is the frequency dependent part. Table I shows the activation energy obtained from the fitting. Taking 0.72 as an average value of n obtained from the curves of $G(\omega)$ vs. F at low temperatures in Fig.4, it can be seen from the table that the relation $Q_2=(1-n)Q_1$ is valid within experimental error at the tested frequencies. Therefore, it is very likely that the a.c. conductance and the dispersion behavior described in the present paper are mainly governed by electrical charge hopping mechanism.

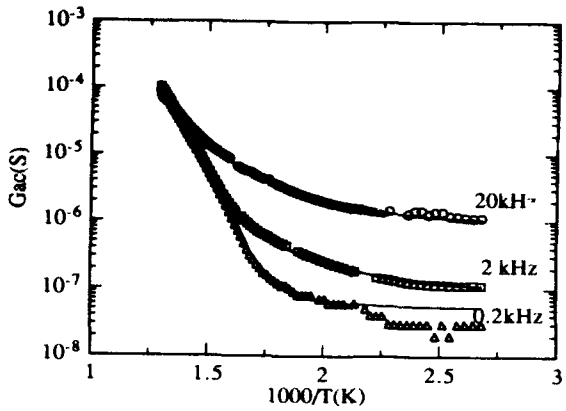


Fig.6 AC conductance vs. 1000/T at three different frequencies. The cycles, squares and triples are experimental data. The solid lines are fitting curves utilizing Eq.(7). The deviation of the experimental points from the fitting curve at low temperatures on the 0.2 kHz curve is an artifact.

Table I The activation energy of the two components of a.c. conductance at three different frequencies obtained by fitting G_{ac}~1/T in Fig.6 using Eq.(7).

F (kHz)	Q_1(ev)	Q_2(ev)
0.2	1.3	0.33
2	1.3	0.34
20	1.2	0.36

Conclusions

1. At high frequencies, phase transformation peak of real dielectric constant was observed. At low frequencies, real dielectric constant monotonically increases with temperature. Space charge blocking model and electric charge hopping model are discussed. The latter is more likely the mechanism governing the observed phenomena.
2. Similar to that in laser ablation PZT thin films, a strong low frequency dispersion of real dielectric constant was observed at high temperatures, which is closely related to a d.c. component of a.c. conductivity.
3. The a.c. conductance at high temperatures are much more sensitive to temperature than that at low temperatures. The activation energy Q_1 at high temperatures is about 1.3 ev. The apparent activation energy Q_2 at low temperatures is about 0.35 ev. Q_1 and Q_2 have the relation of $Q_1=(1-n)Q_2$. Here n is the exponent in the formula $G(\omega) \sim \omega^n$, which was found to dominate at low temperatures. Electric charge hopping model was employed to interpret these phenomena.

Acknowledgements

This work was supported by DAPAR under contract number of 90F131300. The authors thank S.E.Bernacki of Raytheon Equipmemt Division for providing sol-gel PZT film and K.D.Gifford of NCSU for the help in top contact deposition.

References

[1] Yuhuan Xu, Ferroelectric Materials and Their Applications, New York: North-Holland, 1991, Ch.1, pp.11-24.

[2] W.D.Kingery, H.K Bowen and D.R.Uhlmann, Introduction to Ceramics , New York: John Wiley & Sons, 1976, Ch.18, pp.931-937; Ch.5, pp.190-197..

[3] C.Hamann, H.Burghardt and T.Frauenheim, Electrical Conduction Mechanisms in Solids , Berlin: VEB, 1988, Ch.8, pp.190-206.

[4] S.M.Sze, Physics of Semiconductor Devices, New York: John Wiley & Sons, 1981, Ch.5, pp.245-311.

[5] A.R.Von Hippel, Dielectrics and Waves , New York: John Wiley & Sons Inc, 1954, Ch. II, pp.228-234.

[6] P.B.Macedo, C.T.Moynihan and R.Bose, " The role of ionic diffusion in polarisation in vitreous ionic conductors", Phys. and Chem. of Glasses, vol.13, pp.171-179, Dec. 1972.

[7] M.E.Lines, " Interfacial polarization effects in ionic conductors", Phys. Rev.B, vol. 19, pp. 1189 -1195, Jan. 1979.

[8] X.Chen, A.I.Kingon, L. Mantese , O.Auciello and K.Y.Hsieh, "Characterization of conduction in PZT thin films for ferroelectric memory applications", in Proceedings of the 4th International Symposium on Integrated Ferroelectrics, Monterey, California, 1992.

[9] A.K.Jonscher, " Low frequency dispersion in carrier-dominated dielectrics", Phil Mag. B, vol.38, pp.587-601, 1978.

[10] A.K.Jonscher, " Universal Dielectric Response", Phys. Thin Films, vol.11, pp.222-232, 1980.

[11] A.K.Jonscher, Dielectric Relaxation in Solids, London: Chelsea Dielectrics Press, 1983, Ch.4-Ch.8.

[12] D.P.Almond, A.R.West and R.J.Grant, "Temperature dependence of the a.c. conductivity of Na β-Alumina", Solid States Communication. vol.44, pp.1277-1280, 1982.

[13] S.R. Yang and K.N.R.Tay, "Ionic conductivity in single-crystal proustite Ag_3AsS_3," J. Appl. Phys. , vol. 69 (1), pp.420-428, Jan. 1991.

Thin Films: Electrical Properties

MEASUREMENT OF ELECTRO-OPTIC COEFFICIENT OF FERROELECTRIC PLZT THIN FILMS

Wei-Gen Luo, Ai-Li Ding and Rui-Tao Zhang
Shanghai Institute of Ceramics, Chinese Academy of Sciences, Shanghai 200050 China
K.S. Chan and G.G. Siu
Department of Applied Science, City Polytechnic of Hong Kong, Hong Kong

A new and simple method is described for measuring the quadratic electro-optical (E-O) coeffecients of thin ferroelectric PLZT films. A magneto-optical modulator is positioned between a polarizer and analyzer in the conventional measurement system for E-O coefficient. The polarization state of light passing through the magneto-optical modulator will be modulated due to Faraday effect. The proposed technique measures phase retardation shift through determing the frequency change of the modulated light. The main error of the measuring system comes from reading goniometers with precision of 10^{-5} radiant. So measurable retardation of optical path is the order of a few Angstroms. The expermental results are present with thin ferroelectric PLZT films made by magnetron sputtering. The quadratic E-O coefficient of PLZT films varies in the range of $0.1X10^{-16}$ to $1.0X10^{-16}(m/v)^2$ depending on the sputtering conditions.

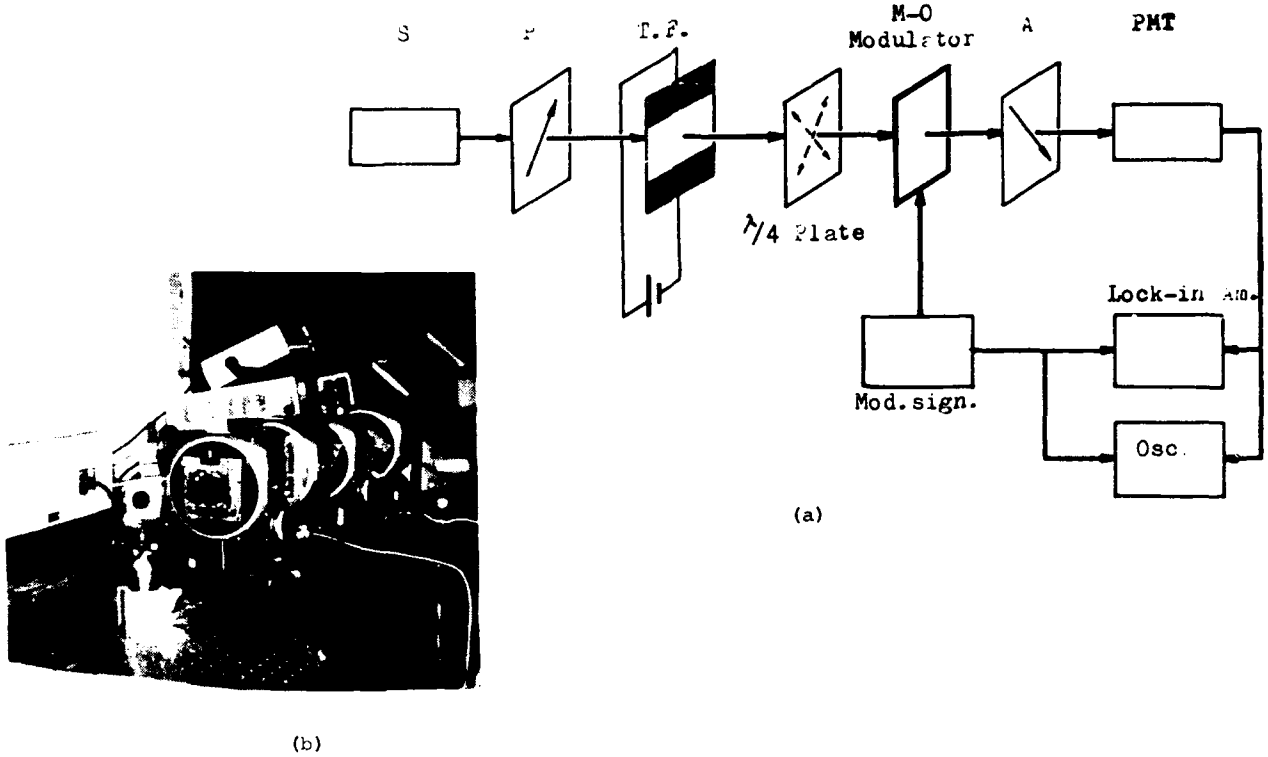
Introduction

Though PLZT ferroelectric ceramics have been applied to electro-optic devices for many years[1,2], increasing interest are focused on the PLZT thin films due to its unique properties: fast response speed, low drive voltage and great potential for integrated optic devices on Si or GaAs. One of the most favorable materials is(28/0/100)PLZT which has been successfully prepared on various substrates such as Al_2O_3,$SrTiO_3$ and glass(3-5) by using various techniques. Most reports on PLZT thin film concerned the preparation processes and structure analysis, but few dealt with the measurement technique of electro-optic property[3,6]. This is due to the fact that the phase retardation caused by the field-induced birefrigence of PLZT film is so small that it is quite difficult to measure it using conventional ellipometric method. It is therefore important how to determine the small phase retardation precisely. Adachi et al[3] proposed an ellipometric technique in which the phase retardation shift was detemined through a Wollaston prism to divide the linear polarizer light into two crossed polarized components. And Wang et al [6] developed a phase modulating technique by a photoelastic modulator. We present a more simple and precise technique to determine small phase retardatio shift of PLZT ferroelectric thin film using a magneto-optic modulator based on Faraday effect.

Measurement System

As known, the transmitted intensity $I(\alpha)$, where α is the angle between a polarization direction of polarizer and an analyzer, varies as $\cos^2\alpha$:

$$I(\alpha)=I_0\cos^2\alpha,$$



(a)

(b)

Fig.1. Block diagram (a) and photo (b) of measuring electro-optic coefficient of ferroelectric thin film

CH3080-0-7803-0465-9/92$3.00 ©IEEE

where I_0 is the maximum output light intensity at $\alpha=0°$. Now a magneto-optic (M-O) modulator is positioned between the polarizer and analyser. The M-O modulator is made from a YAG crystal. When an alternating signal of frequency ω is applied to M-O modulator, the polarization direction of polarized light passing through the M-O modulator will deflect an angle $\theta=\theta_0\cos\omega t$ due to Faraday effect(7), where θ_0 is maximum deflection at $\omega=0$. We have

$$I(\alpha-\theta)=I_0\cos^2(\alpha-\theta).$$

The modulating signal is small enough to satisfy the approximation: $\cos\theta\cong1$ and $\sin\theta\cong\theta$. This leads to $\cos(\alpha-\theta)=\cos\alpha+\theta\sin\alpha$ and

$$I(\alpha-\theta)=I_0[(\cos^2\alpha+1/2\theta_0^2\sin^2\alpha)+\theta_0\sin2\alpha\cos\omega t - \tfrac{1}{4}\theta_0^2\sin^2\alpha\cos2\omega t]$$

The modulated light have a dc and two ac components with the fundamental and the double-frequency. In the case of $\alpha=90°$(i.e. the polarizer and analyzer is crossed), the fundamental frequency component is extinguised and the output intensity is only modulated by the double-frequency of the modulation signal. Now if a sample with very small phase retardation is positioned between the crossed polarizer and analyzer, α will be changed, resulting in recurrence of the fundamental frequency component. This is a very sensitive system to determine the small phase retardation shift.

Our experimental set-up is shown in Figure 1. The light source S is a 1mw He-Ne laser at the wavelength of 6328Å. The transmission axes of two crossed polarizers (P and A respectively in Fig.1) are at 45° to the applied electric field to PLZT film. The analyzer A is mounted on goniometer with precision of 0.001°. The modulating frequency of M-O modulator is taken to be 1KHz and the signal received by a photomultiplier tube (PMT) transmits to a lock-in amplifier as well as an oscillator which are used for monitoring the component of the recurring fundamental and the background double-frequency. The monitoring is essential for precise determination of vanishing or appering of the fundamental frequency signal. Once the fundamental frequency recurs, the analyzer is rotated by an angle β to achieve null-extingnishing. The birefrigence shift $\Delta(\Delta n)$ is expressed as

$$\Delta(\Delta n)=\lambda_0\beta/\pi d,$$

where λ_0 is the wavelenth of the incident light and d is the thickness of the film. In this measurement system there is no contribution from instability of light source and background intensity due to the optical system or the sample. The retardation shift as small as $1X10^{-5}$ radiant can be detected. The error of the measurement system comes from reading of goniometer. We adopt a reading device with a precision of 0.001°.

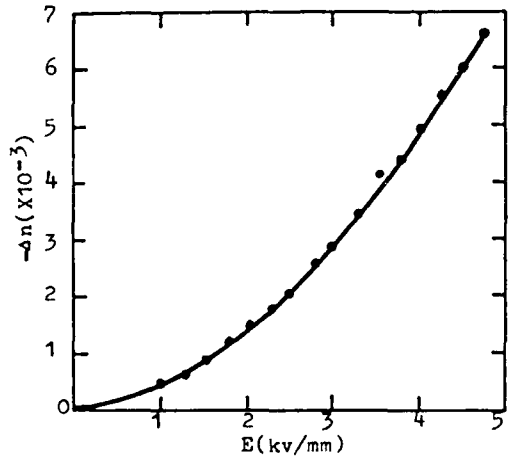


Fig.2. Δn vs E for PLZT(28/0/100) thin film on glass

Electro-optic Coefficient of PLZT Film

The PLZT(28/0/100) thin films were deposited in-situ on glass substrate by RF magnetron sputtering from a powder target [8]. The film was colourless and transparent. Its transmittance was about 80% in visible region. The thickness of film was about 4000Å. The narrow gap(0.4mm) electrodes of gold-chromium were evaporated on surface of the PLZT film. An electric field was applied perpendicularly to PLZT film. Figure 2 shows the measured results of the birefrigence shift as a function of electric field applied to a PLZT(28/0/100) film using the M-O modulating technique. The calculated electro-optic coefficient R is in a range of $0.1X10^{-16}$ to $1.0X10^{-16}(m/v)^2$ depending on the sputtering conditions.

Conclusions

A new and simple technique using a M-O modulator based on Faraday effect is proposed for measuring the electro-optic coefficient of ferroelectric PLZT thin films. The proposed technique measures phase retardation shift through determing the frequency change of the modulated light. It is a very sensitive and precise method for used evaluation in ferroelectric film electro-optic effect. There is no contribution from instability of light source, optical pathway and background intensity due to the optical system, surrounding or sample. It enable hence the precise measurement of very small shift of phase retardation. The main error of the technique comes from reading deflection angle. A reading device with precision of 10^{-5} radiant was adopted. We succeeded in measuring the electro-optic properties of other ferroelectric thin films.

Acknowledgement

We gratefully acknowledge the support of this work by National 863 highly technology committee. The authors wish to express their sincerely thanks to Professor Y.X.Chen and Mr. Y.T.Zhang for helpful discussions.

References

1. C.E.Land and P.D.Thacher, "Ferroelectric ceramic electrooptic material devices," Proc. IEEE Vol.57, pp.751, 1969.
2. G.H.Haertling and C.E.Land, "Hot-pressed (Pb,La)(Zr,Ti) O_3 ferroelectric ceramic for electrooptic applications," J.Am.Cer.Soc. Vol.54, pp.1, 1971.
3. H.Adachi, T.Kawaguchi, K.Setsune, K.Ohjiand K.Wasa, "electro-optic effects of $(Pb,La)(Zr,Ti)O_3$ thin films prepared by rf planar magnetron sputtering," Appl.Phys.Lett.Vol.42, pp.867, 1983.
4. K.D.Budd, British Cer.Soc. Proc. Vol.36, pp.107, 1985.
5. Y.H.Huang, W.G.Luo, A.L.Ding, M.Ge and X.T.Chen, "Oriented growth PLT thin films on amorphous substrate," Proc.SPIE-Int.Soc.Opt.Eng.Vol.1126,pp.36, 1989.
6. F.Wang, C.-B.Juang, C.Bustamante and A.Y.Wu, "Electr0-optic properties of $(Pb,La)(Zr,Ti)O_3$, $BaTiO_3$, $(Sr,Ba)Nb_2O_6$ and $Ba_2NaNb_5O_{15}$ thin films by a confocal scanning differential polarization microscope," Inter.SAMPE Electronic Conf. Series, Vol.4,

pp.712, 1990.
7. G.Liu and X.Liu, Acta Optica Sinica, Vol.4, pp. 1984.
8. W.G.Luo, A.L.Ding, R.T.Zhang and M.Ge, "Deposition and properties of PLT thin films by magnetron sputtering from powder target," Presented at THE IEEE '92 ISAF, Greenville, SC.Aug.31-Sept.2, 1992.

TRANSVERSE ELECTROOPTIC PROPERTIES OF ANTIFERROELECTRIC LEAD CONTAINING THIN FILMS

Feiling Wang, Kewen K. Li and Gene H. Haertling
Department of Ceramic Engineering
Clemson University
Clemson, South Carolina 29634-0907

The transverse electrooptic effect was observed in solution coated lead zirconate thin films. The electric-field-induced birefringent shift exhibited a characteristic response which differed from the normal butterfly-like loops for ferroelectric materials. The observed unique response in lead zirconate thin films was related to their antiferroelectric nature and the electric-field-induced antiferroelectric-ferroelectric phase transition. The possible applications of the materials for optical memory are discussed.

Introduction

Ferroelectric (FE) thin films, owing to their high dielectric constant and two electrically switchable remanent states, have attracted great interest for the development of nonvolatile memory devices and other applications[1,2]. A variety of ferroelectric materials are also known to possess transverse electrooptic properties, i.e. the electric-field-controlled birefringence; however, ferroelectric switching (polarization reversal with an electric field) has not proved equally useful in integrated optical and/or optoelectronic devices. To facilitate an optical memory function in optoelectronic devices, it is desirable for the waveguide materials to possess two electrically switchable birefringent states. However, the two remanent polarization states are not distinguishable for the index ellipsoid in ferroelectric materials. Therefore, it is not feasible to realize optical memory in ferroelectric materials by switching between the two remanent polarization states.

Recently the transverse electrooptic effects in antiferroelectric (AFE) lead zirconate ($PbZrO_3$) thin films were observed[3]. The electric-field-induced birefringent shift in the lead zirconate thin films showed a characteristic response not exhibited in ferroelectric materials. The unique electrooptic response in the antiferroelectric thin films was found to stem from the electric-field-induced antiferroelectric-ferroelectric phase transition. Besides its importance as a fundamental material property, the transverse electrooptic effect in the antiferroelectric thin films may also furnish a mechanism for optical memory in optoelectronic devices. In this report the latest measurements of the transverse electrooptic properties in antiferroelectric lead zirconate thin films are presented.

Experimental Method

Lead zirconate thin films were deposited onto fused silica and Pt/Ti coated silicon substrates by a solution coating technique from an acetate precursor[4,5]. The antiferroelectric crystal structure of the resultant thin films was confirmed by the appearance of the X-ray diffraction peak at $2\theta^o$ = 16.9, characterizing the antiferroelectric double cell structure. For the measurement of the dielectric properties of the materials, copper dots were evaporated onto the thin films deposited on the Pt/Ti-coated silicon substrate. For the detection of the transverse electrooptic properties, copper intedigitated electrodes with gap widths ranging from 5 to 40 μm were deposited on top of the thin films grown on the fused silica substrates.

The electric-field-induced birefringent shift of the thin film was measured by means of a phase-detection technique[6], using a He-Ne laser of wavelength of 632.8 nm as the light source. The phase modulation of the incident light was provided by means of a modulator. The measurements were performed with a transmission mode. In the phase detection scheme, the amplitude of the output signal (from a lock-in amplifier) at the modulating frequency was directly proportional to the phase retardation of the sample, provided that the total phase retardation of the sample was sufficiently small. A slow varying dc voltage was applied to the interdigitated electrodes during the measurement. An optical compensator was used to calibrate the measuring system.

Results and Discussion

A typical electrooptic response of the lead zirconate thin film is shown in Figure 1 where the birefringent shift of the thin film is plotted as a function of the slow varying dc electric field. The thickness of the film was 1 μm. Interdigital electrodes with a gap width of 10 μm was used in the measurement. As shown in the figure, the electrooptic response of the antiferroelectric thin film exhibits a number of features different from that of ferroelectric materials. For the purpose of comparison, a typical birefringence verses E-field curve for a ferroelectric thin film, i.e. PLZT[7] of composition 2/55/45, is shown in Figure 2. The birefringence verses E-field curve for the lead zirconate thin film is characterized by (1) enhanced hysteretic

CH3080-0-7803-0465-9/92$3.00 ©IEEE

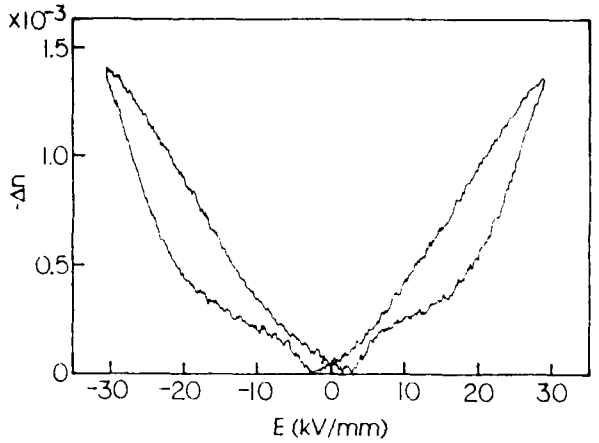


Figure 1 Measured birefringent shift as a function of the external dc electric field for a lead zirconate thin film deposited on a fused silica substrate.

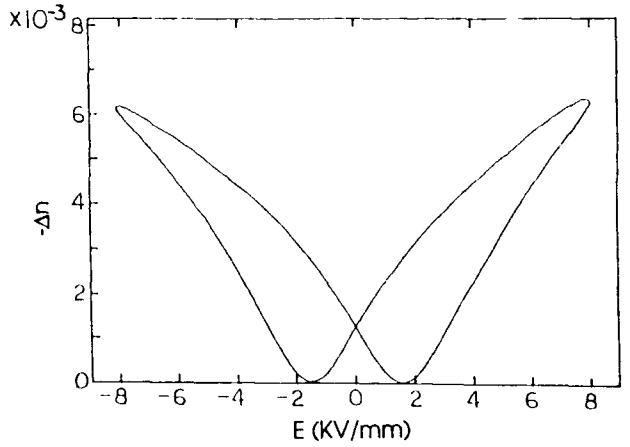


Figure 2 Measured birefringent shift as a function of the external dc electric field for a ferroelectric PLZT thin film deposited on a sapphire substrate.

behavior in the region of field strength above 10 kV/mm, (2) diminished hysterestic behavior in the region of field strength below 5 kV/mm and (3) rapid increase of the slope when the increasing electric field exceeds 20 kV/mm. It was found that the characteristic response of the lead zirconate thin films was attributed to the electric-field-induced AFE-FE structural transition[3].

With the help of a phenomenological model, the correlation between the field-induced birefringent shift of a material and electric polarization P(E) can be described by the following relation:

$$\Delta n \propto [\, E + \beta P(E)]^2, \qquad (1)$$

where β is a constant dependent on the crystal structure of the material ($4\pi/3$ for cubic structure). The main features for the electrooptic response of the lead zirconate thin films shown in Figure 1 are consistent with those predicted from the dielectric properties (double hysteresis loop) by using relation (1).

To better understand the nature of the antiferroelectric lead zirconate thin films, a static bias electric field was applied to the thin film material in both the dielectric and electrooptic measurements. Thin films deposited on the Pt/Ti coated silicon substrates were used for the measurement of the dielectric behavior. With the increase of the dc bias, the polarization versus E field curve of the lead zirconate thin film gradually evolves from a double hysteresis loop to a single hysteresis loop. As shown in Figure 3, under an appropriate bias field, the shape of the biased single hysteresis loop very much resembles the normal hysteresis loop for ferroelectric materials. Unlike the ferroelectric materials, however, the two remanent states in the biased single hysteresis loop (denoted by P_A and P_B in Fig.3) possess polarizations of different magnitude, which produce two distinguished birefringent states in the thin films. These two birefringent states are clearly represented in the biased birefringence verses E-field curve, as shown in Fig.4, measured from a lead zirconate thin film grown on a fused silica substrate. A static bias field of approximately 17 kV/mm was applied during the measurement. It is obvious that the two distinguished remanent birefringent states Δn_A and Δn_B are associated with the two remanent polarization states P_A and P_B in the biased single hysteresis loop shown in Figure 3. It should be noted, however, that to avoid the breakdown of the electrodes through the air, the bias electric field and the scan range are lower in the measurement of the electrooptic properties than in the measurement of the dielectric property. In addition, because these two measurements involve thin films deposited on two different types of substrates with different directions of applied electric field, quantitative correlation between these two measurements is not possible.

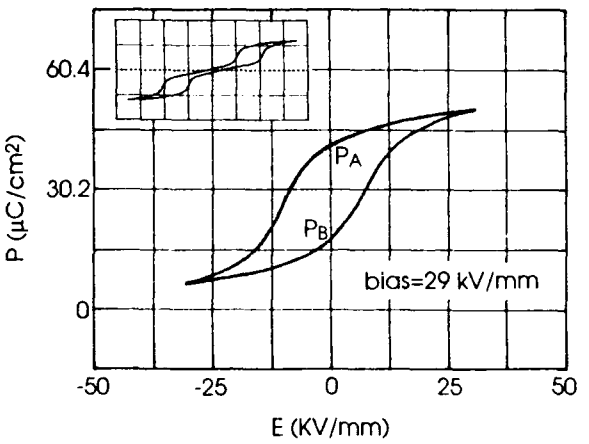


Figure 3 Dielectric properties of a lead zirconate thin film grown on a Pt/Ti-coated silicon substrate, taken under a static bias field of 29 kV/mm. The insert is a hysteresis loop of the same sample taken with zero bias field. The horizontal and vertical scales for the insert plot are 25 kV/mm per division and 30.2 $\mu C/cm^2$ per division, respectively.

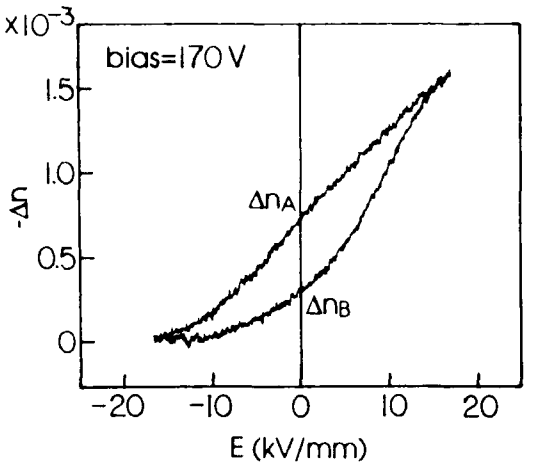


Figure 4 Birefringent shift as a function of the slow varying external field measured with a dc bias field of 17 kV/mm for a lead zirconate thin film on a fused silica substrate.

It was found that the lead zirconate thin films acquired a permanent birefringence once an initial electric field of sufficient magnitude was applied. Shown in Figure 5 is the birefringent shift of a lead zirconate thin film as a function of the slow varying external electric field recorded during the first few cycles of the field scan. In the first half cycle of the field scan, the birefringence of the material drastically increased when the increasing electric field exceeded approximately 16 kV/mm. When the external electric field was reduced to zero, the material retained a significant remanent birefringent shift. During the next few scan cycles, this remanent birefringence kept increasing yet the increment was smaller and smaller after each cycle. A stable remanent birefringence (permanent birefringence) was finally reached as shown previously in the birefringence versus E-field curve of Figure 1. The stable remanent birefringent state, under zero external electric field, was chosen as the zero-birefringence point in plotting both Figure 1 and Figure 4. After testing a few lead zirconate thin film samples, it was found that this initiating process of the material was reproducible.

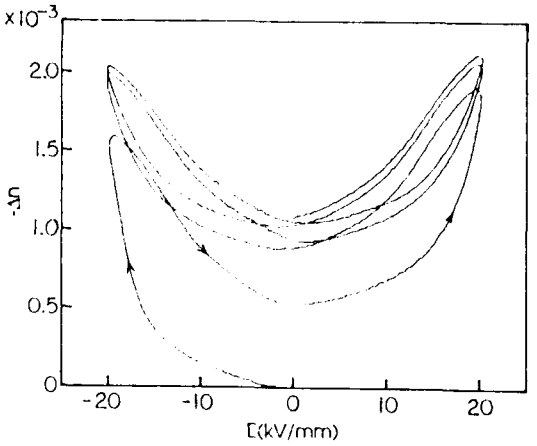


Figure 5 The evolution of the electrooptic response of a lead zirconate thin film on a fused silica substrate during the first few cycles of the electric field scan.

The observed permanent birefringence in the antiferroelectric thin films mentioned above may be related to other types of memory behavior previously observed in antiferroelectric lead zirconate materials[8]. A possible explanation for this birefringence memory is that when the AFE-FE phase transition occurred under a sufficiently high electric field the ferroelectric domains are forced to align along the direction of the E-field; although the structure of antiparallel dipoles was restored after the withdrawal of the external E-field, the antiferroelectric dipoles remained preferentially aligned in the direction along which the E-field was previously applied. Such an explanation for the birefringence memory is supported by an optical study of the lead zirconate crystal which showed that the index of refraction is the smallest for the light polarized along the a axis of the antiferroelectric unit cell[9]. This mechanism of birefringence memory is distinguished from that of ferroelectric materials where birefringence memory is mainly caused by the remanent polarization.

The characteristic electrooptic response of the lead zirconate thin films may furnish a means of realizing optical memory in optoelectronic devices. Two different mechanisms may be utilized in optical memory devices. In the first type of memory, the information may be stored in a virgin material by applying a sufficiently high electric field. After the withdrawal of the electric field, as shown in Figure 5, the thin film material becomes permanently oriented and possesses a permanent birefringence of approximately 1.3 10^{-3}. The second type of memory is associated with the two distinguished birefringent states of the thin film materials in the presence of a bias electric field as shown in Figure 4. Because these two birefringent states, Δn_A and Δn_B, are produced by the two remanent states of polarization, P_A and P_B, of the material, they are stable under the bias field. The merit of the second type of memory is that the two birefringent states are electrically switchable. For example, a TIR switch[10] made of the antiferroelectric thin film would allow the inter-switching of the light between the two waveguide channels by electric pulses of opposite polarities, operated under a static bias field. Such a switch is not possible with ferroelectric materials in which the two remanent polarization states are optically equivalent.

Conclusions

The transverse electrooptic property of the solution coated lead zirconate thin film exhibits a characteristic response which is attributed to the electric-field-induced antiferroelectric-ferroelectric phase transition. Under an appropriate static bias electric field, the material possess two distinguishable birefringent states

associated with the two remanent polarization states of the material. The thin films were also found to acquire a permanent birefringence once a sufficiently high electric field was applied to the virgin materials.

Two types of mechanisms are proposed for utilizing the antiferroelectric thin films for optical memory in optoelectronic devices. The first type of memory makes use of the permanent orientation of the material induced by an initial electric field. The second type of memory involves the inter-switching between the two distinguishable birefringent states of the material under a bias field with electric pulses.

Acknowledgment

This study was partially sponsored by the Office of Naval Research under contract No. N00014-91-J-508.

References

[1] G.H. Haertling, "Ferroelectric Thin Film for Electronic Applications," J. Vac. Sci. Technol. A, 9, 414(1991)

[2] D. Bonsurant and F. Gnadinger, "Ferroelectrics for Nonvolatile RAMs," IEEE Spectrum, July 1989, p.30

[3] F. Wang, K.K. Li, and G.H. Haertling, "Transverse Electro-Optic Effect of Antiferroelectric Lead Zirconate Thin Films," Optics Lett. 17, 1122(1992)

[4] K.K. Li, F. Wang, and G.H. Haertling, "Antiferroelectric Lead Zirconate Thin Films Derived from an Acetate Precursor System," J. Mater. Sci. (to be published)

[5] G.H. Haertling, "PLZT Thin Film Prepared from Acetate Precursors," Ferroelectrics, 116, 51(1991)

[6] F. Wang, C.B. Juang, C. Bustamante, and A.Y. Wu, "Electro-optic Properties of (Pb, La)(Zr, Ti)O_3, $BaTiO_3$, (Sb, Ba)Nb_2O_6 and $BaNaNb_5O_{15}$ Thin Films," in Proc. of 4th International SAMPE Electronic Conference, p.712

[7] G. H. Haertling and C.E. Land, "Hot-pressed (Pb, La)(Zr, Ti)O_3 Ferroelectric Ceramic for Electronic Applications," J. Am. Ceram. Soc. 54, 1(1971)

[8] K. Uchino, "Digital Displacement Transducer Using Antiferroelectrics," Japan. J. Appl. Phys. 24, suppl., 24(1985)

[9] F. Jona, G. Shirane, and R. Pepinsky, "Optical Study of $PbZrO_3$ and $NaNbO_3$ Single Crystals," Phys. Rev. 97, 1585(1955)

[10] H. Higashino, T. Kawaguchi, H. Adachi, T. Makino and O. Yamazaki, "High Speed Optical TIR Switchs Using PLZT Thin Film Waveguides on Sapphire," Jap. J. Appl. Phys. 24, suppl., 284(1985)

Fatigue Effect on the I-V Characteristics of Sol-Gel Derived PZT Thin Films *

S.C. Lee†, G.Teowee††, R.D. Schrimpf†, D.P. Birnie, III††, D.R. Uhlmann†† and K.F. Galloway†

† Department of Electrical and Computer Engineering
†† Department of Materials Science and Engineering
University of Arizona, Tucson, AZ 85721

Abstract

A static I-V measurement method for ferroelectric thin films was developed to distinguish the leakage current from the switching current. The initial polarization state and the exponential decay behavior of the switching current were considered in this method. The fatigue effects on sol-gel derived PZT thin films were analyzed using this I-V measurement method. Changes in polarization due to the bipolar stress were correlated with the changes in the switching current and the leakage current. No degradation was found due to unipolar cycling.

I. INTRODUCTION

Ferroelectric materials have properties useful for non-volatile memories and dynamic random access memories (DRAMs). Non-volatile memories use the hysteresis behavior of the polarization versus the electric field. The one-transistor/one-capacitor DRAM cell can be implemented by replacing the conventional silicon dioxide with a ferroelectric thin film having a high dielectric constant [1]. In these applications, the quality of films is generally characterized by the charge storage capability. Even though the static current, such as the leakage current, is closely related to the charge storage capability, not many studies have been performed on the static current. In this paper, a static current-voltage measurement method is developed to distinguish the leakage current from the switching current. Fatigue effects on the lead zirconate-titanate (PZT) thin films are examined in terms of the variation in the static currents. Based on these results, the degradation mechanism due to the fatigue is discussed.

II. EXPERIMENTAL PROCEDURES

A. Review on the Switching Current

The switching current of a ferroelectric capacitor is generally measured by means of a modified Sawyer-Tower circuit using a small (typically 10 ~ 10,000 Ω) resistor in place of a linear capacitor as shown in Fig. 1 (a) [2, 3]. Because of the hysteresis behavior, the transient responses to the same input signal are different for the different initial polarization states. For the positive step voltage, the response of the initially negatively poled capacitor is defined as a full-switching current, while that of the initially positively poled capacitor is defined as a non-switching current as shown in Fig. 1 (b).

Fig. 2 shows the experimental full-switching and non-switching currents. These switching currents were measured by applying a ± 6 V bipolar or a 0 to 6 V unipolar, 50 Hz, square wave to the modified Sawyer-Tower circuit with a 100 Ω resistor. If a positive step voltage is applied to a ferroelectric capacitor with an initial polarization state of the negative remanent polarization ($-P_r$) and switches the capacitor to the positive maximum polarization ($+P_{max}$), the full-switching current consists of an initial spike due to charging the linear dielectric and a following humped curve due to switching the non-linear dielectric [4].

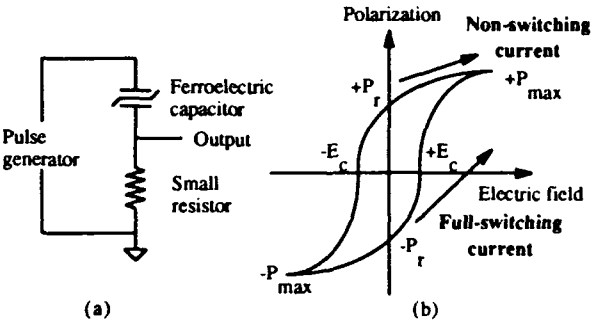


Fig. 1 Switching current measurement method
(a) A modified Sawyer-Tower circuit
(b) A hysteresis curve and the definition of a full-switching and a non-switching current

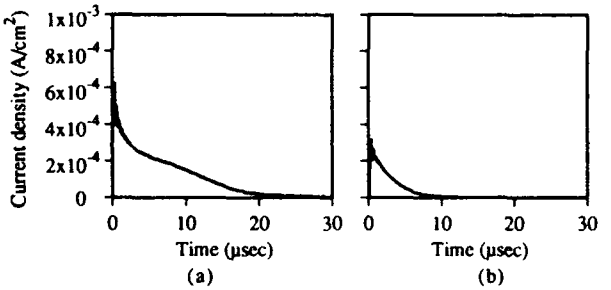


Fig. 2 Switching current of a PZT capacitor
(a) Full-switching current from $-P_{max}$ to P_{max}
(b) Non-switching current from $+P_r$ to P_{max}

In this experiment, because the bipolar square wave switches the capacitor immediately from $-P_{max}$ (negative maximum polarization) to $+P_{max}$, instead of from $-P_r$ to $+P_{max}$, the full-switching curve obtained here shows a larger initial spike than that seen in the traditional measurement [4]. The comparison of the experimental full-switching and non-switching current shows that switching with the complete polarization reversal takes longer time than that with the partial polarization reversal. Both switching

* This work was supported in part by the U. S. Navy through contract number N00014-90-C and in part by the Air Force Office of Scientific Research.

CH3080-0-7803-0465-9/92$3.00 ©IEEE

currents decay exponentially at the end of the switching process. Therefore, the initial polarization state and the exponential decay behavior of the switching current should be considered in the static current measurement.

B. Static I-V Measurement Method Set-Up

A static current measurement method using a HP4145A Semiconductor Parameter Analyzer was developed as shown in Fig. 3.

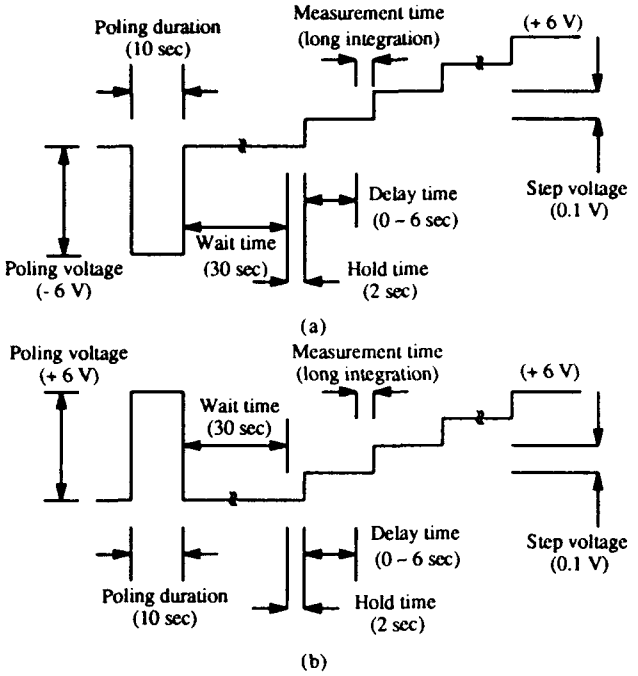


Fig. 3 Static current measurement method
(a) Full-switching static current measurement
(b) Non-switching static current measurement

Initializing the polarization state of a ferroelectric capacitor precedes the measurement of the static current. As shown in Fig. 3 (a), the full-switching static current is measured after setting the ferroelectric capacitor in a state of the negative remanent polarization ($-P_r$). On the contrary, the capacitor remains in a state of positive remanent polarization ($+P_r$) prior to a non-switching static current measurement as shown in Fig. 3 (b). The magnitude and the duration of the poling voltage determine the number of domains with a preferred orientation. However, some of the domains relax or lock into favorable energy configurations [4] and lose their initial orientations during the wait time, defined from the end of the poling voltage to the beginning of the current measurement. To stabilize the initial polarization state, relatively long poling duration (10 sec) and wait time (30 sec) were used. After initializing the polarization state and an additional 2 sec hold time, the static current is measured by applying a DC bias from 0 V to 6 V, increasing in 0.1 V steps. A delay time is inserted between the application of the forcing voltage and the current measurement to consider the exponential decay of the switching current. The current is measured in a long integration mode rather than a short integration mode. In the long integration mode, the current is the average value of 256 measurements for 267 msec. The short integration mode, which measures current directly without integration, usually results in an unstable I-V curve.

Fig. 4 shows the static current density vs. voltage curves for different delay times. In these I-V curves, the full-switching static current is larger than the non-switching static current by an order of magnitude for the same delay time. Smaller current density is measured with a longer delay time for both the full-switching and non-switching static currents. Because of the large switching current at the positive coercive electric field ($+E_c$), the full-switching static current has a peak at ~ 20 kV/cm. These results indicate that complete elimination of the switching current is difficult. However, non-switching static current with a long delay time is considered a good method for the leakage current measurement. In the experiment described below, a 2 sec delay time is used to reduce the total measurement time.

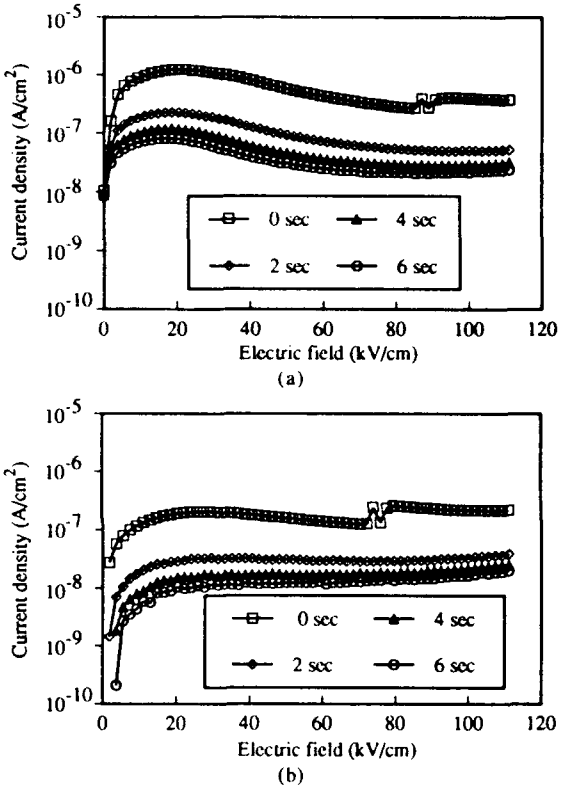


Fig. 4 Static current as a function of electric field for different delay times
(a) Full-switching static current (b) Non-switching static current

C. Application of Static I-V Measurement to Fatigue Effect

The fatigue effects on the PZT thin films were examined with the static current measurement method established previously. PZT thin film capacitors with a zirconium to titanium ratio of 53/47 were fabricated using a sol-gel process [5]. On an oxidized 2" silicon wafer, platinum was sputtered for the bottom electrode and multiple layers of sol-gel PZT were spin-coated to a thickness of approximately 5400 Å. The films were annealed at 700 °C for 30 min. in oxygen. Subsequently, the platinum top electrodes with an area of 2.4×10^{-4} cm^2 were formed by a lift-off process. Finally, the films were heat-treated at 700 °C for 5 min. for better ohmic contact.

The continuous hysteresis curve and the pulse polarization [6] were measured using the virtual ground mode of a RT66A standardized ferroelectric tester [7]. For the continuous hysteresis curve, a one-period triangle wave with a period of 200 msec was

applied as an input signal to the virtual ground circuit. In the pulse polarization method shown in Fig. 5, the first pulse sets the ferroelectric capacitor in a state of having the negative remanent polarization. During the rise and fall times of the four consecutive pulses, eight different polarizations are measured as noted in Fig. 5. Because the switching polarization (P^*) and the non-switching polarization ($P^\wedge$) are important in the memory operation, the fatigue effects were analyzed in terms of these polarizations. The electrical cycling for fatigue was performed at frequencies from 10 kHz to 1 MHz using a ± 6 V or a ± 8 V square wave. Besides the bipolar stress, unipolar cycling was examined at frequencies up to 1 MHz using a 0 to 8 V square wave. The fatigue testing was periodically interrupted to measure the polarization. The full-switching and non-switching static currents before and after the stress were compared.

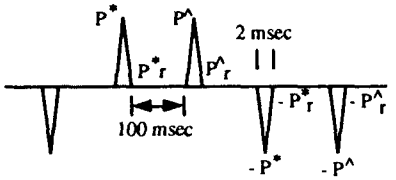


Fig. 5 The pulse polarization method and its parameters [7]

III. RESULTS AND DISCUSSION

Fig. 6 and Fig. 7 show the changes in the hysteresis curves and the pulse polarizations due to bipolar (± 8 V) and unipolar (0 to 8 V) electrical cycling at 100 kHz.

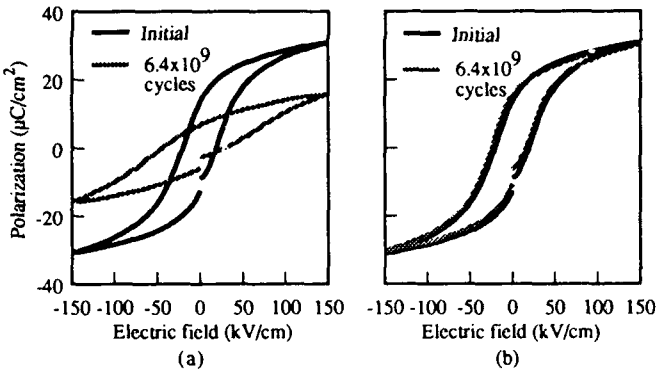


Fig. 6 Changes in the hysteresis curves due to (a) bipolar and (b) unipolar stress

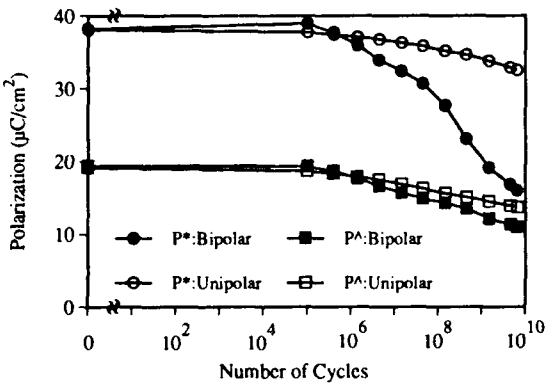


Fig. 7 Changes in the switching (P^*) and non-switching ($P^\wedge$) polarization due to bipolar and unipolar stress

Bipolar cycling decreases the switching polarization (P^*) rapidly after 10^8 cycles and changes the shape of the hysteresis curve. In contrast to the bipolar stress, no significant degradation in the polarization is observed for the unipolar stress.

The changes in the static currents after the bipolar stress (± 8 V, 100 kHz) up to 8.4×10^9 cycles are shown in Fig. 8. In the full-switching static current in Fig. 8 (a), the initial bipolar cycling increases the peak current and decreases the current at 6 V (~110 kV/cm). The increase in the switching polarization in Fig. 7 and the peak current in Fig. 8 (a) after the initial bipolar cyclings indicate that the domain reorganization activates some domains, otherwise unswitchable, to increase the number of domains in the switching process. Simultaneously, more domains switch at the lower electrical field with the faster switching time. Therefore, the switching current increases at the low electrical field and decreases at the high field. The further cycling reduces the number of the switching dipoles and decreases the switching current at low voltage. However, the increase of the current at high voltage shows that the film is degraded by the bipolar stress. The non-switching static current after 8.4×10^9 cycles in Fig. 8 (b) clearly shows the increase of the leakage current.

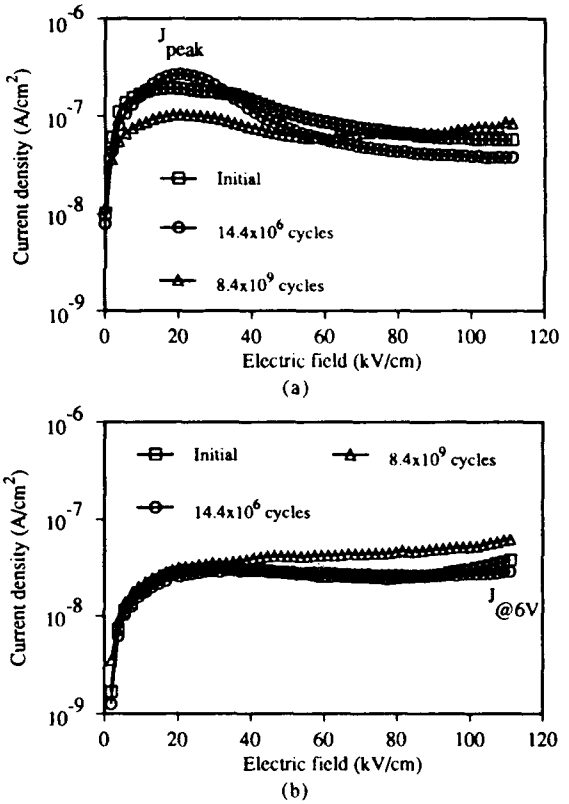


Fig. 8 I-V curves after the ± 8 V, 100 kHz bipolar stress
(a) Full-switching static currents (b) Non-switching static currents

For the various bipolar cycling conditions, fatigue effects on the static currents are examined by correlating the changes in the switching polarization with the changes in the key parameters of the static currents such as the peak current density in the full-switching static current (J_{peak}) and the non-switching static current density at the maximum electric field ($J_{@6V}$). Fig. 9 (a) shows that the decrease in the switching polarization is strongly correlated with the decrease of the peak current in the full-switching static current. As

shown in Fig. 9 (b), a larger decrease in the switching polarization generally accompanies the larger leakage current.

Unipolar stress, as might be expected from Fig. 7, changes the static currents in the same way as the initial bipolar stress. In Fig. 10, the changes in the non-switching static current density at the maximum electric field ($J_{@6V}$) due to the 100 kHz unipolar (0 to 8 V) and the bipolar (± 8 V) stresses are shown as a function of the number of cycles. The unipolar stress only decreases the leakage current up to $6x10^9$ cycles, while the bipolar stress increases the leakage current after 10^8 cycles.

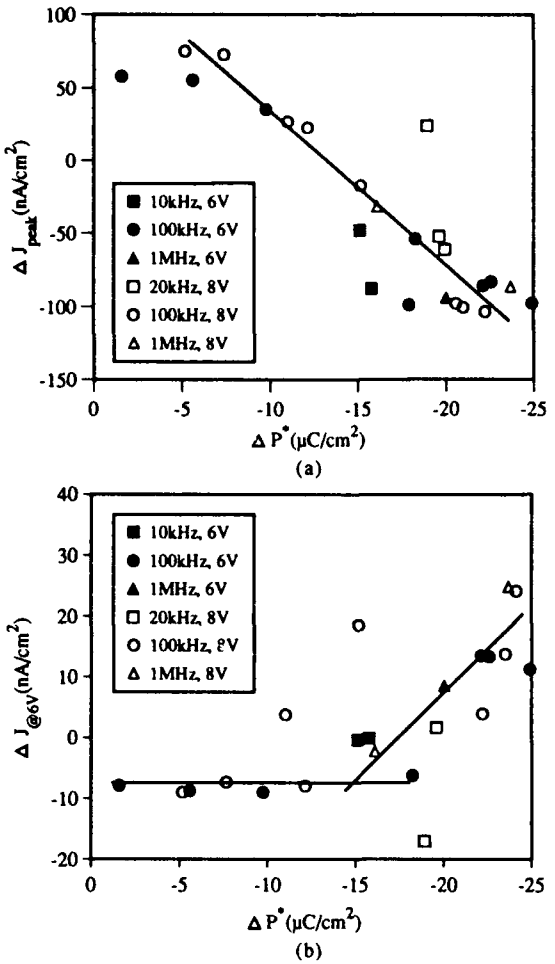


Fig. 9 Correlation of (a) ΔJ_{peak} with ΔP^* and (b) $\Delta J_{@6V}$ with ΔP^*

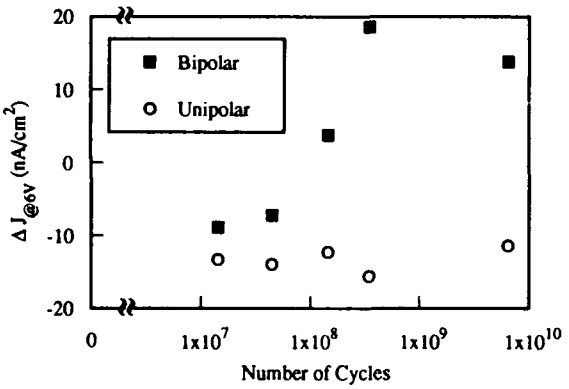


Fig. 10 Changes in $\Delta J_{@6V}$ due to the 100 kHz unipolar (0 to 8 V) and the bipolar (± 8 V) stresses

These results can be explained by the space-charge build-up or the oxygen-deficient dendrite growth [8]. The bipolar cycling will increase the space-charge layers adjacent to the electrodes or disseminate the dendrite away from the electrodes. These processes will reduce the number of switching dipoles and cause micro-shorts through the narrowing switching layer.

IV. Summary and Conclusion

A static I-V measurement method for ferroelectric thin films was developed considering the initial polarization state and the exponential decay behavior of the switching current. Depending on the polarity of the initializing voltage, the static currents are divided into a full-switching and a non-switching static current. A delay time is inserted between the application of the forcing voltage and current measurement to reduce the switching current component. Complete elimination of the switching current was difficult. However, non-switching static current with a long delay time was found to be a good method for the leakage current measurement. The fatigue effects on sol-gel derived PZT thin films were analyzed using this I-V measurement method. In the bipolar stress, the polarization reduction was correlated with the decrease in the switching current and the increase in the leakage current. Neither the significant decrease in the polarization nor the increase in the leakage current was observed in the unipolar stress. The fatigue effects are explained by the increase in the space-charge regions near the electrodes or the oxygen-deficient dendrite growth.

V. References

[1] R. M. Moazzami, C. Hu and W. H. Shepherd, "A Ferroelectric DRAM Cell for High-Density NVRAM's", IEEE Electron Device Lett., vol. 11, no. 10, pp. 454 - 456, Oct., 1990.

[2] C. B. Sawyer and C. H. Tower, "Rochelle Salt as a Dielectric", Phys. Rev. 35, pp. 269 - 273, 1930.

[3] J. C. Burfoot, *Ferroelectrics : An Introduction to the Physical Principles*, D. Van Nostrand, Ltd., London, 1967.

[4] J. C. Burfoot and G. W. Taylor, *Polar Dielectric and Their Applications*, The MacMillan Press, Ltd., London, 1979.

[5] G. Teowee, J. M. Boulton, S.C. Lee and D. R. Uhlmann, "Electrical Characterization of Sol-Gel Derived PZT Films", *presented at MRS symposium, Fall 1991.*

[6] J. T. Evans, M. D. Ivey and J. A. Bullington, "Testing for Fatigue and Aging in Ferroelectric Thin-film Capacitors", The Proceedings of the first symposium on integrated ferroelectrics, pp. 217 - 224, 1989.

[7] RT66A Standardized Ferroelectric Tester V 2.0 Operating Manual, Radiant Technologies, 1990.

[8] H. M. Duiker, P. D. Beale, J. F. Scott, C. A. Paz de Araujo, B. M. Melnick, J. D. Cuchiaro, L. D. Mcmillian, "Fatigue and switching in ferroelectric memories: Theory and experiment", J. Appl. Phys. 68, pp. 5783 - 5791, 1990.

DEFECT STRUCTURES AND FATIGUE IN FERROELECTRIC PZT THIN FILMS

Zheng Wu and Michael Sayer
Department of Physics, Queens University
Kingston, Ontario, Canada K7L 3N6

A thermally stimulated current (TSC) technique has been used to characterize natural and electric field induced defect distributions in PZT films. The principal defects give rise to TSC peaks near 400K and 500K, with defect concentrations ≈ 10^{2} cm^{-3}, and an activation energy of ≈ 0.8 eV. Changes in the defect structures as a function of number of switching cycles and processing conditions are described, and their relationship to the phenomena of fatigue are discussed. It is suggested that the defects measured by TSC arise from extended defects rather than from point defects. Domain splitting and pinning as a result of such defects generated during polarization reversals may account for fatigue in PZT films.

Introduction

There have been intensive studies on ferroelectric thin films due to their promising applications in nonvolatile memories, high density DRAMs, microactuators, and nonlinear optical devices. Memory devices made from ferroelectric films have high access speed, low operating voltage, and radiation hardness. However, large scale applications of ferroelectric memories are limited currently by reliability problems concerned with fatigue, aging and retention. A number of experimental and theoretical studies have been dedicated to fatigue and aging, but the data is still insufficient to give a complete understanding of the problem. Theoretical models proposed to account for the fatigue mechanisms have been based on the effects of mobile charged point defects [1] and on domain pinning [2]. It is still controversial as to which mechanism is dominant in thin films in comparison to that in bulk materials and each model is only successful in explaining some aspects of fatigue and aging.

For the sake of clarity, the distinction between fatigue and aging must be made. Fatigue is the degradation of ferroelectric properties observed under repeated polarization reversal when a material is subjected to a large switching field. It is a non-equilibrium process in a system excited by external stresses. Aging is the time-dependent static degradation of ferroelectric properties under no applied field. It is a relaxation process in which a closed system relaxes from a nonequilibrium state. Fatigue is the main concern of this paper. It occurs as a result of interactions of a ferroelectric system with lattice defects during polarization reversals. To understand the fatigue mechanism, it is therefore necessary to study the static and dynamic properties of the defect stuctures of the ferreoelectric lattice and to correlate these with electrical measurements.

In general, lattice defects can be categorised as point defects such as impurities, vacancies and interstitials, or extended defects such as dislocations, planar defects, and grain boundaries. To gain understanding of how the behavior of defects during polarization reversals relates to the understanding of fatigue mechanisms, we have used a thermally stimulated current (TSC) technique to characterize natural and electric field induced defect distributions in ferroelectric films. The TSC experiments consist of photoexciting thin film samples by UV light at low temperature. Excited carriers are trapped at centers associated with lattice defects. The samples are then heated in the dark at a constant rate. The current which results when the carriers are released from traps by thermal excitation is measured as a function of temperature. For each discrete energy level, a maximum is displayed in the current-temperature thermogram at a temperature related to the depth of the level. The area of the peak is proportional to the concentration of traps. A model for ferroelectric fatigue based on domain splitting and pinning will be discussed based on the results obtained from TSC measurements.

Experimental

Ferroelectric PZT thin films were fabricated by sol gel methods on Pt/Ti coated silicon and on conducting indium tin oxide (ITO) coated 7059 glass substrates. Both the acetic acid based [3] and 2-methoxyethanol based [4] sol gel routes were used. Rhombohedral PZT with compositions having a Zr/Ti ratio of 54/46 and 90/10 were employed. In order to dope films with either donor or acceptors impurities, 1 mol% of Ta ethoxide or Mg acetate were added to the stock solutions respectively. Multilayer-coated films of thickness ranging from 2000 to 4500 Å on both Pt and ITO were initially fired at 400°C for 5 min. Rapid thermal annealing (RTA) at 650°C for 30 s was used to anneal films on Pt, while conventional furnace annealing was used to anneal films on ITO at 650°C for 2hrs. For some samples, a subsequent oxidation or reduction process was carried out in which the samples were annealed for various times at 400°C either in flowing oxygen, or in a flowing hydrogen/nitrogen (10/90) mixture. Gold or silver top electrodes were deposited by vacuum evaporation to form a capacitor structure. The electrodes had a thickness of about 500 Å and were transparent to 365 nm wavelength ultraviolet (UV) light.

Ferroelectric hysteresis loops were measured using a Sawyer-Tower (ST) circuit without compensation for dielectric loss. The samples were fatigued at a frequency of 100 Hz to 100 kHz by subjecting the PZT thin film capacitors to a sinusoidal voltage of Vp= ± 10 volts using the same ST circuit. The I-V characteristics of the films were measured with a Keithley Model 236 source-measure unit (SMU). This was of importance to examine the nature of the contacts made to the PZT films.

TSC was measured using a two probe method. The experimental arrangement is shown in Fig.1. It consists of an air-tight chamber with a sample holding stage facing a quartz window, a liquid nitrogen container, a heater mounted inside the stage, an Omega temperature controller connected to a thermocouple positioned very close to the sample, a photoexciting light source (a 100W Blak-ray UV lamp having a characteristic emission line of 365nm), and the Keithley SMU unit. The data acquisition was automated by a PC computer. The operating temperatures ranged from 130K to 650K. The heating rate of the sample cell provided a uniform rate of temperature change from 0.1 to 0.5K/s. The photon energy of 3.4eV from the UV source was large enough to excite PZT in the fundamental absorption band. PZT has a bandgap of about 3.35eV. The samples were photoexcited at low temperature for about ten minutes. No dc bias was applied during UV irradiation, while the dc bias during heating was constant from 0.0005 to 0.1V.

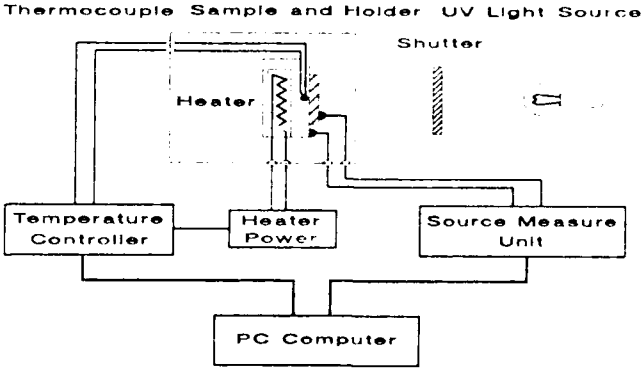


Figure 1. System for thermally stimulated current measurements

CH3080-0/92/0000-0244 $3.00 © 1992 IEEE

The TSC current-temperature thermograms were reconstructed from the difference between the current obtained after UV irradiation and the current obtained in a second run at the same dc bias and heating rate but with no optical excitation. Care was taken that the inherent pyroelectric effect in ferroelectrics which can generate a large depolarization current during heating did not mask the desired TSC current. All samples were depolarized before each measurement.

Electrode Contacts

TSC measurements are sensitive to the nature of the electrode contacts. Ideally, a four probe method could separate the bulk properties from contact effects. However the sample geometry made this difficult to achieve. Fortunately, the I-V characteristics for voltages less than 1V measured using a two probe technique were linear for top gold films on Pt and ITO. This is shown in Fig.2. For applied voltages above 1V, some films showed evidence for space charge limited conduction. The results were virtually the same in films in which Ag was used as the top electrode, despite the difference in the work function of gold (5.28eV) and silver (4.29eV). The TSC results obtained with a dc bias of 0.0002 to 0.1V are therefore considered to represent a volume rather than a contact effect.

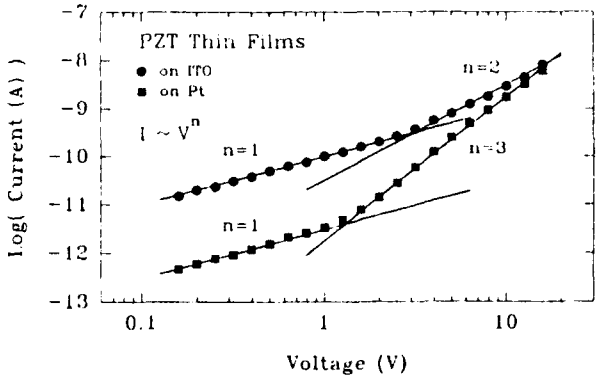


Figure 2. I-V characteristics for Au/PZT/ITO and Au/PZT/Pt devices.

TSC Measurements

Fig.3 shows a typical TSC current-temperature thermogram for a PZT film following UV-irradiation at 130K for 10 min. Two current peaks appear at temperatures of about 400K for peak I and 500K for peak II respectively, indicating the existence of trapping centers of two different kinds.

Fig.4 shows a series of thermograms of peak I obtained with various heating rates. As the heating rate is increased, both the temperature T_s of the peak maxima and the peak heights and areas increase. Such TSC thermograms were repeatable under the same measurement conditions. The trapping parameters of the defects - the activation energies E_t and capture cross sections were estimated from the shape of the TSC peaks. Activation

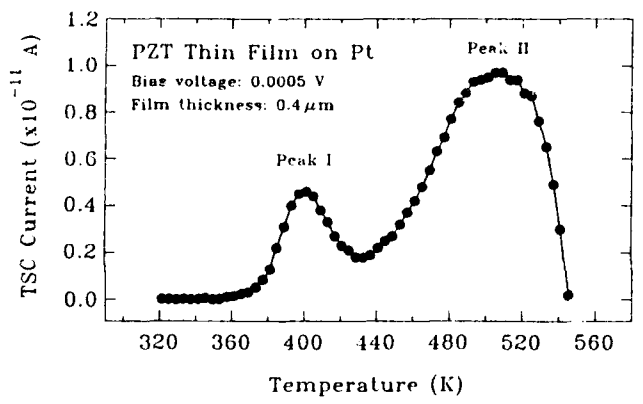


Figure 3. Thermograms after 365 nm UV excitation at 130K for 10m. Heating rate 0.4 K/s.

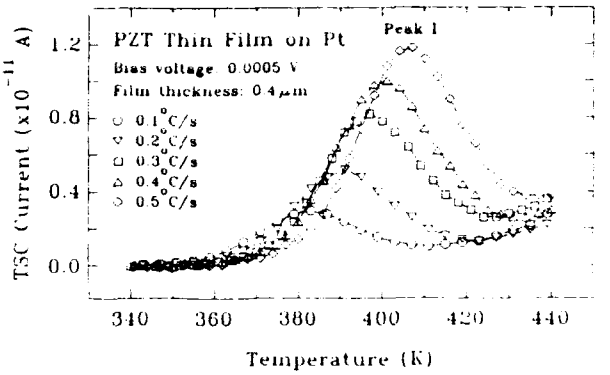


Figure 4. Thermograms for various heating rates

energies were determined by a heating rate method for peak I, and by an initial rise method for peak II. The results gave a value of E_t=0.80eV for peak I and E_t=0.76eV for peak II respectively. Although the activation energy of both traps is nearly the same, their capture cross sections are very different. They are 1.0×10^{-21} cm^2 for peak I and 1.0×10^{-23} cm^2 for peak II respectively, indicating that they indeed correspond to two different traps.

The concentration N_t of trapping centers was determined from the area of the TSC peak assuming that the mobility μ and the lifetime τ of nonequilibrium electronic carriers were known,

$$N_t = \frac{Q_t}{eU} = \frac{A_t\, d^2}{e\, \beta\, \tau\, \mu\, V\, U}$$

where Q_t is the total charge of nonequilibrium carriers, e the electronic charge, U the sample volume under test, A_t the area under a TSC peak, β the linear heating rate, d the film thickness, and V the applied voltage. The mobility and lifetime of carriers in PZT was estimated from values published for $BaTiO_3$ and $SrTiO_3$. These are also perovskite compounds, and the carrier parameters should be comparable to those of PZT within an order of magnitude. With μ=0.1 cm^2/v. [5] and $\tau=1.4\times10^{-8}$ s [6], the concentration of traps is in the order of 10^{21} cm^{-3}, which is a large value compared to the atomic density in PZT. The nature of the trapping centers, and whether they involve electron or hole trapping were not obtainable from these experiments.

Fatigue in PZT Films

Fatigue in PZT films can be represented by curves of polarization P_r and coercive voltage V_c versus the number of polarization reversal cycles N. The fatigue behavior can be approximately divided into two stages, an initial state in which the polarisation is constant and a second stage during which the polarisation degrades. This is shown in Fig.5(a) for a film annealed in O_2 for 2h.

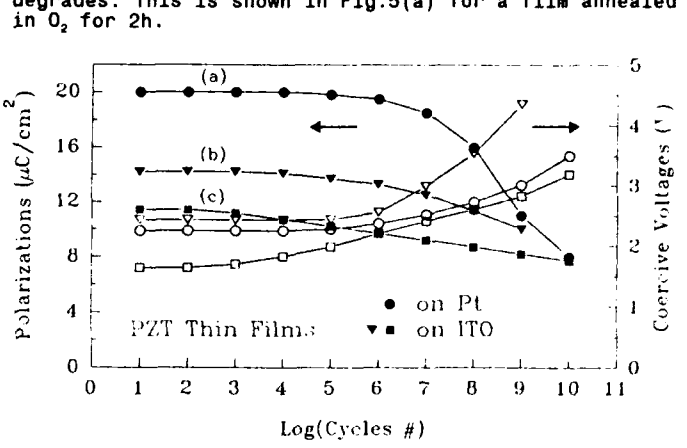


Figure 5. (a) Fatigue of stoichimetric PZT;
(b) Fatigue of Ta doped PZT;
(c) Fatigue of Mg doped PZT.

In the first stage, both the remanent and the spontaneous polarization remain unchanged up to 10^4 to 10^7 cycles. In the second stage, the polarization decreases almost linearly on a logarithmic plot vs number of cycles. The degraded polarizations fall to 50 to 80% of the initial values after 10^{10} cycles. The detailed behaviour varies from sample to sample. On the other hand, the coercive voltage or field increases steadily with reversal cycles, becoming double or even triple the initial value. As a result, the degraded P-E hysteresis loops after fatigue look poorer in the degree of squareness analogous to the hardening effect of mechanical fatigue in metals subjected to cyclic stress. One of the most interesting features of ferroelectric fatigue is that the degradation of polarization depends only on the number of reversal cycles, and is independent of the cycling frequency from 100Hz to 100kHz and thus the total cycling time. This differs markedly from ferroelectric aging effects which are time-dependent.

The ferroelectric properties of bulk PZT can be modified by the introduction of dopants. Dopants can be either of the donor or acceptor type. According to the defect chemistry of titanate perovskites, introduction of charged impurities can change the content of oxygen and lead vacancies. This can lead to modification of the dc conductivity by several orders of magnitude. It was therefore of interest to know if dopants had any effect on the rate of fatigue in PZT films. No significant difference was found in the fatigue rates for PZT films doped respectively with 1 mol % of tantalum (Fig.5(b)) or magnesium (Fig.5(c)), although the initial ferroelectric properties of the doped films were different.

TSC in Fatigued Films

TSC measurements were carried out on fatigued PZT films as a function of number of cycles. Each TSC thermogram was taken after a film was subjected to a certain number of polarization reversals. It was confirmed experimentally that repeated TSC runs did not cause any degradation in the PZT films, since the highest temperature for the TSC measurements did not exceed 330°C. The electrochemical properties of perovskite oxides do not vary significantly over short periods in this range of temperature. Therefore, any variation in TSC peaks were considered to be an effect of fatigue and due to the changes in local order induced by the polarization reversals. Fig.6 shows a series of TSC thermograms as a function of switching cycles following UV-irradiation of an oxidized PZT film at 300K for 10 m.

The room temperature UV irradiation caused peak I and peak II in Fig.3 to merge into one peak at 460K. This may be due to a dependence of the capture cross sections of the trapping centers on temperature. It is obvious that the areas under the TSC peaks which are proportional to the defect concentration increase with the number of polarisation cycles, indicating that more defects of the same type as those already existing in as-deposited films were generated during polarization reversals.

Estimates of the concentrations of traps at different fatigue states is shown in Fig.7(a). The concentration of trapping centers increases by a factor of two after 10^{10} switching cycles. This moderate change in defect concentration is correlated with a significant

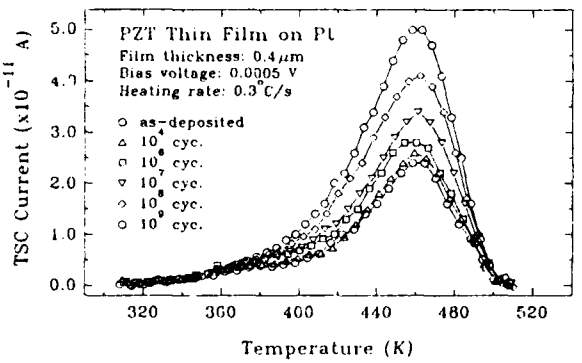


Figure 6. Thermograms as a function of number of switching cycles.

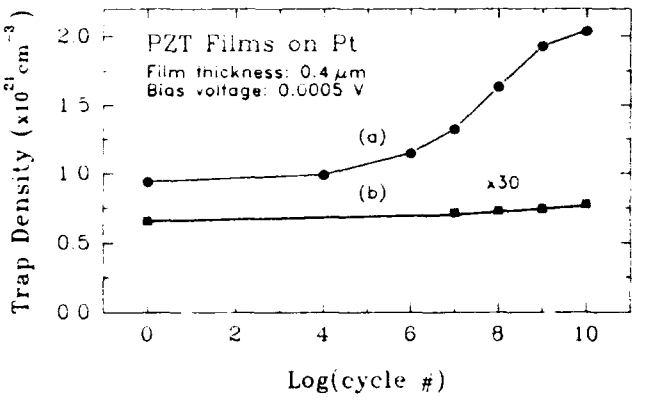


Figure 7. Trap concentration versus number of cycles for a stoichiometric film (a), and for a reduced film (b).

deterioration in the ferroelectric properties. The concentration of traps is $\approx 10^{21}cm^{-3}$, which is a appreciable fraction of the available lattice sites. TSC measurements in which UV irradiations were performed at 10K showed that upon fatigue cycling only the areas of peak II increased, while those of peak I remained virtually constant.

Effects of Processing Conditions

As-fired PZT films processed at 400°C have an amorphous structure and are not ferroelectric. The amorphous films contain distorted perovskite structures and lack long range order. A comparison of TSC in amorphous films to that in well crystallized films may provide evidence which might identify the nature of defects which give rise to TSC peaks that vary with fatigue. No TSC peaks are found in the thermograms for amorphous PZT. This indicates that peaks I and II in well-crystallized films (Fig.3) are associated either with the crystallographic structure of the perovskite, or with defects created during the 650°C annealing process.

It is well known that the dc conductivity of titanate perovskites are controlled by intrinsic point defects such as oxygen and lead vacancies [7]. In PZT, the volatility of PbO at high processing temperature causes a deficiency of lead and oxygen ions and a large number of lead and oxygen vacancies. It has been postulated that fatigue in PZT may be caused by mobile oxygen vacancies [1]. To investigate if any relationship exists between the trapping centers observed from TSC peaks and such intrinsic point defects, we have carried out TSC measurements on reduced PZT films. To minimise the loss of lead, films were reduced at 400°C for 1 min in flowing hydrogen/nitrogen (10/90). The X-ray diffraction patterns of reduced samples showed no significant changes in crystallo-graphic structure. The dielectric constant decreased by a few percent upon reduction, while the overall ferroelectric properties deteriorate. It is believed that the loss of oxygen during reduction leads to a distorted oxygen octahedral structure surrounding a titanium ion which inhibits the motion of the Ti ion which contributes to ferroelectric polarization. TSC measurements for reduced PZT films show only a single peak corresponding to peak II in stoichiometric films. Peak I completely disappears after reduction. The area under the single peak in reduced samples is approximately 60 times less than that of peak II in oxidized samples. The absence of any correlation of the defect concentration with reduction tends to exclude any connection between the trapping centers and intrinsic point defects such as oxygen vacancies. A sinusoidal voltage of the same amplitude as before was applied to a reduced PZT film to induce fatigue. The number of polarization reversals was small because of the poor ferroelectric properties in the reduced film. TSC measurements of the same sample at different stages of fatigue cycling showed that the concentration of trapping centers only increased slightly as shown in Fig.7(b), compared to the doubling in stoichiometric films subjected to similar fatigue cycling. This is consistent with the fact that fatigue in ferroelectrics depends only on polarization reversal. In other words, without polarization reversals no ferroelectric fatigue

occurs. This behavior is distinguished clearly from other time-dependent effects. On the other hand, a film re-oxidized from a reduced state by heating in oxygen at 400°C exhibited a recovery of both the ferroelectric properties and the TSC characteristics implying that the oxygen octahedra are restored by absorbing oxygen ions from the ambient. By comparison, films fatigued by polarization reversals could not be rejuvenated at the same heating condition.

Discussion

The use of TSC to study defects in ferroelectric perovskites has been shown to be of value. The fact that the defect densities correlate with fatigue demonstrates that TSC can assist in the identification of fatigue mechanisms. The two TSC peaks at 400K and 500K respectively in PZT are associated with two different discrete levels even though their energy levels are close. This is confirmed by differences in the capture cross sections of the two traps, and in their response to oxidation and reduction. Trap I, which is associated with peak I, is little affected by the process giving rise to fatigue, but is strongly affected by nonstoichiometry. In contrast, the trap II associated with peak II, is not only affected by nonstoichiometry, but also sensitive to the fatigue process. It is postulated that TSC peaks in PZT are related to the band conduction of nonequilibrium carriers instead of hoping conduction. This may justify the use of transport parameters of band conduction in the estimation of trap concentrations.

The experimental evidence for the origin of the trapping centers obtained from TSC suggests that the traps are not directly associated with point defects. The negative correlation of TSC peaks with oxygen vacancies generated in oxidation-reduction experiments has excluded the direct association of trapping centers with oxygen vacancies. Although oxygen vacancies are considered to be electron donors in titanate perovskites, the expected activation energy is about 0.2eV for the ionization of the second electrons, compared to 0.80eV and 0.76eV in the current TSC measurements. Similarly the fact that reduction was carried out in a temperature range in which the loss of lead was insignificant, and the fact that TSC peaks can be regenerated in an oxidation-reduction-reoxidation process also excludes the direct association of trapping centers with lead vacancies. Impurities may also act as extrinsic point defects. The impurities were introduced either accidentally from the source chemicals in undoped PZT or deliberately by doping. The amount of impurities were established by a specific fabrication process and the concentration was unaffected by the subsequent reduction process. No correlation was observed with the volume concentration of defects. From these arguments, we conclude that point defects do not directly account for TSC trapping centers which are related to fatigue.

The fatigue process in ferroelectric thin films is caused by polarization reversals only and is thus time-independent. This is also confirmed by fact that non-ferroelectric films do not show fatigue and the density of trapping centers in these films is relatively unaffected by repeated cycling. Any models for the fatigue mechanism in ferroelectrics should take these characteristics into account. Our results suggest the fatigue models based directly on the effects of point defects such as oxygen vacancies are unjustified experimentally. Domain pinning models based on the pinning effects of point charged defects which accumulate inside the grain or domain boundaries during the fatigue process are also not consistent with TSC experiments. We therefore have to resort to other fatigue mechanisms which firstly are only polarization reversal dependent and secondly are point defect independent.

The possible defects associated with the trapping centers in the TSC measurements are, in our view, extended defects. Fatigue in ferroelectrics is then caused by the pinning of domains by extended defects, whose concentrations can be altered by polarization reversals. The extended defects may be associated with either linear defects such as dislocations, or planar defects such as antiphase boundaries. However, taking into account the large density of defects measured in TSC, we associate the trapping centers preferably with planar faults. Prisedsky et al. have reported the existence of regular oriented arrays of planar faults in PZT [8]. The distances between these planes are smaller than the usual sizes of ferroelectric domains as revealed under TEM and the fault planes are about 100 Å apart [8][9]. If we assume that the width of a plane fault is 8 Å (the length of two lattice constants) and in such a fault plane each perovskite unit cell contributes one electronic state which acts as an trapping center, the concentration of such centres is $\approx 10^{21} cm^{-3}$ and the distance of 120 Å between plane faults is in good agreement with the TEM observations. Since antiphase boundaries (APB) are real physical disturbances in the otherwise regular lattice structures, we believe that APB may act as the boundaries of microdomains which together form the larger domains seen in TEM. The interaction between the APB and the domains should then affect the motion of ferroelectric domain walls which determine ferroelectric properties such as polarization and coercive fields. In other words, the APBs are able to pin the domain walls.

On the other hand, it has been observed that the major domain wall configuration induced in the PZT system by electric fields are 90° [10]. The switching of 90° domains is accompanied by the redistribution of strain and stress fields in a lattice. If stresses build up around local inhomogeneities with each polarization reversal cycle, the shear motion of the lattice forced by those stresses may create more antiphase boundaries. This may explain the increase of the TSC trapping centers with polarization reversals. Increase of the number of APB in the fatigue process is equivalent to the splitting of microdomains into smaller ones. This intensifies the pinning effect of domain walls, leading to smaller polarizations and larger coercive fields. Obviously, this fatigue mechanism is dependent only on the polarization reversals but not on time. This model is analogous to mechanical fatigue in metals due to the interlocking of dislocations. The hypothesis proposed here is consistent with much of the experimental data on ferroelectric fatigue, although the model may be oversimplified keeping in mind the complexity of formation of the APB boundaries. The detailed interactions between APBs and domain walls are still not clear and have to be further clarified. TEM experiments to confirm the fatigue mechanism proposed here are in progress.

Conclusions

We have correlated ferroelectric fatigue in PZT thin films with lattice defects using a thermally stimulated current technique. The TSC measurements have excluded the direct effects of point defects of either an intrinsic or an extrinsic nature on the fatigue process. The observed trapping centres have been attributed to extended defects such as antiphase boundaries or other planar faults. It is suggested that fatigue is caused by domain splitting and pinning due to interactions with APB boundaries during polarization reversals.

Acknowledgements

This work was supported by the Natural Sciences and Engineering Research Council of Canada.

References

[1] H.M. Duiker, P.D. Beale, J.F. Scott, C.A. Paz de Araujo, B.M. Melnick, J.D. Cuchiaro and J.D. McMillan, J.Appl.Phys., vol 68, 5783(1990)
[2] I.K. Yoo and S.B. Desu, Mat.Res.Soc.Conf.Proc., 1991.
[3] G. Yi, Z. Wu, and M. Sayer, J.Appl.Phys., vol 64, 2717(1988).
[4] K.D. Budd, S.K. Dey and D.A. Payne, Brit.Ceram.Soc.Proc., vol 36, 107(1985).
[5] E. Weise and M. Andrews. Hall effect measurements on some alkali earth titanates. Urbana, Illinois, 1958.
[6] H. Yasunaga, J.Phys.Soc.Japan, vol 24, 1035(1968).
[7] V.V. Prisedsky, V.I. Shishkovsky and V.V. Klimov, Ferroelectrics, vol 17, 465(1978).
[8] V.V. Prisedsky, G.F. Pan'ko and V.V. Klimov, Ferroelectrics, vol 64, 257(1985).
[9] C. Michel and A. Sicignano, Appl.Phys.Letts., vol 24, 559(1974).
[10] E.T. Keve and K.L. Bye, J.Appl.Phys., vol 46, 810(1975).

Piezoelectrics and Electrostrictives: Composites

NEW FERROELECTRIC AND PIEZOELECTRIC POLYMERS

J.I. Scheinbeim, B.A. Newman, B.Z. Mei and J.W. Lee
Polymer Electroprocessing Laboratory
Department of Materials Science and Engineering
Rutgers University
P.O. Box 909
Piscataway, NJ 08855-0909

Abstract: Recent investigations in our laboratory have led to the discovery of a new class of ferroelectric polymers - the odd-numbered nylons. X-ray diffraction and infrared absorbance (FTIR) studies of nylon 11 and nylon 7 films with 3-dimensional orientation (texture) provided an understanding of the polarization process in these polymers. More importantly, these studies led to an electroprocessing technique which allowed for the stabilization of the polarization and therefore, the piezoelectric response of these odd-numbered nylons to their crystalline melting points, which for nylon 5 is ~250°C. A comparison of the properties of these ferroelectric nylons and the only other class of ferroelectric polymers, polyvinylidene fluoride and its copolymers will be made.

These studies were supported by ONR and DARPA.

Recent studies in our laboratory (The Polymer Electroprocessing Laboratory, Rutgers University) have led to the discovery of a new class of ferroelectric polymers—the odd-numbered nylons [1,2]. The ferroelectric switching behavior of these nylons can be seen in Figures 1 and 2, which show the current density (J) versus electric field (E), and electric displacement (D) versus electric field (E) behavior, respectively, of nylon 11, nylon 9, nylon 7 and nylon 5. Figure 3 shows the remanent polarization as a function of dipole density for these nylons. The remanent polarization appears to linearly increase from a value of ~55 mC/m^2 for nylon 11 to a value of ~135 mC/m^2 for nylon 5. If we project this linear increase to the dipole density of nylon 3, we obtain a value ~180 mC/m^2. The actual value for nylon 3 will hopefully be determined in the near future and will be compared with the projected value.

In addition, we have also discovered an electroprocessing technique for stabilizing the polarization of these materials to about their crystalline melting points, which has resulted in a new class of piezoelectric polymers that can be used at high temperatures [3]. We have extended our previous work on nylon 11 and nylon 7 to include studies of nylon 9 and nylon 5. Nylon 5, which has the highest melting point of any of the odd-numbered nylons we have studied, has now been shown to exhibit stable piezoelectric response up to a use temperature of ~250°C.

The temperature dependence of the piezoelectric strain constants, d_{31}, for the odd-numbered nylons studied are shown in Figure 4, and the temperature dependence of the corresponding piezoelectric stress constants are shown in Figure 5.

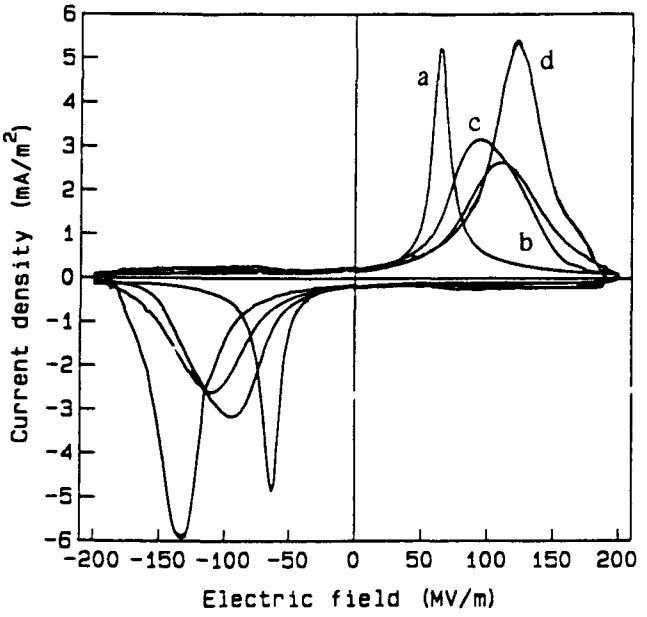
In all cases, the piezoelectric response of these odd-numbered nylons is low at room temperature, which is below their glass transition temperature, T_g. As temperature increases through T_g, piezoelectric response exhibits a sigmoidal shaped increase followed by a plateau region, and sometimes a decrease in response as the maximum annealing temperature of each sample is reached. Each of the polarized nylon samples was first annealed for two hours at the highest measurement temperature shown, in order to stabilize their response.

References

[1] J.W. Lee, Y. Takase, B.A. Newman and J.I. Scheinbeim, "Ferroelectric Polarization Switching in Nylon-11," J. of Polymer Sci., Part B: Polymer Physics, 29, pp. 273-277, 1991.

[2] J.W. Lee, Y. Takase, B.A. Newman and J.I. Scheinbeim, "Effect of Annealing on the Ferroelectric Behavior of Nylon-11 and Nylon-7," J. of Polymer Sci., Part B: Polymer Physics, 29, pp. 279-286, 1991.

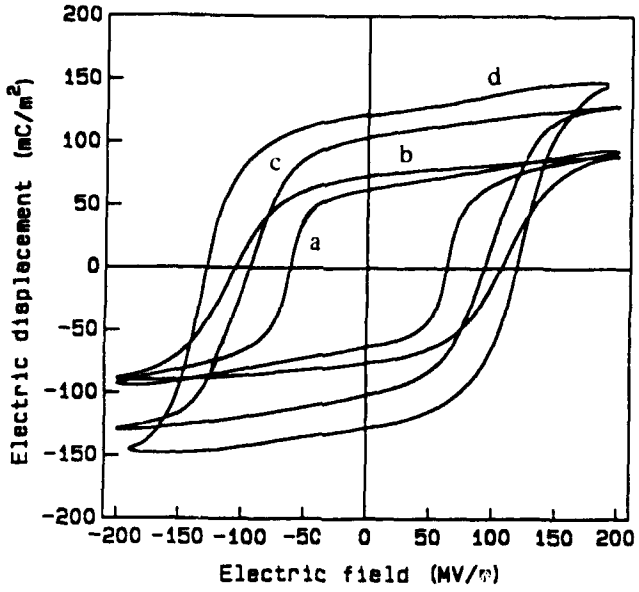
[3] Y. Takase, J.W. Lee, J.I. Scheinbeim and B.A. Newman, "High-Temperature Characteristics of Nylon-11 and Nylon-7 Piezoelectrics," Macromolecules, 24, pp. 6644-6652, 1991.



Current density versus electric field for a) Nylon 11, b) Nylon 9, c) Nylon 7, and d) Nylon 5

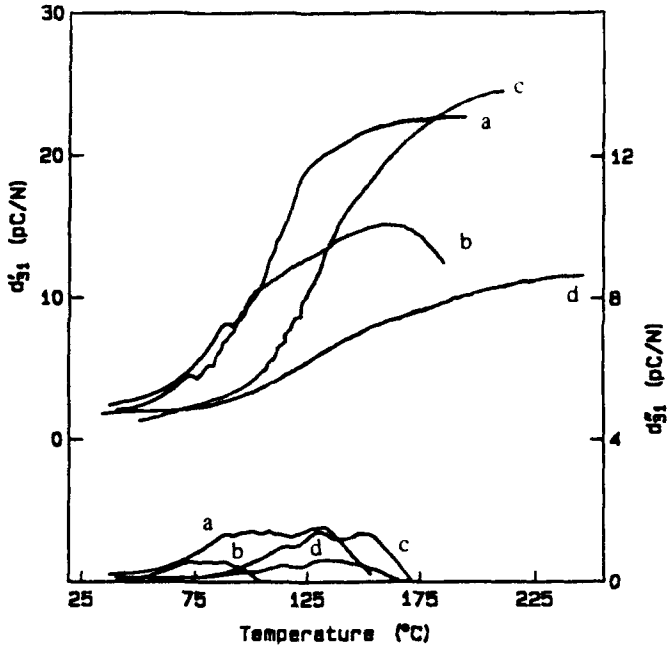
Figure 1

CH3080-0/92/0000-0248 $3.00 ©IEEE



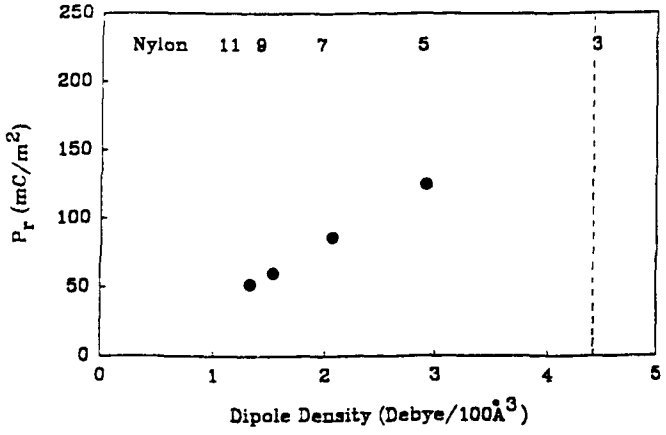
D - E hysteresis loops of odd Nylons. a) Nylon 11, b) Nylon 9, c) Nylon 7 and d) Nylon 5

Figure 2



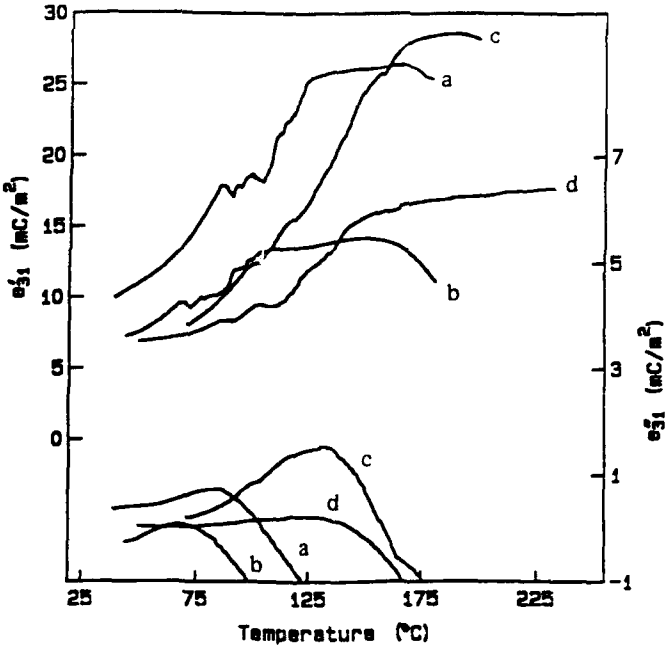
Temperature dependence of the piezoelectric strain constants, d_{31} of samples of a) Nylon 11, b) Nylon 9, c) Nylon 7 and d) Nylon 5 measured at 104 Hz

Figure 4



Dependence of remenant polarization on the dipole density of odd Nylons

Figure 3



Temperature dependence of the piezoelectric stress constants, e_{31} of samples of a) Nylon 11, b) Nylon 9, c) Nylon 7 and d) Nylon 5 measured at 104 Hz

Figure 5

NEW FERROELECTRIC AND PIEZOELECTRIC POLYMERS

J.I. Scheinbeim, B.A. Newman, B.Z. Mei and J.W. Lee
Polymer Electroprocessing Laboratory
Department of Materials Science and Engineering
Rutgers University
P.O. Box 909
Piscataway, NJ 08855-0909

Abstract: Recent investigations in our laboratory have led to the discovery of a new class of ferroelectric polymers - the odd-numbered nylons. X-ray diffraction and infrared absorbance (FTIR) studies of nylon 11 and nylon 7 films with 3-dimensional orientation (texture) provided an understanding of the polarization process in these polymers. More importantly, these studies led to an electroprocessing technique which allowed for the stabilization of the polarization and therefore, the piezoelectric response of these odd-numbered nylons to their crystalline melting points, which for nylon 5 is ~250°C. A comparison of the properties of these ferroelectric nylons and the only other class of ferroelectric polymers, polyvinylidene fluoride and its copolymers will be made.

These studies were supported by ONR and DARPA.

Recent studies in our laboratory (The Polymer Electroprocessing Laboratory, Rutgers University) have led to the discovery of a new class of ferroelectric polymers--the odd-numbered nylons [1,2]. The ferroelectric switching behavior of these nylons can be seen in Figures 1 and 2, which show the current density (J) versus electric field (E), and electric displacement (D) versus electric field (E) behavior, respectively, of nylon 11, nylon 9, nylon 7 and nylon 5. Figure 3 shows the remanent polarization as a function of dipole density for these nylons. The remanent polarization appears to linearly increase from a value of ~55 mC/m^2 for nylon 11 to a value of ~135 mC/m^2 for nylon 5. If we project this linear increase to the dipole density of nylon 3, we obtain a value ~180 mC/m^2. The actual value for nylon 3 will hopefully be determined in the near future and will be compared with the projected value.

In addition, we have also discovered an electroprocessing technique for stabilizing the polarization of these materials to about their crystalline melting points, which has resulted in a new class of piezoelectric polymers that can be used at high temperatures [3]. We have extended our previous work on nylon 11 and nylon 7 to include studies of nylon 9 and nylon 5. Nylon 5, which has the highest melting point of any of the odd-numbered nylons we have studied, has now been shown to exhibit stable piezoelectric response up to a use temperature of ~250°C.

The temperature dependence of the piezoelectric strain constants, d_{31}, for the odd-numbered nylons studied are shown in Figure 4, and the temperature dependence of the corresponding piezoelectric stress constants are shown in Figure 5.

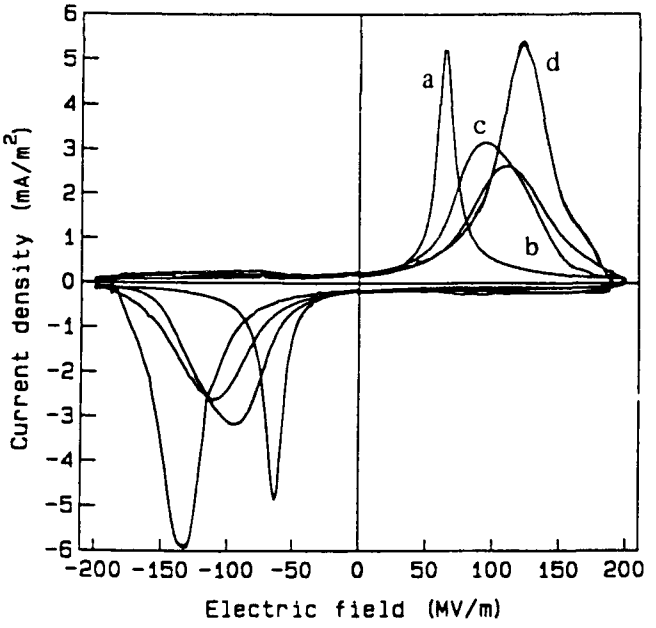
In all cases, the piezoelectric response of these odd-numbered nylons is low at room temperature, which is below their glass transition temperature, T_g. As temperature increases through T_g, piezoelectric response exhibits a sigmoidal shaped increase followed by a plateau region, and sometimes a decrease in response as the maximum annealing temperature of each sample is reached. Each of the polarized nylon samples was first annealed for two hours at the highest measurement temperature shown, in order to stabilize their response.

References

[1] J.W. Lee, Y. Takase, B.A. Newman and J.I. Scheinbeim, "Ferroelectric Polarization Switching in Nylon-11," J. of Polymer Sci., Part B: Polymer Physics, 29, pp. 273-277, 1991.

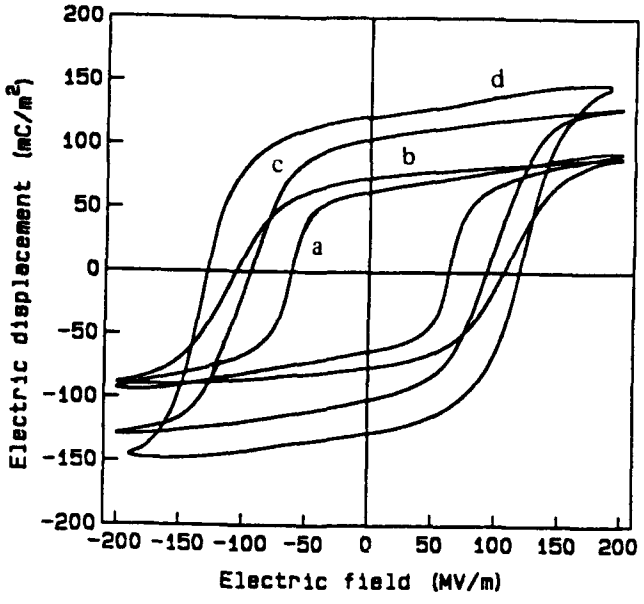
[2] J.W. Lee, Y. Takase, B.A. Newman and J.I. Scheinbeim, "Effect of Annealing on the Ferroelectric Behavior of Nylon-11 and Nylon-7," J. of Polymer Sci., Part B: Polymer Physics, 29, pp. 279-286, 1991.

[3] Y. Takase, J.W. Lee, J.I. Scheinbeim and B.A. Newman, "High-Temperature Characteristics of Nylon-11 and Nylon-7 Piezoelectrics," Macromolecules, 24, pp. 6644-6652, 1991.



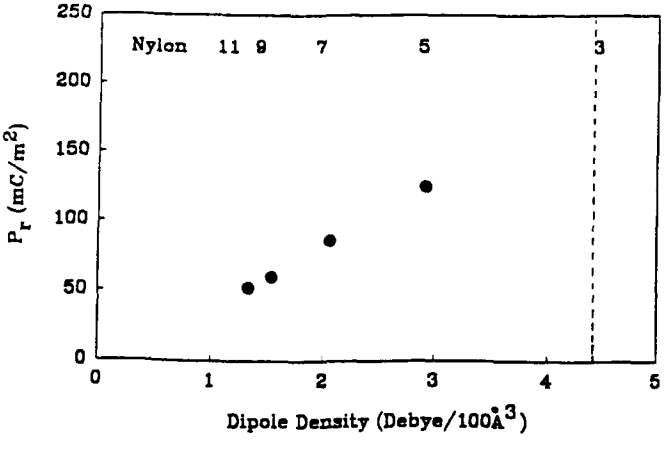
Current density versus electric field for a) Nylon 11, b) Nylon 9, c) Nylon 7, and d) Nylon 5

Figure 1



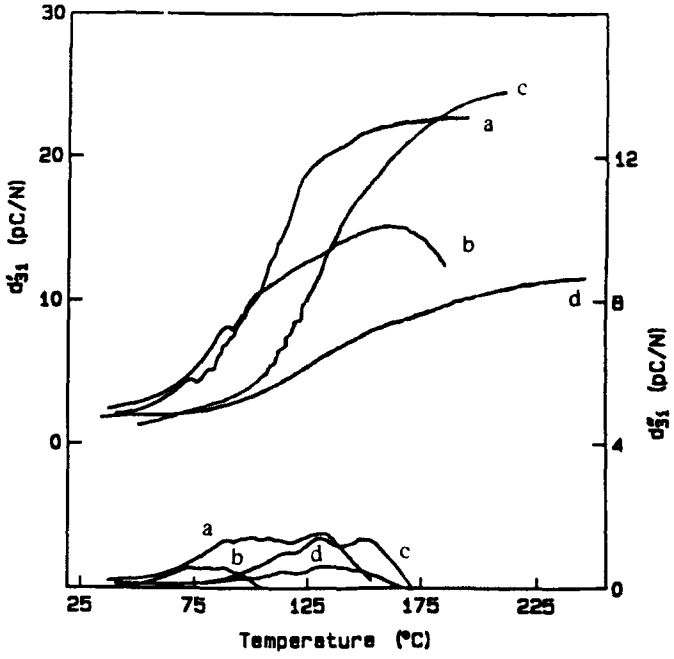
D - E hysteresis loops of odd Nylons. a) Nylon 11, b) Nylon 9, c) Nylon 7 and d) Nylon 5

Figure 2



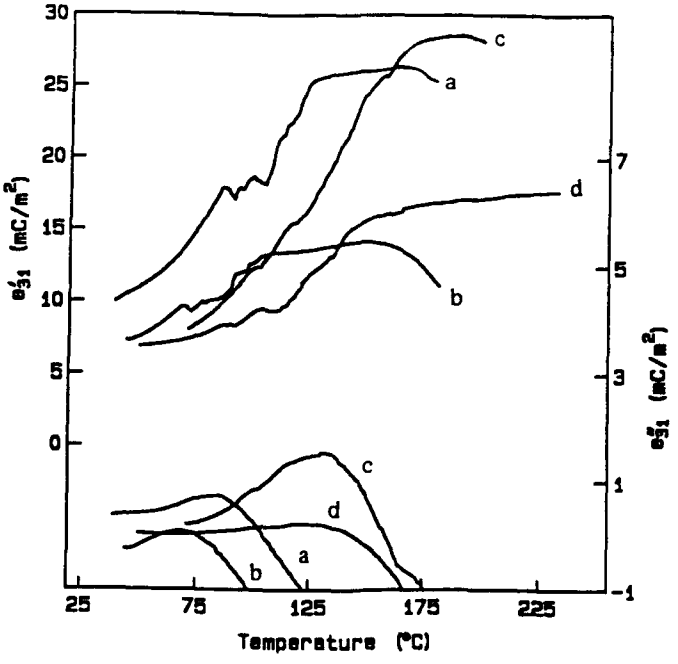
Dependence of remenant polarization on the dipole density of odd Nylons

Figure 3



Temperature dependence of the piezoelectric strain constants, d_{31} of samples of a) Nylon 11, b) Nylon 9, c) Nylon 7 and d) Nylon 5 measured at 104 Hz

Figure 4



Temperature dependence of the piezoelectric stress constants, e_{31} of samples of a) Nylon 11, b) Nylon 9, c) Nylon 7 and d) Nylon 5 measured at 104 Hz

Figure 5

STRAIN PROFILE AND PIEZOELECTRIC PERFORMANCE OF PIEZOCOMPOSITES WITH 2-2 AND 1-3 CONNECTIVITIES

Q. M. Zhang, Wnewu Cao, H. Wang, and L. E. Cross
Materials Research Laboratory, The Pennsylvania State University
University Park, PA 16802

Abstract: The piezoelectric performance of 1-3 type composite depends critically on the stress transfer between the two constituents phases. This paper presents the results of our recent investigation on the elastic and piezoelectric behaviors of composites with 2-2 and 1-3 connectivities. By taking into account the nonuniform strain profiles in the constituent phases, the theoretical model presented can quantitatively predict the performance of these composites. Theoretical predictions agree quantitatively with the experimental results.

Introduction

The quantitative study of the performance of piezoceramic-polymer composites is an interesting and challenging problem. In the past, a great deal of studies have been devoted to this subject.[1-3] Nevertheless, most of these studies are based on the effective medium theory, where the material properties in each constituent phase are assumed to be uniform, and the effective material parameters of a composite are calculated using either the parallel model (Voigt averaging) or series model (Reuss averaging). Although these studies provided general guidelines in predicting the composite properties, the quantitative predictions of the effective material parameters deviate from the experimental observations in most cases.

In this paper, we will present the results of our recent study on piezoceramic-polymer composites with 2-2 and 1-3 type connectivity.[4-6] Since the most important factor of a composite structure is the stress transfer between the two constituent phases, the key to establish a working model for the composites is to understand how this stress transfer is realized. Illustrated in figure 1 is a 2-2 composite structure in which the ceramic plates and polymer are arranged parallel with each other. When subjected to a uniaxial stress, the composite will deform as illustrated by the dashed lines in figure 1(b). For comparison, we have also plotted in the same figure the deformation profile assuming no elastic coupling between the two constituent phases. The effectiveness of the stress transfer between the two phases depends on how much the strain in the polymer phase differs in the two situations [the area between the dash-dotted line and the dashed line in figure 1(b)]. This is determined by the elastic properties of the constituent phases and geometric factors of the composite. Clearly, the stress transfer in the composite is through the shear force and the strain in both phases is not uniform. When the strain is uniform in the composite, there is a maximum stress transfer between the two phases. This is the base for the isostrain model. However, to achieve that situation, the shear modules of the polymer phase needs to be infinity, which is not practical. This explains why the theoretical calculations based on the isostrain model always overestimate the piezoelectric response of composites. Shown in figure 2 is the strain profile for a 1-3 composite manufactured by Fiber Materials, Inc.. The strain profile was measured by the double beam laser interferometer. Clearly, the strain in the polymer phase is much smaller than that expected from the isostrain model. The major advance of our model is to take into account this nonuniformity of the strain profile in the constituent phases explicitly. Therefore, this model can make quantitative predictions on the dependence of the effective material properties of a composite on the properties of its constituent phases and the sample geometric factors.

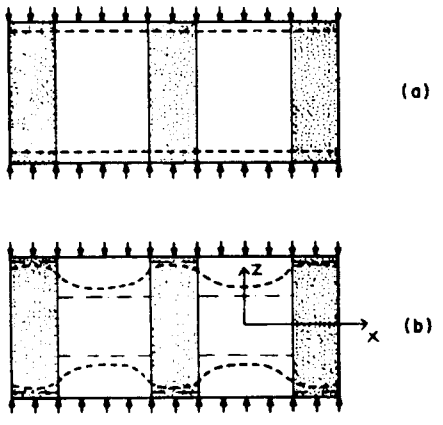


Figure 1: Schematic drawing of the 2-2 composite: (a) strain profile (dashed line) of the composite from the isostrain model when subjected to a uniaxial stress; (b) real strain profile (dashed line).

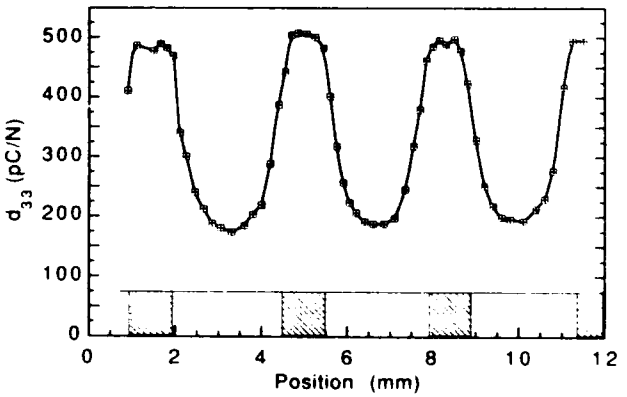


Figure 2: Strain profile for a 1-3 composite measured by the double beam laser interferometer. Hatched regions are PZT rods

The strain profile in 2-2 composites

The cross section of a 2-2 lamellar ceramic-polymer composite is shown in figure 3, where a and d are the dimensions of the ceramic plate and the polymer respectively in the x-direction, and L is the thickness of the composite in the z-direction. The dimension of the composite in the y-direction is much larger than L, a and d.

Under a uniaxial stress T_3, both the polymer and the ceramic are either stretched or compressed depending on the sign of T_3. From symmetry consideration, the z=0 plane (mirror plane) does not move at all in the z-direction. In the near static case, one can assume the strain to be uniform in the z-direction for any given x.
Taking a segment as shown in figure 3 with unit length in the y-direction (h=1), the total shear force in the z-direction fs is

$$fs=(L/4)\,\mu\, u_{xx}(x, L/2)\,dx$$

where u(x, L/2) is the displacement profile at the top surface of the polymer, μ is the shear modulus of the polymer. In the x-direction the composite can move freely and the stress component in this direction is therefore zero. In the y-direction, the polymer is bounded by the ceramic plates and the total stress in this direction is lumped into T_2 since we are not interested in the details of this stress component. From these conditions, one can write down the constitutive relations for this elastic body:

$$\frac{2\,u(x,L/2)}{L} = s_{33}\left(\frac{L}{4}\mu\, u_{xx}(x, L/2) + T_3\right) + s_{32}\,T_2 \qquad (1a)$$

$$S_2 = s_{22}T_2 + s_{32}\left(\frac{\mu L}{4}\, u_{xx}(x,L/2) + T_3\right) \qquad (1b)$$

where S_2 is the y-component of the strain in the polymer phase, s_{ij} is the elastic compliance. For the polymer, one has the relations: $s_{22}=s_{33}$ and $s_{32}/s_{33}=-\sigma$, where σ is the Poisson's ratio. For a 2-2

CH3080-0-7803-0465-9/92$3.00 ©IEEE

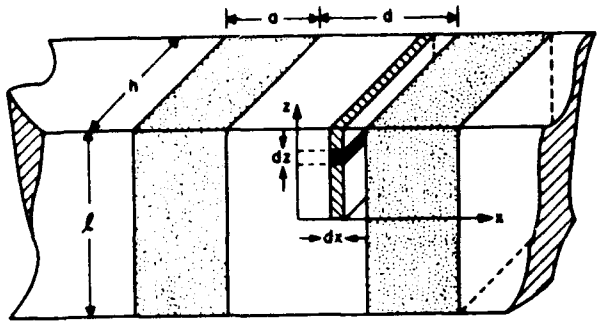


Figure 3: A section of 2-2 composite for our analysis.

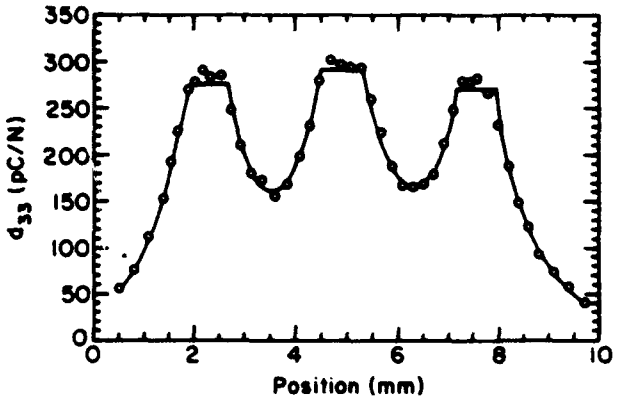


Figure 4: Comparison between the experimentally measured strain profile (dots in the figure) of a 2-2 composite and the theoretical curves (solid lines).

composite with its y-dimension much larger than L, a and d, S_2 is practically a constant and is independent of x. That is, the strain in this direction can be modelled by the isostrain approximation. Combining eqs (1a) and (1b) to eliminate T_2 yields

$$\frac{2\,u(x, L/2)}{L} = s_{33}(1-\sigma^2)\frac{L}{4}\mu\, u_{xx}(x, L/2) + s_{33}(1-\sigma^2)T_3 - \sigma S_2 \qquad (2)$$

If one neglect the stress effect in the y-direction, eq. (1) will be reduced to

$$\frac{2\,u(x, L/2)}{L} = s_{33}\frac{L}{4}\mu\, u_{xx}(x, L/2) + s_{33}T_3 \qquad (3)$$

Hence, the effect of the y-direction stress on the strain in the z-direction is to modify the elastic compliance s_{33} to $s_{33}(1-\sigma^2)$ and to add an additional constant term (Poisson's ratio effect) in the equation. It does not affect the functional form of the equation. Considering the fact that both T_3 and S_2 are constants, we can make variable substitution: $v=u+(L/2)(\sigma s_2 - s_{33}(1-\sigma^2)T_3)$ and equation (2) becomes

$$\frac{2\,v(x, L/2)}{L} = s_{33}(1-\sigma^2)\frac{L}{4}\mu\, v_{xx}(x, L/2) \qquad (4)$$

Therefore, the strain profile in the polymer phase between the two neighboring ceramic plates is

$$\frac{2u}{L} = A\cosh\left(2\frac{x}{L}\sqrt{2Y/(\mu(1-\sigma^2))}\right) + \frac{T_3}{Y} - \sigma S_2 \qquad (5)$$

where A is the integration constant, $Y=1/s_{33}$ is the Young's modulus of the polymer phase. x=0 is at the center of the polymer filling. A can be determined from the boundary condition: $A=(2u_0/L - T_3/Y + \sigma S_2)/\cosh\left(\frac{d}{L}\sqrt{2Y/(\mu(1-\sigma^2))}\right)$, where $2u_0/L$ is the strain in the polymer-ceramic interface. For the situation when there is only one ceramic plate in the composite, the longitudinal strain of the polymer phase is

$$2u/L = B\exp\left(-\frac{(x-a/2)2}{L}\frac{d}{L}\sqrt{2Y/(\mu(1-\sigma^2))}\right) + \frac{T_3}{Y} - \sigma S_2 \quad (x>a/2)$$

and (6)

$$2u/L = B\exp\left(\frac{(x-a/2)2}{L}\frac{d}{L}\sqrt{2Y/(\mu(1-\sigma^2))}\right) + \frac{T_3}{Y} - \sigma S_2 \quad (x<-a/2)$$

where x=0 is set at the center of the ceramic plate.

To compare with the theory, several 2-2 composites were made using PZT-5A plates embeded in spurs epoxy matrix. The longitudinal strain $S_3=2u/L$ of the sample was mapped out along a path parallel to the x-axis (refer to figure 1) using the double beam laser interferometer. Presented in figure 4 is the profile taken from one of these scans. The solid line in the figure is the fitting using eq. (5) for the polymer regions between the PZT plates and eq. (6) at the two edges of the sample. Clearly, the theoretical curve describes the data quite well. From fitting the data, one can obtain the value of $Y/(\mu(1-\sigma^2))=3.35$. For an isotropic medium, we have the relationship $Y/\mu = 2(1-\sigma)$. Therefore, from the value of $Y/(\mu(1-\sigma^2))=3.35$, we can derive $\sigma=0.4$, which is a reasonable value for the spurs epoxy used.

Single rod 1-3 composite

Although the basic stress transfer mechanism between the two constituent phases in a 1-3 type composite is similar to that in the 2-2 type, the problem of solving the strain profile in a regular 1-3 composite is more involved and may be calculated numerically. Here we will only treat one special case, a single rod 1-3 composite subjected to a hydrostatic pressure, to show quantitatively how various parameters affect the performance of a 1-3 composite. The single rod composite is schematically drawn in figure 5, where a cylindrical coordinate system is used. This configuration is a reasonable approximation to the composite with triangularly arranged ceramic rods (for which the unit cell has hexagonal symmetry) and at low ceramic content, the results here could even be used for composites with other rod arrangements.[6]

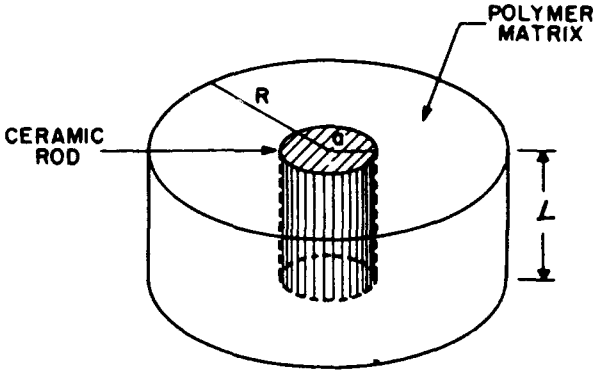


Figure 5: Schematic drawing of a single rod 1-3 composite.

Similar to the 2-2 composite situation, the force equilibrium condition for the polymer phase can be written in the following form[6]

$$\frac{\mu L}{4}\left(u_{rr}(r, L/2) + \frac{u_r(r, L/2)}{r}\right) - (1-2\sigma)p = \frac{2Y\,u(r, L/2)}{L} \qquad (7)$$

where the meaning of each quantity is similar to that in the preceding section and p is the hydrostatic pressure. One can write down similar equation for the strain profile in the ceramic rod. The strain profile for the polymer phase is therefore given by

$$2u/L = A K_0(r/\xi) + B I_0(r/\xi) - (1-2\sigma)p/Y \qquad (8)$$

where $K_0(\rho)$ and $I_0(\rho)$ are zeroth order modified Bessel functions. A and B can be determined from the boundary conditions. From the

strain profile, one can calculate the stress transfer between the two constituent phases and hence the effective piezoelectric hydrostatic strain constant d_h:

$$d_h = V_c (\gamma_h d_{33}^c + 2 d_{31}^c) \qquad (9)$$

where Vc is the volume content of the ceramic in the composite, d_{33}^c and d_{31}^c are the piezoelectric constants of the ceramic phase, and γ_h is the stress amplification factor:[6]

$$\gamma_h = 1 + \frac{\frac{L}{a} I_1(\rho_R^c)[I_1(\rho_R)K_1(\rho_a) - I_1(\rho_a)K_1(\rho_R)][(1-2\sigma)/Y - (1-2\sigma^c)s_{33}]}{\sqrt{\frac{2s_{33}}{c_{44}}} I_0(\rho_a^c)[I_1(\rho_R)K_1(\rho_a) - I_1(\rho_a)K_1(\rho_R)] + \sqrt{\frac{2}{Y\mu}} I_1(\rho_a^c)[I_1(\rho_R)K_0(\rho_a) + I_0(\rho_a)K_1(\rho_R)]} \qquad (10)$$

where s_{33} and c_{44} are the elastic compliance and the shear constant of the ceramic, σ^c is the Poisson's ratio of the ceramic, $\rho_r = (2\,r/L)\sqrt{\frac{2Y}{\mu}}$ and $\rho_r^c = (2\,r/L)\sqrt{\frac{2}{s_{33}c_{44}}}$. One can see that the stress amplification factor depends on the elastic properties of the constituent phases and most importantly, on the aspect ratio of the ceramic rod. Plotted in figure 6 is the calculated results for d_h from eq. (9) for several different aspect ratios for a PZT5H-Spurs epoxy composite. The input data can be found in reference 6. Clearly, aspect ratio of the PZT rod is an important parameter in determining the piezoelectric performance of 1-3 composites.

Shown in figure 7 is the comparison between the experimentally measured d_h for a 1-3 composite with 1% PZT volume content in spurs epoxy matrix and that calculated from equation (9). The parameters used in the calculation are listed in reference 6, and d_{33} and d_{31} were treated as fitting parameters. The agreement between the experimental result and theoretical calculation is satisfactory.

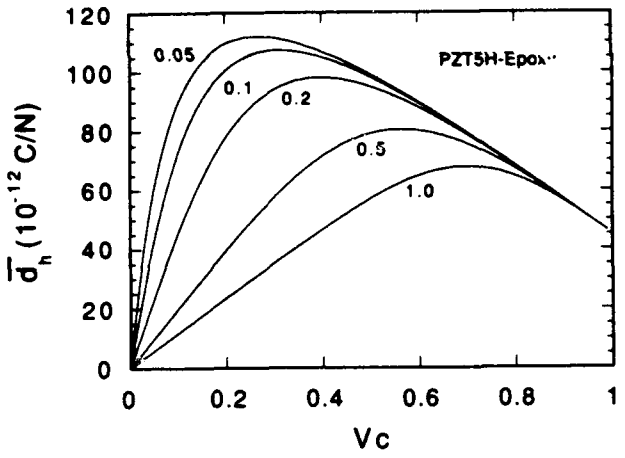


Figure 6: The hydrostatic piezoelectric constant d_h, as a function of the ceramic content at the aspect ratio of a/L=0.05, 0.1, 0.2, 0.5 and 1.0 for a single rod PZT5H-Epoxy 1-3 composite.

Conclusions

In general, the response of the constituent phases of a composite to an external field is not uniform spatially. By taking into account the nonuniform strain profiles in the constituent phases, the theoretical model presented in this paper can quantitatively predict the performance of these composites. Theoretical predictions agree quantitatively with the experimental results.

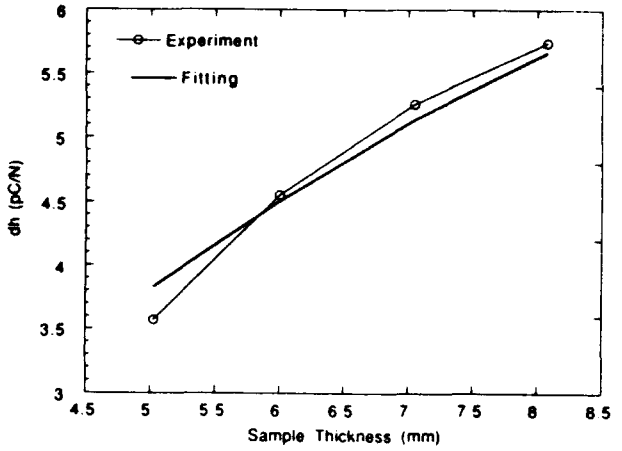


Figure 7: Thickness dependance of d_h for a 1-3 composite and the comparison with the theoretical prediction. The radius of the PZT rod is 0.405 mm.

References

[1] Newnham, R. E., D. P. Skinner, and L. E. Cross, "Connectivity and Piezoelectric-Pyroelectric Composites," Materials Res. Bull, vol 13, pp. 525-536, 1978.

[2] Gururaja, T. R., A. Safari, R. E. Newnham, and L. E. Cross, "Piezoelectric Ceramic-Polymer Composites for Transducer Applications," in Electronic Ceramics, ed. L. M. Levinson, pp. 92-128, New York: Marcel Dekker,1987.

[3] Smith, W. A., B. A. Auld, "Modeling 1-3 Composite Piezoelectrics: Thickness-Mode Oscillations," IEEE Trans. on Ultrasonics, Ferro., and Freq. Control, vol 38, pp. 40-47, 1991.

[4] Wenwu Cao, Q.M. Zhang, and L. E. Cross, " Theoretical Study on the Static Performance of Piezoelectric Ceramic-Polymer Composites with 2-2 Connectivity," IEEE Trans. Ultrasonics, Ferro., and Freq. Control, in press, 1992.

[5] Q. M. Zhang, Wenwu Cao, H. Wang, and L. E. Cross, "Characterization of the Performance of 1-3 Type Piezocomposites for Low Frequency Applications," submitted to J. Appl. Phys., 1992.

[6] Wenwu Cao, Q. M. Zhang, and L. E. Cross, "Theoretical Study on the Performance of Piezoelectric Ceramic-Polymer Composites with 1-3 Connectivity," accepted by J. Appl. Phys., 1992.

AN OPTIMIZATION OF 1.3.1 PZT-POLYMER COMPOSITE FOR DEEP UNDERWATER HYDROPHONE APPLICATION

C.RICHARD, P. EYRAUD, L.EYRAUD and D. AUDIGIER
INSA - Laboratoire de G.E. et Ferroélectricité
69621 VILLEURBANNE Cedex - FRANCE

M. RICHARD
CERDSM - DCN Le Brusc - 83140 SIX FOURS LES PLAGES - FRANCE

Abstract

The strong dependence of the sensitivity on the hydrostatic pressure is a well known problem for sensitive hydrophones. Hydrophones stable up to a 10 MPa or a 15 MPa hydrostatic pressure and with a gh.dh figure of merit respectively equal to $28.10^{-12}Pa^{-1}$ or $16.10^{-12}Pa^{-1}$ are proposed.

Those hydrophones are made on the 1.3.1 piezocomposite basis. For this kind of connectivity, there is no lateral contact between the polymer matrix and the PZT rods. The PZT rods are inserted in holes made in the polymer matrix and are held between two metallic armature plates.

The hydrophone sensitivity and figure of merit variations versus the hydrostatic pressure are compared to the PZT piezoelectric coefficients dependence on the uniaxial stress applied along the polarization direction.

An optimalization approach is proposed based on a complete characterization of the PZT under uniaxial stress and on a FEM model of the piezocomposite.

Introduction

A lot of studies have been made during the fifteen past years in order to make piezoelectric materials presencing a large hydrostatic mode sensitivity. One of these materials, the 1.3 PZT-Polymer piezocomposite, early investigated by Newnham and al.[1], consists of parallel PZT rods embedded in a polymer matrix. This composite is based on the most widely exploited stress transfer principle involving shear stresses at the matrix-rod interface [2]. However, in order to be efficient, this kind of stress transfer requires very thin PZT rod shapes. An other difficulty is the parasitic transverse coupling due to the high Poisson's ratio of very compliant polymers. Very sensitive devices have been made, taking account of these problems, by using foamed polymer matrices[3], fiber reinforced matrices[4] or matrices with a single large void[3] and needle shaped PZT rods for all of them.

In order to make 1.3 piezocomposites with a common industrial PZT rod shape, a transducer, shown on Fig.1, was designed with the rod shape not directly involved in the stress transfer accuracy. This device presents the general properties of a 1.3 piezocomposite but without any lateral contact between the polymer matrix and the PZT rods. No charges are by this way generated by the lateral coupling of the PZT. The stress transfer, not directly based on the interface, is carried out by two metallic armature plates used as electrodes and providing also a reinforcement of the polymer matrix in the transverse directions. This device is referenced as 1.3.1 PZT-Polymer-Air composite, the air surrounding the PZT rod in the matrix hole corresponds to the last figure in the connectivity expression. First studies [5] showed the influences of the different parts of the composite. In this paper, a characterization of the 1.3.1 piezocomposite under high hydrostatic pressure is given and an optimization taking account of the pressure stability is proposed.

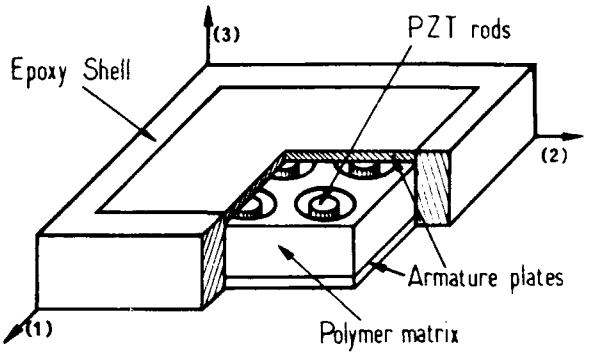


FIGURE 1: A 1.3.1 Piezocomposite device (not embedded)

Experimental

Sample Preparation

The polyurethane matrix (Flexcomet 94SA) is primarily cut to the desired size (30mm x 30mm x 5mm). Holes are drilled following a square or hexagonal arrangement, as numerous as necessary to get the right volume ratio. The armatures plates are cut in sheet steel of various thicknesses. The piezoelectric rods are 2.7mm in diameter and 5mm high. This size was initially chosen because it is the smallest size industrially made in quantities for high voltage igniters. Two kinds of PZT have been used : a Navy I type, TDK FM91e used in the first experiments and a hard one, Fe and Mn doped referenced here as LG262 and used in the present work. Tables 2 and 3 list the main properties of those materials.

The PZT rods are first aligned and bonded on the first armature plate ith a conductive adhesive (epoxy + silver). The matrix is then stuck with epoxy. The rods are grinded in order to equalize exactly their height to the matrix thickness. The second armature is bonded simultaneously on the PZT rods and the matrix. Some samples have been reinforced with an epoxy shell added on the lateral sides of the composite. The devices are finally entirely embedded in polyurethane.

Measurements

The piezoelectric hydrostatic coefficients are directly measured in an oil filled volume where a low frequency (120 Hz) low amplitude (400 Pa RMS) sinusoidal hydrostatic pressure is applied. A high hydrostatic pressure up to 15 MPa can also be applied.

CH3080-0-7803-0465-9/92$3.00 ©IEEE

TABLE 1 : 1.3.1 Piezocomposites made with PZT LG262 and PU 94SA. Experimental results and fabrication data. $\Delta(g_h.d_h) = 10 . \log (g_h.d_h \text{ (x MPa)} / g_h.d_h \text{ (initial)})$. The variations are reversible.

sample number	PZT volume %	numb of rods	hole ϕ (mm)	plate thickn. (mm)	epoxy shell	gh.dh initial TPa^{-1}	β	Δ(gh.dh) 1 cycle 10 MPa	Δ(gh.dh) 1 cycle 15 MPa	Δ(gh.dh) 35 cycles to 10MPa	Δ(gh.dh) 35 cycles to 15MPa	Δ(gh.dh) 24 hours at 10MPa	Δ(gh.dh) 24 hours at 15MPa
3204	10.2	16	6	1	no	24.4	5.8	+0.8	-0.8	not meas.	not meas.	not meas.	not meas.
3208	12.7	20	5	1	no	18.5	4.6	+0.7	-0.1	-0.4	-1.2	not meas.	not meas.
3209	15.9	25	4.5	1	no	16.9	4.0	0	-0.1	-0.5	-0.7	-1	-1.3
3213	15.9	25	4.5	1.5	no	16.5	4.1	+0.3	0	-0.1	-0.5	-0.6	-0.8
3219	10.2	16	6	1	yes	28.2	6.5	+1	-0.9	+0.2	-1.5	-0.9	-3.3
3226	10.2	16	6	1.5	yes	28.3	6.6	+1.1	+0.2	+0.4	-0.5	-0.5	-1.9
3239	12.7	20	5	1.5	yes	21.8	4.9	+0.9	+0.8	not meas.	not meas.	+0.5	-0.3
3255	12.7	20	5	1.5	yes	18.4	4.6	+0.8	+0.2	+0.2	0	-0.15	-1.5

The hydrostatic parameters are first measured under a 0.1 MPa hydrostatic pressure characterizing the initial stress-free state of the composite. The hydrostatic coefficients are measured during 2 stress cycles: a 4 hours long one up to 10 MPa and a 6 hours long one up to 15 MPa. Then, two series of 35 cycles (20 min) are applied up to 10 MPa and 15 MPa. The hydrostatic figure of merit is finally recorded during two 24 hours periods under 10 Mpa and 15 MPa. Each of these 6 experiments are separated by at least a 24 hours recovering period at atmospheric pressure.

Table 1 lists the results obtained with the PZT LG262 / PU 94SA 1.3.1 Piezocomposites. Figure 2 shows typical hydrostatic sensitivity (Sh) variations with the pressure up to 15 MPa for some of them.

Discussion

It is observed that the first pressure cycle is not long enough to evaluate the piezocomposite resistance to hydrostatic pressure. Repetitive pressure cycles are necessary to separate the stable piezocomposites from the unstable ones. Roughly, the decrease of gh.dh with pressure is an increasing function of the sensitivity. However, some other parameters should be considered. Composites with thicker armature plates are generally more stable. The composites with the small lateral epoxy shell are also more stable. Composites without the shell can even be destroyed when the 15 MPa pressure is released (Sample 3204). As it will be shown afterwards , the PZT material has a direct influence on the piezocomposite behavior under pressure, but the matrix can also be involved and particularly in the regions where the strains are too important for a viscoelastic material. Both the armature plate thickness and the epoxy shell lower the stress supported by the lateral edges of the matrix and then limit its lateral strain and the related effects. Considering that point, the piezocomposites with a gh.dh equal to $16.10^{-12} Pa^{-1}$ could be used up to 15 MPa whereas the ones with a gh.dh comprised between 16 and $28.10^{-12} Pa^{-1}$ could still be used up to a 10 Mpa pressure.

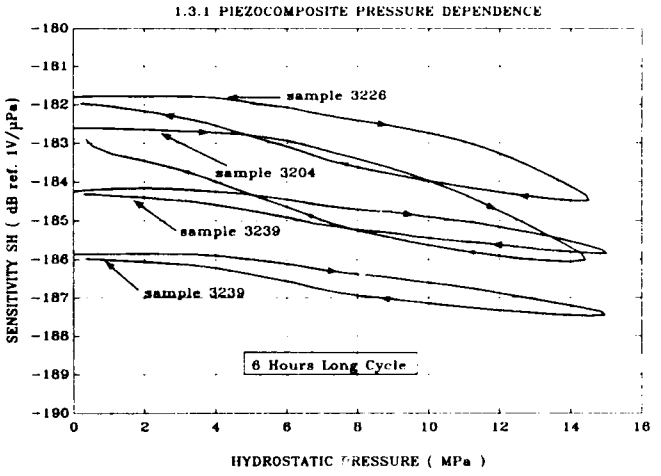


FIGURE 2 : Hydrostatic sensitivity pressure dependence measured during a 6 hours long pressure cycle up to 15 MPa. Sh is expressed in dB ref. 1V/μPa.

Hydrostatic pressure dependence interpretation

Uniaxial scheme of the 1.3.1 Piezocomposite

As a consequence of the piezocomposite constitution, it can be assumed that the PZT rods are uniaxially stressed along their polar axis. If d_{33}, g_{33} and ε^T_{33} are the piezoelectric and dielectric parameters of the PZT material and if $<d_h>$, $<g_h>$ and $<\varepsilon^T_{33}>$ are the hydrostatic and dielectric coefficients of the piezocomposite , then:

$$<g_h> = \beta . g_{33} \quad (1) \qquad <d_h> = \beta . v . d_{33} \quad (2)$$

$$<\varepsilon^T_{33}> = v . \varepsilon^T_{33} \quad (3) \qquad <g_h.d_h> = \beta^2 . v . g_{33}.d_{33} \quad (4)$$

where v is the PZT volume fraction and β is the stress amplification coefficient defined as follows:

$$T_3 = \beta . p_o \quad (5)$$

T_3 is the uniaxial stress applied to the PZT rods and p_o is the hydrostatic pressure .
β is also the ratio of $<g_h>$ to g_{33} and is calculated by this way from the measurements under atmospheric pressure of both the PZT rods and the piezocomposite.

PZT longitudinal stress dependence and limits

The longitudinal uniaxial stress effects on the PZT coefficients, early investigated by Berlincourt and Krueger[6] , have been measured on a special device allowing the measurements of d_{33} and ε^T_{33} with a pre-stress (1 to 200 MPa) applied to a PZT rod (cylindrical PZT sample, 5mm in diameter and 15mm high). Figure 3 shows the $g_{33}.d_{33}$ figure of merit variations versus the uniaxial stress T_3 for various PZT materials including PZT LG262 and PZT TDK FM91e used in our experiments and P1.88 and P1.89 soft and hard PZT made by Quartz et Silice (Saint-Gobain - France). As observed on multiple stress cycles[5], the maximum uniaxial stress T_{3max} that the PZT material can support continuously without important decrease of $g_{33}.d_{33}$ is assumed to correspond to the maximum of the $g_{33}.d_{33}$ versus stress plot. Those limits can therefore be easily obtained from Figure 3.

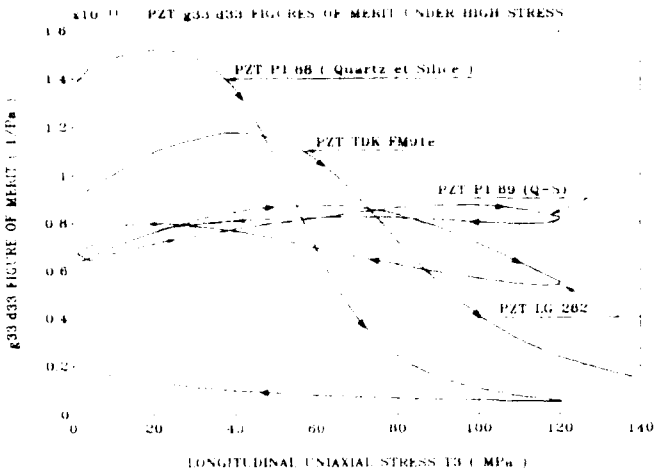


FIGURE 3 : $g_{33}.d_{33}$ pressure dependence of various PZT materials showing the superiority of Navy III PZT (P1.89 - Quartz & Silice - St. Gobain - France).

PZT and Piezocomposite comparison

According to equations (1) to (5), it would be possible to derive the PZT d_{33} variations versus stress from the piezocomposite hydrostatic coefficient variations versus hydrostatic pressure. This is represented on Figure 4. The continuous curve, also plotted on Figure 4, corresponds to the direct measurement on a PZT rod. The rather good agreement between both results shows the consistency of the assumptions and the interest of the direct PZT characterization under uniaxial stress for the piezocomposite design.

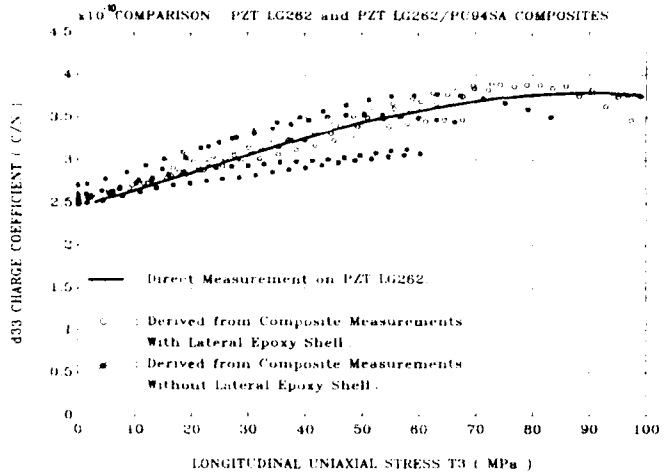


FIGURE 4 : Comparison of the piezocomposite d_h pressure dependence (points and asterisks: the d_{33} is derived from the d_h measurements) to the PZT rod d_{33} stress dependence (continuous curve).

TABLE 2 : Properties of the polymer materials used in the experiments.

Polymer	Epoxy	Polyureth.
Reference	Resin D Ciba-Geigy	94 SA Framet
ε_r	4	4
s_{11} (10^{-12} m^2/N)	217	3300
Poisson's ratio	0.35	0.49

Piezocomposite Optimization

FEM modeling of the 1.3.1 Piezocomposites

Early attempts to model 1.3.1 piezocomposites with an analytical model essentially based on armature plate deflection hypotheses gave good orders of magnitude and some of the general tendencies experimentally observed [5]. However, this kind of model is unable to predict the right deflection state of the armatures, specially in the case of multi-rods composites. Static FEM analysis of the 1.3.1 piezocomposites have been made with the FEM ATILA program[7]. Figure 5 shows the gh variations versus the PZT volume fraction for a 30mm x30mm x 5mm PZT LG262/ PU 94SA 1.3.1 piezocomposite and for various plate thicknesses. For each PZT volume fraction the matrix hole diameter is chosen in order to get the holes tangent to each others in a square arrangement while keeping a 1mm margin between two adjacent holes and a 0.5 mm one between a hole and the external sides of the matrix. These margins are the minimum ones allowing a realistic bonding of the armatures on the matrix. The previous experimental results, obtained in very similar conditions, are also plotted showing a good agreement between the experimental and theoretical results.

Figure 6, obtained by FEM shows the g_h variations versus the lateral size of the composite while the other parameters are kept constant. The g_h coefficient is an increasing function of the composite lateral size. This result is partly due to the transverse reinforcement of the matrix by the armature plates. This effect is combined with the influence of the multiplicity of the PZT rods on the plate deflection. These combined effects saturate when the lateral size is 5 to 6 times the matrix thickness, giving that way a value of the minimum lateral size of the composite.

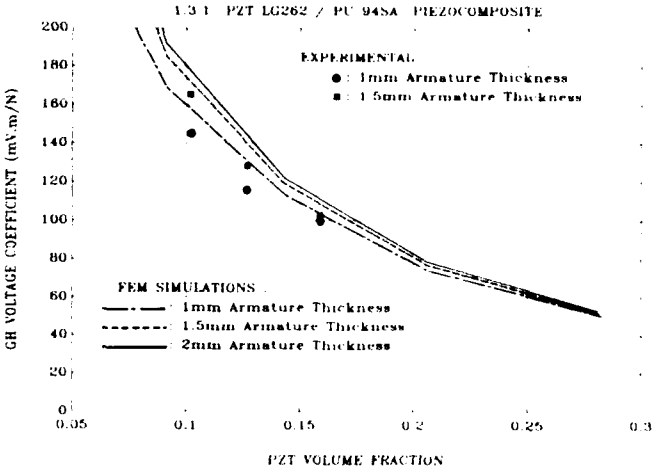


FIGURE 5 : Finite Element Simulations of the g_h variations versus the PZT volume fraction for various armature plate thicknesses(1mm ,1.5mm, 2mm). Calculated for a 30mmx30mmx5mm square composite.

TABLE 3: Properties of the PZT materials used in the experiments.

PZT type	TDK FM91e (TDK)	PZT LG262 (LGEF)
d_{33} (pC/N)	309	260
s^E_{33} (10^{-12} m^2/N)	16.4	14.1
ε^T_{33} / ε_o	1300	1170
$g_{33}.d_{33}$ ($10^{-15} Pa^{-1}$)	8300	6500
T_{3max} (MPa)	40	60

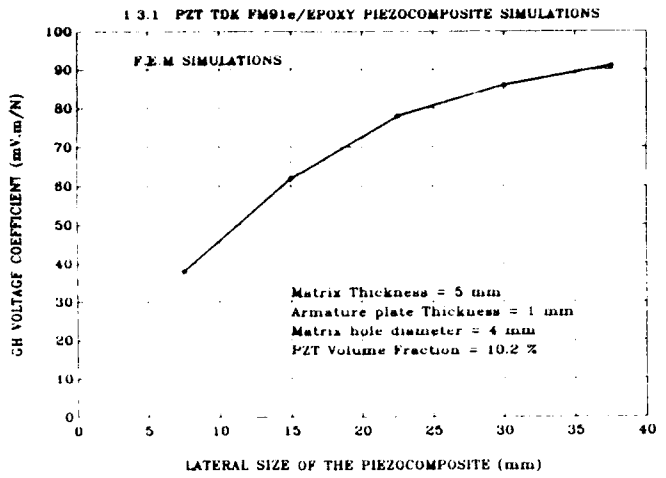


FIGURE 6 : g_h variations versus the lateral size of the piezocomposite. This is a consequence of the reinforcement of the matrix by the armature plates.

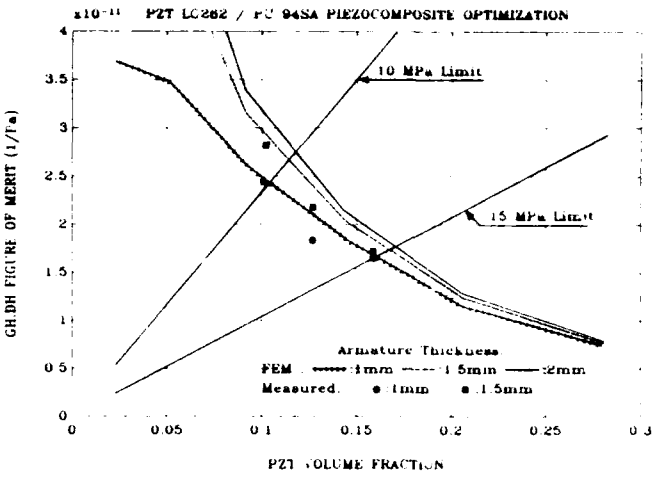


FIGURE 7 : Optimization diagram in the (v , $g_h.d_h$) plane for a 1.3.1 PZT LG262 / PU94SA piezocomposite.

Stability domain - Optimization

As a consequence of the uniaxial compression of the PZT rods, equation (4) means that the β constant locus in the plane defined by the $g_h.d_h$ versus the PZT volume fraction is a straight line. Its slope is proportional to $\beta^2.g_{33}.d_{33}$ .According to the PZT uniaxial stress T_{3max} defined previously as a limit, a maximum useful hydrostatic pressure allows to calculate a β_{limit} value equal to T_{3max} divided by the maximum pressure. The β_{limit} line shares the plane in one stable area below the line and one unstable area for a given PZT and a working hydrostatic pressure. Now, if the theoretical $g_h.d_h$ versus PZT volume fraction plot is superimposed, the intersection point defines the best sensitivity-stability trade-off in these conditions. Figure 7 illustrates this optimization procedure in the case of PZT LG262 and PU 94 SA. The upper straight line (β=6) is representative of a 10 MPa working pressure. The lower one (β=4) corresponds to 15 Mpa. The optimum trade-offs derived are approximately $g_h.d_h = 27.10^{-12}Pa^{-1}$ (v=11%) up to 10 MPa and $g_h.d_h = 17.10^{-12}Pa^{-1}$ (v=16%) up to 15 MPa. The experimental points are also plotted on Figure 7. Keeping in mind the remarks about the epoxy shell or the plate thickness influences on the stability, the experimental data agree quite well to the optimization diagram.

Choice of the PZT material

The optimization procedure has been followed for a 1.3.1 piezocomposite made with the 3 Navy types PZT and polyurethane 94 SA. Table 4 lists the maximum uniaxial stresses and the best trade-offs in the 3 cases for a 10 Mpa and a 15 MPa uses.

It is then shown that ideally, a Navy type III PZT should be the best suitable material for deep underwater hydrophone application of the 1.3.1 piezocomposites.

TABLE 4 : gh.dh optimized values ($10^{-12}Pa^{-1}$) for various PZT materials. The corresponding PZT volume fraction is written between the parenthesis.

PZT type	Navy I P7.62 (QS)	Navy II P1.88 (QS)	Navy III P1.89 (QS)
T_{3max} (MPa)	50	20	95
$g_h.d_h$ (10 Mpa use)	26 (14%)	17 (28%)	44 (7.5%)
$g_h.d_h$ (15 MPa use)	18 (20%)	14 (100%)	30 (11.5%)

Conclusions

It is experimentally shown that the 1.3.1 composite solution allows to get $g_h.d_h$ figures of merit up to $28.10^{-12}Pa^{-1}$ without using needle shaped PZT rods. Moreover, a rather small pressure dependence is demonstrated making those composites interesting up to a 10 or a 15 MPa hydrostatic pressure. Finite Element Modeling of these structures gave good results allowing a realistic optimization. The optimization, based on an efficient characterization of various PZT materials under high uniaxial stress, showed the best suitability of Navy III type PZT for 1.3.1 piezocomposite hydrophones. Figures of merit up to $30.10^{-12}Pa^{-1}$ could be reached while keeping a good pressure stability up to 15 MPa.

Ackowledgements

This work is supported by the CERDSM department of the DCN Toulon and by the DRET. The authors gratefully acknowledge Roger Vignat for his help in the fabrication of the composite parts.

References

[1] NEWNHAM R.E -BOWEN L.J -KLICKER K.A -CROSS L.E Composite Piezoelectric Transducers. Material in Engineering, 1980 Vol. 2, pp. 93 - 106.

[2] COX H.L : The Elasticity and Strength of Paper and other Fibrous Materials. British J. Appl. Sciences 1952, Vol.3, pp. 72-79.

[3] HAUN M.J - NEWNHAM R.E : An Experimental and Theoretical Study of 1.3 and 1.3.0 Piezoelectric PZT Polymer Composites for Hydrophone Applications. Ferroelectrics 1986, Vol. 68, pp. 123-139.

[4] HAUN M.J - MOSES P. - GURURAJA T.R - SCHULZE W.A NEWNHAM R.E : Transversely Reinforced 1.3 and 1.3.0 Piezoelectric Composites. Ferroelectrics , 1983, Vol. 49, pp. 259-264.

[5] RICHARD C.: Etude Experimentale et Théorique de Composites Piézoélectr. de Connectivité 1.3.1 pour Hydrophone. Thèse INSA Lyon 1992 ,ref. 92ISAL0039.

[6] KRUEGER H.H.A : Stress Sensitivity of Piezoelectric Ceramics - Part I : Sensitivity to Compressive Stress Parallel to the Polar Axis. J.Acoust.Soc.Amer. 1967, Vol.42, N°3, pp.636-645.

[7] HAMONIC B.F. : ATILA : Finite Element Code for Piezoelectric and Magnetostrictive Transducer Modeling . Version 5.01 . Lille: ISEN ,1991

PIEZOELECTRIC TRANSDUCERS FOR MEDICAL ULTRASONIC IMAGING

T. R. Gururaja
Hewlett-Packard Company
3000 Minuteman Road
Andover, MA 01810-1099

In clinical pulse-echo ultrasonic imaging, the piezoelectric transducer provides the link between the human body being imaged and the processing electronics. The requirements of a transducer for diagnostic applications are illustrated in this paper with specific examples. Furthermore, the material parameters that influence transducer design are discussed. The current status of the piezoelectric transducer design and common approaches taken to improve the design are also presented.

Introduction

The applications of ultrasound medical imaging span a wide frequency range starting from approximately 1.5 MHz up to 30 MHz depending on the organs to be imaged. For abdominal, obstetrical, and cardiological applications, the ultrasonic frequencies employed range from 2 to 5 MHz. For pediatric and peripheral vascular applications, the range is from 5 to 7.5 MHz. For imaging small objects such as the eye and for many other emerging modalities such as intracardiac and intravascular imaging, frequencies range from 10 to 30 MHz.

In any imaging system, one of the factors which limits the attainable resolution is the wavelength of the radiation used to form the image. The relationship between the wavelength and frequency of sound is given by: wavelength (λ) x frequency (f) = velocity in the propagating media. The velocity of sound in the human body is approximately 1500 m/sec. Thus, the attainable resolution span from 1 mm to 50 micrometers for the frequency range from 1.5 to 30 MHz. The highest frequency that can be used for a particular application is limited by frequency dependent attenuation (approximately 0.5 dB/cm/MHz) within the body.

Principle of Ultrasonic Imaging

Acoustic impedance (Z) of the propagating medium is a key property on which ultrasonic imaging is based. The acoustic impedance of the medium is defined as the product of density of the medium and the velocity of sound in the medium. The unit of acoustic impedance is kg/m^{2}sec and is termed Rayl. The acoustic impedance of biological materials such as blood, muscle, fat, and tissue range from 1.3 to 1.7 MRayl. Bones exhibit relatively high acoustic impedance of 3.8-7.4 MRayl. The phenomenon of reflection and transmission of acoustic signals at an interface between two media is the basis for the ultrasonic imaging.

The pulse-echo modality in which a piezoelectric transducer acts as both acoustic source and detector of ultrasound is the most common technique used for ultrasonic imaging (Figure 1). In this method, the transducer is excited by an electrical signal to emit short duration acoustic waves into the medium to be interrogated. When the acoustic wave encounters an impedance discontinuity, some of the energy is reflected backwards and some travels forward. When the reflected echo reaches the transducer, the transducer generates a voltage proportional to the acoustic impedance mismatch at the interface. The time duration between the signal and the returned echo is proportional to the distance of the interface from the transducer. The acoustic signal transmitted through the interface serves to detect other impedance discontinuities that may be present at farther distances.

In medical diagnostic applications, the existence of an acoustic impedance difference between the various biological materials in the body and also the impedance variation from one tissue to another is used to generate a two-dimensional grey scale image [1]. The fact that the acoustic impedance variation from one soft tissue to another is relatively small is beneficial since energy is allowed to propagate across several interfaces providing imaging capability with fairly large depth ranges. The human body, to a large extent, is compiled of water-like media and cannot support transverse waves. Thus, in all of the diagnostic applications, only longitudinal ultrasonic waves are used.

The mode most frequently used in today's ultrasound equipment is the B-mode. B-mode is a method of echo display in which echo signals are represented as intensity modulated lines on a display. In the early stages of development, transducer was translated manually to form a two-dimensional image on a cathode ray tube (Figure 1). Presently, the transducer is rapidly rotated or scanned electronically to form a real-time image.

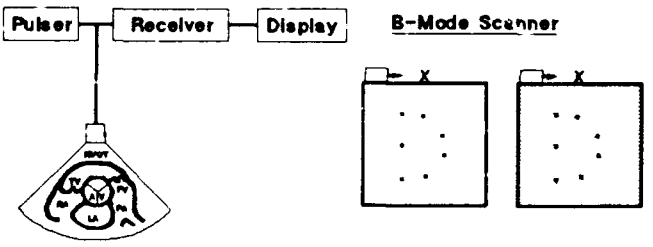


Figure 1: Principle of Ultrasonic Imaging

The electronic scanner uses an array transducer for scanning in which small elementary transducers are placed side by side on a straight or a curved line. Typical scanning formats are linear and sector scanning.

In linear scanning (Figure 2a), a group of elements are driven simultaneously and echo signals are received by the same group. In the second transmission, one or more elements are deactivated while new elements are activated to drive and receive as in the first transmission. This function continues through all of the array elements to complete one scan and produces one cross-sectional image or frame. Real-time instruments acquire, process, and display

CH3080-0-7803-0465-9/92$3.00 ©IEEE

images at a rate of 20-30 frames per second. Figure 3 shows the rectangular format of an image produced by a linear array. A transducer in which the elements are arranged on a curved line is called curved-linear array. Such an array provides a trapezoidal format of the image to facilitate wider area of viewing at deeper depths.

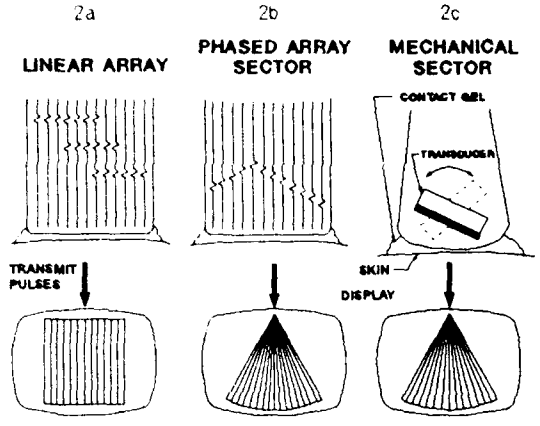


Figure 2: Types of Real-Time Transducers

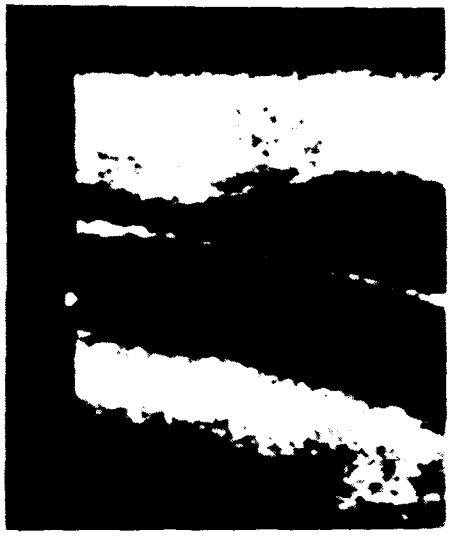


Figure 3: Rectangular Format of a Peripheral Vascular Image Produced by a Linear Array Transducer

In sector scanning (Figure 2b), each element is driven appropriately delayed in relation to its partners, so that the ultrasound beam generated from the transducer propagates at a direction determined by the delaying conditions. By sequentially varying these delaying conditions, the ultrasound beam scans in sector format. This type of transducer is called a phased array transducer. In both linear and sector scanning, an appropriate phase delay can be superposed to focus the acoustic beam at a certain penetration depth in the human body. Figure 4 shows the sector image of the four chambers of a heart.

In a phased array, the elements are approximately $\lambda/2$ wide at the frequency of operation to avoid the problem of grating lobes. However, in linear arrays which do not steer, the width of each element could be as wide as 3 $\lambda/2$. The width for linear and phased array elements with a center frequency of 5 MHz is approximately 450 and 150 micrometers, respectively. The elevation dimension, which is perpendicular to the scanning plane, is chosen based on the desired focal distance and depth of penetration.



Figure 4: Image of a Four Chamber View of a Heart Produced by Phased Array Transducer in a Sector Format

In one type of mechanical scanning, a circular shaped, single element transducer is wobbled inside a fluid medium to generate a 90^0 sector scan (Figure 2c). In such a mechanical scanner, a single element can be replaced by a concentric circular ring array element to facilitate electronic focusing at different distances along the axis. Such a transducer is called an annular array.

Figure 5 shows a 30 MHz image of an artery from one of the emerging modalities, namely intravascular ultrasonic imaging. In this modality, the transducer located at the tip of a catheter is rotated along the axis of catheter at approximately 1800 rpm to generate a real-time image. Each division in the figure corresponds to 1 mm.



Figure 5: Image of an Artery Produced by an Intravascular Transducer in a Circular Format

Broad Bandwidth Transducers

For medical ultrasonic imaging, it is desirable to use a broad bandwidth transducer for the reasons listed below. Broad bandwidth is a relative term, which usually means that the 6dB fractional bandwidth of the pulse-echo spectral response is in excess of 50%.

1. Broad bandwidth response, in most circumstances, corresponds to a short pulse length, which results in better axial resolution.

2. Short driving pulses, which are used to excite transducers, have broad frequency content. Therefore, narrow bandwidth transducers cannot be driven efficiently.

3. Broad bandwidth offers deeper penetration into the body. This is because of the frequency dependent attenuation of ultrasound in the tissue. The effect of tissue attenuation on the broad bandwidth impulse response of a transducer (approximately 70% with center frequency at 5 MHz) is illustrated in Figure 6. As shown in the figure, the signal at 5 MHz is significantly attenuated in traversing 12 cms. If the impulse response did not contain much component at lower frequencies, the penetration would be limited.

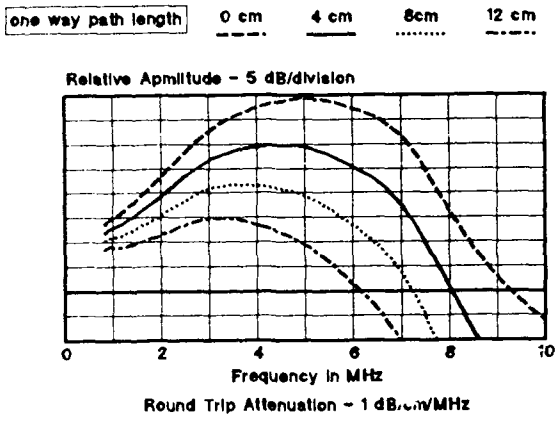


Figure 6: Effect of Tissue Attenuation on the Spectral Response

4. Broad bandwidth also offers the advantage of operating the transducer at multiple frequencies. For deeper penetration the transducer can be operated at lower frequencies, and for better resolution the transducer can be operated at higher frequencies. The concept of a multiple frequency transducer is illustrated in Figure 7, where we compare the images of a pediatric heart from a dual frequency transducer operating at 5.5 and 7.5 MHz. The concept of multiple frequency transducers have a major impact in transesophageal echocardiography, where the transducer attached to a gastroscope is positioned in the esophagus for imaging the heart. It becomes extremely inconvenient to replace the transducer to obtain a better resolution or a deeper penetration. A broad bandwidth transducer can also be operated in a broad band transmitting mode associated with a sliding filter on receive to optimize the resolution and penetration in one image.

5. Broad bandwidth also lets us perform 2D imaging at a higher frequency and perform Doppler mode and color mapping for blood flow velocities at lower frequencies for better penetration and detecting wider range of blood flow velocities.

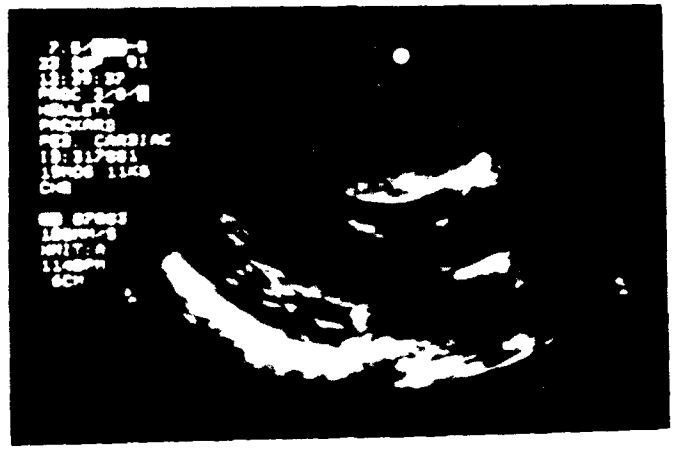


Image at 5.5 MHz



Image at 7.5 MHz

Figure 7: Phased Array Image of a Pediatric Heart at 5.5 and 7.5 MHz Obtained Using a Dual Frequency Transducer

Transducer Design

In order to design an ultrasonic transducer with broad bandwidth response, we have to satisfy the following two criteria:

1. Effectively couple electrical energy from the driving electronics to the transducer across the frequency range of interest. This is referred to as electrical impedance matching.

2. Effectively couple acoustic energy from the transducer to the load and back across the frequency range of interest. This is referred to as acoustic impedance matching.

For electrical impedance matching, it is ideal to have the transducer (acoustically loaded on the front face) to exhibit 50 Ohm as the real part and zero Ohm as the imaginary part of impedance. For acoustic impedance matching, it is ideal to use a piezoelectric material with an acoustic impedance of 1.5 MRayl.

Acoustic Impedance Matching

The piezoelectric materials most commonly used in transducers for medical imaging are soft piezoelectrics such as PZT-5A and PZT-5H. Acoustic impedance of PZTs vary from 30 to 36 MRayl depending on the composition and geometry of array elements. Acoustic impedance of PZT is relatively large compared to that of the human body (1.5 MRayl). If we try to couple the acoustic energy from an air-backed PZT to the human body, large acoustic impedance mismatch leads to pulse response with long ringdown as shown in Figure 8a. This transducer structure will have good sensitivity at the cost of poor resolution. To improve the axial resolution, we can provide PZT with an acoustically matched backing material. This results in an extremely short pulse length at the expense of sensitivity (Figure 8b). We can lower the backing impedance and provide a front matching layer to improve both pulse length and sensitivity (Figure 8c). The matching layer could be one or more in number or a single layer with graded acoustic impedance. Thus, the acoustic impedance matching is tailoring of the pulse-echo response by optimizing the backing and front matching layer(s) impedances relative to that of the piezoelectric material. The transducers are also provided with a lens material in front of the matching layer(s) to collimate the ultrasound beam at a specified distance.

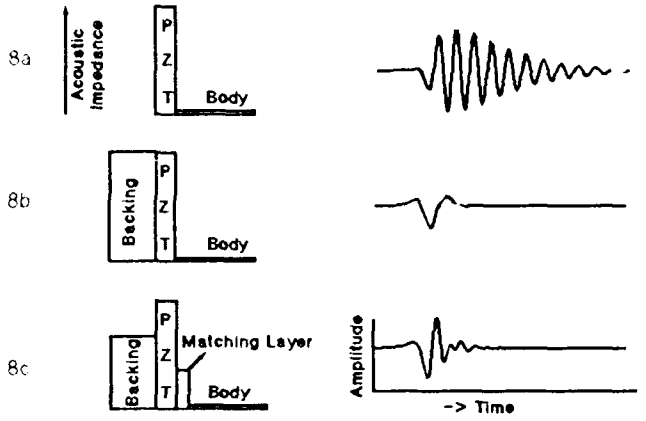


Figure 8: Transducer Design

Electrical Impedance Matching

Real and imaginary part of impedance of a transducer element loaded on the front side with water (Z of water = 1.5 MRayl is similar to biological materials) is shown in Figure 9. Contrary to the ideal solution for electrical impedance matching, both the real and imaginary part vary as a function of frequency. The peak value and variation of impedance as a function of frequency are inversely proportional to frequency, dielectric constant of the piezoelectric material and area of the element. Acoustic impedance of piezoelectric material and the matching layer design also influences the electrical impedance.

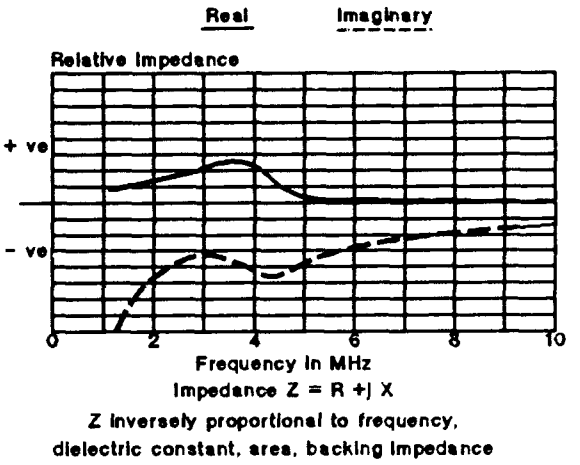


Figure 9: Real and Imaginary Part of Impedance of a Transducer Element

It is evident from this analysis that an appropriate material choice for one type of transducer element operating at a particular frequency may not be appropriate for another type. In designing phased array elements, we are faced with the task of looking for high dielectric constant material to lower the electrical impedance. On the contrary, for a single element transducer, we have to choose materials with lower dielectric constant to increase the electrical impedance. The material criteria might be quite unique in designing an intravascular transducer operating at 30 MHz.

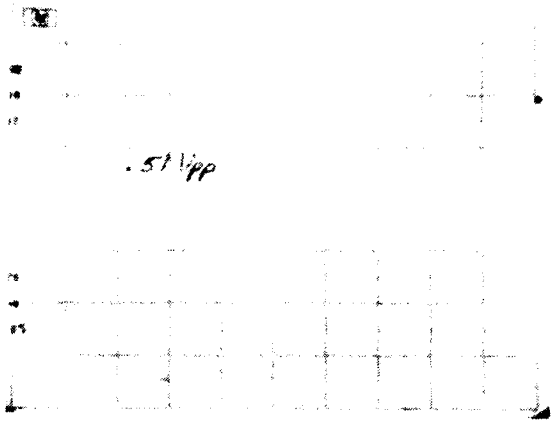
One more factor that needs to be considered in designing a transducer is the attachment of approximately 2 meter long cable for each transducer element. In special instances such as a transesophageal transducer, the cable length is approximately 4 meters. In general practice, an electrical matching network is connected either at the beginning or at the end of the cable to minimize the magnitude and variation of imaginary part of impedance.

Table 1 compares the relevant properties of piezoelectric ceramics, PVDF based copolymers, and ceramic-polymer composites. Next to the properties of PZT ceramic and polymer are positive and negative signs indicating the advantages and limitations, respectively, of the corresponding properties. The ceramic piezoelectrics are most commonly used because they offer relatively high electromechanical coupling, wide range of dielectric constant, and low dielectric loss factor. Polymer piezoelectrics offer desirably low acoustic impedance and reasonable coupling. However, several limitations such as extremely low dielectric constant and relatively large dielectric loss at high frequencies restrain their extensive use in ultrasonic imaging transducers. It is clear from the table that ceramic-polymer composites exhibit properties which are a good combination of ceramic and polymer piezoelectrics. A detailed analysis of the composite materials and their advantages in ultrasonic imaging transducers are presented in excellent reviews [2, 3].

Table 1: Comparison of Material Parameters for Piezoelectric Ceramic, Polymer, and Composites

PARAMETER	CERAMIC	POLYMER	COMPOSITE
Acoustic Imp Mrayls	30 (-)	4.3 (+)	10 (can be tailored)
Coupling Factor	.50 - .70 (+)	0.1-0.3(-)	0.5-0.7
Spurious Modes	many (-)	weak (+)	weak
Dielectric Const.	200-5000 (+)	6-10 (-)	proportional to vol% PZT
tan Δ_m	0.0125 (-)	0.1 (+)	0.05
tan Δ_e	0.02 (+)	0.25 (-)	0.02
Cost & Ease of Fabrication	cheap (+)	expensive (-)	medium

Figure 10 compares pulse-echo response of one of the rings of an annular array fabricated using a PZT ceramic and PZT ceramic-polymer composites. The pulse length of the composite array element is shorter by approximately one wavelength. The 6dB bandwidth of the spectral response of a composite element is in excess of 70% (Figure 11). The composite array in this illustration is an example of optimum electrical and acoustic impedance matching. In an annular array, electrical impedance matching can be achieved because of a relatively large area of individual elements.

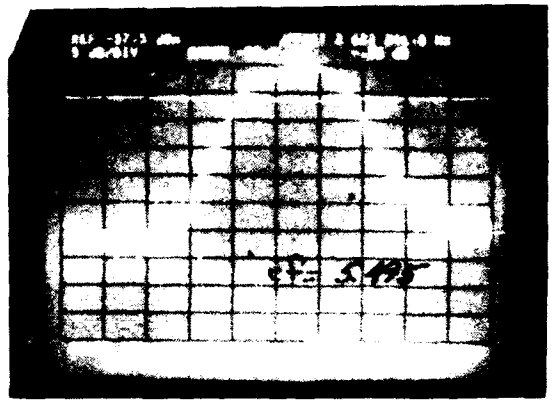


Ceramic Element

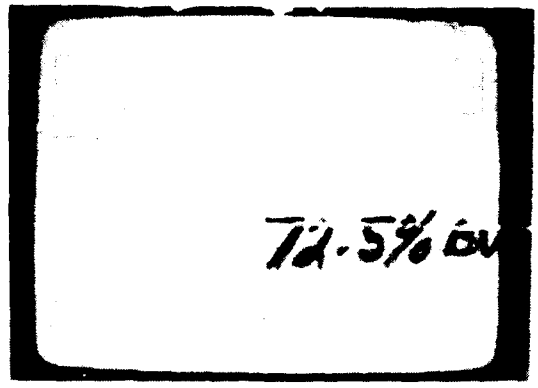


Composite Element

Figure 10: Comparison of Pulse-Echo Responses of an Annular Array Element Fabricated Using a Ceramic and a 1-3 Composite Element



Ceramic Element



Composite Element

Figure 11: Comparison of Spectral Responses of an Annular Array Element Fabricated Using a Ceramic and a 1-3 Composite Element

For accomplishing electrical impedance matching, three main approaches are taken:

1. Materials with high dielectric constant - this is a materials science approach. In the beginning, PZT-5A with low frequency dielectric constant of 1800 was the material of choice for most array elements. For phased arrays, the element widths are narrow and require higher dielectric constant material such as PZT-5H. In PZT-5H, the dielectric constant at room temperature is raised to approximately 3200 by lowering the curie temperature close to 200°C. There are many compositions in the modified lead nickel niobate family with lower curie temperature where the room temperature dielectric constant is above 6000 [4]. However, the main concern in using these piezoelectrics is their susceptibility to depoling at elevated temperatures used in processes during the fabrication of a transducer. It is also required that the transducer not deteriorate under extreme temperature fluctuation experienced during shipping or storage. Ferroelectric relaxor materials which have dielectric constant maxima of up to 30,000 near room temperature appear to be excellent candidates for tiny transducer elements [5]. However, the sensitivity of dielectric constant in these materials to temperature, frequency, and dc bias, are major limitations.

2. Multi-layer ceramic material - this is a materials engineering approach to increase the effective dielectric constant [6]. The multi-layer configuration is widely employed in the capacitor industry. It employs two or more ceramic layers with electrodes in between connected acoustically in series. One set of alternating electrodes are

connected to one polarity, and the other set of alternating electrodes are connected to the opposite polarity of the signal. Thus, the layers are connected electrically in parallel. The resonance frequency of the structure is defined by the total thickness of the configurations and is independent of the number of layers. This configuration will decrease the electrical impedance of the array elements proportional to the square of the number of layers in the multi-layer structure.

3. *Preamplifier for each transducer element* - this is an electrical engineering approach where an emitter follower is used to transform the high source impedance of a transducer element to the low output impedance. This reduces the loading of the impedance by the long cable and results in a better electrical matching with the low impedance system in the receive mode. To improve electrical matching on the transmit, a transformer could be employed.

Effect of Change in Material Properties

This analysis has showed that piezoelectric materials with appropriate properties are critical in designing transducers. It is also the objective of this paper to emphasize the importance of consistency in the properties across a sample, from sample to sample, and from lot to lot. The images are formed by superposition of responses from a number of elements. It is critical that all of the elements exhibit similar characteristics.

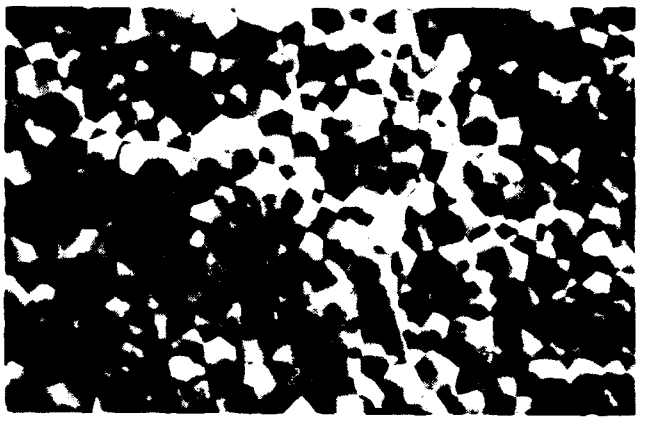
Variation in coupling constant and dielectric constant result in a drift in sensitivity and bandwidth. Because the ultrasound systems are approved by FDA, a transducer with sensitivity higher than the approved limit cannot be used in clinical applications. Similarly, reduction in sensitivity might make the diagnosis more difficult.

Longitudinal velocity of sound in the piezoelectric material influences the center frequency of the transducer. Since the transducers are low Q devices, a shift in center frequency by a few percentages is not a major concern. The variation of acoustic impedance has a relatively minor influence on the pulse length.

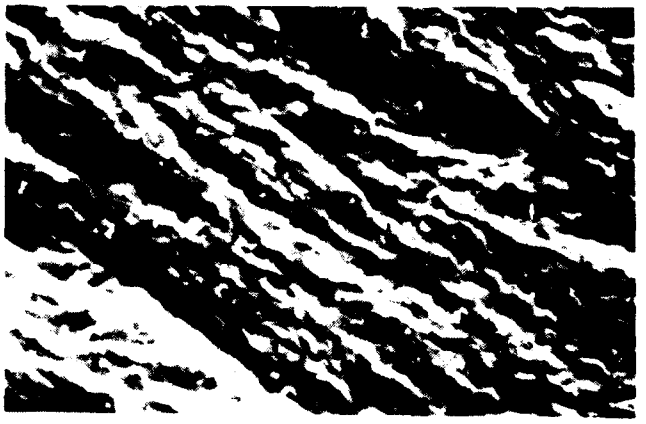
The mechanical strength has a major impact on the yield of transducers. Because the wafers go through many operations such as lapping, polishing, dicing and handling, mechanically weak ceramics result in poor yields. The mechanical strength also influences the adhesion of conducting films used for electroding. Although PZT ceramics are relatively easy to process, small variations in sintering temperatures and atmosphere control can sometimes lead to dramatic changes in the microstructure and mechanical behavior. For example, Figure 12 shows the fractured surfaces of two different batches of PZT ceramics from the same vendor. Thus, homogeneity and consistency in dielectric, piezoelectric, and mechanical properties is as important as obtaining the materials with desired properties.

Summary

Designing a transducer involves many compromises [7]. Figure 13 illustrates some of the cyclic paradoxes that confront a transducer designer. However, the developments over the past decade of several different types of composite materials, PVDF based co-polymers, piezoelectric ceramics with low transverse coupling and electrostrictive materials offer opportunities to overcome some of the compromises.



Intergranular Fracture



Transgranular Fracture

Figure 12: Intergranular and Transgranular Fracture in Two Samples of PZT from Separate Lots, Supposedly Equal

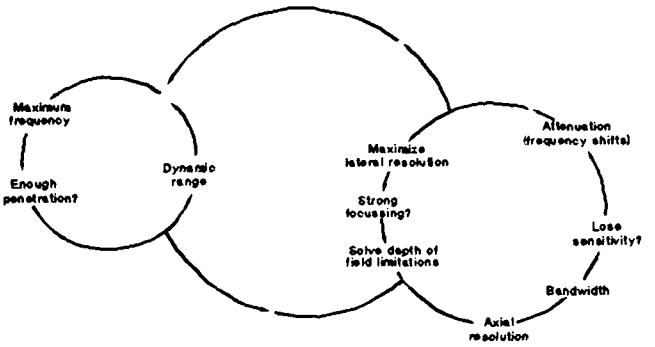


Figure 13: Transducer Compromise
(After J. W. Hunt et. al., IEEE Trans. on Biomedical Engineering, No. 8, August 1983)

References

[1] P. N. T. Wells, Biomedical Ultrasonics, Academic Press, London (1977).

[2] W. A. Smith, "The Role of Piezocomposites in Ultrasonic Transducers", Proceedings of the 1989 IEEE Ultrasonics Symposium, pp. 755-766 (1989).

[3] W. A. Smith, "The Applications of 1-3 Piezocomposites in Acoustic Transducers", Proceedings of the 7th International Symposium on Applications of Ferroelectrics, pp. 145-152 (1990).

[4] D. Luff, R. Lane, K. R. Brown, and H. J. Marshallsay, "Ferroelectric Ceramics with High Pyroelectric Properties", J. Brit. Ceram. soc. 73, pp. 251-264 (1974).

[5] H. Takeuchi, H. Masuzawa, and C. Nakaya, "Relaxor Ferroelectric Transducers", Proceedings of the 1990 IEEE Ultrasonics Symposium, pp. 697-705 (1990).

[6] S. Saitoh, M. Izumi, and K. Abe, "A Low-Impedance Ultrasonic Probe Using a Multilayer Piezoelectric Ceramic", Japanese Journal of Applied Physics 28-1, 54-56 (1989).

[7] J. W. Hunt, M. Arditi, and F. S. Foster, Ultrasound Transducers for Pulse-Echo Medical Imaging", IEEE Transactions on Biomedical Engineering, BME-30, No. 8, pp. 453-480 (1983).

Piezoelectrics and Electrostrictives: Polymers, Transducers, Processing

PIEZOELECTRIC PROPERTIES OF "d_{31}-ZERO", "d_{33}-ZERO" OR "d_h-ZERO" 1-3 OR 2-2 TYPE COMPOSITE CONSISTING OF 0-3 SUBCOMPOSITE OF POLYMER/$PbTiO_3$ AND THAT OF POLYMER/PZT.

H. Banno and K. Ogura

NTK Technical Ceramics Division, NGK Spark Plug Co., Ltd.

14-18 Takatsuji-cho, Mizuho-ku, Nagoya, 467, Japan

Abstract

Piezoelectric constants (d_{33}, d_h and d_{31}) of 1-3 and 2-2 composites consisting of 0-3 subcomposite of polymer /$PbTiO_3$ ceramic powder and that of polymer/PZT ceramic powder were investigated in order to obtain "d_{31}-zero", "d_{33}-zero" or "d_h-zero" composite by changing volume fraction of subcomposites and arranging their polarities to be opposite each other. The experimental results were compared with the theoretical ones, and good agreements between experimental and theoretical ones were observed.

Introduction

Piezoelectric ceramics with almost zero kp (i.e. almost zero d_{31}) have been obtained in $(Pb,Ca)(Ti,W_{1/2}Co_{1/2})O_3$[1] and $(Pb,Sm)(Ti,Mn)O_3$[2] Recently, "d_{31}-zero", "d_{33}-zero" or "d_h-zero" were also obtained in 0-3 composites, consisting of polymer and ceramic powder mixture of PZT and $PbTiO_3$, by applying an appropriate poling electric field to the prepoled ones in the reverse direction.[3]

In this paper, piezoelectric properties of "d_{31}-zero", "d_{33}-zero" or "d_h-zero" 1-3 or 2-2 type composite consisting of 0-3 subcomposite of polymer/ $PbTiO_3$ and that of polymer/PZT are reported.

Theory

As to 1-3 and 2-2 composites consisting of phases 1 and 2 shown in Fig.1(a) and (b), Banno,[4] Skinner et al.[5] and Safari[6] have derived theoretical equations for dielectric, elastic and piezoelectric constants.

The equations for piezoelectric d constants in the case that the elastic constant of phase 1 is equal to that of phase 2 are expressed in the following eqs. (1) and (2) for the 1-3 and 2-2 composites, respectively.

$$d = {}^1v \cdot {}^1d + {}^2v \cdot {}^2d \quad (1)$$

$$d = [{}^1v \cdot {}^2\varepsilon \cdot {}^1d + {}^2v \cdot {}^1\varepsilon \cdot {}^2d] / [{}^1v \cdot {}^2\varepsilon + {}^2v \cdot {}^1\varepsilon] \quad (2)$$

where $\varepsilon = \varepsilon_{33}$, d is d_{33}, d_{31} or d_h. The notation used in the present paper is similar to Newnham's[7] and the previous paper's[4].

Now let us consider the requirement that the piezoelectric constants d_{31} of the composites become zero. Since $d_{31}=0$ in eqs.(1) and (2) for d_{31}, we obtain for the 1-3 and 2-2 composites respectively as follows;

$${}^1v \cdot {}^1d_{31} + (1 - {}^1v) \cdot {}^2d_{31} = 0 \quad (3)$$

$${}^1v \cdot {}^2\varepsilon \cdot {}^1d_{31} + (1 - {}^1v) \cdot {}^1\varepsilon \cdot {}^2d_{31} = 0. \quad (4)$$

Volume fractions ${}^1v(d_{31})$ for the d_{31}-zero are obtained for the 1-3 and 2-2 composites respectively, as follows;

$${}^1v(d_{31}) = 1/[1-({}^1d_{31}/{}^2d_{31})] \quad (5)$$

$${}^1v(d_{31}) = 1/[1-({}^1d_{31}/{}^2d_{31})({}^2\varepsilon/{}^1\varepsilon)]. \quad (6)$$

From $0 < {}^1v(d_{31}) < 1$ (and of course ${}^2\varepsilon/{}^1\varepsilon > 0$), we have

$$({}^1d_{31}/{}^2d_{31}) < 0. \quad (7)$$

Next, let us consider the other requirement that the piezoelectric constant d_h of the composites at ${}^1v(d_{31})$ does not become zero even at the d_{31}-zero volume fraction.

We obtain piezoelectric constant d_h of the compo-

CH3080-0-7803-0465-9/92$3.00 ©IEEE

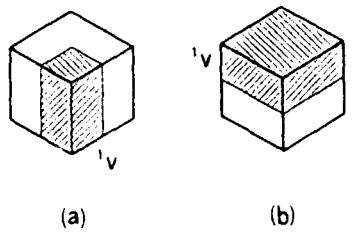


Fig. 1. Schematic representation of models for (a) 1-3 and (b) 2-2 composites.

sites at $^1v(d_{31})$, for both the 1-3 and 2-2 composites as follows;

$$d_h\{^1v(d_{31})\} = {}^2d_h\{(^1d_h/{}^2d_h)-(^1d_{31}/{}^2d_{31})\} / \{1-(^1d_{31}/{}^2d_{31})\} \quad (8)$$

Therefore, we obtain the requirement that the piezoelectric d_h constant of the composite does not become zero even at the d_{31}-zero volume fractions, as follows;

$$(^1d_h/{}^2d_h) \neq (^1d_{31}/{}^2d_{31}) \quad (9)$$

As to "d_{33}-zero", "d_h-zero" 1-3 and 2-2 composites, one can obtain $d_h\{^1v(d_{33})\}$ by substituting d_{33} for d_{31}, and $d_{33}\{^1v(d_h)\}$ by substituting d_h and d_{33} for d_{31} and d_h in the above mentioned equations, respectively.

Accordingly, we have the requirments for "d_{33}-zero" and "d_h-zero" composites as follows;

$$(^1d_{33}/{}^2d_{33}) < 0 \quad (10)$$

$$(^1d_h/{}^2d_h) < 0 \quad (11)$$

and $$(^1d_h/{}^2d_h) \neq (^1d_{33}/{}^2d_{33}) \neq (^1d_{31}/{}^2d_{31}). \quad (12)$$

From eq. (12), we have

$$(^1d_{31}/{}^1d_{33}) \neq (^2d_{31}/{}^2d_{33}) \quad (13)$$

where the value of (d_{31}/d_{33}) is a kind of piezoelectric anistoropy of the subcomposite.

To realize the above-mentiond requirements for the "d_{31}-zero", "d_{33}-zero" or "d_{33}-zero" composite, the poling direction and the piezoelectric anisotropy of the subcomposite of phase 1 are necessary to be opposite and not equal to those of phase 2, respectively.

This theory is applicable not only to 1-3 or 2-2 composite/composite-Composite but also 1-3 or 2-2 ceramic/ceramic-Composite (for example, PZT ceramic /$PbTiO_3$ ceramic 1-3 or 2-2 Composite).

Experimental procedures

The subcomposites (phases 1 and 2 of the present

Table 1. Piezoelectric consta... d_{33}, d_h and d_{31} ... bcomposites of con... ZT or $PbTiO_3$.

50vol% / 50vol%	d_{31}	d_{33}	d_h	ε	phase
PZT / polymer	7.1	-16.3	2.2	60.3	phase 1
$PbTiO_3$ / polymer	-4.2	25.8	17.4	35.5	phase 2

[unit] d : $\times 10^{-12}$ C / N

composite) were prepared by the method described in the previous paper[8]. The volume fraction of ceramic powder was 50 percent, and the ceramic powder of soft PZT (for the phase 1) and pure $PbTiO_3$ (for the phase 2) with average particle sizes of approximately 3 μm were used.

The ceramic powder of PZT or $PbTiO_3$ and chloroprene rubber were mixed and rolled down into 1.8mm for the 1-3 composite, 0.3mm, 0.6mm, 0.9mm 1.2mm and 1.8mm for the 2-2 composite, at 40℃ by using a hot roller, and then heated at 170℃ for 15min. under a pressure of 14 MPa. A thin coat of conductive rubber was attached on both major surfaces of the subcomposites (40mm × 40mm × tmm) as electrodes. Then, they were poled at 20℃ by applying a DC field of 70kv/cm for 1 hour.

The specimens were fabricated by joining the two subcomposites opposing polarity each other so as to form the 1-3 and 2-2 composites, and their sizes

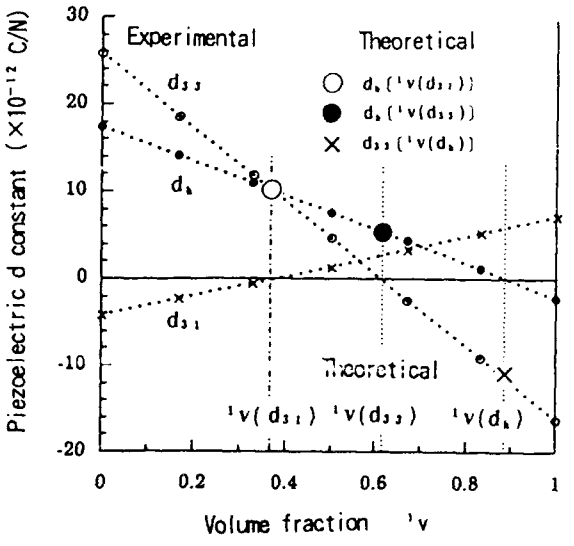


Fig. 2. Piezoelectric constants (d_{33}, d_h and d_{31}) of 1-3 composite consisting of 0-3 subcomposite of polymer/PZT (phase 1) and that of polymer/$PbTiO_3$ (phase 2) as a function of phase 1 in the case that a polarity of phase 1 is opposite to that of phase 2.

were approximately 40mm(L) × 40mm(W) × 1.8mm(T).

The volume fraction of phase 1 was changed from 0/6, to 1/6, 2/6, 3/6, 4/6, 5/6 and 6/6 by area of the 1-3 composite and by thickness of the 2-2 composite, respectively.

The piezoelectric d_{33} constant was measured by a Berlicourt d_{33} meter manufactured by Channel Products, Inc. The piezoelectric d_h constant was measured by the method described in the previous paper[8]. The piezoelectric d_{31} constant was obtained by the calculation of $d_{31}=(d_h-d_{33})/2$.

Results and discussion

Table 1 shows piezoelectric and dielectric constants of the subcomposites (phases 1 and 2). From the values in the Table 1 and eqs.(5) (6) and (8), we obtain theoretical values of the volume fractions for "d_{31}-zero", "d_{33}-zero" and "d_h-zero" in the following eqs. (14)-(16) for the 1-3 and 2-2 composites

$$^1v(d_{31})=0.37 \text{ and } 0.57 \quad (14)$$

$$^1v(d_{33})=0.61 \text{ and } 0.73 \quad (15)$$

$$^1v(d_h)=0.89 \text{ and } 0.97 \quad (16)$$

respectively, and theoretical values of the piezoelectric constants at the volume fractions, in the following eqs.(17)-(19) for the both the 1-3 and 2-2 composites.

$$d_h\,[^1v(d_{31})] = 10.1\times10^{-12}\,C/N \quad (17)$$

$$d_h\,[^1v(d_{33})] = 5.4\times10^{-12}\,C/N \quad (18)$$

$$d_{33}\,[^1v(d_h)] = -11.6\times10^{-12}\,C/N\,. \quad (19)$$

Experimental results for piezoelectric constants of the 1-3 and 2-2 composites are shown in Figs.2 and 3, respectively, where good agreements between experimental and theoretical results were observed.

As mentioned above, we obtained the "d_{31}-zero", "d_{33}-zero" and "d_h-zero" composites at the volume fractions expressed in the eqs.(14)-(16).

From eqs.(3) and (4), we obtain

$$-^1d_{31}=(1/^1v-1)(^2d_{31}) \quad (20)$$

$$-^1d_{31}=(1/^1v-1)(^2d_{31})(^1\varepsilon/^2\varepsilon). \quad (21)$$

Accordingly, at a volume fraction of phase 1, we can obtain "d_{31}-zero" composite by controlling the values of $^1d_{31}$ and/or $^2d_{31}$ (for example, by controlling the the poling electric field or by applying a reverse poling field to the prepoled subcomposites).

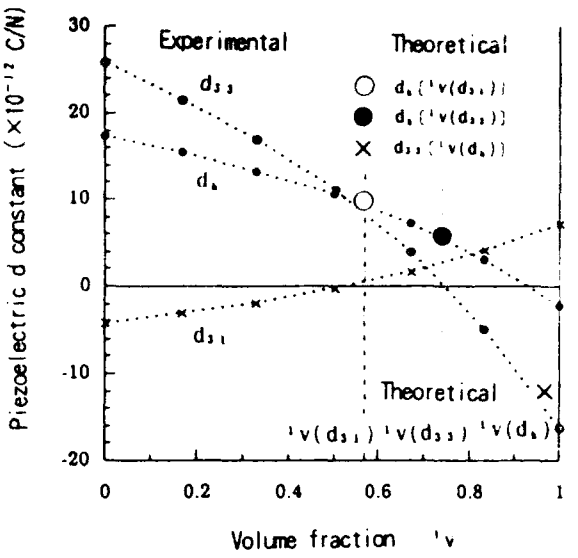


Fig.3. Piezoelectric constants (d_{33}, d_h and d_{31}) of 2-2 composite consisting of 0-3 subcomposite of polymer/PZT (phase 1) and that of polymer/$PbTiO_3$ (phase 2) as a function of phase 1 in the case that a polarity of phase 1 is opposite to that of phase 2.

Conclusions

1) Theoretical values of volume fractions for "d_{31}-zero", "d_{33}-zero" and "d_h-zero" and piezoelectric constants at the volume fractions were obtained in 1-3 and 2-2 composites consisting of two subcomposites with opposite polarity, different piezoelectric anisotsopy and identical elastic constant.

2) Good agreements between the theoretical and experimental results were observed.

References

[1] Y.Yamashita, K.Yokohama, H.Honda and H.Okuma, Jpn. J.Appl.Phys. 20 Suppl. 20-4, 183(1981).

[2] H.Takeuchi, S.Jyomura, E.Yamamoto and Y.Ito, J. Acoust.Soc.Amer. 72, 1114(1982).

[3] H.Banno and K.Ogura, Jpn.J.Appl.Phys. 30 (98) 2050 (1991).

[4] H.Banno, Jpn.J.Appl.Phys. 24 Suppl.24-2, 2050 (1985).

[5] D.P.Skinner, R.E. Newnham and L.E.Cross, Mater. Res.Bull. 13, 599(1978).

[6] A.Safari, Ph.D.Thesis; the Penn. State Univ. pp. 34-48 (1983).

[7] R.E. Newnham, D.P.Skinner and L.E.Cross, Mater. Res.Bull., 13, 525(1978)

[8] H.Banno, K.Ogura, H.Sobue and K.Ohya: Jpn.J. Appl.Phys.26 (1987) Suppl. 26-1, pp.153-155.

PIEZOELECTRIC PZT TUBES AND FIBERS FOR PASSIVE VIBRATIONAL DAMPING

S. Yoshikawa, U. Selvaraj, K.G. Brooks, and S.K. Kurtz
Materials Research Laboratory
The Pennsylvania State University, University Park, Pennsylvania 16802

Abstract: Passive vibrational damping was demonstrated in piezoelectric lead-zirconium titanate (PZT) tubes incorporated into a hard epoxy matrix. For a poled tube, the coupling constant, k_{33} measured from the resonance frequency, was about 0.66. Sol-gel methods were used to fabricate piezoelectric fibers of $Pb(Zr_{0.52}Ti_{0.48})O_3$, and niobium and $CdBO_3$ substituted PZT. Continuous and fine gel fibers of about 5 to 100 μm in diameter were prepared by extruding and drawing spinnable-viscous resins through a spinneret. These fibers fired at 600°C for 1 h exhibited well-crystallized perovskite phases of PZT. Fibers fired between 700° and 1250°C were dense with varying grain sizes (0.1 to 5 μm). The dielectric constant of $Pb(Zr_{0.52}Ti_{0.48})O_3$ fiber fired at 700°C for 1 h was about 800. These fibers will be incorporated into structural materials to obtain maximum damping properties.

1. Introduction

In recent years, there has been growing interest, among researchers in various fields, to minimize and control vibration in machines and devices. Vibration can be significantly reduced by increasing the damping of the dominant modes of vibrations through passive and active damping mechanisms. In active vibrational damping devices, the vibration is minimized by using a certain active elements such as actuators that alter the dynamic response of the structure. These devices, however, require the use of special hardware and real-time control-design algorithms for individual structural elements. The active vibrational damping system is therefore complicated and is still in its developmental stages. By contrast, in passive vibrational damping devices, vibrational energy is dissipated through the added external damping media such as isolation- or constrained-viscoelastic layers. These devices are simple and offer a reliable solution for vibrational suppression over a limited range of frequency. A more realistic future damping control device is likely to have a balanced combination of both active and passive systems.

For passive and active damping applications, piezoelectric ceramics with large electromechanical coupling coefficients (k_{ij}) are potential candidates [1,2]. Based on theoretical and experimental studies [1,2], it has been established that piezoelectric ceramics can provide a large mechanical loss factor and thus can be effective in passive damping. Until now, however, it is not apparent that how and in what forms these piezoelectric ceramics have to be incorporated into structural materials in order to achieve maximum damping. Hence, our goal is to develop methods that allow an effective piezoelectric-passive damping in large structural materials.

The first section of the paper describes the incorporation of commercially available fine PZT tubes in a relatively hard polymer matrix. The PZT tube-polymer configuration (1-3 composite) is such that maximum electromechanical coupling and hence an effective damping is achieved for optimum external resistance. The second section deals with the sol-gel processing of continuous PZT and modified PZT fibers, which would be incorporated into the polymer matrix in the future.

2. PZT/Polymer Composites

Piezoelectric-ceramic tubes (PZT-5H) obtained from Morgan Matroc, Inc. were used to study the passive vibrational damping. The dimensions of these tubes were: 1.28 mm outer diameter, 0.81 mm inside diameter and 10 cm length. In order to obtain maximum k_{33} from these tubes, 10 circumferential silver/glass electrodes of 1 mm in width and 1 cm apart were applied to each tube. These tubes were then fired at 800°C for 30 min. After firing, they were individually poled with an applied field of ~10 kV/cm at 80°C for 10 min. The coupling constant, k_{33}, calculated from the resonance frequency, for a poled tube was 0.66.

Fine silver wires were attached to the silver electrodes using a silver epoxy and cured at room temperature. A two-tube module constructed according to the above procedure is shown in Figure 1. A hard epoxy was applied to the two-tube module, leaving the silver wires outside the module for connecting to the external resistor, and keeping the hollow parts of the tubes without filling with any epoxy. The epoxy was cured at room temperature for 24 h, and then heat-treated at ~65°C for 45 min.

The damping measurement was performed by exciting the middle portion of the sample. The intensities of resonance peaks were measured, while varying external resistance. Figure 1 shows the damping circuit with external resistors. The variation of mechanical loss factor with external resistance for the two-tube module is shown in Figure 2. The mechanical loss tangent, calculated from the resonance frequency (3500 to 4000 Hz) arises from the bending vibration of the sample. From the peak of mechanical loss tangent, it was found that the maximum piezoelectric damping was achieved for an external resistance of ~8 MΩ.

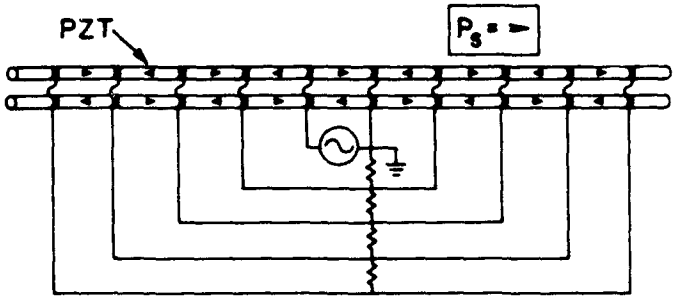


Figure 1 Schematic diagram of the poling configuration and resistive circuit for the two-tube module.

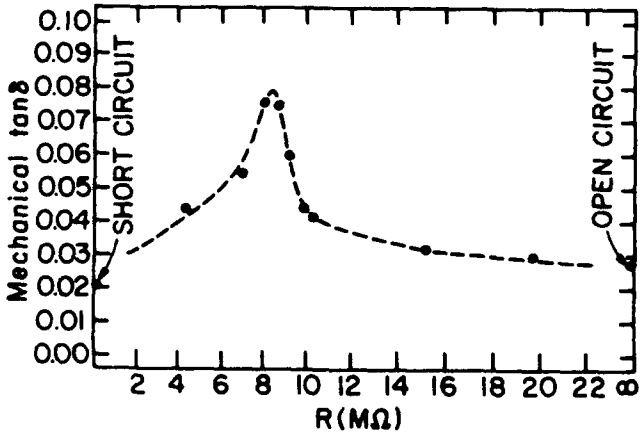


Figure 2 Mechanical loss tangent as a function of external resistance for the two-tube module.

CH3080-0-7803-0465-9/92$3.00 ©IEEE

I. Sol-Gel Fabrication of Continuous PZT and modified PZT Fibers

From practical viewpoint, incorporation of 1.28 mm iameter piezoelectric-ceramic tubes into structural materials leads to iany problems of feasibiilities. Hence, efforts were directed towards roducing fine piezoelectric-ceramic fibers, which can be easily mbedded into various types of structural materials, like glass-fiber einforced plastics.

In $Pb(Zr_xTi_{1-x})O_3$, compositions close to the morphotropic-hase boundary ($x \approx 0.52$ to 55), exhibit high dielectric constants, nd electromechanical coupling coefficients [3]. Addition of a few ercentages of niobium enhances the dielectric and piezoelectric roperties of PZT ceramics. Sol-gel processing of PZT fibers has ained much interest because of its simplicity, low processing emperature, chemical homogeneity and stoichiometry control and he ability to produce fibers of uniform microstructure [4,5]. Accurately-controlled microstructures and special shaping by hemical processes like sol-gel technique are essential for obtaining lense PZT ceramics for high-performance applications. The sol-gel eramic materials of PZT and modified PZT in the fibrous form may xhibit increased response in small scale devices. Because of the olatility of lead at processing temperatures, PZT fibers cannot be abricated by the melt process in the same way as silica fibers. PZT ibers have been prepared using a variety of precursors [6,7]. In his paper, we report the fabrication of continuous $Pb(Zr_{0.52}Ti_{0.48})O_3$, and niobium and $CdBO_3$ substituted PZT $Pb_{0.988}(Zr_{0.52}Ti_{0.48})_{0.976}Nb_{0.024}O_3$ and [97% $Pb(Zr_{0.52}Ti_{0.48})O_3$ - 3% $CdBO_3$]] fibers. Different firing schedules were followed in rder to obtain fibers with varying grain sizes.

Preparation of Viscous Resins for Fiber Drawing:

The scheme for the preparation of spinnable-viscous resins of PZT, and niobium and $CdBO_3$ substituted PZT is outlined in Figure 3. Lead acetate trihydrate [$Pb(CH_3COO)_2.3H_2O$], zirconium n-butoxide, [$Zr(OBu)_4$] 80% solution in 1-butanol, titanium isopropoxide [$Ti(OPr^i)_4$], niobium ethoxide [$Nb(OC_2H_5)_5$], cadmium acetate hydrate [$Cd(CH_3COO)_2.xH_2O$] and boron methoxide [$B(OCH_3)_3$] obtained from Aldrich Chemical Company were used as the starting materials. Lead acetate trihydrate dissolved in 2-methoxyethanol was distilled off three times. A stoichiometric quantity of $Zr(OBu)_4$ was added to the lead solution and refluxed at 125°C for ~6 h. $Ti(OPr^i)_4$, $Nb(OC_2H_5)_5$, $Cd(CH_3COO)_2.xH_2O$ and $B(OCH_3)_3$ were then added to the Pb-Zr solution and again refluxed at 125°C for ~6 h to form the precursor solutions of PZT, and niobium and $CdBO_3$ substituted PZT. A solution of 1 ml of water and 1 ml of conc. HNO_3 diluted in 25 ml of 2-methoxyethanol was added to a vigorously stirred precursor solution of 0.2 M PZT or niobium or $CdBO_3$ substituted PZT. The solution was concentrated by stirring at ~120°C, and then cooled to ~40°C to form a viscous resin. As a result of the forgoing treatment the viscous resin was suitable for extrusion and drawing. The viscosity of the resin in the fiber drawing region was at least 10^6 mPa.s.

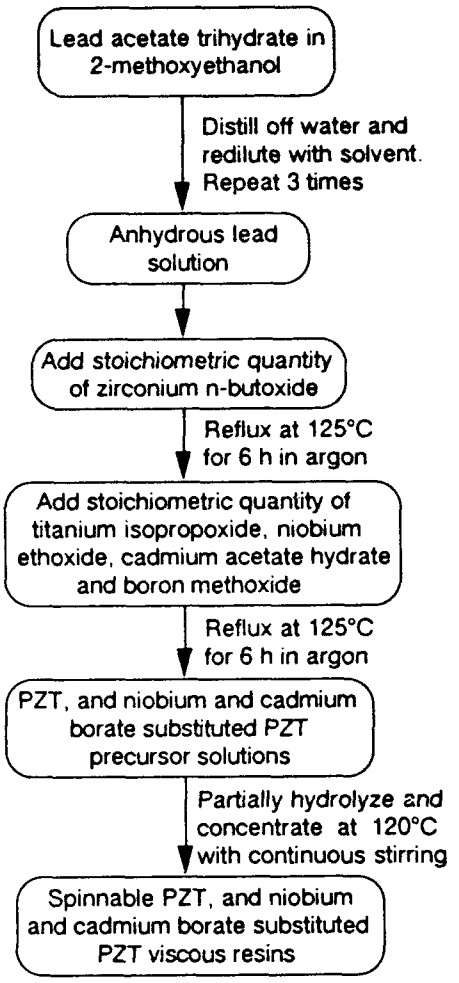


Figure 3 Scheme for the preparation of the spinnable PZT, and niobium and cadmium borate substituted PZT viscous resins.

Drawing and Final Consolidation:

The gel fibers were extruded through a spinneret (e.g., with 12 holes of 200 μm in diameter) at less than 100 PSI. The complete fiber drawing, fiber take-up spool and spinneret assemblies are illustrated elsewhere [8]. These fibers were stretched or drawn by mechanical means to less than 200 μm in diameter. The pulled gel fibers from the spinneret were collected on a rotating drum with a variable-speed control. The drawn gel fibers retained the shape of the spinneret because of the cohesive property of the resins. Because of the viscoelasticity of the resins, the drawn fibers were from approximately 1/20 to 1/3 of the spinneret nozzle diameter. The fibers obtained were of the order of 5 to 100 μm in diameter.

Rapid Thermal Processing:

Niobium substituted PZT fibers preheated at 400°C for 12 h were annealed by a rapid thermal process (RTP) in a Heat Pulse 210T rapid thermal annealer. These fibers were supported on a 4" Si wafer coated with Platinum. Before each run the system chamber was purged with high-purity oxygen. Typical run conditions were: i) a 10 s ramp to 700 °C, ii) hold at 700 °C for 10 s, and iii) cooled down to room temperature. No apparent reaction occurred between the fiber and the coated Si wafer during the brief RTP anneal.

Characterization:

Phase transformations and the weight loss of the gel fibers of PZT, and niobium and $CdBO_3$ substituted PZT obtained from the spinnable resins were studied using Perkin-Elmer differential thermal (Model DTA 1700) and thermogravimetric (Delta Series TGA7) analyzers interfaced with a computerized data acquisition and manipulation system. Phases crystallizing in the heat-treated samples were identified using a Scintag (Model DMC 105) diffractometer with Ni filtered CuKα radiation. The microstructure and the diameter of the heat-treated fibers were studied by a scanning electron microscope (ISI-DS 130, Akashi Beam Technology Corporation, Japan). The dielectric constant of single fiber of PZT was obtained using a precision capacitance bridge (Model GR 1621, General Radio, MA). Capacitance was measured using a three-terminal shielded measurement at 1 kHz. The test fixture capacitance was compensated by open-circuit subtraction. Fibers of 1 to 2 mm in length were attached to sputtered gold electrode pads using a silver paint.

The spun gel fibers were dried at room temperature and heated to 400°C at a heating rate of 1°C/min to eliminate organic

constituents and most of the residual carbon. Figure 4 shows DTA and TGA curves for PZT fibrous gel previously heat treated at 400°C for 24 h. The pre-heated PZT gel exhibited a weight loss of ~3% in the temperature range of 50° to 700°C. The gel exhibited a sharp exotherm at 482°C, followed by a shoulder at 530°C in DTA. These peaks can be attributed to the crystallization of a pyrochlore phase and its conversion into a perovskite PZT. XRD results of the fibrous PZT gel heat treated at 500°C for different durations indicated the formation of pyrochlore and perovskite phases, while heat treatment at 600°C resulted in only the perovskite phase (Figure 5).

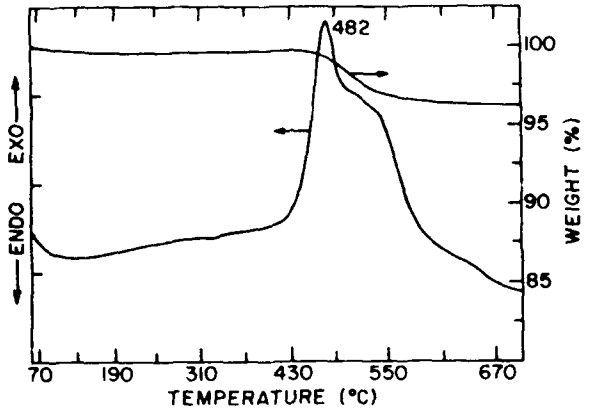


Figure 4 DTA and TGA curves for the fibrous PZT gel pre-heated to 300°C for 24 h.

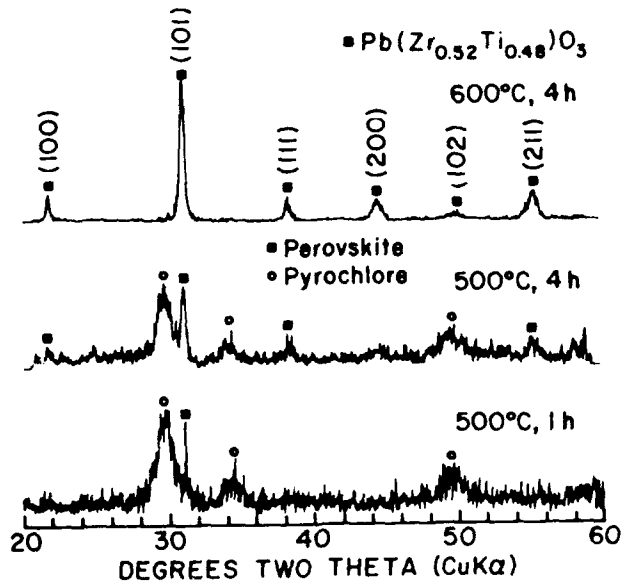


Figure 5 XRD patterns for the fibrous PZT gel heat-treated at different temperatures.

Scanning electron microscope (SEM) pictures of PZT, and niobium and $CdBO_3$ substituted PZT fibers heat treated at 700 °C for 1 h and etched with 1% HCl are shown in Figures 6(a & b), (c & d) and (e & f) respectively. Under higher magnification, PZT and niobium substituted PZT fibers showed fine grains of 0.10 to 0.2 μm (Figures 6(b) and 6(d)). Addition of $CdBO_3$ to PZT resulted

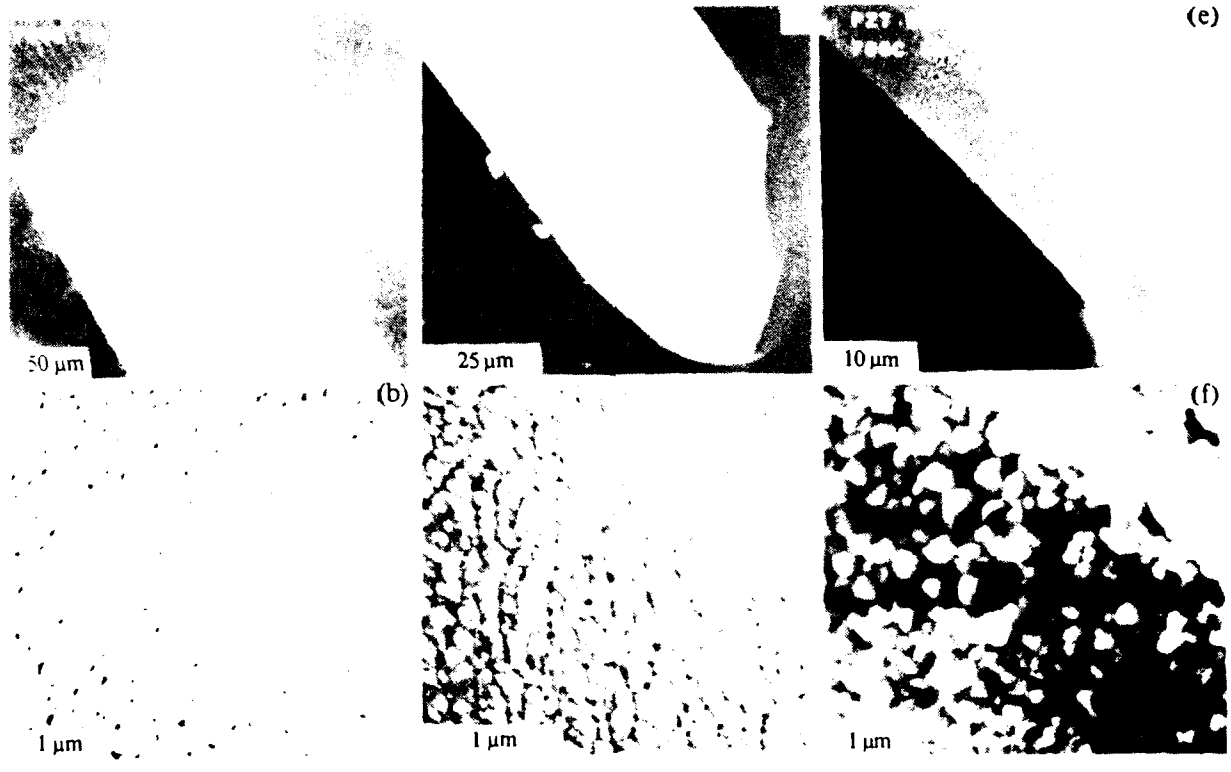


Figure 6 (a) & (b), (c) & (d) and (e) & (f) are respectively the low- and high-magnification micrographs of PZT, niobium and $CdBO_3$ substituted PZT fibers heat-treated at 700°C for 1 h.

in larger grains (~0.1 to 0.35 μm) for fibers annealed at 700°C for 1 h (Figure 6(f)). Figure 7 shows the SEM micrographs of niobium substituted PZT fibers fired at 700°C for 10 s by the RTP (~4100°C/min). This resulted in a denser fiber with more uniform microstructure (grain size ~0.1 μm) compared to the one fired at a heating rate of 1°C / min (Figures 6(b)). PZT fibers were also fired at 1250°C for 0.2 h in a closed lead oxide atmosphere. Lead zirconate powder was used as the source to create lead oxide atmosphere. SEM micrographs of these fibers (Figure 8) show that they are dense and possess grains of about 0.5 to 5 μm.

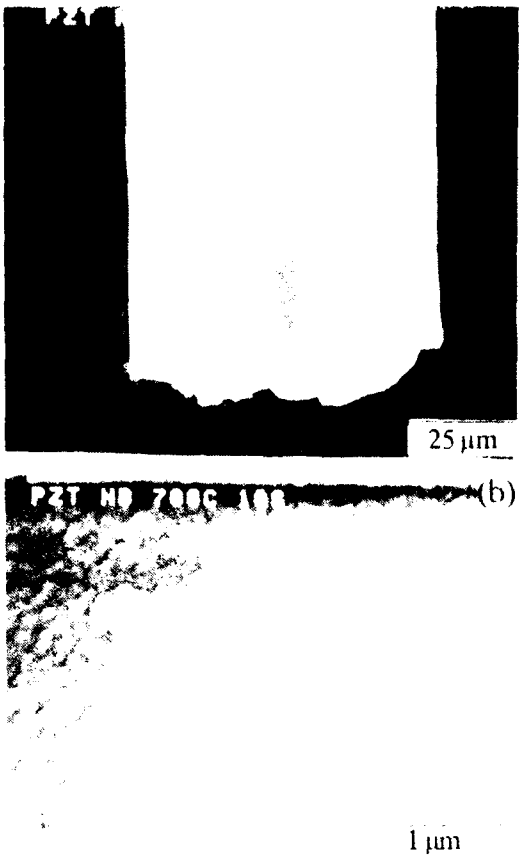


Figure 7 (a) & (b) are respectively the low and high-magnification micrographs of the niobium substituted PZT fibers fast fired at 700°C for 10 s.

The room temperature dielectric constant of the PZT fiber fired at 700°C for 1 h was found to be ~800. The corresponding loss value (tanδ) for the fiber was of the order of 0.06 to 0.08. These values are in agreement with those reported for sintered ceramics of the same composition [3]. Experiments are being carried out to pole these ultrafine PZT, and niobium substituted PZT fibers and embed them in polymer matrix for passive vibrational damping studies.

4. Conclusions

Piezoelectric ceramic tubes, poled and embedded in a polymer matrix, exhibited passive damping with optimum external resistance. By sol-gel processes, uniform PZT, and niobium and $CdBO_3$ substituted PZT gel fibers of unlimited length were obtained from the spinnable viscous resins by extrusion and drawing through a spinneret. The diameter of these fibers were between 5 and 100 μm. The fibrous gels yielded well-crystallized PZT at 600°C. PZT, and niobium and $CdBO_3$ substituted PZT fibers fired at 700°C for 1 h were found to be dense with submicron (0.1 to 0.35 μm) grains. PZT, and $CdBO_3$ substituted PZT fibers with grain sizes of

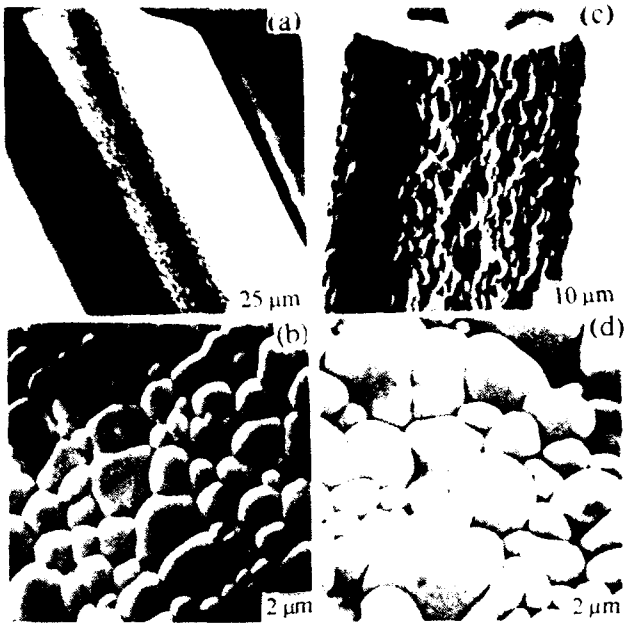


Figure 8 (a) & (b) and (c) & (d) are respectively the low and high-magnification micrographs of PZT and $CdBO_3$ substituted PZT fibers heat treated at 1250°C for 0.2 h.

about 0.5 to 5 μm were obtained on firing the fibers in a closed lead oxide atmosphere at 1250°C for 0.2 h. The room temperature dielectric constant of the PZT fiber fired at 700°C for 1 h was about 800.

Acknowledgement. This research was supported by office of Naval Research under grant No. No. 00014-92-J-1391. The authors would like to thank Prof. D. Edie of Clemson University, in providing access and guidance in the use of fiber manufacturing facilities.

5. References

1. A.R. Ramachandran, Q.C. Xu, L.E. Cross and R.E. Newnham, "Passive Piezoelectric Damping, presented at the IEEE Conference on Ultrasonic Symposium, Honolulu, HI, Dec. 1-7, 1990.
2. N.W. Hagood, W.H. Chung and A. von Flotow, "Modeling of Piezoelectric Actuator Dynamics for Active Structural Control," J. Intell. Mater. System Structure, vol 1, pp. 327-54, July 1990.
3. B. Jaffe, W.R. Cook and H.J. Jaffe, "Piezoelectric Ceramics," New York, Academic Press, 1971, Ch. 7, pp. 135-146.
4. U. Selvaraj, A.V. Prasadarao, S. Komarneni, K.G. Brooks and S.K. Kurtz, "Sol-Gel Processing of $PbTiO_3$ and $Pb(Zr_{0.52}Ti_{0.48})O_3$ Fibers," J. Mater. Res., vol. 7, pp. 992-96, April 1992.
5. S.C. Zhang, G.L. Messing, W. Huebner and M.M. Coleman, "Synthesis of $YBa_2Cu_3O_{7-x}$ Fibers from an Organic Solution," J. Mater. Res., vol. 5, pp. 1806-12, Sept. 1990.
6. D.J. Walter, A. Safari, R.J. Card and M.P. Toole, "Lead Zirconate Titanate Fiber/Polymer Composites Prepared by a Replication Process," J. Am. Ceram. Soc., vol. 73, pp. 3503-506, Nov. 1991.
7. K.C. Chen, H. Zheng and J.D. Mackenzie, "Method for Making Piezoelectric Ceramic Fibers," US Patent No. 5,072,035, Dec. 1991.
8. U. Selvaraj, K.G. Brooks, S. Komarneni and S.K. Kurtz, D. Edie and P. Liu, "Fabrication of PZT and Modified PZT Fibers for Vibrational Damping," The Pennsylvania State University Invention Disclosure, No. 92-1121, University Park, PA, March 1992.

PIEZOELECTRIC RESPONSE OF PRECISELY POLED PVDF TO SHOCK COMPRESSION GREATER THAN 10 GPa

F. BAUER*, R.A. GRAHAM**, M.U. ANDERSON**, H. LEFEBVRE*, L.M. LEE*** and R.P. REED**

*Institut franco-allemand de Recherches, 68301 SAINT LOUIS, France
** Sandia National Laboratories, Albuquerque, NM 87185
*** Ktech Corporation, Albuquerque, NM 87110

Abstract

Prior work has shown that the piezoelectric response of shock-compressed PVDF film prepared with attention to mechanical and electrical processing exhibits precise, well-defined, reproducible behavior to 10 GPa. Higher pressure response continues to pressures approaching 50 GPa, and appears to provide a basis for a very high pressure stress-rate gauge. Previous work shows that differences in response were sometimes observed. The present report describes studies in progress undertaken to increase the precision of the polarization of the PVDF and to develop optimum sensors and shock gauge package designs. Results obtained on such careful prepared PVDF shock gauges show that differences in electrical charge response less than few percent are observed between 10 and 25 GPa.

1. Introduction

The progress of shock-compression science has been strongly influenced by the time resolution of instrumentation systems used to study the response of condensed-matter samples. Historically, the progression of improved time resolution of measurement has followed a pattern from discrete displacement-time (pins), to continuous displacement-time (optics), to direct stress- or particle velocity-time(quartz or VISAR); i.e. a progression of direct measurement of higher kinematic derivatives.

In 1981 Bauer [1] called attention to the strong, and well characterized electrical signals observed from shock-compressed, piezoelectric films of the polymer PVDF. In the intervening period there has been a continuing effort from the authors to develop a high quality, reproducible sensor material, and to determine its physical characteristics under high pressure shock compression. It is now apparent that such a material is useful in time-resolved, stress-rate gauges from 10 MPa to 10 GPa with response characteristics not available with any other existing gauge [2].

At pressures greater than 10 GPa, well-defined signals are observed, but the usefulness as a gauge was hampered by reports of differences in responses by various investigators. At these high pressures a number of distinctive conditions exist compared to lower pressure. Accordingly, the present work is in progress to define the physical processes which might lead to consistent behavior of shock-compressed PVDF films and to develop sensor packages which control the high pressure response problems.

In the present report, background information will be presented on the PVDF material and its response characteristics. Following this information, some of the problems and conditions unique to high pressure experiments will be outlined. Experimental studies on precisely poled PVDF will then be presented. Finally, the status of high pressure response work will be assessed.

2. Background

The PVDF material of the present report is the same standardized Bauer film used for earlier studies by the authors [2-8]. Each piezoelectric element is prepared with precisely controlled mechanical and electrical processing, and is furnished with measured electrical properties including a ferroelectric hysteresis loop which provides a sensitive measure of all the physical properties. Active area, displacement current (Figure 1) and remanent polarization (Figure 2) are given for each PVDF gauge.

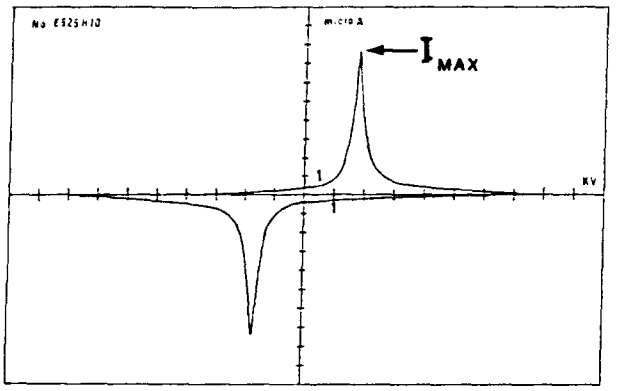


Figure 1: Displacement current versus voltage for a standardized, precisely poled PVDF gauge.

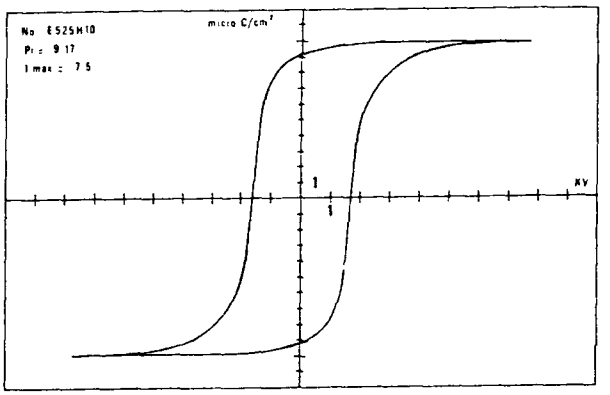


Figure 2: Hysteresis curve for a standard PVDF gauge.

At Sandia National Laboratories the principal experimental tool used to study the shock response is the compressed-gas gun which

CH3080-0-7803-0465-9/92$3.00 ©IEEE

subjects the piezoelectric samples to precise, controlled shock loading with impactors and targets of well-defined standard materials to control the stress input. Impact velocities are measured to accuracies and precisions of 0.1%.

At the Institute of Saint-Louis, the experimental measures of electrical response of shock compressed PVDF film are carried out on a new impact-loading facility which is a powder gun 20 mm in diameter. The accuracy and precision are about 0.3%.

In both laboratories, low loss coaxial cables and 1 GHz digitizers provide the high-frequency recording capability required to properly interpret the sensor responses. The responses are measured in the "current mode" to provide both a simple circuit and the most revealing electrical behavior.

Previous observations of the PVDF piezoelectric charge response data to 50 GPa (Figure 3) show significant deviations from idealized, continuous behavior between about 12 and 20 GPa. These differences were observed for both sapphire and copper standard impactors. Above about 16 GPa, the observed behavior appears to follow a well-defined relationship, but more scatter is observed than at pressures less than 10 GPa.

As indicated in Figure 3, various PVDF film materials have been investigated and the difference in response does not appear to be related to the starting film.

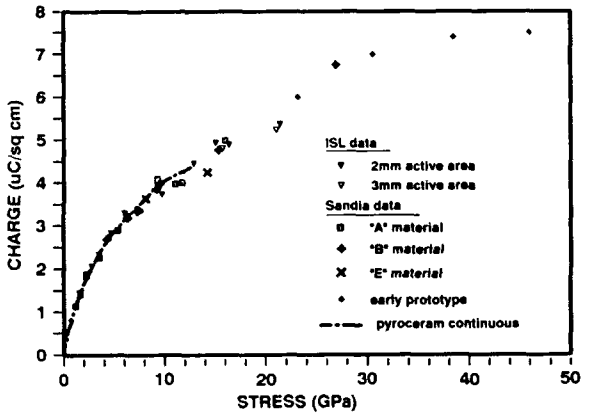


Figure 3: Piezoelectric polarization data for shock-compressed Bauer PVDF reported in prior work [8] is shown over a wide stress range. Note the continuous response data obtained with Pyroceram loading and the scatter in shock response data above 10 GPa.

3. High-pressure response: situation analysis

Given the observations summarized above, it was important to seek to identify distinctive features of high-pressure efforts on PVDF sensors.

A brief review [8] of the effects of shock properties of standard materials, electronic circuit, the PVDF material and the gauge package follows.

3.1 Standard shock materials

At pressures above 10 GPa there are no precise standard materials for use in the impact experiment to determine the impact stresses. Sapphire is thought to be elastic to about 15 GPa [8] but the degree of elasticity can be questioned. Higher impedance materials such as tungsten carbide do not have precisely known properties and the degree of reproducibility is questionable. Copper provides a good standard.

3.2 Electronic circuits

The currents achieved under the high-pressure highly planar loading are large (tens of amperes) and the peak values may be achieved in times of a few nanoseconds. Thus, the rates of change of current are very large (10^9 amperes per second). Very small amounts of inductance in the vicinity of the gauge will lead to inductive ringing under these conditions.

The current densities in the sputtered leads to the gauge are in the range of 10^7 to 10^8 amperes/cm^2. Such current densities are sufficiently large that there is concern for increases in lead resistance.

3.3 Changes in PVDF sensor material

There are potentially a number of both stress-induced and electric-field-induced effects which can act to alter sensor behavior at high pressure.

3.4 Gauge package

The typical PVDF gauge package configuration consists of insulating film of Teflon on both sides of the 25 micron PVDF elements. Both electrical conductivity in the insulating film and mechanical loading history may affect the gauge response.

4. Experimental

Based on the consideration above, we have investigated the effect of sensor remanent polarization on gauge response and have investigated methods of controlling inductive effects in the sensor electrode design.

Our program involves the study of the shock compression response of the standardized gauge elements (Figure 4) under controlled impact loading.

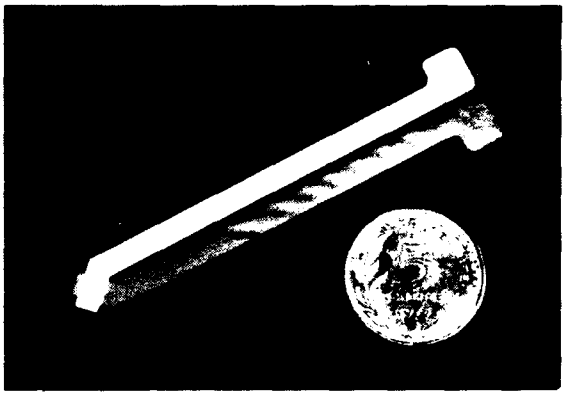


Figure 4: Standardized PVDF shock gauge.

Impact loading is produced by controlled impact in a powder gun (caliber 20 mm) at ISL, or compressed gas gun (SNLA). The symmetrical impact of an impactor and target copper provides the loading. The gauge element is placed on the impact surface of the target material. The PVDF gauge is insulated on both sides with a Kel-F film of 110 μm in thickness. Kel-F matches the shock impedance of the PVDF. In this configuration the initial stress wave produced by impact is that typical of the impact of the copper impactor on the PVDF gauge. This wave then reverberates between the impactor and target until stress is reached equal to that for the standard impactor and target.

Shock pressures are computed with $U=3.91+1.51\ u_p$ (km/s) density 8.924 for copper (U: shock velocity, u_p particle

velocity). The electrical signal from the shock compressed PVDF gauge is recorded in the current mode: the gauge provides a signal dependent on the stress rate called here "multiple shock". Upon integration of the current pulse, the electrical charge versus - time is obtained.

Figure 5 gives an example of the current and electrical charge released versus time for a standardized gauge (shock pressure: 16.3 GPa). The maxima of the current i(t) correspond to shock reverberations within the gauge package. The observed waveform show inductive ringing. Nevertheless, the correct charge will be observed for time after the ringing subsides, but, at best, the ringing behavior complicates the data analysis.

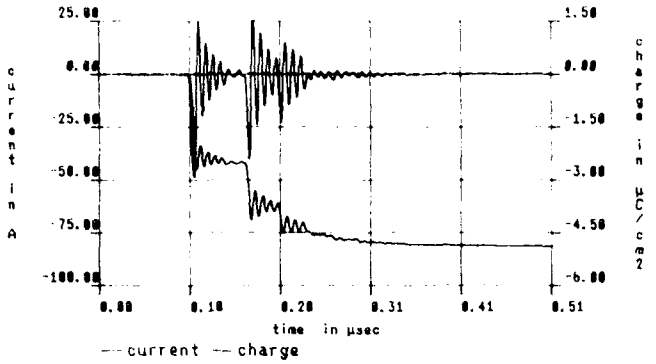


Figure 5: Current pulse and electrical charge versus time for a precisely poled standard PVDF gauge (shock pressure 16.3 GPa). This standard gauge exhibits non-negligible inductance due to the spacing between the leads.

4.1 Effects of inductance

After many trials over a considerable period of time, we have been successful in electrically poling the PVDF film with a new procedure based upon the original cyclic poling method but with the capability of achieving more flexibility in the electrode and lead design. With the new procedure, electrode designs have been developed and tested. The ideal low inductive design would have leads closely spaced which do not overlap.

Figure 6 gives an example of the current and electrical charge released versus time for a low inductance gauge poled at the same level of that of a standardized gauge. As we can see less ringing are observed and such a gauge can lead to better data analysis.

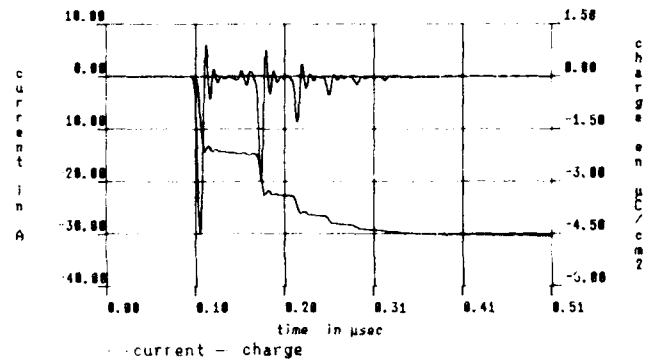


Figure 6: Current pulse and electrical charge of a low inductance PVDF gauge versus time (shock pressure 13.6 GPa).

4.2 Effects of remanent polarization

The effect of remanent polarization (standardized at lower pressure studies at 9.1 $\mu C/cm^2$) on sensor response has been investigated at values of 6.2, 7.5, 8.2 and 9.1 $\mu C/cm^2$. As shown in Figure 7, impact experiments have been carried out at pressures from 3.4 GPa to 5.2 GPa, 9.3 GPa, 12 GPa, 21 GPa and 34 GPa. It is observed that there is a change in behavior at for remanent polarization over 8.5 $\mu C/cm^2$ in particular for the 3 x 3 mm gauges poled at 9.1 $\mu C/cm^2$ by Metravib in using the ISL process [5]. It appears (Figure 7) that the gauges are responding distinctively and are deviating from the expected response.

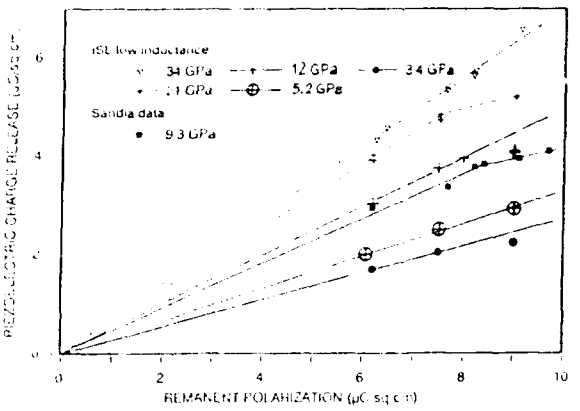


Figure 7: The response data for PVDF in various states of remanent polarization are indicated at various shock stresses. At lower polarizations an approximate linear relation is observed. There appears to be change in behavior for the Metravib standard gauges poled at 9.1 $\mu C/cm^2$.

In order to identify the origin of the deviations observed (section 2), we subject carefully prepared and poled 3 x 3 mm PVDF gauges to shock loading. Such precisely poled gauges are prepared as follows.

- active area A is precisely measured;
- the precision of the measured remanent polarization is enhanced by the controlling the mechanical clamping under pressure during poling. This leads to value of the displacement current achieved in poling to be equal to 7.6 μA at 0.08 Hz;
- the gauge thickness ranges from 22.5 to 23.5 μm.

5. Response of precisely poled PVDF gauges

The precisely poled PVDF gauges were subjected to shock loading between 10 and 25 GPa and have presented following characteristics:

- area ranges from 9.1 to 9.15 mm^2 after poling. Before poling the area is equal to 8.95 mm^2.
- maximum value of displacement current ranges from 7.5 to 7.7 μA;
- remanent polarization is between 9.1 and 9.2 $\mu C/cm^2$.

It should be pointed out that these two last values were measured for 7.7 kV sine wave high voltage applied during poling at a frequency equal to 0.08 Hz. The piezoelectric response of such highly precise poled PVDF gauges is depicted on Figure 8.

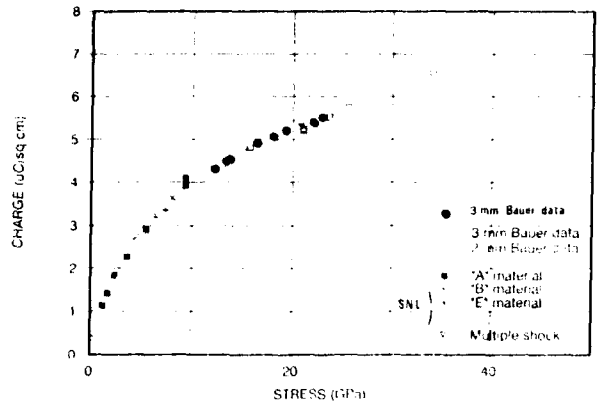


Figure 8: Piezoelectric polarization data for precisely-poled Bauer PVDF from 10 MPa to 35 GPa. Data below 10 GPa are from references 3 and 4.

It is observed that PVDF stress rate gauges show continuous response to pressures approaching 30 GPa. In particular, we do not observe deviations in the shock pressure range 10 to 16 GPa. The results included copper impactors and targets as well as tungsten carbide materials. For the last material there are some uncertainties on the shock pressure attained (the tungsten carbide reproducibility is questionable). Nevertheless, the results obtained and presented on Figure 9 show deviations of less than 2% in charge released, along a fit of the experimental results.

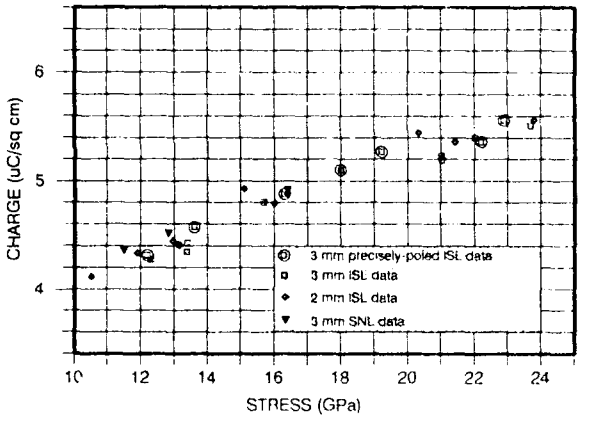


Figure 9: Piezoelectric polarization data for precisely-poled Bauer PVDF from 10 GPa to 35 GPa. The 3 mm data with filled circles is shown in Table I.

The following table gives the obtained experimental values:

TABLE 1. Results obtained with Precisely Poled PVDF (copper impactor and target)

Impact Velocity (m/s)	Shock Pressure using LANL shock data (GPa)	Electric Charge ($\mu C/cm^2$)	Final Area (cm^2) after poling	Thickness of PVDF Gauge (μm)	Max displacement current (μA)	Remnant Polarization ($\mu C/cm^2$)
625	12.2	4.31	0.0940	23.5	7.68	9.01
690	13.6	4.57	0.0915	22.6	7.98	9.06
808	16.3	4.88	0.0915	21.6	7.76	9.26
882	18.0	5.1	0.0910	[illegible]	7.75	9.05
933	19.2	5.27	0.0905	23.4	7.71	9.01
1057	22.2	5.36	0.0915	24.3	7.59	9.09
1085	22.9	5.56	0.0910	22.3	7.75	9.23

6. Discussions, conclusions

PVDF stress rate gauges show continuous response with high reproducibility to pressure approaching 35 GPa.

It appears that low inductance electrode lead designs and reproducible remanent polarization are (significantly) improving the precision of the piezoelectric response of the PVDF gauges under shock loading especially for the 3 x 3 mm gauges.

However, more work needs to be completed to develop sensors with small active areas (1 mm^2) with the same precision in polarization.

Control of loading rate to the sensor with thickness of insulating film appears to offer potential for more reliable response.

These results show that selected and precisely poled PVDF can respond precisely to pressures of 25 GPa. It appears there is considerable potential for use of PVDF gauges in very high pressure materials investigations. In addition to the precise control on the value of remanent polarization, reproducible behavior of high pressure requires control of the maximum displacement current achieved during poling. The maximum current provides a sensitive measure of the degree of deformation to a gauge element during the poling process.

7. References

(1) F. Bauer, "Behavior of Ferroelectric Ceramics and PVF_2 Polymers Under Shock Loading," Shock Waves in Condensed Matter-1981 eds., W.J. Nellis, L. Seaman and R.A. Graham (Amer. Inst. Phys. 1982), pp. 251 266.

(2) R.A. Graham, F. Bauer, L.M. Lee and R.P. Reed, "Standardized Bauer PVDF Piezoelectric Polymer Shock Gauge," Proceedings of Shock Waves in Condensed Matter (Duvall Symposium), ed. Y.M. Gupta (Wash. State Univ. 1988), pp.47-50.

(3) L.M. Lee, R.A. Graham, F. Bauer and R.P. Reed, "Standardized Bauer PVDF Piezoelectric Polymer Shock Gauge," Journal de Physique, Collection C3, Suppl. N° 9,49, 1988, pp. 651-657.

(4) R.A. Graham, M.U. Anderson, F. Bauer and R.E. Setchell, "Piezoelectric Polarization of the Ferroelectric Polymer PVDF from 10 MPa to 10 GPa: Studies of Loading - Path Dependence," Shock Waves in Condensed Matter-1991, eds., S. C. Schmidt, et. al. North Holland (1992), pp. 883-886.

(5) F. Bauer, "Method and Device for Polarizing Ferroelectric Materials", U.S. Patent 4, 611, 260 and 4,4684337 French Patent 8,221,028.

(6) L. Moore, R.A. Graham, L.M. Lee, F. Bauer, J.W. Warren, R.P. Reed, "Standardized Piezoelectric Polymer (PVDF) Gauge for Detonator Response Measurements," 3rd International Symposium High Dyanmic Pressures, ed. R. Cheret (Commissariat a l Energie Atomic, Paris), 1989, pp. 35-43.

(7) F. Bauer, "Improved Ferroelectric and Piezoelectric Polymers for Stress Gauges," Ferroelectrics, 1989, Vol. 92, pp. 29-34.

(8) F. Bauer, R.A. Graham, M.U. Anderson, H. Lefevbre, L.M. Lee, R.P.Reed, "Response of the Piezoelectric Polymer PVDF to Shock Compression Greater Than 10 GPa," Shock Waves in Condensed Matter-1991, eds., S. C. Schmidt, et. al. North Holland (1992), pp. 887-890.

NEW EXTREMELY BROADBAND FERROELECTRIC POLYMER ULTRASOUND TRANSDUCERS

Lewis F. Brown
Electrical Engineering Department
South Dakota State University
P.O. Box 2220, HH-201
Brookings, SD 57007

Abstract

Ferroelectric polymers have been widely investigated for use in ultrasound transducers for both medical and nondestructive testing (NDT) applications. The low acoustic impedance and high electromechanical coupling of PVDF copolymers make them well suited for the design of ultrasound transducers with frequency bandwidths that rival those achieved with other transducer materials. Custom immersible ultrasound transducers were recently developed for an application requiring -6 dB fractional bandwidths in excess of 150%, spanning a frequency range of approximately 5-100 MHz. The copolymer transducers were optimally designed for maximum bandwidth and efficiency for operation in water. The design is also custom optimized for the specific dielectric and piezoelectric properties of the P(VDF-TrFE) copolymer used. This paper reviews the design, fabrication, and testing of these new transducers.

Introduction

Ferroelectric polymers continue to play an important role in ultrasound transducers for medical and nondestructive testing applications. In general, they are best suited for applications which are uniquely served by their low cost, high compliance, low acoustic impedance, availability in large areas, and broadband performance. These unique inherent properties are the underlying reasons for their successful use in commercial products for applications including acoustic microscopy, invasive medical ultrasound imaging, and nondestructive testing [1].

Although the piezo polymers have been widely investigated for "conventional" immersion probes (i.e., low-frequency planar devices), because of their low electromechanical coupling and permittivity, they are generally unable to compete with piezo ceramics unless other physical requirements (high-frequency, large area, flexibility, etc.) rule out the use of ceramics.

Besides their unique material properties, research has also shown that planar ferroelectric polymer ultrasound transducers can produce plane wave perform-ance in the acoustic near field which is superior to that of piezo ceramics [2-4]. Their low radial/lateral mode coupling reduces the effects of edge waves and near field distortion which is typical of piezo ceramic disc transducers. The low radial mode coupling and high k_t of 1-3 piezo composite materials also offer good all-around performance for insertion loss, bandwidth, and plane wave performance, but the 1-3 materials are thus far limited to low frequency (< 10 MHz) applications [5,6].

A recently developed particle analyzer system requires planar through-transmission operation in the near field, with ideal plane wave performance and maximum bandwidth/sensitivity in the 5-100 MHz range. Rather than utilize several pair of commercial ceramic transducers, necessary to cover the frequency range, new ferroelectric polymer transducers were developed for their superior bandwidth and "clean" plane wave performance, despite the higher efficiency (lower insertion loss) of the ceramic transducers. This paper describes the transducer requirements, design, construction, and testing of these new ultrasound transducers.

Transducer Requirements

The requirements for the new transducers include exceptionally broadband through-transmission performance in the 5-100 MHz range. It was desirable to cover the frequency range with a minimum number of transducer pairs. The mathematics utilized in the system's analysis technique requires undistorted plane wave operation with close (i.e., 0-2") transducer spacings. A large diameter (0.25-1.2") active area was also desired so that a large cylindrical volume could be insonified at all frequencies. The transducers are housed in large diameter precision-ground stainless steel housings, as shown in Figure 1, to provide a precise fit to the alignment/positioning hardware of the particle analyzer system.

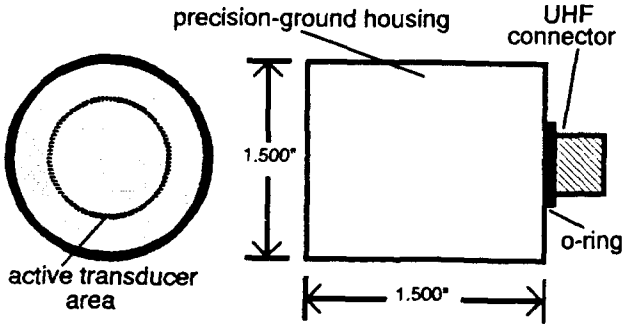


Fig. 1. Required transducer housing design.

Transducer Design

The transducer design is based on high-activity P(VDF-TrFE) copolymer which has been specially treated for high electromechanical coupling. Since the transducers are of a planar active area design, the high compliance of the copolymer could be sacrificed for enhanced crystallinity and high k_t. The typical properties of the copolymer

CH3080-0-7803-0465-9/92$3.00 ©IEEE

materials used for the transducers are summarized in Table 1.

Table 1. Typical copolymer properties

Parameter	Typical Values
Electro. coupling, k_t	0.3
Mechanical Q, $(1/\tan\delta_m)$	25
Dielectric constant, ϵ_r	3.5 - 5.0[1]
Loss tangent, $\tan\delta_e$	0.10 - 0.15[1]
Acoustic imped. (MRayl)	4.3
Thickness, (μm)	10 - 100

[1] Measured at 5-100 MHz.

A half-wave resonator design was selected to maximize bandwidth at the expense of efficiency. Half-wave resonance was achieved by using a lossy low-impedance backing material as shown in Figure 2.

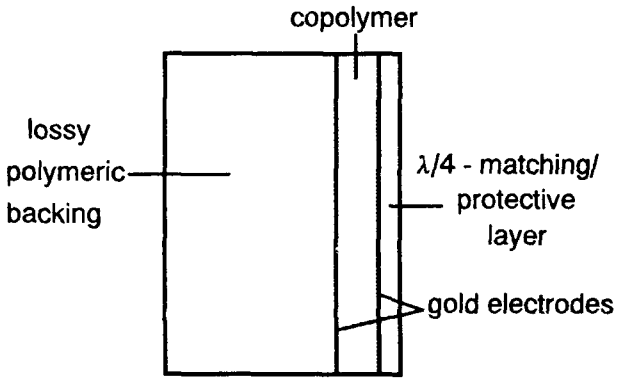


Fig. 2. Transducer substrate assembly.

The thickness of the copolymer material was selected for the desired frequency range, while the diameter of the active area was optimized for maximum power transfer in the electronics of the characterization system, using a technique similar to those reported by others [7-9]. The electromechanical properties of the copolymer, required for the optimization, were characterized using conventional immittance curve fitting techniques [10-12]. To provide the necessary wear resistance, and to enhance insertion loss and bandwidth, a polymeric quarter-wave matching layer was also incorporated in the design as shown in the figure.

The resulting design has provided extremely low-Q (≈0.6-1.0) broadband performance in the particle analyzer system. The completed transducers show little or no discernible electrically excitable mechanical resonances in their immittance spectra, as illustrated in Figure 3. This behavior is indicative of a very low-Q transducer material which is well-matched to both its forward and backing acoustic loads.

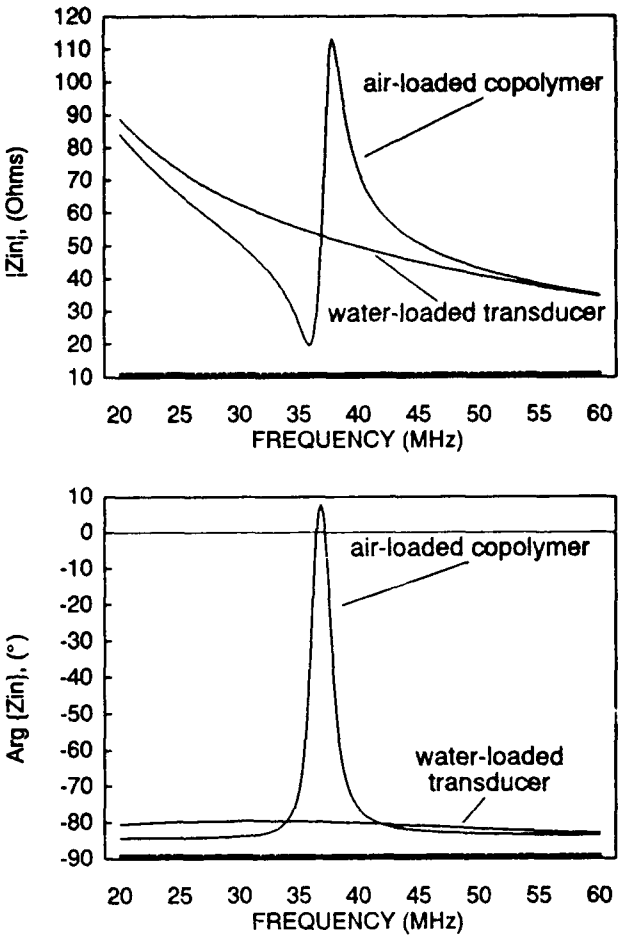


Fig. 3. Typical input impedance magnitude and phase spectra for air-loaded copolymer only, and completed transducer.

Through-Transmission Test Method

The transducer pairs were tested for their through-transmission performance in several different test systems. The transducers were focussed in a test chamber at close spacing in pure water. A network analyzer was used to acquire the broadband through-transmission voltage transfer function (magnitude and phase) of the transducer pair. This spectrum, which contains electrical feed-through and multiple reflection artifacts, is then corrected for the water's attenuation over the particular frequency spectrum and temperature. The transfer response of the electronics system, including all cables, adapters, etc., is also deconvolved from the spectrum. An inverse FFT is then performed so that the time domain response of the transducers can be observed. The portion corresponding to the first arrival acoustic waveform is then gated out of this response, eliminating the feed-through and reflection artifacts, and a forward FFT is applied to compute the transfer function (i.e., the insertion loss spectrum) for the transducer pair.

The technique has proven particularly useful for characterizing very high frequency transducers (i.e., 50-200 MHz)

where the means for conventional sinusoidal tone burst measurements become more difficult without sophisticated instrumentation. To verify the accuracy of the technique at low frequencies, the results were correlated with conventional tone burst measurements (typically 5-10 cycles) and showed excellent results in computing the insertion loss spectra. To verify the accuracy of the technique at high frequencies, the transducers were used to measure the high-frequency attenuation spectra of pure water at known temperatures. The measurements showed excellent agreement with the well known absolute attenuation spectra for water at multiple transducer spacings (i.e., from very low to very high levels of attenuation in the water path). The measurement technique is carried out under computer control and, once the transducers are aligned in the liquid-filled chamber, requires only seconds to complete.

Through-Transmission Test Results

Various transducer pairs have been tested using both conventional tone burst measurements and the previously discussed network analyzer technique. Examples of typical insertion loss spectra for both high and low frequency transducer pairs are shown in Figure 4.

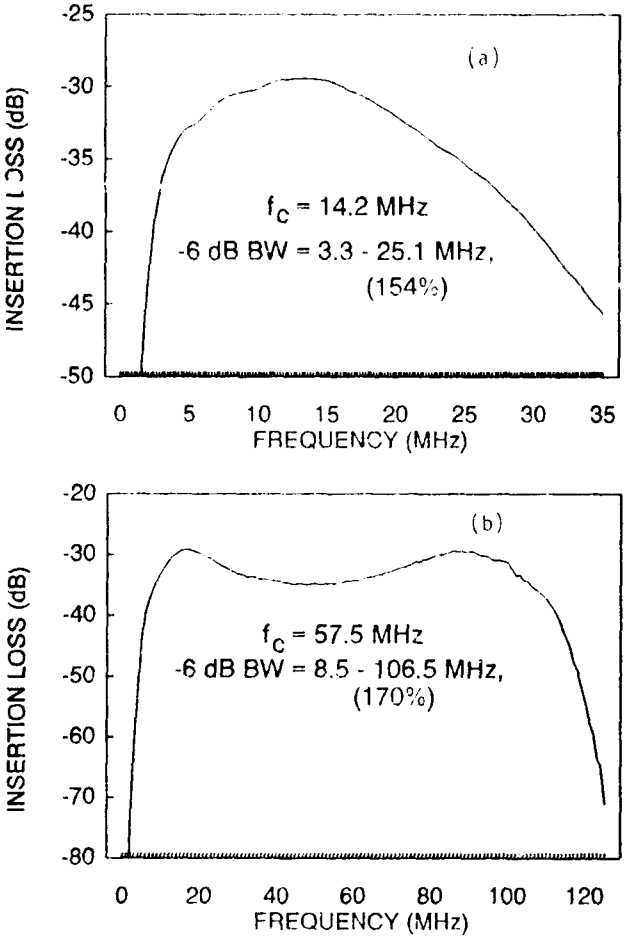


Fig. 4. Typical measured through-transmission insertion loss spectra for a (a) low-frequency, and (b) high-frequency transducer pair.

The low-frequency pair shows a minimum insertion loss of 29.4 dB, with a -6 dB bandwidth of 3.3-25.3 MHz (154%). The high-frequency pair shows a minimum insertion loss of 29.2 dB, with a -6 dB bandwidth of 8.5-106.5 MHz (170%). The results show that excellent broadband performance was achieved, with -6 dB bandwidths often extending more than 1.5 decades of frequency. The minimum insertion losses ranged from 22 to 35 dB, with center frequencies of 15-90 MHz. While these insertion loss values are still high, the transducers have provided excellent performance and long-term repeatability in prototype analyzer systems over approximately two years. Improvements in the insertion loss are now the focus of future work.

Future Development Work

Although the broadband performance of the transducers has been excellent, improvements in the insertion loss of the transducers would greatly enhance the overall capability of the measurement system. While recent works have focussed much attention on improving the bandwidth performance of ferroelectric polymer ultrasound transducers [13-15], little significant work has been noted in major improvements to their poor efficiency. Continued developments in ferroelectric polymer film-forming and processing for enhanced crystallinity (high k_t) will no doubt benefit this work. Computer simulations also show that further improvements in insertion loss can be gained for these transducers through novel copolymer film/substrate fabrication techniques which will be explored.

Conclusions

Extremely broadband ferroelectric polymer ultrasound transducers have been described for a new particle analyzer system based on broadband through-transmission measurements of acoustic plane waves. The basic system requirements, design, fabrication, and testing of the transducers have been described. The transducers have shown excellent broadband performance, capable of extending beyond 1.5 decades of frequency, with improvements in insertion loss still desirable. Improvements in ferroelectric film-forming techniques and material properties will further improve the insertion loss of the transducers.

Acknowledgements

The author wishes to thank Christopher P. Guerin, of Elf Atochem Sensors, Inc. (Valley Forge, PA), for his excellent fabrication skills on the transducers. A debt of gratitude is also owed to Joseph Cero, also of Elf Atochem Sensors, Inc., for his work and suggestions on the design of the transducer housings. This work was largely carried out while the author was with Elf Atochem Sensors.

References

[1] L.F. Brown, "New Developments in Piezoelectric Polymer Ultrasound Transducers and Transducer Systems", presented at The 1992 SPIE International Symposium, Technical Conference No. 1733, San Diego, CA, July 21-22, 1992.

[2] D.A. Hutchins, H.D. Mair, and R.G. Tay[illegible], "Transient Pressure Fields of PVDF Transducers", J. Acoust. Soc. Am., Vol., No. 1, pp. 183-192, July 1987.

[3] D.A. Hutchens, et. al., "Continuous-Wave Pressure Fields of Ultrasonic Transducers", J. Acoust. Soc. Am., Vol. 80, No. 1, pp. 1-12, July 1986.

[4] D.I. Crecraft and C.J.S. Davies, "Visualisation of Ultrasonic Waves Launched by PVF_2 Piezofilm Transducers", Electronics Letters, Vol. 18, No. 1, pp. 16-17, Jan. 7, 1982.

[5] W.A. Smith, "New Opportunities in Ultrasonic Transducers Emerging From Innovations in Piezoelectric Materials", presented at The 1992 SPIE International Symposium, Technical Conference No. 1733, San Diego, CA, July 21-22, 1992.

[6] W.A. Smith, "The Role of Piezocomposites in Ultrasonic Transducers", in Proc. of 1989 IEEE Ultrasonics Symposium, Vol. 2, pp. 755-766.

[7] C.S. DeSilets, J.D. Fraser, and G.S. Kino, "The Design of Efficient Broad-Band Piezoelectric Transducers", IEEE Trans. Son. and Ult., Vol. SU-25, No. 3, pp. 115-125, 1978.

[8] M.D. Sherar and F.S. Foster, "The Design of High Frequency Poly(Vinylidene Fluoride) Transducers", Ultrasonic Imaging, Vol. 11, No. 2, pp. 75-94, 1989.

[9] G.S. Kino. Acoustic Waves. Englewood Cliffs, NJ: Prentice-Hall, 1987, Chapter 1, pp. 27-71.

[10] H. Ohigashi, "Electromechanical Properties of Polarized Polyvinylidene Fluoride Films as Studied by the Piezoelectric Resonance Method", J. Appl. Phys., Vol. 47, No. 3, pp. 949-955, 1976.

[11] D.H. Turnbull, M.D. Sherar, and F.S. Foster, "Determination of Electromechanical Coupling Coefficients in Transducer Materials With High Mechanical Losses", in Proc. 1988 IEEE Ultrasonics Symposium, Vol. 2, pp. 631-634.

[12] L.F. Brown and D.L. Carlson, "Ultrasound Transducer Models for Piezoelectric Films", IEEE Trans. Ult., Ferro., Freq. Cont., Vol. 36, No. 3, pp. 313-318, May 1989.

[13] K. Sakaguchi, et. al., "Wide-band Multi-layer Ultrasonic Transducers Made of Piezoelectric Films of Vinylidene Fluoride-Trifluoroethylene Copolymer", Jap. Jour. Appl. Phys. Suppl., Vol. 25, Sup. 25-1, pp. 91-93, 1986.

[14] P.L. Lewin, Q. Zhang, and P.E. Bloomfield, "Enhanced Bandwidth Ultrasound Transducers with Multiple Piezoelectric Polymer Layers", presented at The 1992 SPIE International Symposium, Technical Conference No. 1733, San Diego, CA, July 21-22, 1992.

[15] M. Platte, "PVDF Ultrasonic Transducers", Ferroelectrics, Vol. 75, No. 3, pp. 327-337, 1987.

PZT-Based Stacked Acoustic Filters

J.Kosinski*+, E.Baidy*, J.Shannon*+, A.Safari+, and A.Ballato*

*US Army Electronics Technology and Devices Laboratory
ATTN: SLCET-MA Fort Monmouth NJ 07703-5601

+Rutgers, The State University of New Jersey
College of Engineering, New Brunswick NJ 08903

Abstract: The stacked-crystal filter for use as a bandpass electrical filter with bandwidth of several percent at HF frequencies and low insertion loss was first proposed in the early 1970s. The filter contains two piezoelectric plates mechanically attached with a grounded electrode along the interface. The electrical input signal is converted to an acoustic signal by the input transducer, and the acoustic signal is propagated across the ground plane to the output transducer which reconverts the acoustic signal to an electrical output signal. The concept was verified experimentally; however the use of single crystal quartz resonators with gold electrodes limited the filter bandwidths and power handling capabilities of the original devices. For applications requiring wider bandwidths and higher RF power levels, other materials such as PZT piezoceramics may be used. Prototype PZT-based stacked acoustic filters exhibiting 30% RF bandwidth, less than 1dB insertion loss, and RF power handling capability on the order of 5 W/cm^2 of transducer area have been demonstrated.

Introduction

The stacked-crystal filter for use as a simple, robust electrical bandpass filter with bandwidth of several percent at HF frequencies and low insertion loss was first proposed in the early 1970s [1-4]. As shown in Figure 1, such a filter is simply formed from two piezoelectric plates mechanically attached with an electrode along the interface which is connected to ground. The electrical input signal is converted to an acoustic signal by the input transducer, and the acoustic signal is propagated across the ground plane to the output transducer which then reconverts the acoustic signal to an electrical output signal. The concept was verified experimentally using single crystal quartz resonators with thin gold electrodes, and a design methodology employing equivalent electrical circuits was set forth by Ballato et al. [5]. The use of single crystal quartz resonators placed distinct limitations on the filter bandwidths and power handling capabilities of the original devices.

Design Considerations

The application of the stacked-crystal filter (here denoted stacked acoustic filter since the piezoelectric elements are not single-crystal) for wider bandwidths and high RF power levels requires consideration of both electrical and acoustic aspects of the constituent materials and filter structure. Important electrical aspects include the insertion loss and frequency response of the

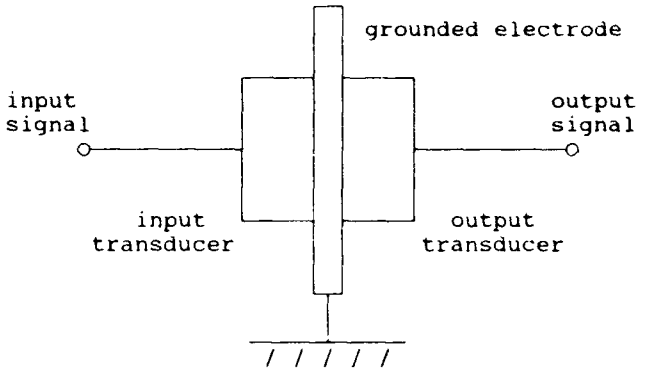


Figure 1. Stacked-crystal filter.

stacked filter. Important acoustic aspects include the piezoelectric coupling of the transducers, acoustic attenuation in the ground plane, and acoustic impedance matching at material interfaces in the stacked filter. All of these parameters are closely interrelated. The primary issues involved are as follows:

Filter Charactertistics

The stacked acoustic filter is an electrical bandpass filter characterized by such parameters as center frequency, bandwidth, shape factor, insertion loss, out-of-band attenuation, input impedance, output impedance, etc. The current work has focused on achieving the desired center frequency, insertion loss, and out-of-band attenuation, with the other parameters being of somewhat lesser importance.

Acoustic Wave Propagation

The conversion of the electrical input signal to an acoustic wave, its propagation through the ground plane, and its reconversion to an electrical signal must be done as efficiently as possible in order to minimize dissipation in the filter. The primary factors affecting the efficiency of acoustic power transmission include the piezoelectric coupling of the transducer material, the bonding of the transducers to the ground plane, the acoustic attenuation in the ground plane, and the acoustic impedance mismatches at the boundaries between the various layers in the stack. These factors are influenced by both materials selection and stack configuration.

Power Handling Capability

The power handling capability of the stacked acoustic filter is determined primarily by the transducer material and the

CH3080-0-7803-0465-9/92$3.00 ©IEEE

transducer to ground plane bonding technique. The frequency of operation also plays a role in determining power handling capability.

In order to implement the foregoing design considerations, the relationships between the physical properties of the constituent materials and the various electrical and acoustic design parameters must be known. These relationships are most clearly modeled by the transmission line analogs of Ballato (see Figures 2-4) [6], wherein the equivalent electrical circuit corresponding to a layer of an arbitrary material with a thickness-directed electrical field exciting acoustic modes with wave vectors along the thickness direction may be determined from the physical properties of the material layer. A multi-layer structure is easily modeled as a cascade of such networks with appropriate port

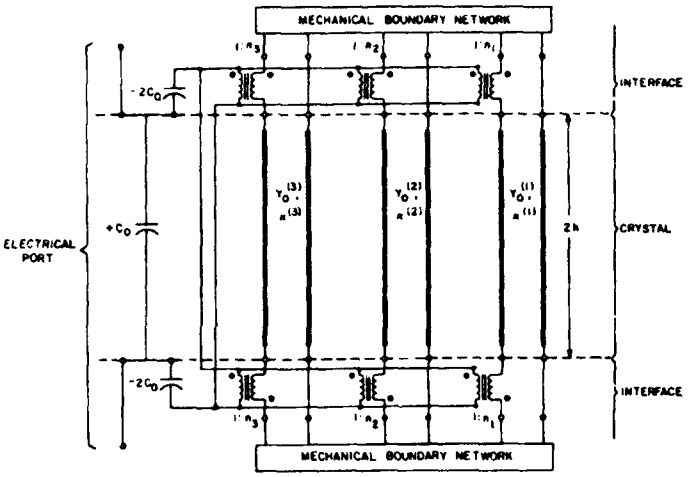
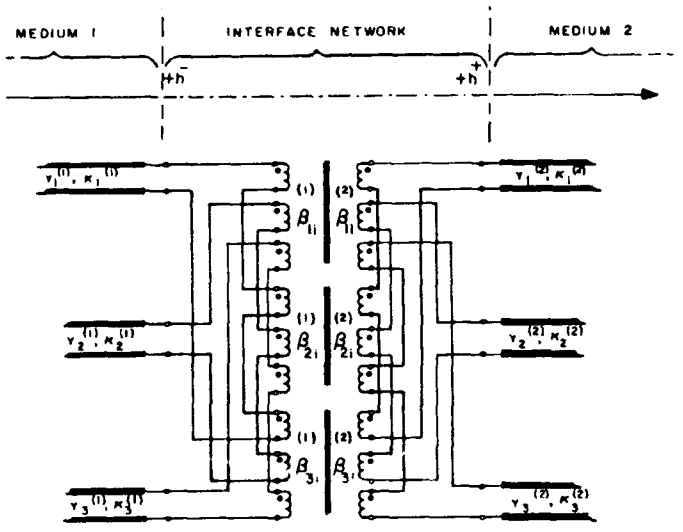


Figure 2. Exact network analog of thickness modes excited by a thickness directed electric field in a piezoelectric plate with arbitrary mechanical boundary loadings.



igure 3. Exact representation of mechanical coupling at the interface of two anisotropic media with plane acoustic wave propagation normal to the boundary. Piezoelectric drive transformers are omitted for clarity.

interconnections. The equivalent circuit model is able to accommodate arbitrary materials for transducers, electrodes, and ground planes as well as the various methods for attaching such.

Materials Considerations

The stacked acoustic filter is composed of three general components, namely the piezoelectric transducers, the groung plane, and the bonding agents joining these two. The material properties of importance differ slightly for each component type. The important properties can be summarized as follows:

Piezoelectric Transducers

The maximum achievable bandwidth, electroacoustic efficiency, and power handling capability of the piezoelectric transducers is directly proportional to the piezoelectric coupling factor of the transducer material. This consideration leads to the use of high coupling lead-zirconate-titanate (PZT) piezoelectric ceramic for the transducer material, for which transducer structures with electroacoustic efficiency exceeding 90% have been reported.

Ground Plane

The ground plane must provide a good electrical ground and at the same time not impede the propagation of the acoustic wave. The quality of the electrical ground depends on the conductivity of the material, while the wave propagation depends on the material density, wave velocity, and acoustic attenuation.

Bonding Agents

The primary requirement for the bonding agent is obviously good adhesion between the bonded layers. However, beyond this purely

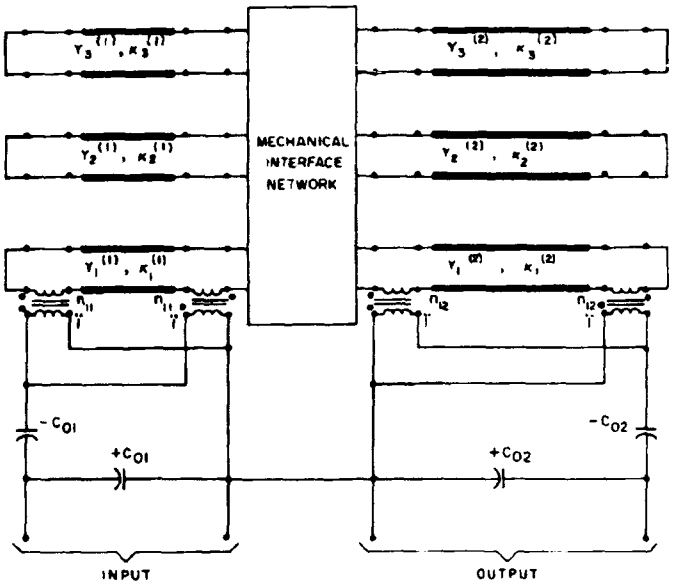


Figure 4. Exact analog representation of a two-layer stack where one thickness mode in each layer is piezoelectrically driven by a thickness directed electric field.

mechanical consideration, the acoustic behavior of the bonding agent is critical to obtaining efficient acoustic wave propagation.

Filter Fabrication

The fabrication of the stacked acoustic filter is in general a simple procedure, although a few pitfalls have been discovered through experimentation. Early attempts at fabricating the stacked acoustic filters with "off-the-shelf" components succeeded in demonstrating acoustic power transmission, but with unacceptably high insertion loss. These filters were made with various combinations of ground plane material and thickness, PZT type, and adhesive type. The fabrication procedure entailed cleaning the components, screen printing adhesive onto the ground plane, clamping the PZT plates to the ground plane, curing the adhesive, and attaching electrical leads.

Several different formulations of various adhesive types were experimented with initially; a Cu-epoxy, Ag-epoxy, and indium paste were chosen for further experimentation based on the preliminary results. The various adhesives used in this experiment have somewhat different physical properties which result in a number of fabrication-related differences. First, the Cu-epoxy is difficult to screen print due to its high viscosity. As a result, the Cu-epoxy cures into an adhesive layer that is not only thicker than that of the silver and indium adhesives but possesses voids and air gaps between the PZT plate and the ground plane. Second, the indium paste screen prints well but due to the solder-like nature of the paste, reflowing procedures produce voids and gaps in the adhesive layer. The voids and gaps are probably caused by flux entrapped between the PZT and the ground plane. Third, the Ag-epoxy exhibits excellent screen printability and flows laterally when clamped and cured. This results in a very thin and uniform adhesive layer. In fact, it should be noted that the Ag-epoxy occasionally flowed to such an extent that it contacted the top electrode on the PZT, forming an electrical short-circuit. A resistor-trimming laser was used to correct such conditions with no noticeable damage being done to the filter structure.

As a measure of the uniformity of the indium and Ag-epoxy adhesive layers, the deviation between the surface normal of the ground plane and the surface normal of the PZT transducer was measured at each corner on several samples. The Ag-epoxy was found to produce slightly wedged bonding layers albeit with good planarity. The indium paste was found to produce bonding layers that are not only more highly wedged but distinctly non-planar. Ideally, the stacked structures being investigated here should have planar transducers which propagate plane-waves at normal incidence to the ground plane. As such, the measured wedging and non-planarity represent sources of acoustic loss in the structures as fabricated.

Based on the acoustic impedance and attenuation of epoxy compared to that of indium, the indium bond was expected to yield the lowest loss. However, void formation, wedging, and non-planarity of the indium bond resulted in unexpectedly poor performance of the indium bond.

Experimental Results

Analysis of the equivalent electrical circuit for longitudinal mode propagation in a three-layer stack with welded contact leads to the expectation that the passband transmission efficiency should be maximized when the ground plane thickness is an integer number of half-wavelengths thick [4]. This is readily seen from the equation describing the acoustic input impedance Z_{in} of the ground plane,

$$Z_{in} = Z_p \frac{Z_t + j\, Z_p \tan(kl)}{Z_p + j\, Z_t \tan(kl)}$$

wherein Z_p, k, and l are the acoustic impedance, propagation constant, and thickness of the ground plane and Z_t is the acoustic impedance of the output transducer. When the ground plane thickness is an integer multiple of half-wavelengths, the tangent factors are zero and Z_{in} is just Z_t. Thus the acoustic wave can propagate from the input transducer (also with acoustic impedance Z_t) to the output transducer with minimum reflection loss when this condition is met. This was verified experimentally, and insertion loss less than 1dB corresponding to a power transmission efficiency of 86% was demonstrated.

Two types of piezoceramic material were tested here representing "hard" and "soft" PZT. The difference which is of note here is the order-of-magnitude greater mechanical Q of the "hard" PZT as compared to the "soft" PZT. The mechanical Q is the ratio of energy stored to energy dissipated per vibrational cycle, and as such the higher Q material produced lower loss stacked filters.

The propagation of the acoustic wave through the stacked filter depends in part on the type of mode (longitudinal or shear) being used. In the filters being discussed here, only longitudinal modes are employed. Additional acoustic losses may arise as 1) part of the acoustic wave which is generated by the input transducer may "leak" laterally along the ground plane and thereby not arrive at the output transducer and 2) friction generated by the atmosphere ("air-loading") may dampen the acoustic wave. Lateral losses were examined by fabricating multiple stacked filters near each other on a single ground plane. No measurable cross-talk (lateral energy transfer) was observed. "Air-loading" was examined in a test fixture which had been modifed for connection to a vacuum pump. No changes in insertion loss were observed as the samples were tested at atmospheric pressure and under vacuum.

The ability of the stacked acoustic filter to transmit useful power loads on the order of several watts has been demonstrated through a series of RF power transmission tests. Starting from 1mW incident power, the test procedure involved applying RF power in successively higher levels until seriously

degraded performance was observed. Each power level was maintained at least two days to check for long term degradation. The prototype units performed well at power densities below 5 W/cm^2 of transducer area, whereas above this level the passband transmission efficiency decreased with increasing RF power. One unit was driven until failure, which occured at an incident power density of 16 W/cm^2 of transducer area. The failure mechanism has not been determined. Another unit is currently in the fourteenth month of continuous life testing at 5 W/cm^2 with no performance degradation.

Conclusion

Stacked acoustic filters exhibiting less than 1dB insertion loss corresponding to passband efficiencies as high as 86% have been demonstrated. The best results to date have been obtained with half-wavelength thick ground planes, Ag-epoxy adhesive, and high-Q ("hard") PZT transducers. Results indicate that further improvements can be achieved through a combination of lower-loss materials and more accurate fabrication. Filter structures developed here have demonstrated high RF power handling capability on the order of 5 W/cm^2 of transducer area.

APPENDIX - Relationship of Filter Bandwidth to Piezocoupling in Stacked Acoustic Filters

McSkimin [7] showed that fractional bandwidths for structures like the stacked crystal filter of about $\sqrt{(2/r)}$ can be achieved with virtually zero loss by coupling to a delay medium through a quarter- or half-wavelength mechanical transmission line. Thurston [8] investigated the further effects of terminating impedances on loss and bandwidth. The fractional bandwidth arising in [7] corresponds to the spacing of the equi-immittance points of the Butterworth-Van Dyke equivalent circuit [9] divided by the series resonance frequency. Using the notation of [9], it may be determined that $(f_g f_h)=f_s^2$ exactly, so that $\delta=(f_h-f_g)/\sqrt{(f_g f_h)} \equiv\sqrt{(2/r-1/Q^2)}$. Defining δ as the stacked crystal filter fractional bandwidth, and using the relation between capacitance ratio r and piezoelectric coupling factor k derived in [6], viz., $2/r=(4k/\pi)^2$, one obtains the percentage bandwidths given in Table 1. The quantity $E=Q^2/r$ is the figure of excellence.

For quartz cuts, k is approximately 10% or less. PZT and other piezoceramics have values of coupling factor that range from 30% to 70% in most instances. As a rough rule-of-thumb, one may use the value of k directly as the fractional bandwidth, except in those cases where $E=Q^2/r$ is of the order unity.

TABLE 1. FRACTIONAL BANDWIDTH, DELTA.

k(%)	δ (%)				
	E=1	3	10	30	∞
10	9.0	11.6	12.4	12.6	12.7
30	27.0	34.9	37.2	37.9	38.2
50	45.0	58.1	62.1	63.1	63.7
70	63.0	81.4	86.9	88.4	89.1
90	91.0	104.6	111.7	113.6	114.6

References

[1] A. Ballato, H. L. Bertoni, and T. Tamir, "Systematic Network Approach for Piezoelectrically Driven Crystal Plates and Stacks," presented at the 1972 IEEE Ultrasonics Symposium, Boston, MA, 4-7 October 1972; abstract in IEEE Transactions on Sonics and Ultrasonics, Vol. SU-20, No. 1, p. 43, January 1973.

[2] A. Ballato and T. Lukaszek, "A Novel Frequency Selective Device: The Stacked-Crystal Filter," in Proceedings of the 27th Annual Symposium on Frequency Control, May 1973, pp. 262-269.

[3] A. Ballato and T. Lukaszek, "Stacked-Crystal Filters," Proceedings of the IEEE (Letters), Vol. 61, No. 10, pp. 1495-1496, October 1973.

[4] A. Ballato, "The Stacked-Crystal Filter," in Proceedings of the 1975 IEEE International Symposium on Circuits and Systems, April 1975, pp. 301-304.

[5] A. Ballato, H. L. Bertoni, and T. Tamir, "Systematic Design of Stacked-Crystal Filters by Microwave Network Methods," IEEE Transactions on Microwave Theory and Techniques, Vol. MTT-22, No. 1, pp. 14-25, January 1974.

[6] A. Ballato, "Transmission-Line Analogs for Piezoelectric Layered Structures," Ph.D. Dissertation, Polytechnic Institute of Brooklyn, Brooklyn, NY, June 1972, 245 pp.

[7] H. J. McSkimin, "Transducer Design for Ultrasonic Delay Lines," Journal of the Acoustic Society of America, Vol. 27, No. 2, pp. 302-309, March 1955.

[8] R. N. Thurston, "Effect of Electrical and Mechanical Terminating Resistances on Loss and Bandwidth According to the Conventional Equivalent of a Piezoelectric Transducer," in the IRE National Convention Record, Part 6, March 1959, pp. 260-278; also IRE Transactions on Ultrasonic Engineering, Vol. UE-7, No. 1, pp. 16-25, February 1960.

[9] A. Ballato, "Resonance in Piezoelectric Vibrators," Proceedings of the IEEE, Vol. 58, No. 1, pp. 149-151, January 1970.

Thin Films: Processing

REACTIVE COEVAPORATION SYNTHESIS AND CHARACTERIZATION OF $SrTiO_3$ - $BaTiO_3$ THIN FILMS

Hironu Yamaguchi, Shogo Matsubara, Koichi Takemura and Yoichi Miyasaka
Fundamental Research Laboratories, NEC Corporation,
4-1 1 Miyazaki, Kawasaki 216 Japan.

Abstract

$(Ba_xSr_{1-x})TiO_3$ thin films were prepared by reactive coevaporation on Pd-coated sapphire substrates. Ba and Sr metals were evaporated by K-cells and Ti metal was evaporated by an E-gun. The films of 80 to 90 nm thickness were deposited at 500°C and were crystallized in perovskite phase for the whole Ba content (x) range. The leakage current density of as-deposited films was fairly large and could be reduced by rapid thermal annealing. ε_r decreased with increasing the (Ba+Sr)/Ti atomic ratio. The leakage current characteristics were improved with increasing the (Ba+Sr)/Ti atomic ratio.

Introduction

In recent years, the interest in ferroelectric thin films has grown rapidly because of their possible application as capacitor dielectrics in memory cells of both nonvolatile memories and dynamic random access memories (DRAMs)[1,2]. Strontium titanate and $(Ba,Sr)TiO_3$ are promising materials for DRAM application because of their high dielectric constant (ε_r) and chemical stability. Many deposition techniques such as rf-sputtering[3 - 6], ion beam sputtering (IBS)[7,8], metal-organic chemical vapor deposition (MOCVD)[9] and liquid source chemical vapor deposition (LSCVD)[10] have been investigated to prepare $SrTiO_3$ and $(Ba,Sr)TiO_3$ thin films.

Reactive coevaporation using metal sources is expected to present advantages such as flexible composition control, preparation under high vacuum and plasma free deposition environment. The authors have previously reported on reactive coevaporation synthesis of $SrTiO_3$ thin films[11]. ε_r value of 170 was obtained for 75 nm thick films.

In this paper, preparation of $(Ba,Sr)TiO_3$ thin films by reactive coevaporation and the film structure and electrical properties are described.

Experimental

A schematic diagram of reactive coevaporation system is shown in Figure 1. The apparatus consists of a source chamber and a deposition chamber, which are separated by a gate valve and are independently evacuated by a diffusion pump and a turbo molecular pump, respectively. Two Knudsen cell (K-cell) are used to evaporate Ba and Sr metal sources and an electron beam gun (E-gun) is used to evaporate Ti metal source. During deposition, the pressure in the source chamber is lower by one order of magnitude than in the deposition chamber. This pressure difference is attained not only by the aforementioned differential pumping system but also by the gettering effect of active Ti, Sr and Ba atoms. Consequently, the E-gun works steadily and the source metals are hardly oxidized. The evaporation rates of each source are measured independently with three quartz crystal monitors, one for each sources, located above the sources. Single-crystal R-plane Sapphire (α -$Al_2O_3(10\bar{1}2)$) coated with a Pd(500 nm) bottom electrode layer was used as the substrate.

After the chambers were pumped down to less than $1x10^{-7}$Torr, oxygen gas was introduced toward the substrate through a stainless steel tube. In order to oxidize the films sufficiently during deposition, as much oxygen gas as

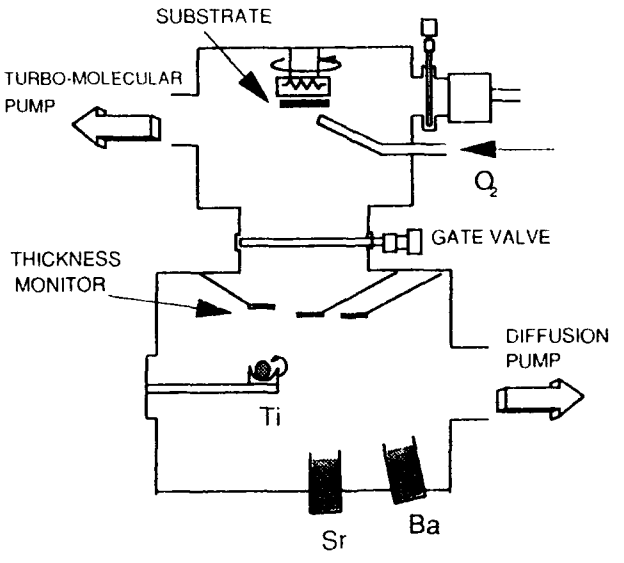


Fig. 1. Schematic diagram of the reactive coevaporation system.

CH3080-0-7803-0465-9/92$3.00 ©IEEE

possible should be introduced. When the pressure was higher than $2x10^{-5}$ Torr, however, the deposition rate decreased rapidly and it was difficult to evaporate source metals steadily at higher oxygen pressure. Therefore, the appropriate oxygen gas pressure in the deposition chamber during deposition was determined to be $2x10^{-5}$ Torr. The deposition temperature was 500 °C. The temperature of the K-cells was varied from 320 to 380 °C for Sr and from 420 to 500 °C for Ba, respectively. In a previous paper on $SrTiO_3$[11], the authors reported that the evaporation rate of Sr gradually decreased with time even when the K-cell temperature was kept constant. After 30 minute deposition, the evaporation rate of Sr became 10% lower than the initial rate. It was found that uniform composition depth profile could be obtained by controlling the Ti evaporation rate according to the Sr evaporation rate change. In this study, evaporation rate of Ba also decreased with time. The decreasing rate of Sr and Ba were almost same. Therefore, the same composition control technique, which is the control of Ti evaporation rate according to the Sr and Ba evaporation rate change, was used. Experiment was performed with thickness in the range of 80 to 90 nm. $(Ba,Sr)TiO_3$ deposition rate was estimated to be 2.5 - 4.5 nm/min by measuring the film thickness with a surface profiler (DEKTAK-3030). Electrical properties were measured on a Au(300 nm)/Ti(50 nm)/$(Ba,Sr)TiO_3$/Pd(500 nm)/R-sapphire capacitor structure. Capacitance and tanδ were measured in the 100 Hz to 10 MHz frequency range with a Hewlett-Packard 4194A impedance analyzer. Saying precisely, ε_r which will be discussed hereafter were calculated from the capacitance at 10 kHz, although no notable frequency dispersion was observed within the measurement range. Leakage current was measured with a Keithley 617 electrometer/source. Crystal structure was studied by X-ray diffraction (XRD), and film composition was measured by inductively coupled plasma spectrometry (ICP).

Results and Discussion

The XRD patterns of $(Ba_xSr_{1-x})TiO_3$ thin films (x= 0 1.0) are shown in Figure 2. Perovskite crystal structure was obtained in the whole Ba content (x) range. It was cubic perovskite structure even in the $0.7 \leqq x \leqq 1.0$ range, where bulk $(Ba_xSr_{1-x})TiO_3$ is known to be tetragonal. The (110) peak intensity decreased and the (100) intensity increased with increasing the Ba content (x). Lattice constant of the films, which were calculated from the (110) peak location are shown in Figure 3 along with the well-known data on bulk[12]. The lattice constant of the films increased with increasing the Ba content (x).

As-deposited films showed the large leakage current, and therefore rapid thermal annealing (RTA) was carried out after deposition. The RTA temperature was varied from 500 to 700 °C, and the RTA time was varied from 1 to 4 minutes.

ε_r of $(Ba_xSr_{1-x})TiO_3$ films, which were annealed by RTA at 600°C for 1 minute, depended on the Ba content (x). The value of ε_r was approximately 450 in the range of

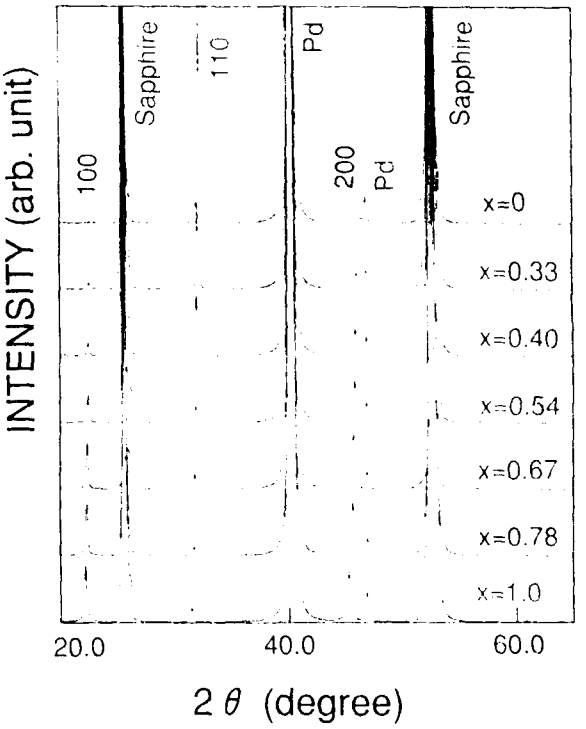


Fig. 2. XRD patterns of $(Ba_xSr_{1-x})TiO_3$ thin films (x= 0 to 1.0) deposited at 500°C.

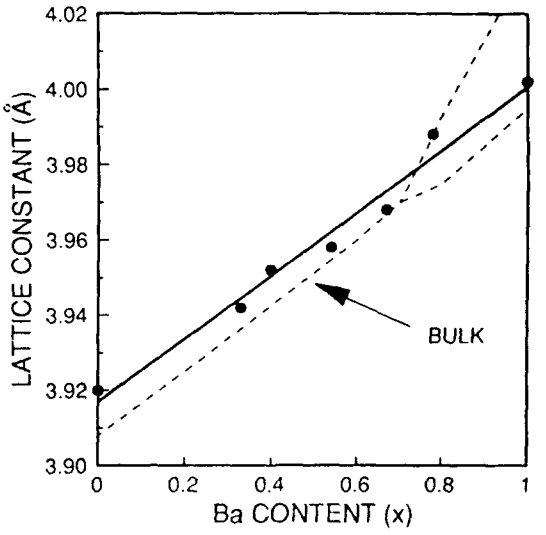


Fig. 3. Lattice constants of $(Ba_xSr_{1-x})TiO_3$ thin films (solid line), and of $(Ba_xSr_{1-x})TiO_3$ bulk (broken line). The values for thin films were calculated from the (110) peak.

$0.3<x<0.7$, and 170 for x=0 ($SrTiO_3$), and 208 for x=1 ($BaTiO_3$). This Ba content(x) dependence of ε_r was similar to that for rf-magnetron sputtering and IBS[6,8].

ε_r for $(Ba_{0.5}Sr_{0.5})TiO_3$ films, which were annealed by RTA for 2 minutes, was slightly lower than that annealed for 1 minute, as shown in Figure 4. When the annealing time was longer than 3 minutes, films were extremely conductive and their surface became rough. This result shows that the RTA time should be lower than 2 minutes. The RTA temperature dependence of ε_r is shown in Figure 5. The RTA time was 2 minutes. ε_r did not depend on the RTA temperature.

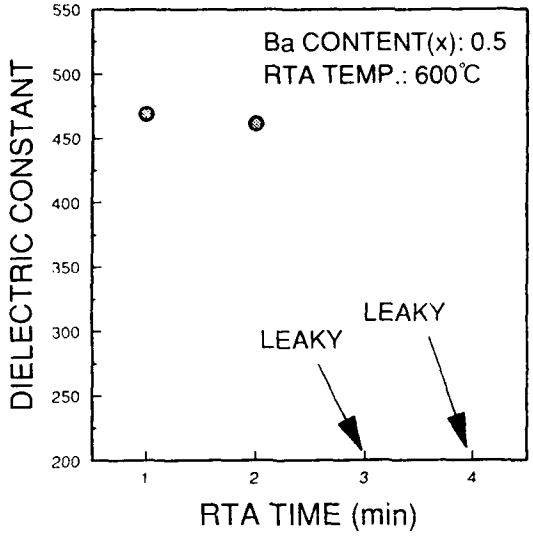


Fig. 4. RTA time dependence of ε_r for $(Ba_{0.5}Sr_{0.5})TiO_3$ films annealed at 600°C.

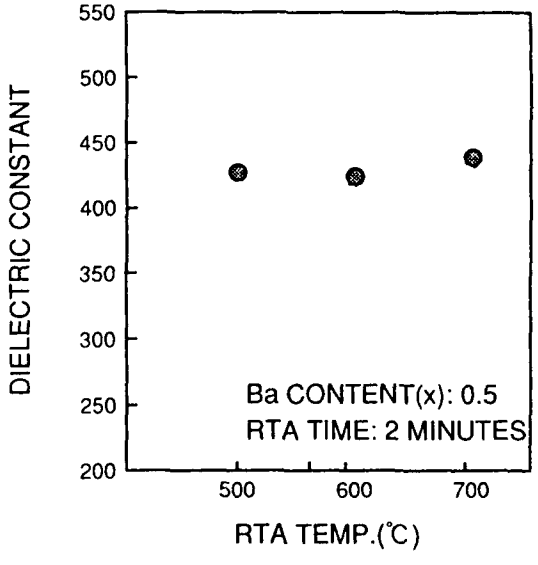


Fig. 5. RTA temperature dependence of ε_r for $(Ba_{0.5}Sr_{0.5})TiO_3$ films.

Figure 6 shows the (Ba+Sr)/Ti atomic ratio (y) dependence of ε_r for as-deposited and annealed films with Ba content (x) of 0.5. ε_r decreased with increasing y. As-deposited films with $y \leq 1.02$ were highly conductive and ε_r could not be measured. On as-deposited films with $y>1.02$, ε_r could be measured, but the leakage current was fairly large. No difference could be observed on the XRD patterns for the films presented in Figure 6. The leakage current density could be reduced by RTA treatment as shown in Figure 7. Thus, RTA was effective to improve the leakage current density.

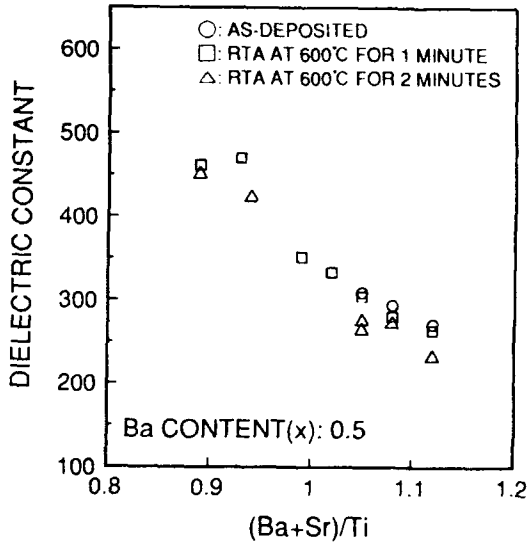


Fig. 6. (Ba+Sr)/Ti atomic ratio dependence of ε_r for $(Ba_{0.5}Sr_{0.5})TiO_3$ thin films.

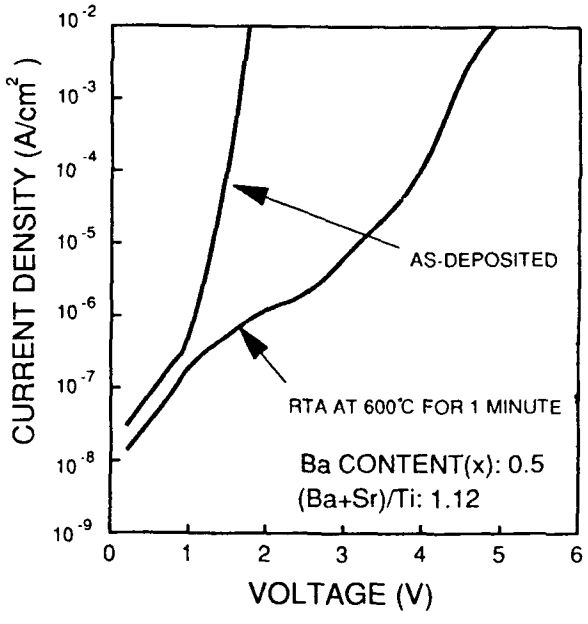


Fig. 7. Leakage current characteristics of as-deposited and annealed films at 600°C for 1 minute.

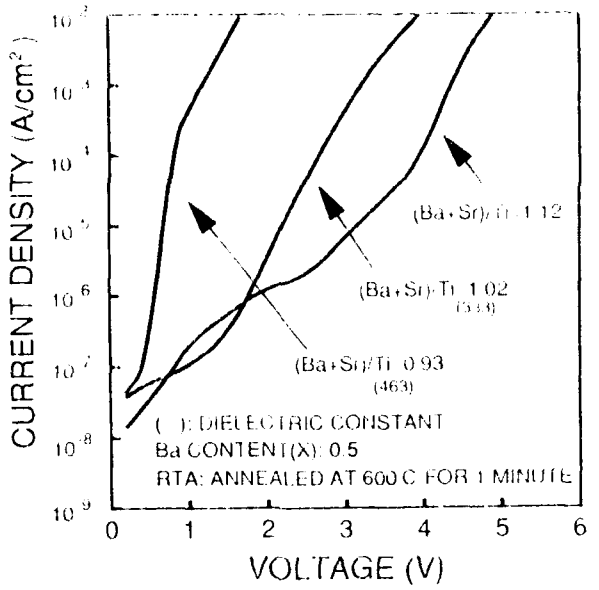


Fig. 8. Leakage current characteristics for various (Ba+Sr)/Ti atomic ratios. The films were annealed by RTA at 600 C for 1 minute.

The leakage current characteristics, after RTA treatment for 1 minute, of $(Ba_{0.5}Sr_{0.5})TiO_3$ films with y=0.93, 1.02 and 1.12 are shown in Figure 8. The leakage current characteristics were improved with increasing the (Ba+Sr)/Ti atomic ratio.

Conclusion

$(Ba_xSr_{1-x})TiO_3$ films (x= 0 to 1.0) were synthesized by reactive coevaporation at 500 C. Films were crystallized in the perovskite phase in the whole Ba content (x) range. As deposited films were leaky. RTA treatment for 1 or 2 minutes reduced the leakage current density. ε decreased with increasing the (Ba+Sr)/Ti atomic ratio. The leakage current characteristics were improved with increasing the (Ba+Sr)/Ti atomic ratio.

Acknowledgment

The authors would like to thank Dr. H. Rang and Dr. N. Shohata for their encouragement and support in this study. Thanks are also due to Dr. S. Yoshida, T. Sakuma, S. Yamamichi, Dr. P.Y. Lesaicherre, T. Hase, H. Yabuta, N. Tawarayama and A. Nakai for their useful discussion and assistance.

References

1) E. H. Parker and A. F. Tasch ," Ferroelectric materials for 64 Mb and 256 Mb DRAMs," IEEE Circuits and Devices Magazine, pp. 17-26, January 1990.

2) C. A. Paz de Araujo, J. D. McMillan, B. M. Melnick, J. D. Cuchiaro and J. F. Scott, "Ferroelectric Memories," Ferroelectrics, vol. 104, pp. 241-256, 1990.

3) W. P. Pennebaker, "RF sputtered strontium titanate films," IBM J. Res. Develop., pp. 695-698, November 1969.

4) S. Matsubara, T. Sakuma, S. Yamamichi, H. Yamaguchi and Y. Miyasaka, "Interface Structure and Dielectric Properties of $SrTiO_3$ Thin Films Sputter Deposited onto Si Substrates," in the Proceedings of the MRS spring meeting, 1990, pp. 243-253.

5) T. Sakuma, S. Yamamichi, S. Matsubara, H. Yamaguchi and Y. Miyasaka, "Preparation of $SrTiO_3$ Thin Film Capacitor with Barrier Layer on Silicon for DRAMs," Appl. Phys. Lett., vol. 57, pp. 2431-2433, 1990.

6) Y. Miyasaka and S. Matsubara, "Dielectric Properties of Sputter-Deposited $BaTiO_3$-$SrTiO_3$ Thin Films," in the Proceedings of the 2th ISAF, 1990, pp. 121-124.

7) S. Yamamichi, T. Sakuma, T. Takemura and Y. Miyasaka, "$SrTiO_3$ Thin Film Preparation by Ion Beam Sputtering and Its Dielectric Properties," Jpn. J. Appl. Phys., vol. 30, B, pp. 2193-2295, September 1991.

8) S. Yamamichi, T. Sakuma, T. Hase and Y. Miyasaka, "$SrTiO_3$ and $(Ba,Sr)TiO_3$ Thin Films Preparation by Ion Beam Sputtering and Their Dielectric Properties," presented at the 1991 MRS Fall Meeting, Symposium I, Boston, MA, December 2-6, 1991.

9) P. C. Van Buskirk, R. Gardiner, P. S. Kirlin and S. B. Krupanidhi, "Plasma Enhanced MOCVD of $(Ba_xSr_{1-x})TiO_3$ Films," presented at 4th ISIF, Monterey, CA, March 9-11, 1992.

10) L. C. McMillan, T. L. Roberts, M. C. Scott and C. A. Paz de Araujo, "Deposition of $(Ba_xSr_{1-x})TiO_3$ and $SrTiO_3$ Via Liquid Source CVD (LSCVD) for ULSI DRAMs," presented at the 4th ISIF, Monterey, CA, March 9-11, 1992.

11) H. Yamaguchi, S. Matsubara and Y. Miyasaka, "Reactive Coevaporaton Synthesis and Characterization of $SrTiO_3$ Thin Films," Jpn. J. Appl. Phys. vol. 30, B, pp. 2197-2199, September 1991.

12) K. H. Hellwege and A. M. Hellwege (Ed.), Landolt Bornstein Numerical Data and Functional Relationships in Science and Technology, New Series vol. 16, New York: Springer-Verlag, 1981, pp. 416.

SOL GEL PROCESSING OF THICK PZT FILMS

Guanghua Yi and Michael Sayer
Department of Physics, Queen's University
Kingston, Ontario, Canada K7L 3N6

Techniques are described for the sol-gel fabrication of ferroelectric PZT films on different substrates up to 1.5 μm in thickness by a single coating and up to 8 μm by multiple coating. The objectives of additives to control drying and firing will be reviewed. A mechanical model is presented which guides the development of such films.

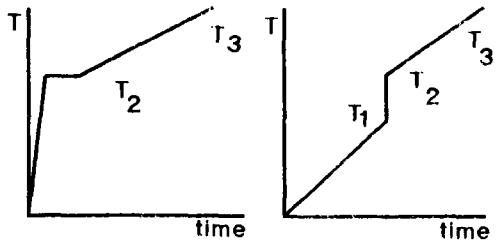
Introduction

The metallorganic processing of thin films of piezoelectrics such as PZT involves the drying and firing of a metallorganic gel coated on a surface, followed by a high temperature anneal to crystallize the film [1]. Sol gel processes based on alcohol [2] and water [3] based solvents respectively and metallorganic decomposition methods for PZT [4,5] have become widely established. During this process, approximately 70 wt% of the starting materials are evaporated or calcined away, and the final ceramic film has to adjust at least to a thermal cycle in which the substrate is cooled from the crystallisation temperature to ambient.

The purpose of this paper is to establish guidelines and procedures to optimise the fabrication of PZT films >1 μm in thickness on specific substrates. In practice, this concerns whether a single or multiple coating technique is used, what is the best temperature schedule for firing, and what is the value of additives in controlling the drying and firing of the film. In principle, the analysis does not directly depend on the details of the specific metallorganic process employed.

Sol Gel Fabrication Procedures

After formation of a gel film on a substrate, commonly used firing schedules are shown in Figure 1.



(a) (b)

Figure 1: Firing schedules for sol gel films
(a) thin films (<0.3μm)
(b) thick films (>1μm)

If the film is thin (of final thickness <0.4μm) it is often placed directly on a surface heated to T_2 = 400°C until carbonisation and oxidation has occured, and is then annealed at a higher temperature. The firing schedule is as shown in Fig.1(a). For films of thickness in the micron range, the firing schedule shown in Figure 1(b) is preferable. The film is initially dried slowly to about T_1 = 285°C, then rapidly fired to T_2 = 400°C, followed by a final anneal at a temperature T_3 from 450°C to 650°C depending on the material and the substrate. T_1 = 285°C corresponds to the decomposition temperature of lead acetate, a key ingredient of most sol gel solutions for PZT, while at T_2 = 400°C most organic components of the film will pyrolyse and oxidise leaving an amorphous inorganic layer. A rapid temperature rise between T_1 and T_2 is generally of value and carrying out part of the process in a partial vacuum can be of use. The phenomena which occur during these stages are shown in Figure 2.

Network Generation		Carbonisation Oxidation		Crystallisation Annealing
20°C	285°C		400°C	650°C
Solvent Evaporation		Byproduct removal		
liquid	wet gel	gel	amorphous	crystal

Figure 2: Stages of processing a sol gel film

Stresses which lead to cracking of the film may occur during (i) drying, (ii) firing, (iii) annealing and crystallisation, and (iv) on cool down. It is found that the most critical time is often in the later stages of steps (i) and (ii). It will be shown that the microscopic phenomena which occur during drying and firing are comparable and lead to a tensile stress in the film. A model based on elasticity is shown to provide guidance for the development of crack-free films.

Drying of a Gel Film $T \rightarrow T_1$

During drying gel films are constrained by the substrate. In order to avoid cracking, an understanding is required of the interaction between the film and the substrate, between the solid network and the liquid, liquid transport, the forces imposed on the solid network, and the fracture mechanism of gel films during drying. It is assumed that on its formation, the solid network bonds strongly to the substrate and has its own internal rigidity and mechanical properties.

Although the solution commences at atmospheric pressure, as the solution gels, due to chemical and osmotic effects the pressure of the liquid within the solid network becomes much higher than the pressure in the liquid layer that covers the surface of the gel [6]. As the solid network forms it is therefore stretched and expanded due to the high pressure of the liquid.

The microscopic stages of drying a gel are illustrated schematically in Figures 3(a)-3(d) [1]. Initially the surface is covered with a layer of liquid as shown in Figure 3(a). This surface is shown as a reference in subsequent diagrams. The initial polymeric network is highly stretched and expanded by the liquid. As the liquid phase in the gel is removed, if it is not constrained the network will spontaneously shrink to release this tensile stress.

The liquid evaporates from the surface of the gel during drying - Figure 3(b). Since the liquid in a gel usually shows a very high affinity to the solid network, the liquid wets the solid network and tends to cover all the gel surface. Therefore, liquid flows from the interior of the gel to compensate for liquid evaporated from the surface. A pressure gradient is developed within the liquid due to this flow. The solid network in the surface region, where the pressure of the liquid is reduced, tends to shrink as a result. However, the region is also constrained by the interior part of the gel where the pressure of the liquid is not reduced, or where forces may be introduced by the substrate. Therefore, the solid network in the surface region shrinks primarily in the direction normal to the surface of the gel with a tensile stress remaining parallel to the surface.

CH3080-0-7803-0465-9/92$3.00 ©IEEE

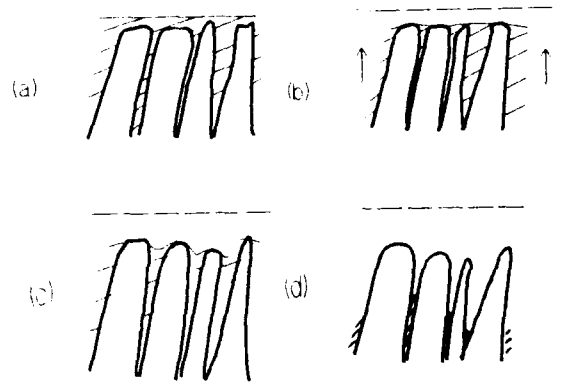


Figure 3: Stages in drying of a gel
(a) Wet film (b) meniscus beginning to penetrate the network (c) outer layer shrinkage taking place (d) flaws developing from large size pores.

The vapor/liquid interface now starts to move into the solid network, menisci are formed in the pores as shown in Figure 3(c), and these menisci begin to move into the interior of the gel. A capillary force will be imposed on the solid network which will further cause the network to shrink as the liquid evaporates. The menisci in the bigger pores have a greater radii of curvature so that the liquid in the larger pores has greater vapor pressure and therefore evaporates faster. If the bigger pores are connected with the smaller ones, the liquid in the bigger pores will also flow to the smaller pores since the liquid in the smaller pores is subject to a greater capillary action. Therefore, the menisci in the bigger pores recede farther into the body so that the bigger pores dry much faster as shown in Figure 3(d). As the gel shrinks, its stiffness increases because the solid network is more tightly bound and further crosslinking takes place. When the gel is too stiff to contract under the capillary force, shrinkage stops. The vapor/liquid interface then moves completely into the solid network and some bigger pores dry fully. Since the interior walls of these pores are not subject to capillary force, while the smaller pores around the bigger pores may still be filled with liquid this causes a stress concentration at the bottom of the bigger pores. The dry, larger pores therefore act as microscopic flaws and propagate under the tensile stress to form cracks.

This mechanism explains why cracks generally appear just when the shrinkage of the gel stops and the vapor/liquid interface moves into the network solid phase, and why gels with different pore sizes have a greater tendency to crack during drying. The critical phenomenon is the increase of the stiffness of the network as it enters its later stages of development. If the drying rate is high, the pressure gradient between the surface and the substrate developed by the evaporation of the liquid is greater and cracks are also more likely to occur. This is not consistent with observation for thin films, and other effects must compensate.

Firing of Dried Films $T_1 \rightarrow T_2$

As the temperature increases, densification, pyrolysis and oxidation of the film takes place. For a water/acetate based PZT film [3], thermogravimetric measurements and studies of the gas species emitted by the film at given temperatures are shown in Table 1. Significant weight losses occurred at 250°C and at 450°C.

Temperature °C	Gas species
56	water, alcohols
73	water, alcohols, acetic acid
87	water, acetic acid, alcohols
121	acetic acid, trace water
175	acetic acid, water
255	acetic acid, water
299	acetic acid, CO_2
368	CO_2, trace acetic acid
450	CO_2, trace CO
558	CO_2
754	trace CO_2

Table 1: Thermogravimetric data for acetic acid/water based sol gel as a function of firing temperature.

The first materials driven off at about 80°C are water, alcohols and acetic acid which are the main components of the gel liquid. Acetic acid was evolved between 73°C to 368°C. A weight loss occurred just below 300°C which can be assigned to the decomposition of lead acetate. Carbon dioxide was initially evolved at a sample temperature of 299°C, a substantial emission occurred at 450°C, and trace carbon dioxide was evolved even at 750°C. This suggests that carbonaceous material can be trapped within the film material.

Thus, substantial amounts of material have to be lost from the film by controlled diffusion over a wide range of temperature. This release will reflect the bonding of the organic species to the inorganic components of the gel. For example, acetic acid is evolved from the coating in different temperature regions. The acetic acid vaporized in the temperature region from 70°C to 120°C is free in the solution. As water is lost, more acetate groups are bonded to titanium and zirconium ions. The bonded acetate groups are driven off around 175°C. For thin films, diffusion is not the limiting factor and desorption is important. However, for thick films, the rate at which components move is critical. Processing in a reduced partial pressure of oxygen can first remove the maximum amount of volatile solvents, and then provide additional control over the way the diffusion constant for various species in the film change during processing.

In the range of temperature from 220°C to 260°C, gel films crack readily. As the volatile components vaporize, the films must shrink. However, because it is constrained by the substrate and by internal parts of the network, the surface cannot shrink freely and internal tensile stresses will be created. If these cannot be relaxed the film will crack when the internal tensile stress achieves a critical value.

An intrinsic stress relief mechanism is inherent to PZT processing. When the gel films are heated to T_1=285°C, lead acetate melts and starts to decompose to the more stable lead carbonate. The amount of acetic acid driven off increases drastically, carbon dioxide is evolved, and network movement takes place. However, part of the shrinkage which takes place arises from continued condensation reactions such as

$$M\text{-}OH + HO\text{-}M > M\text{-}O\text{-}M + H_2O$$

which lead to densification of the solid network. If this occurs in a non-uniform manner, and particularly in the surface regions the diffusion constant for organic products from the interior may be reduced and residues can become trapped leading to subsequent pitting or crack propagation in subsequent thermal cycles. Defects arising from this source are shown in Figure 5. Similarly densification of the surface regions can give rise to tensile stresses relative to the substrate.

Since most stress relaxation processes are thermally activated, the stress relaxation time of the films can be decreased markedly by increasing the temperature. It is advantageous to heat the film to the temperature of T_2 as rapidly as possible. The stress relaxation time is drastically reduced and high internal tensile stress cannot develop. Therefore, a rapid temperature transition from T_1 to T_2 is of qualitative importance in the preparation of crack-free films.

There is a quantitative comparison between both drying and firing in that tensile stress arises in a film bonded to a rigid substrate. In order to examine the parameters of this system, a macroscopic model for crack propagation based on linear elasticity theory has been developed based on Figure 4.

Linear Elastic Model for a Sol Gel Film

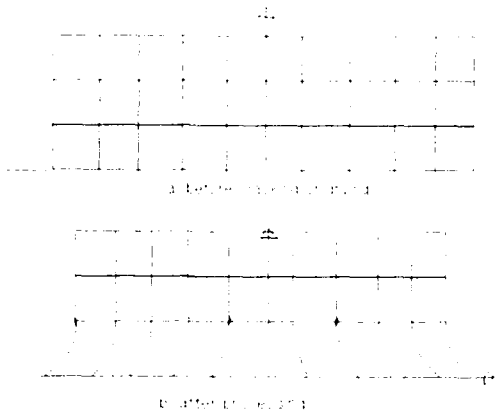


Figure 4: Dried or fired film constrained by a substrate (a) prior to processing (b) after processing.

The substrate is assumed to be a rigid, semi-infinite body and the bonded film is assumed to be thin and isotropic and have a constant thickness. The elastic constants can be clearly defined for fired films and for the later stages of drying gel coatings. As a result of shrinkage due either to a process of drying or of firing, a homogeneous tensile stress is generated in the film. In the case of gel drying, the magnitude of the tensile stress will be approximately equal to that of the pressure of the liquid on the wet gel film. According to the Griffith criterion for crack propagation, a microcrack will propagate if the decrease in elastic strain energy resulting from the propagation of the crack is greater than the increase in surface energy due to the increase in the surface area of the crack [7]. This implies that a critical thickness exists. The elastic energy released by cracking a film which is thinner than the critical thickness cannot compensate for the surface energy created by the formation of the crack. Therefore, the cracking of the film is not a thermodynamically favorable process and the film can be dried or fired without cracking. If the thickness is larger than the critical thickness, this is not the case and it is thermodynamically favourable for cracking to take place.

In the case where no effects of thermal expansion of a substrate were included, the stress distribution in a film segment between two long and parallel cracks and the elastic energy released by the film segment after the formation of the cracks was calculated. When cracks form, the film in the region near the crack is deformed and the stress distribution in this region will change. If a tensile stress σ, which is exactly equal to the tensile stress of the film before cracking, is imagined and applied normally to the crack surfaces, it will bring the film segment back to its original form and stress state. After appropriate calculations, it can be shown that the critical thickness T is given by [8]

$$T = 0.83 \frac{\Gamma E}{\sigma^2 (1+\nu)\sqrt{1-\nu}}$$

The critical thickness is directly proportional to Young's modulus E and the surface energy per unit area Γ of the film, and is inversely proportional to σ^2 the square of the internal tensile stress of the film. ν is Poisson's Ratio.

This expression was checked for alumina. Since all the data for sintered alumina could easily be obtained, a comparison of strength between the film and bulk material of sintered alumina was made. Published data for sintered alumina gives the critical thickness T = 0.5 μm, the Young's modulus E = 3.65×10^{12} dynes/cm^2, the surface energy per unit area Γ = 1000 ergs/cm^2 and the Poisson ratio ν = 0.25 [9]. The calculated strength of a sintered alumina film with critical thickness on a rigid substrate with critical thickness was σ_c = 750 kg/mm^2. This value is more than double the strength of bulk sintered alumina. This is as expected since a film bonded on a rigid substrate would show a much higher strength than the bulk material due to the interaction between the film and the substrate.

Qualitative features of this model suggest that during firing, the dimensions of the substrate should be as large as possible before gel shrinkage takes place. When the substrate is cooled, thermal contraction may then place the film into compression. The firing method and temperature schedule should reflect these requirements. This is consistent with the experimental observation of the suprising effectiveness of hot plate heating of sol gel samples, where the substrate is heated before the film, and of rapid thermal annealing of silicon where the absorption of heat occurs within the silicon wafer.

Application to PZT

The incentive for this model was the observation that a gel film can be dried on a substrate, but only if the thickness of the film is less than a critical thickness. This shown in Figure 5. The critical thickness is less than 1 μm for ordinary PZT gel films. It was also observed that the cracks in a gel film stop at the edges where the thickness of the film is reduced.

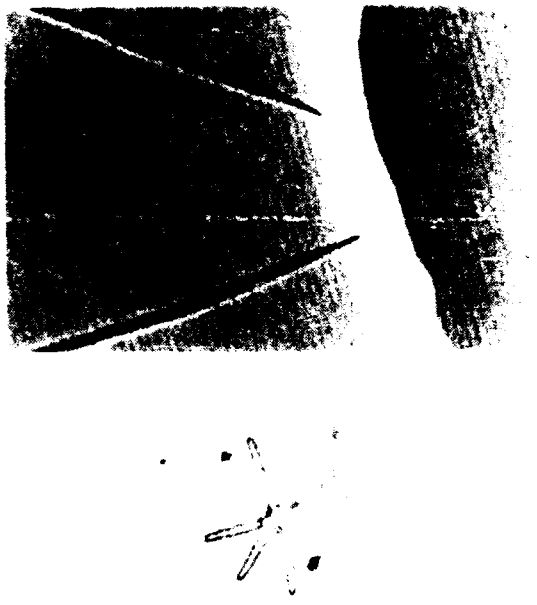


Figure 5: Micrographs of crack propagation in dried PZT gel films (a) Films of varying thickness (b) stress cracks due to included organics

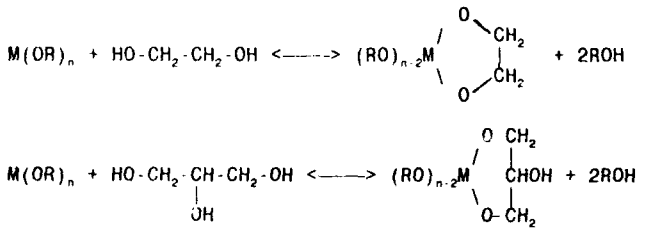
According to the analysis above, the cracking of a gel film on a rigid substrate depends on the Young's modulus, the specific surface energy and the internal tensile stress of the gel film. Qualitative judgements may be made with respect to PZT.

In both the dried and fired gels, the internal tensile stress has the most significant impact on the film and this should clearly be reduced to avoid cracking. This may be done by either chemical or physical means.

In the case of drying, since the internal tensile stress of the gel film is produced by the high pressure of the liquid in the gel, the probability of cracking can be reduced by decreasing this pressure. Chemically this can be achieved by reducing the affinity between the liquid and the solid network and increasing the pore size. Cracking is reduced by adding long chain alcohols or polyethylene glycol into the solution. A gel film formed with a solution containing long chain alcohol or polyethylene glycol is translucent after drying, indicating that the pore size is large. Both of the above compounds act as a poor solvent of the inorganic polymeric species in the solution. Therefore, the affinity between the liquid and the solid network is reduced and the structure of the gel film is coarsened. This reduces the force imposed on the solid network. and after drying, the gel film will have a lower internal tensile stress. However, since coarse structures will require higher firing temperatures and longer annealing times the microstructure and electrical properties can be degraded by this route.

Alternative agents such as ethylene glycol and glycerol can be used. Gel films prepared from solutions containing glycerol are transparent after drying, indicating that the pore size of the gel films is very small or that pores may be totally absent. Fired films prepared from these solutions are clear and transparent, indicating that the components of the films are homogeneously mixed. Such films prepared can be crystallized into the perovskite structure at temperatures as low as 450°.

The mechanism for the use of ethylene glycol and glycerol in precursor solutions for PZT films is still under study. They do not increase the viscosity of the solution, but may simply act as solvents in the presence of water. It was also observed that solutions containing ethylene glycol and glycerol gel at higher temperatures. Since the ethylene glycol and glycerol have more than one functional group, they also act as chelating agents to form chelated derivatives with metal complexes as shown



Since the chelated derivatives are more resistant to hydrolysis than their counterpart metal complexes, the formation of the chelated derivatives may be the reason why such solutions gel at higher temperatures.

Thermogravimetric studies show that the glycerol probably does not evaporate, but is retained in the solid network or in the pores of the gel films and acts as an organic plasticizer. High tensile stress cannot be built up in the gel film and the tendency of the film to crack during drying and firing is substantially reduced. Glycerol and other organics retained in the gel films can be carbonized and oxidized by a proper firing procedure. By this method, thick transparent PZT films up to 2 μm thick at one coating have been made. An example of such a film is shown in Figure 6(a).

The critical thickness is an important parameter which indicates whether multiple coatings are more effective than a search for large thickness single coatings. Figure 6(b) shows a 7.5 μm thick PZT film prepared as 5 successive coats. This thickness is below the critical thickness for PZT and no layering is detected within the body of the film.

The rate of crystallisation of films is affected by the substrates. For example, PZT films on aluminum can be fully crystallized at 500 C [10]. To achieve the same degree of crystallisation, PZT films on platinum, ITO or oxides such as RuO_2 have to be heated to 650°C. Epitaxial growth has also been achieved using sol gel processing. These effects are due to the probability of heterogeneous nucleation of crystals on a specific substrate. This can be illustrated by reference to aluminium. Since aluminum is very active, the surface of an aluminum substrate oxidizes in air to form a layer of alumina.



Figure 6: Scanning electron micrograph of cross-sections of PZT film.
(a) 1.5 μm thick prepared in a single coat.
(b) 7.5 μm thick prepared as 5 coats

The PZT nuclei formed on the aluminum substrate are stablized by contact with alumina. The critical radius of the nuclei is not changed, but the required number of atoms to form a nucleus is reduced and the probability of crystal embroyos achieving a critical radius is increased. Therefore, more nuclei are formed in films on aluminum than on platinum . Since the overall rate of growth of the crystalline phase depends also on the number of particles that are growing, films with more nuclei crystallize more rapidly. Studies of the growth kinetics of ceramic films are therefore of importance [12].

Conclusions

A microscopic and macroscopic review of the sources of stress in films during drying and firing suggest procedures for fabricating thick PZT films. These include the use of additives such as glycerol to reduce internal stress during firing, and appropriate firing schedules to accomodate the film thickness.

[1] G. Yi and M. Sayer, "Sol Gel Processing of Complex Oxide Films," Ceram.Bull., vol 70, pp.1173-1170, 1991.

[2] S.K. Dey, D.A. Payne and K.D. Budd, "Thin Film Ferroelectrics of PZT by Sol-Gel Processing," IEEE Trans.Ultrason.Ferroelectr.Freq.Control, vol 35, pp.80-81, 1988.

[3] G. Yi, Z. Wu and M. Sayer, "Preparation of Pb(Zr,Ti)O_3 Thin Films by Sol Gel Processing: Electrical, Optical & Electro-Optic Properties," J.Appl.Phys., vol 64, pp.2717-2724, 1988.

[4] R.W. Vest, "Metallo-Organic Decomposition (MOD) Processing of Ferroelectric and Electro-Optic Films: A Review," Ferroelectrics, vol 102, pp.53-68, 1990.

[5] G.H. Haertling, "PLZT Thin Films Prepared From Acetate Precursors," Ferroelectrics, vol 116, pp.51-63, 1991.

[6] P.J. Flory. Principles of Polymer Chemistry. Ithaca, N.Y.:Cornell University Press, 1953,

[7] B. Chalmers. Physical Metallurgy. New York:John Wiley and Sons, Inc., 1959, pp. 196.

[8] G. Yi. Ph.D Thesis· Queen's University, 1992,

[9] Table 98, Ceramic Source '90, American Ceramic Society, Westerville, OH, 1990

[10] M.Sayer, "Ferroelectric Memory Programs in Canada",Integ.Ferroelectr., vol 1, (2). 1992

Lead Titanate Thin Films Deposited by Metallorganic Chemical Vapor Deposition (MOCVD)

Warren C. Hendricks, Chien H. Peng, S. B. Desu
Department of Materials Science and Engineering
Virginia Polytechnic Institute & State University
Blacksburg, VA 24061

ABSTRACT

Highly transparent lead titanate ($PbTiO_3$) thin films were deposited on both platinum-coated silicon wafers and sapphire disks. The results were characterized using XRD to determine the phases present and the presence of preferred orientation. SEM was used to examine the morphology of both the surface and cross-section. UV-VIS-NIR spectrophotometry was used to determine the dispersion relationship and the optical band gap energy.

INTRODUCTION

Lead titanate ($PbTiO_3$) based ceramics have been well known for their interesting piezoelectric, pyroelectric, ferroelectric, and electro-optic properties. In recent years, the thin film forms of $PbTiO_3$ (PT) and PT derived materials such as PZT and PLZT have generated considerable interest due to their application in nonvolatile ferroelectric RAMs. These thin films also find applications in optoelectronic devices, sensors and transducers.

While many processing techniques are available to synthesize PT thin films, metallorganic chemical vapor deposition (MOCVD) is a promising technique for several reasons: the equipment is relatively simple, film thickness uniformity is excellent, film density is high, deposition rate is high, step coverage is excellent, and it can be incorporated into large scale processing [1].

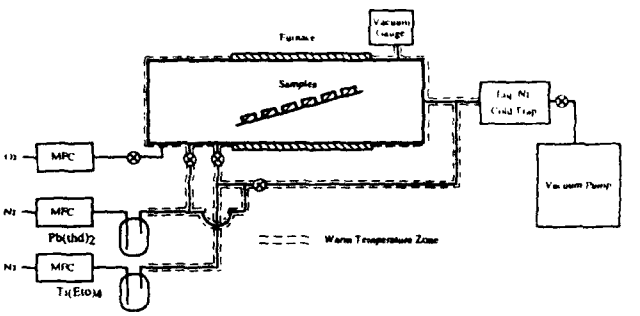


Figure 1: Schematic Diagram of MOCVD System for $PbTiO_3$ Thin Films

EXPERIMENTAL PROCEDURE

In this paper, the MOCVD process was used in a hot-wall reactor to deposit quality $PbTiO_3$ thin films. A schematic diagram of the apparatus used is shown in Fig. 1. The reactor consists of a stainless steel tube with a 2" inner diameter. A liquid nitrogen cold trap in series with the vacuum pump protects the vacuum pump from harmful exhaust products. A resistively heated furnace is used to heat the reactor tube to the desired deposition temperature.

Precursors were sealed in stainless steel bubblers which were resistively heated to a uniform temperature using customized mantle heaters; the variation in bubbler temperature was less than ±1.0 C. The flow rates of the O_2 dilute gas and the N_2 carrier gases were monitored and controlled using microprocessor equipped mass flow controllers (MFCs). The pressure was stabilized using the vacuum pump valve while the system had reached steady state behavior.

A closeable bypass was installed in the reactor to allow the precursors to bypass the reactor prior to beginning the deposition. This is required to insure that the system has already reached equilibrium. All pipes in the system were heated to about 130 C using heating cords to prevent the condensation of the precursor.

The metallorganic precursors chosen were lead (II) tetraheptanedione ($Pb(thd)_2$) and titanium (IV) ethoxide ($Ti(OEt)_4$); a summary of their important properties is provided below [1]:

TABLE I : Summary of Precursor Properties

Precursor	Form at RT	Air Stability	T_m	T_b	T_d
$Pb(thd)_2$	Powder	Stable	128	320	300
$Ti(OEt)_4$	Liquid	Stable	-	122	300

CH3080-0-7803-0465-9/92$3.00 ©IEEE

Selection was based on their volatility and compatible decomposition temperatures as well as the safety and ease of handling the materials. A suitable concentration of oxygen provided by the dilute gas is necessary to provide an oxidizing atmosphere for the pyrolysis of these precursors. $Pb(thd)_2$ is a white powder at room temperature and must be heated near its melting point to achieve significant volatility. 5g were used in the bubbler each time and was replaced with fresh precursor for each deposition to prevent degradation of the precursor due to oligimerization. $Ti(OEt)_4$, on the other hand, is a liquid and while relatively stable in dry air, it reacts readily with moisture. Consequently it was kept sealed up under vacuum in the bubbler and was generally replaced only after ten to fifteen depositions. No apparent degradation in volatility or deposition rate was observed to occur. The optimum deposition parameters used are given below:

TABLE 2 : MOCVD Parameters

	$Pb(thd)_2$	$Ti(OEt)_4$
Bubbler Temperature, T_B	128 C	83 C
Carrier Gas	N_2	N_2
Carrier Gas Flow Rate	25 sccm	5 sccm
Deposition Temperature, T_D	500 C	
Pressure	6 torr	
Dilute Gas	O_2	
Dilute Gas Flow Rate	550 sccm	
Deposition Time, t	30 min.	

The substrates used were of three different materials: single crystal sapphire oriented within a 30 degree cone of the c-axis, platinum coated silicon wafers ($Pt/Ti/SiO_2/Si$), which will hereafter be referred to as platinum substrates, and polycrystalline alumina wafer. Sapphire substrates were used for the purpose of obtaining optical properties by means of UV-VIS-NIR spectrophotometry. The platinum substrates were used to evaluate the deposition behavior of the PT on an electrode material commonly used for determining electrical properties. Polycrystalline alumina was used to monitor the overall deposition rate and phase constitution for positions on the substrate holder not occupied by the platinum or sapphire substrates.

RESULTS AND DISCUSSION

The lead titanate films produced in this way were found to be nearly stoichiometric $PbTiO_3$; energy dispersive spectrometry (EDS) revealed compositions generally of about 54% PbO and 46% TiO_2. To measure the film thickness, weight measurements were taken before and after deposition with an electronic balance having a precision of 10 micrograms. The deposition rate in the uniform temperature zone for the stated experimental parameters was generally about 13 nm/min resulting in a film thickness of about 400 nm after 30 minutes. There was a noticeable substrate effect on the deposition rate; the deposition rate on the Pt samples tended to be much higher than on an adjacent sapphire or alumina substrates. This phenomenon was also reported by Swartz et al.[3]

The $PbTiO_3$ films were generally found to be smooth, specular and crack-free at 500 C, but blistering and peeling was found to occur on the Pt substrates at the higher deposition temperatures of 525 C and 550 C. This phenomenon is most likely stress related and may be a result of the phase transformation occurring at the Curie temperature, which would be avoided at the lower temperature.

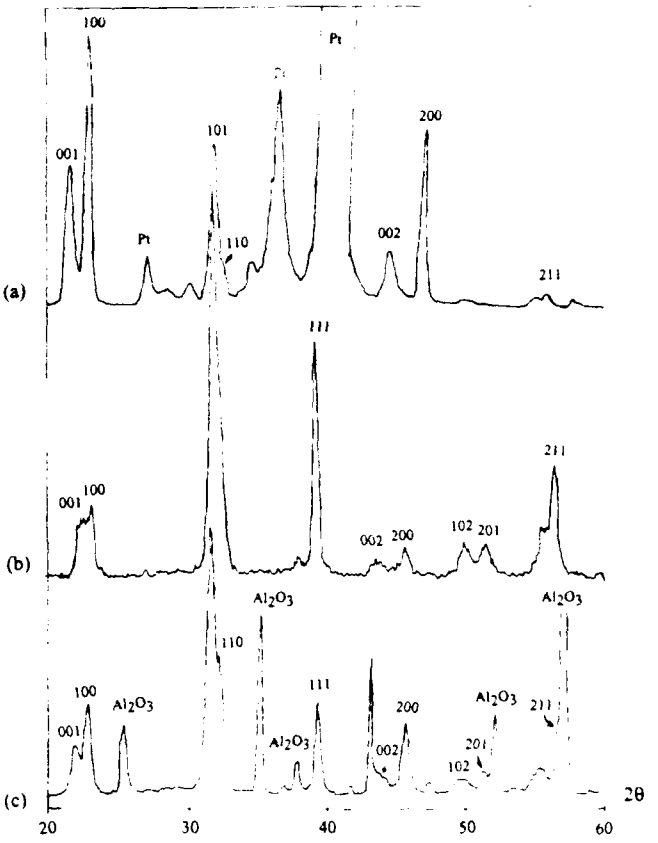
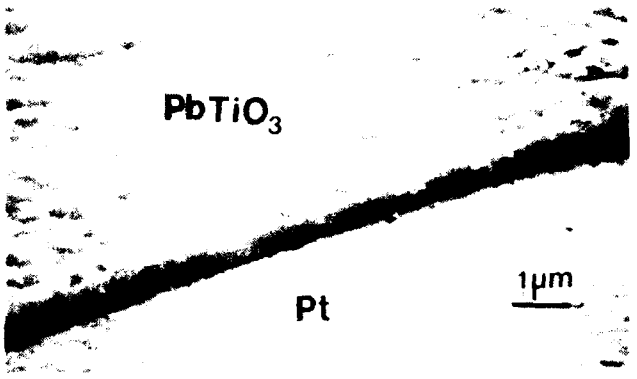


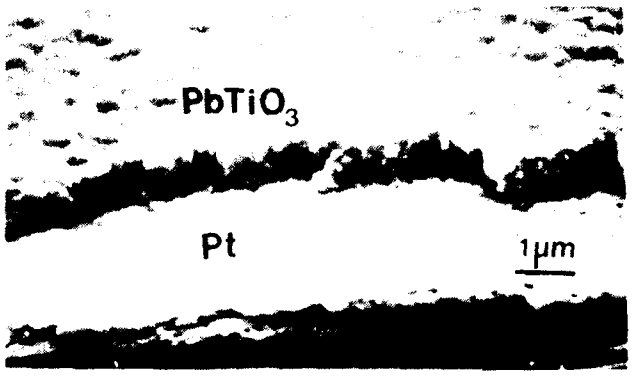
Figure 2: 500 nm thick $PbTiO_3$ film on (a) $Pt/Ti/SiO_2/Si$ (b) sapphire disk (oriented within 30 degree cone of c-axis) (c) polycrystalline alumina

XRD using Cu-Kα radiation was used to monitor phase constitution and reveal possible crystallographic orientation; a comparison of the typical XRD pattern for each of the three substrate materials is given in Fig. 2. In the as-deposited condition, XRD revealed only the presence of the single perovskite phase of $PbTiO_3$. However, some substrates exhibited a very noticeable improvement in their XRD pattern following a 600 C anneal in air for 1 hour, implying that there may be a mixture of both the amorphous and perovskite phases in some of the films prior to annealing. This effect was particularly noticeable on samples which were placed outside the uniform temperature zone and hence were at a lower temperature.

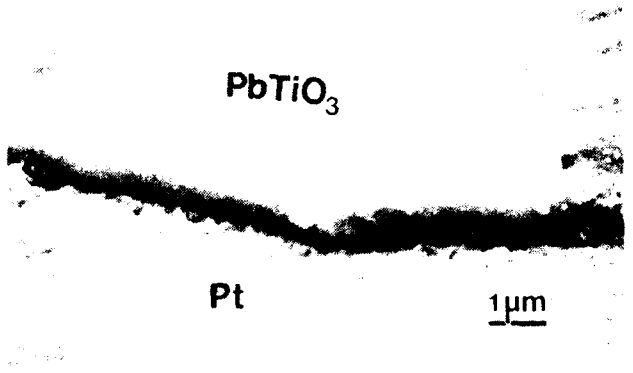
Platinum substrates also showed the formation of a Pb-Pt intermetallic compound at the interface. The XRD patterns also demonstrated the tendency for the preferred orientation of films on Pt substrates as evidenced by the extremely intense x-ray peaks corresponding to the [001] and [100] directions. This phenomenon has also been reported in the literature for Pt substrates[2, 3]. There was no discernible orientation relationship for the sapphire and alumina substrates.



(a) as deposited

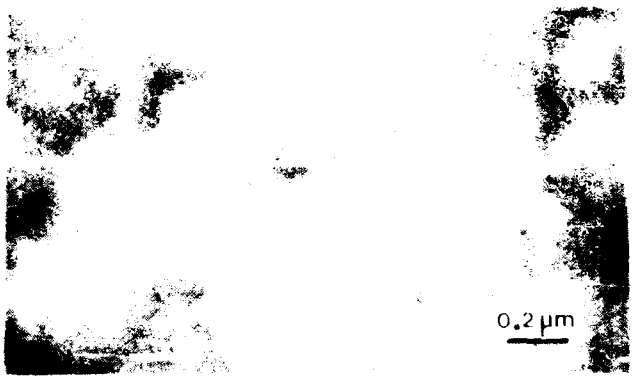


(b) 500 C anneal for 1 hour

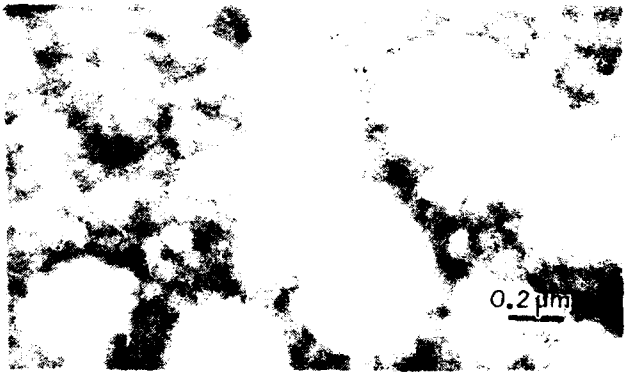


(c) 600 C anneal for 1 hour

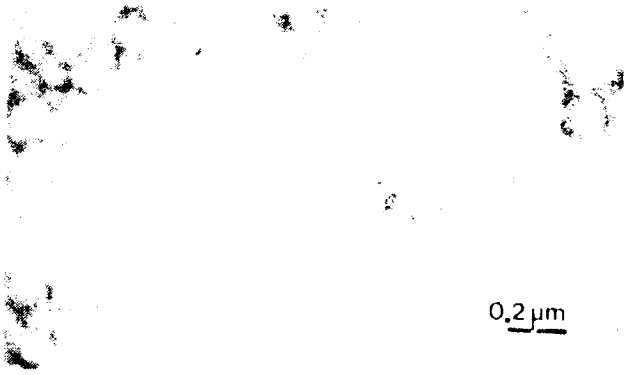
Figure 3 : SEM Photographs (mag. = 50,000 X) of $PbTiO_3$ on $Pt/Ti/SiO_2/Si$



(a) as deposited



(b) 500 C anneal for 1 hour

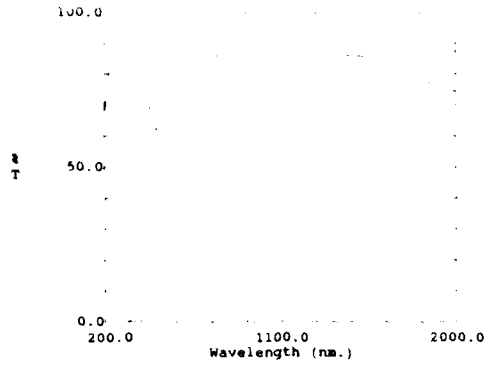


(c) 600 C anneal for 1 hour

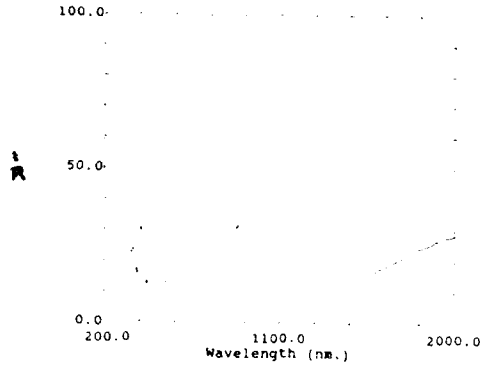
Figure 4 : SEM Photographs (mag. = 10,000 X) of $PbTiO_3$ on $Pt/Ti/SiO_2/Si$

Scanning Electron Microscopy (SEM) was used to image the film morphology and surface topography of a typical $PbTiO_3$ film deposited on a Pt substrate. In addition to including part of the film in the as-deposited state, the sample was broken into two more pieces which were annealed for one hour at 500 C and 600 C, respectively. Edge profiles of the fractured films, which were taken by tilting the microscope stage, are shown in Fig. 3. The cross-sections of the films show a dense, noncolumnar structure, although the surface is slightly rough.

High magnification images of the surfaces are shown in Fig. 4. The annealed samples show evidence of the formation of a fine structure during the heat treatment cycle with what appears to be an extremely small grain size that is not apparent in the as-deposited state. XRD reveals that the annealed samples contained only the perovskite phase. Estimating from the SEM photographs, the apparent grain size of the 500 C annealed sample is about 50 nm. The 600 C annealed sample, due to further growth, shows an average grain size of about 100 nm. A relatively fine grained structure is generally desirable from the standpoint of electrical properties.

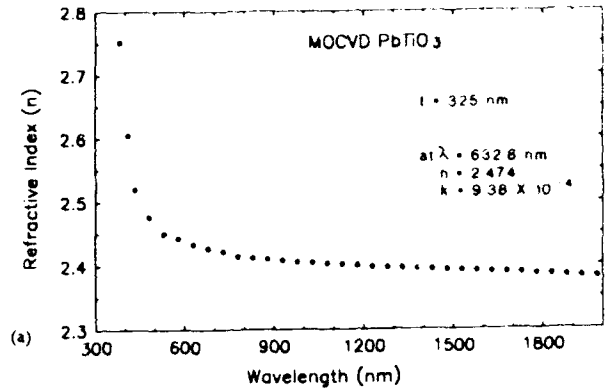


Optical Transmission Spectrum for $PbTiO_3$ Thin Film



Optical Reflectance Spectrum for $PbTiO_3$ Thin Film

Figure 5 : UV-VIS-NIR spectra for 325 nm thick film on sapphire



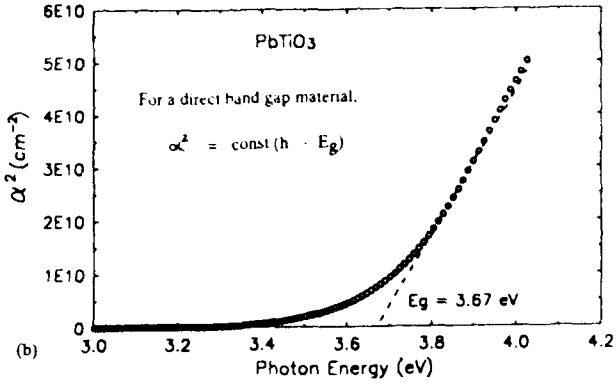


Figure 6: (a) Refractive index, n, as a function of wavelength

(b) Determination of the direct band gap energy, E_g, based on the absorption coefficient, α, and the photon energy

The UV-VIS-NIR transmission spectrum and reflectance spectrum were obtained for the as-deposited PT film on a sapphire substrate in order to obtain the optical constants, film thickness and packing density. The transmission properties of the film revealed a highly specular, nonabsorbing film as evidenced by the fact that the maxima in the interference fringes approach the transmitted intensity of the uncoated sapphire disk at higher wavelengths.

The dispersion relationship for the refractive index, n, and the behavior of the absorption coefficient with photon energy were both determined using the envelope method, as was the film thickness, which, for the spectra shown was 325 nm. Using this method, the optical band gap energy was found to be 3.67 eV. This is slightly greater than the 3.6 eV reported for the bulk solid [4]. For a wavelength of 632.8 nm, the wavelength of a He-Ne laser, the refractive index was found to be 2.474 which is somewhat less than the literature value for the bulk of 2.668 [5]. Using an effective medium approximation for the refractive index, the film packing density was estimated to be about 89%.

SUMMARY

In summary, high quality $PbTiO_3$ thin films were deposited on sapphire and platinum-coated substrates. XRD revealed a nonoriented film on sapphire while the film on the platinum substrate was preferrably oriented in the (100) and (001) directions. A relatively dense morphology was observed using SEM. Additionaly, the formation of a very fine structure was also observed upon annealing the films following deposition. The optical dispersion relationship and absorption coefficient behavior were both determined using the envelope method and UV-VIS-NIR spectrophotometry. The refractive index was 2.474 at 632.8 nm from which the packing density was estimated to be about 89%.

ACKNOWLEDGEMENTS

This project was partially funded by DARPA through a contract from ONR. The author is also grateful to members of the Thin Films Laboratory at Virginia Tech for providing assistance.

REFERENCES

1. C. H. Peng, Ph. D. Thesis, Virginia Polytechnic Institute & State University, Blacksburg, VA (1992).

2. T. Nakagawa, J. Yamaguchi, M. Okuyama, Y. Hamakawa, Jpn. J. Appl. Phys. 21, L655, (1982).

3. S. L. Swartz, D. A. Seifert, G. T. Noel, Ferroelectrics, 93, 37, (1989).

4. V. I. Zametin, Phys. Stat. Sol. (B), 124, 625, (1984).

5. P. D. Thacher, Applied Optics, 16, 3210 (1977).

BULK VS. THIN FILM PLZT FERROELECTRICS

D.E. Dausch and G.H. Haertling
Department of Ceramic Engineering, Clemson University
Clemson, SC 29634-0907

Abstract: Lead lanthanum zirconate titanate (PLZT) ferroelectrics were produced in bulk ceramic and thin film form in order to compare their electrical and physical properties. Both bulk and thin film samples of selected compositions were produced from the same acetate precursor solutions. Properties examined were dielectric permittivity, dissipation factor, remanent polarization, coercive field, Curie temperature and crystallinity. Bulk ceramics were hot pressed from chemically coprecipitated powders, and chemically derived thin films were fabricated by spin coating. Typical conditions for hot pressing were 1200°C for 4 hours at 14 MPa (2000 psi), whereas the thin films were sintered at 700°C for 4 minutes per layer. The similarities and differences between the materials are described.

Introduction

Ferroelectric thin films have been the subject of years of ongoing research in the study and optimization of their processing and properties. The importance of ferroelectric thin films is evident in their many applications ranging from nonvolatile memories to electrooptic devices.[1] These thin film applications stem from the many ferroelectric bulk ceramic components successfully developed over the years. In some instances, however, thin films possess advantages over bulk ceramics which make them more desirable for many devices and broaden the range of applications for ferroelectric materials. Lower operating voltage, higher speed, easier integration with silicon technology and lower cost are among the advantages favoring thin film ferroelectrics.

In order to more fully understand and optimize thin film ferroelectric behavior, a comparison is necessary to bulk ferroelectric phenomena. Direct correlation between the bulk and thin film materials is difficult since the precursors and processing techniques of each are typically so dissimilar; however, a study is presented here that diminishes this disparity. This research focuses on the fabrication and characterization of PLZT bulk ceramics and thin films produced from the same acetate precursor solutions. It is believed that this process allows for a close comparison of PLZT bulk and thin film ferroelectrics by minimizing or eliminating differences in the processing of these materials induced by batching variations, precursor impurities and differences in mixing, reactivity and chemical composition of the precursor materials. A study of several PLZT compositions is presented to explore similarities and differences in the behavior of hot pressed bulk ceramics produced from chemically coprecipitated powders and spin coated thin films produced by a metallorganic decomposition (MOD) process.

Experimental Procedure

Processing

PLZT hot pressed ceramics and spin coated thin films were fabricated using a process similar to previously reported processes using a water soluble acetate precursor system.[2] The acetate precursors were chosen primarily for their chemical stability, insensitivity to moisture and low cost. The starting precursors included lead subacetate (PbAc) powder, lanthanum acetate (LaAc), zirconium acetate (ZrAc) and titanium acetylacetonate (TiAAc) solutions. For processing simplicity and accuracy, PbAc was mixed into solution by the addition of acetic acid and methanol so that all of the acetate precursors were in liquid form. This ensured that the beginning acetate formulation was readily and completely mixed into solution. This step becomes important since only a small portion of the total acetate formulation is used for spin coating. Incomplete mixing would produce compositional fluctuations between bulk and thin film solutions. It should be noted that all of the precursors were assayed before experimentation, and the same stock solution of each precursor was used throughout these experiments. These precautions were taken to reduce the possibility of batching variations between bulk and thin film materials so that similarities and differences in their properties were not a result of these variations.

After initial acetate formulation, the solution was separated into bulk and thin film portions. The bulk portion was coprecipitated in a high speed blender with oxalic acid and methanol and then vacuum dried at 70°C to produce a solid, friable cake. The cake was crushed, calcined at 500°C for 8 hours and milled in trichloroethylene for 6 hours to produce a PLZT oxide powder. Typically, 100g of powder was produced for hot pressing. Hot pressing conditions were 1200°C for 4 hours at 14 MPa. To prepare samples for electrical measurement, the hot pressed parts were sliced on a diamond saw and lapped to 0.5 mm (20 mil) thickness. Electroless nickel electrodes were plated onto the samples.

For thin film production, a small portion (usually 5g) of the acetate solution was decanted and diluted with methanol at a 2:1 ratio by weight. The solution was spun onto silver foil substrates using a photoresist spinner at 2000 rpm for 15 seconds, allowed to dry for 15 seconds and pyrolyzed at 700°C for 4 minutes. Repeating this process for 10 layers produced a PLZT thin film approximately 0.9 um thick. For measurement of electrical properties, copper electrodes were applied to the surface of the films via vacuum evaporation. This process allowed for the fabrication of both bulk and thin film materials from the same batch.

Measurements

Bulk and thin film samples were analyzed using several electrical and physical measurement techniques. The dielectric properties (virgin and poled capacitance and dissipation factor) were measured on bulk and thin film samples using a Leader LCR meter at a measuring frequency of 1 kHz. Polarization (P) vs. electric field (E) hysteresis loops were also measured for both materials. The bulk samples were measured using a Sawyer-Tower circuit with a dc applied voltage of ±1400 V. The hysteresis loops were plotted with a Goerz Metrawatt X-Y plotter. Hysteresis loops of the thin film samples were customarily measured using a 60 Hz Sawyer-Tower circuit and an oscilloscope readout; however, in order to more accurately compare measurement of bulk and film hysteresis loops, the thin films were also measured using a low voltage (±30-50 V) dc looper.

The Curie temperature of bulk samples was determined for several PLZT compositions. Bulk samples were placed in a stirred oil bath and heated while taking capacitance and loss tangent measurements at 5°C increments. The Curie temperature was indicated by a maximum in the measured capacitance. X-ray diffraction analysis was also performed on bulk and thin film samples using a Scintag XDS 2000 diffractometer with Cu K-alpha radiation.

CH3080-0-7803 0465-9/92$3.00 ©IEEE

Results and Discussion

Several compositions were chosen for study near phase boundaries in the PLZT system. The morphotropic phase boundary compositions consisted of 2/55/45, 2/53/47 and 2/51/49 which regularly exhibit ferroelectric memory behavior. Compositions approaching and entering the paraelectric phase region with 65/35 Zr/Ti ratios included those with 6, 7, 8, 9, 9.5 and 10% La. These materials typically are memory materials at 6% La and range toward slim-loop ferroelectric materials in the 9 to 10% La range. Hot pressed bulk ceramics and spin coated thin films on Ag foil substrates were fabricated, and a comparison of properties was established.

Dielectric Properties

Dielectric and ferroelectric properties are listed for bulk and thin film samples in Table 1 including virgin and poled dielectric constants for each. As expected, thin film dielectric constants were generally lower than their bulk counterparts. These effects have previously been reported to be due to several effects caused by the obvious differences between bulk and thin film configurations including small grain size of the thin films, mechanical clamping effects and voltage sensitivity of the dielectric measurement due to the high electric field applied to a <1 um thin film.[2] The difference in dielectric properties found in the present results, however, was not as significant as that reported earlier.

In comparing bulk 2% La samples to thin films, some similarities and differences were noted. Unsurprisingly, both bulk and thin film data showed maxima in K_{vir} and K_{pol} at the 2/53/47 composition indicating the existence of the morphotropic phase boundary near this composition, although the position of the boundary for the thin films seemed to be slightly different than that of the bulk samples. K_{pol} and K_{vir} for 2/51/49 thin films was essentially equal to that of 2/55/45 films, while bulk 2/51/49 had a much greater poled dielectric constant than bulk 2/55/45. This result suggested that thin films and bulk ceramics did not behave equivalently near the morphotropic phase boundary since the dielectric constant was expected to peak at this boundary. A comparable result occured for x/65/35 compositions when the paraelectric phase boundary was encountered. The dielectric constant was expected to reach a maximum at this phase boundary which was previously reported at the 9/65/35 composition for mixed oxide processes.[3] Though both bulk and thin film samples seemed to have maximum dielectric constants at the 9.5/65/35 compositions, the 9/65/35 thin films were closer to 9.5/65/35 than the bulk. Note the occurance of the high K_{pol} for the 8/65/35 bulk sample despite the lower K_{vir} shown by this sample. The bulk ceramics demonstrated a larger difference in dielectric constants between the 9 and 9.5/65/35 compositions. Additionally, the thin film 6/65/35 composition revealed a higher dielectric constant than the bulk 6/65/35. These results would suggest that bulk and thin film samples showed dissimilar behavior also near the paraelectric phase boundary.

As mentioned above, the expected maximum dielectric constant for x/65/35 bulk ceramics produced via mixed oxide processes was 9/65/35; however, the results in Table 1 for the chemical process generally indicate a maximum at the 9.5/65/35 composition. Furthermore, the dielectric constants for all of these compositions were higher than values reported for mixed oxide processes.[3] These results could possibly be explained by realizing the type of process used in this study for fabricating bulk ceramics and thin films; i.e. thoroughly mixed acetate precursor solutions to produce chemically derived powders and thin films. This process may provide improved mixing of components which could slightly alter stoichiometry in the bulk and thin film samples-- especially Zr/Ti ratio and dispersion of the La dopant in PLZT. This could have produced higher dielectric constants and shifted the maximum in dielectric constants of these materials to 9.5% La. In order to explore this supposition, Curie temperatures of bulk x/65/35 samples were measured and are shown in Table 2 and Figure 1.

	K_{pol}	tan d (pol)	K_{vir}	tan d (vir)	E_C (dc) [kV/cm]	P_R (dc) [uC/cm^2]	E_C (ac) [kV/cm]	P_R (ac) [uC/cm^2]
BULK CERAMICS								
2/55/45	1328	.029	1293	.033	8	46	--	--
2/53/47	1885	.025	1391	.028	10	40	--	--
2/51/49	1630	.024	1234	.034	16	33	--	--
6/65/35	1355	.036	1774	.056	6	33	--	--
7/65/35	2712	.033	2479	.036	5	31	--	--
8/65/35	5700	.055	4692	.050	3	20	--	--
9/65/35	5147	.054	5007	.050	0	0	--	--
9.5/65/35	5658	.048	5603	.046	0	0	--	--
10/65/35	5548	.036	5538	.033	0	0	--	--
THIN FILMS								
2/55/45	997	.122	1228	.133	27	34	43	32
2/53/47	1265	.132	1619	.160	28	47	44	45
2/51/49	972	.122	1237	.146	28	38	46	37
6/65/35	1871	.142	1995	.141	14	21	28	25
7/65/35	2499	.170	2460	.145	14	18	27	21
8/65/35	3211	.194	3172	.176	11	15	22	19
9/65/35	4221	.195	4001	.172	9	11	22	17
9.5/65/35	4234	.190	4092	.164	7	8	19	18
10/65/35	4157	.193	4157	.209	7	10	18	16

Table 1. Electrical properties of PLZT bulk ceramics and thin films.

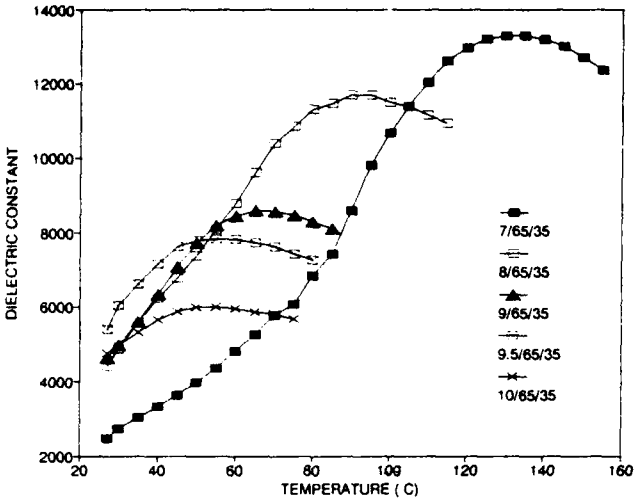


Figure 1. Curie temperature measurements of bulk x/65/35.

Table 2. Curie temperatures of PLZT x/65/35 bulk ceramics.

Composition	T_c
7/65/35	140
8/65/35	100
9/65/35	70
9.5/65/35	65
10/65/35	60

The Curie temperatures measured were consistently 10°C lower than previously reported for bulk samples produced by a mixed oxide process.[3] This result further emphasizes the possibility that the stoichiometries of the chemically prepared materials presented here were slightly different than the mixed oxide materials.

Crystallinity

X-ray diffraction patterns of thin film 8/65/35 and bulk 8/65/35 samples are shown in Figures 2a and 2b, respectively, and d-spacings are labeled for the PLZT peaks. Due to their greater intensities, the three Ag substrate peaks labeled on the thin film pattern masked three PLZT film peaks expected at the same angles. The thin film sample produced lower intensity PLZT peaks than the corresponding bulk sample. This could be a result of the thin film having either a lower degree of crystallinity than the bulk sample or simply a smaller quantitiy of material being analyzed by the diffractometer. In analyzing the lattice spacings of the materials, it was found that the thin film d-spacings were slightly larger than in the bulk material. Watanabe et al.[4] proposed that mechanical stress present in PZT thin films caused by lattice or thermal expansion mismatch between the film and the substrate can cause differences in lattice constant between bulk and thin film materials. This may be the cause of the difference in d-spacing observed here. The increase in d-spacing for the thin films is quite small--approximately 0.6 to 1% between the bulk and thin film samples. An absence of larger differences in d-spacings could be attributed to the Ag substrates used which are quite ductile and may allow the films to be relatively stress free compared to films fabricated on more rigid substrates (i.e. Si, sapphire, MgO).

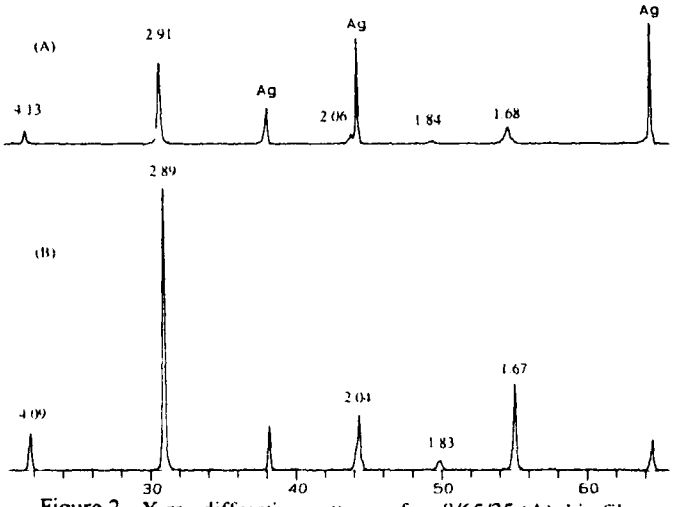


Figure 2. X-ray diffraction patterns of an 8/65/35 (A) thin film and (B) bulk ceramic. D-spacings are in angstroms.

Ferroelectric Properties

The ferroelectric properties calculated in Table 1 were taken from the P vs. E hysteresis loops shown in Figure 3. As stated above in the discussion of dielectric properties, both bulk and thin film materials indicated a transition across the morphotropic phase boundary. This transition was also evident in the hysteresis loops of the materials. In the bulk materials, the transition was obvious with a widening of the hysteresis loop signaling the emergence of the tetragonal phase in the 2/51/49 material. This phenomenon, however, did not occur in the thin film samples. The tetragonal phase was evident in the dc hysteresis loops of the thin films by a slightly more square hysteresis loop for 2/51/49 than for the rhombohedral 2/55/45 film. The phase transition was apparent in both ac and dc hysteresis loops of the films by a rise in remanent polarization in the 2/53/47 film. Previous work mentioned that thin films have a lower P_R and higher E_C than bulk materials for reasons similar to differences in dielectric properties mentioned above (grain size, clamping, voltage sensitivity).[2] Although the thin films presented here with 2% La had a higher E_C, the P_R of these films was not necessarily lower than for bulk materials. In fact, 2/53/47 and 2/51/49 films had a higher P_R than bulk samples of the same composition. Again, as with dielectric properties, the ferroelectric properties of the thin films seemed to be different across the phase boundary than the bulk ceramics. This was also the case for x/65/35 materials.

In PLZT bulk x/65/35 samples, the hysteresis loops obtained were similar to those expected for these compositions. The remanent polarizations and coercive fields calculated were lower than reported mixed oxide values[3], and this can possibly be attributed to the difference in processing between the coprecipitation and mixed oxide processes as discussed above. As anticipated, the 6, 7 and 8% La materials were memory materials, and the 9, 9.5 and 10% La materials were slim-loop materials. For the memory materials, E_C was higher and P_R was lower for thin films than for bulk materials which was similar to previously reported results.[2] Although both bulk and thin film memory materials experienced narrowing of their hysteresis loops with increasing %La, the bulk materials transformed to slim-loop materials at 9% La, while the thin films maintained ferroelectric memory hysteresis loops beyond 9% La. Research by Gu et al.[5] on quenched PLZT 9.5/65/35 ceramics showed that internal stresses induced in quenched samples can enhance polar region ordering and produce a more ferroelectric-like response. This produced higher remanent polarizations in quenched samples than in annealed samples. These findings could explain the memory behavior observed in the 9, 9.5 and 10/65/35 thin films in this study. Residual stresses in the thin films which could have produced the differences in d-spacings discussed above may have caused these films to retain ferroelectric memory hysteresis loops that were not observed in the bulk materials of the same compositions. Nevertheless, thin film behavior again differed from bulk ceramic behavior near the paraelectric phase boundary.

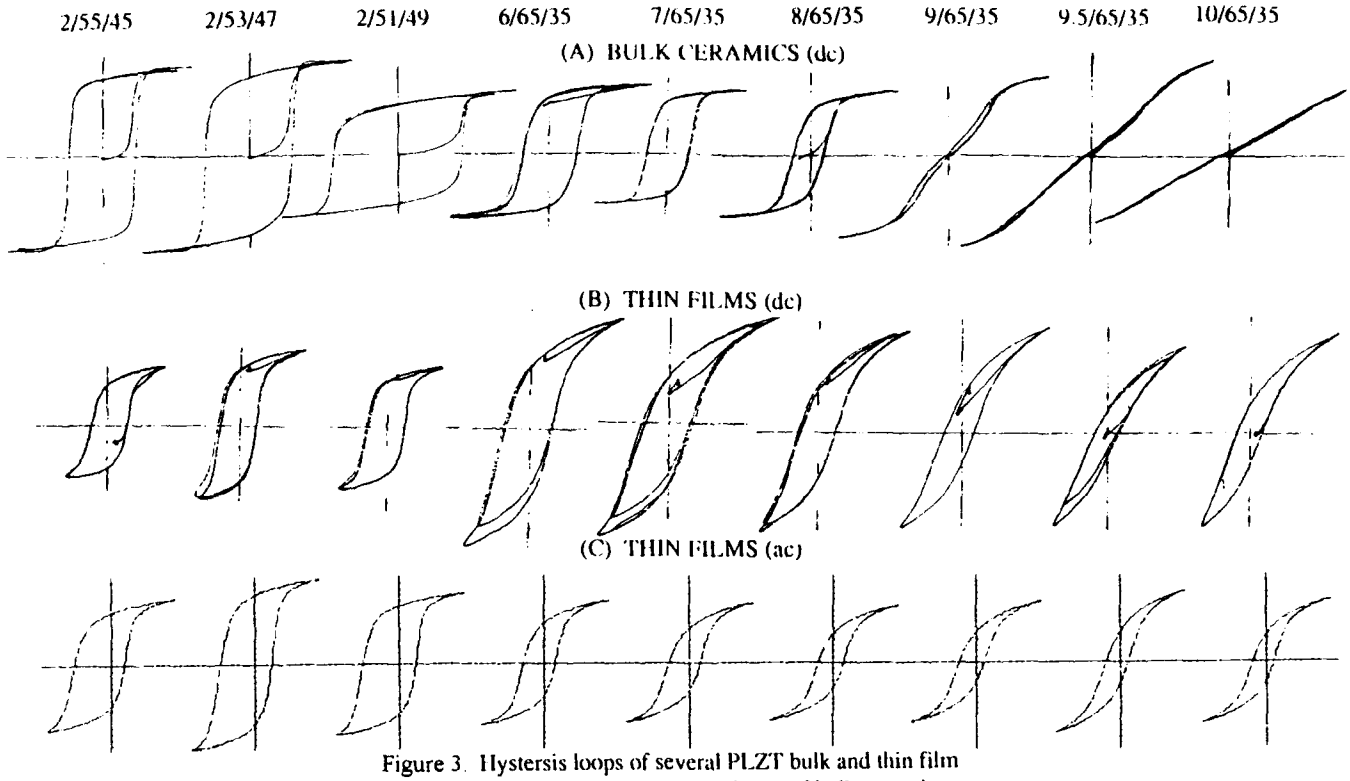


Figure 3. Hystersis loops of several PLZT bulk and thin film materials including (A) dc loops of bulk ceramics, (B) dc loops of thin films and (C) ac loops of thin films.

Summary and Conclusions

PLZT bulk ceramics and thin films were fabricated from the same acetate precursor solutions in order to minimize batching variations and accurately compare properties between bulk and thin film samples of the same compositions. It was found that materials near the morphotropic phase boundary with 2% La differed in behavior. Maximum dielectric constants were found at 2/53/47 for both materials; however, the bulk 2/51/49 had a proportionally higher dielectric constant than the thin film when compared to their respective 2/55/45 samples. The hysteresis loops of the bulk samples indicated a transition to a tetragonal phase with a widening of hysteresis loops (increased E_C, decreased P_R). Thin films also indicated a transition but with a maximum in P_R for the 2/53/47 composition.

Bulk x/65/35 materials behaved as expected with the exception of slightly lower Curie temperatures, coercive fields and remanent polarizations and slightly higher dielectric constants than previously reported. The 6, 7 and 8/65/35 materials produced memory hysteresis loops, and the 9, 9.5 and 10/65/35 materials produced slim hysteresis loops. The thin film memory loops were somewhat thinner than the bulk memory loops, and continual narrowing of the loops occurred toward the paraelectric phase boundary; however, slim-loop ferroelectrics were never completely achieved in the thin film materials. X-ray diffraction analysis showed that thin film lattice spacings were only slightly greater than the corresponding buik spacings as indicated by diffraction peaks slightly shifted in diffraction angle between the two materials.

This comparison of bulk and thin film ferroelectrics is believed to be an accurate comparison of properties caused only by the inherent differences in configuration between bulk ceramics and thin films. It is believed that the current process used to fabricate these materials is one in which complete mixing of precursors and accurate batching of materials provided a minimization of batching differences that could cause serious variations in composition and properties of bulk and thin film PLZT ferroelectrics. Hence, this process provided a valid comparison between these materials.

Acknowledgement

This work was supported by ONR under contract #N00014-91-J-1508

References

[1] L.M. Sheppard, "Advances in Processing of Ferroelectric Thin Films," Am.Cer.Soc.Bull., vol. 71(1), pp. 85-95, 1992.

[2] G.H.Haertling, "An Acetate Process for Bulk and Thin Film PLZT," in IEEE 7th International Symposium on Applications of Ferroelectrics, pp. 292-5, 1990.

[3] G.H.Haertling, "Electrooptic Ceramics and Devices," in Engineered Materials Handbook, vol. 4 (Ceramics and Glasses), ASM International, pp. 1124-30, 1991.

[4] H.Watanabe, T.Mihara and C.A.Paz De Araujo, "Device Effects of Various Zr/Ti Ratios of PZT Thin-Films Prepared by Sol-Gel Method," in Proceedings of the 3rd International Symposium on Integrated Ferroelectrics, pp. 139-50, 1991.

[5] W.Y. Gu, E.Furman, A.Bhalla and L.E.Cross,"Effects of Thermal Treatment on the Electrical Properties in Relaxor PLZT Ceramics," Ferroelectrics, vol. 89, pp. 221-30, 1989.

HIGHLY ORIENTED (Pb,La)(Zr,Ti)O_3 THIN FILMS ON AMORPHOUS SUBSTRATES

A. Y. Wu[a], D. M. Hwang[b] and L. M. Wang[c]

[a]Center for High Technology Materials, University of New Mexico, Albuquerque, NM 87131
[b]Department of Geology, University of New Mexico, Albuquerque, NM 87131
[c]Bell Communications Research, Red Bank, NJ 07701

PLZT thin films have been deposited on various substrates, particularly on amorphous SiO_2, and on Si, or GaAs with a buffer layer such SiO_2. Regardless if the substrate is single crystal or not, many films are highly oriented with one of the [100], or [110], or [111] direction normal to the substrate surfaces. Depending on the PLZT composition, substrate material and deposition conditions, there are ten different film categories: For the distorted perovskite (cubic, tetragonal, or rhombohedral) structure, (1) single crysal film; (2) quasi single crystal film; (3) orientationally locked epitaxial film; (4) uniaxially-oriented film with unique crystallographic direction normal to substrate surface; (5) polycrystalline film; and for other crystal structures: (6) highly oriented film with the pyrochlore crystal structure; (7) polycrystalline film with the pyrochlore crystal structure; (8) amorphous film; (9) film showing perovskite, pyrochlore, and amorphous structures; and (10) film showing different phases. Among these films the most interesting ones are the highly-oriented films deposited on amorphous SiO_2 substrate because of the possibility of monolithic integration of integrated optical thin film devices onto Si and GaAs with a non-lattice matched buffer layer of SiO_2, the best optical transparent material for waveguiding and integrated optics. Since there is no lattice matching condition between the film and the amorphous substrate, it is very interesting to know the growth condition at the interface. Crystal structure, grain size, morphology, composition, and symmetry of the thin film on SiO_2 have been studied using a JEOL 2000FX and a JEOL 4000FX transmission electron microscope systems and interesting results have revealed that 1) very large single crystal grain up to 2 μm in size, with the [100] direction normal to the substrate surface are frequently grown on amorphous substrate; and 2) clusters of orientationally-locked, highly-oriented grains are also frequently formed on amorphous substrate. These interesting but unusual thin film growth behavors will be discussed.

INTRODUCTION

PLZT thin films have been deposited using sputtering method on various substrates including SiO_2, Si, GaAs, Al_2O_3, MgO, stainless steel, Pt, etc., and SiO_2, Si, or GaAs with a buffer layer such as $SrTiO_3$, In_2O_3-SnO_2, Pt, Ti/Pt and PLT [1]. Regardless if the substrate is single crystal or not, many films are highly oriented with one of the [100], or [110], or [111] direction normal to the substrate surfaces. Depending on the PLZT composition, substrate material and deposition conditions, there are ten different film categories. We will describe these ten different films only briefly but concentrate mainly on the film deposited on fused silica substrate because of its importance.

For the distorted perovskite (cubic, tetragonal, or rhombohedral) structure, the following films have been and can be deposited:

(1) Single crysal film: Using a lattice matched PLZT 9/65/35 wafer as substrate with the wafer surface optically polished and slightly etched in very dilute HF solution, it is possible to deposite single crystal film of the size of 8 μm, the average grain size of the PLZT wafer.

(2) Quasi single crystal film: Using a nearly lattice matched MgO or $SrTiO_3$ single crystal substrate, it is possile to deposit large single crystal with a lot of strain, stress and defects due to both lattice and thermal expansion mismatch. This is because the lattice mismatch between PLZT film and the substrate is about 5%, while the maximum strain PLZT material can tolerate is about 3%.

(3) Orientationally locked epitaxial film: Highly oriented PLZT films deposited on MgO or $SrTiO_3$ single crystal substrate are likely to be orientationally locked also. Grain and grain boundaries may be formed due to the lattice and thermal expansion mismatch. Grain size may be larger than a few μm.

(4) Uniaxially-oriented film with a unique crystallographic direction normal to substrate surface: Highly oriented film with the unique [100], or [110], or [111] direction normal to the substrate surface. The substrates can be fused silica, polycrystalline (100), or (110) highly-oriented $SrTiO_3$ film of 1000 Å thick, polycrystalline ITO film of 1000 Å, polycrystalline (111) highly-oriented Pt or Pt/Ti film of 1000 Å, single crystal substrates such as Si(100), Si(111), Si(110), GaAs(100), Al_2O_3(0001), Al_2O_3(1$\bar{1}$02), etc. Although lattice mismatches are very large in above-mentioned substrates, orientationally-locked, highly oriented films can be obtained frequently. Grain size in the film may be a few hundred Å up to 2 μm.

(5) Polycrystalline film: This is the type of film reported in most publications. In such film, most of the (100), (110), and (111) peaks would show up in powder x-ray diffraction pattern. Our experience is that these films have much inferior optical quality with large scattering, attenuation, etc. than that in highly-oriented films. Researchers obtained this kind of films because their deposition parameters such as deposition rate, gas mixture, flow rate, substrate temperature, etc. were not optimized.

For other crystal structures, the following films have been and can be deposited:

(6) Highly-oriented film with the pyrochlore crystal structure: It is easy to deposit a pyrochlore structured film with the [100] direction normal to the substrate surface providing that the deposition conditions are the same as that for depositing perovskite structrued film but the substrate temperature should be kept lower. Fused silica substrate is useful for obtaining highly-oriented pyrochlore structured film consistently.

(7) Polycrystalline film with the pyrochlore crystal structure: In this film all the pyrochlore peaks would show up in the powder x-ray diffraction pattern. Again, researchers obtained this kind of film because their deposition parameters were not optimized.

(8) Film showing perovskite, pyrochlore, and amorphous structures: This poor film usually indicates that the substrate temperature is still not high enough and the deposition parameters are not optimized.

(9) Amorphous film: When the substrate temperature is too low, only amorphous film can be obtained. However, it is possible to deposite amorphous film of good optical quality because there is no crack in the film.

(10) Film showing different phases: This kind of film is caused by an unsteady or disturbed plasma discharge in the deposition chamber. Also the substrate temperature may be not uniform.

Among these films the most desired film should be large single crystal but it is difficult to deposite it mainly due to the lattice

CH3080-0-7803-0465-9/92$3.00 ©IEEE

mismatch problem. Even if a proper substrate can be used, the cost is likely very expensive. The next choice would be the epitaxial film but the cost of single crystal substrate is still a problem. For practical purpose, Si and GaAs are the only two substrates with potential for monolithical integration. Since the lattice mismatch between PLZT and Si or GaAs is more than 25% and the refractive index of Si and GaAs is higher than PLZT, it is necessary to use a buffer layer. It is natural to use SiO_2 as a buffer layer not only because fused silica is more economic but also because of the monolithic integration of SiO_2 or its device onto Si and GaAs substrate is a rather mature technology. Althouth there is non-lattice matching between crystalline PLZT and amorphous SiO_2, the question now is why large grain, orientationally locked, highly oriented PLZT film can be deposited on fused silica? We may not answer this question now but we will first provide hard evidence in this paper.

We have used TEM to study the growth condition, crystal structure, grain size, morphology, composition, and symmetry of PLZT films, because all these properties are very important for the understanding of optical scattering, attenuation, and optical nonlinearity in PLZT thin film optical, nonlinear optical, and waveguide devices.

EXPERIMENTAL RESULTS AND DISCUSSION

PLZT films of the composition 28/0/100, about 4500 A thick, were deposited on fused silica substrate (Optosil 1, Optosil II, or TO8 from Amersil Inc.) or onto Si(100) substrate with a SiO_2 buffer layer of 2 μm thick thermally grown on the Si surface. The substrate temperature was 400°C and the deposition method is rf magnetron sputtering [2]. Two different types of TEM samples were prepared: (1) Thin film foil parallel to the film surface for studying the film properties, and (2) Thin cross-sectional foil prepared by stacking several PLZT/SiO_2/Si or PLZT/SiO_2 samples together using epoxy and then sliced the stack perpendicular to the film. All TEM foils were polished to desired thickness using standard Ar ion milling perforation method. A few PLZT 7/0/100 films of 900 Å thick were also deposited directly onto pure Si(100) substrate. TEM PLZT 7/0/100 sample were obtained by totally dissolving Si away and collecting the remaining PLZT films in a warm KOH/water solution. Film debris larger than 2mm X 2mm could be easily collected and scooped onto meshed or pinholed TEM copper or Be sample disks for TEM study. The films were cleaned thoroughly by acetone and acohol.

TEM studies were performed at various different times using the JEOL 2000FX TEM system at the University of New Mexico for studying the film itself and the JEOL 4000FX TEM system at Belcore for studying the cross-sectional structure at interface. Several micrographs and corresponding electron diffraction patterns of PLZT 28/0/100 and PLZT 7/0/100 thin film samples were obtained. Figure 1 is a bright-field micrograph and its

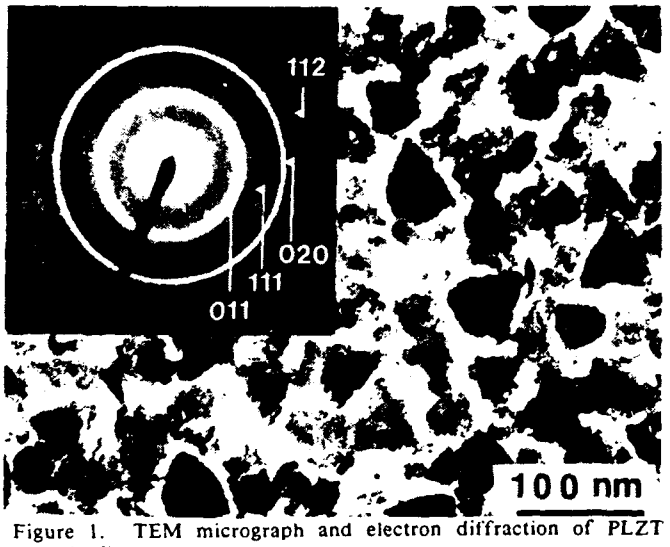


Figure 1. TEM micrograph and electron diffraction of PLZT 7/0/100 film.

corresponding electron diffraction pattern of a PLZT 7/0/100 film deposited directly on a clean Si(100) substrate (Si substrate was etched in HF solution just before it was loaded into deposition chamber, so there might be only very thin native SiO_2 formed at the interface which may not be dissolved away by KOH/water solution). In this case the film thickness is 900 Å without any perforation procedure. The micrograph shows the random distriution and orientation of small PLZT grains of the size of about 500 Å. From the diffraction pattern in the insert of the Figure, the film is a polycrystalline commonly seen in many published reports. Figure 2 is a TEM bright-field micrograph and the corresponding electron diffraction pattern of a PLZT 28/0/100 film deposited on a SiO_2/Si(100) substrate. The film is highly oriented with the [100] direction normal to the substrate surface. The most interesting thing about this Figure is that there are many grains having the shape of square in the sample, as can be seen clearly in the Figure. These grains have the size of about 2000 to 5000 Å and many of them are clustered together as if their orientation in the plane of the original substrate are all the same. (The original substrate is thermally grown SiO_2 on Si, which has been ion-milled away). The clusters are large in size that it is possible for us to focus the electron beam of the size 1 μm in diameter inside one cluster area and obtain a single-crystal-like diffraction pattern. For example, the electron diffraction pattern on the upper left corner shows a four-fold symmetry representing the crystallographic (100) diffraction with very little containmination. This indicates that the beam was possibly probing a "single crystal" region of the size larger than 1 μm. It is not easy for us to say for sure that this large region is indeed a true PLZT single crystal for the following reason: Just about 1 μm away from the probed region, we can see several large clusters consisting of square-shaped grains, and the grains in each cluster are all "aligned" in one direction in the plane of the film. Thus we conclude that not only the surface normal of the grains in one cluster has the [100] orientation but also that all the grains in the cluster are orientationally locked in the plane with respect to the original SiO_2 substrate surface so that a clean, almost pure four-fold symmetry diffraction pattern was observed.

Figure 3 shows several TEM micrographs on cross-sectional views of PLZT 28/0/100 deposited on Optosil 1 or SiO_2/Si(100) substrate. The acceleration voltage for the JEOL 4000FX system was 400 KV and the beam aperature was 1 μm. Both bright and dark field and double exposure techniques have been employed. From the figures it is clear that (1) The size of some individual region (grain or cluster of grains) is large, larger than 1 up to 2 μm, but these region contains some defects and possibly stress and strain because the image inside each individual region is not homogeneous or uniform. Several corresponding electron diffraction patterns of these grains or regions show clean diffraction patterns suggesting that they are very similar to single crystal in nature. But some other patterns occationally do show two or more single crystal diffraction patterns superimposed closely on top of each other, suggesting that there are several grains in that region, and each grain makes a small angle with another grain. This suggests that small angle grains and boundaries exist in our films. On a higher magnification, it can be seen that the single-crystal-like region become more and more defective when the film is closer to the PLZT/SiO_2 interface. It can also be seen that the interface boundary line in most samples are very sharp to within about 100 Å, which is also about the surface roughness of the thermally grown SiO_2 surface. By analyzing our micrographs it seems that there is no strong evidence that there might be any second phase at the PLZT/SiO_2 interface to within our resolution of 20 to 30 Å. In order to find out whether there is any second phase or not, it is necessary to use a TEM with much higher magnification and resolution and to study the crystal structure and chemical composition in both PLZT and SiO_2 regions to within 30 Å from the interface.

CONCLUSIONS

Orientationally locked, highly oriented PLZT films have been deposited on amorphous SiO_2 substrates. Large single crystal grains or cluster of grains up to 2 μm in size, with the [100] direction normal to thin film surface are frequently grown on SiO_2 substrates. The film structures are examined and reported in this



Figure 2. TEM micrograph and electron diffraction of PLZT 28/0/100 film.

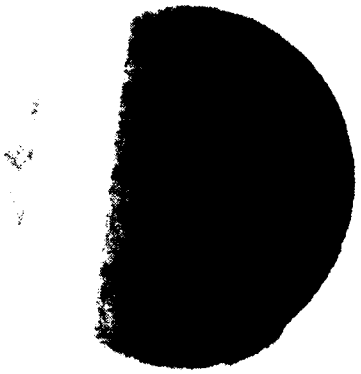


Figure 3(a). TEM cross-sectional micrograph of PLZT 28/0/100 film and SiO_2 substrate. X15K.

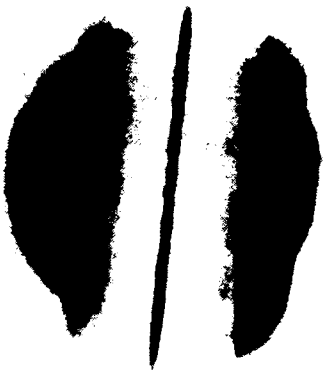


Figure 3(b). TEM cross-sectional micrograph of PLZT 28/0/100 film and SiO_2 substrate. X30K.

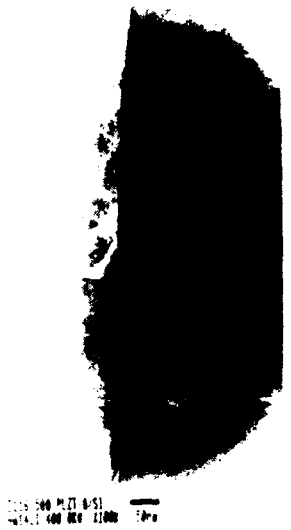


Figure 3(c). TEM cross-sectional micrograph of PLZT 28/0/100 film and SiO_2 substrate. X100K.



Figure 3(d). TEM cross-sectional electron diffraction pattern of PLZT 28/0/100 film and SiO_2 substrate showing large single crystal grain or cluster of grains.

work by using TEM methods.

Acknowledgements

This work was supported in part by AFOSR, DARPA, NSF, DOE-BES, Office of Basic Energy Sciences, US Department of Energy, and the University of New Mexico.

REFERENCES

[1] A. Y. Wu, private communications.

[2] A. Y. Wu, Preceedings of the 4th International SAMPE Electronics Conference, 722 (1990).

Thin Films: Processing

BARIUM STRONTIUM TITANATE THIN FILMS BY MULTI-ION-BEAM REACTIVE SPUTTERING TECHNIQUE

C.-J. Peng*, H. Hu and S.B. Krupanidhi#
Material Research Laboratory
Pennsylvania State University, University Park, PA 16802
* Also with Material Research Laboratories, Industrial Technology Research Institute, Hsinchu, Taiwan, R.O.C.
# Also with Department of Engineering Science & Mechanics

ABSTRACT

Thin films of barium strontium titanate including $BaTiO_3$ and $SrTiO_3$ end members were deposited by multi-ion-beam reactive sputtering (MIBERS) technique using alkaline earth oxides (BaO and SrO) and Ti-metal targets. The MIBERS technique showed convenient and flexible control of the film compositions. The dielectric constants of the films deposited on Pt-coated Si substrates showed thickness dependence. A dielectric constant of 219 at 100 KHz was found for 1.2 μm thick films. Charge storage density of 15 fC/μm^2 at 5 volt and leakage current density of 5.8 $\mu A/cm^2$ at an electric field of 0.1 MV/cm can be obtained for 0.3 μm thick films and are suitable for the application of 64 Mb dynamic random access memories (DRAM). However, a charge storage density of >30 fC/μm^2 is achievable provided that some extrinsic factors which lowering the overall dielectric constant can be eliminated, and can be used for higher memory density DRAMs. Thin interface layers were likely present between film and silicon substrate in the case of metal-insulator-silicon configuration. The overall results showed that barium strontium titanate thin films by multi-ion-beam reactive sputtering technique are suitable candidates for DRAM applications.

I. Introduction

Ferroelectric materials are well recognized to be the promising capacitor materials for ultra large scale integration (ULSI) dynamic random access memory (DRAM) applications, especially for memory densities higher than 64 Mb[1]. The most attractive advantage of ferroelectric materials over conventional nitride-oxide materials is that the former have much higher (at least one order magnitude) dielectric constants. The higher dielectric constant of ferroelectric materials allows the capacitor remaining to be planar and still maitain high enough charge storage. Thus the manufacturing processes can be dramatically simplified.

Among numerous ferroelectric materials, barium strontium titanate ($Ba_{1-x}Sr_xTiO_3$) is a promising candidate dielectric material to be used in ULSI DRAMs due to its paraelectric phase (for $x < 0.7$) at room temperature and thus no aging and fatique effects. Besides, $Ba_{1-x}Sr_xTiO_3$ solid solution ceramics has high dielectric constant at room temperature (K~2500 for $x=0.7$)[2], low temperature coefficient of capacitance and is a thermally stable compound (compared with lead-based ferroelectrics). Barium strontium titanate solid solution ceramics also have low dissipation factors (~0.0015 for $x=0.5$)[2].

In this paper, results on barium strontium titanate thin films including end members prepared by multi-ion-beam reactive sputtering (MIBERS) technique are reported. MIBERS has been successfully applied to the growth of other ferroelectric materials, such as PZT thin films[3]. Compared with other sputtering techniques, it has some inherent advantages such as (a) independent control flux density and energy of the sputtering speices which allows greater flexibility and better control of process, (b) lower operating pressure (~10^{-4} torr) ensures better quality of films, (c) the plasma is localized within the ion sources which are away from target and sustrate, so that the unwanted bombardment is avoided, (d) flexibility of the control of the film composition by independent sputtering source for multi-component thin film materials and (e) controllable bombardment by secondary low energy ion source to assist thin film growth. This technique was also demonstrated to have very uniform thickness and composition over large area and good process reproducibility. Details of the MIBERS technique have been described elesewhere[3].

II. Experimentals

Three focused Ar^+ beams were used to sputter a SrO, BaO and a Ti-metal target respectively. The chamber was first pumped down to a base pressure of ~$2x10^{-6}$ torr by cryopump. Then the argon (as the precursor of Ar^+) was bled through the ion guns and oxygen was bled into the chamber directly (molecular ratio of Ar/O_2 was 1), give rise to a total pressure about $4x10^{-4}$ torr. The $SrTiO_3$ thin films were deposited onto unheated Pt-coated Si and bare Si substrates. Figure 1 shows the variation of Ba/Ti and Sr/Ti ratio (by current plasma spectrochemical analysis) with ion flux density, in which the ion beam voltage and current for Ti target were kept at 1100 V and 30 mA respectively, and the ion beam voltage for BaO and SrO target was at 900 and 1000 V respectively. The linear relationship between Ba/Ti or Sr/Ti ratio and the ion beam current for BaO and SrO targets provides convenient and flexible control of the film compositions. The growth rates of near stoichiometric barium strontium titanatethin films were estimated to be ~13 nm/min. The deposited films were amorphous, and post-deposition annealing by conventional oven was performed in oxygen atmosphere in order to induce crystallization. 0.3 mm diameter gold dots were deposited onto film surface as top electrodes. Low signal dielectric properties and capacitance-voltage (C-V) characteristics were measured with HP 4192A impedance analyzer. I-V characteristics were measured using Keithley 617 ampmeter. Time dependent dielectric breakdown were measured by RT66A program of Radiant Technologies.

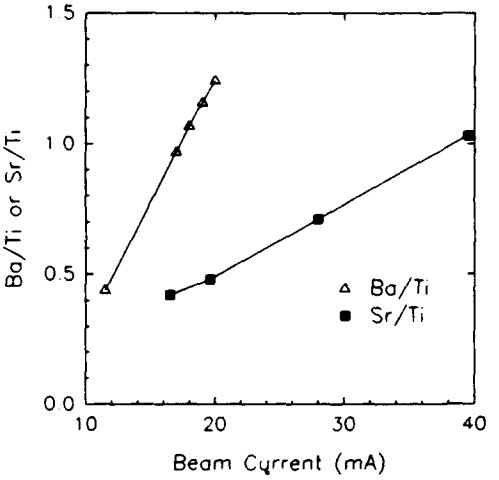


Fig.1: Variation of Ba/Ti and Sr/Ti ratio with ion beam current for BaO and SrO target respectively.

CH3080-0-7803-0465-9/92$3.00 ©IEEE

III. Results and Discussions

Figure 2 shows the x-ray diffraction patterns of 1.2 μm films for $BaTiO_3$, $SrTiO_3$ (Ba/Ti and Sr/Ti = ~1.03) and $Ba_{0.54}Sr_{0.48}TiO_3$ (BST) compositions annealed at 700°C for 2 hrs. No alkaline earth oxides or alkaline earth rich titanate phases were observed in all films although the alkaline earth /Ti ratio are all more than 1. The second phases probably exist in the form of amorphous phase or crystalline phase but undetectable by x-ray diffraction. The peaks of $SrTiO_3$ are much sharper and higher, which indicates much better crystallinity than that of $BaTiO_3$ for films annealed at 700°C for 2 hrs. The presence of second phase, if it is a low dielectric constant material, will affect the electric properties of films which will be discussed later.The broad peak of $BaTiO_3$ films may also come from the pseudo-cubic nature of $BaTiO_3$ with very fine grain size and

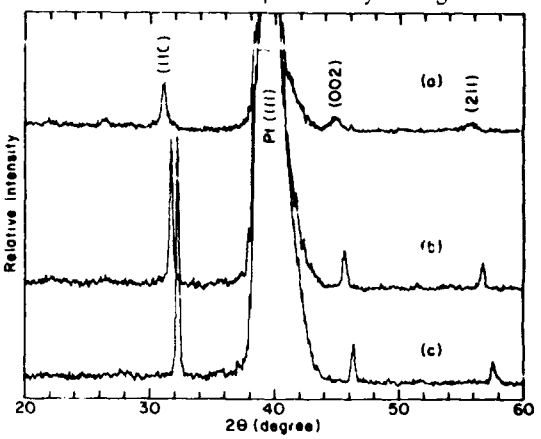


Fig.2: X-ray diffraction patterns of 1.2 μm films for (a)$BrTiO_3$, (b)$Ba_{0.54}Sr_{0.48}TiO_3$ (c)$SrTiO_3$ annealed at 700°C for 2 hrs.

stress on grian boundaries[4]. The extremely low intensity of the $BaTiO_3$ films also implies that the crystallization is not as easy as $SrTiO_3$ films at 700°C annealing temperature.

Figure 3 shows the x-ray diffraction patterns for 1.2 μm films of $SrTIO_3$ by conventional oven annealing at various temperatures for 2 hrs. It can be seen from the relative peak intensities that the crystallinity improved with the annealing temperature. However, a pure perovskite phase was noticed in films annealed at all temperatures. The subsequent improvement in crystallization with annealing temperature may be ascribed to the increase in grain size as well as reduction of second non-crystalline phase. Often, the presence of such second phase strongly affects the electrical properties, in terms of the lowering dielectric constant. In the present case, it was observed that the dielectric constant of these films measured at 100 KHz were 81, 151, and 219 for $SrTiO_3$ films annealed at 500°C, 600°C and 700°C respectively.

Figure 4 shows the dielectric constant and dissipation factor as a function of frequency for $SrTiO_3$ films of various thicknesses annealed at 700°C for 2 hrs. The dielectric constants measured at 100 KHz are 99, 127 and 219 for films with 0.3, 0.7 and 1.2 μm thickness respectively. The dielectric constant increases as film thickness increases, which is consistent with other reports in literatures[5]. Several reasons for lowering the dielectric constants with decreasing film thickness are possible, including surface layer effect, residual stress and structural inhomogenieties. The surface layer effect may be visualized in terms of an oxygen absorption layer on either surface or grain boundaries and/or nonstoichiometric surface layer[6]. The stress resulting from the different thermal expansion coefficients between films and substrates, which are generally thickness dependent, may also contribute to the thickness dependence of dielectric behavior. For thin films deposited at low substrate temperatures (in this case, at room temperature), the structure of the films are generally columnar structure and contain voids between columnars. Subsequent annealing may not eliminate these voids. The density of voids increases as film thickness decreases and thus the dielectric constant decreases. However, these factors need to be separated to see the individual effect. The dielectric constant of 219 for 1.2 μm $SrTiO_3$ films is consistent with the value of 220 reported for films by ion-beam sputtering using single target[7]. This value also approaches the $SrTiO_3$ single crystal dielectric constant of 300 measured at room temperature and 1 KHz[8]. It is expected that the dielectric constant of thinner films can reach ~ 220 provided that the films can be made without these factors which lowering the overall dielectric

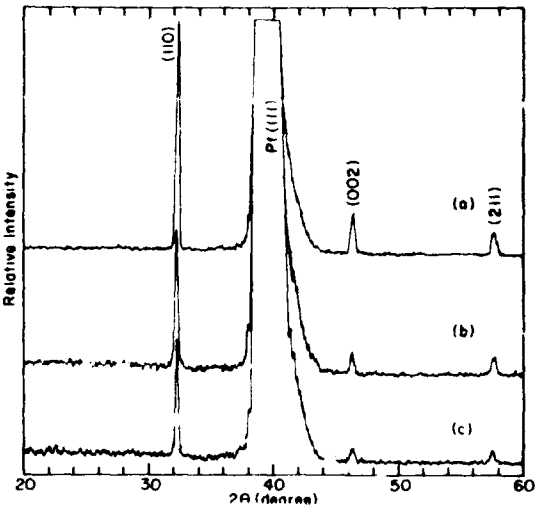


Fig.3: X-ray diffraction patterns for 1.2 μm $SrTiO_3$ films annealed at (a)700, (b)600, (c)500°C for 2 hrs.

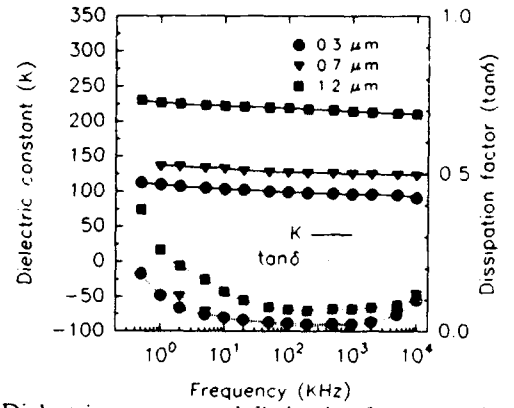


Fig.4: Dielectric constant and dissipation factor as a function of frequency for $SrTiO_3$ films of various thicknesses.

constant. One of the methods may be in-situ crystallization, which, at least can partly eliminate the surface effect, residual stress and structure inhomogeneities. More stoichiometric composition of the films is also very important. No frequency dependent dielectric dispersion was noticed and indicates the absence of extrinsic electrode contact effects[9].

Figure 5 summarizes the dielectric constants and dissipation factors for $BaTiO_3$, $SrTiO_3$ and BST films of various thickness annealed at 700°C for 2 hrs. Unlike $SrTiO_3$ films, the dielectric constants do not increase as film thickness increases from 0.7 to 1.2 μm for $BaTiO_3$ and BST films. This difference may be attributed to the less crystallinity of $BaTiO_3$ and BST films as can be seen in x-ray diffraction pattern (Fig. 2). Miyasaka et al[10]. also reported that for a given crystallization temperature, the degree of crystallization for $SrTiO_3$ thin films reaching to

that of bulk crystal is higher than that for $BaTiO_3$ by in-situ crystallization via rf-magnetron sputtering. The dielectric constant of BST films for 1.2 μm thickness does not show maxima in $BaTiO_3$-$SrTiO_3$ solid solutions, as reported by Miyasaka et al.[10], mainly due to the incomplete crystallization of films. In-situ crystallization and more stoichiometric films are needed to increase the dielectric constant of BST films, the work on which is in progress.

Typical C-V characteristics (measured at 100 KHz) of both MIM (metal-insulator-metal) and MIS (metal-insulator-silicon) configurations are shown in Fig. 6 for 0.3 μm $SrTiO_3$ films oven-annealed at 700°C for 2 hrs. The C-V characteristics of MIM configuration is found to be almost independent of bias voltage within the experimental range. The absence of hysteresis loop also indicates the paraelectric nature of $SrTiO_3$ films. The charge storage density can be calculated from this C-V measurement, and is found to be 15 fC/μm^2 at 5 V for 0.3 μm $SrTiO_3$ thin films. The charge storage densities for 0.7 and 1.2 μm films can be similarly calculated to be 8.0 and 6.7 fC/μm^2 at 5 V respectively. Note that the charge storage density is not inversely proportional to the thickness, due to the thickness dependent of dielectric constant. It is expected that charge storage density higher than 30 fC/μm^2 can be achieved provided that the extrinsic effects are minimized, such that the dielectric constant of the films is improved to ~ 220. Although bulk $BaTiO_3$ is ferroelectric at room temperature, the C-V characteristics of $BaTiO_3$ films is similar with Fig. 6, which indicates that $BaTiO_3$ thin films exhibit very little or no ferroelectric property under present processing conditions. The C-V characteristics of $SrTiO_3$ films in MIS structure resemble the ideal C-V curve of metal-SiO_2-Si structure[11], except that

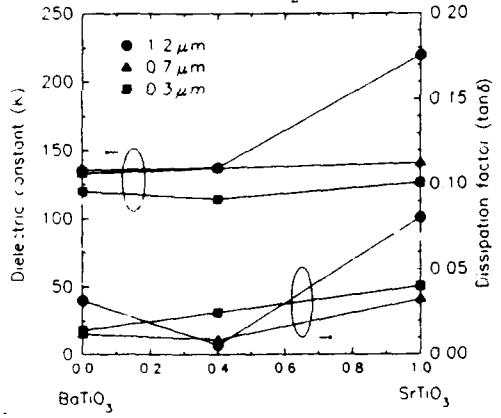


Fig.5: Dielectric constants and dissipation factors for $BaTiO_3$, $SrTiO_3$ and BST films annealed at 700°C for 2 hrs.

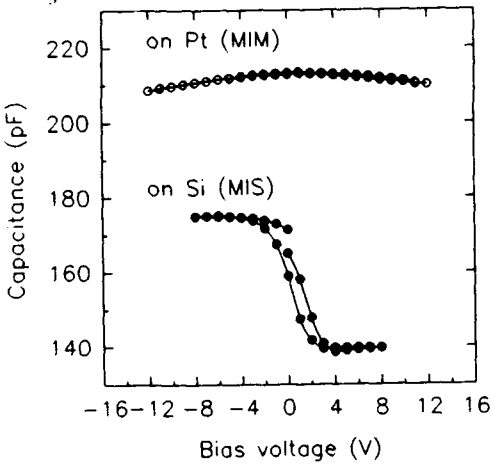


Fig.6: C-V characteristics of both MIM and MIS configurations for 0.3 μm $SrTiO_3$ films.

there exists a hysteresis loop. The calculated flat-band voltage is small (~-0.5 V) and so, the hysteresis may be attributed to the physcial interface layer effect. The presence of such interface layer can also be realized when we compare the accumulation capacitance (175 pF) with the value of 213 pF for MIM configuration at 0 bias voltage. Although the crystallinity (which will affect the values of dielectric constants as mentioned before) of $SrTiO_3$ films on Pt-coated Si and bare Si may not be the same, the results of X-Ray diffraction pattern show minor differences. The amorphous SiO_2 between films and Si substrates was reported for RF magnetron sputtered[12] $SrTiO_3$ and excimer laser ablated[13] $Ba_{0.7}Sr_{0.3}TiO_3$ films. The SiO_2 interface layer between films and Si can be formed either during deposition or post-deposition annealing processes. During deposition, Si is very easily oxidized in the plasma environment[14]. If we assume the lowering of capacitance is due to the low dielectric constant (K=3.9) SiO_2 layer in series with films, the thickness of this layer can be calculated to be ~25 Å, which is close to the results (30-100 Å) obtained by transmission electron microscopy (TEM) studies[13].

The I-V characteristics (measured by Keithley 617 ampmeter with metal-shielded sample box) of $SrTiO_3$ films with various thickness is shown in Fig. 7. If the film qualities are the same for films with different thickness, the three curves should have overlapped and the leakage current should have been linearly inverse to film thickness. The slopes of the curves can be estimated to be 1 and 4 for low and high voltage region respectively. The low voltage region (slope=1) is ohmic conduction, while the conduction mechanism may be attributed to trap filled space charge conduction at high field region, as the slope >2 normally indicates such mechanism[11]. The slopes changed gradually from 1 to ~4 for 1.2 μm films. One can see that the behavior of 0.7 μm films in Fig. 7 seems to be the combination behavior of 0.3 and 1.2 μm films. At low voltage (ohmic region) the conductivity is almost the same as that of 0.3 μm films, while at higher fields, it switches to the values of 1.2 μm films. This may imply that the surface layer effect or structure inhomogeneity mentioned previously dominates the I-V behavior in the ohmic region, while at higher fields, the effect is deminished. The leakage current density at electrical field of 0.1 MV/cm is calculated to be 5.8, 46 and 38 μA/cm^2 for films with thickness of 0.3, 0.7 and 1.2 μm respectively. Again, the lower leakage current density in the case of thinner films may be attributed to the higher density of voids for those films.

Figure 8 shows the I-V characteristics of 0.7 μm films for the three compositions, in which all curves can be devided into two

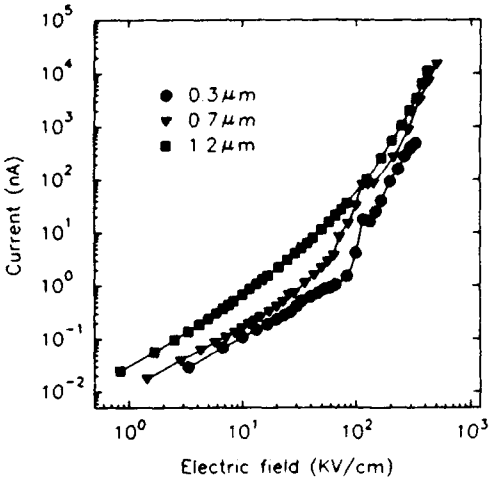


Fig.7: I-V characteristics of $SrTiO_3$ films with various thickness.

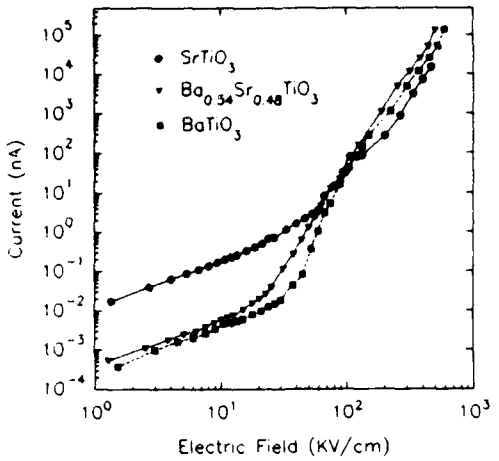


Fig.8: I-V characteristics of 0.7 μm films for the three compositions.

regimes, namely, low field (ohmic) and high field regimes. The leakage current of $SrTiO_3$ films in ohmic regime is about 1 order of magnitude higher than $BaTiO_3$ and BST films. The slope of high field regime for $SrTiO_3$ films is ~4, while that for $BaTiO_3$ and BST is ~5. These differences may be attributed to the structure nature of the films. As mentioned before, $SrTiO_3$ films contain higher degree of well developed crystallines (although contain some second phases due to nonstochiometry), while $BaTiO_3$ and BST films have lower degree of crystallinity. The well developed crystallized regions can be regarded as, to some extent, stress and defect-relaxed regions. So, the I-V characteristics of $SrTiO_3$ films would behave more like bulk materials, while that of $BaTiO_3$ and BST films is prevailed by extrinsic factors such as structure inhomogeneities. The lower leakage currents for $BaTiO_3$ and BST films at ohmic regime maybe due to such structure inhomogeneities such as non-crystalline phases (which, in general, has high small- signal resistivity). The different slopes at high field regime indicates that the conduction mechanisms are different for these films. It is well known that the electric field will develop mainly across the low dielectric constant high resistivity material in composites containing both high and low dielectric constant materials. The steeper slopes of $BaTiO_3$ and BST films at high fields are porbably due to the higher electric field concentration on the relative high defect-containing amorphous phases, causing ionization of defects and thus high leakage current. This argument can also explain the relatively faster time dependent dielectric breakdown (TDDB) for $BaTiO_3$ and BST films, in comparison with $SrTiO_3$ films, as shown in Fig. 9 where the 0.3 μm films were continously subjected to an electric field of 0.5 MV/cm. The TDDB failure mode is generally attributed to the migration of charged defects[15]. The above mentioned amorphous phases are probably responsible for the breakdown routes for the migration of charged defects, particularly in $BaTiO_3$ and BST films at such high field.

IV. Conclusions

In conclusion, the barium strontium titanate thin films and also the end members with perovskite structure have been successfully prepared by multi-ion-beam reactive sputtering technique. The MIBERS technique is shown to provide flexible control of the film compositions. The dielectric constants of barium strontium titanate films showed thickness dependent, with higher dielectric constants for thicker films. The interface layer, deducing from the C-V characteristics, exists between films and Si substrates. The charge storage density and leakage current density of 0.3 μm $SrTiO_3$ films are in the range projected for 64 Mb DRAM applications[1]. The electric properties of the films can be improved while the extrinsic factors lowering the dielectric constant are minimized. Due to the thickness dependence of dielectric constant, the thickness of the films has to be optimized for the application of higher memory density DRAMs. The overall results showed that barium strontium titanate thin films by MIBERS technique are suitable candidates for DRAM applications.

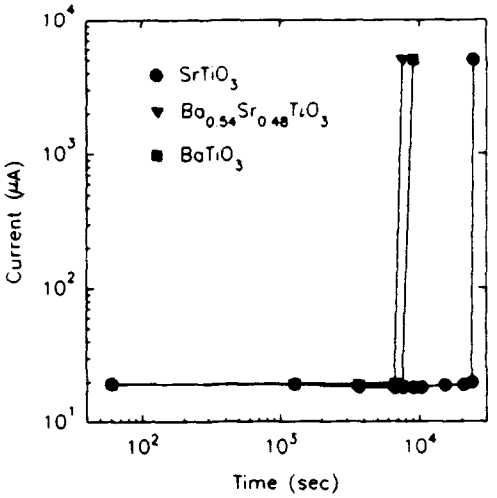


Fig.9: TDDB curves of 0.3 μm films for the three compositions.

ACKNOWLEDGMENT

This work was supported by a DARPA contract.

References

[1] L.H. Parker and A.F. Tasch, IEEE Circuits and Devices Magazine, p.17-26, Jan. 1990.

[2] U. Syamaprasad, R.K. Galgali and B.C. Mohanty, Mater. Lett., 7 [5/6] 197 (1988).

[3] S.B. Krupanidhi, H. Hu and V. Kumar, J. Appl. Phys., 71 [1] 376-88 (1992).

[4] G. Arlt, D. Hennings and G. deWith, J. Appl. Phys., 58, 1619 (1985).

[5] C. Feldman, J. Appl. Phys., 65, 872 (1989).

[6] J.C. Burfoot and J.R. Slack, Jpn. J. Appl. Phys., 28, Suppl. 417 (1970).

[7] S. Yamamichi, T. Sakuma, T. Takemura and Y. Miyasaka, Jpn. J. Appl. Phys., 30, 3193 (1991).

[8] A. Linz., Phys. Rev., 91, 753 (1953).

[9] M. Sayer, A. Mansingh, A.K. Arora and A. Lo, Integrated Ferroelectrics, 1, 129-46 (1992).

[10] Y. Miyasaka and S. Matsubara, 1990 IEEE 7th International Symp. on Appl. of Ferroelectrics, Urbana, Illinois, eds. S.B. Krupanidhi and S.K. Kurtz. p.121 (1992).

[11] S.M. Sze, *Semiconductor Devices Physics and Technology*, (Wiley, New York, 1985), p.

[12] S. Matsubara, T. Sakuma, S. Yamamichi, H. Yamaguchi and Y. Miyasaka, in Mat. Res. Symp. Proc., vol. 200, edited by R. Myers and A.J. Kingon (MRS Pittsburg, 1990) p. 243-53.

[13] R.F. Pinizzotto, E.G. Jacobs, H. Yang, S.R. Summerfelt and B.E. Gnade, Mater. Res. Soc. Fall Meeting, Boston, MA (1991).

[14] W.B. Pennebaker, IBM J. Res. Develop., Nov. p. 680 (1969).

[15] R. Waser, T. Baiatu and K.H. Haerdtl, J. Am. Ceram. Soc., 73 [6] 1645-53, 1654-62 (1990).

CONTROLLED ION BOMBARDMENT INDUCED MODIFICATION OF PZT THIN FILMS

H. Hu and S. B. Krupanidhi
Materials Research Laboratory
The Pennsylvania State University
University Park, PA 16802

ABSTRACT

The properties of PZT thin films can be modified by low-energy oxygen ion bombardment. The degree of (100) orientation, remanent polarization (P_r), coercive field (E_c) and dielectric constant (k) of the films were chosen to properly quantify the bombardment effect. It was found that these properties are strongly dependent on the ion beam flux and bombarding ion energy. The ion/atom ratios between 1.0 and 1.3 and the bombarding energies within the range of 60 to 80 eV are optimal to realize desirable property modification. Relative to the non-bombarding case, the bombardment could increase the P_r and k by up to 60% and 25% respectively, and reduce the E_c by about 20%. The improved properties also include crystallization temperature, switching characteristics, I-V behavior and time dependent dielectric breakdown.

I. INTRODUCTION

Controlled ion bombardment of thin films during growth has long been recognized as an important tool in modifying the growth process, microstructure and properties of resultant films.[1,2] Among most of the physical vapor deposition techniques, intrinsic energetic particle bombardment of the depositing films is generally observed. However, in plasma based deposition techniques such as magnetron sputter deposition, the flux density and the energy of the sputtering species are inseparable, unwanted bombardment is unavoidable and limited opportunities exist to introduce controlled bombardment. On the contrary, it is ideal for technique of ion beam sputter deposition to include a secondary low energy ion bombardment, since it is in this technique that the most controllable bombardment can be realized due to the unique features of the ion source (independent monitoring of ion flux and energy, localized plasma and low operating pressure).[2]

In a recent paper,[3] effects of low-energy oxygen ion bombardment on multi-ion-beam reactive sputter (MIBERS) deposited ferroelectric PZT films has been briefly reported. In this paper, property modification of the PZT thin films by the bombardment are systematically described.

II. EXPERIMENTAL

The MIBERS was used to deposit PZT films with a Zr/Ti ratio of 50/50 on Pt coated Si substrates at room temperature and at a deposition rate about 18 Å/min.[3] During the deposition, the growing films were directly bombarded by a low-energy oxygen ion (O_2^+/O^+) beam from a 3-cm Kaufman ion source in single grid configuration. The beam was directed to the substrates with an angle of incidence at about 25° from the normal of substrate surface. To compensate for the Pb resputtering by the direct bombardment and maintain nearly the same Pb content in the deposited films, the Pb flux was increased by about 15-19% excess (relative to the non-bombarding case) depending on bombarding conditions.[3] This was done by increasing the voltage and current of the sputtering ion beam of the Pb target. While all the other deposition parameters were fixed the same, the bombarding ion energy (E_b) and beam flux (I_b) were changed, one at a time, from run to run to render different bombardment conditions. The I_b was changed by adjusting the current of cathode filament of the ion source only, without varying the O_2 flow, so that the oxygen partial pressure of the deposition chamber was kept the same at 0.01 Pa for all the runs.[3] From the values of I_b and the measured deposition rates, ion/atom arrival ratio was calculated as one of the parameters expressing the bombardment effects.[2] Electron probe microanalysis (EPMA) showed that most of such deposited films have nearly the same Pb content (about 3% excess relative to the stoichiometry of PZT perovskite phase), except for a few deposited at too high E_b or I_b which are slight Pb deficient. The as-grown films were annealed at temperatures from 550 to 700°C in an oxidizing ambient to achieve crystallization.[3] The crystallized films were characterized in terms of structure and electrical properties to examine the bombardment effects with reference to the non-bombarded films.

The study was done in the following strategy. First, effects of the bombardment were qualitatively scanned, and several bombardment-sensitive properties were chosen in order to quantify the bombardment effect. Second, the dependencies of such properties on the bombarding parameters (ion/atom ratio and E_b) were investigated, thus defining an optimal range of the bombardment conditions.

III. RESULTS AND DISCUSSION

A. Qualitative descriptions

The first obvious effect of the bombardment is the reduction in crystallization temperature as shown in Fig.1. Films grown with the bombardment at an energy of 75 eV and an ion/atom ratio of 1.2 showed a dominant perovskite phase after annealing at 550°C for 2 h, while films grown without the bombardment assumed only a pyrochlore phase by the same annealing. This bombardment induced enhancement in crystallization was expected, since similar results have been widely reported for other materials.[1,2] The same effect was also observed for PZT films on bare Si substrates. It was found[3] that excess amount of Pb as high as 20-25% were needed for near

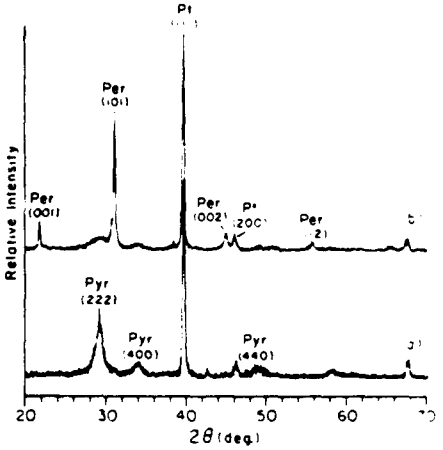


Fig. 1. XRD patterns of the films, annealed at 550°C for 2 h: (a) deposited without the bombardment; (b) deposited with bombardment at E_b = 75 eV and ion/atom = 1.2.

CH3080-0-7803-0465-9/92$3.00 ©IEEE

morphotropic phase boundary composition PZT films on bare Si substrates to attain perovskite phase by post-deposition annealing, and it was hard to induce perovskite phase in PZT films of near-stoichiometric Pb content (about 3% excess Pb) on bare Si substrates as shown in Fig.2.a. However, the PZT films of the same Pb content on bare Si substrate and annealed at the same condition assumed a dominant perovskite phase when the film growth was assisted by secondary ion

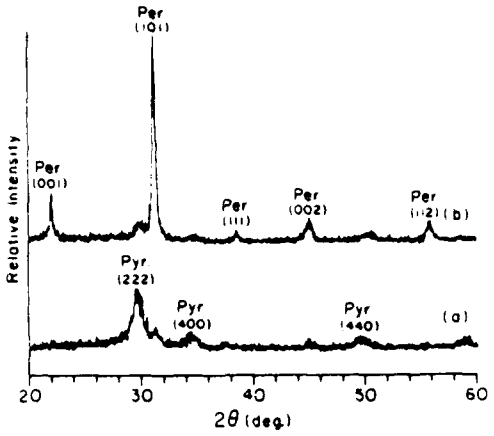


Fig. 2. XRD patterns of the films with near-stoichiometric Pb on bare Si and annealed at 650°C for 2 h: (a) without the bombardment; (b) with the bombardment at E_b=75eV and ion/atom=1.2.

bombardment, as shown in Fig.2.b. Such crystallization enhancement may in part be attributed to enhanced adatom mobility by the bombardment. Muller visualized the possible mechanism for such effect in molecular dynamics simulations of crystal growth.[2] Low energy ion bombardment provides local atomic rearrangement allowing atoms to relax into lower energy sites. In the present case, although the as-grown films were mainly amorphous, it was quite possible that nucleation may have been initiated during deposition by these local atomic rearrangement and relaxation, so that some micro-crystallites have already existed in the as-grown films although they were too small to be detected by x-ray diffraction (XRD). In addition, enhanced incorporation of oxygen in the films by the reactive oxygen ion (O_2^+/O^+) bombardment, as similarly reported,[4] may be the other reason for this crystallization enhancement. It has been noted that sufficient oxygen concentration is crucial for PZT films in forming and maintaining the perovskite structure.[5] It may also be worth mentioning that the as-grown amorphous films may have stored some extra energy due to the bombardment which may tend to be released during annealing process.[6] This would tend to lower the minimum annealing temperature of the films as well.

Figure 3 indicates that while non-bombarded films usually exhibits a random orientation with the XRD pattern similar to those of randomly oriented PZT ceramics, bombarded films can assume preferred (100) orientation. The degree of such preferred orientation seems highly dependent on the bombardment conditions (Fig.3(b) and (c)). This effect has often been attributed to the occurrence of recrystallization associated with channelling. Since there was no appreciable *in-situ* crystallization in the present case, it is thought that this preferred orientation might initiate from the possible *in-situ* nucleated micro-crystallites (as so mentioned above) which would act as seeds for the following crystallization. The other possible reasons may be associated with bombardment induced anisotropic stress[7] and the bombarding energy stored in the as-grown amorphous films[6] which may tend to cause a preferred

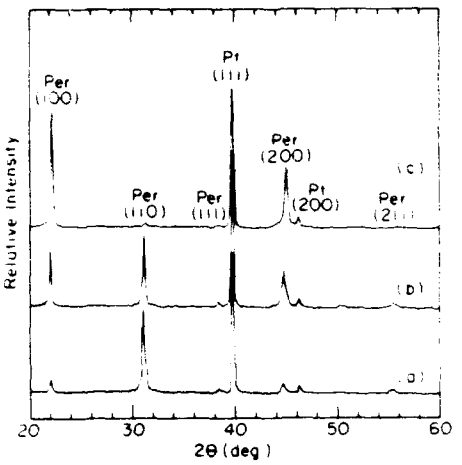


Fig. 3. XRD patterns of the films deposited (a) without bombardment, (b) with bombardment at E_b = 80eV and ion/atom=1.1, and (c) at E_b=80eV and ion/atom=1.4. (annealed at 580°C)

orientation of film upon instantaneous release during post-deposition annealing.[8]

Scanning electron microscopy shows the films grown with secondary ion bombardment showed denser structure and smoother surface than the non-bombarded ones. According to molecular dynamics simulations, the densification by off-normal incident ion beam bombardment was thought to be a natural consequence of the bombardment.[2] The surface smoothness would, of course, be improved with film density. Besides, enhanced adatom mobility makes a significant contribution to smoothing the surface.[2] The other aspect of the surface smoothing might be a consequence of resputtering. Since the sputter yield is strongly dependent on the angle of incidence of sputtering species, the result of energetic bombardment during deposition is often that topographical features which protrude up from the rest of the surface plane are more rapidly etched than the flat surface, resulting in a smoother and more featureless films.[2]

Figure 4 shows the evolution of both remanent polarization (P_r) and coercive field (E_c) of both kinds of the films with annealing temperature (T_a). It can be seen that for each T_a the bombarded films have higher P_r and lower E_c than

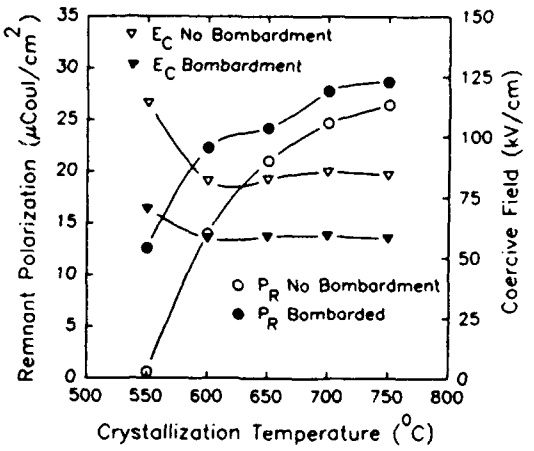


Fig. 4. Evolutions of P_r and E_c of the films (7000Å thick) with annealing temperature. Bombardment parameters were E_b = 75 eV and ion/atom = 1.2. Measuring frequency was 60 Hz.

the non-bombarded films. The following reasons were noted responsible for this superiority of the bombarded films: a) better crystallinity for each corresponding T_a since the bombarded films started to form perovskite phase at lower temperature, b) higher degree of (100) orientation, and c) better electrode-film interfaces attributed to denser and smoother film surfaces. Therefore, degree of (100) orientation and values of P_r and E_c were chosen as the basic bombardment-sensitive properties to quantify the bombardment effect. Low-field dielectric response, as a highly structure-sensitive property,[9] was also examined versus bombardment parameters. However, the effect of reduction in crystallization temperature (T_c) is not suitable to be used as a quantitative parameter since in the present case T_c can not be easily defined and detected due to the limit in sensitivity of XRD.

In addition to those mentioned above, some other electrical properties such as switching characteristics, I-V behaviors and time dependent dielectric breakdown were also found strongly affected by the bombardment, and are reported elsewhere.[10]

B. Bombarding-flux-dependent properties

The following results are based on films with similar thicknesses ranging from 1700 to 2100 Å, and the same annealing condition (580°C for 20 min).

Figure 5 shows the XRD intensity ratio $I_{(100)}/(I_{(100)}+I_{(110)})$ of the crystallized films as a function of the ion/atom ratio. For clarity, it is worth mentioning that in the present case "ion" denotes both O_2^+ and O^+, and "atom" includes Pb, Zr and Ti. It is noted from Fig.5 that the degree of (100) orientation increases monotonically within the range of

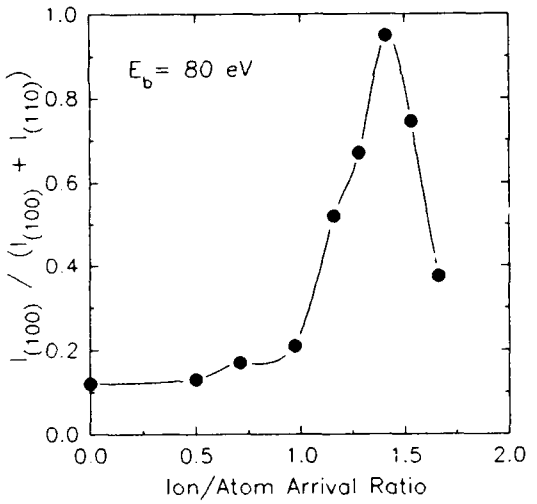


Fig. 5. XRD intensity ratio $I_{(100)}/(I_{(100)}+I_{(110)})$ of the crystallized films as a founction of ion/atom ratio.

ion/atom ratio from 0 to about 1.4, gradually from 0 to 1.0, and sharply from 1.0 to 1.4. Afterwards, however, it steeply decreases with ion/atom ratio. The trend of the evolution of preferential orientation with ion/atom ratio in the region lower than 1.4 is consistent with the behaviors of low-energy ion bombardment modified properties in general,[2] and confirms the strongly flux-dependent nature of the bombardment effect. It is of interest to note that there is a highly sensitive range between 1.0 and 1.4 of ion/atom ratio, which may be of particular importance in practice of property modifications. The abnormal steep decrease in the degree of (100) orientation in the higher ion/atom ratio region (>1.4) was presumably attributed to the deviation in the film stoichiometry, namely the resputtering-induced Pb deficiency by the high ion flux, as revealed by EPMA.

Figure 6 shows the P_r and E_c values as functions of the ion/atom ratio. Basically, the curve of P_r versus ion/atom ratio follows a trend similar to that of orientation in Fig.5, although it increases more steadily over the entire lower ion/atom region (from 0 to 1.3). It may be noted, however, that the peak position of ion/atom ratio is shifted to about 1.3, compared to 1.4 for the preferential orientation. This discrepancy may be stress related, since the films deposited at ion/atom ratio near 1.4 seemed highly stressed, as evidenced by the fact that thicker films (about 5000 Å) of this condition tended to buckle off after crystallization. It has been noted that the stress and preferential orientation are often highly correlated.[2] The further decrease in

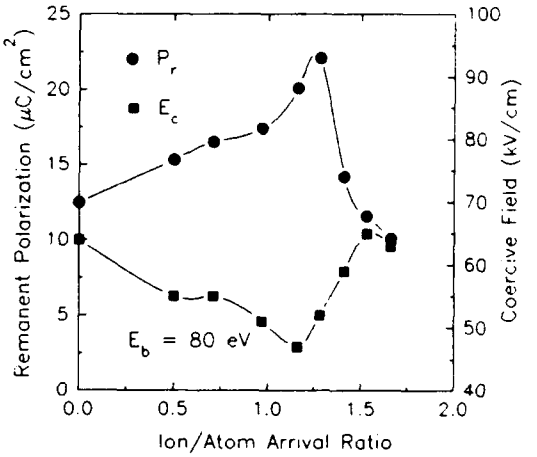


Fig. 6. Remanent polarization and coercive field of the films as functions of ion/atom ratio.

P_r with ion/atom>1.4 was again thought to be the consequence of Pb deficiency. It can also be seen from Fig.6 that the E_c changes with ion/atom ratio the other way against the P_r. This fact is of great significance as it allows optimum conditioning to attain as high P_r and as low E_c as possible simultaneously.

The dielectric constant (k) of the films at 100 kHz also showed a strong dependence on the ion/atom ratio, while the dissipation factor (tanδ) remained in the vicinity of 0.02 (Fig.7). Again, the k curve roughly mimics the P_r curve or orientation

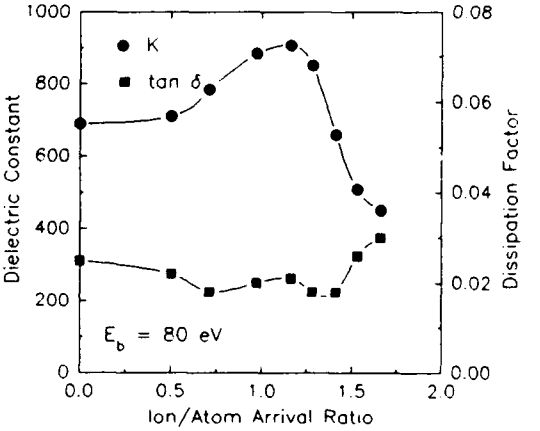


Fig. 7. Dependence of dielectric constant (k) and dissipation factor (tan δ) of the films (at 100 kHz) on ion/atom ratio.

curve, except for a little further shift in the peak position towards the lower ion/atom side and some broadening of the peak. Comprehensively, the ion/atom ratio for optimum combination of P_r, E_c and k in the present conditions seems within the range from 1.0 to 1.3. Relative to the non-bombarding case (zero point of ion/atom ratio), the increments in P_r and k could be about 60% and 25% respectively, while the reduction in E_c could be about 20%.

While the ion/atom ratio was kept constant at 1.28, the bombardment effect was also studied in terms of P_r and E_c versus the bombarding ion energy E_b. The results were summarized in Fig.8. It is shown that for E_bs from 60 eV to 80 eV, P_r had almost equally high values of about 20-22 $\mu C/cm^2$, while beyond 80 eV it continuously decreased as E_b increased.

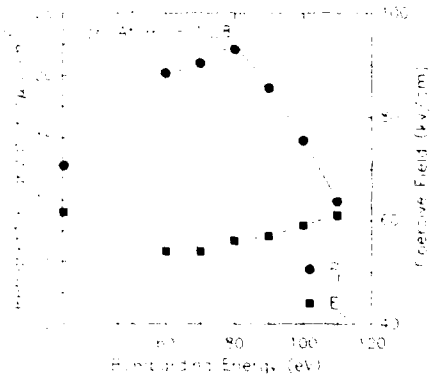


Fig. 8. Variation of remanent polarization and coercive field with bombarding ion energy.

Therefore, it seems that, within the range of experimental condition explored in the present work, the bombarding energies between 60 and 80 eV are optimal to realize effective property modification. Higher E_b was not suitable because it led to significant Pb resputtering,[3] which may have resulted in less effective bombardment for desirable modification[2] as well as Pb deficient in the films (observed by EPMA in the case of 110 eV).

IV. CONCLUSIONS

low-energy oxygen ion bombardment was successfully used to modify and enhance the physical properties of ferroelectric PZT thin films. The degree of (100) orientation, remanent polarization, coercive field and dielectric constant of the films were chosen to properly quantify the bombardment effect. It was found that these properties are strongly dependent on the ion beam flux (characterized by ion/atom ratio) and bombarding ion energy, and the ion/atom ratios between 1.0 and 1.3 and the bombarding ion energies from 60 to 80 eV are optimal to realize desirable property modification.

ACKNOWLEDGMENT

This work was supported by DARPA.

REFERENCES

1. J.E.Greene, S.A.Barnett, J.-E.Sundgren and A.Rochett, in *Ion Beam Assisted Film Growth*, edited by T.Itoh (Elsevier, Amsterdam, 1989), p.101.
2. E.Kay, S.M.Rossnagel, R.A.Roy, D.S.Yee, K.-H.Muller and R.M.Bradley, in *Handbook of Ion Beam Processing Technology*, edited by J.J.Cuomo, S.M.Rossnagel and H.R.Kaufman (Noyes, Park Ridge, New Jersey, 1989), pp.170, 194, 241, 300.
3. S.B.Krupanidhi, H.Hu and V. Kumar, J. Appl. Phys. 71, 376 (1992).
4. J.M.E.Harper, J.J.Cuomo, and H.T.G.Hentzell, J. Appl. Phys. 58, 550 (1985).
5. R.N.Castellano and L.G.Feinstein, J. Appl. Phys. 50, 4406 (1979).
6. S.V.Krishnaswamy, R.Messier, P.Swab, L.L.Tongson, and K.Vedam, J. Electron. Mat. 10, 433 (1981).
7. D.W.Hoffman, Thin Solid Films 107, 353 (1983).
8. R.Messier, T.Takamori and R.Roy, J. Non-crys. Solids 8-10, 816 (1972).
9. A.K.Jonscher, in *Physics of Thin Films, Vol.11*, edited by G.Hass and M.H.Francombe (Academic, New York, 1980), p.205.
10. H.Hu and S.B.Krupanidhi, in this issue of the proceedings.

MICROWAVE ASSISTED LOW TEMPERATURE SOLID PHASE CRYSTALLIZATION OF FERROELECTRIC THIN FILMS

Jiayu Chen, K. R. Udayakumar, and L. E. Cross
Department of Electrical Engineering & Materials Research Laboratory,
The Pennsylvania State University, University Park, PA 16802

Abstract

Sol-gel derived ferroelectric thin films (PZT, PLZT) have been successfully processed using the novel internal heating mechanism of microwave energy. Pyrolysis and crystallization of films in the microwave field was fast, and showed good selectivity. The nature of xerogel plays an important role in the pyrolysis and crystallization of these films because of good coupling of the microwave with these dipole containing species. The microwave processed films exhibit respectable dielectric and ferroelectric properties.

Introduction

The potential applications of ferroelectric thin films in microelectronics and micromechanics has been extensively researched in the past few years. It is a well established fact now that the quality of ferroelectric thin films is directly related to the fabrication process. A number of studies have shown, for instance, that rapid thermal annealing (RTA) is desirable in thin film processes; it supresses interface diffusion and evaporation of possible surface elements [1].

The use of microwave energy for the sintering of ceramics, although a relatively new development, has proliferated in recent years [2,3]. The potential of microwaves for reducing the processing temperature and maintaining uniform microstructure compared to conventional sintering techniques has been demonstrated unequivocally. This has been attributed to higher diffusion and lower activation energy for sintering that is characteristic of microwave energy. Fast heating speed as well as higher diffusion rates that are associated with microwave heating may be the reason for low temperature crystallization process. The microwave sintered PZT and PLZT ceramics have shown some superior properties compared to conventional sintering [4]. However, although the use of microwave energy for sintering serves to accelerate the process, due to the poor coupling between the microwave and the materials at room temperature, preheating the material upto a critical temperature at which it starts to couple effectively with the microwave is still a problem, especially at the low frequency of 2.45 GHz. Long time is expended in heating the samples to the critical temperature range, above which the dielectric loss of materials increase drastically, and consequently, rapid heating occurs.

In contrast to microwave heating, conventional heating takes place by radiation. There is a positive temperature gradient from the surface of the sample to its interior, which is not desirable in many cases. The overheated surface can cause strong reaction, change the stoichiometry, and form a surface layer. Another disadvantage of conventional heating is unselective heating; that is, the heat flux is merely related to the distance of the sample from the surface rather than the material properties. The microwave heating technique can overcome these two drawbacks. This is because the heat generated by microwave is due to the dielectric loss of materials.

In sol-gel processed thin films, prepyrolysed gel films contain many polar ionic groups, such as $CH_2CH_2OCH_3$, and other metal alkoxide polymers. These polar groups vibrate thermally and nonthermally under the electromagnetic field and are good microwave absorbers. Microwave energy couples to sol-gel films easily at room temperature, and heats the film to higher temperature; microwave energy couples with pockets of crystallized regions in the film, aided by the dielectric dissipation, to form grains until crystallization is completed. Many substrate materials, such as metals and quartz, are poor microwave energy absorbers [5,6]. Metals, for example aluminum and platinum, are good conductors which reflect microwave effectively. On the other hand, quartz and fused silica are almost microwave transparent at a wide temperature range. Ferroelectric thin films have great potential in being used as "smart coatings". Therefore, it is of interest to study the possible approaches to obtain high quality film coated composite.

The objective of this research has been to explore the feasibility of using microwave energy to process ferroelectric thin films with different substrates. The processing and properties of PZT and PLZT thin films with microwave treatment are described in this paper. Further details will be published elsewhere.

Experimental

The films were fabricated on platinized silicon by the sol-gel spin-on technique; the details of the procedure has been outlined in Reference 7. The samples were placed in the microwave cavity of a commercial 800 W microwave oven (2.45 GHz). The temperature was

CH3080-0-7803-0465-9/92$3.00 ©IEEE

measured by a thermo-couple which contacted the surface of the samples; to overcome the electromagnetic field interference of microwave, the actual value of the temperature was noted immediately upon switching off the power. The temperature versus time curve is shown in Figure 1.

The heated samples were characterized by x-ray diffraction (XRD) to determine the crystalline phase; the microstructures were examined by scanning electron microscope (SEM). Sputtered gold and/or platinum, over a 250 μm x 250 μm area, served as the top electrode of the films, forming metal-insulator-metal (MIM) capacitor structure for electrical characterization. The dielectric properties were measured by HP4191A impedance analyzer, and the ferroelectric polarization by a modified Sawyer-Tower circuit.

Results and Discussion

A constant microwave power input was applied. In the first few seconds, the temperature of the film rose very rapidly; the temperature shot up to 300 °C within 3-5 seconds and then slowed down. This is different from the sintering of bulk materials; the films have a large surface area for heat dissipation, and small mass. During microwave sintering, heat is generated from within the material; larger the sample area, faster is the heat dissipated. At a given input power, the sample reaches an equilibrium temperature. This feature is helpful in preventing a fast thermal runaway and controlling the processing temperature. Thermal runaway is not desirable in the pyrolysis and crystallization process of thin films since temperature control is difficult, and can cause overheating, even partial melting of the specimen.

Figure 1 is a plot of the film surface temperature as a function of time. The rapid rise in temperature proves that the gelled films contain polar groups which have good coupling with microwave energy. Polymer components can be considered as sintering aids which couple microwave at a lower temperature range and burns off at higher temperatures. This is an advantage in using microwave to treat sol-gel derived thin films. The temperature difference measured between the substrate and the surface of the films was larger than several hundred degrees which proves the selective feature of microwave heating.

Crystallization of thin films is a function of the local annealing temperature. The local temperature depends most importantly on the local dielectric constant and other properties, such as heat capacity and density; the temperature in turn affects the local dielectric constant. The XRD patterns, displayed in Figure 2 as a function of temperature, reveals that the film is completely crystallized when annealed at 500° C for 5 minutes. The enhanced crystallization characteristics were most likely the result of the extremely fast heating rates achievable by the unique direct heating and nonthermal excitation mechanism. Fig. 3 illustrates the x-ray diffraction pattern of PZT films coated on NiTi alloy substrate.

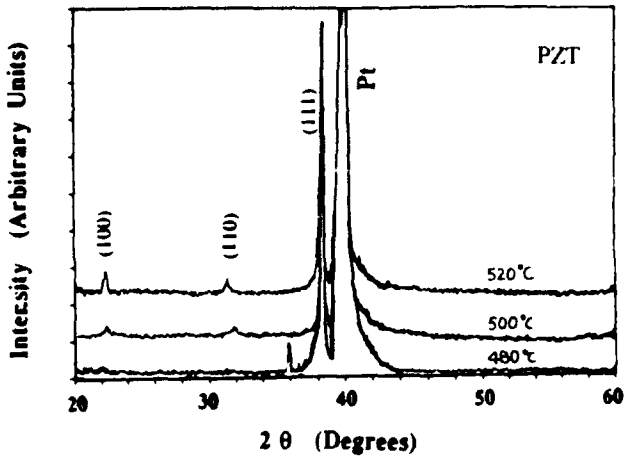


Figure 2 XRD patterns of the PZT films microwave annealed in the range of 480-520 °C for 5 minutes. The films are completely crystallized by 500 °C

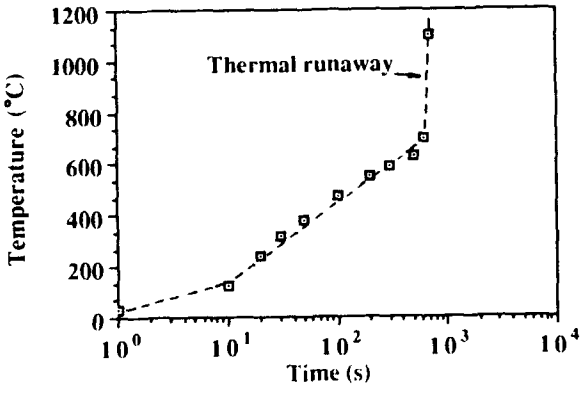


Figure 1 Plot showing the surface temperature of the film as a function of time. Note the three distinct regions in the temperature profile.

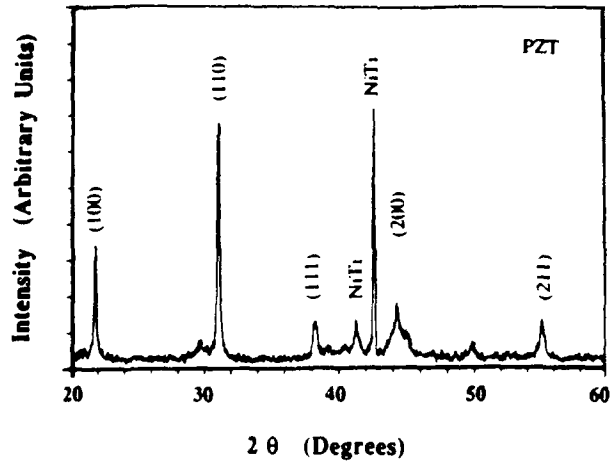


Figure 3 XRD pattern of PZT film on TiNi shape memory alloy substrate.



Figure 4 Planar SEM micrograph of PZT film microwave annealed at 500 ^{0}C for 5 minutes.

The microstructure of the sample, shown in Figure 4, is a testimony to the ability of the fast thermal process to produce high quality microstructure. Using a linear intercept method, the average grain size of the microwave processed films was found to be 0.1-0.2 μm. The uniform microstructure accrues from the microwave field interacting with the material at the molecular level and exciting more nuclear sites than simple thermal excitation.

Figure 5 is a plot of the dielectric permittivity and loss factor (tan ∂) of 0.48 μm thick PZT films against microwave annealing temperature; the dielectric constant and tan∂ were 820 and about 0.03 respectively at 530^{0}C, which are comparable to the conventionally processed thin films. The P-E hysteresis loop oscillographs of the films constitute Figure 6; the remanent polarization show respectable values of approximately 9 μC/cm^2 and 6 μC/cm^2 for the PZT and PLZT films respectively.

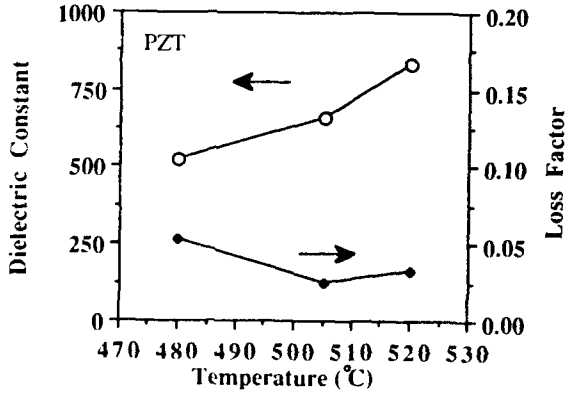


Figure 5 Plot of weak field dielectric constant and loss factor as a function of annealing temperatures

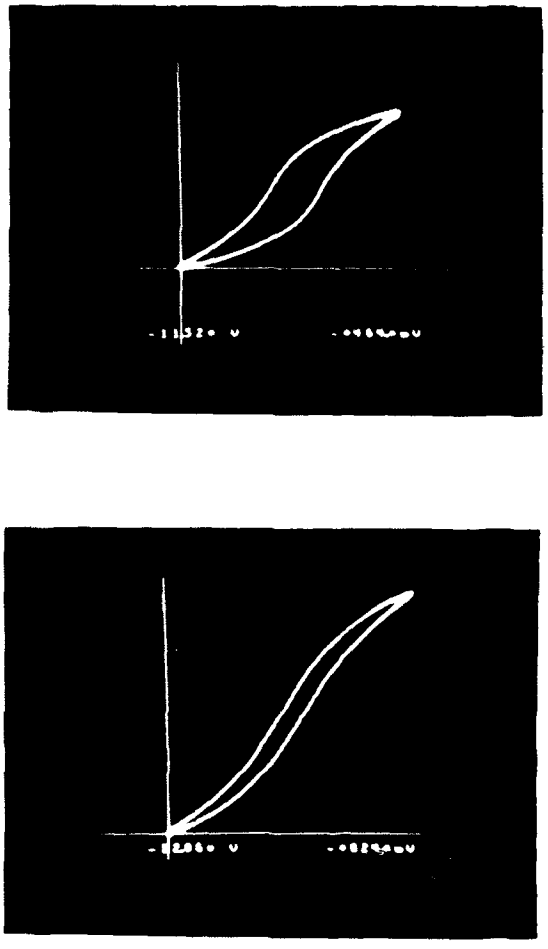


Figure 6 Polarization-Electric field hysteresis loops of PZT (top) and PLZT (bottom) thin films

Conclusions

Sol-gel derived ferroelectric thin films, such as PZT and PLZT, have been processed by microwave energy; the attractive feature of the process resides in quickly completing the pyrolysis and crystallization steps. The pre-pyrolysed gel films have good microwave absorption which may be attributed to the existence of polar groups in the films. Selective heating is another unique characteristic of the microwave process which holds promise for composite materials fabrication.

References

[1] J. Chen, K. R. Udayakumar, K. G. Brooks, and L. E. Cross, "Rapid thermal annealing of sol-gel derived PZT thin films" J. Appl. Phys., pp. 4465-69, May 1992.

[2] W. Sutton," Microwave processing of ceramic materials", Ceramic Bulletin, vol. 68, pp. 376-386, Feb. 1989.

[3] R.E. Newnham, S. J. Jang, M. Xu, and F. Jones, "Fundamental interaction mechanism between microwaves and matter", Proc. of the Symposium on Microwaves, 93rd Annual Meeting of the ACS, Cincinnati, OH, Apr. 29-May 3, pp. 51-68, 1991.

[4] W.B. Harrison, M. Hanson, and B. G. Koedke, "Microwave processing and sintering of PZT and PLZT ceramics", Mat. Res. Soc. Symp. Proc., vol 124, pp. 279-285, 1988.

[5] Z. Fathi, I. Ahmad, and D. E. Clark, "Microwave processing of sol-gel derived potassium niobate", Mat. Res. Soc. Symp. Proc., vol. 180, pp. 401-406, 1991.

[6] S. Sirapanan, M. E. Mullins, and B. C. Cornilsen, "Microwave drying of borosilicate gels" Mat. Res. Soc. Symp. Proc., vol. 189, pp. 309-325, 1991.

[7] K. R. Udayakumar, J. Chen, S. B. Krupanidhi, and L. E. Cross, "Sol-gel derived PZT thin films for switching applications", Proceedings of the 7th IEEE International Symposium on Application of Ferroelectrics, 1990, pp. 741-43.

PREPARATION OF LEAD-ZIRCONATE-TITANATE THIN FILMS BY REACTIVE RF-MAGNETRON COSPUTTERING USING MULTI-ELEMENT METALLIC TARGETS AND THEIR EVALUATIONS

TAKASHI YAMAMOTO, TOSHINORI IMAI AND *TADASHI SHIOZAKI
DEPT. OF ELECTRICAL ENG., NATIONAL DEFENSE ACADEMY, YOKOSUKA 239 JAPAN
*DEPT. OF ELECTRONICS ENG., KYOTO UNIVERSITY, KYOTO 600 JAPAN

Abstract

As-sputtered ferroelectric lead-zirconate-titanate (PZT) thin films were prepared on a Pt(800nm)/Ti(350nm)/SiO_2(150nm)/Si(100) substrate at a comparatively low temperature around 500°C. The compositional variation of Zr/Ti ratio in the deposited $Pb(Zr_{0.53}Ti_{0.47})O_3$ film were discussed as a function of rf-power, sputtering gas pressure and substrate temperature. Dielectric constant in a 2.0 um-thick film was εs = 370 by an oscillation level of 1V at 60 Hz. The remanent polarization polarization and the coercive field were 5.2 uC/cm^2 and 20 KV/cm, respectively.

§1. Introduction

Lead-zirconate-titanate, $Pb(Zr_xTi_{1-x})O_3$, thin films have attracted much attention for non-volatic randam access memory (ferro-RAM) for their polarization reversal characteristics by electric field and for dynamic-RAM capacitors due to their high dielectric constants compared with SiO_2 on Si.

Several deposition methods have been reported using mixed oxide powder of PbO and TiO_2 , $Pb(Zr_xTi_{1-x})O_3$ ceramics target[1] and metal target[2,3]. The mixed oxide powder supperting has disadvantage such as the difficulty in applying a large rf-power due to the low melting temperature of PbO. The ceramic-target sputtering has also disadvantages such as difficulty in fabricating a large target, the difficulty in applying a large rf-power due to the low thermal conductivity of ceramic target, and as a both common disadvantage, poor compositional transferability from the target to the film.

In this paper, $Pb(Zr_{0.53}Ti_{0.47})O_3$ (MPB) thin films were prepared by a reactive rf-magnetron sputtering in $Ar:O_2$ = 50:50 pre-mixed gas using Pb, Zr and Ti metal targets. Metal target sputtering has several advantages compared with the abovementioned other sputterings ; 1) highly stability and purity of target, 2) possiblity to apply a large rf-power due to the high thermal conductivity. However there existed some complexities related with sputtering coefficients of metal used as a target.

§2. Experimental procedure

Typical schematic diagram of the multi-element metal targets is given in Fig. 1. The diameter of metal Pb and the ratio of the Zr/Ti area were determined by the modified Sigmund's method[6] ; 1) coefficient of utilization for target (magnetic flux distribution), 2) coefficient of sputtering for Pb, Zr and Ti metal (calculated by 350 and 700 eV as a Ar/O_2 = 50/50, 3) Pb diameter due to Pb/(Zr+Ti)=1/1, 4) ratio of Zr/Ti. Figure 2 shows the calculated areas of component metal (Pb, Zr and Ti) as a function of Zr ratio in the $Pb(Zr_xTi_{1-x})O_3$ component, where solid and broken lines (marks) show the calculation using the coefficients of sputtering of 350 and 700 eV, respectively. The quantity of Pb became slightly larger in $PbZrO_3$ than in $PbTiO_3$. From calculation, the diameter of Pb metal was 41.08mm and the outside and inside diameters of Zr metal were 90.00 and 41.08 mm, respectively in the case of 350 eV (correspond to the rf-power of 100 W). The 21 pieces of Ti metal (5x48.92x 0.5 mm) were prepared in the case of $Pb(Zr_{0.53}Ti_{0.47})O_3$ composition and rf- power of 100 W.

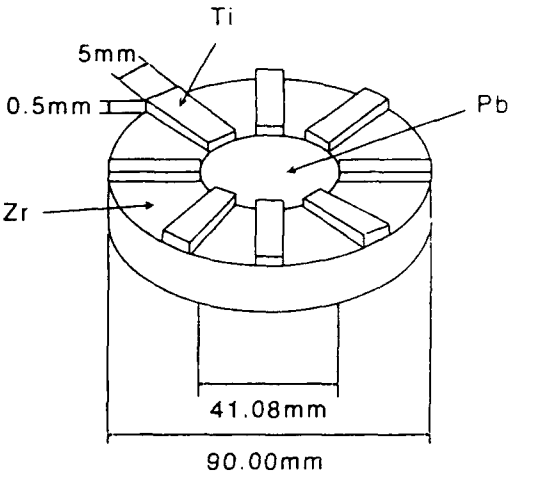


Fig. 1 Shematic figure of the multi-element target

Table 1 shows the fabrication conditions

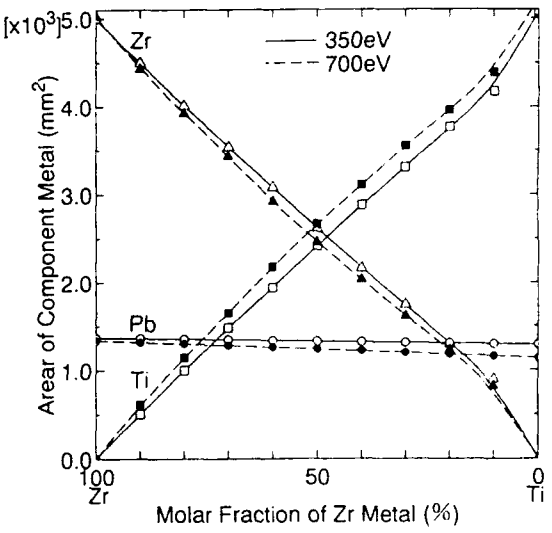


Fig. 2 Calculated area of Pb, Zr and Ti metal as a function of Zr mole ratio in $Pb(Zr_xTi_{1-x})O_3$

CH3080-0-7803-0465-9/92$3.00 ©IEEE

		Ti	Pt
RF Power	(W)	100	100
Temperature	(°C)	220	600
Gas Pressure	(Pa)	1.0	1.0
Sputtering Time	(min)	15	2
Target-Substrate Distance	(mm)	35	35
Sputtering Gas		Ar	Ar
Thickness	(Å)	3500	8000

Table 1 Sputtering conditions for Ti and Pt films as lower electrodes

RF Power	(W)	100~200
Temperature	(°C)	450~550
Gas Pressure	(Pa)	0.5~4.0
Sputtering Time	(min)	60~300
Target-Substrate Distance	(mm)	35
Sputtering Gas		Ar/O2=50/50

Table 2 Sputtering conditions for as-sputtered PZT53/47 film

of Ti and Pt lower electrodes on SiO2/Si substrate. The Ti film was (010)-oriented. The Pt film was (111)-oriented and the rocking curve, 2θ, of (111)-oriented Pt film was 0.085. Table 2 shows the fabrication conditions of $Pb(Zr_{0.53}Ti_{0.47})O_3$ (PZT53/47) film. As sputtered PZT53/47 film were a perovskite single phase by the substrate temperature above 500°C, a pyroclore single phase below 450°C and a mixed phase from 450 to 500°C. The typical deposition rate of as-sputtered PZT53/47 film was 0.26 um/h by a rf-power of 100 W and 1 Pa.

The film configuration in this study was a Au/PZT film/Pt/Ti/SiO_2/Si(100) substrate. Figure 3(a) and (b) show the stress and displacement distribution in PZT (1000nm)/Pt (300nm)/Ti(100nm)/SiO_2(100nm)/Si(1mm) substrate, when cooled to 25°C from 500°C by a finite element method. The compressive force (marked by ⟷) in the upper half-part of the PZT film and the tensional force (marked by ——) in the lower half-part of the PZT film were predominant. The PZT film was uniformly shrinkaged, because the compressive and tensinal forces maintained the balance. On the other hand, in the PZT film/Si(100) configuration, i.e. without the lowder electrode of Pt, the compressive force in PZT film was predominant and as a result PZT film was bended with a concave surface.

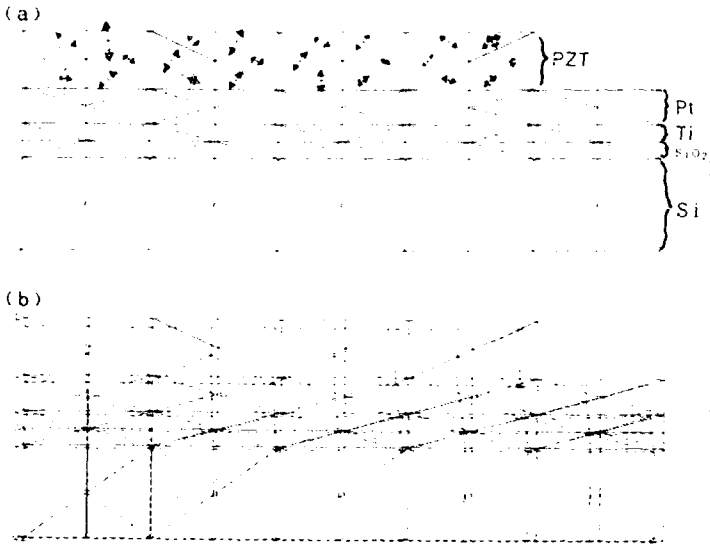


Fig. 3 (a) stress (b) displacement distribution in PZT film (1um))/ Pt(300nm)/Ti(100nm)/SiO2(100nm)/ Si(1000um)

(a) compressive stress : ⟷ tensional stress : ——
(b) solid line : 500°C broken line : 25°C

§3. Results and discussion

Figure 4(a) and (b) show the X-ray diffraction pattern (XRD) of as-sputtered PZT53/47 film on (111)Pt/(010)Ti/SiO_2/Si(001) and on non-oriented Pt/(010)Ti/SiO_2/Si(001). The relations of XRD peak intensities in Fig. 4(b) were the same as those of powder pattern in PZT53/47, i.e. the (101) peak was most strongest and this PZT53/47 film was identified as a non-oriented film, while in the case of PZT53/47 film on (111)Pt, the XRD intensity of (111) peak from PZT became stronger compared with other XRD peaks, i.e. the (111) orientation of PZT film became dominant.

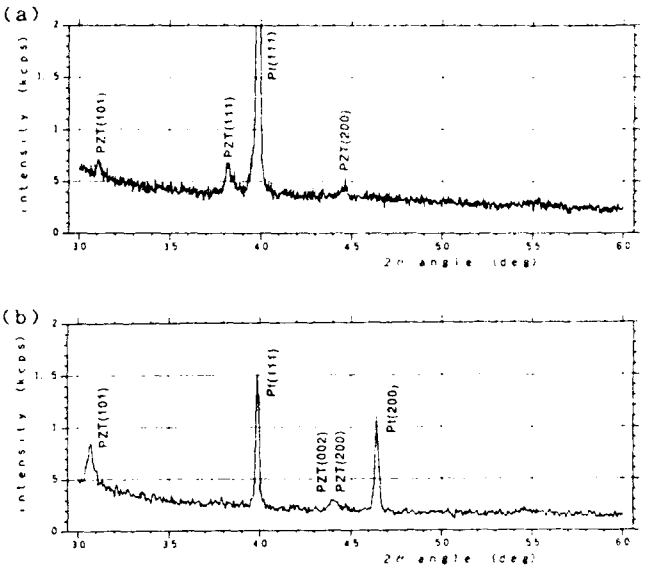


Fig. 4 XRD patterns as sputtered PZT53/47 films on (111)Pt/(010)Ti/SiO_2/Si (a) and on non-oriented Pt/(010)/ SiO_2/Si(b)

Various characteristics depend on strongly the composition in $Pb(ZrxTi_{1-x})O_3$, i.e. Zr/Ti ratio. The composition near the Zr/Ti=53/47 is well known as a MPB and a mixed phase of tetragonal and rhombohedral. The chemical composition of the deposited film was identified by the XRD method ; d constant(Å) and 2θ of XRD was almost linearly changed by the x in $Pb(ZrxTi_{1-x})O_3$, as shown in the measured values (white circles and squares) of $Pb(Zr_{0.53}Ti_{0.47})O_3$, $PbTiO_3$ and $PbZrO_3$ powder as a reference in Fig. 5, while the chemical composition of the deposited film depends on the area of metal (Fig.1) calculated by the coefficients of sputtering for individual metal. The d-constant and 2θ from the (111) XRD peak in PZT film prepared by a rf-power of 100 W , a sputtering gas pressure of 1 Pa and a

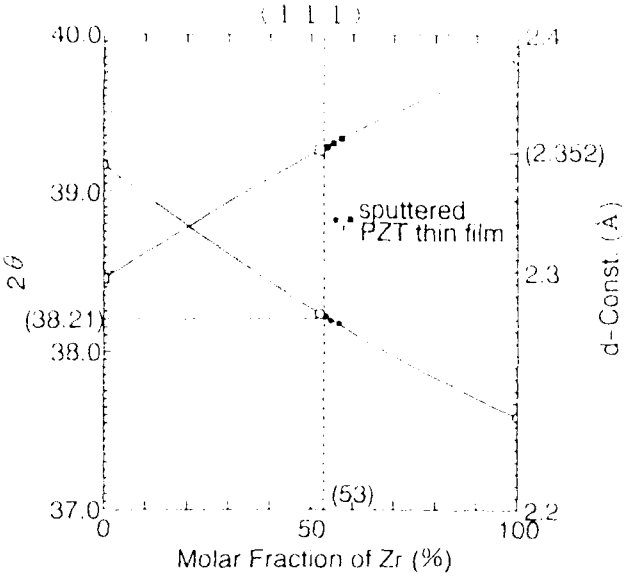


Fig. 5 d-constant and 2θ in (111) peak as a function of Zr in $Pb(Zr_xTi_{1-x})O_3$
White circles and squares : ceramics
Black circles and squares : film

substrate temperature of 500°C. As can be seen in good agreement between the expected chemical composition calculated from area of component metal and d-constant and 2θ measured from as-sputtered PZT film, the chemical variation in as-sputtered PZT film can easily be estimated from (010),(111), (002) XRD peaks. Figure 6 shows the comparisions of d-constant in PZT film

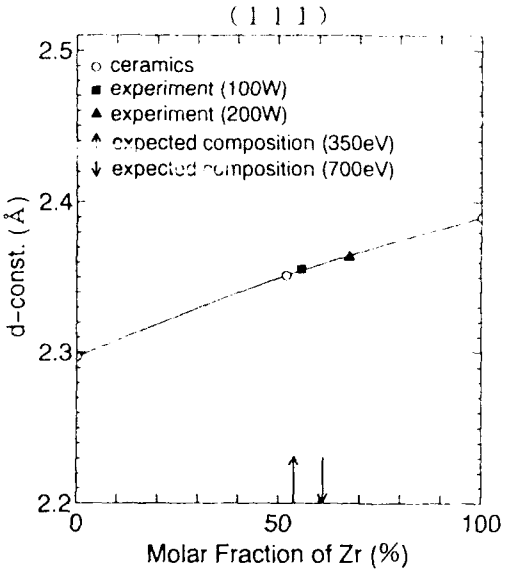


Fig. 6 d-constant in (111) peak from PZT film prepared by the rf-powers of 100 W (■) and 200 W (▲) and the expected composition calculated from 350 eV (↑) and 700 eV (↓) as a function of Zr in $Pb(Zr_xTi_{1-x})O_3$

prepared by the rf-powers of 100 and 200 W and other fabrication conditions were the same.

As can be seen, the d-constant in PZT film prepared by a 100 W was shifted to those of Zr-rich PZT. These results suggests that the coefficient of sputtering (350 eV) used for Pb, Zr and Ti was suitable value for a rf-power of 100 W. Therefore, when applied the rf-power of 200 W (700eV as a linear relation), the quantities of Pb and Zr for PZT53/47 film should be decreased, and that of Ti should be increased, respectively as shown in Fig. 2 compared with those for 100 W. however due to change only a rf-power, the chemical composition of as-sputtered PZT film prepared by a 200 W shifted to Zr-rich side in $Pb(Zr_xTi_{1-x})O_3$.

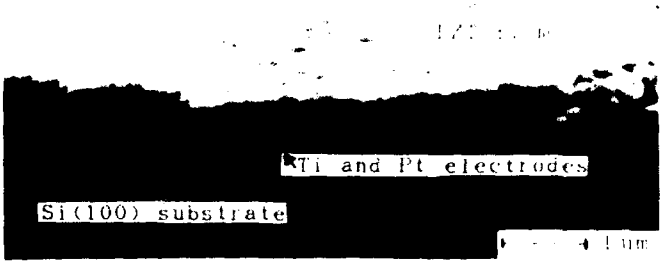


Fig. 7 Cross section of PZT film on Pt/Ti/SiO2/Si substrate

Figure 7 show the SEM micrograph of as-sputtered PZT53/47 film on (111)Pt/(010)Ti/SiO_2/Si substrate. Preparation conditions are as follows : substrate temperature = 500°C, sputtering gas pressure = 1 Pa, rf-power = 100 W. Typical columm structure could be observed from the cross section. These film surface wassmooth compared with that of PZT film on non-oriented Pt/(010)Ti/SiO_2/Si substrate.

Dielectric constants in 2.0 um thick film were almost εs = 370 by the oscillation level of 5 mV to 1 V. The remanent polarization and the coercive field were 5.2 uC/cm^2 and 20 KV/cm, respectively. These values were small compared with those of ceramics, due to the stress in PZT film as discussed in Fig. 3 and the film thickness effect.

References

1) K.Iijima, I.Ueda and K.Kujimiya, "Preparation and Properties of Lead Zirconate-Titanate Thin Film", Jpn. J. of Appl. Phys. ,30, 9B (1991) 2149-2151.
2) A.Croteau, S.Matsubara, Y. Miyasaka and N. Shohata, "Ferroelectric Pb(Zr,Ti)O_3 Thin Film prepared by Metal Target Sputtering" Jpn. J. Appl. Phys., 26 (1987) Supplement 26-2, 18-21.
3) T.Hase, T. Shiozaki, "Preparation and Switching Kinetics of Pb(Zr,Ti)O_3 Thin Films deposited by reactive Sputtering" Jpn. J. of Appl. Phys., 30, 9B (1991) 2159-2162.

A CRITICAL REVIEW OF PHYSICAL VAPOR DEPOSITION TECHNIQUES FOR THE SYNTHESIS OF FERROELECTRIC THIN FILMS

Orlando Auciello[1,2] and Angus I. Kingon[2]
1. MCNC, Center for Microelectronics, 3021 Cornwallis Rd., RTP, NC 27709-2889
2. N. C. State University, Department of Materials Science and Engineering, Raleigh, NC 27695-7919

Physical vapor-deposition techniques such as plasma and ion beam sputter-deposition and pulsed laser ablation-deposition are extensively used for synthesizing single and multicomponent and multilayered thin films, particularly multicomponent oxide ferroelectric thin films. The optimization of deposition conditions, thus film composition, microstructure and properties requires a good understanding of the basic phenomena involved in ion and laser-solid target interaction and related processes such as sputtering, ablation, transport, and deposition of material onto appropriate substrates. Basic phenomena related to these techniques and their influence on processing-composition-microstructure-property relationships of ferroelectric thin films are discussed in view of recent experimental and theoretical work performed by several groups, with the ultimate goal of optimizing the mentioned deposition techniques and scale them up for application in the fabrication of ferroelectric thin film-based devices.

Introduction

Intensive research on the synthesis, characterization, and determination of processing-microstructure-property relationships of multicomponent oxide thin films has been performed during the last five years on the new oxide high temperature superconductor (HTSC) materials, and on ferroelectric and electro-optic multicomponent oxides. Research is being performed to develop both the scientific bases for the synthesis and characterization of oxide films and the technological applications to devices.

There are various areas of scientific interest related to the study of oxide thin films, which can have important implications for technological applications of these materials in manufacturing advanced thin film-based devices. The areas of interest include:

- New properties or phenomena (especially via heterostructures and superlattices).
- High permitivities such as those characteristics of ferroelectric materials, which result from their high spontaneous polarizations, partly originated in the atomic structure of the material and partly as a result of polarization reversal in the presence of an electric field applied on either a macro- or a nano-scale (relaxor materials).
- Higher permitivities achieved via modulated structures.
- Induced birefringence using a "superalloy."
- Metal - metal oxide heterostructures.
- Field induced ferroelectric - antiferroelectric phase transition in ferroelectric materials, such as that observed in certain lead zirconate titanate (PZT) and lead lanthanum zirconate titanate (PLZT) solid solutions.
- Low permitivity dielectric (≤2) materials, which are required for use as substrates and interlayers in microwave devices. One method of engineering low permitivity materials is to produce porous (composite) materials, which can be achieved by vapor phase deposition under controlled conditions.

The technological importance of multicomponent oxide ferroelectric thin films is reflected in the wide range of applications in microelectronic hybrid and discrete devices, which are currently under investigation [1]. It is of value to consider their current application in discrete devices, which utilize the full range of bulk oxide properties, including dielectric, ferroelectric, piezoelectric, electrostrictive, pyroelectric, optical, electro-optic and magnetic properties, as well as electronic and ionic conduction. Applications include multilayer capacitors, boundary layer capacitors, varistors, PTC devices, NTC devices, gas sensors, radiation detectors, temperature sensors, transducers, switches, shutters, MHD electrodes, fuel cell electrolytes, concentration cell electrolytes, and electrolytes for high energy density batteries [1].

In reviewing the device applications mentioned above, it is worth noting that the use of oxide films integrated with semiconductors has been limited to the simple oxides. The wide range of properties which are available via the multicomponent oxides are currently not being exploited in microelectronic devices. The reason is primarily because of the difficulty in reliably producing device-quality films directly on large semiconductor substrates, in a way that is fully compatible with existing semiconductor process technology. As it has been pointed out in recent reviews [2], these requirements have not yet been met, despite studies of a variety of deposition processes. Various vapor phase deposition techniques [plasma and ion beam sputter-deposition (PSD and IBSD respectively), pulsed laser ablation deposition (PLD), electron beam or oven-induced evaporation for molecular beam epitaxy (MBE), and chemical vapor deposition (CVD)] have been applied to produce multicomponent oxide thin films (see refs. [3-5] for recent reviews).

Currently, a large part of research efforts on multicomponent oxide films is directed at establishing suitable synthesis/processing methods, and at investigating processing–microstructure-property relationships. Physical vapor-deposition techniques are among the most utilized methods currently applied to the synthesis of ferroelectric thin films. Plasma sputter-deposition (PSD), ion beam sputter-deposition (IBSD) and pulsed laser ablation-deposition (PLAD), three of the most extensively used techniques are the subject of this review.

Plasma Sputter-Deposition: Systems, Basic Deposition Processes and Films Characterization

Several variations of the plasma sputter-deposition technique have been developed and are still under investigation to produce multicomponent oxide thin films, including HTSC, ferroelectric, and electro-optic materials. The development of plasma sputter-deposition techniques for the application described in this review is being done with a view at using them not only in research laboratories, but also for applications in the industry for manufacturing thin film-based devices. In the later case, the development of automated systems for the production of oxide films in an integrated deposition/processing cycle will help meet the requirements for large scale integration of oxide materials in the fabrication of oxide/semiconductor thin film-based devices.

A manufacturing process for producing multicomponent oxide thin films should at least include the following characteristics: (1) applicability of the processes to deposition of materials with different physical and chemical properties, (2) compatibility with integrated device processing, which includes production of as-deposited films with specific microstructures (perovskite, for HTSC, ferroelectric and electro-optic materials) on substrates at the lowest possible temperature, (3) production of device-quality, epitaxial films with specific properties (high transition temperature T_c and critical currents, for HTSC thin films; high electrical polarizability for ferroelectric materials; or high light transmission coefficients for electro-optical thin films) (4) simple and low cost deposition with capacity for high deposition rates, (5) ability to produce patterned structures, superlattices and layered heterostructures, and (6) reproducibility of the deposition process.

Basic phenomena occurring during the interaction of plasmas with the targets and substrates, used to synthesize films, are important in that they can determine to a large extent the composition, microstructure and properties of the films. Therefore, a brief discussion of basic plasma-material interaction and transport of species through the plasma is presented when describing the plasma sputter deposition technique. A more extensive review can be found elsewhere [6]. It is impossible to cite all the literature in this rapidly growing field of research; therefore, only representative references are cited. In addition, the discussion of plasma sputter-deposition of ferroelectric thin films is limited to the lead-titanate family of materials.

CH3080-0-7803-0465-9/92$3.00 ©IEEE

Plasma Sputter-Deposition Systems and Related Phenomena

In most plasma processing techniques [6], deposition of ferroelectric films is achieved by sputtering targets exposed to a dc or rf plasma discharge generated in a high vacuum chamber back-filled with an inert (commonly Ar) or oxidant (generally O_2) gas, or a mixture of both, to a pressure of 0.5-170 mTorr (dc or rf diode sputtering, or magnetron sputtering). Most studies on plasma sputter-deposition of ferroelectric films have been performed in the 5-50 mTorr pressure range. Various target-substrate geometries have been used as knowledge on plasma-target/substrate interaction effects progressed, revealing the existence of phenomena that can strongly affect the film deposition process. For example, the most common geometry, initially used to deposit HTSC and ferroelectric thin films, consisted of a multicomponent oxide target facing a substrate such that both surfaces were parallel to each other with typical separations of 2 to 10 cm (see Fig. 1 for example). The initial work on HTSC and ferroelectric thin film synthesis, involving mainly the magnetron sputtering technique and bulk HTSC targets (Fig. 1), immediately revealed several problems in relation to controlling the film stoichiometry: (a) the well known preferential sputtering phenomenon occurring during ion bombardment of multicomponent materials, particularly oxides, can alter the surface composition of the target and result in films with different stoichiometry than that characteristic of the target; (b) the development of an ion bombardment-induced surface topography can affect the sputtered flux and consequently the film thickness and composition uniformity; (c) the impact of plasma ions on multicomponent oxide targets results in the emission of a large amount of O^- ions, which are accelerated by the plasma sheath in front of the target, acquiring enough kinetic energy to produce, upon impact on the films, resputtering and compositional changes ("negative ions effect") [7, 8]; (d) in addition to the "negative ion effects, films are also bombarded by secondary electrons emitted from the oxide targets, and these electrons can also produce compositional alterations through the well known electron bombardment-induced oxide breakdown phenomenon.

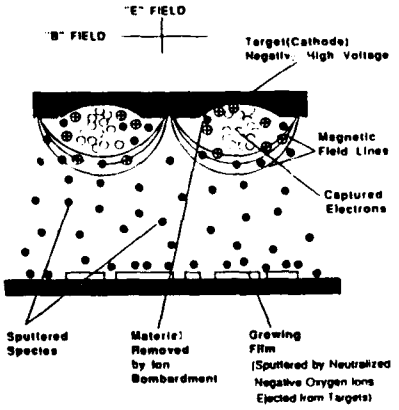


Figure 1. Cross-sectional view of a magnetron sputtering system for deposition of multicomponent oxide, including ferroelectric thin films, by sputtering of a multicomponent oxide target.

A number of different methods have been implemented in order to control the negative ion and electron bombardment effects. A straightforward method is to increase the plasma pressure such that the energy of the neutralized negative ions is reduced, by multiple collisions with plasma species, until it is below the energy necessary to resputter the growing film [9]. A second means of obtaining the appropriate film stoichiometry is to modify the target composition in order to compensate for the preferential sputtering associated with the negative ion effect [10]. This method is time-consuming and somewhat unreliable since any change in processing parameters may alter the final film stoichiometry. Unconventional sputtering geometries, in which the substrate is not subject to ion impact (termed "off-axis sputtering, Fig. 2 [7, 11]), may ameliorate the negative ion effect, at the cost of film thickness uniformity and deposition rate. This latter factor can be reduced by as much as two orders of magnitude, which may represent an undesirable situation for commercial applications of this deposition technique. Other researchers [12] have investigated various methods (Fig. 3) for minimizing the bombardment of growing films by secondary electrons and ions emitted from the target.

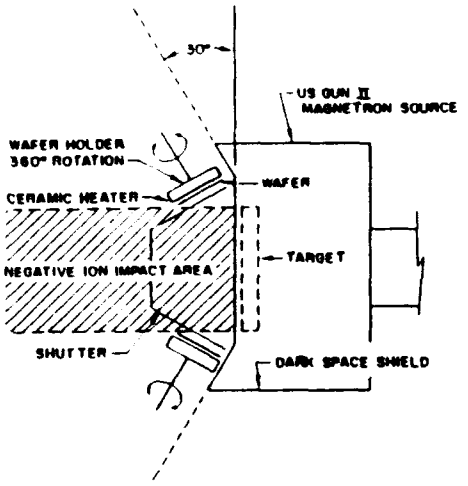


Figure 2. Sketch of an unconventional geometrical arrangement of substrates out of the main stream of sputtered-neutralized negative ions to minimize the plasma-induced negative ion effect in plasma sputter- deposition of ferroelectric films (Roy et al. [7]).

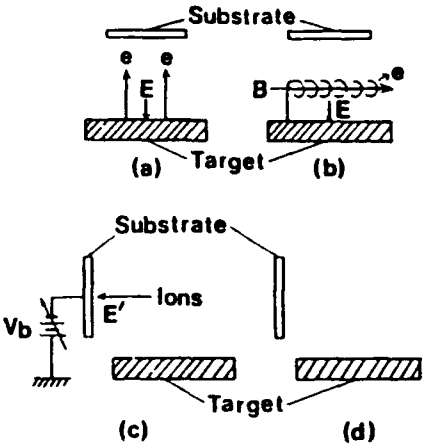


Figure 3. Methods for minimizing or eliminating secondary electron and/or ion bombardment of growing oxide films in plasma sputter-deposition (Terada et al. [12]).

To overcome the various problems related to the use of multicomponent oxide targets, various groups have used elemental metals (Pb, Zr, Ti), or their oxides (PbO, ZrO_2, TiO_2), for example, in multitarget arrangements, where each material constitutes a cathode of a magnetron sputtering system.While this method addresses the issue of preferential sputtering and the "negative ion effect", other problems are raised. Simultaneous sputter-deposition from elemental target materials exposed to independent magnetron sources may lead to compositionally inhomogeneous films. Because the targets are located in different positions, the overlapping deposition fluxes will not be identical at all points on the substrate [14]. This may present a problem in relation to coverage of large

areas with films of uniform stoichiometry and thickness, since fabrication of HTSC thin film-based devices will require processing of single large wafers (≥ 5 inches). One method to improve compositional homogeneity with multiple sources is to increase the substrate to target distance, but this results in a very inefficient use of target materials. An alternative is to maintain a fixed substrate-target geometry by moving the substrate sequentially into position in front of each fixed source and alternately depositing thin layers of each material.

Deposition Processes and Film Characterization

Both single multicomponent oxide and multiple elemental metallic targets have been used to synthesize a wide range of ferroelectric materials in thin film form, including $BaTiO_3$ (BTO)[13-15], $PbTiO_3$ (PTO)[16], $Pb_{1-x}La_xTi_{1-x/4}O_3$ (PLTO)[17], $PbZr_{1-x}Ti_xO_3$ (PZT) [18], and $Pb_{1-x/100}La_{x/100}(Zr_{y/100}Ti_{z/100})_{1-x/400}O_3$ (PLZT) [19]. Due to space limitations, only the work on the Pb-based family of materials is reviewed in some detail in this paper, and only a brief discussion of laser ablation-deposition of other ferroelectric thin films is presented.

Iijima et al. [16] demonstrated that highly c-axis oriented PTO thin films (98% of the film had the c-axis oriented perpendicular to the substrate surface) can be produced by r.f. magnetron sputtering only when using low deposition rates (< 20 Å/min), low gas pressure (~ 7×10^{-3} Torr), and PbO-rich targets (see Table 1). According to Iijima et al. [16], high gas pressures in the magnetron system would increase the sputtering rate because of the production of a larger amount of ions in the plasma, but at the same time would decrease the mean kinetic energy of the sputtered species arriving at the substrate, due to collisions with the plasma species. A reduced kinetic energy of the depositing species would result in a lower mobility on the substrate surface at the deposition temperature. The combination of high sputtering rate (hence high deposition rate) and low mobility of the depositing species would tend to inhibit the epitaxial growth of the film. The work of Iijima et al. [16] demonstrates the importance of controlling the deposition parameters to optimize certain film properties for particular device applications. In the case of the PTO films discused above, the main objective was to minimize the relative dielectric constant ε_r and maximize the pyroelectric coefficient γ, to maximize the figure of merit $F_v = \gamma/\varepsilon_r c_v$ (c_v: volume specific heat) for application of PTO films as pyroelectric infrared sensors. The parameter ε_r was minimized and g maximized by growing highly c-axis oriented films [16]. Similar work on PLTO [17] demonstrated that an accurate control of dopants introduction in the films is also necessary to achieve optimized film properties tailored for a particular application.

Sayer et al. demonstrated that magnetron sputtering can be used to produce PZT films with controlled stoichiometry and properties, utilizing metallic elemental targets [18]. They designed a disk-shaped target consisting of several sectors of the Pb, Zr, and Ti [20], in which they could change the size of the targets to control the amount of each material deposited on the substrate at a particular temperature. They performed extensive studies of the basic plasma-target-substrate interaction phenomena and their effects on the deposition processes. These investigations [20] revealed that the growth of stoichiometric highly oriented films with good electrical properties, by their particular magnetron sputter-deposition method, is governed by three main processes: (a) formation of a reproducible oxide layer on the target surface, (b) the stability of oxide species formed during transport through the plasma towards the substrate, and (c) the nucleation and growth of the film on the substrate surface. Sayer et al. observed that in order to obtain PZT films with good stoichiometry, microstructure, and electrical properties they needed to use relatively high gas pressure of pure oxygen (~ 3×10^{-3} Torr) and a target-substrate distance of approximately 10 cm. Computer simulations of the transport of sputtered species in the plasma and experimental measurements of deposition rate vs. gas pressure and film composition vs. substrate-target distance indicated that complex plasma-surface interaction and material transport processes control many of the film characteristics [18]. For example, the metallic species sputtered from the Pb, Zr, and Ti targets undergo multiple collisions with the plasma species and among themselves during transport to the substrate. The collisions serve to thermalize and mix the sputtered species. Once the sputtered species are thermalized, they reach the substrate by diffusion through the plasma. However, the diffusional fronts of Pb, Zr, and Ti or their oxide species are formed at different distances from the target [18], which have a direct influence on the deposition profiles and composition of the resulting films.

Sayer et al. were unable [18] to produce as-deposited PZT films at the temperature needed (550-600 °C) to produce the perovskite structure, mainly because of poor control on the sticking coefficient of Pb and the reaction on the substrate surface. Therefore, films were synthesized at 200-250 °C and subsequently annealed in air at 550 °C for 10-20 hrs. X-ray diffraction of as-deposited films at 200-250 °C revealed a (100) peak characteristic of the massicot or litharge phases of PbO, which indicated that the as-deposited film contained crystalline PbO grains, while the ZrO_2 and TiO_2 seemed to be deposited in an amorphous form. Annealing of the as-deposited films resulted in structural transformations at about 450 °C, which lead to a tetragonal or rhombohedral structure at 550 °C depending on the Zr:Ti ratio in the film (rhombohedral for Zr:Ti = 58/42, and tetragonal for Zr:Ti = 45/55). The surface topography of the films depended strongly on the annealing temperature and cooling time, with rapid cooling leading to film cracking and hillock formation, depending strongly on the state of stress of the films [18], while long time annealing (20 hrs.) and very slow cooling resulted in smooth films with practically no hillock formation. Experiments involving annealing at different temperatures revealed that the lattice strain of the films was reduced from -0.01 to -0.001 as the annealing temperature increased from 450 °C to 700 °C. The electrical properties of the PZT films produced by magnetron sputter-deposition of metallic targets [18] are presented in Table 1. Generally, good electrical properties were obtained for the films deposited under the optimized conditions described above. It is interesting to notice that other researchers have also produced good quality PZT films by magnetron sputter-deposition of multi-element metal targets [21].

Adachi et al. were able to growth epitaxial PLZT films on c-plane sapphire with epitaxial relations (111)PLZT // (0001) sapphire and [1$\bar{1}$0] // [10$\bar{1}$0] sapphire, by planar magnetron sputter-deposition involving powder pressed PLZT targets of various compositions (see Table 1) [19]. They also determined that the film stoichiometry is largely controlled by the Pb incorporation into the films, which in their particular experiments appeared to be independent of the deposition rate. Adachi et al. also observed, as most other researchers, that films deposited at temperatures ≤ 550 °C presented a pyrochlore structure, although in Adachi et al.'s case the films appeared to be remarkable rich in Pb content. Stoichiometric PLZT was obtained at substrate temperatures above 550 °C [19] for the case in which the films were Pb-rich. On the other hand, epitaxial PLZT stoichiometric films were produced with the same magnetron sputtering system at about 450 °C by using a PLZT (28/0/100) target with a reduced Pb content [19]. This later result of Adachi et al. [19] seems to disagree with the work of Ishida et al. [22] and Okada [23], whom needed a Pb-rich PLZT target to produce stoichiometric PLZT films with a conventional diode sputtering system. Based on the work of Sayer et al. discussed above [18], related to the control of Pb incorporation in the films due to transport processes in the plasma, the seemingly contradictory results of Adachi et al.[19] and Ishida et al. [22] may be explained in terms of different transport processes in the plasma. In the diode sputtering system [22], the higher gas pressure needed may reduce the transport of Pb towards the substrate, and therefore a larger supply of Pb from the target may be needed. On the other hand, the magnetron sputtering system used by Adachi et al. [19] requires lower gas pressure to sustain the plasma, which would result in a more effective transport of Pb, and therefore a less enriched Pb target would be needed to incorporate the required Pb content in the film.

The limited discussion presented above indicates that the geometry and deposition conditions play fundamental roles in the synthesis of ferroelectric thin films by plasma sputter-deposition. Unfortunately, there is not enough systematic data, particularly related to the sputtering, transport and deposition processes, for many of the ferroelectric materials being investigated to synthesize films. Therefore, further work is necessary to determine the optimum conditions needed to produce films of different ferroelectric materials with the best composition, microstructure, and properties.

Table 1a Deposition / processing conditions and compositional and microstructural characterization of ferroelectric thin films produced by plasma sputter-deposition

MATER	TECHN	TARGET	SUBSTR	DEP TP (° C)	ANNEAL (° C)	GAS	PRESS (Torr)	POWER (w)	COMP	MICROSTR	MORPHOL	REF
PTO	RF MAG SPT	PTO/PbO	(100)MgO	≤550		Ar90:O(10)	7.00E-02	170	A2 B2 O7	PYROCL		LIJIMA [16]
		PTO/PbO(0)		550-600		" "	" "	"		NO C-PEROVSK		" "
		PTO/PbO(0.3)		550-600		" "	1.00E-02	"	PbTiO(3)	C-PEROVSK	MOSAIC	" "
PLTO	RF MAG SPT	PLTO/PbO10	(100)MgO	550-600		Ar90:O(10)	1.00E-02	170				
		PL(0.05)	" "	" "		" "	" "	"		C-PEROVSK (.86)		LIJIMA [17]
		PL(0.10)	" "	" "		" "	" "	"		C-PEROVSK (.71)		" "
		PL(0.15)	" "	" "		" "	" "	"		C-PEROVSK (.67)		" "
PZT	RF DIOD SPT	PbO10/PZT	Pt, FQ, InO/FQ	≤ 300		Ar20:O(80)	1.00E-03		Pb(-7%)	AMORPH		OKADA [23]
		PZO52/PTO48	" " " "	350-450		" "	" "		Zr50 Ti50	PYROCL		" "
		PZO42/PTO58	" " " "	350-450		" "	" "		Zr47 Ti53	" "		" "
									Pb (stoich)	PEROVSK		OKADA [23]
		PZO52 PTO48	" " " "	≥550		" "	" "		Zr60 Ti40	" "		" "
		PZO42 PTO58	" " " "	≥550		" "	" "		Zr47 Ti53	" "		" "
PZT	DC MAG SPT	Pb, Zr, Ti	Si,GI,FQ	200		O(100)	4.00E-02	50	PbO,ZrO2,TiO2	(100)PbO		SAYER [18]
	" "	" "	" " " "	"	550	"	" "	"	Zr(58):Ti(42)	(101) PZT/RHOM	SMO+HILL	" "
	" "	" "	" " " "	"	750	"	" "	"	Zr(45):Ti(55)	(101) PZT/TETR	SMO+HILL	" "
	" "	" "	ALUMINA	"	550	"	" "	"	Zr(58):Ti(42)	(101) PZT/RHOM	ROUGH	" "
PLZT	RF MAG SPT	PLZT(28/0/100)	C-SAPPHIRE	≤550		Ar(60)O(40)	3.00E-02	200	A2 B2 O7	PYROCL		ADACHI [19]
	" "	" "	" "	580		" "	3.00E-03	200	PLZT(STOICH)	(111)PLZT	SMOOTH	" "

Table 1b Deposition / processing conditions and electrical characterization of ferroelectric thin films produced by plasma sputter-deposition,

MATER	TECHNIQUE	TARGET	SUBSTR	DEP TP (° C)	ANNEAL (° C)	GAS	PRESS (Torr)	POWER (w)	PR (μC/cm2)	RR (μC/cm2)	EC (KV/cm)	K	∂	REF
PTO	RF MAG SPT	PTO/PbO	(100)PT/MgO	≤550		Ar90:O(10)	7.00E-02	170						
		PTO/PbO(0)		550-600		" "	" "	"	20	16	60	190	0.15	LIJIMA [16]
		PTO/PbO(0.3)		550-600		" "	1.00E-02	"	40	35	160	97	0.15	" "
PLTO	RF MAG SPT	PLTO/PbO10	Ni-Cr(100)MgO	550-600		Ar90:O(10)	1.00E-02	170						
		PL(0.05)	" "	" "		" "	" "	"	30	19	52	100	0.01	LIJIMA [17]
		PL(0.10)	" "	" "		" "	" "	"	45	30	36	200	"	"
		PL(0.15)	" "	" "		" "	" "	"	52	39	32	280	"	"
PZT	RF DIOD SPT	PbO10/PZT	Pt, FQ, InO/FQ			Ar20:O(80)	1.00E-03							
		PZO52/PTO48	" " " "	≥550		" "	" "		26.1	20.4	23.3	751	0.03	OKADA [23]
		PZO42/PTO58	" " " "	≥550		" "	" "		7.33	6.37	12.2	644	0.04	" "
PZT	DC MAG SPT	Pb, Zr, Ti	Si,GI,FQ	200	550	O(100)	4.00E-02	50	50	30	25	800	0.1-0.3	SAYER [18]

PTO: Lead Titanate, PLTO: Lead Lantanum Titanate, PZT: Lead Zirconium Titanate

Ion Beam Sputter-Deposition: Systems, Basic Deposition Processes and Film Characterization

Ion beam sputter-deposition (IBSD) of multicomponent oxide films has been less extensively used than plasma sputter-deposition. However, this method is well suited for deposition of oxide films, as recently demonstrated by various groups, which synthesized HTSC [2], ferroelectric [24-26], and electro-optic [24] thin films. The IBSD technique is a suitable alternative to plasma sputter-deposition, because many of the undesirable effects (substrate bombardment by energetic negative ions and electrons, impurity introduction in films from plasma-wall interaction in the deposition chamber, etc.) already discussed for the later method are not present or are much smaller in the ion beam sputter-deposition case.

The IBSD deposition method was used for synthesizing multicomponent oxide thin films as early as in 1979, when Castellano and Feinstein used this technique to produce PZT thin films [27]. A major problem with the IBSD method as applied by Castellano and Feinstein was that they used PZT hot pressed oxide targets, which were exposed to an Ar^+ ion beam directed at ~ 45 ° with respect to the target surface normal. Apparently, these researchers were not aware of problems such as preferential sputtering of multicomponent oxides, that results in alterations of target surface, hence film composition; nor about extensive scattering of low mass ions (Ar) on heavy mass targets (Pb, Zr), which leads to resputtering of the films as well as ion bombardment-induced damage and incorporation of gas into the films. These phenomena were studied recently in detail [28, 29] and a brief discussion about them is presented below. Because these processes were not properly recognized by Castellano and Feinstein, it was difficult for them to control of the PZT films composition and microstructure, which resulted in films with relatively poor electrical properties (see Table 2a and 2b). In relation to ion beam-target/substrate interaction effects, early work on IBSD of HTSC films also involved the utilization of ion beams under rather uncontrollable conditions to sputter $YBa_2Cu_3O_{7-x}$ bulk superconductor targets, which resulted in films with uncontrolable composition, microstructure, and properties.

More recently, a computer controlled IBSD technique has been developed by Auciello et al. [30, 31], which involves a series of unique design features described below:

(1) A high current broad ion beam is directed at near normal incidence with respect to the target (see Fig.4). Fundamental studies

on ion-solid interactions have revealed that the optimum geometry depends on the bombarding ions mass and kinetic energy, and the mass of the sputtered atom being deposited onto the substrate [28,29].
(2) A rotating target holder driven by a computer-controlled stepper motor serves to sequentially position elemental material (or their single oxide) targets in front of the sputter-beam (Fig. 4).
(3) A QCR (Fig. 4) measures the amount of each elemental material deposited and sends a feedback signal to the computer when the pre-programmed necessary amount of an element, to produce a desired film composition, is reached. The QCR feedback signal activates the computer for shutting off the ion beam while rotating the target holder to position the next target under the beam.
(4) Various computer-operated controls are especially programmed into the computer [30, 31] to regulate:(a) the introduction of processing gases (oxygen for example) into the target chamber or in a sub-eV atomic or energetic ion beam source directed at the substrate, (b) the interposition of shutters or masks between targets and substrates, (c) the substrate temperature, including rump-up and down cycles, and (d) other processing steps.

The potential of this technique has recently been demonstrated by producing superconducting $YBa_2Cu_3O_{7-x}$ [32], ferroelectric PZT [24] and electro-optic $KNbO_3$ [24'] films with controlled composition, microstructure, extremely smooth surfaces, and good electrical properties (see Table 2a and 2b). In addition, it has been recently demonstrated that the automated IBSD technique described above can produce multicomponent oxide thin films with $\leq \pm$ 0.2-1% composition and thickness uniformity across 10 cm substrates [25]. Comprehensive experimental and computer simulation studies performed in our laboratory [28, 29] were undertaken in order to achieve a good understanding of the processes involved in the IBSD technique. Those studies [28, 29] were the bases for optimizing the IBSD method. Briefly, the studies mentioned above have shown that light ions such as Ar^+ impacting at 45^o with respect to the target surface normal results in an undesirably high scattered ion flux, involving species with energies in the hundreds of eV range, when the ions impacting on the target have energies in the range of 1000-1400 eV. The flux of neutralized scattered ions from the target is directed at the substrate, which leads to a deleterious erosion of, and gas incorporation into the growing film. It was found that by using Kr^+ or Xe^+ ions, the scattered ions effect can be minimized or eliminated [28, 29]. Additionally, A mapping of the sputtered flux angular distribution was obtained and successfully used to optimize the deposition geometry.

Other groups have developed ion beam sputter-deposition techniques involving the use of various beams to sputter elemental materials from different spatial locations and simultaneously deposit them onto an appropriately situated substrate [26]. However, the automated ion beam sputter-deposition method described above has various advantages over those featuring multiple ion beams, namely:
(a) The use of only one ion beam simplifies hardware design and reduce cost, particularly when producing films with more than three components. This makes computer control more manageable and avoids having to accurately control various ion beam currents simultaneously.
(b) The sputtered fluxes of all elemental target materials originate from the same spatial location in the computer-controlled single ion beam system, which should contribute to the production of more uniform films across the substrate surface both in thickness and composition.
(c) The ion scattering fluxes and angular distributions of the sputtered fluxes may be more easily controlled in the single ion beam system.
(d) The geometry of the single ion beam system permits the installation of oxygen sources directed at the substrate, and focused beams for in-situ ion, electron, or laser beam-induced patterning.

Compared with the plasma sputter-deposition techniques, the ion beam method offers the following advantages:
(a) A much lower partial pressure of impurities in the target chamber during deposition, since the focused beam can be made to mainly interact with the target, contrary to the plasma sputtering case, where the plasma has a rather strong interaction with the target chamber walls.
(b) Controllability of the ion angle of incidence with respect to the target surface, and better control of the ion current and energy .
(c) No negative ion bombardment of the growing film as in the plasma sputter-deposition case, which requires extra attention in relation to the target-substrate relative positioning.

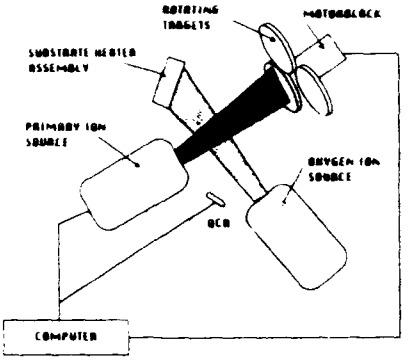


Figure 4. Schematic of the automated ion beam sputter-deposition system developed by Auciello et al. [30, 31].

The automated IBSD technique described above has been used to demonstrate the feasibility of producing device-quality $Pb(Zr_{1-x}, Ti_x)O_3$ (PZT) thin films. PZT was selected because of its technological importance, and the known difficulty associated with the synthesis. The results may be grouped as follows:

Processing: Conditions have been determined for obtaining single phase PZT with perovskite structure. At low processing temperatures, a deleterious "pyrochlore" phase is commonly obtained. We have shown that perovskite phase formation can be achieved through strict control of A:B-site cation ratio, via the substrate temperature, oxygen partial pressure, and composition of the fluxes [34]. It has become clear that the lead oxide sticking coefficient is strongly p_{O_2} and substrate temperature dependent at the process temperatures generally used. It should be noted that we have achieved deposition of PZT films with good properties at substrate temperatures as low as 480°C, with no subsequent annealing. This is significantly lower than process temperatures reported by other researchers , and represents an advantage for integrated devices.

We have also observed that the tendency for "pyrochlore" formation is strongly influenced by the choice of the substrate. This effect requires further study.

Microstructures: A significant effort has been focused on the development of heteroepitaxial ferroelectric films. The primary studies were on films deposited upon single crystal (100)MgO substrates. The lattice mismatch is ~5% versus PZT near the morphotrophic boundary ($PbZr_{0.5}Ti_{0.5}O_3$), and this mismatch is accommodated, not by partial misfit dislocations, but rather via small angle tilt and twist of the film lattice with respect to that of the substrate. This results in films which are best described as "topotactic", containing grains 20-50 nm in diameter, connected via low angle boundaries of 0-2° (see Fig. 5). The grains retain a 3-dimensional relationship with respect to the substrate lattice, as confirmed by cross-sectional and plan view SAD in the TEM. The films diffraction spots, however, show a characteristic elongation corresponding to the 0-2° tilt (or twist) [35]. It is important to note that no ferroelectric domain walls are observed in these films; each grain is single domain. The described microstructure may be responsible for the relative good electrical properties observed in the first films produced with the automated IBSD method. In order to measure the properties of "epitaxial" PZT films in a standard MIM configuration, we developed procedures for deposition of epitaxial (100)Pt metal films on MgO(100) substrates. There is an approximately 6.8% mismatch between Pt and MgO, and <1% between Pt and PZT. Surprisingly, the mismatch between the Pt film and the substrate seems to be accommodated by the more usual dislocation mechanism, while the close match between PZT and Pt indicates that the previously described tilt/twist accommodation

mechanism may not occur. Thus the microstructures no longer have the characteristic low angle boundaries. We are therefore currently exploring the ferroelectric domain structure, by TEM, but x-ray diffraction indicates that the polarization directions are normal to the film plane (only (00l) no (h00) reflections are observed). Properties are described in (c), below.



Figure 5. HRTEM micrograph of an ion beam sputter-deposited epitaxial PZT film containing low angle tilt and twist grain boundaries.

We have also studied other microstructural defects in the perovskite films. We have observed (221)-type growth twins, which appear to nucleate from (110) slip steps on the MgO surface [36]. These can be eliminated by appropriate substrate pretreatment [36]. We have also observed inversion domain boundaries in $KNbO_3$ films, but not in PZT films. It is not clear at this time the reasons for the different microstructures in the films mentioned above, and therefore further investigation is needed. The issue is important, as these fixed subgrain boundaries will have an effect on the mobility of the ferroelectric domain walls

Properties: Good ferroelectric and dielectric properties have been achieved for the PZT films synthesized by the in-situ automated ion beam sputter deposition technique. Typical values for 90 nm thick films are as follows: P_{max} ~50 $\mu C/cm^2$; P_r ~20 $\mu C/cm^2$; E_c ~1.1×10^7 V/m; K_{eff} ~1300, resistivity ~1×10^{10}Wcm. A comment should be made about the relatively large value for the coercive field, E_c. First, the films we produce are extremely thin, typically 60-150 nm, and E_c is known to increase with decreasing film thickness. However, the films are expected to show switching behavior which more closely resembles single crystal than polycrystalline material. However, coercive fields for free single crystals are usually low, and we therefore deduce that constraint imposed by the substrate lattice markedly increases E_c.

Measurements of conductivity and ferroelectric fatigue of the PZT films produced by the automated IBSD method have shown that the films display characteristic hopping conduction [38], and that fatigue results in only a loss of ~50% in P_r out to 10^9 cycles. These fatigue results are extremely encouraging. The fatigue characteristics are very similar to those obtained for polycrystalline PZT films of 170 nm thickness [37]. The implication is that the heteroepitaxial films do not display markedly improved fatigue behavior over polycrystalline ones (on Pt electrodes).

Electrode effects: The nature of a bottom electrode can have a significant effect on the microstructure and properties of a PZT film. We have conducted extensive comparison tests of a number of potential lower electrodes, including Pt/MgO, Pt/SiO_2/Si, Pt/Ti/SiO_2/Si, RuO_2/SiO_2/Si, TiN/MgO, $TiSi_2$/Si, $CoSi_2$/Si, and several others. These studies have included examination by transmission electron microscopy (TEM), high-resolution and analytical TEM, X-ray diffraction, scanning electron microscopy, Auger depth profiling, and Rutherford back scattering. Some of these results were reported at three recent conferences and in a paper currently in press [37]. Some of the phenomena discovered in our studies on electrodes include: a) the rapid diffusion of lead beneath platinum films on silicon dioxide; b) strong interdiffusion of PZT films and some substrates, including TiN and silicides; c) the deformation of platinum films during anneals, including the formation of potentially disastrous hillocks which can penetrate through the PZT film.

One of the main advantages of the ion beam sputter-deposition technique is its capability for independent control of the energy, current and angle of incidence of the ion beam on the target. In addition, dual ion beam systems can be easily implemented in such a way that a secondary ion can be independently directed at the substrate in order to produce ion-assisted growth. In this respect, it has been demonstrated in recent years that controlled ion bombardment of growing films can be used to tailor different deposition processes as well as mechanical, microstructural, physical, and chemical properties of the films [39] Processes and/or properties that can be affected include: (a) surface reaction rates; (b) active gas incorporation into the films, such as oxygen in high temperature superconductor (HTSC) or ferroelectric (FE) and electro-optic (EO) materials; (c) film sticking coefficient; (d) nucleation and growth kinetics; (e) interdiffusion rates at homo- and heterojunction interfaces; (f) microstructure; (g) stress; (h) and electrical conduction. Currently, ion assisted deposition (IAD) is being used in conjunction with different vapor-phase deposition techniques such as plasma and ion beam sputter-deposition (PSD and IBSD) [39], electron beam evaporation (EBE), and molecular beam epitaxy (MBE). Advantages of IAD schemes characteristic of the ion beam-assisted sputter-deposition (IBASD) technique, which are not commonly shared by other deposition techniques, include:

(1) The possibility of easy independent control of the energy, ion flux density, and angle of incidence of both the primary ion beam on the target and the secondary ion beam on the substrate, which gives great flexibility for controlling synthesis and in-situ processing of films.

(2) The possibility of attaining a lower background pressure in the deposition chamber that can be advantageously used to control the deposition process.

(3) The creation of ions in a plasma localized in the ion beam source keeps the plasma from contacting the target, substrate, and deposition chamber walls, therefore contributing to minimize or eliminate uncontrollable plasma-substrate/target/chamber walls interaction effects, characteristic of plasma systems, that could affect the film growth.

(4) Perhaps the most important feature of the IBASD technique is the possibility of independently controlling the energy of the secondary-processing ion beam, which appears to be the most influential parameter in ion-assisted film processing [39]. In the case of ferroelectric thin films, initial research on ion-assisted deposition has been performed by bombarding the growing film with low energy (60-80 eV) O_2^+ or O^+ ions [40]. The impact of these ions on the film during growth can activate chemical processes necessary to produce the required composition and microstructure; it can provide extra energy to the film constituents arriving at the substrate, to increase their surface mobility at lower substrate temperatures than required for thermal processing alone, therefore contributing to reduce the film crystallization temperature; it can also induce film densification, and beneficially affect surface morphology, and structural, electrical, and optical properties. In this respect, Krupanidhi et al. [40] have recently shown that low energy O^+ ion bombardment of growing PZT films can enhance their electrical properties. In particular, it was demonstrated [40] that the remnant polarization and dielectric constant of PZT films can be enhanced up to about 60% and 25%, respectively, over the values characteristics of films produced without ion bombardment (see Table 2b). In addition, it was demonstrated [40] that the coercive field can be reduce by about 20%. The initial results on ion assisted-deposition of ferroelectric thin films are promising (see Table 2a and 2b).

Table 2a Deposition / processing conditions and compositional and microstructural characterization of ferroelectric thin films produced by ion beam sputter-deposition

MATER	TECHN	TARGET	SUBSTR	DEP TP (°C)	ANNEAL (°C)	ION	ENERG (keV)	CURR DENS (mA/cm2)	GAS	PRESS (Torr)	COMP	MICROSTR	MORPHOL	REF
PZT	IBSD	HOT PRES PZT	NiCr,Au/Pyre	0-250		Ar	2.00	1.00	O2	1.00E-04	Pb2 Ti2 O6	PYROCHLORE	MICROCRACKS	CASTELLANO [27]
PZT	IBSD	HOT PRES PZT	NiCr,Au/Pyre	0-250	750	"	"	"	"	"	PZT+PZT2O6	PYROCH+PERVSK		" "
PZT	IBSD	HOT PRES PZT	NiCr,Au/Pyre	450		"	"	"	"	"	PZT	PEROVSKITE		" "
PZT	IBSD	Pb, Ti, Zr	(100)MgO	450-550		Kr	1.2-1.4		O2	2.00E-04	PZT	(100)PEROVSK	SMOOTH	GIFFORD [24]
"	"	"	(100)PT/MgO	"		"	"		"	"	"	"	HILLOCKS	" "
PZT	IBSD	Pb, Ti, Zr	(100)MgO,Si,OTHER	100	500	Ar	0.3-1.0			2.00E-04	PZT(Zr/Ti=50/50	(101)PERV(222)PY	(Pb-RICH)ROUGH	KRUPANIDHI [26]
"	"	"	"	"	>550	"	"			"	"	PURE PEROVSK	(SOICH Pb)SMOOT	"
"	"	"	"	"		"	"		O2+(75eV)		~ 8% Pb reqmt	(101)(100) PERVSK	DENSE+ SMOOTH	"
PLZT	IBSD	PZT(28/0/100)	Ti/Pt/(100)Si	480		Ar	1.1	1.00	O2	2.00E-04	PZT	PEROVSKITE	SMOOTH	BYER [25]
KNBO3	IBSD	KO2, Nb	(100)MgO	550		Kr	1.2-1.4		O2	2.00E-04	KNbO3	NO ORIEN+EPY	RELATIVE SM	AMEEN [24]
"	"	"	"	600		"	"		"	"	"	EPYTAXIAL	"	" "
"	"	"	(100)Si	550		"	"		"	"	"	CRYST+AMORPH	"	" "
"	"	"	"	600		"	"		"	"	"	POLY+LITT ORIEN	"	" "

Table 2b Deposition / processing conditions and electrical characterization of ferroelectric thin films produced by ion beam sputter-deposition

MATER	TECHN	TARGET	SUBSTR	DEP TP (°C)	ANNEAL (°C)	ION	ENERG (keV)	CURR DENS (mA/cm2)	GAS	PRESS (Torr)	PS (μC/cm2)	PR (μC/cm2)	EC (KV/cm)	K	d	REF
PZT	IBSD	HOT PRES PZT	NiCr,Au/Pyre	450		Ar	2.00	1.00	O2	1.00E-04	10	4.9	25	350		CASTELLANO [27]
PZT	IBSD	Pb, Ti, Zr	(100)MgO	450-550		Kr	1.2-1.4		O2	2.00E-04	59	35	100	500-600		GIFFORD [24]
PZT	IBSD	Pb, Ti, Zr	(100)MgO,Si,OTHER	100	500	Ar	0.3-1.0			2.00E-04						
"	"	"	"	"	>550	"	"			"		23	80	850	0.02	KRUPANIDHI [26]
"	"	"	"	"		"	"		O2+(75eV)			26	60	1000	0.02	
KNBO3	IBSD	KO2, Nb	(100)PT/MgO	600		Kr	1.2-1.4		O2	2.00E-04	32	25	90-100			NCSU(Unpublished)

However, more work is necessary to understand and control the processes involved in ion-assisted deposition of ferroelectric films, if this technique is to be considered for application in industrial processing of ferroelectric film-based devices.

The work performed recently by various groups on ion beam sputter-deposition indicates that this is a very versatile and powerful technique for application to the synthesis of multicomponent oxide thin films, not only at the laboratory scale, but also in industrial manufacturing of thin film-based devices.

Pulsed Laser Ablation Deposition: Systems, Basic Deposition Processes and Film Characterization

The application of laser beams to different branches of basic science and technology have multiplied rapidly since the laser was discovered as a source of energy in the form of monochromatic and coherent photons in the 1960's. Shortly after the demonstration of the first laser, the most intensively studied theoretical topics were related to laser beam-solid interactions. Experiments were performed to verify different models developed to explain various phenomena observed during the interaction of laser beams with materials. These experiments and models were the bases for the subsequent evolution of the many applications of laser beams, of which pulsed laser-ablation deposition (PLAD) is only a small part.

Pulsed laser deposition is conceptually and experimentally a relatively simple technique. A simplified schematic with the main features of the PLAD method, as currently implemented by different groups, is shown in Fig. 6. The main components include a pulsed excimer laser beam, generally in the ultraviolet wavelength range (193 nm or 248 nm) [41, 42]. The laser beam is directed at a target located in a vacuum chamber in such a way that it generally impacts on the target surface at a 45° angle of incidence. The laser beam pass through both a quartz suprasil lens and window before entering into the deposition chamber. The lens and window material is chosen so there is a minimum absorption of laser light and therefore maximum attainable laser energy deposited on the target. The impact of the laser beam on the target surface results in various complicated processes including ablation, melting, and evaporation of material, and production of a plasma due to excitation and ionization of the species ejected from the target by the laser photons. All these processes are triggered by the transformation of electromagnetic energy into electronic excitation, followed by a transformation into thermal, chemical, and mechanical energy. The material ejected from the target is deposited on a substrate generally positioned opposite the first, as indicated in Fig.6.

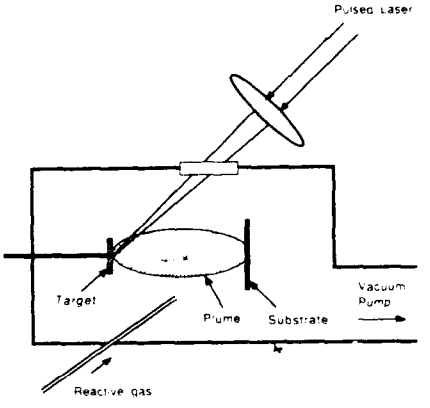


Figure 6. Schematic of a common PLAD system. Various groups have introduce variations of this general arrangement, which will be described in the following sections [44].

In the PLAD technique, species are ejected from the surface of a target forming part of a "plume" controlled by a hydrodynamic flow regime in which a large number of molecular and atomic collisions occur. The physicochemical conditions of the plume depend to a large extent on the laser wavelength through the dependance of the laser-solid interaction process on this particular parameter. Since currently there are numerous lasers available which provide a broad spectrum of wavelengths and pulse energies and widths, the PLAD technique can be used to deposit thin films of almost any material that can absorb the laser light up to a minimum level. The versatility of the PLAD technique is demonstrated by the fact that close to 128 different materials have been deposited in thin film form using the PLAD method [43]. However, the development of PLAD has been slow up until recently, when researchers realized that this technique has several features that can be used advantageously to synthesize multicomponent oxide thin films, including high temperature superconductors (HTSC), ferroelectric (FE), electro-optic (EO), and optical materials [41, 44]. The PLAD technique has been particularly successful in the production of HTSC thin films [21, 24], and for that reason the groups using the PLAD method have been very enthusiastic in promoting the technique as one of the best for this particular application. In reality, however, the technique has advantages and disadvantages like any other vapor phase deposition methods that currently are being extensively investigated to produce multicomponent thin films. A balanced description of advantages and disadvantages of the PLAD technique to synthesize HTSC and ferroelectric films has been presented only in isolated reviews [41, 42]. The main objective of this review is to present a brief overview of the application of the PLAD method and update previous descriptions published in the literature by including a discussion of new developments in the use of the PLAD method to synthesize ferroelectric thin films.

The PLAD technique has only recently been extensively applied to ferroelectric thin film growth, and it was a logical extension to the work done on deposition of HTSC thin films. Key advantageous features of the PLD technique include: (1) the possibility of a straightforward replication, under certain conditions, of the target stoichiometry on the films; (2) the ability to deposit in high background pressures, which in this case minimizes vaporization of volatile species from the film; (3) the ease of *in-situ* deposition which enables epitaxial film growth and can minimize thermal budget during processing, and (4) the demonstrated high deposition rate (~10 Å/s). These features of PLAD method have been successfully used to grow films of $BaTiO_3$ [45, 46], $Bi_4Ti_3O_{12}$ [47, 48] $K(Ta,Nb)O_3$ (KTN) [48], $Pb(Zr,Ti)O_3$ (PZT) [49, 50], $(Pb,La)(Zr,Ti)O_3$ (PLZT) [51], and $Bi_4Ti_3O_{12}$ on an $YBa_2Cu_3O_{7-x}$/MgO substrate [52]. Because many applications either require an epitaxial film or may benefit from a reduced thermal budget, the synthesis of ferroelectric films by the PLAD technique has involved *in-situ* deposition at relatively high temperatures (500-600 °C).

Since there is not enough space to discuss in detail aspects related to the synthesis of all the ferroelectric thin films mentioned above, only key deposition conditions used in the synthesis of PZT films will be described as an example. In one set of experiments, by Grabowski et al. [44], the deposition conditions used for synthesizing PZT films include focus of an excimer laser beam (248 nm, 5 Hz, 35-100 mJ/pulse) to about 1 J/cm^2 per pulse onto a rotating mixed-oxide PZT target. The heated substrate was held in a high pressure atmosphere (~300 mtorr) of pure O_2, located about 4 cm from the laser target. Films would be grown at about 510 Å/s to a thickness of about 4,000 Å in this manner [44].

Two deposition parameters are critical to obtaining phase-pure ferroelectric PZT, namely, substrate temperature and oxygen background pressure. For example, Grabowski et al. [44], observed that to maintain stoichiometric Pb content in laser ablation-deposited PZT (Zr/Ti = 0.54/0.46) films, a high oxygen pressure (at least 300 mTorr) is required, and the substrate temperature must not exceed about 550 °C (Fig. 7). A metastable non-ferroelectric pyrochlore phase forms in Pb-deficient films and for MgO substrate temperatures below about 500 °C. Therefore, there is a narrow operational window to obtain phase-pure ferroelectric PZT. However, XRD analysis of PZT films produced within the narrow pressure-substrate temperature window range mentioned above indicates that there is still a remaining pyrochlore phase [44]. The appearance of the pyrochlore phase is believed to be associated with the high volatility of Pb and its low reactivity with diatomic oxygen, leading a reduced incorporation of Pb in the film. Other substrates, such as $SrTiO_3$ which can provide a better lattice match to perovskite PZT, enable perovskite film growth at temperatures as low as 350 °C, where Pb volatility is not as great a problem [53. Similar problems have been observed for laser ablation-deposition of $BaTiO_3$ [45] and KTN [49].

To increase the likelihood of deposition of single-phase epitaxial PZT on poorly lattice-matched substrates (i.e., substrates other than $SrTiO_3$), the potential for Pb reaction with oxygen during film deposition must be maximized to limit Pb volatilization. This may be accomplished by using higher oxygen background pressures (1 Torr) [54], or a more reactive oxygen source (N_2O) [55]. Another innovative method that has been particularly successful is to place an electron emitting filament between the laser target and substrate, and to bias the target to collect excited diatomic oxygen anions created by electron attachment. This effectively introduces more reactive oxygen close to the substrate [56]. The dramatic effect on crystal structure of this approach is shown in Fig. 8. Initially, the electrons emitted from the filament diminished the pyrochlore phase and enhanced epitaxial perovskite PZT dramatically. However, at high emission currents, the generated oxygen anions promoted additional orientations of the perovskite phase to nucleate. Another benefit produced by the greater oxygen reactivity is an improved film surface morphology. Filament-assisted PLD appears to produce a continuous and smooth topography as opposed to a porous and rough one observed on films grown under O_2 exposure. In-situ epitaxial PZT films produced with the filament-assisted PLD method have have shown remnant polarizations P_r of 15-20 μC/cm^2 and coercive fields E_c of 35-50 kV/cm. In general, the ferroelectric properties obtained from in-situ deposited PZT films grown either by sputtering or PLD without some enhancement of oxygen reactivity have not been remarkable. Low values of remnant polarization and high coercive voltages have been reported. Post-deposition annealing has been found to improve the ferroelectric properties [57], but as described before, the problem might be better addressed by increasing oxygen reactivity during deposition.

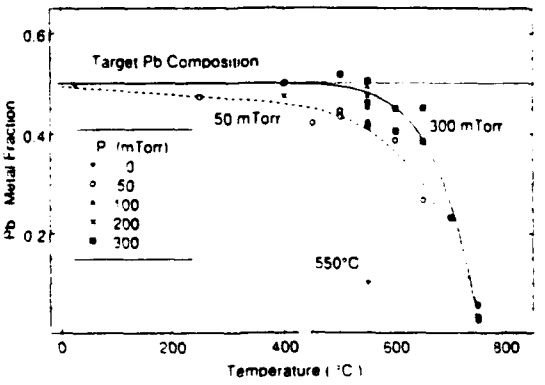


Figure 7. Pb content of PZT films (Zr/Ti = 0.54/0.46) films, measured by RBS, as a function of substrate temperature and ambient oxygen pressure. The line at 550 °C marks the temperature at which numerous different pressures were examined, and indicates the threshold for pure-phase-perovskite film formation [44].

More recently, Auciello et al. have developed an automated PLD deposition technique [31, 58], which involves ablation of elemental targets (metals or their single oxides) sequentially exposed to an excimer laser beam using a computer-controlled system (Fig. 9). For the initial experiments performed to demonstrate the automated laser ablation-deposition technique, ZrO_2,TiO_2,and PbO were sequentially exposed to an excimer laser beam (KrF, ~ 1J/cm^2 on target, 3 Hz, 45 ° angle of incidence) via a computer-controlled rotating target holder driven by a high vacuum motor (see Fig. 9). The films were deposited on MgO (100) substrates at 200 °C, in such a way that the first layer in contact with the MgO substrate was

ZrO_2, and the subsequent layers were TiO_2, and PbO. A quartz crystal resonator, functioning as a film thickness monitor, is located on the side of the substrate and measures the amount of each elemental material or oxide deposited and sends a feedback signal to the computer.

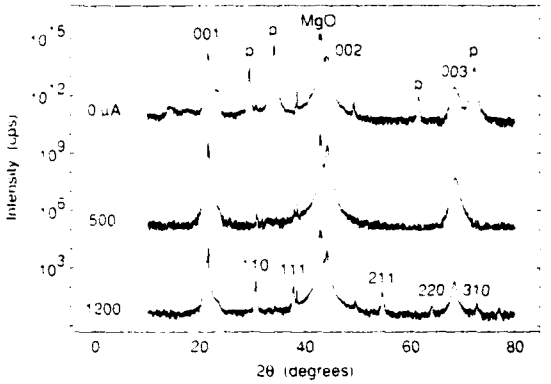


Figure 8. XRD patterns of PZT (Zr/Ti = 0.54/0.46) films deposited on MgO substrates using three different filament emission currents. The ferroelectric perovskite peaks are identified by their miller indices while peaks corresponding to the metastable pyrochlore phase are identified by a "p". The patterns are offset by 10^5 cps for clarity of presentation [44].

When the pre-programmed necessary amount of an element, to produce a desired film composition, is reached, the QCR feedback signal activates the computer to shut off the laser beam and rotate the target holder to position the next target in front of the beam. This sequence is repeated until the programmed total film thickness is achieved. This new automated PLD method can be used to control the amount of Pb deposited and overcome the problems of Pb deficiency when producing PZT films by ablation of PZT targets, as discussed above. The XRD pattern of a film deposited with the layer by layer method (Fig. 10a) [58], on MgO at 200 °C, indicates that the film consist of a highly oriented (100) PbO microstructure, which upon annealing at 600 °C in an oxygen atmosphere turns into a highly oriented (101) PZT film with no evidence of a pyrochlore phase (Fig. 10b). Work under way in our laboratory will demonstrate whether layer by layer deposition can be used to produce as-deposited PZT films at substrate temperatures in the range 500-550 °C, with less stringent control on the oxygen background pressure during deposition, as it is necessary in the case of PZT film synthesis by ablation of PZT targets. Further details about the working principle of the automated PLD technique can be found elsewhere [31].

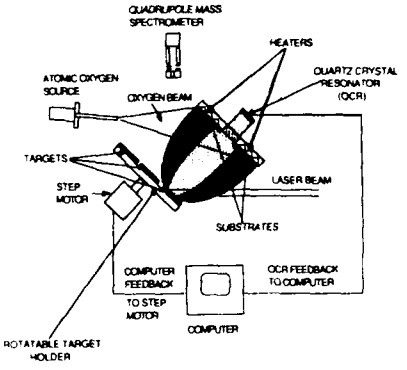


Figure 9. Schematic of the automated PLD system developed by Auciello et al. The system is controlled via an especially developed computer program, and the technique has the potential for industrial applications [31].

The automated PLAD technique described above was also used to deposit PZT films by ablation of a 10%PbO-rich PZT target with Nb doping. Films were synthesized under similar conditions as those described above for the layered films. The films grown by ablation of the bulk PZT target presented a (100) orientation (Fig. 11). The particular crystallographic orientation of the layered PZT films (Fig. 10b) can be explained in terms of a controlled growth from the crystalline PbO layers nucleated in the as-deposited films (Fig. 10a), since the lattice matching between a (100) PbO layer and a (101) PZT layer is favorable for the nucleation of the later during a post-deposition annealing process, as used in the work reported [58]. On the other hand, the growth of PZT films produced by ablation of bulk PZT targets appears to be dominated by the crystallographic orientation of the substrate.

Extensive electrical characterization of the PZT films produced by Auciello et al. [58] have shown that these films have device-compatible remnant polarizations (see Table 3b). In addition, first capacitance and film conductivity measurements ever performed on a laser ablation-deposited film revealed that electron and ion hopping may be two important conduction mechanisms in PZT films [58].

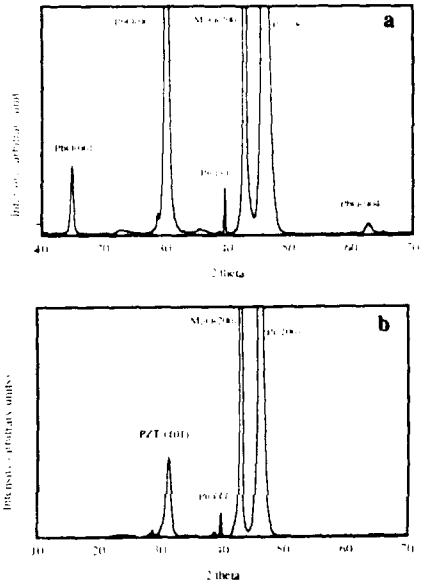


Figure 10. (a) XRD pattern of an as-deposited (at 200 °C) layer by layer film on an (100) Pt/(100) MgO substrate. (b) XRD pattern of the film described in (a) after annealing at 600 °C in an oxygen atmosphere. Notice the (100) oriented PbO structure in the as-deposited film (a), which controls the growth of a highly oriented (101) PZT film (b) during the post-deposition annealing [58].

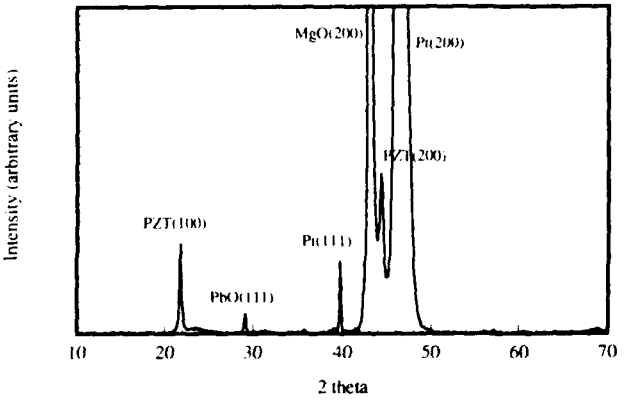


Figure 11. XRD pattern of a PZT film deposited on (100)MgO, by ablation of a 10%PbO-rich PZT target, at 200 °C and later annealed at 600 °C.

Other researchers have synthesized PZT films using the PLAD technique, but utilizing different laser wavelengths and energy density, as well as different deposition parameters. Information on the deposition conditions, and compositional, microstructural, topographical, and electrical characteristic of the films are presented in Tables 3a and 3b. There are various noticeable aspects related to the works cited in Tables 3:

- Films deposited by ablating bulk PZT targets with excimer lasers have varying degrees of composition close to the stoichiometry corresponding to the targets [51, 52, 57-60];
- Films deposited by ablation of PZT targets with lasers of longer wavelengths [50, 62] generally do not have as good an stoichiometry as those produced with the excimer lasers;
- The excimer lasers are very appropriate to produce films with the desired perovskite structure and electrical characteristics [51, 52, 57-60].
- Laser ablation-plasma-assisted deposition of ferroelectric thin films [59, 60] may provide a suitable technique to synthesize the films at relatively low substrate temperature, improve the amount of perovskite microstructure present in the film, and produce smoother films.
- Laser ablation deposition with assisted laser in-situ annealing of the films during growth [63] is a promising method to produce multicomponent oxide thin films as-deposited without post-deposition annealing, and with smoother surface topographies than without a laser beam impactir g on the growing film.

In conclusion, the work of several research groups has demonstrated that the PLAD technique is a very suitable method to synthesize multicomponent oxide thin films, particularly those of ferroelectric materials. However, further work is necessary to understand better the processes involved in film deposition, in order to optimize the films properties. In addition, work is also needed to scale-up the technique to cover large area substrates (> 4 inch diameter) with uniform films, if the technique is going to be applied for manufacturing film-based devices.

Table 3a Deposition / processing conditions and compositional and microstructural characterization of ferroelectric thin films produced by pulsed laser ablation-deposition.

MATER	PVDT	TARGET	SUBSTR	T-S DIS (cm)	DEP TP (°C)	ANNEAL (°C)	GAS	PRESS (Torr)	(nm)	PULSE (ns)	ENG DENS (J/cm2)	COMP	MICROSTR	MORPHOL	REF
PZT	PLAD	Pb1.25Ti1.6Zr.4O3.25	(100)MgO,Pt/MgO	3 or 5	525		O2	3.00E-03	248	30	8	PZT(Ti/Zr=61/39)	(100)PERSK(222)PY	PARTICLES	SAENGER [57]
"	"	"	"	"	525	575	"	"	"	"	"	"	"	"	"
PZT	PLAD	PZT 501A(COMMERC)		2.0-5	25	400-600	O2	2.00E-03	10(+4)	10(+3)	1.6	Pb0.87Ti0.1Zr0.05	PEROVSK+PYROC		RAMKUMAR [62]
PZT	PLAD	PZT(Zr/Ti = 53/47)	Pt, Pt/(100)Si	2	25-200	650-800	O2	1.00E-01	1064	15	204	PZT	CUBIC+PEROVSK	ROUGH+PART	CHIANG [50]
PZT	PLAD	PZT(Zr/Ti = 52/48)	Pt/(100)Si	4	25	650	O2	1.00E-04	248		2	PZT	PEROVSK+PYROC		KRUPANIDHI
PZT	PLAD	PZT(Zr/Ti = 52/48)	Pt/(111)Si	3	400-600		O PLASM	1.00E-03	248		2				KRUPANIDHI [59]
"	"	"	"	"	"	"	(0 VOLT)	"	"	"	"	PZT	(100)/(110) POLYC	"	"
"	"	"	"	"	"	"	(300 VOL)	"	"	"	"	PZT	(100)/(220)/(110)POL	"	"
PZT	PLAD	PZT(Zr/Ti = 54/46)	(100)Pt/(100)MgO	4	550		O PLASM	3.00E-01	248		1				GRABOWSKI [60]
							(0uA)					PZT(Zr/Ti=54/46)	(001)PERVSK/PYR	ROUGH	"
							(1200uA)					PZT(Zr/Ti=54/46)	(001)/(110)/(220)PYR	SMOOTH	"
PZT	PLAD	PZT(Zr/Ti = 52/48)	r-SAPPHIRE		LAS ON SUB										
"	"	"	"		1000 (10nm)		O2	5.00E-02	193		8	PZT(Zr/Ti = 52/48)	PEROVSK-LESS PY	ROUGH	MINAMIKAWA[63]
"	"	"	"		700(NO LAS)		"	"	"		"	"	PEROVSK-LARG PY	SMOOTH	
PZT	PLAD	PbO(10%)+PZT(Nb)	(100)Pt/(100)MgO	5	200	600	O2	3.00E-03	248		1	Pb1.0Zr0.57Ti0.43	(001)PEROVSK	SMOOT+SM PAR	AUCIELLO [58]
"	"	PbO, ZrO2, TiO2	"	"	200	"	"	"	"	"	"	Pb1.0Zr0.45Ti0.55	(101)PEROVSK	SMOOT+LG PAR	"
PZT	PLAD	PZT (Zr/Ti =20/80)	YBCO/(001)LaAlO	4	550-750		O2	1.00E-01	248	30	2	Pb1.0Zr0.2Ti0.8	(001)PEROVSK	SMOOT+SM PAR	RAMESH [52]
PLZT	PLAD	PLZT(7/0/100)/(28/0/100)	(100)Si, FUS SIL	4.0-12	450		O2	1.00E-01	24o			Pb/Ti=3-5	(100)PERVSK+PYR		PETTERSEN [51]
"	"	"	"	"	500		"	"	"			"	(100)/(200)PEROVSK		
BTO	PLAD	Bi4 Ti3 O12	Pt/(100)Si	3.5	550-700		O2	1.00E-03	248	20-30	2	Bi4 Ti3 O12	(001)PEROVSK	FIBER TEXTURE	BUHAY [61]

Table 3b Deposition / processing conditions and electrical characterization of ferroelectric thin films produced by pulsed laser ablation-deposition.

MATER	PVDT	TARGET	SUBSTR	T-S DIS (cm)	DEP TP (°C)	ANNEAL (°C)	GAS	PRESS (Torr)	(nm)	PULSE (ns)	ENG DENS (J/cm2)	PS (μC/cm2)	PR (μC/cm2)	EC (KV/cm)	ε	d	REF
PZT	PLAD	Pb1.25Ti1.6Zr.4O3.25	(100)MgO,Pt/MgO	3 or 5	525		O2	3.00E-03	248	30	8				200		SAENGER [57]
"	"	"	"	"	525	575	"	"	"	"	"	12			652		"
PZT	PLAD	PZT(Zr/Ti = 53/47)	Pt, Pt/(100)Si	2	25-200	650-800	O2	1.00E-01	1064	15	204		36		600		CHIANG [50]
PZT	PLAD	PZT(Zr/Ti = 52/48)	Pt/(100)Si	4	25	650	O2	1.00E-04	248		2	50	32	180	800-900	0.03	KRUPANIDHI
PZT	PLAD	PZT(Zr/Ti = 52/48)	Pt/(111)Si	3	400-600		O PLASM	1.00E-03	248		2						KRUPANIDHI [59]
"	"	"	"	"	"	"	(0 VOLT)	"	"	"	"		40	40	400	0.03	"
"	"	"	"	"	"	"	(300 VOL)	"	"	"	"		22	24	860	0.01	"
PZT	PLAD	PZT(Zr/Ti = 54/46)	(100)Pt/(100)MgO	4	550		O PLASM	3.00E-01	248		1		15-20	35-50			GRABOWSKI [60]
							(1200uA)										
PZT	PLAD	PbO(10%)+PZT(Nb)	(100)Pt/(100)MgO	5	200	600	O2	3.00E-03	248		1	21.4	10.3	117	450		AUCIELLO [58]
"	"	PbO, ZrO2, TiO2	"	"	200	"	"	"	"	"	"	21	11	59.6	1074		"
PZT	PLAD	PZT (Zr/Ti =20/80)	YBCO/(001)LaAlO	4	550-750		O2	1.00E-01	248	30	2	38	26	80-100	250	0.05-0.1	RAMESH [52]
BTO	PLAD	Bi4 Ti3 O12	Pt/(100)Si	3.5	550-700		O2	1.00E-03	248	20-30	2	28	19 3	250	138		BUHAY [61]

Conclusions

The extensive basic and applied research performed in the field of synthesis and characterization of ferroelectric thin films has advanced the materials science and the technology bases of this materials for application in the manufacturing of advanced film-based devices. It has been demonstrated that physical vapor-deposition techniques are at the forefront of the ferroelectric materials technology and they will continue to provide the means for studying and producing films needed for advancing the device technology.

Acknowledgements

The authors gratefully acknowledge the continuous support of the Defense Advanced Research Project Agency, the Office of Naval Research, and the National Science Foundation. The authors also acknowledge the important contribution of all members of the NCSU group.

References

[1] R.D. Schwartz, B.A. Tuttle, D.H. Doughty, C.E. Land, D.C. Goodnow, C.L. Hernandez, T.J. Zender, and S.L. Martinez, IEEE Trans. on Ultrasonic, Ferroelectric and Freq. Control, vol. 38, p. 677, 1991.

[2] O. Auciello, A.R. Krauss, A.I. Kingon, and M.S. Ameen, Scanning Microscopy, vol. 4, p. 203, 1990.

[3] E.R. Myers and A.I. Kingon (Eds.), various reviews and contributed papers in Ferroelectric Thin Films, MRS Symp. Proc. Materials Research Society, Pittsburg, vol. 200, 1990.

[4] G.K. Hubler (Ed.), Pulsed Laser Deposition, Special Issue of the MRS Bulletin (USA), vol. 17, 1992.

[5] O. Auciello and J. Engemann (Eds.), various chapters in Multicomponent and Multilayered Thin Films for Advanced Microtechnologies: Techniques, Fundamentals, and Devices, NATO/ASI Series, The Netherlands: Kluwer Academic Publishers, in press, 1993.

[6] O. Auciello, D.J. Lichtenwalner, A.I. Kingon, and A.R. Krauss, in Multicomponent and Multilayered Thin Films for Advanced Microtechnologies: Techniques, Fundamentals and Devices, NATO/ASI Series, The Netherlands, Kluwer Academic Publishers, in press, 1993.

[7] S. M. Rossnagel and J. J. Cuomo, Thin Film Processing and Characterization of High Temperature Superconductors, J. M. E. Harper, R. J. Colton, and L.C. Feldman (Eds.), American Institute of Physics Conf. Proc., No. 165, p. 106, 1988.

[8] R.A. Roy, K.F. Etzold, and J.J. Cuomo, Ferroelectric Thin Films, E.R. Myers and A.I. Kingon (Eds.), MRS Symp. Proc. Materials Research Society, Pittsburg, vol. 200, p. 77, 1990.

[9] H. Adachi , K. Hirochi, K. Setsune, M. Kitabatake, and K. Wasa, Appl. Phys. Lett., vol. 51, p. 2263, 1987.

[10] K. Moriwaki, Y. Enamoto, S. Kubo, and T. Murakami, Jap. J. of Appl. Phys., vol. 27, L2075, 1988.

[11] R. L. Sandstrom, W. J. Gallagher, T. R. Dinger, R. H. Koch, R.H. Laibowitz, R.B. Kleinsasser, R. J. Gambino, B. Bumble, and M. F. Chisholm, Appl. Phys. Lett., vol. 53, p. 444, 1988.

[12] N. Terada, H. Ihara, M. Jo, M. Hirabayashi, Y. Kimura, K. Matsutani, K. Hirata, E. Ohn, R. Sugise, and F. Kawashima, Jap. J. of Appl. Phys., vol. 27, L639, 1988.

[13] V.S. Dharmadhikari and W.W. Grannemann, J. Appl. Phys., vol. 53, p. 8988, 1982.

[14] I.H. Pratt, Proc of the IEEE, vol. 59, p. 1440, 1971.

[15] Y. Shintani and O. Tada, Electron. Commun. Jpn., vol 56, p. 74, 1973.

[16] K. Iijima, Y. Tomita, R. Takayama, and I. Ueda, J. Appl. Phys., vol. 60, p. 361, 1986.

[17] K. Iijima, R. Takayama, Y. Tomita,, and I. Ueda, J. Appl. Phys., vol. 60, p. 2914, 1986.

[18] K. Sreenivas, M. Sayer, and P. Garrett, Thin Solid Films, vol. 172, p. 251, 1989.

[19] H. Adachi, T. Mitsuyu, O. Yamazaki, and K. Wasa, J. Appl. Phys., vol. 60, p. 736, 1986.

[20] A. Crouteau and M. Sayer, Proc. of the 6th Intern. Symp. on Applications of ferroelectrics, V.E. Wood (Ed.), IEEE, New York, p. 606, 1986.

[21] T. Fukami and M. Naoe, Trans. IEE Jpn., vol. 103-A, p. 278, 1983.

[22] M. Ishida, S. Tsuji, Y. Hamawaka, and T. Nakagawa, Appl. Phys., vol. 21, p. 339, 1978.

[23] A. Okada, J. Appl. Phys., vol. 49, p. 4495, 1978.

[24] K.D. Gifford, H.N. Al-Shareef, S.H. Rou, P.D Rhen, O. Auciello, and A.I. Kingon, MRS Symp. Proc., Fall 1991, in press, 1992.

[24'] M.S. Ameen, T.M. Graettinger, S.H. Rou, H.N. Al-Shareef, K.D. Gifford, O. Auciello, and A.I. Kingon, Ferroelectric Thin Films, E.R. Myers and A.I. Kingon (Eds.), MRS Symp. Proc. Materials Research Society, Pittsburg, vol. 200, p. 65, 1990.

[25] L.L. Boyer, A.Y. Wu, and J.R. McNeil, Ferroelectric Thin Films, E.R. Myers and A.I. Kingon (Eds.), MRS Symp. Proc. Materials Research Society, Pittsburg, vol. 200, p. 97, 1990.

[26] S.B. Krupanidhi, H. Hu, and V. Kumar, J.Appl. Phys., vol. 71, p. 376, 1992

[27] R.N. Castellano and L.G. Feinstein, J. Appl. Phys., vol. 50, p. 4406, 1979.

[28] O. Auciello, M.S. Ameen, A.R. Krauss, A.I. Kingon, and M.A. Ray, Beam-Solids Interaction: Physical Phenomena, MRS Symp. Proc., Pittsburg, vol. 157, p. 287, 1990.

[29] A.R. Krauss and O. Auciello, MRS Symp. Proc., in press, 1992.

[30] A.R. Krauss and O. Auciello, US patent No.4,493,525.

[31] A.R. Krauss, O. Auciello, A.I. Kingon, M.S. Ameen, Y.L. Liu, T. Barr, T.M. Graettinger, S.H. Rou, C.N. Soble, and D.M. Gruen, Applied Surface Science, vol. 46, p. 67, 1990.

[32] D.J. Lichtenwalner, O. Auciello, R.R. Woolcott, C.N. Soble, S.H. Rou, and A.I. Kingon, J. Vac. Sci. and Technol., vol. A10, p.1537, 1992.

[33] D.J. Lichtenwalner, R.R. Woolcott, C.N. Soble, O. Auciello, and A.I. Kingon, J. Appl. Phys., vol. 70, p. 6952, 1991.

[34] H. N. Al-Shareef, K.D. Gifford, M.S. Ameen, S.H. Rou, P.D. Hren, O. Auciello, and A.I. Kingon, Ceramic Transactions, vol. 25, p. 97, 1992

[35] A.I. Kingon, M.S. Ameen, O. Auciello, K. Gifford, H. Al-Shareef, T.M. Graettinger, S.H. Rou, and P. Hren, Ferroelectrics, vol. 116, p. 35, 1991.

[36] S.H. Rou, P.D. Hren, T.M. Graettinger, M.S. Ameen, O. Auciello, and A. I. Kingon, High Resolution Electron Microscopy of Defects in Materials, MRS Proc. Symposium, vol. 183, p. 285, 1990.

[37] P.D. Hren, S.H. Rou, K.D. Gifford, H.N. Al-Shareef, O.Auciello, and A.I. Kingon, Ferroelectrics, in press, 1992.

[38] S.X. Chen, A.I. Kingon, L. Mantese, O. Auciello, K. Gifford, K. Hsieh, Ferroelectrics, in press, 1992.

[39] J.E. Greene, S.A. Barnett, J.E. Sundgren, and A. Rochett, in Ion Beam Assisted Film Growth, T. Itoh (Ed.), Elsevier, Amsterdam, p. 101, 1989.

[40] H. Hu and S.B. Krupanidhi, Appl. Phys. Lett., vol. 61, p. 1, 1992.

[41] J.T. Cheung and H. Sankur, CRC Critical Reviews in Solid State and Materials Science, vol. 15, p.63, 1988.

[42] O. Auciello, Materials and Manufacturing Processes, vol. 6, p. 33, 1991.

[43] F.Beech and I.W. Boyd, in Photochemical Processing of Electronic Materials, I.W. Boyd and R.B. Jackman (Eds.), Academic Press, NY, p. 387, 1991.

[44] C.M. Cotell and K.S. Grabowski, Special Issue of the MRS Bulletin on Pulsed Laser Deposition, G.K.Hubler (Ed.), vol. 27, p. 30, 1992.

[45] S.B. Ogale, S.M. Kanetkar, S.M. Chaudhari, V.P. Godbole, V.N. Koinkar, S. Joshi, R. Nawathey, R.D. Vispute, S.K. Date, and A.R. Moghe, Ferroelectrics, vol. 102, p. 85, 1990.

[46] M.G. Norton C. Scarfone, J. Li, C.B. Carter, and JW. Mayer, J. Mater. Res., vol. 6, p. 2022, 1991.

[47] R. Ramesh, K. Luther, B. Wilkens, D.L Hart, E. Wang, and J.M. Tarascon, Appl. Phys. Lett., vol. 57, p. 1505, 1990.

[48] H. Buhay, S. Sinharoy, W.H. Kasner, and M.H. Francombe, Appl. Phys. Lett.,vol. 58, p. 1470, 1991.

[49] S. Yilmaz, T. Venkatesan, and R. Gerhard-Multhaupt, Appl. Phys. Lett., vol. 58, p. 2479, 1991.

[50] C.K. Chiang, L.P. Cook, P.K. Schenck, P.S. Brody, and J.M. Benedetto, in Ferroelectric Thin Films, E.R. Myers and A.I. Kingon (Eds.), Mater. Res. Soc. Symp. Proc., Pittsburg, No. 200, p. 133, 1990.

[51] G.A. Petersen, L.C. Zou, W.M. Van Buren L.L. Boyer, and J.R. McNeil, in Ferroelectric Thin Films, E.R. Myers and A.I. Kingon (Eds.), Mater. Res. Soc. Symp. Proc., Pittsburg, No. 200, p. 127, 1990.

[52] R. Ramesh, A. Inam, W.K. Chan, F. Tillerot, B. Wilkens, C.C. Chang, T. Sands, J.M. Tarascon, K. Remschnig, V.K. Keramides, Appl. Phys. Lett., vol. 59, p. 3542, 1992.

[53] H. Tabata, T. Kawai, S. Kawai, O. Murata, J. Fujioka, and S-I. Minakata, Appl. Phys. Lett., vol. 59, p. 2354, 1991.

[54] H. Kidoh, T. Ogawa, A. Morimoto, and T. Shimizu, Appl. Phys. Lett., vol. 58, p. 2910, 1991.

[55] A. Morimoto, S. Otsubo, T. Shimizu, T. Minamikawa, Y. Yonezawa, H. Kidoh, and T. Ogawa, in Laser Ablation for Materials Synthesis, D.C. Paine and J.C. Bravman (Eds.), Mater. Res. Soc. Symp. Proc., No. 191, p. 31, 1990.

[56] R.E. Leuchtner, K.S. Grabowski, D.B. Chrisey, and J.S. Horwitz, Appl. Phys. Lett., in press, 1992.

[57] K.L. Saenger, R.A. Roy, K.F. Etzold, and J.J. Cuomo, in Ferroelectric Thin Films, E.R. Myers and A.I. Kingon (Eds.)Mater. Res. Soc. Symp. Proc., Pittsburg, No. 200, p. 115, 1990.

[58] O. Auciello, L. Mantese, J. Duarte, S.H. Rou, A.I. Kingon, A.R. Krauss, and A.F. Schreiner, J. Appl. Phys., in press, 1992.

[59] S.B. Krupanidhi and D. Roy, J. Appl. Phys., vol. 72, p. 620, 1992.

[60] R.E. Leuchtner, K.S. Grabowski, D.B. Chrisey, and J.S. Horwitz, Appl. Phys. Lett., in press, 1992.

[61] H. Buhay, S. Sinharoy, W.H. Kasner, M.H. Francombe, D.R. Lampe, E. Stepke, 7th Inter. Symp. Appl. Ferroelectrics, June 6-8, 1990.

[62] K. Ramkumar, J. Lee, A. Safari, and S.C. Danforth, in Ferroelectric Thin Films, E.R. Myers and A.I. Kingon (Eds.)Mater. Res. Soc. Symp. Proc., Pittsburg, No. 200, p. 121, 1990.

[63] T. Minamikawa, Y. Yonezawa, K. Segawa, A. Marimoto, T. Shimizu, S. Otsubo, H. Kidoh, and T. Ogawa, Proc. US-Japanese Workshop on Ferroelectrics, Japan, p. 304, 1991.

Thin Films: Applications and CVD

$LiNbO_3$ THIN FILM CAPACITOR AND TRANSISTOR PROCESSED BY A NOVEL METHOD OF PHOTO-INDUCED METALLO-ORGANIC DECOMPOSITION

Charles H.-J. Huang, He Lin, and Thomas A. Rabson
Rice University
Department of Electrical and Computer Engineering
Houston, TX 77251

Abstract

A novel technique of photo-induced metallo-organic decomposition (PIMOD) was developed to deposit dielectric thin films without interdiffusion and cracking which were frequently found in the films derived by the conventional furnace-processed MOD method. Results of XRD and RBS confirm that polycrystalline stoichiometric thin films of lithium niobate can be produced under a much lower temperature and within a shorter processing time compared to the MOD process. $LiNbO_3$-based capacitors and transistors in an metal-ferroelectric-semiconductor (MFS) structure have been made via the PIMOD process. The MFS capacitors have yielded ferroelectric switching properties shown by hysteresis in capacitance vs. voltage characteristics. Large photocurrents were measured for 900 mil^2 capacitors. Recent MFSFETs have achieved an amplification factor of 92.3, and the channel conductance of the devices has been demonstrated to be highly affected by the application of voltage pulses from the gate to the substrate.

Introduction

Since the metal-ferroelectric-semiconductor field-effect transistor (MFSFET) was first proposed by Wu [1] in 1974, the device has drawn great attention by integrating the ferroelectric film into a conventional semiconductor device [1-6]. By replacing the gate oxide of a conventional metal-oxide-semiconductor (MOS) transistor with a ferroelectric material, the device may possess several advantages over other computer memory cells, including nonvolatility, fast switching speeds, and radiation hardness. The use of a thin film of lithium niobate ($LiNbO_3$) as the gate oxide offers the possibility of two different types of computer memory architectures. In addition to the operation controlled based on ferroelectric switching, the transistor characteristics of the device can be altered optically, which, based on the bulk photovoltaic effect, involves a shift in the transistor threshold by exposing the gate to laser light with different intensities. This, incorporated with other optical and electrooptic properties of $LiNbO_3$ [7, 8], makes the device extremely useful in building the optical computer.

A $LiNbO_3$-based MFSFET fabricated on silicon using the r.f. magnetron sputtering technique and a molybdenum liftoff process was recently reported by Rost *et al.* [6]. Considering the high cost for mass production due to the use of a vacuum technology, non-vacuum deposition methods such as sol-gel [9] and metallo-organic decomposition (MOD) [10] have recently received much attention. Due to the relatively long processing time (> 1 hr) and the high processing temperature (600-800°C) required for the MOD process, interdiffusion was found at the $LiNbO_3$-Si interface [11]. Utilization of rapid thermal annealing reduces the interdiffusion while increasing the chance of forming cracks. Moreover, the molybdenum layer could be highly oxidized at a temperature higher than 500°C (in air), which would totally foil the liftoff process. Huang has recently developed a novel technique of photo-induced metallo-organic decomposition (PIMOD) to overcome these problems [11]. At a much lower temperature (500°C) for a shorter processing time than required for the MOD process, crack- and interdiffusion-free thin films of $LiNbO_3$ have been grown by the PIMOD process. This is the first attempt to study the feasibility of fabricating the $LiNbO_3$ MFSFET via the PIMOD process.

Thin Film Growth

The metallo-organic precursor solutions, $C_9H_{19}COOLi$ and $Nb(OC_2H_5)_3(C_9H_{19}COO)_2$ (both in xylene), were mixed in the appropriate cation ratio to form the formulation solution. Thermogravimetric analysis (TGA) was implemented to measure the weight loss of the individual solutions as a function of temperature. A summary of the TGA results is given in Table 1. The thermogram for a $LiNbO_3$ formulation solution heated 10°C/min in air is shown in Fig. 1. The residue of the formulation solution heated at a temperature higher than 480°C was determined by x-ray diffraction to be stoichiometric lithium niobate.

Table 1: Thermal decomposition behavior of metallo-organic compounds.

Compound in Xylene	Xylene loss	Decomposition	Residue
$C_9H_{19}COOLi$	25-175°C	175-480°C	480°C - (Li_2O)
$Nb(OC_2H_5)_3(C_9H_{19}COO)_2$	25-150°C	150-360°C	360°C - (Nb_2O_5)
Mixed	25-150°C	150-480°C	480°C - ($LiNbO_3$)

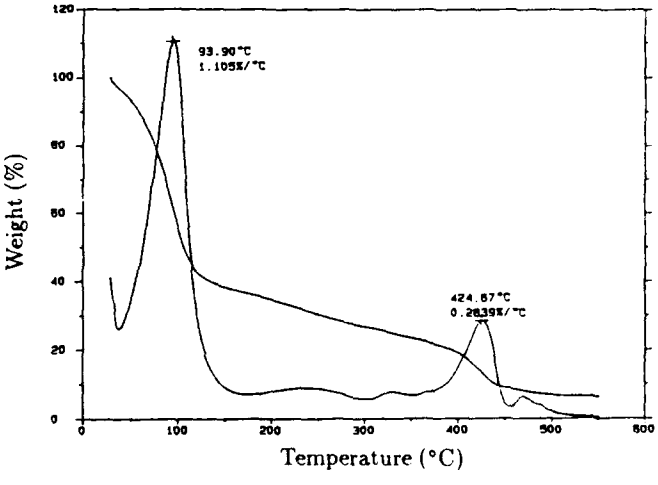


Figure 1: Thermogram for a $LiNbO_3$ formulation solution heated 10°C/min in air.

The formulation solution was spun onto a substrate at 3000 rpm for 30 sec to produce a uniform wet film. The sample was then rapidly heated by a tungsten halogen lamp to 500°C, which was determined according to the thermogram, and the time of

exposure was about 5 minutes to allow for the completion of the involved reactions including evaporation of the solvent, decomposition of the metallo-organic compounds, and sufficient oxidation of the film. The thickness of a single-layer film is about 0.19 ± 0.1 μm. The processes of deposition and pyrolysis can be repeated as many times until the film is of the required thickness. The films were often subjected to a post annealing process to reduce the porosity and to improve the crystallinity. X-ray diffraction and Rutherford backscattering (RBS) confirm that the films deposited by the PIMOD process are polycrystalline stoichiometric lithium niobate [7].

Device Fabrication

Capacitor

To form the MFS (Metal-Ferroelectric-Semiconductor) capacitors, gold-on-chromium top electrodes with areas about 0.0025 and 0.0050 cm^2 were evaporated onto the lithium niobate films on p-type (111) Si. A thin layer of Cr is necessary to help adhesion of the Au electrodes on the films. The thickness of the Au and Cr layers is 0.10 and 0.04 μm, respectively. The electrodes possess some degree of transparency (3-4%) which allows for optical measurement.

Transistor

For fabricating transistors with a 25×25 μm gate and capacitors with an area of 900 mil^2, a molybdenum liftoff process developed at Texas Instruments was used to isolate small areas of lithium niobate. The liftoff process is outlined in Fig. 2. A gold-on-chromium overlayer, the same as those described previously, was thermally evaporated onto a patterned silicon wafer. The thickness of the lithium niobate film in the MFSFET devices investigated was 0.19 μm. A 30% H_2O_2 etch removed all of the molybdenum and thus all the lithium niobate not directly in contact with the silicon. A second etch step, 4.9% HF solution, removed the plasma oxide, allowing electrical connection to the source and drain areas. MFSFET transistors and 900 mil^2 capacitors were now completely fabricated and ready for testing. A picture of two transistors, with a 25×25 μm gate, after going through all the etch steps is shown in Fig. 3.

The most critical parameter in making the $LiNbO_3$ MFSFET transistor using the PIMOD process is the temperature of the wafer. Since the PIMOD process is generally carried out in air, high oxidation of the molybdenum occurs at a temperature higher than 500°C, which can totally foil the liftoff process. However, the decomposition process can not be completed if the surface temperature does not exceed 480°C. In this case extra C and H in the $LiNbO_3$ films form defects which decrease the chemical resistance of the films thereby making the HF etch step more difficult to implement. A substrate temperature of 490°C and an exposure time of 5 minutes are thus considered to be the optimal parameters to be compatible with the molybdenum liftoff process. After the H_2O_2 etch step, a post annealing in 10 mTorr oxygen at 520-550°C for one hour is often performed to improve the crystallinity of the film.

Device Properties

Capacitor Characteristics

For electrical measurements the wafer was placed on a gold-coated wafer chuck in a shielded, light tight enclosure. A small

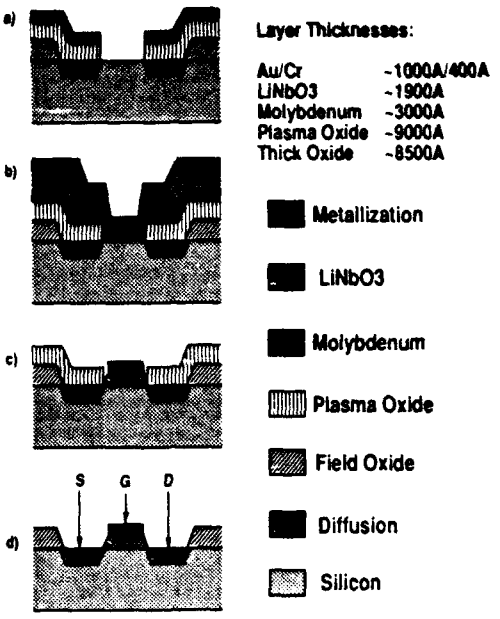


Figure 2: Molybdenum liftoff process for fabricating $LiNbO_3$ MFS transistors: a) prior to deposition, b) after $LiNbO_3$ and Au/Cr deposition, c) after H_2O_2 etch step, and d) after HF etch step.

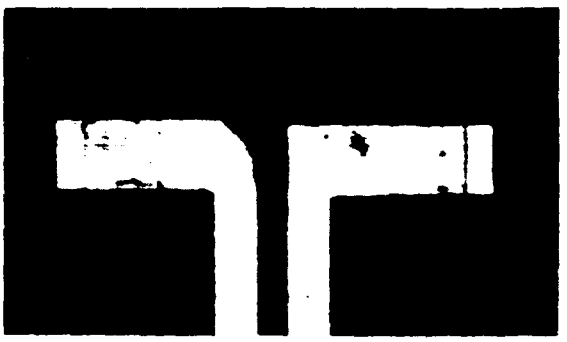


Figure 3: $LiNbO_3$ MFS transistors (gate area = 25×25 μm) after etching is complete.

tungsten probe was positioned to make contact with the electrode. By I-V measurement, the resistivity of the thin films of lithium niobate is determined to be in the range of 10^{15} Ω·cm. Capacitance vs. voltage characteristic curves were measured by applying a signal of 30 mV amplitude at 1 MHz while linearly ramping the DC offset of the signal slowly in time. Fig. 4 shows a curve taken without light exposure of a $LiNbO_3$ MFS capacitor on p-type (111) Si wafer. The hysteresis loop is due to the polarization reversal in the ferroelectric film. The dielectric constant of the films can be calculated from the capacitance provided the thickness of the film and the area under the electrode are given. The dielectric constant of a 2000 Å thick $LiNbO_3$ film was calculated to be 22. The value is slightly smaller than the bulk value, which might be attributed to the existence of an oxide buffer layer acting as a series capacitor.

To measure the photo-properties of the films, green (543.5 nm) and red (632.8 nm) He-Ne lasers, with a power of 0.9 mW, were directed onto the electrode being probed, and the photocurrent was recorded as a function of time. Fig. 5 shows the

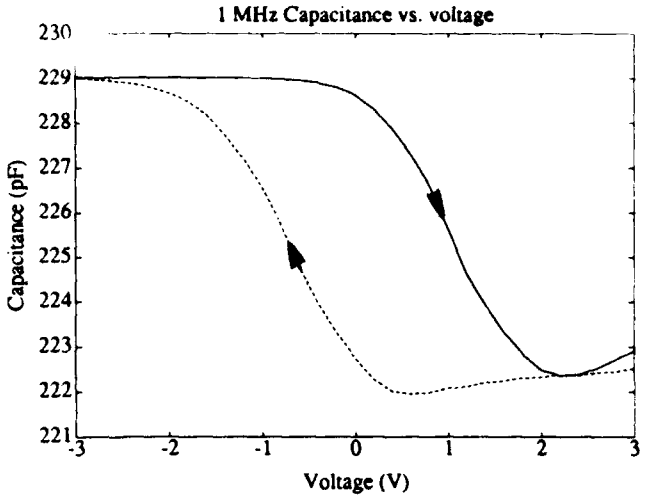


Figure 4: C-V curve for a 2000 Å thick $LiNbO_3$ film PIMOD-processed on a p-type (111) Si wafer. (0.20 V steps, 1 sec intervals, 3 sec hold at voltage extremes. Electrode area $\sim$ 0.0025 cm^2.)

photocurrents generated by shining the green laser on a 900 mil^2 capacitor. A smaller response was observed if a red light was used. This could be attributed to a higher absorption for $LiNbO_3$ in the green region. Moreover, the photocurrent was flowing in the opposite direction when the laser was incident onto a p-n junction, which excluded the possibility that the photocurrent might be generated in the depletion layer. Therefore, it is concluded that the photocurrent is produced by the pyroelectric effect and the bulk photovoltaic effect in the $LiNbO_3$ film, and the direction of the photocurrent corresponds to the +c axis of the film being oriented into the silicon substrate. It is encouraging that a large photocurrent of 3.3 nA has been observed. This indicates that the $LiNbO_3$-based devices possess a great potential on various applications in the optoelectronics and integrated optics areas.

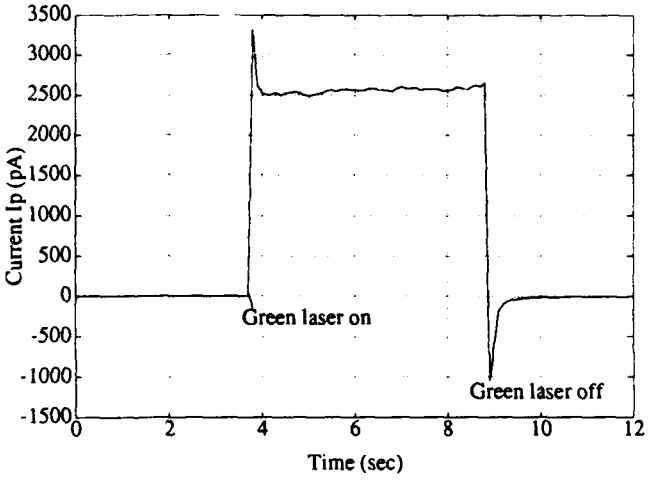


Figure 5: Photocurrents measurement for a 900 mil^2 capacitor after isolation.

MFSFET Characteristics

The characteristics of the resulting transistors were measured with the HP4145 semiconductor parameter analyzer. The gate leakage for the devices was about 1 nA (V_G = 1 V, V_{DS} = 2 V), indicating that the liftoff process was successful, and the areas of the devices were correctly defined. Fig. 6 shows the transistor curve trace of a device with a 25×25 μm gate. From these curve traces, basic transistor parameters can be calculated. The output conductance is given by

$$g_d = \left.\frac{\partial I_{DS}}{\partial V_{DS}}\right|_{V_G} \quad (1)$$

and the transconductance is

$$g_m = \left.\frac{\partial I_{DS}}{\partial V_G}\right|_{V_{DS}} \quad (2)$$

The amplification factor can then be defined by

$$\mu = \frac{g_m}{g_d}. \quad (3)$$

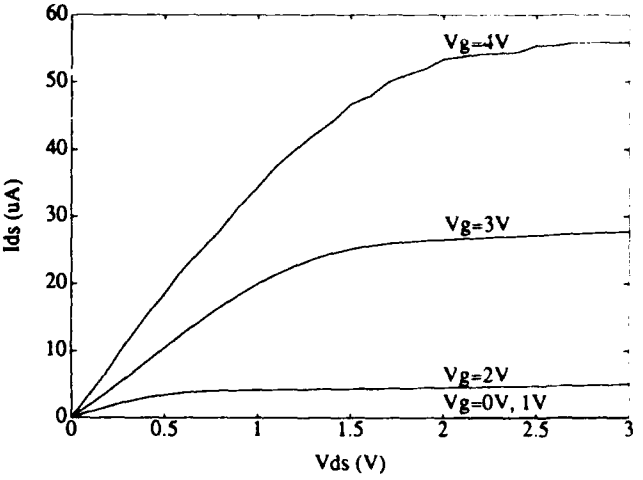


Figure 6: Transistor curve trace for a 25 × 25 μm device.

In saturation, the output conductance (g_d) was calculated, at V_G = 2 V, to be 0.24 μS. The transconductance (g_m) was measured to be 22.24 μS at a V_{DS} of 2 V with V_G from 2 to 3 V. The amplification factor of the device was then determined to be 92.3, which compares superably with the only other published data (μ = 64) on MFS transistors [6]. For a conventional MOS transistor, the channel current in saturation, $I_{DS_{sat}}$, can be approximated by

$$I_{DS_{sat}} = k(V_G - V_T)^2 \quad (4)$$

where k is a constant and V_T is the threshold voltage. By using this equation, a threshold voltage of about 1.33 V was determined for this device. The results of the measurements are shown in Table 2.

A pulsing experiment was implemented to study the switching performance of a 25×25 μm device. Voltage pulses of 1 μs were applied from the gate to the silicon substrate. As shown in Fig. 7, the channel current in saturation with 3 V on the gate can be decreased from 27.7 to 3.0 μA by applying a +10 V pulse. The curve was then restored to the original when a pulse of opposite polarity (-10 V) was applied. This shows that a feasible $LiNbO_3$-based MFSFET logic device can be fabricated by the molybdenum liftoff process. The simplicity of the PIMOD process ensures low cost for mass production.

Table 2: Measured transistor parameters for a $LiNbO_3$ MFSFET with a 25×25 μm gate area.

Parameter	Value
Gate current (V_G = 1 V, V_{DS} = 2 V)	1 nA
Output conductance (V_G = 2 V)	0.21 μS
Transconductance (V_{DS} = 2 V, V_G = 2 → 3 V)	22.24 μS
Amplification factor	92.3
Threshold voltage	1.33 V

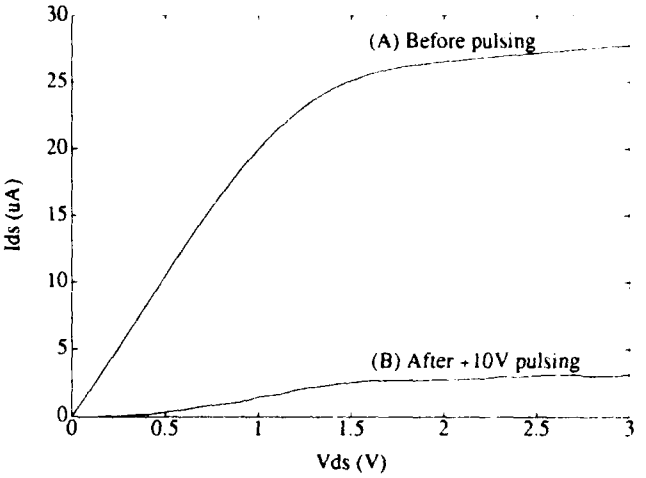


Figure 7: Channel current vs. channel voltage for an n-channel $LiNbO_3$ MFSFET before and after voltage pulses are applied from the gate to the silicon substrate, all at a gate voltage of 3 V. Curve B is then restored to curve A when -10 V pulses are applied.

Conclusions

A novel PIMOD process has been used to grow thin films of $LiNbO_3$ acting as the gate oxide of an MFSFET device. Small areas of $LiNbO_3$ on silicon and a $LiNbO_3$ MFS transistor with a gate area of 25×25 μm have been successfully fabricated by a molybdenum liftoff technique. The first measurements of the $LiNbO_3$ MFSFET device are encouraging. The transistor parameters compare favorably with other published data as well as conventional MOS devices. The channel current was shown to be greatly change by the application of voltage pulses from the gate to the substrate. The fatigue and retention characteristics of the device are currently under investigation.

References

[1] S. Y. Wu, "A New Ferroelectric Memory Device, Metal-Ferroelectric-Semiconductor Transistor," IEEE Trans. Electron Devices, vol. ED-21, pp. 499-504, 1974.

[2] S. Y. Wu, "Memory Retention and Switching Behavior of Metal-Ferroelectric-Semiconductor Transistors," Ferroelectrics, vol. 11, pp. 379-383, 1976.

[3] K. Sugibuchi, Y. Kurogi, and N. Endo, "Ferroelectric Field-Effect Memory device Using $Bi_4Ti_3O_{12}$ Film," Journal of Applied Physics, vol. 46, pp. 2877-2881, 1975.

[4] J. Schulz, ST. Koch, P. Würfel, and W. Ruppel, "Interface State Density at the Contact of Ferroelectric $NaNO_2$ and Silicon," Ferroelectrics, vol. 99, pp. 87-100, 1989.

[5] H. Buhay, S. Sinharoy, W. H. Kasner, M. H. Francombe, D. R. Lampe, and E. Stepke, "Pulsed Laser Deposition and Ferroelectric Characterization of Bismuth Titanate Films," Applied Physics Letters, vol. 58, pp. 1470-1472, 1991.

[6] F. Rost, H. Lin, and T. A. Rabson, "Ferroelectric Switching of a Field-Effect Transistor with a Lithium Niobate Gate Insulator," Applied Physics Letters, vol. 59, pp. 3651-3653, 1991.

[7] C. H. J. Huang, H. Lin, and T. A. Rabson "Integrated Optic Devices Based on Thin Film Lithium Niobate," Proceedings of the 4th International Symposium on Integrated Ferroelectrics (ISIF '92), Monterey, CA, March 9-11, 1992, (to be published).

[8] T. A. Rabson and C. H.-J. Huang, "Electronic and Optical Applications on Thin Film Lithium Niobate," Proceedings of the 4th International Symposium on Integrated Ferroelectrics (ISIF '92), Monterey, CA, March 9-11, 1992, (to be published).

[9] D. P. Partlow and J. Greggi, "Properties and Microstructure of Thin $LiNbO_3$ Films Prepared by a Sol Gel Process," Journal of Materials Research, vol. 2, pp. 595-605, 1987.

[10] R. W. Vest and R. C. R. Wu, "The Electrical Properties and Epitaxial Growth of $LiNbO_3$ Films by the MOD Process," Proceedings of the 1990 IEEE 7th International Symposium on the Applications of Ferroelectrics, Urbana, IL, pp. 170-176, June 6-8, 1990.

[11] C. H.-J. Huang, "Thin Film Lithium Niobate Optical Waveguides for Integrated Optics," PhD Thesis, Rice University, Houston, 1992.

PHOTO-CVD OF FERROELECTRIC $Pb(Zr,Ti)O_3$ THIN FILMS

Takuma Katayama, Masataka Sugiyama, Masaru Shimizu
and Tadashi Shiosaki
Department of Electronics, Kyoto University, Kyoto 606,Japan

Abstract: $Pb(Zr,Ti)O_3$ thin films were grown by the photo-CVD method using $Pb(C_2H_5)_4$, $Zr(O\text{-}t\text{-}C_4H_9)_4$, $Ti(O\text{-}i\text{-}C_3H_7)_4$ and O_2. In this growth system, both tetragonal $Pb(Zr,Ti)O_3$ films and rhombohedral $Pb(Zr,Ti)O_3$ films were successfully obtained, and the (111)-orientation of the tetragonal films was affected by the photoirradiation. It was also proven that the photo-process enhanced the reactions involving the Zr precursors and this enhancement caused compositional changes and an increase in growth rates. Some electrical properties of the films, which were related to the ferroelectric memory device qualities, were also detailed.

Introduction

Ferroelectric thin films integrated with semiconductors have a high potential for use as essential materials of future electronic and optical devices. In particular, thin films of lead zirconate titanate ($Pb(Zr,Ti)O_3$) and related perovskite oxides are the most attractive for applications to ferroelectric nonvolatile memories, high-density DRAMs, piezoelectric microactuators, pyroelectric sensors and so on. For the realization of ferroelectric thin film devices, there are some technological issues to be solved, such as film deposition, annealing, etching and formation of electrodes. Regarding the film deposition, the chemical vapor deposition (CVD) method using metallorganic sources is one of the most promising techniques to obtain device-quality $Pb(Zr,Ti)O_3$ films. The advantages of the CVD method are fairly high growth rate, high productivity, good controllability of the film composition and excellent step coverage characteristics. Moreover, it is of great interest to combine the CVD technique with the plasma-enhanced and the photo-enhanced processes in order to reduce growth temperature and to improve thin film quality.

We have proposed the photo-enhanced CVD method as a new technique for the growth of ferroelectric thin films and have been developing this method to obtain $PbTiO_3$ and $Pb(Zr,Ti)O_3$ films. In our previous study, it was clearly established that the photo-enhanced process during the CVD growth had some effects on the structural, compositional and electrical properties of both $PbTiO_3$ and $Pb(Zr,Ti)O_3$ thin films.[1-6] In this paper, we will report new experimental results on the growth of $Pb(Zr,Ti)O_3$ thin films by our photo-CVD method and discuss in detail effects of the photoirradiation on crystallinity, composition and growth rate. Several electrical properties of $Pb(Zr,Ti)O_3$ thin films related to the memory device applications are also described.

Experimental procedure

The photo-CVD system for the formation of $Pb(Zr,Ti)O_3$ thin films was the same one as has been already reported.[6] The growth conditions are summarized in Table I. Tetraethyl lead ($Pb(C_2H_5)_4$), zirconium tetratertiarybutoxide ($Zr(O\text{-}t\text{-}C_4H_9)_4$), titanium tetraisopropoxide ($Ti(O\text{-}i\text{-}C_3H_7)_4$) and oxygen ($O_2$) were used as source materials. The concentration of each metallorganic precursor was controlled by both source tank temperature and Ar carrier gas flow rate. Substrates used were (111)$Pt/SiO_2/Si$, SiO_2/Si and (0001)sapphire. The $Pb(Zr,Ti)O_3$ films were grown at substrate temperatures ranging from 525 to 660°C. In the photo-CVD experiments, the substrates were directly irradiated by the UV light emitted by a Xe-Hg lamp.

Table I. Growth conditions of $Pb(Zr,Ti)O_3$ thin films.

Source Temperature	$Pb(C_2H_5)_4$: 0°C
	$Zr(O\text{-}t\text{-}C_4H_9)_4$: 35°C
	$Ti(O\text{-}i\text{-}C_3H_7)_4$: 35°C
Ar Carrier Flow Rate	$Pb(C_2H_5)_4$: 80sccm
	$Zr(O\text{-}t\text{-}C_4H_9)_4$: 20-70sccm
	$Ti(O\text{-}i\text{-}C_3H_7)_4$: 26-76sccm
O_2 Flow Rate: 240sccm	
Substrate Temperature: 525-660°C	
Total Pressure: 6Torr.	
UV Light Source: Xe-Hg Lamp (220-600nm)	

Results and Discussion

Structural Nature

The crystalline phases and orientation properties of the films deposited on $Pt/SiO_2/Si$ and sapphire substrates were investigated. In the case of the growth onto $Pt/SiO_2/Si$, both $Pb(Zr,Ti)O_3$ thin films with a tetragonal phase and those with a rhombohedral phase could be obtained without annealing. The crystalline phases of the films were significantly affected by the substrate temperatures and source supply conditions, and higher substrate temperatures were required to grow rhombohedral $Pb(Zr,Ti)O_3$ films than tetragonal $Pb(Zr,Ti)O_3$ films. Details of the crystalline phases of the films deposited by the conventional thermal-CVD method (without photoirradiation) were reported elsewhere.[7] When the photo-CVD was carried out, we obtained films with the same crystalline phases as were grown by the thermal-CVD method, and it was difficult to reduce the growth temperature for the formation of perovskite single

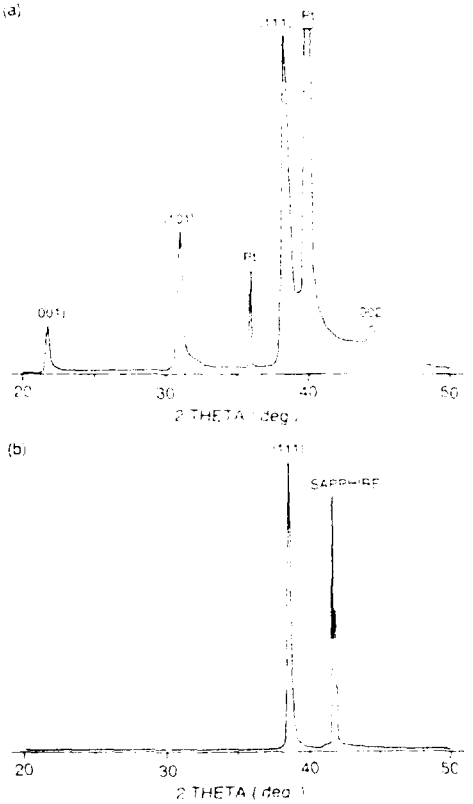


Fig.1. X-ray diffraction patterns of the tetragonal $Pb(Zr,Ti)O_3$ thin films grown at 605°C by photo-CVD. Substrates used were (a)$Pt/SiO_2/Si$ and (b)(0001)sapphire.

CH3080-0-7803-0465-9/92$3.00 ©IEEE

phase $Pb(Zr,Ti)O_3$ in the present photo-CVD system. It seems necessary to select more effectual source materials and/or light sources in order to achieve low temperature growth. On the other hand, orientation properties of the films were affected by the photoirradiation. In particular, the photodeposited tetragonal $Pb(Zr,Ti)O_3$ showed higher (111)-orientation than the films grown by thermal-CVD. However, (111)-single-oriented $Pb(Zr,Ti)O_3$ films could not yet be obtained, perhaps because of the low (111)-orientation of the sputtered Pt layers of the substrates. Figure 1(a) shows an X-ray diffraction pattern of a $Pb(Zr_{0.47},Ti_{0.53})O_3$ thin film grown on $Pt/SiO_2/Si$ by the photo-CVD method. (substrate temperature; 605°C)

When the (0001)sapphire substrates were used, tetragonal $Pb(Zr,Ti)O_3$ thin films were obtained, but rhombohedral films could not be grown because ZrO_2 was formed more easily. In the case of the growth onto sapphire, there was a distinct improvement in the (111)-orientation of the tetragonal $Pb(Zr,Ti)O_3$ films in the photo-CVD process. Figure 1(b) shows an X-ray diffraction pattern of a photodeposited tetragonal $Pb(Zr,Ti)O_3$ film (the composition was not investigated yet) grown on sapphire at 605°C. These results indicate that the effects of the photoirradiation on film orientation were dependent on the substrate materials.

Film Composition

The compositions of the tetragonal $Pb(Zr,Ti)O_3$ films grown on SiO_2/Si substrates were methodically analyzed by inductively coupled plasma (ICP) emission spectrometry. Figure 2 shows the dependence of the Zr/(Zr+Ti) compositional ratio of the films on relative supply ratio of the Zr source ([Zr]/([Zr]+[Ti])). The symbols of [Zr] and [Ti] indicate the supply rates of the Zr and Ti source materials, respectively, which were changed by controlling the vapor pressure and carrier gas flow rate of each sources. As shown in Fig.2, the photodeposited films had higher Zr/(Zr+Ti) ratios than the films obtained without photoirradiation. In order to evaluate these data theoretically, we assume that the number of a metal cation:M contained in a film (N_M) was proportional to the source supply rate of M ($[M]$), that is;

$$N_M = k_M \cdot [M] \cdot t_d \quad (1),$$

where t_d is a deposition time. The new constant of k_M was equivalent to the yield of M during the CVD growth run. Under this assumption, the relative Zr compositional ratio of the films ($X=Zr/(Zr+Ti)$) was considered to be a function of the relative Zr supply ratio ($x=[Zr]/([Zr]+[Ti])$) as;

$$X = \frac{k_{Zr} / k_{Ti}}{(k_{Zr} / k_{Ti}) + ((1-x)/x)} \quad (2).$$

The theoretical curves calculated from the experimental data by the least squares method are also drawn in Fig.2. This statistical evaluation revealed that the atomic yield ratio between Zr and Ti (k_{Zr}/k_{Ti}) was 0.41 when the films were grown without photoirradiation. On the other hand, in the photo-CVD process, k_{Zr}/k_{Ti} was estimated to be 0.48, which was higher than that of the thermal-CVD. Therefore, it was probable that the UV light irradiation enhanced the reactions of the Zr precursors more drastically than these of Ti precursors.

Growth Rate

The growth rates of the tetragonal $Pb(Zr,Ti)O_3$ films obtained on Pt/SiO2/Si at various [Zr]/([Zr]+[Ti]) supply ratios and substrate temperatures were investigated. Figures 3(a) and 3(b) show the substrate temperature dependence of the growth rate of the films grown at [Zr]/([Zr]+[Ti]) ratios of (a)0.41 and (b)0.65, respectively. When the [Zr]/([Zr]+[Ti]) ratio was 0.41, the growth rates of the films were in the range from 17 to 19nm/min. at substrate temperatures higher than 578°C, where the perovskite $Pb(Zr,Ti)O_3$ thin films were dominantly grown. At this gas supply condition, the photoirradiation enhanced the growth rates of the films, but only slightly. On the other hand, the films grown at the [Zr]/([Zr]+[Ti]) ratio of 0.65 had lower growth rates than the films grown at the [Zr]/([Zr]+[Ti]) ratio of 0.41. This decrease in the growth rates was related to the value of k_{Zr}/k_{Ti} less than unity, as mentioned in the previous para-

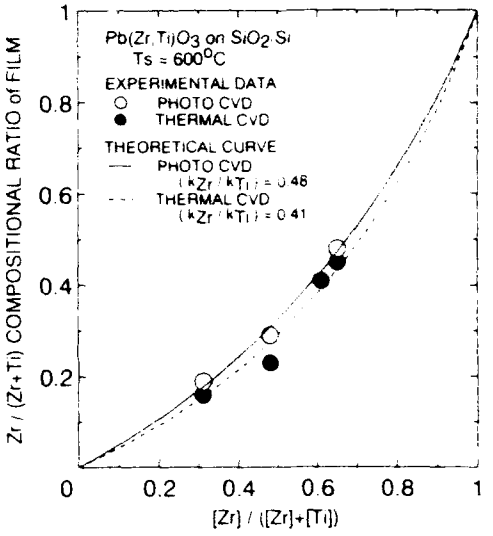


Fig.2. The dependence of Zr/(Zr+Ti) compositional ratio of films on relative supply ratio of the Zr source ([Zr]/([Zr]+[Ti])).

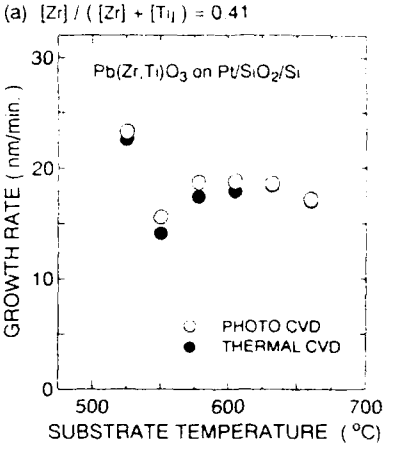


Fig.3. The dependence of growth rate of films on substrate temperature. [Zr]/([Zr]+[Ti]) ratios were (a)0.41 and (b)0.65.

graph. That is to say, it was difficult to achieve the high-rate growth of $Pb(Zr,Ti)O_3$ at the high Zr source concentrations because the yield of the Zr source in the CVD growth was lower than that of the Ti source. However, the presence of photoirradiation during the growth run helped to increase the growth rates of the films obtained at the [Zr]/([Zr]+[Ti]) ratio of 0.65. This means that the effects of the UV light irradiation on the growth rate were dependent on the gas supply conditions, and tended to become greater as the relative Zr supply ratio increased. Therefore, it was probable that the photo-process significantly promoted the chemical reactions involving the Zr precursors in the CVD growth. As for the effects of the photo-enhancement, the result on the growth rate concurred well with that on the film composition, as described above.

Electrical Properties

We also measured several electrical properties of the films, such as dielectric constants, ferroelectric hysteresis properties, polarization switching characteristics and current-voltage characteristics. In this paper, we will report the electrical properties of the $Pb(Zr_X,Ti_{1-X})O_3$ thin films (some of them included the other crystalline phases) grown either by thermal-CVD or photo-CVD, where the values of X were 0.43-0.48. These films were obtained at the [Zr]/([Zr]+[Ti]) supply ratio of 0.65 and at substrate temperatures ranging from 525 to 660°C. The thicknesses of the films measured were between 280 and 320nm. Au upper electrodes with areas in a range from 3.8×10^{-5} to $1.0\times10^{-2}cm^2$ were prepared on the $Pb(Zr,Ti)O_3$ films for the various electrical measurements.

The relationship between the relative dielectric constant of the films and the substrate temperature is shown in Fig.4. The dielectric constants were drastically affected by the substrate temperature because the crystalline properties of the films depended on the substrate temperature. At substrate temperatures around 578°C, where the $Pb(Zr,Ti)O_3$ films with perovskite single phase were successfully obtained, the relative dielectric constants of the films were as high as 500-600. Moreover, the photodeposited thin films had higher dielectric constants than the films grown without photoirradiation at this temperature range. This increase in the dielectric constant was due to the compositional and/or structural changes caused by the photoirradiation

The ferroelectric properties of the $Pb(Zr,Ti)O_3$ thin films were evaluated by observing the D-E hysteresis loops at 1kHz using the conventional Sawyer-Tower circuit. Figure 5 illustrates a typical hysteresis loop of a 320nm-thick $Pb(Zr,Ti)O_3$ film grown at 550°C by our photo-CVD method. The films grown at substrate temperatures lower than 632°C showed distinct ferroelectric hysteresis loops, regardless of whether the photoirradiation was present or not. As shown in Fig.4, most hysteresis loops of the films obtained in our experiments were asymmetric because of the existence of an internal bias field. The cause of this bias field is not clear yet. Though the asymmetric shapes of the hysteresis loops prevented us from measuring accurate values of the remanent polarizations and coercive fields of the films, they were approximately estimated as 20-35μC/cm² and 70-90kV/cm, respectively. The remanent polarizations of the films tended to decrease as the substrate temperature increased, because the crystalline structures of the $Pb(Zr,Ti)O_3$ films changed from the c-axis (the polarization axis) oriented structure to the (111)-preferential oriented structure with the substrate temperature.

The polarization switching characteristics of the $Pb(Zr,Ti)O_3$ thin films were investigated, by applying double bipolar pulses with amplitudes ranging from 2 to 8V. The widths of the pulses used were varied from 1 to 20μs. Figure 6 shows the polarization switching current characteristic of the $Pb(Zr,Ti)O_3$ thin film grown at 550°C by photo-CVD. This figure indicates the difference between the switching current transient generated by the first and third pulses and the non-switching current transient generated by the second and forth pulses, which were observed using a 51Ω sense resistor. The switched charge densities measured were 20-30μC/cm², which were less than double the remanent polarizations of the films, because pulse amplitudes higher than 8V were required to switch the ferroelectric domains in the $Pb(Zr,Ti)O_3$ films completely. On the other hand, the switching times of the films monotonically shortened as the area of the upper electrode decreased. When electrodes with the areas less than $5.0\times10^{-5}cm^2$ were used, switching times as short as 50-70ns could be achieved, as shown in Fig.6.

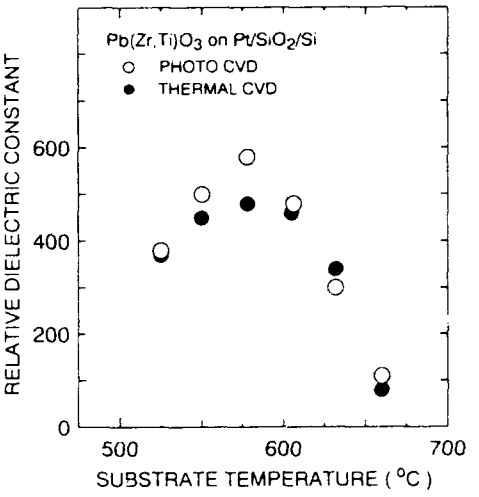


Fig.4. The dependence of relative dielectric constant of films on substrate temperature.

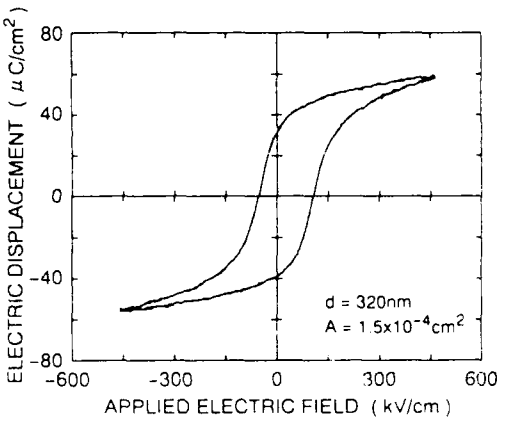


Fig.5. D-E hysteresis loop of a 320nm-thick $Pb(Zr,Ti)O_3$ film grown at 550°C by photo-CVD.

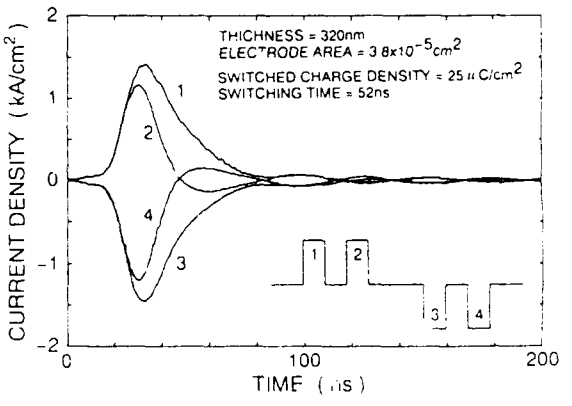


Fig.6. Polarization swithing current characteristic of the $Pb(Zr,Ti)O_3$ film grown at 550°C by photo-CVD.

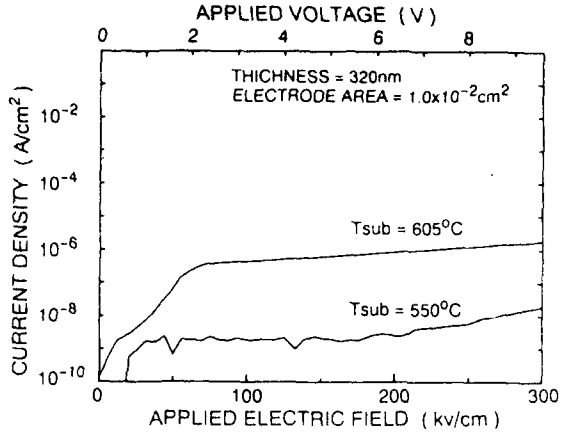


Fig.7. Leakage current characteristics of $Pb(Zr,Ti)O_3$ thin films grown by photo-CVD.

The current-voltage characteristics of the $Pb(Zr,Ti)O_3$ films were also investigated. Figure 7 shows the leakage current densities of the films grown by photo-CVD as a function of the applied electric field. The leakage currents became lower as the substrate temperature decreased, in a temperature range from 550 to 632°C. Especially, the photodeposited film obtained at 550°C had a leakage current density lower than $10^{-8}A/cm^2$ at electric fields below 250kV/cm (at applied voltages below 8V). This improvement in tolerance for leakage was due to a change of the microstructures of the thin films, which were much dependent on the substrate temperature.

The photoirradiation during the growth run affected the dielectric constants of the tetragonal $Pb(Zr,Ti)O_3$ thin films, as mentioned above. Moreover, some differences in the other electrical properties, such as the shape of the hysteresis loop, internal bias field and leakage characteristics, were also observed between the films grown by photo-CVD and those by thermal-CVD. It is probable that these differences in the electrical properties relate to the structural and compositional changes caused by the photo-process. The details of the effects of the photoirradiation on the dielectric and ferroelectric properties of the $Pb(Zr,Ti)O_3$ thin films are now being studied.

Conclusions

The photo-CVD of the $Pb(Zr,Ti)O_3$ thin films was carried out using tetraethyl lead ($Pb(C_2H_5)_4$), zirconium tetratertiarybutoxide ($Zr(O\text{-}t\text{-}C_4H_9)_4$), titanium tetraisopropoxide ($Ti(O\text{-}i\text{-}C_3H_7)_4$) and oxygen ($O_2$) as source materials. The films were grown at relative Zr source supply ratios below 0.65 and substrate temperatures ranging from 525 to 660°C. The UV light source used was a Xe-Hg lamp.

In our experiments, two types of perovskite $Pb(Zr,Ti)O_3$ films, tetragonal films and rhombohedral films, were successfully obtained by controlling the growth conditions. In the photo-enhanced CVD process, growth of (111)-oriented tetragonal $Pb(Zr,Ti)O_3$ thin films was observed, particularly on (0001)sapphire substrates. However, it was difficult to reduce the substrate temperatures required to grow the perovskite $Pb(Zr,Ti)O_3$ in the present photo-CVD system. The UV light irradiation during the CVD growth helped to increase both the relative Zr compositional ratios and growth rates of the films. These results revealed that the photo-process enhanced the chemical reactions involving the Zr precursors.

The electrical properties of the obtained tetragonal $Pb(Zr,Ti)O_3$ thin films and their dependence on the substrate temperature were also investigated. The $Pb(Zr,Ti)O_3$ films with the highest dielectric constants were grown around 578°C. On the other hand, the films with good ferroelectric properties and excellent leakage current characteristics were successfully obtained at substrate temperatures as low as 550°C. These films showed high-speed polarization switching behaviors. We also observed some effects of the photoirradiation on the electrical properties, e.g., an increase in dielectric constants. Therefore, detailed investigations of the relationship between the photo-process and the electrical properties are now conducted.

Acknowledgements

The authors would like to thank Mr. Y. Takamatsu of Tri-Chemical Laboratory Inc. for the metallorganic source materials. They are also much indebted to Mr.C. Hashimoto and Mr. K. Hayashi of Ube Industries Co.,Ltd. for the ICP emission analysis. This work was partly supported by Grants-in-Aid for Scientific Research (B) (No.04452176) and for Scientific Research on Priority Areas (2) (No.04205075) from the Ministry of Education, Science and Culture of Japan, and by research grants from the Mazda Foundation's Research Grant and the Foundation for the Promotion of Material Science and Technology of Japan.

References

[1] M.Shimizu, T.Katayama, T.Shiosaki and A.Kawabata, "Preparation of $PbTiO_3$ Thin Films by Photo-MOCVD," in *Proc. 7th IEEE Int.Symp. Applications of Ferroelectrics*, 1991, pp.669-672.

[2] M.Shimizu, T.Katayama, M.Fujimoto and T.Shiosaki, "Growth of $PbTiO_3$ Films by Photo-MOCVD," in *Proc.Int.Conf. Thin Film Physics and Applications*, 1991, pp.122-127.

[3] T.Katayama, M.Fujimoto, M.Shimizu and T.Shiosaki, "Growth and Properties of $PbTiO_3$ Thin Films by Photoenhanced Chemical Vapor Deposition,"*Jpn.J.Appl.Phys.*, vol.30, pp.2189-2192, 1991.

[4] T.Katayama, M.Fujimoto, M.Shimizu and T.Shiosaki, "Photo-MOCVD of $PbTiO_3$ Thin Films," *J.Cryst.Growth*, vol.115, pp.289-293, 1991.

[5] T.Katayama, M.Shimizu and T.Shiosaki, "Photoenhanced Chemical Vapor Deposition of $PbTiO_3$ and $Pb(Zr,Ti)O_3$ Thin Films," to be published in *Proc. 4th Int.Symp. Integrated Ferroelectrics*.

[6] T.Katayama, M.Sugiyama, M.Shimizu and T.Shiosaki, "Growth of $Pb(Zr,Ti)O_3$ Thin Films by Photoenhanced Chemical Vapor Deposition and Their Properties," to be published in *Jpn.J.Appl.Phys.*, vol.31, Part 1, No.9B, 1992.

[7] M.Shimizu, K.Hayashi, T.Katayama and T.Shiosaki, "Compositional Control of Ferroelectric $Pb(Zr,Ti)O_3$ Thin Films Prepared by Reactive Sputtering and MOCVD," in *Proc. 8th IEEE Int.Symp. Applications of Ferroelectrics*, 1992.

MOCVD GROWTH OF $BaTiO_3$ IN AN 8" SINGLE-WAFER CVD REACTOR

P. C. Van Buskirk, R. Gardiner, P. S. Kirlin
Advanced Technology Materials, 7 Commerce Dr., Danbury CT. 06810

S.B. Krupanidhi
MRL, Pennsylvania State University, University Park PA., 16802

Abstract

Standard ONO capacitors may be replaced by high dielectric constant materials such as $Ba_{1-x}Sr_xTiO_3$ (BST) in 256 megabit (Mb) and 1 gigabit (Gb) dynamic random access memories (DRAMs). A reduced pressure MOCVD process for the growth of $BaSrTiO_3$ thin films was developed in a 2" inverted-vertical reactor and preliminary studies were carried out to scale this process to a commercially available single-wafer tool. Novel process technology was used as the CVD sources were dissolved in a liquid which was metered into a vaporizer with a high precision pump . Implementation of this process gave uniform deposition of perovskite phase $BaTiO_3$ over the entire surface of a 150 mm Pt metallized Si wafer. These films exhibited crystallographic texture in the [100] direction and thickness uniformity better than ±10%. The $BaSrTiO_3$ thin films grown in the 2" reactor were predominantly [111] oriented; dielectric constants greater than 400 and dc leakage of 7 x 10^{-6} A/cm were achieved.

Objectives

$BaTiO_3$-$SrTiO_3$ is a set of solid solutions with exceptional electronic properties; the temperature dependence and amplitude of the dielectric constant can be engineered via manipulation of the Ba:Sr ratio and the grain size.[1] These properties enable many applications for this material, which include storage capacitors in conventional as well as low temperature Si-based integrated electronics[2], pyroelectric detector array elements in room temperature infrared sensors,[3] cell capacitors in dynamic and static random access memories (DRAMs and SRAMs), decoupling capacitors for E-M noise suppression[4], and filters for cellular communications.

The use of BST thin films for 256 Mb and 1 Gb DRAMs is being actively investigated by several groups; high capacitance per unit area and low dc leakage have been demonstrated using various film deposition methods that include physical vapor deposition (PVD), chemical vapor deposition (CVD) and "wet" techniques. These methods include ion[5] and magnetron sputtering[6], reactive co-evaporation[7], metalorganic chemical vapor deposition (MOCVD)[8] and metal-organic decomposition, which entails either spin-on or nebulized liquid application of metalorganic precursors followed by heat treatments[9]. The primary focus of these efforts has been to deposit BST thin films with electrical properties suitable for use as storage capacitors in ULSI DRAMs. Miyasaka et al. have recently reviewed BST film performance and compared present performance to the projected capacitance/area required at storage nodes for 256 Mb and 1 Gb DRAMs[10]. Equivalent SiO_2 thickness[11] (t_{eq}) of approximately 0.3 nm is required for planar capacitors in 256 Mb devices. Present ONO multilayers[12] have t_{eq} = 5 nm., Ta_2O_5 films have t_{eq} = 2.5 nm. and results to-date for BST films deposited using PVD methods are limited to t_{eq} = 1 nm. While this falls short of required capacitance/area by a factor of 3, required capacitance may be realized by moderate increases in the effective capacitor area by conformal BST deposition over a 3 dimensional bottom electrode of moderate topography.

Chemical vapor deposition (CVD) is uniquely capable of uniform, conformal deposition over submicron features which, in addition to the ease of scale-up to manufacturing volumes, is the main reason for its widespread acceptance in the semiconductor IC industry. The development of a BST MOCVD process in a research tool and subsequent scale-up to a state-of-the-art commercial CVD system is described below.

Technical approach

MOCVD of complex oxides (both ferroelectric perovskites and high T_c films) has been ongoing at ATM for the past five years and during that time we have identified the key process parameters which substantially impact film stoichiometry and crystallinity. This experience provides the basis of our technical approach for scaling processes developed in relatively small "research" CVD reactors to a larger CVD reactor which is described below.

Thermal vs. plasma-enhanced MOCVD

An important consideration in the development of the BST MOCVD process was the energy source for activation of the precursors (both cation and oxygen) and film crystallization; a standard thermal process employing a N_2O/O_2 oxidizer gas mixture was selected. In previous efforts an RF plasma was used to remotely generate atomic oxygen (and other active species), which were then transported to the substrate via gas flow in the reactor. Remote generation of short-lived, excited species such as atomic oxygen results in large reactant concentration gradients making control of growth conditions over a large area difficult. Another shortcoming is the strong tendency of the O_2 plasma by-products to stimulate premature gas-phase reactions with the metalorganics, even at very low plasma powers. Particulates resulting from premature reactions are not acceptable in a VLSI device manufacturing step; stringent cleanliness requirements are being driven by ever decreasing device feature size and increasing yield requirements, especially for DRAMs.

Standard thermal MOCVD processes are much simpler to control their plasma assisted analogs and once developed, scaling to different reactor geometries is less difficult. Recent results obtained by ATM[13] and reported in the literature[14,15,16] in the MOCVD of related Ba and Sr containing compounds (high temperature superconductors) indicate that replacing oxygen with N_2O or ozone (O_3) has a similar effect as a remote oxygen plasma in lowering the temperature required for the in-situ formation of the perovskite phase. Both N_2O and ozone are thermally more liable than oxygen leading to higher concentration of atomic oxygen (vs. molecular) at moderate temperatures and it has been widely speculated that this is the underlying mechanism responsible for reducing the deposition temperature of the Ba- and Sr- based perovskites. Thermal decomposition of N_2O may in fact be a significant (or predominant) mechanism in plasma-enhanced processes that employ this gas. The scaling of the BST MOCVD process has therefore focused on thermal decomposition of N_2O as a low temperature source of atomic oxygen. Figure 1 schematically illustrates this approach for scaling the BST deposition process to the Watkins-Johnson Select 7000 reactor. Development of a thermal process was the first step; initial work in the 8" reactor utilized a ternary system, $BaTiO_3$, to simplify process and thin film characterization.

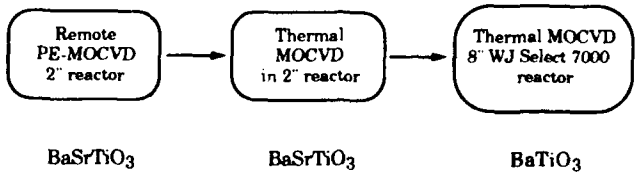


Figure 1. Schematic of technical approach. A thermal process for BST deposition has been implemented in a 2" reactor; initial work in the 8" reactor will use this process and concentrate on $BaTiO_3$.

CH3080-0/92/0000-0465 $3.00 ©IEEE

Precursor delivery to the reactor

A second major issue in the development of a BST MOCVD process is the controlled introduction of relatively involatile precursors to the reactor. Regardless of the type of compound (inorganic, metalorganic, alkoxide, etc.) the desirability of CVD for film deposition has intensified the search for CVD precursors for many materials where obvious choices (gaseous compounds) do not exist, and in general the volatility of these new sources is somewhat less than what is desired. Quite often liquid sources (and sometimes solid sources) are the only viable precursor choice[17], and conventional techniques for controlled vaporization and delivery of these compounds utilizing bubblers do not give reproducible results.[18] Consequently, an alternative approach[19] which uses liquid solutions of the metalorganic precursors was developed. In this approach, the liquid solutions were supplied to a vaporization zone using a high precision pump. (Figure 2) Downstream of the vaporization zone a homogeneous gas of the precursors flows to the reactor; this part of the system must be heated to prevent condensation of the reactants. The major advantage of the liquid delivery approach is that liquids can be mixed just prior to vaporization; besides the simplicity of this approach the ability to make slight composition adjustments via computer control makes this approach highly desirable. Once the process has optimized, the simultaneous delivery of all the cation species to the substrates via a single solution is possible and this is inherently superior to separate precursor manifolds in terms of both film stoichiometry and system complexity. This technique has been successfully used by ATM for growth of $BaSrTiO_3$ and $YBaCuO$[20]. Properties of HTSC and ferroelectric films deposited using this process have been comparable to films grown by any technique and to the best of our knowledge in the case of the BST superior to all published CVD results. The controlled delivery of relatively involatile CVD precursors offered by this technique opens the doors to a broad range of CVD processes, especially those which employ simultaneous delivery of several compounds. The possibility of donor-doping to suppress dc leakage may also be addressed in a simple way by use of this technique.

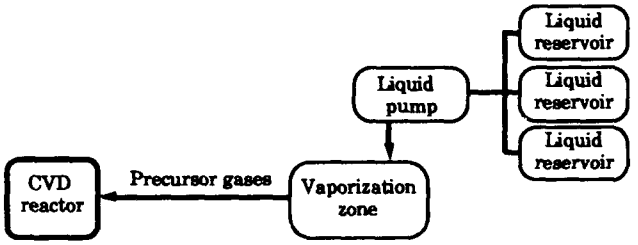


Figure 2. Schematic of liquid delivery technique for simultaneous, controlled introduction of metalorganic compounds to the CVD reactor.

$BaSrTiO_3$ film properties (2" reactor)

Process description

As described above a thermal CVD process for BST was first developed in the research scale reactor and the single solution liquid delivery technique was used to introduce the metalorganic precursors: $Ba(thd)_2$-tetraglyme, $Sr(thd)_2$-tetraglyme and $Ti(OPr)_2(thd)_2$. Reactor geometry was the inverted-vertical type with a 2" wafer capability described in earlier publications.[21,22] The Ba/Sr ratio was 75:25. Growth temperature was 650°C and total pressure was 525 mTorr. A mixture of nitrous oxide (N_2O) and oxygen were used as the oxidizer gas; flow rates were 100 sccm for each component. Ar was used as a carrier gas at 100 sccm and the BST films were grown on a Pt/Ta metallized Si wafer; typical film thickness was in the 1400-3300Å range.

BST film morphology and crystallinity

X-ray diffraction indicates that films grown under these conditions were perovskite phase with preferred orientation (texture) in the [111] direction. (Figure 3) The Pt film substrate also had this predominant orientation. In contrast; BST films grown using an O_2 plasma-enhanced process[23] with otherwise similar deposition conditions were typically random oriented; the reason for this difference is not known at present.

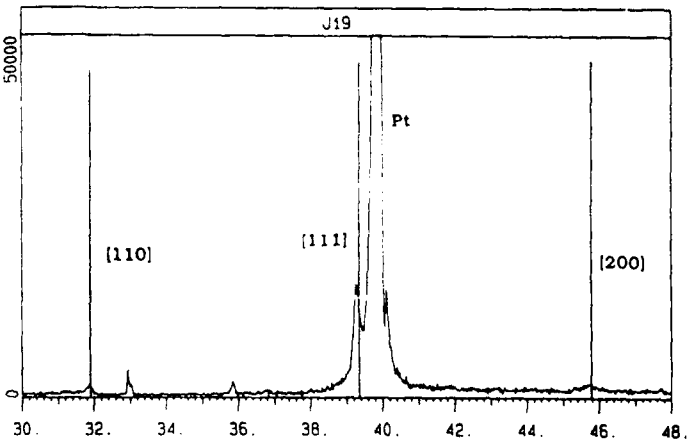


Figure 3. X-ray diffraction, BST deposited using the thermal process on metallized Pt. JCPDS Card# 34-411 ($Ba_{0.6}Sr_{0.4}TiO_3$) is overlaid.

Film morphology was quite smooth, comprised of a homogeneous, tightly packed system of crystallites that were less than 1000Å in diameter. Surface roughness was measured using stylus profilometry.[24] Poughness of the BST films on the Pt metallization was typically 50-70Å RMS, although this value was not significantly different from that of the metallized Si which was exposed to the growth conditions without the metalorganics present, indicating that the BST film contributed little additional roughness. Roughening of the Pt bottom electrode coupled with partial oxidation of the refractory metal binder layer has also been reported by other workers.[25,26]

BST film electrical properties

Dielectric properties from 100 Hz to 1 MHz were measured with an HP 4192A impedance analyzer, using evaporated gold contacts and the Pt base layer as the top and bottom electrodes, respectively. Polarization vs. E-field was measured using a modified Sawyer-Tower circuit configuration. DC conductivity was measured using a Keithley 617 electrometer. The field dependence of the dielectric constant or "quasi-static C-V characteristic" of the BST films was determined with the impedance analyzer at 1 MHz (1 mV) and a sweeping dc voltage (+10 to -10 V).

Films typically showed slight ferroelectricity, for example a coercive field of 9kV/cm and a remnant polarization of 2 $\mu C/cm^2$ were obtained for a film of 3300 Å thickness. Capacitance-voltage (Figure 4) similarly shows slight hysteresis and decrease in the dielectric constant as polarization becomes partially saturated. The macroscopically observed dielectric constant was found to depend on film thickness (Figure 5); this could be caused by a low dielectric constant interface layer at the BST-Pt interface, compositional or microstructural inhomogeneities (with depth), or intrinsic grain size effects which are poorly understood at present. The dielectric constant showed almost no dependence on temperature (Figure 6) which, along with the suppressed dielectric constant (relative to ceramics) is consistent with the published data on the dielectric properties in fine-grained $BaTiO_3$ and $SrTiO_3$ ceramics.[27]

Leakage current at 3V was 7 x 10^{-6} A/cm^2 and resistivity was as high as 10^{10} Ω-cm, although there was significant variability in the conduction characteristics which suggests that extrinsic defects (pinholes, particulates, bottom electrode discontinuities) may be responsible.

While these leakage properties are not yet suitable for DRAMs, the achievement of high dielectric constant films using a thermal N_2O/O_2 CVD process is significant and demonstrates the viability of the approach. At this stages efforts to scale the BST MOCVD process to the Select 7000 CVD system were initiated; preliminary results are describe in the next sections.

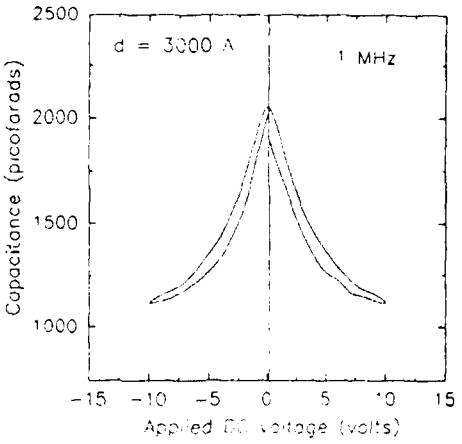


Figure 4. C-V for thermally grown BST (2" reactor)

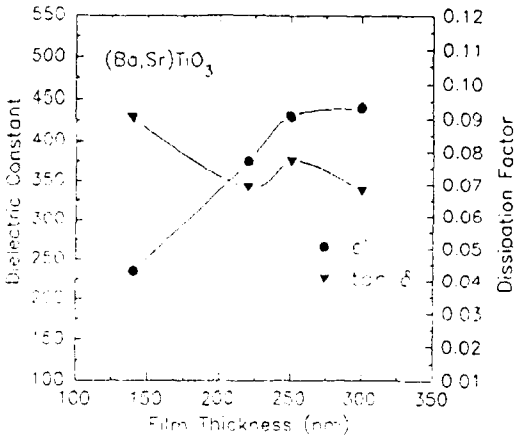


Figure 5. Thickness dependence of dielectric constant

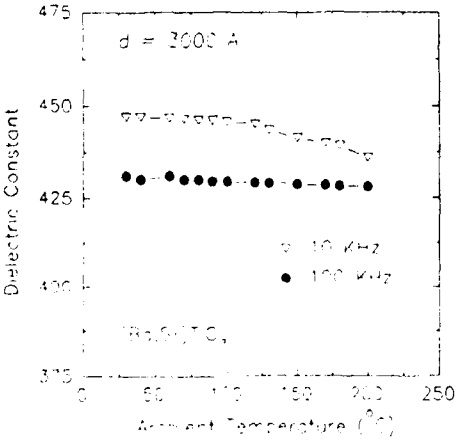


Figure 6. Temperature dependence of dielectric constant.

WJ Select 7000 modifications

The Watkins Johnson[28] Select 7000 is a low-pressure CVD module designed for use in a cluster tool configuration (Figure 3). This tool conforms to Modular Equipment Standards Committee (MESC) specifications for semiconductor equipment. The reactor uses a "shower head" inlet to the reactor chamber; both the shower head and the wafer are nearly vertical during film deposition. As mentioned above the inlet sub-system needs to be heated to prevent condensation or decomposition of the metalorganics downstream of the vaporization zone and modifications to the standard Select 7000 inlet were made in two phases to achieve uniform heating. The liquid delivery technology developed in smaller reactors was also adapted to the Select 7000 hardware. Vaporizer design and operation were essentially unchanged from the initial work demonstrating the versatility of the liquid delivery approach.

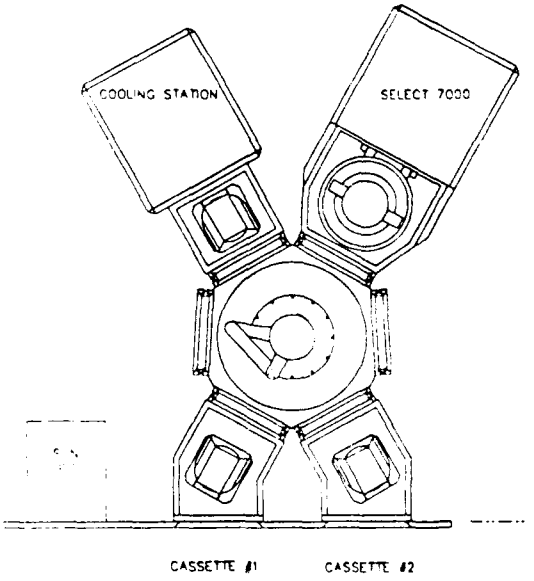


Figure 7. Schematic (top-view) of Watkins Johnson Select 7000 CVD tool in a cluster tool configuration. "Footprint" of the Select 7000 module is approximately 3' x 3'.

$BaTiO_3$ film results on 150 mm wafers

$BaTiO_3$ films were deposited on Pt metallized Si wafers under conditions similar to those used for BST films in the 2" diameter research reactor described above. Relatively simple adjustments in pressure, flow and precursor concentrations gave single phase $BaTiO_3$ films in the perovskite structure, with strong texture in the [100] orientation. (Figure 8.) Films deposited thus far were 500-1500Å thick with a typical thickness non-uniformity of less than ±10%. Buoyancy effects (convection) caused by the vertical substrate orientation is the most probable cause of the non-uniformity, and future experiments will investigate the use of lower pressures to suppress this influence.

The dielectric constants for films 1200Å thickness were greater than 450, which corresponds to capacitance/area greater than 35 fF/μm^2. Films at present have relatively low resistivity (< 10^6 Ω-cm) which may be a consequence of microstructure resulting from a reduction in the deposition temperature to 600°C. The susceptor temperature is presently limited to this temperature because of thermal non-uniformities in the injector region. The next iterations in the reactor design will address the issue of active temperature control of all regions in the injector assembly, and will be accompanied by numerical modelling of the fluid flow through the shower head and in the proximity of the heated substrate.

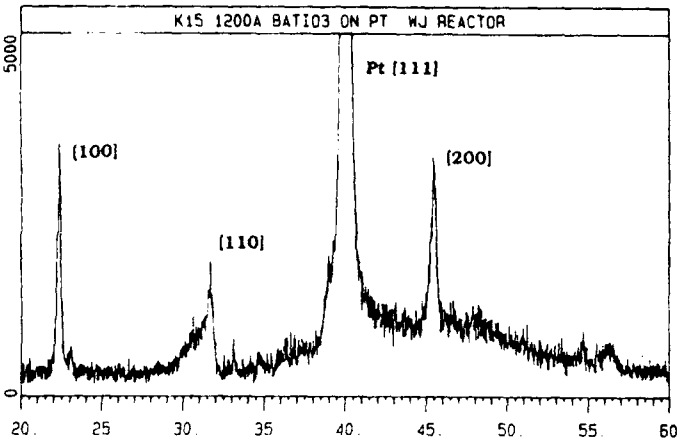


Figure 8. X-ray diffraction for a $BaTiO_3$ film deposited on a 150 mm Pt metallized Si wafer. Film thickness is 1200 Å. Thickness nonuniformity is less than ±10%.

Conclusions

A MOCVD process for deposition of $BaSrTiO_3$ thin films suitable for DRAMs was developed. The CVD process utilizes a novel technique for controlled introduction of metalorganic compounds to the reactor via a single liquid solution. The viability of a thermal MOCVD process using N_2O/O_2 as the oxidant was demonstrated; $BaSrTiO_3$ films with dielectric constants greater than 400 and dc leakage of 7×10^{-6} A/cm were achieved on 50 mm wafers. Implementation of this process in a commercial single wafer tool resulted in the deposition of perovskite phase $BaTiO_3$ over the entire surface of a 150 mm Pt metallized Si wafer. The films were polycrystalline, single phase, single orientation [100] with thickness uniformity better than ±10%.

References

1 M.E. Lines, A.M. Glass, Principles and Applications of Ferroelectrics and Related Materials, 1970, Oxford: Claredon Press, p 240-2 and 620-31.

2 See, for example, L.H. Parker, A.F. Tasch, "Ferroelectric materials for 64 Mb and 256 Mb DRAMs." , IEEE Circuits and Devices Mag., January 1990, 17-25

3 Private communication with Bob Smythe, Uncooled IR Detector Programs at Texas Instruments.

4 Private communication with Yoichi Takemura, Fundamental Research Laboratories, NEC Corporation.

5 K. Koyama, T. Sakuma, S. Yamamichi, H. Watanabe, H. Aoki, S. Ohya, Y. Miyasaka, T. Kikkawa, "A stacked capacitor with (Ba,Sr)TiO_3 for 256 Mb DRAMs.", Proc. IEDM'91, Washington DC, 823-826

6 Y. Miyasaka, S. Matsubara, "Dielectric properties of sputter-deposited $BaTiO_3$-$SrTiO_3$ thin films.", Proc. ISAF 1990, Urbana, Ill. 121-124.

7 H. Yamaguchi, S. Matsubara, Y. Miyasaka, "Reactive coevaporative synthesis and characterization of $SrTiO_3$-$BaTiO_3$ thin films.", Proceedings ISAF'92, August 31-Sept. 2, 1992, Greenville, SC., these Proceedings.

8 P.C. Van Buskirk, R.A. Gardiner, P.S. Kirlin, S.B. Krupanidhi, S. Nutt, "Plasma Enhanced MOCVD of $BaSrTiO_3$ Films for ULSI Applications." , Proceedings ISIF 92., in press.

9 J.F. Scott, A. Azuma, E. Fujii, T. Otsuki, C.A. Paz de Araujo, L.D. McMillan, M.C. Scott, "Microstucture-induced Schottky-barrier effects in barium strontium titanate thin films for 16 and 64 Mb DRAM cells.", Proceedings ISAF'92, August 31-Sept. 2, 1992, Greenville, SC., these Proceedings.

10 Y. Miyasaka, T. Sakuma, S. Matsubara, "High dielectric constant thin films for DRAMs: Present research status in Japan.", Proceedings ISAF'92, August 31-Sept. 2, 1992, Greenville, SC., these Proceedings.

11 Equivalent SiO_2 thickness characterizes the capacitance/area of a film of thickness t and dielectric constant ϵ in terms of the capacitance of an SiO_2 film. It is defined $t_{eq} = t \cdot \epsilon(SiO_2) / \epsilon$

12 Communication with Pierre Fazan, Micron Technology, Boise Idaho.

13 P.S. Kirlin, "MOCVD and PE-MOCVD of HTSC Thin Films.", AIP Conf. Proc., 251, 175 (1991).

14 H. Ohnishi, H. Harima, Y. Goto, K. Tachibana, "Influence of Ozone Concentration on the Preparation of Stoichiometric Superconducting Y-Ba-Cu-O Films by Metalorganic Chemical Vapor Deposition Technique.", Jpn. J. Appl. Phys., 30, L1477 (1991).

15 "Y-Ba-Cu-O Film Growth by OMCVD Using N_2O." Tsuruoka, T., Kawasaki, R., Abe, H., Jpn. J. Appl. Phys., 28, L1800 (1989).

16 K. Yamamoto, R.H. Hammond, J.S. Harris, "The relative effect on the oxygen concentration in $YBa_2Cu_3O_{7-x}$ of atomic and ionic oxygen fluxes, produced by a small compact cyclotron resonance source.", J. Vac. Sci. Technol., A9, 2587 (1991).

17 Not only must a CVD precursor have useful vapor pressure at reasonable temperatures, but it must also be sufficiently stable to evaporate or sublime without decomposition.

18 Bubblers require very tight control of temperature, carrier gas flow and total pressure for repeatable delivery of precursor. Total pressure at the bubbler requires constant conductance of the downstream manifold; slight conductance changes over time cause drift in bubbler pressure and hence the growth rate and film properties experience drift too.

19 This technique has been developed at ATM over the last four years, and a variety of complex oxide thin film have been deposited using the liquid delivery method. At present five CVD reactors are configured with this system for growth of $BaTiO_3$, $BaSrTiO_3$, YBaCuO, TlBaCaCuO and $MgAl_2O_4$.

20 J. Zhang, R.A. Gardiner, P.S. Kirlin, "In-Situ Growth of C-Axis Oriented YBaCuO on Silicon with Composite Buffer Lyers by Plasma Enhanced Metalorganic Chemical Vapor Deposition.", Proceedings MRS Spring Symposium, San Francisco, April 29 (1992).

21 P.C. Van Buskirk, R.A. Gardiner, P.S. Kirlin, "Microstructure of $BaTiO_3$ Thin Films Prepared by Reduced-Pressure CVD," , MRS Proceedings, 202, 235 (1991).

22 P.C. Van Buskirk, R.A. Gardiner, P.S. Kirlin,"MOCVD Growth of $BaTiO_3$." , J. Vac. Sci. Tech., A10, 1578 (1992).

23 P.C. Van Buskirk, R.A. Gardiner, P.S. Kirlin, S.B. Krupanidhi, S. Nutt, "Plasma Enhanced MOCVD of $BaSrTiO_3$ Films for ULSI Applications." ISIF 92 Proceedings, in press.

24 A Dektak IIa was used. Measurement parameters were: 12μ stylus, 500 μ scan at slow speed, roughness calculated using the R_a function over a 200 μ section of the scanned region.

25 J.O. Olowolafe, R.E. Jones, A.C. Campbell, P.D. Maniar, C.J. Mogab, "Analyses of Pt/Ti electrodes for for application to PLZT capacitors.", MRS Proceeding, 1991 Fall Mtg., Boston, MA, to be published.

26 R. Bruchhaus, D. Pitzer, O. Eibl, U. Scheithauer, W. Howler, "Investigation of Pt bottom electrodes for 'in-situ' deposited PZT thin films.", MRS Proceeding, 1991 Fall Mtg., Boston, MA, to be published.

27 G. Arflt, D. Hennings, G. de With, "Dielectric properties of fine-grained barium titanate ceramics.", J. Appl. Phys., 58(4) 1620-1625 (1985)

28 Watkins Johnson Company, 440 Kings Village Rd., Scotts Valley, CA 95066

CHEMICALLY PREPARED $Pb(Zr,Ti)O_3$ THIN FILMS: THE EFFECTS OF ORIENTATION AND STRESS

Bruce A. Tuttle, James A. Voigt, Terry J. Garino, David C. Goodnow, Robert W. Schwartz, Diana L. Lamppa, Thomas J. Headley, and Michael O. Eatough,
Sandia National Laboratories, Albuquerque, NM 87185

Abstract

We have determined the effects that orientation and stress have on chemically prepared $Pb(Zr,Ti)O_3$ (PZT) film properties. Systematic modification of the underlying substrate technology has permitted us to fabricate suites of films that have various degrees of orientation at a constant stress level, and to also fabricate films that are in different states of stress, but have similar orientation. We have fabricated highly oriented films of the following compositions: PZT 60/40, PZT 40/60 and PZT 20/80. Remanent polarizations (≈60 $\mu C/cm^2$) greater than the best bulk polycrystalline ferroelectrics were obtained for PZT 40/60 films that were under compression and highly (001) oriented. While we show that systematically varying orientation influences ferroelectric properties, film stress also has a considerable effect. Perhaps the most important concept presented in this paper is that the sign of the film stress at the Curie point controls the type of ferroelectric behavior exhibited by PZT thin films. Further, our stress measurements as a function of thermal history indicate that the coefficient of thermal expansion of the paraelectric state is critical in determining the type of film ferroelectric behavior.

Introduction

Our work is one of the first attempts to isolate the effects that orientation and stress have on ferroelectric thin film properties. We have fabricated highly oriented pseudocubic (100) PZT films by meshing two diverse technologies: 1) RF magnetron sputtering of (100) oriented, topotactical, Pt electrodes, and 2) rapid thermal processing of solution derived PZT thin films using a temperature gradient. The degree of orientation, in otherwise identical PZT films, has been controlled by manipulating the sputter deposition parameters of the bottom Pt electrode. Thus, we have an excellent property comparison of oriented and randomly oriented PZT films that have the following similarities: 1) the same thickness (340 nm), 2) both films were deposited from the same solution at the same time, 3) both films were thermally processed under identical conditions at the same time, and 4) identical substrate materials were used, 100 nm thick Pt films deposited on (100) MgO single crystals. A range of stress levels were obtained in PZT films by appropriate control of thermal processing parameters and the use of either silicon, sapphire or MgO substrates.

Oriented ferroelectric thin films of $Pb(Zr,Ti)O_3$ with large polarizations offer technological advantages for a range of optical and electronic applications. Previous work[1] has indicated that as material structure evolves from randomly oriented, complex, polycrystalline ensembles to single crystals in tetragonally distorted simple perovskite ferroelectrics, such as PZT 40/60, distinct trends in electrical properties occur. $BaTiO_3$ and $KNbO_3$ are examples of simple perovskite ferroelectric materials that have the same nonpolar, cubic, prototypic symmetry (m3m) and the same polar, tetragonal symmetry (4mm) as PZT 40/60. If the same property - structure relationships hold for PZT 40/60, as for $BaTiO_3$ and $KNbO_3$, then (001) oriented PZT 40/60 films should have higher polarizations, lower coercive fields, lower dielectric constants, higher electrooptic coefficients, and potentially lower optical loss than similar PZT 40/60 films that are not preferentially oriented. Among the applications for which oriented PZT films will be of interest are pyroelectric detectors, optical disk storage systems, optical waveguide devices, and spatial light modulators. A further benefit of orientation may be to enhance process integration of ferroelectric thin film and semiconductor technologies.

A specific application for which highly oriented ferroelectric thin films with high polarizations enhance device performance is eraseable nonvolatile optical disk storage. Dimos[2] has demonstrated that thin (<1 μm) films can be utilized in such a device. This device consists of a PZT thin film sandwiched between two transparent conducting electrodes. The device write operation consists of focussing a laser beam to the PZT element which changes the polarization state and thus the birefringence of the pixel. The disk read is obtained by focussing a laser beam to the desired pixel and monitoring the change in optical retardation via a photodetector. Highly oriented films with large polarizations will possess large electrooptic coefficients and thus enhance the signal to noise ratio of these devices. For the multiple pass technique of measurement, the high degree of orientation may lessen optical loss; and thus, further enhance device performance.

Several workers[3-5] have reported on fabrication of oriented PZT and PLZT films by vapor deposition techniques. Kingon and coworkers[3] deposited (100) oriented PZT 40/60 films by ion beam deposition on platinized MgO. Ogawa and coworkers[4] deposited c-axis oriented $(Pb,La)TiO_3$ thin films on MgO substrates using RF magnetron sputter deposition. We have used the work of Iijima and coworkers[5] as a model for our studies. Iijima and coworkers deposited oriented (100) PLT films by RF magnetron sputter deposition on (100) Pt film // (100) MgO substrates. Highly oriented (100) Pt films on (100) MgO single crystal substrates were deposited at a deposition temperature of 600°C and a sputtering gas mixture of 50:50 Ar:O. Although our sputter gas composition and deposition temperature were slightly different than Iijima's, we have followed a similar procedure for the fabrication of (100) oriented Pt films on (100) MgO. Iijima and coworkers were able to RF sputter deposit highly oriented PLT films with good ferroelectric properties using the following process parameters: a PLT target with excess Pb, a deposition temperature of 600°C, and a 50/50 O/Ar gas mixture.

Deposition on insulating substrates of oriented ferroelectric thin films, fabricated by solution chemistry techniques, have been reported by several workers.[6-8] For example, Hirano[6] and Payne[7] have deposited highly oriented $LiNbO_3$ films on sapphire substrates. Swartz and coworkers[8] have deposited highly oriented $Pb(Mg_{0.33}Nb_{0.67})O_3$ films on $SrTiO_3$ substrates. Transmission electron micrograph lattice images indicate epitaxial relationships between film and substrate exist. However, reports of deposition of highly oriented ferroelectric films fabricated by solution chemistry on conducting substrates and associated electrical measurements have been limited to date.

Experimental Procedure

We fabricated PZT thin films using a modification of the hybrid solution deposition procedure[9] developed by Sayer and coworkers. Our 0.4 M solutions were synthesized using an inverted mixing order (IMO) process[10] for which the Zr and Ti alkoxides are blended first before the addition of the lead precursor. Excess Pb (5 mol%) was added to enhance formation of the perovskite phase; and thus, improve electrical properties. First, titanium isopropoxide* was added to zirconium butoxide-butanol& and stirred for 5 min. Methanol and acetic acid were then added to the solution, followed by addition of lead (IV) acetate.& The solution was then heated to 85°C to dissolve the lead precursor. Additional acetic acid, methanol and distilled water were added to control solution viscosity and to improve solution stability. Our thin films were deposited by spin-coating at 3000 rpm for 30 seconds. Following deposition, we heat treated the thin film layer at 300°C for 5 min on a hot plate. Three film layers were deposited to attain the final film thickness of 3400Å.

We developed a novel rapid thermal processing (RTP) procedure using a temperature gradient to crystallize our films into the perovskite phase. First, the films were loaded onto a Si wafer susceptor and the RTP system# was evacuated and backfilled with oxygen twice. A heating rate of 125°C/min and a soak temperature and time of 650°C for 10 min were typical RTP parameters used to crystallize the films. Further, for the most highly oriented films, only the quartz lamps below the samples were used, such that, a significant temperature gradient existed between the top and bottom of the PZT film. Our goal was to have the perovskite PZT nucleate at the electrode interface; and thus, enhance the epitaxial / topotactical relationships between film and substrate that are necessary for the formation of highly oriented PZT thin films.

* Aldrich Chemical Company, Inc.; Milwaukee, WI
& Alfa Products; Ward Hill, MA
# Addax Model RMV4; Zurich, Switzerland

CH3080-0/7803-0465-9/92$3.00©IEEE

We have used RF magnetron sputter deposition to fabricate (100) oriented Pt thin films on (100) single crystal MgO substrates and to fabricate (111) oriented Pt thin films on sapphire substrates. For highly oriented Pt film growth, MgO substrates** with an epitaxial surface finish were used. These substrates were thermally annealed at 400°C in air for 10 min and then placed in vacuum (10^{-6} Torr) at 500°C for 5 min to remove any surface contamination. We used the following sputter deposition parameters: 4" diameter targets, a target - substrate separation distance of 10 cm, a pressure of 6 mTorr during sputter deposition, and an RF power of 13 watts. Deposition rates were on the order of 20Å/min. Deposition temperatures ranging from 450°C to 625°C and O/Ar sputter gas ratios ranging from 0/100 to 50/50 were investigated in this study. Our best conditions for fabricating highly oriented (100) Pt films were a deposition temperature of 625°C and 100% Ar sputtering gas. Amorphous Pt films, which were used for fabricating randomly oriented PZT films, were deposited under conditions of 600°C and a 50/50 Ar/O sputter gas mixture.

Electrical characterization of PZT 40/60 films consisted of low field (≈ 3 kV/cm) dielectric measurements and ferroelectric hysteresis loop measurements using an applied field of 300 kV/cm. While a Hewlett-Packard model HP1492A network analyzer was used for the low field dielectric constant measurements, most of the ferroelectric measurements were made with a Radiant Technologies model RT66A ferroelectric tester. A virtual ground test configuration was used, with a triangular wave period of approximately 20 ms. For consistency, and to obtain a truly representative comparison of ferroelectric films in the same poled state, we dc poled all capacitors with +5 volts (150 kV/cm) for 2 seconds at ambient before dielectric measurement. Low field dielectric property measurements were then performed before the high field ferroelectric measurements. Further validation of the ferroelectric properties of these films was accomplished by measuring hysteresis loops over a relatively wide range of frequencies (0.1 Hz to 20 kHz) using a modified Diamant-Pepinsky Bridge. Platinum electrode dots of 300 μm and 700 μm diameter were sputter deposited at ambient on top of the PZT films. A blunt (≈50 μm) Be-Cu probe tip was used for the electrical measurements.

Results and Discussion

Crystallization by our novel RTP technique of PZT 20/80 films deposited directly onto single crystal (100) MgO substrates resulted in PZT films with a high degree of pseudocubic (100) orientation. From the X-ray diffraction pattern of this PZT film, shown in Fig. 1, there is no evidence of the pseudocubic (111) diffraction peak. Further, the pseudocubic (110) peak is substantially suppressed; the integrated intensity ratio of the pseudocubic (100) to the (110) peak is 500:1. These results indicate that our thermal processing procedure of a 125°C/second heating rate, 650°C / 10 min soak, and implementation of a temperature gradient is adequate to produce highly oriented PZT 20/80 films on an appropriate substrate. We have previously demonstrated[10] that highly oriented PZT 40/60 films could be deposited in a similar manner.

The tetragonal anisotropy of the PZT 20/80 film, deposited directly onto the MgO substrate, is clearly evident in Fig. 1. The c/a ratio is 1.042, which is slightly less than the value of 1.048 expected for bulk PZT 40/60 ceramics. Further, the (001) or c-axis diffraction peak has twice the magnitude of the (100) or a-axis peak. For a stress free, random, polycrystalline, tetragonal PZT ceramic, the (100) diffraction peak should be approximately twice as large as the (001) diffraction peak. We speculate that compressive film stress, primarily due to the thermal expansion mismatch between the PZT film and the MgO substrate, causes preferential c-axis alignment upon cooling through the Curie point. Formation of 90° domains occurs in response to transformation induced strain so as to minimize the overall elastic energy of the film. Because of the origin of (100) domains in the film, it is not surprising that the relative intensity ratio of the PZT film (001) to (100) diffraction peaks should be different than that of randomly oriented material.

An X-ray diffraction trace of an (001) oriented PZT 20/80 film on a Pt film - MgO substrate is shown in Fig. 2. For the oriented PZT film, the structure of the underlying Pt layer is topotactical (100) oriented, with an enhanced integrated intensity ratio of I_{100} to I_{111} of 200:1. The crystal structure of the PZT film mimics the underlying Pt film crystal structure quite well.

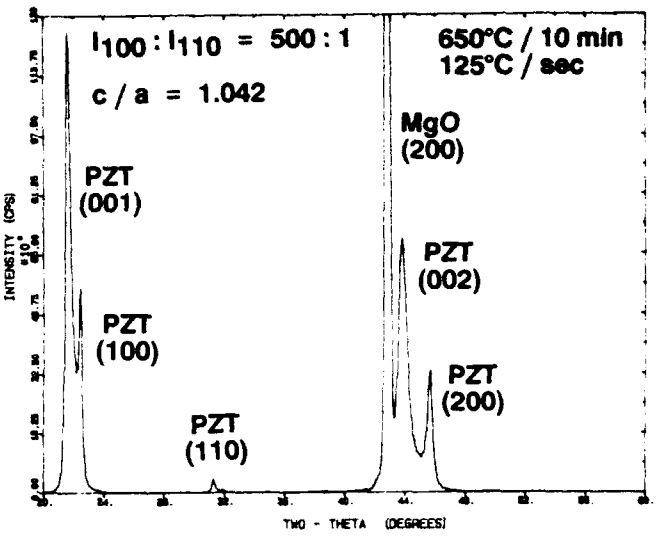


Fig. 1. X-ray diffraction pattern of a 3400 Å thick PZT 20/80 film deposited directly on a (100) MgO single crystal and rapidly thermal processed (125°C/sec) at 650°C for 10 min in flowing oxygen.

The integrated intensity ratio of the oriented PZT film pseudocubic (100) to (111) diffraction peaks is approximately 500:1. Further, the lattice spacing associated with the pseudocubic (100) peak is 4.098Å which is closer to the c lattice constant (4.157Å) than the a lattice constant (3.96Å) of the bulk polycrystalline material. Unlike the PZT 20/80 film deposited directly on MgO, no splitting of the pseudocubic (100) into its tetragonal (001) and (100) components is observed. Although peak broadening due to crystallite size can not entirely be ruled out, we attribute the lack of splitting to the suppression of 90° domain formation in this fine grain film.

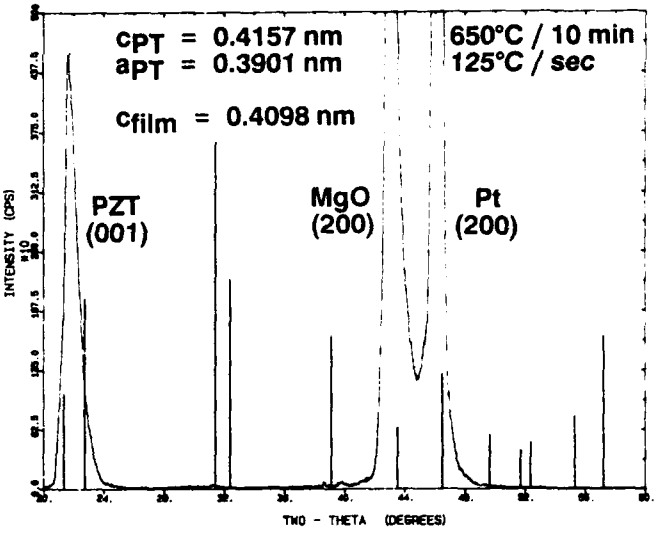


Fig. 2. X-ray diffraction pattern of 3400 Å thick PZT 20/80 film deposited on a highly (100) oriented Pt film // (100) MgO single crystal substrate processed identically to the film in Fig.1.

PZT film microstructures were substantially influenced by the underlying substrate. We previously reported[11] that grain sizes of PZT 40/60 films deposited directly on MgO were 20 times greater than those of identically processed films deposited on (100)Pt // MgO. Cross-sectional transmission electron micrographs indicated formation of no 90° domains in the fine (0.1 μm) film; whereas, 90° domains were detected in every grain investigated for the coarse grain film. Further, the rough calculations of the volume percent (18%) of a domains detected by TEM diffraction contrast was in good agreement with the volume percent (23%) of c to a domains from the integrated intensity ratio of the corresponding c to a diffraction peaks. For the fine grain film, no evidence of

porosity or the presence of surface layers were detected. The grain size of the PZT 20/80 film deposited on (100) MgO was approximately three times smaller than the grain size of the PZT 40/60 film deposited on the same substrate.

Ferroelectric and low field dielectric properties are tabulated as a function of film orientation for three different PZT 40/60 films in Table I. In addition to the properties of the previously discussed highly (001) oriented PZT film, we also fabricated a randomly oriented PZT 40/60 film and a film that was not as highly (001) oriented by manipulating the underlying substrate technology. The randomly oriented film was deposited on an initially amorphous Pt film deposited at 500°C in 50:50 Ar:O sputtering gas. The PZT film of intermediate orientation was fabricated identically to the highly (001) oriented film, with the exception that the underlying MgO substrate surface was submicron polished rather than epitaxial. All the electrical properties tabulated in Table I were the mean of measurements of 10 different electrode dots on each of the films. Standard deviations for the measurements are indicated by the values after the ± signs in Table I. The tabulated dielectric constant was measured at a frequency of 10 kHz and a field of 3 kV/cm ac rms (0.1 volt). Dissipation factors of 0.025 and 0.030 were measured at 10 kHz for the oriented and randomly oriented film, respectively.

Most of the relationships between dielectric properties and orientation were as expected for the three films shown in Table I. Remanent polarization increased and dielectric constant decreased with increase in c-axis orientation, similar to that observed in tetragonally distorted simple perovskite ferroelectrics as structure approaches that of a single crystal. Semiquantitative agreement between the calculated and measured values of remanent polarization as a function of orientation was obtained. While orientation appears to be the dominant factor for the ferroelectric property relationships, other factors, such as, microstructure also influence ferroelectric properties. While the coercive fields of the oriented and randomly oriented film were statistically indistinguishable from one another, the coercive field of the film of intermediate orientation was slightly (≈ 10%) less than that of the other two films. A large number of factors can influence the measured coercive field. Among these factors are stress, crystallite size and electrode-ceramic interface characteristics. Grain size may be the dominant effect for the coercive field relationship of our

Table I. Electrical Property Vs. Orientation Behavior

Enhanced Integr. Int. Ratio $[I_{100}/I_{111}]$ $[I_{100}/I_{111}]$	Remanent Polarization ($\mu C/cm^2$)	Coercive Field (kV/cm)	Dielectric Constant (10 kHz)
300:1 [7.0:1]	60.9 ± 1.4	75.7 ± 0.7	368 ± 11
20:1 [2.5:1]	57.8 ± 3.2	68.0 ± 1.1	378 ± 17
4.6:1 [2.1:1]	41.0 ± 3.4	77.8 ± 1.8	466 ± 18

films, as the mean value of the coercive field montonically decreased with increasing average grain size.

An increase in polarization is expected with increase in (001) film orientation as the c-axis is the polar axis for PZT ceramics with 4mm symmetry. Due to compressive stress, primarily caused by the film - substrate thermal expansion mismatch, c-axis rather than a-axis orientation is preferred in the PZT film. Tominaga and coworkers[12] have verified that $PbTiO_3$ thin films deposited on MgO substrates have a c+ orientation. The decrease in dielectric constant with c-axis orientation is expected, based on the property-orientation behavior of 4mm perovskite single crystals. Typically, κ_{33} is significantly less than κ_{11} for simple perovskite ferroelectrics of 4mm crystal symmetry. For example, $BaTiO_3$ single crystals have the following dielectric constants: $\kappa_{33} = 200$ and $\kappa_{11} = 4000$. The reason[1] for the substantial anisotropy in dielectric constant is because the displaced atoms are tightly bound by the ferroelectric polarization in the polarization direction, but relatively free to move in the direction perpendicular to the polarization direction.

After having systematically investigated the effects of orientation for films that are under a constant stress, we now investigate PZT films that have similar orientation, but substantially different stress levels. The substantial effect that stress can have on ferroelectric properties is illustrated in Figure 3. Dielectric hysteresis loops are shown for two identically processed PZT 60/40 films with the exception that one film was deposited on a platinized (0001) sapphire substrate, while the other film was deposited on a platinized Si substrate. Both films are highly oriented in the pseudocubic (111) crystallographic direction. We have fabricated these films of rhombohedral symmetry with essentially the same degree of (111) orientation by controlling the deposition conditions of the underlying Pt film. The Pt film deposited on sapphire was deposited at 600°C at a slow rate (2 nm/min); whereas, the Pt film deposited on silicon was deposited at 600°C at a higher deposition rate of 30 nm/min. Grain growth orientation is responsible for the high degree of (111) orientation of the Pt film on Si.

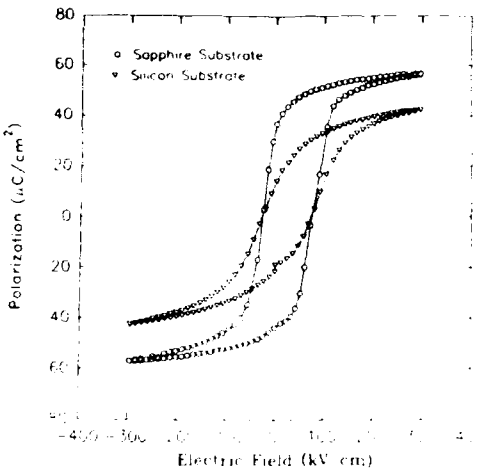


Fig. 3. Dielectric hysteresis loops of identically processed PZT 60/40 thin films on the following platinum coated substrates: a) (0001) Sapphire and b) (100) silicon.

Although the two PZT films have similar orientation, their dielectric hysteresis characteristics are substantially different. While a large remanent polarization of 40 $\mu C/cm^2$ is measured for the PZT 60/40 film deposited on sapphire, a remanent polarization of only 20 $\mu C/cm^2$ is measured for the PZT 60/40 film deposited on silicon. Further, the film deposited on sapphire has a very sharp, square, well saturated dielectric hysteresis shape, while the film on sapphire has a slanted hysteresis characteristic. We have determined similar trends in stress-orientation property relationships for PZT 40/60 films of tetragonal symmetry deposited on MgO and Si substrates, respectively. The PZT 40/60 film deposited on MgO exhibited dielectric hysteretic behavior similar to the PZT 60/40 film deposited on sapphire, while the PZT 40/60 film and PZT 60/40 film deposited on Si had relatively low (≈20 $\mu C/cm^2$) remanent polarizations and a similar type of hysteresis characteristic.

For the rest of this paper, we shall term the two different hysteresis characteristics, described above, as type c and type a. Type c behavior is typified by a dielectric hysteresis characteristic with high remanent polarization (in this case,40 $\mu C/cm^2$) and very square, sharp, well saturated hysteresis loop shape. Conversely, type a behavior is typified by a lower remanent polarization and a slanted hysteresis loop shape. We attribute the difference in behavior to crystallite orientation. Films with a majority of crystallites preferentially oriented such that their polar directions are perpendicular to the film plane are type c; whereas, films with a majority of crystallites oriented such that the polarization vector is parallel to the film surface are type a. We postulate that the sign of the film stress as the film is cooled through the Curie point determines whether the film exhibits type a or type c behavior. Specifically, if the film is under compression at the Curie point type c behavior is observed; whereas, if the film is under tension, type a behavior is obtained.

Because film stress has been shown to have such a substantial effect on ferroelectric behavior, it is important to quantify the stress in PZT thin films. We have measured stress in PZT thin films by two different techniques: 1) wafer curvature measurements and 2) X-ray diffraction. Wafer curvature has been measured by laser reflectance techniques and surface profilometry. Our laser reflectance technique has been previously described,[13] and allows PZT film stress to be measured through out the entire thermal processing history. The residual stress at ambient is confirmed by surface profilometer measurements of the substrate curvature. For our X-ray diffraction measurements of the macrostrain of PZT thin films, a $\sin^2\psi$ technique[9] is used. Thin film glancing angle X-ray diffraction coupled with parallel beam optics allow accurate measurements of strain as a function of film depth.

Figure 4 depicts the change in thermal stress with processing for two essentially identical PZT 53/47 thin films deposited on two different platinum coated substrates: 1) silicon and 2) (100) MgO. From these characteristics, it is obvious that the coefficient of thermal expansion (CTE) of the substrate is one of the major factors that controls PZT film stress. Further, we propose that the type of film stress, either tensile or compressive, which is present upon cooling the film through the Curie point controls the PZT crystallite orientation. Crystallite orientation, in turn, strongly influences the stress vs. temperature characteristics in the low temperature ferroelectric state. Both of the films in Figure 4 were heated at 5°C/min and held at 650°C for 30 min as stress was monitored by our laser reflectance technique.

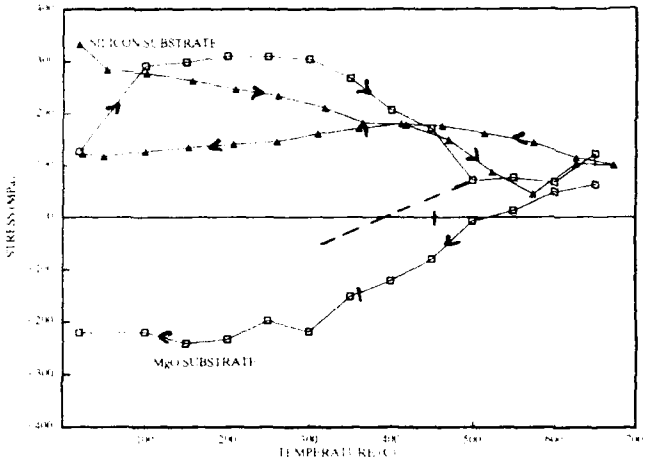


Fig. 4. PZT thin film stress as a function of temperature for films deposited on two platinum coated substrates: a) (100) MgO and b) (100) silicon.

The initial stress levels of the two PZT films, after a 300°C 5 min drying treatment, are as expected. The PZT film deposited on MgO has less tensile stress than the film deposited on the lower CTE silicon substrate. We consider the as-deposited film to have a higher thermal expansion coefficient than either the MgO or Si substrate; and thus, both films should be in tension after the drying treatment. Since the CTE for MgO is greater than that of Si, the film on the MgO substrate has less tensile stress than the film on Si. For the Si substrate, an initial decrease in tension occurs as the film is heated, since the high thermal expansion film expands more than the Si substrate. PZT film stress continues to decrease even as the film crystallizes into the pyrochlore phase at approximately 450°C. During transformation of the pyrochlore phase to the perovskite phase considerable film volume shrinkage occurs as evidenced by the increase in tensile stress. Because the pyrochlore phase consists[14] of two interpenetrating nanophases: 1) crystalline pyrochlore and 2) an amorphous phase containing Pb, Zr and Ti, the volume contraction is substantial.

The tensile stress increases for the PZT 53/47 film deposited on Si upon cooling from the soak temperature. A relatively high CTE of 6.7 X 10^{-6} for the high temperature paraelectric phase is the cause of this increased tensile stress. Conversely, the PZT film deposited on the MgO substrate is put into compression upon cooling from the soak temperature. This behavior is also attributed to the CTE mismatch between film and substrate. At the Curie point, of approximately 375°C, the PZT film on MgO is in 150 MPa of compression; whereas, the PZT film deposited on Si is in 150 MPa of tension. PZT 53/47 has a thermal expansion coefficient of approximately 2.0 X 10^{-6} in the ferroelectric state. The stress of the two films at 25°C are 120 MPa tensile and 210 MPa compressive for the Si and MgO substrates, respectively. While these stress values measured by laser reflectance and surface profilometry agree well with calculations of stress from macrostrain measurements from X-ray diffraction for the PZT film deposited on the Si substrate, there is some discrepancy between the film stress measurements for the PZT film deposited on MgO. However, both measurement techniques indicate that the film is in high compression. From X-ray diffraction measurements, a residual tensile stress of 100 MPa was calculated for the PZT film on silicon, while a residual compressive stress of 470 MPa was calculated for the PZT film on MgO.

It is quite surprising that the PZT film deposited on MgO is not under considerably more compressive stress at ambient given that the CTE for the ferroelectric state (2.0 X 10^{-6}) is considerably less than that of the high temperature paraelectric phase. We propose that as the film cools through the transformation temperature that the sign of the stress will preferentially orient film crystallites in the a or c crystallographic direction. For simplicity, we will assume that the PZT 53/47 film is of tetragonal symmetry. For the film on the MgO substrate, the film is under compression at the Curie point; and thus, crystallites are preferentially oriented with the c direction normal to film plane. Thus, crystallites have their a direction in the film plane. If one considers the change in crystal parameters[1] with temperature of $PbTiO_3$ and the superimposed linear expansion of Si and MgO, shown in Fig. 5, it is obvious that the change in the a lattice constant is close to that of the MgO substrate. Thus, the change in film stress below the Curie point is very slight, as shown in Fig. 4. The relative change in lattice parameter, not the absolute magnitudes, for Si and MgO are shown in Fig.5.

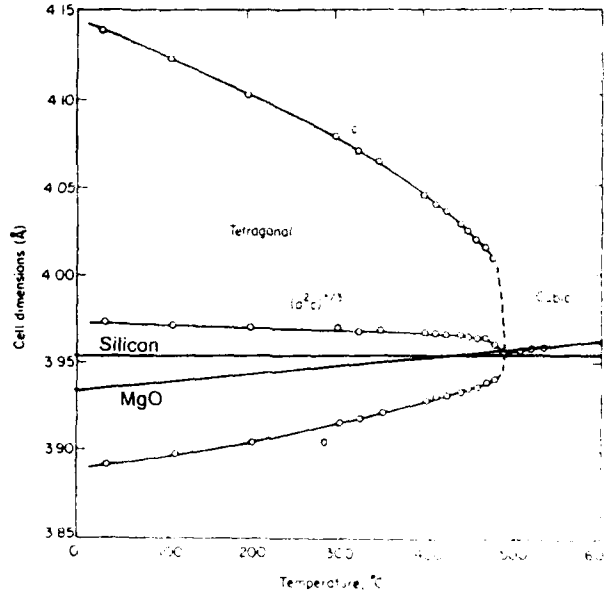


Fig. 5. Thermal expansion behavior of platinum, MgO, and a and c axes of $PbTiO_3$.

While we have shown that stress vs. temperature characteristics are substantially influenced by the type of stress at the Curie point, our premise is that the sign of film stress at the Curie point controls type a and c ferroelectric behavior. From this postulation one can make both obvious and not so obvious predictions. Among the obvious predictions are that films fabricated using our solution chemistry technique and fired at 650°C would exhibit type a behavior when deposited on Si substrates, and type c behavior when deposited on MgO substrates. A less obvious prediction is that it is possible for a PZT 52/48 film to have type a behavior while an identically processed PZT 40/60 film would exhibit type c behavior. These films would have to be deposited on a substrate with appropriate intermediate CTE to Si and MgO, such that, the PZT 52/48 film is in tension and the PZT 40/60 film is in compression at the Curie point. What permits this behavior is that the CTE for the PZT 53/47 paraelectric state is 6.7 X 10^{-6} while the CTE for the PZT 40/60

paraelectric phase is significantly higher (9.4 X 10 ^{6}). This example illustrates the important contribution that the CTE of the high temperature paraelectric state has on determining the type of ferroelectric behavior in PZT thin films.

Another prediction, which one would not make from consideration of ambient CTEs alone, is that despite the high CTE of MgO, it is possible to fabricate PZT 20/80 films deposited on MgO substrates that exhibit type a behavior. Specifically, we demonstrate in Fig. 6 that a PZT 20/80 film fired at 500°C exhibits type a behavior; whereas, an otherwise identically processed PZT 20/80 film fired at 650°C exhibits type c behavior. X-ray diffraction traces of three PZT 20/80 films deposited on MgO substrates and rapidly thermal processed at 500°C, 550°C, and 650°C,respectively, are shown in Fig. 6. The film fired at 500°C has only a diffraction peak corresponding to the a lattice parameter and there is no evidence of a diffraction peak corresponding to the c lattice parameter. The film fired at 550°C shows X-ray diffraction peaks of approximate equal magnitude corresponding to both the a and c lattice parameters. The film fired at 650°C has type c behavior as the integrated intensity ratio of the diffraction peak for the c lattice parameter is more than twice the value of the integrated intensity ratio of the peak that corresponds to the a parameter.

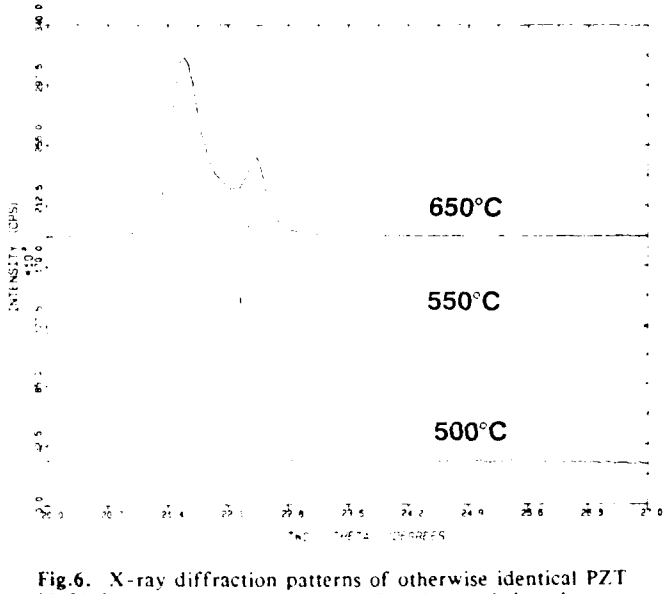


Fig.6. X-ray diffraction patterns of otherwise identical PZT 20/80 films deposited on (100) MgO and annealed at three different temperatures: 500°C, 550°C, and 650°C.

These relationships are easily explained by incorporating our knowledge of the stress vs. temperature behavior of the films with our postulation that the sign of Curie point stress controls the type of ferroelectric behavior. We assume that the stress versus temperature characteristics for a PZT 20/80 film deposited on MgO are qualitatively similar to that of the PZT 53/47 film deposited on an MgO substrate shown in Fig. 5. From Fig. 5, the stress of two PZT 53/47 films deposited on MgO substrates are approximately equal at the annealing temperatures of 500°C and 650°C, respectively. Because the film annealed at 500°C is closer to the transformation temperature (≈450°C), upon cooling, it is still in tension at the Curie point, thus, forcing type a behavior. The dotted line in Fig. 5 indicates the stress of the PZT film as a function of temperature as it is cooled from the 500°C annealing temperature. Conversely, the film fired at 650°C has a considerable temperature range to allow the CTE mismatch between film and substrate to put the film into compression at the Curie point, as shown shown by the original solid line in Fig. 5. This compressive stress forces the PZT film crystallites to preferentially orient towards the c axis, resulting in type c ferroelectric behavior.

Summary

We have investigated the effects that orientation and stress have on PZT thin film properties. Our approach was to fabricate and characterize a suite of films that have similar stress levels with systematically varying orientation, and another suite of films that have similar orientation, but that have different levels of stress. PZT 40/60 films that had a high degree of c-axis orientation had higher polarization and lower dielectric constants than films oriented with their a crystallite axes perpendicular to the top film surface. This property behavior was expected as tetragonally distorted, simple perovskite ferroelectric films structurally evolve from random polycrystalline ensembles to single crystals. We postulated that the Curie point stress controls crystallite orientation and the type of ferroelectric behavior. Electrical, structural and stress versus temperature data were presented that supported this hypothesis.

Acknowledgements

The authors would like to acknowledge the support of DARPA and DOE for this work. Further, the authors would like to thank Ray Goehner, Angus Kingon, Gary Zender, and Duane Dimos for many enlightening discussions.

References

[1] B. Jaffe, W.R. Cooke, and H. Jaffe, Piezoelectric Ceramics, Academic Press, Inc., (1971).
[2] D. Dimos and R.W. Schwartz, "Electrooptic Properties of PZT Thin Films For Image Storage Applications," Matls. Res. Symp. Proc., Volume 243, (1992).
[3] K. Gifford and A.I. Kingon, "Oriented PZT Films," Ferroelectrics, Proc. of 3rd Int. Symp. on Int. Ferroelectrics, accepted for publication (1992).
[4] T. Ogawa, A. Senda, T. Kasnami, "Controlling the Crystal Orientations of Lead Titanate Thin Films," Jap. J. of Appl. Phys., 30 8 2145-8 (1991).
[5] K. Iijima, R. Takayama, Y. Tomita, and I. Ueda, "Epitaxial Growth and the Crystallographic, Dielectric, and Pyroelectric Properties of Lanthanum Modified Lead Titanate Thin Films," J. Appl. Phys., 60 (8) 2914-19 (1986).
[6] S. Hirano, K. Kukuta, and K. Kato, "Processing of Stoichiometric and Ti Doped $LiNbO_3$ Films with Preferred Orientation From Metal Alkoxides," Matls. Res. Soc. Symp. Proc. Vol. 200, April 16-20, 1990, San Francisco, CA 3-11 (1990).
[7] D.J. Eichorst, D.S. Hagberg, and D.A. Payne, "Processing and Properties of Sol-Gel Derived Lithium Niobate Thin Layers," Proc. of IEEE 7th Int. Symp. on Appl. of Ferroelectrics, 250-3 (1991).
[8] S.L. Swartz, S.D. Ramamurthi, J.R. Busch, and V.E. Wood, "Sol-Gel Processing of Ferroelectric Films For Optical Waveguides," Proc. of MRS Symp. Ferroelectric Thin Films II, Boston, MA Dec 2-6, 1991, accepted for publication (1992).
[9] G. Yi, Z. Wu, and M. Sayer, "Preparation of $Pb(Zr,Ti)O_3$ thin films by Sol Gel Processing: Electrical, Optical and Electro-optic Properties," J. Appl. Phys., 64 (5), 1 2717-24 (1988).
[10] R. Schwartz, B. Bunker, D. Dimos, R. Assink, B. Tuttle, D. Tallant, I. Weinstock, and D. Haaland, "Solution Chemistry Effects in $Pb(Zr,Ti)O_3$ Thin Film Processing," Proc of 3rd Int. Symp. on Int. Ferroelectrics, 535-46, (1991).
[11] B.A. Tuttle, J.A. Voigt and coworkers, "Highly Oriented, Chemcially Prepared $Pb(Zr,Ti)O_3$ Thin Fil. .," J. Am. Ceram. Soc., submitted (1992).
[12] K. Tominaga, M. Miyajima, Y. Sakashita, H. Segawa, and M Okada, "Preparation of C-Axis Oriented PLT Thin Films By The Metalorganic Chemical Vapor Deposition Method," Jap. J. of Appl. Phys., 29 [10] L 1874-6 (1990).
[13] T.J. Garino and M. Harrington, "Residual Stress in PZT Thin Films and its Effect On Ferroelectric Properties," Mat. Res. Soc. Symp. Proc. Vol. 243, Ferroelectric Thin Films II, (1992).
[14] B.A. Tuttle, T.J. Headley, B.C. Bunker, R.W. Schwartz, T.J. Zender, C.L. Hernandez, D.C. Goodnow, R.J. Tissot, and J. Michael, and A.H. Carim, "Microstructural Evolution of $Pb(Zr,Ti)O_3$ Thin Films Prepared By Hybrid Metallo-Organic Decomposition," J. Mater. Res., 7, 7 1876-82 (1992).

Thin Films: Applications and Processing

DAAS TECHNIQUE FOR SYNTHESIZING DOPED PZT AND PLZT THIN FILMS

C.T. Lin, Li Li, and J.S Webb
Department of Chemistry
Northern Illinois University
DeKalb, IL 60115-2862

and

R.A. Lipeles and M.S. Leung
The Aerospace Corporation
PO Box 92957
Los Angeles, CA 90009-2957

Abstract

The Deposition by Aqueous Acetate Solution (DAAS) technique has been developed for the preparation of 5% Fe-doped $Pb(Zr_{0.53}Ti_{0.47})O_3$ (PZT) and $(Pb_{0.93}La_{0.07})(Zr_{0.65}Ti_{0.35})_{0.983}O_3$ (PLZT) thin films on Pt<111>/Ti/SiO_2/Si<100> substrates. PZT films, crystallized at 600°C for 10 min, display good electrical properties and fatigue characteristics. Iron doping suppressed the crystallization of the films as measured by XRD and FTIR spectroscopy. When 5% of the zirconium and titanium were replaced by iron in the stoichiometric precursor solution, the film crystallized predominantly in the (110) orientation. When 5% excess iron was added to the precursor solution, the film crystallized in the (100) orientation. The electronic states and charge species responsible for photoconductivity were investigated by emission/excitation and photocurrent action spectroscopy. The low photoemission at 77K and high photoconductivity at 298K in the doped thin films, as compared with thermally iron-doped ceramics, are attributed to the surface energy quenching and low trapping state density.

Introduction

Extrinsic metal ions can increase photoconductivity in wide-bandgap ceramics of lead zirconate titanate (PZT) and lead lanthanum zirconate titanate (PLZT). However, weak photoconductivity measured at visible wavelengths in ceramic PLZT was attributed to the presence of trapping states and the lack of optically absorbing states in the band gap. [1] Extension of the photoresponse into the visible region would make these materials ideal for photonic applications using commonly available laser sources. The visible light photoresponse in PZT/PLZT has been increased by ion implantation of inert gases and metals [2,3] by thermal diffusion of metal with [4] and without [5,6] subsequent ion implantation, and by sintering a mixture of metal oxide and presynthesized perovskite powder. [1] Lead perovskite thin films made by a sol-gel technique were shown [7] to have a higher photoconductivity than the bulk ceramic, which was attributed to the films having fewer trapping states. [7]

Recently, we have developed an aqueous, low-temperature process termed Deposition by Aqueous Acetate Solution (DAAS) [8] for synthesizing $Pb(Zr_{0.53}Ti_{0.47})O_3$ [PZT (53,47)] thin films on Pt<111>/Ti/SiO_2/Si<100> substrates. The process offers a number of advantages that include: (1) the formulated precursor solutions are stable with no discernible gelation or precipitation over several months; (2) the precursor solutions can be formulated to within better than 1% of the desired stoichiometry; (3) because this is an aqueous process, it is a non-moisture-sensitive alternative to the sol-gel technique; (4) water soluble acetate, acetylacetonate, or carbonate salts of various metal ions can be easily added to the solution to prepare extrinsically doped perovskites; and (5) the process uses water as the solvent, which is considered "environmentally friendly." The low processing temperature together with the ability to control the stoichiometry and dopant level accurately makes the DAAS process ideally suited for synthesizing doped PZT and PLZT thin films for a wide range of applications.

In this paper, the crystallinity/orientation and electrical properties/fatigue characteristics of PZT thin films on Pt<111>/Ti/SiO_2/Si<100> substrates are described. Two ways of preparing doped PZT and PLZT thin films are adopted: in one, 5% of the of zirconium and titanium in the precursor solution was replaced by iron, and, in the other, 5% excess iron was added to the stoichiometric precursor solution. The effects of iron on the crystallinity and orientation of both films were determined by X-ray diffraction and FTIR spectroscopy. The defect states and active-ion sites responsible for photoconductivity of doped films were investigated by emission/excitation and photocurrent action spectroscopy. The results were compared to those of thermally iron-doped bulk ceramics.

Experimental

The DAAS technique and its formulation and synthesis of PLZT (7/65/35) bulk powders [9] and PZT (53,47) perovskite films [8] on Pt<111>/Ti/SiO_2/Si<100> substrates have been described elsewhere. The same precursors and procedure were used to prepare the iron-doped PZT and PLZT. $Pb(Zr_{0.53}Ti_{0.47})O_3$+5% Fe and $(Pb_{0.93}La_{0.07})(Zr_{0.65}Ti_{0.35})_{0.983}O_3$+5% Fe are referred to as 5% excess iron formulations, and $Pb\{(Zr_{0.53}Ti_{0.47})_{0.95}Fe_{0.05}\}O_3$ and $(Pb_{0.93}La_{0.07})\{Zr_{0.65}Ti_{0.35})_{0.933}Fe_{0.05}\}O_3$ are referred to as the 5% Fe stoichiometric formulations. Iron (III) acetylacetonate was added into the coating solution to supply the iron dopant for the DAAS-deposited films. The films were dried at 100°C for 10 min and consolidated at 400°C for 10 min before subsequent layers were added. After the desired thickness was attained, the films were annealed at 650°C for 10 min.

Fourier transform infrared (FTIR) spectroscopy [8], X-ray diffraction (XRD) [8], and emission/excitation spectroscopy [5] used in this work have been reported previously. In photocurrent action spectroscopy, the photocurrent was measured as a function of the irradiated light wavelength and intensity, and the applied voltage and polarity. Two small platinum or copper electrodes (about 2 mm x 2 mm with a 0.25-mm gap) were deposited on the sample surface (film or plate) for photoconductivity measurements. A 1/4-meter monochromator was placed in front of a 450-W enhanced UV xenon lamp source (Oriel, 66203) and was used to scan the excitation wavelengths via a stepper motor controller (Oriel, 20025). Light of selected wavelengths was focussed onto the gap between the electrodes. Current was measured using a Keithley model 617 electrometer, which also supplied the applied voltage. The data were acquired and stored on an HP 7090A plotter with the aid of an NEC PowerMate 286 Plus computer.

Results and Discussion

Crystallinity and Fatigue of PZT (53,47) Films

The top panel of Fig. 1 shows the XRD spectrum of a PZT(53,47) film prepared by the DAAS technique on a Pt<111>/Ti/SiO_2/Si<100> substrate and annealed at 650°C for 10 min. Spectral peaks at 2θ = 22.11° {100}, 31.28° {110}, 38.62° {111}, 44.92° {200}, and 50.51° {210} are perovskites, whereas the peak at 2θ = 33.16° is a broad band and is assigned to a pyrochlore phase

CH3080-0-7803-0465-9/92$3.00 ©IEEE

probably related to $Pb_2Ti_2O_6$. [9] The film is highly crystalline as represented by a small FWHM (full width at half maximum). The preferential film orientations are PZT{110} and PZT{111}.

For measuring the electrical properties, gold electrodes (0.63 mm in diameter) were deposited on a PZT (53,47) film (about 0.4 μm thick) by evaporation through a shadow mask and were annealed at 550°C for 15 min in air. Contact was made to the lower platinum electrode and to the deposited gold contacts using a gold whisker mounted on mechanical probes. The P-E hysteresis loops were obtained using an RT66A (Radiant Technologies, Albuquerque, NM) curve tracer. The dc resistance and coercive field of the film is about 1×10^8 ohm-cm and 2×10^5 V/cm, respectively. The relative dielectric constant is about 1000, and the dissipation factor is 0.014, based on measurements using an HP model 4276A LCZ meter operated at 1 kHz. The bottom trace of Fig. 1 shows the fatigue behavior of PZT (53,47) film cycled with a 12-V sine wave. At 10^6 cycles, no fatigue was observed, and only a slight amount of fatigue, about 10%, was noticeable at 10^{11} cycles. These excellent fatigue results are due, in part, to the accurate control of stoichiometry and the high degree of crystallinity obtainable through the use of the DAAS process.

Crystallite Orientations of Doped PZT and PLZT Films

The effect of iron doping on the crystallization of PZT and PLZT films should depend on how iron incorporates into the lattice. Iron was introduced into PZT and PLZT films as a substitutional dopant for zirconium and titanium, i.e., $Pb[(Zr_{0.53}Ti_{0.47})_{0.95}Fe_{0.05}]O_3$ (film 1) and $(Pb_{0.93}La_{0.07})[(Zr_{0.65}Ti_{0.350})_{0.933}Fe_{0.05}]O_3$ (film 2), and as an additive to the stoichiometric DAAS solutions, i.e., $Pb(Zr_{0.53}Ti_{0.47})O_3$ +5% Fe (film 3) and $(Pb_{0.93}La_{0.07})(Zr_{0.65}Ti_{0.350})_{0.983}O_3$+5% Fe (film 4). Figure 2 shows the XRD spectra of film 1 (top) and film 3 (bottom) on Pt<111>/Ti/SiO_2/Si<100> substrates. Film 1 displays a more conventional randomly orientated perovskite PZT similar to that shown in Figure 1 having a dominant (110) peak. In the 5% iron stoichiometric formulation, the iron was incorporated into the PZT lattice and did not affect the normal nucleation and crystallization of the films. On the other hand, film 3 shows that the 5% excess iron resulted in crystallization preferentially with (100) and (200) orientations.

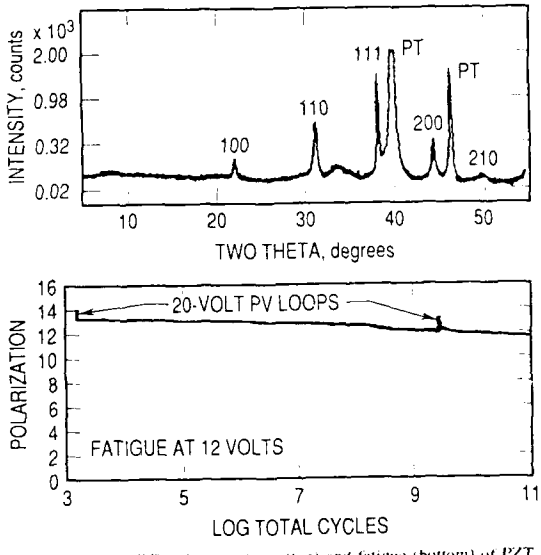


Figure 1. X-ray diffraction spectrum (top) and fatigue (bottom) of PZT (53,47) film on Pt<100>/Ti/SiO_2/Si<100> substrate annealed at 650°C for 10 min.

The intensity ratio of XRD peaks (on the same intensity scale) are I (100)/I (110) = 114/346, 353/331, 272/67, and 66/18 for film 1, film 2, film 3, and film 4, respectively. The pyrochlore broad bands at 2θ = 19.90°, 29.99°, and 33.73° appear in all four films, with the intensity in descending order of film 4 > film 2 > film 3 > film 1. The pyrochlore phase is also evidenced as a broad-base [8] FTIR spectral band at 676 cm^{-1}. The addition of 5% excess iron to the stoichiometric PLZT (film 4) suppressed the crystallization of the perovskite film. PLZT has been shown in many studies to have a higher crystallization temperature than PZT, and more difficulty in crystallization. Substitutional iron-doping of PLZT (film 2) resulted in crystallization with both (110) and (100) orientations, i.e., a higher than normal (100) orientation.

Defect Chemistry and Photoconductivity of Iron-doped PLZT Perovskites

To study the creation of chemically active doped ions and the generation of photoconductivity in iron-doped PLZT thin films for the comparison to those in iron-doped PLZT (7/65/35) ceramic, the emission/excitation and photocurrent action spectra of thermally diffused iron-doped samples were recorded. A 100 Å thick film of iron on $(Pb_{0.92}La_{0.07})(Zr_{0.65}Ti_{0.350})_{0.98}O_3$ ceramic wafer (0.25 to 0.30 mm thick, Honeywell) was prepared by vacuum evaporation in an electron beam evaporator. The iron was diffused into the ceramic in a furnace under O_2 atmosphere for 8 h at 800°C.

Figure 3(a) shows the 77K emission spectrum of iron-doped ceramic with broad band spectral peaks at approximately 430, 520, 540, and 570 nm. The first three bands are the intrinsic emission spectrum of the undoped PLZT sample whereas the fourth band at 570 nm is the characteristic emission maximum of Fe^{3+}-doped PLZT ceramics. [5] The band gap energy of undoped PLZT ceramic is = 3.35 eV (or 370 nm). [10]

The intrinsic emission of the undoped perovskite PLZT samples comes mainly from the transitions between the valence band and the conduction band. The valence and conduction bands have been calculated for similar ferroelectric crystals, i.e., barium titanate and strontium titanate. [11,12] The results indicate that the conduction band consists primarily of empty t_{2g} titanium bands while the valence band consists of filled oxygen 2p states. The 77K excitation spectrum of an iron-doped PLZT sample monitored at the 570-nm emission peak is

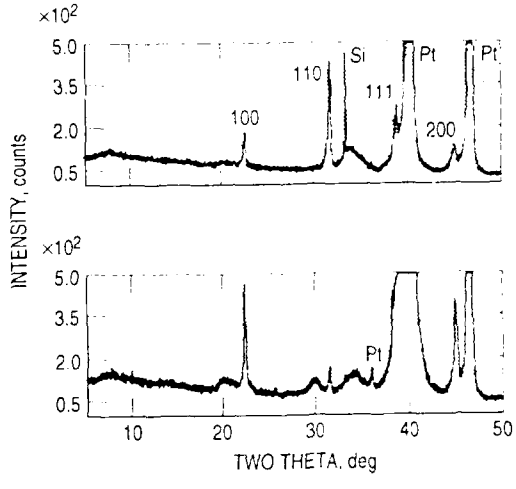


Figure 2. X-ray diffraction spectra of $Pb[(Zr_{0.53}Ti_{0.47})_{0.95}Fe_{0.05}]O_3$ (top) and $Pb(Zr_{0.53}Ti_{0.47})O_3$ + 5% Fe (bottom) on Pt<111>/Ti/SiO_2/Si<100> annealed at 650°C for 10 min.

illustrated in Fig. 3(b). The excitation spectrum consists of a strong broad band maximum at 341 nm (referred to as band system I) and a relatively strong multiple structure extended from 400 to 500 nm (referred to as band system II) with a peak maximum at 465 nm. The band edge of the low-energy side of band system I corresponds well with the band gap energy of 370 nm. Band system II originates from optically absorbing states at visible light wavelengths generated by the thermally diffused Fe^{3+} in PLZT ceramics.

Figure 3(c) shows the photocurrent action spectrum of iron-doped PLZT ceramic. The photocurrent was measured as a function of the irradiated light wavelength (200 to 600 nm), intensity, applied voltage (102 V/0.25 mm), and polarity (+). Four photocurrent action peaks are observed: 1.0 nA at 300 nm, 1.7 nA at 370 nm, 1.2 nA at 420 nm, and 1.0 nA at 465 nm. These peaks are correlated well with those of the excitation spectrum in Fig. 3(b), indicating that the photon absorbing states that lead to the photoemission spectrum shown in Fig. 3(a) are also responsible for the production of photoconductivity displayed in Fig. 3(c). As expected, the creation of chemically active iron ions upon doping can generate photocarriers and enhance photoconductivity. It was shown [6] that the photoexcited electrons in iron-doped PLZT ceramic have a good mobility with relatively few deep traps. The studies of low-temperature photocurrent action spectrum and its rise/decay characteristics have confirmed the trapping dynamics.

Figure 3(d) shows the 77K emission spectrum of $(Pb_{0.93}La_{0.07})(Zr_{0.65}Ti_{0.35})_{0.983}O_3$ + 5% Fe thin film on a Pt<111>/Ti/SiO_2/Si<100> substrate. The $(Pb_{0.93}La_{0.07})[(Zr_{0.65}Ti_{0.35})_{0.933}Fe_{0.05}]O_3$ thin film gives a similar emission spectrum. Both iron-doped films made by the DAAS technique display very weak emission compared to the thermally doped PLZT ceramic in Fig. 3(a), suggesting that fewer trapping states have been created or the excitation has been quenched non-radiatively by the substrate surface. The emission extends from 380 nm to 560 nm with a band maximum at 450 nm. When this emission maximum at 450 nm is monitored, the excitation spectrum shows that a single band extends from 270 nm to 380 nm with a peak maximum at 341 nm, which is the band gap transition. Land [7] has shown that PLZT thin films made by a sol-gel technique have a higher photoconductivity than the bulk ceramic, which he attributed to the films having fewer trapping states. This result is in agreement with that of emission/excitation studies of iron-doped PLZT thin films made by the DAAS technique. Weak emission from our Fe-doped PZT films suggests that iron ions are strongly bonded in the perovskite lattice. The energy states of iron substitutionally doped in PZT lie outside the bandgap and will have insignificant effects on enhancing the extrinsic photoconductivity of the doped materials. In the thermally doped ceramic PLZT samples, diffusion occurs mainly at the grain boundary. The dopant tends to modify the surface of the grain and create new energy states near the band edge that are responsible for the enhanced photoconductivity. Fe-doped films are currently being prepared for the measurement of photocurrent action spectra and electrical properties to examine this hypothesis.

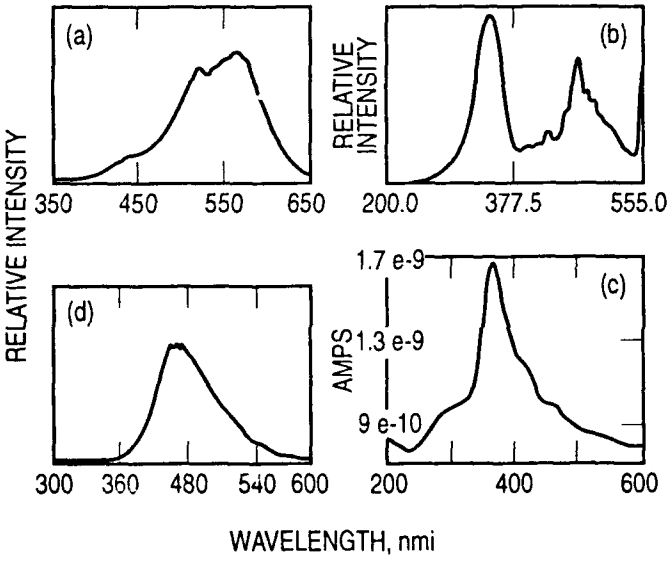


Figure 3. 77K emission (a) and excitation (b), and 298K photocurrent action (c) spectra of iron-doped PLZT (7/65/35) ceramics. (d) 77K emission spectrum of $(Pb_{0.92}La_{0.07})(Zr_{0.65}Ti_{0.35})_{0.983}O_3$+5% Fe thin film on Pt<111>/Ti/SiO_2/Si<100> substrate.

Conclusion

The DAAS technique has been shown to produce highly crystalline and preferentially oriented thin films of undoped and iron-doped PZT and PLZT perovskites on Pt<111>/Ti/SiO_2/Si<100> substrates at relatively low temperatures of 550 to 650°C. The 5% iron stoichiometric formulation produces films that crystallized with a (110) orientation whereas those made of 5% iron excess formulation display a (100) orientation. A precise stoichiometric PZT precursor solution formulated by the DAAS technique has produced a perovskite film of excellent fatigue behavior. The emission/excitation and photocurrent action studies illustrated that the photon absorbing states in the iron-doped ceramics are responsible for the production of photoconductivity. The iron-doped perovskite films show weak photoemission, consistent with energy quenching by the substrate surface, and exhibit high intrinsic photocurrent indicative of fewer trapping states in the films.

Acknowledgements

Financial support from the Aerospace Sponsored Research Program, and Northern Illinois University Graduate School and College of Liberal Arts and Sciences is acknowledged.

References

[1] R.A. Craig, C.R. Batishko, J.L. Brimhall, W.T. Pawlewicz, K.A. Stahl, and L.R. Toburen, "Develop techniques for ion implantation of PLZT for adaptive optics", Report WL-TR-89-26, Kirtland Air Force Base, NM, November 1989.

[2] C.E. Land and P.S. Peercy, "The effects of ion implantation on the photoferroelectric properties of lead lanthanum zirconate titanate ceramics", *Ferroelectrics*, vol. 38, pp. 947-950, 1981.

[3] C.E. Land and P.S. Peercy, "Ion implanted PLZT for photoferroelectric image storage and display devices," *Ferroelectrics*, vol. 27, pp. 131-136, 1980.

[4] C.E. Land and P.S. Peercy, "Photoferroelectric sensitivity enhancement in PLZT by thermal diffusion of metals," *Ferroelectrics*, vol. 50, pp. 85-90, 1983.

[5] C.T. Lin, H.Y. Lee, H.C. Bitting Jr., R.A. Lipeles, M.B. Tueling, and M.S. Leung, "Emission and excitation spectra of thermally diffused ions in PLZT ceramics," *Chem. Phys. Letters*, vol. 174, pp. 269-277, 1990.

[6] R.A. Lipeles, G. Eng, M.S. Leung and C.T. Lin, "Photoconductivity in PLZT thermally diffused ceramic with iron", in *Proceedings of the 1990 IEEE 7th International Symposium on the Application of Ferroelectrics*, Champaign, IL, 6-8 June 1990 (IEEE, New York, NY 1991), pp. 640-642.

[7] C.E. Land, "Longitudinal electro-optical effects and photosensitivities of lead zirconate titanate thin films," *J. Am. Ceram. Soc.*, vol. 72, pp. 2059-2064, 1989.

[8] C. T. Lin, Li Li, J.S. Webb, R.A. Lipeles, and M.S. Leung, "An aqueous, low temperature process for synthesizing PZT (53,47) thin films," in *Proceedings of 4th International Symposium on Integrated Ferroelectrics*, Monterey, CA, 9-11 March 1992.

[9] C.T. Lin, B.W. Scanlan, J.D. McNeill, J.S. Webb, Li Li, R.A. Lipeles, P.M. Adams, and M.S. Leung, "Crystallization behavior in a low-temperature acetate process for PT, PZT and PLZT bulk powders," *J. Mater. Res.*, vol 7, 1992, in press.

[10] C.H. Seager and C.E. Land, "Optical absorption in ion-implanted lead lanthanum zirconate titanate ceramics," *Appl. Phys. Lett.*, vol. 45, pp. 395-397, 1984.

[11] L.F. Mattheiss, "Energy bands for $KNiF_3$, $SrTiO_3$, $KMoO_3$, and $KTaO_3$," *Phys. Rev. B*, vol. 6, pp. 4718-4740, 1972.

[12] T. Wolfram, "Two-dimensional character of the conduction bands of d-band perovskites", *Phys. Rev. Lett.*, vol. 29, pp. 1383-1387, 1972.

CH3080-0-7803-0465-9/92$3.00 ©IEEE

THE STUDY OF PZT FERROELECTRIC THIN FILM AND COMPOSITE WITH AMORPHOUS SILICON

Wang Yong Ling Wu Dao Huai Chen Hui Ting Yu Da Wei
Shanghai Institute of Ceramics, Chinese Academy of Sciences
1295 Ding Xi Road
Shanghai 200050, China

This paper introduced some work done in our lab recently. The first part we study the remanent polarization and coercive field of PZT ceramics in variation with the thickness of specimen. Second, study the properties of PZT thin film which be prepared by RF sputtering. Last, we design a new optical devices with composite amorphous silicon and PZT ceramics.

Introduction

There are a lot of papers have been published in study of the ferroelectric thin film to be used for DRAM or FRAM (Ferroelectric Random Access Memory) devices[1-2].In this paper our first aim is to study the remanent polarization and coercive field of ceramics in variation with the thickness of specimen. Because those properties are also seriously varied by the different processing methods for bulk, thick film and thin film materials in the thickness range from 1 mm down to 100 nm, so only part of result has been obtained. Our second aims is to design a new optical device with composite amorphous silicon and PZT thin films. The applied voltage drop is transferred from amorphous silicon to ferroelectric ceramics by optical exposure. This idea has been demonstrated by experiment in a wide range of thickness match. More data will be published in the next paper.

Materials and Specimen Preparation

PZT bulk materials were prepared by commercial processing method and fine milling. The limit thickness down to 0.04 mm can be obtained. PZT thin film in the thickness range less than 1 um were prepared by RF sputtering Method. The substrate can be heated within the temperature 650°c during deposition and most of the specimen were annealed after deposition. The amorphous silicon thin film which was deposited on the PZT ceramics was prepared by radio frequency glow discharge method in the thickness range usually less than 1 um. The thickness of a-Si thin film are considered to be matched with PZT both in resistance and electric strength. In order to get the good ohm contact, the aluminum electrode were pre-vaporized on the PZT ceramics. Fig. 1 shows the structure of experimental specimen.

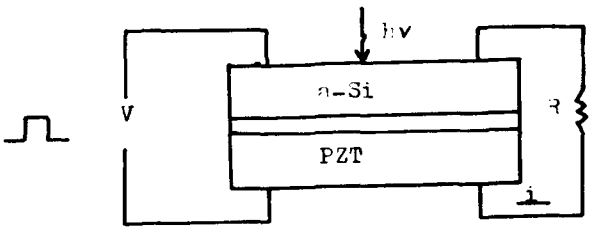


Fig. 1: The Scheme of Composite PZT and a-Si Thin Film.

Results

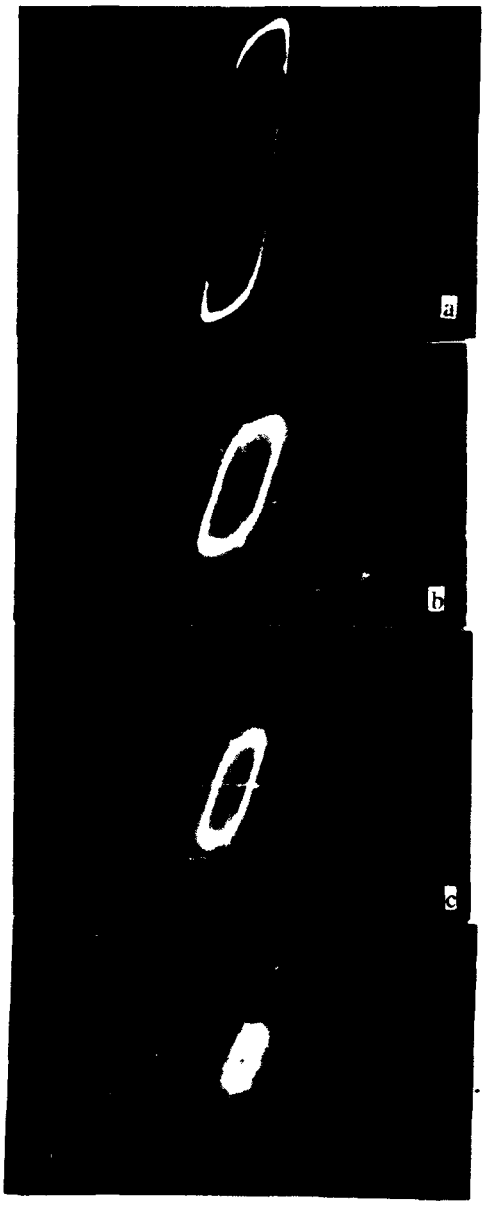


Fig. 2: The Ferroelectric Hysteresis Loop of Ceramics with Different Thickness.
d: Thickness.
(a) d = 0.1 mm, Pr = 24.4uc/cm^2, Ec = 937.5v/mm
(b) d = 0.08mm, Pr = 10.6uc/cm^2, Ec = 1000v/mm
(c) d = 0.06mm, Pr = 8.5uc/cm^2, Ec = 1041.7v/mm
(d) d = 0.04mm, Pr = 6.1uc/cm^2, Ec = 1250v/mm

CH3080-0-7803-0465-9/92$3.00 ©IEEE

Fig. 2 shows the 50 hz hysteresis loops of PZT specimen in the thickness range from 1 mm to 0.04 mm. It can be seen that the remnant polarization decrease and the coercive field increase. Because the quality of specimen and electrode contact is not very good, these data is not very exact.

Fig. 3 shows the differential interference optical microscopic photos (x400) in response of different annealing conditions. Fig.4 shows the x-ray diffraction spectra. It can be seen that the perovskite phase increases with the increase of temperature and time.

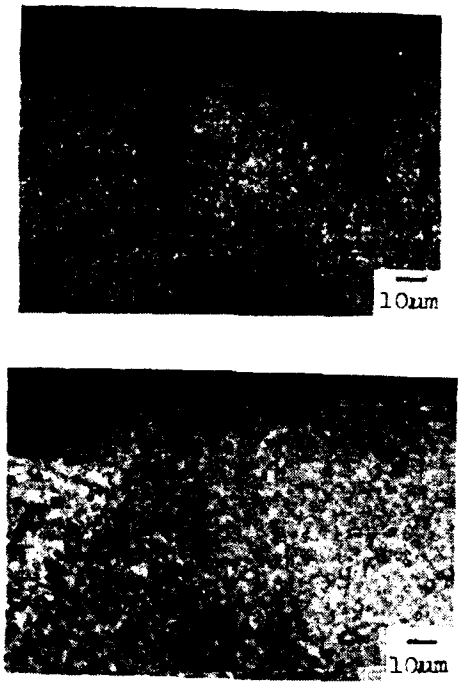


Fig. 3: The Differential interference Optical Micrographs (x400) of PZT film. Annealed at 700 c for (a) 2hr. (b) 1hr.

The resistivity of a-Si thin film are usually in the range of $10^9\Omega$cm in dark field and can be raised to $10^{11}\Omega$cm by doping B. After optical exposure, it will drop more than three orders. The PZT ceramics can be modified by doping U_3O_8 to obtain the resistivity even down to $10^7\Omega$cm . When a-Si thin film composite with thicker PZT ceramics which have been doped U_3O_8, the voltage drop can still be transferred from a-Si thin film to PZT ceramics by optical exposure. Table 1 shows the results and Fig. 5 shows the specimen structure. Fig. 6 is the SEM picture of the interface between PZT ceramics and a-Si thin film. It can be seen that the interface is quite smooth, no pin hole or obvious zig-zag.

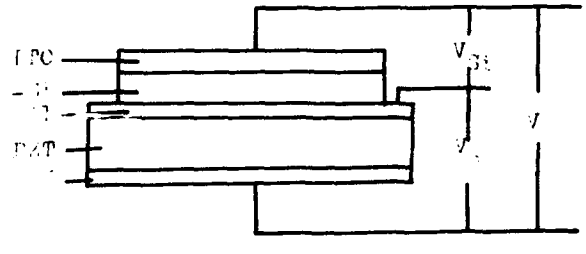


Fig. 5: The Specimen Structure of the Optical Devices Which is Composite PZT and a-Si Thin Film.

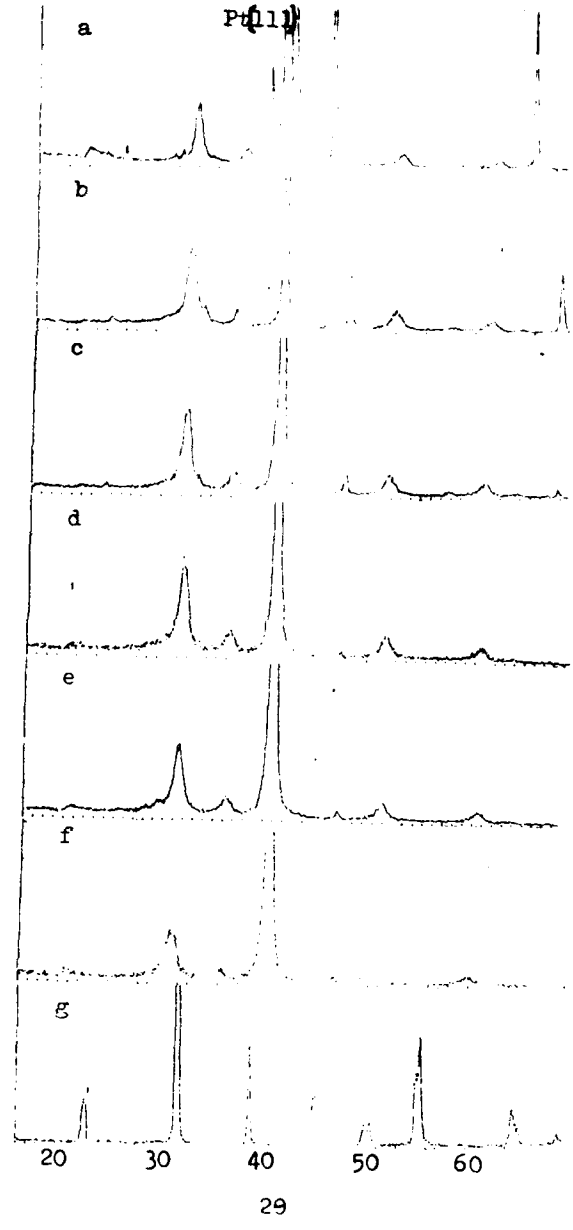


Fig. 4: XRD spectra of the PZT film annealed at
(a) 700°c for 2hr., (b) 700°c for 1 hr.,
(c) 700°c for 30 min., (d) 650°c for 2 hr.,
(e) 650°c for 1 hr., (f) 650°c for 20 min.,
(g) PZT ceramics as target.

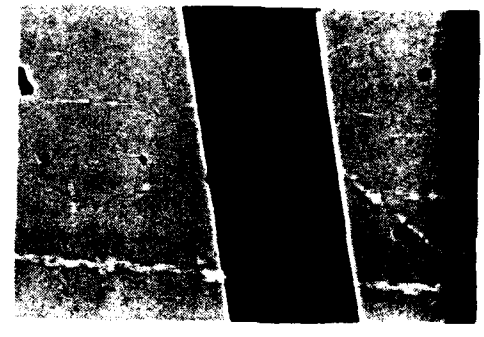


Fig. 6: The SEM Picture of the Interface of PZT and a-Si.

Table I: The Variation of applied voltage drops with the light.

	Dark		Light	
V(v)	Vsi(v)	Vp(v)	Vsi(v)	Vp(v)
2.0	1.3	0.7	0.03	1.97
4.0	2.6	1.4	0.06	3.94
6.0	4.0	2.0	0.10	5.90

In condition of the high quality PZT thin film instead of PZT ceramics, this kind of match will be very easy to obtain and a lot of devices can be designed. This kind of devices show following advantages:

1) Fast response (switch time 10^{-9}s).
2) High density.
3) Easily matched with integrated circuit.
4) No need P-N junction.
5) Cheap price.

The further work is being done in our lab, and more data will be published in the next paper.

References

[1] J. F. Scott and C. A. Paz De Araujo, "Ferroelectric memories", Science, Vol. 246, pp. 1400-1405, Dec. 1989.

[2] L.H. Parker and A. F. Tarsch " Ferroelectric materials for 64 MB and 256 Mb DRAMs", IEEE on circuits and Devices, Jan. 1990, pp17-26.

MICROSTRUCTURE-INDUCED SCHOTTKY BARRIER EFFECTS IN BARIUM STRONTIUM TITANATE (BST) THIN FILMS FOR 16 AND 64 MBIT DRAM CELLS

J. F. Scott,+ M. Azuma,* E. Fujii,* T. Otsuki,*
G. Kano,* M. C. Scott,+ C. A. Paz de Araujo,+
L. D. McMillan,+ and T. Roberts+

+ Symetrix Corp., 5055 Mark Dabling Blvd., Colorado Springs, CO 80918 and Univ. of Colorado (Boulder, CO 80309-0390 and Colorado Springs, CO 80933-7150)

* Electronic Research Laboratory, Matsushita Electronics Corp., Takatsuki, Osaka, Japan

Abstract

Barium strontium titanate is the material of choice for advanced DRAM cells with simple structures. The linearity of the dielectric properties of this system of solid solutions is controlled by the composition and microstructure. Recent results show that the leakage current is also very dependent on the acceptor-to-donor ratio at the grain boundaries, inducing Schottky barrier effects. This problem does not void the application of BST to ULSI DRAMs, but it must be controllable in order to achieve repeatability. This paper shows a model and pertinent data for integrated BST capacitors used in 16/64 Mb DRAM cells. The results confirm in detail the earlier conclusion of R. Waser and M. Klee [Ferroelectrics, in press, Aug. 1992] that conduction in ceramic $SrTiO_3$ is Schottky-dominated and that the Schottky barriers arise from depletion regions at grain boundaries and not only at the ferroelectric/electrode interface.

Introduction

The present trend toward replacement of SiO_2 and Ta_2O_5 capacitors in DRAMs (dynamic random access memories) with very high dielectric films has emphasized strontium titanate ($SrTiO_3$) and (BST) barium strontium titanate ($Ba_xSr_{1-x}TiO_3$). A planarized (i.e., without trenching) 64 Mb cell design with sol-gel BST is being presented this autumn,[1] and work with sputtered BST has gone on at NEC for several years.[2] Although some authors believe[3] that lead zirconate-titanate (PZT) is suitable for ULSI (ultra large scale integrated) DRAMs, that is not our opinion. In PZT the dielectric constant is ca. 1300 at 1 MHz but rolls off to ca. 40 at about 1 GHz; similarly, its loss tangent diverges to ca. 0.1 at such frequencies. Thus, at the high clock rates envisioned for ULSI DRAMs (≥ 100 MHz), PZT is completely unsuitable. By comparison, BST retains its dielectric constant of ε = 400 - 800 up to 2 - 3 GHz, and a loss tangent of 0.001 to 0.02 at such frequencies.[4]

In the present paper we examine the current-voltage and capacitance-voltage characteristics of fine-grained, ceramic BST thin films for ULSI DRAM applications.

Experiment

I(V) Current-Voltage Data:

The sample geometry is illustrated in Fig. 1. Typical specimen dimensions are: Specimen #20. 70% Ba. 143 nm thickness. ε' = 504. Tan δ = 0.015. Specimen #25. 80% Ba. 142 nm thickness. ε' = 436. Tan δ = 0.017. The capacitor areas were both 6940 μm^2. Measurements were at 50 mV at 1 MHz.

In Figs. 2 and 3 we replot these data versus different powers of applied voltage (viz., $V^{1/2}$ and V^{-1}). These plots will show that the behavior is that of Schottky tunneling [or Frenkel-Poole; the two mechanisms differ only by a factor of two in slope in such graphs, and we will discuss the evidence that this is truly Schottky and not Frenkel-Poole in a separate paper] up to ca. 6.5V and that of Fowler-Nordheim tunneling (field emission) above ca. 6.5V. Fig. 2 shows the I(V) characteristics of sample #20 from 20 to 200°C. The results for sample #25 are extremely similar. The dashed curves are the theoretical

CH3080-0-7803-0465-9/92$3.00 ©IEEE

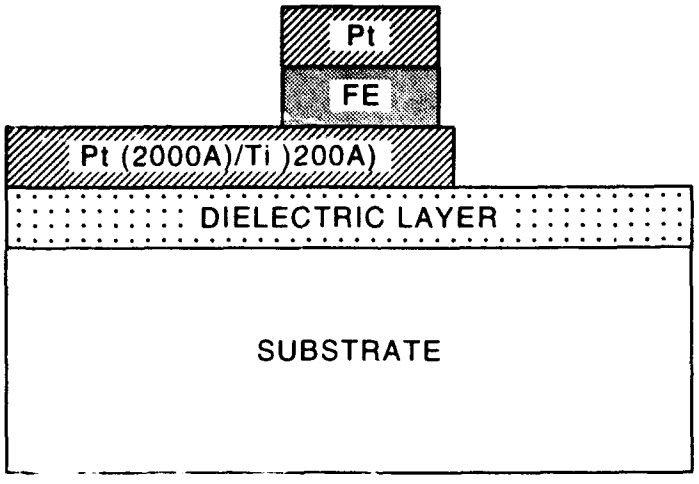


Figure 1. Device structure: BST ceramic film, 140-210 nm thick, sandwiched between 200 nm Pt electrodes, with 20 nm Ti adhesion layer.

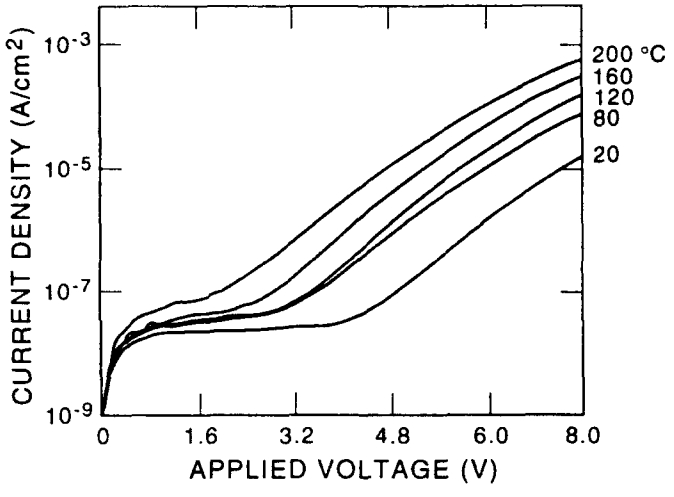


Figure 2. Semilogarithmic plot of current density versus applied voltage for 70% Ba BST sample, 143 nm thick, at temperatures of 20, 80, 120, 160, and 200°C. Note that the 2.5V ULSI operating voltage at room temperature the leakage current is 20 nA/cm^2.

form for Schottky conduction:

$$\log (J/T^2) = \text{const. x } V^{1/2} \qquad (1.)$$

And in Fig.3, with Fowler-Nordheim tunneling:

$$\log (J/V^2) = \text{const. x } V^{-1}. \qquad (2.)$$

These graphs show that over the full temperature range studied (20 - 200°C) the conduction mechanism is Shottky at voltages less than 6.5V, but that Fowler-Nordheim tunneling is dominant from 6.0 - 12.0V.

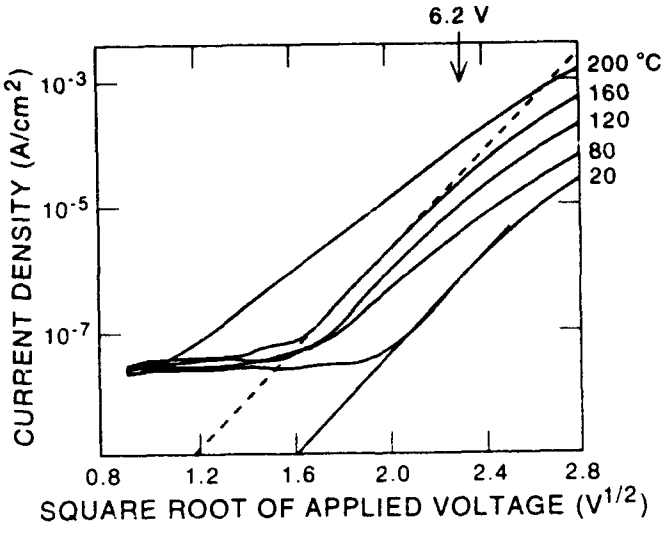


Figure 3a. Semilogarithmic plot of current density versus the square root of applied voltage for 80% Ba BST sample, 142 nm thick, at temperatures of 20, 80, 120, 160, and 200°C. The straight lines are the predictions for Schottky conduction, found to be valid below 6.5V (455 kV/cm).

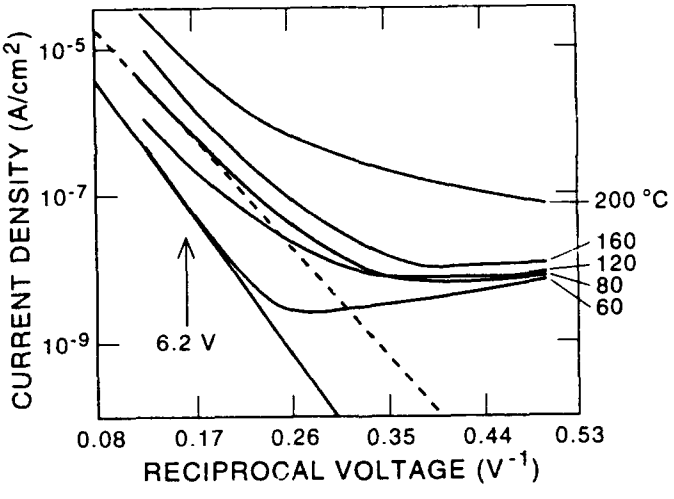


Figure 3b. Semilogarithmic plot of the data in Fig.3a versus 1/V; the straight lines show agreement with Fowler-Nordheim tunneling (field emission) above 6.5V (455 kV/cm).

Strictly speaking, field emission is quite independent of temperature, whereas our data in Fig.3 are slightly dependent upon T even at the highest fields employed (12V/200 nm = 600 kV/cm). This indicates that the mechanism is not strictly Fowler-Nordheim (field emission) but perhaps a mixed phenomenon.

Since Schottky conduction appears dominant at the intended operating voltage of this device, on the basis of the voltage dependence shown in the figures above, we complete the demonstration of Shottky conduction by showing in Fig. 4 below the

temperature dependence:

$$\log (J/T^2) = \text{const. x } T^{-1}. \quad (3.)$$

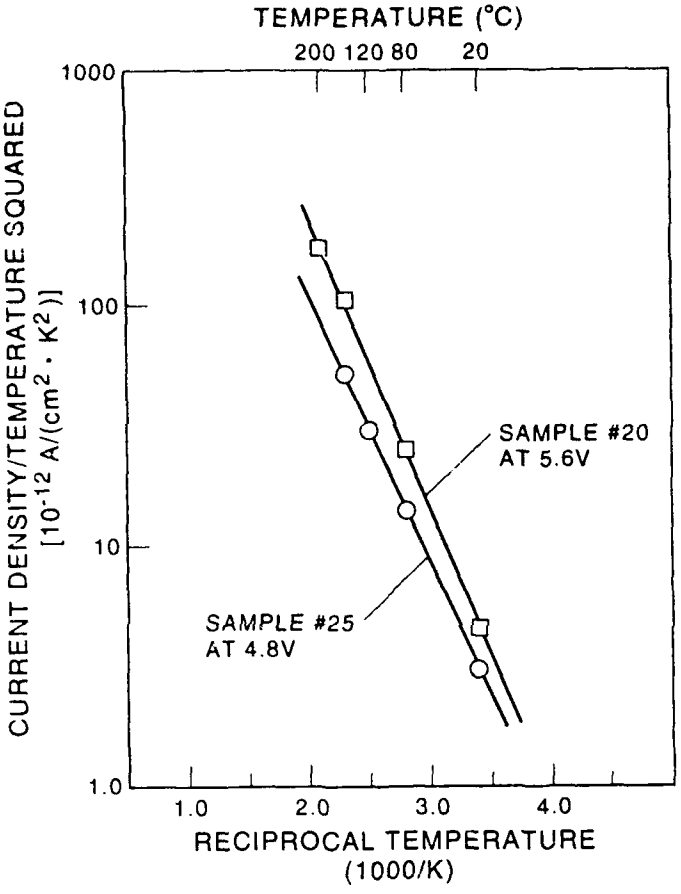


Figure 4. Temperature dependence of leakage current density J in ceramic BST samples #20 and #25. $\log(J/T^2)$ is plotted versus 1/T. The straight lines confirm Schottky-dominated currents at voltages up to 6V (400 kV/cm).

C(V) Capacitance-Voltage Data:

Fig. 5 shows the capacitance-voltage data on one ofthese two samples. If we assume that BST near the electrodes is an n-type semiconductor, due to oxygen vacancies, then the capacitance of the depletion region, under reverse bias voltage V_b, is given by:[5,6]

$$Cd = A \{q\epsilon N_D/(2\Delta V)\}^{1/2}, \quad (4.)$$

from which one can obtain

$$\log (1/C) = \text{const. x } V. \quad (5.)$$

Here C is capacitance; d, a depletion thickness which can be either film thickness in our case or an inter-grain parameter; q, electron charge; ϵ, dielectric constant; A, capacitor surface area; $\Delta V = V_b - V$; and N_D, donor concentration.

This dependence is confirmed in Fig. 6, where we use d = constant = film thickness for numerical values (but since d is not a variable in these data, only the relation $1/C \propto \exp V$ is being tested).

These data, plus the observation that neither conductivity nor dielectric constant of our BST films exhibit a strong dependence upon film thickness, support a model that the nonlinear C(V) characteristics are due to strong depletion that cannot originate from the BST/electrode interface, but must come internally from the BST ceramic itself.[7] This confirms the conclusions of Waser and Klee.[8]

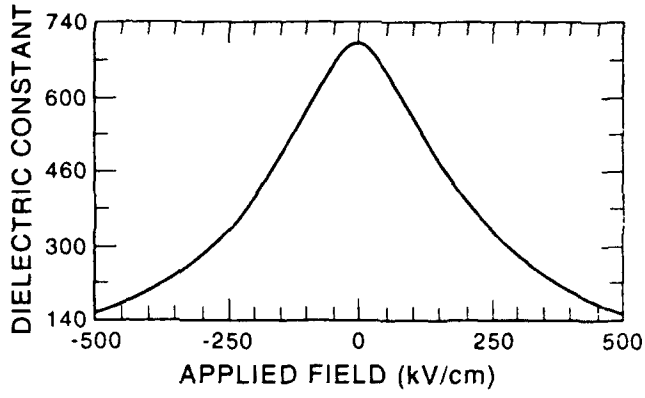


Figure 5. Capacitance-voltage C(V) data for ceramic BST samples #20 and #25. Dielectric constant is plotted versus field from -0.5 MV/cm to +0.5 MV/cm (ca. -8V to +8V). The small-signal dielectric constant κ is ca. 700. At the intended operating voltage of 2.5V, it is about 530.

References

[1.] M. Azuma et al., "A 64 Mb Ferroelectric DRAM Cell," IEDM Conf., Dec. 1992 (in press).

[2.] Y. Miyasaka et al., Proc. TMS Conf., Boulder, Colorado, June 1991 (in press).

[3.] R. Moazzami, C. Hu, and W. H. Shepherd, IEEE Electron Device Letters 11, 454 (1990); L. H. Parker and A. F. Tasch, IEEE Circuit and Devices Mag. 17, (1990); R. Moazzami et al., IEEE Trans. Elec. Devices (in press, Aug. 1992).

[4.] J. F. Scott, C. A. Paz de Araujo, L. D. McMillan, H. Yoshimori, H. Watanabe, T. Mihara, M. Azuma, Toshiyuki Ueda, Tetsuko Ueda, D. Ueda, and G. Kano, "Ferroelectric Thin Films in Integratred Microelectronic Devices," Proc. 25th Int. Conf. Polar Dielectrics (London, April 1992, edited by Roger Whatmore et al.), [Ferroelectrics, in press, 1992].

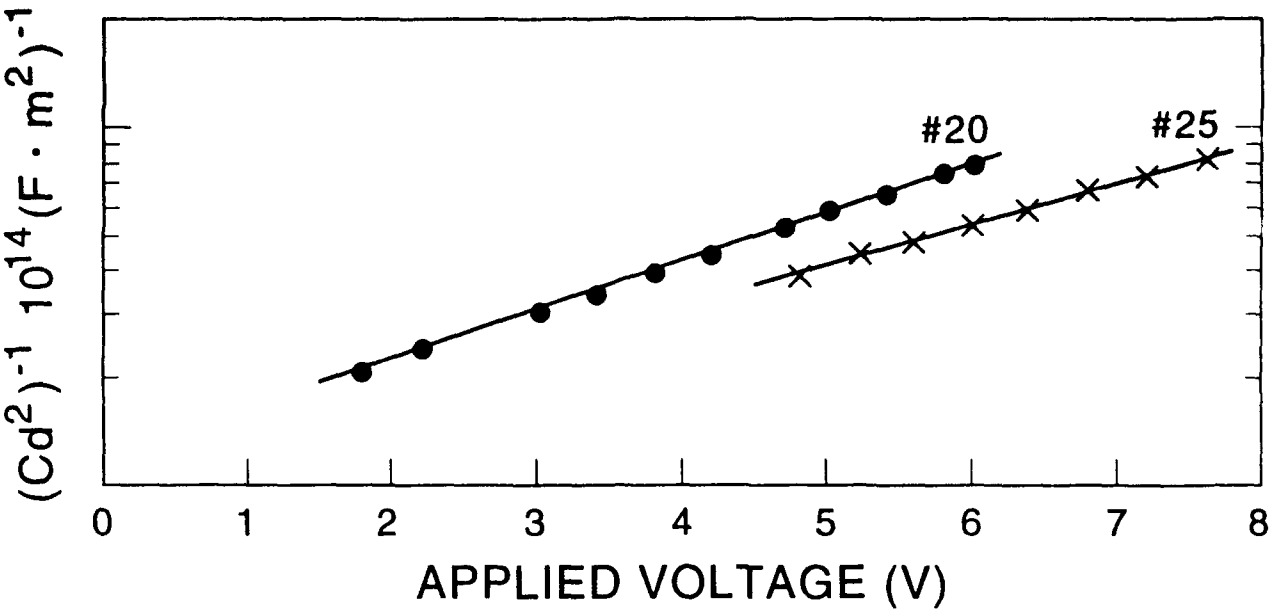


Figure 6. Capacitance-voltage relationships in ceramic BST specimens #20 and #25. The logarithm of reciprocal capacitance is plotted versus applied voltage (thickness d is actually not a variable in the data plotted).

[5.] In-Chyuan Ho and Shen-Li Fu, "Effect of Reoxidation on the Grain-Boundary Acceptor-State Density of Reduced $BaTiO_3$ Ceramics," J. Am. Ceram. Soc. 75, 728-30 (1992).

[6.] Ben Huybrechts, Kozo Ishizaki, and Masasuke Takata, "Experimental Evaluation of the Acceptor-States Compensation in Positive-Temperature-Coefficient-Type Barium Titanate," J. Am. Ceram. Soc. 75, 722-4 (1992).

[7.] S. Roberts, "Dielectric and Piezoelectric Properties of Barium Titanate," Phys. Rev. 71, 890-5 (1947).

[8.] R. Waser and M. Klee, "Theory of Conduction and Breakdown in Perovskite Thin Films," Proc. Int. Symp. Integrated Ferroelectrics (ISIF '91), Colorado Springs, CO, April 1991, edited by C. A. Paz de Araujo, pp.288-305 [Ferroelectrics, in press, August 1992].

Ferroelectric

NEW FERROELECTRICS $Ba_{1-x}M_x(Li_{2x}Al_{2-2x})O_{4-4x}F_{4x}$ (M=Pb,Sr)

Sui-Yang HUANG, R.VON DER MÜHLL, J.RAVEZ and P.HAGENMULLER
Laboratoire de Chimie du Solide du CNRS, Université Bordeaux I,
351 Cours de la libération, 33405 Talence Cedex, FRANCE

bstract

New ferroelectric ceramics $Ba_{1-x}M_x(Li_{2x}Al_{2-2x})$ $O_{4-4x}F_{4x}$ with $x\in[0,0.07]$ for M = Pb and $x\in[0,0.1]$ for M = Sr ave been studied. The behavior of T_C with composition as been determined. For Pb T_C decreases first from 396 o 233K when x rises from 0 to 0.04 and then, for x ising from 0.04 to 0.07, T_C increases from 233 to 320K. 'he thermal variation of P_S was determined. The ariation of T_C for the Sr-compound is rather similar: 'c decreases first from 396 to 238K when x rises from 0 o 0.05 and then remains constant when x increases up to).1.

1.INTRODUCTION

More than twenty compounds isostructural with $BaAl_2O_4$ ıave been reported yet, some of them have been claimed ır predicted as ferroelectric [1]. The first one was he solid solution $Ba(Li_{2x}Al_{2-2x})O_{4-4x}F_{4x}$ investigated ıy Dunne et al. on single crystals with composition ∈[0.15,0.30] [2]. We also studied the same compositions ıs ceramics for $x\in[0,0.3]$ [3]. Crystals of $Ba_{0.98}(Al_{0.999}\ Cu_{0.001})_2O_{4-\delta}$ were investigated by Bush ınd al.[4]; the materials with composition $Ba_{1.05}Ga_2O_{4.05}$ and $Sr_{1.1}Al_2O_{4.1}$ were also reported as ɔeing ferroelectric [5]. It could be concluded that naterials with a structure close to that of $BaAl_2O_4$ ɔould be ferroelectrics. The purpose of the present ıtudy is to investigate the dielectric and pyroelectric ɔroperties of some new compounds derived from $BaAl_2O_4$ by he mixed substitutions Ba/M - Al/Li - O/F (M=Pb,Sr).

2.SAMPLE PREPARATION

A $BaAl_2O_4$ powder was prepared as starting material by ɔolid state reaction at 1300°C:

$2BaCO_3 + 4Al(OH)_3 \rightarrow BaAl_2O_4 + 6H_2O + 2CO_2\uparrow$

The reagents were Merck 99.0% purity products. The X-ray liffraction patterns may be indexed with an hexagonal ınit cell with parameters: a=10.449(1)Å c=8.793(1)Å ɔlose to those of $BaAl_2O_4$ single crystals [6]. The solid ɔolution ceramics were then synthetised by solid state eaction:

$(1-x)BaAl_2O_4 + x(MF_2+2LiF) \rightarrow$

$Ba_{1-x}M_x(Li_{2x}Al_{2-2x})O_{4-4x}F_{4x}$ (M=Pb,Sr).

The reagent were 99.9% purity Merck products for PbF_2, SrF_2 and LiF and previously prepared $BaAl_2O_4$ powder. The mixture was ground and then uniaxially pressed as pellets, heated in vacuum for 2 h at 120°C and sintered in platinum sealed tubes at 1450-1500°C. The XRD patterns show only one phase up to the upper values observed for $x_{Pb}=0.07$ and $x_{Sr}=0.1$.

3.X-RAY DIFFRACTION

The XRD patterns of the two kinds of new obtained ceramics can be indexed with an hexagonal unit cell; the examination of the positions and the intensities of the reflexions shows that they are isostructural with $BaAl_2O_4$. This structure can be considered as deriving from that of β-tridymite [7]. The three dimensional framework is built up by layers of $[AlO_4]$ tetrahedra sharing three corners, the layers are linked by the remaining corner. Large tunnels parallel to the c-axis are filled by 9-coordinated Ba atoms. The lattice parameters were determined by least-square fitting. The Fig. 1 shows the variation of a and c , of the c/a ratio and the cell volume V vs. x for the $Ba_{1-x}Pb_x(Li_{2x}Al_{2-2x})O_{4-4x}F_{4x}$ ceramics. We shall discuss

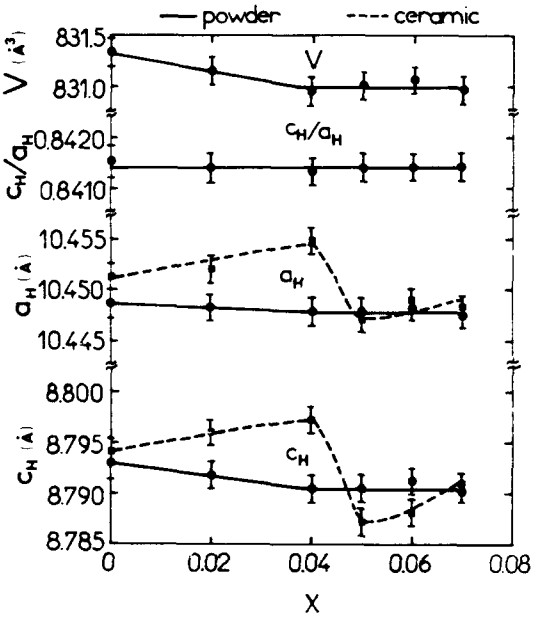


Fig.1 Variation of a, c, the c/a ratio and unit cell volume V with x for $Ba_{1-x}Pb_x(Li_{2x}Al_{2-2x})O_{4-4x}F_{4x}$.

080-0-7803-0465-9/92$3.00 ©IEEE

ıe values measured on ground ceramic powders, some ifferences appear for the values obtained from the urface of the ceramics probably due to internal tresses developed during sintering. For the Pb-ontaining solid solutions, a, c and V decrease first or rising x up to x=0.04 and then remain constant. The eplacement of larger Ba^{2+} ions by Pb^{2+} ($r_{Ba^{2+}}(IX)=1.47Å$ $r_{Pb^{2+}}(IX)=1.35Å$) explains the cell contraction observed or $x<0.04$. For x exceeding 0.04 this effect seems to be ompensated by the substitution of bigger Li^{+} for Al^{3+} ($r_{Al^{3+}}(IV)=0.39Å, r_{Li^{+}}(IV)=0.59Å$) with a probable slight earrangement of the structure. For the Sr-solid olution (Fig.2), the values of a,c and V decrease inearly with rising x in the whole domain between 0 and).1. The smaller size of strontium ($r_{Sr^{2+}}(IX)=1.31Å$) explains indeed the stronger decrease of the cell parameters and volume.

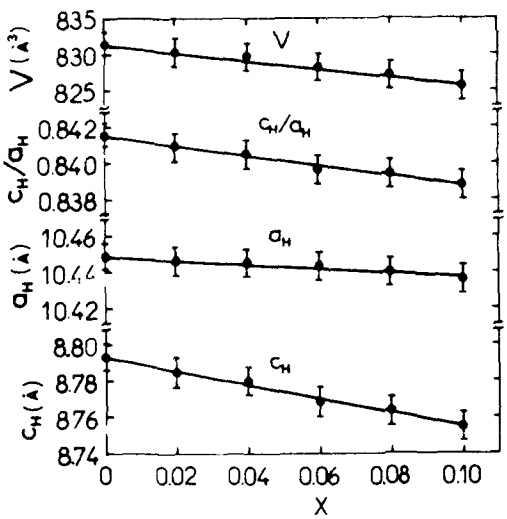


Fig.2 Variation of a, c, the c/a ratio and unit cell volume V with x for $Ba_{1-x}Sr_x(Li_{2x}Al_{2-2x})O_{4-4x}F_{4x}$.

4.FERROELECTRIC PROPERTIES

The dielectric constant ε_r' and tanδ were obtained by capacitance measurements on gold electroded pellets between 80 and 500K in the frequency range [20, 300k]Hz. In the thermal variation of ε_r' for $Ba_{0.93}Pb_{0.07}Li_{0.14}Al_{1.86}O_{3.72}F_{0.28}$(Fig.3) a small peak corresponding to T_C can be observed at 320K. The dielectric loss due to ionic conductivity increases quickly above 350K. The variation of T_C vs x rate is given in Fig.4 for two solid solutions. For the Pb-containing solid solutions T_C decreases first for x increasing up to 0.04, and then increases. This minimum behavior was already observed for the $BaLi_{2x}Al_{2-2x}O_{4-4x}F_{4x}$ solid solutions [3]. The

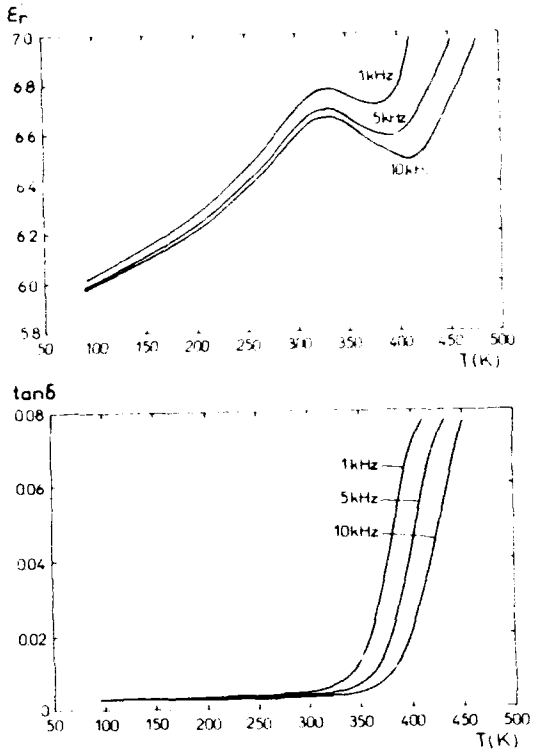


Fig.3 Temperature dependences of ε_r' and tanδ for a $Ba_{0.93}Pb_{0.07}Li_{0.14}Al_{1.86}O_{3.72}F_{0.28}$ ceramic.

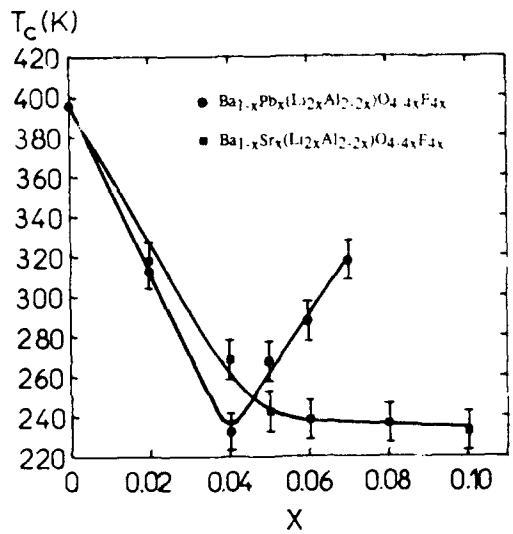


Fig.4 Evolution of the Curie point T_C vs x for $Ba_{1-x}M_x(Li_{2x}Al_{2-2x})O_{4-4x}F_{4x}$(M=Pb,Sr) ceramics.

variation of T_C with x results from the competition of the Al-Li, O-F against Ba-Pb substitutions. The Δz shift of the central atom Al(Li) in the tetrahedra along the polar axis from its position in the paraelectric phase is mainly responsible of the spontaneous polarization in the solid solutions with low substitution rates. The replacement of Al^{3+} by bigger Li^{+} ions limits its displacement in the corresponding tetrahedral site. This effect as well as reduced covalency due to Al-Li

cationic and O-F anionic substitution leads to decreasing T_C. For $x>0.04$ the Ba-Pb cationic substitution favor an increase of T_C. The polarization of Pb^{2+} is stronger than that of Ba^{2+} [8]; this may modify the atomic framework more that the O-F substitution and even if the fluoride anions are not statistically distributed.

Fig.5 shows the temperature dependence of ε_r' for a $Ba_{0.9}Sr_{0.1}Li_{0.2}Al_{1.8}O_{3.6}F_{0.4}$ ceramic. The dielectric peak is diffuse at T_C=238K. The conductivity effect becomes obvious above 350K. The relation between T_C and x is shown in Fig.4. T_C decreases first with rising x up to 0.05 and becomes practically constant for $0.05\leq x\leq 0.1$. The replacement of Ba^{2+} by smaller Sr^{2+} ions in the

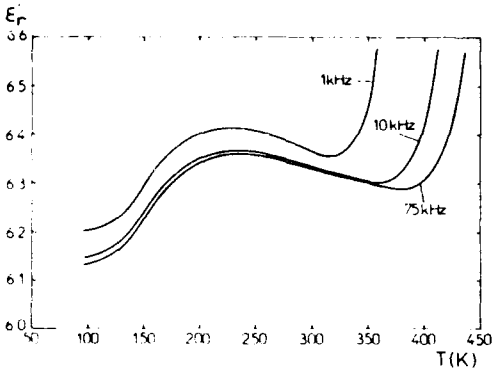


Fig.5 Temperature evolution of ε_r' for a $Ba_{0.9}Sr_{0.1}Li_{0.2}Al_{1.8}O_{3.6}F_{0.4}$ ceramic.

large 9-coordinated site gives more space for cation shifts. The spontaneous polarization related to the displacement of Sr^{2+} becomes considerable when the substitution rate x is bigger than 0.05. This may compensate the decrease of T_C due to the coupled substitutions of Li for Al and F for O.

5.PYROELECTRIC PROPERTIES

Thermal variation of the pyroelectric coefficient p and spontaneous polarization P_S are reported in Fig.6 and Fig.7 for $Ba_{0.93}Pb_{0.07}Li_{0.14}Al_{1.86}O_{3.72}F_{0.28}$. The ceramic samples have been previously poled by heating at the poling temperature $T_p=T_C$-30K with a dc field during 3 min. After polarization the samples are short-circuited at the same temperature for 10h in order to eliminate the space charges. The measurements were performed by a thermal depolarization method with a heating rate of 6K/min. The direction of the polarization vector can be reversed by application of an electric field. p presents a sign reversal around 200K and P_S shows a maximum at the same temperature. This unsual behavior had, nevertheless, been previously observed for $BaAl_2O_4$ and $BaLi_{2x}Al_{2-2x}O_{4-4x}F_{4x}$[3,4].

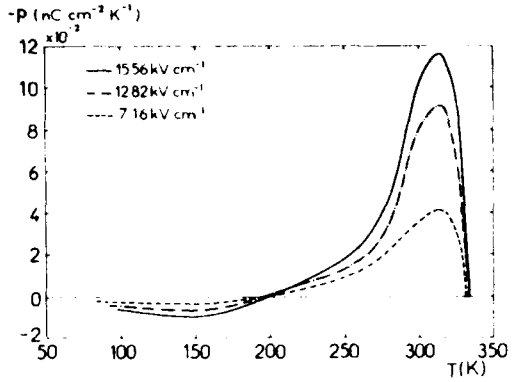


Fig.6 Thermal variation of the pyroelectric coefficient p for a $Ba_{0.93}Pb_{0.07}Li_{0.14}Al_{1.86}O_{3.72}F_{0.28}$ ceramic

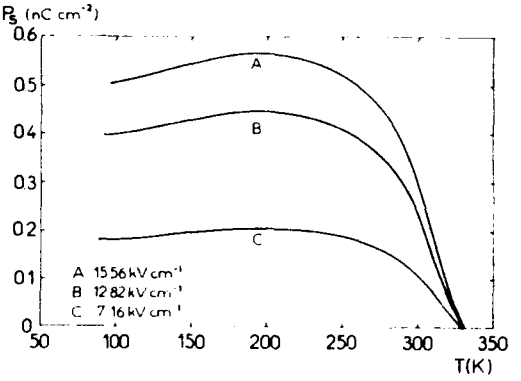


Fig.7 Temperature dependence of the spontaneous polarization P_S for a $Ba_{0.93}Pb_{0.07}Li_{0.14}Al_{1.86}O_{3.72}F_{0.28}$ ceramic.

It was not possible to observe an hysteresis loop for the ceramic samples between 200 and 350K, probably due to the low value of the spontaneous polarization ($P_S$max(200K)=0.57nC.cm^{-2}) by comparison with the sensitivity limit of the equipment ($\Delta P_S=\pm 10$nC.cm^{-2}).

The pyroelectric measurement cannot be performed on the solid solutions $Ba_{1-x}Sr_xLi_{2x}Al_{2-2x}O_{4-4x}F_{4x}$ because of the sintering temperature limit and the very bad compactness of the ceramics ($d_{obs.}/d_{calc.}<0.75$).

6.CONCLUSION

New ferroelectric ceramics have been prepared. A correlation between the Curie point T_C and substitution rate x is observed. For Pb-containing ceramics T_C decreases with x and then increases again linearly; for Sr containing ceramics T_C decreases first and then becomes constant with x. The spontaneous polarization is measured on the $Ba_{0.93}Pb_{0.07}Li_{0.14}Al_{1.86}O_{3.72}F_{0.28}$ ceramic sample, the maximum value is 0.57nC.cm^{-2}.

REFERENCE

[1]S.C.Abrahams, "Systematic Prediction of New Ferroelectric Inorganic Materials in Point Group 6," Acta Cryst., Vol.B46, pp.311-324, 1990.

[2]T.G.Dunne and N.R.Stemple, "Ferroelectric Properties of $BaLi_{2x}Al_{2-2x}F_{4x}O_{4-4x}$," Phys. Rev., Vol.120, n.6, pp. 1949-1950, December 1960.

[3]S.Y. Huang, R.Von Der Mühll, J.Ravez and P.Hagenmuller, " nvestigaton of Ferroelectric and pyroelectric Properties of ceramics with composition $Ba(Li_{2x}Al_{2-2x})O_{4-4x}F_{4x}$ ($0 \le x \le 0.3$)," to be published in ISAF'92.

[4]A.A.Bush and A.G.Laptev, "Dielectric and Pyroelectric Properties of $BaAl_2O_4$ single crystals,"Fiz.Tverd.Tela, Vol.31, pp.317-318, March 1989.

[5]V.V.Zhurov, A.A.Bush, S.A.Ivanov, S.Yu.Stefanovich and B.N.Romanov, "Oxygen-tetrahedral AB_2O_4 crystals (A=Ba,Sr; B=Al,Ga): preparation, properties and phase transition characteristics," Fiz.Tverd.Tela, Vol.33,pp. 1706-1712, June 1991.

[6]R.H.Arlett, J.G.White and M.Robbins, "Single crystals of $BaAl_2O_4$," RCA Laboratories, Acta Cryst. Vol.22, pp.315,1967.

[7]W.Hörkner and HK.Müller-Buschbaum," Zur Kristallstruktur Von $BaAl_2O_4$," Z.anorg.allg.Chem., Vol.451, pp. 40-44, 1979.

[8]J.R.Tessman and A.H.Kahn,"Electronic Polarizabilities of Ions in Crystals," Phys. Rev., Vol.92, n.4 1953.

OPTICAL CHARACTERISTICS OF $Pb_5Al_3F_{19}$ - TYPE CRYSTALS

R. Von der MÜHLL, J. RAVEZ, , V. ANDRIAMAMPIANINA, J.P. CHAMINADE, A. SIMON

Laboratoire de Chimie du Solide du CNRS, Université Bordeaux I,
351 cours de la Libération, 33405 TALENCE cedex.

S.C. ABRAHAMS,
Physics Department, Southern Oregon State College, ASHLAND, OR 97520, USA.

Abstract

Determination of the crystal structure of $Pb_5Cr_3F_{19}$ at room temperature reveals an atomic arrangement that satisfies the structural criteria for ferroelectricity. Ferroelectric $Pb_5Cr_3F_{19}$ forms a complete series of solid solutions with $Pb_5Al_3F_{19}$. Large colorless crystals of the latter type, with dimensions approaching $1cm^3$, have been grown in sealed platinum tubes by the Bridgman technique. The phase transitions in $Pb_5Al_3F_{19}$ have been studied by optical microscopy on crystals oriented along different crystallographic directions. Ferroelastic domains have been observed; a reversible and reproducible ferroelastic-prototype transition has been shown. The thermal dependence of the birefringence has also been determined. The ferroic properties of $Pb_5Al_3F_{19}$ are discussed in relation to the crystral symmetry.

I - INTRODUCTION

The determination of the crystal structure of $Pb_5Cr_3F_{19}$ at room temperature has revealed an atomic arrangement that satisfies the structural criteria for ferroelectricity (1). Various studies on powders, ceramics and single crystals have confirmed this hypothesis. There is in addition a family of compounds with formula $Pb_5M_3F_{19}$ (M = Al, Ti, V, Cr, Fe, Ga) (2). Ferroelectric $Pb_5Cr_3F_{19}$ forms a complete series of solid solutions with $Pb_5Al_3F_{19}$ (3). Crystal growth of lead fluoroaluminate has been carried out in order to investigate the phase transition by optical measurements.

II - CRYSTAL GROWTH

The PbF_2-AlF_3 phase diagram has been previously determined by Shore and Wanklyn and more recently by Moulton and Feigelson (4,5). We have partially checked their results. The diagram exhibits a eutectic point at about 933 K (around 65 mole % PbF_2). As $Pb_5Al_3F_{19}$ melts incongruently, a PbF_2 rich composition (72 mole % PbF_2) has been selected as starting mixture for crystal growth. PbF_2 is a pure Merck (99.99 %) powder. Anhydrous AlF_3 is obtained by thermal decomposition of $(NH_4)_3AlF_6$ under dry argon atmosphere.

The operation has been performed in a platinum crucible sealed under dry argon. After preliminary interaction of pure PbF_2 and AlF_3 (15 hrs at 825 K) the crucible was heated up to 995 K in the isothermal zone of the furnace. Cooling was achieved from 995 K to 825 K at a 0.5 $deg.h^{-1}$ rate and from 825 to 293 K at a 10 $deg.h^{-1}$ rate. A transparent block of about 2 cm^3 and of $Pb_5Al_3F_{19}$-type has been obtained.

A microprobe study leads to a composition of 63 $\pm$ 2 moles % PbF_2 combined with AlF_3. This result includes the value 0.625 which corresponds to $Pb_5Al_3F_{19}$; the measurement nevertheless does not exclude a possible solid solution of $Pb_5Al_3F_{19}$-type at high temperatures.

OPTICAL OBSERVATION BY POLARIZED TRANSMITTED LIGHT.

Experimental procedure

A Ortholux II Pol polarising microscope was used with transmitted light for all observations. A low temperature stage using a cooled nitrogen stream allows experiments from 77 to 300 K. In the temperature range from 300 to 600 K, the specimens were set in a Leitz high temperature cell heated by a Pt resistance controlled furnace. The temperature was recorded with a thermocouple. The birefringence was measured with a Nikitin-Berek compensator using a 543 nm interferometer.

Optical characterization

A crystal of $Pb_5Al_3F_{19}$-type was first cut parallel to the (001) plane of the prototype tetragonal (P.T.) phase and then polished. This sample cannot be totally darkened between crossed polarizers and its behavior thus corresponds to a very weak birefringence. Observation in convergent polarized light (conoscopic observation) shows an interference figure with a slightly deformed cross close to that of an uniaxial material. The addition of a λ crystal plate allows clearly the determination of the optical sign as positive.

A second crystal was cut and polished as a plate of 80 μm thickness parallel to the (110) plane. The observation between crossed polarizers shows this direction to be birefringent. The orientation of the low speed axis was determined to be parallel to the c axis of the P.T. phase.

CH3080-0-7803-0465-9/92$3.00 ©IEEE

Observation of the domain walls and thermal behavior

At room temperature, on (110) oriented plates, two kinds of ferroelastic domain wall orientation can be observed, parallel or perpendicular to the c-axis of the P.T. phase. The thickness of the domains is about 2 μm. The thermal behavior of the domains was observed from the temperature range 77-400 K for crystals cut at different places in the original ingot. Cooling from 300 K to 77 K does not result in a total disappearance of the domain walls. On heating, from 300 to 400 K, the domain walls vanish at a definite temperature lying in the range 330 to 360 K depending on the specific crystal i.e. its position in the original ingot. Such a result involves a composition gradient. On cooling from 400 to 300 K the domains reappear at a temperature close to the vanishing temperature observed on heating. The domain pattern reappears without modification of the previous aspect. We may thus conclude that this temperature corresponds to the ferroelastic-prototype transition without apparent hysteresis. The unchanging domain pattern after several transitions suggests that strong internal stresses develop inside the crystal. Figure 1 shows the domain pattern below the ferroelastic Curie temperature.



Fig.1 - Domain structure of a $Pb_5Al_3F_{19}$-type single crystal at room temperature.

Birefringence measurements

A study of the birefringence for a (100) crystal plate $\Delta n = n_a - n_c$ was measured between 300 and 600 K. The curve shows a discontinuity at the ferroelastic-prototype temperature (Fig.2).

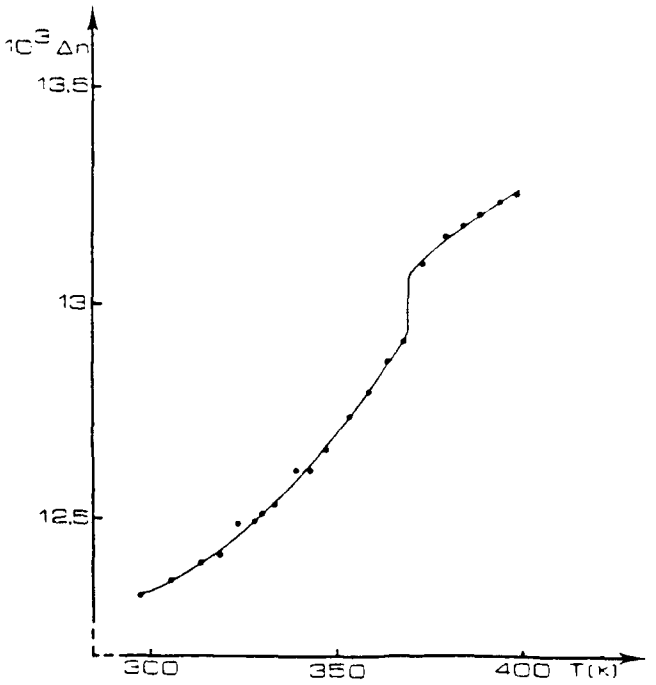


Fig.2 - Temperature dependence of the birefringence of a $Pb_5Al_3F_{19}$-type single crystal.

DISCUSSION

A crystal about 2 cm^3 and of $Pb_5Al_3F_{19}$-type has been prepared. Optical measurements have revealed only one phase transition from a ferroelastic to a prototype phase whose symmetries are monoclinic and tetragonal respectively as was recently shown by electron diffraction (6). Compared to X-ray diffraction on powder studies, there is no doubt that the crystal obtained is of $Pb_5Al_3F_{19}$-type but has a slightly different composition (7). In fact for 0.625 mole % PbF_2 corresponding to $Pb_5Al_3F_{19}$ there are three transitions rather than only one in the temperature range 77 to 600 K.

REFERENCES

[1] S.C. ABRAHAMS, J. ALBERTSSON, C. SVENSSON and J. RAVEZ, Structure of $Pb_5Cr_3F_{19}$ at 295 K. Polarization reversal and the 555 K phase transition, Acta Cryst., Vol. B 46, pp. 497-502, 1990.

[2] J. RAVEZ, A. SIMON, A. ANDRIAMAMPIANINA, J. GRANNEC and S.C. ABRAHAMS, Ferroelectric-paraelectric phase transitions in $Pb_5M_3F_{19}$ with M = Al, Ti, V, Cr, Fe, Ga, J. Appl. Phys., Vol. 70, pp. 1331-1336, 1991.

[3] J. RAVEZ, V. ANDRIAMAMPIANINA, A. SIMON, J. GRANNEC, P. HAGENMULLER and S.C. ABRAHAMS, Composition dependent ferroelectric Curie temperature of $Pb_5(Cr_{1-x}Al_x)_3F_{19}$ from 555 to 280 K and of $Pb_5(Cr_{1-x}Fe_x)_3F_{19}$ from 555 to 725 K for $0 \leq x \leq 1$, J. Appl. Phys., Vol. 68, pp. 3529-3531, 1990.

[4] R.G. SHORE and B.M. WANKLYN, The systems PbF_2-AlF_3 and GaF_2-AlF_3, J. Amer. Ceram. Soc., Vol. 52, n°2, pp. 79-81, 1969.

[5] V. MOULTON and R.S. FEIGELSON, Phase equilibria and solidification behavior in the PbF_2-AlF_3 system, J. Mat. Res., Vol.6, n°10, pp. 2188-2192, 1991.

[6] V. ANDRIAMAMPIANINA, J. RAVEZ, J.P. CHAMINADE, F. WEILL, P. HAGENMULLER and S.C. ABRAHAMS, Croissance et caractérisation de monocristaux de type $Pb_5Al_3F_{19}$, C.R. Acad. Sc. Paris, t. 314, sér. II, pp. 1319-1323, 1992.

[7] J. RAVEZ, V. ANDRIAMAMPIANINA and J. IHRINGER, Phase transition sequence in $Pb_5Al_3F_{19}$, J. Appl. Cryst. (to appear).

POLING AND SWITCHING BEHAVIOR OF FERROELECTRIC SINGLE GRAINS STUDIED BY PIEZOELECTRIC RESONANCE

Y. I. Ryu, J. S. Kim and I. Yu
Department of Physics, Seoul National University, Seoul 151-742, Korea

ABSTRACT

Piezoelectric resonance signal from minute (~10 μg) single grain ferroelectric sample is observed by using an inductive pulse method. The inductive pulse detection method does not require electrodes to be coated on the samples and is suitable for the small size samples. Examples of the temperature dependent resonance signal from Rochelle salt, KH_2PO_4(KDP), and $NH_4H_2PO_4$(ADP) single grains are shown. Poling and switching behavior of a single grain Rochelle salt in an external electric field is studied. Time dependence of the resonance frequency and decay time constant of the transient piezoelectric resonance signal reflects the change in sample polarization due to variation of domain structure. Another advantage of the inductive pulse detection method is its capability of observing fast initial change just after the application of electric field. The *in-situ* detection characteristic is facilitated by the well isolated detection and poling systems inherent to inductive methods.

Introduction

In the application of ferroelectric materials two mostly used bulk forms are single crystals and ceramics. Naturally ceramics consists of many random grains and this fact introduces inherent inhomogeneities to the system. Even in single crystalline system the ferroelectric domains are formed spontaneously due to the symmetry breaking phase transition. These provide complexity in the study of ferroelectric materials. Electric fields are routinely applied to pole the ferroelectric specimens as single domain-like as possible. The change of domain structure with time represents its approach to a more stable one in an electric field.

When the size of ferroelectric sample becomes smaller than the typical domain size (*0.1 μm ~ 1 μm*), *it is hard to form multi*-domain structure and the sample remains in a single domain form in ferroelectric phase. [1] On the other hand, the small size makes the sample more susceptible than bulk to the influence of surface. It is very important to study the sample size dependent ferroelectric properties, however, experimental studies are hampered by the difficulty in attaching electrodes onto minute samples. Noncontact methods which do not require electrode attachments will be suitable for the study of fine grain samples.

An electrodeless detection method of piezoelectric resonance signal has been developed. [2] We modify the method and apply it to the study of minute single grain samples.

Method

The electrodeless detection method of piezoelectric resonance employs the techniques used in pulse nuclear magnetic or quadrupolar resonance(NMR or NQR) experiments. [3] The schematic diagram of the detection system is shown in Fig. 1. In this non-contact method the sample is placed in a sample coil, rather than in a parallel plate capacitor, in contrast to conventional methods. [2] The piezoelectric excitation and detection of resonance are done by rf electric field of the sample coil. The detection system is a conventional phase coherent pulse NMR spectrometer which is operated at frequencies near 3.5 MHz. Certainly, the dc magnetic field which is necessary for NMR experiments is not relevant. The detected piezoelectric resonance signal is a form of free induction decay (FID) signal in NMR terminology [3] and two quantities, the resonance frequency f_r and the decay time constant T_2^* can be measured. The frequency f_r is actually the antiresonance frequency f_a in piezoelectrics terminology. The decay time constant is related to the width of resonance spectrum by

$$(\Delta f_r)_{HWHM} = \frac{1}{2\pi T_2^*} \qquad (1)$$

where $(\Delta f_r)_{HWHM}$ is the half-width at half-maximum height of the spectrum which is determined by the efficiency of decay mechanisms of the electromechanical energies stored in the sample.

The measured quantities are related to the complex elastic stiffness constants C_{ij}^{K*}, size l and density ρ of the sample [4].

$$f_r^K = \frac{n}{2l}\sqrt{\frac{\mathrm{Re}(C_{ij}^{K*})}{\rho}} \qquad (2)$$

$$\tan\delta_m = \frac{\mathrm{Im}(C_{ij}^{K*})}{\mathrm{Re}(C_{ij}^{K*})} = \frac{1}{\pi T_2^* f_r^K} \qquad (3)$$

where i, j and K are the indices representing appropriate directions of stress and strain and the surface condition of measurements, respectively. In the above n is the order of harmonics being measured, $\tan\delta_m$ the mechanical loss which is inverse of the mechanical Q-factor, and l the size of sample in the direction of propagating mechanical waves.

The couplings between sample and sample coil are modified as in Fig. 2 to be more appropriate for orienting and poling a minute grain sample. The sample is placed in a parallel plate capacitor cell and oriented by applying a small dc electric field. The sample is coupled to the detection system by passing the wire from an electrode of the cell through the sample coil. One can also connect the wire to a high voltage dc power supply for the poling measurements.

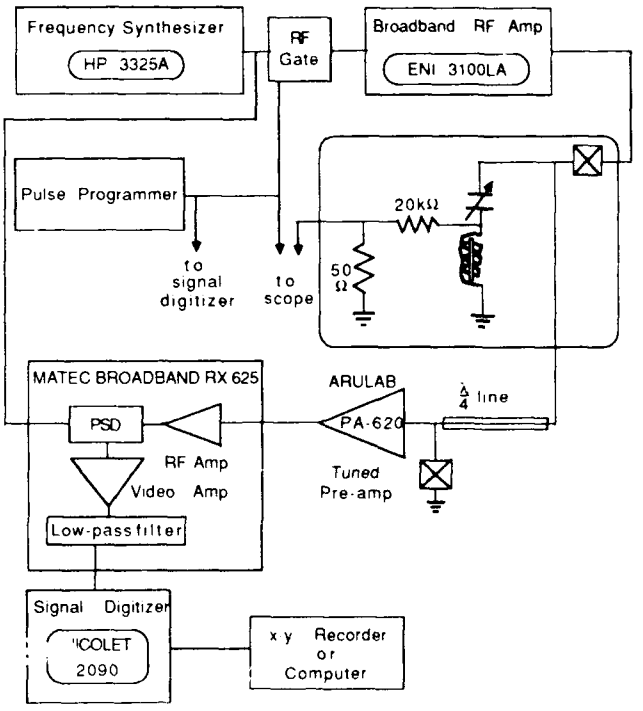


Fig. 1: Block diagram of inductive pulse detection system. This is a conventional pulse NMR spectrometer system with phase sensitive detector (PSD). A piezoelectric sample is placed in sample coil. The crossed square represents a back-to-back pair of diodes.

CH3080-0-7803-0465-9/92$3.00 ©IEEE

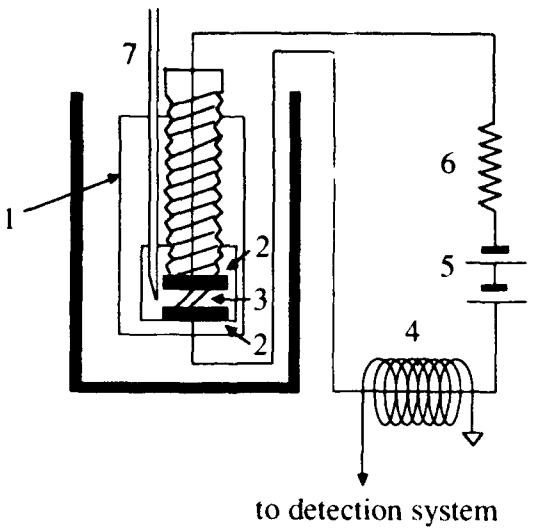


Fig. 2: Sample cell geometry for minute single grain samples. A teflon bolck(1) contains hollow where parallel plates(2) and sample (3) are placed. Electric wire passes through sample coil(4) and connects to a high voltage dc power supply(5) with a current limiting resistor(6). The temperature of sample in a temperature controlled dewar is measured by a thermocouple(7).

Results and interpretation

We present some of the measurements made on Rochelle salt, KDP, and ADP single grains. The grain samples are selected out from commercial granular powders (Junsei Chemical Co., Japan GR grade). First of all, we observe as strong resonance signal from a minute single grain sample (size ~ 0.4 mm x 0.4 mm x 0.6 mm) as bulk plate (size ~ 0.4 mm x 1 cm x 1 cm) in spite of the large volume ratio ~ 400. This reflects the sample volume independent piezoelectric resonance signal intensity and opens up a possibility of studying even a molecular thin piezoelectric wire by our detection method.

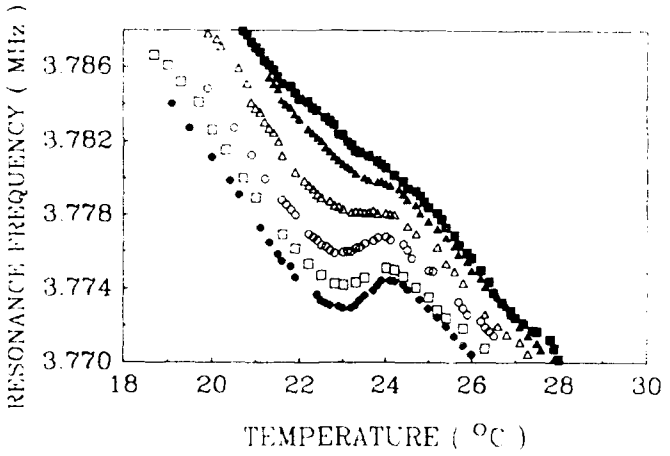


Fig. 3: Temperature dependent piezoelectric resonance frequencies from a Rochelle salt grain. The measurements are for cooling runs with electric fields; 0 V/cm (•), 50 V/cm (□), 200 V/cm (o), 500 V/cm (△), 700 V/cm (▲) and 900 V/cm (■).

Examples of the temperature dependent resonance frequencies are shown in Figs. 3, 4 and 5 for Rochelle salt, KDP and ADP single grain samples, respectively. Rochelle salt is unusual in that the ferroelectric phase appears between two nonferroelectric phases separated by two Curie points T_{ch} = 24 °C and T_{cl} = - 18 °C. [5] Antipolar ordering of dipoles into two sublattices was claimed for the nonferroelectric phases. [6] Rochelle salt is also known as consisted of many domains in its ferroelectric phase and the domain structure can be changed easily by applying electric fields. [7] The relevant elastic stiffness component to the measurements in Fig. 3 is C_{44}^{P*} for the thickness shear mode at constant polarization, and dc electric fields are applied parallel to the crystalline a-axis. The temperature dependent changes in resonance frequency f_r^P possess a kink at the upper transition temperature. The kink structure, which was attributed to morphic effects [8], depends on the strength of dc electric field applied to the sample and smears out when the field exceeds 900 V/cm as can be seen in Fig. 3.

The s-shaped kink and its influence on electric field resemble the Van der Waals' equation of state for gas-liquid transitions and the influence of temperature to the shape of transition in a *P-V* diagram. We interprete the kink as the gas-liquid-like transition of interacting dipoles. The gaseous state is the high temperature nonferroelectric phase and the dipoles undergo random fluctuations between two symmetric potential wells. The liquid-like state is the ferroelectric phase where interactions of dipoles generates built-in asymmetry in potential and the dipoles condense in the lower energy well. The kink represents buildup of two types of domains below the transition temperature and the domain formation becomes inhibited when dc electric field of sufficient strength let one of the two domains be more preferable.

In Fig. 4 we show the temperature dependence of two different resonance frequencies f_r^P and f_r^E of KDP measured with constant polarization (P) and field (E) conditions, respectively. Experimentally the different conditions are achieved by changing the resistance values connected in series with the parallel plate sample cell. [9] For the f_r^P 2 MΩ is used to mimic an open circuit for rf and 94 kΩ is used for the f_r^E. Although the induction coupling scheme of our detection method allows short circuit measurements, the small resistance is added to limit the currents and to protect the sample from overheating. The sample is oriented in electric field with the crystalline c-axis parallel to the field. The relevant elastic stiffness components are C_{66}^{P*} and C_{66}^{E*}, respectively. The results are in accord with the previous measurements [10] on bulk sample by conventional method.

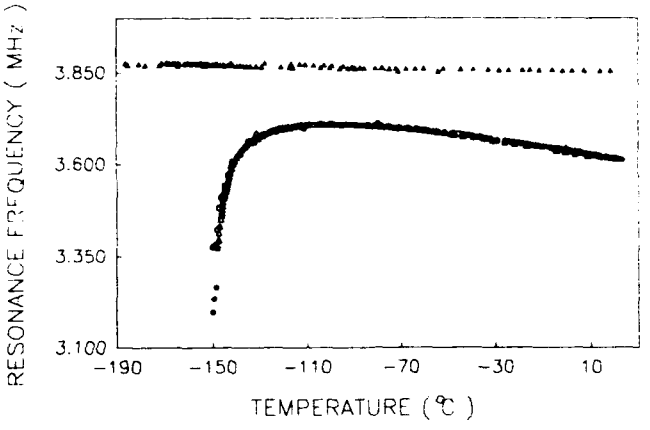


Fig. 4: Temperature dependent resonance frequencies of a KDP grain. The open circuit resonance frequency (circles) has no noticeable hysteresis (filled and open circles for the cooling and heating measurements) or field dependence upto 2.5 kV/cm in the scale of the figure. There is a strong decrease in resonance frequency as the ferroelectric transition is approached. We could not find resonance signal in ferroelectric phase. The short circuit resonance frequency (triangles), on the other hand, is not influenced by the ferroelectric transition.

One interesting outcome of the studies on small grain ADP is that the minute crystal, especially when it is under dc electric field, is free from the notorious shattering problem which is experienced by the bulk ADP when it is cooled below the antiferroelectric transition temperature T_c = -122 °C. The cooling and subsequent heating measurements in Fig. 5 show no evidence of shattering when dc electric field of 1 kV/cm is applied to the sample continuously throughout the transition. This opens up a new possibility of studying single crystalline properties of ADP in its antiferroelectric phase.

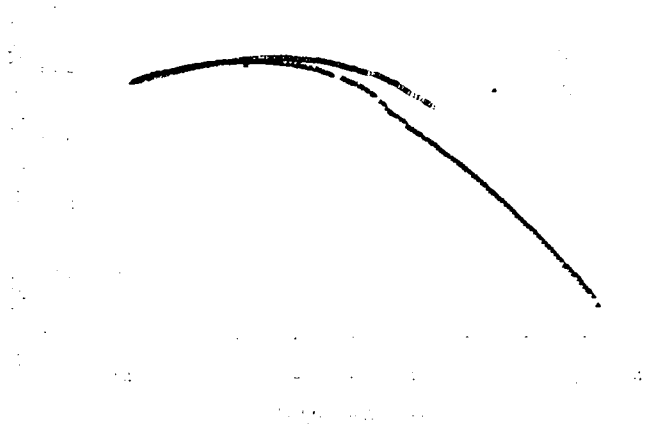


Fig. 5: Temperature dependent resonance frequencies of ADP minute grain. When electric field(1 kV/cm) is applied to the sample continuously the heating run follows the previous cooling measurements even though the crystal was experienced the antiferroelectric phase transition.

We now concern about the time dependent piezoelectric resonance frequencies and decay time constants of Rochelle salt in dc electric field. Only in ferroelectric phase the time depen-dent changes are observed as the example in Fig. 6 which is measured at 13 °C with 16 kV/cm field applied in the direction of c-axis. There is an indication of strongly correlated behavior between the two time dependences such that at the same time when the fastest change in f_r with respect to the logarithm of time occurs, the T_2* becomes maximum. The correlation is actually between the real and imaginary parts of complex elastic stiffness and is similar to what was seen [11] in PZT ceramics.

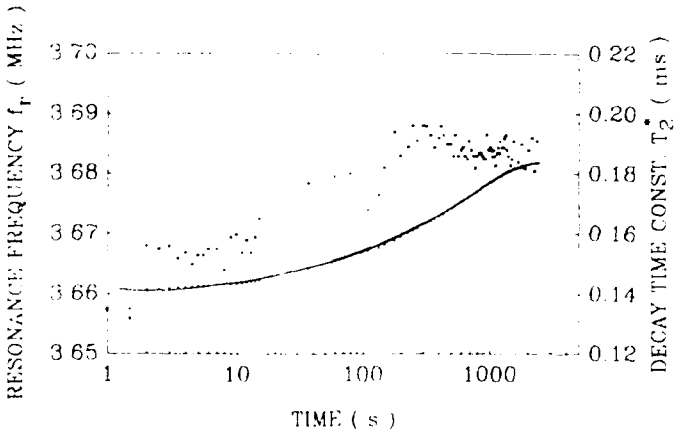


Fig. 6: Time dependent changes in f_r (curve) and T_2* (dots) for a Rochelle salt grain. The sample is kept at constant temperature (13 °C) in its ferroelectric phase and an electric field (16 kV/cm) is applied at time t = 0.

Summary

The inductive pulse method of piezoelectric resonance detection is very useful in the study of minute granular ferroelectric crystals. The electrodeless nature of the detection method suits to the small sized samples. The grain samples can be easily obtained from commercial granular powders. The intensity of piezoelectric resonance signal hence detected from a minute grain is not weakened in spite of its small volume and this fact will allow us the study of effects of small size on ferroelectric and piezoelectric properties. Some interesting results including the evidence of condensation-like phase transition properties of Rochelle salt and the different shattering behavior in ADP grains on cooling have come out already through the study.

Acknowledgments

The authors aknowledge grateful contributions of J. O. Kwag and Y. W. Song for their help in some of the experiments. This work was supported in parts by the Ministry of Education, Korea through the Research Institute for Basic Sciences in Seoul National University and also by the Korea Science and Engineering Foundation through the Research Center for Dielectric and Advanced Matter Physics.

References

[1] P. Marquardt and H. Gleiter, "Ferroelectric phase transition in microcrystals," Phys. Rev. Lett., vol. 48, pp. 1423-1425.

[2] K. Choi and I. Yu, "Inductive detection of piezoelectric resonance by using a pulse NMR/NQR spectrometer," Rev. Sci. Instrum., vol. 60, pp. 3249-3252, 1989.

[3] E. Fukushima and S. B. W. Roeder, Experimental Pulse NMR - A Nuts and Bolts Approach. Reading : Addison, 1981, p. 12.

[4] W. P. Mason, Piezoelectric Crystals and Their Application to Ultrasonics. New York: Nostrand, 1950, ch. 5, pp. 65-66.

[5] W. G. Cady, Piezoelectricity. New York: MaGraw, 1946 ch. 20, pp. 510-530.

[6] B. Zeks, G. C. Shukla, and R. Blinc, "Dynamics of ferroelectric Rochelle salt," Phys. Rev. B, vol. 3, pp. 2306-2309, 1971.

[7] J. Kobayashi, K. Uchino, H. Matsuyama, and K. Saito, "Optical study on domain switching of ferroelectric triglycine sulfuric acid and Rochelle salt," J. Appl. Phys., vol. 69, pp. 409-413, 1991.

[8] H. Mueller, "Properties of Rochelle salt, IV", Phys. Rev. vol. 58, pp. 805-811, 1940.

[9] J. S. Kim, K. Choi, and I. Yu, "A new method of determining the equivalent circuit parameters of piezoelectric resonators and analysis of the piezoelectric loading effect," IEEE Trans. Ultrason. Ferroelec. Freq. Contr., in press.

[10] K. -H. Hellwege and A. M. Hellwege, Eds., Landolt-Bornstein - Numerical Data and Functional Relationships in Sicence and Technology. vol. 3. Heidelberg: Springer, 1969, p. 427.

[11] J. S. Kim and I. Yu, "Correlations in the real and imaginary parts of time dependent elastic stiffness of a system with distributed time constants," in Proceedings of the Symposium '92 on Theoretical Solid State Physics, Daeduk, Korea, January 7-9, 1992, pp. 22-23.

THE INFLUENCE OF La CONTENT IN PLZT-x/95/5 CERAMICS (x = 0.5 to 4 %) ON THE DIELECTRIC, PYROELECTRIC, THERMALLY STIMULATED CURRENT AND RAMAN SCATTERING MEASUREMENTS AND MODEL INTERPRETATION.

J. Handerek[1], Z. Ujma[1], D. Dmytrow[1], C. Carabatos-Nédelec[2] and I. El-Harrad[2]

[1] Institute of Physics, Silesian University, 40-007 Katowice, ul. Universitecka 4, Poland.

[2] Centre Lorrain d'Optique et Electronique des Solides, Université de Metz et Supélec, 2 Belin, F-57078 Metz Cedex 3.

Abstract

PLZT-x/95/5 ceramics with low La concentration, x = 0.5 to 4wt%, exhibit an Antiferroelectric (AFE) - Ferroelectric (FE) - Paraelectric (PE) phase sequence. The FE phase exists in both AFE and PE phases in a wide range. Dielectric, pyroelectric, thermally stimulated current and Raman scattering measurements have been performed as functions of temperature in all phases. The diffuse character of the phase transitions was confirmed and the width of the phases coexistence was proved to depend upon the La concentration. An interpretation model is proposed for the defects and the phases balance.

Dielectric measurements

The PLZT-x/95/5 ceramics with La content of 0.5, 1, 2, 3, and 4 wt% were prepared using a conventional method of thermal synthesis of mixed-oxides. The final sintering was performed at 1250°C during 3 hours in a double crucible with a PbO atmosphere. As a result of the small size of the grains (10μm and less) and the low porosity [1, 2], the obtained ceramics were partially transparent (~30% in the visible ligth for a 1mm thick sample)

The samples were coated with silver electrodes. The temperature dependence of the permittivity (ε) and of the dissipation factor (tanδ) were measured at nine fixed different frequencies between 0.1 and 20 kHz using a computerized automatic system based on a Tesla BM-595 RLCG-merter. The remanent polarization (P_r) vs. temperature was obtained from hysteresis loop measurements in a field of frequency 50 Hz and strength of 5 kV/cm. Before measurements, the samples were deaged by a thermal treatment at 600 °C for one hour. An example of (ε) and $P_r(T)$ curves on heating and cooling, for PLZT-1/95/5 ceramics are shown in Figure 1.

The La dopant has a special strong influence on the remanent polarization. In the case of 0.5 and 1% of La, the $P_r(T)$ behaves similarly as shown in Figure 1. The P_r values are the biggest for the PLZT-0.5/95/5 sample. In the case of 2, 3 and 4% of La content, however, only slim hysteresis loops and very small P_r values were observed in the whole temperature range of the transient FE phase.

The comparison of the ε(T) curves for PLZT-x/95/5 (x = 0.5 to 4wt%), measured on heating at a 1kHz frequency is shown in Figure 2.

The AFE-FE and FE-PE phase transitions temperatures as functions of the La concentration are also shown in the Figure 2a.

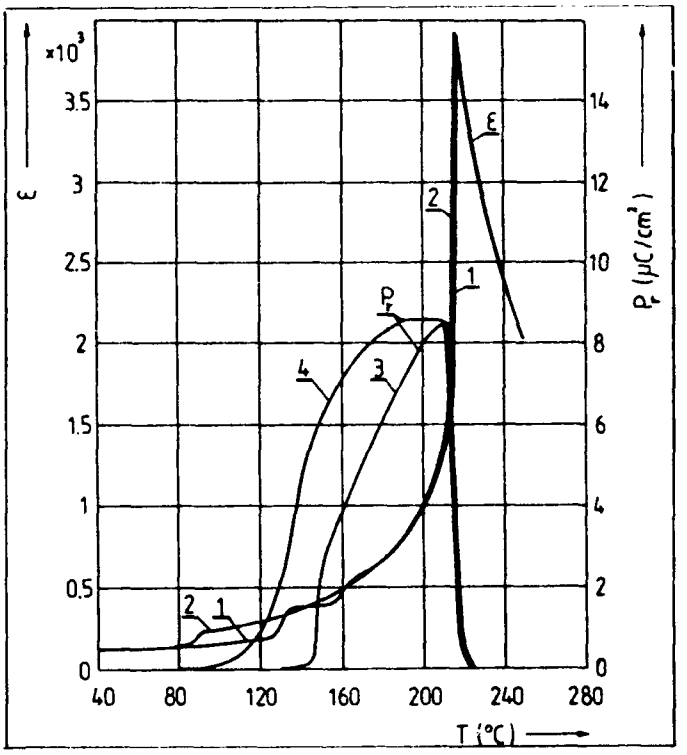


Figure 1: Temperature dependence of the permittivity (f = 1kHz) and of the remanent polarization on heating (curves 1 and 3) and on cooling (curves 2 and 4) for PLZT-1/95/5.

CH3080-0-7803-0465-9/92$3.00 ©IEEE

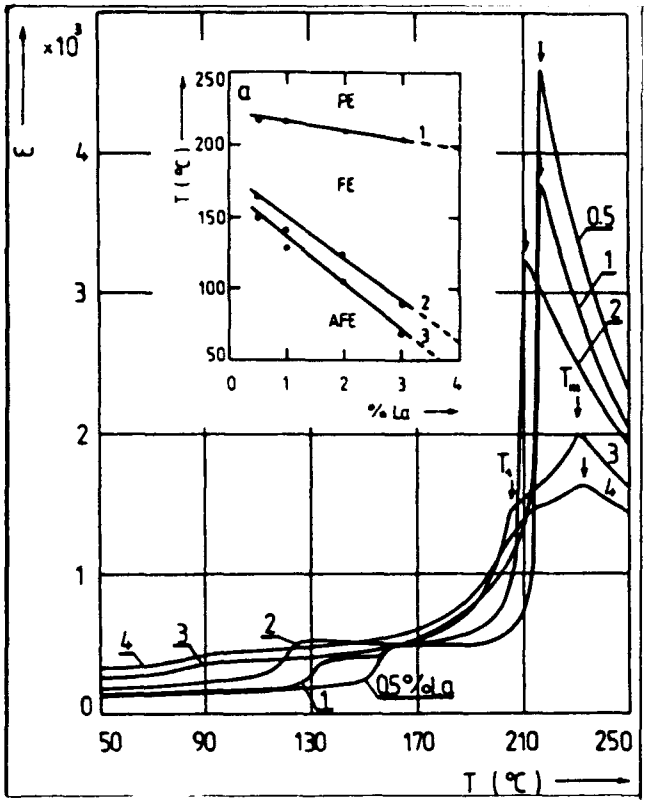


Figure 2: Comparison of the ε(T) curves, at 1kHz on heating, for PLZT-x/95/5 ceramics with La content x = 0.5 to 4wt% and the phase transition temperatures (FE-PE curve 1, AFE-FE region between curves 2 and 3) as a function of La content (a).

This phase diagram is compatible with part of that for Zr-rich PLZT materials, given by Haertling and Land [3]. The dopant causes a strong decreasing of the ε_{max} values at the Curie temperature, which is shifted downwards with increasing La concentration.

The diagram of the natural logarithm of the frequency vs. the reciprocal absolute temperature proved that the frequency dependence of the temperatures at which local maxima in the tanδ(T) curves occur can be described by the known equation $f = f_0 \exp\{-E_a/k_B T\}$ [4]. The activation energies E_a obtained from these data are approximately of 1eV and 0.65eV for the 0.5/95/5 and the 3/95/5 ceramics, respectively.

Pyroelectric and thermally stimulated depolarization current mesurements

An example of the pyroelectric current behaviour around the AFE-FE and FE-PE phase transitions, recorded for the PLZT-0.5/95/5 ceramics is shown in Figure 3.

The sample was pre-polarized in a dc field of 5kV/cm strength applied at 180°C (i.e. inside the FE phase) during 10 min. and then heated through the FE-PE phase transition with the rate of 10K/min.

The metastable polarization formed during the process of prepolarization arises usually from the combination of various components and namely heterocharge (dipolar orientation, ionic and electronic drift) and homocharge (electronic and ionic injection from electrodes). The thermally stimulated depolarization current can, in this case, occur at temperatures much higher than the temperatures at which the sample was pre-polarized [5]. Just such a behaviour of TSDC was observed in the case of the investigated PLZT-x/95/5 ceramics.

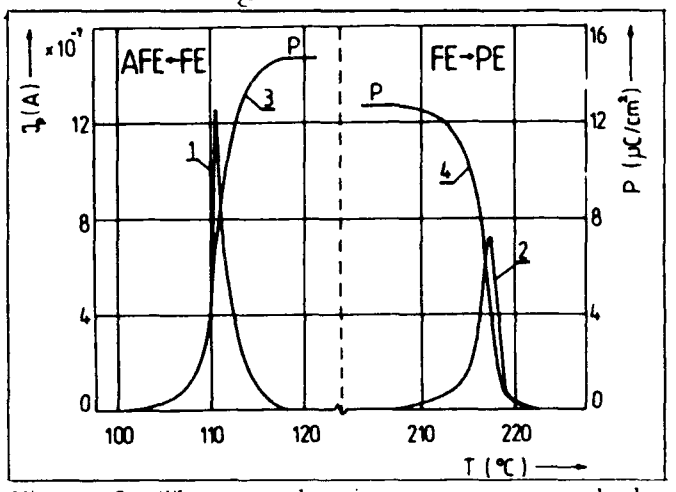


Figure 3: The pyroelectric current arround the AFE-FE and FE-PE phase transitions (curves 1 and 2) and polarization vs temperature (curves 3 and 4) for PLZT-0.5/95/5 ceramics.

Raman scattering measurements

Raman scattering measurements have also been performed for the same La concentrations of 0.5, 1, 2, 3 and 4%, in the temperature range 20 to 250°C, after deaging at 600°C for approximately one hour before any new experiment; in this way, strong memory effects, as well as the increasing absorption of the samples, due to laser illumination were eliminated.

Our Raman scattering results show that both Ti and La dopants influence strongly the lattice dynamics, relative to the particular phase transition

and to the relaxor properties of PLZT-x/95/5 ceramics. They influence as well and especially the neighbour AFE, FE and PE phases coexistence in the vicinity of the phase transition temperatures. The investigation of these phases coexistence by Raman scattering measurements indicated that : 1°) the transition temperatures decrease as the Lanthanum content increases and 2°) the hysteresis cycle broadens indicating that the character of the transitions becomes more diffuse with increasing Lanthanum concentrations from 0.5 to 4 wt%, in other words, the width of the phases coexistence increases.

For the first time, a new peak at 25 cm^{-1} was observed; it is present only in the FE phase (even mixed) of the PLZT ceramics for all the La concentrations under consideration.

Figure 4 illustrates the temperature behaviour of all low frequency peaks and especially of this new peak at 25 cm^{-1} for the PLZT-2/95/5 ceramic.

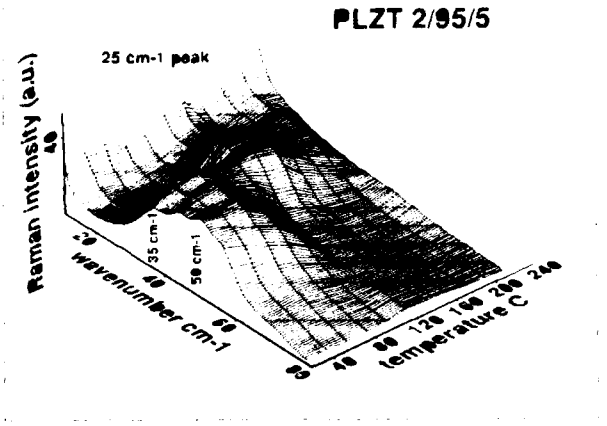


Figure 4: Raman spectra of PLZT-2/95/5 ceramics as a function of temperature.

All the obtained spectra have been analysed in terms of an adequate superposition of : 1°) a relaxor contribution in order to take into account the Rayleigh scattering, 2°) a second relaxor contribution in order to take into account the central peak due to structural defects, 3°) an appropriate number of lorentzian shape peaks in order to take into account the light scattering due to low frequency collective vibrations of the constituant atoms. Figure 5 illustrates such a spectrum analysis for the case of PLZT-2/95/5 at room temperature.

On the basis of this analysis of the Raman spectra, it has been possible to draw the variation with the

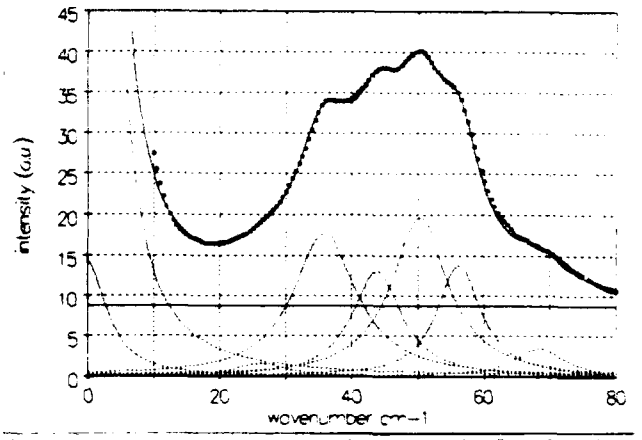


Figure 5: Experimental (dots) and fitted (line) Raman spectrum of PLZT-2/95/5 at room temperature, showing the different components. The spectrum has been corrected for the thermal population function.

temperature of the intensities (integrated areas) of the second relaxor and of the three selected lorentzian peaks; we observed a remarquable similarity between the second relaxor curve as a function of temperature and the corresponding dielectric constant curve for all La concentrations under consideration.

The selected peaks are : 1°) at 50cm^{-1} because it is characteristic of the AFE phase, 2°) at 35cm^{-1} because it is characteristic of the particular perovskite structure and 3°) at 25 cm^{-1} because it is characteristic of the FE phase (presumably it corresponds to a zone edge longitudinal acoustic vibration of the host $PbZrO_3$ structure, activated by the presence of defects). Their integrated intensity variation with temperature allowed to draw the phase diagrams. In Figure 6 is shown the case of the PLZT-2/95/5 ceramic.

Discussion

The obtained experimental data show that the dopant has a strong influence on all the investigated properties of the PLZT-x/95/5 (x = 0.5 to 4wt%) ceramics. Lanthanum replaces mainly Lead creating vacancies in its sublattice.

The La sites are also considered as donors, whereas Pb vacancies behave as acceptors. The pair La^{3+}-Pb^{2+} can also be considered as dipoles giving rise to dipolar polarization. In the vicinities of the AFE-FE phase transitions they can play the role of nucleation centres of FE domains, similar to Nb^{5+}-Pb^{2+} dipoles in Nb doped $PbZrO_3$ and PZT ceramics [6].

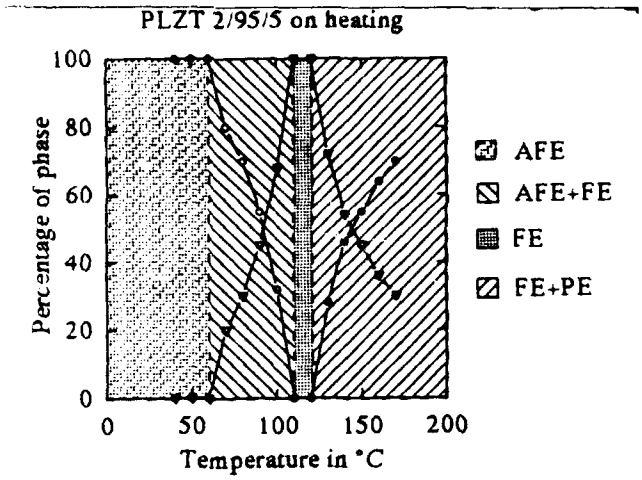


Figure 6: Phase diagram of the PLZT2/95/5 ceramic based on the appropriate Raman peak intensities functions of temperature.

The La dopant has also an influence on the quality of the PLZT ceramics, causing a decrease of the grain size and of the porosity, increasing in this way their transparency [3]. In the case of the investigated ceramics, the vacancies in the Pb and O sublattices, caused by PbO sublimation, should be also taken into account.

To explain the observed strong broadened AFE-FE and FE-PE phase transitions, the compositional and polarization fluctuations should be taken into account. The occurence of the compositional fluctuations is beyond any doubt in the studied ceramics. The fluctuations occur in the Pb, La and vacancies in Pb and O sublattices distribution. The same holds for the Zr/Ti distribution. The broadening of the phase transitions is much stronger if the two-phase AFE-FE and FE-PE regions are approached at higher La concentration. The polarization fluctuations also play an important role, espacially around the AFE-FE transition, on account of the small free energy difference between these phases. It causes the coexistence of these phases in the region surrounding the AFE-FE phase transitions. The same holds partially for the FE-PE transition.

The dielectric properties inside the transient FE phase and around the AFE-FE and FE-PE phase transitions depend on the mutual proportion of the compensated FE domains. This proportion depends obviously on the concentration and kind of defects and on the thermal and electric history of the sample. The high degree of the PE domain screening and small number of the non-screened domains allows us to understand the slim hysteresis loop and the small P_r values for the higher La concentration samples.

The separated donors (La ions and vacancies in the O sublattice behaving as traps) and acceptors (mainly vacancies in the Pb sublattice) form simultaneously n- and p-type conducting cathodic and anodic surface layers, respectively. The electrons released due to thermal generation from donors and traps in the n-conducting cathodic layer diffuse towards the bulk under a concentration gradient. The emptied donor and trap centres change the electrochemical properties of the cathodic contact, causing an injection of electrons, which refill again these centres. If this process is not effective enough, a change of the electric conductivity type takes place.

Considering this phenomenological model illustrated in Figure 7, one can understand the different aspects of our measurements.

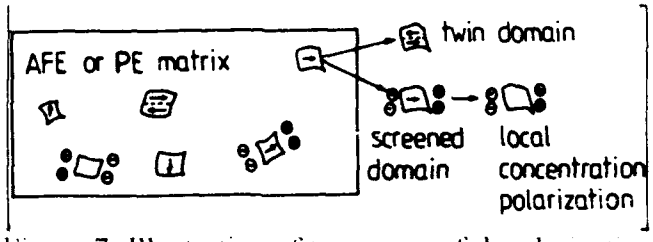


Figure 7: Illustration of two ways of depolarization field energy minimalization of FE domains remaining in an AFE or PE phase matrix.

References

[1] C. Carabatos-Nedelec, I. El-Harrad, J. Handerek, F. Brehat and B. Wyncke, Ferroelectries, vol. 125, p. 48, 1992.

[2] J. Handerek, Z. Ujma, C. Carabatos-Nedelec, G. E. Kugel, D. Dmytrow and I. El-Harrad, J. Appl. Phys., (under press), 1992.

[3] G. H. Haertling and C. E. Land, J. Amer. Ceram. Soc., vol. 54, p. 1, 1971.

[4] M. Kuwabara, K. Goda and K. Oshima, Phys. Rev., vol. B42, p. 10012, 1990.

[5] P. Braunlich, Thermally stimulated relaxation in solids, Topics in Applied Physics vol.37, New York: Springer-Verlag, 1979.

[6] L. Benguigui, J. Sol. State Chem., vol. 3, p. 381, 1971.

PROCESSING AND CHARACTERIZATION OF NEW MEMBERS OF Pb-K-NIOBATE SERIES

P. Jana, V. A. Kallur, M. A. Drummond, S. Nigli and R. K. Pandey
Center for Electronic Materials
Department of Electrical Engineering
Texas A&M University
College Station, TX 77843-3128

ABSTRACT

Two new members in the tungsten-bronze family of ferroelectric lead-potassium-niobate (PKN) have been identified. Ceramic samples with general formula $Pb_{1-x}K_{2x}Nb_2O_6$ have been processed with different values of x. PKN with x = 0.20 is the leading material for high speed broad band surface acoustic wave devices. The new materials are of compositions x = 0.23 and x = 0.34. The processing of these materials involves charge preparation, solid state reaction, isostatic pressing and annealing. These samples have been characterized for ferroelectric properties between 25 °C to 500 °C. The samples exhibit well pronounced and characteristic peaks of a ferroelectric material in the thermal behavior of dielectric constant and conductivity. The Curie point for x = 0.23 is found to be at 396 °C ± 2 °C; whereas it is at 242 °C ± 2 °C for x = 0.34. These values are in close agreement with values obtained from other measurements. The differential thermal analysis and thermo gravimetric analysis show these ceramics to be of single phase with melting points at approximately 1280 °C for x = 0.23 and 1220 °C for x = 0.34, respectively. The paper will present the method of ceramic processing, the results of ferroelectric characterization; and the DTA, TGA and X-ray diffraction analyses. Efforts are now being made to synthesize large bulk single crystals of these compositions to determine the anisotropic and optical properties for identifying their applications in electro-optics, sensor and transducing devices.

INTRODUCTION

Ferroelectric tungsten-bronze (TB) oxides in general exhibit ferroelasticity and are attractive for electrooptic and pyroelectric devices [1]. Single crystals of PKN with x = 0.20 have been found to possess attractive physical properties which make it a very desirable substrate material for surface acoustic wave (SAW) devices [2,3]. Current materials for this application such as α-quartz and lithium niobate are of marginal value because of their intrinsic physical properties in the upper frequency limit of operation [4]. The largest electromechanical coupling factors ever observed in a TB structure are those of $Pb_2KNb_5O_{15}$ crystals with $\kappa_{15} = 0.69$ and $\kappa_{24} = 0.73$ [5]. However PKN, though satisfactory in performance over a much wider frequency bandwidth, has been shown to contain innumerable cracks all across the bulk when synthesized as single crystals [5,6]. Thus there is a growing need for materials which may exhibit superior properties of PKN with x = 0.20 but can be grown as large single crystals without mechanical flaws.

Four new members of the PKN family have been processed in the ceramic form from stoichiometric charges. The composition of the charge has been altered progressively to include more of potassium into lead in the composition $Pb_{1-x}K_{2x}Nb_2O_6$. The value of x varied from 0.23 to a high value of 0.5. The ferroelectric properties of these samples were studied and the results are compared with those of original and traditional composition with x=0.2 ($Pb_2KNb_5O_{15}$).

PROCESSING

PKN charge processing involved the mixing of chemical compounds in appropriate ratios, developing a solid state reaction and densification.

Highly pure (99% or better) powders of PbO_2, Nb_2O_5 and K_2CO_3 are mixed in the necessary molar ratios as required for each member of the compound (i.e., value of x in $Pb_{1-x}K_{2x}Nb_2O_6$). The charge is then ball milled for several hours, stopping the process intermittently to remove any packed material from the inner walls of the container and mixing with the rest of the charge. The powdered mixture is rich purple to brown in color and soft in texture.

Each of these charges (mixtures for the different members of the PKN family) are placed in a separate clean alumina crucible and heated to 300 °C in a resistively heated furnace at the rate of about 120 °C per hour. Soaking for half an hour at 300 °C allows decomposition of PbO_2 to provide the required PbO and release of oxygen.

$$2PbO_2 \text{ -----> } 2PbO + O_2 \qquad (1)$$

Further heating and soaking at 900 °C for three hours decomposes K_2CO_3 according to the equation:

$$K_2CO_3 \text{ -----> } K_2O + CO_2. \qquad (2)$$

Also, PbO melts at 886 °C and diffuses into the charge mixture which allows a chemically homogeneous compound of desired stoichiometry to be formed. Then the furnace is cooled to room temperature. The resulting powder is pale yellow in color and the texture is maintained.

The formation of PKN charge is governed by the following chemical equation

$$(1-x)PbO + (x)K_2O + Nb_2O_5 \text{ -----> } Pb_{1-x}K_{2x}Nb_2O_6. \qquad (3)$$

Equations (1) and (2) show that there is an evolution of carbon dioxide and oxygen during processing from the above mentioned chemicals. By calculating the weight of gases evolved and comparing with the weight loss measured in the samples after cooling, the completion of reaction can be ascertained.

The first phase of increasing the material density is by cold pressing. Then the charge is compacted into pellets in a hydrostatic

CH3080-0-7803-0465-9/92$3.00 ©IEEE

press by applying a pressure of 380MPa for about 10 seconds by means of a water-oil bath. This removes voids and increases the interface boundary. The pellets are a few millimeters thick and 1 inch in diameter. A high temperature sintering for 9 hours at 1100 °C causes an intimate mixture to be formed and enables further densification. The pellets were free of any cracks or mechanical defects. Small specimens, 5mm x 3mm x 1mm, are cut, polished and electroded for various measurements to ascertain their ferroelectric properties.

CHARACTERIZATION

Thermal, ferroelectric and x-ray analyses were performed on each of the ceramic samples obtained. Netzsch Inc. analyzer was used to conduct the Differential Thermal Analysis (DTA) and Thermogravimetric Analysis (TGA). DTA and TGA show the compounds x = 0.23 and x = 0.34 to be congruent melting in nature. Melting point is seen to be around 1280 °C for x = 0.23 and 1220 °C for x = 0.34. The other two samples with x = 0.43 and x = 0.50 are not stable melts and are suspected to be incongruent. Their melting points are found to be approximately 1180 °C and 1120 °C, respectively. The TGA reveals hardly any weight change in the compounds, ruling out any oxygen absorption by the material.

Ferroelectric characterization involved obtaining the dielectric constant (ε_r) and conductivity (σ) as a function of temperature. Instrumentation for these studies was developed in the laboratory. The primary technique was studying the capacitive behavior of the samples. Electrodes were applied to two parallel faces of the pressed dense ceramic specimens using silver epoxy. It was found that it diffuses into the material during the curing step at 150 °C causing dielectric breakdown. Hence gold ink was applied on both sides of the sample and fired at 700 °C for 10 minutes. Silver epoxy is then used as an adhesive to bond the tin coated copper wires as external leads on both sides of the sample. Thickness of the sample was typically 1 mm.

An integrated system was employed for measurement of ferroelectric parameters. A resistive furnace with a sample holder arrangement was hooked to a controller that can be programmed for heating, soaking and cooling cycles. A chromel-alumel thermocouple was placed within 2 millimeters of the sample and connected to the computer through a thermometer. Capacitance across the sample was determined using an LCR meter, also connected to the computer. Knowing the dimensions of the sample and the area of applied electrodes the dielectric constant was determined. The instrumentation was activated through National Instruments' LABVIEW data acquisition software that samples temperature and electrical voltage values and stores as the two axes readings. Fig. 1 and Fig. 2 show the dielectric constant plots. For x = 0.23, the dielectric constant reached a peak value of 4570 at the Curie point of T_c = 396 °C ± 2 °C. The room temperature value was found to be 498 and there is a sharp rise in the curve above 350 °C. The decline in the graph above T_c is not as rapid. For x = 0.34 dielectric constant rose from 858 at room temperature till T_c = 242 °C ± 2 °C where the peak was found to be at 2914. The curve dropped off symmetrically till the higher end of measurement range at almost 300 °C. The change in the Curie point for the different samples is in accordance with the molar ratio of the lead and potassium contents. The transition temperature for the more commonly known PKN with x = 0.20 is T_c = 469 °C ± 4 °C [5] while lead niobate, $PbNb_2O_6$, has a curie point of T_c = 570 °C [7]. Samples with x = 0.43 and x = 0.50 did not show any ferroelectric behavior.

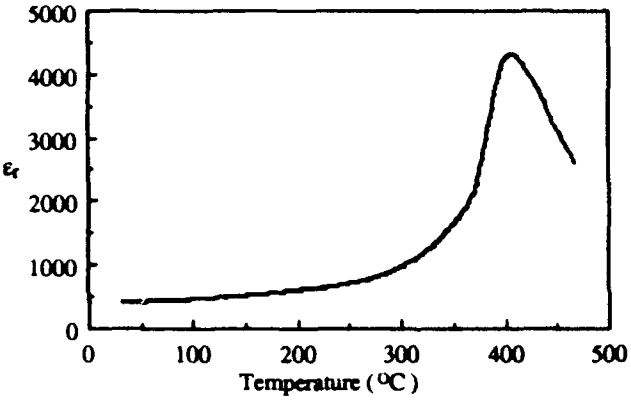


Fig. 1 Relative Dielectric Constant (ε_r) vs. Temperature of PKN, x = 0.23

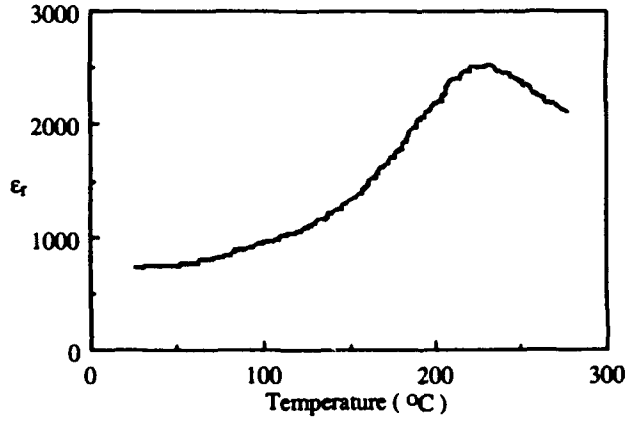


Fig. 2 Relative Dielectric Constant (ε_r) vs. Temperature of PKN, x = 0.34

AC conductivity (σ) measurements were carried out only on samples with x = 0.23 and x = 0.34. Instrumentation was similar to the dielectric constant measuring setup where the LCR meter had the conductance display also. In both the cases data are obtained using

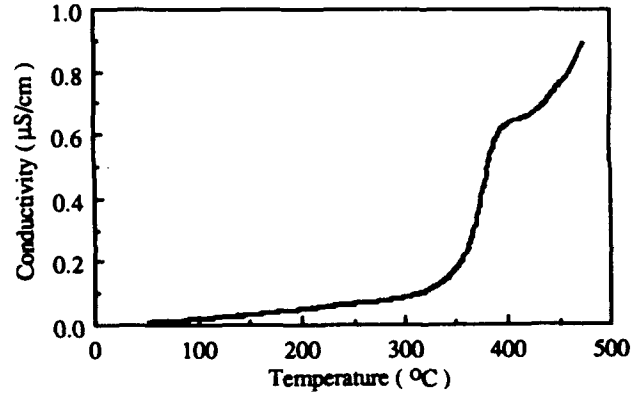


Fig. 3 Thermal behavior of ac conductivity of PKN, x = 0.23

Table I
Pertinent parameters for PKN members

PKN	Lattice Constants (Å)			T_c	ε_r		σ at 25 °C	d
x	a	b	c	(°C)	25 °C	T_c	(μS/cm)	(g/cc)
0.20 (single crystal [8,9])	17.723	17.987	3.895	469 ± 4	1500	12500	0.012	6.12
0.23	17.792	18.096	3.867	396 ± 2	498	4570	0.0095	5.167
0.34	17.526	18.443	3.898	242 ± 2	858	2914	0.0096	5.6

a reference signal of frequency 1kHz. Conductivity curves are shown in Fig. 3 and Fig. 4. The Curie points obtained from the ac conductivity measurements are in full agreement with the T_c values found from the temperature dependence of the relative dielectric constant.

°C)

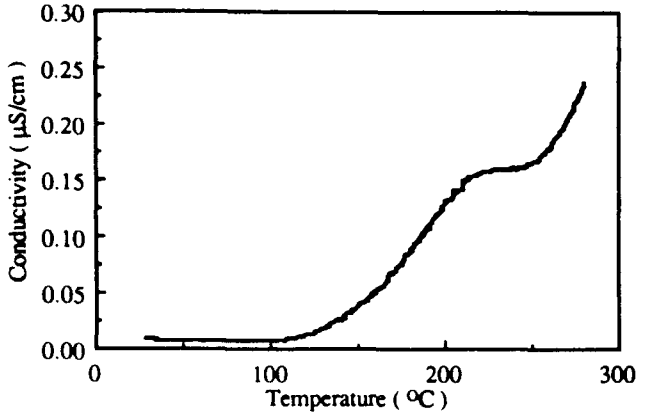


Fig. 4 Thermal behavior of ac conductivity of PKN, x = 0.34

X-ray analysis was performed with Cu-Kα radiation to determine the lattice parameters of the unit cell. PKN has orthorhombic crystal structure. All phases of the powder diffraction pattern could be attributed to the PKN composition. The lattice constants were found to be a = 17.792Å, b = 18.096Å and c = 3.867Å for x = 0.23 and a = 17.526Å, b = 18.443Å and c = 3.898Å for x = 0.34. These are comparable to the ideal PKN values of a = 17.723Å, b = 17.987Å and c = 3.895Å [5].

Density (d) measurements are also obtained and showed a departure from the standard PKN with x = 0.20.

CONCLUSION

It has been shown that by mixing the two ferroelectric compounds lead niobate and potassium niobate in different proportions a whole set of new materials can be obtained. Some of these compositions are found to be ferroelectric in nature and behave in accordance with the amount of potassium doping into the lead niobate. The new materials have the general formula of $Pb_{1-x}K_{2x}Nb_2O_6$. Four new members have been processed with values of x as 0.23, 0.34, 0.43 and 0.50. The densified ceramic samples were characterized and it has been found that the first two are ferroelectric while the other two are not. Results for PKN with x = 0.23 and x = 0.34 have been tabulated in Table I in comparison with the standard material x = 0.20.

It can be seen that at room temperature the values of ε_r and σ for the sample with x = 0.34 are higher than those of x = 0.23. This is due to the presence of a small peak around the room temperature.

Efforts are underway for the synthesis of bulk single crystals of x = 0.23 and x = 0.34. Further studies are needed to ascertain their piezoelectric and optical properties to find out their potential applications.

Acknowledgement: The authors acknowledge the support of Center for Space Power, a division of Texas Engineering Experiment Station (TEES) for this work; Grant No. NAGW-1194. We also thank Professor A. M. Gadalla and his co-workers at Texas A&M University for their active support and participation in the development of this work.

REFERENCES

[1] S. T. Liu, "New polar materials: Their application to SAW and other devices", Journal of Electronic Materials, vol. 4(1), pp. 91-100, 1975.

[2] T. Yamada, "Elastic and piezoelectric properties of lead potassium niobate", Journal of Applied Physics, vol. 46(7), pp. 2894-2898, 1975.

[3] R. M. O'Connell, "Cuts of lead potassium niobate, $Pb_2KNb_5O_{15}$, for surface acoustic wave (SAW) applications", Journal of Applied Physics, vol. 49(6), pp. 3324-3327, 1980.

[4] R. W. Whatmore, "New polar materials: Their application to SAW and other devices", Journal of Crystal Growth, vol. 46, pp. 530-547, 1980.

[5] R. K. Pandey and U. Sridhar, "Synthesis and dielectric characterization of Pb-K-Niobate SAW single crystal", Ferroelectrics, vol. 51, pp. 681-687, 1983.

[6] T. Yamada, "Single crystal growth and piezoelectric properties of lead potassium niobate", Applied Physics Letters, vol. 23(5), pp. 213-214, 1973.

[7] M. E. Lines and A. M. Glass, Principles and Applications of Ferroelectrics and Related Materials. Oxford: Clarendon Press, 1977, Appendix F, pp. 620-632.

[8] J. Nakano and T. Yamada, "Ferroelectric and optical properties of lead potassium niobate", Journal of Applied Physics, vol. 46(6), pp. 2361-2365, 1975.

[9] A. Hossain, Temperature and Frequency Dependent Dielectric Behavior of Lead Potassium Niobate Single Crystal. M. S. Thesis, Texas A&M University, 1984, pp. 45-47.

PYROCHLORE / PEROVSKITE PHASE TRANSFORMATION IN LEAD ZINC-NIOBATE BASED CERAMICS

Xiaoli Wang, Xi Yao
Electronic Materials Research Laboratory
Xian Jiaotong University
Xian, Shaanxi, 710049, China

Abstract

A phase transformation from pyrochlore to perovskite takes place during the firing of $Pb(Zn_{1/3}Nb_{2/3})O_3$ (PZN) based ceramics. Stabilization of the perovskite phase in PZN based ceramics is closely related to the type of additive and its amount. A thermodynamic model based on the chemical potential of the system is proposed in this paper, which is able to give account to the stabilization of the perovskite phase in terms of the internal stress introduced by the additives.

Introduction

$Pb(Zn_{1/3}Nb_{2/3})O_3$ (PZN) single crystals with the perovskite structure can be grown from a PbO flux.[1] It is very difficult to prepare pure PZN ceramics with the perovskite structure by conventional ceramic processing. The product obtained by a two step, columbite route via $PbO+ZnNb_2O_6$, is a mixture of a cubic pyrochlore phase, $Pb_2ZnNb_2O_8$ and PbO[2]. Perovskite PZN ceramics can be prepared by the addition of ABO_3 perovskite compounds, such as $BaTiO_3$ (BT), $SrTiO_3$ (ST), $PbTiO_3$ (PT) etc.[3,4,5] The stabilization of the perovskite structure in PZN based ceramics is directly related to the type and amount of the additives. In PZN–BT system, a BT content of 6 to 7 mol% stabilizes the perovskite structure, while in the PZN–PT system, the perovskite phase is stabilized only when the PT content exceeds 25 mol%. The minimum amount of various perovskite compounds needed to stabilize the perovskite structure in PZN by conventional ceramic processing is given in Table I.

Perovskite additives with strong ionic bonding and a large tolerance factor are suggested by Halliyal et. al[6] to be favorable to the stabilazation of the perovskite phase in PZN based ceramics, as shown in Figure 1. It is clearly evident that BT, which is located at the top right of Figure 1, is the most suitable additive for stabilizing the perovskite phase in PZN based ceramics. However, from Figure 1, both $Ba(Zn_{1/3}Nb_{2/3})O_3$ (BZN) and $BaZrO_3$ (BZ) should be better to stabilize the perovskite phase in PZN than ST which is in the left side of BZN and BZ. However, the experimental results are in contradiction. The performance of ST is inferior to that of BT, but superior to those of BZN and BZ.

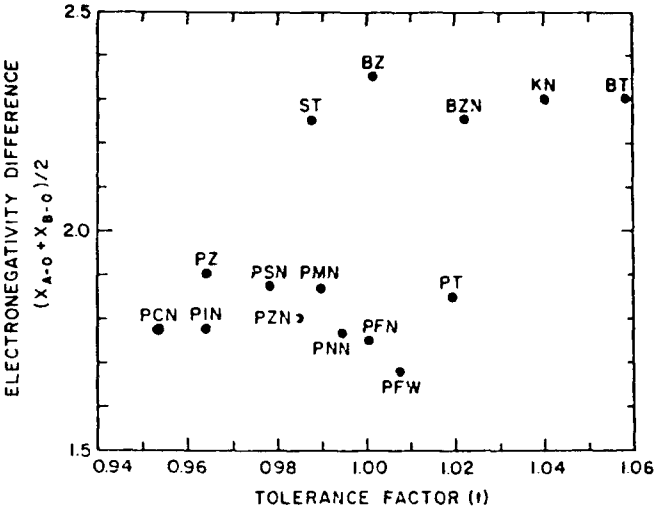


Fig. 1 Plot of electronegativity difference vs tolerance factor for several perovskite compounds.

In the present work, the phase transformation of the PZN based system during synthesis is discussed on the basis of thermodynamics .

Chemical potential and stress

In thermodynamics, the definition of chemical potential μ_i is defined as

$$\mu_i = \left(\frac{\partial G}{\partial n_i}\right)_{T,P,n_{j\neq i}}$$

which means the change rate of the total Gibbs free energy in the system at constant temperature and pressure when an infinitesimal amount of the component i is added to the system without changing the number of moles of the other components j. The difference in chemical potential μ_i is the driving force for material i to change from one phase to another.

The chemical potential of component i is related to many factors, including stress. Evaluating the partial derivative of μ_i with respect to stress we find that

$$\left(\frac{\partial \mu_i}{\partial X}\right)_{T,P,n_{j\neq i}} = \left(\frac{\partial^2 G}{\partial X \partial n_i}\right)_{T,P,n_{j\neq i}} \qquad (1)$$

Because thermodynamic functions are state functions, the second order derivative does not depend on the order of differentiation, i.e.

$$\frac{\partial^2 G}{\partial X \partial n} = \frac{\partial^2 G}{\partial n \partial X}$$

CH3080-0-7803-0465-9/92$3.00 ©IEEE

Combining Maxwell's relation $(\frac{\partial G}{\partial X}) = -x$(where x is the strain), eqn (1) then yields,

$$(\frac{\partial \mu_i}{\partial X}) = (\frac{\partial^2 G}{\partial n_i \partial X}) = -(\frac{\partial x}{\partial n_i}) = -\bar{x}_i \quad (2)$$

where $\bar{x}_i$ is the partial molar strain of component i under constant temperature and pressure. In the range of the elasticity of materials, $\bar{x}_i$ may follow Hook's law,

$$\bar{x}_i^{\delta} = s^{\delta} X^{\delta} \quad (3)$$

where s^{δ} is the elastic compliance of phase δ before the concentration of component i changes, X^{δ} expresses the stress caused by the variation of the concentration of component i in phase δ.

Substituting eqn (3) into eqn (2), and integrating the chemical potential with respect to x at constant temperature and pressure, generates

$$\mu_i = \mu_o \ (T,p,n_j) \ -\frac{1}{2} s X^2 \quad (4)$$

The chemical potential of the material in a phase depends on whether stress is introduced into the phase. At constant temperature and pressure, the stronger the stress induced by component i entering into phase δ, the lower the chemical potential of component i in phase δ. It means, that the component i will shift continuously into phase δ until the stress induced by component i in phase δ becomes zero.

Phase equilibrium and thermodynamics in PZN based ceramics

Numerous experimental results indicate that, either between PbO and $ZnNb_2O_6$ or among PbO, ZnO and Nb_2O_5, the perovskite phase cannot be formed by solid state reaction under general presure.[2,7] The process of transformation from pyrochlore to perovskite takes place during sintering of PZN based ceramics. Figure 2 shows the X-ray diffraction patterns of 0.95PZN-0.05BT calcined at 880 °C (A) and fired at 1100 °C (B). The relative fraction of the perovskite phase of calcined 0.95PZN-0.05BT is only about 5%, while the relative fraction of the perovskite phase of fired 0.95PZN-0.05BT is 85%. From the evidence it is suggested:

During the solid state reaction, additives to stabilize the perovskite phase in PZN based ceramics should initiate formation of perovskite sub-grains. These perovskite sub-grains are surrounded by a number of pyrochlore and PbO particles. The perovskite sub-grains grow constantly with time, while the pyrochlore and PbO particles become continuously smaller, and eventually disappear.

At constant temperature and pressure, the tendency for material i to shift spontanously from phase β to phase δ depends on material i having a lower chemical potential in phase δ than in phase β, i.e.

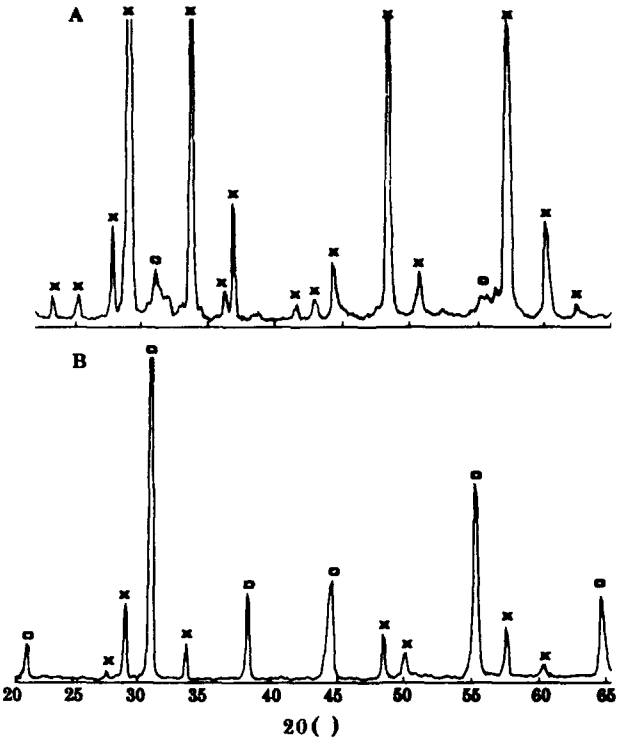


Fig. 2 XRD patterns for 0.95PZN-0.05BT specimen calcined at 880 °(A) and fired at 1100 °C (B). o — Perovskite, x — Pyrochlore.

$$\mu_i^{\delta} < \mu_i^{\beta}$$

The flow of material will stop automatically when $\mu_i^{\delta} = \mu_i^{\beta}$. Eqn. (4) indicates that the chemical potential of material i in a phase is dependent on whether one introduces stress in the phase.

The sintering process of PZN-BT ceramic can be analyzed using this model. During initial process of sintering, there are introduction of Pb^{2+}, Zn^{2+}, Nb^{5+} and O^{2-}into BT sub-grain. As A-site ions in perovskite, the radius of Pb^{2+} (1.63A) is smaller than that of Ba^{2+} (1.74A). That Pb^{2+} relocates at A-site of $BaTiO_3$ lattice may make the lattices contract and distort, thus causing stress in $BaTiO_3$ lattice. According to eqn. (4), in BT perovskite phase, Pb^{2+} will have lower chemical potential, so there are constantly net Pb^{2+} ions relocating on BT sub-grains. There exist vacancies in BT sub-grains, especially at the surface. The ion density difference and the stress caused by lattice distortion may make Ba^{2+} diffuse outward, and Pb^{2+} diffuse inward. Similarly, as B-site ion in perovskite, the radius of Zn^{2+} (0.89A) is larger than that of Ti^{4+} (0.75A), so the relocation of Zn^{2+}at sub-grain BT may distort lattice and introduce intrinsic stress too. Thus Zn^{2+} will constantly relocate at B-site on the surface of BT grain according to equ. (4). As the B-site ion, the electrovalence of Zn^{2+} is low. In order to maintain

electro-neutrality, there are net Nb^{5+} ions relocate at B site of sub-grains. Diffusion will occur among Zn^{2+}, Nb^{5+} and Ti^{4+}. When no distortion of lattice can be caused by transitions of Pb^{2+} and Zn^{2+} in perovskite phase, the chemical potentials of Pb^{2+} and Zn^{2+} in perovskite and pyrochlore tend to equilibrium. There are not any net Pb^{2+}, Zn^{2+} entering perovskite phase. Thermodynamical equilibrium is achieved between perovskite and pyrochlore. If a complete layer of $Pb(Zn_{1/3}Nb_{2/3})O_3$ extends from the perovskite sub-grain, the growth of the perovskite grain due to the disappearence of the pyrochlore phase will cease. The inference accords with the experiments. The stabilization of the perovskite phase in PZN based ceramics is closely related to the additive content and type.

Thus, in PZN based ceramics, the effect of additives stabilizing perovskite phase is closely related to the radius ratios of Pb^{2+}, Zn^{2+} and Nb^{5+} at A-sites, B-sites respectively. The more that $r_A / r_{Pb^{2+}}$ deviates from 1, the stronger the stabilization. Table I lists the values of $r_A / r_{Pb^{2+}}$ and $r_B / r_{\frac{1}{3}Zn^{2+}+\frac{2}{3}Nb^{5+}}$ of some additives.

When each $r_B / r_{\frac{1}{3}Zn^{2+}+\frac{2}{3}Nb^{5+}}$ of additives is same, the size of the A-site ion in an additive determines the amount of the additive needed to stabilize the perovskite structure in PZN based ceramics. For instance, if the B-site ions in additives are Ti^{4+}, when $r_A / r_{Pb^{2+}} = 1.067$ ($BaTiO_3$), the minimum amount is 6-7 mol%; when $r_A / r_{Pb^{2+}} = 1.058$ ($SrTiO_3$), the minimum amount is 9-10 mol%; while if $r_A / r_{Pb^{2+}} = 1.000$ ($PbTiO_3$), the minimum amount increases to 25-30 mol%. When each $r_A / r_{Pb^{2+}}$ of additives is same, the size of the B-site ion has a smaller effect on the amount of an additive needed to stabilize the perovskite structure in PZN based ceramics. For example, the minimum amount of $Ba(Zn_{1/3}Nb_{2/3})O_3$ is 15 mol%, while the minimum amount of $BaZrO_3$ is 15-18 mol%.

In the perovskite structure, diffusion is easiest for O site ions, then the A-site ions, and most difficult for B-site ions. If $PbTiO_3$ is selected as an additive, according to the assumption mentioned above, the expansion of the perovskite phase in PZN based ceramics during the sintering process will depend on the diffusion of B-site ions only. Since the diffusion of B-site ions is relatively difficult, the growth of perovskite grains is restricted, and more PT is needed to stabilize the perovskite phase in PZN based ceramics.

Summery

The additives that stabilize the perovskite phase in PZN based ceramics are those materials which can initiate formation of perovskite sub-grains. The radius ratio ($r_A / r_{Pb^{2+}}$) is an important criterion for stabilization of the perovskite phase in PZN based ceramics. The larger the deviation of $r_A / r_{Pb^{2+}}$ form 1, the better the stabilizing effect of the additive.

References

[1] Y.Yokomizo, T.Takahashi and S.Nomura, "Ferroelectric Properties of $Pb(Zn_{1/3}Nb_{2/3})O_3$," J.Phys. Soc. Jpn, vol.28, pp.1278-1284, May 1970.

[2] Xiaoli Wang, Xi Yao, "The Process of Phase Transformation in Solid State Reaction of $Pb(Zn_{1/3}Nb_{2/3})O_3$Based Ceramics," J. Chinese Ceram., (to be published).

[3] S.Nomura, M.Yonezawa, K.Doi, S.Nanamatsu, N.Tsubouchi and M.Takahashi "Crystal Structure and Piezoelectric Properties of PZN-PT Solid Solution," NEC Res. Dev., No.29, pp.15-21, April 1973.

[4] J.R.Belsick, A.Halliyal, U.Kumar and R.E.Newnham, "Phase Relations and Dielectric Properties of Ceramics in the System PZN-ST-PT," Am. Ceram. Soc. Bull., vol.66, pp.664-667, 1987.

[5] A.Halliyal, U.Kumar, R.E.Newnham and L.E.Cross, "Dielectric and Ferroelctric Properties of Ceramics in the PZN-BT-PT System," J. Am. Ceram. Soc., vol.70, pp.119-123, 1987.

[6] A. Halliyal, U. Kumar, R. E. Newnham and

Table I Relations and amount of additives in PZN based ceramics

Additive	$r_A / r_{Pb^{2+}}$	$r_B / r_{\frac{1}{3}Zn^{2+}+\frac{2}{3}Nb^{5+}}$	Amount (mol%) [6]
$BaTiO_3$	1.067	0.912	6-7
$SrTiO_3$	0.945	0.912	9-10
$PbTiO_3$	1.000	0.912	25-30
$BaZrO_3$	1.067	1.053	15-18
$Ba(Zn_{1/3}Nb_{2/3})O_3$	1.067	1.000	15
$PbZrO_3$	1.000	1.053	55-60

L.E.Cross, "Stabilization of the Perovskite Phase and Dielectric Properties of Ceramics in the PZN–BT System," Am. Ceram. Bull., vol.66, pp.671–676, 1987.

[7] M.Dambekalne, I.Brante and A.Sternberg, "The Formation Process of Complex Lead–containing Niobates," Ferroelectrics, vol.90, pp.1–14, 1989.

DIELECTRIC PROPERTIES OF BISMUTH LAYER TYPE CERAMICS WITH LANTHANUM AND NICKEL CO-SUBSTITUTIONS

Huang Biao, Wang Xiaoli and Yao Xi
Electronic Materials Research Laboratory
Xian Jiaotong University, Xian, China, 710049

Abstract: Dielectric properties of bismuth layer type ceramics with lanthanum and nickel co-substitutions $Bi_2(Pb_{1-x}La_x)(Nb_{2-x/3}Ni_{x/3})O_9$ are presented. Above the Curie temperature, the dielectric constant decreases at a rate that can approximately be described by the quadratic law of Smolensky showing relaxor behavior. At room temperature, the dielectric constant and loss tangent of the new materials are all higher than those of the parent BPN. High resistivity and break-down strength make these materials very attractive for applications such as a high voltage ceramic capacitor dielectric.

1.Introduction

The ferroelectric compound $Bi_2PbNb_2O_9$ is a member of a family of bismuth layer type compounds, the general formula of which is $(Bi_2O_2)^{2+}(A_{n-1}B_nO_{3n+1})^{2-}$, where A can be mono-, di-, or trivalent ions or a mixture of them, B represents Ti^{4+}, Nb^{5+}, Ta^{5+}, etc., and n (=2,3,4,5) is the number of perovskite-like layers of oxygen octahedra between Bi_2O_2 layers[1].

In the parent $Bi_2PbNb_2O_9$ (BPN, n=2), Pb^{2+} and Nb^{5+} can be co-substituted by La^{3+} and Ni^{2+} resulting in a kind of layer type ceramic, $Bi_2(Pb_{1-x}La_x)(Nb_{2-x/3}Ni_{x/3})O_9$ ($0 \le x \le 1$). The tolerance factors t of the substituted materials are lie in the range 0.81-0.93Å (n=2), which are the limits of t for the perovskite-like units of bismuth compounds with layer type structure[2]. The vacancies are avoided in the lattice sites to improve the structure stability of bismuth layer type ceramic. Structures and dielectric properties of the new ceramics were studied.

2.Preparation and Microstructure

The value of x in $Bi_2(Pb_{1-x}La_x)(Nb_{2-x/3}Ni_{x/3})O_9$ was chosen as 0, 0.25, 0.5, 0.75, 1.0, and five compositions were selected for the present study (listed in Table 1). Samples were prepared by a solid state reaction, using the chemical reagents PbO, La_2O_3, Nb_2O_5, NiO and Bi_2O_3 as starting materials. They were calcined at 725°C for 2 hours, then sintered in a covered alumina crucible between 1060°C and 1120°C for 1 hour.

SEM pictures of the materials (Fig.1) show that the grains are flakes with an average diameter about 2 μm and a thickness 0.9 μm. The phase of the sintered products was identified by X-ray diffraction powder techniques using Cu Kα radiation. The XRD patterns show that the lanthanum and nickel substituting materials have the same structure as the parent BPN ceramics. The ceramic disks used for dielectric measurement had over 95 per cent

Table 1. Dielectric constant of $Bi_2(Pb_{1-x}La_x)(Nb_{2-x/3}Ni_{x/3})O_9$

Abbrev.	Composition	x	k(25°C)	tg δ	Tc(°C)	Δ Tm(°C)*
BPN	$Bi_2PbNb_2O_9$	0	140	0.008	552	—
BPLNN(0.25)	$Bi_2(Pb_{0.75}La_{0.25})(Nb_{1.92}Ni_{0.08})O_9$	0.25	215	0.035	465	—
BPLNN(0.5)	$Bi_2(Pb_{0.5}La_{0.5})(Nb_{1.83}Ni_{0.17})O_9$	0.5	205	0.028	322	16
BPLNN(0.75)	$Bi_2(Pb_{0.25}La_{0.75})(Nb_{1.75}Ni_{0.25})O_9$	0.75	185	0.027	155	12
BLNN	$Bi_2La(Nb_{1.67}Ni_{0.33})O_9$	1	165	0.020	—	12

* $\Delta T_m = T_m(100KHz) - T_m(2KHz)$.

CH3080-0-7803-0465-9/92$3.00 ©IEEE

theoretical density.



Fig.1:SEM picture of $Bi_2(Pb_{0.75}La_{0.25})(Nb_{1.92}Ni_{0.08})O_9$

3.Dielectric properties

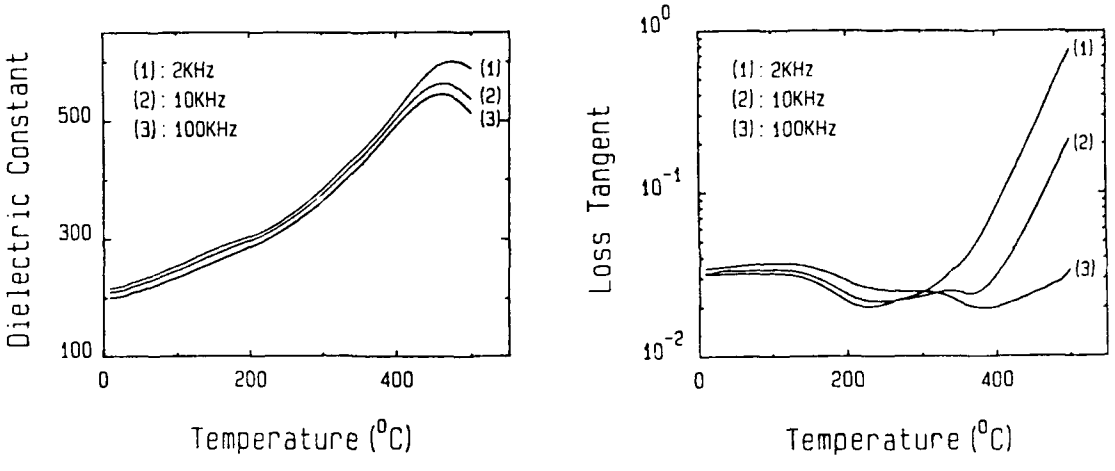
Dielectric constant and loss

Strong frequency dispersion was observed in the temperature dependences of the dielectric constant and loss tangent of these samples (Fig.2). At temperatures higher than T_c, the inverse dielectric constant 1/k obeys quadratic law of Smolensky[3]: $1/k=1/k_c+B(T-T_c)^n$. The values of n lie in the range 2.12 to 2.74. The temperature difference between the T_m measured at 2KHz and 100KHz reaches 12°C-16°C (listed in Table 1) and gives an estimation of the diffused characteristic of transition.

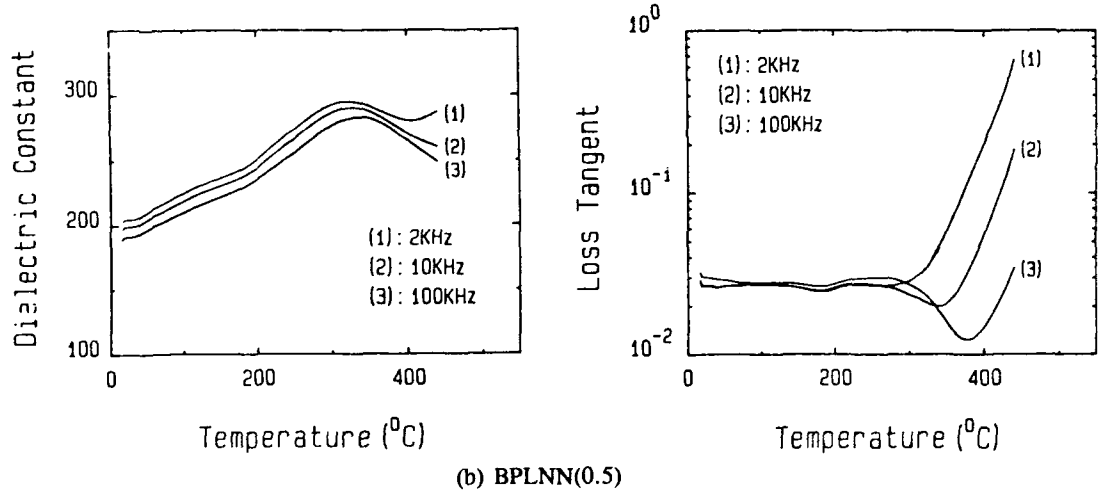
With increasing x, the Curie temperature of $Bi_2(Pb_{1-x}La_x)(Nb_{2-x/3}Ni_{x/3})O_9$ decreases and the dielectric constant peak broadens. Therefore, at room temperature, the dielectric constant and loss tangent of the substituted materials are all higher than those of the parent BPN, as listed in Table 1. Because of the internal stress and composition fluctuation[3], broadened peaks were evident in the temperature variation of the dielectric constants of BPLNN(0.75) and BLNN samples, which show that a low temperature diffused phase transition (DPT) was presented (Fig.2).

Hysteresis

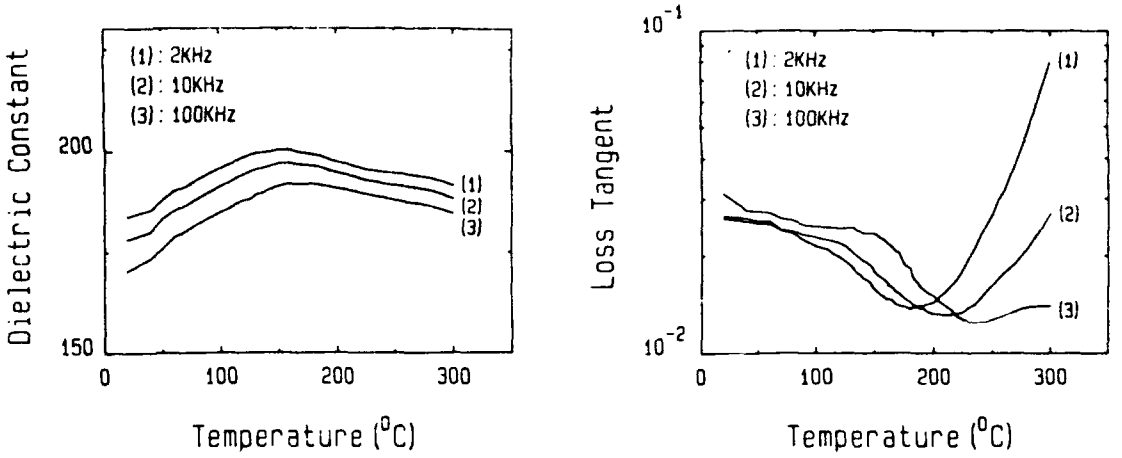
Using a resistance-compensation Sawyer-Tower circuit, a hysteresis loop was observed in BPLNN(0.25) between 100°C and 180°C (Fig.3). The coercive force E_c of BPLNN (0.25) decreases significantly from 9 Mv/m of the parent BPN to 7.5 Mv/m at 160°C. The maximum polarization was approximately 0.098c/m^2 and the estimated spontaneous polarization was about 0.085



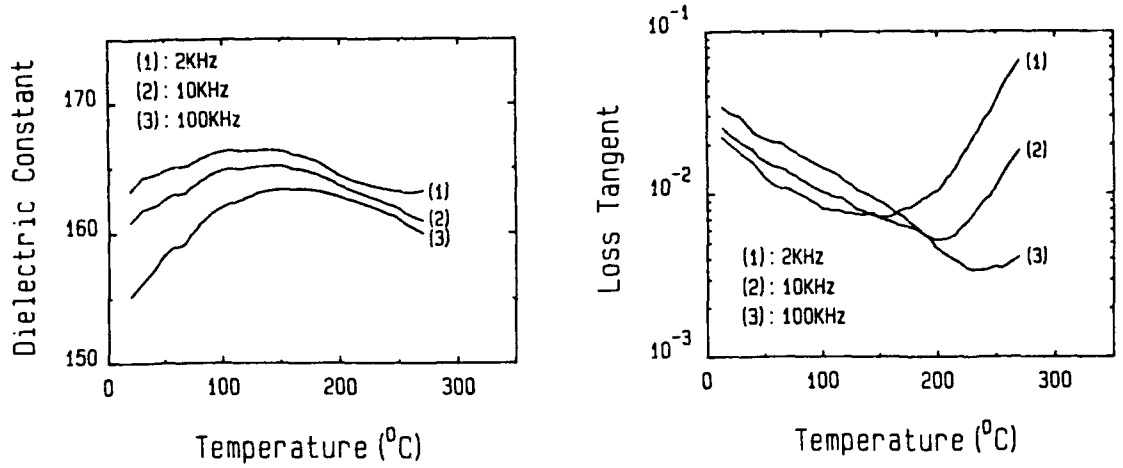
(a) BPLNN(0.25)



(b) BPLNN(0.5)



(c) BPLNN(0.75)



(d) BLNN

Fig.2: Temperature dependences of dielectric constant and loss tangent of $Bi_2(Pb_{1-x}La_x)(Nb_{2-x/3}Ni_{x/3})O_9$ ceramics

c/m^2. With increasing x, the ferroelectric behaviors of the substituted bismuth layer type materials become more and more weak, and hysteresis loops were difficult to detect in BPLNN(0.5), BPLNN(0.75) and BLNN samples.

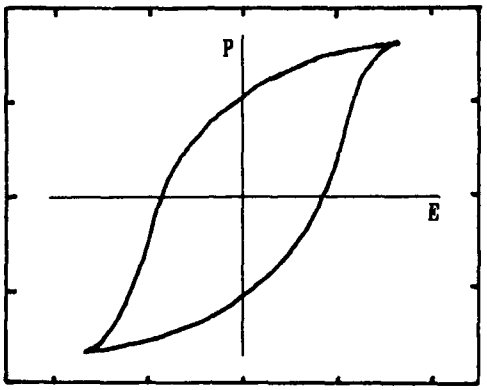


Fig.3: Hysteresis loop of BPLNN(0.25) ceramic at 160°C (x: 8.25 Mv/m/div, y:0.061c/m^2/div)

Resistivity and break-down strength

The resistivities of all the bismuth layer type materials are in the range of 10^{11}-10^{12}ohm.m, which are higher than that of the parent BPN. The valence compensated co-substitution of the La^{3+} and Ni^{2+} for the Pb^{2+} and Nb^{5+} are thought to be responsible for the improvement of the resistivity.

Because of the dense packing of small flaky-like grains of the materials, the break-down strength of all the samples under DC voltage is very high (higher than 30 Mv/m), which is very attractive for applications such as high voltage ceramic capacitor dielectrics.

4.Summary

(1) The lead and niobium ions in the bismuth layer type parent material $Bi_2PbNb_2O_9$ can be partially and completely co-substituted by lanthanum and nickel ions within the layer structure.

(2) The Curie temperature and coercive force

of the substituted materials are all lowered due to the substitution. The substituted materials are ferroelectric relaxors.

(3) The dielectric constant and resistivity of the co-substituted materials at room temperature are all higher than the parent material. The break-down strength of the materials is high, making these materials very promising for capacitor dielectrics.

References

[1] E.C.Subbarao, " A family of ferroelectric bismuth compounds", J.Phys.Chem.Solids, vol. 23, pp.665-676, 1962.

[2] E.C.Subbarao, "Crystal chemistry of mixed bismuth oxides with layer-type structures" J.Amer.Ceram.Soc, vol. 45, pp.166-169, April 1962.

[3] G.A.Smolensky, " Physical phenomena in ferroelectrics with diffused phase transition", J.Phys.Soc.Japan, vol. 28, Supplement, pp26-37, 1970.

PREPARATION AND PHASE TRANSITION OF NANOPHASE FERROELECTRIC $PbTiO_3$ FINE POWDERS

LU Shengguo, ZHANG Liangying and YAO Xi

Electronic Materials Research Laboratory (EMRL)
Xi'an Jiaotong University, Xi'an, 710049
China

ABSTRACT

Nanophase ferroelectric $PbTiO_3$(PT) fine powders are prepared through sol-gel and hydrolysis-aging processes. The lattice constants and grain size are determined by XRD analysis. The phase transition is examined by DSC analysis with different heating rates. The relation of onset temperature to grain size is obtained. Results indicate that the grain size is in the range of 10-100 nm, the phase transition temperature is lower than that of bulk material, and the transition region is broadened. The small grain size and surface electric charge compensation are accounted for the reduction of phase transition temperature, and the former may dominate. The distribution of particle size may be responsible for the broadening of the phase transition. The phase transition of PT fine powders is compared with the diffused phase transition (DPT) in relaxor ferroelectrics. The nm structure, nm transition and critical size of fine powders are discussed.

1. INTRODUCTION

Recently, studies on fine particles, especially the nanometer (nm) particles, are very active. The nanosized metals, oxides, carbonides, nitrides, compound semiconductors, etc., have been successfully prepared by various methods. Investigations on their electric, thermal, optical, and mechanical properties have been reported. [1-4]

Because of the multi-elements of chemical composition and high crystallization temperatures, it is very difficult to prepare nanosized ferroelectric particles through conventional ceramic method.

However, the studies of ferroelectric nanophase in bulk materials may be traced to the early fifties, when Kanzig observed the nanosized polar region at temperature slightly higher than the Curie temperature. The polar region now is called Kanzig region, which has a size of 10-100 nm[5]. Later on, the researches on diffused phase transition [6-9], micro-macro domain transition [10-11] all adapted to this concept.

The grain sizes of several ferroelectric powders are listed in Table 1, where the grain sizes are in the range of Kanzig region except for the PZT powders.

The phase transition temperature of $PbTiO_3$ fine powders has been observed shifting to a lower temperature compared to bulk materials (T_c = 490 °C) by K. Ishikawa et al. using high temperature laser Raman spectrum [13], which was accounted for the depolarization effect, as Betra et al. did in thin films.[17-18]

Table 1, Grain sizes of fine ferroelectric powders

Material	Grain size minimum	preparation method	measurement	Ref.
$PbTiO_3$	12nm	coprecipitation	XRD	12
$PbTiO_3$	22nm	precipitation	XRD	13
$BaTiO_3$	36nm	milling	light beating	14
PZT	8.7nm	precipitation	XRD	15
PLZT	16nm	coprecipitation	/	16

It seems that the phase transition of nanosized fine powders is still unclear in the following aspects: characteristics of phase transition, relation between the phase transition and the powder size distribution, and effect of nanosized crystalline structure.

In this paper, the sol-gel and hydrolysis-aging processes are used to prepare $PbTiO_3$ fine powders with nanosized grains. The phase transition of different grain sizes are investigated by DSC analysis with different heating rates. The relation of specific heat vs. temperature is observed. The crystalline lattice constants and grain size are determined by XRD patterns. The nm structure, nm phase transition, and critical size of nm ferroelectric particles are discussed.

2. EXPERIMENTAL

Two steps were used to prepare the nanophase ferroelectric $PbTiO_3$ fine powders. First, preparation of Pb, Ti complex alkoxide; Second, Pb, Ti complex alkoxide hydrolyzed in a basic solution, and fired at a temperature of about 600 °C.

The method using lead acetate and titanium butoxide [19] is used to prepare the Pb, Ti complex alkoxide. Lead acetate [$Pb(CH_3COO)_2 \cdot 3H_2O$] is dissolved in ethyleneglycol monoethyl ether [$C_2H_5OC_2H_4OH$], heated to 125 °C to remove water, then cooled to 100 °C. Titanium butoxide [$Ti(OC_4H_9)_4$] then added at this stage. A gold colored Pb, Ti complex alkoxide is obtained after the solution is reheated to a temperature of 135 °C or so.

The Pb, Ti complex alkoxide is diluted in ethanol alcohol [C_2H_5OH] (or iso-propyl alcohol [$(CH_3)_2CHOH$],) and dropped into a basic solution

CH3080-0-7803-0465-9/92$3.00 ©IEEE

(ph=11.5) mixed with water and ethanol alcohol. The ratio of water to alkoxide is about 4-6 : 1. After stirred for 5-10 hours at room temperature, hydrolyzed solution is kept in a glass tube, and aged for 20-30 hours at 60-80 ^{o}C. The gel like material then dried, crushed, sieved, and fired at 600 ^{o}C for 5 minutes to 2 hours. The powders obtained is light-yellow in color.

XRD was analyzed by RIGAKU D/MAX-RB, calibrated with polycrystalline silicon powders. Particle size distribution was taken by HORIBA CAPA-700. Thermal analysis was completed with a PERKIN-ELMER DSC-7.

3. RESULTS AND DISCUSSION

(1). Particle size distribution

Particle size distribution of $PbTiO_3$ powders was taken from CAPA-700, with a rotating rate of 3000 rpm, the bulk density of $PbTiO_3$ 7.90 g/cm^3 was used as the density of powders. The distribution of particle sizes is shown in Fig.1. The median size is 300 nm, with a std. dev. of 180nm.

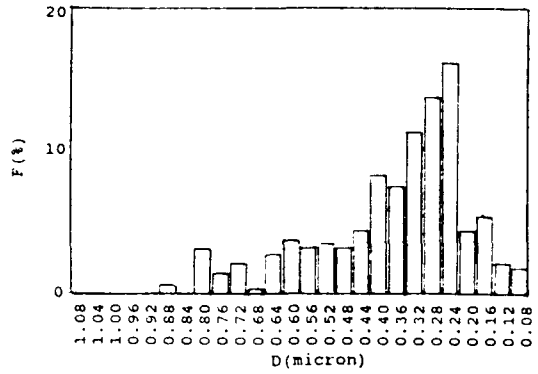


Fig.1 Particle size distribution (in volume) of $PbTiO_3$ powders.

(2). Particle size, grain size and lattice constants

To obtain the lattice constant, polycrystalline silicon powders are used to correct the diffraction peaks. The calibrated peaks of polycrystalline silicon powders are (111), (220), (400), (511), (531), (533). A calibration formula of the full width of half maximum (FWHM) is

$$(2\theta)_r = 0.11203 - 8.01462 \times 10^{-4} (2\theta)_m + 1.18958 \times 10^{-5} (2\theta)_m^2 \quad (1)$$

where

$(2\theta)_r$ ---real 2θ value.
$(2\theta)_m$ ---measured 2θ value.

After slowly scanning several selected peaks of (101), (111), (200), (202), (311), and (312) of $PbTiO_3$ powders, separating the $k_{\alpha 1}$, $k_{\alpha 2}$ peaks, correcting these peaks with calibrated formula, and according to the Scherrer's formula

$$D = k\lambda/(\beta\cos\theta) \quad (2)$$

where D is the grain size in diameter, k the Scherrer's constant(k=0.9 for FWHM), λ the X-ray wavelength , β the FWHM of a diffraction peak, θ the diffraction angle, the grain sizes obtained are listed in Table 2. The Cauchy-Cauchy, Gaussian-Gaussian, and Cauahy-Gaussian methods are used to evaluate the distortion of crystalline structure, the results is shown in Table 3.

Table 2 The grain sizes of a few peaks of PT powders

No.	h k l	D(H,G)(nm)	D(H,C)(nm)	k
1	1 0 1	41.7	38.4	0.9
2	1 1 1	51.2	45.2	0.9
3	2 0 0	44.7	40.8	0.9
4	2 0 2	28.1	27.6	0.9
5	3 1 1	37.2	35.5	0.9
6	3 1 2	33.8	50.4	0.9

Table 3 The distortion of crystalline structure of PT powders

Method	Grain size (nm)	lattice distortion
Cauchy-Cauchy	66.1 (Gaussian)	0.09%
	36.9 (Cauchy)	-0.00%
Gaussian-Gaussian	46.3(Gaussian)	0.13%
	35.7(Cauchy)	-0.03%
Cauchy-Gaussian	48.1(Gaussian)	0.10%
	39.4(Cauchy)	0.07%

Then the least square method is used to calculate the lattice constants. The results are a=b=3.093 A, c=4.142 A, with a standard derivations of 0.001 and 0.003 respectively. The c/a ratio is 1.061, which is smaller than that of bulk material (a=b=3.899, c=4.1532c/a=1.0652).[20]

From the XRD results we can conclude that the lattice distortion of $PbTiO_3$ fine powders is very small, the crystalline structure of nanosized fine powders seems still perfect.

(3). DSC analysis

The DSC analysis of PT powders with various grain size is performed for the above sample with different heating rates. The results are shown in Fig.2 and Fig.3. A relation between the onset temperature and grain size D is demonstrated in Fig.4.

The apparent activation energy of phase transition E obtained from the Arrhenius dependence [21]

$$k_h = v \exp(-E/(RT_{peak})) \quad (4)$$

is about 308.6kJ/mol. Here k_h is the heating rate,

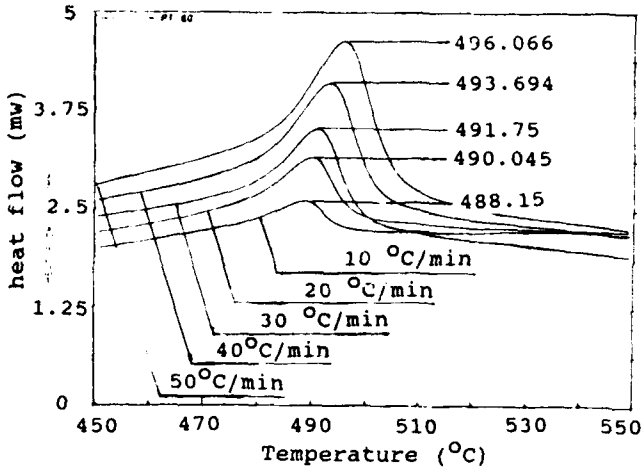


Fig.2 DSC curves with different heating rates.

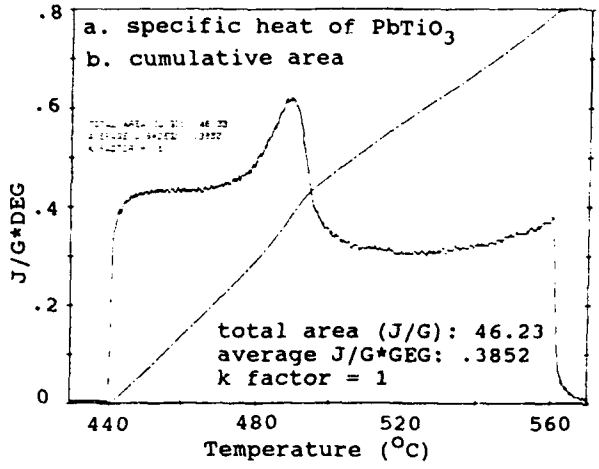


Fig.3 Specific heat of PT fine powders.

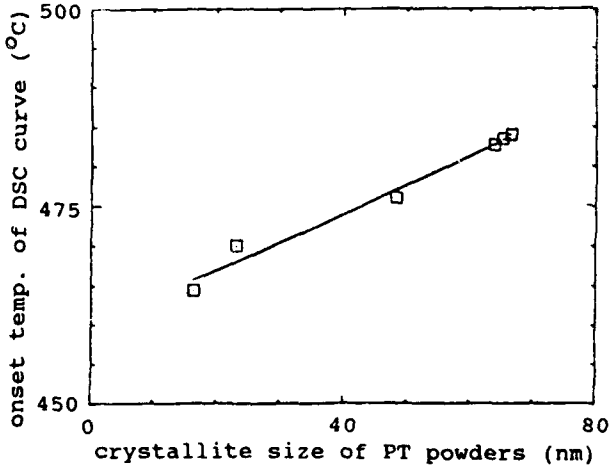


Fig.4 Relation of onset temperature vs. grain size.

T_{peak} is the peak temperature, v the frequency factor. The transformation heat is about 0.92 kJ/mol. For the crystallization process of PZT powders, heat transformation is 4.6 kJ/mol, E is 309.6 kJ/mol. [21] It seems that the transformation heat of phase transition is much smaller than that of crystallization.

(4). The nm structure of $PbTiO_3$ fine powders

Considering the calculated value of peak (111) 51.2 nm (Table 2), and the median particle size of 300 nm (Fig.1), it seems that a particle may consist of about 2-9 grains. The grains may agglomerate to a powder, and there are lots of surfaces exposed to the surrounding. It is obvious that the agglomerate structure is difficult to be dispersed. Sometimes electronic beam can disperse the agglomerate into crystallites during the TEM observation.

(5). Phase transition of fine powders with nanosized grains

The endothermal peaks of DSC curve suggests that there is a latent heat involved, which means that the phase transition is of first-order. However, because the specific heat vs. temperature showes a gradual change (Fig.3), it seems that there is the characteristic of second-order phase transition. It might suggest that the phase transition is diffused here.

(a). Decrease of the Curie temperature T_c

Because the grain size is in the range of Kanzig region (10-100 nm), and c/a ratio is smaller than the value of bulk material, the polarization value may be less than that of a bulk crystal, as occurred in the diffused relaxor ferroelectrics. This phenomenon has been observed in PT, PLT, PLZT and other thin films,[22-24] (PT: P_s=10.59 uC/cm^2 , ε_m=115; PLT: P_s=11.4 uC/cm^2, ε_m=115; PLZT: P_s=14.7 uC/cm^2, ε_m=450), where the grain sizes are also in the range of Kanzig region. But for PT single crystal, P_s=75 uC/cm^2, ε_m=200; PLZT ceramic, P_s=22 uC/cm^2, ε_m=13,000. Betra et al. accounted for this result by means of the depolarization field[17-18] compensating the polarization to the electrodes. Although free electric charges may exist on the surfaces of the grains, the small grains with smaller polarization vector may dominate the lowering of the Curie temperature. For a smaller polarization vector, the elastic Gibbs free energy G[25]

$$G = G_0 + 1/2\ aP^2 + 1/4\ bP^4 + 1/6\ cP^6 \quad (5)$$

where G_0---free energy of paraelectric phase
a, b, c---constants

will be small, and can be easily overwhelmed by the thermal energy of phonons. So at temperatures lower than the Curie temperature T_c of the bulk materials, the ferroelectricity will partially disappear, and part of ferroelectric crystallites will be changed into paraelectric ones.

On the other hand, the absorbed surface electric charges could compensate the polarization, if a grain is a crystallite. Assuming the surface charge density

is n_s, the effective polarization intensity could be written as

$$P_{eff} = P - 2en_s \qquad (6)$$

The compensation will further lead to the reduction of polarization and the free energy of ferroelectric phase. The phase transition temperature will be reduced as[25]

$$\Delta T = 2lC/(\varepsilon D) \qquad (7)$$

where l---thickness of surface layer
C---Curie-Weiss constant
ε---relative dielectric constant
D---grain size

Then, we can obtain that the reduction of phase transition temperature is related to the grain size.

(b). Broadening of the phase transition

The broadening of phase transition of $PbTiO_3$ fine powders may be from the size distribution of the powders (Fig.1). Since the reduction of phase transition temperature T_c is related to the grain size D, the distribution of powder size will result in the distribution of T_c , hence the phase transition peak of DSC curves will be broadened.

(c). Comparison with the DPT in relaxor ferroelectrics

The phase transition here differs from that in relaxor ferroelectrics in following aspects: first, the distribution of T_c originated from different mechanisms, for PT fine powders, is the distribution of particle size and grain size, and for DPT relaxor ferroelectrics, is the fluctuation of the composition (in PMN). Second, the reduction of phase transition temperature is from size reduction and charge compensation of PT grains, while for relaxor ferroelectrics, is from the different B-site ions composition.

(6). Critical size of ferroelectric nm particles

The critical size of ferroelectric phase evaluated by F. Glasse in bulk materials was about 6.4 nm.[26] The experimental value of polar region is 10-100 nm in $BaTiO_3$[5], 5 - 30 nm in PLZT.[27] Ishikawa obtained that the critical size of ferroelectric size is 12.6 nm. The critical size cannot be obtained according to relation of onset temperature vs. grain size in Fig.4, although the minimum grain size is 16.4 nm. Since the particle size of precursor of $PbTiO_3$ crystallites is about 500 nm,[28] the lower thermal heat treatment temperature will lead to a insufficient of crystallization, which will affect the XRD patterns.

REFERENCES

1. H. Gleiter, *Mater. Sci. Eng.*, **52**(1982)91.
2. *"Fine particles"*, Proceeding of seminar onsolid state physics and metal physics (in Japanese), Agre Technology Center, (1984).
3. "Special issue on nonlinear optics", *Solid State Physics* (in Japanese), **24**(11)(1989).
4. R. W. Siegel et al. *MRS Bull.*, **15**(1990)60.
5. W. Kanzig, *Helv. Phys. Acta*, **24**(1951)175.
6. G. A. Smolensky, *J. Phys. Soc. Jpn.*, **28**, suppl., (1970)26.
7. V. A. Isupov, *Ferroelectrics*, **90**(1989)113.
8. N. Setter and L. E. Cross, *J. Mat. Sci.*, **15** (1980)2478.
9. Lu Shengguo, Chen Zhixiong, *Ferroelectrics*, **110** (1990)57.
10. Yao Xi, Chen Zhili and L. E. Cross, *J. Appl. Phys.*, **54**(1983)3399.
11. Yao Xi and Chen Zhili, *Piezoelectrics and Acoustooptics*, (6)(1984)1. (in Chinese)
12. M. H. Lee, A. Halliyal and R. E. Newnham, *J. Am. Ceram. Soc.*, **72**(1989)986.
13. K. Ishikawa et al., *Phys. Rev.*, **B37**(1988)5852.
14. R. Bachmann and K. Barner, *Solid State Commun.*, **68**(1988)865.
15. R. W. Schwartz et al., *"Ultrastructure of advanced ceramics"*, ed. by J. D. Mackenzie, D. R. Ulrich, John Wiley & Sons Inc.,(1988)487.
16. Y. Yoshikawa and Tsuzuki, *J. Am. Ceram. Soc.*, **73**(1990)31.
17. I. P. Betra et al., *Phys. Rev.*, **B8**(1973)3257.
18 I. P. Betra et al., *Phys. Rev. Lett.*, **30** (1973)384.
19. J. B. Blum, S R. Gurkovich, *J. Mat. Sci.*, **20**(1985)4479.
20. Yuxuan Xu, *Ferroelectric and Piezoelectric Materials*, Science Press, (1978)118. (in Chinese)
21. K. C. Chen et al., *"Better ceramics through chemistry"*, Materials Research Society, ed. by C. J. Brinker, D. E. Clark, and D. R. Ulrich, Pittsburgh, (1986)731.
22. Wei Ren et al., *"Composition, microstructure and properties of advanced ceramics"*, ed. by Yao Xi and Sun Hongtao, Xi'an Jiaotong Univ. Press, (1989)172.(in Chinese)
23. Ping Sun, Liangying Zhang and Xi Yao, ICECM'92, Hangzhou, China,(1992).
24. Ping Sun, Liangying Zhang and Xi Yao, *"Composition, microstructure and properties of advanced ceramics"*, ed.by Yao Xi and Sun Hongtao, Xi'an Jiaotong Univ. Press, (1992).(in Chinese)
25. V. M. Fridkin, *"Ferroelectric semiconductors"*, translated by Chen zhixiong et al.,Huazhong University of Sicence and Technology Press, (1985).(in Chinese)
26. F.Glasse, *Ferroelectrics Letter*, **5**(1986)101.
27. Xiangyun Song et al., *Science in China* (Scientia Sinica), A(12)(1988)1310.
28. Jiming Ma (internal report on the preparation of $PbTiO_3$ fine powders by hydrolysis of alkoxide) (1989).

AMORPHIZATION OF BULK AND THIN FILM PLZT MATERIALS BY 1.5 MeV KRYPTON ION IRRADIATION WITH in situ TEM OBSERVATION

L. M. Wang[a] and A. Y. Wu[b]

[a]Department of Geology and [b]Center for High Technology Materials
University of New Mexico, Albuquerque, NM 87131

PLZT (lanthanum modified lead zirconate-titanate) materials for high performance electrical and optical non-volatile memory device may encounter high-level irradiation environment either during ion-beam assisted device fabrication process or in service. It is especially important to understand the critical irradiation conditions under which PLZT material become amorphous, because this will result in the loss of ferroelectricity in the material and the memory in the device.
In this study, transmission electron microscopy (TEM) samples prepared from both bulk and thin film PLZT materials have been irradiated with 1.5 MeV krypton ions at various temperatures in the HVEM-Tandem Facility at Argonne National Laboratory. *In situ* TEM observation was performed during irradiation, which made the determination of the critical amorphization dose possible. At room temperature, a PLZT 9/65/35 ceramic sample was found to become completely amorphized after a dose of ~$2x10^{14}$ ions/cm^2, much less than the critical amorphization dose for silicon. The sputter-deposited, fine-grained PLZT thin film took even smaller dose to become amorphous. However, at 450°C, the upper temperature limit for the material to retain its desirable physical properties, the PLZT 9/65/35 was not amorphized even after a dose of $1.1x10^{15}$ ions/cm^2. The results will be discussed with a recent model for ion-beam induced amorphization of ceramic materials.

Introduction

Ferroelectric PLZT [(Pb,La)(Zr,Ti)O_3 or lanthanum modified lead zirconate-titanate] in bulk or thin film form can be used for various device applications including non-volatile memories [1], piezoelectric transducers, pyroelectric sensors, spatial light modulators [2], and optical image storage [3]. In order for PLZT materials to have these useful properties, the material must possess the correct chemical composition and crystal structure. For example, PLZT films deposited below certain substrate temperatures by sputtering or solution coating methods frequently are either amorphous or with the pyrochlore structure. These films do not exhibit the Pockels or Kerr effect and are not useful for electrooptic applications. On the other hand, radiation damage caused by ion implantation in PLZT material may greatly enhance the photosensitivity of the photo-ferroelectric effect [3]. Such observations suggest that variations in ferroelectric property of PLZT may be caused by variations in composition, crystal structure, dopant level and defect structure. Land and Peercy [3] have noted that a damaged thin layer of a few hundred nanometers beneath the surface of bulk PLZT may be created by ion implantation using ion beams of the energy 200 to 500 keV. Depending on the ion beam energy, this thin layer may not have the perovskite structure and thus not be electrooptic. However, this thin layer apparently can enhance the photosensitivity of the optical storage capability of the bulk device. Still, there has been little detailed study of the structure of the ion beam damaged layer in PLZT. Radiation damage in PLZT is important because PLZT materials are frequently ion-milled to form structures for electrooptic applications [4] and PLZT films are known to be deposited by ion beam assisted deposition techniques. Also PLZT devices may encounter high-level irradiation environments, such as in ionosphere and Van Allen radiation belts or in a nuclear reactor or a high energy particle accerlerator so that the material may be amorphized and lose its ferroelectric properties. In this study, we have used an *in-situ* transmission electron microscopy (TEM) during 1.5 MeV Kr ion irradiations to investigate radiation-induced amorphization of PLZT single crystal samples prepared from bulk ceramic material, highly-oriented PLZT thin film samples, and polycrystalline PLZT thin film samples, in the temperature range between 25-450°C. The results for the room temperature irradiation are compared with that obtained from pure silicon of the (110) orientation under the same irradiation condition and the data can be extrapolated to predict the critical amorphization dose required under other irradiation conditions.

Experimental

PLZT materials normally have the slightly distorted perovskite structure which is common among ABO_3 compounds. The structure, to the first approximation, consists of cubic closest packing of oxygen ions and A-site cations (Pb and La). B-site cations (Zr and Ti) occupy one-fourth of the octahedral interstices in the close-packed array, filling only those octahedral sites not adjacent to A-sites. A-sites are coordinated by twelve oxygens, B-sites are coordinated by six oxygens. Each oxygen is in contact with the adjacent four A-type and two B-type cations.

TEM samples were prepared from hot pressed PLZT 9/65/35 wafer. The density of the sample is 7.81 g/cm^3 and the average grain size is about 8 μm. After Ar ion milling perforation for preparing several TEM thin foils, we were able to select single crystals of the [111] orientation inside individual crystal grain for TEM study because TEM beam size is smaller than the grain size. Several PLZT fine-grained, thin films samples of the composition 7/0/100 and about 1000 Å thick have also been prepared. These films were deposited on Si(111) substrate by rf magnetron sputtering at 400°C. The PLZT thin film samples for TEM study were obtained by dissolving Si away using a warm KOH/water solution. A typical TEM micrograph of the grain structure of the thin film sample is shown in Figure 1.

As mentioned above, TEM sample foils from bulk ceramic wafer were prepared by Ar ion milling to perforation. TEM examination after ion milling did not reveal any "amorphous halo" in the electron diffraction pattern for the bulk ceramic sample. Samples were irradiated with 1.5 MeV Kr^+ ions in the HVEM-

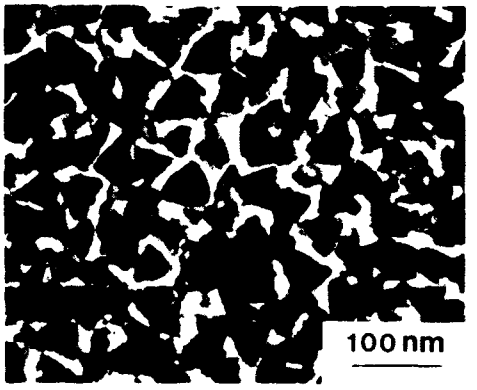


Figure 1. TEM micrograph of PLZT 7/0/100 thin film.

CH3080-0/92/0000-0389$03.00 ©IEEE

Tandem Facility at the Argonne National Laboratory [6] at a dose rate of $3.6x10^{11}$ ions/cm^2. The facility links a modified Kratos/AEI EM7 high-voltage electron microscope (HVEM) with a 2 MV tandem ion accelerator, so that *in-situ* TEM observations can be made during the ion irradiations. The ion beam enters the microscope column at an angle of 30°, and the sample on a double-tilt heating stage was tilted 25-27° toward the ion beam during the experiment. A defocused 300 keV electron beam was used for the *in situ* observation in several selected area of the electron diffraction mode. The experimental arrangement is shown schematically in Figure 2. Ion irradiations were performed at 25, 200, 325 and 400°C. The sample temperature was continuously monitored, and its increase due to beam heating was less than 50°C. A pure silicon sample of the (110) orientation was also irradiated with 1.5 MeV Kr ions at room temperature for comparison. Because of their high energy, most of the Kr ions completely penetrate through the electron transparent thickness (<300nm) of the sample, and the Kr concentration introduced in the sample region of study is negligible for all the doses used in our experiments.

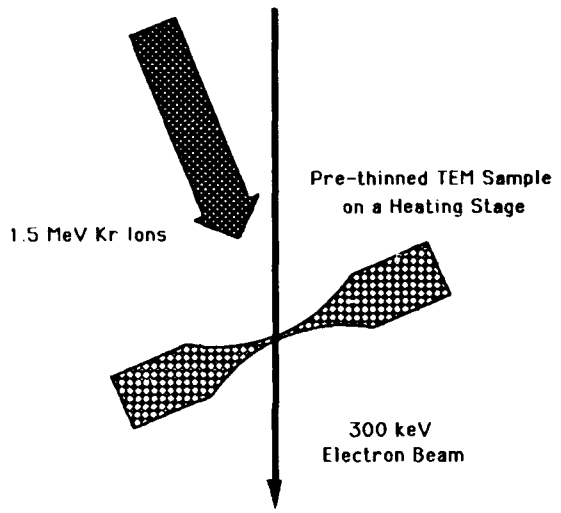


Figure 2. In-Situ TEM/ion irradiation experimental arrangement with the HVEM-Tandem Facility at the Argonne National Laboratory.

Results and Discussion

At room temperature, the electron transparent region of the silicon sample was completely amorphized with 1.5 MeV Kr ions irradiation after a critical dose of $1x10^{15}$ ions/cm^2. The progressive amorphization process was evidenced by the changes in the electron diffraction pattern as is shown in Figure 3. At first, a diffuse halo, whcih is the characteristic of an amorphous material, appeared and its intensity increased with increasing ion dose. Concurrently, the diffraction maxima intensity decreased until the diffraction maxima completely vanished at the critical amorphization dose. For PLZT 9/65/35, this process proceeded much more rapidly at room temperature. As shown in Figure 4, a diffuse halo was observed at doses as low as $5.1x10^{13}$ ions/cm^2, and amorphization was completed after only $1.9x10^{14}$ ions/cm^2, a dose less than one fifth of that required for the complete amorphization of silicon. For the sputter-deposited PLZT films, we found that the amorphization was completed after only $3.4x10^{13}$ ions/cm^2, about one fifth of that required for hot-pressed PLZT ceramic bulk samples.

Because of the large differences in chemical composition and density between silicon and PLZT, and also because most ions penetrate through the thickness of the sample examined, the stopping power of the target materials for the ions is an important parameter in determining the effectiveness of a certain ion dose in damaging the target. Therefore, it is better to compare the total energy loss due to nuclear collision events in the samples which became amorphous, rather than to compare the critical amorphization doses directly. The energy loss doe to nuclear collisions can be estimated by a Monte Carlo simulation using the TRIM code [7], although TRIM does not explicitly provide output for this result [8]. Based on the TRIM results, the energy loss per unit length due to nuclear interactions by 1.5 MeV Kr ions is calculated to be 1.03 keV/nm/ion in the PLZT material and 0.35 keV/nm/ion in silicon (using data from the depth of 150 nm for the average of the first 300 nm thickness). In other works, the PLZT material has a higher nuclear stopping power for the ions than silicon, so for a specific ion dose, more energy is transfered through nuclear collision within the PLZT sample, thus causing more severe rediation damage. This is expected because PLZT has a much higher density (7.8 g/cm^3) than silicon (2.33g/cm^3). However, at the critical amorphization dose, the estimated total energy loss due to nuclear collisions in silicon is 3.5 keV/nm^3, and in PLZT 9/65/35, only 2 keV/nm^3. Thus, the higher nuclear stopping power can not completely account for the lower critical amorphization dose in the PLZT. One of the other important parameters affecting damage efficiency is the displacement threshold energy, E_d. Unfortunately, no data are available at present for PLZT. Assuming E_d equals 15 ev for both silicon and PLZT, the displacement damage levels at the critical amorphization dose are 1.8 and 0.7 displacements per atom (dpa) for silicon and PLZT, respectively. Previous studies on many complex ceramic materials suggest that the critical amorphization dose decreases with increasing chemical and structure complexity and decreasing average bond ionicity [9]. The relatively complex crystal structure of PLZT must also be a factor which makes it more sensitive to radiation-induced amorphization.

The results obtained from 1.5 Mev Kr irradiation can be extrapolated based on TRIM simulations to predict the critical amorphization dose required under other irradiation condition. For example, assuming nuclear collision events (energy loss due to nuclear collision) are mainly responsible for the radiation-induced amorphization [9], it can be predicted that a thin amorphous layer centered at a depth of 200 nm forms under 500 keV Ar ion irradiation after a dose of $3.5x10^{14}$ ions/cm^2. Land and Peercy [3] have observed a three orders of magnitude increase in photosensitivity in 500 keV Ar irradiated PLZT 9/65/35 ($5x10^{14}$ ions/cm^2) and have attributed the effect to decreased dark conductivity and dielectric constant in a near surface damaged layer less than 1 μm thick without specifying the damaged structure. According to our estimate, an amorphous layer approximately 100 nm thick has been created at that dose.

The critical amorphization dose for the PLZT material increased with increasing irradiation temperature as is shown in Figure 5. This behavior is common for other materials [10,11] due to the competition between damage production and thermally activated recovery. At 450°C, no evidence of amorphization was observed above a dose of $1.1x10^{15}$ ions/cm^2 indicating an equilibrium between the two competing processes has probably been attained. The reason why sputter-deposited PLZT has a much lower dose for amorphization must be attributed to its lower density and higher porosity and more defective structures in comparison with that in the hot-pressed ceramic bulk material.

Conclusions

At room temperature, PLZT 9/65/35 single crystal samples prepared from bulk ceramic wafer were amorphized under a 1.5 MeV krypton ion irradiation with a dose of only $1.9x10^{14}$ ions/cm^2, less than one fifth of the critical amorphization dose for silicon ($1x10^{15}$ ions/cm^2), and the sputter deposited PLZT film took even smaller dose to become amorphous. The critical amorphization dose for the PLZT material increased with increasing irradiation temperature. At 450°C, amorphization was not observed above a dose of $1.1x10^{15}$ ions/cm^2. PLZT is sensitive to ion irradiation induced amorphization because of its high nuclear stopping power and complex crystal structure.

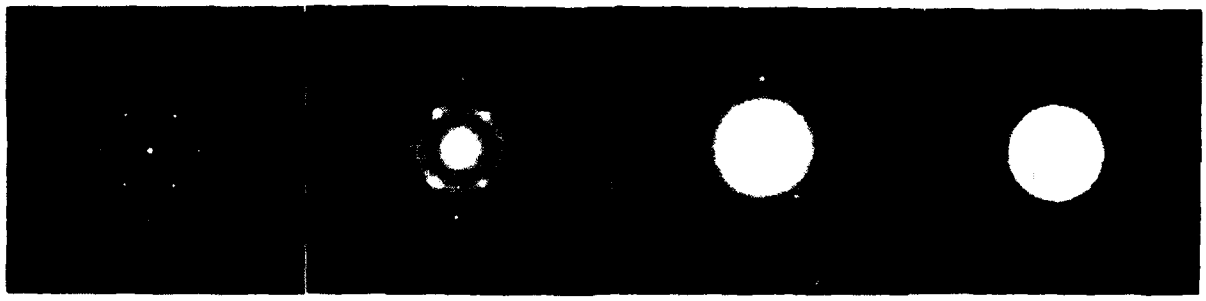


Figure 3. Electron diffraction patterns of Sa[110] zone irradiation at room temperature (a) unirradiated, (b) 5.4×10^{14}, (c) 8.8×10^{14}, and (d) 1.3×10^{15} ions/cm^2.

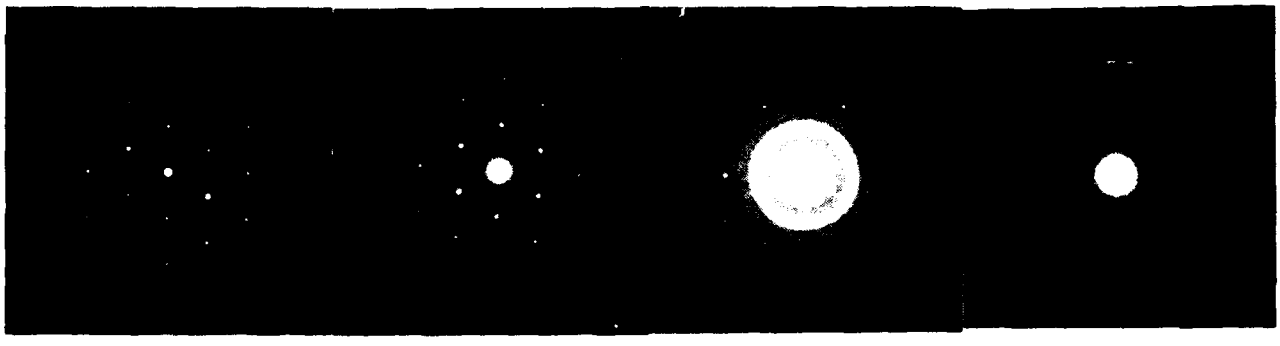


Figure 4. Electron diffraction patterns of <111> oriented PLZT 9/65/35 during irradiation at room temperature (a) original, (b) 5.1×10^{13}, (c) 1.2×10^{14}, (d) 1.9×10^{14} ions/cm^2.

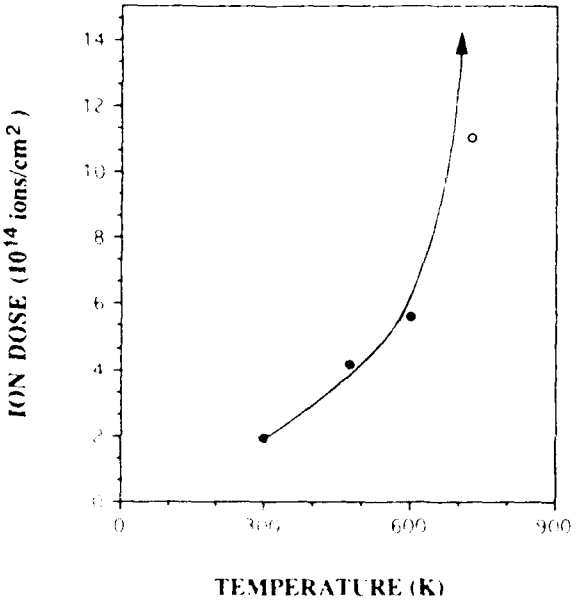


Figure 5. Temperature dependence of critical amorphization dose of 1.5 MeV Kr ion irradiated PLZT 9/65/35 single crystal TEM samples. Solid dots: amorphization completed, Open circle: no evidence of amorphization.

Acknowledgements

The authors wish to thank the HVEM-Tandem Facility Staff at the Argonne National Laboratory for assistance during ion irradiations. The electron microscopy was completed, in part, in the Electron Microbeam Analysis Facility of the Department of Geology of the University of New Mexico supported by NSF, NASA, DOE-BES, and the state of New Mexico. This work was supported by the Office of Basic Energy Sciences, US Department of Energy under grant DE-FG04-84ER45099, and Air Force Office of Scientific Research.

References

[1] Y. Higuma, Y. Matsui, M. Okuyama, T. Nakagawa, and Y. Hamakawa, Jap. J. Appl. Phys. Suppl. 17, 269 (1978).

[2] A. Y. Wu, F. Wang, C. B. Juang, and C. Bustamante, *Proceedings of the 7th International Conference on the Applications of Ferroelectrics* (Urbana, Illinois, 1990) p.643.

[3] C. E. Land and P. S. Peercy, Ferroelectrics, 45, 25 (1982).

[4] M. A. Tikle, I. M. Walpita, W. Chen, S. H. Lee, and W. S. C. Chang, Applied Optics 25, 1908 (1986).

[5] A. Navrotsky and D. J. Weidner, *Perovskite: A Structure of Great Interest to Geophysics and Materials Science* (American Geophysical Union, 1989), p. 146.

[6] C. W. Allen, L. L. Funk, L. A. Ryan, and S. L. Ockers, Nucl. Instr. and Meth. B40/41, 885 (1989).

[7] J. F. Ziegler, J. P. Biersack, and U. Littmark, *The Stopping and Range of Ions in Solids* (Pergamon, New York, 1985).

[8] D. E. Alexander (private communication).

[9] L. M. Wang and R. C. Ewing, MRS Bulletin 18(5) (1992), in Press.

[10] L. M. Wang and R. C. Birtcher, Philos. Mag. A64, 1209 (1991).

[11] R. C. Birtcher and L. M. Wang, Nucl. Instr. and Meth. B59/60, 966 (1991).

THE TEMPERATURE DEPENDENCE OF SOUND VELOCITIES, ELASTIC CONSTANTS AND ACOUSTIC ATTENUATION OF LEAD LANTHANUM ZIRCONATE TITANATE $(Pb,La)(Zr,Ti)O_3$

A. Y. Wu,[a] G. Nicolaides,[b] and D. M. Hwang[c]

Department of Physics
University of Illinois at Chicago
Chicago, Illinois 60680

[a]Now at the Center for High Technology Materials, University of New Mexico, Albuquerque, NM 87131.
[b]Now at the Department of Physics, Iowa State University, Ames, IA 50010.
[c]Now at Bell Communications Research, Red Bank, NJ 07701.

Sound velocities, elastic constants and acoustic attenuation in PLZT 9/65/35 bulk ceramic material have been determined by ultrasonic techniques between 1.2 and 470 K. Anomalous elastic behaviors, including broad dip in sound velocity and sharp cusp in attenuation were observed around the diffuse phase transition at 330 K. The sound velocity increases strongly and linearly with decreasing temperature at low temperatures. This behavior is different from that predicted by Debye lattice model. An unusually large 42% discrepancy between the elastic Debye temperature and the calorimetric Debye temperature was found which may be attributed to the disorderness nature in this ceramic material.

INTRODUCTION

Lanthanum modified lead zirconate titanate, $(Pb,La)(Zr,Ti)O_3$, or PLZT, is a ferroelectric ceramic of the perovskite structure with a diffuse phase transition [1-4]. The broadness of the dielectric constant maximum at T_C suggests a gradual transition from an unpolar high temperature phase to a polar ferroelectric phase. It has been found that the polarization is reversible above a temperature T_t ($T_t < T_C$, where T_C is the transition temperature) and irreversible below T_t [3]. The high disorderness in PLZT suggests a finite correlation length at the phase transition similar to that of glass transitions and one might expect that PLZT behaves like an amorphous dielectric material [3,4].

The purpose of this work is to measure the sound velocities and acoustic attenuation of PLZT in serach of anomalies due to phase transitions and glass-like behaviors, and to determine the elastic Debye temperature which is important in interpreting calorimetric results at low temperatures [5,6].

EXPERIMENTAL

A hot pressed PLZT ceramic sample of composition 9/65/35, or $Pb_{0.91}La_{0.09}Zr_{0.6211}Ti_{0.3421}O_3$, manufactured by Motorola Inc., was used in this sutdy. The sample was ground and polished into parallelepiped shapes suitable for sound velocity measurements and was thermally depoled at 600 °C for one day to eliminate residue stresses and strains. Elastic properties were determined by an ultrasonic phase comparison technique [7]. Electric pulses of width 1 μm, gated and amplified using a c.w. oscillator at 11 MHz, were converted into ultrasonic pulses by quartz transducer bonded on the sample. The echo trains were picked-up by the same transducer and phase-compared with the c.w. signal. The transit time t, or the round trip time-of-flight, of the echo was determined to within an accuracy of 1 nsec or 0.05%, at temperatures away from phase transitions. From the transit time, and the thickness and density of the sample, the sound velocity can be calculated. The ultrasonic measurement system has been described elsewhere [7].

The longitudinal and shear sound waves were generated by activating X- and AC-cut quartz transducers with active area of 2.5 mm in diameter, bonded onto the PLZT sample of thickness 0.5984 cm, respectively. For the longitudinal mode, Dow Corning DC200 fluid was used as the bonding agent in the temperature range of 1.2 and 470 K. For the transverse mode, DC200 fluid, DC276V9 resin, and Ren Plastic epoxy were used in the temperature ranges of 1.2-200 K, 120-300 K, and 250-405 K, respectively. The low temperature measurement system has been described elsewhere [7].

RESULTS

The longitudinal and shear sound velocities v_L and v_s, where $v = 2d/t$ and d is the sample thickness, were measured from the phase comparison method. The corresponding elastic constant C_L and C_S, where $C = \rho v^2$ and $\rho = 7.810$ gm/cm^3 is the sample density, determined from the Archimedes method, were deduced from the sound velocities. (The theoretical density, however, is 7.84 gm/cm^3 as calculated by using the molecular weight of 323.4 gm/mol and the lattice constant $a = 4.091$ Å from our x-ray powder diffraction determination). The ultrasonic attenuation was determined by measuring the amplitudes of successive sound echoes and the best least square linear fit of the logarithms of amplitudes of the sound echo trains. Because of the lack of complete published thermal expansion data of PLZT ceramic material at low temperatures, sample thickness and thus density were not corrected for temperature changes. The results of the sound velocities, elastic constants, and attenuation as a function of temperature are shown in Figure 1 to 6. Within our experimental errors we found that there is no significant hysteresis in the sound volecity or attenuation measurements as a function of temperature scans.

As can be seen from Figure 1, 2, 4 and 5, both the longitudinal and shear velocities and elastic constants exhibit a broad and diffuse depression at 330 K. This depression lies between T_C = 360 K and the reversible-irreversible transition temperature T_t = 290 K. The ultrasonic attenuations shown in Figure 3 and 6 show strong temperature dependence. The longitudinal elastic constant

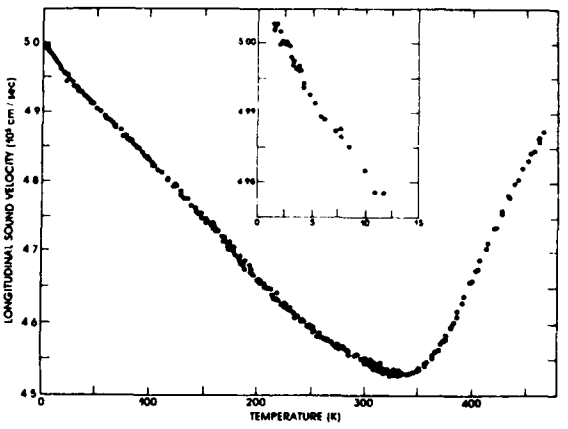


Figure 1. The longitudinal sound velocity of PLZT 9/65/35.

CH3080-0-7803-0465-9/92$3.00 ©IEEE

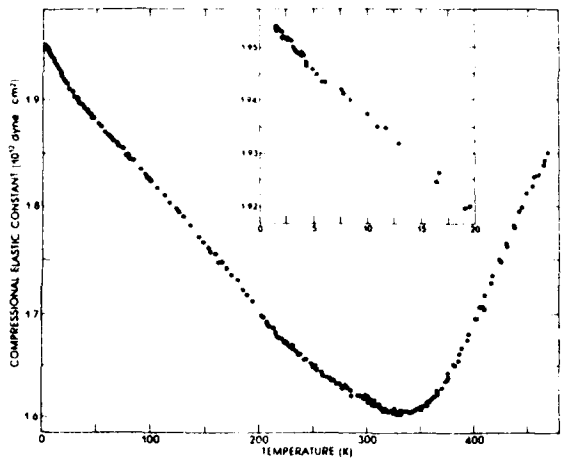


Figure 2. The compressional elastic constant of PLZT 9/65/35.

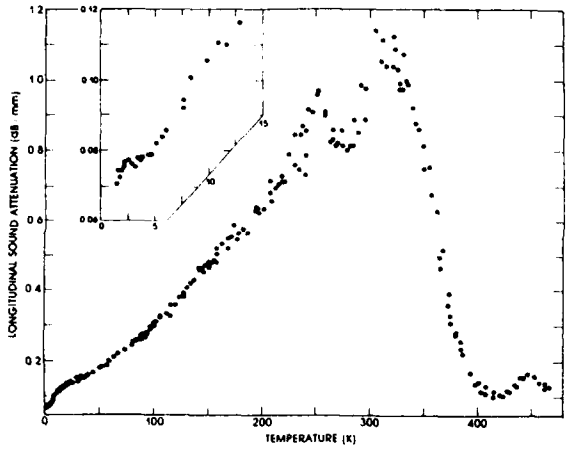


Figure 3. The longitudinal ultrasonic attenuation of PLZT 9/65/35.

has a major attenuation peak at 315 K and minor peaks at 250 and 450 K. In the case of the transverse mode, the major attenuation peak is at 290 K and the minor peaks are at 250 and 350 K. There are also small fluctuations in the shear elastic constant at 280 and 350 K, associated possibly with the attenuation peaks.

The details of the low temperature behavior are shown in the inserts of Figure 1 to 6. The sound velocity and elastic constant increase while the sound attenuation decreases as the temperature decreases, and the sound velocity shows a linear temperature dependence for both the longitudinal and shear modes, suggesting that the material has a glass-like behavior [8]. It is very interesting to see that there is no sign of any "leveling-off" effect for both of the velocity modes at the lowest temperature of 1.2 K. This phenomenum can not be explained by the Debye lattice theory [9] because in that theory the elastic constant of ordinary solid dielectric material should have a temperature dependence of $(1-cT^4)$, where c is a constant, at the absolute zero.

DISCUSSION AND CONCLUSIONS

The existence of the unusually broad and strong softening of the elastic constants and the drastic changes in the attenuation at the diffuse phase transition in PLZT suggest that the long range orders associated with the polar to unpolar phase transition are accomplished at around 330 K, and both the volume and linear piezoelectric couplings are strong in this material. However, the fact that phase transition is diffuse and not sharp must be due to the randomness and ceramicity nature of the material: That is, the very diffuse mode softenings and attenuation peaks at the transition are caused by the fluctuations of medium or short range orders inside the randomly distributed ceramic grains directly related to the variations in the ferroelectric moments, grain boundaries, domains, domain walls, etc. We speculate that this medium or short range correlation length should be on the order of a few Å up to the domain or domain wall sizes which may be much smaller than the grain size which in this sample has an averaged value of 8 μm.

It is interesting to note that the attenuation peak and the velocity dip have a one-to-one correspondence: The broad and diffuse peak in the attenuation corresponds to the broad and diffuse dip in the velocity. This suggests that the observed anomalies in attenuation and velocity change all stem from a same relaxation process through the following Kramers-Kronig type relations [8,11]:

$$\ell^{-1} = \frac{D^2}{4\rho v^3 kT} \int_0^\infty P(V) \frac{\omega^2 \tau(V)}{1 + \omega^2 \tau^2 (V)} dV , \qquad (1)$$

and

$$\frac{\Delta v}{v} = \frac{D^2}{8\rho v^2 kT} \int_0^\infty P(V) \frac{dV}{1 + \omega^2 \tau^2 (V)} , \qquad (2)$$

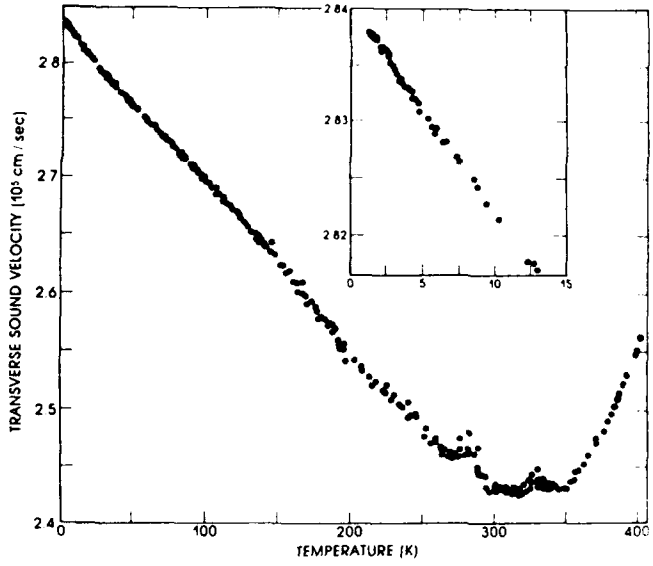


Figure 4. The transverse sound velocity of PLZT 9/65/35.

where D is the deformation potential or the energy shift of the relaxing state due to acoustic strain, P(V) is the distribution of the activation energy V, $\tau = \tau_0 \exp(V/kT)$ is the Arrhenius relation for the relaxation time τ, and ω is the sound frequency. These relations have proven to be useful for describing both the crystalline and the disorder systems [8] and might be useful for describing PLZT material qualitatively. Unfortunately, material parameters such as D, P(V), and $\tau(V)$ in PLZT can not be obtained uniquely by a simple curve fitting precedure using

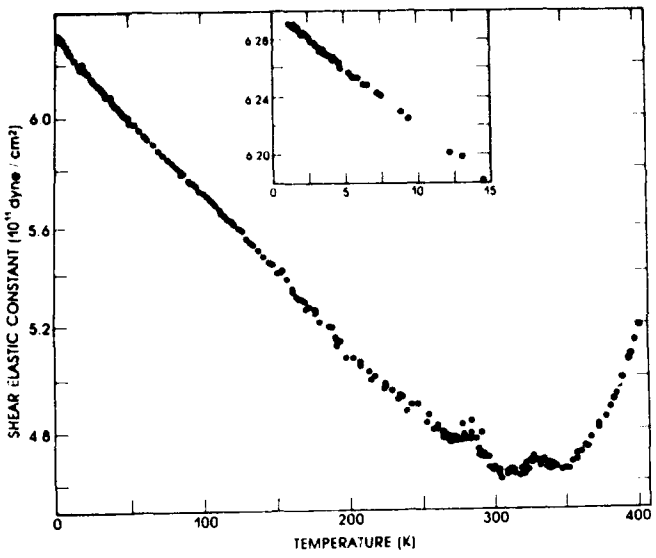


Figure 5. The shear elastic constant of PLZT 9/65/35.

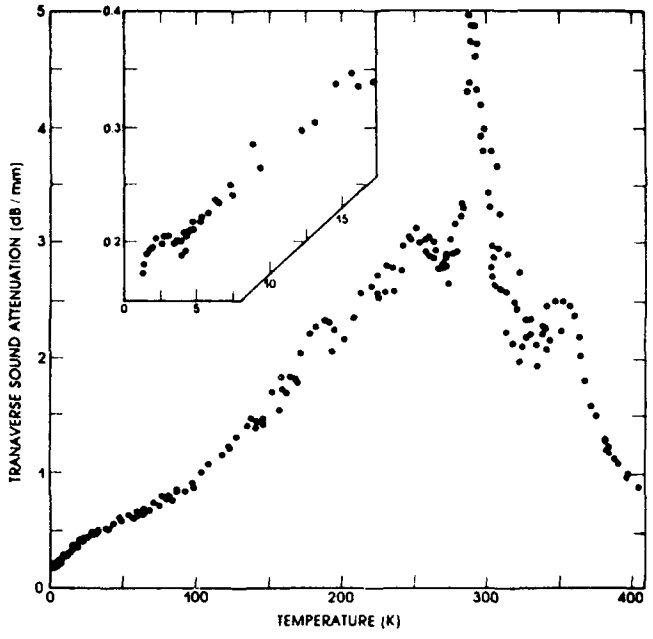


Figure 6. The transverse ultrasonic attenuation of PLZT 9/65/35.

formulae (1) and (2) because the phase transition in PLZT is too strong, too broad, and too diffuse which prohibit us from estimating the true background velocity or attenuation value in the entire temperature range so that it is difficult from our data to deduce the actual velocity or attenuation changes due to the phase transition. Furthermore, because of the ceramicity nature of PLZT, D, P(V), and τ (V) may not be single-valued but may have broad spectrum of values because of the random distribution of grain and domain sizes.

It is clear that PLZT material does not behave like an ordinary Debye solid at all because an ordinary Debye solid must have a leveling-off effect at the absolute zero. The non leveling-off of the elastic constants down to 1.2 K suggests that some unusual mode vibrations other than the zero point lattice vibrations may not be totally frozen out near the absolute zero.

To further explore the unusual behavior, we have calculated the elastic Debye temperature of PLZT from the following relation [11]:

$$\Theta^{elast} = \frac{h}{k}\left(\frac{3QN_0\rho}{4\pi W}\right)^{1/3}\left(\frac{1}{3v_L^3}+\frac{2}{3v_S^3}\right)^{-1/3}, \quad (3)$$

where h is the Plank constant, k is the Boltzmann's constant, Q = 5 is the number of atoms per formula unit, N_o is the Avogadro's number, and W is formula weight. Using the measured sound velocities at 1.2 K, v_L = 5.00 x 10^5 cm/sec and v_s = 2.84 x 10^5 cm/sec, we deduced the elastic Debye temperature Θ_D of 392 ± 4 K, which is 42% larger than the calorimetric Debye temperauture Θ_D of 225.7 K reported by Lawless from specific heat measurements [5,6]. This unusually large discrepancy between the elastic and calorimetric Debye temperatures suggests that the acoustic lattice vibrations can not account for all the Debye terms in the specific heat, and at the lowest temperature, *about 80% of the measured specific heat in PLZT material is due to contributions from some excitations other than ordinary acoustic vibrations.* We suggest that the random distributions of ceramic grains, the substitutional Pb and La on the A-site and Zr and Ti on the B-site in PLZT lattice, the A-site and B-site vacancies, the possible interstitial species, and the multiple orientational states of ferroelectric moment are all intrinsic in the defective perovskite structure of PLZT ceramic material. These randomnesses may result in many low lying modes in PLZT, similar to the two-level systems caused by double-well potentials in glass or disordered solid from a statistical calculation [12]. These low lying modes, on the average, can contribute an extra large term to the heat capacity of PLZT and caused the observed linear velocity dependence at low temperatures. Other low lying modes may involve domain walls excitations or quantized ferroelectric polarization waves similar to quantized spin waves in magnetic materials, but we do not have direct evidence of the existence of such modes at the present time.

Acknowledgement
This work was supported in part by the Atlantic Richfield Foundation Grant for Research Corporation No. 9422.

REFERENCES

[1] J. T. Krause, H. M. O'Bryan, Jr., J. Am. Ceramic Soc. **55**, 497 (1972).
[2] G. A. Smolensky, J. Phys. Soc. Japn. **28**, 26 (1970).
[3] E. T. Keve and A. D. Annis, Ferroelectric **5**, 77 (1973).
[4] (a) G. Schmidt, H. Arndt, G. Borchardt, J. Von Cierminski, T. Petzsche, K. Borman, A. Sternberg, A. Zirnite, and V. A. Isupov, Phys. Stat. Sol. (a) **63**, 501 (1981). (b) E. Fischer, W. Hassler, E. Hegeabarth, and V. I. Fritsberg, Phys. Stat. Sol. (a) **66**, K1, 69 (1981).
[5] W. N. Lawless, Ferroelectric **14**, 134 (1976).
[6] W. N. Lawless, Ferroelectric **15**, 61 (1977).
[7] D. M. Hwang, Sol. Stat. Commu. **46**, 177 (1983).
[8] S. Hunklinger and W. Arnold, in *Physical Acoustics*, edited by W.P. Mason and R.N. Thurston (Academic Press, New York, 1976), Vol. XII, p. 155.
[9] M. Born and K. Huang, *Dynamical Theory of Crystal Lattices* (Oxford University, London, 1968), Chap. III.
[10] O. L. Anderson, in *Physical Acoustics*, edited by W.P. Mason (Academic Press, New York, 1965), Vol. IIIB, p. 43.
[11] J. Jackle, L. Piche, W. Arnold, and S. Hunklinger, J. Non-Cryst. Solids, **20**, 365 (1976).
[13] P. W. Anderson, B. I. Halperin, and C. Varma, Philos. Mag. **25**, 1 (1972).

DIELECTRIC, PYROELECTRIC AND PIEZOELECTRIC PROPERTIES IN THE RELAXOR FERROELECTRIC (1-x-y) $Pb(Mg_{1/3}Nb_{2/3})O_3$-x$PbTiO_3$-y$PbZrO_3$ SYSTEM.

J. S. Ko, Y. J. Kim, Y. H. Shin*, and S.W.Choi
Department of Physics, Dankook University,
29 Anseodong, Cheonan, Chungnam, Korea
* Cheonan National Junior Technical College

Abstract

Dielectric, pyroelectric and piezoelectric properties of relaxor ferroelectric in the (1-x-y)$Pb(Mg_{1/3}Nb_{2/3})O_3$-x$PbTiO_3$-y$PbZrO_3$ solid solution series have been investigated. The dielectric constant and loss of poled ceramic samples were determined. The pyroelectric coefficient was measured by the static Byer-Roundy method as a function of temperature. Electromechanical coupling factor (Kp) was measured by using the resonance-antiresonance method. The addition of $PbZrO_3$ affects the dielectric and pyroelectric properties of PMN-PT and transition temperature is continuously shifted to lower temperature with increase of a small amount of $PbZrO_3$. The composition with the maximum electromechanical coupling factor exhibits the high dielectric and pyroelectric properties.

Introduction

In the composition PMN-PT system, morphotropic phase boundary exists near 35mol% of PT[1,2]. The composition near MPB shows a large dielectric, pyroelectric coefficient, much larger than those of PZT ceramics. In the case of the most of PMN-PT series transition temperature is above room temperature. With an addition of $PbZrO_3$ (Tc = 230°C) the transition temperature can be suitably adjusted for the pyroelectric and piezoelectric applications.

In this paper, we used the columbite precursor method[3] so as to stabilized perovskite structure. Dielectric constant and electromechanical coupling factor of the PMN-PT-PZ system are high at the compositions near the morphotropic transformation[4]. The dielectric, pyroelectric and piezoelectric properties of the PMN-PT-PZ system near the morphotropic phase boundary system (PMN-PT) are described.

Experimental procedure

In the ternary system 0.60PMN-(0.40-x)PT-xPZ and 0.70PMN-(0.30-x)PT-xPZ compositions were prepared at x = 0.05 to 0.30. The raw materials were reagent grade oxide powders. We first prepared the columbite structure $MgNb_2O_6$, and the precursor materials were then mixed in stoichiometric ratio with PbO, TiO_2, and ZrO_2. Mixed powders were dried and calcined at 700°C for 2 hr. After ball milling, powders were cold pressed to form disks, followed by sintering at 1250°C for 2 hr. PbO volatilization during sintering was minimizing by surrounding each pellet with " atmosphere powder" of identical chemical compositions. The sintered samples were characterized by X-ray diffraction to insure phase purity. For electrical measurements, the samples were polished down to have same physical dimension, and gold electrodes were sputtered on the surfaces of pellet.

Temperature dependence of dielectric constant and loss tangent were measured of 0.1, 1, 10 and 100kHz at the temperature rate of 4°C/min with a multi-frequency LCR meter. Pyroelectric coefficient was measured by the static Byer-Roundy method[5] as the samples were heated, again at a rate of 4°C/min, through the phase transition region. Prior to the dielectric, pyroelectric and piezoelectric measurements the specimens were poled by applying a DC field of about 20 kV/cm while cooling from well above the transition to a temperature well below. Electromechanical coupling factor was measured by using the resonance-antiresonance method[6].

Results and Discussion

Dielectric properties

Figure 1 shows the typical plot of the dielectric constant and loss tangent at various frequencies(100 Hz - 100 kHz) as a function of temperature for a composition 0.60PMN-0.22PT-0.18PZ. The dielectric constant vs. temperature data depict the typical relaxor behavior of this composition.

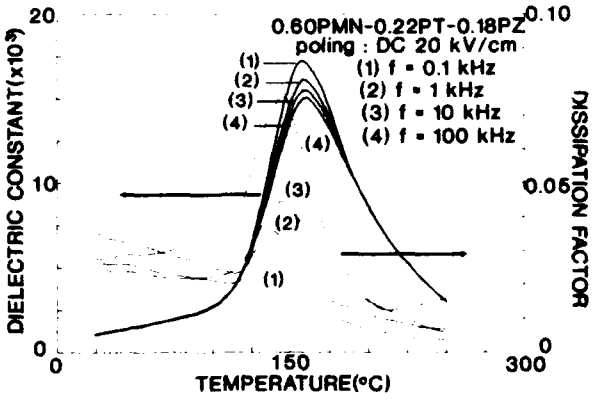


Figure 1. Temperature dependence of dielectric constant and dissipation factor at various frequencies for 0.60PMN-0.22PT-0.18PZ system.

When the samples were poled and x varied from 0.05 to 0.30, the dielectric behavior on various compositions showed a increase in Tc with decreasing of mole fraction of PZ. Dielectric constant increases with increasing mol%PZ. However, for x more than 0.18, the dielectric constant decreased(Fig. 2). Figure 3 shows the dielectric behavior on the 0.70PMN-(0.30-x)PT-xPZ (x = 0.05 - 0.28) solid solution system might be similar to that observed in the dielectric constant vs. temperature studies for the composition 0.60PMN-(0.40-x) PT-xPZ. In each series the maximum dielectric constant is observed for the compositions 0.60PMN-0.22PT-0.18PZ and 0.70PMN-0.15PT-0.15PZ, respectively.

Transition temperature of PMN, PT and PZ are -15°C 490°C and 230°C, respectively. As the transition temperature is expected to vary with the compostition, in each series. Figure 4 shows the variation in transition temperature with composition x of system PMN-PT-PZ series.

CH3080-0-7803-0465-9/92$3.00 ©IEEE

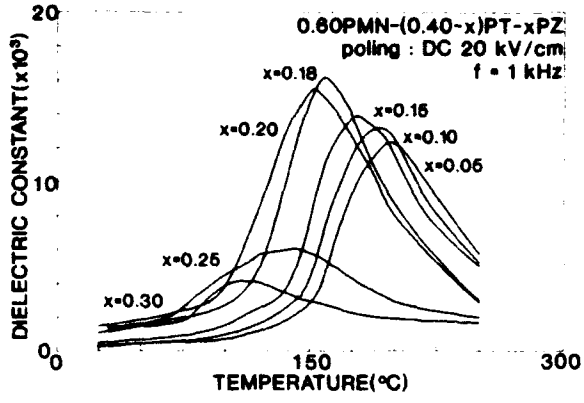


Figure 2. Dielectric constant vs. temperature in the 0.60PMN-(0.40-x) PT-xPZ system.

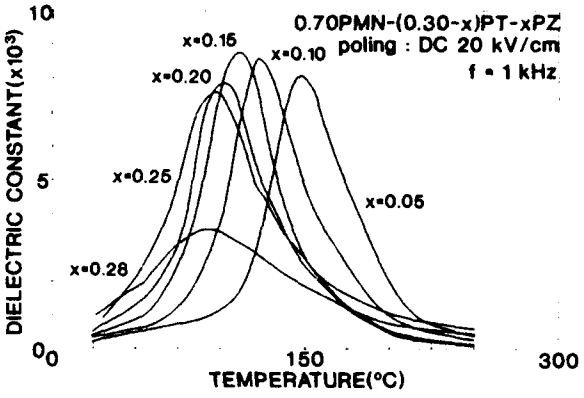


Figure 3. Dielectric constant vs. temperature in the 0.70PMN-(0.30-x)PT-xPZ system.

The addition of $PbZrO_3$ affected the dielectric properties of PMN-PT and the phase transition temperature is continuously shifted to lower temperature with increase of a small amount of $PbZrO_3$, their rates of decrease are about 3-5°C/mol%. With an addition of $PbZrO_3$ the transition temperature of the(1-x-y) PMN-xPT-yPZ can be suitably adjusted for the room temperature dielectric applications.

Pyroelectric and piezoelectric properties

Figures 5 and 6 show the pyroelectric coefficient for various compositions in the 0.60PMN-(0.40-x)PT-x PZ and 0.70PMN-(0.30-x)PT-xPZ solid solutions, respectively, as a function of temperature. In the compositions 0.60PMN-(0.40-x)PT-xPZ and 0.70PMN-(0.30-x)PT -xPZ pyroelectric coefficient increases with mol% PZ. However, in each series for x less than 0.18 and 0.15, respectively, the pyroelectric coefficient decreased. The composition with maximum pyroelectric coefficient might be similar to that observed in K vs. T studies.

The variation of peaktemperature with composition is shown in Figure 7. The peak temperature of pyroelectric coefficient is continuously shifted to lower temperature with increase of an amount of $PbZrO_3$, their rates of decrease are about 2-3°C/mol%. However, especially at x = 0.22-0.30 it is observed that two peaks are existed in the P vs. T measurements as

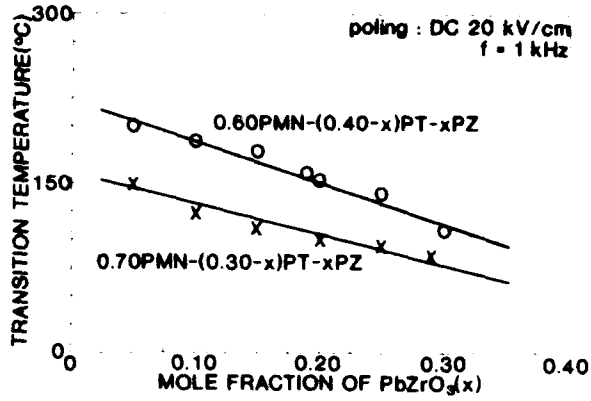


Figure 4. Variation of the transition temperature as a function of the mole fraction of PZ.

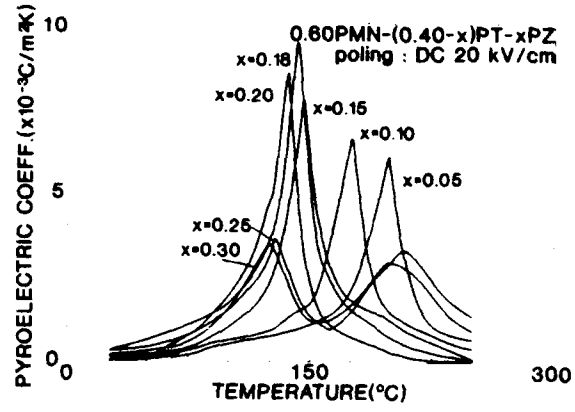


Figure 5. Pyroelectric coefficient vs. temperature in the 0.60PMN-(0.40-x)PT-xPZ system.

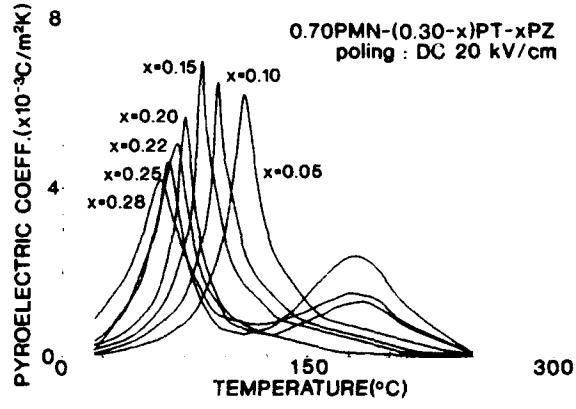


Figure 6. Pyroelectric coefficient vs. temperature in the 0.70PMN-(0.30-x)PT-xPZ system.

shown in Figures 5 and 6. This suggests a change of property behavior of ferroelectric materials in such regions. The broadening of the two peaks in P vs. T may be due to the coexistence of the ferroelectric and paraelectric phases. But this phenomena can not be fully explained at present work.

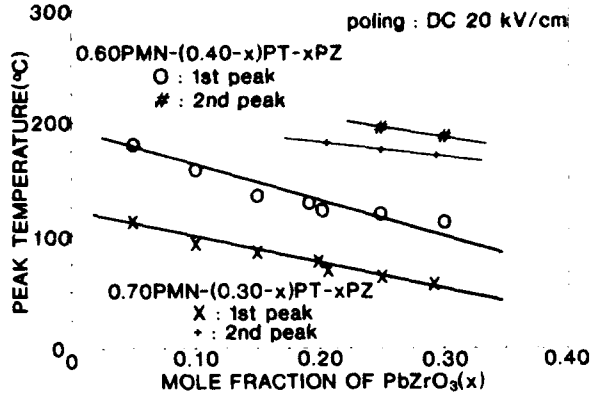


Figure 7. Peak temperature of pyroelectric coefficient plotted as a function of the mole fraction of PZ.

Figure 8 shows the electromechanical coupling factor at room temperature of the compositions 0.60 PMN-(0.40-x)PT-xPZ and 0.70PMN-(0.30-x)PT-xPZ solid solution series as the mole fraction of PZ. The maximum of the electromechanical coupling factor occurs in the compositions 0.60PMN-0.22PT-0.18PZ(0.40) and 0.70PMN-0.15PT-0.15PZ(0.35). The compositions are in good agreement with those exhibiting maximums in dielectric constant and pyroelectric coefficient.

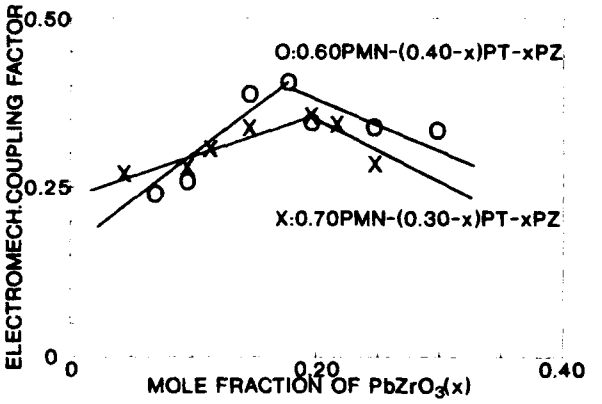


Figure 8. Electromechanical coupling factor as a function of mole fraction of PZ at the room temperature.

Conclusions

The addition of $PbZrO_3$ affects the dielectric, pyroelectric and piezoelectric benavior of PMN-PT system. With an addition of $PbZrO_3$ to the PMN-PT system the phase transition temperature of the PMN-PT-PZ system is continuously shifted to lower temperature with increase of an amount of $PbZrO_3$. The composition with the maxmium electromechanical factor exhibits relatively superior dielectric and pyroelectric properties. With an addition of $PbZrO_3$ to the PMN-PT system the phase transition temperature of the PMN-PT-PZ solid solution series can be suitably adjusted for the room temperature dielectric applications.

Acknowledgement

This work was supported by the Korea Science and Engineering Foundation (KOSEF) through the Science Research Center (SRC) of Excellence Program.

References

(1) S.W.Choi, T.R.Shrout, S.J.Jang and A.S.Bhalla, "Morphotropic Phase Boundary in $Pb(Mg_{1/3}Nb_{2/3})O_3$-$PbTiO_3$System," Materials Letters, vol.8, pp.253-255, July 1989.

(2) S.W.Choi, T.R.Shrout, S.J.Jang and A.S.Bhalla, "Dielectric and Pyroelectric Properties in the $Pb(Mg_{1/3}Nb_{2/3})O_3$-$PbTiO_3$ System," Ferroelectrics, vol. 100, pp.29-38, 1989.

(3) S.L. Swartz and T.R.Shrout, "Fabrication of Perovskite Lead Magnesium Niobate," Mater.Res.Bull., vol. 17, pp.1245-1250, 1982.

(4) H.Ouchi, K.Nagane and S.Hayakawa, "Piezoelectric Properties of $Pb(Mg_{1/3}Nb_{2/3})O_3$-$PbTiO_3$-$PbZrO_3$ Solid Solution Ceramics," J.Am.Ceram.Soc., vol.48(12), pp. 630-635,1965.

(5) R.L. Byer and C.B. Roundy, "Pyroelectric Coefficient Direct Measurement Technique and Application to a NSEC Response Time Detector," Ferroelectrics, vol.3. pp.333-338, 1972.

(6) IRE Standands on Piezoelectric Crystal: Measurement of Piezoelectric Ceramics, Proc. 1961," IRE(Inst.Radio Engrs.) vol.49 (7), pp.1161-1169, 1961.

INFLUENCE OF HIGH ENERGY GRINDING ON THE TEXTURE, STRUCTURE AND ELECTRICAL PROPERTIES OF BARIUM TITANATE

JM Criado, F Gotor, L Perez-Maqueda, C Real, M Mundi and J del Cerro
Material Science Institute P Box 1065 Sevilla Spain

Abstract

It is shown that nanocrystalline barium titanate can be obtained from high energy ball-milling of conventional barium titanate powder available in the market X-ray investigations, surface determination and dielectric studies have been carried out on several samples obtained with different periods of grinding It is deduced that the stabilization of the cubic phase at room temperature occurs for values of grain size and coherently diffracting domain size of 0.12 μm and 2.5×10^2 A respectively.

Introduction

It has been found that the stabilization of the cubic phase in $BaTiO_3$ (BT) depends on its microstructure Uchino et al.[1] have compared the crystallographic structure of BT with the sample grain size (**g**) as determined from the BET surface, concluding that at room temperature the change from tetragonal to cubic symmetry occurs at a critical particle size of 0.12 μm.

The Constant Rate Thermal Analysis (CRTA) technique has been used[2] under different experimental conditions to obtain BT powders of very small grain size. These particles are formed by small crystallites welded in a mosaic structure in such a way that **g** is not equivalent to the coherently diffracting domain size (**D**). Both a crystallographic and a dielectric studies were carried out[3-5] on these samples and it was deduced that the stabilization of the cubic phase at room temperature depends on **D** rather than **g** and this stabilization occurs when **D** is lower than 2.5×10^2 A.

For this paper, commercial BT powder has been ground in a high energy ball-milling as a function of time. X-ray investigations, surface area determinations and dielectric study of these samples ascertain the above results.

Experimental

Several samples were obtained by grinding Aldrich commercial $BaTiO_3$ powder between 0 to 150 min For grinding, a high energy ball- mill (whose characteristics are 7.5 cm, 730 r.p.m. and Tungsten Carbide balls) has been used

X-ray investigations of the above samples were carried out with a diffractometer (Philips 1750) using CoKα radiation and graphite monochromator The size of the coherently diffracting domain of BT samples has been determined from the analysis of the (111) profiles by Sherrer's method[6] that supplies reliable values of this parameter On the other hand, the (200) peaks have been also studied to see the vanishing of the tetragonality.

Surface area determination of BT powders was carried out using a single point BET method with an Adsorptmeter Micromeritic model 2000.

With the above samples, several pellets were prepared and later sintered The dielectric constant of these samples was measured using a SP-5240 ESI Capacitance Bridge.

Results and discussion

In table 1 the influence of the grinding time on the textural characteristics of the samples is shown. As it was expected, these data indicate that the increase of the grinding time leads to a decrease of both **g** and **D**.

Table 1

Textural characteristics of the samples

Sample	Grinding time (min)	**g** (μm)	**D** (Å)
A	0	0.26	1688
B	2	0.22	682
C	5	0.18	539
D	10	0.17	400
E	15	0.15	315
F	30	0.14	264
G	45	0.12	256
H	60	0.10	213
I	90	0.09	202
J	150	0.04	192

CH3080-0-7803-0465-9/92$3.00 ©IEEE

The (200) XRD profile of the samples in table1 have been studied, in Figure 1 the peaks corresponding to samples A, C and F are shown. We can see that the tetragonal splitting decreases with the grinding time and it practically dissapears at sample F, whose **g** and **D** are 0.14 μm and 264 A respectively.

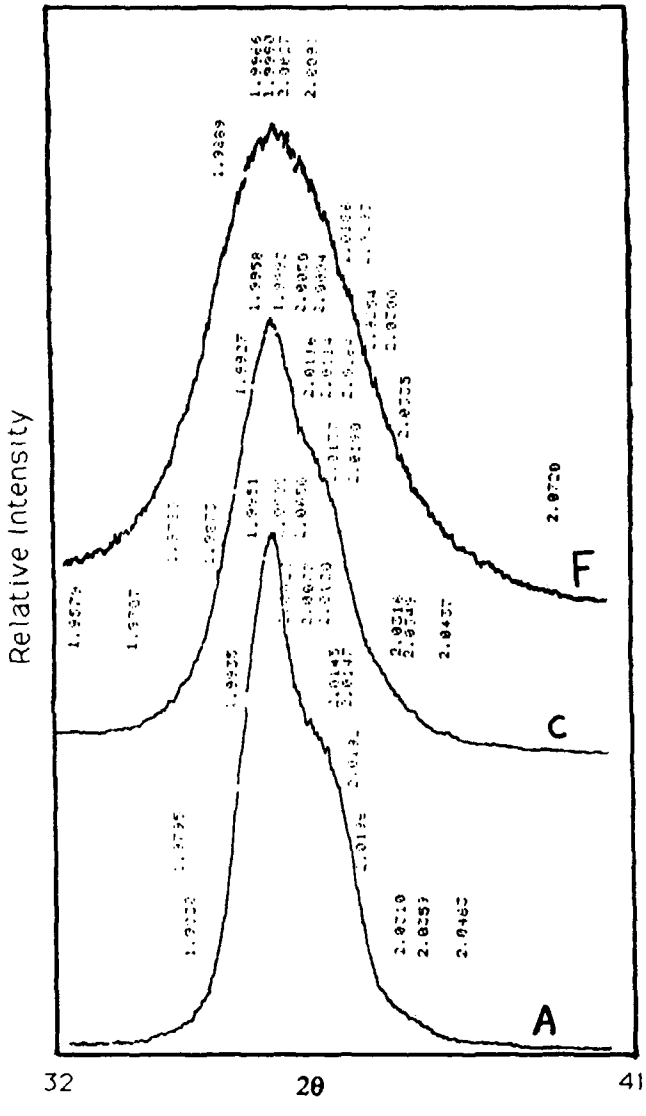


Figure 1.- Powder X-ray diffraction (200) peak of barium titanate milled for: A) 0 min, C) 5 min and F) 30 min.

The dielectric constant of sample G (without sintering and whose **g** and **D** are 0.12 μm and 256 A respectively) is represented as a function of the temperature in Figure 2a. This curve shows that sample E is cubic at room temperature. When this sample was later sintered, the tetragonal phase is recovered at room temperature as we can see in Figure 2b.

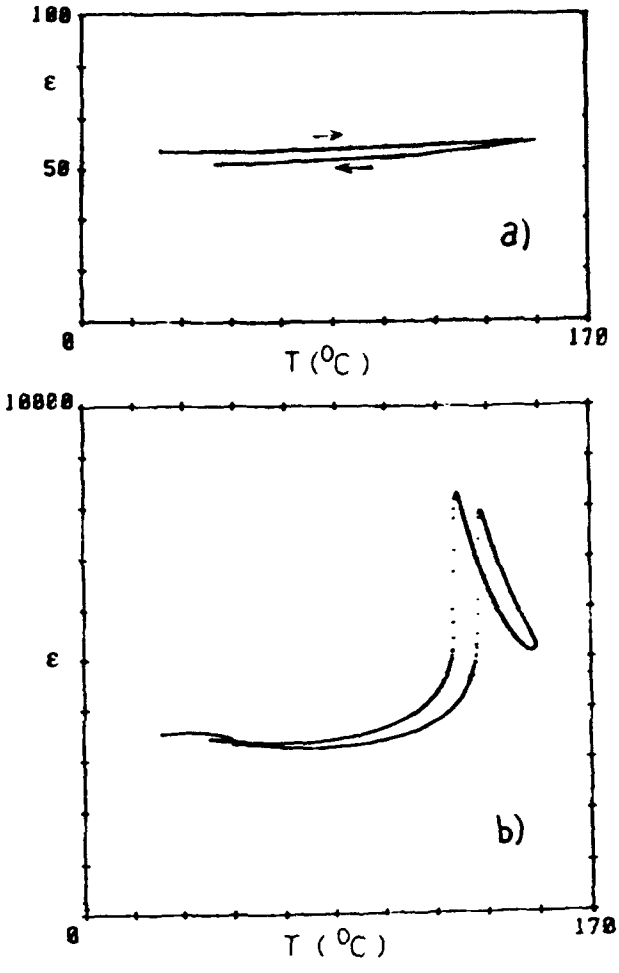


Figure 2.- Dielectric constant of sample G versus temperature: a) without sintering and b) sintered at 1700 K.

According to the above results, which are in agreement with those found by Uchino et al.[1] and in our previous papers[4,5], we can deduce that the stabilization of the cubic phase at room temperature occurs for values of **g** and **D** lower than 0.12 μm and 2.5×10^2 A respectively.

On the other hand, using CRTA method at a pressure of 10 mbar, barium titanate powder was obtained[4] with values of **g** and **D** equal to 0.15 μm and 246 A respectively. It was shown that this sample, whose particles are formed by small crystallites welded in a mosaic structure, is cubic at room temperature.

From the above data it is possible to conclude:

a) nanocrystalline barium titanate can be obtained from high energy ball-milling of conventional BT powder available in the market.

b) when the particles behave as single crystals, (like the ones studied by Uchino et al.[1] and in this paper),

the stabilization of the cubic phase at room temperature occurs for values of **g** and **D** lower than 0.12 μm and 2.5×10^2 Å respectively.

c) when the particles do not behave as single crystals, (like the ones obtained by means of CRTA method[3-5]), the stabilization of the cubic phase at room temperature depends on **D** rather on **g**, and it occurs for **D** lower than 2.5×10^2 Å.

Acknowledgement

This work has been supported by the projects PB88-267 and MAT87-195 of the Spanish DGICYT.

References

[1] K. Uchino, E. Sadanaga and T. Hirose, "Dependence of the crystal structure on particle size in barium titanate", J. Am. Ceram. Soc. **72**, 1555-1558, 1989.

[2] J.M. Criado, F. Gotor, C. Real, F. Jimenez, S. Ramos and J. del Cerro, " Application of the CRTA technique to the microstructure control of barium titanate yielded from coprecipitated oxalate", Ferroelectrics, **115**, 43-48, 1991.

[3] J.M. Criado, M.J. Dianez, F.Gotor, C. Real, F.Jimenez, S.Ramos and J. del Cerro, "Influence of particle size on the crystalline structure and both the sintering and electrical properties of barium titanate", 1990 IEEE, Proceedings of 7th International Symposium on Applications of Ferroelectrics, pp 36-39.

[4] J.M. Criado, M.J. Dianez, F. Gotor, C. Real, M. Mundi, S.Ramos and J. del Cerro, "Correlation between synthesis conditions, coherently diffracting domain size and cubic phase stabilization in barium titanate", Ferroelctric Lett. **14**(3), 79 (1992)

[5] J. del Cerro, M. Mundi, C. Gallardo, J.M. Criado, F.Gotor and A.S. Bhalla, "Sintering temperature influence on phase stability in barium titanate ceramics with very small grain size" Ferroelectrics, **127**, 59-64 , 1992.

[6] H.P. Klug and L.E. Alexander, "X-ray diffraction procedures for polycrystalline and amorphous materials", John Wiley, New York, 1974.

90° - Domain Reversal in $Pb(Zr_xTi_{1-x})O_3$ Ceramics

Shaoping Li*, Chi-Yuen Huang**, A.S. Bhalla*, L.E. Cross*

* Materials Research Laboratory, The Pennsylvania State University, University Park, PA 16802

** Department of Mineral Engineering, National Cheng Kung University, Tainan, Taiwan, 70101

Abstract

In this study, a simple and direct method has been proposed, which allows to be used for quantitatively distinguishing the mechanisms of domain reorientation processes in polycrystalline materials. By using this method, the 90° - domain reorientation in the $Pb(Zr_xTi_{1-x})$ ceramic under the electric field was examined through the X-ray diffraction analysis. It was found that the polarization switching in the PZT ceramic with the composition near the morphotropic phase boundary is predominantly controlled by the two successive 90° domain processes rather than 180° domain wall reversal. Experimental results also indicate that the coercive field of the ceramics is related to the cooperative deformation associated with each grain, which arises from 90°- domain reversal process.

I. Introduction

The interrelationship between the dynamic behaviors and the microstructures (intrinsic domain structures) of ferroelectric ceramics is of great significance. The investigation of polarization reversal in ferroelectric ceramics is of both theoretical and practical interest. Recently, a lot of efforts have been put into developing polycrystalline ferroelectric thin films as non-volatile memory devices using the capability of switching the direction of remnant polarization under the influence of an electric impulse. In fact, the polarization reorientation processes are intimately associated with the basic dynamic memory capability and the switching threshold of polycrystalline thin film memory devices, as well as the basic fatigue and degradation behavior of thin film devices. With regard to this, the mechanisms of the domain reversals in PZT polycrystalline systems have a special and important aspect.

Early investigations for the dynamical behavior of 90° type domain walls (90° in tetragonal, 71° and 109° in the rhombohedral phase) and 180° domain walls in PZT ceramics have been carried out in the past three decades [1-6]. Based on the bias dependence measurements of dielectric constants, polarization, and spontaneous strain in certain PLZT ceramic systems, it has been suggested that the processes of polarization reversal may be characterized by two successive 90° type domain processes rather than by the direct 180° domain switching processes. Apparently, all previous research results seemed to be adequate, however, they are by no means quantitatively conclusive because no any direct experimental methods could distinguish the mechanisms of the polarization reversal processes in the polycrystalline materials.

In general, the mechanism of polarization reversal processes in single crystals is explained by the nucleation and growth of new antiparallel domains. Ferroelectric ceramics consists of many randomly orientated grains. Therefore, the polarization reversal mechanism and switching behavior in ferroelectric polycrystalline materials is rather complicated and depends upon many conditions[7]. Usually, the polarization reversal processes in ferroelectric polycrystalline materials is substantially different from those in single crystals. In this work, a simple and direct method has been proposed, which can be used for quantitatively distinguishing the mechanisms of domain reorientation processes in polycrystalline materials. It has been directly confirmed that the polarization switching processes in PZT ceramic with the composition within the morphotropic phase boundary is predominantly dependent upon two successive 90° domain reversal processes.

II. Experimental Procedure

The specimens used here are of chemical composition: $Pb(Zr_{0.52}Ti_{0.48})O_3$ + 0.5 wt.% Nb_2O_5, which is within the morphotropic phase boundary. The ceramics were prepared by the conventional mixed-oxide process. The final sintering temperature is 1180 °C -- 1250 °C for 2- 3 hrs. The scanning electron micrographs (Fig.1.) show the average grain size of the ceramic to be 3μm - 3.5μm. The domain structures can be clearly observed through the environmental scanning electron microscope without coating the samples [7].



Figure 1. The SEM micrographs of the PZT ceramic with the composition within the morphortropic phase boundary.

The samples were cut in the dimensions of (8mm × 8mm × [0.5 - 0.8 mm]) and electroded with gold for the dielectric and strain measurements. For the X- ray analysis measurements, the thin vacuum deposited silver electrodes were used on the faces exposed to the X - rays in order to reduce the extra- diffraction of the electrodes. Before making silver electrodes, the surfaces of the samples were polished and etched. X- ray diffraction measurements were performed on an automatic X-ray diffractometer using CuKα

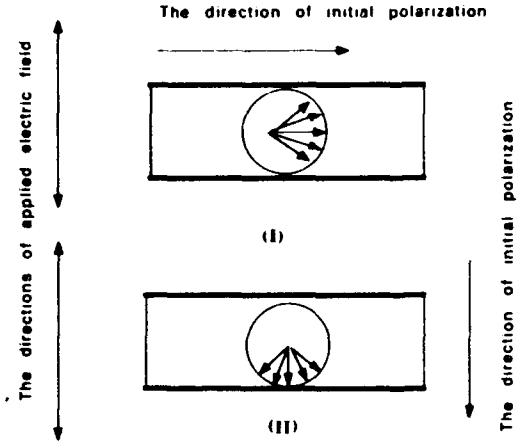


Figure.2. Shape and initial polarization orientation of specimens for two different cases.
(a) The initial direction of remnant polarization parallel to the surface of the plate sample.
(b) The initial direction of remnant polarization perpendicular to the surface of the plate sample.

CH3080-0-7803-0465-9/92$3.00 ©IEEE

radiation (λ = 1.5418 Å). The experimental data were processed with the software developed by the Materials Research Lab at Penn State. The X-ray patterns were recorded at a scan rate of $2\theta = 0.3^0$ min^{-1}. The low scanning rate was chosen in order to enhance the intensity of the diffraction. The ceramic specimens were initially poled in two different ways in accordance with the sample shape, as shown in Fig.2. The depth of X- ray penetration in this PZT system is estimated to be 1μm.

III. Results and Discussions

3.1. Principle of X- ray analysis

It is well known that PZT ceramics contain many 90^0 and 180^0 domains. The electric field will force them move toward the direction favorable to the total system energy. According to Friedel's law, *the reversal of 180^0 domains during the polarization process could not be detected by the X-ray diffraction method*. Therefore, it is believed that the change of ratio I(002)/I(200) is caused by the switching of 90^0 domain alone [8,9]. In general, the intensity of any (hkl) reflection , relative to that from a random specimen, is proportional to the volume fraction of domains having their (hkl) planes parallel to the plate surface. Regarding this study, the intensity of I(002) reflection is proportional to the volume fraction of domain having the polarization direction parallel to the normal of surface of plate specimens.

Based on the general principle of X-ray diffraction, the diffractive intensity I(hkl) for (hkl) plane can be usually expressed by [9]

$$I_{(hkl)} = C\, A\, I_0\, L\, |F_{(hkl)}|^2\, N_{(hkl)}\, \rho_{(hkl)} \qquad (1)$$

where, I_0 stands for incident X-ray diffraction, L, Lorentz angle factor; F(hkl), structure factor for (hkl) plane; N(hkl), iterating factor; A, absorption factor and C is known as measuring system constant. Once the measuring conditions and specimens are defined, C can be calculated. *ρ(hkl) is the crystal plane orientation density which is defined as the volume fraction of the crystal grains with (hkl) plane parallel to specimen surface*. Obviously, for a specimen with the preferened orientation of the (hkl) plane, its ρ(hkl) should be constant and can be taken as 1, therefore, one has

$$I_{p(hkl)} = C\, A\, I_0\, L\, |F_{(hkl)}|^2\, N_{(hkl)} \qquad (1')$$

From the definition of diffraction intensity, it easily follows that the diffraction intensity for the (hkl) planes should be proportional to the volume fraction of domains (both 90^0 and 180^0 domains) in which the (hkl) planes are parallel to the surface of the plate specimens. Since there may be two possible kinds of domain reversal processes during the polarization switching, the measured I(002) and I(200) should contain the contributions of the planes (002) and (200) within both 90^0 reversal domains and 180^0 reversal domains, respectively, that is:

$$I(002) = n_1 [90^0]\, I_p(002) + n_2 [180^0]\, I_p(002) \qquad (2)$$

$$I(200) = g_1 [90^0]\, I_p(200) + g_2 [180^0]\, I_p(200) \qquad (3)$$

and,

$$n_1 + n_2 + g_1 + g_2 = 1$$

where, n_1 and n_2 are the 90^0 and 180^0 domain volume fractions, respectively, which have the (002) plane parallel to the surface of the plate specimens. g_1 and g_2 are the 90^0 and 180^0 domain volume fractions, respectively, which have the (200) plane parallel to the surface of the plate specimens. It should be noted that n_1 and g_1 are the function of applied electric field, whereas the n_2 and g_2 are always constants during the domain reversal processes. The domain volume ratio between the domains with the polarization direction perpendicular to the surface and those having the direction of their polarizations parallel to the surface of the plate specimen could be expressed as follows:

$$R' = K \frac{I(002)}{I(200)} \qquad (4)$$

here, K is special coefficient. Since the change in diffraction intensities are only caused by 90^0 domains, the X- ray intensities of I(002)/I(200) under the influence of the electric field could represent the characteristics of 90^0 domain reversal. The changing rate of I(002)/I(200) may reveal some information about the mechanism of the domain reorientations.

In the following, we shall discuss two different cases of polarization reorientation to distinguish the polarization reorientation processes between 90^0 domain reversal and 180^0 domain reversal processes. It should be noted that in reality the domains can never be perfectly aligned. The distribution of polarization directions always obey the certain axial distribution, as shown in Fig.3. The I(002) and I(200) are measured by their average values.

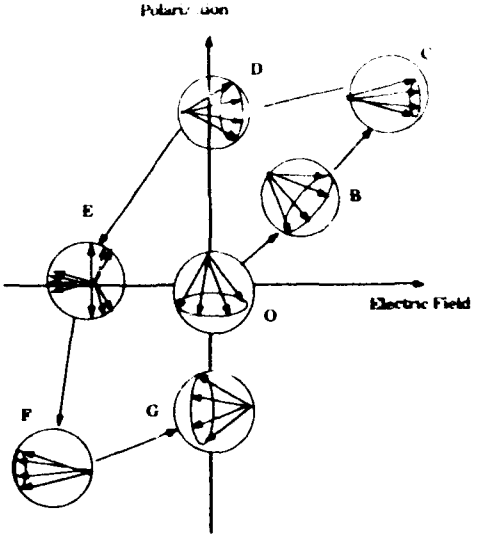


Figure 3. Two dimensional representation of the vector model showing the spatial distribution of domains at different stages of the polarization reversal.

The Case I.

For the case I of Fig.2., the initial directions of polarization in most domains are parallel to the surface of the plate specimen. If an electric field is applied to the direction normal to the surface of the plate specimen, the polarization reversal process will be expected to be following the model in Fig.3. As the applied electric field increases, the direction of polarization will gradually be changed. With a sufficiently strong electric field, the polarization directions in the ceramic will change their distribution direction. Eventually, all polarization directions will be lined up nearly parallel to the plus direction shown at point C via *the 90^0 domain wall reversal* process. The intriguing feature is that in this process only 90^0 domain reorientation is involved and no 180^0 domain wall reversal process occur since the initial direction of polarization is perpendicular to the applied electric field. From eq (3) and eq (4), one obtains

$$R|_{O\,C} = \frac{I(002)}{I(200)} = \frac{n_1 [90^0]\, I_p(002)}{n_2 [90^0]\, I_p(200)} \qquad (5)$$

and $n1+n2 = 1$. Eq.(5) means that R is equal to the diffractive intensity ratio of $\{n_1[90^0]I_p(002)/ n_2[90^0]I_p(200)\}$ within the *unit volume of per 90⁰ domain*. It should be noted that, in geneart, the unit volum of per 90^0 domain is not necessarily equal to the unit volum of per domain if considering the coexistence of both 90^0 and 180^0 domains. From eq.(5), the changing rate of R as a function of electric field can be expressed as

$$\left.\frac{dR}{dE}\right|_{D\ C} = \frac{d\{n_1[90^0]I_p(002)/n_2[90^0]I_p(200)\}}{dE} \qquad (6)$$

where R is the measured value of ratio I(002)/I(200). The changing rate of I(002)/I(200) from point O to the point C reflects only the feature of 90^0 domain wall reorientation.

The Case 2

When the intensity of electric field is decreased from the point C to point D, the domain polarization turns back to the nearest easy direction in the favour of lowing the internal energy. If the applied electric field is increased further in the minus direction from the point D to point F, the domain polarizations pointing in the plus direction are reversed. This may involve both the 90^0 and 180^0 domain switching processes. Thus, from eqs.(2) and (3), we have

$$R|_{D\ F} = \frac{I(002)}{I(200)} = \frac{n_1[90^0]I_p(002) + n_2[180^0]I_p(002)}{g_1[90^0]I_p(200)} \qquad (7)$$

where, $n1+n2+g1 = 1$. It should be noted that no 180^0 domain reversal occurs in the direction perpendicular to the applied field. Thus, eq.(7) can expressed as

$$R|_{D\ F} = \frac{I(002)}{I(200)} = \frac{n_1[90^0]I_p(002) + n_2[180^0]I_p(002)}{g_1[90^0]I(200)} \qquad (8)$$

$$= (n_1 + g_1)\alpha \text{ ; where: } \alpha = \frac{\{n_1[90^0]I_p(002) + n_2[180^0]I_p(002)\}}{g_1[90^0]I_p(200)(n_1 + g_1)}$$

where: $(n1+g1) = (1-n2)$, which is a constant representing the voulme fraction of total 90^0 domains in the material. α is the ratio of diffrative intensity within the uint volume of per 90^0 domain. α is a fuction of electric field and dependent upon the entire domain polarization reversal process. Precisely speaking, since only the (n1 + g1) portion of 90^0 domains contributes to the diffraction intensity of R (or I(002)/I(200)) in eq.(8), thus, the contribution of 90^0 domains to R in the process from point D- point F should not be exactly the same as that to the intensity R in the process from point O- point C. In order to compare the features of these two domain reversal processes, we can define that the changing rate of diffration intensity is the same within the unit volume of per 90^0 domain with respect to these two domain switching processes. Therefore, from eq.(8), one should have]

$$\left.\frac{dR}{dE}\right|_{D\ F} = (n_1+g_1)[90^0]\frac{d\alpha}{dE} \qquad (9)$$

$$= (n_1+g_1)[90^0]\left.\frac{dR}{dE}\right|_{O\ C}$$

Naturally, unlike eq.(6), which describing a pure 90^0 domain wall reorientation process, it can be found that from eq.(9), the changing rate of R as a function of the electric field will also be affected by (n1+g1). Obviously, if (n1+g1) is equal to 1, the polarization reversal process will be a pure type of 90^0 domain one and eq.(9) will become exactly the same as eq.(6). In contrast, if (n1+g1) is equal to zero, this means that no 90^0 domain reversal will occur, and no X-ray information can be obtained. Eq.(9) is an approximate expression which is precisely valid only if large amounts of 90^0 domains are involving in the polarization switching processes. The detail discussions can be found in Ref.[7]. Compared to eq.(9) and eq.(6), it could be asserted that if 90^0 domain wall reorientation is the main process in the polarization switching process from point D to point F, the changing rate of the measured ratio dR/dE would be slightly less than those from the point O to the point C according to eq.(9). In other words, the feature of domain reversal process from point D to point F is most likely a pure type of 90^0 domain reorientation between point D and point F. Conversely, if 180^0 domains are predominantly involving the polarization reversal process from the point D to the point F, the changing rate of the measured dR/dE would be much smaller than that from point O to point C because of the small (n1+g1). Here we assume the internal energy states at points O and D are the same. This assumption is, in practice, almost fulfilled. In short, eq.(9) could be used as the criterion for qualitatively evaluating the characteristics of the dynamic behavior of domain reorientation processes in ceramics in terms of X-ray analysis techniques.

3.2. Experimental Results and Conclusions

In practice, in order to sort out the mechanisms of domain reorientation in the ceramic specimens, we have to examine both the features of the dependence of I(hkl) as a function of applied electric fields and the changing rate of I(002)/I(200) as a function of the applied electric field (or d{I(002)/(200)}/dE) in some details.

Fig.4 show the XRD profiles of (002) and (200) peaks for plate PZT samples in the case of different polarization orientations. It can be seen from Fig.(4a) that when the normal direction of the plate is perpendicular to the polarization direction, the (200) peak is much higher than the (002) peak of the sample. Conversely, for samples with the normal direction of the plate parallel to the poling direction,

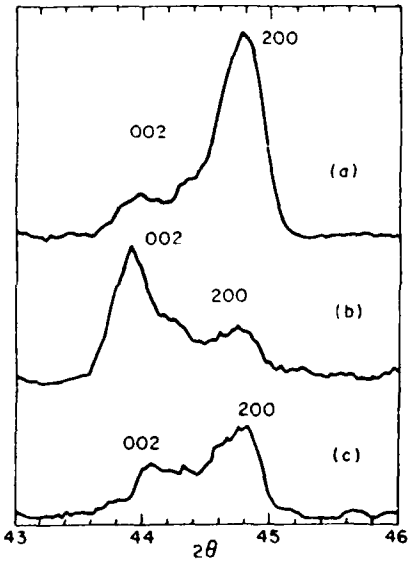


Figure 4. The XRD profiles of (002) and (200) peaks for plate PZT samples of different orientation of polarization. (a) X-ray intensity profile of a poled ceramic plate sample with its normal direction perpendicular to the poling direction. (b) X-ray intensity profile of a poled ceramic plate sample with its normal direction parallel to the poling direction. (c) X-ray intensity profile of an unpoled ceramic sample.

as shown in Fig.(4b), the (002) peak is much higher than (200) peak. Fig.(4c) is the case of an unploed sample. Since no preferred orientation exists, the intensity of (200) peak is about twice as that of (002) peak.

Fig.5. presents the ratio I(002)/I(200) as a function of the applied electric field in the case (II) of Fig.2. In Fig.5, the magnitude of the applied electric field at points D and D' are almost exactly equal to the coercive fields of the P- E (polarization - electric field) hystersis loop and S-E (strain- electric field) hysterisis loop measured at uitra- low frequency.

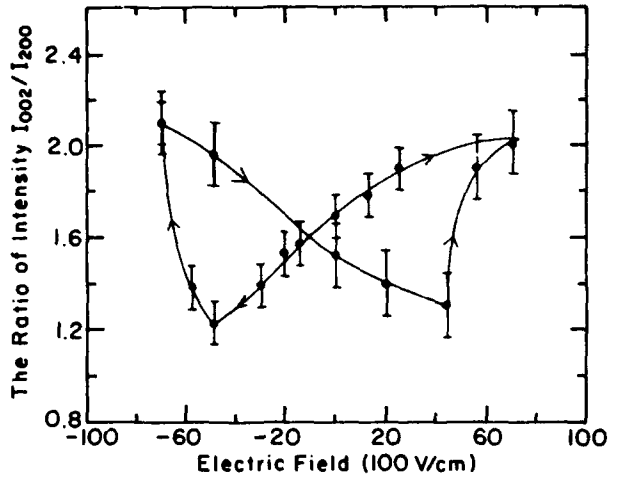


Figure 5. The ratio of I(002)/I(200) as a function of the applied electric field for the case II of Fig.2.

Since the ratio I(002)/I(200) represents the characteristics of 90^0 domain reversal, it indicates that the cocevice field of polarization switching is closely related to the 90^0 domain reversal in this ceramic sample.

Fig.6 presents the ratio of I(002)/I(200) as a function of the applied electric field from point O to point D' for the case I of Fig.2.

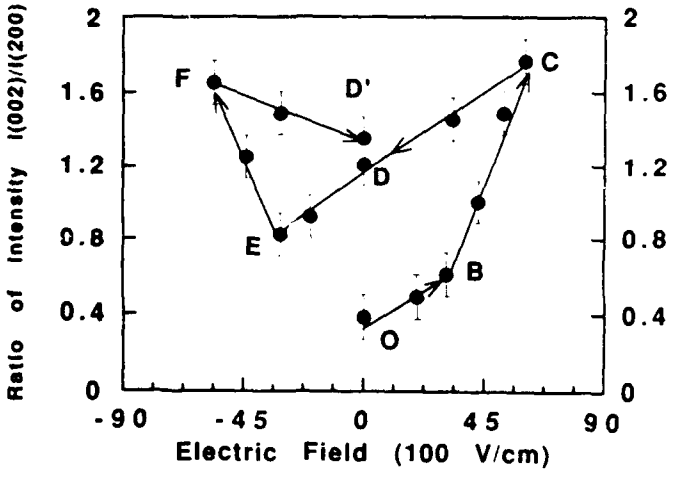


Figure 6. The ratio of I(002)/I(200) as a function of the applied electric field for the case I of the Fig.2.

As discussed above, from the point O to point C, the domain reorientation is a pure 90^0 domain type. If polarization reorientations involving both the 180^0 and 90^0 domain reversal processes from point D to point F, then the slopes of I(002)/I(200) as a function of electric fields from the point D to the point F should be substantially smaller than those from point O to point C. The slopes of the dR/dE in the Fig.6. are listed in the Table I

Table1. Changing rate of I(002)/I(200) v.s. the applied electric field for the cases of Fig.6

Lines	Slopes
O---B	$(0.95 \pm 0.2) \times 10^{-2}$ (100 v/cm) $^{-1}$
B---C	$(4.2 \pm 0.3) \times 10^{-2}$ (100 v/cm) $^{-1}$
D---E	$(1.1 \pm 0.2) \times 10^{-2}$ (100 v/cm) $^{-1}$
E---F	$(3.2 + 0.3) \times 10^{-2}$ (100 v/cm) $^{-1}$

From Table.1. it can be clearly found that there is no substantial difference in the absolute values of the slopes between the O-- B line and the D--E line or between the B--C line and the E--F line. This argument strongly suggests that the entire polarization reorientation process from point O to point F is predominantly controlled by the 90^0 domain reversal process. In other words, eq.(9) could be approximately satisfied by the experimental data. The estimated value of $(n_1 + g_1)$ is around 0.7 - 0.8.

Therefore, it can be concluded that the 90^0 domain reorientation plays a major role in terms of the polarization switching in the PZT bulk ceramic with the composition within the morphotropic phase boundary.

Acknowledgements

This research has been supported in full by the Office of Naval Research.

Reference

1. N.B. Chaim, M. Brunstein, J. Grunberg and A Seidman, " Variations of the Dielectric Constant of PZT Ferroelectric Ceramics with Electric Field", Ferroelectrics, Vol.6 pp299-305 (1974) and "Electric field dependence of the dielectric constant of PZT ferroelec ceramics", J. Appl. Phys. Vol.45(6) pp2398-2405 (1974)

2. N.A. Schmidt, "Coercive Force and 90^0 Domain Wall Motion in Ferroelectric PLZT Ceramics with Square Hystersis Loops", Ferroelectrics, Vol.312 pp105-112 (1981)

3. P. Gerthsen and G.Kruger, "Coercive Field in Fine -Grained PLZT Ceramics", Ferroelectrics Vol.11 pp489-492 (1976)

4. G.Kruger, " Domain Wall Motion Concept to Describe Ferroelectric Rhombohedral PLZT Ceramics", Ferroelectrics Vol.11 pp417--422 (1976)

5. N.Uchida and T.Ikeda, " Temperature and Bias Characteristics of Pb(Zr, Ti) O_3 Families Ceramics", Jan. J. Appl. Phys. 4 (11) pp867--874(1965)

6. Y. Masuda and A. Baba, "D.C. Bias and Frequency Dependence of the Dielectric Constant PZT Family Ferroelectric Ceramics", Jan J.Appl. Phys. Vol.24 pp113 -116(1985)

7. Shaoping Li, " Extrinsic Contributions to the Response in Ferroelectric Ceramics", Ph.D. Thesis, Penn State University, 1992

8. J.Mendida and L. Pardo, " A XRD Study of 90^0 Domains in Tetragonal PLZT Under Poling", Ferroelectrics, Vol.54 pp199--203 (1984)

9. Y.W.Zeng, W.R.Xue and G.F. Fu, " Investigation on Switching Behavior of 90^0 Ferroelectric Domains in $(Pb_{0.85}Sm_{0.10})Ti_{0.98}Mn_{0.02})O_3$ Piezoelectric Ceramics of Ultera-High Electromechanical Anisotropy by the X-ray diffraction Technique", J.of Mat. Sci. 22 pp4294 -4299(1991)

PHENOMENOLOGICAL TREATMENT OF DIELECTRIC LOSS OF FERROELECTRICS UNDER HYDROSTATIC PRESSURE

Sanji Fujimoto, Yoshinobu Kato and Ken Kanai
Fukui Institute of Technology, Fukui 910, Japan

Abstract

This work is concerned with the phenomenological analysis of the dielectric loss tangent in the ferroelectric phase and its application to iodinated trissarcosine calcium chloride.

1. Introduction

In this paper, the dielectric loss tangent in the ferroelectric phase under hydrostatic pressure is phenomenologically presented, and the effect of hydrostatic pressure on the dielectric loss tangent of iodinated trissarcosine calcium chloride is reported.

2. Phenomenological Treatment of Dielectric Loss Tangent

The electric field E^* and the permittivity ε^* as a function of polarization P^* in the ferroelectric phase are expressed on the basis of the free energy function for ferroelectrics under hydrostatic pressure p as follows [1]:

$$E^* = (u^* + g^* p)P^* + \xi^* P^{*3} + \zeta^* P^{*5} \tag{1}$$

$$\frac{1}{\varepsilon^* - \varepsilon_0} = u^* + g^* p + 3\xi^* P^{*2} + 5\zeta^* P^{*4} \tag{2}$$

where the expansion coefficients u^*, g^*, ξ^* and ζ^* are phenomenological constants, and all complex numbers are shown by mark $*$.

As the polarization P^* in the ferroelectric phase is the sum of the spontaneous polarization P_S and the polarization $P_E{}^*$ induced by the applied electric field $E^* = Ee^{j\omega t}$ with angular velocity ω,

$$P^* = P_S + P_E{}^* = P_S + P_0 e^{j(\omega t - \delta_1)} \tag{3}$$

where P_0 is the magnitude of induced polarization, and δ_1 is the phase lag of the induced polarization P_E^* behind the phase of the applied electric field E^*.

As there is no induced polarization when an external field is not applied to ferroelectrics, $P_0 = 0, P_S \neq 0$ at $E^* = 0$.

On putting the above relation into eqs. (1) and (3), we obtain the following equation:

$$u^* + g^* p + \xi^* P_S{}^2 + \zeta^* P_S{}^4 = 0 \tag{4}$$

On substituting P^* in eq. (3) for eq. (1), and putting $A = P_0/P_S$, the following equation is obtained:

$$\begin{aligned} Ee^{j\omega t} = {} & A\{2(\xi + 2\zeta P_S{}^2)P_S{}^3 e^{j\omega t} \\ & + A(3\xi + 10\zeta P_S{}^2)P_S{}^3 e^{j(2\omega t - \delta_1)} \\ & + A^2(\xi + 10\zeta P_S{}^2)P_S{}^3 e^{j(3\omega t - 2\delta_1)} \\ & + 5A^3\zeta P_S{}^5 e^{j(4\omega t - 3\delta_1)} \\ & + A^4\zeta P_S{}^5 e^{j(5\omega t - 4\delta_1)}\} \end{aligned}$$

By neglecting terms in A of an order higher than 2 in the above equation because of $A << 1$, we can confirm that the phase of the left hand side in the above equation is equal to that in the right hand side.

When the complex permittivity is expressed by the relation $\varepsilon^* = \varepsilon_1 - j\varepsilon_2$, the dielectric loss tangent is given by the formula $\tan\delta = \varepsilon_2/\varepsilon_1$.

On the other hand, by neglecting terms in P^* of an order higher than 2 in eq. (2), the reciprocal permittivity of ferroelectrics in the paraelectric phase is obtained as follows:

$$\frac{1}{\varepsilon^* - \varepsilon_0} = u^* + g^* p = (u + gp)e^{j\delta_1}$$

For the case $\varepsilon_1 >> \varepsilon_0$ applying to ordinary ferroelectrics, the dielectric loss tangent in the paraelectric phase is expressed to be $\tan\delta = \tan\delta_1$ from the above equation.

This means that the dielectric loss tangent of ferroelectrics in the paraelectric phase corresponds to that in usual dielectrics, whose polarization is caused by the lag from the applied electric field.

In view of the facts mentioned above, we can confirm that phase lags of all the expansion coefficients are equal to δ_1.

The complex permittivity ε^* in the ferroelectric phase can be obtained on substituting eqs. (3) and (4) for eq. (2) as follows:

$$\begin{aligned} \frac{1}{\varepsilon^* - \varepsilon_0} = {} & 2(\xi + 2\zeta P_S{}^2)P_S{}^2 e^{j\delta_1} \\ & + 2A(3\xi + 10\zeta P_S{}^2)P_S{}^2 e^{j\omega t} \\ & + 3A^2(\xi + 10\zeta P_S{}^2)P_S{}^2 e^{j(2\omega t - \delta_1)} \\ & + 20A^3\zeta P_S{}^4 e^{j(3\omega t - 2\delta_1)} \\ & + 5A^4\zeta P_S{}^4 e^{j(4\omega t - 3\delta_1)} \end{aligned}$$

By comparing the real and imaginary parts in the right hand side with those in the left hand side, the following relations must be satisfied:

CH3080-0-7803-0465-9/92$3.00 ©IEEE

$$\frac{\varepsilon_1 - \varepsilon_0}{(\varepsilon_1 - \varepsilon_0)^2 + \varepsilon_2^2} = 2(\xi + 2\zeta P_S^2)P_S^2 \cos\delta_1 + 2A(3\xi + 10\zeta P_S^2)P_S^2 \cos\omega t + 3A^2(\xi + 10\zeta P_S^2)P_S^2 \cos 2(\omega t - \frac{1}{2}\delta_1) + O(A^3)$$

$$\frac{\varepsilon_2}{(\varepsilon_1 - \varepsilon_0)^2 + \varepsilon_2^2} = 2(\xi + 2\zeta P_S^2)P_S^2 \sin\delta_1 + 2A(3\xi + 10\zeta P_S^2)P_S^2 \sin\omega t + 3A^2(\xi + 10\zeta P_S^2)P_S^2 \sin 2(\omega t - \frac{\delta_1}{2}) + O'(A^3)$$

where $O(A^3)$ and $O'(A^3)$ stand for the small quantity including terms A of an order higher than 3.

By putting the above relations into $\tan\delta = \varepsilon_2/\varepsilon_1$, the dielectric loss tangent in the ferroelectric phase is obtained as follows:

$$\tan\delta = \left\{1 + \frac{3\xi + 10\zeta P_S^2}{(\xi + 2\zeta P_S^2)\sin\delta_1} \times A\sin\omega t + O''(A^2)\right\} \times \tan\delta_1$$

where $O''(A^2)$ stands for the small quantity including terms A of an order higher than 2.

The root mean square of $\tan\delta$ with respect to time t is as follows:

$$< \tan\delta > \simeq \sqrt{1 + \frac{1}{2}A^2\frac{(3\xi + 10\zeta P_S^2)^2}{(\xi + 2\zeta P_S^2)^2 \sin^2\delta_1}} \times \tan\delta_1 \quad (5)$$

By using eq. (5), we will show the pressure and dc electric field dependence of $\tan\delta$ in the ferroelectric phase for the second and the first phase transitic

2.1 Second order phase transition

On putting $\zeta = 0$ into eq. (5), we obtain the following equation:

$$< \tan\delta > \simeq \sqrt{1 + \frac{9}{2}A^2\mathrm{cosec}^2\delta_1} \times \tan\delta_1 \quad (6)$$

By substituting relations $A = P_0/P_S$ and $P_S^2 = -(u + gp)/\xi$ [1] for eq. (6),

$$< \tan\delta > \simeq \sqrt{1 - \frac{\alpha}{\sin^2\delta_1}} \times \tan\delta_1 \quad (7)$$

where

$$\alpha = \frac{9\xi P_0^2}{2(u + gp)} \quad (8)$$

The above equation shows the pressure dependence of $\tan\delta$ in the ferroelectric phase.

When $\zeta = 0$, and the applied electric field is expressed by

$$E^* = E_0 + Ee^{j\omega t}$$

where E_0 is the dc electric field and E is the very small ac electric field ($E << E_0$) which is applied for measuring $\tan\delta$, the electric field dependence of $\tan\delta$ is obtained by putting $A\ (= P_0/P_S)$ in eq. (6) and P_S into eq. (1) as follows:

$$E_0 = \left\{u + gp + \xi\left(\frac{3P_0}{\sqrt{2}}\frac{1}{\sqrt{\tan^2\delta - \tan^2\delta_1}}\right)^2\right\} \times \frac{3P_0}{\sqrt{2}}\frac{1}{\sqrt{\tan^2\delta - \tan^2\delta_1}} \quad (9)$$

where $\tan^2\delta_1 << 1$ and $A << 1$.

2.2 First order phase transition

The spontaneous polarizations as a function of hydrostatic pressure p is expressed as follows [1]:

$$P_S^2 = -\frac{(1 + \beta)\xi}{2\zeta}$$

and

$$P_{SC}^2 = -\frac{3\xi}{4\zeta}$$

at a transition pressure p_C or a transition temperature T_C.

On putting the above relations into eq. (5),

$$< \tan\delta > \simeq \sqrt{1 - \frac{\zeta P_0^2(2 + 5\beta)^2}{\xi(1 + \beta)\beta^2 \sin^2\delta_1}} \times \tan\delta_1 \quad (10)$$

where

$$\beta^2 = 1 - \frac{4(u + gp)\zeta}{\xi^2} \quad (11)$$

and

$$< \tan\delta > \simeq \sqrt{1 - \frac{54\zeta P_0^2}{\xi \sin^2\delta_1}} \times \tan\delta_1 \quad (12)$$

at a transition pressure p_C.

3. Pressure Dependence of Dielectric Loss Tangent of Iodinated Trissarcosine Calcium Chloride

Iodinated trissarcosine calcium chloride $(CH_3NHCH_2COOH)_3CaCl_{2(1-x)}I_{2x}$ (abbreviated as $TSCC_{1-x}I_x$) is a ferroelectric with a second order phase transition, and it changes from the ferroelectric phase to the paraelectric phase with increasing temperature and with decreasing pressure.

The $TSCC_{1-x}I_x$ crystal was grown from an aqueous solution of calcium chloride and calcium iodide and sarcosine in stoichiometric proportions by the slow evaporation method

at 30°C. Since the growth features of $TSCC_{1-x}I_x$ are multitwinned, non-twinned parts were chosen by means of a polarizing microscope. The molar fraction of iodide in a specimen was determined to be $x = 0.1$ by the chemical absorptiometric method. Each plate was cut out perpendicular to the b-axis from a crystal and mirror-polished with No. 1500 Al_2O_3 powder.

From the dielectric measurement of $TSCC_{0.9}I_{0.1}$ at −165°C and −156.5°C, the phenomenological coefficients are [2]:

$$g = -3.8 \times 10^{10}\text{m/Fkbar}$$
$$\xi = 4.1 \times 10^{16}\text{m}^5/\text{FC}^2$$
$$u = 1.45 \times 10^{10}\text{m/F for } -165°\text{C}$$
$$u = 4.1 \times 10^{10}\text{m/F for } -156.5°\text{C}$$

, the polarization induced by the ac electric field of 5V/cm is $P_0 = 3.2 \times 10^{-6}\text{C/m}^2$, the value of the dielectric loss tangent in the paraelectric phase is $\tan\delta_1 = 1.5 \times 10^{-4}$, and $A = P_0/P_S = 7.11 \times 10^{-3}$.

The pressure dependence of the dielectric loss tangent $\tan\delta$ calculated from eq. (7) is shown by Fig. 1.

It is found that the dielectric loss tangent in the ferroelectric phase at pressures above the transition pressure p_C (= 0.38kbar for −165°C, 1.07kbar for −156.5°C) decreases rapidly near p_C and then gradually with increasing pressure.

References

[1] S. Fujimoto and N. Yasuda, "Phenomenological Treatment of Ferroelectricity under Hydrostatic Pressure," Trans. Inst. Elect. Eng. Japan, vol. 93-A, pp. 361-368, August 1973.

[2] S. Fujimoto, N. Yasuda, A. Kawamura and T. Hachiga, "Temperature and Pressure Dependence of Dielectric Properties of Iodinated Trissarcosine Calcium Chloride," J. Phys. D, Appl. Phys., vol. 17, pp. 1019-1028, May 1984.

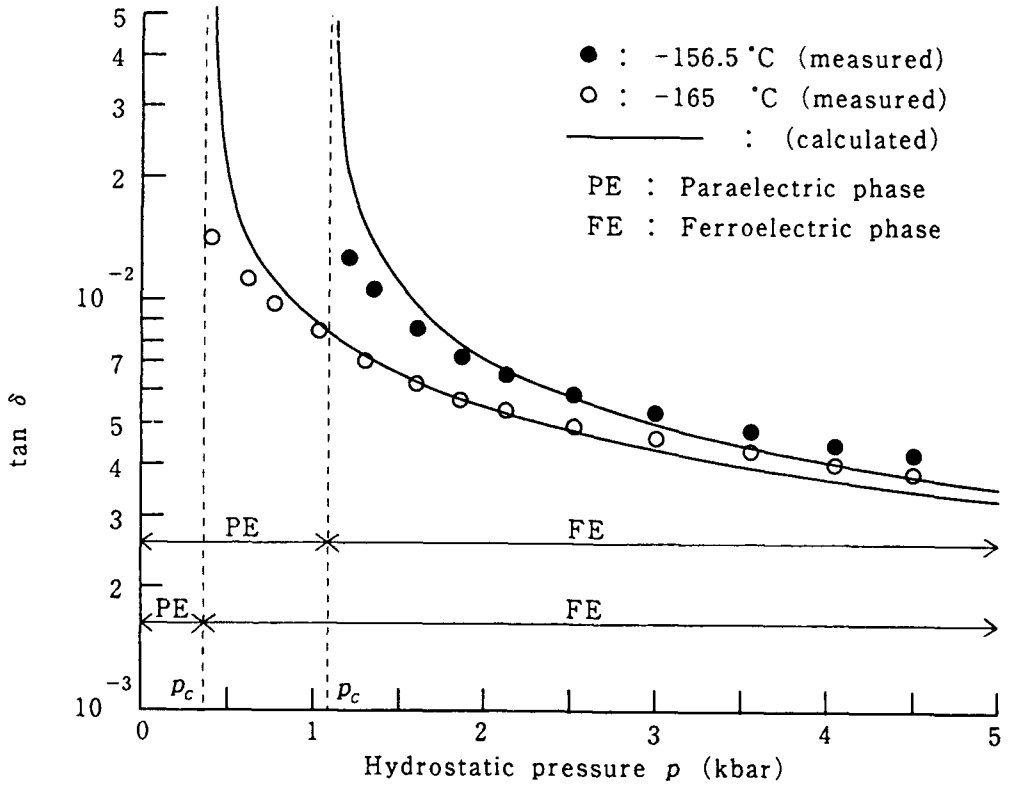


Fig. 1 Pressure dependence of the dielectric loss tangent (tan δ) of iodinated trissarcosine calcium chloride $TSCC_{0.9}I_{0.1}$ in the ferroelectric phase at −156.5 °C and −165 °C.

Thin Films

ELECTRODE EFFECTS ON ELECTRICAL PROPERTIES OF FERROELECTRIC THIN FILMS

D.P. Vijay, C.K. Kwok, W.Pan, I.K.Yoo, S.B. Desu
Department of Materials Engineering
Virginia Polytechnic Institute and State University
Blacksburg, VA

ABSTRACT

The electrical properties of lead zirconate titanate (PZT) films were investigated on Pt and RuO_x electrodes. Films with compositions close to the morphotrophic phase boundary showed high P_r and low E_c values on RuO_x electrodes. No significant fatigue was observed in the films on RuO_x electrodes up to 2×10^{11} test cycles. The degradation properties were studied as a function of film thickness by an accelerated unified test which can evaluate fatigue and breakdown simultaneously. It was observed that thinner PZT films on RuO_x electrodes show better electrical properties.

INTRODUCTION

Recently, there has been a renewed interest in ferroelectric materials for nonvolatile memory applications. Ferroelectric memories offer distinct advantages over other nonvolatile memories in terms of faster access times, lower operating voltages, wider operating temperature range and radiation hardness. However, the lifetime of ferroelectric memories is an important factor that needs to be considered before it can be applied commercially. Degradation problems such as fatigue, ageing and low voltage breakdown are known to affect the lifetime of ferroelectric devices.

In an earlier work Desu and Yoo[1] have proposed an electrochemical model for failure in oxide perovskites (a promising class of ferroelectric materials for memory applications). In the present work, an attempt has been made to improve the degradation properties of oxides ferroelectrics based on the conclusions of this model.

According to the model, the degradation phenomena such as fatigue can be minimized by controlling the nature of the electrode-ferroelectric interface. The model also suggests ceramic conducting oxide electrodes as possible replacements for metal electrodes in thin film ferroelectric capacitors.

This paper investigates the degradation phenomena in ceramic electrode ferroelectric capacitors. Lead zirconate titanate (PZT) films were used in this study as the ferroelectric material because of their good electrical properties, wide operating range and very good stability under a wide range of operating conditions. In an earlier work[2], we have shown that ruthenium oxide electrodes show excellent barrier properties to interdiffusion of various elements in the ferroelectric PZT material and the Si substrate during high temperature processing (around 650°C) compared to other ceramic electrodes such as indium tin oxide (ITO), ZrN and TiN[3]. Thus, the obvious choice of the ceramic electrode for this study was ruthenium oxide. The PZT films were deposited on $Si/SiO_2/RuO_x$ substrate using the sol-gel method and characterized thereafter to investigate the degradation properties.

EXPERIMENTAL PROCEDURE

Thin films of ruthenium oxide were reactively sputtered in an argon-oxygen atmosphere at a gas pressure of 10 mTorr and at a substrate temperature of 200°C. The films were deposited to a thickness of 400 nm on thermally oxidized Si substrate.

Sol-gel derived PZT films were then spin coated on the electrodes. The PZT precursors were prepared from a metallorganic (0.4M) solution of lead acetate, zirconium n-propoxide and titanium iso-propoxide dissolved in acetic acid and n-propanol. The solutions were hydrolyzed to form the precursors. Precursors of different compositions were prepared by varying the ratios of zirconium n-propoxide and titanium iso-propoxide to obtain PZT films with different Zr/Ti content. The precursor preparation method was similar to that suggested by Yi et al[4] and more specific details can be obtained from this reference. The films were spin coated at 1500 rpm for 20 sec and dried subsequently at 150°C for 5 min to obtain a thickness of 150 nm. The spin-dry cycle was repeated to obtain any other desired thickness of the films.

The coated films were then annealed at 650°C for 30 min in air. The films were characterized using EDAX and XRD to confirm the composition and the formation of complete perovskite phase in the films, respectively. Ruthenium oxide top electrodes were then sputter deposited on the films under conditions similar to the bottom electrode deposition.

Hysteresis, fatigue and breakdown properties of the films were evaluated using the RT66A standardized ferroelectric test system. An external pulse generator (HP8116A) was used to obtain the desired input signal during the test. DC leakage current measurements were performed using a Keithley 617 electrometer.

RESULTS AND DISCUSSION

The hysteresis properties of PZT films of different compositions (30/70, 40/60, 53/47, 65/35 and 75/25 : all annealed at 650°C for 30 min in air) on RuO_x electrodes were measured using the RT66A standardized tester. All the samples were coated to a thickness of 450 nm. The films with Zr/Ti ratio of 53/47 showed higher remanent polarization ($\sim$20 $\mu C/cm^2$) and lower coercive field values ($\sim$30 kV/cm). A typical hysteresis loop obtained from this sample is shown in figure 1. The 53/47 composition is close to the morphotrophic phase boundary (MPB) in the PZT phase diagram. At compositions close to the MPB, both tetragonal and rhombohedral phases co-exist and therefore there are a larger number of polarization directions that can be used for domain switching. This explains the higher P_r values and lower E_c values that we observe for the 53/47 films.

CH3080-0-7803-0465-9/92$3.00 ©IEEE

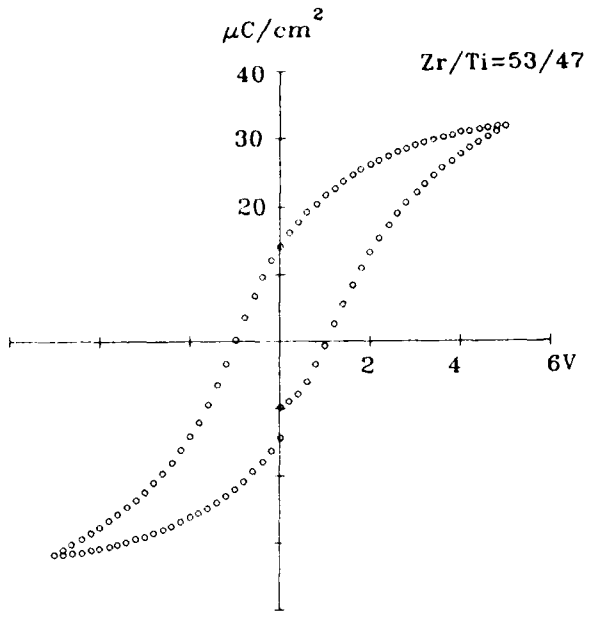


Fig.1 A Typical Hysteresis Loop Obtained from RuOx/PZT/RuOx Capacitors.

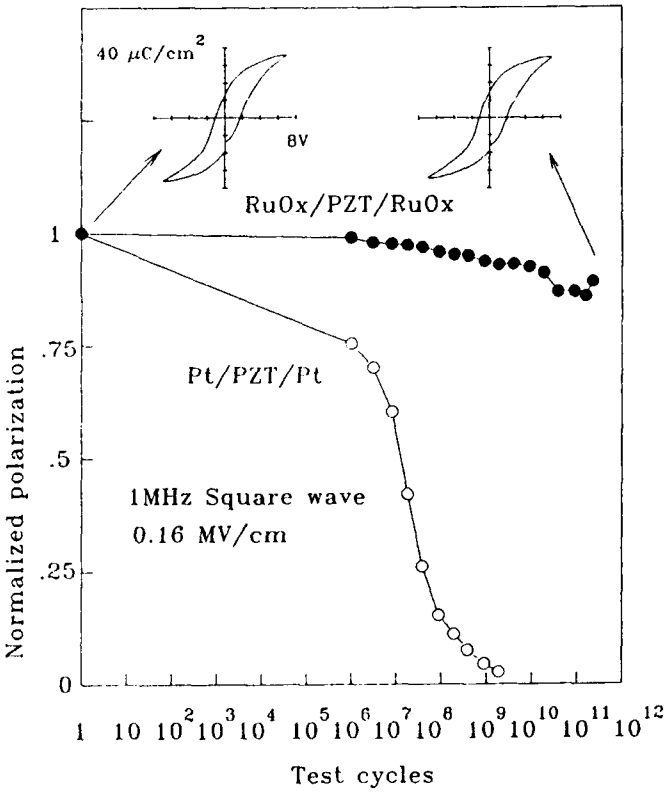


Fig. 2 Comparison of Fatigue Properties of PZT films on Pt and RuOx Electrodes.

The fatigue properties of RuO_x/PZT/RuO_x films and Pt/PZT/Pt are compared in figure 2. The fatigue properties were measured under accelerated test conditions using 1 MHz square wave and an electric field of 0.16 MV/cm. As expected, the films showed early loss of polarization on Pt electrodes. PZT films did not show any fatigue on RuO_x electrodes up to 2×10^{11} cycles. As shown in figure 2, there was no significant difference in the hysteresis properties of the films before and after the fatigue cycling. This result is consistent with the model proposed by Desu and Yoo[1] for fatigue of oxide ferroelectrics on ceramic electrodes. The use of a ceramic electrode for a ferroelectric ceramic capacitor reduces the work function difference and lattice mismatch at the interface. Thus, the interface is relatively more stable when compared to metal electrode-oxide ferroelectric capacitors. Under an alternating polarity, the tendency for oxygen vacancies to become entrapped at the interface is reduced. The reduced entrapment decreases the structural damage to the interface and hence, no significant loss in polarization is observed in the films.

An accelerated unified test developed by Yoo and Desu[5] was used to evaluate the breakdown phenomena in PZT films on RuO_x electrodes. This test combines the effect of temperature, voltage and cycling frequency to accelerate the test conditions and can measure the fatigue and breakdown properties of the films simultaneously. The films were fatigued at 200°C at a frequency of 1 MHz (square wave) and electric field of 0.16 MV/cm. The results of this test are shown in figure 3[5]. While the films show very early breakdown (within 2×10^7 cycles) on Pt electrodes, no fatigue or breakdown was observed on RuO_x electrodes.

Similar tests were performed on RuO_x/PZT/RuO_x capacitors as a function of PZT film thickness. The measurements were conducted at 200°C and 300°C. Figure 4 compares the results of the fatigue/breakdown test for 150 nm and 450 nm films at 200°C. At this temperature, either of the films do not show any fatigue or breakdown. Although the polarization values for both the films do show some degree of asymmetry in the positive and negative cycling, the effect is more pronounced in the thicker sample. The asymmetry is estimated to arise form differences in contact between RuO_x and PZT at the top and bottom electrodes. The bottom electrode has undergone a thermal annealing cycle with the PZT film on top of it while the top electrode in the final device structure remains as-deposited.

At 300°C, the thicker films begin to show electrical degradation above 10^6 cycles as shown in figure 5. However, there is a high degree of asymmetry in the degradation. As is evident form fig. 5, the degradation occurs essentially at the bottom electrode. We believe that this may be due to a low Schottky barrier height at the bottom electrode at higher temperatures. It is possible that there is interlayer formation at the interface between the bottom electrode and the PZT films due to thermal processing at high temperatures that causes the compositional gradient at the interface to be low. At high temperatures, the oxygen vacancy migration through the interface is greater leading to ionic conduction and consequent degradation of the films. For the thinner films, the low concentration of defects could result in reduced migration of vacancies through the interface. Thus the possibility of ionic conduction leading to degradation is less.

Earlier work[5] on the current-voltage characteristics of PZT films on Pt and RuO_x electrodes have shown that the films on RuO_x electrodes show higher leakage current levels compared to platinum. However, it has been pointed out that the pre-breakdown range is longer on RuO_x electrodes whereas, the breakdown occurs abruptly on Pt electrodes. This is evident from the results of the accelerated test shown in figure 3. In general, at high temperatures there is a loss in polarization and an increase in leakage current level in the ferroelectric films. In this

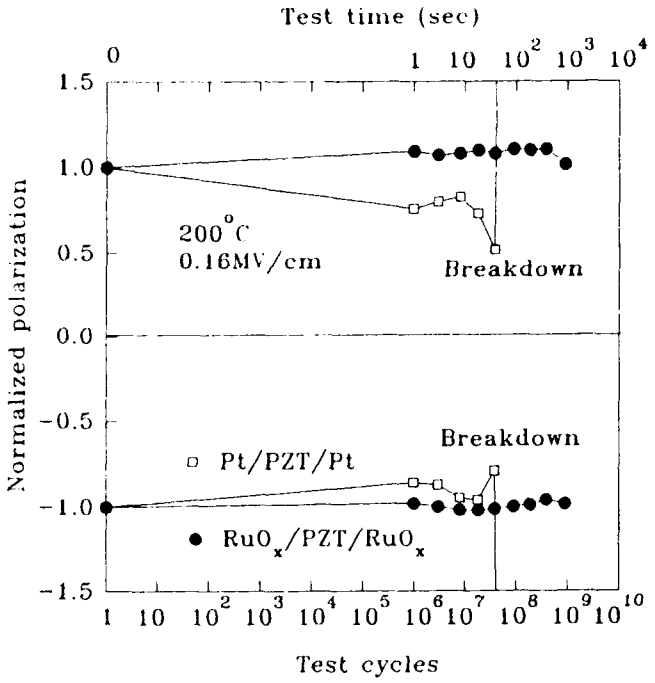


Fig. 3 Unified Test for PZT Capacitors (Ref. 5)

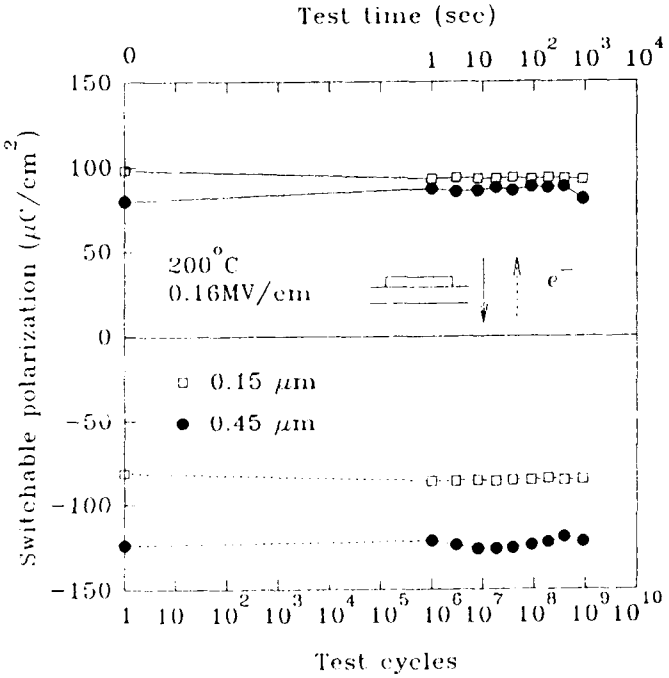


Fig. 4 Comparison of Fatigue/Breakdown of RuOx/PZT/RuOx Capacitors at 200°C

case, under an alternating field the leakage current level remains almost constant at high temperatures on RuO_x electrodes whereas the films show an abrupt breakdown at 2×10^8 on Pt electrodes. The I/V characteristics of RuO_x/PZT/RuO_x films under a DC field were studied as a function of film thickness. The results are shown in figure 6. At any particular electric field, a lower current level is observed for thinner films. Also, the breakdown field is higher for thinner films. The increase in breakdown field for thinner films could be the result of better contact between the electrode and the PZT films, resulting in relatively higher Schottky barrier height at the interface. Thus, the passage of ions through the interface is low over a wide range of applied voltages leading to a longer pre-breakdown range.

SUMMARY

The degradation phenomena in PZT thin films capacitors was investigated using Pt and RuO_x electrodes. The hysteresis properties of PZT films were measured for different compositions (Zr/Ti ratios) on RuO_x electrodes. The films with composition close to the morphotrophic phase boundary showed higher P_r and lower E_c values. PZT films did not show any significant fatigue up to 2×10^{11} cycles on RuO_x electrodes while early fatigue was observed on Pt electrodes. The degradation properties of the films on RuO_x electrodes were evaluated as a function of measurement temperature and film thickness using an accelerated unified test that combined the effect of voltage, temperature and cycling frequency. The thinner films showed better degradation properties even at high temperatures. Also, under a DC field the thinner films showed lower leakage current and higher breakdown fields. The reasons for these observations could be attributed to the differences in the Schottky barrier height due to better contact between the electrode and the ferroelectric and lower defect concentration with decreasing thickness of the films.

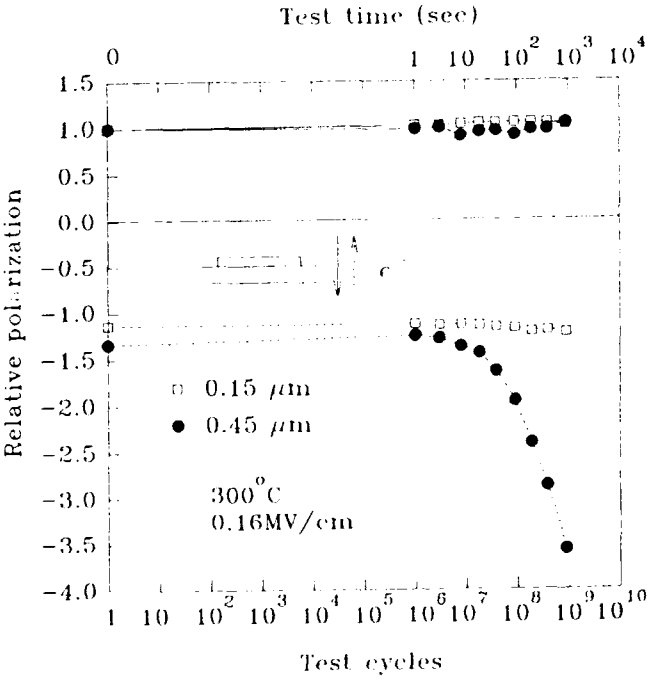


Fig. 5. Thickness Effect on Electrical Degradation

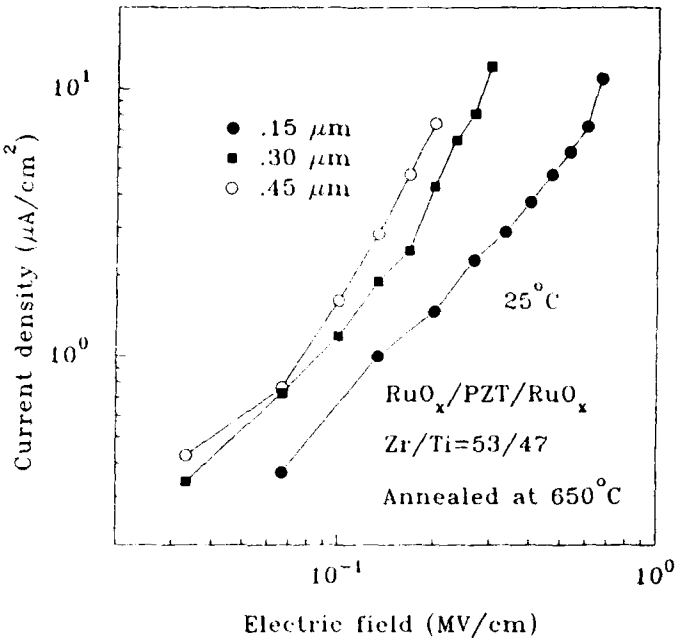


Fig. 6 Thickness Effect on I/V Characteristics

ACKNOWLEDGEMENTS

This work is partially supported by DARPA through a project from ONR.

REFERENCES

[1] S.B. Desu and I.K. Yoo, "Electrochemical Models of Failure in Oxide Perovskites", ISIF 92 Proceedings, 1992.

[2] C.K. Kwok, D.P. Vijay, S.B. Desu, N.R. Parikh and E.A. Hill, "Conducting Oxide Electrodes for Ferroelectric Films", ISIF 92 Proceedings, 1992.

[3] N.R. Parikh, J.T. Stephen, M.L. Swanson and E.A. Myers, Mat. Res. Soc symp. Proc., 200, p.193, 1990.

[4] G. Yi and M. Sayer, Ceram. Bull., 70(7), p.1173, (1991).

[5] I.K. Yoo and S.B. Desu, "Leakage Current Mechanism and Accelerated Unified Test of Lead Zirconate Titanate Thin film Capacitors", ISAF 92 Proceedings, 1992.

Preparation and Characterization of Lead Lanthanum Titanate Thin Films by Metalorganic Decomposition

Ashraf R. Khan, In K. Yoo, and Seshu B. Desu
Department of Materials Science and Engineering
Virginia Polytechnic Institute and State University
Blacksburg, VA 24061

ABSTRACT

Lead Lanthanum Titanate (PLT) thin films corresponding to 28 mol% of La were fabricated by metalorganic decompositon (MOD) process . The films were made from two solutions of different compositions. In the first case it was assumed that the single unbalanced positive charge of La^{3+} gives rise to A-site or Pb vacancies whereas the other solution assumed the creation of B-site or titanium vacancies. Optical and electrical measurements indicated that the films made assuming B-site vacancies had better properties. It was also found from x-ray diffraction patterns that the films were cubic at room temperature. The films showed high resistivity and good permittivity values. The highest permittivity at room temperature was 1285. The resistivity values at room temperature were as high as 10^{12} ohm-cm.

INTRODUCTION

Increasing demand for miniaturization in the electronics industry has sparked a special interest in high dielectric constant materials. PLT materials owing to their very high dielectric constant in bulk form are among the most sought after candidates for the potential application in 64- and 256- *Mb Dynamic Random Access* Memories(DRAMs) among other applications. Also preparation and characterization of PLT in the thin film form makes it directly compatible for integration in the memory technology.

With the above mentioned motivation thin films of PLT were fabricated using metalorganic decomposition process. The MOD process offers several advantages such as low processing temperatures, close compositon control, ease of fabrication, relative inexpense, and greater homogeneity.[1]

Because La^{3+} has an ionic radius comparable to the Pb^{2+} ions it occupies the corners or A-sites in the tetragonal perovskite structure of $PbTiO_3$.[2] There are two possible ways of neutralizing the extra positive charge from the La addition--creation of the lead or titanium vacancies. The chemical formula for PLT can, therefore, be expressed in either of two forms depending on the type of vacancies :

(A) $Pb_{1-1.5x}La_xTiO_3$, or

(B) $Pb_{1-x}La_xTi_{1-.25x}O_3$

In the present study, thin films were fabricated using both the formulae and their properties were compared.

EXPERIMENTAL PROCEDURE

Solution Preparation

The precursors used to make the solution for PLT film fabrication were lead acetate trihydrate $Pb(CH_3COO)_2{\cdot}3H_2O$ from Fisher, aqueous solution of lanthanum acetate $La(CH_3COO)_3$ Molycorp, and titanium isopropoxide $Ti(OCH(CH_3)_2)_4$ from Fisher. Acetic acid and n-propanol were both used as the solvent and chemical modifier. The essential steps of the solution making procedure are shown in Fig. 1. To prepare a 0.4M solution, approximately 10g of propanol was added to a weighed amount of titanium isopropoxide and stirred in an ultrasonic bath for 5 minutes to facilitate proper mixing. Then approximately 5g of acetic acid was added to this system and was mixed in the ultrasonic bath ('USB' in the figure) . Then lanthanum acetate was added to the system followed by the addition of lead acetate. Proper dissolution was obtained by heating the system to 60-70 °C in the ultrasonc bath (USB) for 10-15 minutes. After the precursors dissolved completely approximately 5g of acetic acid was added. And finally propanol was added to make the total volume 50 ml. By this process, very clear solutions were consistently obtained. The solution, however, didnot have a long batch life.

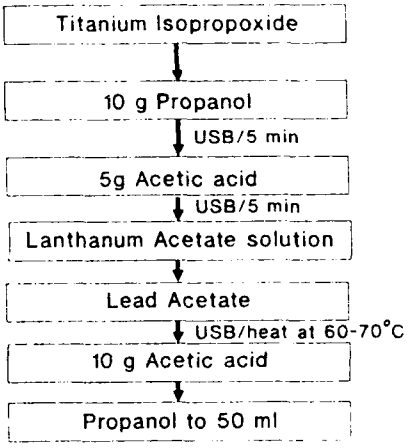


Fig.1 The flow diagram for solution preparation.

Fabrication of Thin Films

Thin films were spin-coated on the substrates using a photoresist spinner (Headway Research Inc) at an rpm of 1500 for 30 seconds. Sapphire substrates were used for optical property characterization while Pt/Ti/SiO2/Si substrates were used for dielectric measurements. After coating the films were baked at 150C for 5 minutes to dry out the volatile organic medium. This cycle was repeated until the desired thickness was obtained. After the last coating, the films were dried for 15 minutes.
The films were then annealed at elevated temperatures and their structure was studied. The heat treatment was always done in air for 30 minutes.

Characterization Procedure

The crystal structure of the films was characterized by x-ray diffraction. Scanning electron microscopy was used to study the microstructure. The thickness of the film was estimated by weight difference and also more accurately by the optical transmission spectra.

CH3080-0-7803-0465-9/92$3.00 ©IEEE

The optical properties of the films deposited on sapphire were measured using a UV-VIS-NIR spectrophotometer (UV-3101PC, Shimadzu Corpn). The envelope method was employed to calculate the refractive index and the thickness of the film.[3]

For electrical measurements the films were spin coated on Pt/Ti/SiO2/Si and after appropriate heat treatment top electrodes of palladium were sputtered using vacuum evaporation. The area and thickness of the top electrode were 2.1×10^{-4} cm^2 and 400 nm respectively. The dielectric constant and loss measurements were done using the HP4192A impedance analyzer. The time dependent dielectric breakdown study was done on the RT66A standardized ferroelectric tester.

RESULTS AND DISCUSSION

Crystal Structure

As mentioned in the introduction thin films were prepared assuming both A- and B-site vacancies. For convenience they will be referred to as type-A film and type-B film, respectively. The x-ray diffraction patterns for both films were very similar. The variation in the x-ray diffraction pattern as a function of annealing temperature for the type-A film is shown in Fig. 2. The structure is single phase cubic with lattice parameter a = 3.924 A. Also before perovskite phase formation no other phases, such as the pyrochlore phase appeared. There was no change in the intensity of the diffraction peaks beyond 600C indicating that the perovskite phase formation completed somewhere between 550 and 600 C.

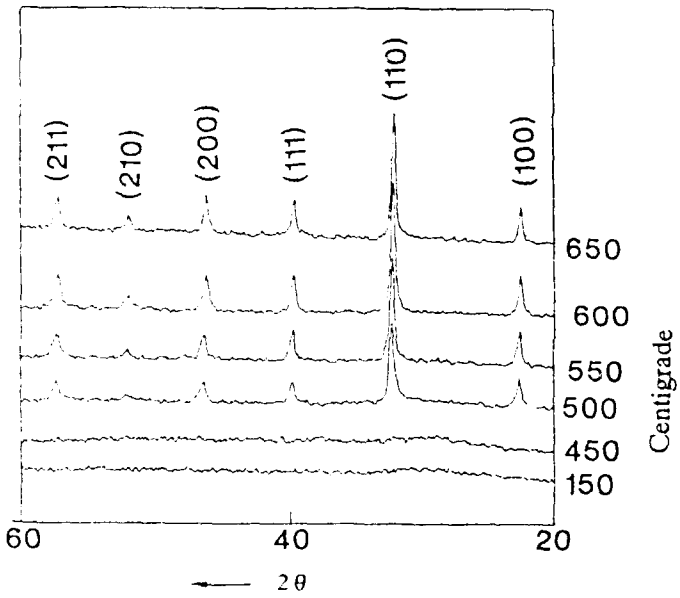


Fig.2 XRD pattern as a function of annealing temperature (film A on sapphire).

The film surfaces do not show much morphological features. Two typical SEM micrographs are shown in Fig. 3 for films annealed at 600°C for 30 minutes. Fig. 3 shows the structure of type-A film and as can be seen the film has small dark regions throughout the micrograph. This could be either due to porosity or the presence of amorphous phase. The micrograph of film-B in Fig. 3(b) shows very fine microstructure. Typical grain size for these films range from 0.1 micron to 0.2 micron. The larger regions on the film might be clusters of grains.



Fig.3a SEM micrograph of film A annealed at 600°C for 30 min

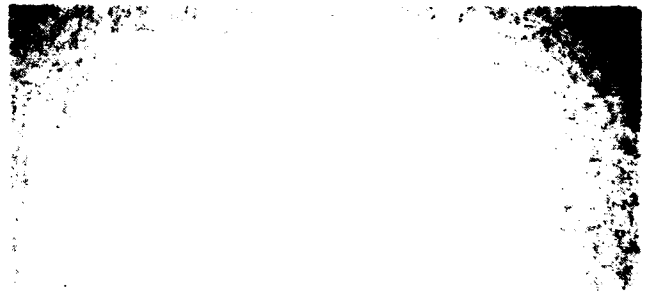


Fig.3b SEM micrograph of film B annealed at 600°C for 30 min

Optical Properties

Measurement of optical properties brought about the most striking difference between type-A and type-B films. Upon heat treatment the films-A invariably start becoming cloudy after 500°C though they are quite transparent before that temperature and yield transmission curves more or less similar to the type-B films. The dark regions in the micrograph of type-A film in Fig. 3(a) might have some deleterious effect on the optical properties. Even in the case of bulk PLT formula A consistently does not give transparent samples.[4] Further work in this direction is underway.

The transmittance vs. wavelength pattern is therefore not reliable after 500C for type-A films. On the other hand type-B films give excellent transmittance curves and the transparency is always very good. However, it was found that for a given annealing temperature below 500C refractive index was higher for type-A than for type-B films.

The refractive index and the thickness calculated from the transmittance vs. wavelength curve using the envelope method are shown in Fig. 4 for bothtype-A and type-B films. The refractive index value was found to be around 1.96 for perovskite(above 500C) type-B films.

DIELECTRIC PROPERTIES

The dielectric constant and the loss tangent values as a function of applied frequency at 1 V (or,field of 30kV/cm) for type-A and type-B films are plotted in Fig. 5. The permittivity and the loss in general both decrease with increasing frequency. The type-B films showed higher dielectric constant as well as slightly higher dielectric loss than type-A. As is shown in the figure, at around 1MHz the dielectric permittivity as well as the loss value starts increasing rapidly with frequency. It might be due to resonance in the electrical test circuit.[5] It was also observed that decreasing the applied field value results in an increase in the dielectric permittivity value.

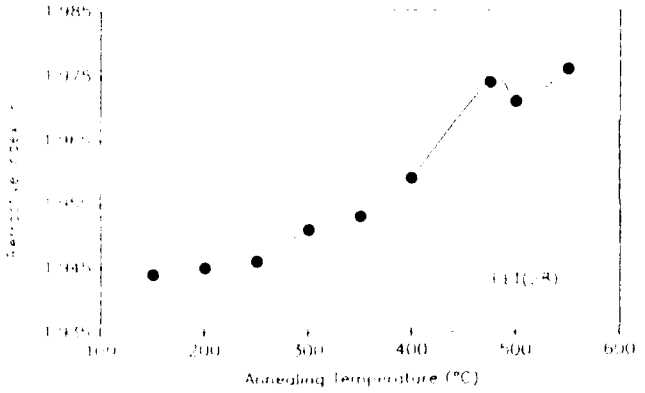


Fig.4a Refractive index of film A as a function of annealing temperature

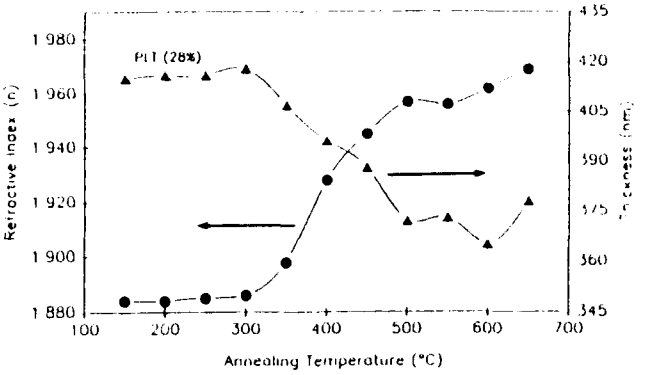


Fig.4b Refractive index and film thickness of film B as a function of annealing temperature.

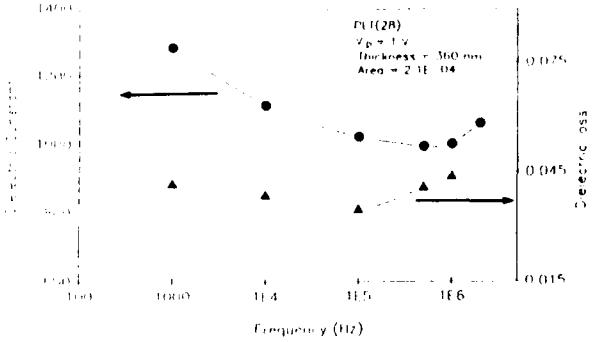


Fig.5a Dielectric constant and loss tangent for film A as a function of applied frequency.

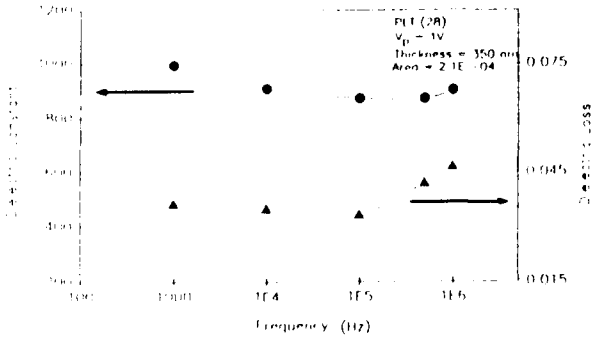


Fig.5b Dielectric constant and loss tangent for film B as a function of applied frequency.

The change in the value of permittivity with temperature is shown in Fig. 6 for the type-A film. The behavior for type-B was similar.

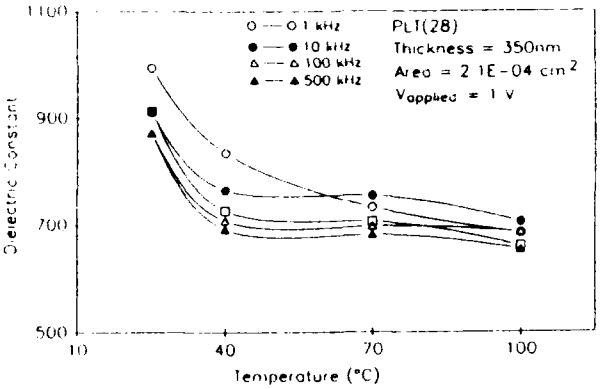


Fig.6 Variation in the dielectric constant of PLT (28) films with temperature (film A).

Time Dependent Dielectric Breakdown

The breakdown of the dielectric after a certain period of time under a fixed applied field lower than its breakdown strength is an important parameter that governs the performance of the dielectric in the memory capacitor. RT66A tester was used to measure the performance of PLT thin film with time at a fixed applied dc voltage of 20 volts. At room temperature the value of resistivity is very high and even at the voltage level as high as 20 V no breakdown was observed for more than three decades. However the same film showed much lower levels of resistivity and a sharp drop in resistivity after one and half decades when the measurement was done at 300C(Fig. 7(a) and 7(b)) indicating the drastic impact of temperature on the performance of the memory cell.

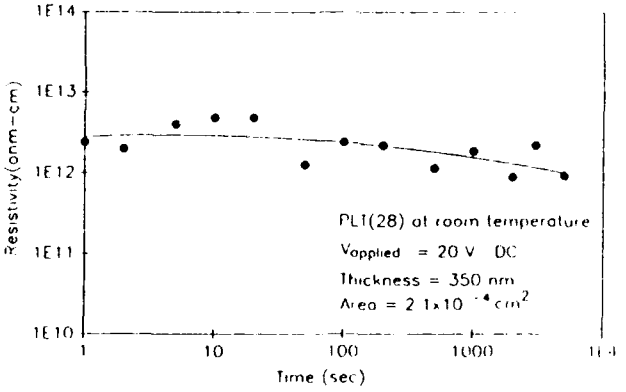


Fig.7a Time dependent dielectric breakdown (TDDB) behavior of PLT (28) at room temperature at an applied voltage 20 V.

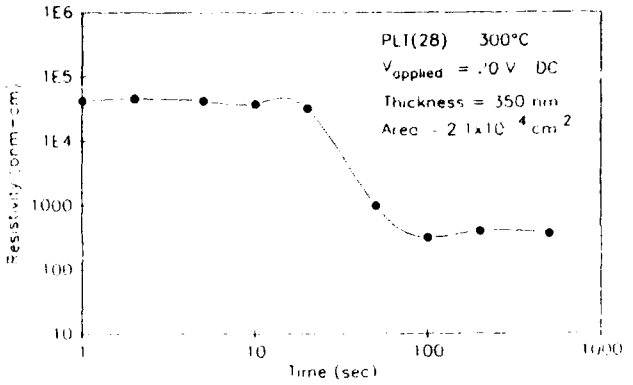


Fig. 7b TDDB behavior of PLT (28) at 300°C at an applied voltage of 20 V.

CONCLUSIONS

PLT thin films having 28 mol% La were fabricated successfully using metalorganic decomposition. The films were made corresponding to two different formulae; assuming A site and B-site vacancy compensation, respectively. The dielectric permittivity was higher for type-B films. Moreover, type-A films became cloudy as the annealing temperature was increased over 500C. In other words, type-B film, which had an excess lead gave more transparent films. Therefore it can be concluded that assuming B-site vacancies results in better quality PLT films. The best dielectric permittivity value obtained at the applied voltage level of 1.0V was 1285 while the lowest loss value was 0.03.

ACKNOWLEDGMENT

This project was partially supported by DARPA through a project from ONR.

REFERENCES

1.Y. Shimizu, K. R. Udaykumar, and L. E. Cross, "Preparation and Electrical Properties of Lanthanum-Doped Lead Titanate Thin Films by Sol-Gel Processing", J. Am. Ceram. Soc., vol. 74, no. 12, pp 3023-3027, Dec 1991.

2.D. Hennings and K. H. Hardtl, "The Distribution of Vacancies in Lanthana-Doped Lead Titanate", Phys. Stat. Solidi., (a) 3, pp 465-474, (1970).

3.C. H. Peng, "Optical Property Studies and Metalorganic Chemical Vapor Deposition of Ferroelectric Thin Films", Ph. D. thesis, Virginia Polytechnic Institute and State University, Aug 1992.

4.G. H. Haertling and C. E. Land, "Hot-Pressed (Pb,La)(Zr,Ti)O_3 Ferroelectric Ceramics for Electrooptic Applications" J. Am. Ceram. Soc., vol 54, no 1, pp1-11, Jan1971.

5.S. K. Dey and J. J. Lee, "Cubic Paraelectric (Nonferroelectric) Perovskite PLT Thin Films with High Permittivity for ULSI DRAM's snd Decoupling Capacitors",IEEE Transactions on Electron Devices, vol 39, no. 7, July 1992.

THE USE OF DESIGN OF EXPERIMENTS TO EVALUATE THE RELIABILITY OF FERROELECTRIC NONVOLATILE MEMORIES

T. D. Hadnagy, S. N. Mitra, D. J. Sheldon
Ramtron International Corporation, 1850 Ramtron Drive, Colorado Springs, CO 80921

Abstract

A full factorial experiment was performed on 4K ferroelectric random access memory (FRAM®) devices to determine their fatigue performance as a function of fatigue temperature, fatigue voltage, read/write voltage, pattern, and number of cycles of fatigue. The resulting response surface of short term retention (10 seconds at 80°C) and long term retention (40 hours at 100°C), as well as product functionality were the metrics used to evaluate the product performance. An empirical model was used to predict yields and product performance. Based on this model, process modifications were undertaken to improve the performance of the product fabricated with PZT (nominal composition — $Pb_{1.10}Zr_{0.48}Ti_{0.52}O_{3.10}$). As a result, better than two orders of magnitude improvement in product performance over operating conditions was seen. The paper will discuss in detail the nature of the experiments performed and the results of process modifications. In addition, the resulting technique has been used to evaluate present product as a benchmark to assure our ability to continuously improve product performance.

Introduction

One of the important capabilities of a nonvolatile memory is not only its ability to store information but how many different times this can be done. There is a concern that data retention interacts with fatigue. A fatigue cycle (endurance cycle) is defined as one read/write cycle. Ramtron was interested in knowing the functional behavior of retention in response to number of fatigue cycles. To that end, a great deal of work has been done at Ramtron and within the industry on the functional fatigue behavior from a capacitor standpoint. Capacitor data is useful in order to determine the mean behavior of different design and process combinations. It is not proven that all large area capacitor data can be mapped directly into product performance. Therefore it is important to measure this material and process interactions on the circuits in question. It was also of great interest to understand the statistical behavior of our product and to be able to model it. In particular, we had a specification on the product that 1e8 cycles at use conditions would not adversely affect the product performance from both a functional and retention standpoint.

Capacitor Data

Individual capacitors were measured using the standard Sawyer-Tower circuit. The pulse sequence and nomenclature are shown in Figure 1. Figure 2 shows how the positive and negative switching and non-switching (P, N, U, and D, respectively) portions of the hysteresis loop are measured.

Figure 1.

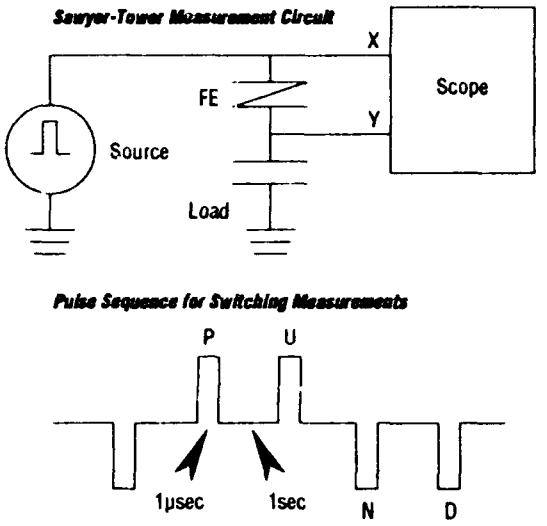
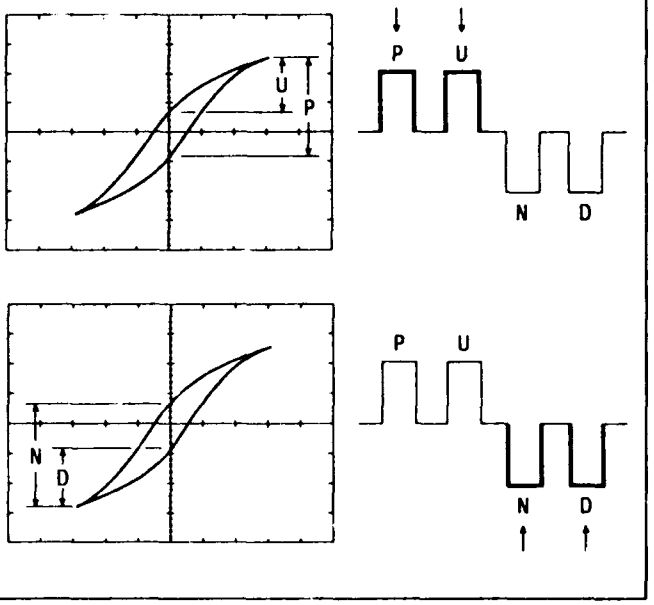


Figure 2.



CH3080-0-7803-0465-9/92$3.00 ©IEEE

Figure 3.

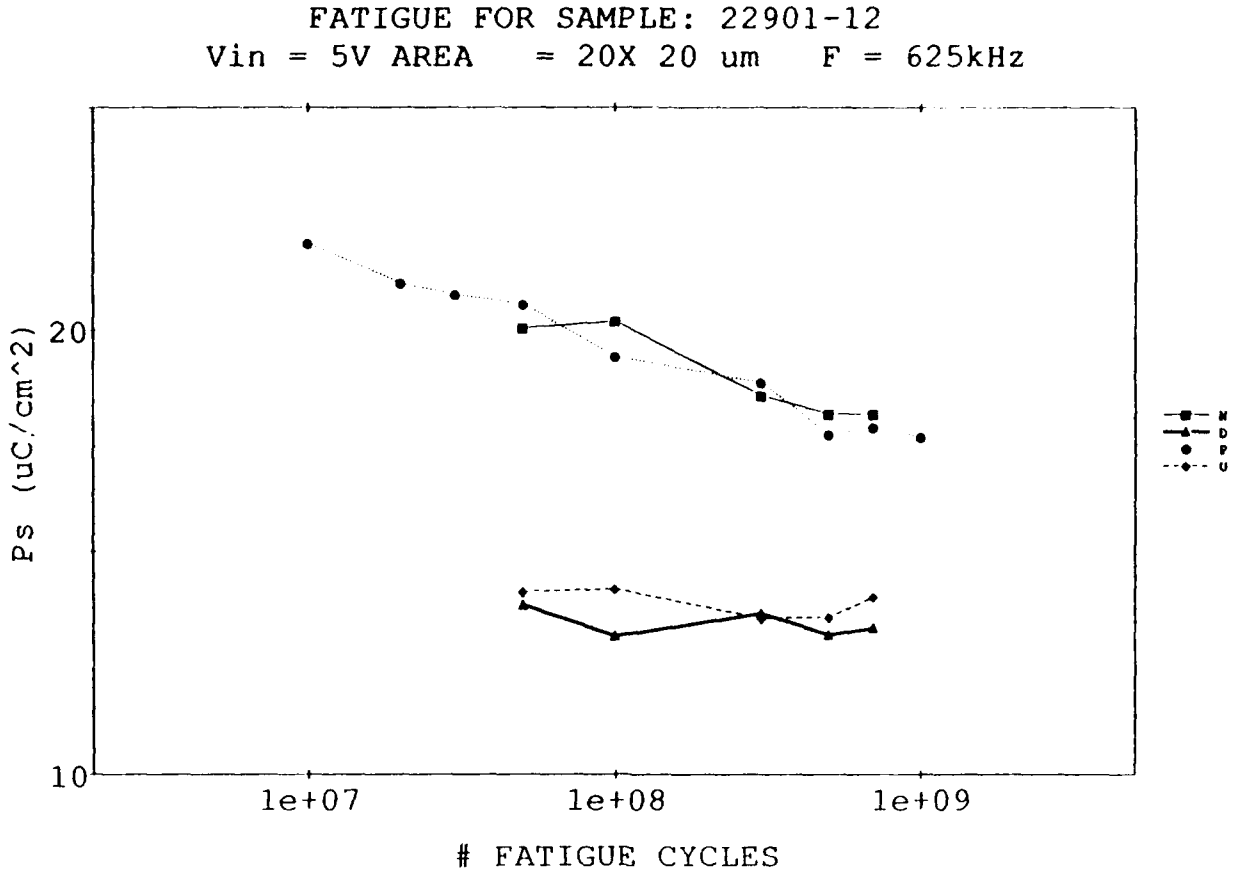


Figure 3 shows the degradation of switch charge as a function of room temperature, 5.0V, bipolar switching pulses for the material that was used for our first generation product. This capacitor data showed that the amount of switched charge was greatly decreased after 1e9 cycles of fatigue. In addition, there was indication that the available charge was degraded and was within 20 percent of the value that was detectable by the circuitry of the part. Our objective was to determine if product manufactured from the same material and process would show similar sensitivities to fatigue cycles as shown by the capacitor data and whether it would continue to retain data after 1e8 cycles.

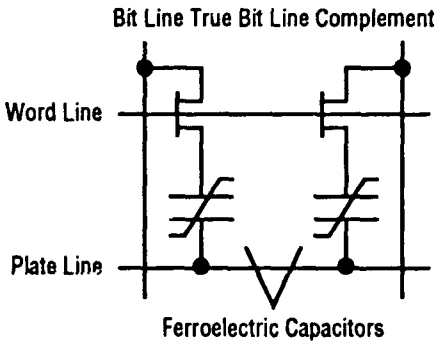
Device Performance

The basic memory cell of the 4,096-bit (FRAM) device organized as 512w x 8b is shown in the circuit diagram of Figure 4. This memory cell uses a two-transistor, two-capacitor structure and is manufactured in a 1.5-micron Si gate CMOS technology.

The application of an electric field can polarize a ferroelectric cell. A reversal of the electric field orients the polarization of the dipoles in the opposite direction. The ferroelectric crystals retain their orientation or polarization even after the electric field is removed. The ferroelectric crystals therefore have two permanent or stable states, and it is this property that is used to store digital data within the ferroelectric cell.

During a write operation to the memory cell (refer to Figure 4), data is transferred from the I/O pins to the bit lines. When the word line is enabled and the plate is pulsed via the plate line, the data will be stored by polarizing the ferroelectric cell in one of its two stable states.

Figure 4. Circuit Diagram of the Basic Memory Cell



To read data from the memory cell, the N channel pass transistors are enabled with the word line going active high, and the difference in polarization is sensed by the sense amplifier to determine the data state stored in the cell. The read operation requires the data to be rewritten or restored to the original data in the cell. This is done by switching the polarization and is done automatically as part of the read cycle.

Test Fixture

A fatigue or burn-in oven was designed that would allow for reading and writing different patterns at different temperatures and voltages. The system is capable of cycling product with a cycle time of 1 microsecond from room temperature to 150°C. In addition, the fatigue cycles can be performed from 4 to 7 volts in increments of 200 millivolts.

Tests

The fatigue tests were done on our 4K product from two different production lots. The capacitor is made of lead zirconate titanate (PZT) with a top and bottom electrode as published in *IEEE Spectrum*, Volume 18, No. 7[1]. The maximum read access is 250 nanoseconds and 500 nanoseconds maximum read or write cycles. Parts were packaged in standard 24-pin SOPs (small outline packages).

A designed experiment was developed with the following factors: temperatures of fatiguing, fatigue cycles, fatigue voltage, pattern, and read or write voltage. The responses that were of interest were short term retention (10 seconds) and long term retention (40 hours at 100°C). All measurements were made at 80°C. The part failure rate and bit failure rate were measured for each test. The experiment was a full factorial design with a total of 54 cells. The fatigue cycling was done with a "solid zero" pattern. Figure 5 lists the factors and related levels that were used in the experiment.

Figure 5.

Experimental Factor	***Range of Factor***
Fatigue Temperature	25, 85°C
Fatigue Voltage	4, 5, 6 Volts
Fatigue Cycles	1e6, 1e7, 1e8 Cycles
Read/Write Voltage	4.5, 5.0, 5.5 Volts
Read/Write Pattern	Row and Rowbar

Analysis

The resulting experiment was completed and then modeled using a statistical software package called "RS Discover" created by BBN Software[2]. The results indicated that the fatigue voltage and the number of fatigue cycles were the only parameters that were important in modeling the behavior of the product. There was a weak dependence on the read or write voltage of the retention tests. This behavior was the same for the bit failure rate as well as the part failure rate. The model indicated that the part failure rate at nominal conditions (5 volts, room temperature) would be more than 60 percent and that same 60 percent would also fail long term retention. In addition, the failure rate was independent of the pattern written or the temperature at which the fatigue was performed. The bit failure rate was predicted to be about 400 bits per die. Figure 6 gives a response surface model of the results. This model allows us to predict product performance under a number of different conditions. This in turn allows us to predict what our customer base might see for product performance. The result was that the product was not performing to the stated specification conditions.

Ramtron therefore embarked on a series of designed experiments using this technique to evaluate the effect of different process changes to improve product performance. The process changes resulted in the following behavior as measured over five production lots and over 1,000 parts.

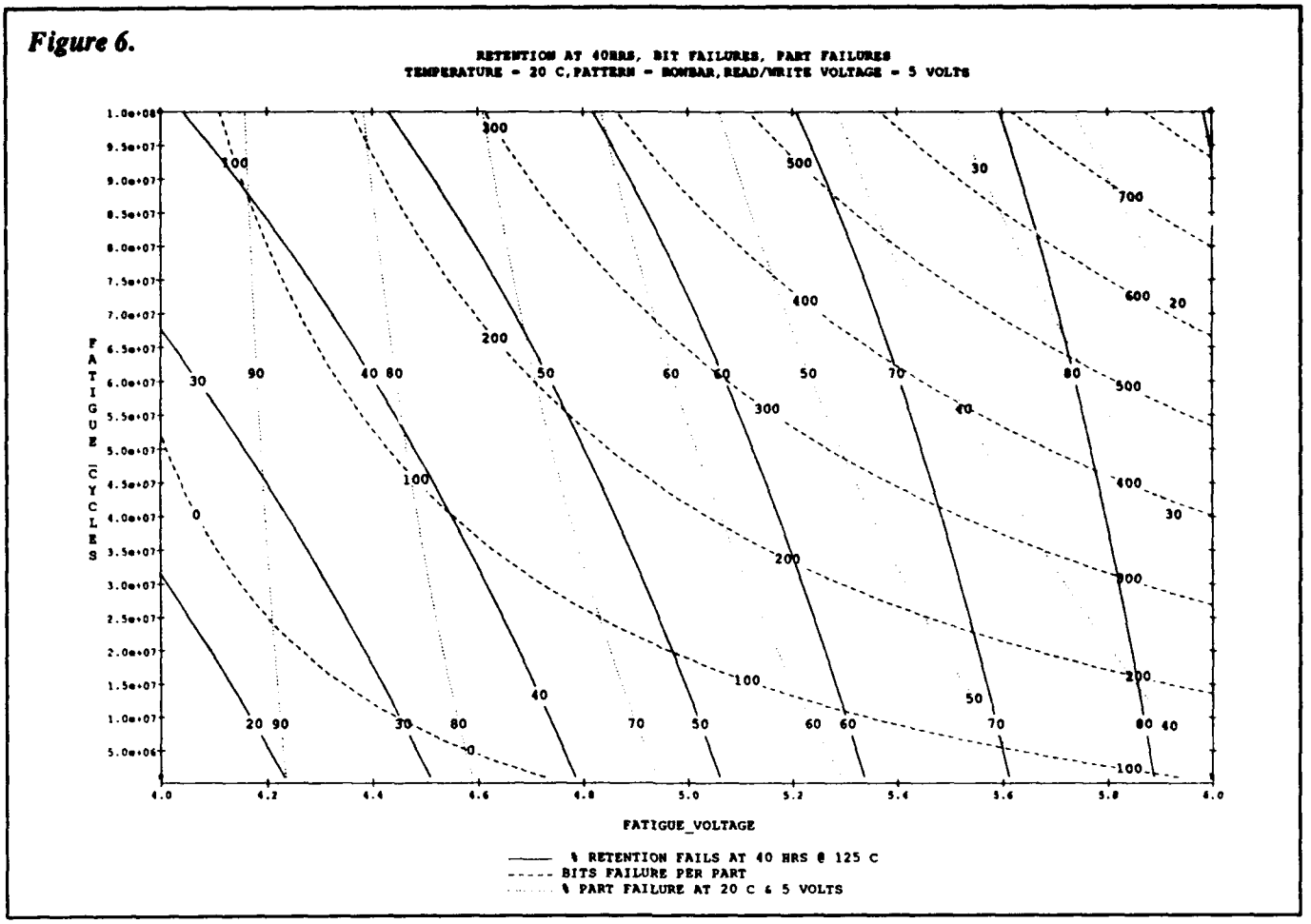
1) The short term retention (shown to a 95 percent simultaneous confidence interval) indicated that at 1e8 cycles the failures were between 0 to 1.3 percent of the product with a mean of .2 percent.

2) The long term retention behavior (to a 95 percent simultaneous confidence interval) indicated that at 1e8 cycles the failure rate was the same as zero cycles of fatigue.

3) Long and short term retention and functional tests after 3.5e9 cycles at 125°C showed to a 95 percent confidence level no change in the failure rate as compared to zero cycles. These results indicate a better than two orders of magnitude improvement in the fatigue performance of our product. This low level of failures prevented us from developing a response surface model.

To ensure that this level of performance is maintained, Ramtron has put in place a SPC based monitoring program. The parameters being monitored are percentage retention loss after 1e9 cycles as well as retention loss at zero cycles.

Figure 6.



Conclusion

The use of a designed experiment allowed the development of a model that would predict part performance. Using this information as a metric of product reliability and quality allows one to improve performance by more than two orders of magnitude. In addition, this also allowed us to develop a statistically based monitoring program to insure product performance.

References

[1] "Ferroelectrics for Nonvolatile RAMs," IEEE Spectrum, vol. 18, no. 7, pp. 30-33, 1989.

[2] BBN Software Products, A Division of Bolt Beranek and Newman Inc., 150 Cambridge, MA 02140.

PURE AND MODIFIED LEAD TITANATE THIN FILMS BY SOL-GEL

D. M. Tahan and A. Safari
Department of Ceramic Science and Engineering
Rutgers, The State University of New Jersey
Piscataway, N. J. 08855-0909

Abstract

Pure and modified lead titanate thin films were fabricated by spin coating an alkoxide based solution onto platinum coated silicon substrates. The solution was made by combining lead acetate trihydrate, titanium IV isopropoxide and diethanolamine in isopropanol with lanthanum as a dopant. Various heating schedules and techniques were examined to optimize the dielectric and microstructural properties of the films. The films were tested for dielectric and hysteresis properties, and were characterized by XRD, SEM, DTA, and TGA. Perovskite $PbTiO_3$ was found to form at approximately 400°C and could be obtained by heating for short soaking durations of 10 minutes per layer. Measured at 1 kHz, an average dielectric constant of 410 was obtained for pure lead titanate films heated at 500°C for 1hr. Hysteresis measurements taken on these films at 100 Hz revealed an average remanent polarization of 11 $\mu C/cm^2$ with a coercive field of approximately 75 kV/cm. The films doped with 5% lanthanum exhibited a dielectric constant of 825 with a coercive field of 52 kV/cm and a remanent polarization of 25 $\mu C/cm^2$.

Introduction

Ferroelectric pure and lanthanum modified lead titanate, $PbTiO_3$ (PT) and $(Pb_{1-1.5x},La_x)TiO_3$ (PLT), thin films have many applications due to the piezoelectric, pyroelectric, and electro-optic properties of these materials. Some of these applications include IR detectors, pyrodetectors, SAW substrates, and waveguide devices.[1,2] The use of PT and PLT in the thin film geometry as opposed to the bulk form allows for greater design flexibility and more economical processing.[2]

Ferroelectric thin films can be fabricated by sputtering, chemical vapor deposition (CVD), and metal-organic chemical vapor deposition (MOCVD). These methods involve drawbacks such as expensive equipment, complicated chemistry, and high reaction temperatures. Other problems with these techniques are difficulties in adjusting composition for the optimization of properties, inhomogeneities, and the fabrication of suitable targets.[1,3] The major disadvantage of these methods is the difficulty in controlling the stoichiometry while fabricating multicomponent oxide films. This problem results from differences in the sputtering rates of the components or the vapor pressures of the CVD precursor reagents.[4]

Sol-gel processing has recently been receiving attention as an alternative method for the fabrication of ferroelectric thin films. This technique provides a solution to some of the problems encountered in conventional fabrication techniques. Modern ceramic technology requires high purity which can be obtained by the sol gel process. Extremely homogeneous thin films with lower processing temperatures can be synthesized because the precursors are mixed as liquids. Also, compositions can be easily adjusted for the optimization of properties of the films.[4] Another advantage of sol-gel is that it facilitates the fabrication of films on substrates with large or complex areas.

There are several different methods by which the gel can be applied to the substrate. The first is dip coating which involves withdrawing a substrate out of a solution at a constant rate. A similar technique involves keeping the substrate stationary and lowering the liquid level. Another method is spin coating which involves spinning the substrate at high RPM and spreading the solution by centrifugal force. Spraying is a technique which is mostly used for applications which do not require thin films with strict thickness tolerances.[5]

Although most of the research on ferroelectric thin films by sol-gel to date follows the techniques reported by Gurkovich et al[6] and Budd et al[3], a method similar to that used by Takahashi et al[7,8] was chosen for this study.[9] Although metal alkoxides, such as titanium isopropoxide, are very unstable to hydrolysis, the addition of a small amount of diethanolamine (DEA) aids in the stabilization of the alkoxide solution.[7,8] Also, DEA enables lead acetate trihydrate to be soluble in an alcoholic solution. Another interesting point about this process is that additional hydrolysis and polymerization steps are not necessary to convert the sol to a gel. The water present in the lead acetate trihydrate is sufficient to cause the reactions to occur, producing a water to alkoxide ratio of 3:1.[7,8] In this study PT and PLT thin films prepared by spin coating were analyzed for their microstructure and ferroelectric properties. The effect of different processing conditions on the properties of the films is studied extensively and discussed.

Experimental

A lead titanate solution was made following the procedures of Takahashi, et al.[7,8] Figure 1 is a flow diagram illustrating this process. The first step in the solution preparation was to make a 0.5M solution of titanium IV isopropoxide in isopropanol.

CH3080-0-7803-0465-9/92$3.00 ©IEEE

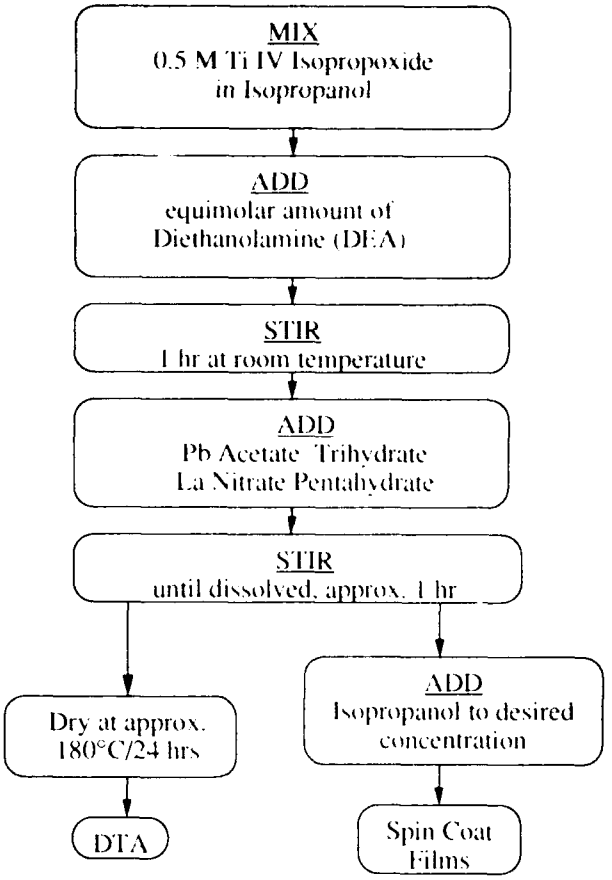


Figure 1. Flow chart illustrating the solution preparation process.

An equimolar amount of DEA was added to this solution, and it was stirred at room temperature for 1 hour. Lead acetate trihydrate and lanthanum nitrate pentahydrate were added in the appropriate stoichiometric proportions. This was stirred until a clear solution developed (approximately 1 hour). This process yielded a 0.5M solution of $(Pb_{1-1.5x}La_x)TiO_3$. To decrease the concentration, isopropanol was added. A sample of the solution was dried at 180°C for 24 hours. DTA and TGA analyses were then performed on the dried gel.

The films were spun onto platinum sputtered Si substrates* at various RPM and spinning times with an Integrated Technologies P-6000 spin coater** . After each coating, the substrates were placed on a hot plate at 180°C for 10 minutes to dry. In this step the gel shrank and lost weight through the evaporation of solvent and adsorbed water. This is a critical step in the processing of the films because cracks and other defects are most likely to develop in this stage. The hot plate temperature was then increased to approximately 350°C and the film was heated for 15 minutes. This was done to pyrolyze the organics, which left tiny pores throughout the film. These pores were later eliminated by a viscous flow sintering mechanism[4] when the films were heated in a furnace at 400-600°C for 1 hour. This process was repeated until the desired film thickness was achieved.

The films were analyzed by XRD, SEM and optical microscopy. The dielectric constants of the films were calculated from capacitance measurements taken at 1 kHz. The remanent polarization and coercive field values of the films were measured at 100 Hz using a hysteresis bridge circuit. These properties were determined for films which were prepared with various processing parameters and were compared.

* Silicon Quest, Monterey, CA.

** Integrated Technologies, Inc., Acushnet, MA.

Results and Discussion

The DTA/TGA analysis of the dried PT gel shown in Figure 2 illustrates that the pyrolysis of organics begins at approximately 300°C and continues until approximately 360°C. Also, crystallization of PT is seen to occur at approximately 440°C.

Several parameters, such as spinning speed and time affect the quality of thin films fabricated by spin coating. Films coated six times at 3000 RPM for 25 seconds developed cracks which ran throughout the samples. Each layer was measured to be approximately 250 nm thick. A second set of samples was made in a similar manner but with a higher spinning speed of 7500 RPM and with the same spinning time. Each layer was measured to be 110 nm in thickness, and the quality of the films was greatly improved. The cracks in the samples only existed on the outer perimeter of the films, leaving the center of the films free of defects. A third set of samples was fabricated at a medium spinning speed of 5000 RPM for an extended spinning time of 1 minute. Each layer of these samples was measured to have a thickness of approximately 180 nm, and the resulting films were very similar to the previous samples with cracks only on the outer perimeter of the films. These results indicated that each layer of the films should be no greater than 200 nm in thickness in order to develop crack free films.

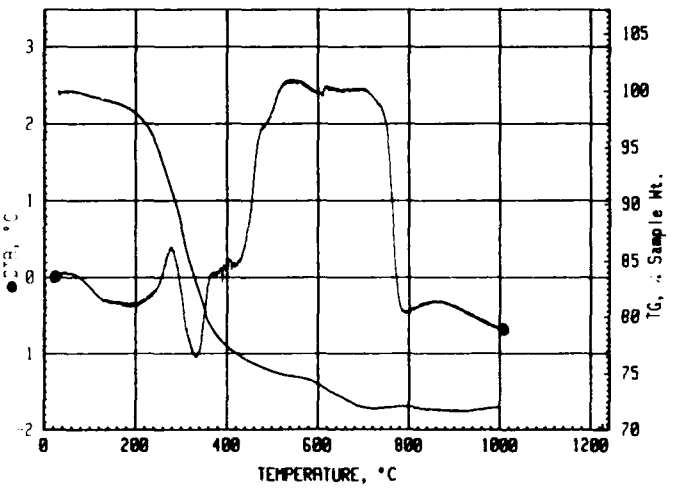


Figure 2. DTA/TGA analysis of dried PT gel.

To increase the thickness of the spin coated films, thicker samples were made by spinning several layers onto the substrate, employing a pyrolysis step between each layer and heating the films once the desired thickness was obtained. It was noticed that after the application of 4 layers (approximately 440 nm) cracks began to develop. To ensure crack free films, a heating step was performed after each coating.

A set of samples heated at various temperatures for 1 hour was fabricated in this manner until a thickness of 6 layers was obtained. The XRD patterns for these samples can be seen in Figure 3. All of the patterns appear similar and exhibit the formation of perovskite lead titanate.

Table 1 shows the dielectric constant and loss values for these films. It can be seen that the samples exhibited a maximum dielectric constant of 410 at 500°C and a minimum of 170 at 400°C. The maximum tan δ, 0.065, occurred at 400°C and the minimum of approximately 0.035 occurred at 500°C. Figure 4 graphs the remanent polarization and coercive field against heating temperature. The remanent polarization was maximum (11 $\mu C/cm^2$) at 500°C, and then saturated at a value of approximately 6.5 $\mu C/cm^2$ with heating temperatures above 550°C. The coercive field increased almost linearly with temperature from a value of approximately 75 kV/cm at 500°C to 115 kV/cm at 600°C.

All of these results were obtained from samples which were heated from room temperature to 600°C at a rate of 3.5°C/minute. The samples were held for a soak of 1 hour, and were then cooled to room temperature. Because it was necessary to implement this schedule after every coating to prevent cracking, the fabrication time for one film was quite long. To shorten the fabrication time of the films, various other heating techniques were tested.

The first method was to place the films directly into a furnace preheated to a set temperature. Figure 5 shows the XRD spectra of samples made in this fashion and heated at 600°C

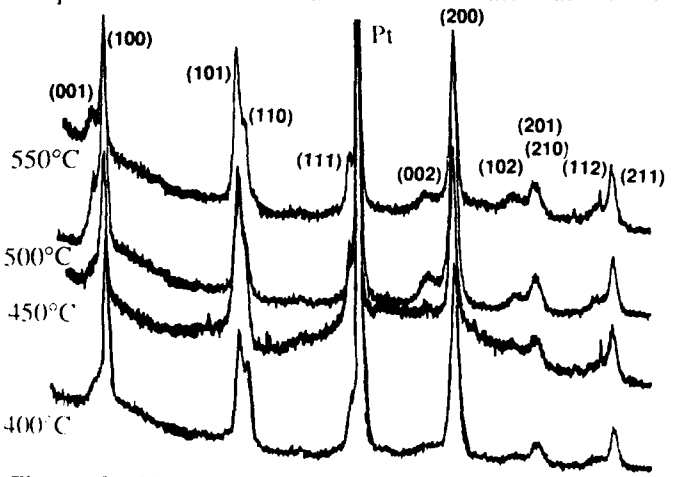


Figure 3. XRD analysis of PT films heated at various temperatures.

Table 1. Dielectric constant and tan δ values at various heating temperatures.

Temperature	400°C	500°C	600°C
Dielectric Constant	170	410	375
Tan δ	0.065	0.035	0.055

for 1 and 0.5 hours, respectively. The XRD patterns exhibit the diffraction peaks characteristic of perovskite PT, even for the shortened soaking time of 0.5 hours. Table 2 lists the measured electrical properties for these films. It can be seen that the dielectric constant decreased with shortened soaking time from 350 to 210. The coercive field for the samples increased with shortened soaking time from 55 to 80 kV/cm, and the remanent polarization remained constant with a low value of 2 $\mu C/cm^2$.

A second heating technique was used to reduce the fabrication times of the films. This method involved ramping the films up to the soaking temperature at a very fast rate of 600°C/minute in a tube furnace. The films were then heated at this temperature for short times of 10 and 15 minutes, and were cooled down at the same rate. The XRD patterns for these samples can be seen in Figure 6. Perovskite PT peaks were present in the XRD spectra of the films processed with these short soaking times. The electrical properties for these samples are also listed in Table 2. The dielectric constant again decreased with shortened soaking time from 240 to 150, and the tan δ increased from 0.05 to 0.10. A coercive field of 60 kV/cm and a remanent polarization of 1 $\mu C/cm^2$ were obtained for the samples with a soaking time of 15 minutes, although the sample with a soak of 10 minutes did not exhibit hysteresis.

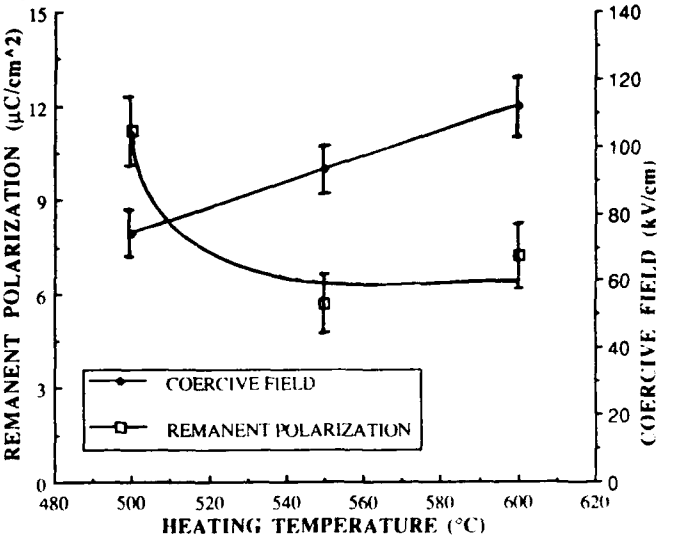


Figure 4. Remanent polarization and coercive field vs. heating temperature.

Pure $PbTiO_3$ Table 2. Electrical Properties.

Heat Treatment at 600°C	Time/ layer	K 1 kHz	tan δ 1 kHz	E_c (kV/cm) 100 Hz	P_r (μ C/cm²) 100 Hz
Preheated Furnace	60 min	350	0.080	55	2
	30 min	210	0.025	80	2
Fast Fire	15 min	240	0.050	60	1
	10 min	150	0.100	-----	-----

$(Pb_{.925}, La_{.05})TiO_3$

Conventional Heat Treatment at 600°C	1 hr	825	0.085	52	25

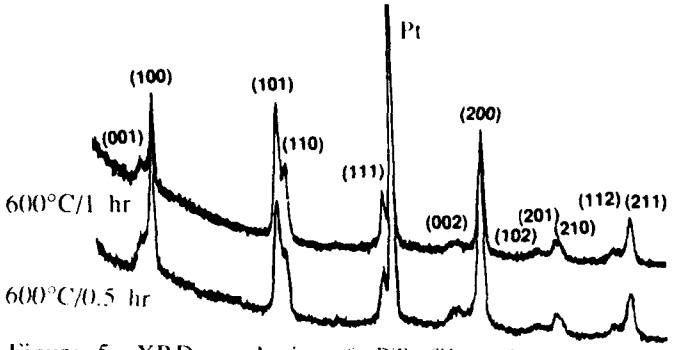


Figure 5. XRD analysis of PT films heated in a preheated furnace.

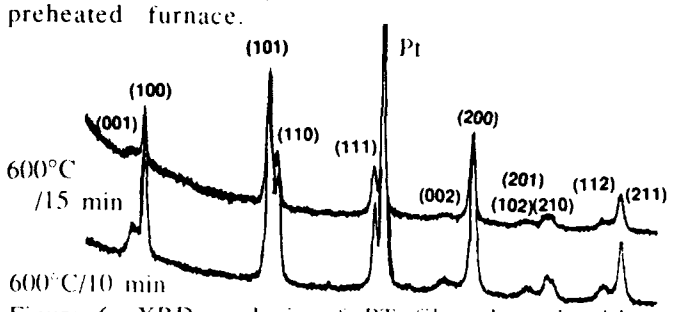


Figure 6. XRD analysis of PT films heated with a rate of 600°C/min.

Lanthanum-doped lead titanate films, $(Pb_{.925}, La_{.05})TiO_3$, were prepared by heating to 600°C for 1 hour after each coating. The dielectric constant was measured to be 825 with a tan δ of 0.085. The coercive field and remanent polarization for these samples was 52 kV/cm and 25 $\mu C/cm^2$, respectively (Table 2).

Conclusions

Homogeneous lead titanate thin films were made by a sol-gel technique, with crystallization temperatures as low as 400°C. Parameters, such as spinning speed and spinning time affected the quality of the films. A thickness of approximately 200 nm was determined to be the maximum thickness for each layer in order to prevent cracking of the film. To produce high quality thicker films, a multilayer technique was performed by heating the film after each coating. It was also concluded that different heating techniques and temperatures have an effect on the quality of the films, and small additions of La have a significant effect on the dielectric and ferroelectric properties of the films.

Acknowledgements

The authors would like to thank the National Science Foundation and Alcoa Research Foundation for their support of this research.

References

[1] S. L. Swartz, S. J. Bright, J. R. Busch and T. R. Shrout, "Sol-Gel Processing of Ferroelectric Thin Films", presented at the Ceramic Science and Technology Congress, Anaheim, CA, November 2, 1989.

[2] L. M. Sheppard, "Advances in Processing of Ferroelectric Thin Films", Ceramic Bulletin, Vol. 71, No. 1, pp. 85-95, 1992.

[3] K. D. Budd, S. K. Dey and D. A. Payne, "Sol-Gel Processing of PbTiO3, PbZrO3, PZT and PLZT Thin Films", British Ceramics Proceedings, Vol. 36, pp. 107-121, 1985.

[4] G. Yi and M. Sayer, "Sol-Gel Processing of Complex Oxide Films", Ceramic Bulletin, Vol. 70, No. 7, pp. 1173-1179, 1991.

[5] L. E. Scriven, "Physics and Applications of dip coating and spin coating", Materials Research Symposium Proceedings, Vol. 121, pp. 717-729, 1988.

[6] S. R. Gurkovich and J. B. Blum, "Preparation of Monolithic Lead Titanate by a Sol-Gel Process", Ultrastructure Processing of Ceramics, Glasses and Composites, L. L. Hench and D. R. Ulrich, New York: Wiley-Interscience, 1984, pp. 152-160.

[7] Y. Takahashi and K. Yamaguchi, "Dip-Coating Conditions and Modifications of Lead Titanate and Lead Zirconate Titanate Films", Journal of Materials Science, Vol. 25, pp.3950-3955, 1990.

[8] Y. Takahashi, Y. Matsuoka, K. Yamaguchi, M. Matsuki, and K. Kobayashi, "Dip Coating of PT, PZ, and PZT Films Using an Alkoxide-Diethanolamine Method", Journal of Materials Science, Vol. 25, pp. 3960-3964, 1990.

[9] S. J. Milne and S. H. Pyke, "Modified Sol-Gel Process for the Production of Lead Titanate Films", Journal of the American Ceramics Society, Vol. 74, pp. 1407-1410, 1991.

EFFECT OF Zr/Ti STOICHIOMETRY RATIO ON THE FERROELECTRIC PROPERTIES OF SOL-GEL DERIVED PZT FILMS

G. Teowee, J.M. Boulton, E.A. Kneer, M.N. Orr,
D.P. Birnie III, and D.R. Uhlmann
Arizona Materials Laboratories
Department of Materials Science and Engineering
University of Arizona
4715 E. Ft. Lowell Road
Tucson, AZ 85712

S.C. Lee, K.F. Galloway and R.D. Schrimpf
Department of Electrical and Computer Engineering
University of Arizona
Tucson, AZ 85721

Abstract

A series of sol-gel derived PZT films with Zr:Ti ratios including 100:0, 94:6, 80:20, 65:35, 53:47, 35:65, 20:80 and 0:100 was prepared on platinized Si wafers. The precursor chemistries were based on lead acetate and Zr/Ti alkoxides containing the appropriate amounts of cations in the required stoichiometries. Excess PbO was incorporated to compensate for PbO loss during processing. Films were fired to 700C where they were all single-phase perovskite as determined by XRD. Microlithography was performed to obtain Pt-PZT-Pt monolithic capacitors with 130 μm square electrode pads. Ferroelectric properties were obtained on these pads using a Radiant Technologies RT-66A Tester while the leakage characteristics were measured using a Keithley 617 Electrometer. The dielectric and ferroelectric properties of the PZT films were highly dependent on composition and processing conditions.

Introduction

Lead zirconate titanate (PZT) is a widely explored ferroelectric (FE) material utilized for its FE, dielectric, electro-optic, acousto-optic, pyroelectric and piezoelectric properties in both bulk and thin film forms[1]. PZT is a solid solution containing lead titanate (PT) and lead zirconate (PZ) in various stoichiometric ratios. PZT x/y refers to $Pb(Zr_{x/100}Ti_{y/100})O_3$ where x,y≤100 and x+y = 100. The PZT phase diagram is shown in Fig. 1.

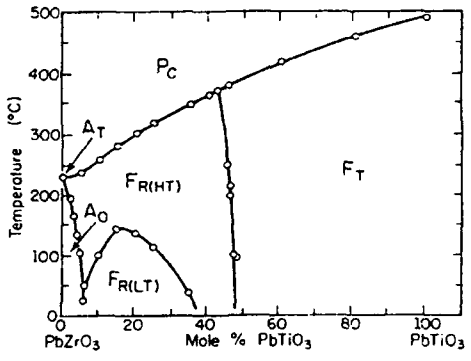


Fig. 1 - Phase diagram of PZT (P_c-cubic paraelectric, A_T-tetragonal antiferroelectric, A_o-orthorhombic antiferroelectric, $F_{R(HT)}$-high temperature rhombohedral ferroelectric, $F_{R(LT)}$-low temperature rhombohedral ferroelectric and F_T-tetragonal ferroelectric).[1]

Note that PZ is antiferroelectric (AF) while PT is ferroelectric; and solid solutions of these two end numbers produce mostly FE materials with fascinating properties which are highly dependent on the Zr/Ti ratio. Examples of the effect of this stoichiometry ratio on material properties include dielectric constant, planar coupling constant and T_c, the Curie point. PT-rich and PZ-rich compositions belong to the tetragonal and rhombohedral modifications respectively of the perovskite crystal structure. In the PZ-PT phase diagram, the rhombohedral-tetragonal boundary is the most important feature, termed the morphotropic phase boundary (MPB). It is located at about 53 atom % Zr or 47 atom % Ti (PZT 53/47). Not only is the dielectric constant highest at this boundary, but also the electromechanical coupling factor and piezoelectric coefficients achieve their maximum values here[1].

Recently PZT films have attracted considerable attention for applications in ferroelectric memory. The numerous techniques used to prepare PZT films include magnetron sputtering[2], diode sputtering[3], e-beam evaporation[4], laser ablation[5], plasma spraying[6], MOCVD[7], and sol-gel methods[8].

Most of the attention has been focused on the MPB composition, namely PZT 53/47[9,e.g.]. There is, unfortunately, scant attention in the literature on exploring the effect of Zr/Ti ratio on the FE properties of PZT films[10-13]. The film properties are expected to vary since the crystal structure and ferroelectric nature (whether ferroelectric or antiferroelectric) change with Zr/Ti ratio.

Experimental

The general chemical formula PZT x/y for the various PZT compositions studied consisted of $Pb_{1.1}Zr_{x/100}Ti_{y/100}O_{3.1}$ where x,y≤100 and x+y=100. The specific compositions chosen cover the range of tetragonal, orthorhombic or rhombohedral modifications of PZT, namely PZT 0/100, PZT 20/80, PZT 35/65, PZT 53/47, PZT 65/35, PZT 80/20, PZT 94/6 and PZT 100/0.

The precursor solutions were prepared using lead acetate and Ti/Zr alkoxides. The derived stoichiometrics were achieved in these precursor solutions by adding the appropriate molar ratios of Pb, Zr and Ti (where applicable). 10 mole % excess PbO was also incorporated as shown by the chemical formulae. After refluxing for 3 hours, the solutions were concentrated to 1.0 M.

Substrates chosen were Si(100) wafers which had previously been thermally oxidized before being sputtered with Pt to yield Pt(2000Å)/SiO_2(1500Å)/Si. Spincoating was performed in a Class 100 clean room using a Headway Spinner at 2000 rpm for 30s. The precursor solutions were filtered using a syringe filter (0.2 μm) to minimize particle contamination. The green films were fired at 500C to burn off the organics, yielding films ~1700A thick per coating. In order to achieve thicker films, multiple coatings were performed. Typically three coatings were required to obtain films about 0.5 μm. Later these films were fired at 700C to crystallize them fully into single-phase perovskite.

Microlithography was used to define 130 μm x 130 μm Pt top electrode pads using a lift-off technique. The monolithic Pt-PZT-Pt capacitors were completed by obtaining back-contact through acid-

CH3080-0-7803-0465-9/92$3.00 ©IEEE

etching one portion of the films. These capacitors were later post-metallization annealed at 100C for 5 mins. to consolidate the top electrodes.

The phase assembly in the films was monitored by X-ray diffraction (XRD) using a Scintag XRD Diffractometer. The ferroelectric properties were measured using a Radiant Technologies RT-66A Ferroelectric Tester. The leakage characteristics were obtained using a Keithley 617 Electrometer.

Results and Discussions

XRD results indicated that the phase assemblages depended on composition and processing temperature. PZT 0/100 (i.e., $PbTiO_3$) crystallized the easiest on Pt substrates, forming single-phase perovskite at 500C. With increasing Zr content, perovskite crystallization is hindered. Crystallization behavior of the PZT films is substrate-dependent. For PZT films on Pt fired to 500C, with Zr content $x>35$, pyrochlore phase was found; while $PbTiO_3$-rich compositions (i.e., $x<35$) were all perovskite at the same firing temperature. All films fired to 700C or 750C, regardless of Zr/Ti ratio, became single-phase perovskite. Fig. 2 shows the XRD scans of various PZT perovskite films fired to 700C. As expected, PZ-rich compositions are rhombohedral while PT-rich films exhibit tetragonal structures (note the tetragonal splitting in the XRD peaks which denotes a high degree of crystallinity).

Films on Pt fired above 600C show no pyrochlore phase. In constrast, Zr-containing PZT films on Corning 7059 glass remained perovskite-free even when fired up to 750C[14].

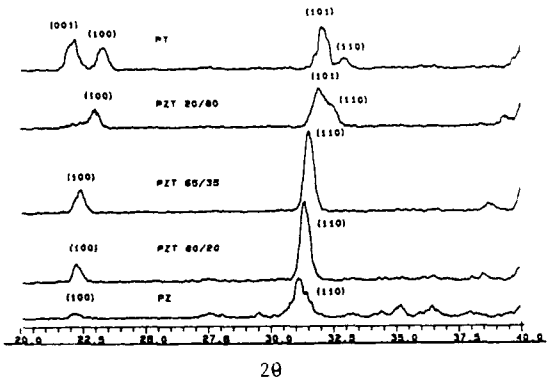


Fig. 2 - XRD scans of the perovskite PZT films fired to 700C as a function of Zr/Ti ratio.

Optical microscopy revealed that rosette perovskite grains tended to predominate in Zr-rich PZT compositions. The PT film appeared slightly porous; however, $PbTiO_3$-rich PZT films were observed to consist of dense microstructures with no intergranular phase. The rosette grain size increased with Zr content, and in Zr-rich PZT films, large percolated rosettes were seen in films fired to 700C. Note that 10 mole % of excess PbO was incorporated in these PZT films since it was found that 10-15 mole % excess PbO was optimal in achieving PZT 53/47 films with superior dielectric and FE properties[15]. It was found previously that, at least in the specific example of PZT 53/47 films, without excess PbO, the stoichiometric PZT 53/47 films tend to display rosette-containing microstructures. With 10 mole % excess PbO, the microstructures become denser and rosette-free. It is expected that since Pb diffusion becomes exacerbated in containing higher concentrations of Zr[16], the optimal amount of excess PbO needed to eliminate rosette formation will depend on the specific Zr/Ti ratio in the films. It was also observed that PZT films with high Zr/Ti ratio tended to crack even on Pt when subjected to elevated firing temperatures, e.g. 700C. The coefficient of thermal expansion increases with Zr content[16] and in films containing large amounts of Zr, the thermal expansion mismatch with the Pt substrate worsens, increasing the tensile stresses upon cooling and leading to film cracking.

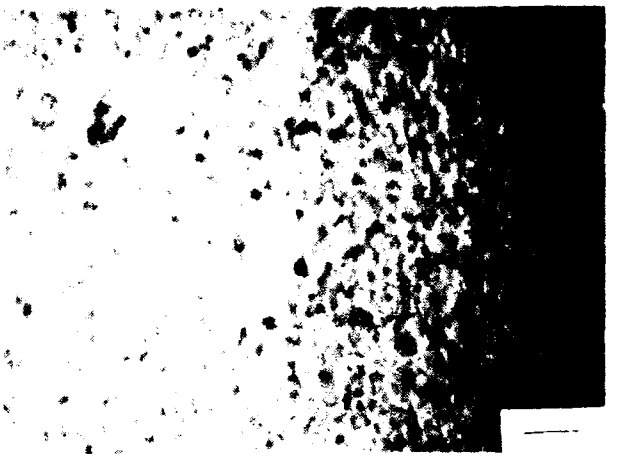


Fig. 3 - Optical micrographs of a sol-gel derived PZT 53/47 film fired to 700C (bar = 10 μm).

The dielectric constants, ϵ_r's, of the PZT films fired to 700C are shown in Fig. 4. The ϵ_r shows a maximum at the MPB, namely in a PZT 53/47 film exhibiting a value of 2100; while in compositions away from the MPB, ϵ_r decreases with increasing Zr or Ti content. This trend follows the behavior of bulk samples (also shown in Fig. 4). Note that the ϵ_r's of the films obtained in this study are consistently higher than those of their corresponding bulk ceramic counterparts regardless of the Zr/Ti ratio.

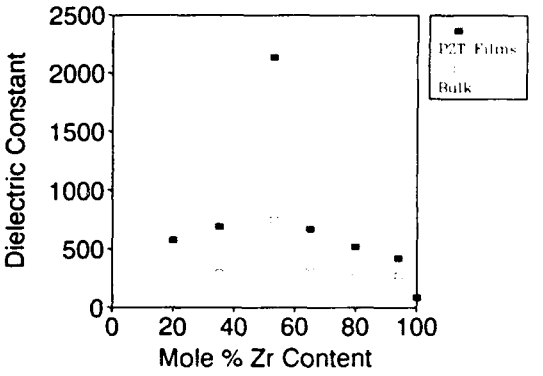


Fig. 4 - Dielectric constants of sol-gel derived PZT films fired to 700C as a function of Zr content. Also shown for comparison on the values for bulk ceramics[1] of the same compositions.

The remanent polarizations and coercive fields of the PZT films fired to 700C are shown in Fig. 5. Note that both the remanent polarization and coercive field are highest near the MPB. Being antiferroelectric, PZ films exhibit low values of P_R and E_c, namely 0.15 $\mu C/cm^2$ and 10 kV/cm respectively.

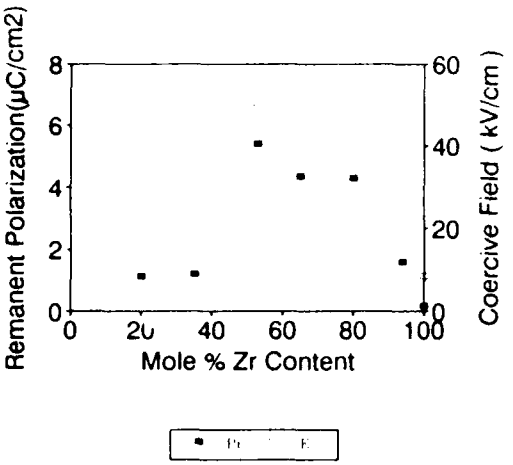


Fig. 5 - Remanent polarizations and coercive fields of sol-gel derived PZT films fired to 700C as a function of Zr content.

Note that the PZT FE capacitors, being non-linear dielectrics, do not exhibit ohmic or linear resistance, i.e., the resistances depend not only on the applied field but also on the electrical history, namely the polarization state. The films show a rapid rise of current at low voltages and an exponential dependence at higher voltages, reflecting the presence of a Schottky barrier at the PZT-Pt interfaces.

Fig. 6 shows the bulk resistivities of the PZT films fired to 700C measured at 8V as a function of Zr content. The resistivities are mostly in the range 10^{10}-10^{11} Ω-cm. Such values are encouragingly higher than those reported in the recent literature[12], e.g., 10^{8} Ω-cm, and reflect a high level of homogeneity/stoichiometry as well as the large grain size of the present films. Bulk resistivities increase with Zr content, reaching $2.5x10^{11}$ Ω-cm in a PZ film, while PT-rich films tend to be relatively conductive. The increase in bulk resistivity with Zr content has been reported in bulk PZT ceramics[17]. Resistivity is a strong function of domain structure and microstructure. While the PZ-rich films tend to be biphasic, consisting of rosettes and an intergranular phase, their composite resistivities are quite high (10^{11} Ω-cm). The PT film was not fully densified even when fired to 700C; and PT-rich films develop severe stresses from the highly anisotropic c/a lattice ratio upon cooling below their Curie temperatures. Microcracks can occur, leading to conductive paths between electrodes. The microstructures of the PZ-rich (Zr > 53 mole %) films indicated that the size of the rosettes increases with Zr content. The increase of resistivity with grain size is expected since with larger grains there are fewer grain boundaries for possible conduction pathways.

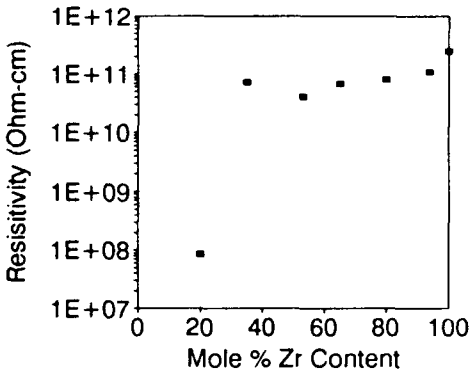


Fig. 6 - Bulk resistivities of sol-gel derived PZT films fired to 700C as a function of Zr content.

The capacitors were also annealed at 400C and 700C after depositing the top Pt electrodes. It was found that the post-metallization annealing had a considerable effect on the dielectric and FE properties of the films. Such annealing helps to consolidate the top Pt electrodes onto the PZT films and renders the top Pt-PZT interfacial characteristics similar to those of the bottom Pt-PZT interfaces which had previously been fired to 700C. The resulting capacitors are more symmetrical in their electrical behavior. Higher post-metallization annealing tends to increase P_R and ϵ_r while decreasing the bulk resistivity. Leakage currents also increase with post-metallization annealing temperature as shown in Fig. 7. Upon post-metallization firing to 700C (i.e., the same temperature at which the PZT films were fired), the leakage current increases by about 5 orders of magnitude; while lower firing temperatures (i.e., 100 or 400C) resulted in insignificant changes. In films containing higher concentrations of Zr, the increase in leakage current is exacerbated even at lower post-metallization temperatures (e.g., 400C). This is due to the diffusion of Pb into the Pt electrodes, an effect which worsens with increasing Zr content since the partial vapor pressure of PbO is higher in films containing higher Zr concentrations[14,e.g.] Such diffusion not only affects the PZT-Pt interfaces, but also renders the PZT films more conducting due to Pb vacancies resulting from the Pb loss.

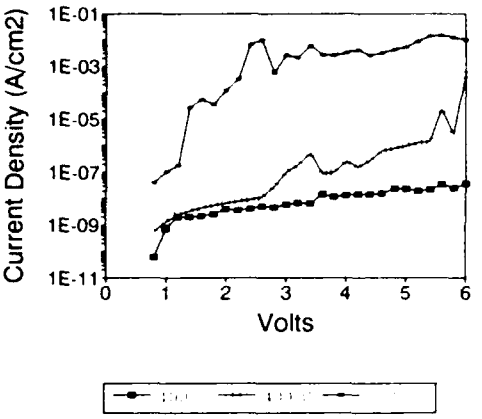


Fig. 7 - Effect of post-metallization annealing temperature on the leakage characteristics of a sol-gel derived PZT 35/65 film fired to 700C.

Conclusions

In the sol-gel derived PZT films obtained in the present study, the Zr/Ti ratio significantly affects the phase assemblage, crystallization behavior and microstructure, as well as the dielectric and ferroelectric properties.

The desired perovskite phase forms at lower firing temperatures on Pt in films with high PT contents, while the presence of high amounts of PZ favors the pyrochlore phase. Crystallized PT-rich and PZ-rich films are tetragonal and rhombohedral respectively.

With increasing Zr content, rosettes tend to form (x > 53 mole %); and the size of the rosettes increases with higher Zr contents. PT and PT-rich films exhibit dense, uniform microstructures. Different amounts of excess PbO may be needed to eliminate rosette formation, depending on the Zr content in the films. The bulk resistivity increases and the leakage current decreases with Zr content.

In films fired to 700C, the values of ϵ_R, P_R and E_c reach their maxima near the MPB, i.e., in the PZT 53/47 films. The values of the dielectric constant observed were consistently higher than those reported for bulk ceramics regardless of the Zr/Ti ratio.

The post-metallization annealing temperature considerably affects the FE and dielectric properties of the films. High post-metallization annealing temperatures increase the values of P_R, E_c, ϵ_r and leakage current. The degradation in leakage characteristics was more significant in higher Zr-containing films where Pb diffusion into Pt electrodes is exacerbated.

The low leakage currents (or high bulk resistivities) and superior values of dielectric constant compared to bulk values indicate that the various PZT films obtained in this study exhibit high degrees of homogeneity and stoichiometry.

Acknowledgment

Financial support for the present work was provided by the Air Force Office of Scientific Research (GT, JMB, DRU) and by the Office of Naval Research (EAK, SLL, MNO, KFG, RDS and DPB). This support is gratefully acknowledged.

References

[1] B. Jaffe, W.R. Cook and H. Jaffe, Piezoelectric Ceramics, Acad. Press, NY 1971.

[2] K. Sreenivas and M. Sayer, "Characterization of $Pb(Zr,Ti)O_3$ Thin Films Deposited from Multi-element Metal Targets," J. Appl. Phys., Vol 64 (3), pp 1484-1493, 1988.

[3] A. Okada, "Some Electrical and Optical Properties of Ferroelectric Lead Zirconate-Lead Titanate Thin Films," J. Appl. Phys., Vol. 48 (7), pp 2905-2909, 1977.

[4] M. Oikawa and K. Toda, "Preparation of $Pb(Zr,Ti)O_3$ Thin Films by an Electron Beam Evaporation Technique," Appl. Phys. Lett., Vol. 29 (8), pp 491-492, 1976.

[5] S. Otsubo, T. Maeda, T. Minamikawa, Y. Yonezawa, A. Morimoto and T. Shimizu, "Preparation of $Pb(Zr_{0.52}Ti_{0.48})O_3$ Films by Laser Ablation," Jpn. J. Appl. Phys., Vol. 29 (1), pp L133-L136, 1990.

[6] B. Malric, S. Dallaire and K. El-Assal, "Crystal Structure of Plasma-Sprayed PZT Thick Films," Mater. Lett., Vol. 5 (7,8), pp 246-249, 1987.

[7] M. Okada, K. Tominaga, T. Araki, S. Katayama and Y. Sakashita, "Metalorganic Chemical Vapor Deposition of C-axis Oriented PZT Thin Films," Jpn. J. Appl. Phys., Vol. 29 (4), pp 718-722, 1990.

[8] K.D. Budd, S.K. Dey and D.A. Payne, "Sol-gel Processing of $PbTiO_3$, $PbZrO_3$, PZT and PLZT Thin Films," Br. Ceram. Proc., Vol. 36, pp 107-121, 1986.

[9] G.A.C.M. Spierings, M.J.E. Ulenaers, G.L.M. Kampschöer, H.A.M. van Hal and P.K. Larsen, "Preparation and Ferroelectric Properties of $PbZr_{0.53}Ti_{0.47}O_3$Thin Films by Spin Coating and Metalorganic Decomposition," J. Appl. Phys., Vol. 70 (4), pp 2290-2298, 1991.

[10] K. Iijima, I. Ueda and K. Kugimiya, "Preparation and Properties of Lead Zirconate-Titanate Thin Films," Jpn. J. Appl. Phys., Vol. 30 (9B), pp 2149-2151, 1991.

[11] R. Takayama and Y. Tomita, "Preparation of Epitaxial $Pb(Zr_xTi_{1-x})O_3$ Thin Films and Their Crystallographic, Pyroelectric and Ferroelectric Properties," J. Appl. Phys., Vol. 65 (4), pp 1666-1670, 1989.

[12] K. Sreenivas, M. Sayer and P. Garrett, "Properties of D.C. Magnetron-Sputtered Lead Zirconate Titanate Thin Films," Thin Solid Films, Vol. 172, pp 251-267, 1989.

[13] N. Tohge, S. Takahashi and T. Minami, "Preparation of $PbZrO_3$-$PbTiO_3$ Ferroelectric Thin Films by the Sol-gel Process," J. Amer. Ceram. Soc., Vol. 74 (1), pp 67-71, 1991.

[14] G. Teowee, J.M. Boulton, S. Motakef, D.R. Uhlmann, B.J.J. Zelinski, R. Zanoni and M. Moon, "Optical Properties of Sol-gel Derived PZT Thin Films," to be published in SPIE Proc., Vol. 1528, 1992.

[15] G. Teowee, J.M. Boulton, and D.R. Uhlmann, "Optimization of Sol-gel Derived PZT Films by the Incorporation of Excess PbO," to be published in MRS Symp. Proc., Vol. 241, 1992.

[16] G. Shirane, K. Suzuki and A. Takeda, "Phase Transitions in Solid Solutions of $PbZrO_3$ and $PbTiO_3$ (II) X-ray Study," J. Phys. Soc. Jpn., Vol. 7, pp 12-18, 1952.

[17] Z. Wrobel and G. Kus, "Electric Properties in Solid Solutions of $Pb(Zr_xTi_{1-x})O_3$ Near the Morphotropic Phase Boundary," Ferroelectrics, Vol. 22, pp 801-803, 1978.

COMPOSITIONAL CONTROL OF FERROELECTRIC $Pb(Zr,Ti)O_3$ THIN FILMS BY REACTIVE SPUTTERING AND MOCVD

Masaru Shimizu, Koji Hayashi*, Takuma Katayama and Tadashi Shiosaki

Department of Electronics,Faculty of Engineering,Kyoto University
Yoshida Honmachi, Sakyo-ku, Kyoto 606, Japan
*Ube Laboratory, Ube Industry, Ltd.,
1978-5 Kogushi, Ube City, Yamaguchi Prefecture 755, Japan

Abstract

The preparation and compositional control of $Pb(Zr,Ti)O_3$ films obtained using two kinds of reactive sputtering processes and MOCVD were investigated. When a metal composite target was used in reactive sputtering, the film composition Zr/(Zr+Ti) could be controlled from 0.25 to 0.81 by changing the total area of Ti in the target. When an alloy target was used in reactive sputtering, there was no change in the Zr/(Zr+Ti) ratio of the films up to 196 hours of target usage, and the reproducibility of the film compositional control was very good. Using the MOCVD method, the compositions of the films and crystalline structures could be easily controlled by changing the amounts of gases supplied.

1. Introduction

Ferroelectric thin films, such as lead titanate [$PbTiO_3$], lead zirconate titanate [$Pb(Zr,Ti)O_3$:PZT], lantanium modified lead zirconate titanate [$(Pb,La)(Zr,Ti)O_3$], strontium titanate [$SrTiO_3$] and barium titanate [$BaTiO_3$], have been extensively studied for many application devices. Especially, the interest in the use of these ferroelectric thin films for memory applications has increased in recent years. These thin films have been obtained by various kinds of techniques such as electron beam evaporation, sputtering, sol-gel process, chemical vapor deposition (CVD) and metalorganic chemical vapor deposition (MOCVD).

In any thin film growth technique, the compositional control of the films is a very important key factor, because the compositional changes of the films affect the crystalline structure and electrical properties of the films.

In memory device applications of PZT thin films, if the PZT films will be used as a capacitor of DRAM, films with high dielectric constants are required. On the other hand, films with relatively small dielectric constants are useful for application to nonvolatile ferro-RAM. Therefore precise control of the film composition is essential.

In order to investigate the most effective and reproducible method for control of $Pb(Zr,Ti)O_3$ film composition, we developed two kinds of reactive sputtering methods. In one method, reactive sputtering using a metal composite target was employed[1,2]. In the other method, an alloy of Zr and Ti was used as a target.

Recently the MOCVD method for ferroelectric films has attracted much attention because of its great usefulness and the recent development of new source materials. We have also obtained PZT films by MOCVD and photo-MOCVD[3,4]. Therefore, by comparing with our sputtering method, the controllability of the film composition using MOCVD was also investigated.

In this paper, from the point of view of the compositional control we will describe the preparation of $Pb(Zr,Ti)O_3$ thin films obtained using the two types of reactive sputtering processes and MOCVD. The effects of compositional change of films on crystalline structure will be also described.

2. Experimental procedure

In order to prepare $Pb(Zr,Ti)O_3$ thin films, two types of reactive sputtering were used. One type was reactive sputtering using a metal composite target. A typical shape of the metal composite target used is illustrated in Fig.1. The fan shaped Ti pieces used had included angles of 3 and 8 degrees. By increasing or decreasing the number of Ti pieces, the composition of the films could be controlled. The diameter of metal Pb and the ratio of the Zr/Ti area were determined from the sputtering yield of Pb, Zr and Ti, which were modified to the values at Ar/O_2(=50/50) gas mixture according to Sigmund's theory[5]. In our experiment, the number of Ti peaces was changed from 8 to 16 in order to investigate the ratio change of the Zr/(Zr+Ti) area on the crystalline structure of the films. The sputtering system used was a conventional planer magnetron sputtering device. The sputtering conditions are listed in Table 1.

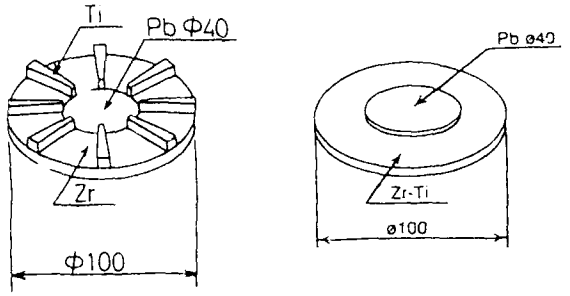
In the other type of sputtering method, an alloy target of Zr and Ti was used. A schematic diagram of the alloy target is also shown in Fig.1. When the alloy target was used, the composition of the target could be changed by changing the alloy ratio of Zr and Ti. In this type of reactive sputtering, the planer magnetron equipment was also used. The sputtering conditions are also listed in Table 1.

$Pb(Zr,Ti)O_3$ thin films were also obtained by MOCVD. In our study, tetraethyl lead [$Pb(C_2H_5)_4$:TEL],zirconium tetratertiarybutoxide [$Zr(O\text{-}t\text{-}C_4H_9)_4$:ZTB] and titanium tetraisopropoxide [Ti(i-

CH3080-0-7803-0465-9/92$3.00 ©IEEE

$OC_3H_7)_4$:TIP] were used as source materials. O_2 was used as an oxidizing gas. The MOCVD system used is shown schematically in Fig.2. The Zr/(Zr+Ti) compositional ratio of the films were significantly controlled by changing the carrier gas flow rates of Zr and Ti sources. In this experiment, substrate temperatures varied from 600 to 650°C and reaction pressure was 6 Torr during the growth run. The growth conditions for $Pb(Zr,Ti)O_3$ are also listed in Table 2.

In our experiments, the substrate used was $Pt(111)/SiO_2/Si(100)$. The crystalline structures of the films grown were determined by the X-ray diffraction method. The film composition was analyzed by the inductively coupled plasma (ICP) emission spectrometry method.



a) b)

Fig.1. Schematic diagrams of the targets; a) metal composite target, b) alloy target.

Table 1. Sputtering conditions for $Pb(Zr,Ti)O_3$ thin films.

Substrate temperture(℃)	560～665
Gas pressure($\times 10^{-2}$Torr.)	0.8～6
Target substrate distance(mm)	45
rf input power(W)	100
Sputtering gas	Ar/O_2=50/50
Substrate	$Pt(111)/SiO_2/Si(100)$
Sputtering time(min)	60
Target(Zr/(Zr+Ti))	
metal composite target	0.64～0.93
alloy target	0.78
Deposition rate (Å/min)	40～120

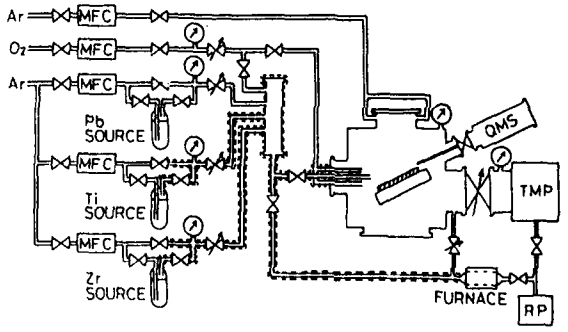


Fig.2. Schematic diagram of the MOCVD system.

Table 2. Growth conditions for $Pb(Zr,Ti)O_3$ thin films using MOCVD.

Source temperature(℃)	$Pb(C_2H_5)_4$	0
	$Zr(O\,t\,C_4H_9)_4$	35～50
	$Ti(O\,i\,C_3H_7)_4$	35～50
Ar carrier flow rate(sccm)	$Pb(C_2H_5)_4$	80
	$Zr(O\,t\,C_4H_9)_4$	20～70
	$Ti(O\,i\,C_3H_7)_4$	26～76
O_2 flow rate(sccm)	240～300	
substrate temperature(℃)	525～660	
Total pressure(Torr.)	6	

3. Results and discussion

3.1. Reactive sputtering using a metal composite target

When a Pb plate with a diameter of 40mm, and 8 to 16 fan shaped Ti pieces were used, $Pb(Zr,Ti)O_3$ thin films with a perovskite phase were grown on $Pt/SiO_2/Si$ at substrate temperatures from 605 to 635°C. The compositional change of the films was achieved by changing the total number of the Ti pieces in the target. The dependence of the film compositional ratio Zr/(Zr+Ti) on area of Ti is shown in Fig.3. It can be seen that film composition could be controlled by changing the area of the Ti. However there were differences in the composition between the films and the theoretical values calculated from the ratio of the Zr/(Zr+Ti) area of the target.

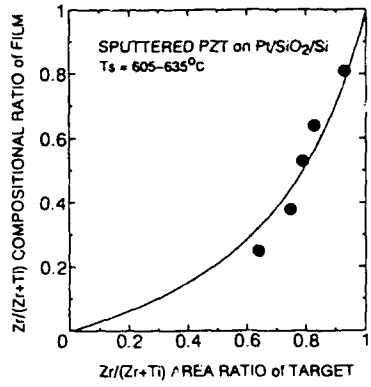


Fig.3. Dependence of the film composition on the area of Ti in the target.

3.2. Reactive sputtering using an alloy target.

$Pb(Zr,Ti)O_3$ thin films were also grown by the reactive sputtering method using an alloy target. The compositional ratio of the Zr/(Zr+Ti) in the alloy target used was 0.78. The crystalline structure of the films grown were influenced by the substrate temperature and the sputtering pressure. Highly (111)oriented $Pb(Zr,Ti)O_3$ films with the perovskite phase were grown at substrate tempera-

tures higher than 620°C and at pressures higher than 2×10^{-3}Torr. X-ray diffraction peaks from perovskite PZT(111), (110) and (001) planes were observed when films were grown higher than 605°C. X-ray diffraction patterns of films grown at substrate temperatures from 590 to 665°C and at a sputtering pressure of 4×10^{-2}Torr are shown in Fig.4. From this figure,it was found that the highly (111) oriented $Pb(Zr,Ti)O_3$ film was grown at a substrate temperature of 620°C.

The composition of the film obtained at 620 °C was investigated by the ICP emission spectrometry method. This analysis revealed that the Zr/(Zr+Ti) atomic ratio of film was 0.78, which was the same ratio as the target's. It was found that there were no differences in the Zr/(Zr+Ti) ratio between the films and the target. The dependence of the Zr/(Zr+Ti) atomic ratio of the films on the elapsed time of target usage was also studied. When the alloy target was used for 196 hours, the Zr/(Zr+Ti) ratio of the film obtained using this target was 0.78, which was also the same ratio as the target's. There was no change in the Zr/(Zr+Ti) ratio of the films up to 196 hours of target usage as shown in Fig.5. This means that the reproducibility and stability of the film compositional control were quite good when an alloy target was used.

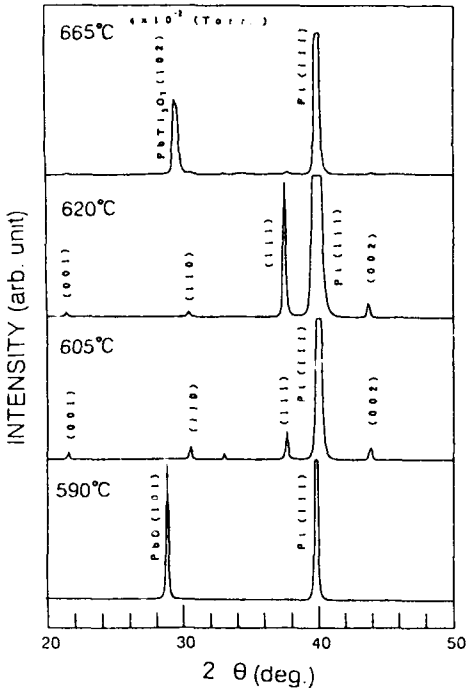


Fig.4. X-ray diffraction patterns of $Pb(Zr,Ti)O_3$ films.

3.3. MOCVD

In our study, the compositional control of the films was also performed using the MOCVD method. In MOCVD, the film composition was controlled by changing the Ar carrier gas flow rates of the Zr and Ti sources. The Ar carrier gas flow rate of Pb

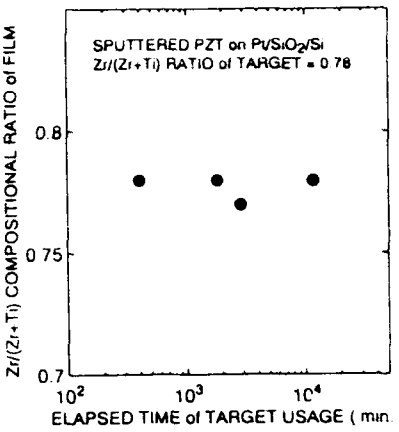


Fig.5. Dependence of the film compositional ratio Zr/(Zr+Ti) on the elapsed time of target usage.

was kept at 240sccm in this experiment. The crystalline structures of the films were influenced by both the ratio of [Zr]/([Zr]+[Ti]), where [Zr] and [Ti] were the amounts of the Zr and Ti gases supplied, and substrate temperature, as shown in Fig.6. $Pb(Zr,Ti)O_3$ films with a tetragonal phase were obtained at [Zr]/([Zr]+[Ti]) ratio smaller than 0.65. By increasing the ratio of [Zr]/([Zr]+[Ti]), $Pb(Zr,Ti)O_3$ with a rhombohedral phase could be grown at substrate higher than 635°C. However, when the ratio of [Zr]/([Zr]+[Ti]) was higher than 0.7, films with a mixture of rhombohedral phase and other phases ($Pb(Zr,Ti)_3O_7$, ZrO_2, $Pb_2(Zr,Ti)_2O_{7-\delta}$, $ZrTiO_4$) were grown. It can be also seen that the growth of the $Pb(Zr,Ti)O_3$ films with a rhombohedral phase required higher substrate temperatures than were required in the growth of the tetragonal $Pb(Zr,Ti)O_3$ films.

The dependence of the film composition on the ratio of [Zr]/([Zr]+[Ti]) was also investigated, which is shown in Fig.7. The experimental data coincided with a theoretical curve, when the ratio k_{Zr}/k_{Ti} was 0.41. Here, K_{Zr} and k_{Ti} are given by $N_{Zr}=k_{Zr}\cdot[Zr]\cdot t_d$ and $N_{Ti}=k_{Ti}\cdot[Ti]\cdot t_d$, where N_{Zr} and N_{Ti} are the

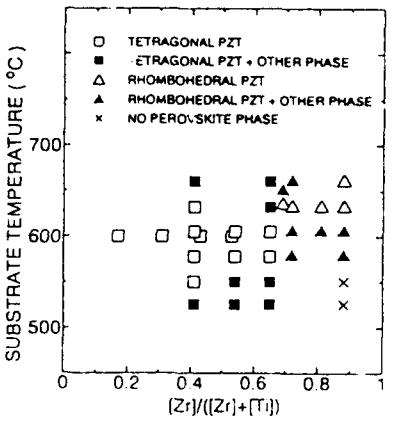


Fig.6. Schematic quality diagram of the $Pb(Zr,Ti)O_3$ films grown by MOCVD.

amounts of Zr and Ti included in the films, and [Zr] and [Ti] are amounts of Zr and Ti gases supplied, respectively. The details is described in reference [6]. From Fig.7, we can see that the compositional ratio of films was not proportional to the ratio of [Zr]/([Zr]+[Ti]). This means that the Zr content could not easily be deposited in the films. The film composition was also affected by substrate temperature. The compositional ratio of Pb/(Pb+Zr+Ti) for the films increased with an increasing substrate temperature.

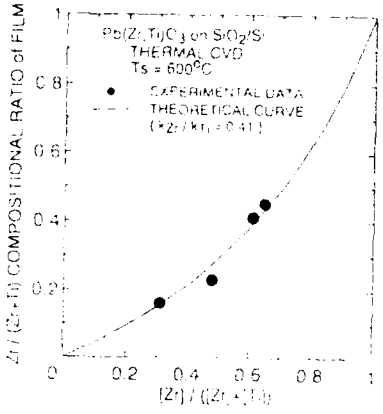


Fig.7. Dependence of the film compositional ratio Zr/(Zr+Ti) on the ratio of gases supplied.

4. Conclusions

In our study, the preparation and the compositional control of the $Pb(Zr,Ti)O_3$ thin films obtained using the reactive sputtering and MOCVD methods were investigated. Two kinds of reactive sputtering were carried out. When a metal composite target was used in reactive sputtering, the perovskite $Pb(Zr,Ti)O_3$ films were grown at substrate temperatures ranging from 605 to 635°C. The film composition Zr/(Zr+Ti) could be controlled from 0.25 to 0.81 by changing the total area of the Ti pieces in the target. However differences in the composition between the films and the theoretical values calculated from the ratio of Zr/(Zr+Ti) area of the target were observed. On the other hand, When an alloy target was used, there were no differences in composition (Zr/(Zr+Ti)=0.78) between the films and the target. There was also no change in the Zr/(Zr+Ti) ratio of the films up to 196 hours of target usage, and the reproducibility of the film compositional control was very good.

Using the MOCVD method, $Pb(Zr,Ti)O_3$ films both with tetragonal and rhombohedral phases were grown at substrate temperatures from 550 to 675°C by changing the ratio of [Zr]/([Zr]+[Ti]), where [Zr] and [Ti] were the amounts of the Zr and Ti gases supplied. There were also differences in composition between the films and the theoretical amounts of the Zr and Ti gases supplied. Moreover it was found that it was easy to control the film composition within a wide range, and the reproducibility was also good.

Acknowledgements

This work was partly supported by Grant-in-Aid for Scientific Research(B)(No.04452176) and for Scientific Research on Priority Areas(2)(No.04205075) from the Ministry of Education, Science Culture of Japan, and by research grants from the Mazda Foundation's Research Grant and the Foundation for the Promotion of Material Science and Technology of Japan.

References

[1] T.Okamura,M.Adachi,T.Shiosaki and A.Kawabata, "Epitaxial Growth and Electrical Properties of Ferroelectric $Pb(Zr_{0.9}Ti_{0.1})O_3$ Films by Reactive Sputtering," Jpn.J. Appl. Phys.,Vol.30,pp.1034-1037,1991.

[2] T.Hase and T.Shiosaki,"Preparation and Switching Kinetics of $Pb(Zr,Ti)O_3$ Thin Films Deposited by Reactive Sputtering," Jpn.J.Appl.Phys.,Vol.30,pp2159-2162,1991.

[3] M.Shimizu,T.Katayama,T.Shiosaki and A.Kawabata,"Preparation of $PbTiO_3$ Thin Films by Photo-MOCVD," in Proceedings of the 7th Int.Sym.on the Applications of Ferroelectrics, 1990,pp.669-672.

[4] T.Katayama,M.Shimizu and T.Shiosaki,"Photoenhanced Chemical Vapor Deposition of $PbTiO_3$ and $Pb(Zr,Ti)O_3$ Thin Films," in Proceedings of the 4th Int.Sym.on Integrated Ferroelectrics, 1992.

[5] P.Sigmund, "Theory of sputtering.I.Sputtering Yield of Amorphous and Polycrystalline Targets," Phys. Rev., Vol.184, pp.383-416,1969.

[6] T.Katayama,M.Sugiyama,M.Shimizu and T.Shiosaki,"Photo-CVD of Ferroelectric $Pb(Zr,TiO_3$ Thin Films," in Proceedings of 8th Int.Sym.on the Application of Ferroelectrics, 1992.

CRYSTALLIZATION AND DIELECTRICAL PROPERTIES OF PLZT FILMS DERIVED FROM METALLO-ORGANIC PRECURSORS

SUN Ping, ZHANG Liang-ying and YAO Xi
Electronic Materials Research Laboratory (EMRL)
Xi'an Jiaotong University, Xi'an Shaanxi, 710049, China

Abstract: Lead Lanthanum Zirconate Titanate (PLZT) films were deposited by the metallo-organic decomposition (MOD) process using multilayer spinning. The crystallization kinetics, evolution of the crystallographic structure, dielectric behavior and ferroelectric properties were studied.

Introduction

Recently much work has been focussed on the processing of PLZT ferroelectric thin films by Sol-Gel [1] and metallo- organic decomposition (MOD) [2] methods because of their potential as excellent dielectric, ferroelectric and optical devices. MOD is a thermal process which can produce homogeneous polycrystalline phases at low processing temperatures. For the $PbZrO_3$-$PbTiO_3$ system crystallization always results in a mixture of the desired perovskite phase and a nonferroelectric pyrochlore phase, especially in the case of the thin films. A study of the crystallization mechanism may lead to better control of the microstructure, film properties and annealing of a pure perovskite phase transformation.

The present research investigates the crystallization kinetic parameters and their electrical properties.

Experimental

The initial metallo-organic compounds evaluated as precursors for PLZT films are commercial lead acetate trihydrate, tetra- n-butyl titanate and others, such as lead heptanoate, zirconyl heptanoate, zirconyl butyrate and lanthanum butyrate, which were synthesized in this laboratory by double decomposition [3].

The PLZT(8 / 0 / 100) and PLZT(8 / 65 / 35) solutions and films were prepared following the procedures given in Reference 3 and 4.

For crystallization kinetic studies, PLZT(8 / 0 / 100) and PLZT(8 / 65 / 35) solutions, and PLZT(8 / 65 / 35) films were used as samples. The films were prepared by dipping onto silicon substrates. Thermogravimetry (TG) and Differential Thermal Analysis (DTA) studies were conducted on a Beijing Analyzer I.CT and a Dupont 1090A. X- ray diffraction data were obtained on a Regaku D / MAX-III A diffractometer using monochromatic Cu K_α radiation at room temperature. The thickness of the films was measured by a multi- beam interference method. For electrical measurements, films were deposited on Pt / glass ceramic or indium tin oxide (ITO) / glass substrates. Pt and ITO films as bottom electrodes were deposited by RF sputtering. An array of Au films in the form of dot electrodes wassputtered on top of the PLZT film, where the diameter of dots is 1 mm. Dielectric properties were measured by HP4274A and 4275A LCR meters. Ferroelectric measurements were made using a modified Sawyer-Tower circuit.

Results and Discussion

Figs.1 and 2 show the TG and DTA analyses of solutions of PLZT.

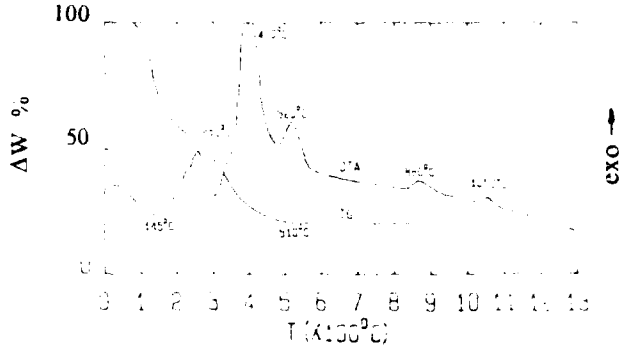


Fig.1 TG and DTA of the metallo-organic solution of PLZT(8 / 0 / 100).

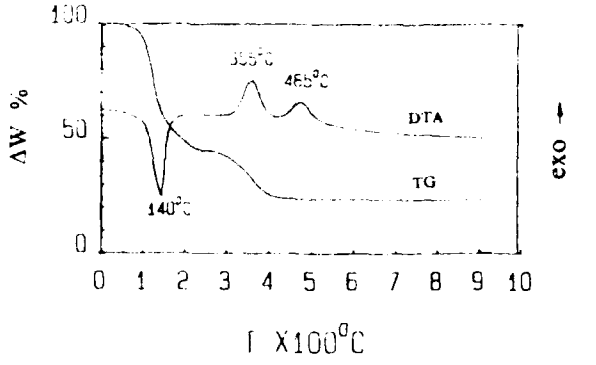


Fig.2 TG and DTA of the metallo-organic solution of PLZT(8 / 65 / 35).

For the PLZT(8 / 0 / 100) solution, the total weight loss (in static air) is about 81 %, which is consistent with the calculated values. There are three major stages of weight loss. The first stage, occurring at 145 ℃, is due to solvent evaporation while in the temperature range 260℃ ~ 510℃ the weight loss consists of two stages at which the organics burn off. In the DTA curve of PLZT(8 / 0 / 100), there is an exothermic peak at 520 ℃ because of

crystallization; the exothermic peak at 860 ℃ is due to the transformation from a rhombohedral structure to a tetragonal structure, and the exothermic peak at 1050℃ is due to the transformation from one tetragonal structure to another tetragonal structure.

As shown in Fig. 2, the total weight loss of the PLZT(8 / 65 / 35)solution is about 79 % , which also agrees with theoretical calculations. There are two major stages of weight loss; the first stage, occurring at 140℃, is also attributed to solvent evaporation while that at 355℃ corresponds to burning off the organics. At 465℃, only one exothermic peak due to crystallizing appears.

After removal of organics by firing at 390℃ in air, amorphous powders and films of PLZT(8 / 65 / 35) are obtained. Fig.3 shows the DTA study on the crystallization kinetics of PLZT(8 / 65 / 35) powders and films on Si substrates. By increasing the heating rate β, the peak temperature T_p shifted to higher temperatures. The apparent activation energy E and frequency factor ν are calculated using Kissinger's method[5].

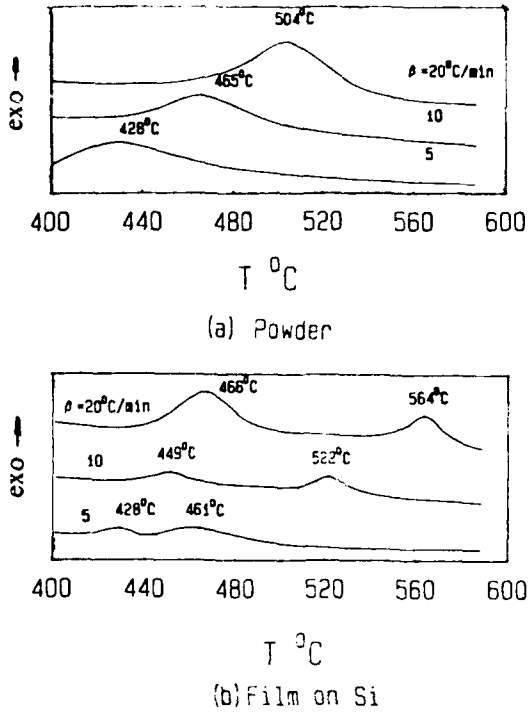


Fig.3 DTA plots at different heating rates, for the amorphous PLZT(8 / 65 / 35) (a) powder and (b) film.

The PLZT Powder has a ν value of 1.4×10^{4} s^{-1}, and an E value of 70 kJ / mol. The same experiments on the PLZT film gave lower values of ν and E of 451 $s^{-1}$and 55 kJ / mol. The ν value of the powder is higher than that of the film so that the powder crystallized more easily than the film at same temperature, though its E value is slightly higher than that of the film.

As shown in Fig. 3 (b) , there is an exothermic peak at an even lower temperature, which may be due to the film transforming to the pyrochlore phase from the amorphous phase, and has values of ν and E of 7.8×10^{9} s^{-1} and 143 kJ / mol. This means that metastable pyrochlore always forms before the perovskite structure from an amorphous structure because its ν value is much higher than that of the perovskite structure, even though its E value is higher than that of the perovskite structure.

Figs. 4 and 5 show the XRD patterns for the powder and films of PLZT(8 / 0 / 100) at various firing temperatures. For PLZT(8 / 0 / 100) , two modifications of the perovskite structure can be obtained: one is rhombohedral (a = 0.3948 nm, $\alpha = 89.61^{\circ}$) when annealed in air at 550 ℃ , another is tetragonal (a = 0.3909 nm, c = 0.4046 nm, c / a = 1.035) when annealed in air over 1050℃. This agrees with the results of the DTA.

Fig. 6 shows the XRD patterns for films of PLZT(8 / 65 / 35). A pure perovskite structure can be obtained by annealing in air at 550 ℃.

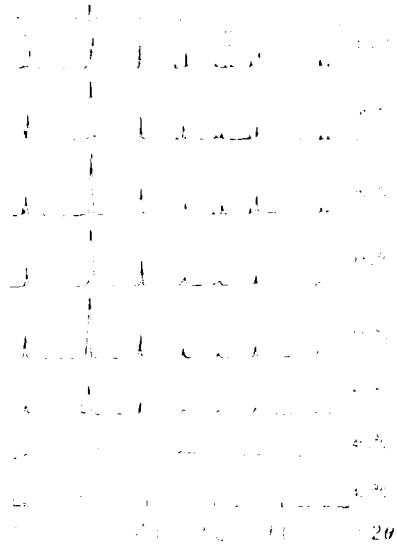


Fig.4 The XRD pattern for PLZT(8 / 0 / 100) power.

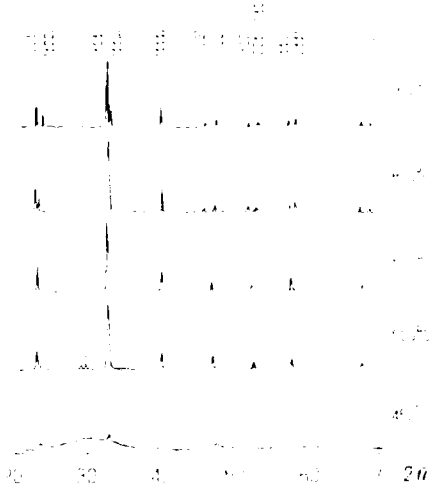


Fig.5 The XRD pattern for films of PLZT(8 / 0 / 100) on sapphire substrates. The indicated peaks are not characteristic of PLZT

The thick crack-free final films consist of several single layer crack-free films, whose formation is dependent on the precursors and substrate, the time- temperature profile of annealing, and more importantly the heating rate. According to the processing method given in Ref 4,

at a heating rate of 3 ℃ / min to the firing temperature, we can obtain a crack-free single layer film with a thickness of about 136 nm.

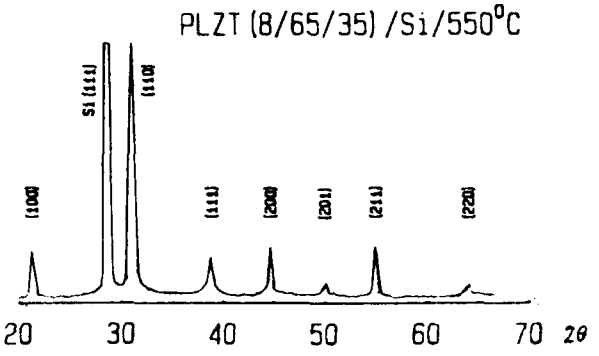


Fig.6 The XRD pattern for films of PLZT(8 / 65 / 35) on a silicon substrate.

The electrical properties of films with thicknesses from 408 nm to 1632 nm are measured. At room temperature, the measured capacitance values for PLZT(8 / 0 / 100) films indicate values of the dielectric constant K in the range 100–150. Fig.7 shows the frequency dependence of the dielectric constant K and dissipation factor D of the PLZT(8 / 0 / 100) films. The dielectric constant decreases with increasing frequency below 400 kHz, then increases sharply. The dielectric loss varies little between 100Hz–100kHz.

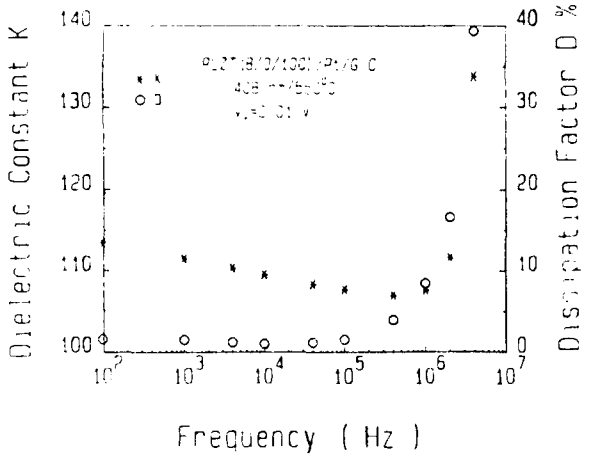


Fig.7 Dielectric constant and dissipation factor versus frequency for PLZT(8 / 0 / 100) films.

The temperature dependence of the dielectric properties is presented in Fig.8 for a 660 nm PLZT(8 / 65 / 35) film on ITO / glass substrate heat treated at 550 ℃ for 1 hour.

The dielectric constant K of the film is much lower than in the bulk ceramic PLZT(8 / 65 / 35) [5], the Curie point is about 244℃ which is much higher than that of the bulk, and the temperature dependence of K shows a broad transition range. This behavior is supposed to related to the nano grain sizes of the films.The grain sizes of the films annealed at 550 ℃ are below 50 nm[6]. It is reasonable to believe that no normal ferroelectric domains still exist in such nanosized grains. Another reason is that the La molar fraction and the ratio of Zr / Ti in the film sample are lower, as the results of X- ray micro- analysis using an electronic probe indicated. At room temperature, the films have a dielectric constant K of 450 and a dissipation factor D of less than 4 % at 1kHz. The K values of the films were smaller than the corresponding values for bulk PLZT(8 / 65 / 35) [5], and this behavior is also mainly related to the smaller grain sizes of the films.

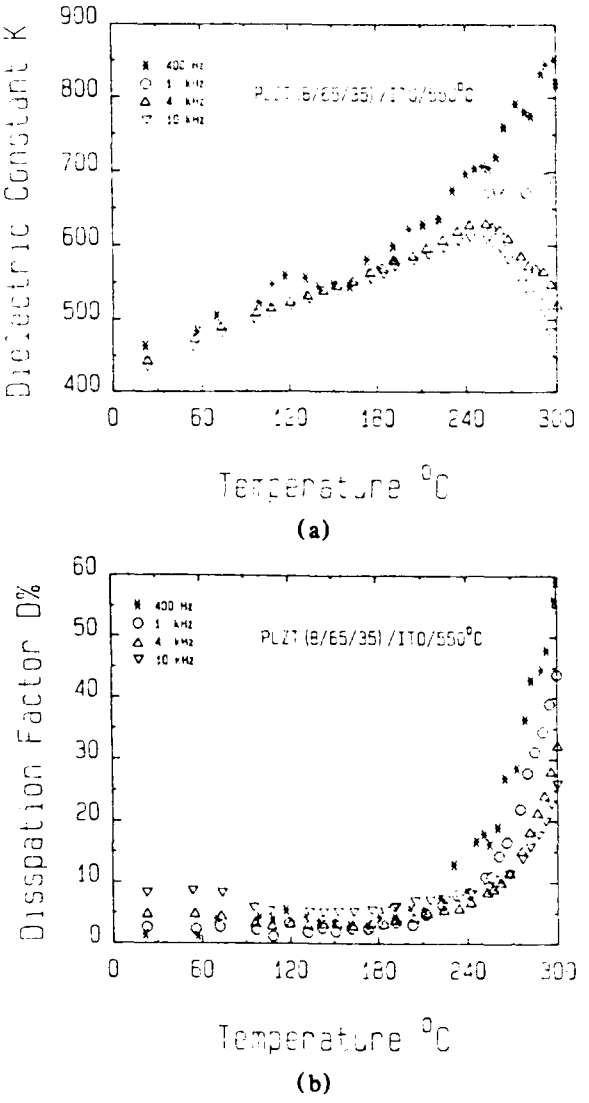


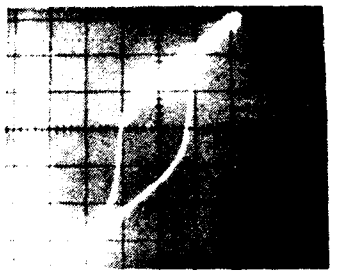
Fig.8 (a) Dielectric constant and (b) dissipation factor versus temperature for a PLZT (8 / 65 / 35) film on a ITO / Glass substrate.

Fig. 9 shows the hysteresis loop for PLZT(8 / 0 / 100) film at room temperature, with a spontaneous polarization P_s of 11.4 $\mu C / cm^2$ and a coercive field E_c of 90 kV / cm at 50 Hz. The thickness of the film is 1632 nm. At 1 kHz, the P_s and E_c are 12.2 $\mu C / cm^2$ and 35 kV / cm respectively.

The hysteresis loop for PLZT(8 / 65 / 35) film (660 nm) at room temperature is shown in Fig.10. The spontaneous polarization P_s is 14.7 $\mu C / cm^2$ and the coercive field E_c is 114 kV / cm at 50 Hz.

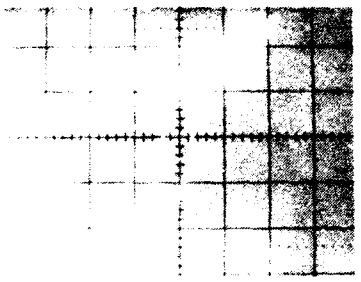
Conclusions

Lead Lanthanum Zirconate Titanate (PLZT) films were prepared by metallo-organic decomposition (MOD) method. The crystallization kinetics of PLZT powders and films (on Si substrates) have been studied using DTA. A perovskite structure crystallizes from decomposed amorphous precursors in the temperature range 420- 570 ℃. With apparent activation energies of crystallization E are 55 kJ / mol and 70 kJ / mol with pre-exponential frequency factors ν 450 s^{-1} and 1.4×10^{4} s^{-1}. A metastable pyrochlore phase always forms during the crystallization of the films from amorphous phase, with an activation energy and a frequency factor of 143 kJ / mol and 7.9×10^{9} s^{-1}. Two modifications of the perovskite structure can be obtained for PLZT(8 / 0 / 100): one is rhombohedral with a = 0.3948nm and $\alpha = 89.61°$ when annealed in air at 550℃, and the other is tetragonal with a = 0.3909 nm, c = 0.4046 nm and c / a = 1.035. Dielectric constant, dissipation factor and P-E hysteresis loops were measured. For PLZT(8 / 0 / 100) annealed at 550 ℃, the dielectric constant K is 115, the loss tangent D is 0.01 (1 kHz), the spontaneous polarization P_s is 11.4 $\mu C / cm^2$ and the coercive field E_c is 90 kV / cm (50 Hz), all at room temperature. For PLZT(8 / 65 / 35) annealed at 550℃, K = 450, D = 0.02 (1 kHz), P_s = 14.7 $\mu C / cm^2$ and E_c = 114 kV / cm(50 Hz).



(a)

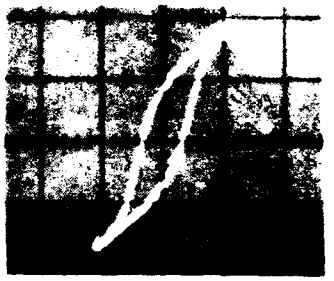
(x: 100 kV / cm / div; y: 8.14 $\mu C / cm^2$ / div)



(b)

(x: 117 kV / cm / div; y: 7.58 $\mu C / cm^2$ / div)

Fig.9 P-E hysteresis loop at (a) 50 Hz, and (b) 1 kHz for a PLZT(8 / 0 / 100) film on a Pt / G.C substrate.



(x: 326 kV / cm / div; y: 18.7 $\mu C / cm^2$ / div)

Fig.10 P-E hysteresis loop at 50 Hz for a PLZT (8 / 65 / 35) film on a ITO / Glass substrate.

Acknowledgment

This work is supported financially by the Chinese National Natural Science Foundation.

References

1. K.D.Budd, S.K.Dey and Payne, " Sol- Gel Processing of $PbTiO_3$, $PbZrO_3$, PZT and PLZT Thin Film, " British Ceramic Proc., vol. 36, pp. 107-121, 1985.
2. R.W.Vest and J.Xu, " Preparation and Properties of PLZT Films from Metallo-organic Precursors, " Ferroelectrics, vol. 93, pp. 21-29, 1989.
3. Sun Ping, Zhang Liangying and Yao Xi, "Preparation of PLZT Films from Metallo-organic Precursors, " Vacuum Science and Technology (china), vol. 12, pp. 191-194, 1992.
4. Sun Ping, Zhang Liangying and Yao Xi, "Crystallization and Dielectric Properties of PLZT Films Derived from Metallo-organic Precursors, " Composition, Microstructure and Properties of Advanced Ceramics (china), vol. 4, pp. 183-196, 1992 (in Chinese).
5. H.E. Kissinger, " Reaction Kinetics in Differential Thermal Analysis, " Anal. Chem., vol. 29, pp. 1702-1706, 1957.
6. G. H. Heartling and C. E. Lend, " Hot-pressed (Pb, La)(Zr, Ti)O_3 Ferroelectric Ceramics for Electrooptic Applications, " J. Amer. Ceram. Soc., vol. 54, pp. 1-11, 1971.
7. Wei REN, Xiaoqing WU, Zhang Liangying and Yao Xi, "Structures and Properteis of $PbTiO_3$ Thin films by Thermal Decomposition of Metallo- organic compounds, " Composition, Microstructure and Properties of Advanced Ceramics (china), vol. 2, pp. 172-181, 1989 (in Chinese).

STRUCTURAL INVESTIGATION OF THIN FILM PLZT USING X-RAY ABSORPTION SPECTROSCOPY

R. B. Greegor, F. W. Lytle and A. Y. Wu[1]
The Boeing Company, MS 2T-05, Seattle, WA 98124
[1]Center for High Technology Materials, University of New Mexico, Albuquerque, NM 87131

Abstract

Thin film electro-optic (EO) and non-linear optical (NLO) materials are of interest for applications in high speed integrated optical devices. Materials of the system $Pb_{1-x/100}La_{x/100}(Zr_{y/100}Ti_{1-y/100})_{1-x/400}O_3$ or PLZT x/y/(100-y) are attractive since they can be integrated into Si and GaAs substrates using suitable deposition techniques. In this investigation we examine the structural properties of RF magnetron sputter-deposited PLZT using x-ray absorption near edge spectroscopy (XANES). For XANES analysis four samples were selected: 1) a highly-oriented PLZT 28/0/100 film (~4500Å) deposited on Al_2O_3 (1$\underline{1}$02), 2) a highly-oriented PLZT 28/0/100 film (~4500Å) deposited on SiO_2 (2um) over Si(100), 3) a highly-oriented PLZT 28/0/100 film (~4500Å) deposited on SiO_2, and 4) a commercial ceramic wafer of PLZT 9/65/35. The XANES experiments were performed at the Stanford Synchrotron Radiation Laboratory (SSRL) using electron yield and fluorescence techniques. Data was taken at the Ti K-edge (4966 eV) and compared to reference spectra. Of the reference spectra, the Ti K-edge spectra of the PLZT most closely resemble perovskite ($SrTiO_3$). The surface and bulk thin film are similar and all the 28/0/100 spectra resemble 9/65/35, indicating similar cubic perovskite structures for these materials.

Introduction

Thin film (<= 1μm) PLZT has large EO or NLO effects as compared to the corresponding bulk material. These effects make it a possible candidate for use in integrated electro-optical devices such as, waveguides, modulators, mixers, shutters, frequency doublers, and memory devices. In such applications the PLZT is sputter deposited onto a Si or GaAs base which has been overlaid with a SiO_2 buffer layer. The PLZT film deposited by sputtering has a cubic perovskite structure with the [100], [110] or [111] direction normal to the plane of the substrate [1]. For films deposited by the sol-gel method the grains are randomly distributed with no preferred orientation [2]. The electro-optic effects demonstrated by PLZT vary depending on the composition, thermal history and applied voltages. Field-induced birefringence and field-induced secondary harmonic generation are thought to be related to a) the field-induced anisotropic orientation of ferroelectric domains and b) a contribution of the nonlinear susceptibilities of the material which contain electronic and ionic contributions [3]. The susceptibilities of the material have been modeled using an anharmonic oscillator which represents the motion of the octahedrally coordinated cation (e.g. Ti) in the perovskite structure [4]. When applied external fields are large the centrosymmetry of the films may be broken due to field induced polarization, polarization switching or induced phase changes. The fundamental building blocks of the oxygen octahedra or the lattice structure of the materials is affected and high-order EO effects appear.

In this paper we make measurements of the Ti K X-ray absorption near edge structure (XANES). XANES is very sensitive to the structural environment in which the absorbing atom is located. Slight changes in the symmetry, bond lengths and species of the coordinating atoms have significant effects on the measured absorption spectra. The XANES was measured for thin film PLZT on differing substrates and bulk ceramic material.

Experimental

Thin film PLZT of the system $Pb_{1-x}/100\ La_{x/100}\ (Zr_{y/100}\ Ti_{1-y/100})_{1-x/400}\ O_3$ or PLZT x/y/(100-y) was prepared using a radio frequency magnetron sputtering technique incorporating compound ceramic targets. For the investigation three samples were prepared: 1) a highly-oriented PLZT 28/0/100 film (~4500Å) deposited on Al_2O_3 (1$\underline{1}$02), 2) a highly-oriented PLZT 28/0/100 film (~4500Å) deposited on SiO_2 (2-μm) over Si(100), 3) and a highly-oriented PLZT 28/0/100 film (~4500Å) deposited on SiO. In addition, a commercial ceramic wafer of PLZT 9/65/35 was also used.

Figure 1 shows the layer structure for a PLZT waveguide modulator using the above materials and deposition techniques. The SiO_2 is used as a buffer

CH3080-0/92/0000-0436 $3.00 © 1992 IEEE

layer since its index of refraction (n~1.5) is less than the PLZT film (n~2.5). A ~1000Å ITO (indium tin oxide, n~1.8)) superstrate serves as a capping layer and contact electrode. As can be seen, the set of samples selected for this investigation permit an examination of the effect of the PLZT / substrate interaction and comparsion to bulk ceramic material of a different composition (28/0/100 vs 9/65/35).

For the XANES several reference spectra samples were used: 1)5μm Ti foil, 2)powdered TiO_2 (anatase, rutile, brookite, 3)powdered Ti_2O_3, 4)powdered $NiTiO_3$ and 5)powdered $SrTiO_3$. For XANES experiments, all the powdered samples were ground to a fine mesh (400), suspended in duco cement diluted with acetone and spread in a thin layer (~25μm) on aluminum foil.

The Ti foil was used to determine the K-edge position (4966.4 eV) of Ti metal. The remaining oxides were aligned with respect to the metal edge. Anatase, rutile and brookite show the sensitivity of the XANES technique to slight changes in the coordination geometry about the absorption site. Anatase is tetragonal [5] with the each Ti atom having 6 oxygen neighbors ranging in distance from 1.91 to 1.95 Å, while rutile (having the cassiterite form, also tetragonal) has Ti-O bondlengths ranging from 1.95 to 1.98 Å. Brookite is orthorhombic with each Ti atom having near neighbor oxygen bondlengths from 1.87 to 2.04 Å. In rutile there is one, and anatase two short oxygen-to-oxygen separations at 2.43 Å. Brookite also has close anion-anion contact with oxygen-oxygen separations varying upwards from 2.49 Å. Ti_2O_3, is rhombohedral, having Ti in a higher oxidation state (+3) with octahedrally coordinated oxygen distances from 2.01 to 2.08 Å. This structure can be considered as a slightly distorted hexagonal close-packing of oxygen ions with the small Ti ions lying in some of the interstices. The arrangement is illustrated by ilmenite ($FeTiO_3$) if its two types of metallic atoms are taken as identical. $LiTaO_3$ has the ilmenite structure and is a ferroelectric crystal. The $NiTiO_3$ standard used in this study also has the ilmenite structure. $SrTiO_3$, has the cubic perovskite structure with Ti coordinated by six oxygen atoms in the faces of the cube and Sr at the corners. $SrTiO_3$ may be paraelectric down to at least 1K and is possibly induced ferroelectric by an electric field at low temperature.

The XANES experiments on the above samples were performed at the Stanford Synchrotron Radiation Laboratory (SSRL). At SSRL, beam line IV-1 (a

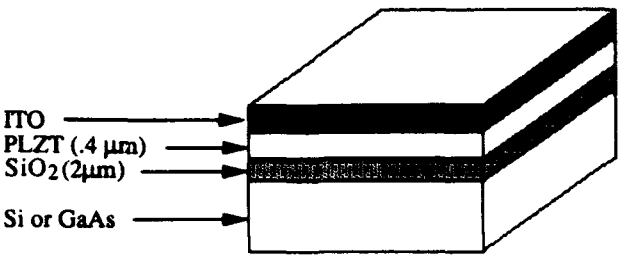


Figure 1. PLZT wafer structure for waveguide modulator.

wiggler side station) was used while the storage ring was being run in a dedicated mode with the electron beam energy at 3 GeV and a stored beam current of 30-80mA. A Si (220) double crystal monochromator detuned approximately 50% to reduce beam harmonics was used to select the desired X-ray energy in the vicinity of the Ti K-edge at 4966.4 eV. The monochromator slits were adjusted to 1mm which provided a resolution of approximately 0.3eV at the Ti K-edge. Scans were made from 100eV below the Ti K-edge energy to 350eV above the Ti K-edge energy. At the K-edge the monochromator was moved in steps of approximately 0.25eV and above the edge (+20eV) the step size was adjusted to produce a step of 1-2 eV or a step less than or equal to 0.06 $Å^{-1}$. Both fluorescence and total electron yield data were collected. The fluorescence yield data were taken in the standard manner with the sample at a 45 degree angle to the incident X-rays. The total electron yield data were collected simultaneously with fluorescence data. The simultaneous collection of fluorescense and total electron yield data allows a comparison of surface (~ top 500 Å) and bulk signals originating from different depths within the sample.

Results and Discussion

The XANES for ploymorphs of TiO_2 (anatase, rutile and brookite) are shown in Figure 2. In this figure the zero of energy is taken at the K-edge for the Ti metal which is at 4966.4 eV. In all of these samples the Ti is surrounded by 6 oxygen near neighbors. Note the sensitivity of the spectra to the changes in the bondlength and coordination geometry as described previously. The features from approximately 0 to 12 eV are 1s -> 3d bound state transitions which are dipole forbidden but quadrapole (very weak transition) allowed. If the center of inversion at the Ti site is distorted then the dipole transition becomes allowed and

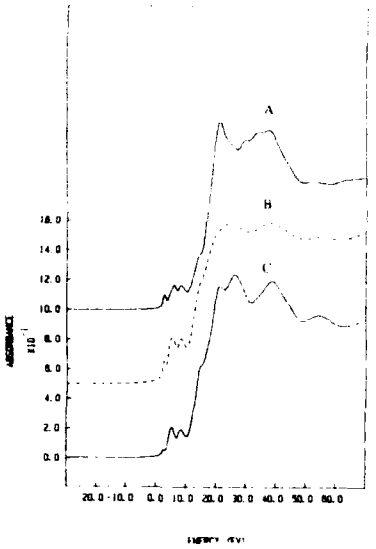


Figure 2. Ti K-edge XANES of TiO_2 a)anatase, b)brookite, and c)rutile. The zero of energy is taken at the Ti metal K-edge (4966.4 eV).

becomes stronger for more distorted octahedra. The features at the top of the absorption rise are due to 1s -> 4p transitions and multiple scattering effects which are followed at higher energy by the oscillations due to the extended X-ray absorption fine structure (EXAFS). This region begins at 30 to 50 eV above the K absorption edge and is not examined in this investigation.

In Figure 3 the XANES of Ti_2O_3, $NiTiO_3$ and $SrTiO_3$ are compared to thin film PLZT (28/0/100) on a Si substrate with a SiO_2 buffer layer. Note that the $SrTiO_3$ exhibits the closest resemblance to the PLZT film. As discussed above, $SrTiO_3$ has a cubic perovskite structure. The match of $SrTiO_3$ is not outstanding because the reference sample was polycrystalline and the PLZT is highly oriented in the direction perpendicular to the substrate and randomly oriented in the substrate plane. Since synchrotron radiation is highly polarized in the plane of the storage ring, bonds along the polarization direction are enhanced, whereas for the polycrystalline reference all bonds are equally sampled by the x-radiation. The Ti_2O_3 and $NiTiO_3$ spectra are quite different from the PLZT film but resemble each other except in the 1s -> 3d region where $NiTiO_3$ shows a more intense transition indicative of higher distortion in the Ti-O octahedral cage. This similarity is not totally surprising since $NiTiO_3$ and Ti_2O_3 can both be represented by a HCP array of oxygen atoms with the metal cations in some of the intersties.

Figure 4 shows the XANES for the various PLZT samples considered in this investigation. It should be noted that the features from ~50 to 60 eV above the Ti K absorption edge are due to artifacts in the Si (220) monochromator used and are not part of the absorption features or the EXAFS. All of the spectra in Figure 4 were collected in the fluorescence mode except for the 28/0/100 on SiO_2 which was examined in both the fluorescence and electron yield mode. Note that the data for the electron yield is noisier than for the fluorescence data. This is due to charge build-up and subsequent discharging in the insulator. However, the major features of the e-yield and fluorescence data are identical. This indicates that the structure in the top ~500 Å is the same as in the lower ~4000 Å since e-yield is sensitive to the surface, and fluorescent yield samples to depths (~50,000 Å) well beyond the film thickness.

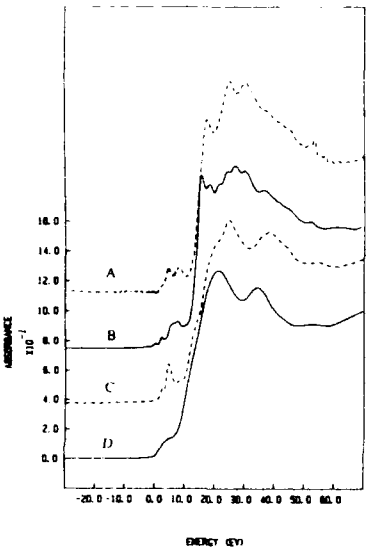


Figure 3. Ti K-edge XANES of a)thin film PLZT 28/0/100 on SiO_2/Si, b) $SrTiO_3$, c)$NiTiO_3$, and d)Ti_2O_3.

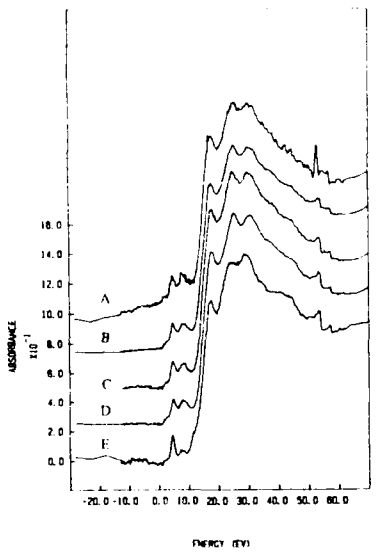


Figure 4. Ti K-edge XANES of PLZT materials (all taken in fluorescent yield except a which was taken in electron yield) a) 28/0/100 PLZT on SiO_2, b) 28/0/100 PLZT on SiO_2, c)28/0/100 PLZT on Al_2O_3, d)28/0/100 PLZT on SiO_2/Si, e)9/65/35 commercial wafer.

Comparison of the fluorescence data for the 28/0/100 PLZT on SiO_2, Al_2O_3 and SiO_2/Si shows that these spectra are essentially identical. The spinel structure of alumina or the tetrahedrally coordinated Si in silica have no apparent effect on the resulting structure of the PLZT overlayer. Further comparsion of all the 28/0/100 data and the 9/65/35 PLZT shows only minor differences. Bulk 9/65/35 also has the cubic perovskite structure as does 28/0/100 PLZT. The 1s -> 3d transition for the 9/65/35 sample is more intense which indicates a higher degree of disorder in the Ti-O octahedral cage than in the thin film 28/0/100 PLZT.

Bulk ceramic 28/0/100 PLZT is paraelectric and has a cubic perovskite crystal structure. However, thin film 28/0/100 possesses the largest EO coefficient among (x/0/100) series [6]. Comparison of the delta n vs. E curves of 28/0/100 with normal and Pb deficient compositions shows that the normal composition has a considerably larger field induced birefringence (FIB) [3]. It has been suggested that this birefringence is due to a variety of effects including distortions in the Ti-O octahedral building blocks of the material [7]. From the investigation conducted here it should be possible to make a direct structural measurement of such distortions since XANES is very sensitive to such effects.

Conclusion

The XANES of four PLZT samples have been measured and compared to standard reference spectra for which the structures are known. Thin film (~4500Å) 28/0/100 PLZT on SiO_2, Al_2O_3, and SiO_2/Si all have similar spectra indicating that the substrate or substrate buffer layer does not influence the bulk properties of the thin film overlayer. Also, the surface layer (top ~500Å) of 28/0/100 PLZT on an SiO_2 substrate is the same as the underlying bulk thin film. All of these spectra were similar to the spectra of bulk ceramic 9/65/35 PLZT which has the cubic perovskite structure. Of the reference spectra used (TiO_2(anatase, rutile, brookite), Ti_2O_3, $NiTiO_3$ (ilmenite structure), and $SrTiO_3$ (perovskite structure)) the PLZT thin film and bulk ceramic exhibited spectra most similar to $SrTiO_3$. This work demonstrates that the XANES technique is very sensitive to distortions in the Ti-O octahedral building blocks of these materials and should be a useful diagnostic for structural changes.

Acknowledgements

The work of RBG and FWL was supported in part by DOE grant DE-FG06-84ER45121. AYW was supported by AFOSR and DARPA. We wish to thank SSRL for excellent beam time and experimental assistance.

References

[1]A. Wu, F. Wang, C. Juang, C. Dustamante, C. Yeh and J. Diels, "Electro-Optic & Non-Linear Optical Properties of (Pb,La)(Zr,Ti)O_3, $BaTiO_3$, (Sr,Ba)Nb_2O_6, $Ba_2NaNb_5O_{15}$, and beta-BaB_2O_4 Thin Films," in Proceeding of 7th International Symposium on Applications of Ferroelectrics, Urbana, Illinois, pp. 135-138, June 9, 1990.

[2]A. Wu, F. Wang, C. Juang and C. Bustamante, "2-D High Definition & High Resolution PLZT Thin Film Spatial Light Modulators," in Proceedings of 7th International Symposium on Applications of Ferroelectrics, Urbana, Illinois, pp. 643-646, June 9, 1990.

[3]A.Wu, F. Wang, C. Juang and C. Bustamante, "Electro-Optical and Nonlinear Optical Coefficients of (Pb,La)(Zr,Ti)O_3, $BaTiO_3$(Sr,Ba)Nb_2O_6, and $Ba_2NaNb_5O_{15}$ Thin Films," Materials Research Society Proc. Vol. 200, pp.261-266, 1990.

[4]F. Wang and A. Wu, "Electro-Optical and Nonlinear Optical Properties of Thin Film Materials Containing Oxygen-Octahedra Under High DC Electric Fields," in Proceedings of 7th International Symposium on Applications of Ferroelectrics, Urbana, Illinois, pp. 131-134, June 9, 1990.

[5]For Crystal Structures see, R. Wyckoff, Crystal Structures, Interscience Publishers, 1963, Vol. I & II.

[6]H. Adachi,T. Kawaguchi and M. Kitabatake, Jap. J. Appl. Phys. Vol. 22, 11, 1983.

[7]F. Wang, C. Juang, C. Bustamante and A. Wu, "Electro-Optic Properties of (Pb,La)(Zr,Ti)O_3, $BaTiO_3$(Sb,Ba)Nb_2O_6 and $Ba_2NaNb_5O_{15}$ Thin Films by a Confocal Scanning Differential Polarization Microscope," in Proceedings of 4th International SAMPE Electronics Conference, pp. 712-721, June 12, 1990.

ELECTRICAL CHARACTERIZATION OF MULTI-ION BEAM REACTIVE SPUTTER DEPOSITED PZT THIN FILMS

H. Hu and S. B. Krupanidhi
Materials Research Laboratory
The Pennsylvania State University
University Park, PA 16802

ABSTRACT

The electrical properties of multi-ion-beam reactive sputter (MIBERS) deposited PZT(50/50) thin films were characterized in terms of low-filed dielectric response, high-field polarization hysteresis, switching characteristics, fatigue and retention behaviors, I-V response, time dependent dielectric breakdown, and C-V behavior. Many of the properties are found quite processing-sensitive. This opens much opportunity of property modification of the films. The techniques of rapid thermal annealing (RTA) and low energy oxygen ion bombardment seem very useful for such a purpose.

I. INTRODUCTION

Detailed electrical characterization is essential to the development of ferroelectric thin films for device application. Being thin, the ferroelectric films behave differently from bulk materials, and their properties are usually highly processing-dependent. Therefore, processing optimization is critical to obtain desirable properties, and in return property measurement offers a convenient reference in the optimization of processing conditions.

Among various deposition techniques used in growth of ferroelectric thin films, multi-ion-beam reactive sputter (MIBERS) deposition holds high promise mainly due to its easy control over film composition and great flexibility in processing modification.[1] In this paper, most properties of interest to memory applications are characterized for MIBERS deposited PZT thin films, including low-field dielectric response, high-field polarization (P-E) hysteresis, switching characteristics, fatigue and retention behaviors, capacitance-voltage (C-V) hysteresis, dc current-voltage (I-V) characteristics and time dependent dielectric breakdown (TDDB) behaviors. Meanwhile, their dependence on processing is highlighted.

II. EXPERIMENTAL

PZT films with Zr/Ti ratio of 50/50 were deposited by the MIBERS technique on Pt coated Si and bare Si substrates, and crystallized by either conventional furnace annealing or rapid thermal annealing (RTA).[1] Gold was sputter-deposited to make the top electrodes, whose area was either 0.0028 cm^2 or 0.0007 cm^2. Thus metal-ferroelectric-metal (MFM) capacitors or metal-ferroelectric-semiconductor (MFS) transistors were formed. The MFS transistors were used for C-V measurement, while MFM capacitors were used for all the other measurements.

The frequency dependent dielectric responses and C-V characteristics were measured by a computer-controlled HP 4192A low frequency impedance analyzer. P-E hysteresis loops were measured by either a computer-controlled modified Sawyer-Tower circuit or a RT66A ferroelectric tester (Radiant Technologies, Inc.). Switching characteristics were recorded by a LeCroy 9310M Dual 300 MHz oscilloscope following a standard switching circuit. I-V and TDDB measurements were carried out on a HP 4140B pA meter/dc voltage source. Fatigue and retention behaviors were characterized by using the RT66A tester.

III. RESULTS AND DISCUSSION

A. Dielectric response

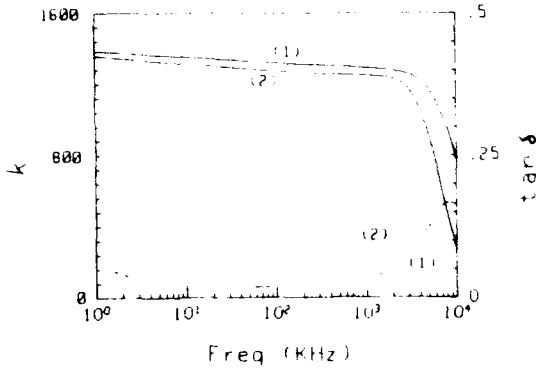


Fig.1. Frequency-dependence of k and tanδ of the films (0.5μ thick) annealed by (1) RTA at 650°C for 1 s, and (2) furnace at 650°C for 2 h. (oscillation level 0.01V).

Figure 1 comparatively shows the typical results of frequency-dependence of room-temperature low-field dielectric constant and loss of the PZT films annealed by the two different methods, at the same temperature of 650°C. Roughly speaking, over a fairly wide frequency range (10-1000kHz) both films have nearly the same dielectric constant (about 1400) and dissipation factor (about 0.02) with very small dispersion. In other words, crystallization by RTA is so fast that in 1 s the films can attain the same crystallinity as in the case of furnace annealing for 2 h. Such a fast process appears much like an "explosive crystallization".[2] However, distinctions can be point out at the two ends of the measured frequency range. At the

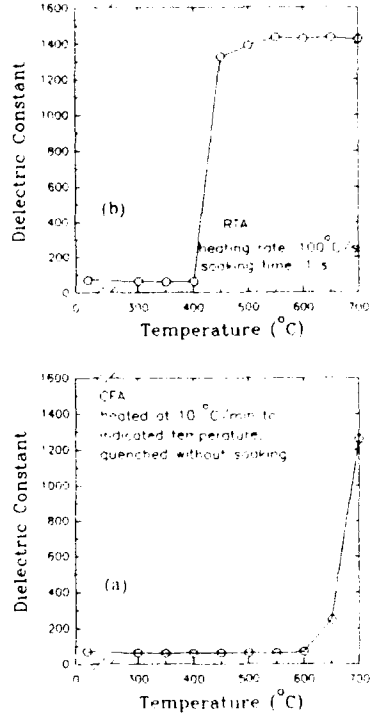


Fig.2. Evolutin of dielectric constant (at 100kHz) of the films with (a) temperature during the heating process of furnace annealing, and (b) temperature of RTA.

CH3080-0-7803-0465-9/92$3.00 ©IEEE

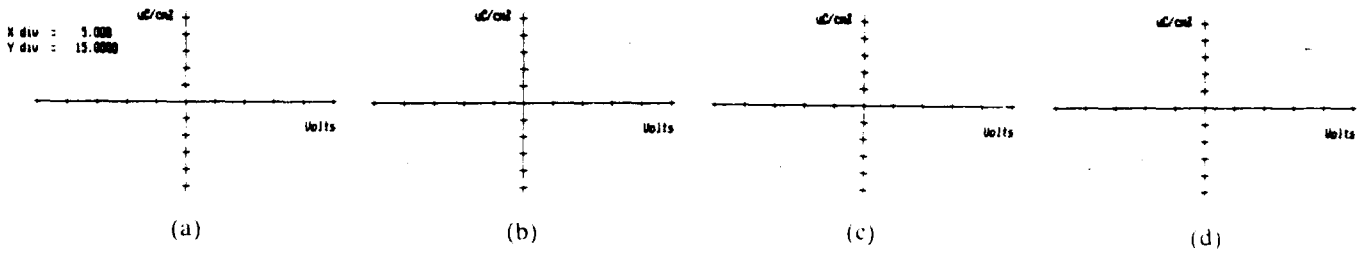


Fig.3. Conduction-compensated P-E hysteresis loops of the films (0.5μ thick) annealed by RTA at 650°C for varied time; (a) 1 s, (b) 15 s, (c) 30 s, (d) 60 s.

low frequency range (<10kHz), small dispersion in the dissipation factor can be found for the RTA films but not for the furnace annealed films. This is attributable to relatively higher conductivity in the RTA films caused by a higher residual Pb content. At the high frequency range (>1000kHz), the furnace annealed films are more dispersive than the RTA films, which is characteristic of thicker interface barriers.[3] Therefore, it can be suggested that RTA is definitely better in the sense of minimizing interface reaction, while it should take a little longer to reduce the residual Pb content although 1 s looks enough for crystallization of perovskite phase.

The evolutions of dielectric constant of the films with annealing temperature were shown in Fig.2 for both annealing methods. As can be seen, while the evolution of dielectric constant during furnace annealing is rather slow, an abrupt increase to the saturation value in the dielectric constant is observed in the case of RTA within the temperature range from 400 to 450°C. These results further substantiates the effectiveness of RTA.[2]

B. Polarization versus field

Figure 3 shows a set of P-E hysteresis loops of the films annealed by RTA at 650°C for different time. It can be noted that they all have nearly the same remanent polarization of about 20 μC/cm^2, although the coercive field seems decreasing slightly with increasing annealing time. This is consistent with the results of dielectric measurements described above, and again exhibits the nature of "explosive crystallization" by RTA. The lower coercive field in the case of longer annealing time is presumably due to relative higher crystallinity and "purer" structure of the films, as more defects (including residual Pb) and grain boundary phase would be annealed out as annealing time increased.

C. Switching characteristics

It has been found that with the assistance of low-energy oxygen ion beam, many electrical properties of MIBERS deposited ferroelectric films can be favorably modified.[1,4] The switching characteristics were studied comparatively between PZT(50/50) films grown with and without low-energy oxygen ion bombardment. Typical switching characteristics of the films are shown in Fig.4, in which only V(t) transients resulting from the two positive pulses of double bipolar pulse input were recorded. In the measurement, the sample was initially polarized negatively with negative pulses. The first positive pulse resulted in a gross switching transient (GS) caused by the ferroelectric domain reversal (charge density of the capacitor changed by $\delta Q \sim 2P_r$) plus a normal capacitor charge transient ($\delta Q \sim P_s$-P_r), where P_s and P_r denote respectively the spontaneous polarization and remanent polarization of the films under the measurement condition. The second positive pulse

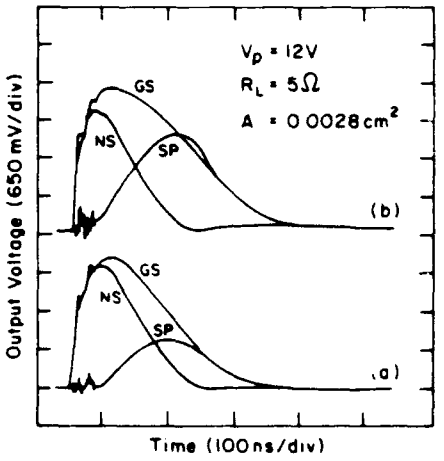


Fig.4. Switching characteristics of (a) the non-bombarded films and (b) the bombarded films, both annealed at 650°C for 1 h.

gave rise to a non-switching transient (NS) merely due to the normal capacitor charge. The difference of these two curves then leads to a net switching transient (SP) due to sole ferroelectric domain reversal.

The switched charge density (Q_s) can be determined by the area under the SP curve divided by the load resistance R_L and the electrode area A and should be close to $2P_r$. It can be seen from Fig.4 that, under the same measurement conditions, the SP-covered area (and thus the Q_s) for the bombarded films is much larger than that for the non-bombarded films, and is consistent with the fact that the low-energy oxygen ion bombardment largely enhanced the remanent polarization of the films.[4]

It can be found in Fig.4 that the switching time t_s, defined as the time from the onset to a point 90% down from the maximum value of the SP curve,[5] is about 230 ns for the non-bombarded films and about 260 ns for the bombarded films. Noting the values of Q_s in the respective cases are 10.8 μC/cm^2 and 18.5 μC/cm^2 as determined from Fig.4, the difference in t_s is small and not proportional to the large difference in Q_s. As the relation $t_s \propto Q_s$ holds in each case and the coercive field comes into the proportional coefficient,[6] comparison can be made between these two kinds of the films by using the ratio t_s/Q_s. It is this ratio, rather than t_s, that reflects the easiness of a switching process. For the bombarded films this ratio is appreciably smaller than that for the non-bombarded films. This fact implies that the domain reversal in the bombarded films is dynamically more favorable and can be related to the lower coercive fields of these films compared with the non-bombarded films.[4]

The switching time in the present case appears rather large, ranging from tens of nanosecond to a few microsecond. This is due to the relatively large electrode areas used.[7] Figure 5 shows both load resistance (R_L) and electrode area (A) dependencies of the switching time. Assuming a linear dependence of switching time on the electrode area as reported,[7] the switching time is estimated to be about 6 ns for A=1000 μm^2 and less than 1 ns for A=1 μm^2 at V_p=12V and R_L=50 Ω, being consistent with other reported results.[8]

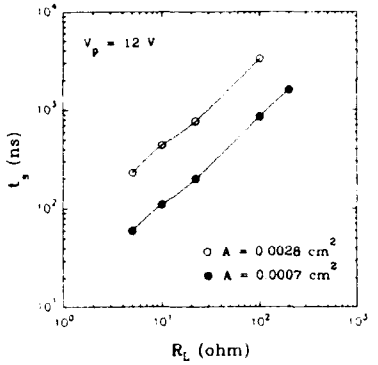


Fig.5. Dependence of t_s on R_L and A. Measured from the non-bombarded films annealed at 650°C.

To further quantify the dynamics of domain reversal, the relation[9] $t_s=t_o\exp(\alpha/E)$, i.e. $\log t_s=\log t_o+\alpha/(2.303E)$ was used to determine the activation field α for both bombarded and non-bombarded films. Figure 6 shows data on field dependence of switching time and the fitting lines to the above relation, yielding an α of 284 kV/cm for the non-bombarded films and an α of 197 kV/cm for the bombarded films. As expected,[9] the α value in either case is about 4 times the respective coercive fields (E_c). The E_c is about 55 kV/cm for the bombarded films and about 75 kV/cm for the non-bombarded films, obtained from the polarization hysteresis loop under a 60 Hz sinusoidal electrical field.[4]

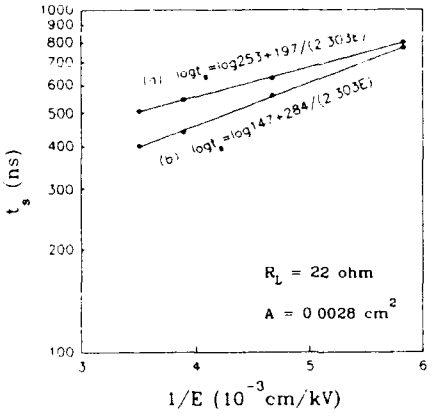


Fig.6. Dependence of t_s on the applied field (E) for (a) the bombarded films and (b) the non-bombarded films, both annealed at 650°C.

D. Fatigue and Retention

Figure 7 shows fatigue behavior in polarization of the non-bombarded films under ±170 kV/cm bipolar pulse cycling. It can be seen that the decay in polarization is less than 20% after 10^{10} switching cycles.

Figure 8 shows the retention of the polarization of such films, measured by applying initially a -5 V write pulse and afterwards +5 V and -5 V read pulses. The loss in the stored charge is less than 10% after 10^5 s.

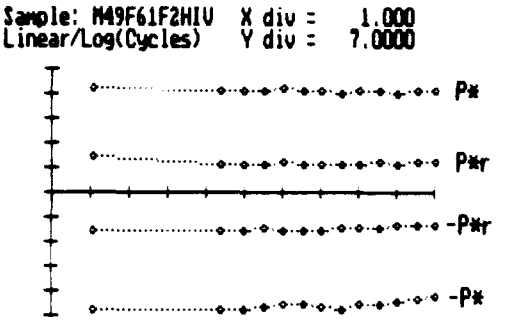


Fig.7. Fatigue behavior of the films under ±170 kV/cm bipolar pulse cycling, shown are $P = P_s(+)-P_r(-)$, and $P^*_r = P_r(+)-P_r(-)$, and alike.

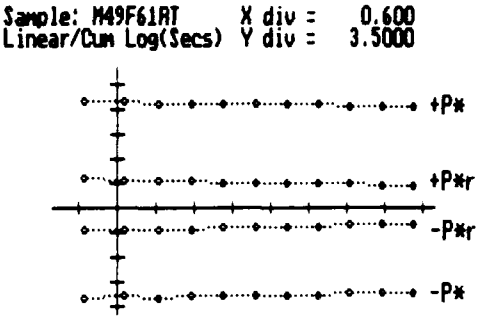


Fig.8. Retention of the polarization of the films, written by a -5V pulse and then read by +5V and -5V pulses.

The difference in fatigue and retention behaviors between the bombarded and non-bombarded films is that for the bombarded films the initial polarization is higher but decays faster, and becomes similar to that of non-bombarded films after 10^{10} switching cycles or 10^5 s retention.

E. I-V and TDDB behaviors

Figure 9 shows the results of measurement on I-V response of both the bombarded and non-bombarded films, annealed at 600°C for 2 h. Several interesting differences can be noted between the bombarded films and the non-bombarded films: (a) The ohmic resistivity of the bombarded films (~3×10^{11} Ωcm) is about one order of magnitude higher than that of the non-bombarded films (~3×10^{10} Ωcm). (b) The onset voltage of the space-charge-dominant conduction is much higher for the bombarded films (~12 V) than for the non-bombarded films (~3 V). (c) The bombarded films have much higher dielectric breakdown strength compared with the non-bombarded films (~770 kV/cm versus ~350 kV/cm, under the indicated measurement conditions). It was also found that for films annealed at higher temperatures, these differences

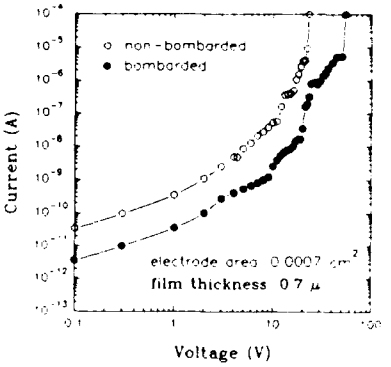


Fig.9. I-V curves of the films (annealed at 600°C for 2h).

become less significant while the values of the non-bombarded films approaches those of the bombarded films. These differences may be due to the difference in the microstructure and the degree of non-stoichiometry between these two kinds of films,[1] and are being under further investigation.

TDDB of the ferroelectric films is believed to have close relation to the I-V behavior since both of them are due to the motion of charge carriers.[10] Figure 10 shows the TDDB characteristics of the above mentioned films annealed at 680°C for 2 h. As expected, the bombardment induced effect on

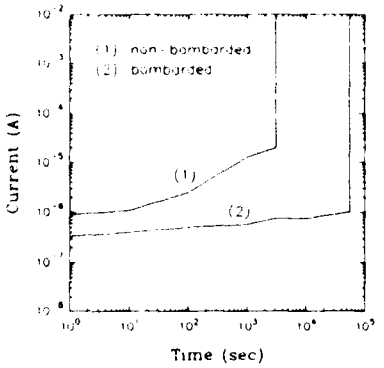


Fig.10. TDDB behavior of the films under a constant dc field of 450kV/cm (0.7μ thick, annealed at 680°C for 2h).

TDDB is amazingly large. Under the same dc field of 450 kV/cm, the non-bombarded films break down in about 50 min, while the bombarded films can last for 925 min.

F. C-V characteristics

Ferroelectric films on semiconductors have been proposed to be used in metal-ferroelectric-semiconductor (MFS) configuration for non-destructive read-out (NDRO) memory devices by making use of the ferroelectric field effect which can be observed in terms of the typical capacitance-voltage (C-V) characteristics.[11] Therefore, C-V measurements were carried out in the MFS configuration with the PZT films on bare Si substrate to study the ferroelectric field effect. Figure 11 shows typical C-V patterns for both furnace annealed films and RTA films. It can be seen that in both cases there exist C-V hysteresis loops which reflect the ferroelectric nature of the films and are necessary to realize the memory function.[11] However, significant difference between the two can be pointed out from the different rotation directions of the hysteresis loops. In the case of RTA films, the C-V loop is dominated by the ferroelectric polarization limited mode (Fig.11.a), while for the furnace annealed films, the rotation direction of the C-V loop indicates a trap limited or carrier injection limited mode (Fig.11.b)[11]. This difference can be again attributed to the different interface conditions between the RTA films and the furnace annealed films.[11]

IV. SUMMARY

A series of electrical properties of MIBERS deposited PZT films were characterized in relation to the processing conditions. Many of them are found quite processing-sensitive, particularly dielectric constant, remanent polarization, switching characteristics, I-V response, TDDB, and C-V response. This opens much opportunity of property modification of the films. The techniques of RTA and low-energy oxygen ion bombardment seem very useful for such modification.

ACKNOWLEDGMENT

This work was supported by a DARPA contract.

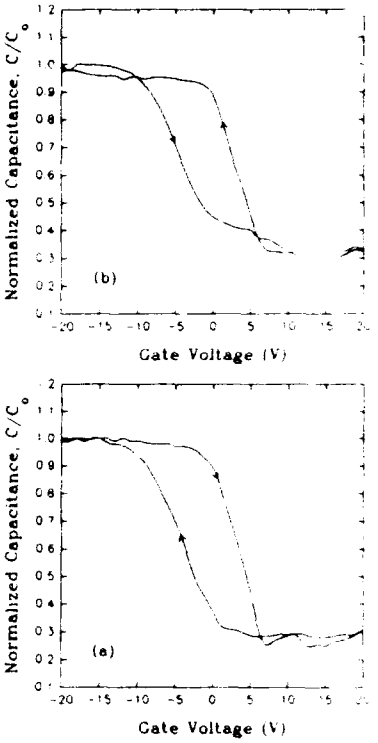


Fig.11. Typical C-V loops of MFS configuration of films (a) RTA annealed at 650°C for 15 s, and (b) furnace annealed at 650°C for 2 h.

REFERENCES

1. S.B.Krupanidhi, H.Hu and V.Kumar, J. Appl. Phys. 71, 376 (1992).
2. H.Hu, C.J.Peng and S.B.Krupanidhi, Submitted to Thin Solid Films.
3. M.Sayer, A.Mansingh, A.K.Arora and A.Lo, Integrated Ferroelectrics 1, 129 (1992).
4. H.Hu and S.B.Krupanidhi, in this issue of proceedings.
5. J.F.Scott, L.Kammerdiner, M.Parris, S.Traynor, V.Ottenbacher, A.Shawabkeh and W.F.Oliver, J. Appl. Phys. 64, 787 (1988).
6. W.J.Merz, J. Appl. Phys. 27, 938 (1956).
7. B.P.Maderic, L.E.Sanchez and S.Y.Wu, Ferroelectrics 116, 65 (1991).
8. S.K.Dey, C.K.Barlingay, J.J.Lee, T.K.Gloerstad and C.T.A.Suchicital, in Proceedings of the Third Symposium on Integrated Ferroelectrics, Colorado Springs, Colorado, April 1991, p.30.
9. J.C.Burfoot and G.W.Taylor, *Polar Dielectrics and Their Applications* (Macmillan, London, 1979), chap.12.
10. B.M.Melnick, C.A.Paz de Araujo, L.D.McMillan, D.A.Carver and J.F.Scott, Ferroelectrics 116, 79 (1991).
11. S.Y.Wu, IEEE Trans. Electron Devices 21, 499 (1974).

SOL-GEL LEAD ZIRCONATE-TITANATE THIN FILMS: EFFECT OF SOLUTION CONCENTRATION

C. Lavage, A. Safari and L. C. Klein
Rutgers-the State University of New Jersey
Department of Ceramics
P.O. Box 909
Piscataway, NJ 08855-0909

Abstract: The microstructure development of PZT compositions near the morphotropic phase boundary, PZT (50 PT/50 PZ) and PNZT (2 Nb_2O_5/53 PT/45 PZ), has been investigated by scanning electron microscopy (SEM), optical microscopy, and X-ray diffraction analysis (XRD). The molar concentration of the precursor alkoxide solution has been increased to 0.75M from that of previous studies, around 0.20M. Thin films have been fabricated by spin coating Pt/Ti/SiO_2/Si substrates with the alkoxide solution. It is found that in the solutions with high molar concentrations, perovskite phase forms at lower temperatures than found previously in dilute solutions. In addition, the microstructure of the films is dense and uniform, showing none of the spherulites found previously [1].

Introduction

The fabrication of ferroelectric PZT, $Pb(Zr_xTi_{1-x})O_3$ in thin film form has generated considerable interest recently for nonvolatile semiconductor memory cells [2,3,4]. A number of deposition methods have been investigated including RF sputtering, laser ablation, chemical vapor deposition (CVD) and chemical solution processes such as sol-gel or metallo-organic decomposition (MOD). Solution processing circumvents many of the problems associated with the synthesis of complex multi-component materials, since it offers the possibility of the preparation of homogeneous compositions by molecular mixing in solution. This can lead to uniform incorporation of dopants and reduced temperature processing which allow integration with semiconductors. Another advantage is that the rheological properties of solutions facilitate the formation of fibers, composites or thin films by techniques such as spin-casting, dip-coating or impregnation.

The chemistry of the sol-gel process is based on hydrolyzation and polycondensation of molecular alkoxide precursors. The effects of the formation of polymeric structures during the hydrolysis-condensation process on the development of properties in the products is not fully understood [5]. The reactions between alkoxides, the solvents, the molarity and the hydrolysis rates are all factors in determining the characteristics of gels and films.

This work describes the preparation of PZT precursor solutions by an improved chemical method. These solutions, in which we control the hydrolysis of suitable metal alkoxide precursors, are used to spin-cast thin layers of PZT (50/50) and PNZT (2/53/45) doped with 2 mole % of niobia. We show the effects of the hydrolysis rates and alkoxide concentration on the deposition characteristics, the microstructure of the thin layers, and the crystalline phase development. Comparing the experimental result obtained between PZT and PNZT, we study also the effects of dopants on PZT thin layers. Finally, we find from comparisons with bulk powders that in thin layers the formation of the perovskite phase is affected by stress and substrate interactions.

Experimental Procedure

The choice of the solvent and precursors was based on the following requirements. The solvent should have the proper boiling point, viscosity and surface tension for the coating process. The solution formed should have a high concentration of the components and be stable under ambient conditions. With these considerations, a procedure was adapted from earlier works [6,7]. Lead acetate trihydrate, $Pb(CH_3CO_2)_2.3H_2O$, zirconium propoxide, $Zr(C_3H_7O)_4$, titanium isopropoxide $Ti[(CH_3)_2CHO]_4$ and niobium ethoxide, $Nb(C_2H_5O)_5$ were used as starting materials with 2-methoxyethanol as a solvent. To prevent hydrolytic reactions lead acetate was first dissolved in methoxyethanol and associated water was boiled off by heating at 110°C for 2 hours under nitrogen. After dehydration, the lead solution was cooled to 60°C and then zirconium, titanium and niobium alkoxides, mixed in a methoxyethanol solution, were added in the required stoichiometric ratio. The resulting mixture was refluxed at 125°C for 2 hours, cooled to room temperature and adjusted to 0.75 M to form the precursors solution. As described earlier by Lakeman et al., an FT-IR analysis of the precursor solution showed that all alkoxy groups and part of the acetate groups were replaced by the chelating 2-methoxyethyl group [8]. Since individual metallic species were bonded to the same ligand, a close rate of hydrolysis and condensation can be expected, leading to a high degree of homogeneity of metal distribution in gels or thin layers [9].

Gels were obtained by mixing different amounts of water with the precursor solutions. At room temperature the homogeneous solutions set to a transparent gel, in one week for a solution prepared adding 10 moles of water per lead, and two days with 20 moles. Entrapped solvent was removed from the gels by heating at 100°C for two days, leading to a desiccated gel.

Thin layers were obtained by a multi-layering spin-casting technique. The precursor solutions were applied to platinum coated silicon substrates (Pt/Ti/SiO_2/Si) through a filtered (0.2 µm) syringe, and then the substrates were spun at 4000 rpm for 30 s. The films were subjected to low temperature treatment (300°C) for solvent removal and partial organic pyrolysis; then further deposition could be made without redissolving the layers. By adjusting either the concentration of the solution or the number of coatings, the required thickness was achieved. After the final spin-coating, densification and crystallization into the perovskite structure were achieved by firing the substrate at 600°C for 1h.

A systematic study was made in order to examine the effects of process parameters such as the amount of water and alkoxide molarity on the crystallinity of the perovskite phase and on film microstructure Microstructural information was obtained by scanning electron microscopy (SEM) and characterization of crystalline phases by X-ray diffraction (XRD). In order to investigate the different steps of formation of the inorganic network, thin films and desiccated gels were subjected to increasing heat treatment from 400 to 600°C.

CH3080-0-7803-0465-9/92$3.00 ©IEEE

Results and Discussion

Effects of solution concentration: The first series of experiments was designed to study the effects of sol concentration on the casting properties of the solution and to determine their consequences on the microstructure of PZT films. Various amounts of methoxyethanol were mixed with the starting alkoxide solution in order to adjust the molarity of the solution. Five formulations with varying concentrations were used for these studies. The viscosity of each solution was measured, and wet films were produced by spinning at 4000 rpm for 30s. Crystallization of the perovskite phase was achieved by heat treating at 600°C for 1h. The thickness of the films was measured using a profilometer.

Fig. 1 shows that the viscosity increases rapidly with the alkoxide concentration. As described by Scriven, with the spin-coating technique, controlling the viscosity of the precursor solution is a way to adjust the thickness of the film [10,11]. For example, using the 0.75 M spin-casting solution, typically a thickness of 0.1 µm/layer is obtained, whereas using a 0.25 M solution the thickness of a single layer is around 0.02-0.03 µm.

For good ferroelectric properties, the films must be uniform, dense and crack-free. All these qualities are more likely achieved with submicron films (0.2-0.7 µm) produced using the higher concentration solution (0.75 M). SEM photomicrographs (not shown here) of a 0.5 µm thick film show uniform films with fine grained microstructures. This microstructure was also observed on a film with an equivalent thickness, but which required more layers deposition of a more dilute solution (0.50 M).

Comparing the microstructure of a variety of thin films, we observed that increasing the molarity of the casting solution lead to a very dense microstructure, appearing fully dense for the 0.75 M solution. This reduction of film porosity may be attributed to the smaller proportion of solvent evaporated during the firing process. Using a higher concentration solution increased not only the thickness of the films but also its quality. Additionally, a reduced number of deposition steps is more desirable because it makes the process cleaner and less time-consuming [12].

By XRD all films show pure perovskite phase with good crystallinity. The mean crystallite size was estimated by the Scherrer equation [13] analyzing the line-broadening for the (110) peak of the X-rays pattern. Correction of the instrumental broadening was made using the (111) silicon peak of the substrate as internal standard. The mean crystallite sizes are more or less the same for the different concentration solutions, around 50-70 nm.

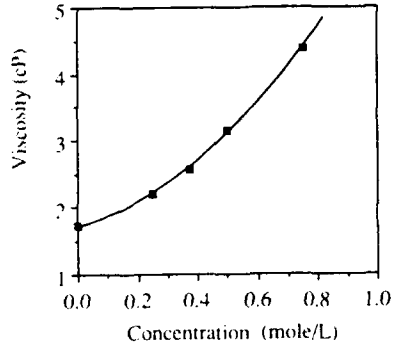


Fig. 1: Viscosity of the sol as a function of the molarity of the precursors solution.

Influence of water: Addition of water to the alkoxide solution results in hydrolysis followed by condensation reactions and the eventual development of a polymeric gel network. The purpose of this investigation was to vary the hydrolysis rates in the formation of PZT (50/50) and PNZT (2/53/45) films. Then we characterized the evolution of structure and determine which processing conditions were most suitable for the fabrication of a thin dielectric layer.

Various amounts of water were added to the 0.75 M precursor solution. The quantity of water was defined as the number of moles added for one mole of lead dissolved in the solution ($R_w=[H_2O/Pb]$). The prehydrolyzed solutions were aged for 24 hours prior to spinning. Due to the chelating properties of the methoxyethoxide ligand, the solutions have a low sensitivity to moisture during the coating process [9].

XRD patterns of PZT and PNZT films obtained with solutions made increasing the amount of water are shown in Fig.2 and 3. All composition films, heat treated at 600°C for 1hour, transformed to well crystallized perovskite phase. However, PNZT thin layers appeared to have a small proportion of a pyrochlore phase as shown by the very broad peak at 30° (2θ). In contrast PZT films show only pure perovskite phase. As shown by the similar X-ray patterns of films made with $R_w \geq 2$, increasing the hydrolysis rate during the sol-gel process does not affect significantly the crystallinity of the perovskite phase. Grain size, estimated by the Scherrer equation, appeared to be relatively independent of water content, with values from 60 to 80 nm.

Another feature to note is that layers derived from prehydrolyzed solutions tended to be more oriented in the [110] direction as shown by the different x-ray values of peak height ratios (100)/(110) (Table 1). This ratio for films prepared without water was similar to that for powder samples (JCPDS) with a value around 5-6. In contrast, all prehydrolyzed films show a peak height ratio value two time greater around 10-12. This difference in crystallization may be attributed to different oligomeric species, or polymeric structures, produced during hydrolysis and condensation [14,15]. In addition, analyses of the microstructure of the films, show that non hydrated solutions produced dense, crack-free layers, while those containing water showed a tendency to form cracks. This may be attributed to a faster gelation rate in the prehydrolyzed solutions compared to the rate of evaporation of the solvent.

As described for the MOD process, based on the use of high molecular weight precursors and solvents, with a lower condensation rate, the films first shrink with the evaporation of solvent and then crosslinking occurs during the decomposition of the metallo-organic compounds [16,17]. Films made with non-prehydrolyzed solutions seem to be able to lose solvent and shrink concurrently with the formation of a continuous polymeric gel during the coating process.

From the experimental results, it is clear that additions of water do not improve the crystallinity of the films and, instead, lead to microstructure defects. Better PZT thin films using the chemical process described above can be easily prepared with non-prehydrolysed solutions.

Electrical properties were measured by depositing platinum electrode dots on the top of a 0.5 µm PZT film prepared with the 0.75 M solution with no water added. The films presented typical P-E symmetrical hysteresis loops. The remanent polarization and the coercive field were measured to be 6.5 $\mu C/cm^2$ and 55 KV/cm.

Table 1: Characteristics of PZT and PNZT Thin Films

Composition	R_w	Layers #	Thickness (μm)	(100)/(110)	Xtal Size (nm)
PZT (0.75M)	-	5	0.5	4.5	65
	2	5	0.5	11.8	70
	5	5	0.5	12.1	67
	10	5	0.7	10.1	77
PNZT (0.75M)	-	5	0.5	5.5	85
	2	5	0.5	10.1	75
	5	5	0.5	10.0	77
	10	5	0.7	9.8	62

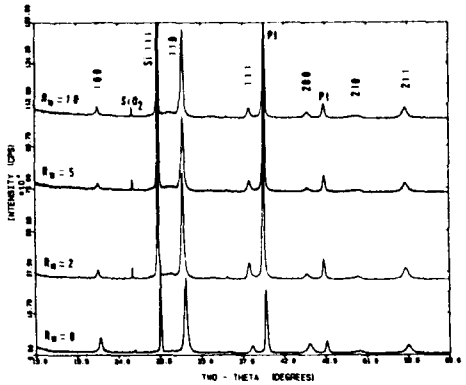


Fig. 2: X-ray diffraction pattern of PZT thin films on platinized silicon substrates, increasing the amount of hydrolysis water (heated at 600 C for 1h).

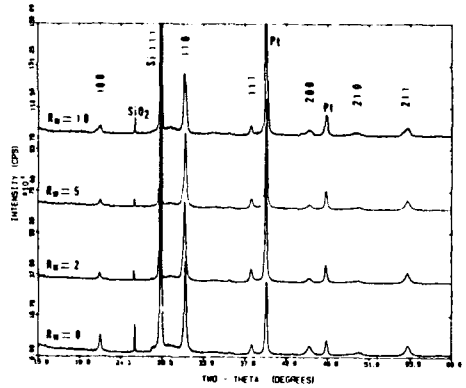


Fig. 3: X-ray diffraction pattern of PNZT thin films on platinized silicon substrates, increasing the amount of hydrolysis water (heated at 600 C for 1h).

Crystalline phase development: In order to investigate the steps of formation of the perovskite phase, PZT and PNZT films treated at 400, 450, 500 and 600°C for 1 hour have been studied by XRD analysis. X-ray diffraction results for non prehydrolyzed PZT films and PZT films prepared with R_w=5 are shown in Figs. 4(a) and 4(b), respectively.

For all compositions with different amounts of water, thin films show the same crystallization process: Heat treatment at 400°C resulted in the formation of a very broad "amorphous" hump at 30° (2θ), the only diffraction peaks present being due to the silicon and platinum constituents. Broads peaks, 29.5, 34.5, 49.5 and 59° (2θ), corresponding to a pyrochlore phase ($A_2B_2O_6$ or AB_2O_7) appear at 450°C. Further heating promotes development of the perovskite phase so that by 600°C virtually all pyrochlore has been eliminated and thin layers exhibit pure perovskite phase. As reported before by earlier works [18], heating the film at 600°C for 1 min using the rapid thermal annealing (RTA) process, a direct transition from amorphous to perovskite phase occurs, thus avoiding the formation of the pyrochlore phase.

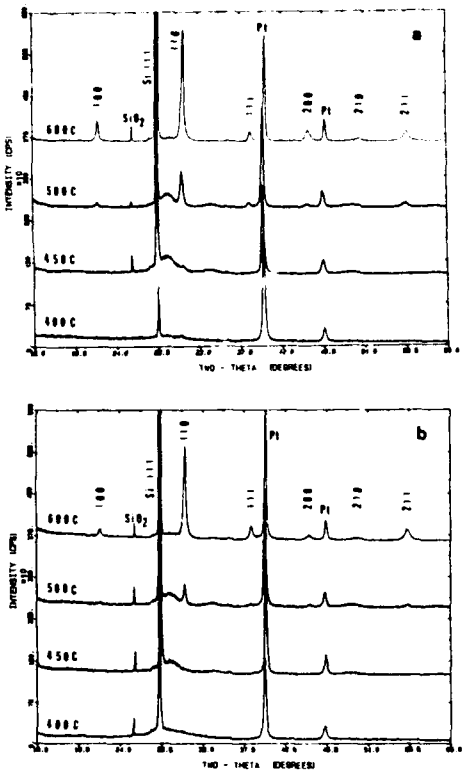


Fig. 4: Effect of heat treatment temperature; XRD patterns of PZT thin films on platinized silicon substrates, heat treated 1 h, (a) R_w=0 and (b) R_w=5.

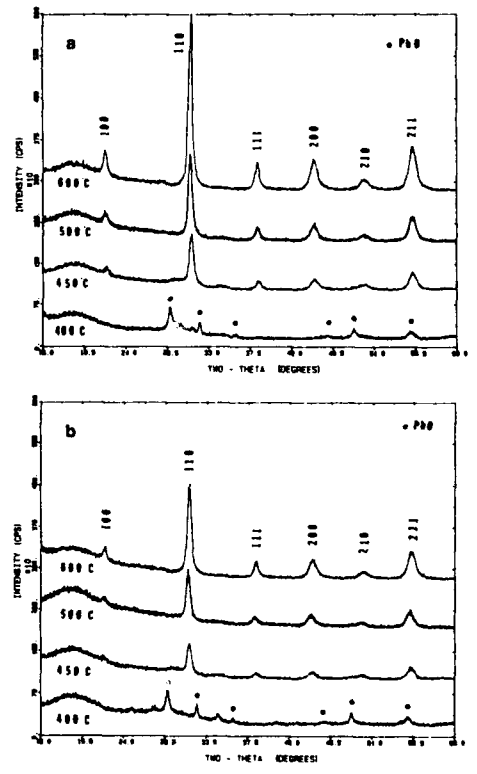


Fig. 5: Effect of heat treatment temperature; XRD patterns of PZT gel powders (a) R_w=10 and (b) R_w=20.

The XRD patterns of PZT gel powder (R_w=10) heat treated at 400, 450, 500 and 600°C for 1h, are shown in Fig 5(a), in comparison with a PZT gel (R_w=20) in Fig. 5(b). Below 300°C gel powders were amorphous; between 400 and 450°, PbO litharge structure was obtained; and above 450°, the gel exhibited a pure perovskite phase. This sequence was typical for all compositions with different amounts of water. Surprisingly, perovskite formation in gel powders was not inhibited by a low temperature pyrochlore formation.

For thin layers, no additional crystalline phases other than pyrochlore and perovskite could be detected by XRD. The presence of a Pb deficient pyrochlore phase in thin layers instead of the PbO phase in gels could arise from the lost of Pb during the heating process of films. This related to the higher evaporation rate for films than for desiccated gels due to the high surface area compared to the surface/volume ratio of a powder [19].

Another feature to note is that the initial formation of the nonferroelectric pyrochlore in thin layers is detrimental to the crystallization of the perovskite phase. With a heat treatment at 450°C, only peaks corresponding to the pyrochlore phase are observed for the PZT and PNZT films. In contrast, at this low temperature, we observed the formation of pure crystalline perovskite in the heat treated powders. This result shows that the development of the perovskite structure is more difficult in thin films integrated on substrates in comparison with the crystallization of bulk powders gels. This has been described recently for a $Pb[(Mg_{1/3}Nb_{2/3})_{1-x}Ti_x]O_3$ system and could arise from the substrate-film interaction, in particular, because of the stresses developed during the unidirectional shrinkage of films [19].

Comparing the perovskite phase development in gels formed with different amounts of water, we observed that the temperature at which the initial presence of perovskite phase was observed was lowered by decreasing the amount of water in the precursor solution. This is evidenced by the relative intensities of the (110) peak on the X-ray pattern. For example, at 600°C $[I(R_w=10)/I(R_w=20)]=2$ and $[I(R_w=10)/I(R_w=20)]=3$, respectively, for PZT and PNZT gels. Lowering the hydrolysis rate for PZT and PNZT gels induced a better crystallization of the perovskite phase, evidenced by higher and sharper XRD peaks at lower temperature.

Conclusions

Crack-free, submicron ferroelectric PZT (50/50) and PNZT (2/53/45) thin films were prepared on platinum coated silicon with a 0.75 M precursors solution. Using a lower concentration solution the coating process requires more layers deposition to achieve the desired thickness. In addition, the porosity of the film seems to increase when the molarity of the precursor solution decreases.

Adding water in the spin-casting solution showed no further improvement in the crystallinity of the films and in contrast, leads to microstructure defects. We found that perovskite phase prepared with the prehydrolyzed solution shows a tendency to be more oriented in the [100] direction. We show that good PZT thin films using the described chemical process with non prehydrolyzed solutions can be easily prepared.

From this investigation, it is clear that doping PZT with 2 mole% of niobium has very little effect on the crystallization or microstructure of thin layers. This is attributed to the solution process which allows the preparation of a very homogeneous solution by incorporating the dopants at the molecular level. The temperature at which the initial presence of perovskite phase is detected is 500°C for thin films.

Acknowledgement: The financial support of the Center for Ceramic Research, A New Jersey Commission on Science and Technology Center, is greatly appreciated.

References

[1] J-M. Wu, L.C. Klein and A. Safari, "Microstructure development of sol-gel prepared niobium doped lead zirconate-titanate thin films", J. Am. Ceram. Soc., Vol. 76 (1993) to appear.

[2] S.K. Dey and R. Zuleeg, "Integrated sol-gel PZT thin films on Pt, Si, and GaAs for non-volatile memory applications", Ferroelectrics, Vol. 108 (1990) 1643-1652.

[3] S.K. Dey and R. Zuleeg, "Processing and parameters of sol-gel PZT thin-films for GaAs memory applications", Ferroelectrics, Vol. 112 (1990) 309-319.

[4] J.F. Scott, L. Kammerdiner, M. Parris, S. Traynor, V. Ottenbacher, A. Shawabkeh and W.F. Oliver, "Switching kinetics of lead zirconate titanate submicron thin-film memories", J. Appl. Phys. Vol. 64 (1988) 787-792.

[5] C.J. Brinker and G.W. Scherer, Sol-Gel Science, The Physics and Chemistry of Sol-Gel Processing, Academic Press, Boston (1990).

[6] J. B. Blum and S. R. Gurkovich, "Sol-gel derived $PbTiO_3$", J. Mat. Sci., Vol. 20 (1985) 4479-4483.

[7] K. D. Budd, S. K. Dey and D. A. Payne, "Sol-gel Processing of $PbTiO_3$, PZT and PLZT thin films", Proc. Br. Ceram. Soc., Vol. 36 (1985) 107-121.

[8] C.D.E. Lakeman, J-F Campion and D. A. Payne, "Ferroelectric films", Ceramic Transaction, Vol. 25 (1992) 413-439.

[9] G. Yi and M. Sayer, "Sol-gel processing of complex oxide films", Ceramic Bulletin, Vol. 70, No. 7 (1991) 1173-1179.

[10] L.E. Scriven,"Physics and Applications of Dip Coating and Spin Coating", Mat. Res. Soc. Symp. Proc., Vol. 121 (1988); Materials Research Society.

[11] P. Gaucher, S. Lequien, J-P Ganne, S. Faure and P. Barboux, IEEE, 7 Th International Symposium on Applications of Ferroelectrics, (1990) 267-270.

[12] A. Gupta and S. K. Dey, "Ferroelectric films" Ceramic Transaction, Vol. 25 (1992) 243-250.

[13] B. D. Cullity, Elements of X-ray Diffraction, Addison-Wesley, Reading, MA (1978).

[14] R. C. Mehrotra, "Synthesis and reactions of metal alkoxides", Journal of Non-Crystalline Solids, Vol. 100 (1988) 1-15.

[15] J. Livage, M. Henry and C. Sanchez, "Sol-gel chemistry of transition metal oxides", Prog. Solid St. Chem., Vol. 18 (1988) 259-341.

[16] T.J. Garino, "The cracking of sol-gel films during drying", Mat. Res. Soc. Symp., Vol. 180 (1990) 497-502.

[17] R. W. Vest, Ferroelectrics, Vol. 102 (1990) 53-68.

[18] H. Hu, L. Shi, V. Kumar and S. B. Krupanidhi, "Ferroelectric films" Ceramic Transaction, Vol. 25 (1992) 113-120.

[19] L. Falter Francis and D. A. Payne, "Thin-layer dielectrics in the $Pb[(Mg_{1/3}Nb_{2/3}O_{1-x}Ti_x]O_3$ system" J. Am. Ceram. Soc., Vol. 74 [12] (1991) 300-310.

ELECTRICAL CHARACTERIZATION OF SOL-GEL DERIVED PZT THIN FILMS

Kashyap R. Beliur, H. N. Al-Shareef, S. H. Rou,
K. D. Gifford, O. Auciello* and A. I. Kingon.

Department of Materials Science and Engineering,
N. C. State University, Raleigh, NC 27695-7919.
*Also, Microelectronics Center of N. C., Research
Triangle Park, NC 27909-2889

ABSTRACT

Thin films of lead zirconate titanate (PZT) were deposited on a variety of substrates using the sol-gel process. These included $Pt/Ti/SiO_2/Si$, $RuO_2/SiO_2/Si$, RuO_2/MgO, Pt/MgO and Pt/Ti/MgO. Epitaxial, oriented and polycrystalline films were obtained after annealing at 700°C for 10 min. Polycrystalline PZT films with RuO_2 as top and bottom electrodes show superior hysteresis and fatigue behaviour as compared to such films on Pt. Epitaxial films on Pt/MgO and Pt/Ti/MgO display excellent fatigue behavior, large remnant polarization as compared to their polycrystalline counterparts on $Pt/Ti/SiO_2/Si$. The results suggest that different fatigue mechanisms may be simultaneously operating.

INTRODUCTION

Extensive research is being carried out on ferroelectric thin films of lead zirconate titanate ($PbZr_xTi_{1-x}O_3$) because of their potential applications in DRAMs and non-volatile memories [1,2]. Ferroelectric memory devices have many attractive features such as non-volatility, radiation hardness and speed. The basic requirements of such a memory device are: a) the switching voltage should be less than 5V and b) the films should be able to withstand 10^{15} read/write cycles, although 10^{10} cycles also offers device possibilities [3]. PZT is a promising candidate among the various ferroelectric materials for memory applications. It has a large remnant polarization and a low coercive field among other properties. However, fatigue is of major concern in terms of reliability of devices made from PZT films.

The various techniques that have been investigated for PZT thin film deposition include sputtering [4,6], laser ablation [5], organometallic chemical vapor deposition (CVD), metalorganic decomposition (MOD) [3] and sol-gel processing [7]. In this study, the sol-gel technique has been used to deposit films with a composition of $PbZr_{0.53}Ti_{0.47}O_3$. An attempt has been made to understand the role of the electrode type and film crystallinity on fatigue. We have compared two sets of PZT capacitors with different electrodes, viz. $RuO_x/PZT/RuO_2/SiO_2/Si$ and $Pt/PZT/Pt/Ti/SiO_2/Si$. Polycrystalline thin films of $Pt/PZT/Pt/Ti/SiO_2/Si$ are also compared with epitaxial films of Pt/PZT/Pt/MgO and Pt/PZT/Pt/Ti/MgO in terms of hysteresis and fatigue behavior. These films were processed under identical conditions.

RESULTS AND DISCUSSION

Ruthenium Oxide vs Platinum Electrodes

Polycrystalline PZT films were deposited on RuO_2 and Pt electrodes. Hysteresis and fatigue tests were performed on $Pt/PZT/Pt/Ti/SiO_2/Si$ and $RuO_x/PZT/RuO_2/SiO_2/Si$. Fig. 1 and Fig. 2 show the hysteresis loops on the above films. The $RuO_x/PZT/RuO_2/SiO_2/Si$ capacitor shows higher remnant polarization values in comparison to the $Pt/PZT/Pt/SiO_2/Si$ capacitor. However the resistivity of the PZT film with ruthenium oxide electrodes is about two orders of magnitude lower(10^8-10^9 ohm-cm). Both films were of comparable thickness (0.15 and 0.18 μm). The coercive fields for both films are of similar magnitude (100-120 kV/cm).

EXPERIMENTAL

The procedure for the preparation of stock solution is based on an inverted mixing order technique developed at Sandia National Laboratories [8]. The precursors used were lead (IV) acetate, zirconium-n-butoxide and titanium-iso-propoxide. These were dissolved in methanol and acetic acid. Water was added to make the final molarity 0.4 M PZT. Both spin on and dip coating techniques were employed to make films. Each film was formed by multiple layer deposition with each layer being heated at 300° C for 5 min. in order to convert the film into an inorganic amorphous structure [7]. Finally the films were annealed at 700° C for 10 min. and rapidly cooled by removing them directly out of the furnace.

Thin films of PZT were deposited on $RuO_2/SiO_2/Si$, $Pt/Ti/SiO_2/Si$, RuO_2/MgO, Pt/MgO and Pt/Ti/MgO. XRD, TEM and field emission SEM were used to characterize the films. The top contacts were fabricated by lift-off photolithography. In the case of RuO_x top electrodes, ruthenium metal was first sputtered and then patterned by lift off. Subsequently, the ruthenium metal contacts were oxidized in pure oxygen at 500° C for 30 min. Measurements were done on electrodes of size 100 by 100 μm^2 or 50 by 20 μm^2. The electrical measurements included hysteresis and fatigue using the RT-66A ferroelectric tester from Radiant Technologies.

CH3080-0-7803-0465-9/92$3.00 ©IEEE

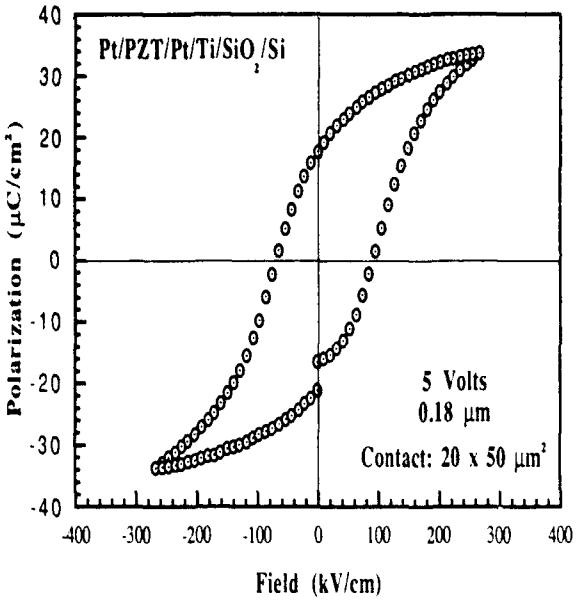


Fig. i Hysteresis loop of a Pt/PZT/Pt/SiO_2/Si film

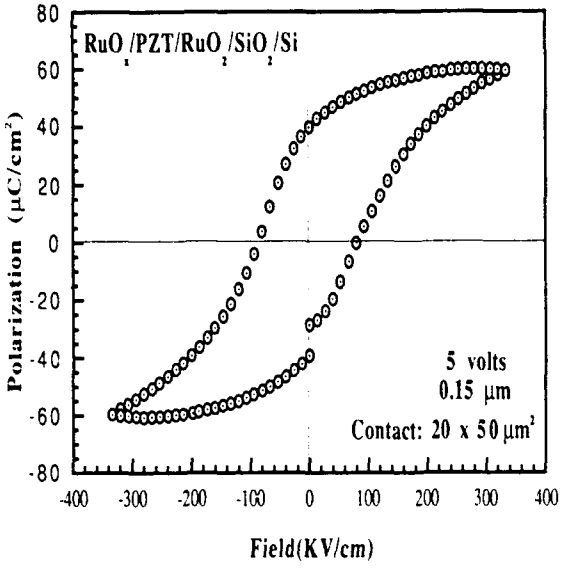


Fig. 2 Hysteresis loop of an RuO_x/PZT/RuO_2/SiO_2/Si Film

Fig. 3 shows the fatigue curves of the two capacitors. Here, one clearly notices the superior performance of RuO_x/PZT/RuO_2/SiO_2/Si. After extrapolating to 10^{10} cycles, the value of (P*r-P^r) is about 15 $\mu C/cm^2$ for RuO_x/PZT/RuO_2/SiO_2/Si whereas it is only about 0.5 $\mu C/cm^2$ for Pt/PZT/Pt/Ti/SiO_2/Si. P*r and P^r refer to the switched and non-switched polarization, respectively. The difference (P*r-P^r) is equivalent to 2Pr (assuming a symmetric loop). In memory applications a capacitor is considered to have failed if P*r-P^r is smaller than 0.5-2.0 $\mu C/cm^2$ [9]. In our experiments we have chosen 2.0 $\mu C/cm^2$ as the criterion for capacitor failure. This implies that the polycrystalline PZT film on RuO_2 is device worthy while that on Pt is not.

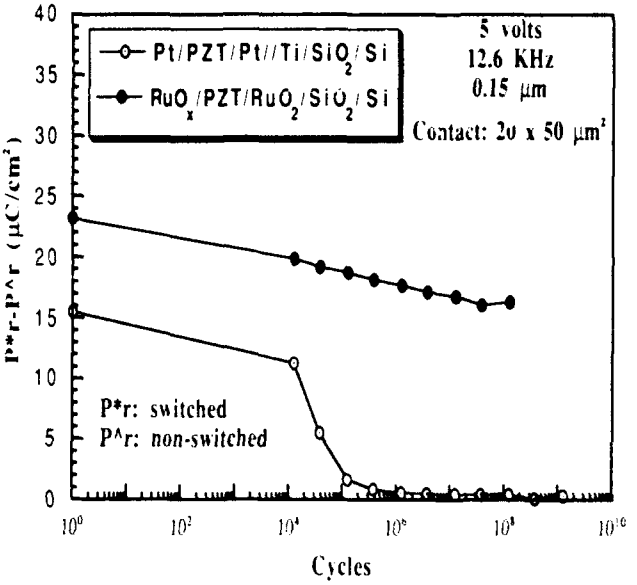


Fig. 3 Comparison of fatigue on Pt and RuO_2 electrodes

Limited research has indicated that the conduction process in PZT based capacitor systems is bulk controlled, especially at low fields [10,11]. It was observed that microstructure of PZT film on RuO_2 was different from that grown on Pt. This difference may contribute to the higher leakage current observed in RuO_2/PZT/RuO_2 system as compared to that in Pt/PZT/Pt system. In contrast, the higher leakage current can possibly be due to the lower work function mismatch between RuO_2 and PZT as compared to that between Pt and PZT [12]. This difference in leakage currents may be related to the observed difference in fatigue.

Epitaxial vs Polycrystalline Films

The properties of epitaxial PZT films in the Pt/PZT/Pt/MgO and Pt/PZT/Pt/Ti/MgO systems were compared with those of polycrystalline PZT in the Pt/PZT/Pt/Ti/SiO_2/Si system. To separate the effect of film crystallinity from other variables (such as electrode type, processing parameters), we fabricated PZT capacitors under the following conditions: a) Pt/Ti layers were simultaneously deposited on MgO and SiO_2/Si in the same deposition chamber, b) PZT films on both substrates were made under identical processing conditions.

The films on Pt/Ti/MgO were epitaxial (the polarization vector oriented only perpendicular to the plane of the film), while those on Pt/Ti/SiO_2/Si were polycrystalline. The grain size of the epitaxial film and polycrystalline film were about 0.22 μm and 0.15 μm respectively, as observed by TEM. It can clearly be seen from Fig. 4 that the epitaxial film displays better properties (higher polarization values and a more square loop) as compared to the polycrystalline film. The higher polarization values for the epitaxial film can be attributed to the high c-axis orientation of

the film. Besides,the more square loop results because there is no stress induced polarization reversal process operative to slim the loop. Thus it is behaving more like a single crystal. The coercive field is nearly the same for the two films.

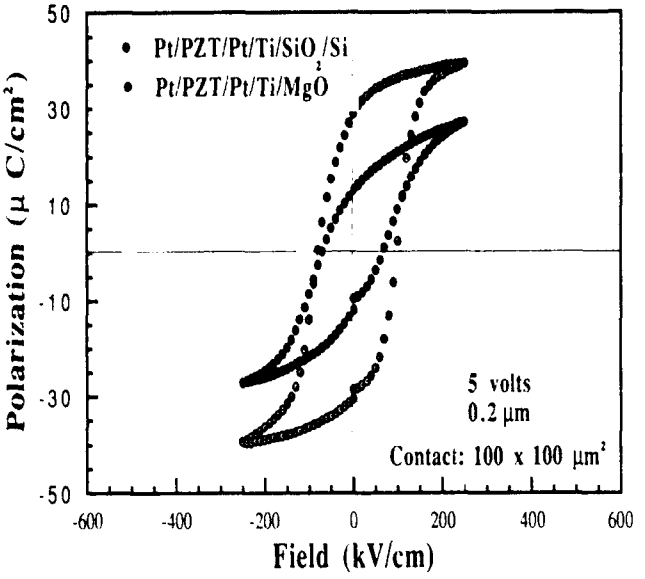


Fig.4 Hysteresis loops of epitaxial and polycrystalline films.

A comparison of the fatigue profiles of the two films is shown in Fig. 5. It is evident that the epitaxial film has a better fatigue life. After 10^{11} cycles, the value of P*r-P^r is about 22 μC/cm² for Pt/PZT/Pt/Ti/MgO whereas it is only 0.5 μC/cm² for Pt/PZT/Pt/Ti/SiO_2/Si. Both the top and bottom contacts for these two films were deposited under identical conditions. However, they display very different fatigue behavior. This leads us to believe that some other mechanism besides interface and electrode effects is also responsible for fatigue. This other mechanism could involve domain wall pinning at structural defects in the film. These could include point defects such as oxygen vacancies [13] and possibly planar defects . Stress could be an important parameter. It should be noted that, in distinct contrast to the polycrystalline films the virgin and the switched states of the epitaxial films have the same stress condition (ie. there is no strain associated with the switched state). There is therefore no stress-driven mechanism of polarization reversal. This is also consistent with the observation that loss of retention is also significantly less in the epitaxial films (see Fig. 6).

An epitaxial PZT film was also grown on Pt/MgO omitting the Ti adhesion layer. This too displayed larger polarization and better fatigue behavior than PZT films on Pt/Ti/SiO_2/Si as shown in Fig. 6. The polarization values of of this film are higher than those of the PZT/Pt/Ti/MgO indicating a higher degree of (001) orientation.

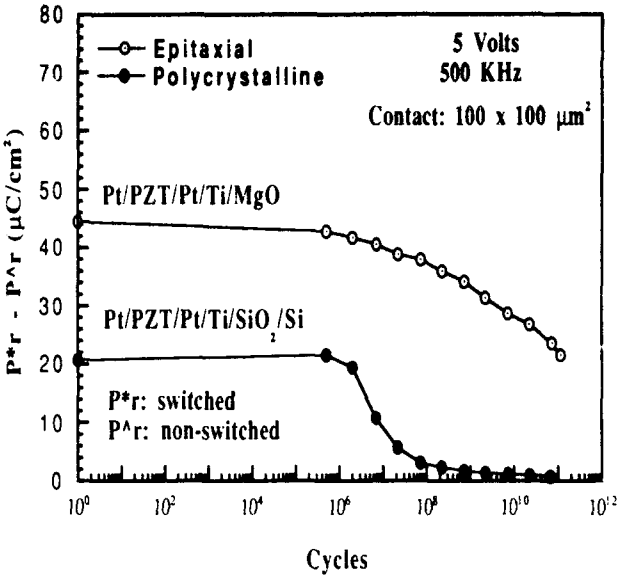


Fig. 5 Fatigue profiles of epitaxial and polycrystalline films

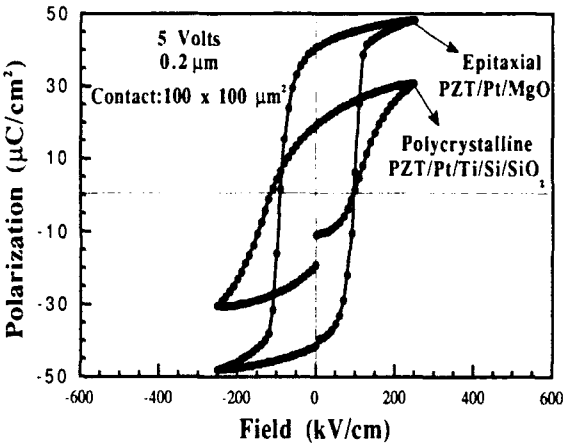


Fig. 6 Hysteresis loops on Pt/ MgO and Pt/Ti/SiO2/Si

A similar study on the effect of orientation on film properties has been reported by Tuttle et al.[14].

REVERSIBILITY OF FATIGUE

It is possible to restore the original hysteresis loop of a fatigued film. This can be done in more than one way. For example, Scott et al. [15] showed that the original loops of fatigued films can be restored by applying a voltage much larger than the fatigue voltage for a period of 30 μsec. This worked for sol-gel films only. Ramesh et al. [9] were able to restore the original loop of fatigued films by applying a voltage of the same magnitude as the fatigue voltage for a period of two seconds (This was simply done by acquiring a resistance measurement using the RT66A ferroelectric tester). They reported such an effect on PZT films grown by laser ablation on YBCO/$LaAlO_3$ substrates.

We have been able to restore the loops of epitaxial films after they were fatigued at 5 volts. This required the application of 8-10 V for a period of 2 seconds (see Fig. 7). For polycrystalline films, we were unable to completely restore the original loop even after applying up to 15 V for 2 seconds. This again, may indicate that domain wall pinning is more pronounced in the case of polycrystalline films than in epitaxial ones.

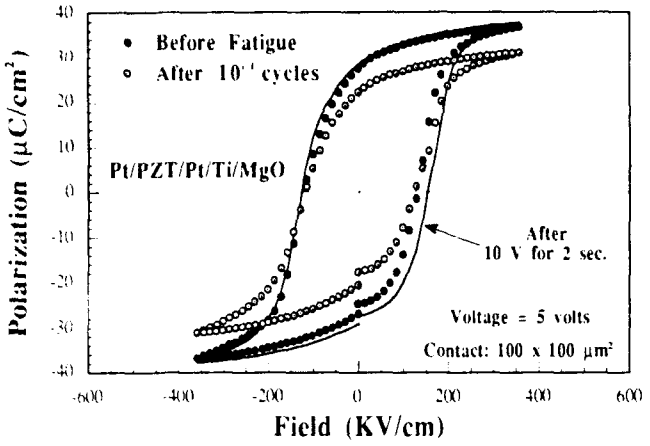


Fig. 7 Fatigue reversibility in epitaxial films

SUMMARY

Our analysis of the RuO_2 electrode has shown that it has the potential for use in PZT based ferroelectric memories. Films grown on RuO_2 display better properties in comparison with those on platinum in terms of fatigue and polarization values. However, these films have higher leakage currents. Epitaxial films show superior properties in comparison to polycrystalline films. In particular, they show excellent fatigue and retention performance even on Pt electrodes The study on fatigue has revealed that more than one failure mechanism may be simultaneously operating. Loop restoration after fatigue can be more easily achieved in epitaxial films than in polycrystalline ones.

ACKNOWLEDGMENTS

Support for this work was provided by the Defense Advanced Research Projects Agency (DARPA).

REFERENCES

[1] C. A. Araujo et. al.,"Ferroelectric Memories", Ferroelectrics, Vol 104, pp 241-256, 1990.
[2] W. A. Geideman,"Progress in feroelectric memory technology",IEEE Trans. Ultrasonics Ferroelectrics and Frequency Control, Vol 38, No 6 pp 704-711, Nov 1991.
[3] G. A. C. M. Spierings et. al., " Preparation and ferroelectric properties $PbZr_{0.53}Ti_{0.47}O_3$ thin films by spin coating and metalorganic decomposition", J. Appl. Phys., Vol 70(4), pp 2290-2298, 15 Aug 1991.
[4] M. S. Ameen et. al.," Processing and structural characterization of ferroelectric thin films deposited by ion beam sputtering", in Proceedings of MRS Symposium, Vol 200, 1990, pp 65-76.
[5] O.Auciello et al.,"Synthesis and characterization of PZT thin films by an automated laser ablation deposition technique", J. Appl Phys.,(in press, 1992)
[6] O. Auciello and A. I. Kingon, "A critical review of physical vapor deposition techniques for the synthesis of ferroelectric thin films", to be published in the Proceedings of the International Symposium on the Applications of Ferroelectrics, Greenville, SC, 1992.
[7] G. Yi, Z. Wu and M. Sayer," Preparation of $Pb(Zr,Ti)O_3$ thin films by sol-gel processing : Electrical, optical, and electro-optic properties ",J. Appl. Phys., 64(5), pp 2717-2723, 1 Sep. 1988.
[8] R.W.Schwartz et. al.," Spectroscopic and microstructural characterization of solution chemistry effects in PZT thin Film processing", in Mat. Res. Soc. Symp. Proc., Vol 243, " Ferroelectric Thin Films II", Eds. A.I.Kingon, E.R.Myers and B.Tuttle, MRS, Pittsburgh, 1992.
[9] R.Ramesh et.al. ,"Fatigue and aging in ferroelectric $PbZr_{0.2}Ti_{0.8}O_3$/ $YBa_2Cu_3O_7$ heterostructures", Integrated Ferroelectrics, Vol.1, pp1-15, 1992.
[10] X. Chen et al.,"Electric transport properties of PZT thin films for ferroelectric memory applications", (submitted to J. Appl. Phys., 1992)
[11] J. F. Scott et. al., " Quantitative measurement of space-charge effects in lead zirconate titanate memories", J. Appl. Phys., 70(1), pp 382-388, 1 July 1991.
[12] I.K.Yoo et al.," Leakage current studies of lead zirconate titanate thin films", to be published in the Proceedings of the International Symposium on the Applications of Ferroelectrics, Greenville, SC, 1992.
[13] H. M. Duiker et. al.,"Fatigue and switching in ferroelectric memories: Theory and Experiment", J. Appl. Phys., 68 (11), pp 5783-5791, Dec 1 1990.
[14] B.A.Tuttle et al., " Highly oriented chemically prepared $Pb(Zr,Ti)O_3$ thin films ",in Mat. Res. Soc. Symp. Proc., Vol 243, " Ferroelectric Thin Films II", Eds. A.I.Kingon, E.R.Myers and B.Tuttle, MRS, Pittsburgh, 1992.
[15] J. F. Scott et al.,"Raman Spectroscopy of submicron KNO_3 films. II. Fatigue and space charge effects", J. of Appl. Phys., 64(3), pp1547-1551,1 Aug. 1988.

CONTROL OF LEAD CONTENT IN PLZT THIN FILMS PRODUCED USING CLUSTER MAGNETRON SPUTTERING

K F Dexter, K L Lewis and J E Chadney
DRA Malvern, St Andrews Road, Malvern, Worcs WR14 3PS, UK

ABSTRACT

The deposition of PLZT thin films by cluster magnetron techniques is described. X-ray photoelectron spectroscopy has been used to determine film composition over a range of substrate temperatures. As-deposited films have been studied by X-ray diffraction techniques and the role of post deposition annealing has been assessed. The morphology and growth rates have been determined.

INTRODUCTION

Thin films of PLZT have been studied extensively in order to exploit their ferroelectric and electro-optic properties [1,2]. Deposition of PLZT (x/y/z), where x, y and z are defined [3] by:

$$Pb_{1-x/100}La_{x/100}(Zr_{y/100}Ti_{z/100})_{1-x/400}O_3$$

is achieved in this study using r.f cluster magnetron sputtering. This technique offers advantages over other routes in terms of film quality, surface morphology and compositional control. In common with other methods, such as sol-gel deposition [4,5], and single target r.f. sputtering [6,7,8] control of lead stoichiometry is a key issue and using a cluster magnetron (Fig 1), we report incorporation of Pb into our PLZT films up to and in excess of the chosen stoichiometric value. This allows the exploration of two step deposition/anneal processes, where films containing an excess of Pb can be sputtered at room temperature and annealed into the perovskite phase [9]

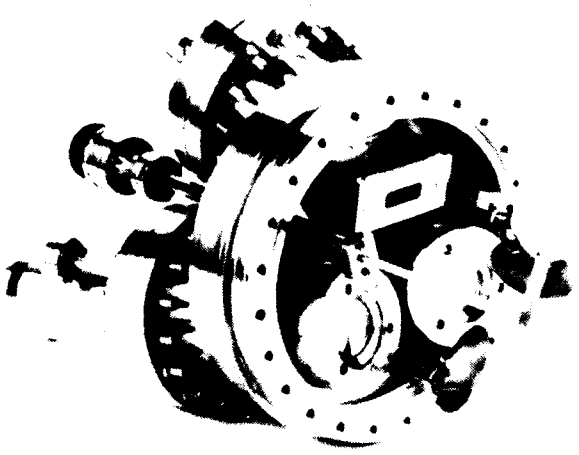


Fig. 1: UHV cluster of 50mm magnetron sputter sources with shutters, gas rings and a fast atom source (courtesy of Atom Tech Ltd).

EXPERIMENTAL

The work was carried out in a UHV system with 50mm planar magnetrons (Fig 1). The sputtering targets used in this work are PLZT (8/75/31.5) ceramic and metallic lead (99.9% purity). Polished c-plane sapphire substrates, 25mm diameter, were positioned at 110mm from the targets. A calibrated substrate heater was used to generate temperatures of up to 640°C. Sputtering was carried out in mixtures of argon and oxygen, whose composition was controlled using Brooks 5850R series mass flow controllers. The effect of plasma thermalisation was studied by variation in deposition pressure over the range $1x10^{-1}$ to 8Pa. All experiments reported in this work were carried out at $2x10^{-1}$Pa. The composition of the films was determined after deposition by X-ray photoelectron spectroscopy (XPS). These measurements were calibrated using a PLZT 9/65/35 optical grade ceramic standard. All surfaces were etched in Ar^+ at 5000μA, 2.5kV for 30 mins to remove surface contamination before analysis. Studies of films deposited *in situ* in the UHV system used for XPS analysis confirmed the reliability of this technique, and demonstrated the absence of preferential sputtering effects. One particular advantage of using this technique is the ability to determine reliably the oxygen content of the films. The crystal structure was determined using a Siemens D5000 diffractometer, using Ni filtered CuKα radiation.

A Wyko TOPO 3 white light interferometer was used to assess the effects of a post-deposition anneal on film morphology. Growth rate data has also been determined using this technique and cross-referenced with a Dektak 2000 step meter. Annealing experiments were carried out using a fused silica resistive heater furnace with *in situ* temperatures monitored by a Pt:Pt/Rh thermocouple.

RESULTS AND DISCUSSION

The effect of power applied to the secondary lead source can be seen in Fig 2. The Pb content value required for stoichiometric 9/65/35 PLZT is 0.91 (for oxygen =3), and so an excess of lead can clearly be incorporated into the films, provided that 5% oxygen is added to the sputtering gas. The importance of oxygen in controlling the incorporation of lead into the films is clearly evident from Fig 3, which is consistent with other work in this field [10]. This is fundamental to the achievement of the correct stoichiometry of films at growth temperatures in excess of 600°C (Fig 4). However, both the input of oxygen during deposition, and the application of power to the secondary lead target have the effect of reducing the growth rate. Films deposited at room temperature are amorphous. At intermediate temperatures (<500°C), mixed phase deposits

CH3080-0-7803-0465-9/92$3.00 ©IEEE

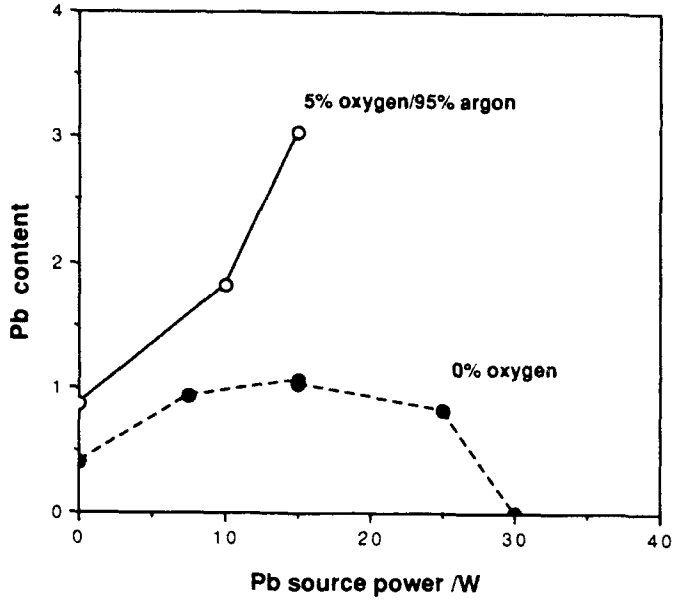


Fig. 2: Variation of Pb content (normalised to oxygen = 3) with RF power applied to Pb source for films grown with and without oxygen, substrate temperature 540°C. This emphasises the role of oxygen in controlling the Pb content of PLZT films.

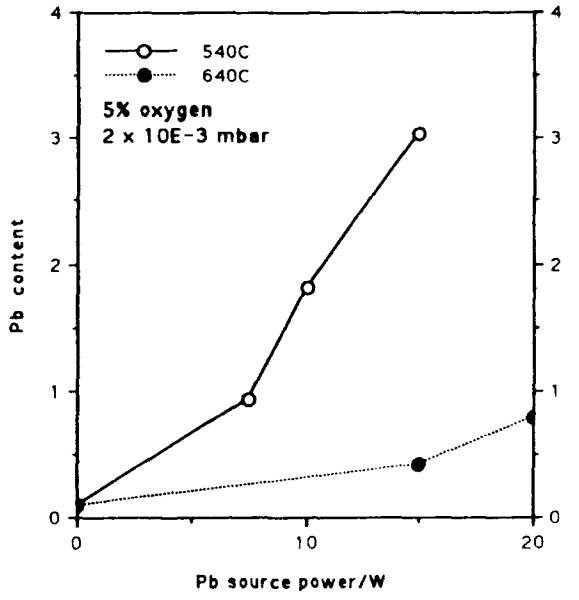


Fig. 4: Variation of Pb content with RF power applied to Pb source for films grown at two different temperatures. This shows the steep variation in Pb content with change in deposition temperature

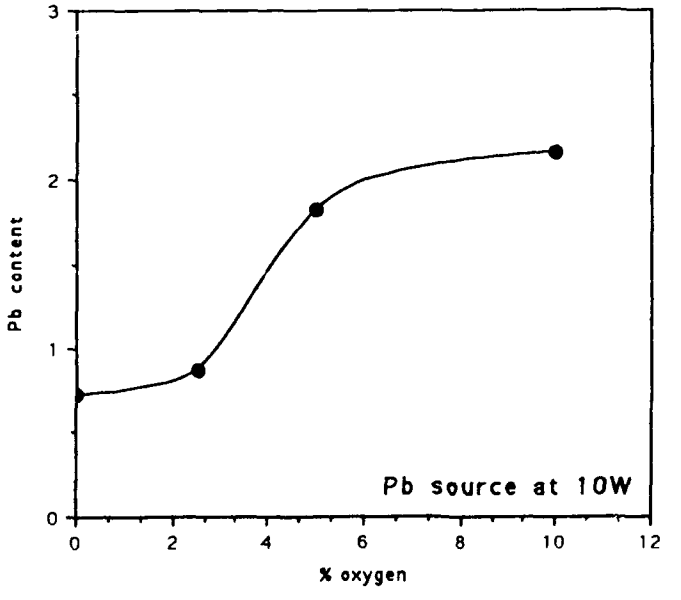


Fig. 3: Variation of Pb content (normalised to oxygen = 3) with oxygen level for a fixed power level to the Pb source of 10W and substrate temperature 540°C.

are obtained, but even at the highest temperatures examined it has been difficult to produce 100% phase pure perovskite material. Films of highly oriented pyrochlore (Fig 5) are readily obtained at temperatures between 500 and 640°C.

The ability to deposit films containing excess Pb allows the exploration of 2-step annealing for the production of perovskite films. This process uses a room temperature growth stage followed by post deposition anneal. Films deposited at room temperature can have lead contents in excess of 200% of the required value, and in common with the higher temperature deposition excess lead films, they are black in colour. Subsequent annealing at 600°C for 2 hours in air produced single phase 110 perovskite films (a_0 = 4.153Å). The films then have an optical transmission close to the Fresnel limit of 75% at 632.8nm.

Studies of surface morphology using white light interferometry have highlighted an increase in surface morphology produced as a result of the anneal process. This is related to the exact amount of lead present in the as-deposited films, and in the worst cases can be in excess of 5nm, with pinholes 2-3μm in diameter. These are clearly the result of grain growth phenomena and the ensuing crystallisation of the film.

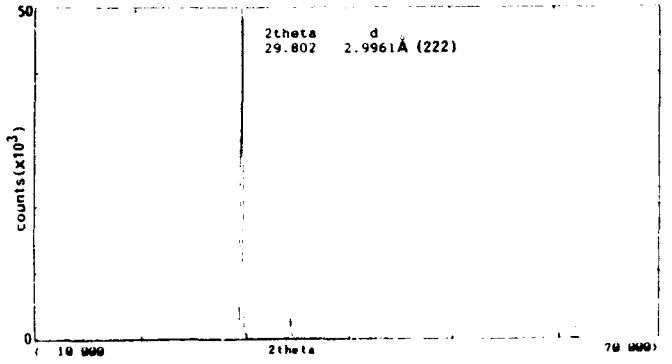


Fig. 5: X-ray diffraction spectrum of a thin film of PLZT grown at 560°C, showing the high level of preferred orientation found in pyrochlore films.

SUMMARY

Cluster magnetron techniques have proved to be a very effective method for controlling the incorporation of lead in PLZT thin films. As-deposited films can be either amorphous or pyrochlore phase. Subsequent annealing of films can produce single phase perovskite layers.

REFERENCES

[1] G Haertling, Ferroelectrics 75 25 (1987)
[2] S Krishnakumar, V H Ozguz, C Fan, C Cozzolino, S C Esener and S H Lee, IEEE Trans. on Ultrasonics, Ferroelectrics and Frequency Control, 38 585 (1991)
[3] H Adachi, T Mitsuyu, O Yamazaki, K Wasa, J Appl Phys 60(2) 1432 (1986)
[4] G Yi, Z Wu and M Sayer, J Appl Phys 64(5) 2717 (1988)
[5] S J Milne and S H Pyke, J Am Ceram Soc 74, 1407 (1991)
[6] E S Ramakrishnan and W Y Yowng, J Van Sci Technol A10(1) 69 (1992)
[7] K Torii, T Kaga, K Kushida, H Takeuchi and E Takeda, Jap J Appl Phys 30 3562 (1991)
[8] M Ishida, H Matsunami and T Tanaka, J Appl Phys 48(3) 951 (1977)
[9] R M Hazen, Sci American, p52 (1988)
[10] H N El-Shareef, K D Gifford, M S Ameen, S H Rou, P D Hren, O Auciello and A I Kingon, Ceram Trans 25, 97 (1992)

© Controller, HMSO, London, 1992.

Dielectric

EFFECT OF CORE SHELL MORPHOLOGY ON DIELECTRIC PROPERTIES OF Zr DOPED $BaTiO_3$

T.R. Armstrong, R.D. Roseman and R.C. Buchanan, Dept. of Materials Science and Engineering University of Illinois at Urbana-Champaign, IL 61801

Abstract

The dielectric properties of modified $BaTiO_3$ are highly dependent upon dopant type, concentration and heat treatment. Substitution of isovalent dopants, such as Zr^{4+}, can result in significant changes in grain morphology, such as the development of core-shell grains. In these modified $BaTiO_3$ ceramics enhanced dielectric and mechanical properties can result from the volume concentration of these core-shell structures. In this investigation, characterization of the core-shell grains and lattice structure in Zr modified $BaTiO_3$ was carried out. Through TEM, CBED and EDS techniques, the shells were identified as diffuse regions of pseudocubic structure surrounding a tetragonal $BaTiO_3$ core. This condition leads to the development of internal stresses, which significantly modify the dielectric properties.

Introduction

In $BaTiO_3$, the ferroelectric phase transition near T_c (Curie temperature) is associated with the development of a complex stress state, as expansion in the c-directions becomes constrained. Large crystals adjust by formation of 90° domains, so as to lower the residual internal stress state. In smaller grains, the unrelieved stresses leads to a decrease in the concentration of 90° domains. It has been shown that this increase in stress level leads also to an increase in the permittivity [1].

$BaTiO_3$ can be doped with isovalent ions, such as Zr^{4+}, in small concentrations to modify its dielectric behavior and to control densification and grain size [2-5]. These dopants have the effect of shifting the transition temperatures and of broadening or enhancing the magnitude of the permittivity peak. ZrO_2 acts as a grain growth inhibitor due to incomplete solid solution at temperatures where the additive resides primarily at the grain boundaries [6-8]. Broadening of the permittivity peak with temperature due to Zr additions has been attributed variously to local variation in composition, to biphasic grains and to structural changes in the unit cell which result in high internal stresses and a distribution of Curie temperatures [4,9,10]. The microstructural refinement and dielectric behavior changes which are a result of the doping are highly dependent upon heat treatment and dopant concentration. Several investigators [2,15] have shown that Zr additions decreased the axial ratio, resulting in a pseudocubic structure. Under controlled processing conditions, a complex stress state was found to exist, the result core-shell grains being developed [3,10].

As in most ferroelectric materials, device properties depend upon grain morphology as well as defect and grain boundary states. These characteristics in doped $BaTiO_3$ ceramics are dependent upon developed microstructures as well as on the domain and lattice structures, which are a result of processing parameters. In this investigation, the objectives were to study the effects of grain morphology and grain domain structure on internal stress and dielectric properties in Zr^{4+} modified $BaTiO_3$.

Experimental

Samples were prepared by ball-milling high purity $BaTiO_3$[a] (Ba/Ti = 0.997) for 12h with and without 2 wt % unstabilized ZrO_2[a] powder using ZrO_2 balls. This amount of ZrO_2 was determined to be the lowest concentration necessary to achieve a uniform fine-grained microstructure [16]. Milling was carried out in a 1.5:1 solution of isopropyl alcohol : deionized water with 1 wt % Menhaden fish oil added as a dispersant. A binder/lubricant solution composed of PVA (5 % solution) and Carbowax 4000, 1 wt% each, was added and the slurry milled an additional 1.5 h. ZrO_2 contamination due to ball milling was less than 0.1 wt % per 150-g batch. The dispersed slurry was spray-dried and the powder uniaxially pressed into discs and sintered in air in the range 1300°-1320° C/2h and furnace cooled.

Capacitance and tan δ measurements were made using an automatic capacitance bridge at 1 and 10 kHz upon heating from -50° to 150 C. Measurements of the aging rate were carried out at 25°, 50° and 90 C for upto 200 h on samples that had been thermally de-aged at 150 C for 15 min. The apparent internal stress was determined using the microindentation technique described by Okasaki [11]. From the indentation analysis the fracture toughness was determined for applied loads in the range 0.1 to 0.5 kg using a loading time of 90 s. The measurements were carried out as a function of time (1, 10, 100 h). The indentation size and Vickers indentation crack length were measured immediately after loading. The apparent stress was determined from the slope of a plot of the fracture toughness versus the square root of the crack length. All microscopic examinations and selected area diffraction analyses were conducted on a Philips EM 420 TEM, operated at 120 keV. The convergent beam electron diffraction studies were carried out with an operating voltage of 80 keV.

Results and Discussion

The effects of ZrO_2 additions to $BaTiO_3$ are compared in the SEM micrographs of Figure 1 for samples sintered at 1320°C. A dense microstructure of essentially large grains was found for the unmodified $BaTiO_3$ (no ZrO_2 additions) as shown in Fig. 1A. With 2.0 w/o ZrO_2 addition (Fig. 1B), a microstructure consisting entirely of uniform small grains (average grain size ~0.8 μm) was obtained. The microstructure shown in Fig. 1B is comprised of approximately 50 vol.% core-shell grains, with lesser amounts being present at slightly lower temperatures. The core-shell grains are characterized by a center of pure $BaTiO_3$ surrounded by a diffused shell of grain boundary modified material, as depicted in Figures 1C and 1D, which shows transmission electron microscope (TEM) microstructural images of the core shell structures. As indicated, there is a discontinuity between the domains in the central core and the surrounding shell which is free of domains. The x-ray intensity distribution, derived from energy dispersive x-ray spectroscopy (EDS) data, given in Figure 2, show the relative concentration of Zr to decrease as the core is approached with no Zr being present in

CH3080-0-7803-0465-9/92$3.00©IEEE

the core region. From selected area diffraction (SAD) and convergent beam electron diffraction (CBED) analysis of the high-order Laue zone (HOLZ) lines in the [421] beam direction, the shell was found to be tetragonal, but highly strained and with expanded lattice parameters, giving a higher unit cell volume as indicated in Table 1. The volume expansion mismatch between the two regions (shell and core) was determined to be ~4.4%. This places the core in compression, directed mainly along the c-axis, as evidenced by the overall pseudocubic structure which is developed.

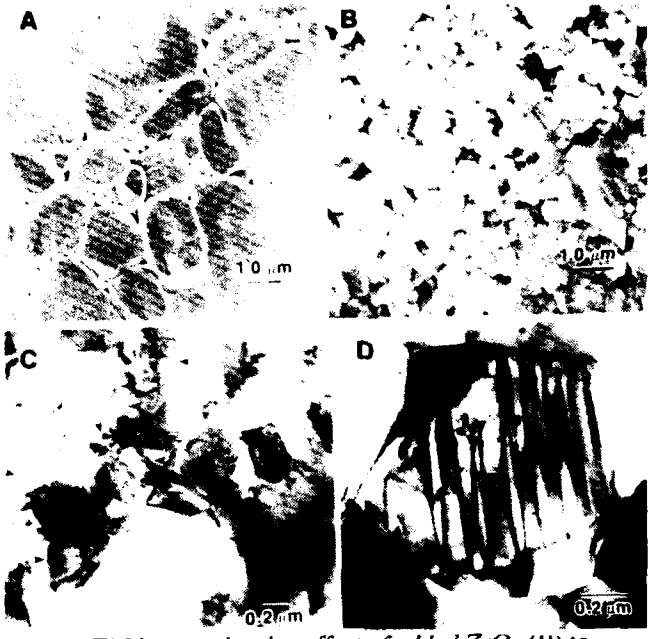


Fig. 1 SEM images showing effect of added ZrO_2 (B) to $BaTiO_3$ (A). TEM images (C, D) of core-shell grains in $BaTiO_3$ modified with 2.0 wt% ZrO_2. Sintered at 1320°C/2h.

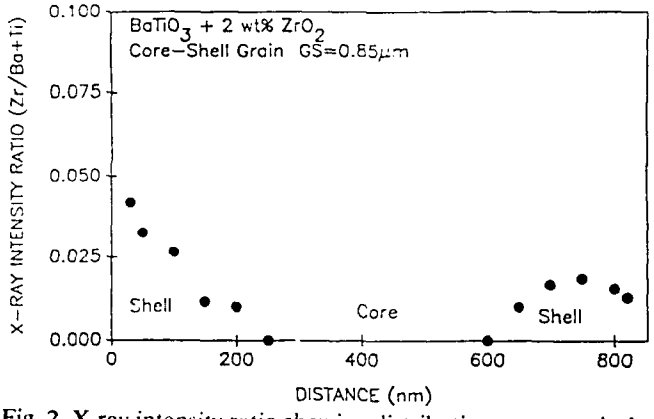


Fig. 2 X-ray intensity ratio showing distribution across typical core-shell grain.

The apparent internal stress level was determined by use of the microindentation technique described by Okazaki [11]. Data on the internal stress states, as a function of static aging by heat treatment (at 25°, 50°and 90°C under a constant applied field of 0.1 V rms) and as a function of grain size (sintering temperature), are given in Table 2. Accompanying the decrease in grain size is a decrease in the concentration of 90° domains, and a pseudocubic modification of the tetragonal structure, as indicated by the lattice parameter data in Table 1. From these tables, specimens with core shell grains show much higher internal stress levels, a decrease in c-lattice parameter and a corresponding decrease in c/a ratio. The permittivity response of the $BaTiO_3$ modified with 2.0 wt % ZrO_2 is shown in Figure 3. The measured permittivity is seen to be relatively flat with respect to temperature and shows a suppressed ferroelectric transition region.

Table 1

Lattice Parameters of ZrO_2 Doped $BaTiO_3$, Core Region, Shell and Unmodified $BaTiO_3$

Sample	a(nm)	c(nm)	c/a	Vol. (nm^3)	Volume %Strain
Core	.4000	.4026	1.007	.0644	4.89
Shell	.4050	.4117	1.017	.0675	
$BaTiO_3$ + 2 wt% ZrO_2	.4004	.4027	1.006	.0645	0.23
$BaTiO_3$	.3994	.4038	1.011	.0644	

The overall effect of the ZrO_2 additions to $BaTiO_3$, therefore, is formation of a diffused boundary phase and a distribution of Curie points related to the diffuse phase transition, where a Curie region rather than a Curie point is found. These changes explain the flat permittivity response with temperature.

Table 2

Internal stress as a function of aging temperature, time and grain size for $BaTiO_3$ modified with 2.0 wt% unstabilized zirconia.

Average Grain Size (μm)	Sintering Temperature (°C)	Time (h)	Aging Temperature (°C) 25	50	90
			Internal Stress (MPa)		
0.28	1300	1	134	113	106
		10	128	82	75
		100	70	68	62
0.36*	1310	1	119	85	68
		10	75	69	52
		100	55	68	48
0.43*	1320	1	355	136	115
		10	292	105	91
		100	184	80	78

* Core-shell grains in the microstructure

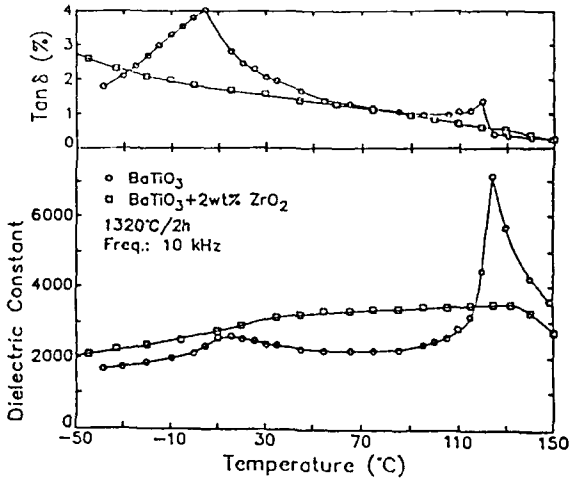


Fig. 3 Dielectric response for $BaTiO_3$ and $BaTiO_3$ modified with 2.0 wt% ZrO_2.

Several models have been proposed to describe and predict this permittivity response [12-14]. A model developed from this research relates the permittivity (ε) to internal stress (σ) and to grain size (gs) as a function of temperature. Trends between internal stress, grain size and the volume fraction of core shell grains (v_f) were developed using a multivariable regression analysis. From the analysis, an expression relating the dependence of internal stress on grain size, the volume fraction of core shell grains and on temperature was developed. The resulting equation is given as:

$$\sigma = K_1 (1/gs)^n \exp(k_2 v_f)\, T^m$$

Where the constants (K_1 = 52.7; n = 1.07; k_2 = 1.83; and m = -.029) were obtained from plots of experimentally measured internal stress as a function of the natural log of the inverse of grain size, for various volume fractions of core-shell grains, all as a function of temperature (T = °C).

The relationship between permittivity, internal stress and temperature was also analyzed. This analysis was carried out for temperatures less than T_c. The Curie temperature, for a 2.0 wt % modified samples where a flattened permittivity response is found, was taken to be the point where the permittivity response begin to decrease. The data used for this analysis was from experimental data at 25°, 50°and 90°C and from calculated internal stresses. The relationship is given by the following equation.

$$\varepsilon = K \sigma^x T^y$$

Where: K is 686.1; x is 0.22; and y is 0.12 are empirically determined constants. For a $BaTiO_3$ sample, using average grain size of 0.43 nm and a volume fraction of core-shell grains of 0.50, Figure 4 shows a plot of actual data versus a plot of generated data using the above equations. The plot shows that the flattened permittivity response, due to Zr doping, is satisfactorily explained by considering the stress dependence upon grain size and volume fraction of core-shell grains, along with a temperature dependence.

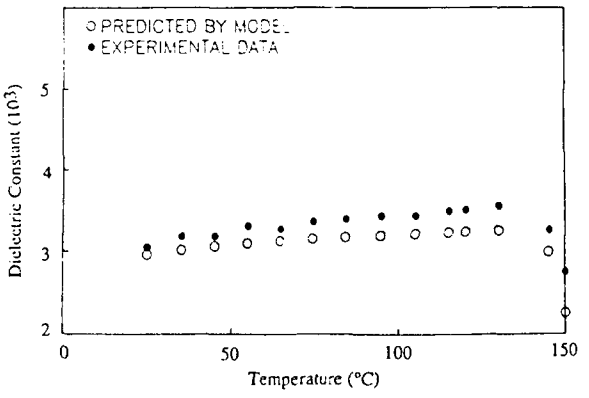


Fig. 4 Comparison of the actual permittivity response of $BaTiO_3$ modified with 2.0 wt% unstabilized ZrO_2 with a curve of generated data using the model based on internal stress.

Conclusions

Grain morphology and developed internal stresses in $BaTiO_3$ based high dielectric materials have been shown to be a dominant factor in the development and stability of those properties. Core-shell grains were formed in $BaTiO_3$ with ZrO_2 doping, upon sintering in the range 1300 -1320°C. A diffused boundary phase led to high internal stresses, suppression of T_c, a distribution of Curie points and a flattened permittivity peak. The internal stress was found to be an accurate basis for estimating the permittivity response to temperature. The stability of these highly stressed samples was also found to be improved as the concentration of core-shell grains increased. Under controlled processing parameters, therefore, significantly enhanced dielectric properties can be achieved.

i Ticon-HPB, TAM Ceramics, Inc., Niagara Falls, NY. (0.997); Lot # 719, Product # 5018

ii Zircar Products, Inc., Florida, NY.

Acknowledgements

This work was supported by ONR DARPA contract N00014-88-K-0317 and in part by NSF under contract number NSF-DMR89-20538. Microanalysis was carried out in the Center for Microanalysis of Materials at the University of Illinois, which is supported by the U.S. Department of Energy under contract number DE-AC-02-76ER-01198.

References

1) A.J. Bell and A.J. Moulson,"The Effect of Grain Sise on the Permittivity of $BaTiO_3$," Ferroelectrics, Vol. 54, pp. 147-150 (1984)

2) J. M. Herbert, Ceramic Dielectrics and Capacitors, Gordon and Breach Science Publishers, London, 1985.

3) T. R. Armstrong, R. C. Buchanan, "Influence of Core-Shell Grains on the Internal Stress State and Permittivity Response of Zirconia-Modified Barium Titanate," *J. Am. Ceram. Soc.*, 73 [5] 1268-73 (1990).

4) T. R. Armstrong, L. E. Morgans, A. K. Maurice, R. C. Buchanan, "Effects of Zirconia on Microstructure and Dielectric Properties of Barium Titanate Ceramics," *J. Am. Ceram. Soc.*, 72 [4] 605-11 (1989).

5) M. Kahn, "Effects of Sintering and Grain Growth on the Distribution of Niobium Addition in Barium Titanate Ceramics"; Ph. D. Thesis, Pennsylvania State University, University Park, PA, 1969.

6) A. K. Maurice, "Powder Synthesis, Stoichiometry, and Processing Effects on Properties of High Purity $BaTiO_3$," M. S. Thesis, University of Illinois, Urbana, IL, 1984.

7) N.M. Molokhia and M.A. Issa,"Dielectric Properties of $BaTiO_3$ Modified With ZrO_2," *Pramana*, Vol 11, No. 3, pp. 289-293 (1978).

8) D. Hennings, G. Rosenstein,"Temperature-Stable Dielectrics Based on Chemically Inhomogeneous $BaTiO_3$," *J.Am. Ceram. Soc.*, 67 [4] 249-254 (1984).

9) W. Heywang,"Structural Engineering in Ferroelectrics," *Ferroelectrics*, 49, 3-14 (1983).

10) B.S. Rawal, K. Kahn, W.R. Buessern,"Grain Core-Shell Structure in Barium Titanate Based Dielectrics," pp. 172-88 in Advances in Ceramics, Vol. 1, Grain Boundary Phenomena in Electronic Ceramics. Edited by L. Levinson, American Ceramic Society, Columbus, OH (1981).

11) K. Okasaki,"Mechanical behavior of Ferroelectric Ceramics," *Bull. Am. Ceram. Soc.*, 63 [9] 1150-57 (1984).

12) K. Yamashita, S. Yamasaki, K. Koumoto and H. Yangida,"Numerical Estimation of the Dependence of the Dielectric Constant of BaTiO3," *Jpn. J. Appl. Phys.*, 20 [10] 1833-40 (1981).

13) H. Diamond,"Variation of Permittivity with Electric Field in Perovskite-Like Ferroelectrics,"*J. Appl. Phys.*, 32 [5] 909-15 (1961).

14) G.A. Smolenski, Ferroelectric and Related Phenomena Vol. 3, Gorden and Breach Science Pub., New York, 1984.

15) R.C. Kell and H.J. Hellicar,"Structural Transitions in Barium Titanate Transducer Materials," *Acustica*, 6 [2] 235-38 (1956).

HIGH FREQUENCY DIELECTRIC RELAXATION IN $Pb(Mg_{0.317}Nb_{0.633}Ti_{0.05})O_3$ CERAMICS.

C. ELISSALDE and J. RAVEZ
Laboratoire de Chimie du Solide du CNRS, Université Bordeaux I,
351 cours de la Libération, 33405 TALENCE cedex, France.

P. GAUCHER
Thomson-CSF, Laboratoire Central de Recherches,
Domaine de Corbeville, 91401 ORSAY cedex, France.

Abstract

Dielectric measurements have been performed on $Pb(Mg_{0.317}Nb_{0.633}Ti_{0.05})O_3$ ceramics in the frequency and temperature ranges 10^6-10^9 Hz and 110 - 400 K respectively. A dielectric relaxation of Cole-Cole type has been found between 10^7 and 10^9 Hz depending on the temperature. This relaxation exists not only in the ferroelectric phase but also in the paraelectric one. A minimum of the relaxation frequency occurs at temperature close to the Curie temperature T_C.

I - INTRODUCTION

The lead magnesium niobate (PMN) is a well-known example of relaxor ferroelectric : a strong permittivity ε_r' around $T_{max.}$ (267 K), a diffuse phase transition and a low frequency dispersion of ε_r' (1). In addition, a high frequency relaxation which appears in both ferro and paraelectric phases has been recently shown (2). On another way, the lead titanate $PbTiO_3$ presents a classic ferroelectric phase transition with a high value of T_C (3). So, the interest of the $Pb(Mg_{1/3}Nb_{2/3})O_3$ - $PbTiO_3$ solid solution consists in a very high dielectric constant and in the possibility to shift the apparent Curie Point at temperature close to room temperature (4). Such ceramics can be interesting for industrial applications i.e. dielectric for Z5U standard capacitors. The addition of $PbTiO_3$ brings about an increase of both ε_r' and $T\varepsilon_r'max.$ and causes a diminution of the diffuse character of the transition. As an example, a substitution rate of $PbTiO_3$ larger than 30 % leads to a classic "ferroelectric" transition and the ordered (1:1) nanoregions which appear below T_C in PMN, seem to have a less effect (4).

In the present work we have selected the composition corresponding to x = 0.05 in the $(1-x)Pb(Mg_{1/3}Nb_{2/3})O_3$ - $xPbTiO_3$ system in relation with the temperature of $\varepsilon_r'max.$ close to room temperature. The purpose is here to study the influence of the substitution on the high frequency dielectric relaxation. The dielectric properties have been studied in the frequency and temperature ranges 10^6 to 10^9 Hz and 150 to 450 K respectively.

II - PREPARATION OF THE SAMPLES

The powder has been prepared by the columbite method developed by Shrout (5). An excess of magnesium oxide has been used in the $MgNb_2O_6$ preparation to avoid pyrochlore phase. Titane is added in form of TiO_2 when columbite and PbO are mixed. Small pellets are made by conventional axial pressure. They are sintered at 950°C for 4h. in a lead oxide atmosphere. The compactness of the sample is greater than 95 %.

The permittivity ε_r' shows a maximum of about 26500 at 292 K for a frequency of 1 kHz.

III - EXPERIMENT

Dielectric measurements are performed on disk samples (diameter 7 mm). Gold electrodes are previously deposited on ceramics by sputtering. The permittivities ε_r' and ε_r'' are measured at high frequency from 10^6 to 10^9 Hz, using an HP 8753 A network analyser. The broad band analysis of a coaxial line loaded with the disk sample and backed up by a short circuit enables us to calculate the complex permittivity from the reflexion coefficient.

IV - RESULTS

The temperature dependences of ε_r' and ε_r'' at various frequencies are shown in Fig.1 and 2. The curves are characteristic of a typical relaxor behaviour :

- a broad temperature region of the permittivity peak as in the pure PMN.
- when the frequency increases :

the temperature of $\varepsilon_r'max.$ shifts towards higher temperatures,

the value of ε_r'' increases until a frequency close to 2.10^8 Hz and then decreases.

Such evolutions correspond to one apparent relaxation phenomena. The dielectric response versus frequency is represented at two temperatures, either in the paraelectric region (Fig.3 and 4) or in the ferroelectric one (Fig.5). In

CH3080-0-7803-0465-9/92$3.00 ©IEEE

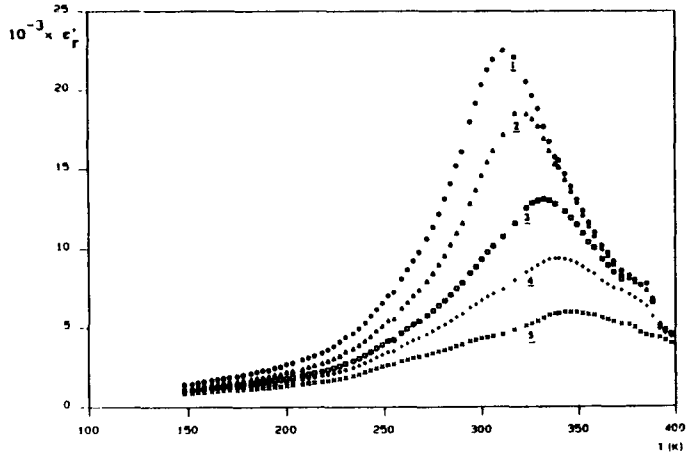


Fig.1 - Thermal dependence of ε'_r at different frequencies : 10^6 (1), 10^7 (2), 5.10^7 (3), 10^8 (4) and $2x10^8$ Hz (5).

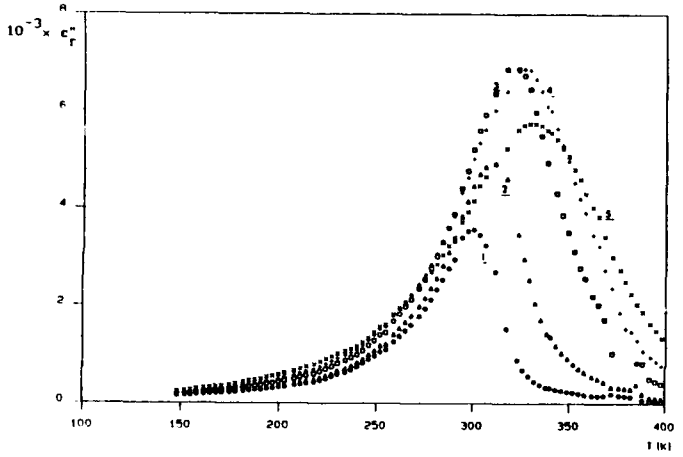


Fig.2 - Thermal dependence of ε''_r at different frequencies :10^6 (1), 10^7 (2), 5.10^7 (3), 10^8 (4) and $2x10^8$ Hz (5).

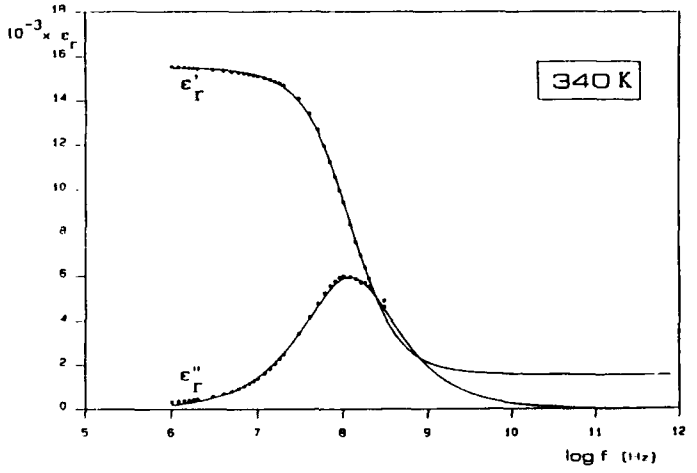


Fig.3 - Frequency dependence of ε'_r and ε''_r at 340 K (o, experimental points ; — theoretical curve).

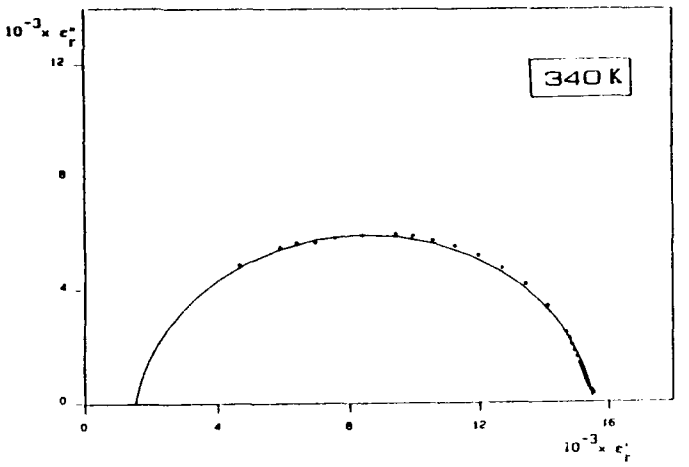


Fig.4 - Cole-Cole plots ε''_r vs. ε'_r at 340 K.

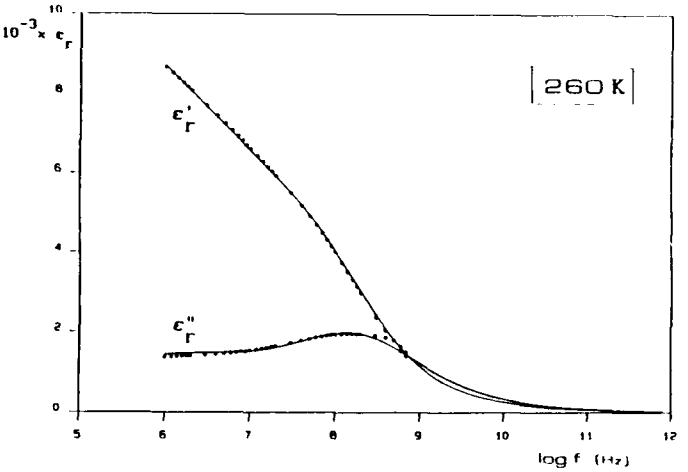


Fig.5 - Frequency dependence of ε'_r and ε''_r at 260 K (o, experimental points ; — theoretical curve).

each case a decrease of ε'_r and a maximum of ε''_r are observed. However it appears clearly some differences :

***T > $T_{\varepsilon'_r max}$.**

A high frequency relaxation appears clearly. The inflexion point of ε'_r corresponds to the maximum of ε''_r close to 10^8 Hz. Argand diagram ε''_r versus ε'_r is drawn in order to characterize the relaxation or the frequency range 10^6 - 10^9 Hz. The obtained curve is very close to a circular arc in agreement with a Cole-Cole model. The complex permittivity ε^*_r is expressed by the formula :

$$\varepsilon^*_r = \varepsilon'_r - i\,\varepsilon''_r = \varepsilon'_\infty + (\varepsilon'_S - \varepsilon_\infty) / 1 + (if / f_r)^{1-\alpha}$$

ε'_S is the static permittivity at low frequency ($f << f_r$), ε'_∞ the value at $f >> f_r$ and f_r the relaxation frequency. The figure 4 shows the good agreement between experimental points and theoretical curve.

* $T < T_{\varepsilon_r' max.}$

The high frequency relaxation is still present but the continuous decrease of ε_r' and the broader maximum of ε_r'' suggest the existence of a low frequency relaxation in the ferroelectric phase. This low frequency relaxation was previously described in relaxor ferroelectric (1). For higher temperatures ($T > T_{\varepsilon_r' max.}$), the value of ε_r' is close to zero for $f < 10^6$ Hz implying no dispersion in the low frequency range.

The three dimensional curves, ε_r' and ε_r'' versus temperature and frequency (Fig.6 and 7), give a good representation of the dielectric response in all the temperature range. The high frequency relaxation occurs not only in the ferroelectric region but also in the paraelectric one.

The temperature dependence of the relaxation frequency f_r is shown in Fig.8. The temperature of the minimum of f_r is close to $T_{\varepsilon_r' max.}$ (at low frequency). A strong decrease of α, the relaxation time distribution, is observed on heating at $T_{\varepsilon_r' max.}$ (Fig.9). The values of α

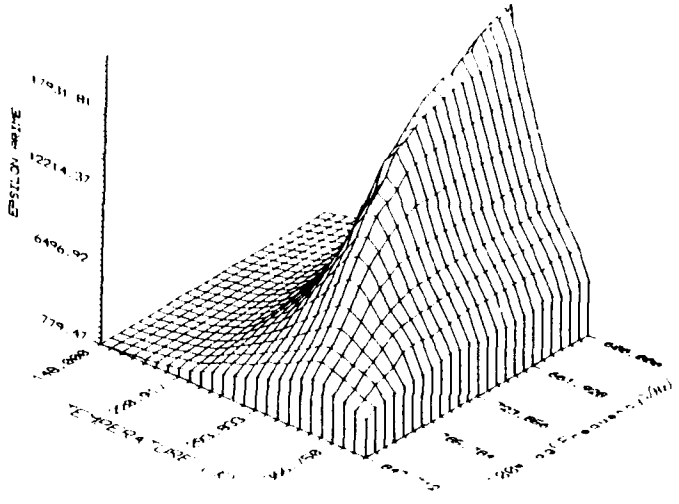


Fig.6 - Temperature and frequency dependences of ε'_r.

below $T_{\varepsilon_r' max.}$ reach about 0.55. Such a value corresponds to a large relaxation time distribution and confirms the increase of the absorption width when the temperature decreases. On the contrary, α is small in the paraelectric region. This is in agreement with a Cole-Cole arc close to a Debye semi-circle obtained in this temperature range ($T > T_{\varepsilon_r' max.}$) The fall of α near $T_{\varepsilon_r' max.}$ is thus characteristic of a dielectric behaviour change from the ferro to paraelectric region.

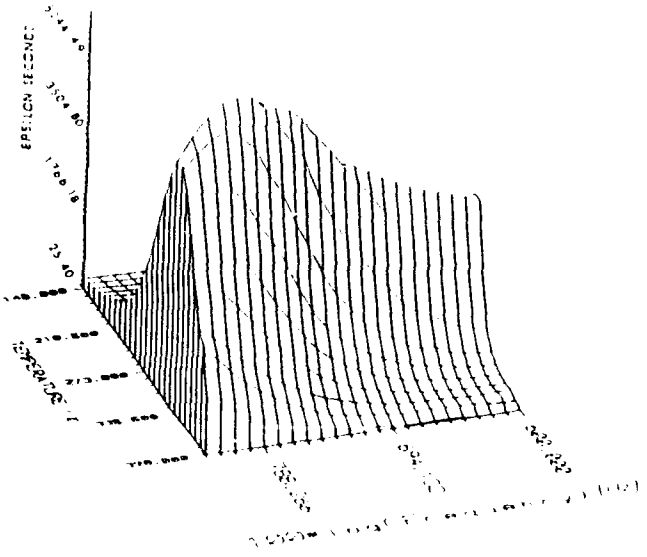


Fig.7 - Temperature and frequency dependences of ε''_r.

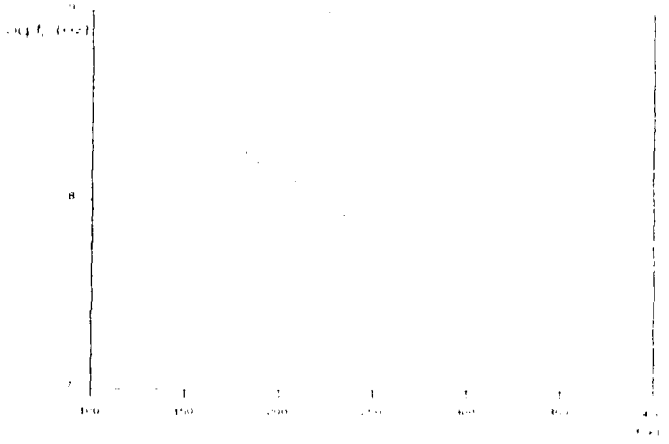


Fig.8 - f_r vs. temperature.

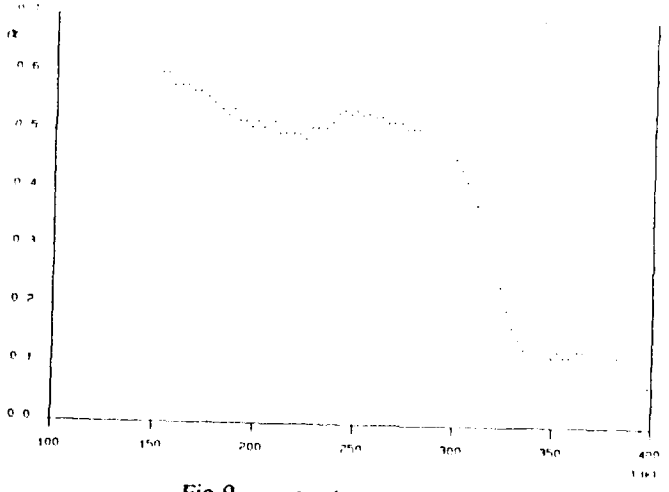


Fig.9 - α vs. temperature.

IV- CONCLUSION

This work allowed us to display a new high frequency relaxation in a ceramic with composition corresponding to x = 0.05 in the (1-x)$Pb(Mg_{1/3}Nb_{2/3})O_3$ - x$PbTiO_3$ system. The origin of the relaxation has been discussed in the case of lead magnesium niobate ceramics in which a similar relaxation was found (2). Fig.10 shows the temperature dependence of f_r for these two systems. As for ε'_r versus temperature variation, the curve corresponding to the pure PMN is more flat. This result can be related to the more diffuse phase transition for PMN. Indeed, the addition of $PbTiO_3$ seems to increase the pure "ferroelectric" behaviour of the transition (4).

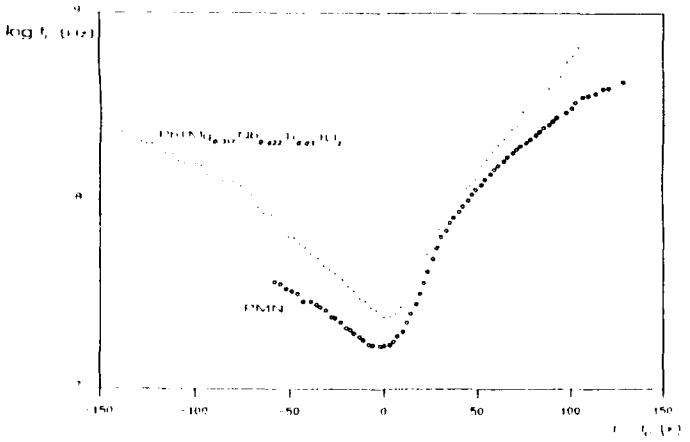


Fig.10- f_r vs. temperature for pure PMN and 95 PMN-5PT system.

REFERENCES

[1] L.E. Cross, "Relaxor Ferroelectrics", Ferroelectrics, vol. 76, pp. 241-267, 1982.

[2] C. Elissalde, J. Ravez and P. Gaucher, "High frequency dielectric relaxation in lead magnesium niobate ceramics" Mat. Sc. Engin.B, Vol.13, pp. 327-333, 1992.

[3] Ferroelectrics and related Substances, Landolt-Börnstein III, Vol. 16, pp. 78-81, Springer, Berlin, 1981.

[4] N. de Mathan, "Etudes structurales de céramiques diélectriques de magnoniobate de plomb $Pb(Mg_{1/3}Nb_{2/3})O_3$ en fonction de la température". Thèse, Paris, 1991.

[5] T.R. Shrout and A. Halliyal, Am. Ceram. Soc. Bull., Vol. 66, pp. 704-711, 1987.

DIELECTRIC AND FERROELECTRIC BEHAVIOURS OF $Ba(Ti_{1-x}Li_x)(O_{3-3x}F_{3x})$ CERAMICS.

C. ELISSALDE and J. RAVEZ
Laboratoire de Chimie du Solide du CNRS, Université Bordeaux I,
351 cours de la Libération, 33405 TALENCE cedex (France).

X. YAO
Electronic Materials Research Laboratory, Xian Jiaotong University,
710049, XIAN (China).

Abstract

$BaTiO_3$ was doped with $BaLiF_3$ to form solid solution of $Ba(Ti_{1-x}Li_x)(O_{3-3x}F_{3x})$ composition. Special care has to be taken to prevent hydrolyse during firing. Curie temperature of solid solution is decreasing from 393 ($BaTiO_3$), to 300 and to 225 K for compositions x = 0, x = 0.025 and x = 0.10 respectively. Temperature dependences of dielectric constant under various frequencies are presented. The three successive phase transitions of pure barium titanate are still preserved for lightly doped materials, while for heavily doped materials only one phase transition can be observed in the same temperature range. Temperature dependences of spontaneous polarization and coercive field taking from ultra low frequency measurements of hysteresis loops of the materials are presented.

I - INTRODUCTION

The oxyfluoride ceramics derived from $BaTiO_3$ with composition $Ba(Ti_{1-x}Li_x)(O_{3-3x}F_{3x})$ ($0 \leq x \leq 0.10$) are attractive type II dielectrics for capacitor due to :

- a lower sintering temperature (1250°C for 2h) compared to that of $BaTiO_3$ (1450°C for 4h),
- a decrease of the ferroelectric Curie temperature from 395 K ($BaTiO_3$) to 225 K (x = 0.10) leading to a high value of the real part of the permittivity, ε'_r, close to room temperature for the composition corresponding to x = 0.025.

If the dielectric and ferroelectric behaviours of $BaTiO_3$ have been widely studied, it can be interesting to study that of the oxyfluoride ceramics of the $BaTiO_3$-$BaLiF_3$ system. The aim is to understand the influence of the fluorine-oxygen substitution on the ferroelectric properties.

II - EXPERIMENTAL

II-1- Preparation

$BaLiF_3$ is prepared from the fluorides BaF_2 and LiF which are mixed and ground in a dry box. The obtained powder is calcinated at 650°C for 15h in a gold tube sealed under dry nitrogen to avoid hydrolysis. Final compositions are prepared from $BaTiO_3$ and $BaLiF_3$. Selected oxyfluoride compositions x = 0.025 and x = 0.10 are sintered at 1300 and 1200°C respectively for 2h in platinum sealed tubes under dry oxygen. Ceramics of $BaTiO_3$ are obtained at 1450°C for 4h under oxygen atmosphere.

II-2- Measurements

Gold electrodes are deposited on both circular faces of the ceramics by cathodic sputtering. Frequency measurements between 10^2 to $3x10^5$ Hz are performed from 150 to 450 K using a Wayne-Kerr component analyzer 6425. Bias measurements of the capacitance are carried out with a Wayne-Kerr capacitance bridge B 605. Electric field is applied using a dc generator. Hysteresis loops are obtained at $3x10^{-2}$ Hz and under bias of 800 V from both a "Polarsine" and a Keithley electrometer using the Sawyer-Tower method (1). They allow us to determine the spontaneous polarization P_S and the coercive field E_C on cooling in the temperature range 320-150 K.

III - RESULTS

The temperature dependence of ε'_r at 1kHz is shown in Fig.1, 2 and 3 for three ceramics with composition corresponding to x = 0, x = 0.025 and x = 0.10. For the two first ceramics, the three phase transitions (rhomb. → orth. → tetr. → cub.) appear clearly. Only one relatively broad peak corresponding to the rhomb.-cub. transition subsists for x = 0.10. The decrease of the Curie temperature T_C when the substitution rate increases (Fig.1 to 3), is related to the covalency decrease of the M-X bonds (M = Ti, Li; X = O, F) when x increases.

The room temperature variations of ε'_r versus the electric field E are given, for several frequencies, in Fig.4, for ceramics with x = 0.025 and 0.10. The dielectric response under bias varies according to the x values :

- concerning x = 0.025 for which $T_C \simeq 300$ K, there is a relatively strong decrease of ε'_r with increasing E, as in $BaTiO_3$ (2). In addition there is a frequency dispersion,

CH3080-0-7803-0465-9/92$3.00 ©IEEE

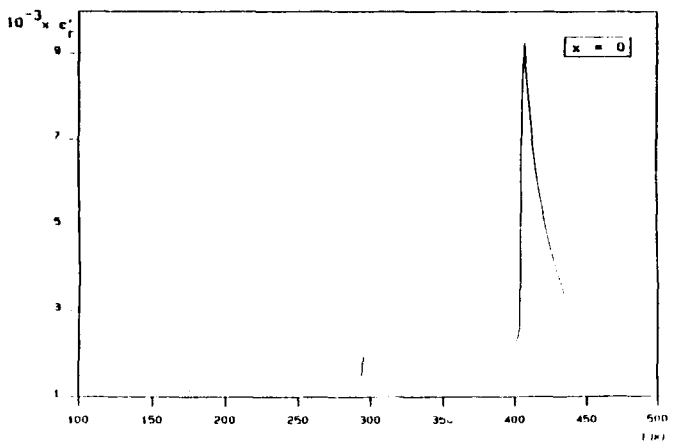


Fig.1 - Temperature dependence of ε_r' for a ceramic with composition corresponding to x = 0 at 1 kHz.

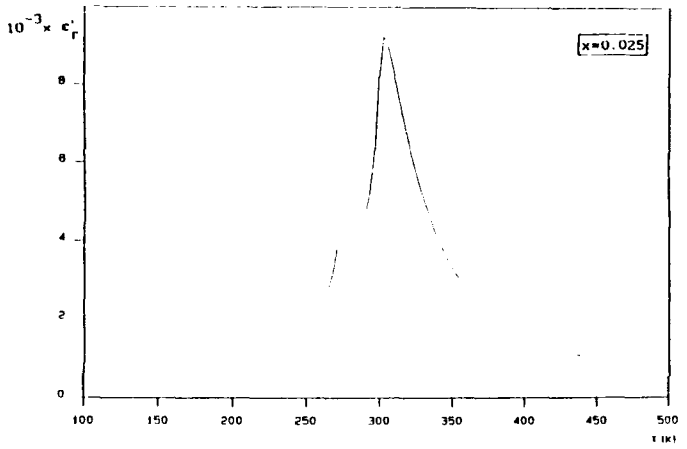


Fig.2 - Temperature dependence of ε_r' for a ceramic with composition corresponding to x = 0.025 at 1 kHz.

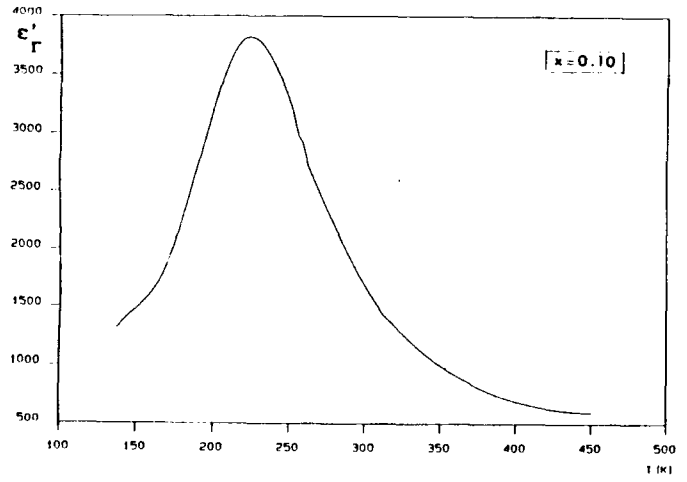


Fig.3 - Temperature dependence of ε_r' for a ceramic with composition corresponding to x = 0.10 at 1 kHz.

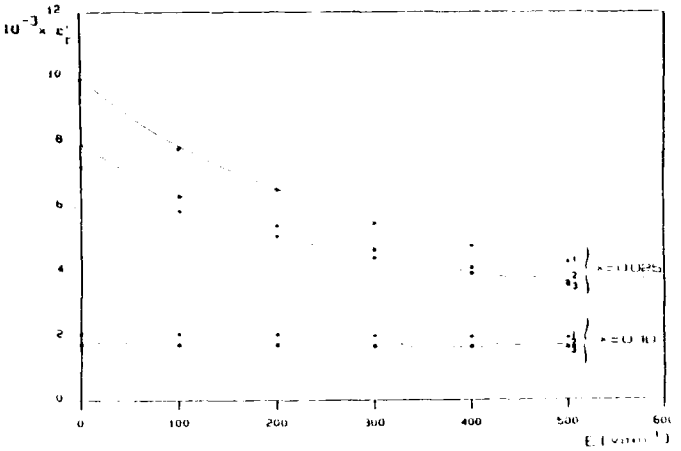


Fig.4 - Field dependence of the dielectric constant of ceramics with compositions corresponding to x = 0.025 and x = 0.10 at room temperature and at various frequencies : 10^2 (1), 10^3 (2) and 10^4 Hz (3).

- for a higher x value (x = 0.10), ε_r' is less dependent on the bias with, nevertheless, still a frequency dispersion.

The value of P_S decreases with temperature (Fig.5). For x = 0.025, there are two change slopes close to T_C and to the orth.-tetr. transition due probably to the loss of ferroelectricity and to the reorientation of the dipoles. Concerning the ceramic with x = 0.10 composition, the curve is very flat with lower values of P_S in relation with the more diffuse phase transition and with the lower values of ε_r' compared to that of x = 0.025 composition or $BaTiO_3$. Moreover, P_S is not equal to zero at T_C and even at $T >> T_C$, for the two oxyfluoride ceramics. This difference with regard to barium titanate may be correlated with the existence of polarization residue due to defects and chemical inhomogeneities in the substituted ceramics.

Fig.6 shows the temperature dependence of the ccercive field. For the ceramic with composition corresponding to x = 0.025, E_c decreases firstly on heating. It then increases suddenly approaching $T_{orth.-tetr.}$, which expresses a more difficult mobility of domains, and finally decreases at T_C. This curve with a maximum close to the orth.-tetr. transition looks like the temperature dependence of the loss tangent in $BaTiO_3$ (2). On heating, for x = 0.10, E_c decreases strongly and becomes constant close to zero at T_C. The hysteresis loop evolution is shown in the figures 7 and 8 for compositions corresponding to x = 0.025 and x = 0.10 respectively. For x = 0.025 slim loops are observed above T_C. Close to square loops with relatively higher rectangularity appear, as in $BaTiO_3$, when the sample cools down through the ferroelectric-paraelectric transition. Approaching the tetr.-orth. transition temperature the loop seems to blow up leading to an increase of E_c as was described before. Concerning x = 0.10, even down to 220K, hysteresis loops are very slim and the determination of both E_c and P_S is rather critical. Below T_C , it broadens out but no rectangularity appears.

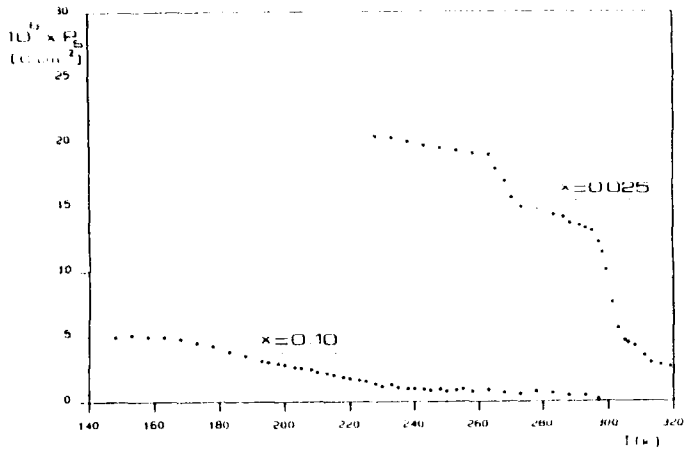


Fig.5 - Spontaneous polarization P_S as function of temperature for x = 0.025 and x = 0.10.

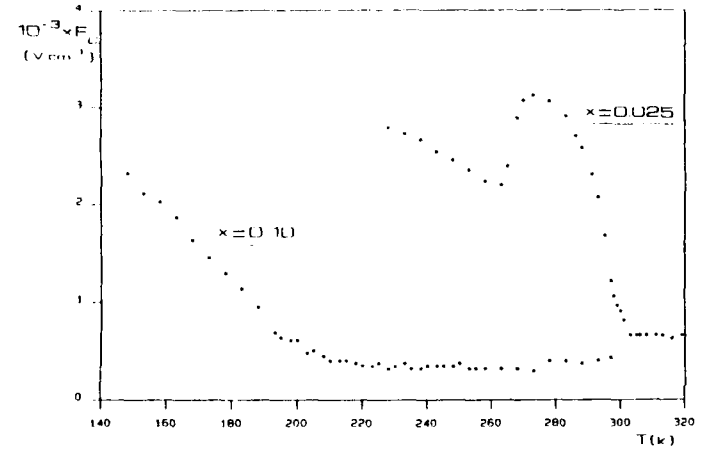


Fig.6 - Coercive field versus temperature for x = 0.025 and x = 0.10.

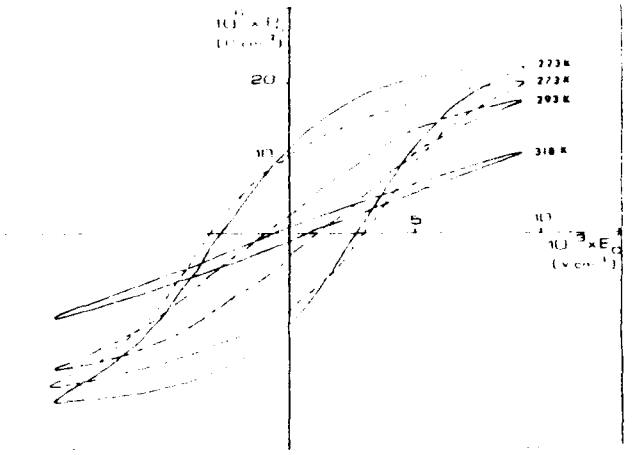


Fig.7 - Hysteresis loops at various temperatures for x = 0.025.

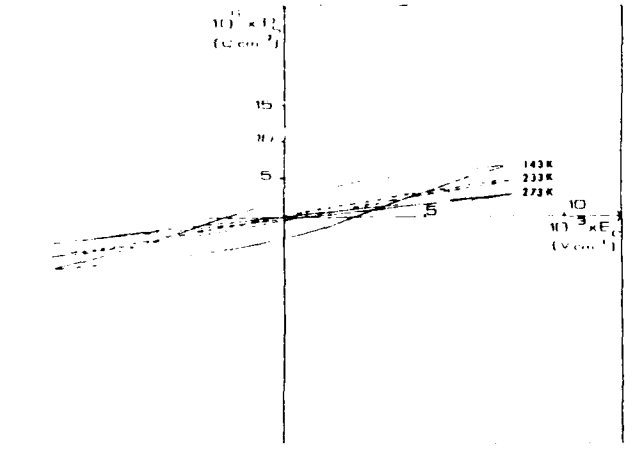


Fig.8 - Hysteresis loops at various temperatures for x = 0.10.

IV - CONCLUSION

The dielectric and ferroelectric behaviours of the selected oxyfluoride ceramics vary according to the composition. For x = 0.025, the dielectric response shows three phase transitions as in $BaTiO_3$ but the value of T_C is lower. Several analogies with the barium titanate have been pointed out in particular a similar temperature evolution of the hysteresis loop on cooling (2). On the contrary , for x = 0.10, there is only one phase transition (rhomb.-cub.) which is more diffuse than the ferroelectric -paraelectric transition of other ceramics. This change leads, of course, to a different ferroelectric behaviour. No anomaly of P_S and E_C occurs as at the orth.-tetr. transition for x = 0.025 and the decrease of P_S and E_C approaching T_C is here much more spread.

The ferroelectric Curie temperature is correlated with various parameters and in particular with chemical bonding. An increase of the substitution rate x in the $BaTiO_3$-$BaLiF_3$ system leads to a decrease of the M-X bonds covalency (M = Ti, Li ; X = O, F). This influences largely the ferroelectric and dielectric properties.

REFERENCES

[1] C.B. SAWYER and C.H. TOWER, Phys. Rev., 35, 269, 1930.

[2] A. Von HIPPEL, " Ferroelectricity, Domain Structure and Phase Transitions of Barium Titanate", Rev. of Modern Physics, Vol. 22, N°3, pp. 221-237, 1950.

DIELECTRIC RELAXATION IN CERAMICS WITH COMPOSITION $(Ba_{1-y}Pb_y)TiO_3$

S. KAZAOUI, J. RAVEZ and C. ELISSALDE

Laboratoire de Chimie du Solide du CNRS, Université Bordeaux I,

351 cours de la Libération, 33405 TALENCE cedex, France.

A systematic study of the dielectric relaxation phenomena is carried out for ceramics with compositions $(Ba_{1-y}Pb_y)TiO_3$ ($y \in [0, 0.2]$derived from $BaTiO_3$ in the frequency and temperature ranges 10^6-10^9Hz and 300-500 K, respectively. A dielectric relaxation appears not only in the ferroelectric phase but also in the paraelectric-one. For each composition a minimum of the relaxation frequency f_r occurs at T_C. The dipolar-type relaxation is correlated to coherent displacements of the Ti^{4+} ions in the octahedron sites ordered either along chains or in 3D-lattice.

I - INTRODUCTION

The present work concerns the dielectric dispersion study in perovskite-type ferroelectric ceramics in the frequency and temperature ranges 10^6-10^9 Hz and 300-500 K, respectively. The ceramics have the composition $(Ba_{1-y}Pb_y)TiO_3$ $(0 \leq y \leq 0.2)$. The permittivity frequency dependence is performed, in particular, close to the Curie temperature T_C both in the ferroelectric and paraelectric phases. The aim of the present paper is to try to fill the gap in our knowledge of frequency and temperature dependences of ε' and ε'' in solid solution derived from $BaTiO_3$.

II - PREPARATION

$(Ba_{1-y}Pb_y)TiO_3$ perovskite-type ceramics for $y=0$, $y=0.05$, $y=0.10$ and $y=0.20$ are sintered under a partial PbO pressure at 1300°C for 2 hours. A survey of the microstructure of the ceramics corresponding to $y=0$, $y=0.10$ and $y=0.20$ shows that the average grain size is 20μm with a narrow size distribution. The compactness of all samples is always higher than 0.92. Gold electrodes are previously deposited on both disk faces of the ceramic by sputtering.

III - EXPERIMENTAL

Dielectric measurements are firstly performed at low frequency, $f=10^3$Hz, on disk samples in the range 150-550 K. The thermal dependence of the permittivity ε' shows a peak both at T_C and at the orthorhombic-tetragonal transition temperature. The phase transition temperatures obtained are in good agreement with previous works (1). However no dielectric dispersion appears in the frequency range 20 to 10^6Hz.

The permittivities ε' and ε'' are then measured at high frequencies from 10^6 to 10^9Hz using a network analyser HP 8753 A, and at various temperature in the range 300-500 K. The figure 1 shows the room temperature frequency dependences of ε' and ε'' : typical relaxation curves appear for each ceramic. Such results are in agreement with previous works : high frequency dielectric dispersions have been already reported in solid solutions derived from $BaTiO_3$ and with compositions $Ba(Ti_{1-x}B_x)O_3$ (B=Zr,Hf) or $(Ba_{1-y}A_y)TiO_3$ (A=Ca,Sr) (2,3,4). The shape of the diagrams ε'' - ε' was found to be close to circular arcs : there is a good agreement between experimental points and theoretical curve. The complex permittivity ε^* is thus expressed by :

$$\varepsilon^* = \varepsilon'_\infty + (\varepsilon'_s - \varepsilon'_\infty) / (1 + (if / f_r)^{1-\alpha}) \quad (5)$$

(f is the frequency, f_r the relaxation frequency, ε'_s the permittivity at $f << f_r$, ε'_∞ the permittivity at $f >> f_r$, α the parameter related to the relaxation time distribution). The analysis of the experimental data concerning the relaxation frequency f_r shows that the Pb-Ba substitution increases strongly the value of f_r from 5.10^8Hz to values higher than 10^9Hz. For $y \geq 0.1$ it is impossible to determine the f_r value at room temperature due to our experimental limitation at 10^9Hz.

The figure 2 illustrates the variation of f_r versus temperature for $y = 0$ and $y = 0.05$. It is interesting to remark that the dielectric dispersion occurs not only in the ferroelectric region but also in the paraelectric-one at least up to T_C + 70°C; such a result has been previously announced for $BaTiO_3$ single crystals and ceramics (6) : for each composition a minimum of f_r appears close to the transition temperature T_C. As the substitution rate y increases the values of T_C, the temperature corresponding to the minimum of f_r is shifted toward higher temperatures.

The temperature dependence of the dispersion step $\Delta\varepsilon' = \varepsilon'_s - \varepsilon'_\infty$ as well as that of ε'_∞ and f_r are reported on the figure 3 for the composition $Ba_{0.95}Pb_{0.05}TiO_3$. The value of $\Delta\varepsilon'$ is calculated from the values of ε'_s and ε'_∞ determined using the Argand diagram by

CH3080-0-7803-0465-9/92$3.00 ©IEEE

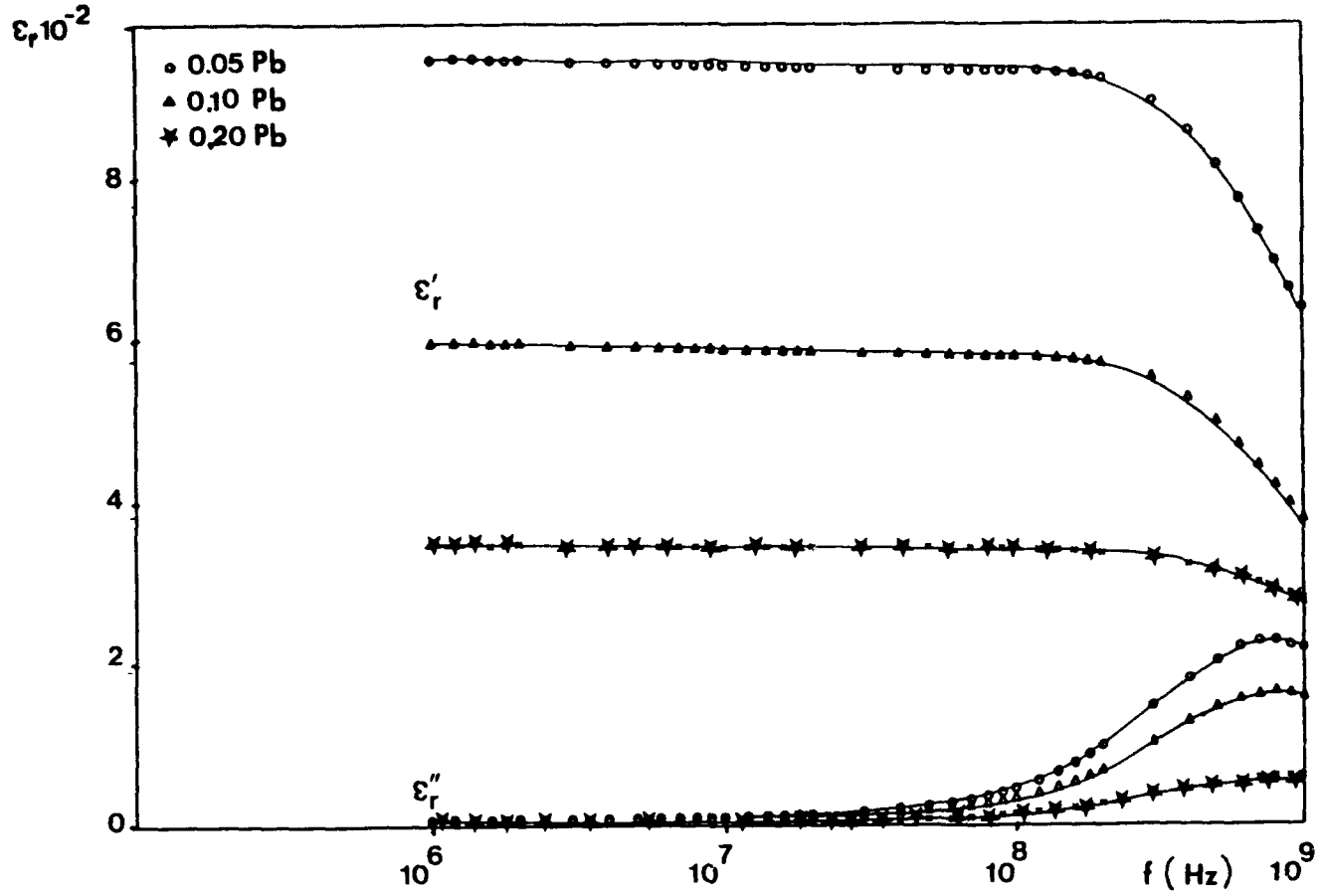


Fig.1 - ε' and ε'' versus frequency for $(Ba_{1-y}Pb_y)TiO_3$ at room temperature (y=0.05 ; y=0.10 ; y=0.15).

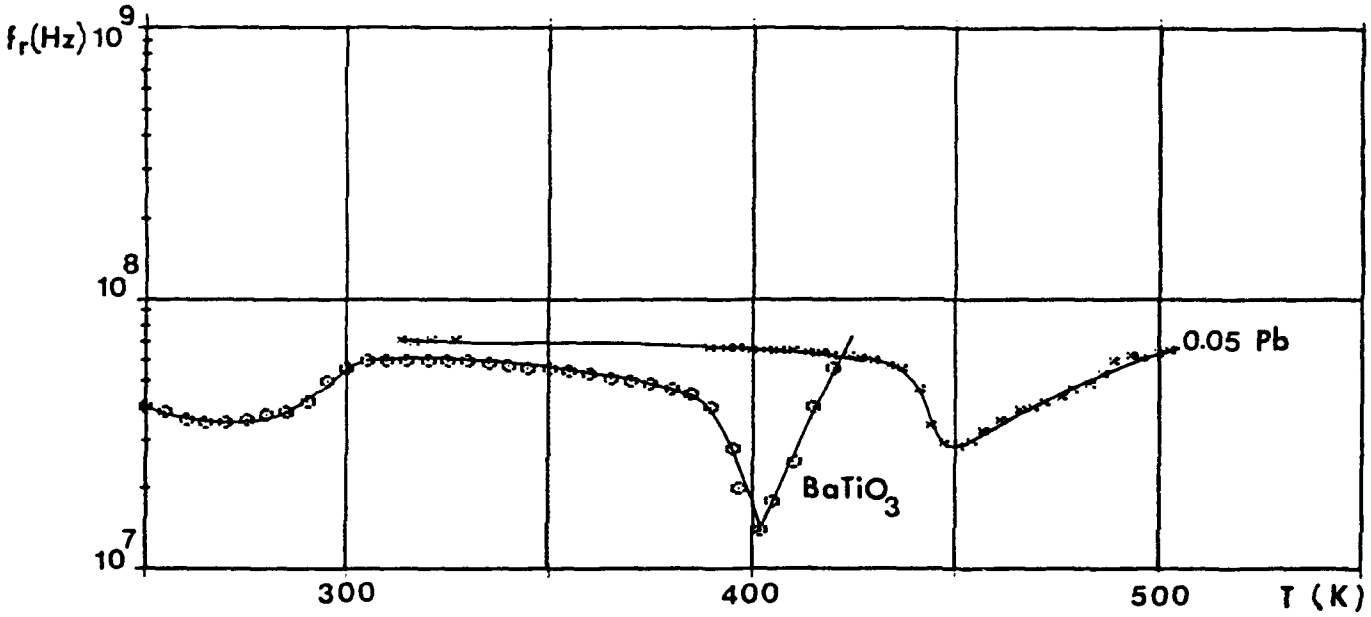


Fig.2 - Relaxation frequency for $BaTiO_3$ and $Ba_{0.95}Pb_{0.05}TiO_3$ ceramics.

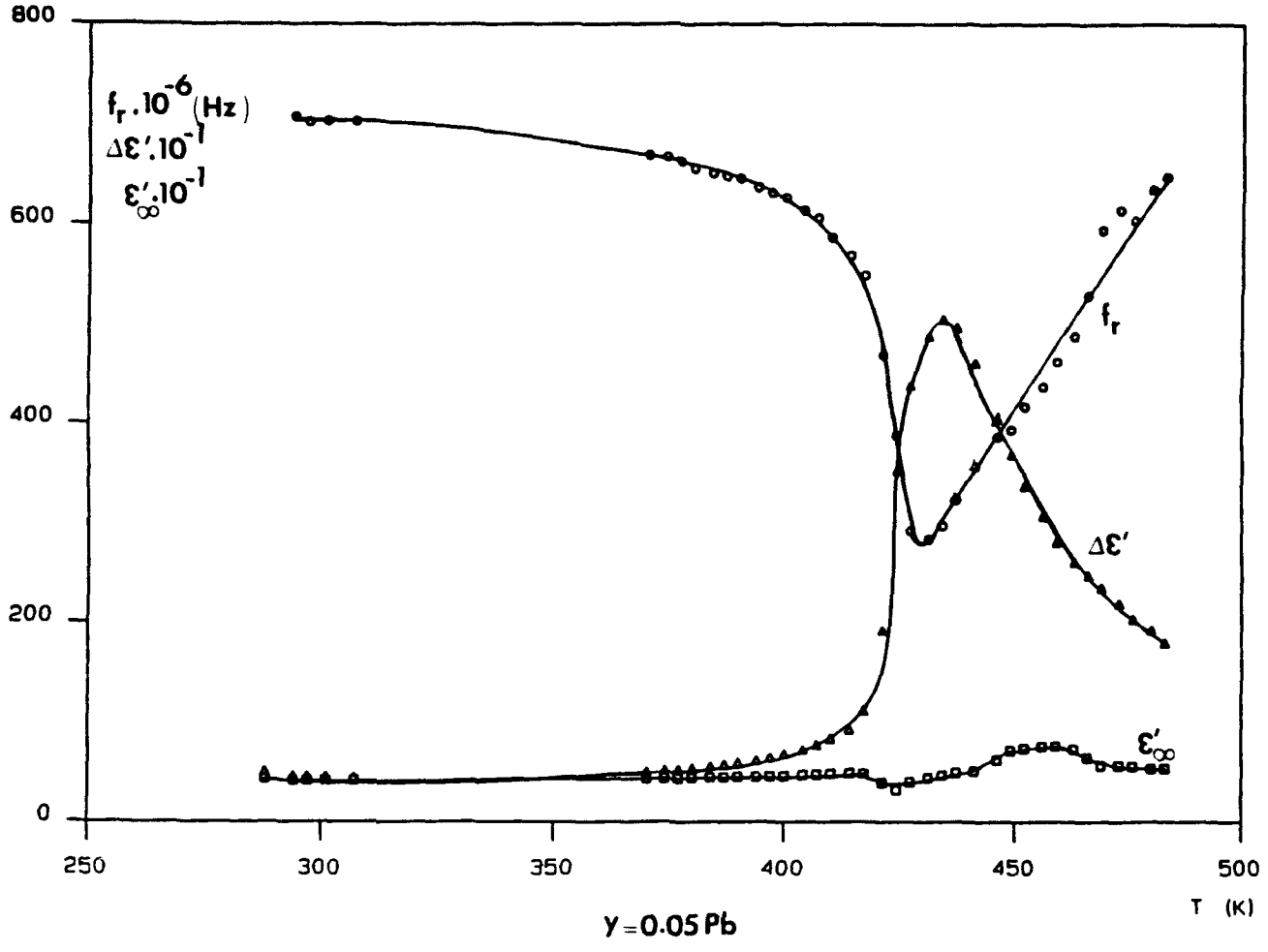


Fig.3 - Thermal dependences of f_r, $\Delta\varepsilon'$ and ε'_∞ for the composition $Ba_{0.95}Pb_{0.05}TiO_3$.

extrapolation at low ($f << f_r$) and high-frequencies ($f >> f_r$), respectively. It appears clearly a maximum of the dispersion step $\Delta\varepsilon'$ at the Curie temperature. The maximum of $\Delta\varepsilon'$ (T) and the minimum of f_r (T) occur at the same temperature which is exactly the Curie temperature measured at low frequency (10^3Hz).

The non-zero value of ε'_∞ suggests an ε' contribution of another nature such as ionic and electronic polarizabilities. $\Delta\varepsilon'$ is correlated to the dipolar moment of off-center Ti^{4+} in the oxygen octahedron and while ε'_∞ is probably related to the ionic and electronic polarizabilities. Indeed ceramics with composition $(Ba_{1-y}Pb_y)TiO_3$ exhibit a great electronic polarizability due to the lone pair of Pb^{2+} which is probably responsible to the strong value of ε'_∞.

The origin of the dielectric relaxation in solid solutions derived from $BaTiO_3$ in the range 10^6-10^9 Hz is still a matter of debate. The main issue is to distinguish between extrinsec and intrinsec mechanisms for this relaxation. The interpretation of such results in $BaTiO_3$ is already in progress.

REFERENCES

[1] B. Jaffe, W.R. Cook and H. Jaffe,"Piezoelectric ceramics" Academic Press, London, 1971, p. 242.

[2] S. Kazaoui and J. Ravez, Céramique de type $BaTiO_3$: influence des substitutions Zr-Ti et Hf-Ti sur la dispersion diélectrique en hyperfréquences, Physica Status Solidi (a), vol. 123, p. 165, 1991.

[3] S. Kazaoui and J. Ravez, Dielectric dipolar-relaxation in ferroelectric ceramics with composition $(Ba_{1-y}Sr_y)TiO_3$, Physica Status Solidi (a), vol. 125, p. 715, 1991.

[4] S. Kazaoui, J. Ravez and J.L. Miane, Correlation between dielectric relaxation and cation size in ceramics with composition related to $BaTiO_3$, J. Non Cryst. Solids, vol. 131, p. 1202, 1991.

[5] K.S. Cole and R.H. Cole, Dispersion and absorption in dielectrics, I-Alternative current characteristics, J. Chem. Phys., vol. 19, pp.341-351, 1941.

[6] M. Maglione, R. Böhmer, A. Loidl and U.T. Höchli, Polar relaxation mode in pure and iron-doped barium titanate, Phys. Rev.B, vol. 40, n°16, pp. 11441-11444, 1989.

A LOW－FIRING HIGH PROPERTIES MLC

Mao zu－you
Hong Ming Electronic Component Factory Chengdu China
Li Long Tu
Qing－Hua University Beijing China
Yao Xi
Xian Jiao－Tong University Xian China

This paper describles a low－firing (the firing temperature is lower than 900℃) multilayer ceramic capacitor, which meets the IEC temperature characteristic code 2E4. The composition of the materials is based on the system Pb$(Mg_{1/3}Nb_{2/3})O_3$ $Pb(Zn_{1/3}Nb_{2/3})O_3$－$PbTiO_3$.

A two－step calcination process was developed to restrain the formation of the pyrechlore phase during the synthesis of PMN ceramic powder. The dielectric properties of the MLC material were: $\varepsilon=14500$, $tg\delta=0.4\times10^{-2}$, $\rho=6.5\times10^{12}\Omega.cm$, $t_c\approx0℃$, $\Delta C/C(-25\sim85℃)\leqslant-50\%$, $E_{BDV}=6kv/mm$.

The binder CK－90 and the electrode materials YS－4, YC－4 were researched also. As a result, a compatible system of three relative materials, i.e., PMN ceramic powder, CK－90 binder and YS－4, YC－4 electrode materials, as well as a relative technological process were obtained. The product MLC have met the IEC standard and reached the five－level reliability.

Introduction

Along with the development of the large scale integration circuits and the surface mounting technologies the reqirements of multilayer ceramic capacitors (MLC) are increasing day by day. There are three categories of MLC, high－firing MLC (>1140℃), middle－firing MLC (1000～1140℃) and low－firing MLC (<1000℃), which are divided by medium ceramic materials and the sintering temperatures suitable to the electrode materials.

This paper present a material system for MLC with 2E4 characteristics. The ceramic powder is PMN relaxor ferroelectric material with low－firing, the casting－film binder is a kind of ethylene resin and the electrode material is complete silver. The three materials are compatible with each other quite well, and the main manufacturing process is suitable for these materials. Finally, the product MLC have met the IEC standard and reached the five－level reliability.

Ceramic Powder PMN

Composition of the powder:

$0.94Pb(Mg_{1/3}Nb_{2/3})O_3$ $0.04PbTiO_3$ $0.02Pb(Zn_{1/3}Nb_{2/3})O_3$－0.1wt%$MnO_2$－0.6mol%MgO

Physical properties of the powder

Average partical diameter: $1\pm0.3\mu m$

Surface area: $3.3\ m^2/g$

Sintering temperature: 880～900℃

Electric properties of the powder

Dielectric constant: 13500～15000

Dielectric loss: $<1.0\%$

Volume resistivity: $>10^{12}\Omega.cm$

Capacitance variation with temp: $<-50\%$

(adding bias 500V/mm: $<\pm30\%$)

Aging (%/Decade): 5%

Breakdown voltage: >5kV/mm

The key to make PMN ceramic powder is to restrain the formation of the pyrochlore phase and to enhance the development of the perovskite main phase. So a two－step synthesis technique at high temperature was used. Fist, $MgNb_2O_6$ and $ZnNb_2O_6$ were synthesized by MgO, ZnO with Nb_2O_5, and then individually mixed with PbO to synthesize $Pb(Mg_{1/3}Nb_{2/3})O_3$ and $Pb(Zn_{1/3}Nb_{2/3})O_3$.

Figure 1 shows the XRD pattern of the PMN powders by one step synthesis and two steps synthesis. It is shown that the pyrochlore content is about 20% in the powder by one step synthesis, but less than 2% by two steps.

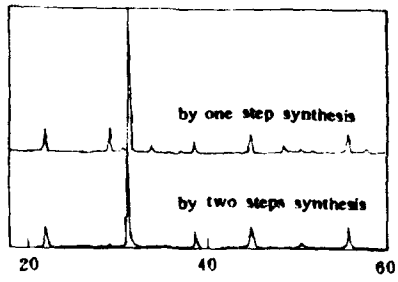


Figure 1. The XRD pattern of the PMN powders

The pure perovskite phase were obtained whether the sintering temperature was 840℃or 860℃ when using the process of two steps synthesis. (Figure 2)

CH3080-0-7803-0465-9/92$3.00 ©IEEE

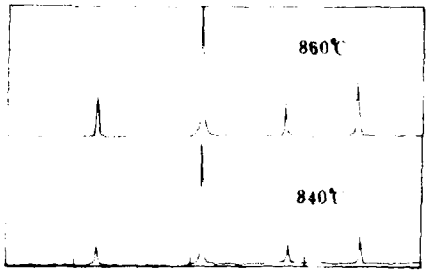


Figure 2. The XRD pattern of the PMN powders sintered at 840 C and 860 C

Figure 3 showes the DC bias character of PMN ceramic

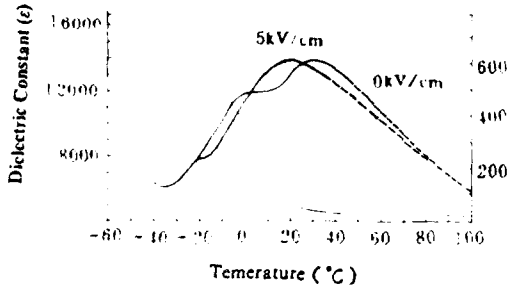


Figure 3. The DC bias character of PMN ceramic

The dielectric breakdown voltage and the mechanical strength of the PMN ceramic will be 15~50% higher by air quenching and annealing under proper temperature than that by furnace cooling. This result is shown in table 1. These values are comparable to that of $BaTiO_3$.

Table 1. The heat treatment conditions for improving the dielectric breakdown and machanical strength of the PMN ceramic

E(kv/mm)	σ(kg/cm²)	Heat treatment condition
4.68	690	Furnace Cooling
5.09	840	Air Quenching
6.12	1077	Air quenching+Annealing

Casting film Binder CK-90

The binder CK-90 is a poly-composition complex of the ethylene category. The optimum proportion of the casting film slurry is as follows:

CK-90 : PMN powder=0.7~0.75 : 1 (wt.)

Physical and chemical properties of the binder CK-90

Appearance: transparent liquid with the color of light yellow.

Intrinsic content: 8~14%

Beginning decompose temperature: 178±1 C

Last decompose temperature: 600±1 C

Average molecular weight of the resin: 6.50×10^4

Distributed coefficient of the resin molecular weight: 2.939

The film made by PMN powder and CK-90 binder is fine and close and well-distributed in texture, which proves that the PMN powder is compatible well with the CK-90 binder (Figure 4)



Figure 4. SEM image of PMN film

Electrode Materials YS-4 And YC-4

The complete silver internal electrode material YS-4 and the extreme One YC-4 were researched in order to make the electrodes materials compatible with casting material and process.

A fine silver powder which had the flat and sphere shape in proper proportion was used to obtain the fine and close conducting layer, and an acid-resisting material was selected as a flux to compound the electroplate-resisting extreme electrode material YC-4.

The thermal analysis pattern of the electrode materials carrier was basically matchable with that of CK-90 binder. It meant that the electrode material and the CK-90 binder was compatible.

The properties of electrode materials

	YS-4	YC-4
Silver content(%)	≥65	≥65
Square resist. (mΩ/□):	≤5	≤25
Viscosity (Pas):	≈30	≈6
Printing thickness by one time (μm):	8-10	≥10
Dry speed (after 3 min.):	80≈85%	
Stick strength (N/mm²)		≥4.9
Firing and permeating temperature (℃):	≤900℃	≤900℃

The ceramic film did not split and be permeated. There were clear printing lines and clear boundaries between the electrodes and the ceramic. That meant the PMN powder and the binder CK-90 and the YS-4 were well compatible. (Figure 5, 6, 7)

The table 2 shows that the square resistance of the YC-4 extreme electrode silver layer do not change before and after being chemically corroded.

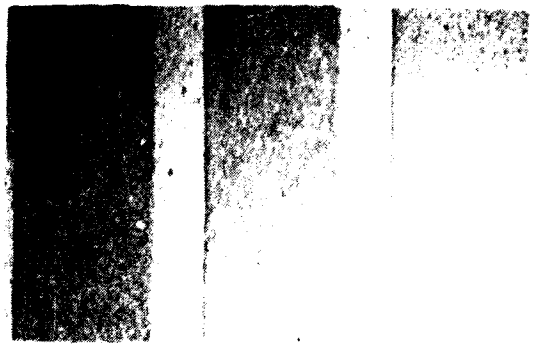


Figure 5. The casting film is compatible with YS-4 (15X)



Figure 6. MLC sectional pattern (100X)

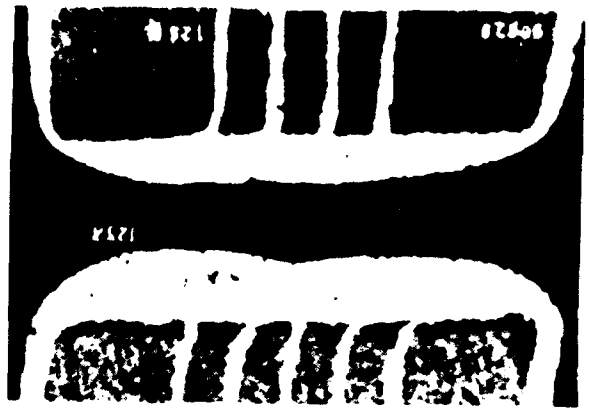
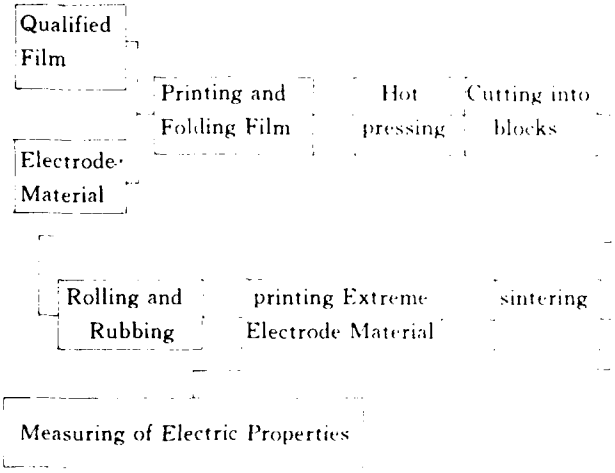


Figure 7. MLC extreme sectional pattern (125X)

Table 2. The change of the YC-4 square resistance before and after being chemically corroded

Square Resist. Before Corrosion (mΩ/□)	Square resist. After corrosion (mΩ/□)	Change of Square resist. (%)
4.70	4.70	0
7.50	7.50	0
9.00	9.00	0
9.50	9.50	0

Technological Process of Low-firing MLC



The parameters of the MLC technological process was determined by the properties of the MLC relative material system. The process must be compatible with these relative materials.

Electric Properties And Reliability

Table 3. The electric properties of the low - firing MLC

Rated Voltage	Medium Film Thickness	Medium Layers	size	Capacit.
63V	$<50\mu m$	8	0805	$5\mu F^{+80}_{-20}\%$

Insulation Resist.	Breakdown Voltage	tgδ
$>1000M\Omega$	$\geqslant 200V$	$\leqslant 1.1\times10^{-2}$

Ninety two of the MLC were sampled for reliability test on the condition of 63V and 85 C for 1000h, and no one wes failure during periodic test.

The MLC was qualified according to IEC standard and the reliability had reached the five - level.

Conclusion

1. The PMN ceramic powder meets IEC temperature characteristic code 2E4.
2. The three relative material system, PMN powder and CK - 90 binder and complete silver electrode materials YS - 4, YC - 4 are well compatible.
3. The low - firing, high properties MLC is qualified according to IEC standard and the reliability has reached the five - level.

ONE-STEP, LOW-TEMPERATURE SINTERING OF $SrTiO_3$ BASED GRAIN BOUNDARY BARRIER LAYER CAPACITOR MATERIALS

Yin Zhiwen, Xu Baomin
Shanghai Institute of Ceramics, Chinese Academy of Sciences, Shanghai 200050, China
Wang Hong
Shanghai University of Science and Technology, Jiading, Shanghai 201800, China

ABSTRACT

A new technology was developed to fabricate the $SrTiO_3$-based GBBL capacitor materials. The main feature of the technology is one-step, low-temperature (1100 -- 1200°C) sintering of the material in a reducing atmosphere with doping of a sintering aid composed of Li_2O and SiO_2. The main dielectric properties of the materials obtained by this technology are: effective dielectric constant $\epsilon_{eff} > 5\times10^4$, dielectric loss $\tan\delta < 5.0\%$, volume resistivity $\rho > 10^9\Omega\cdot$cm, temperature coefficient of $\epsilon_{eff} < 10\%$ (-25 -- +85°C). The effects of doping composition, sintering temperature, atmosphere and Ti/Sr ratio on the sinterability and dielectric property of the capacitor materials were discussed. The mechanism of the sintering aid in the formation of semiconducting grains and insulating grain boundaries were discussed from the results of compositional micro-analyses and microstructural analyses.

INTRODUCTION

In recent years, people paid more and more attention to the $SrTiO_3$-based ceramic grain boundary barrier layer (GBBL) capacitors due to their high dielectric constant, good temperature stability and high dispersive frequency. However, the sintering temperature of $SrTiO_3$-based ceramic GBBL capacitors were as high as above 1400°C, which gave big trouble for their mass production. Although there were some publications on the low-temperature sintering of $SrTiO_3$ GBBL capacitors[1,2], it was not satisfied with their microstructure and dielectric property. In this paper, a new technology was developed to fabricate the $SrTiO_3$-based GBBL capacitor materials with effective dielectric constant $\epsilon_{eff} > 5\times10^4$. The main feature of the technology is one-step, low-temperature (1100 -- 1200°C) sintering of the material in reducing atmosphere with doping of a sintering aid composed of Li_2O and SiO_2.

EXPERIMENTS AND RESULTS

Experiments were carried out on the effects of doping composition, sintering temperature, atmosphere, and Ti/Sr ratio on the sinterability and dielectric property of the $SrTiO_3$-based GBBL capacitor materials. Compositional micro-analyses and micro-structural analyses were also carried out for discussing the mechanism of the sintering aid in the process.

1. Effect of doping composition[3]

Using $SrTiO_3$ + xmol% Nb_2O_5 as base composition, the batch material was synthesized at 1150°C. Then the sintering aid composed of Li_2O and SiO_2 was added to the synthesized material, then grounded and pressed to form small disks and finally sintered in N_2+H_2 atmosphere. The composition of the samples for the experiments were listed in Table 1. It can be seen from the Table that there are two groups of the samples with different amount of dopants, namely, one group of samples with definite amount of Nb_2O_5 (0.1 mol% and 0.5 mol respectively) and variable amount of Li_2O, whereas the other group of samples with definite amount of Li_2O (1.0 mol% and 5.0 mol% respectively) and variable amount of Nb_2O_5. The amount of SiO_2 doping for all samples was kept the same. The dependence of dielectric properties on the variation of Li_2O or Nb_2O_5 content are shown in Fig. 1 and Fig. 2 respectively.

2. Effect of sintering temperature[3]

Select low Nb_2O_5 content (Sample 3) and high Nb_2O_5 content (Sample 7) from Table 1 to carry out this experiment. The sintering temperature used are from 1100 to 1200°C. Fig. 3 shows the dependence of dielectric property on sintering temperatures. Fig. 4(a) and (b) are the microstrucutures of Sample 3 sintered at 1100 and 1200°C respectively.

3. Effect of atmosphere[4]

Select Sample 7 from Table 1 for this experiment. Three different atmosphere, namely air, N_2, and $N_2 + H_2$ were used and the sintering temperature was kept at 1150°C for 3 hours. The properties of Sample 7 sintered in different atmosphere are listed in Table 2. Fig. 5 shows different microstructurers of the sample sintered in various atmosphere.

4. Effect of Ti/Sr ratio[5]

Two groups of samples with different amount of Nb_2O_5 doping, 0.1 mol% (low Nb_2O_5 content) and 0.5 mol% (high Nb_2O_5 content), respectively, was used to study the effect of Ti/Sr ratio on their properties. Definite amount of sintering aid was added to each sample. Fig. 6 and Fig. 7 show respectively the dielectric property dependence on Ti/Sr variation of the high and low Nb_2O_5 content samples sintered at 1100 and 1175°C for 3 hours.

5. Electron diffraction studies of GBBL samples[6]

In order to locate the different doping ions, selective area electron diffraction of the grain and triple grain junctions of the Nb_2O_5 and sintering aid doped $SrTiO_3$ ceramics was studied. The samples were sintered at 1150°C for 3 hours in $N_2 + H_2$ atmosphere and finally either naturally cooled in N_2 (named as G1) or quenched in air (named as G2). Fig. 8 and Fig. 9 show respectively the electron diffraction patterns of Sample G1 and G2.

DISCUSSION

The effective dielectric constant ϵ_{eff} can be simply expressed as

CH3080-0-7803-0465-9/92$3.00 ©IEEE

$\epsilon_{eff}=(d_g/d_i)\epsilon_i$, where d_g is the average dimension of grains, d_i and ϵ_i are respectively the thickness and dielectric constant of the insulating layer[7]. Therefore, lager the grain size and thinner the insulating layer are the key factors to obtain a GBBL capacitor ceramic with high effective dielectric constant.

1. Effect of sintering aid Li_2O and SiO_2

In sintering aid, SiO_2 is a typical glass former and Li_2O is a modifier, they are easily to form glass phase during sintering. The experimental results of electron diffraction studies (see Fig. 8 and 9) also support the conclusion that the Li_2O and SiO_2 ingredients in the batch mainly form glass phase at the grain boundaries during sintering and $Li_4Si_2O_7$ crystallite will be crystallized from the glass phase during slowly cooling. Most of the Li^+ ions will not enter the $SrTiO_3$ lattice as acceptors, they mainly precipitate at the grain boundaries to form the insulating layer. Furthermore, the amount of Li_2O content in the batch plays an important role on the formation temperature, quantity and viscosity of the glass phase. Table 1, Fig. 1 and 2 show that only appropriate amount of Li_2O content can form a glass phase with good characteristics to satisfy the demand of grain growth so as to obtain a ceramic material with high effective dielectric constant.

Besides, the amount of Li_2O content will affect the degree of semiconductorization of the grains. Compare Sample 1, 5 and Sample 2, 6 in Table 1 and Fig. 1, it is clear that with definite amount of Nb_2O_5 content, when the amount of Li_2O content increases from 1.0mol% to 2.5mol%, the ϵ_{eff} of the ceramic will increase 1 to 2 orders of magnitude. This phenomenon can also be explained by the formation of glass phase at grain boundaries to promote grain growth and the volatilization of oxygen so as to promote the semiconductorization of the grains.

2. Effect of donor dopant Nb_2O_5

It was well known that Nb^{5+} ions easily enter the $SrTiO_3$ lattice to replace Ti^{4+} ions as donor, which will promote the volatilization of oxygen to conduct the semiconductorization of grains and grain growth[8,9]. For low Li_2O content samples (No.9 to 12 in Table 1), since the characteristics of the glass phase is not good enough to conduct the volatilization of oxygen, higher Nb_2O_5 content is required to promote the semiconductorization of the grains. However, for high Li_2O content samples (No.13 to 16 in Table 1), the characteristics of the glass phase system seems good enough to promote grain growth and the volatilization of oxygen, so the semiconductorization of grains will proceed well even though the Nb_2O_5 content is low. From our experimental results, it showed that the solubility limit of Nb_2O_5 in $SrTiO_3$ lattice is smaller than 0.5mol%, and the appropriate doping amount of Nb_2O_5 is about 0.3mol%. Over doping of Nb_2O_5 in $SrTiO_3$ will result in precipitation of Nb_2O_5 at grain boundaries, which will give rise to lower the insulating property of the grain boundary so as to decrease the resistivity of the material and increase the dielectric loss (see Fig. 2).

3. Effects of sintering temperature

Curves in Fig. 3 and Fig. 4 show that for one-step, low-temperature sintering $SrTiO_3$-based GBBL capacitor materials, well sintered ceramics with good dielectric properties can be obtained in a rather broad sintering temperature range (1100 to 1200°C). Higher the sintering temperature has the advantage to promote the grain growth so as to increase the effective dielectric constant of the material.

4. Effect of sintering atmosphere

Table 2 and Fig. 5 show along with the decrease of the oxygen partial pressure of the atmosphere during sintering, the grain growth process proceeds well and the dielectric constant of the material increases. For Sample 7 sintered in N_2 + H_2, a strong reducing atmosphere with oxygen partial pressure smaller than 10^{-17} atm, the grain growth proceeded very fast during sintering and a microstructure with large grains and dense grain boundaries was obtained, its effective dielectric constant is several orders of magnitude higher than those materials sintered in atmosphere with higher oxygen partial pressure. According to the mechanism of semiconductorization of grains by oxygen volatilization[10], donor doping (e.g. Nb_2O_5) will weaken the Ti-O bond to promote the volatilization of oxygen. Strong reducing atmosphere will lower the oxygen partial pressure of the surrounding and improve the property of the glass phase, both of them are of great advantage to the oxygen volatilization process. As a result, grain growth and semiconductorization of grains proceed well, a ceramic with desired microstructure and good dielectric properties is obtained.

5. Effect of Ti/Sr ratio

Curves in Fig. 6 and Fig. 7 show that variation of Ti/Sr ratio in a certain range (1.02 to 0.98) will not give great effect on the temperature range of sintering and grain semiconductorization . However, the amount of donor doping and sintering condition is relevant to the effect of Ti/Sr ratio. In case of good sintering condition, excessive SrO (Ti/Sr < 1.00) is profitable to grain growth so as to increase the effective dielectric constant. Nevertheless, the presence of SrO or TiO_2 at grain boundaries is detrimental to the insulating property of the grain boundary layer resulting in the increase of the dielectric loss of the material.

CONCLUSION

1. A new technology was developed to fabricate the $SrTiO_3$-based GBBL capacitor materials. The main feature of the technology is one-step, low-temperature (1100 -- 1200°C)sintering of the material in a reducing atmosphere with doping of a sintering aid composed of Li_2O and SiO_2. The main dielectric properties of the material fabricated by this technology are: effective dielectric constant $\epsilon_{eff}>5\times10^4$, dielectric loss $\tan\delta<5.0\%$, volume resistivity $\rho_v>10^9\Omega\cdot$cm, temperature coefficient of $\epsilon_{eff}<10\%$ (-25 -- +85°C).
2. The formation mechanism of the material during sintering is schematically shown in Fig. 10.
3. Only if the Li_2O doping reaches certain amount, can the characteristics of the glass phase satisfy the demand of grain growth; in the mean time, the glass phase will promote semiconductorization of grains. Besides, a strong reducing atmosphere is necessary to proceed the volatilization of oxygen. Small fluctuation of sintering temperature or Ti/Sr ratio will not give large effect on the sinterability, microstructure and dielectric property of the material.
4. It is possible to use this technology to develop the monolithic GBBL capacitors with base metal (e.g. Ni) as inner electrodes.

References

1. J. M. Haussone, M. J. Laurent et al, J. Phys. Colloq., 47, C1-883 (1986)
2. S. M. Park and D. A. Payne, presented at the Fall Meeting of the Electronics of the American Ceramic Society, Williams, Va., Sept. 16 -- 19 (1979)
3. Xu Baomin, Wang Hong and Yin Zhiwen, J. Chin. Ceram. Soc., 19 (4), 354 (1991)
4. Xu Baomin, Wang Hong and Yin Zhiwen, J. Inorg. Mat., 6 (3), 290 (1991)

5. Xu Baomin, Wang Hong and Yin Zhiwen, Bull. of Chin. Ceram. Soc., 10 (5), 22 (1991)
6. Xu Baomin, Wang Hong and Yin Zhiwen, J. Chin. Ceram. Soc., 20 (1), 16 (1991)
7. R. Wrenicke, Advances in Ceramics, Vol. 1, Ed. by L. M. Levinson and D. C. Hill, ACS, Columbus, 272 (1981)
8. I. Burn and S. Neirman, J. Mat. Sci., 17, 3510 (1982)
9. Zhang Shuren, M. Sc. Thesis, Shanghai Institute of Ceramics, Chinese Academy of Sciences, 1986
10. S. Shirasaki and H. Yamamura, J. Chem. Phys., 73 (9), 4640 (1980)

Table 1. Compositions of Samples

Sample No.	1 2 3 4	5 6 7 8
Li_2O (mol%)	1.0 2.5 5.0 7.5	1.0 2.5 5.0 7.5
Nb_2O_5 (mol%)	0.1	0.5
Feature	low Nb_2O_5 content	high Nb_2O_5 content
Sample No.	9 10 11 12	13 14 15 16
Nb_2O_5 (mol%)	0.1 0.3 0.5 0.7	0.1 0.3 0.5 0.7
Li_2O (mol%)	1.0	5.0
Feature	low Li_2O content	high Li_2O content

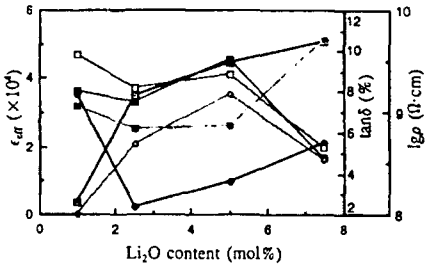


Fig. 1. Dependence of dielectric properties on Li_2O content
- ϵ_{rt}, low Nb_2O_5 content
- tanδ, low Nb_2O_5 content
- ρ, low Nb_2O_5 content
- ϵ_{rt}, high Nb_2O_5 content
- tanδ, high Nb_2O_5 content
- ρ, high Nb_2O_5 content

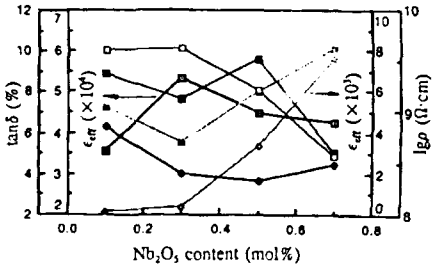


Fig. 2. Dependence of dielectric properties on Nb_2O_5 content
- ϵ_{rt}, low Li_2O content
- tanδ, low Li_2O content
- ρ, low Li_2O content
- ϵ_{rt}, high Li_2O content
- tanδ, high Li_2O content
- ρ, high Li_2O content

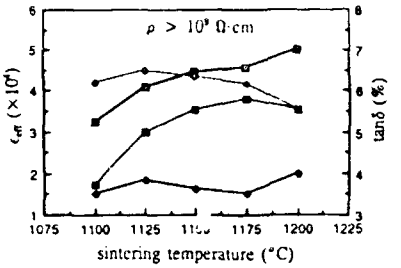
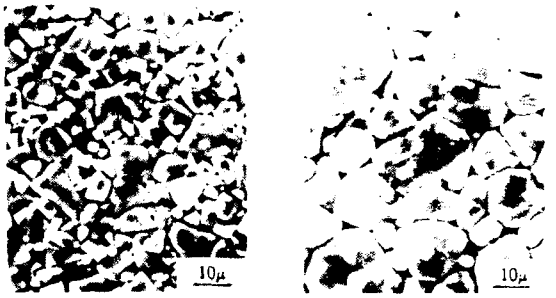


Fig. 3. Dependence of dielectric properties on sintering temperature
- ϵ_{rt}, Sample 3
- tanδ, Sample 3
- ϵ_{rt}, Sample 7
- tanδ, Sample 7

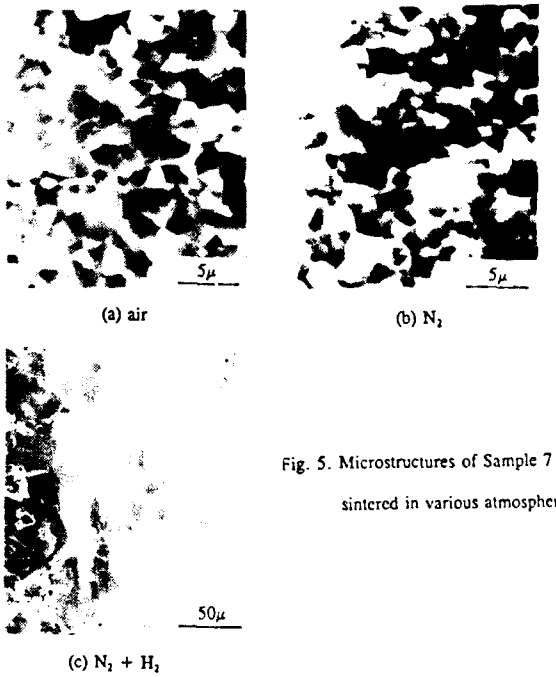


(a) 1100°C (b) 1200°C

Fig. 4. Microstructures of Sample 3 sintered at various temperatures

Table 2. Properties of Sample 7 sintered in various atmosphere

Atmosphere	air	N_2	$N_2 + H_2$
Po_2 (atm)	0.21	8.90×10^{-4}	$<10^{-17}$
ϵ_{rt}	2.11×10^3	2.41×10^3	4.47×10^4
tanδ (%)	2.78	3.15	3.61
ρ (Ω·cm)	3×10^9	2×10^9	3×10^9



(a) air (b) N_2

(c) $N_2 + H_2$

Fig. 5. Microstructures of Sample 7 sintered in various atmosphere

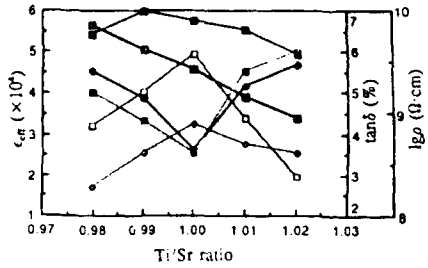


Fig. 6. Dependence of dielectric properties of the samples doped with 0.5mol% Nb_2O_5 on Ti/Sr ratio
- ϵ_{rt}, sintered at 1100°C
- tanδ, sintered at 1100°C
- ρ, sintered at 1100°C
- ϵ_{rt}, sintered at 1175°C
- tanδ, sintered at 1175°C
- ρ, sintered at 1175°C

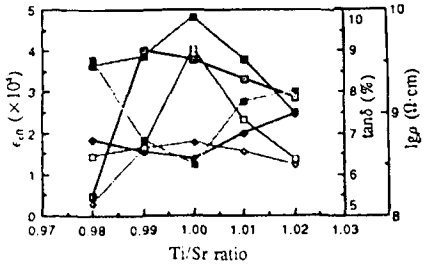
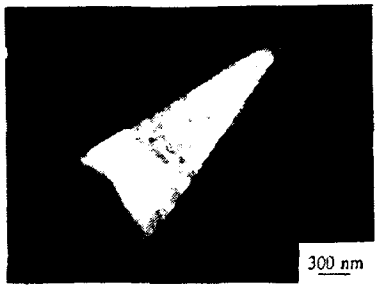
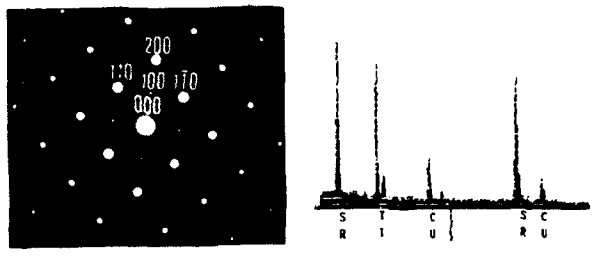


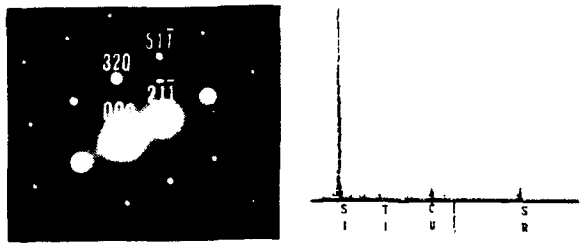
Fig. 7. Dependence of dielectric properties of the samples doped with 0.1mol% Nb_2O_5 on Ti/Sr ratio
- ϵ_{rt}, sintered at 1100°C
- tanδ, sintered at 1100°C
- ρ, sintered at 1100°C
- ϵ_{rt}, sintered at 1175°C
- tanδ, sintered at 1175°C
- ρ, sintered at 1175°C



(a) Triple grain junction



(b) Electron diffraction pattern and X-ray energy dispersive spectrum of grain, which proved to be $SrTiO_3$ crystal

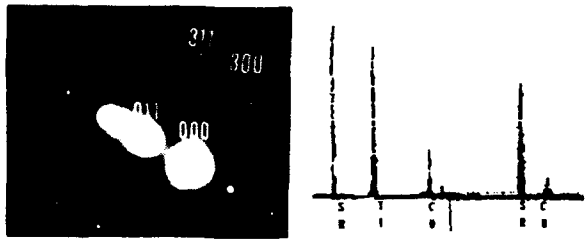


(c) Electron diffraction pattern and X-ray energy dispersive spectrum of the triple grain junction, which proved to be $Li_4Si_2O_7$

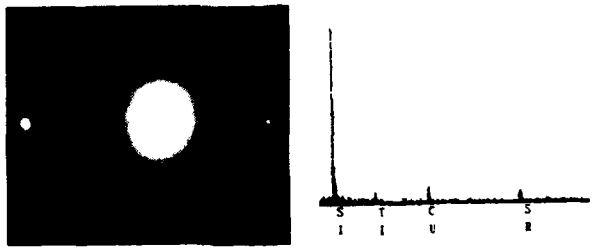
Fig. 8. TEM analyses of Sample G1 (the Cu peak in the X-ray energy dispersive spectrum is caused by the copper net supporting the sample)



(a) Triple grain junction



(b) Electron diffraction pattern and X-ray energy dispersive spectrum of grain, which proved to be $SrTiO_3$ crystal



(c) Electron diffraction pattern and X-ray energy dispersive spectrum of the triple grain junction, which proved to be glassy phase

Fig. 9. TEM analyses of Sample G2 (the Cu peak in the X-ray energy dispersive spectrum is caused by the copper net supporting the sample)

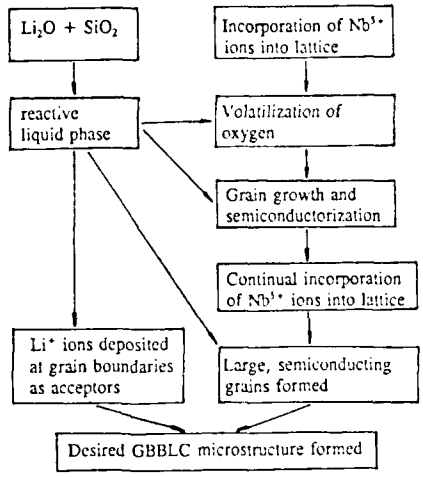


Fig. 10. Schematic diagram to show the mechanism of the $SrTiO_3$ GBBL capacitors single-fired at low-temperature

INFLUENCE OF SINTERING CONDITION ON MICROSTRUCTURE DEVELOPMENT OF $BaTiO_3$ BASED PTCR MATERIALS

Z. Z. Huang, H. M. Lu and Z. W. Yin
The Shanghai Institute of Ceramics, The Chinese Academy of Sciences
Shanghai 200050, China

The influence of sintering condition on the microstructure development of (Ba-Sr)TiO_3 system was studied. The experimental results showed that the samples were densified at a rather low temperature without substantial grain growth. As temperature increased, both discontinuous and continuous grain growth could take place depending mainly on the temperature range and heating rate of sintering schedule, i.e. nucleation and grain growth processes. A good PTCR characteristic was observed with the sample having grain size of 5-10um. Compared to the normal process, sintering in nitrigen and cooling in air for (Ba-Pb)TiO_3 system would produce a finer grain microstructure, which resulted in decreasing resistivity and improving PTCR characteristic. Microanalyses (SIMS and EPMA) indicated that the additive ions would mainly deposite at grain boundary and intergranular region.

Introduction

PTCR effect refers to the positive temperature coefficient of resistivity exhibited by certain n-type semiconducting barium titanate poly-crystalline material, which is properly donor-doped in its composition, sintered or annealed in oxidation atmosphere and yields a certain extent of grain growth in its microstructure development[1].

The mechanism of PTCR effect was considered as a grain boundary effect rather than a bulk phenomenon. Potential barriers at the grain boundary are formed, which are supposed as a result of P-type contamination, adsorbed oxygen and/or cation vacancy after sintering in oxidation atmosphere[2]. The ferroelectric nature of the material allows the potential barriers to be activated above the Curie Point resulting in a sharp rise in resistance. Below the Curie Point, the barriers are weak due mainly to the spontaneous polarization of the ferroelectric materials, which compensates the barrier charge. That leads to PTCR effect observed in barium titanate ceramic materials[3].

PTCR material has found a variety of applications because of the abrupt change of its resistance value near the ferroelectric Curie Point, making it one of the most important ferroelectric ceramic materials[4]. A high performance PTCR material requires low electrical resistivity below Tc, low voltage sensitivity and high temperature shock resistance. In order to achieve these requirements, the ceramic material with a high density, fine grain size and uniform microstructure development is needed.

In this paper, the temperature range and heating rate during the sintering process of (Ba-Sr)TiO_3 solid solution were studied to obtain a fine grain body with a good PTCR characteristic, and the relation between the microstructure development and PTCR characteristic was also discussed. A material with lower resistivity was obtained from the (Ba-Pb)TiO_3 solid solution, which showed that a finer grain microstructure development could be obtained when the ceramics was sintered in nitrigen atmosphere and cooled in air. The different distribution of the main constituents and the additive ions were measured by microanalysis for these PTCR materials.

Preparation and Performance of the Samples

In this experiment, PTCR materials were prepared by using the mixed oxide method. (Ba-Sr)TiO_3 and (Ba-Pb)TiO_3 solid solutions were selected to obtain the samples with different Curie Point, La_2O_3 and Nb_2O_5 as donor were added in the compositions, Al_2O_3, SiO_2, $CaCO_3$ and Mn ion as additives were doped to improve the sintering behavior, microstructure development and the electrical performance of the materials. The powder of mixed oxides with donor doped were calcined at 1150°C for 4 hr. for $BaTiO_3$ composition and (Ba-Sr)TiO_3 solid solution, and 950°C for 2 hr. for $PbTiO_3$ composition, respectively. The sintering process was as follows: the green bodies were first heated to a lower temperature (1200°C or higher) at a rate of 500°C/hr., then fast heating to sintering temperature (1300°C or higher), soaking for a period of time (e.g. 0.5 hr.), and finally cooling to room temperature at a rate of 300-500°C/hr. depending on the desired performance of the sample. The experiment of sintering in nitrigen atmosphere and cooling in air was conducted for the (Ba-Pb)TiO_3 solid solution with the same temperature schedule and heating rate described above.

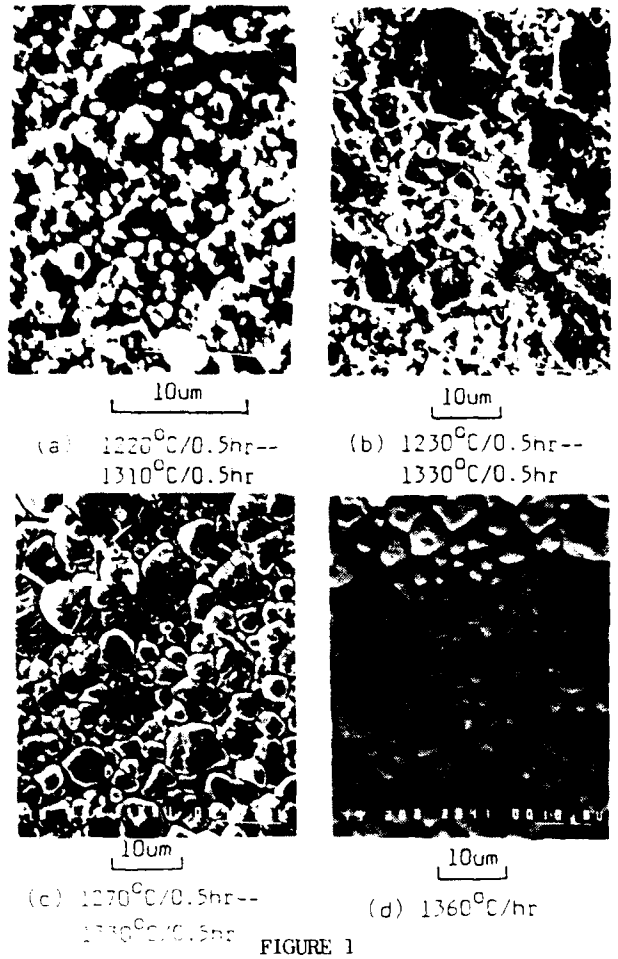
The sintered samples were ground and electroded with electroless nickel, then silver paste. The sample of (Ba-Sr)TiO_3 solid solution exhibited quite a good PTCR characteristic (> 5 orders of magnitude resistance jump) with grain size of 5-10um. The sample of (Ba-Pb)TiO_3 solid solution possesses quite a low resistivity ($< 3 \times 10^2 \Omega$.cm) below Tc with a good PTCR characteristic, which seems to be suitable for the low voltage applications.

Results and Discussion

Influence of Sintering Condition on the Microstructure Development and PTCR Characteristic

The very different microstructure developments were observed for the samples of donor-doped (Ba-Sr)TiO_3 solid solution with some additives (Ca^{2+}, Al^{3+}, Si^{4+}, Mn^{2+}) sintered in different conditions, which are shown in Figure 1, and the resistivity as a function of temperature for these samples are shown in Figure 2. A dense body with fine grain microstructure (grain size~2um) was obtained for the sample sintered at 1220°C/0.5hr. and 1310°C/0.5hr. seen from Fig. 1(a). In other words, the densification process took place with a negligible degree of grain growth at a lower temperature range in presence of certain additives[5]. This sample exhibited an insulating behavior with brown in color. As temperature increased, the grain growth took place. A duplex microstructure development was obtained as shown in Fig. 1(b). This typical discontinuous grain growth phenomenon is not good to PTCR effect seen from Fig. 2. However, a relatively uniform microstructure development was produced for the sample sintered at 1270°C/0.5hr. and 1330°C/0.5hr. It could be deduced that a large number of grains might nucleate at ~1270°C, and then grow to a certain extent (e.g. 5-10um) as shown in Fig. 1(c). This phenomenon seems to be a typical continuous grain growth occuring in titanates, which is beneficial to the PTCR effect as shown in Fig. 2. As the sintering temperature increased

CH3080-0-7803-0465-9/92$3.00 ©IEEE



(a) 1220°C/0.5hr--1310°C/0.5hr (b) 1230°C/0.5hr--1330°C/0.5hr

(c) 1270°C/0.5hr-- (d) 1360°C/hr

FIGURE 1
SEM micrographs of as-fired surface of the samples sintered at different condition

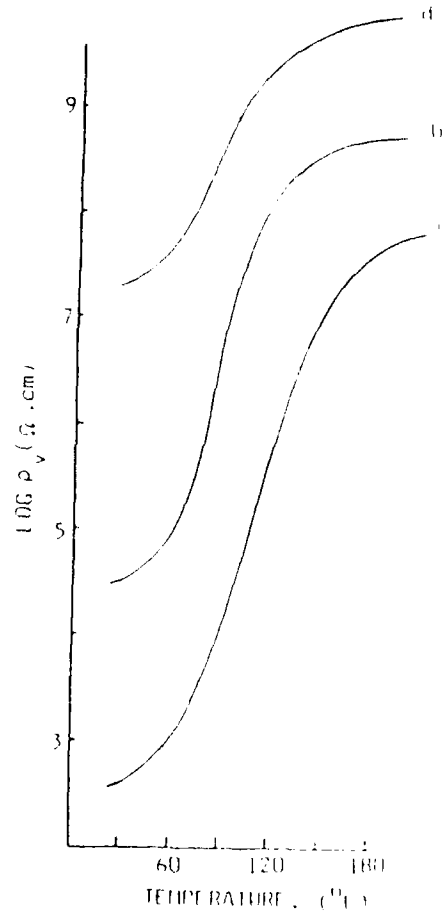


FIGURE 2
Resistivity as a function of temperature for the sample sintered at different condition

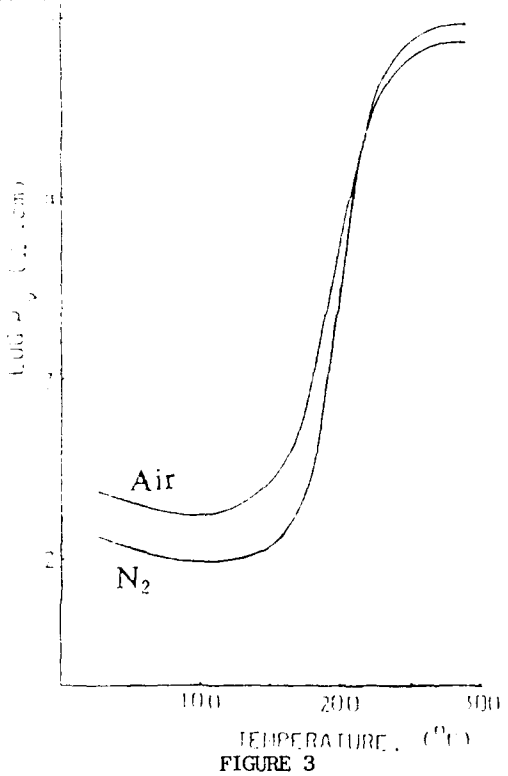
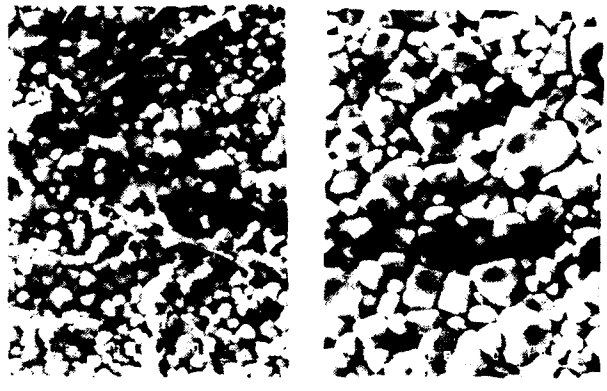


FIGURE 3
Comparison of PTCR characteristic of samples sintered at nitrigen and air atmosphere.



(a) nitrigen (b) air

FIGURE 4
SEM micrographs of as-fired surface of the samples sintered at different atmosphere
(a) nitrigen (b) air

further, e.g. 1360°C/hr., the exaggerating grain growth took place, some grains outgrew in consumption of surrounding small grains as shown in Fig. 1(d). This coarsening phenomenon indicates that the secondary recrystallization process seemed to occur in this temperature range,[6][7] and is harmful to the PTCR effect as shown in Fig. 2. As mentioned above, the microstructure development of the samples of donor-doped (Ba-Sr)TiO_3 solid solution seemed to be determined by two separate processes, nucleation and grain growth, which were strongly influenced by the temperature range and heating rate of sintering schedule.

Influence of Sintering Atmosphere

The experiment of sintering in nitrigen atmosphere and cooling in air was conducted on the samples of donor-doped (Ba-Pb)TiO_3 solid solution. Compared to the normal sintering process, the sample exhibited a lower resistivity below Tc and some improvement in PTCR characteristic as shown in Fig. 3. The relevant microstructure developments are shown in Figure 4. An average grain size of ~3um was observed, which is smaller than that sintered in air. This result could be attributed to the different diffusing rate of ions in nitrigen or in air, and possibly less evaporation of Pb in the form of PbO in nitrigen atmosphere. It could be supposed that this firing process would promote the reduction of grain and prohibit the grain growth during sintering in nitrigen atmosphere[8], thereafter fully reoxidize the grain boundary during cooling in air, which is beneficial to the PTCR effect, especially for the preparation of PTCR material with a lower resistivity (e.g. $\lesssim 100\,\Omega$.cm) to meet the requirement used in low voltage field.

Ion Distribution

The distribution of ions in the depth profile of the sample of (Ba-Sr)TiO_3 solid solution was measured by SIMS (Secondary Ion Mass Spectroscopy) as shown in Figure 5. It could be seen that the distributions of the main constituent ions (Ba^{2+} and Ti^{4+}) and donor ions (La^{3+} and Nb^{5+}) seem to be relatively homogeneous in the depth profile, however, the additive ions (Al^{3+} and Si^{4+}) show some segregation at grain boundary.



FIGURE 6
SEM micrograph of polished surface without any etching treatment and EPMA measurement.

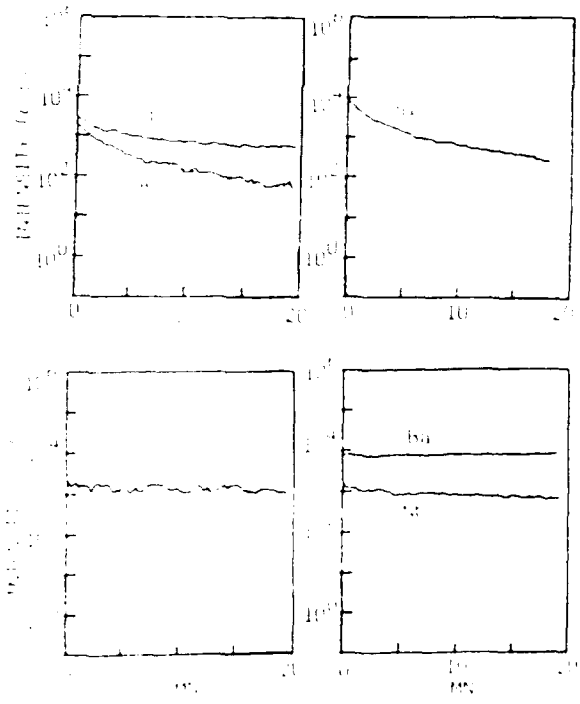


FIGURE 5
Distribution of some ions in the depth profile of samples based on (Ba-Sr)TiO_3 solid solution measured with SIMS.

The EPMA (Electron Probe Microanalysis) was carried out with a polished surface of the sample of (Ba-Pb)TiO_3 solid solution without any etching treatment, which is shown in Figure 6. The scanning operation was conducted along the line depicted in the figure.

The similar results as above were obtained: the main constituent ions (Ba^{2+}, Pb^{2+} and Ti^{4+}) and donor ions (La^{3+} and Nb^{5+}) were detected both at the white areas (grain regions) and at the black areas (grain boundary and intergranular regions), whereas the additive ions (Al^{3+} and Si^{4+}) were only detected at the black areas (grain boundary and intergranular regions).

Apparently, it could be deduced that the role of the additives (Al_2O_3 and SiO_2) would mainly exert on the grain boundary rather than the grain itself.

Conclusion

1) The microstructure development of (Ba-Sr)TiO_3 solid solution with donor and other additives was strongly influenced by the sintering condition. A densification process could take place at a lower temperature with a regligible grain growth. As the sintering temperature increased, both discontinueous and continueous grain growth processes could occur depending mainly on the temperature range and heating rate.

2) Compared to normal process, sintering in nitrigen and cooling in air would produce a finer grain microstructure development, decrease resistivity and improve the PTCR effect in (Ba-Pb)TiO_3 solid

solution.

3) Microanalyses (SIMS and EPMA) indicate that the additive ions in $BaTiO_3$-based PTCR material would mainly deposite at the grain boundary and intergranular regions.

References

(1) M. H. Drofenik: "Grain growth during sintering of donor doped $BaTiO_3$" Am. Ceram. Soc. Bull, 63(5) 1984 pp. 702-704.

(2) H. Ihrig: "Advance in Ceramics" V.7, The American Ceramic Society, 1984, pp.117-127.

(3) J. Daniels and R. Wernicke: "New Aspects of an improved PTC model" Philips Res. Rep. 31(6), 1976. pp.544-559.

(4) B. M. Kulwicki: "Advance in Ceramics" V.1, The American Ceramic Society, 1981, pp,138-154.

(5) J.F. Fernandez et al.: "Dielectric and Microstructural properties of sintered $BaTiO_3$ ceramics prepared from different TiO_2 raw materials" J. Mat. Sci. 26, 1991, pp.3257-3263.

(6) W. Heywang and H. Thomann: "Electronic Ceramics" Elsevier Applied Science, 1991, Chapter 2, pp.29-47.

(7) W. D. Kingery et al.: "Introduction to ceramics" 2nd edition. John wiley & sons, Inc. 1976, pp. 461-464.

(8) V. R. W. Amarakoon et al.: "Auger analysis of $BaTiO_3$ thermistors" presented at the 85th Annual Meeting of the American Ceramic Society, Chicago, Il, U.S.A. April 24-27, 1983.

Quasi Lumped Parameter Method for Microwave Measurements of Dielectric Dispersion in Ferroelectric Ceramics

Shaoping Li, Tyh Sheen, Q. M. Zhang, Sei-Joo Jang, A.S. Bhalla and L.E. Cross

Materials Research Lab., Penn State University, University park, PA 16802

Abstract

In this work, a modified lumped parameter method has been discussed which, we believe, is especially suitable for microwave measurements of dielectric dispersion in high dielectric materials in a particular frequency region. The method combines some of the features of both the lumped parameter method and the distributed parameter method. Dielectric dispersions for $Pb(Zr_{1-x}Ti_x)O_3$, $BaTiO_3$ and $Ba_xSr_{1-x}TiO_3$ ceramics in the frequency domain from 1 MHz to 1GHz are presented. This paper also discusses the principle of the measurement and the accuracy of the experimental data which is retrieved.

I. Introduction

Dielectric properties of ferroelectric materials and their frequency dependence are of great importance in many applications. Dielectric dispersion in ferroelectric materials has been measured and discussed by many authors [1-6]. The measurement of relative dielectric constant (ε) and loss tangent ($\tan\delta$) in ferroelectric materials at microwave frequencies is made difficult by the large dielectric constant and loss tangents exhibited by these materials.

In general, high frequency dielectric measurement techniques are mainly divided into two sections: (1) the transmission techniques, and (2) the resonant techniques, among which only the transmission techniques have the swept frequency capability. The transmission techniques for microwave measurements on dielectric samples can be classified into two categories. One is the lumped capacitance method and the other is the distributed parameter method. In practice, however, the microwave measurements for high dielectric materials in the frequency range 100 MHz -- 2GHz can not be made accurately by either of these two methods, even though the microwave equipments have been improved significantly in the past few decades. The objective of this study is to measure the dielectric dispersions of high dielectric constants materials at the frequency range 1 MHz- 2GHz.

II. Limitations of Conventional Methods

In the lumped capacitance method, a dielectric sample was placed on the end of a shorted coaxial line and the complex reflection coefficient was measured by the time domain reflectmeter (TDR) through the vector voltage ratio of the reflected wave to the incident wave from the sample [7]

$$\Gamma = \frac{V_{ref}}{V_{inc}} = \Gamma_x + j\Gamma_y = |\Gamma| e^{j\theta} \qquad (1)$$

where V_{ref} is the voltage of the reflected wave and V_{inc} represents the voltage of the incident wave. The complex reflection coefficient is a function of the complex permittivity, and thus, the real and imaginary parts of the relative permittivity can be expressed as [7,8]

$$\varepsilon'' = \frac{2|\Gamma|\sin\theta}{\omega C_0 Z_0 \{1-|\Gamma|^2 + 2|\Gamma|\cos\theta + 1\}} \qquad (2)$$

$$\varepsilon' = \frac{1-|\Gamma|^2}{\omega C_0 Z_0 \{1-|\Gamma|^2 + 2|\Gamma|\cos\theta + 1\}} \qquad (3)$$

where C_0 is the capacitance of the test capacitor and Z_0 is the characteristic impedance of the network analyzer. The basic assumption for the lumped capacitance method is that the electric field is uniform throughout the sample. In other words, this means that the measured reflection coefficient is equal to the intrinsic reflection coefficient of samples, which is caused by the complex permittivity of the sample. If this basic requirement could not be satisfied, the accurate results would not be obtained by using the lumped capacitance method. At higher frequencies, the lumped capacitance method breaks down in several respects. (1) The measured capacitance of the sample cannot be simply related to the real dielectric constant of the sample because of the non-uniform variation of the electric field throughout the sample. In other words, for high dielectric constant materials, due to the wave compression, the basic assumption for the lumped impedance technique loses validity at the high frequency. It is, therefore, required that the thickness of the sample should be around the order of a few percent of a wavelength at the highest frequency of interest in order to obtain rather accurate experimental data. If the material has a dielectric constant at about 1000 at the frequency of 1 GHz, the corresponding thickness of the sample should be the order of 100 μm. The other dimensions of specimens should also be much less than the wavelength of light. (2) The fringe field effects [9] and the inability of the measurement equipment also affect the accuracy of measured experimental data severely. At the high frequencies, the fringing field is usually no longer negligible. The smaller cross section of samples decreases the fringe field, however, machining the sample becomes difficult. In addition, due to the limitations of measurement instruments, the maximum readable capacitance value within 5% accuracy is always limited at the higher frequencies. On the other hand, it is known that the distributed transmission method does not require the uniform field assumption. In this method, however, the wave guide is the primary medium of microwave propagation. If the cutoff frequency is around 300 MHz, the wave guide dimensions should be around the order of 0.5 m, which is apparently not reasonable in practical cases.

III. The Principle of the Proposed Measurement Method

As discussed above, due to the influence of fringing fields and the difficulty of sample machining, it is difficult to satisfy the requirement of the critical thickness which is imposed by the assumption of the lumped impedance technique. The question, therefore, arises as to whether or not the lumped impedance method can be modified in order to extend the scope of its applications.

Usually, in the high frequency region, the dimension of the sample does not fulfill the critical requirement of the sample dimension in terms of the basic assumption of the lumped parameter method. Therefore, the measured reflection coefficient is not exactly equal to the intrinsic reflection coefficient of the sample. Hence, the measured reflection coefficient is not solely related to the complex permittivity, which is affected also by the losses and the phase shift of the measuring signal during the electromagnetic wave passing through the sample. In order to overcome these difficulties, to describe the measurement situation accurately, and to make the measurement practical, the measured sample can be considered as a "quasi-transmission" line. Precisely speaking, in this situation we may visualize the measured sample comprising of two parts, as shown in Fig.1. Part I is a very thin layer, which is thin enough to be equivalent to an ideal lumped capacitance system. The reflection coefficient of this part represents the intrinsic properties of the measured material. Part II is the rest of the sample (the shadowed area) , which is a "lossy transmission line " or a distributed

CH3080-0-7803-0465-9/92$3.00 ©IEEE

component, and could be described by a simple two- port net work, as shown in Fig.(1c).

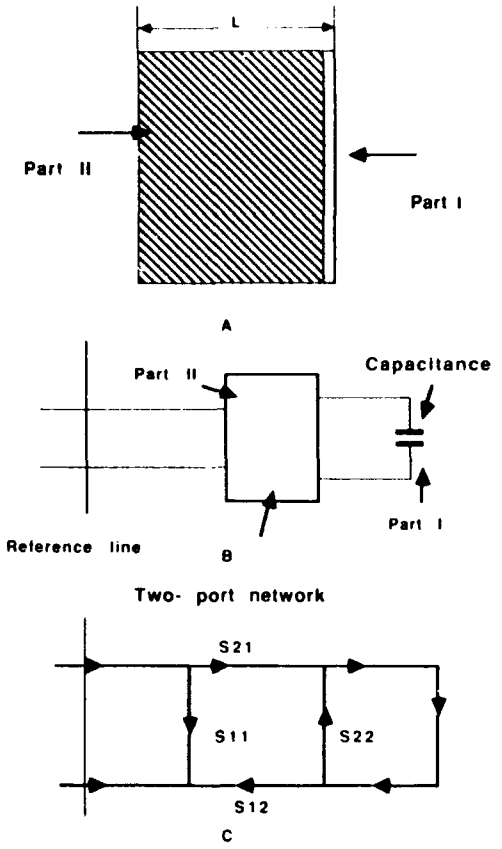


Figure 1. (a) Schematic drawing of the sample imaged as the two parts of a "lossy quasi- lumped transmission line".
(b) Equivalent circuit of the real sample.
(c) Terminated two-port network with the S_{ij} parameters to describe the nature of the sample.

The equivalent circuits of the specimen are also shown in Figs.1(b) and (1c). According to this equivalent circuit, the relationship between the measured reflection coefficient and intrinsic reflection coefficient can be expressed as[10]

$$\Gamma_s = \frac{1}{\left[\frac{S_{12}S_{12}}{\Gamma_m - S_{11}} + S_{22}\right]} \qquad (4)$$

In reality, as long as the thickness of the measured samples does not fulfil the critical requirement of lumped parameter method, it can be considered that part II exists in the measured sample, which will cause attenuation of the signal amplitude and the phase shift of the measured signal when the measured signal goes through the sample. Therefore, by using eq.(4), intrinsic reflection coefficients of the sample can be retrieved and obtained from the measured reflection coefficient provided the S_{ij} parameters are known.
In a simplified case (here we assume $S_{11}=S_{22}$, $S_{12}=S_{21}$), according to the theory of the distributed parameter method [5,11], S_{11} and S_{12} can be expressed in terms of the sum of reflected and transmitted waves and can be numerically evaluated by [11]

$$S_{11} = \rho \frac{1 - \exp(-2\gamma l)}{1 - \rho^2 \exp(-2\gamma l)} \qquad (5)$$

$$S_{12} = \frac{(1 - \rho^2)\exp(-\gamma l)}{1 - \rho^2 \exp(-2\gamma l)} \qquad (6)$$

where

$$\rho = \frac{1 - (\varepsilon^*)^{1/2}}{1 + (\varepsilon^*)^{1/2}}, \quad \gamma = \alpha + j\beta = j\omega(\mu^*\varepsilon^*)^{1/2}$$

l is the thickness of measured sample, and ε^* is the relative complex permittivity. From eqs.(5) and (6), it is very obvious that when the measuring frequency is very low, S_{11} approaches to zero and S_{12} is equal to 1. Thus, from eq.(4), Γ_m is equal to Γ_s. This is the case in an ideal lumped capacitance situation. Fig.2 presents the theoretical calculations of S_{11} and S_{12} as a function of frequencies.

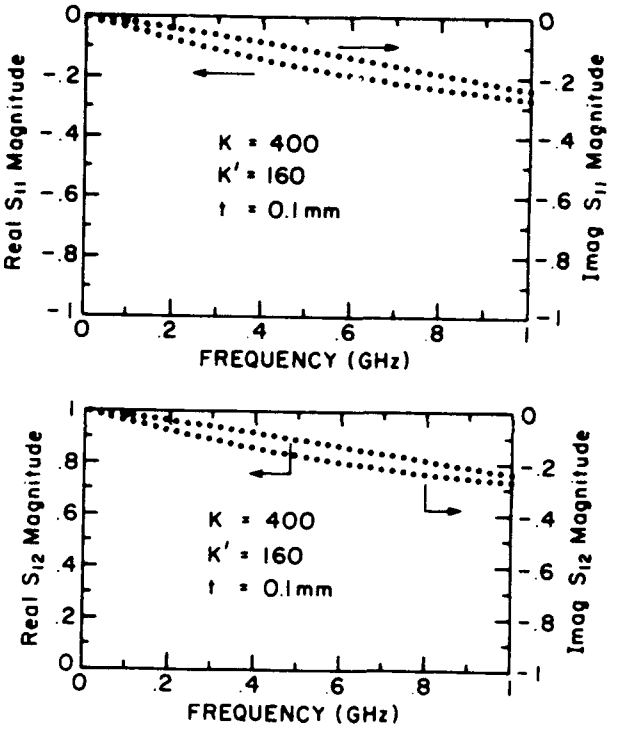


Figure 2. Theoretical calculations of the real and imaginary parts of the S_{ij} parameters v.s. frequency.
(a) Theoretical calculated real and imaginary magnitudes of S_{12}.
(b) The S_{11} versus frequency in the range 1Hz-1GHz.

As discussed above, in the real measurements, if the measured frequency becomes very high, Γ_s will be strongly affected by the electromagnetic wave absorption and phase shift inside part II of the sample. In principle, as long as the influence of part II in the sample is not very large, which may be considered as a small perturbation term in terms of Γ_s, (this condition is easily fulfilled in practice), we can obtain the intrinsic reflection coefficient of the sample (Γ_s) by retrieving the measured reflection coefficients (Γ_m) from eq.(4) through the numerically evaluated S_{ij} parameters in an iterative process. The calculation procedure is that we assumed $\Gamma_m = \Gamma_s$, $S_{12} = S_{21} = 1$, and $S_{11} = S_{22} = 0$ at the lowest measuring frequency , and then we used the measured dielectric coefficients of every preceding frequency spot to evaluate S_{ij} parameters for next neighbor higher frequency spot by Eqs.7.5 and 7.6.

Finally, the complex dielectric dispersion ($\varepsilon^* = \varepsilon' - \varepsilon''$) can be obtained from the intrinsic reflection coefficient of the sample Γ_s by

$$\varepsilon^* = \frac{(1-\Gamma_s)}{\{(1+\Gamma_s)\, 2\pi j f C_0 Z_0\}} \qquad (7)$$

where Z_0 is the characteristic impedance of the impedance analyzer $C_0 = \varepsilon_0 a/d$.

IV. Experimental Results and Discussions

The $Pb(Zr_xTi_{1-x})O_3$, $BaTiO_3$ and $Ba_{0.5}Sr_{0.5}TiO_3$ ceramics were prepared by the conventional mixed- oxide process. The samples were cut to approximately the plate shape. Their dimensions were much smaller than the wavelength of light. Before making the electrodes, the surfaces of specimens were polished, etched and annealed in order to keep the contributions of surface layer low. The complex reflection coefficient of the sample was recorded with HP 4191A impedance analyzer, with a test frequency range from 1MHz to 1 GHz. The frequency dependence of dielectric constants and their losses for PZT ceramics are shown in Fig.3.

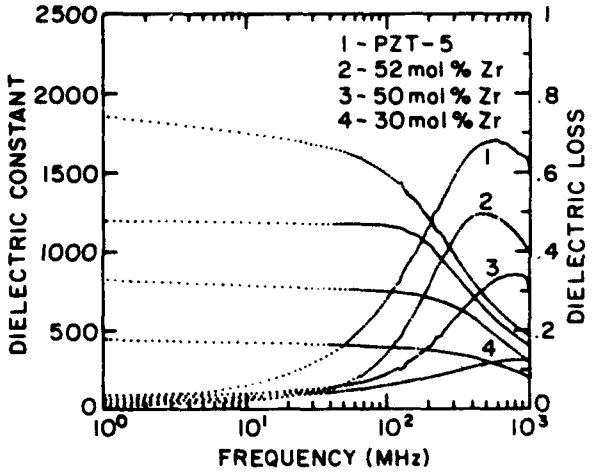


Figure 3. Dielectric constants and losses vs. frequencies in the PZT system.

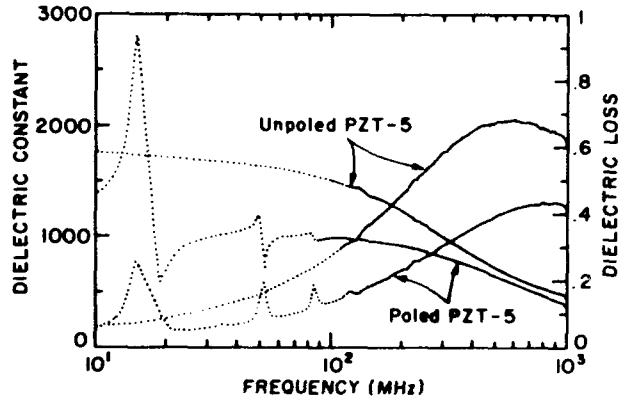


Figure 4. The dielectric dispersion in poled and unpoled PZT ceramics.

These results are similar to those of previous investigations [1]. From our results, however, it can be found that the minimum relaxation frequency (or the resonance frequency of domain wall motions) occurs in the ceramic with the composition near the morphotropic phase boundary. These experimental data are useful for estimating the effective mass of domain wall motions. Fig.4 shows the dielectric dispersions of both poled and unpoled PZT ceramic samples. The piezoelectric resonances can be clearly observed at very high frequency (around 100 MHz) due to the sample dimensions, implying that the measured data are reliable.

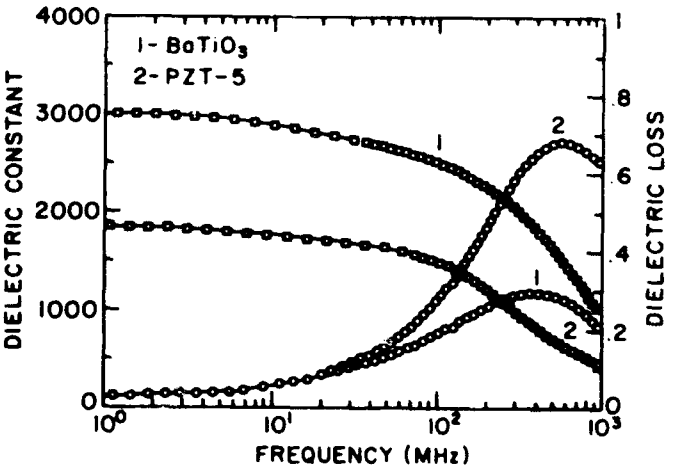


Figure 5. The dielectric dispersion in PZT-5 and $BaTiO_3$ ceramics.

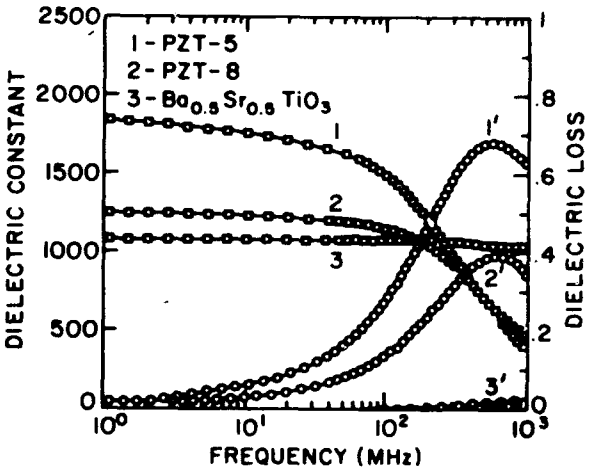


Figure 6. The dielectric dispersion in soft PZT, hard PZT and $Ba_{0.5}Sr_{0.5}TiO_3$ ceramics.

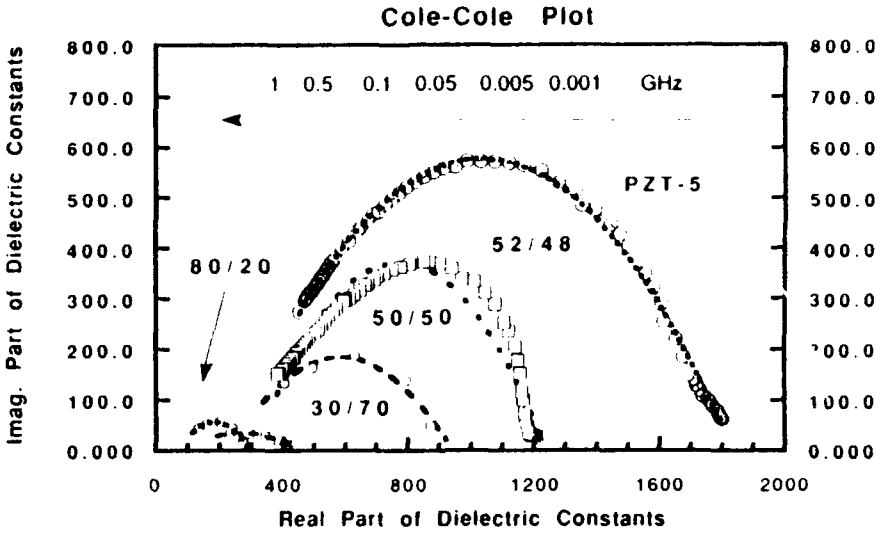


Figure 7. Cole - Cole plot of the complex dielectric constants of PZT ceramics with different Ti concentration

The dielectric dispersion in PZT, $BaTiO_3$ and $Ba_{0.5}Sr_{0.5}TiO_3$ have been presented in Figs(5) and (6). It can be found that the real value of dielectric constant of $Ba_{0.5}Sr_{0.5}TiO_3$ is almost independent of measured frequencies, which is basic consistent with previous studies [5, 12]. It should be noted that since the S_{11} parameter was estimated by the initially assumed dielectric constants, and the measurement instruments have some limitations, the measurement error is still rather significant regarding materials with ultra low loss tangents. In fact, at the frequency of 1 GHz, the measured dielectric losses (0.017--0.02) are almost one order of magnitude larger than the true values [5,12]. Fig.7 presents a Cole- Cole plot of the complex dielectric constants of the PZT system.
In summary, a quasi-lumped parameter method is discussed, which is suitable for the impedance measurements of ferroelectric ceramics in a particular frequency range (1 MHz-- 2GHz).

Acknowledgement

Authors thank Dr. U. Selvaraj for supplying the sol - gel powders of $Ba_{0.5}Sr_{0.5}TiO_3$ for ceramic sample preparation. This research was supported by the Office of Naval Research.

V. Reference

1. O. Kersten and G.Shmidt, "Dielectric Dispersion in PZT Ceramics", Ferroelectrics Vol.67, pp191-197 (1986)

2. A.V. Turik, K.R.Chernshov and V.D. Komarov, "Dielectric Dispersion in Ferroelectrics with Perovskite Structure over the Meter-Wave Range", Ferroelectrics Vol.6 pp45-47 (1973)

3. M.M.Maglione, R.Bohmer A.Loidl and U.T.Hochli, " Polar Relaxation Mode in Pure and Iron-Doped Barium Titanate", Physical Review B. Vol.40(16) pp11441- 11444 (1989)

4. Y.M.Poplavk, V.G.Tsykalov, and V.I. Molchanov, "Microwave Dielectric Dispersion of the Ferroelectric and Paraelectric Phases of Barium Titanate", Sov. Phys.Solid State Vol.10. pp2708-2712 (1969)

5. M.T. Lanagan,"Microwave Dielectric Proerties of Antiferroelectric Lead Zirconate", Ph D. Thesis, The Pennsylvania State University (1987)

6. Von Hippel A.R. "Ferroelectricity, Domain Structure, and Phase Transitions of Barium Titanate ", Rev. Modern Phys. 22(3) pp221-237 (1950)

7. S.S.Stuchly et.al., "Permittivity Measurements at Microwave Frequencies Using Lumped Elements", IEEE Trans Instrum.Meas. Vol.IM-23 pp56-62 (1974); " A Combined Total Reflection-Transmission Method in Application to Dielectric Spectroscopy", IEEE Trans. Instrum. Meas. Vol.IM-27 pp 285-288 (1978); "A Lumped Capacitance Method for the Measurement of the Permittivity and Conductivity in the Frequency and Time Domain-- A Furth Analysis", IEEE Trans. Instrum Meas. Vol.IM-24(1) pp27-35 (1975), and " A Time- Domain Technique for Measurement of the Dielectric Properties of Biological Substances", IEEE Trans. Instram. Meas. Vol.IM-21 pp425--430 (1972)

8. T.Ichino, H. Ohkawara, and N. Sugihara, "Vector Impedance Analysis to 1000 MHz", J. Hewlett-Packard, pp22-31 (1980)

9. M.F. Iskander and S.S.Stuchly, "Fringing Field Effect in the Lumped- Capacitance Method for Permittivity Measurement", IEEE Trans. Instrum. Meas. Vol.IM-27 pp107-109 (1978)

10. S.F.Adams, "Microwave Theory and Applications (Prentice-Hall Engle- W[illegible] Cliffs, NJ, (1969)

11. Van. Gemert M.J.C., "High- Frequency Time - Domain Methods in Dielectric Spectroscopy", Phillips Res. Repts 28 pp530--572 (1973)

12. J.B.Horton and G.A. Burdick, "Measurement of Dielectric Constant and Loss Tangent in Materials Having Large Dielectric Constants", IEEE Trans Microwave Theory Tech Vol.23, pp873--875 (1968) and U. Syamaprasad, R.K.Galgali and B.C. Mohanty, " Dielectric Properties of the $Ba_{1-x}Sr_xTiO_3$ System" Materials Letters 7 (1988) pp197-201

AUTOMATED SYSTEM FOR PROCESSING OF PLZT POWDERS DERIVED FROM ACETATE PRECURSORS

J R Barrett and E C Skaar
Department of Ceramic Engineering, Clemson University
Clemson, S C 29634-0907

Abstract

An IBM-PC based system to produce and control the production of PLZT powders from acetate precursors is described Problems with the development of appropriate sensing systems and algorithms are discussed A proposed prototype system is presented

Introduction

The increasing need for better manufacturing methods for new (and old) materials has been the purpose for this study. In advanced materials systems, it is often necessary to very closely monitor a process, which can be very expensive if the procedure is too complicated or too abstract to be overseen by conventional sensors and computer equipment. The development of advanced sensors can enable the reduction of labor-intensive procedures. [1] The use of advanced sensors in conjunction with high-level control methods, such as artificial intelligence, can result in a cheaper, yet higher quality product in processes that may involve complicated processing steps. This study examines the use of software and hardware combined in an automated process to produce PLZT powders from water soluble acetate precursors.

Intelligent Processing of Materials

The purpose of the method of Intelligent Processing of Materials (IPM) is to reduce the period between materials development and the production of those materials while at the same time increasing the quality of the product. The quality that is achieved through the IPM process is built-in during production and not the result of an inspection after manufacture. [1] IPM is desirable because it can improve the quality, reliability, and the yield of processed materials. [2] IPM combines the expertise of the process engineer and the knowledge of the materials scientist through the use of an expert system. [2] The expert system is a computer's software that is an application of artificial intelligence which utilizes efficient and effective data handling and retrieval to analyze and predict processing events. [3] The system is designed in such a way that corrections and/or compensations may be made instantaneously in a process so that the result is a high-quality product. This system monitors all processing steps from raw material characteristics to the final product during the manufacturing so that changes can be made in each step and in future steps to achieve the highest quality product. Process models and real-time sensors are heavily relied upon in the IPM strategy so that higher levels of control and awareness than in conventional processes can be attained. In-situ sensors can monitor complex characteristics such as microstructure in real time and combine this data with conventionally sensed data, such as temperature or viscosity, and the resulting combination is used by the expert system to make process judgements. [1] It is through these judgements that the process is improved continually to compensate for process and raw material variability.

To implement IPM in the production of powders from PLZT acetate solutions, a production process that is compatible with the requirements of an automated process is needed. The production process must be completely defined The entire process for this system includes the making of PLZT acetate solutions, the precipitation of a solid, the separation of the solid from the liquid, and the processing of the solid into a powder As the process is defined, process variables are defined and assessed These variables must be isolated and treated in a manner that is consistent with the IPM process It is also important that the equipment that makes up the system be compatible so that it can be linked efficiently and effectively. The hardware, such as mixing equipment, valves, and sensors must be linked to the software (computer) that runs the system. The hardware and software are the two major components of any IPM system, and each has its own purpose

Sensors

One of the common measurements in a coprecipitation process is the pH of the solution However, pH measurements have been found to be impractical and not suited for automated processes for this particular material system The presence of acetic acid, either from addition or from the bulk raw materials, and the high methanol concentration of the water soluble solutions prohibits an accurate and reliable measurement of pH because the glass bulb of the pH probe is strongly attacked under these conditions [4] The pH measurement is based on the Nernst equation, which assumes that the hydrogen ion activity is equal to the hydrogen ion concentration However, the Nernst equation is not valid for low hydrogen ion concentrations, and that is the condition that exists with this system In addition, the ammonium hydroxide used as a precipitating agent destroys the hydrated layer that is used to generate the potential difference for a pH reading The potential difference is the signal that is converted to a pH value It is possible to take pH measurements in this system in a laboratory environment, but it is not possible to implement this sensing method in an automated process because of the constant maintenance that is required to keep the pH electrode in operating condition A long stabilization time for a pH reading also contributed to the decision that pH is not suitable for this IPM procedure.

A method of sensing material properties that has been found to be useful for automated processes is the measurement of resistivity/conductivity. A two-conductor probe was constructed and tested for reading stabilization (response) time and stability of the reading over extended time periods with no probe maintenance The first attempts to use the probe were made using direct current as the electrical source It was found that DC measurements would not stabilize or would stabilize only after a long period of time. Because the solutions are polar in nature, it is believed that a polarization of the solution was taking place, causing the readings to drift. As a result, alternating current was used as the electrical source. Using the same probe, as shown in Figure 1, the AC measurement resulted in a quick reading response time, in the range of two to five seconds. The stabilization of the reading was also satisfactory, as the readings stabilized almost immediately. The probe was left in a variety of raw material, solvent, and batch solutions for periods of hours to days, and the readings were extremely stable.

The voltage measurement of the solution, V_2, was used to

CH3080-0-7803-0465-9/92$3.00 ©IEEE

find the resistance of the solution after the current, I, was found using Ohm's Law for the known resistor in the probe system and measuring the voltage across it, V_1. The change in resistance of the solution as the constituents were added to make a 9/65/35 PLZT acetate solution batch for coprecipitation was plotted against the weight of the total batch, as shown in Figure 2. An order of addition of constituents was chosen to best suit the homogeneity of the batch.

Generally, the resistance of the total batch solution increased as each constituent was added. This result is encouraging evidence that an AC resistance probe can be used in an IPM process for PLZT acetate solutions when an expert system has "learned" the characteristics of the batching process with respect to change in solution resistance vs weight of addition. The constituent that shows a possible exception for the upward trend is lead subacetate, for which the resistance decreased after a point. However, the neural network that runs the system can be "trained" to compensate for this result. Naturally, the weight of the batch must be monitored and the process model for this procedure must be available to the network, so that the computer can tailor the batching additions and other parameters to fit the model. At this point in the development of the system, it is believed that the lead subacetate data may actually not be much cause for concern. Because of the difficulty in keeping the material dissolved during this particular test and other conditions, such as the high evaporation rate in this open-air test, there is reason to believe that a test of a larger batch size in a closed container should solve the problem.

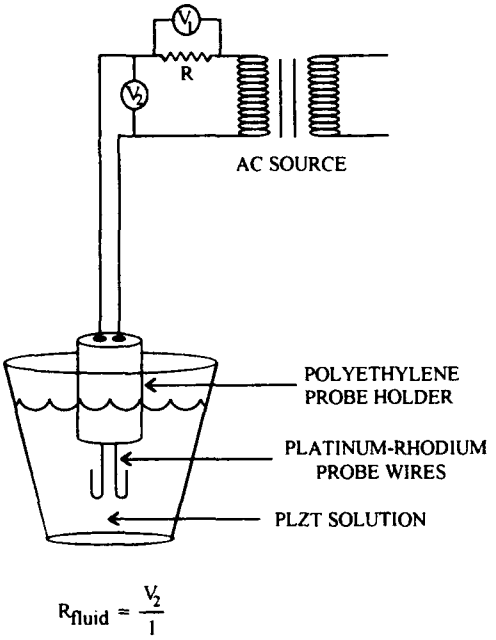


Figure 1. Method of measuring resistance of PLZT acetate solution using alternating current.

Algorithm Development

The control algorithm for this process is a two part algorithm. The first part is a normal weighing or batching algorithm. It contains a database of recipes for the solutions required to make powders of various compositions. As long as the process does not vary, and all the settings remain constant, the process is capable of running with this section of the algorithm alone. The second part of the algorithm (currently under development) is designed to sense problems and make corrections to the process.

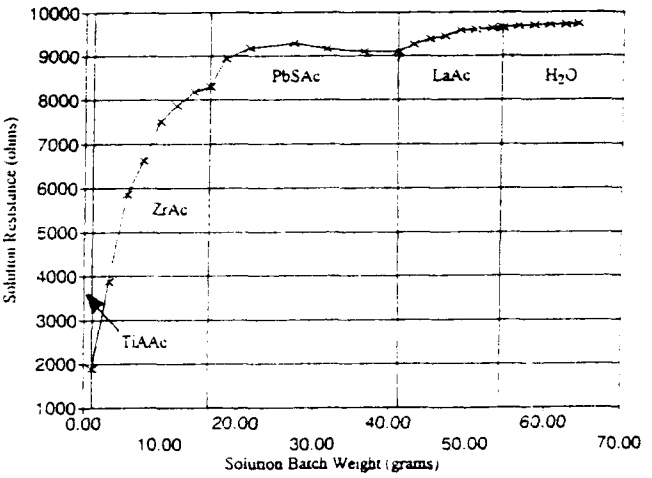


Figure 2. Solution resistance (AC measurement) for the total PLZT acetate batch as constituents were added.

This second section is an artificially intelligent program based on a neural network. It is designed to sense "out of control" conditions and make appropriate corrections to the weighing or batching algorithm.

Neural networks excel at pattern recognition, diagnosis, and decision making.[5] The idea behind this section of the algorithm is to recognize an assignable problem as it develops, and compensate. In a sense, the computer is programmed to utilize statistical process control.

For example, suppose the metering mechanism for one of the constituents became partially clogged. The result would be a variance from normal with respect to the weight and the resistance measurements for the batch. The pattern of these measurements would change. The neural network would be taught to recognize this pattern, and effect the appropriate compensation. Other types of assignable problems would also present their unique patterns which the neural network would be taught to recognize.

The unique beauty of using neural network technology for this application is that the teaching of the network is not a function of programming, but rather simulation. For the network to function, it has to be taught the patterns that specific problems create. We accomplish this by actually simulating the problem in the process. The network is programmed to learn and recognize the resulting sensor patterns. Once the network recognizes the pattern, it is programmed to compensate for the deficiency. A properly designed network, therefore, does not depend upon an exhaustive database of every problem. Rather, as experience is gained with a process, the problems and solutions can be taught to the network. The algorithm improves with operating experience and thus the process can proceed toward optimization.

Automated Batching System

The entire automated process for the production of PLZT acetate powders that is being developed has many parts that need to be both optimized and automated. The section of the process that has received the greatest attention to this point in the development of the total process is the automated batching system. Figure 3 shows this system, which utilizes manually filled reservoirs containing the liquified constituents of the PLZT acetate system which supply smaller, computer-controlled reservoirs that are used to dispense batch amounts. A switch system that consists of two stainless steel screws and a low current is used as a liquid-contact switch such that when the valve from the larger, manually controlled reservoirs is opened, the fluid will flow until the liquid

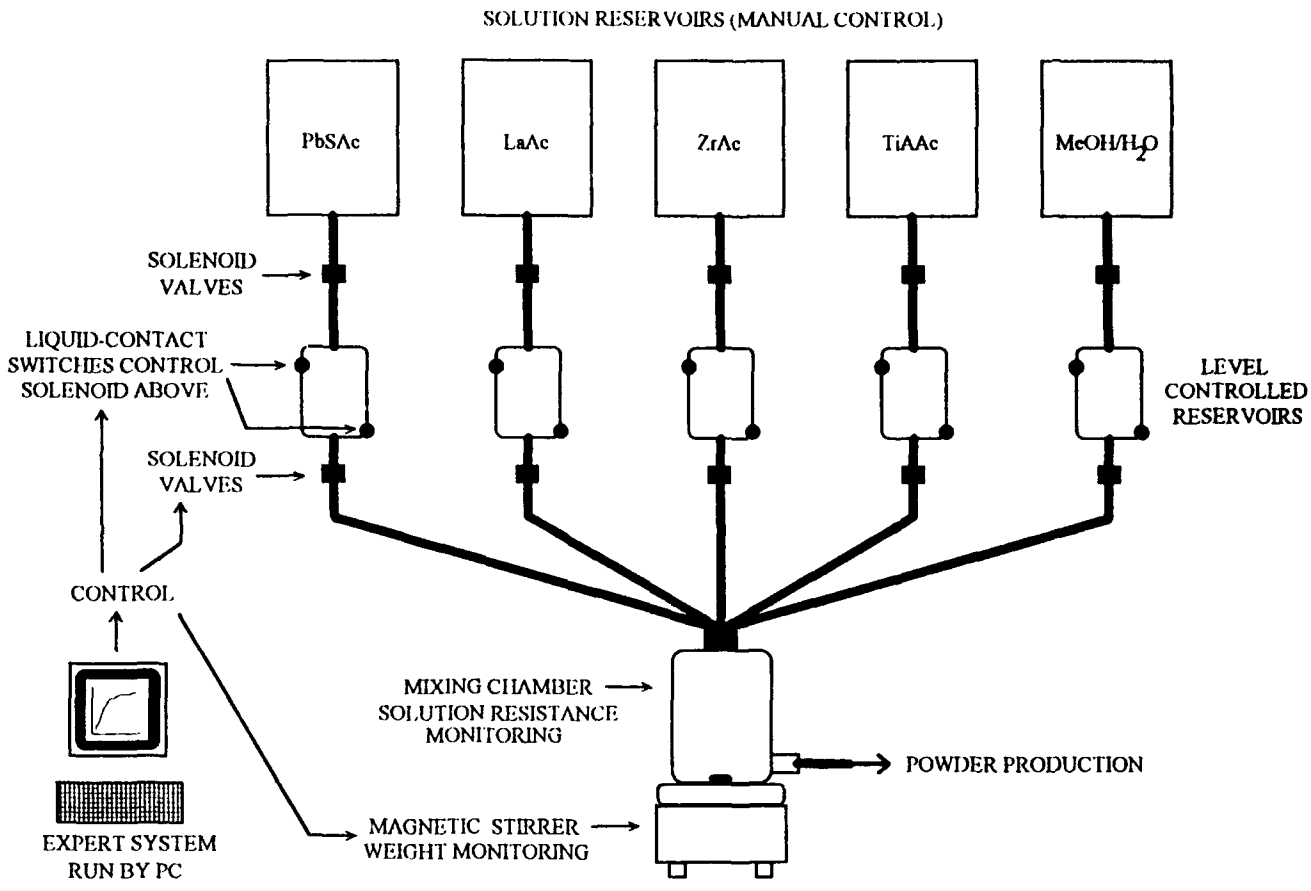


Figure 3. *Automated solution batching system controlled by IBM PC.*

completes the circuit between the two contacts. The contacts are positioned at the top and at the bottom of the reservoir. The flow of fluid in the system is controlled by sets of solenoid valves that are run by the computer. Once the circuit is completed, as the fluid fills the reservoir, the switch will be activated and the solenoid valve will be closed by the computer to stop the fluid flow. Then, the valves of the smaller dispensing reservoirs are opened for a time period that has been previously determined, based on material characteristics, to a larger mixing reservoir. The longer the time that the valve is opened, the more fluid is added to the batch.

The weight of the constituent is checked and recorded by the computer to check the accuracy of the system. The AC resistance probe will also be used here to detect any changes and be a part of the control in the batching procedures. The system is designed to be able to compensate for clogging of the valves and changes in viscosity by taking in data on the raw materials and the trends in the process. The expert system can then execute an order to make a change in the process parameters if it is necessary to keep the process at the correct level, such as leaving the valve open a longer or shorter period of time. The next step is the mixing of the constituents. After mixing, a valve is opened and the constituents will flow into the precipitation reactor for the coprecipitation process

The automated batching system will be run by the expert system in a manner in which it will be possible to enter the desired composition of the PLZT acetate solution to be made, and then the process will be changed to yield the correct amounts of each constituent needed.

Summary

The requirements for the use of better manufacturing methods in the production of materials that normally require labor-intensive procedures have been the reason for this study. The reduction of labor hours and the susbstantial improvement in quality of the materials that is possible are the integral in the theory of Intelligent Processing of Materials. An expert system can be used to develop algorithms to control the system if sensors and sensing methods can be improved or developed to suit the needs of such a data intensive system. The next step in the automation of this process is the linking of the system to the other components that are needed in the process, a coprecipitation step and a calcination/powder production step.

Acknowledgement

This work was supported by the Office of Naval Research under contract number N00014-91-J-1508.

References

[1] H. T. Yolken, "Intelligent Processing of Materials," Materials Research Society Bulletin, April 1988, p. 17.

[2] B. G. Kushner and P. A. Parrish, "The Intelligent Processing of Advanced Materials, " Intelligent Processing of Materials and Advanced Sensors, 1987, pp. 173-184.

[3] P. A. Parrish, "Design and Manufacturing of Advanced Materials and Structures," Intelligent Processing of Materials, 1990, pp. 3-15.

[4] Private Communication, Fisher Scientific, Pittsburgh, February 1992.

[5] NeuroWindows, Ward Systems Group, July 1991, pp. 1-3.

PLZT POWDERS FROM ACETATE PRECURSORS VIA COPRECIPITATION

C. Lin, B. I. Lee, and G. H. Haertling
Department of Ceramic Engineering
Clemson University, Clemson, S.C. 29634

Abstract: Various chemical coprecipitation techniques used for the production of PLZT 2/55/45 (La/Zr/Ti) powders were investigated. The coprecipitation condition corresponding to 0.5 M oxalic acid at a titration rate of 24 cc/min and at a temperature of 21°C yielded the largest surface area calcined powders, hence this condition was selected as the optimum in regard to sinterability of the powders. The characteristics of the PLZT 2/55/45 powders under the best precipitation condition were observed and evaluated. It was found by means of FTIR and XRD that the perovskite phase formation occurred at 550°C .

Introduction

There has been great interest in lead-based perovskite ferroelectric compounds within the $(Pb_{1-x},La_x)(Zr_y,Ti_{1-y})_{1-x/4}\ O_3$ system owing to their distinct electrooptic properties and their utilization for transparent ferroelectric ceramics[1, 2] . The purpose of the present work was to observe the characteristics of PLZT 2/55/45 powders obtained from some specific precipitation conditions. Before selecting the final precipitation condition, some important factors relating to the precipitation process were selected i.e., (1) type, (2) concentration, (3) rate of titration and (4) temperature of precursors. These coprecipitation conditions were then screened in regard to the specific surface area of powders obtained from these conditions. Finally, the condition for the formation of PLZT phase was investigated by heat treatment.

Experimental Procedure

Selection of Experimental Conditions

The system of the experimental design[3] is given as in Table 1.

Table 1. PLZT Coprecipitation Conditions

Type	C	K	T	R
1	0.35M	ox	21°C	12 cc/min
2	0.35M	amc	50°C	24 cc/min
3	0.50M	ox	21°C	24 cc/min
4	0.50M	amc	50°C	12 cc/min
5	0.65M	ox	50°C	12 cc/min
6	0.65M	amc	21°C	24 cc/min
7	0.80M	ox	50°C	24 cc/min
8	0.80M	amc	21°C	12 cc/min

C: Concentration (unit: Molarity)
T: Temperature of precursors.
R: Rate of titration of precipitating agent.
K: Kind of precipitating agents.
(for brevity, ox: oxalic acid solution , amc: $(NH_4)_2CO_{3(aq)}$)

Powder Preparation

The starting precursor chemicals used in this study were lanthanum acetate (LaAc), zirconium acetate (ZrAc), lead subacetate (PbsubAc) and Titanium acetylacetonate (Tiacac). The oxide content (wt%) of each precursor and the stoichiometric batch proportions are given in Table 2.

The flowchart representation for the overall preparation process is shown in Figure 1.

Table 2 Precursor and Batch Weight Proportions for PLZT 2/55/45

Oxide	PbO	La2O3	ZrO2	TiO2
mole ratio	0.96	0.01	0.547	0.448
Precursor oxide wt %	78.6	6.76	22.61	16.96
Precursor	PbsubAc	LaAc	ZrAc	Tiacac
Batch (0.0307 mole)				
Batch weight	8.537g	1.474g	9.144g	6.743g

Powder Production

Type 1 Coprecipitation Process The conditions for this process were C=0.35M, K=ox., T=21°C, and R=12 cc/min. A clear solution of 9.305 g ZrAc, 1.474 g LaAc, 6.970 g Tiacac and 8.536 g PbsubAc was prepared in 75 ml of methanol . The solution was titrated at the rate of 12 ml/min with 100 ml 0.35M oxalic acid solution under constant stirring and a constant temperature of T=21°C by means of a water bath. The precipitate suspension was stirred for 5 additional minutes after the titration was completed. Then, the entire precipitate suspension was poured into a stainless pan and was dried in an oven at 70°C. The dried powder was calcined for 7 hours in air at 550°C. The specific surface area of the powders obtained above was measured using the BET multi-point method (Model: Micromeritics, Gemini 2360).

Types 2-8 Coprecipitation Processes The conditions were the same as Type 1 except concentration, kind, temperature and rate were changed according to Table 1.

Direct Pyrolyzation Process The conditions were the same as that of Type 1 except no precipitating agent was involved.

Spray Pyrolysis Process The conditions were the same as Type 3. After titration, drying was performed by spraying the colloidal precipitate suspension into a tube furnace at 450°C. The powders were collected at the exit of the furnace.

CH3080-0-7803-0465-9/92$3.00 ©IEEE

Characterization of PLZT 2/55/45 Powders

Five samples obtained from the optimum coprecipitation condition Type 3 were processed separately with five different heat treatment conditions: (1) 220°C/2 hrs, (2) 400°C/4 hrs, (3) 500°C/7 hrs, (4) 550°C/4 hrs and (5) 550°C/7 hrs. The properties of the PLZT powders were measured using FTIR (Perkin-Elemer 1600 on KBr pellet absorbance mode), X-ray diffraction (Scintag XDS 2000, Cu Kα-radiation) and electron microscopy SEM (JEOL, JSM-848).

Results and Discussion

Selection of the best coprecipitation condition

The Type 3 coprecipitation condition was evaluated as the best condition in regard to the results of the specific surface area as shown in Table 3.

In Table 3, it was noted that the low surface area of uncalcined powders in Types 2, 4, and 6 resulted from aggregation of powders during degasing (200°C/2 hrs) in the BET test, while the low surface areas of uncalcined powders in Types 7 and 8 were mainly due to supersaturation. Also, as shown in Table 4, it indicates that a higher titration rate (comparison between Types 1 and 3 in oxalates) enhances larger number of nuclei of a new phase as well as more rapid precipitation[4]. This results in finer particles with higher surface area in both uncalcined and calcined powders. The effect of temperature as shown in Table 5 indicates that low temperature was favorable for forming powders with higher surface area. This was interpreted that high temperature affects nucleation and hence larger particles due to growth. The effect of kind of precipitant as shown in Table 6 indicates that oxalic acid was a better precipitant.

Table 3 Specific Surface Area of PLZT Powders

Type	Uncalcined	Calcined (550°C/7 hrs)
1	67.15 (m^2/g)	4.67 (m^2/g)
2	1.55	4.24
3	79.64	16.21
4	1.89	3.50
5	71.21	4.96
6	2.65	2.98
7	2.75	10.60
8	2.92	3.72
MOD	1.82	3.94

Table 4 Mean Effect of Titration Rate on Surface Area of PLZT Powders via oxalate precipitation

Rate	Uncalcined	Calcined (550°C/7 hrs)
12 cc/min	49.13 (m^2/g)	4.82 (m^2/g)
24 cc/min	41.20	3.48

Table 5 Mean Effect of Temperature on Surface Area of PLZT Powders via oxalate precipitation

Temperature	Uncalcined	Calcined (550°C/7 hrs)
4°C	56.93 (m^2/g)	4.74 (m^2/g)
21°C	73.40	10.44

Table 6 Mean Effect of Kind of Precipitant on Surface Area of PLZT Powders

Kind	Uncalcined	Calcined (550°C/7 hrs)
Ox	45.16 (m^2/g)	7.11 (m^2/g)
Ame	2.05	1.11

As shown in Figure 1 , the various processes involve liquid state mixing at the molecular level. The mixed solutions of Pb, La, Zr, and Ti precursors was coprecipitated as the oxalates or carbonates. The selection of the best coprecipitation condition was based on the largest specific surface area of the resulting PLZT 2/55/45 powder. It was found that the conditions of Type 3 coprecipitation (i.e., 0.5M oxalic acid titrated at 24 cc/min at 21°C) were optimum for producing submicron PLZT 2/55/45 powders.

The FTIR spectra of powders prepared under different calcining conditions are shown in Figure 2. The spectra show reduction in the absorbance peaks at ~1700 cm^{-1}, which is due to C-O vibration, as the calcination temperature and/or time increased. On the other hand, the peak at ~575 cm^{-1} is due to metal-oxygen bond, more specifically ZrO_6/TiO_6 octahedra vibrational mode. The increase in the peak size as the degree of calcination increased indicates the formation of crystalline PLZT powder. The small peaks at ~1600 - 1700 cm^{-1} are believed to be originated from the impurities in KBr and at ~1490 cm^{-1} from acetate . The spectra show that calcination at 550°C for 4 hrs is nearly sufficient to calcine PLZT powder for the given coprecipitated powders. There are always absorbance peaks around 2920 cm^{-1} which correspond to the residual carboxylic acid functional groups, i.e., oxalic acid.

The X-ray diffraction pattern shown in Figure 3 indicates that the Type 3 coprecipitated PLZT powder is a mixed phase which is composed of a perovskite PLZT phase and lesser pyrochlore phase (2θ=27.93° only) with an approximate mean particle size[5, 6] of 18 nm. This approximation is a calculated value based on the Scherrer relationship of the X-ray diffraction broadening. Improved results for achieving the perovskite phase were obtained by spray pyrolysis as shown in Figure 4. The reason is that spray pyrolysis provides a looser agglomeration of the uncalcined powders which is favorable to forming a better diffusivity environment for the gaseous products during thermal decomposition.

SEM micrographs in Figures 5-6 show the morphologies of the submicron particles.

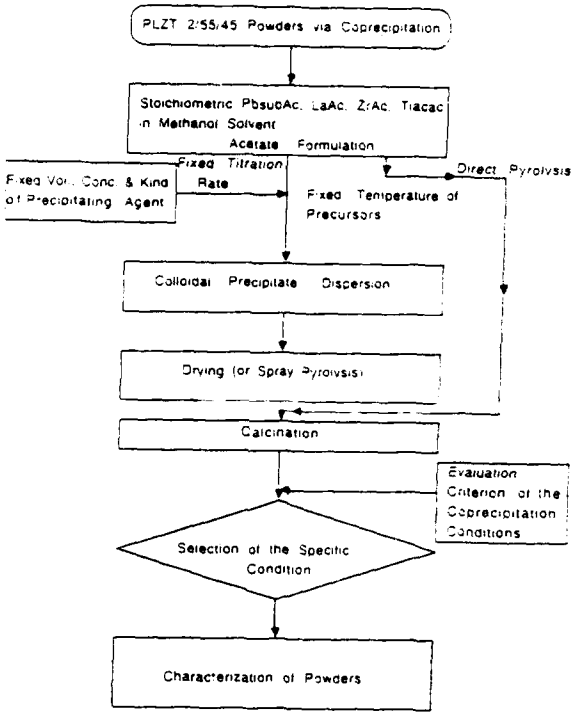


Figure 1. Flowchart of Coprecipitation Processes for PLZT 2/55/45 Powders.

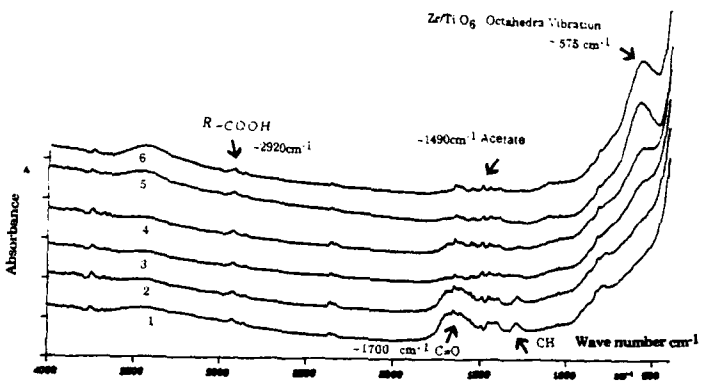


Figure 2. FTIR spectra of PLZT powders: (1) no calcination, (2) 220°C/2 hrs, (3) 400°C /4 hrs , (4) 500°C /7 hrs, (5) 550°C /4 hrs and (6) 550°C /7 hrs.

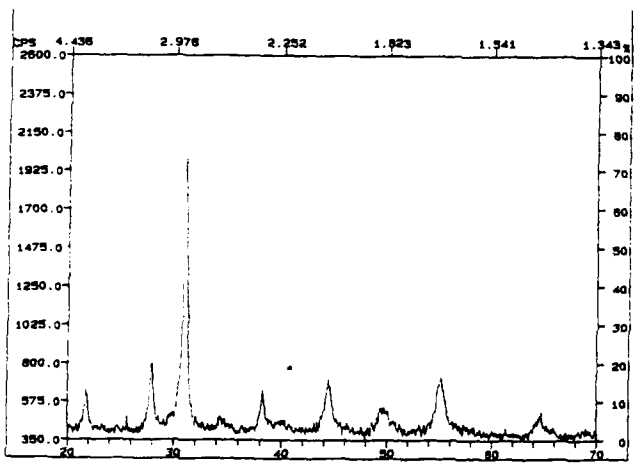


Figure 3. X-ray diffraction pattern of Type 3 calcined (550°C /7 hrs) PLZ powders.

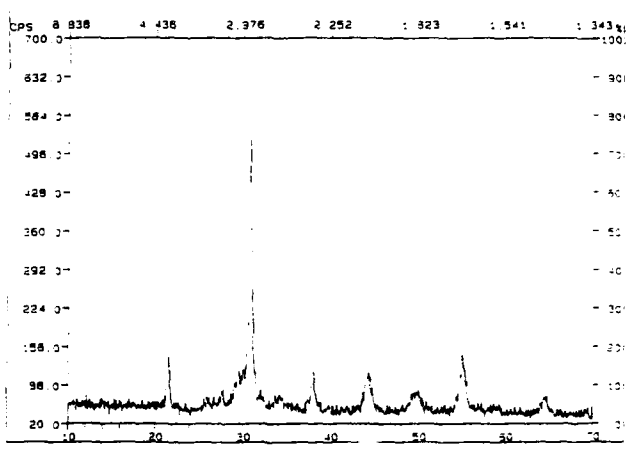


Figure 4. X-ray diffraction pattern of Type 3 calcined (550°C /7 hrs) PLZTpowders (using spray pyrolysis instead of drying).



Figure 5. SEM micrograph of Type 3 uncalcined PLZT powder.

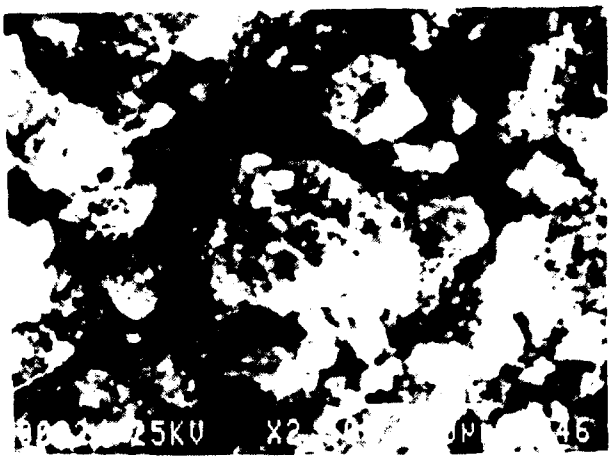


Figure 6. SEM micrograph of Type 3 calcined (550°C/7 hrs) PLZT powder.

Conclusions

There were totally eight coprecipitation processes evaluated in the production of PLZT powders. The oxalates yielded powders with larger specific surface areas (mean value 9.11 m^2/g after calcination) than that of the ammonium carbonates (mean value 3.11 m^2/g).

Under the oxalate conditions, the calcined powders prepared at a lower temperature of precursors yielded higher specific surface area than those at a higher temperature. For the lower temperature cases, the faster titration rate produced calcined powders with higher surface areas than that at the slower rate. Single phase perovskite PLZT powders were produced by using a spray pyrolysis technique for preparing the calcined powders.

Acknowledgement

The project is sponsored by the Office of Naval Research under contract No. N00014-91-J-1508

References

[1] C. E. Land, P. D. Thatcher, and G. H. Haertling, Electrooptic Ceramics, Appl. Solid State Sci. Vol. 4, R. Wolfe, Ed. Academic Press, New York, 1974.

[2] A. E. Krumins and V. Y. Fritsberg, "Semiconductor Properties and General Applications of Optical Ceramics," Ferroelctrics, vol. 35 pp. 149-154, 1981.

[3] G. Taguchi, System of Experimental Design, Unipub/Kraus International Publications, New York, 1988.

[4] M. L. Salutsky and W. R. Grace, Precipitates, Treatise on Analytical Chemistry, Part I, Vol. 1, pp 737-764, I. M. Kolthoff, Ed. The Interscience Enclopedia, New Yotk, 1959.

[5] C. R. Veale, Fine Powders, Applied Science Publishers Ltd. London, 1972.

[6] H. P. Klum and L. P. Alexander, X-ray Diffraction Procedures, Wiley, New york, 1954.

GRAIN SIZE EFFECTS IN BARIUM TITANATE

K. wa Gachigi, U. Kumar and J. Dougherty
Center for Dielectric Studies
Materials Research Laboratory
Pennsylvania State University
University Park, PA 16802

Abstract

Grain size effects in $BaTiO_3$ are examined as a function of porosity in order to evaluate the effect of micro-structurally imposed stresses on the dielectric behavior. For this investigation hydrothermal starting powder was used to minimize any extraneous effects. Fast-firing techniques were successfully used to obtain a variety of grain sizes and densities, and the data were evaluated using an analysis of the Curie-Weiss behavior. A percolation limit between 48% and 60% of theoretical density is proposed below which insufficient flux continuity is thought to limit the dielectric response of the ceramic. Above this limit, increased density appears to increase the room temperature dielectric constant for grain sizes between approximately 0.6 μm and 20 μm.

I. Introduction

The problem of size effects in $BaTiO_3$ have been studied since the mid-1950's and still remain largely unresolved. These effects are of various types including particle size, grain size and thin film effects, depending on the nature of the energetic boundary conditions for the given system.

The grain size effect occurs at grain diameter of approximately 1 μm, and is especially characterized by an anomalously high value of the dielectric constant, K, at room temperature. Various theories have been forwarded to explain this, most significant of which are the *internal stress* [1] and the *domain wall* [2] models. The former states that the absence of 90° domains at the critical grain size means that an unrelieved stress exists in the grains which causes the high values of K. The latter states that there is in fact an increase in the domain wall density at the critical grain size and that this results in an increased extrinsic contribution to K.

In a previous paper the authors reported a significant difference in the dielectric properties for two samples with approximate grain size of 0.6 μm, but with densities of 48% and 60% of theoretical[3]. This paper seeks to study the effects on the dielectric properties of varying the grain size for constant, non-zero porosity levels and vice-versa.

II. Experimental Procedure

1. Materials -

Hydrothermal $BaTiO_3$ powder (HPCP BT8, lot no. 5711-14, obtained from Cabot Corporation) was used for which the BET specific surface area was measured to be 10 m^2/g, corresponding to an equivalent spherical diameter of approximately 100 nm. From S.E.M. micrographs the particle size was found to be 150 nm+/- 33nm, as determined by a count of over 100 particles (the data so obtained was treated as a Gaussian distribution and the standard deviation is quoted as the confidence limits). The grain sizes were obtained in the same way wherever quoted. The (200) peaks on the as-received powder showed no splitting suggesting that it is in the cubic phase, though peak-broadening effects at such small sizes could also be reponsible for this. The chemical analysis of the powder revealed impurities in very low quantities as follows:

Al_2O_3 = 0.41%, CaO = 0.49% and B_2O_3, Fe_2O_3, K_2O, MgO, Na_2O, P_2O_5, SiO_2, SnO_2, SrO_2 and ZrO_2 all < 0.06%.

All other impurities were present in quantities less than 0.01%. The Ba:Ti ratio was approximately 0.99:1.

2. Processing -

The powder was mixed with 5 wt% poly(propyl carbonate) (QPAC 40 obtained from Air Products, Allentown, PA) as the binder and the pellets were pressed uniaxially at a pressure of approximately 40 000 p.s.i.(280 MPa) to a thickness of 0.5 mm in a $^1/_4$" (6.25 mm) die.

The pellets were then fast-fired[4] at temperatures between 1025°C and 1300°C and for soak-times between 5 minutes to 30 minutes by insertion into a conventional furnace which was kept at the requisite temperature. They were removed after the desired soak-time had elapsed. Some of the pellets were subsequently annealed at 600°C for four days to alleviate any thermal stresses that may have developed despite the low thermal mass of the samples. Other samples were sintered using conventional time-temperature regimes.

3. Dielectric Measurements -

The dielectric constant (K) and loss (D) were measured while cooling from 150°C to -120°C, at 0.1, 1, 10, 40,100 kHz, using a 4272 Hewlett-Packard capacitance bridge interfaced to a computer. The cooling rate was 2°C per minute. An alternating voltage of 1 V was applied. The Curie constant and Curie-Weiss temperature (C and T_0 respectively) were calculated from the dielectric data by plotting $^1/_k$ versus temperature and curve fitting. The transition temperatures were determined by plotting $^{dK}/_{dT}$ versus temperature, with the ranges quoted being determined as explained below.

CH3080-0-7803-0465-9/92$3.00 ©IEEE

III. RESULTS AND DISCUSSION

1. Microstructural Development -

As explained in the introduction, the boundary conditions of the system are very influential in determining its dielectric behavior. This is the reason for selecting hydrothermal powder as the starting material as it is highly crystalline and is thought to possess a relatively pristine surface, unlike calcined or milled powders. In addition, the narrow size distribution results in a narrow grain size distribution which is essential for comparison in a study such as this. The fact that the Ba:Ti ratio is slightly below 1 caused exaggerated grain growth and the resulting bimodal grain size distribution only at sintering temperatures above approximately 1250°C.

As expected, fast-firing at high temperatures (though < 1250°C) produced high densities with fine grain size and by this method a variety of grain sizes and densities was obtained as desired.

2. Dielectric Data-

a) Room Temperature K:- Bottcher's mixing rules were applied to the dielectric data to account for the porosity, which in some cases was as high as 50%. Values of dielectric constant measured at 70°C were used since, in many cases, the tetragonal to orthorhombic phase transition temperature (T_{o-t}) rose to around room temperature, thereby additionally increasing the room temperature value of K as has been observed by others[2,5,6] (see section 2. b)).

While for the samples with <75% of theoretical density the K values at 70°C appear independent of grain size (figure 1.A), the trend for samples with higher density is not consistent. The Curie-Weiss analysis for these samples shows that samples with very low densities -approximately 48% dense- have Curie-constants (figure 1.B) and Curie-Weiss temperatures (figure 1.C) significantly lower than they are for the more dense samples . This is believed to reflect the existence of a percolation limit between 48% and 60% density below which there is limited continuity of the electric flux lines during the application of the field. The recorded values of C and T_o appear to generally lie within the ranges of 0.5 - 2.5 E5 °C and 55 - 105°C respectively. The Curie-Weiss analysis was taken as a measure of any deviation from classical ferroelectric behavior, as is seen with Maxwell-Wagner microstructures (see section 2.c) below). To this end, an arbitrarily selected range of acceptable C values was imposed between 1.3 and 1.8 E5 outside of which the dielectric data was assumed to be suspicious. These limits are shown in figures 1B, 2B, and 3B.

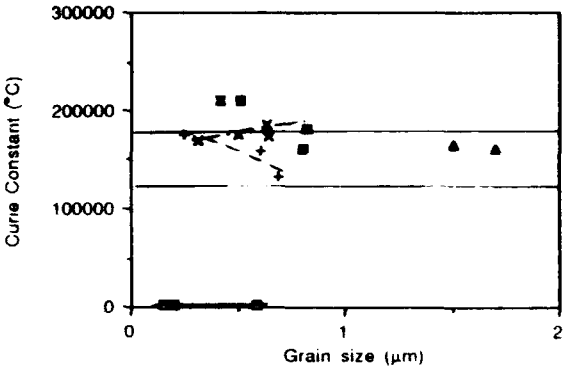


Figure 1B: Curie constant vs grain size for various densities for fast-fired BaTiO3

48% dense 61% dense 75% dense 81% dense 90% dense

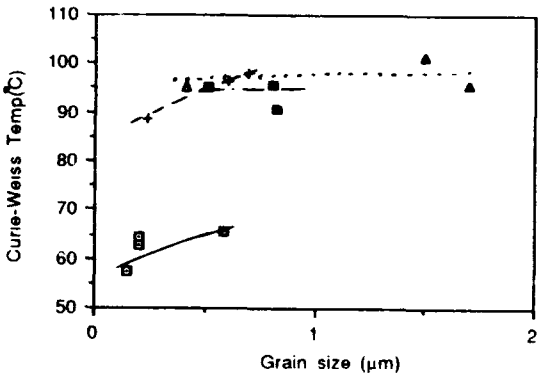


Figure 1C: Curie-Weiss temperature vs grain size for various densities for fast-fired BaTiO3

48% dense 63% dense 81%dense 90% dense

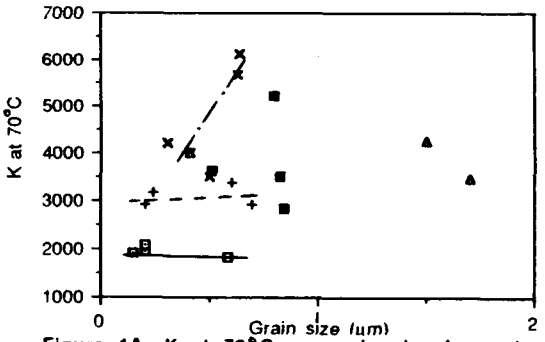


Figure 1A: K at 70°C vs. grain size for various densities for fast fired BaTiO3

48% dense 63% dense 75% dense 81% dense 90% dense

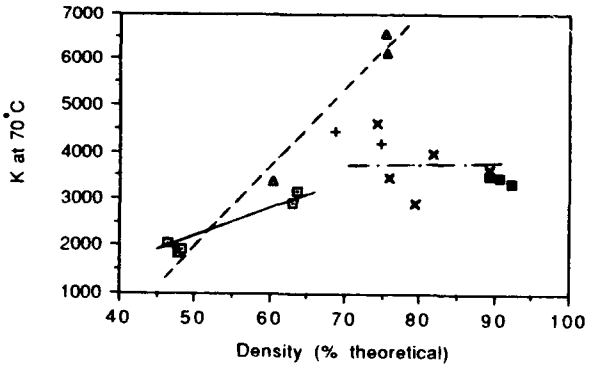


Figure 2A: K at 70°C vs density for various grain sizes for fast fired BaTiO3

0.2 µm 0.3 µm 0.45 µm 0.6 µm 0.82 µm

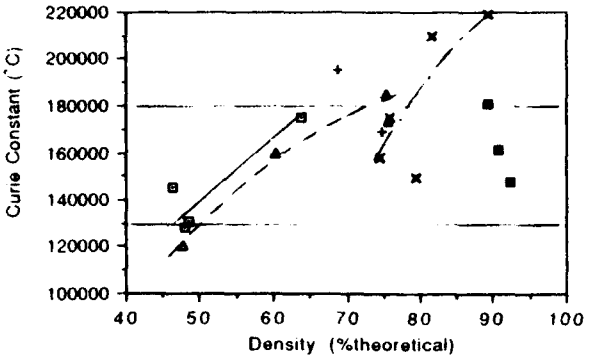


Figure 2B: Curie constant vs density for various grain sizes for fast fired BaTiO3

0.2 μm + 0.3 μm ×—0.45 μm —▲—0.6 μm ■ 0.82 μm

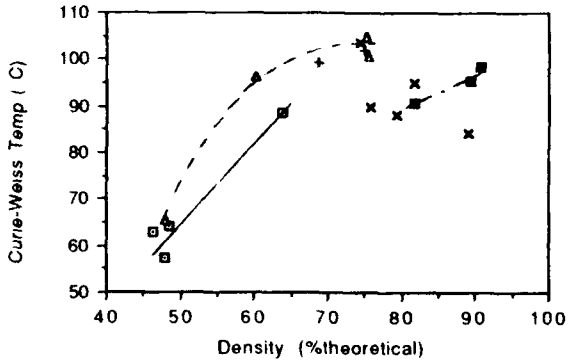


Figure 2C: Curie-Weiss temperature vs density for fast fired BaTiO3

0.2 μm + 0.3 μm × 0.45 μm —▲—0.6 μm —■ —0.81 μm

Figure 3 shows similar plots for samples which were annealed after fast-firing. Here the same percolation limit is observed though only a limited number of density ranges was examined. However for densities above 82% of theoretical, i.e. well above the proposed percolation limit, there is a higher degree of consistency in the trends observed. K is observed to indeed be a function of grain size at each of the fixed densities, initially increasing to a maximum at about 1 μm, and then dropping for the very large grain sizes (90% dense range of samples - figure 3.A). The Curie constant (figure 3. B) is also seen to lie within the selected limits, with the exception of one value at 80% of theoretical density. What is expected but not

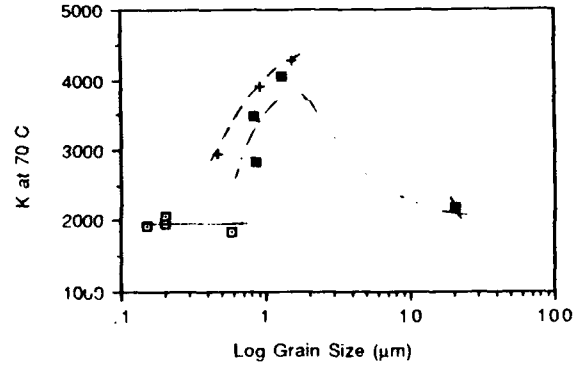


Figure 3A: K at 70 C vs grain size for various densities for fast fired and annealed BaTiO3

48% dense + 80% dense ■—90% dense

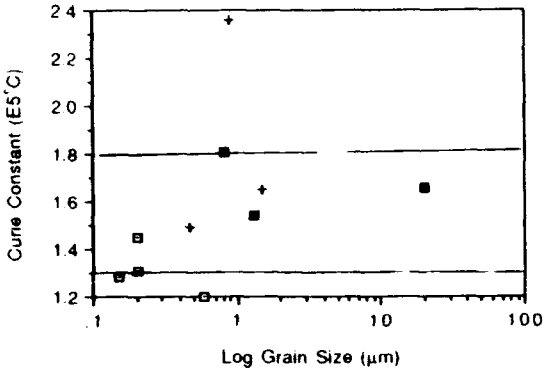


Figure 3B: Curie constant vs grain size for various densities for fast fired and annealed BaTiO3

48% dense + 80% dense ■ 90% dense

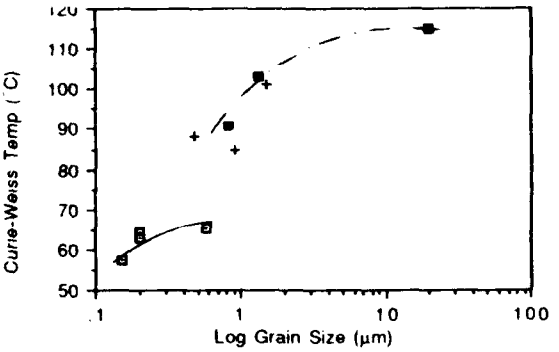


Figure 3C: Curie-Weiss temperature vs grain size for various densities for fast fired and annealed BaTiO3

48% dense + 82% dense —■— 90%dense

seen is generally higher values of K for the samples which are on *average* 90% dense, than those that are about 80% dense, assuming greater stress results at higher densities. Unfortunately the lack of more data points meant that these rather close density values could not be compared with others.

b) <u>Shift of Transition Temperatures:-</u> A second anomaly, the increase in the orthorhombic to tetragonal transition temperature (T_{o-t}) to around room temperature,was observed (figure 4), as has been reported by others[2,5,6]. An increase of the rhombohedral to orthorhombic transition temperature (T_{r-o}) was also seen, although the transitions became very diffuse at grain sizes smaller than around 0.3 μm.

The Curie temperature was observed to decrease gradually as a function of grain size. This appears to fit in well with the internal stress model which envisages a complex stress on grains which has a resultant hydrostatic nature, therefore suggesting that the room temperature tetragonal phase will be forced back to the cubic phase. Such trends have been observed on single crystal $BaTiO_3$ subjected to hydrostatic pressure by Merz[7] and Samara[8] in separate studies. However, Merz[7] observed T_{o-t} to initially decrease as hydrostatic pressure increases, and eventually increase at much higher levels of stress (1500 atm) than can be expected in these ceramics. It can only be concluded therefore that actual stress system on the grains in these ceramics is very complex.

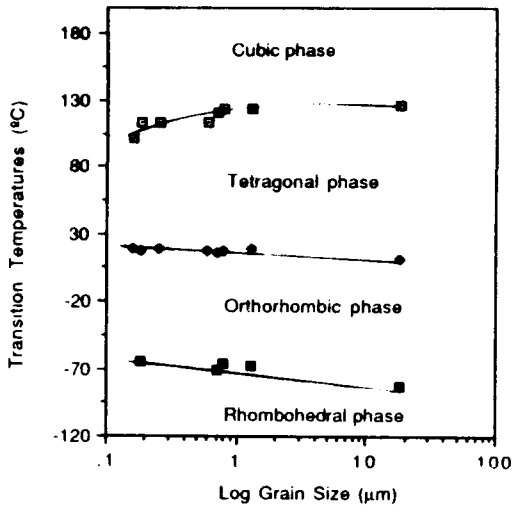


Figure 4: Transition temperatures as a function of grain size

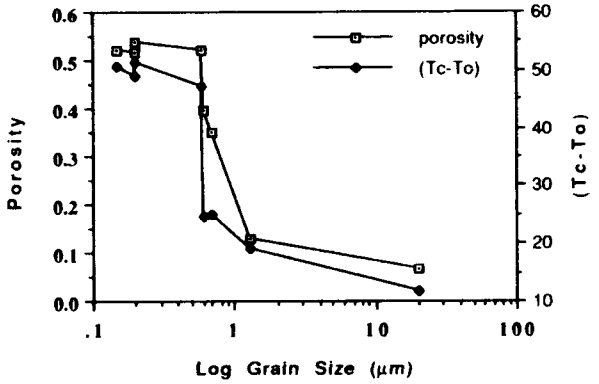


Figure 5: Porosity and (Tc - To) vs Grain Size

c) Curie-Weiss Analysis:- The Curie-Weiss equation is given as:

$$K = C / (T - T_o)$$

where C is the Curie constant, T_o the Curie-Weiss temperature and T is the measuring temperature (the independent variable). For samples with diffuse phase transitions, the relationship was plotted at a temperature above the value of T_c obtained in order to obtain a linear curve. The data indicate a scatter in C as grain size decreases, with a more definite decrease in T_o, especially for densities below the 60% mark. The difference between T_o and T_c is about 10°C for $BaTiO_3$, which is characteristic of ferroelectrics with a first order phase transition. The plots of the log of the grain size versus T_c-T_o and versus porosity were found to coincide closely (figure 5). Lines and Glass note that the difference (T_c-T_o) decreases with increasing pressure[9]. Figure 5 therefore appears to support the theory that increased density increases the stress on the grains.

Graham et al examined the Curie-Weiss behavior of $BaTiO_3$ and reported that their dielectric dispersion characteristics reflected microstructural inhomogeneity of the Maxwell-Wagner type (i.e. conducting grains with insulating grain boundaries) resulting in room temperature and maximum dielectric constants of 15,000 and 50,000 respectively in some of their samples[10]. Such microstructures may be the result of defects carried over from the starting powder. As mentioned earlier, one of the reasons for selecting hydrothermal powder for this work was to avoid such problems. For a range of frequencies between 100 Hz and 100 kHz no appreciable change in the values of C and T_o for the annealed samples was noticed suggesting that conductivity was not a factor in this case.

IV. Conclusions

1) Room temperature K seems to display a maximum for grain size of just above 1μm below which it drops off, for samples with densities greater than approximately 60% of theoretical.

2) The data suggests the existence of a percolation limit between the densities of 48% and 60% of theoretical.

3) Above this limit there appears to be an increase in K as grain size increases while holding density constant, with a peak at about 1.3 μm.

4) The effect of density as a variable appears to be less influential on the dielectric data above the proposed percolation limit, although a more thorough statistical analysis would be desirable to confirm this.

5) T_c decreases with decreasing grain size, while T_{o-t} and T_{t-o} increase, over the range of grain sizes examined.

6) Curie-Weiss analysis was found to be a good measure of the microstructures obtained by fast-firing, e.g. under conditions that prevent adequate diffusional processes from occurring, anomalous Curie-Weiss behavior was witnessed. Annealing for temperature and time conditions selected so as to avoid grain growth (600°C for four days) removed the anomalies.

REFERENCES

1. W.R.Buessem, L.E. Cross and A.K. Goswami, "Phenomenological Theory of High Permittivity in Fine-Grained Barium Titanate", J. Am. Ceram. Soc., vol. 49, pp. 33-36, January 1966.

2. G. Arlt, D. Hennings and G. de With, "Dielectric Properties of Fine-Grained Barium Titanate Ceramics", J. Appl. Phys., vol. 58, pp. 1619-1625, August 1985.

3. K. wa Gachigi, U. Kumar and J. Dougherty, to be published in Ferroelectrics.

4. H. Mostagachi, and R.J. Brook, " Production of Dense and Fine Grain Size $BaTiO_3$ by Fast Firing", Trans. J. Br. Ceram. Soc., vol. 82, pp. 167-170, 19832.

5. A.J. Bell, A.J. Moulson and L.E. Cross, "The Effect of Grain Size on the Permittivity of $BaTiO_3$", Ferroelectrics, vol.54, pp. 147-150, 1984.

6. T. Kanata, T.Yoshikawa and K.Kubota, "Grain-Size Effects on Dielectric Phase Transitions of $BaTiO_3$ Ceramics", Solid State Communications, vol. 62, pp. 765-767, 1987.

7. W.J. Merz, "The Effect of Hydrostatic Pressure on the Curie Point of Barium Titanate Single Crystals", Phys. Rev., vol.77, pp.52-54, April 1950.

8. G.A. Samara, "Pressure and Temperature Dependences of the Dielectric Properties of the Perovskites $BaTiO_3$ and $SrTiO_3$", Phys. Rev., vol. 151, pp. 378-386, Nov. 1966.

9. M.E. Lines and A.M. Glass, Principles and Applications of Ferroelectric and Related Materials, Oxford (Eng.), Clarendon Press, 1977, ch.5, p. 161.

10. H.C. Graham, N.M. Tallan and K.S. Mazdiyasni, "Electrical Properties of High Purity Polycrystalline Barium Titanate", J. Am. Ceram. Soc. , vol. 54, pp. 548-553, Nov. 1971.

Piezoelectric, Electrostrictive

The FLEXIBLE COMPOSITE FERROELECTRIC FUNCTIONAL FILMS*

Daben YANG
Electronic Polymers Research Laboratory (EPRL)
Department of Materials Science and Engineering
University of Electronic Science and Technology of China
Chengdu 610054, Sichuan, P.R. China

ABSTRACT

This paper investigates the concepts of structure, mechanism and characteristics of flexible composite functional films in modern materials science of electronic composites. It also studies the films' basic principles and flexible characteristic features, and utilizes the dispersion model in 2-phase flexible composite framework to effectively explain the properties of composite piezo- and ferroelectirc mechanism. The theory and experiments are consistent.

INTRODUCTION

Electronic materials, components and devices play a leading and fundamental role in new high technology development in modern electronic science. In particular, electronic composite functional materials and their applications are one of the important directions in the worldwide development of electronic materials, components and devices in 1990's. The wide ranges of characteristics and applications of electronic composite functional materials, which have been developed from various kinds of modern electronic functional materials, originate in fact from diverse composite processes[1]. Table 1 summarizes the functional composite principles and characteristic types of modern electronics.

Table 1 Functional composite principles of modern electronics

Principles	Characteristic types
composite effects	summation, (independence, union); multiplication
base states	metallic base, ceramic base; polymer base
phase states	two-phase; multi-phase
connectivity types	1, 2 and 3-dimensional
structural properties	flexibleness; composite class; symmetry; percolation
functional properties	dielectric, sensitive, transducing,electret, conductive, magnetic, bioelectrical, molecular electrical"

Recently, electronic flexible composite piezo- and ferroelectric films have brought up wide research interest and been a focus of international ferro- and piezoelectric study[2]. Within the framework of "flexible composite functional films", flexible composite piezo- and ferroelectric characteristics signify into the following ways:

* This project is funded by the National Natural Science Fundation of China.

(1) flexibleness structure: flexible thin film;
(2) flexibleness parameters: low C_{33}, low density ρ and low acoustic impedance Z_a;
(3) flexibleness functions: flexibleness strength, deformation processing, low density matching, wide frequency band response, sensitive transducing of weak signal,etc.

The author studies the most world-widely typical ferroelectric polymer PVDF and PVDF-based flexible composites PVDF/BT, PVDF/PZT, PVDF/PCM, etc., as well as other kinds of flexible composite piezo- and ferroelectric films of different organic /inorganic systems. They contain remarkable technological and scientific values in modern electronic sensitivity, energy transducing, electret, and electrical power areas[3,4].

EXPERIMENTAL

1. Preparation of Flexible Composite Thin Films

Analysis shows that whether a 2-phase composite film is structurally stiff or flexible depends mainly on base state and connectivity type of the composite system. Obviously, composites with metallic and ceramic bases are stiff while composites with polymer base may be flexible. On the other hand, the connectivity type is also crucial for 2-phase composite systems. According to the classification scheme by R.E. Newnham of The Pennsylvania State University of the U.S.[5], but using polymer base categorization (polymer/ceramic, i.e. P/C composite categorization) instead of using ceramic base categorization (ceramic/polymer, i.e. C/P composite categorization), we may have the following results. As polymer (P) phase exhibits flexibleness while ceramic (C) phase exhibits stiffness, all P/C composite systems can be primarily classified into three types by 2-phase connectivity:
(1) flexible composite (F type), i.e. all those with zero dimension of stiff ceramic phase, for example, 3-0, 2-0, 1-0 and 0-0 types;
(2) stiff composite (S type), i.e. all those with three dimensional stiff ceramic phase, for example, 0-3, 1-3, 2-3, 3-3 types;
(3) semi-stiff-semi-flexible composite (SF type), i.e. all those with flexible polymer phase and ceramic phase taking one or two dimension, for example, 1-1, 1-2, 2-1 and 2-2 types. Fig. 1 shows the flexible, stiff and semi-flexible-semi-stiff connectivity types of the P/C 2-phase composite systems.

CH3080-0-7803-0465-9/92$3.00 ©IEEE

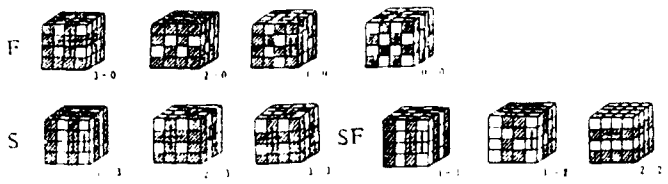


Fig.1 Connectivity types of P/C 2-phase composite systems

Therefore, the flexible composite films for experimental samples adopt electronic polymer PVDF-based resin (SOLEF 1008, Germany; CSFP, China) and ferroelectric ceramics BT, PZT, PCM (puratronic, Philips, China) clusters (50~80% wt), in the form of 3-0 type 2-phase flexible composite system, to prepare 50~200 μm thin films of PVDF/BT, PZT and PCM, etc. by the solution flow extension method. Such composite film technique and structure provide valuable implication for industrial manufacturing and applications.

2. Piezo- and Ferroelectric Treatment

Experiments show that the keys of composite piezo- and ferroelectric functional film technique lie in: (1) composite film itself; (2) piezo- and ferroelectric treatment; (3) energy transducing structure. After the requirements of flexible composite proportion, prescription, cluster size and shape, and uniform film formation are all satisfied, the piezo- and ferroelectric polarization and appropriate treatment become the critical determining factors for composite piezo- and ferroelectric properties[6].

In the piezo- and ferroelectric treatment of this study, the experiments focus on improvement in the following two approaches:
(1) polarization method: thermal polarization, discharge polarization, and polarizations aided by low-frequency impulse or laser;
(2) polarization condition: polarization field strength E_p, temperature T_p, time t_p, pattern P_p and processing techniques. All these factors help to control composite piezo- and ferroelectric micro-domain and polarization structure.

3. Characteristics of Composite Piezo- and Ferroelectric Properties

Research shows that P/C 2-phase flexible composite functional film systems have a distinguishable characteristic of combining mechanical flexibleness and comprehensive piezo- and ferroelectric properties. Such composite functional properties can be represented by:

(1) mechanical flexibleness (C_{33}, ρ, Z_a);
(2) flexible composite functions:

A. composite dielectric (ε_Σ, $tg\delta_\Sigma$);
B. composite piezoelectric (d_{33}, g_{33});
C. composite pyroelectric (P_c);
D. composite ferroelectric (P_r, E_c, T_c);
E. composite coupling (K_{33}), sensitive responsive (V_s).

Due to the similarity between polymer-based flexible composite films and flexible polymer films, the former's piezo- and ferroelectric resonance is much weaker than that of inorganic crystals and ceramics. Hence the flexible composite piezo- and ferroelectric characteristic parameters may be characterized by two approaches: direct test method and indirect calculation method. Some calculational equations of 2-phase flexible composite coupling parameters have been derived in this research and are given as follows:

(1) stiffness constant

$$C_{33} = \frac{3(1-\phi)C_{33}^1 + (2+3\phi)C_{33}^2}{(3+2\phi)C_{33}^1 + 2(1-\phi)C_{33}^2} C_{33}^1 \qquad (1)$$

where C_{33}^1, C_{33}^2 are the stiffness constants of phase I and II respectively, and ϕ is the volume percentage proportion of phase II.

(2) acoustic impedance

$$Z_a = \rho (C_{33}/\rho)^{1/2} \qquad (2)$$

where ρ is the composite volume density, and C_{33} is the composite stiffness constant.

(3) electromechanical coupling factor

$$K_{33} = (C_{33}/\varepsilon_0 \varepsilon_r)^{1/2} d_{33} \qquad (3)$$

where ε_r is the composite relative dielectric constant, and d_{33} is the composite piezoelectric strain constant.

RESULTS AND DISCUSSIONS

1. Flexible Composite Piezo and Ferroelectric Properties

Under the conditions of meeting the key technical requirements for film formation, treatment and structure, the P/C flexible composite films in this study achieve high levels of comprehensive piezo- and ferroelectric properties. As illustrated in Table 2, the 2-phase composites possess a feature of summation of the two single phases[7].

Table 2 Flexible composite piezo- and ferroelectric properties

Films	ρ (10^3Ks/m³)	C33 (10^9N/m²)	εr	d33 PC/N	g33 10^{-3}Vm/N	Za 10^6Kg/m²s	K33 %	Pr μC/cm²	Ec MV/m	Tc °C
PVDF	1.78	2.5	13	12	113	2.1	5.6	0.1	4.6	165
PZT	7.8	36	1300	200	16.5	16.7	34	22.5	1.35	180
PVDF /PZT	5.6 5~6	8.8 8~9	85 40~85	50 30~50	66.5 48~85	6.6 6~7	17 10~17	3.8 2~8	13 10~15	180 180~220

A large experimental data set shows that the PVDF film's piezo- and ferroelectric properties depend on film formation conditions, thin film's one-way or two-way extension and the extension ratio (generally ≥ 3~5), and piezo- and ferroelectric polarization treatment conditions and techniques.

In particular, the causal factor for piezo- and ferroelectric micro structure still lies in the transformation of α crystal type into ß crystal type and the orientation effect of C-F polarized dipole moment in PVDF. Single phased PVDF films have excellent mechanical flexibleness (ρ,C_{33}), absorption piezoelectricity (g_{33}) and water media biological coupling property (Z_a). However, the weak piezo- and ferroelectric domain effect determines their unsatisfactory emission piezoelectricity (d_{33}), electro-mechanical coupling (k_{33}) and ferroelectric storage property (P_r).

In contrast, the ferroelectric ceramics PZT, when meeting the 2-phase system's ferroelectric domain structure and polarization treatment conditions, based on its ferroelectric spontaneous polarization domain mechanism, provides strong piezoelectricity d_{33}, coupling k_{33} and ferroelectricity Pr and E_c, except for that the mechanical stiffness and high acoustic impedance limit a wide application in water media coupling and sensitive transducer testing.

The 3-0 type 2-phase flexible composite P/C system, based on the composite functional summation principle, has achieved the overall composite goal of combining high piezo- and ferroelectric properties. Compared with stiff composites, flexible composites excel in the improved piezo- and ferroelectric properties in addition to a focus of mechanical flexibleness strength, low density match coupling, and sensitivity transducing property. Our experimental tests show that the P/C flexible composite system has remarkably excellent composite dielectric properties (ε'~T°C relation in Fig. 2 and ε"~T°C in Fig. 3), composite piezoelectric property (d_{33}~E_p in Fig. 4), composite ferroelectric properties (P_r~E_p in Fig. 5, ferroelectric hysteresis loop in Fig. 6: a.PVDF, b.PZT, c.PVDF/PZT).

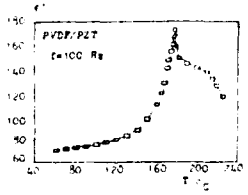


Fig. 2 ε'~T°C relation

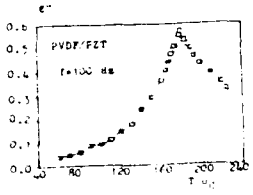


Fig. 3 ε"~T°C relation

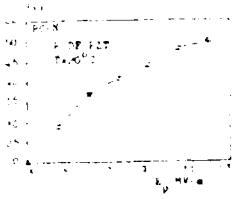


Fig. 4 d_{33}~E_p relation

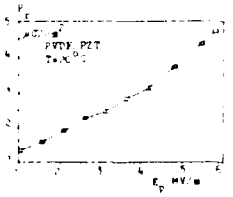
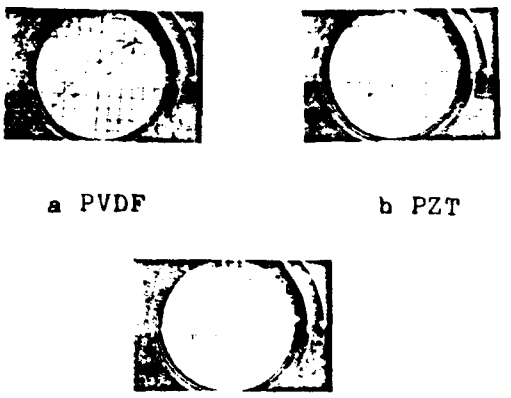


Fig. 5 P_r~E_p relation

In the meantime, the ferroelectric characteristic frequency spectrum and field strength spectrum of flexible composite films show that all ferroelectric response curves exhibit a composite characteristic tendency towards the flexible phase relative to the single stiff phase (ceramic) and single flexible phase (polymer). This is typical "flexible composite effect"[8].



a PVDF b PZT

c PVDF/PZT

Fig. 6 Ferroelectric hysteresis loops

2. Flexible Composite Dispersion Model

Many micro-structural analyses (metallic phase MG, scanning electronic microscopy SEM, infrared ray IR) show that the P/C flexible composite 3-0 type 2-phase system (phase I polymer, phase II ceramic) is a composite structural system with phase II clusters distributed highly uniformly in phase I base.

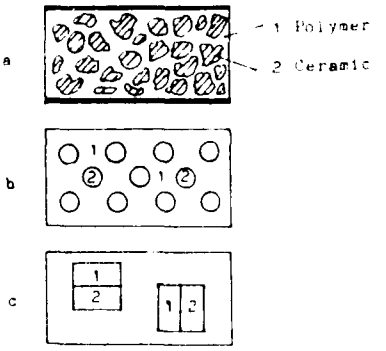


Fig. 7 Flexible composite dispersion model

Based on the 2-phase flexible composite structural characteristics and composite piezo- and ferroelectric effect principles, the author proposes a concept of flexible composite "dispersion model"[1]. The model describes the polymer-based 3-0 type flexible composite film as a 2-phase dispersive composite system with series connection and parallel connection uniformly distributed, as illustrated in Fig. 7. This model gives the system of equations for the dispersive composite with a certain proportion of series connection and parallel connection:

$$\begin{cases} D = (1-\delta)D_1 + \delta D_2 \\ E = (1-\varphi)E_1 + \varphi E_2 \end{cases} \qquad (4)$$

$$\begin{cases} \delta = (\varepsilon_\Sigma - \varepsilon_1)/(\varepsilon_2 - \varepsilon_1) \\ \varphi = (\varepsilon_\Sigma \varepsilon_2 - \varepsilon_2 \varepsilon_1)/(\varepsilon_\Sigma \varepsilon_2 - \varepsilon \varepsilon_1) \\ \varepsilon_\Sigma = f(\phi) \end{cases} \qquad (5)$$

where D is the electrical displacement, E is the field strength, P is the polarization strength, ε is the dielectric constant, ϕ is the volume percentage of phase II, and σ,φ are composite coefficients of series connection and parallel connection.

According to this study's 2-phase flexible composite dispersion model, the author extends the 1-phase piezoelectric composite model by T. Furukawa et al of Japan[9]. The assumptions for adopting the dispersion model are as follows:

(1) Two phases are both homogeneous.
(2) Two phases do not permeate into each other with defectless interfaces.
(3) Phase II is uniformly distributed as sphere in phase I.
(4) Two phases both have piezo/ferroelectric properties.

$$\varepsilon_\Sigma = \frac{2\varepsilon_1 + \varepsilon_2 - 2\phi(\varepsilon_1 - \varepsilon_2)}{2\varepsilon_1 + \varepsilon_2 + \phi(\varepsilon_1 - \varepsilon_2)}\varepsilon_1 \qquad (6)$$

$$d_\Sigma = (1-\phi)\frac{c_1}{c_2} L_{E_1} L_{S_1} d_1 + \phi \frac{c_2}{c_1} L_{E_2} L_{S_2} d_2 \qquad (7)$$

$$P_\Sigma = \frac{\varepsilon_\Sigma - 1}{\varepsilon_1 - 1}(1-\varphi)P_1 + \frac{\varepsilon_\Sigma - 1}{\varepsilon_2 - 1}\varphi P_2 \qquad (8)$$

where ε_1, ε_2; C_1, C_2; d_1, d_2, P_1, P_2 are the relative dielectric constants, stiffness constants, piezoelectric strain constants, and ferroelectric residual polarization strengths of phase I and II respectively.

The repeated computer aided analysis has verified that the dispersion model in this study is consistent with the 1-phase composite piezo- and ferroelectric properties, and is also applicable to the 2-phase piezo- and ferroelectric composites. Therefore the dispersion model extends the T. Furukawa model.

3. Piezo- and Ferroelectric Mechanism of Flexible Composites

Our micro-mechanism study shows that the piezo- and ferroelectric mechanism of P/C flexible composites may originate from three sources:
(1) heterogenous deformation of the composite film,
(2) dipole moment change of the composite phase,
(3) space charge effect in the composite system[9,10,11,12].

From a comparative study of the X-ray diffraction analysis on single-phased P.VDF, single-phased PZT and 3-0 type two-phase PVDF/PZT composite system, it is shown in Fig. 8:

(1) Around $2\theta = 44°$, the diffraction peaks (002) and (200) reflecting the PZT ferroelectric domain have a reversed strength change before and after polarization.

(2) Around $2\theta = 21°$, the change of the two diffraction peak values before and after polarization may correspond to the transformation of two phases of PVDF and PZT.

Therefore if the piezo- and ferroelectric treatment ensures adequate technical conditions, the 3-0 type 2-phase flexible composite system in this study will obtain its comprehensive functional mechanism from the following two sources:
(1) inorganic ferroelectric phase: spontaneously polarized ferro domain of stiff ceramic PZT etc..
(2) organic heterogenous deformation phase: ß crystal type of flexible polymer PVDF molecular chain and the oriented ordering of C-F bond dipole moment. This is a "flexible composite ferroelectric ordered domain" effect[1].

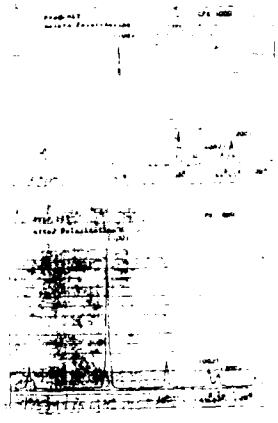


Fig. 8 3-0 type 2-phase composite X-ray diffraction graphs

CONCLUSION

The 3-0 type flexible composite piezo- and ferroelectric thin films of polymer base PVDF and ferroelectric ceramic series PZT, namely PVDF/PZT series, possess remarkable properties of low C_{33} *mechanical flexibleness, high synthesized composite* dielectric ε_Σ, good piezoelectric d_{33} and g_{33}, ferroelectric P_Σ and low Z_a coupled matching features.

The 3-0 type 2-phased flexible composite functional structure exhibits an oriented addition of the stiff ferroelectric domain and the flexible heterogenous deformed dipole moment, namely "flexible composite ferroelectric ordered domain" effect.

REFERENCES

1. Daben YANG, ISE7, CH 3029-6/91/000-0518, IEEE, 1991.
2. D.S. McLachlan, M. Blaszkiewicz, R.E. Newham, J. Am. Ceram. Soc. 73 [8], 1990.
3. YANG Daben, ISE 6, 88/CH/2593-2, IEEE, 1986.
4. YANG Daben, Ferroelectrics, Vol. 101, 1990.
5. R.E. Newnham, et al., Mater. Res. Bull, 13, 1978.
6. Daben YANG, ISAF '90, IEEE, 1990.
7. Daben YANG, et al., *Polymers and Biomaterials*, Elserier Sci. Publ. 1991.
8. D.B. YANG, et al., ISVTS '91, 1991.
9. T. Furukawa, K. Ishida, E. Fukada, J. Appl. Phys., 57, 1979.
10. M.G. Broadhurst, et al., Ferroelectrics, Vol. 60, 1984.
11. G.M. Sessler, *Electrets*, Springer Verlag, 1987.
12. M. Ieda, IEEE trans. on Elec. Insulat., Vol. E1-19, No. 9, 1984.

HYSTERESIS BEHAVIOUR AND PIEZOELECTRIC PROPERTIES OF Nb DOPED PLZT CERAMICS

K.V. Ramana Murty, K.Umakantham, S.Narayana Murty, K.Chandra Mouli and A.Bhanumathi
Solid State Physics Laboratories, Department of Physics
Andhra University, Waltair-530 003 **INDIA**

ABSTRACT

Lanthanam modified PZT ceramics are widely used for device applications. The effect of Niobium doping on the microstructure, hysteresis and piezoelectric properties of PLZT (5/65/35) ceramics is described. Saturation polarisation is obtained in the 0.5 mole % Nb added composition. Niobium doping inhibits the grain growth. Room temperature dielectric constant increased and the ferrolectric Curie temperature decreased with Nb content. Optimum piezoelectric coefficients are obtained in the 0.5 mole % Nb added ceramic composition.

INTRODUCTION

Among the perovskite compounds, Lead Zirconate Titanate (PZT) is extensively used for device applications (1). The properties of these materials are influenced by the amount and type of substitutions. Ferroelectric and piezoelectric properties of PZT are enhanced when doped with Nb, as reported by several authors (2-4). Also La modified PZT (**PLZT**) ceramics are widely used (5) for applications such as high frequency filters, surface acoustic devices etc, requiring high relaibility. It would be interesting to study the effect of **Nb** substitutions in **PLZT** ceramics. In this work, we report the microstructure, ferroelectric and piezoelectric properties of Nb doped **PLZT (5/65/35)**. The composition PLZT (5/65/35) was choosen as the ceramics in the rhombohedral phase exhibit (6) higher polarisation and piezoelectric properties.

EXPERIMENTAL PROCEDURE

Material preparation:

PbO volatalizes at higher termperatures leading to deficiancy of Pb in the final composition. To avoid Pb loss, a carefully calculated excess amount of (5wt %) of PbO is added to the base composition. Using the conventional method of oxide sintering the following ceramic compositions were prepared and studied.

$$Pb_{0.95}La_{0.05}(Zr_{0.65}Ti_{0.35})_{0.9875} - 1.25xNb_xO_3$$

where x = 0, 0.005, 0.010 and 0.015.

The constituent materials, after grinding and homogenising, were calcined in alumina crucibles at 950°C for 3 hrs. The calcined slug was again ground and PVA binder was added to facilitate pressing into pellets. 4 to 5 pellets of each composition were stacked on alumina foil surrounded by coarse powder of the same composition and closed with an alumina crucible. Then the sintering of the pellets was carried out at 1225-1250°C for 4 hrs and the furnace is allowed to cool slowly.

Fired on silver paint was applied to the polished surfaces of the sintered pellets and fired at 500°C for 1 hr.

Poling: For piezolectric measurements and hysteresis beheviour the pellets were poled by the method of Belding and McLaren (7) using fields of 20 KV/cm at elevated temperatures in silicon oil.

Dielectric and Piezoelectric Measurements:

The dielectric measurements and hence the Curie tempeiature, were perfoimed at 1KHz using the HP impedence anlyser model 4192A. Piezoelectric measurements were also carried out on the same HP model 4192A by the method of resonance - antiresonance technique (8). Piezolectric coupling coefficients K_p, K_t, d_{31} and g_{31} are determined from these datas. d_{33} coefficient is measured by using the Berlincourt d_{33} meter.

Grain size and Hysteresis Measurements:

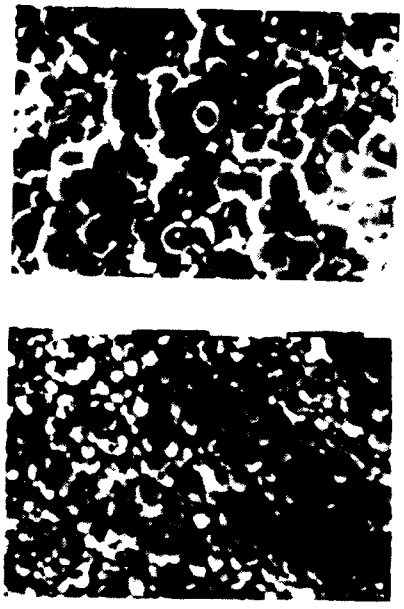
The grain size of the ceramic compositions is determined from the Scanring

CH3080-0-7803-0465-9/92$3.00 ©IEEE

Electron Micrographs taken on the as fired surfaces of the specimens using the Philips SEM model 520M. A modified Sawyer - Tower circuit (9) is used for the hysteresis measurements. The saturation and remanent polarisations and coercive field are obtained from the hysteresis loops.

RESULTS AND DISCUSSION

Ceramic compositions in the PLZT system and their modifications with Nb exhibit highly uniform microstructure consisting of randomly oriented grains. The SEM photographs of Nb doped and undoped PLZT (5/65/35) ceramics is shown in Fig.1.



(a)

(b)

Fig. 1 SEM photographs of (a) undoped and (b) Nb doped PLZT ceramics.

As the niobium concentration increases the grain size decreases indicating that the Nb inhibits grain growth.

The polarisation parameters depend strongly on the grain size of the ceramic compositions. The behaviour of the polarisation parameters with Nb content in PLZT (5/65/35) composition is shown in Fig.2. Saturation in the hysteresis loops could be observed only for 0.5 mole % Nb added composition, yielding a saturation polarisation of 42.6 C/cm^2. Optimum piezolectric coupling coefficients are also obtained for this composition. With

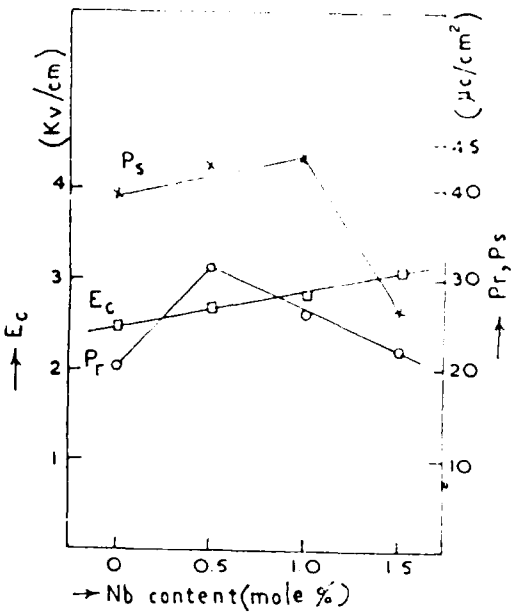


Fig. 2. Variation of P_r, P_s and E_c with Nb content in PLZT ceramics.

increasing Nb concentration the remanent polarisation, P_r decreases and coercive field E_c increases. Similar effect was observed by Nagata (10) in undoped PLZT ceramics. Decrease in remanent polarisation may be due to the decrease in grain size. The decrease in P_r may also be due to the orientation of non 180° domains in these harder compositions. With decreasing grain size i.e. with increasing Nb content, non 180° domain rotation decreases and so P_s decreases, as observed.

The doping of PLZT (5/65/35) ceramics with Nb enhances the dielectric and piezoelectric properties. Fig. 3 shows the variation of dielectric constant with temperature for the Nb doped PLZT compositions. The room temperature dielectric constant increases with Nb content while the Curie temperature decreases. Effect of Nb addition in PLZT (5/65/35) ceramics is that is shows a diffused phase transition for 0.5 mole % Nb content while more Nb concentration the phase transitions becomes sharper. This indicates an increase in the ordering of the structure with increasing Nb content.

As Niobium is introduced into the B positions of the PLZT (5/65/35) ceramics, the coupling factors K_p and K_t increase.

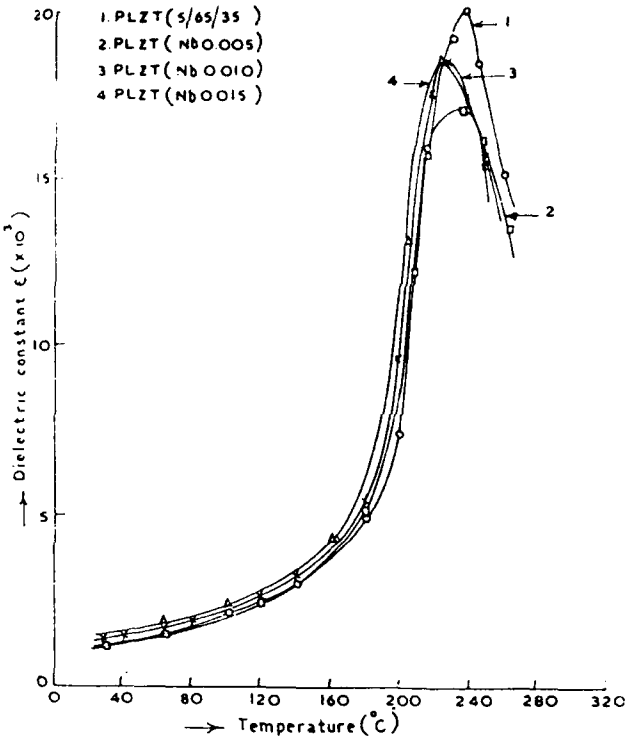


Fig. 3. Variation of dielectric constant with temperature of Nb doped PLZT ceramics.

But as the Nb content is increased, thickness coupling factor K_t decreases while the planar coupling factor K_p decreases upto 1 mole % Nb and then increases. The variation of piezoelectric coupling coefficients is shown in Fig.4. Maximum piezoelectric charge coefficients, d_{31} of 134.5 pC/N and d_{33} of 225 pC/N are obtained in the 0.5 mole % Nb doped composition; which also showed saturation polarisation. But maximum piezoelectric voltage coefficient g_{31} of 10.01 V-m/N is obtained in the 1.5 mole % Nb added composition. Except for the g_{31} coefficient other coupling coefficients decrease with increasing Nb content. It is observed that the doping ions concentrate near the grain boundaries. This mechanism may effect the domain wall motion in Nb doped PLZT ceramics toward an increase in the polarisation. This results in an increase in the dielectric and piezoelectric properties, as observed.

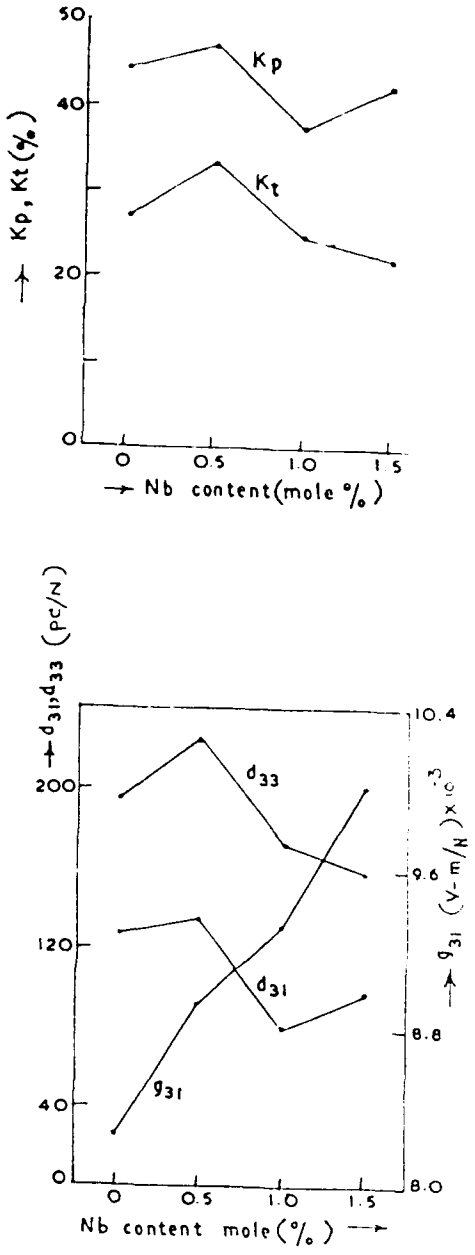


Fig. 4. Variation of piezoelectric properties with Nb content in PLZT ceramics.

Acknowledgements:

One of the others (KVR) wishes to acknowledge CSIR, New Delhi for financial assistance.

References

1. F. Kulscar
J. Am. Cerem. Soc 42(7) 343 (1959)

2. R. Gerson
J. Appl. Phys. 31(1) 188 (1960)

3. B. Jaffe, W.Cook and H.Jaffe
Piezoelectric ceramics, Academic Press, London(1971) p 135.

4. M.M. Abousekkina and A.Tawfik
J.Mat. Sci. Lett. 3 733 (1984)

4. D.Luff, R. Lane, K.R. Brown and
H.J. Marshallsay
Trans. J. Brit. Ceram. Soc.73 251 (1974)

6. G.H. Heartling and C.E. Land
J.Am. Ceram. Soc.54(1) 1 (1971)

7. Belding and Mc Laren
Am. Ceram. Soc. Bull. 49 1025 (1970)

8. I.R.E. Standards on Piezoelectricity
Proc. I.R.E. 49 1161 (1961).

9. J.K. Sinha
J. Sci. Inst. 42 696 (1965)

10.K. Nagata
Elec. Engg. Jpn. 11(4) 1 (1980).

ELECTRICAL DEGRADATION PROCESS AND MECHANICAL PERFORMANCE OF PIEZOELECTRIC CERAMICS FOR DIFFERENT POLING CONDITIONS

Toshio TANIMOTO and Kiyoshi OKAZAKI

Department of Materials Science and Ceramic Technology
Shonan Institute of Technology
Tsujido-Nishikaigan, Fujisawa, Kanagawa 251, Japan

Synopsis

The degradation process of piezoelectric properties under fatigue loading and mechanical performance for piezoelectric ceramics have been investigated with the special emphases on the effects of poling conditions. The materials used in the present study are the commercial piezoelectric ceramics, $PbZrO_3$-$PbTiO_3$ (PZT) and $BaTiO_3$. Poling conditions for PZT samples were varied in the three different ways: Polarization was basically conducted by applying DC field on the samples (Case 1). Then, some of the samples were kept under constant temperature of 85°C for two hours as an aging treatment (Case 2). Moreover, in some samples, re-polarization was performed (Case 3). For $BaTiO_3$, DC field was applied on the samples at the temperature above a Curie point in advance to the ordinary polarization at the temperature below the Curie point.

First, the effect of applied voltage values in poling on the piezoelectric constant and mechanical fatigue properties were evaluated.

Second, the discussion is made on the degradation process of piezoelectric coupling constant under subjected to repeated compressive fatigue loading and static compressive strength properties of PZT samples which were poled in the three different poling conditions as explained above.

Third, the effect of application of DC field at the temperature above a Curie point on the $BaTiO_3$ samples before ordinary poling is discussed on the degradation process of piezoelectric properties under fatigue loading and mechanical strength properties, compressive strength, compressive modulus and so on.

1. Specimen Preparation and Experimental Method

The material used in the present study is the commercially available piezoelectric ceramics, $PbZrO_3$-$PbTiO_3$ including the third component and $BaTiO_3$. Figure 1 shows the specimen configurations. Poling conditions for those piezoelectric ceramics are illustrated in Figure 2. Three different poling conditions, 1) general poling (application of DC field at the temperature below a Curie point of 330°C), 2) aging treatment 85°C for two hours after poling and 3) re-poling after subsequent aging treatment for the poled sample, are adopted for the study on PZT. For $BaTiO_3$, on the other hand, DC field were applied at the temperature above a Curie point of 128°C (hereinafter referred to as a prior treatment) and then aged at 85°C for two hours, in advance to ordinary poling. Also the samples poled without such a prior treatment were prepared for the comparative study. The specimen was loaded to failure at cross-head speed of 3.5mm/min in static compression test.

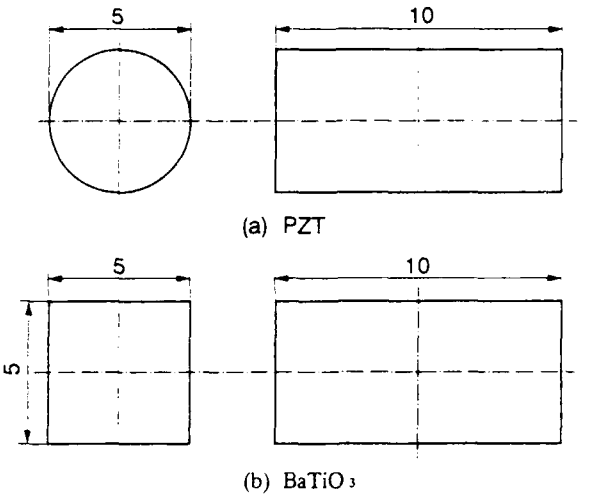


Fig.1 Compressive test specimens.

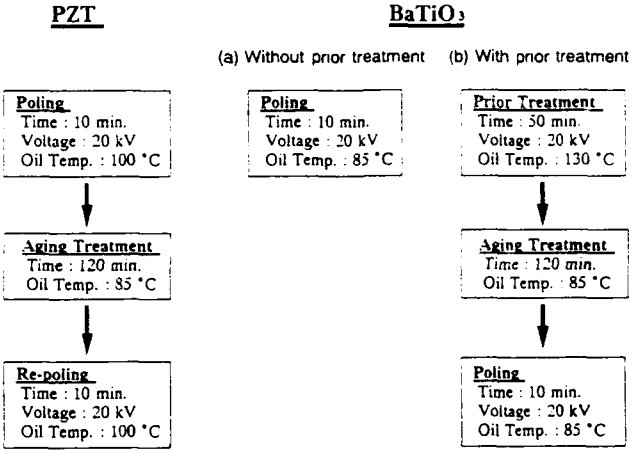


Fig.2 Various poling conditions for PZT and $BaTiO_3$.

Fatigue tests were conducted under axial cyclic compression at a frequency of 30Hz by an electro-hydraulic fatigue testing machine. The stress ratio R (= $\sigma_{min}/\sigma_{max}$) is fixed to a constant value of 10 in all the fatigue tests.

2. Experimental Results and Discussion

2.1 Comparison of Fatigue Properties for PZT and $BaTiO_3$

The basic fatigue S-N diagrams for PZT and $BaTiO_3$ used for the present work are compared in Figure 3.

CH3080-0-7803-0465-9/92$3.00 ©IEEE

Polarization for these samples were performed by a general way without any particular treatment such as aging, prior treatment and re-poling, which was shown in Figure 2. The linear approximation between the maximum cyclic stress and fatigue life is drawn by a solid line. As can be seen in the figure, the poled PZT sample exhibit a better fatigue performance in comparison to the poled $BaTiO_3$ sample.

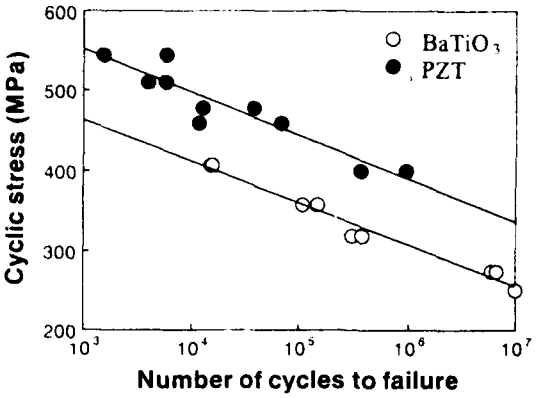


Fig.3 Fatigue S-N diagrams.

2.2 Electrical Properties and Mechanical Performance of PZT

The effect of applied voltage value in poling on the piezoelectric constant and mechanical fatigue properties were examined in Figure 4. Fatigue resistance appears to increase with increasing of applied voltage in poling, particularly in a longer life region.

Figure 5 compared the degradation process of piezoelectric coupling constant under subjected to repeated compressive fatigue loading among three different poling conditions as explained in Figure 2. Aging treatment after poling is found to be effective in suppressing the degradation of piezoelectric coupling constant. and much remarkable improvement is observed when the sample is re-poled via. aging treatment after poling. Re-poled sample increases not only the piezoelectric coupling constant K33, but also compressive strength, as can be seen in Figures 6 and 7. As a result, both the electrical degradation process and mechanical performance of the PZT samples are appeared to be the most favorite when the poling of samples were performed by the third poling condition which means re-poling via aging treatment after poling. We believe that these results are probably brought by the space-charge effects [1] through aging treatment below Curie point. Figure 8 schematically illustrates the space charge effects. Important points of the space charge effects are: 1) During the aging process of poled ceramics, the internal bias field, Ei, gradually generates in the direction of poling field and the residual polarization is stabilized by the space-charge. 2) It is supposed that re-poling increases the amount of space-charge and the internal bias field. Space charge stabilized effects pay an important role against electrical depolarization and stress depolarization, and thus to improve mechanical performance, strength performance and fatigue resistance and so on.

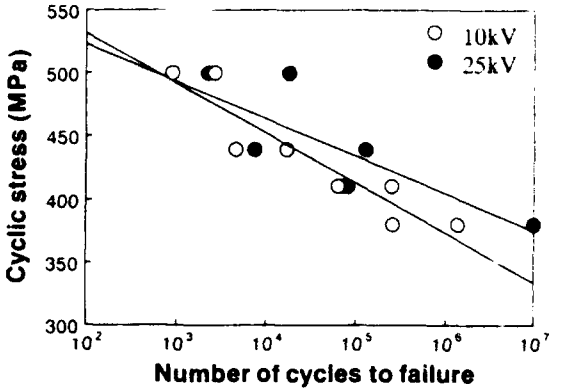


Fig.4 Effect of DC voltage in poling on the fatigue properties.

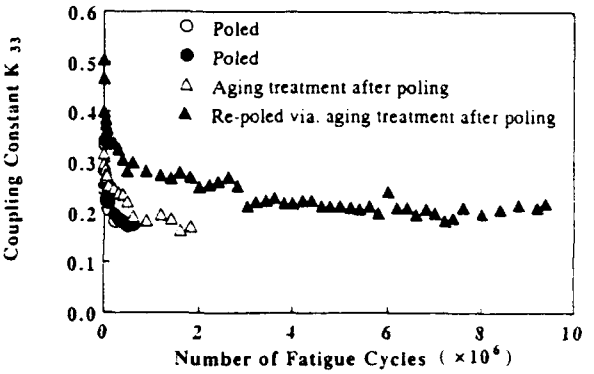


Fig.5 Change of piezoelectric coupling constant with increasing fatigue cycles under a fixed cyclic stress.

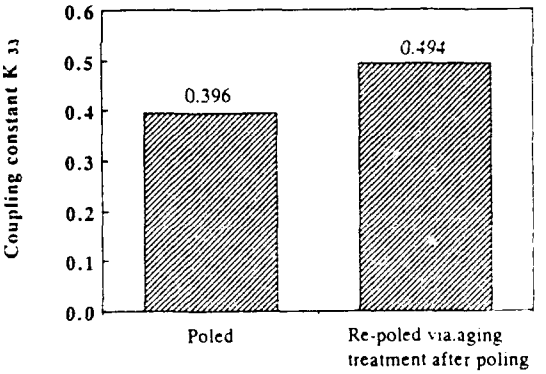


Fig.6 Comparison of piezoelectric coupling constant for poled PZT and re-poled PZT via. aging treatment after poling.

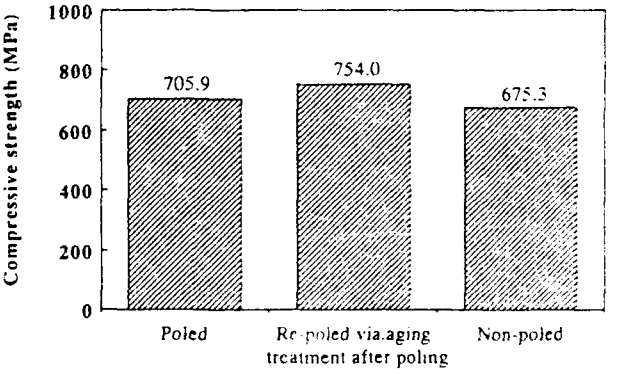
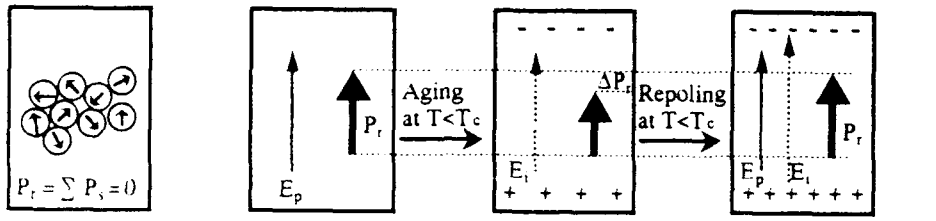


Fig.7 Compression strength of PZT samples at varying the poling conditions.



Virgin sample | Poling at T<Tc | Aging treatment after poling | Re-poling via. aging treatment after poling

P_r : Residual polarization
P_s : Spontaneous polarization
E_p : Applied DC field
E_i : Internal bias field

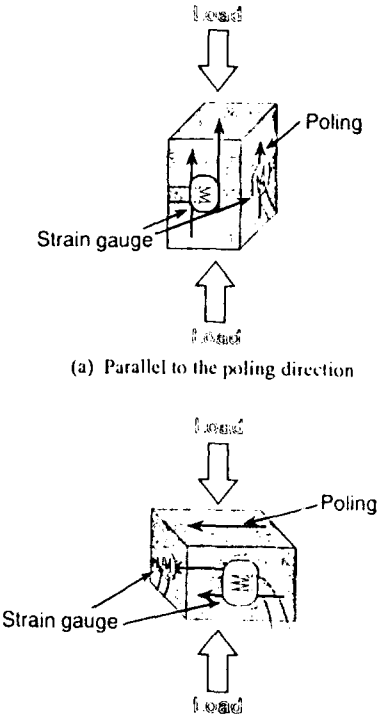
Fig.8 Schematic explanation for space-charge effects and internal bias field.

2.3 Electrical Properties and Mechanical Performance of $BaTiO_3$

In order to investigate the effect of residual polarization produced in the sample on the mechanical performance, axial compressive tests were conducted both in parallel and perpendicular to the poling directions as shown in Figure 9. Strain gauges were mounted on the samples in the two directions, parallel and transverse to the loading directions. Thus, compressive modulus as well as compressive strength can be evaluated.

As previously explained in Figure 2, the effect of application of DC field at the temperature above a Curie point on the $BaTiO_3$ samples before ordinary poling is now discussed here. It was clarified from Figure 10 that such a prior treatment in poling increases piezoelectric coupling constant of the samples. In addition to this, Figure 11 suggests that the prior treatment could be effectively working to suppress the degradation of piezoelectric properties under fatigue loading. Moreover, it should be noted from Figures 12 and 13 that this treatment improves the mechanical strength properties; compressive strength and compressive modulus .

Figures 12 and 13 also indicate that the axial compressive strength and compressive modulus in parallel to poling direction are superior if compared with those in perpendicular to poling direction. Figure 14 explains the reason for this result. Residual tensile stress produced in the sample through poling treatment probably contributes to the difference of mechanical performance. It is quite reasonable to consider that the residual tensile stress occurred in parallel and opposite directions to external load increases the fracture strength. Figure 13 suggests that compressive modulus for the poled sample is lower than that for the non-poled sample. As pointed out in our previous work [2]-[4], the failure mode of non-poled sample in compression is typical transgranular fracture, while intergranular fracture is mainly observed in the poled sample. Therefore, grain boundary in poled sample is supposed to be easy to slip, resulting in the lower compressive modulus in comparison to that in non-poled sample.



(a) Parallel to the poling direction

(b) Perpendicular to the poling direction

Fig.9 Measurements of compressive strength properties.

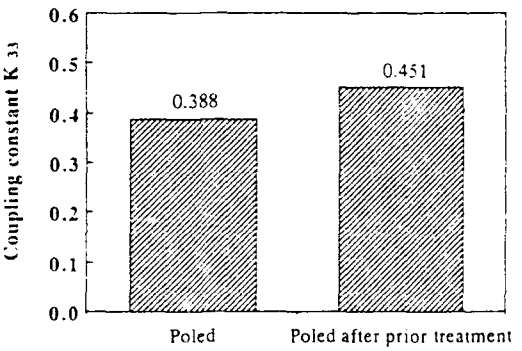


Fig.10 The effect of a prior treatment in polarization on the piezoelectric coupling constant of $BaTiO_3$.

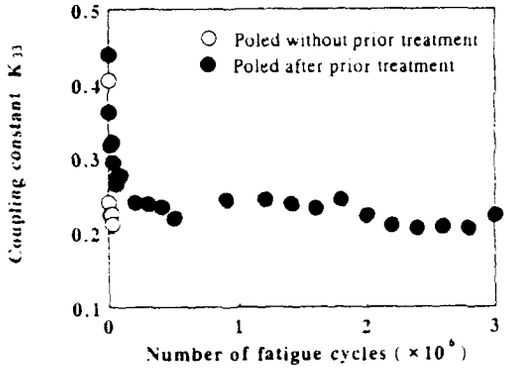


Fig.11 Change of piezoelectric coupling constant with increasing fatigue cycles under a fixed cyclic stress.

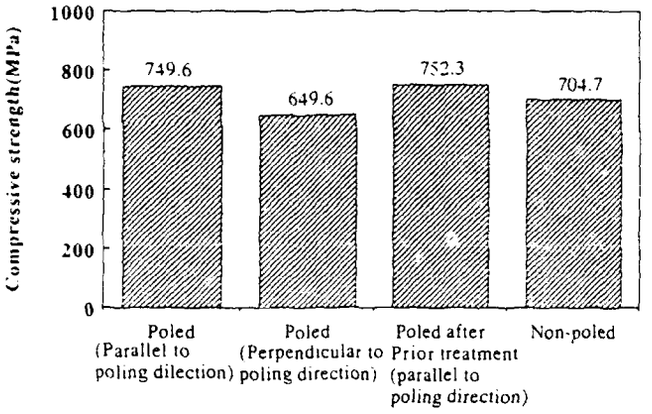


Fig.12 Compressive strength of $BaTiO_3$ samples at varying the poling conditions.

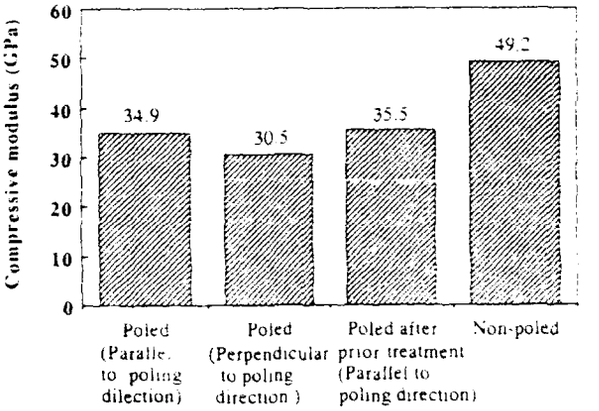


Fig.13 Compressive modulus of $BaTiO_3$ samples at varying the poling conditions.

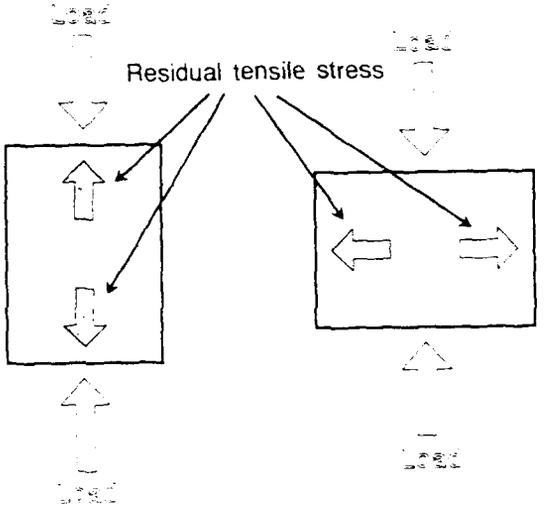


Fig.14 Schematic explanation for the direction of residual tensile stress occurred due to residual polarization.

3. Conclusions

Mechanical and electrical properties of piezoelectric ceramics have been investigated in the present paper with the special emphases on the effects of poling conditions. The materials used in the present study are the commercial piezoelectric ceramics, $PbZrO_3$-$PbTiO_3$ (PZT) and $BaTiO_3$.

This investigation led to the following conclusions;

1. For the effect of applied voltage values in poling on the piezoelectric constant and mechanical fatigue properties, it was revealed that fatigue resistance increases with increasing of applied voltage in poling.

2. The electrical degradation process and mechanical performance of the PZT samples are appeared to be the most favorite when the poling of samples were performed by the third poling condition which means re-poling via aging treatment after poling. This phenomenon was explained based upon space-charge stabilizing effects.

3. The application of DC field at the temperature above a Curie point on the $BaTiO_3$ samples before ordinary poling is very effective for the improvement of electrical and mechanical properties. It was found that such a prior treatment in poling increases piezoelectric coupling constant of the samples. In addition to this, prior treatment could be effectively working to suppress the degradation of piezoelectric properties under fatigue loading and also to improve mechanical strength properties, compressive strength, compressive modulus and so on.

References

[1] K. Okazaki and K. Sakata, Electrotechnical J. of Japan, 7, 1, pp.13-18, 1962.

[2] T. Tanimoto and K. Okazaki, "Mechanical properties and fatigue of electronic ceramics", Proc. the 7th Korea-Japan Seminar on New Ceramics, 1990, pp.91-96.

[3] T. Tanimoto and K. Okazaki, "Reliability-based consideration on the fatigue degradation process of piezoelectric ceramics", Jap. J. Appl. Phys., Vol.30, No.9B, pp.2410-2412, 1991.

[4] T. Tanimoto, T. Yamamoto and K. Okazaki, "Mechanical and electrical properties of piezoelectric ceramics under repeated compression fatigue tests", Proc. 1990 IEEE 7th ISAF, 1990, pp.202-205.

0-3 Piezoceramic-Polymer Composites Prepared Using Thermoplastics and Elastomers

M.A. Williams, D.A. Hall and A.K. Wood

Materials Science Centre, University of Manchester and UMIST,
Grosvenor St., Manchester, U.K. M1 7HS.

Abstract

A number of thermoplastic polymers and elastomers are evaluated with respect to their use in 0-3 piezoceramic-polymer composites. Materials were prepared by dispersing 50 vol% of pure lead titanate powder within various polymer matrices, and characterised by measurement of electrical resistivity, dielectric and piezoelectric properties, and by XRD. It is shown that composites prepared using polypropylene can be poled efficiently and exhibit a reasonable piezoelectric response. Further work on thermoplastic systems is expected to yield useful materials which have distinct advantages over conventional thermosetting systems in terms of flexibility in processing.

Introduction

Composite materials have long been utilised as a means of combining different materials to enhance particular chemical, electrical, or structural properties. One well-known example is the combination of piezoceramics and polymers to overcome the limitations imposed by using homogeneous, single-phase ceramics alone. For example, PZT exhibits only modest hydrostatic piezoelectric coefficients due to a relatively high transverse coupling[1]:

$$d_h = d_{33} + 2d_{31} \qquad (1)$$

and, for PZT, $$d_{31} \approx -\frac{1}{2} d_{33} \qquad (2)$$

In addition, the relatively high physical density of ceramics means that acoustic coupling into air, water, or human tissue is not straightforward, necessitating the use of relatively complex transducer design[2].

Piezoceramic-polymer composites are a class of materials which effectively overcome these limitations and hence are found to be more responsive and versatile materials[3]. Such composites can be fabricated by several methods, for example embedding parallel piezoelectric rods of ceramic in a polymer matrix, producing a 1-3 type composite[4], or by the 'replamine' process, producing a 3-3 type composite[5]. Perhaps the most attractive composite from the point of view of ease of fabrication is the 0-3 type, comprising discrete ceramic particles dispersed within a polymer matrix. This type of composite can be fabricated in a wide variety of forms, for example thin sheets, extruded bars, fibres, and moulded shapes, and has the ability to conform to curved surfaces.

For 0-3 type composites, it has often been found that the greatest piezoelectric sensitivity is attained when the ceramic phase possesses high intrinsic hydrostatic coefficients. For example, the use of pure or modified lead titanate gives substantial improvements over PZT[6].

The properties of the polymer phase are also important, since they result in a lower density (providing an improved acoustic coupling to low-density media) and a lower dielectric permittivity, effectively raising the voltage coefficient and the figure of merit. Examples of polymer systems already reported are chloroprene rubber[7], epoxies[8], polyurethanes[9], and polyethylene-acrylic acid copolymers[10]. Thermoplastic polymers and elastomers are of particular interest since, together with their associated processing technology, they offer a high degree of flexibility in processing and the possibility of producing tailored composite structures, for example particle-oriented composites, which might exhibit piezoelectric coefficients approaching those of the 1-3 type composites.

The major difficulty in the use of common non-polar thermoplastics (such as polyethylene and polypropylene) and elastomers (such as natural rubber) in 0-3 piezoceramic-polymer composites arises in the poling process, when their relatively high electrical resistivities would effectively reduce the poling field which could be applied to the ceramic phase. According to the simple two-layer model, the ratio of electric fields within the two phases of the composite is equal to the ratio of their resistivities :

$$E_c / E_p = \rho_c / \rho_p \qquad (3)$$

where E_c = electric field in ceramic phase;
E_p = electric field in polymeric phase;
ρ_c = resistivity of ceramic phase;
and ρ_p = resistivity of polymeric phase.

If the polymeric phase has a higher resistivity ($\sim 10^{11} \Omega m$) than the ceramic phase ($\sim 10^{8}$ Ωm)[6] at the poling temperature, then only a small fraction of the applied electric field will develop within the ceramic particles.

The present study was carried out in order to assess the suitability of a number of candidate thermoplastics and elastomers for use in 0-3 piezoceramic-polymer composites, with particular emphasis being placed on electrical resistivity and its variation as a function of temperature. Results will also be presented for poling experiments carried out on selected composites and V-I measurements which reveal substantial departures from linearity in certain materials.

Experimental Procedure

Pure lead titanate powder was prepared by conventional solid state reaction between lead(II) oxide and titanium dioxide (>99%, Fluka Chemicals Ltd.). The constituent oxide powders were mixed/milled for 4 hours in propan-2-ol using zirconia grinding media, calcined at 900°C for 1 hour, and then milled for a further 1 hour to

CH3080-0-7803-0465-9/92$3.00 ©IEEE

break down any hard agglomerates.

A range of polymers were chosen for the study, as shown in Table 1. For the thermoplastics, the composites were prepared by mixing the polymer with the relevant processing additives and the ceramic powder on a heated two-roll mill for 20-30 min., the processing temperature being slightly above the melting point of the relevant polymer (170 C for polypropylene, 130 C for polyethylene, and 110 C for the polyethylene-acrylic acid copolymer). A similar procedure was followed for the elastomers, but in this case the two-roll mill was water-cooled and the cross-linking agents (sulphur in the case of natural rubber and zinc oxide for the chloroprene rubber) were added last in order to prevent cross-linking during the mixing process. In each case, the volume fraction of lead titanate powder was 50%.

Table 1. Formulation and Processing Conditions for Polymers

Polymer	Additives	Mixing Temp.	Forming / Curing Temperature
Polyethylene-Acrylic Acid Copolymer (Dow-Chemical Primacor 3460)	none	110 C	110 C
Polypropylene	Stearic Acid, Microcrystalline Wax	170 C	170 C
Chloroprene	Zinc Oxide, Magnesia	40 C	160 C
Natural Rubber	Sulphur	40 C	160 C

After mixing, the composites were pressed in a heated press at 10 MPa (the elastomers at a temperature of 160 C for 20 min., the thermoplastics at the appropriate mixing temperature for 2 minutes), followed by cooling to room temperature at a rate of 15 C/min. Flat, square sheets of the composites were produced measuring 160 mm x 160 mm and having thicknesses in the range 0.5-2 mm. Test specimens were cut from the pressed sheets and electrodes applied using air-drying silver paint (Acheson Electrodag 915).

Electrical resistivity measurements were carried out as a function of temperature on circular specimens having a diameter ~55 mm, using a three-terminal guarded electrode configuration. The applied electric potential for these measurements was 6 Volts, giving an electric field ~5V/mm, and the heating rate was 1 C/min. In addition, two-terminal V-I measurements at high fields (~1kV/mm) were made using a high voltage amplifier (Chevin Research HVA1B) and a current-voltage converter with protected inputs. In this case, the specimen was held in a heated silicone oil bath at temperatures from 60-120 C. Poling experiments were carried out in the same apparatus, with specimens being subjected to the appropriate poling field and temperature for the required time (15-120 min.) and then cooled under field to a temperature of 40 C.

The degree of poling achieved was characterised by scanning over the (001) and (100) peaks using a Philips PW1380 X-ray diffractometer and by piezoelectric measurements made using a custom-built d_{33}-meter. Dielectric properties were measured at 1kHz using a Hewlett-Packard 4284A LCR-meter.

Results and Discussion

Electrical properties of polymers

The electrical resistivities of the thermoplastics were all found to be $>10^{10}$ Ωm over the temperature range investigated. This would seem to indicate that composites prepared using these polymers could not be effectively poled, since it has been noted previously that values ~10^7-10^8Ωm are necessary[12]. However, encouraging results have been reported previously for composites prepared using the polyethylene-acrylic acid copolymer[10] and so work on these materials was continued.

Of the two elastomers investigated, the results for chloroprene rubber gave the clearest indication of achieving the required resistivity at 60 C, as shown in Fig. 1. Natural rubber exhibited a substantially higher resistivity throughout the temperature range, falling to a minimum value ~10^9Ωm at 140 C. Since the level of resistivity for the natural rubber appeared to be a little high, the work was extended to include carbon filled materials prepared by blending natural rubber with a 50% carbon-filled material which is commonly employed to improve the mechanical toughness of rubber-based products. The results for these materials, presented in Fig.2., show a substantial reduction in resistivity at 20 vol% of carbon and a shift from a negative temperature coefficient of resistivity typical of a semi-insulator at low carbon-contents to a positive value at the higher carbon contents. From these results, a carbon content of 15vol% should give a resistivity in the required range at 120 C.

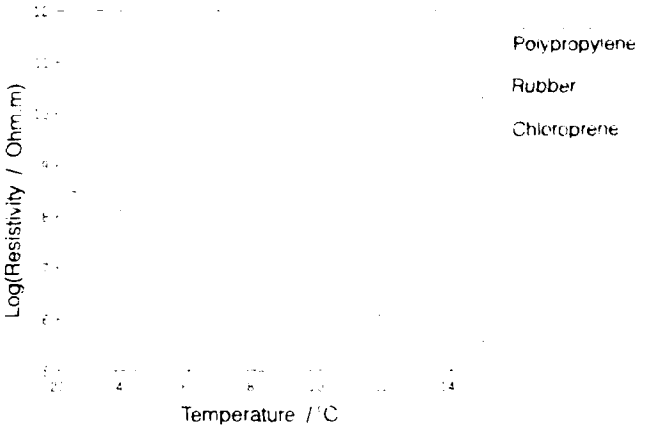


Fig. 1. Resistivity vs. temperature for chloroprene rubber and natural rubber.

Electrical properties of composites

Resistivity measurements carried out on the composites at low field levels, presented in Fig.3., gave some unexpected results. It was generally found that the composites exhibited a reduction in resistivity with increasing temperature, in line with results obtained for the polymers alone. However, in some cases the absolute values of resistivity for the composites showed substantial shifts (both positive and negative) relative to those of the polymers.

The resistivity of the chloroprene rubber composite was approximately an order of magnitude higher than that of the rubber alone throughout the temperature range of interest. It is common practise to include a small amount of a basic oxide (such as magnesia) in the formulation of a chloroprene rubber in order to reduce the residual

concentration of chloride ions. If the conductivity is attributed to the presence of chloride ions, then it is possible that the lead titanate powder might function in a similar manner to magnesia, resulting in the observed increase in resistivity for the composite.

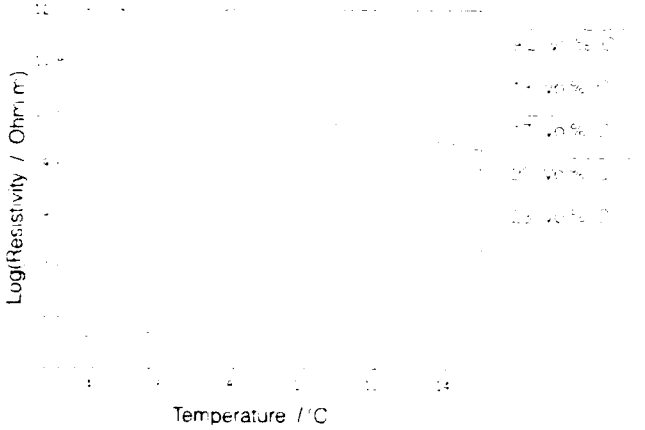


Fig. 2. Resistivity vs. temperature for various carbon-filled natural rubbers.

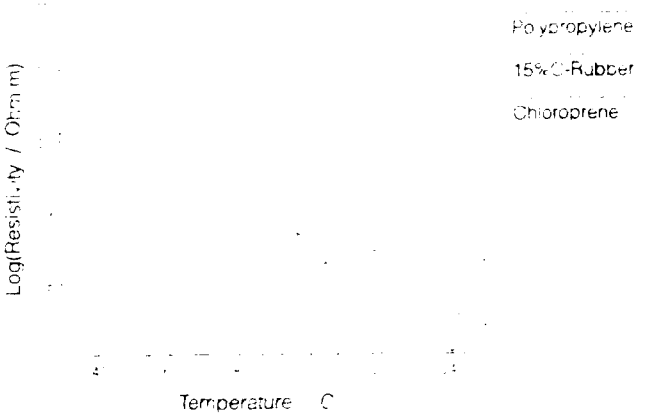


Fig. 3. Resistivity vs. temperature for composites prepared with 50 vol% lead titanate.

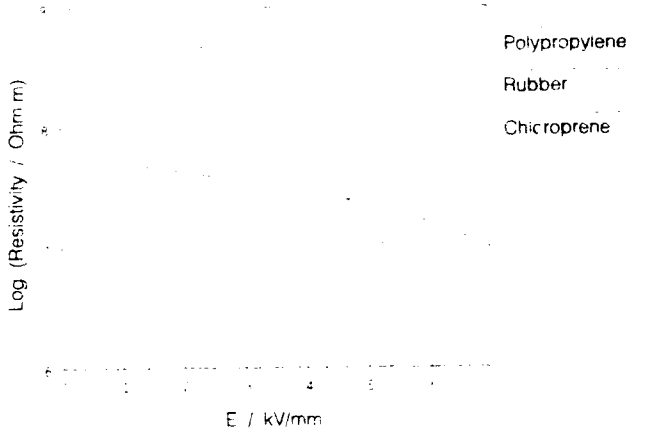


Fig. 4. Resistivity vs. electric field for composites prepared with 50 vol% lead titanate powder.

The introduction of lead titanate powder into the carbon-filled natural rubber had little effect on the resistivity, giving values $\sim 10^9 \Omega m$ at 100 °C which would normally be considered to be above the range required for poling. However, resistivity measurements carried out as a function of electric field strength (Fig.4) showed that the resistivity of this composite was remarkably reduced at electric fields greater than 3 kV/mm, indicating that poling should be possible. Poling studies for the two elastomeric composites gave a good correlation with the high-field resistivity measurements in that the carbon-filled natural rubber composite was more easily poled than the chloroprene composite, as shown in Fig.5 and Fig.6. Dielectric and piezoelectric measurements for these composites are presented in Table 2. It is likely that the chloroprene composite would be more efficiently poled at higher field levels (~10 kV/mm), and that the piezoelectric properties would then be closer to the values reported previously[7].

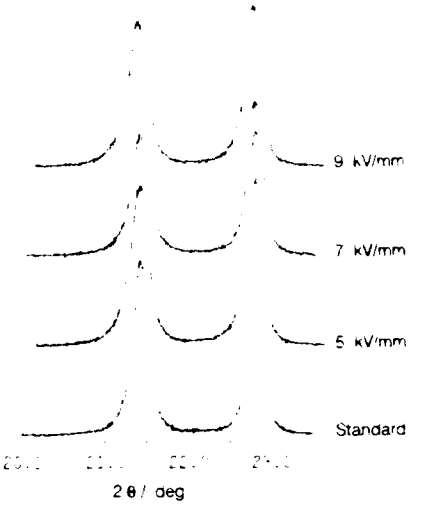


Fig. 5. XRD results for poling study of chloroprene composite (temperature = 120 °C, time = 15 min.)

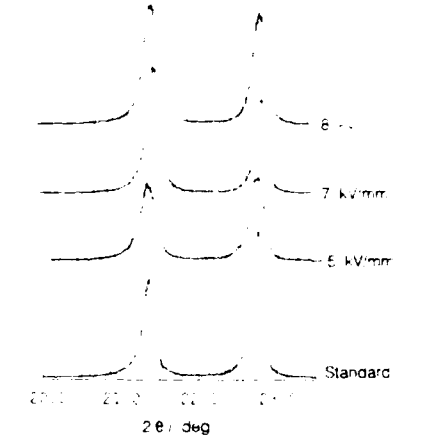


Fig. 6. XRD results for poling study of carbon-filled natural rubber composite (temperature = 120 °C, time = 15 min.)

The polypropylene-based composite showed a pronounced reduction in resistivity with increasing temperature to a value $\sim 10^7 \Omega m$ at 120 °C (Fig.4), in marked contrast to the results obtained for the polymer alone, which indicated a value $>10^{10} \Omega m$ up to 140 °C (Fig.1). It is likely that this reduction in resistivity relative to the polymer is a result of the presence of a small amount of moisture in the composite, introduced via the surface of the ceramic powder. It was noted that the resistivity of the composite was increased substantially after drying the specimen for 60 min. at 140 °C.

Further work showed that the resistivity of the polypropylene-based composite was reduced by approximately an order of magnitude at high fields (Fig. 4)

and that efficient poling of the material was possible, as shown in Fig.7. It was found that the degree of poling, as measured by the relative intensities of the (001) and (100) peaks, increased in a predictable manner as a function of time, temperature, and poling field. The piezoelectric coefficients obtained for this material to date are fairly low, being reduced by a factor of 3 relative to comparable epoxy-based materials[12]. It has yet to be determined whether this is a result of the elastic properties of polypropylene (being a relatively high modulus polymer) which might give a less efficient transfer of stress, or of a non-uniform distribution of polarisation through the thickness of the material (since only the surface region is analysed by XRD).

Table 2. Dielectric and Piezoelectric Properties of Composites (all with 50 vol% lead titanate and poled at 120 C for 15 min.)

Composite I.D.	Poling Field (kV/mm)	ε_r	tan δ	d_{33} (pC/N)	g_{33} (pC/N)
Chloroprene	5	30.0	0.059	3	11
	7	30.7	0.055	4	15
	9	30.0	0.055	6	23
15% Carbon Rubber	5	24.0	0.037	4.5	21
	7	24.4	0.037	7	32
	8	24.2	0.035	8	37
Polypropylene	5	19.53	0.046	6	35
	7	18.33	0.046	10	62
	9	16.56	0.039	12.5	85

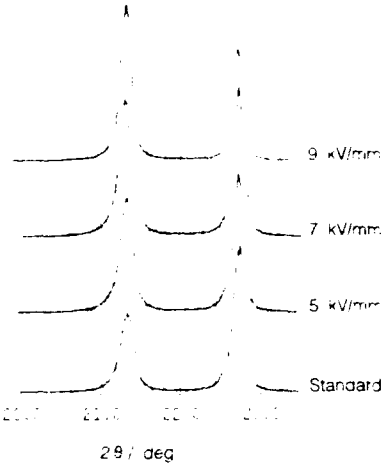


Fig. 7. XRD results for poling study of polypropylene composite (temperature = 120°C, time = 15 min.)

Composites prepared using the polyethylene-acrylic acid copolymer did not show any indication of falling within the required resistivity range for poling. It is possible that the promising results reported previously for this polymer[10] might be due to the use of a ceramic powder (a commercial 'soft' PZT) having a higher resistivity and/or lower coercive field than the pure lead titanate used in the present study.

Conclusions

It has been shown previously that electrical resistivity, and its dependence on temperature, is an important criterion in assessing the suitability of a polymer for use in 0-3 piezoceramic-polymer composites, since the correct resistivity balance must be achieved in order to enable poling of the ceramic phase[6,11]. In the present work, it was found that the electrical behaviour of the composite is not always a true reflection of that of the polymer, since the introduction of the ceramic powder can have a marked effect on electrical conduction through the polymer matrix. This was particularly pronounced for the lead titanate-polypropylene composite, which exhibited a resistivity of $10^7\Omega$m at 120 C, approximately 4 orders of magnitude lower than that of the polymer alone. In this case, the reduction in resistivity was attributed to the introduction of a small amount of residual moisture into the composite. The relatively low resistivity of the polypropylene-based composite enabled poling and allowed the production of an active piezoelectric material, albeit with relatively low piezoelectric activity. The results reported here for polypropylene indicate that it may be possible to produce piezoelectric composites using a wide variety of other non-polar polymers which have previously not been considered suitable on the basis of their high electrical resistivities. Thermoplastic polymers in particular offer benefits in terms of processing (for example, they are well-suited to complex forming operations) and may exhibit characteristics complementary to those of the currently-preferred epoxies or chloroprene rubber.

It was also found that certain composites (notably those prepared with carbon-filled natural rubber and polypropylene) exhibited pronounced non-ohmic behaviour at high electric field strengths, which was of further benefit in allowing the required resistivity balance to be achieved. It can be concluded that the suitability of a given polymer for use in 0-3 piezoceramic-polymer composites can only be fully evaluated by carrying out resistivity measurements on the composite as a function of temperature and electric field strength, since low-field measurements on the polymer alone may give misleading results.

Acknowledgements

The authors would like to thank Mr. A. Zadoroshnyj for technical assistance and the SERC, Ferranti-Thomson Sonar Systems Ltd., and The Royal Society (London) for financial support.

References

1.K.A. Klicker et. al., J.Am.Ceram.Soc. 64, 5-9 (1981).
2. W.A. Smith, ISAF'90, 145-152 (1990).
3. R.E. Newnham et. al., Mat.Res.Bull. 13, 525-536 (1978).
4. M.J. Haun et. al., Adv.Ceram.Mat. 1, 361-65 (1986).
5. R.E. Newnham et. al., Ferroelectrics 27, 49-55 (1980).
6. G.M. Garner et. al., Ferroelectrics 93, 169-176 (1989).
7. H. Banno, Ferroelectrics 50, 3-12 (1983).
8. T. Furukawa et. al., Jap.J.App.Phys. 15, 2119-29 (1976).
9. L.A. Pauer, IEEE Int.Conf.Pec., 1-6 (1973).
10. S. Fidleris et. al., ISAF '90, 309-312 (1990).
11. G. Sa-Gong et. al., ISAF '86, 281-284 (1986).
12. M.A. Williams, unpublished results

FIELD DEPENDENCE OF THE ELECTROMECHANICAL PROPERTIES OF FINE GRAINED HYDROTHERMALLY PROCESSED LEAD TITANATE CERAMICS

L. Pardo, J. Ricote, C. Alemany and B. Jimenez
Instituto de Ciencia de Materiales (Sede A). CSIC
Serrano,144. 28006 - Madrid (SPAIN)

C.E. Millar
Ferroperm A/S. Hejreskovvej 6, 3490 Kvistgård (DENMARK)

ABSTRACT

Fine grained Sm-modified lead titanate ceramics, prepared from hydrothermally processed powders, have been microstructurally characterized by quantitative stereology. The poling field dependence of their dielectric permittivity and losses, and electromechanical and elastic properties determined by the resonance method, has been obtained and compared with that of Ca-substituted titanates. In addition, the results are used to evaluate the influence of grain size on the behaviour of the electromechanical properties with the poling field. This behaviour is considered to determine the most appropriate conditions for the production of ceramics for high frequency applications.

INTRODUCTION

The microstructure is a factor of particular importance that determines the performance of ceramics in high frequency applications. For example, the damping of the planar mode of resonance of thin disks of Ca-modified lead titanate was only observed [1] in ceramics whith remanent porosity. Modified lead titanate ceramics has been considered interesting [2] to be used in surface acoustic waves (SAW) devices. In this application severe limits to the potential use of the ceramic are imposed on the grain size in order to minimize propagation losses due to the scattering by grains [3]. In addition to fine grain and high homogeneity, low dielectric permittivity and losses are required for a ceramic to be used as a SAW substrate. However, the requirements are not so strong for bulk high frequency applications.

The purpose of this work is to determine the variation, as a function of the poling field, of some dielectric, elastic and electromechanical parameters of fine grained Sm- modified lead titanate ceramics with well characterized microstructures, obtained by changing the sintering treatment. The relations observed between the properties of the ceramics with the microstructure and poling field will give a guidance for the selection of the most appropriate ceramics for such applications.

EXPERIMENTAL PROCEDURES

Samarium modified lead titanate ceramics of nominal composition

$$(Pb_{0.88} , Sm_{0.08})(Ti_{0.99} , Mn_{0.01}) O_3$$

were prepared from powder that was hydrothermally processed, at 290°C, by a recently developed method [4], suitable for large scale production of submicron size particles. The powder was dry pressed and sintered at 1050, 1100, 1150 and 1200°C for 2-3 h.

XRD and SEM techniques were used to study the microstructures of these ceramics. The porosity and grain size distribution were measured by computerized image analysis by a semiautomatic process [5] using SEM micrographs, obtained from polished surfaces, and polished and thermally etched surfaces, respectively. The analysis involved four steps, which required specific operations for each measured parameter. First, a processing of the gray level image (SEM micrograh) was performed to allow the second step: the binarization of the image. This was made by manually setting thresholds for the gray levels. As a third step, a processing of the binary image was carried out and, finally, the measurement procedure took place. The equivalent diameter to a circular shape has been chosen as the parameter to quantify grain sizes. This is defined as

$$D = (\text{Area inside grain} \times 4/\pi)^{1/2}$$

For the dielectric and piezoelectric measurements, thin discs with, typically, 0.5 mm thickness and 13 mm diameter were prepared by cutting and grinding the sintered pellets. Silver paint electrodes were then fired onto the largest faces. The samples were poled at 130° C with increasing electric fields until breakdown. After each poling treatment, the d_{33} piezoelectric coefficient, the dielectric permittivity and losses at 1 KHz were determined. Electromechanical and elastic parameters were measured by the resonance method according to IEEE Standards [6].

RESULTS

The lattice parameters, tetragonal distortion and theoretical density of the ceramics were determined from their XRD patterns. The values obtained , $c = 4.05$ Å, $a = 3.89$ Å , $c/a = 1.041$ and $\rho = 7.83$ g.cm^{-3} , were the same for all the ceramics, regardless of their sintering conditions. The presence of a small amount of unreacted TiO_2 was observed in the XRD patterns of all the ceramics.

CH3080-0-7803-0465-9/92$3.00 ©IEEE

Table I

sintering conditions	Porosity (%)	Pore Area (μm^2)	Grain Size (μm)
1050°C-3h	13.7	0.92	0.56
1100°C-3h	8.9	5.51	0.64
1150°C-2h	7.6	15.26	0.81
1150°C-3h	7.3	18.21	0.81
1200°C-2h	10.4	61.96	1.41

Table I. shows the percentage of porosity and the average pore area and grain size resulting from each sintering condition. In addition to these results, image analysis on micrographs of the polished samples revealed that the percentage of TiO_2 did not depend on sintering conditions.

From the values of the pore area in Table I, it is observed that the sintering conditions did not only modify the percentage of porosity, but also the size of the pores.

Figures 1, 2 and 3 show micrographs on polished and thermally etched surfaces of ceramics sintered at 1100, 1150 and 1200°C, respectively.

The grain size distributions obtained by image analysis of these micrograhs are shown in Figure 4.

Results in Table I and Figure 4 reveal a displacement to higher average grain size and wider distributions as sintering temperature increases. The distributions are remarkably narrow for ceramics sintered at 1050 and 1100° C. For the ceramic sintered at 1200°C the width of the distribution suggests a tendency to a bimodal character.

To determine the poling temperature required, the dielectric permittivity as a function of the temperature, and the coercive field were measured on samples sintered at 1150°C-2h. The ferroelectric transition temperature is 319°C and the coercive field is 42 $KV.cm^{-1}$ at 130°C.

Breakdown of the ceramics was found to occur at a poling field of 80 $KV.cm^{-1}$, except for the ceramic sintered at 1050°C-2h, which suffered breakdown at 70$KV.cm^{-1}$.

The values of the dielectric, elastic and electromechanical parameters measured are given in Table II for a poling field of 70 $KV.cm^{-1}$ and for each sintering condition. The changes in d_{33} and K_t are rather small and do not show any obvious correlation with the sintering temperatures. On the contrary, the dielectric permittivity, K^T_{33} , and the frequency constant for the thickness mode, N_t , increase to a maximum at 1150°C and then decrease, whereas the elastic compliance, s^E_{11}, has a minimum at 1150°C.

The variation of these parameters as a function of the poling field was not found to be dependent on the sintering conditions and it can be described as follows.

As expected, a continuous decrease with the poling field is observed for the dielectric permittivity for all the ceramics.

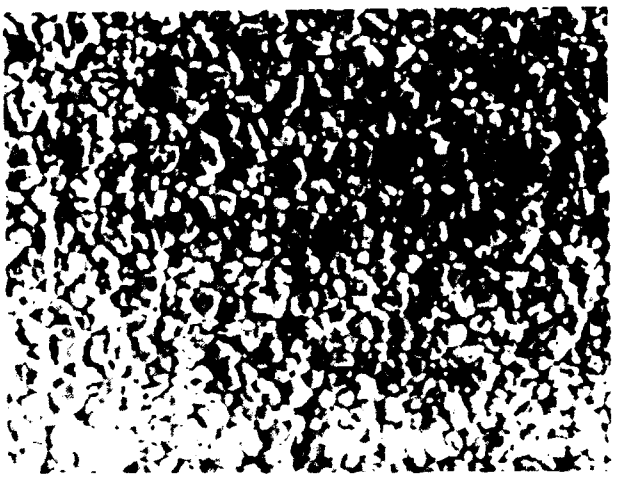


Figure 1. SEM micrograph of ceramic sintered at 1100°C-3h.



Figure 2. SEM micrograph of ceramic sintered at 1150°C-3h.

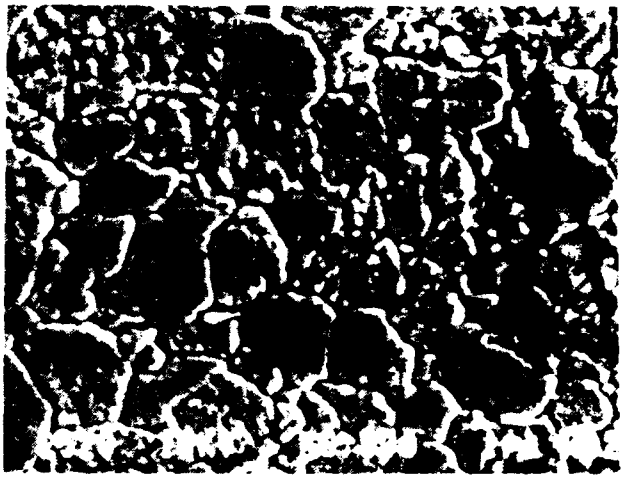


Figure 3. SEM micrograph of ceramic sintered at 1200°C-2h.

The d_{33} and K_t coefficients increase sharply up to a poling field of 40 $KV.cm^{-1}$, which is close to the coercive field. Little increase of these coefficients was found above this field.

The frequency constant for the thickness mode shows a small decrease ($< 5\ \%$) as the poling field increases.

Table II

sintering	K^T_{33}		s^E_{11}	d_{33} pC/N	N_t KHz.mm	K_t %
	before poling	poled	x10^{12} m^2/N			
1050°C-3h	176	147	11.1	57	1880	42
1100°C-3h	211	187	7.9	55	2161	46
1150°C-2h	224	194	7.4	56	2285	42
1150°C-3h	216	187	7.4	54	2309	40
1200°C-2h	196	171	8.4	53	2129	44

The behaviour of the dielectric losses as a function of the poling field for ceramics sintered under different conditions is shown in Figure 5. Increasing losses and a sharper variation with the poling field are found as the sintering temperature increases.

The change of the planar coupling factor with the poling field, K_p , is presented in Figure 6 for different sintering temperatures. The ceramics sintered at 1050, 1100 and 1150°C (2h) showed an increase in the K_p value with the poling field up to 40 KV.cm^{-1}, when saturation is achieved. However, for ceramics sintered at 1150°C (3h) and 1200°C, K_p reached a maximun at 40 KV.cm^{-1} and showed a tendency to decrease with further increases of the poling field. Ceramics sintered at 1050 and 1200°C have the lowest K_p values.

DISCUSSION AND CONCLUSIONS

XRD results showed that there is no change in the crystal structure of the ceramics with sintering conditions. Therefore, the differences observed in the variation with the poling field of the dielectric, elastic and electromechanical parameters or in their saturation values can only be ascribed to the differences in the ceramic microstructures determined by the sintering conditions.

The d_{33} and K_t saturation values compare well with those in the literature for similar compositions [2,7]. Neither their saturation values nor their evolution with the poling field show any obvious microstructural dependence.

From the results of the percentage of porosity (Table I) and of the dielectric permittivity, K^T_{33} , elastic compliance, s^E_{11} , and frequency constant, N_t , (Table II) as a function of the sintering temperatures, the dependence between them is clear. The higher the percentage of porosity, the lower the values of K^T_{33} and N_t , and the higher the values of s^E_{11} , regardless of pore size.

The influence of porosity masks the expected [3] increase of dielectric permittivity with decreasing grain size. However, again, the comparation of the results in Tables I and II, taking into account previous results for ceramics with grain sizes from 1 to 10 μm [3] , shows that grain size seems to be the main factor affecting dielectric losses. The

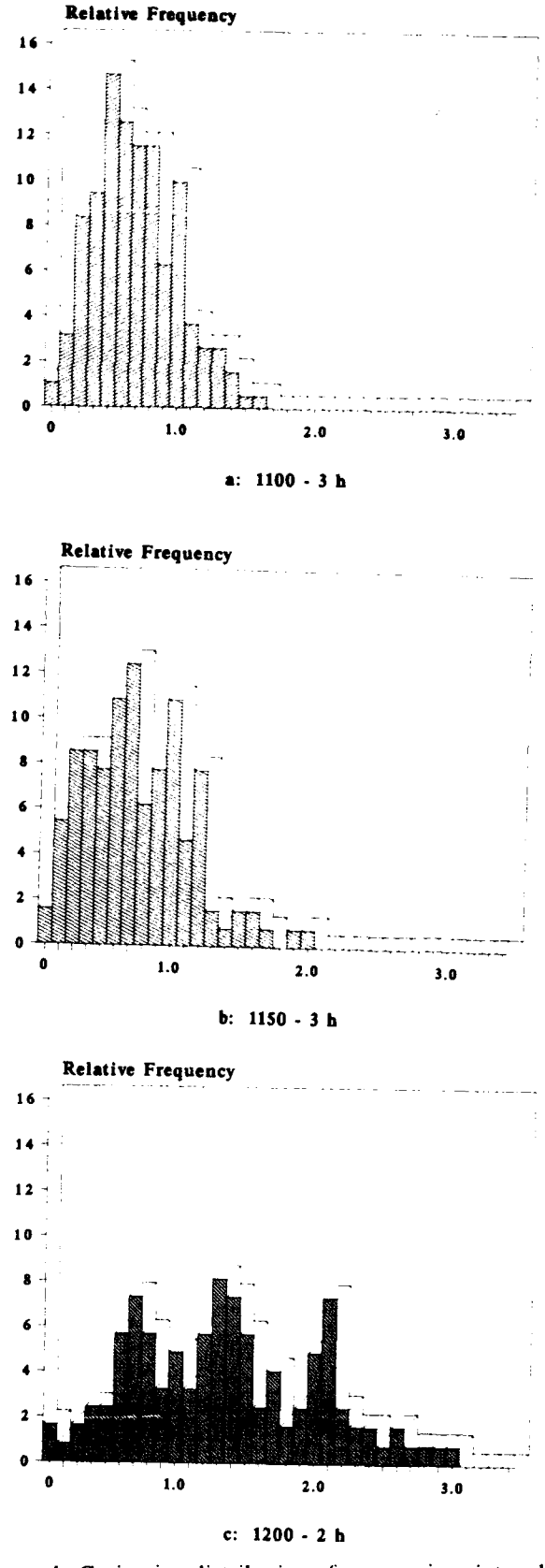


Figure 4. Grain size distributions for ceramics sintered at (a)1100°C-3h, (b) 1150°C-3h and (c) 1200°C- 2h (x-axis: grain size in μm).

Figure 5. Dielectric losses as a function of the poling field for ceramics sintered under different conditions.

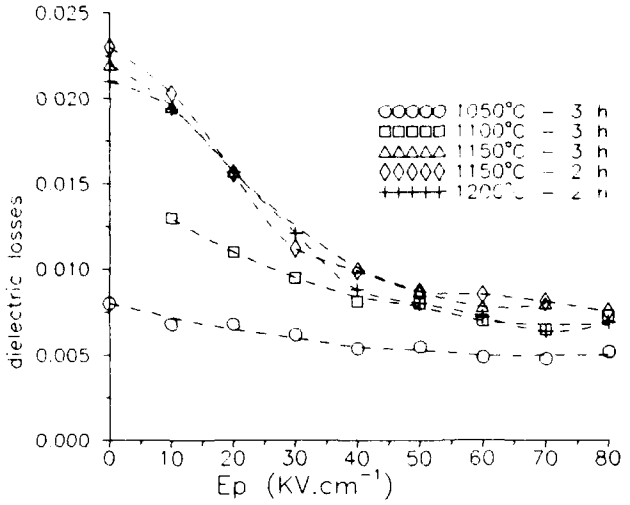
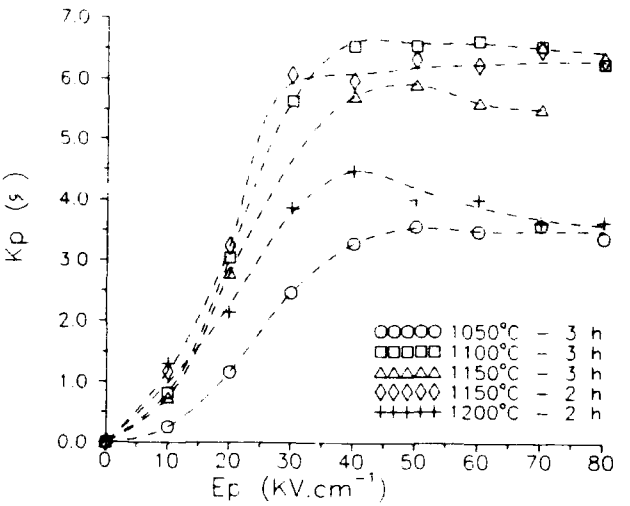


Figure 6. Variation of K_p with the poling field for different sintering conditions.



lower the sintering temperature, the lower the grain size and the dielectric losses.

It can also be seen (Figure 5) that the decrease of the dielectric losses as the poling field increases is higher the higher the grain size.

It is remarkable that when poled to saturation ($E_p > 40$ KV.cm^{-1}) all the ceramics have tanδ < 0.010. This is a low value for most high frequency bulk transducer applications and, when combined with the small grain size, suggests that these ceramics may also be suitable for applications as substrate in SAW devices.

The values of the planar electromechanical coupling factor, K_p , also show a dependence on the percentage of porosity. The higher the porosity (ceramics sintered at 1050 and 1200°C) the lower the K_p values. This is in agreement with previous works [1] on calcium modified lead titanate ceramics. Here, again, the reported tendency of increasing K_p with decreasing grain size [3] is masked by the primary effect of the porosity of the ceramic.

Both in Sm [7] and Ca [8] modified ceramics a clear decrease of K_p with the poling field has been observed from a maximum value achieved at fields of 30 to 40 KV.cm^{-1}. However, our results show (Figure 6) that the poling field dependences of K_p, for the ceramics sintered at 1050, 1100 and 1150°C (2h), do not follow this trend, although they were poled up to fields of 80 KV.cm^{-1}, higher than those reported previously. A small reduction was nevertheless observed for the ceramics sintered at 1150°C (3h) and 1200 °C. This interesting effect can be explained when the variation of grain size (Table I) and grain size distributions with sintering temperatures is considered. The first set of ceramics have smaller average grain sizes together with narrower distributions. As the average grain sizes increase and distributions become wider, the behaviour tends to be that reported for coarser grain ceramics.

In summary, it has been examined the dependence with the sintering conditions of the properties, and, also, of the change of these properties with the poling field, of fine grained Sm-modified lead titanate ceramics. Grain size effects in the behaviour of K_p and tanδ and appropriate overall properties for high frequency applications of these ceramics were found.

ACKNOWLEDGEMENTS

Authors wish to thank C. Fandiño and F. Díaz for ceramic preparation, and D. Gomez (Centro Nacional de Microelectrónica de Madrid) for SEM. This work was funded by BRITE-EURAM project contract number BREU-C91-0504.

REFERENCES

[1] J. Mendiola, C. Alemany, L. Pardo, B. Jimenez, L. del Olmo and E. Maurer, J. Mat. Sci. 22, 4395 (1987).

[2] Y. Ito, K. Nagatsuma, H. Takeuchi and S. Jyomura, J.Appl.Phys. 52 (7), 4479 (1981).

[3] S. Yomura, K. Nagatsuma and H. Takeuchi, J.Appl.Phys. 52 (7), 4472 (1981).

[4] C.E. Millar, W.W. Wolny and L.-Pedersen, ECAPD-2/IWIF, London, U.K., April, 1992.

[5] M.A. Schmidt, M.A. Janney and J.R. Mayotte, Microstructural Science 18 , 47 (1990).

[6] IEEE Standards on Piezoelectricity, ANSI/IEEE Std. 176 (1987).

[7] J.M. Hayes, T.R. Gururaja, L.E. Cross and G.L. Geoffroy J. Mat. Sci. 23 , 2087 (1988).

[8] Y. Yamashita, T. Takahashi and S. Yoshida, Ferroelectrics 54 , 131 (1984).

PROCESSING AND CHARACTERIZATION OF Ca, Ce AND Na ION DOPED LEAD TITANATES

A. Ahmad, T.A. Wheat, J.D. Canaday and A.K. Kuriakose
Mineral Sciences Laboratory, CANMET
Energy Mines and Resources Canada
Ottawa, Ontario, K1A 0G1, Canada

S.E. Prasad and S. Varma
B.M. Hi-Tech Inc.
Collingwood, Ontario, L9Y 4K1, Canada

Precursor powders of both alkaline-earth and rare-earth doped lead titanate based ceramics have been synthesised using an attrition milling process. The influence of dopants and powder processing parameters on the sintering, microstructure, dielectric and piezoelectric properties of the products is discussed.

INTRODUCTION

Piezoelectricity describes the phenomenon of generation of an electric charge in a substance which is directly proportional to the applied mechanical stress, conversely, the application of an electric field produces a proportionate dimensional change in the material. This phenomenon was first discovered in 1880 by J. and P. Curie during their systematic study on the influence of pressure on the electrical response of a variety of crystalline materials.

Initially only single crystal materials, e.g., quartz, rochelle salt, triglycine sulphate etc., that lack a centre of symmetry in their crystal structure were considered to exhibit piezoelectricity. The non-centrosymmetry in the crystal structure is an essential feature for piezoelectricity to occur. However, since the pioneering work of Gray (1) and Roberts (2) who showed that piezoelectricity can be induced in poly-crystalline barium titanate ceramics under the influence of high d.c. fields, and the subsequent discovery of piezoelectricity in solid solutions of lead zirconate-titanate (PZT) by Jaffe and co-workers (3), a variety of poly-crystalline materials have also been shown to exhibit piezoelectricity.

Recently, poly-crystalline lead titanate has been the focus of much attention for various device applications. Lead titanate is a ferroelectric material having a perovskite structure similar to barium titanate. The main features of this ceramic include: 1) an order of magnitude lower dielectric constant (~200) compared to barium titanates and PZT ceramics, 2) a high Curie point of about 500°C, 3) an almost negligible aging effect on the dielectric constant and 4) a large difference between the thickness coupling coefficient (K_t) and planar coupling coefficient (K_p). The disadvantages are, 1) poor sinterability due to a large anisotropy in the crystal structure (large c/a ratio), 2) inhomogeneities in the microstructure caused by the volatilization of lead oxide at high sintering temperatures and 3) severe poling conditions required to induce piezoelectricity in this material. However, the advantages outweigh the disadvantages, and this material is considered to be promising for high temperature, high frequency device applications, e.g., transducer elements for (ultrasonic) non-destructive testing devices, medical diagnostic apparatus, hydrophones etc. Compared to PZT ceramics, lead titanate based ceramic array transducers can be operated at higher frequencies, thus providing better image resolution. This is due to the very small lateral or planar mode coupling coefficient allowing a width-to-thickness ratio of the transducer element to be greater than one ($w/t > 1$). The large planar mode coupling factor in PZT restricts the width-to-thickness ratio of the transducer element to be less than one ($w/t < 1$) in order to prevent lateral vibrations from affecting the acoustic beam. This restriction makes it difficult for PZT ceramics to be used for high frequency array transducers. This dimensional limitation and also difficulties in machining plates into a large number of small elements, limits the operating frequency of commercially available array transducers to the 5MHz region (4-5).

The sinterability of lead titanate has been shown to be improved by doping with a variety of alkaline-earth and rare-earth oxides (6-13). The sintering temperature can also be reduced by adding transition metal oxides along with tungsten oxide as a mineralizer. Furthermore, the addition of MnO increases the insulation resistance and improves the sinterability and poling response of the material.

This improved sinterability of doped material has resulted in lead titanate becoming a practical poycrystalline piezoelectric for a variety of transducer applications, especially at the higher frequencies where the resolution necessary for the detection of subsurface microflaws is crucial if advanced structural ceramic components are to be used extensively in applications such as in high temperature gas turbines and internal combustion engine parts. This would require development of transducer materials that can operate at frequencies of 100 MHz or higher. At present, no such transducer element is commercially available. A number of lead titanate based compositions are therefore being developed by the authors.

This paper describes the effect of processing parameters on the sintering, microstructure, dielectric and piezoelectric properties of lead titanate based ceramics containing alkaline-earth and rare-earth oxides as major dopants.

MATERIALS AND METHODS

The following is a list of the intended elemental composition of the powders:

Powder	Composition
D1	$Pb_{.765}Ca_{.24}(Fe_{.03}W_{.03}Mn_{.015}Ti_{.97})O_3$
D2	$Pb_{.88}Na_{.24}(Co_{.02}w_{.02}Mn_{.02}Ti_{.97})O_3$
D3	$Pb_{.95}Na_{.1}(Co_{.02}W_{.02}Mn_{.02}Ti_{.97})O_3$
D4	$Pb_{.80}Ce_{.1}(Co_{.02}W_{.02}Mn_{.02}Ti_{.97})O_3$

A schematic diagram showing various processing steps involved for the production of modified lead titanate based materials is given in Fig. 1.

CH3080-0-7803-0465-9/92$3.00 ©IEEE

Powders were prepared from high purity commercial raw materials in the form of oxides or carbonates. Initially they were dry mixed in a rotary tumbler and then subjected to attrition milling. Batches of powder weighing 300-400 g were placed in a 1 L attrition mill containing high purity zirconia milling medium (spherical, 3 mm diameter). Water was used for the slurry along with 0.55wt% of the deflocculent 'Darvan C'. The slurry was attrition milled for two to four hours and the slurry was spray dried using a Buchi model 190 mini spray drier with an inlet temperature of ≈200°C and an outlet temperature of ≈125°C.

The powder (50-100g batches) was placed in a zirconia crucible, covered with platinum foil, and calcined in a muffle furnace between 800° and 1000°C for 2 hours.

The calcined batches were re-attrition milled for 2 hours as described previously, to break up any agglomerated particles, and dried by filtration or vacuum evaporation.

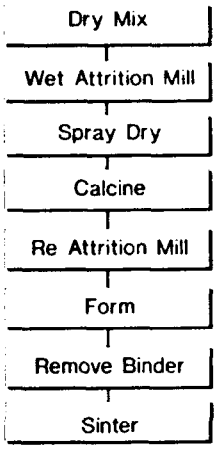


Fig 1 - Synthesis and Processing of $PbTiO_3$

The powders were pressed into 19-mm diameter pellets each weighing between 3.5 and 4.0 g. Enough powder to make 2 pellets was mixed with 5wt% of a 20wt% aqueous solution of the binder polyvinyl alcohol (PVA). The powder was placed in a lubricated (2 machine oil:1 kerosene) die and pressed at 138 MPa for 30 seconds in a hydraulic press.

Before sintering, the PVA was removed by heating the pellets in an oven at 5°C/min to 300°C and holding for 1 hour, followed by raising the temperature at 15°C/min from 300° to 600°C and holding for 2 hours.

The pellets were sintered in an electrically heated furnace at 15°C/min to 600°C and then to their respective sintering temperatures at 5°C/min.

Sintered pellets were parallel lapped with water slurry of 600 mesh silicon carbide grit to ensure the two faces were parallel. Dry polishing with 2/0 and 3/0 SiC-coated paper on a rotary polisher gave a smooth surface for electroding.

Silver electrode paint (Dupont #4731) was applied to each face, the pellet was allowed to dry and then heated at 15°C/min to 660°C and held for 15 minutes. The pellets were allowed to cool to room temperature and a second coat applied by repeating the aforementioned process. Details of the dielectric and piezoelectric measurement system and methods are described in another paper of this proceedings volume (14).

RESULTS AND DISCUSSION

X-ray diffraction (XRD) patterns of powdered samples of the oxides and carbonates that were mixed and attrition milled together showed a (perovskite) $PbTiO_3$ structure after calcination between 800° and 900°C. Only in some cases were trace amounts of unreacted oxides/carbonates or other unidentified phases detected at these temperatures. Heat treatment above 1000°C produced single phase $PbTiO_3$ materials. Typical XRD patterns are shown in Fig. 2.

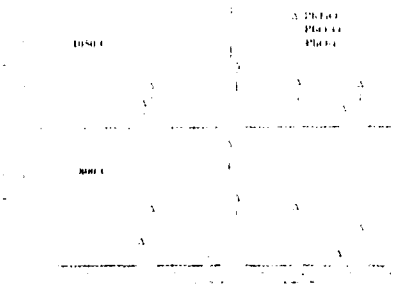


Fig 2 - XRD Patterns of D1 Powders Calcined at (a) 800°C and (b) 1050°C.

The diffraction patterns clearly showed the effect of dopants on the d-spacings of the material. Unit cell volumes and tetragonality (c/a) were calculated by indexing the diffraction patterns and obtaining "a" and "c" values using a lattice parameter calculations program developed at CANMET. Theoretical densities calculated using lattice parameters were useful in determining optimum sintering conditions. Sample densities were calculated from the masses and dimensions of lapped, polished pellets. Densities measured by Archimedes method were 2-3% larger than calculated values. The former procedure was followed because the buoyancy method is not recommended for objects weighing less than 50 g (ASTM C373-72). Data from the XRD studies, optimum sintering temperatures and observed densities for the above compositions are summarised in Table. 1. The cell tetragonality and theoretical density of undoped lead titanate is also given. All sintered materials had densities that were 92% theoretical or better. The optimum sintering temperatures and densities of the materials appear to be influenced by the sample composition. Sample D4 exhibited the highest sinter densities. The high soda content may be responsible for the observed low sintering temperatures of D2.

Table 1. Tetragonality and Density of Various Samples

Powder	c/a	Theoretical Density (g/cc)	% theor. Density (g/cc)	Sintering Temp.(°C)
D1	1.042	7.269	95.20	1150
D2	1.039	7.686	92.17	950
D3	1.045	7.955	94.80	1050
D4	1.028	7.492	96.50	1050
$PbTiO_3$	1.065	7.971	-	-

The c/a ratio for doped materials is significantly lower compared to pure lead titanate. The lower c/a ratio is a desirable feature as the materials showing less tetragonality are less susceptible to thermal shock. The explanation for this is that large differences in lattice dimensions result in large differences between the rates of thermal expansion along different axes. These differences set up mechanical stresses that result in macro or micro cracking of the ceramic body while cooling through the Curie temperature. The large anisotropy in the crystal structure is the reason why pure $PbTiO_3$ will not sinter and must be doped in order to obtain a useable product. Lowering of unit cell tetragonality has also previously been reported (7-13) for other doped lead titanates.

The above compositions also exhibited a narrow temperature range where the materials could be successfully sintered to high densities. A variation in sintering temperatures of 100°C profoundly affected the sintered densities. For example, sample D1 sintered at 1075°C produced poorly sintered/porous material (density≈ 87% of the theoretical value), whereas heat treatment to 1150°C resulted in a well-sintered material (density > 95%) having a uniform microstructure. Above 1200°C, lower densities (< 90 %), exaggerated grain growth and both micro- and macro-cracking of the sintered specimens was observed (Fig.3).

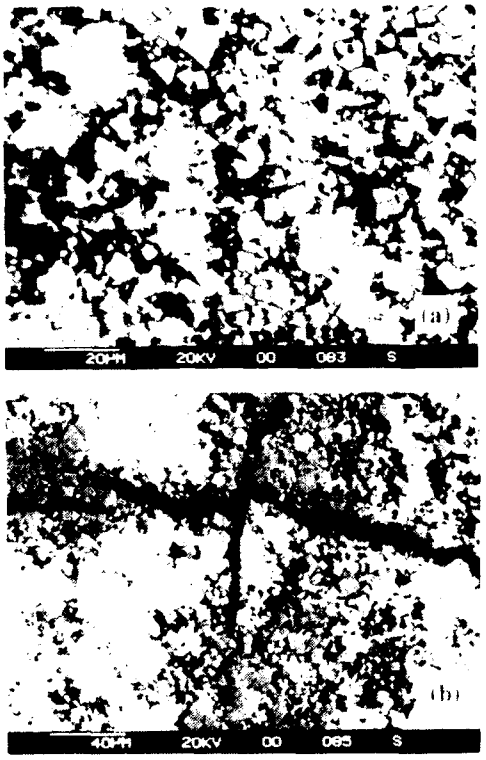


Fig 3 - Effect of Overfiring (1200°C) on sample D1.

Sample composition also appears to have an effect on the fracture behaviour of the materials. Sintered discs made from powders D1 and D4 displayed inter-granular fractures and fine microstructure (1-4 μm size particles), whereas, samples D2 and D3 predominently exhibited intra-granular fracture behaviour (Fig.4). This could be related to the presence of a second phase observed in samples D2 and D3 that appears to be glassy in nature. The glassy phase was more easily detected for D2 having a higher soda content. An EDX analysis of the polished D2 specimen revealed a sodium deficient $PbTiO_3$ type matrix and sodium-rich, lead-deficient glassy inclusions.

Results from the dielectric and piezoelectric property measurements are given in Table 2. An examination of the data indicate that both dielectric and piezoelectric properties of the sintered discs are strongly influenced by the powder compositions. Sodium ion doping (samples D2 & D3) resulted in an increase in the materials conductivity and the dielectric loss factor (tan δ). Compared to D1 & D4, the conductivity increase and dielectric losses were significantly

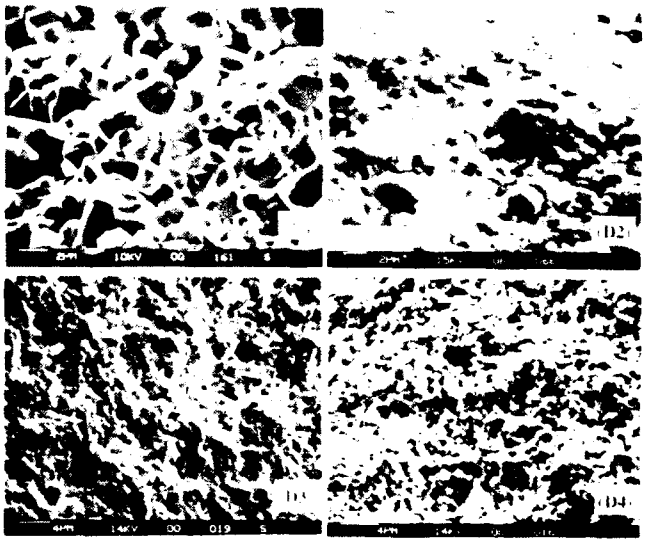


Fig 4 - SEM Micrographs of Fractured Surfaces.

higher in samples D2 & D3 near the poling temperature (≈120°C). The lower resistivity and higher losses made it impossible to electrically pole or induce piezoelectricity in these two materials. Even at small poling fields (≈ 5 kV/cm) these samples experienced electrical breakdown. An increase in soda content (D2 vs D3) also seems to promote an increase in the dielectric constant. For piezoelectric

Table 2. Dielectric and Piezoelectric Properties

Property	Composition			
	D1	D2	D3	D4
ϵ 25°C	235	326	211	322
ϵ 120°C	404	549	401	555
Tanδ @ 25°C	1.4×10^{-2}	1.5×10^{-1}	6.3×10^{-2}	6.3×10^{-2}
Tanδ @ 120°C	2.9×10^{-2}	5.2×10^{-1}	4.3×10^{-1}	1.0×10^{-1}
σ_{ac} 25°C $(\Omega\text{-cm})^{-1}$	1.8×10^{-9}	2.6×10^{-8}	8.0×10^{-9}	1.1×10^{-8}
σ_{ac} 120°C $(\Omega\text{-cm})^{-1}$	6.5×10^{-9}	1.3×10^{-7}	1.2×10^{-7}	3.0×10^{-8}
Curie Temp °C	250	-	-	290
K_p	0.049	-	-	0.12
K_t	0.51	-	-	0.31
Q_m	71	-	-	321
N_p (Hz.m)	2680	-	-	2830
N_t (Hz.m)	1910	-	-	2225
d_{33}	92	-	-	78

property measurements, samples were poled at high electric fields of ≈40kV/cm for a period of 10 minutes in a silicon oil bath kept at temperature of 110°C. The Curie temperatures were determined from the dielectric constant vs temperature plots. The Curie temperatures for cerium-doped samples (D4) are a little higher than D1 suggesting a slightly larger useful transducer operating temperature range for D4. However, the superior piezoelectric properties (i.e. K_p, K_t, Q_m, d_{33}) and the large anisotropy in electromechanical coupling factor (K_t/K_p >10) for sample D1 make it a better candidate for high frequency linear array transducers. The dielectric and piezoelectric properties of D1 samples are comparable to those reported by Yamashita et. al. (12) for Ca doped lead titanates.

CONCLUSIONS

Compared with pure lead titanate, modified lead titanates having alkaline-earth and rare-earth oxides as major dopants exhibit lower crystal tetragonality (c/a ratio ref. Table 1). Similar results have been previously reported for other modified lead titanate compositions(7-13). The data in Table 1, also suggest that, with the exception of D2, these materials can be sintered to high densities (~95% or higher). The high soda content appears to promote the low densification in D2. SEM micrographs and EDX analysis have revealed soda-rich, lead deficient inclusions that may be responsible for the observed low density of this material. SEM studies also indicate composition dependent fracture behavior. Samples D1 and D4 exhibit inter-granular fracture whereas D2 and D3 displayed intra-granular fracture. These materials also demonstrate a fairly narrow temperature range for densification. A mere 100°C variation from the optimum sintering temperatures appears to have adverse effects on both the sample density as well as its microstructure. Although sample D4 had the lowest c/a value of 1.028 exhibited the highest density, no direct correlation between the sample density and unit cell tetragonality can be determined from Table 1.

Both the dielectric as well as piezoelectric properties in these materials are strongly influenced by the sample composition. Doping with sodium ions produces more conductive and lossy material resulting in electrical breakdown of the samples during the poling process. Of all the materials studied, D1 showed the most favourable piezoelectric properties, with a thickness coupling coefficient of 0.51 and a planar coupling coefficient of 0.049 and a mechanical quality factor of 71. These characteristics make it a promising candidate for use as transducer elements for non-destructive testing of materials and similar device applications.

ACKNOWLEDGEMENTS

The authors acknowledge the technical assistance of D. Napier, Co-op student at CANMET from Waterloo University and A.G. McDonald, Technologist, Ceramic Section (CANMET) for sample preparations. The authors would also like to thank P. Carriere and Dr. J.T. Szymanski of the Mineralogy Section (CANMET), for providing XRD data and the computer programs for lattice parameter calculations.

REFERENCES

1. Gray, R.B. "Transducer and Making of the Same"; U.S. Patent, 2,486,560, Nov.1, 1949.
2. Roberts, S. "Dielectric and Piezoelectric Properties of Barium Titanate"; Phys. Rev. 71 850-855; 1947.
3. Jaffe, B., Roth, R.S. and Marzullo, S. "Piezoelectric Properties Of Lead Zirconate Titanate Solid-Solution Ceramic Ware"; J. Appl. Phys. 25:809-810; 1954.
4. Takeuchi, H., Ishikawa, Y., Yamamoto, E. "A 7.5 MHz Linear Array Ultrasonic Probe Using Modified Lead Titanate Ceramics"; Proceedings of the IEEE Ultrasonic Symposium, San Diego, CA. Institute of Electrical and Electronic Engineers, pp. 849-853; 1982.
5. Honda, H., Yamashita, Y. and Uchida, K. "Array Transducer Using Modified Lead Titanate Ceramics"; ibid., pp. 845-848.
6. Ueda, I. "Effect of Additives on Piezoelectric and Related Properties of $PbTiO_3$ Ceramics"; Japanese J. of Appl. Phys. 11(4):450-462; 1972.
7. Ikegami, S., Ueda, I. and Nagata, T. "Electromechanical Properties of $PbTiO_3$ Ceramics Containing La and Mn"; The J. Acoust. Soc. of America 50(4) (Part 1): 1060-1066; 1971.
8. Duran, P., Fadez Lazano, J.F., Capel, F. and Moure, C. "Large Electromechanical Anisotropic Modified Lead Titanate Ceramics"; J. Mater. Sci. 23:4463-4469; 1988.
9. Ueda, I. and Ikegami, S. "Piezoelectric Properties of Modified $PbTiO_3$ Ceramics", Jap. J. Appl, Phys. 7(3):236-242; 1968.
10. Yamashita, Y., Yoshida, S. and Takahashi, T. "Effect of MnO Additive on Piezoelectric Properties of Modified $(Pb,Ca)TiO_3$ Ferroelectric Ceramics", Proceedings Of the 4th Meeting on Ferroelectric Materials and Their Applications, Kyoto, 1983; Jap. J. Appl. Phys. 22: Supplement 22-2, pp.40-42, 1983.
11. Ahmad A. Wheat, T.A., Kuriakose, A.K., Quon, D.H.H. and Berry, R. "The Effect Of Processing Parameters on The Properties of Modified Lead Titanate"; Division Report MSL 88-19(OP), CANMET, EMR, Canada; 1988.
12. Yamashita, Y., Yokoyama, K., Honda, H. and Takahashi, T. "$(Pb,Ca)((Co_{1/2}W_{1/2}),Ti)O_3$ Piezoelectric Ceramics and Their Applications"; Jap. J. Appl. Phys. 20 (Supp. 20-4):183-187; 1981.
13. Ahmad, A., Besso, K., Chehab, S., Wheat, T.A. and Napier, D. "Chemical Processing of Modified Lead Titanate"; J. Mater. Sci. 25:5298-5302; 1990.
14. Ahmad. A, Wheat, T.A., Sherrit, S. and Jones, D. "Microstructure, Dielectric, Piezoelectric and Pyroelectric Properties of Chemically Derived Lead Titanate"; Proc. ISAF'92 (this publication).

MICROSTRUCTURAL, DIELECTRIC, PIEZOELECTRIC AND PYROELECTRIC PROPERTIES OF CHEMICALLY DERIVED MODIFIED LEAD TITANATE

A. Ahmad and T.A. Wheat
Mineral Sciences Laboratory, CANMET
Energy Mines and Resources Canada
Ottawa, Ontario, K1A 0G1, Canada

S. Sherrit and B.K. Mukherjee
Royal Military College of Canada
Kingston, Ontario, K7K 5L0, Canada

Chemical co-precipitation and gel processing techniques have been used to synthesize precursor powders of a modified lead titanate composition. The effects of powder processing parameters and sintering conditions on the microstructure and dielectric, piezoelectric and pyroelectric properties of the products are discussed. A comparison is made between powders and products made by conventional attrition milling process and those produced via chemical processing techniques.

INTRODUCTION

There has been growing interest in the development of lead titanate based ceramics for a variety of piezoelectric/pyroelectric devices applications. Some of the attractive features of lead titanate ceramics include: a high Curie temperature (>250°C), high spontaneous polarisation, low dielectric constant(~200), a very small aging rate of dielectric constant, a large difference between the thickness coupling constant (k_t) and planar coupling constant (k_p) and relatively low mechanical quality factor (Q_m). These characteristics make it a promising candidate for high frequency ultrasonic transducers for non destructive evaluation of materials, medical diagnostics, SAW devices, infrared sensors etc (1-3). However, difficulties are encountered in the sintering and subsequent poling of $PbTiO_3$ due to the high anisotropy in its crystal structure (large c/a ratio), which leads to the development of micro- and macrocracks upon sintering and subsequent cooling through the Curie point. Doping with alkali metals, transition metals or rare earth oxides has been shown to produce crack-free high-density material (1,4-6).

In recent years there has been greater emphasis on the synthesis of precursor powders via chemical routes (7-11). This approach is believed to offer greater control of chemical composition, homogeneity, particle size, shape and other key parameters considered necessary to produce high performance advanced ceramics.

In an earlier study (12) we reported the synthesis and characterization of calcia-doped lead titanate compositions having a general formula,

$$[Pb_{1-x}Ca_x][(Co,W)_yMn_zTi_{1-2y-z}]O_3$$

where

$$x \leq 0.30,\ y \leq 0.03,\ z \leq 0.01$$

Two different chemical routes and also conventional attrition milling methods were used to synthesize the precursor powders. The influence of powder processing methods on the crystal structure, unit cell parameters and the particle size/surface area were discussed. This study provides data on the microstructural, dielectric, piezoelectric and pyroelectric properties of the above materials.

EXPERIMENTAL PROCEDURES

Precursor powders were prepared by a gel-process and a co-precipitation route and also by a conventional attrition milling process. Powders were calcined in air at 750°C for two hours. Green discs 1.3 cm in diameter were formed at ~25,000 psi and sintered at 1050°C for three hours. Coarse powder of the same composition was loosely packed around the samples to provide a PbO atmosphere during sintering. Details of the syntheses are reported elsewhere (12).

For dielectric, piezoelectric and pyroelectric measurements the samples were parallel lapped using wet SiC powder (600 mesh), cleaned in isopropanol using an ultrasonic bath, dried, electroded (using Dupont #4731 silver ink) and fired at 600°C for 15 minutes. For piezoelectric/ pyroelectric measurements samples were poled at 40 kv/cm in a silicone oil bath at 100°C for 10 minutes. The radial mode resonance of the samples were analyzed using the method of Sherrit et al. (13) with slight modifications. When the material k_p is small the analysis can be dependent on 1 Hz shifts in frequency. However the resolution in frequency from the impedance scans is only 10 Hz at best. To fit the data the critical frequencies were determined to 10 Hz resolution as usual and a fit was calculated. The frequencies were then adjusted to 1 Hz to minimize the errors of the fit.

The materials constants of the thickness mode were determined using the method of Smits (14). The constants for both modes were determined at the resonance frequency except for ϵ^t_{33} which was determined at 1 kHz. The impedance scans were measured with an HP 4192 impedance analyzer.

The pyroelectric characteristics were determined using

$$p = I/(dT/dt)A$$

as described by Byer and Roundy (15) where I is the short circuit current, A is the electrode area and dT/dt is the temperature ramp rate. The current was measured using a Keithly 619 electrometer. The ramp rate was set at 1°C per minute. The temperature was measured using a chromel-alumel thermocouple referenced to an ice bath imbedded in a stainless steel stage below the sample.

The hydrostatic measurements were made in a pressure vessel. The sample and a standard of known g_h were placed in the chamber filled with oil. The static pressure is increased to the desired level and an ac hydrostatic pressure of 400 Hz was generated using a volume expander. The response of the standard and sample to the ac hydrostatic pressure was recorded using a lock-in amplifier, and corrections were made to both by noting the stray capacitance of each. The g_h of the sample was then determined from using the relationship:

$$g_h = g_{hs}\,(V_s t_s / V t)$$

where g_{hs} , V_s , t_s are respectively the hydrostatic voltage

CH3080-0-7803-0465-9/92$3.00 ©IEEE

coefficient, the voltage generated by the standard and the thickness of the standard, and V and t are the voltage generated by the sample and the sample thickness respectively. The average value of piezoelectric d_{33} coefficient was measured using a Berlincourt d_{33} meter (model CPDT 3300, Channel Products, Inc. Chagrin Fall, Ohio).

RESULTS and DISCUSSION

The X-ray diffraction patterns of the powders calcined at 750°C are shown in Fig. 1. Only gel-processed material produced single phase lead titanate at this temperature. Both the attrition milled and coprecipitated powders showed the presence of trace amounts of unreacted lead oxide. However, all three materials exhibited single phase lead titanate at the sintering temperature of 1050°C.

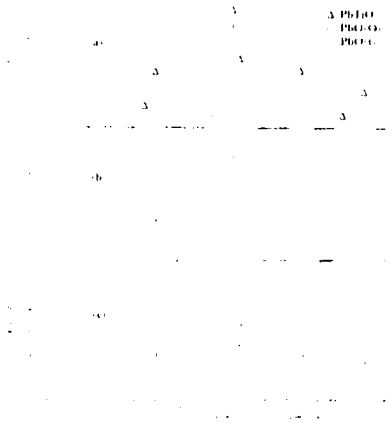


Fig .1 - XRD diffraction patterns of precursor powders heated to 750°C: (a) attrition milled, (b) co-precipitated and (c) gel processed.

The SEM micrographs of the gel-derived, coprecipitated and attrition milled powders heat treated at 750°C are shown in Fig. 2. The gel processed material produced hard agglomerated particles ranging from 1-100 μm in size. Most grains have a smooth glass-like surface and exhibit microporosity and microcracking. A closer examination of the material reveals the formation of $PbTiO_3$ crystals in a glassy type matrix. Green discs made from these powders could not be sintered to > 90% of the theoretical density. However, after attrition milling this material for 30-45 minutes the sintered densities of the pellets improved significantly (> 96%). This is due to the removal of internal micro-porosity in the particles via attrition milling.

The powders prepared by chemical coprecipitation and dried at 750°C produce irregularly shaped particles and small lumps ranging between 1 μm and 100 μm in size. Those in excess of 10 μm were usually multi-phase. Some of the agglomerates have an almost granular appearance and a few of the smaller agglomerates have elongated platelets of PbO, thus indicating compositional inhomogeneity. Like gel-processed materials, these powders also required attrition milling for 30-45 minutes to produce pellets having densities in excess of 95% of the theoretical value.

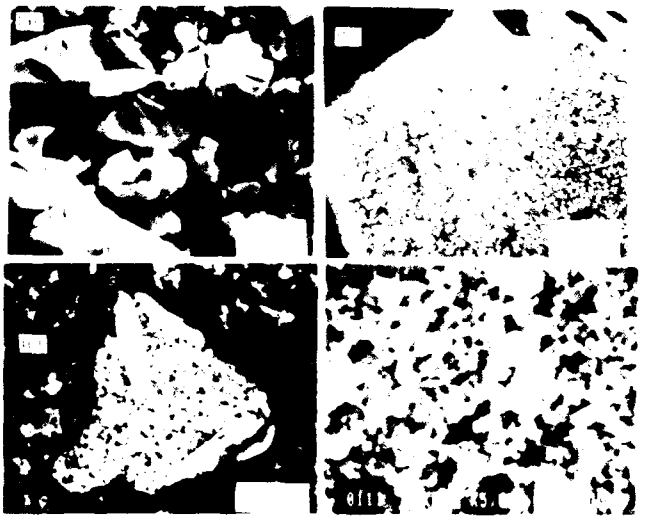


Fig .2 - SEM micrographs (a,b) gel processed, (c) co-precipitated and (d) attrition milled powders heated to 750°C.

The powders produced via attrition milling and dried at 750°C mainly consist of $PbTiO_3$ crystals bound together. The individual grains are from 0.5 to 4 μm. Only trace amounts of PbO were detected. It was impossible to produce sintered discs having densities in excess of 93% even after re-attrition milling for an hour using these powders; however addition of approximately 1-2 weight percent excess PbO in the calcined powders improved the sintered densities to > 96% of the theoretical value.

Fractured surfaces of the sintered samples were also examined using SEM. The micrographs indicated intragranular fracture and low porosity in all three case. The pores generally remained less than 2-5 μm in size.

Results from the dielectric, piezoelectric and pyroelectric property measurements are given in Table 1. Typical examples of both the radial and thickness mode resonance plots along with a polynomial least square fit (13) to the experimental data are also shown in Fig.3. The results clearly indicate that these materials posses attractive properties for potential applications in various practical devices. For example, sintered and poled discs made from the three different powders exhibited very small radial mode coupling coefficients k_p (.012-.032)and large thickness mode coupling coefficients k_t (0.42-0.52). Also the ratio of the coupling coefficients k_t/k_p in all three cases is fairly large (≈13-42). These features enable efficient coupling between transducer and medium without interference from undesirable modes, providing improved resolution (larger signal to noise ratio), hence greater detectability for nondestructive testing (NDT) applications. The higher signal resolution also suggests that transducers made from these materials for medical diagnostics applications can be operated at a lower drive level making ultrasonic imaging a safer diagnostic tool. The large values for longitudinal piezoelectric constant, d_{33}, (≈71 to 88×10^{-12}) and relatively much smaller lateral piezoelectric constants, d_{31} (-1.145 to -3.21×10^{-12}) imply that the hydrostatic piezoelectric coefficient,

Table 1. Dielectric Piezoelectric and Pyroelectric properties

Properties	Gel	Coppt	Milled
Density (10^3 Kg/m^3)	6.88	6.77	6.97
Poisson's ratio σ^E	0.210	0.212	0.216
Curie temperature (°C)	250	280	265
Mech. quality factor Qm	78	85	126
Dielectric const @ 1 KHz	210	208	198
Dissipn. factor @ 1 KHz	0.014	0.025	0.027
Permitivity (x10^{-9} F/m)			
ϵ^T_{33}	1.86	1.85	1.75
ϵ^S_{33}	1.37	1.47	1.31
Coupling factors			
k_p	0.015	0.032	0.012
k_t	0.46	0.42	0.52
k_t / k_p	30.52	13.26	42.2
Piezoelect. const			
d_{31} (x 10^{-12} CN^{-1})	-1.53	-3.21	-1.15
d_{33} (x 10^{-12} CN^{-1})	79	71	88
d_h (x 10^{-12} CN^{-1}) @10 MPa	50.6	41.50	58.50
g_h (x 10^{-3} V m N^{-1}) "	24.25	19.90	28.8
$g_h d_h$ (x 10^{-15} m^2 N^{-1}) "	1228	824	1686
Elastic properties			
S^E_{11} (x 10^{-12} m^2 N^{-1})	8.27	8.18	7.52
S^E_{12} (x 10^{-12} m^2 N^{-1})	-1.74	-1.73	-1.63
C^D_{33} (x10^{11} Nm^{-2})	1.41	1.38	1.6
Q_{11}	-295	-622	-1041
Q_{12}	-329	-708	-1364
Pyroelectric coeff. (p)			
(x 10^{-4} Cm^{-2} K^{-1}) @ 50°C	4.9	4.5	1.4

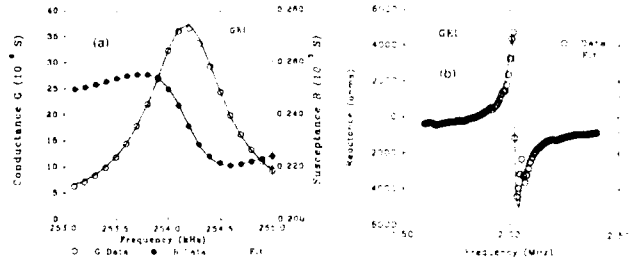


Fig .3 - Conductance, susceptance and reactance as a function of frequency for a gel-processed piezoelectric resonator: (a) radial mode (b) thickness mode.

$$d_h = d_{33} + 2d_{31}$$

is only slightly smaller than d_{33}. These characteristics coupled with a low mechanical quality factor Q_m (75-125) and a low dielectric constant (≤ 210) make them suitable for under water transducer applications. The measured hydrostatic voltage coefficient g_h and the product $g_h d_h$ are more than an order of

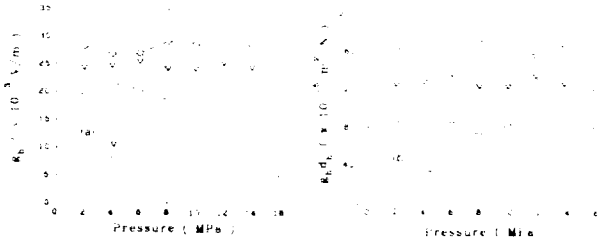


Fig .4 - Variation of (a) g_h and (b) $g_h d_h$ as a function of applied pressure for materials produced using gel-processed, co-precipitated and attrition milled powders.

magnitude higher (Fig. 4) than commercially available PZT ceramics (16). The g_h and d_h values only varied slightly with increasing hydrostatic pressure, however, these parameters showed significant dependence on the methods for producing the precursor powders. The $g_h d_h$ values for sintered and poled specimens produced from attrition milled powders were twice those measured for coprecipitated materials. The large anisotropy in various coupling modes of these materials is also very useful as it allows transducer designs with simple flat plates as opposed to hollow cylindrical or spherical geometries commonly used with PZT ceramics. The measured pyroelectric coefficients (p) of these materials are also comparable or superior to many leading pyroelectric ceramics e.g. $LiTaO_3$, PZT, PZT-PZN, TGS, $(Pb,Ba)TiO_3$, $(Pb,Sr)TiO_3$ etc. (17-20). The high pyroelectric coefficients and the low dielectric constants (≤210) of these materials make them very attractive for various infrared detection and thermal imaging device applications.

The dielectric, piezoelectric and pyroelectric properties of the materials investigated also showed dependence upon the methods used to prepare the precursor powders. Discs produced using the attrition milled powders provided the highest K_t, d_{33}, d_h and g_h values. These discs also displayed the lowest k_p, d_{31} and dielectric constant. The relatively superior piezoelectric properties for attrition milled materials could be due to the excess PbO used to improve the sintered densities as discussed in the previous section. Mendiola et al. (21) have previously suggested that the possible presence of unreacted PbO in the grain boundaries of the modified lead titanate ceramics, presumably, promoted high preferential rotation of 90° domains during poling treatment and yielded an unusually large k_t/k_p value.

The gel-processed materials displayed the highest pyroelectric coefficient and lowest mechanical quality factor (Q_m) and dielectric loss or dissipation (tan δ). In general, samples produced from

coprecipitated powders exhibited relatively inferior piezoelectric properties. This could be related to the compositional inhomogeneities observed in the microstructure due presumably to the variations in precipitation kinetics or undesirable chemical reactions as discussed earlier.

CONCLUSIONS

The above studies indicate that among the three processing methods gel processing provides the most reactive precursor powders. These powders when heat treated to 750°C produce single phase lead titanate; whereas both coprecipitated and attrition milled powders show trace amounts of unreacted lead oxide at this temperature.

The SEM studies indicate that, compared with conventional attrition milling, the chemically-derived powders contain highly agglomerated large particles (1-100μm in size as opposed to < 5 μm for attrition-milled material) when heat treated to 750°C. However, the chemically-derived material can easily be crushed to yield a submicron particle size that can provide high density sintered discs (≈97% of the theoretical). When heat-treated, the chemically-derived powders display microporosity and microcracking presumably due to the decomposition of the organics which may explain the observed high surface area of these powders (12). The chemically derived powders also exhibit a titania-rich glassy phase that may be responsible for the observed higher sintered densities compared with the attrition-milled material. However, attrition milled materials can be sintered to high densities (>96%) using excess PbO (1-2 wt%). Microstructural studies also revealed compositional inhomogeneities in the coprecipitated precursor powders.

The dielectric, piezoelectric and pyroelectric properties of these materials are also significantly influenced by the methods used to produce the precursor powders. Attrition milled materials exhibit the most favourable piezoelectric properties; however, gel processed materials display the highest pyroelectric coefficient. Compared to the leading commercial product (PZT), these materials possess many attractive properties for possible exploitation in a variety of electromechanical and thermal detection and imaging devices.

ACKNOWLEDGMENTS

The authors acknowledge the technical assistance of their colleagues in the Mineral Sciences Laboratories, E.M & R, CANMET, in particular Dr. J.T. Szyamanski and Mr. P. Carriere for providing XRD data on the powders and Mr. A.G. McDonald for powder preparations. The authors would also like to thank Dr. A.K. Kuriakose of the Mineral Sciences Laboratories for very stimulating and invaluable discussions throughout the course of this work.

REFERENCES

1. Y. Yamashita, K. Yokoyama, H. Honda and T. Takahashi, "(Pb,Ca) ($Co_{1/2}$ $W_{1/2}$),TiO_3) Ceramics and their Applications"; Jap. J. Appl. Phys. 20 (Supplement 20-4), pp.183-187; 1981.
2. Y. Ito, H. Takeuchi, K. Nagatsuma, S. Jyomura and S. Ashida, "Surface Acoustic Wave Properties Of (Pb,Ln)(Ti,Mn,In)O_3 Ceramics (Ln = La and Nd)", J. Appl. Phys. 52(5) 3223-3228. 1981
3. N. Ichinose, Electronic Ceramics for Sensors", Amer Ceram. Soc Bull. 64(12) 1581-1585; 1985
4. I. Ueda and S. Ikegami, "Piezoelectric Properties of Modified $PbTiO_3$ Ceramics" Jap. J. Appl. Phys. 7(3) 236-242, 1968.
5. S. Ikegami, I. Ueda and T. Nagata, "Electromechanical Properties of $PbTiO_3$ Ceramics Containing La and Mn"; J. Acoust. Soc. of America 50(4) (Part 1) 1060-1066; 1971.
6. I. Ueda, "Effect of Additives on Piezoelectric and Related Properties of $PbTiO_3$ Ceramics", Jap. J. Appl. Phys. 11(4):450-462, 1972
7. C.J. Brinker, D.E. Clark, D.R. Ulrich "Better Ceramics Through Chemistry", Material Research Society Symposium Proceedings Volume 32, (1984)
8. C.J. Brinker, D.E. Clark, D.R. Ulrich "Better Ceramics Through Chemistry II "; Material Research Society Symposium Proceedings Volume 73, (1986).
9. C.J. Brinker, D.E. Clark, D.R. Ulrich "Better Ceramics Through Chemistry III ", Material Research Society Symposium Proceedings Volume 121, (1988)
10. L.L. Hench and D.R. Ulrich "Ultrastructure Processing of Ceramics, Glasses and Composites"; John Wiley & Sons, Inc. New York (1984).
11. J.D. Mackenzie and D.R. Ulrich "Ultrastructure Processing of Advanced Ceramics" , John Wiley & Sons, Inc. New York (1988).
12. A. Ahmad, K. Besso, S. Chehab, T.A. Wheat and D. Napier, "Chemical Processing of Modified Lead Titanate"; J. Mater. Sci. 25:5298-5302, 1990
13. S. Sherrit, N. Gauthier, H.D. Wiederick, B.K. Mukherjee, "Accurate Evaluation of the Real and Imaginary Material Constant for Piezoelectric Resonator in Radial Mode"; *Ferroelectrics*, 119:17-32, 1991.
14. J.G. Smits, "Iterative Method for Accurate Determination of Real and Imaginary Parts of Material Coefficients of Piezoelectric Ceramics"; IEEE Trans. On Sonics and Ultrasonics, SU-23:393-402, 1976.
15. R.L. Byer, C.B. Roundy, "Pyroelectric Coefficient Direct Measurement Technique", Ferroelectric 3:333-338, 1972.
16. A. Safari "Perforated PZT-Polymer Composites with 3-1 and 3-2 Connectivity for Hydrophone Applications"; Ph.D, Thesis, The Pennsylvania State University, USA, 1983.
17. A.S. Bhalla, R.E. Newnham, L.E. Cross, W.A. Schulze, J.P. Dougherty and W.A. Smith, "Pyroelectric PZT-Polymer Composites", Ferroelectrics 33:139-146, 1981.
18. R.W. Whatmore, "Pyroelectric Devices and Materials"; Rep. Prog. Phys. 49:1335-1386; 1986.
19. V.M. Jamadar, T.A. Patil and S.H. Chavan, "Pyroelectric Properties of Lead-Barium and Lead-Strontium Titante"; Bull. Mater. Sci. (India); 9(4):249-253; 1987.
20. T. Shiosaki, J. Lian, M. Adachi and A. Kawabata, "Pyroelectric and Ferroelectric Properties in the PZT-$Pb(Zn_{1/3}Nb_{2/3})O_3$ System"; Ferroelectrics; 92:23-28; 1989.
21. J. Mendiola, M.L. Pardo and L. Del Olmo, "Electric Poling Effect on Piezoelectricity of Calcium Modified Lead Titanate Ceramics"; Ferroelectrics; 29:1249-1252; 1988.

Fabrication and Piezoelectric Properties of PZT Ceramics Prepared by Partial Oxalate Method

Hyo-Duk Nam* and Hee Young Lee#
Departments of Electronic Engineering and Materials Science and Engineering#, Yeungnam University, Kyongsan, 712-749, Korea

Abstract

$Pb(Zr,Ti)O_3$ powders were synthesized by the partial oxalate method and the modified partial oxalate method, where the difference between the two is the use of pre-reacted $(Zr,Ti)O_2$ in the former method. When compared with conventional mixed oxide method, calcination temperature can be reduced to less than 700 ℃ by both partial oxalate methods, and the resulting particle size was finer and more uniform. Using partial oxalate-derived PZT powders, sintering temperatures can also be reduced as low as 950℃ without sacrificing desired dielectric and piezoelectric properties, such as relative permittivity, electromechanical coupling factor, and piezoelectric coefficient. Two partial oxalate methods yield ceramics with almost the same physical and electrical properties, so that the step of producing ZTO powder does not seem to be necessary.

1. Introduction

Today, most of PZT ceramics are still fabricated from PZT powder obtained by calcining PbO, ZrO_2, and TiO_2 powder mixture[1], although PZT powder from chemically-derived precursor such as alkoxide, oxalate, or sol-gel is available to some extent. The latter has been developed to improve the uniformity, purity and particle shape, and to obtain smaller particle size and narrow distribution of resulting PZT powder. The fine and uniform powder synthesized by such chemical methods is advantageous in many engineering applications as lower firing temperature and improved reproducibility of properties can be realized. However, such chemical synthesis is not suitable for mass production due to low yield and high cost of powder.

The pure chemical methods[2] have shown a lack of productivity and the mechanical milling of conventionally calcined powder[3] have demonstrated a lack of purity of the resulting product. Therefore, it has been necessary to develop novel processes to combine the advantages and to eliminate the disadvantages of the two techniques. An example of newly developed chemical methods is the multi-stage coprecipitation method proposed by Watanabe et al.[4]

Recently, Yamamoto et al.[5-6] proposed the partial oxalate method which combined the conventional mixed oxide method and the chemical method for the synthesis of PZT powder. In this method, $Zr_{0.53}Ti_{0.47}O_2$ is used as starting material with lead oxalate prepared from lead nitrate and oxalate solution. This approach attempted to produce the most active parts by the chemical method and bypass the conventional reaction process, and thereby eliminating the formation of $PbTiO_3$[7] which is formed as an intermediate product during firing of the mixed oxide powder.

In this paper, the synthesis and low temperature firing of fine PZT powder is presented. We have used both the partial oxalate method which was originally proposed by Yamamoto and the modified partial oxalate method to synthesize PZT powder, and have investigated the dielectric and piezoelectric properties of PZT ceramics. The reaction mechanisms for the formation of PZT powder through the partial oxalate method are being proposed. Finally, the piezoelectric properties of PZT ceramics prepared by both the partial oxalate methods and the conventional mixed oxide method are compared as well as the firing temperatures.

2. Experimental Procedure

The chemical composition used in this study is given below. Raw materials were high purity PbO, ZrO_2, TiO_2, $Pb(NO_3)_2$, $(COOH)_2 \cdot 2H_2O$ and Nb_2O_5 chemicals. The types and characteristics of raw materials used in this study were summerized in Table 1.

$$Pb(Zr_{0.53}Ti_{0.47})O_3 + 0.5 \text{ mol\% } Nb_2O_5 \quad \text{or} \quad Pb(Zr_{0.53}Ti_{0.47})Nb_{0.01}O_3 \qquad (1)$$

In the partial oxalate method, the first of three methods tried in this study, weighed ZrO_2 and TiO_2 powders in molar proportion of 0.53 : 0.47 were mixed for 6 hours by wet ball milling, followed by calcination at 1300℃ for 3 hours to form $(Zr_{0.53}Ti_{0.47})O_2$ solid solution (ZTO). In addition, ZrO_2 and TiO_2 powder mixture doped with 0.5 mol % Nb_2O_5 powder was also calcined at 1300℃ (NZTO). In this study, we have used NZTO powders prepared by the above method and/or purchased from Sakai Chemical Co., Japan. Instead of PbO, lead oxalate prepared by mixing lead nitrate and

CH3080-0-7803-0465-9/92$3.00 ©IEEE

Table Raw materials used for various PZT preparation methods.

Method / Raw Materials		Mixed Oxide Method	Partial Oxalate Method		Modified Par. Oxa. Method
Chemical	D_{50}(μm)	PZT	P-ZT(1)*	PZ-T(1)	P-ZT(2)
PbO	3.63	○			
ZrO_2	0.70	○			○
TiO_2	1.18	○			○
Nb_2O_5	0.56	●	●		●
$(COOH)_2 \cdot 2H_2O$	-		○	○	○
$Pb(NO_3)_2$	-		○	○	○
ZTO	1.62		○		
NZTO	0.33			○	
PbC*	0.01				

Preliminary experiments showed similar characteristics for two combinations shown here, and therefore NZTO purchased from Sakai Chemical Co. was used throughout the study.
* Powder produced by thermal decomposition of lead oxalate precipitates.

oxalic acid aqueous solution was used in this method.

At first, ZTO or NZTO powder was dispersed in 1 mol oxalic acid aqueous solution, and 1 mol lead nitrate solution was dropped into the solution to form fine lead oxalate particles which precipitated onto rather large ZTO particles. Then, ZTO precipitates coated with lead oxalate was washed with distilled water until NO_3^{2-} ion was not detected in washing liquid, followed by drying and calcining at 650 ~ 750℃ for the formation reaction of PZT. The ball-milling of calcined PZT agglomerates was necessary to obtain fine PZT powder.

The modified partial oxalate method was devised to eliminate energy-consuming reaction of ZTO or NZTO production. In this method, the mixture of ZrO_2, TiO_2 and/or Nb_2O_5 particles replace ZTO or NZTO of the partial oxalate method. The detailed explanation of two processes are shown in Fig. 1.

The third method to obtain PZT powder was the well-known solid state reaction technique of mixed oxides. The powder produced by this method was used to make PZT ceramic in order to compare its properties with those prepared by partial oxalate methods.

The shape and size of synthesized powder were observed using scanning electron microscope, and the distribution of particle size was examined using particle size analyzer utilizing centrifugal sedimentation. Phase analysis of the powder was done by X-ray diffractometer. Sintering behavior of the powder was examined by pressing the powder into the pellet at 98 MPa and firing at 850 ~ 1200℃ for three hours. Bulk density, crystal structure, dielectric and piezoelectric properties, and poling behavior of PZT ceramics were then examined. Fired-on silver paste was applied onto two faces of discs by heat treatment at 800℃ for 10 minutes. Poling was performed by immersing the ceramic into silicone oil at 130℃ and applying 3 kV/mm field.

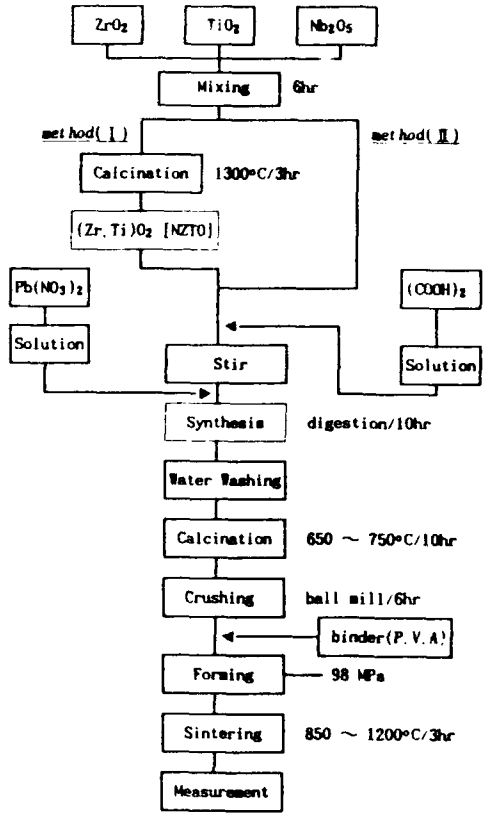


Fig. 1. Flow chart of PZT preparation by partial oxalate method(Ⅰ) and modified partial oxalate method(Ⅱ).

3. Results and Discussion

In order to study the decomposition and/or phase transformation reactions for lead oxalate obtained from mixing lead nitrate and oxalic acid, thermogravimetric and differential thermal analysis were made, and the results are shown in Fig. 2. An exothermic peak at 425 ℃ is due to the formation of free PbO, and an endothermic peak at 900℃ is due to melting of PbO. Above 900℃ weight loss due to evaporation of PbO is evident from TGA curve. Therefore, the PZT formation in partial oxalate methods may be postulated as the series of following reactions.

$$0.53\ ZrO_2 + 0.47\ TiO_2 \rightarrow (Zr_{0.53}Ti_{0.47})O_2 \quad (2)$$

$$Pb(NO_3)_{2(aq)} + (COOH)_2 \cdot 2H_2O_{(aq)} \rightarrow PbC_2O_{4(s)}\downarrow + 2\ HNO_{3(aq)} \quad (3)$$

$$PbC_2O_4 + \tfrac{1}{2}\ O_2 \rightarrow PbO + 2\ CO_2 \quad (4)$$

$$PbO + (Zr_{0.53}Ti_{0.47})O_2 \rightarrow Pb(Zr_{0.53}Ti_{0.47})O_3 \quad (5)$$

or

$$Pb(NO_3)_{2(aq)} + (COOH)_2 \cdot 2H_2O_{(aq)} + [(ZrO_2/TiO_2)] \rightarrow PbC_2O_{4(s)}\downarrow + [(ZrO_2/TiO_2)\ \text{mixture}] + 2\ HNO_{3(aq)} \quad (6)$$

$$PbC_2O_4 + \tfrac{1}{2}\ O_2 \rightarrow PbO + 2\ CO_2 \quad (7)$$

$$PbO + [(ZrO_2/TiO_2)\ \text{mixture}] \rightarrow Pb(Zr,Ti)O_3 \quad (8)$$

From Fig. 2, one can see that reactions (4) and (7) occurred at about 425℃, whereas PZT formation reactions (5) and (8) start to occur at 600℃, which was confirmed by the endothermic peak of DTA curve for the same system reported by Yamamoto et al.[6] In addition, XRD patterns revealed the formation of PZT perovskite phase for partial oxalate methods started to occur in the temperature range of 650 ~ 700℃. This is much lower than the temperature range for mixed oxide method, where typical value is in the range of 850 ~ 900℃.

The lowering of PZT formation temperature in partial oxalate methods can be explained by the following. First of all, in mixed oxide method, as temperature increases, $PbTiO_3$ tends to be formed as an intermediate product[7], which then reacts with remaining ZrO_2 to form PZT at a higher temperature. On the other hand, in the partial oxalate method, ZTO powder is used to avoid the formation of $PbTiO_3$, and therefore PZT is formed at a lower temperature. In addition, the use of ultra fine PbO powder produced by the pyrolysis of lead oxalate powder may lower the calcination temperature, since the diffusion path is reduced in a great deal.

Average particle sizes of calcined PZT powders prepared by various methods used in this study are 0.94 μm for conventional mixed oxide method, 0.47 μm for partial oxalate method, and 0.52 μm for modified partial oxalate method. Calcination temperatures were 850 ℃ for mixed oxide and 710℃ for both oxalate methods. It is evident that two partial oxalate methods yield finer particles than conventional mixed oxide method.

In Fig. 3, the temperature dependence of bulk densities of ceramics fired over the temperature range of 850 ~ 1200℃ is demonstrated for various preparation methods. In Fig. 3 and the following figures, same symbols are used to denote various powder preparation routes. Solid dot, open square and triangle represent mixed oxide [PZT], partial oxalate [PZT(1)] and modified partial oxalate-derived powders [PZT(2)], respectively. PZT powders synthesized by two partial oxalate methods show similar sintering behavior, whereas the powder obtained by mixed oxide method shows much sluggish sintering kinetics, and as a result, higher temperatures are necessary to obtain the same sintering densities. It is noted that almost full density is

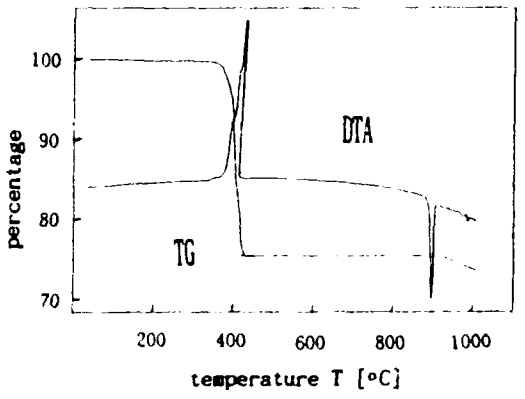


Fig. 2. DTA and TGA curves of lead oxalate powder.

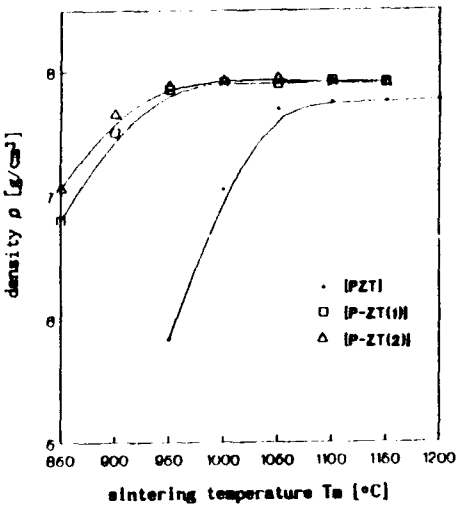


Fig. 3. Bulk density of PZT ceramics as a function of sintering temperature for powders derived by different methods.

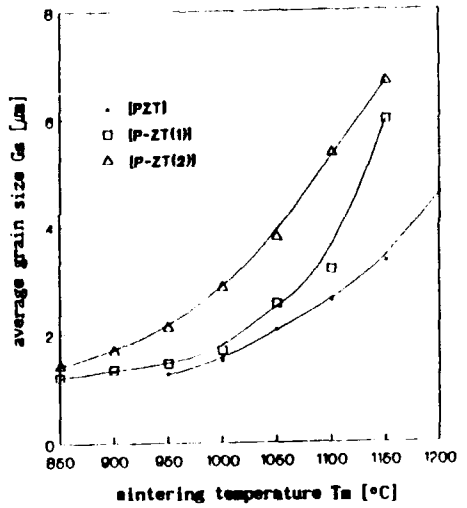


Fig. 4. Average grain sizes of PZT ceramics as a function of sintering temperature.

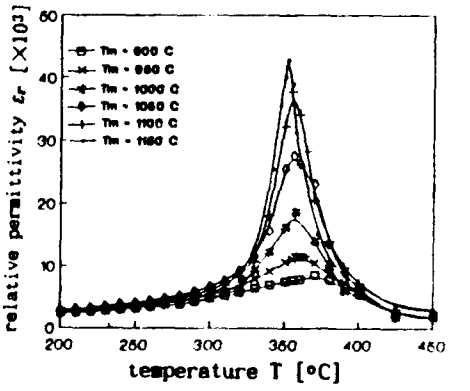


Fig. 5. Temperature dependence of relative permittivity for samples prepared using modified partial oxalate-derived PZT powder at various sintering temperature.

realized at as low as 950℃ for partial oxalate-derived powder, whereas the same density is possible at above 1050℃ for mixed oxide-derived PZT powder. This result again reflects the fact that the partial oxalate-derived powders are smaller in size and chemically more uniform so that the densification can be accomplished at lower temperatures.

Average grain sizes determined from the figure by line intercept method are plotted against the sintering temperature in Fig. 4. It is clear that grain growth occurs at lower temperatures for partial oxalate-derived powder compacts.

The temperature dependences of dielectric constant and Curie temperature for ceramics sintered using modified partial oxalate-derived powder are shown in Fig. 5. It is found that, as sintering temperature increases, Curie temperature decreases whereas the dielectric constant at Curie point increases. This result is in good agreement with that reported by Yamamoto et al.[6] for the similar system. Shrout et al.[8] also found the same temperature dependences of dielectric constant and Curie temperature for $Pb(Mg_{1/3}Nb_{2/3})O_3$ ceramic, and interpreted the data in terms of average grain size instead of sintering temperature. However, since average grain size is proportional to sintering temperature as shown in Fig. 4, the result obtained in this study remains consistent with other studies.

For the sintered samples prepared using three types of PZT powders, the sintering temperature dependence of relative permittivity at room temperature is illustrated in Fig. 6. For two types of partial oxalate methods, relative permittivity reaches maximum at about 1050℃ whereas, for mixed oxide method, the same happens at 1150℃. This result is in accord with Fig. 3, where bulk density values for three methods shows similar trend. The fact that relative permittivity and bulk density show similar temperature dependence can be interpreted due to the influence of pores.

Electromechanical coupling factors for three types of PZT ceramics are shown in Fig. 7 as a function of sintering temperature. It is noticeable that the coupling factors for all samples generally increase with sintering temperature. However, two partial oxalate methods appear to be better than mixed oxide method since the maximum values of the former happen at about 100℃ lower than that of the latter. This trend is similar to that of dielectric constant, and is again the consequence of decrease of sintering temperature for the same bulk density.

Since the coupling factor of 0.55 is sufficient for most piezoelectric applications, two partial oxalate methods can be more adequate in practical applications than mixed oxide method. The sintering temperature for the former can be as low as 950℃, whereas that for the latter must be higher than 1050℃.

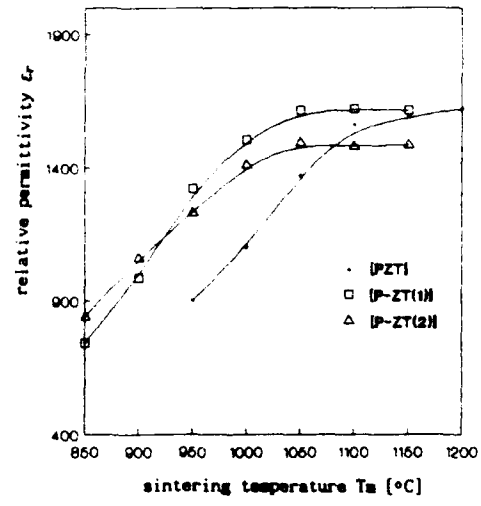


Fig. 6. Relative permittivity as a function of sintering temperature for three types of samples.

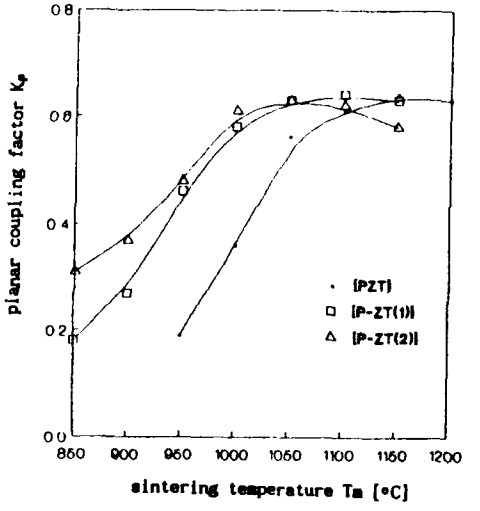


Fig. 7. Planar coupling factor as a function of sintering temperature for three types of samples.

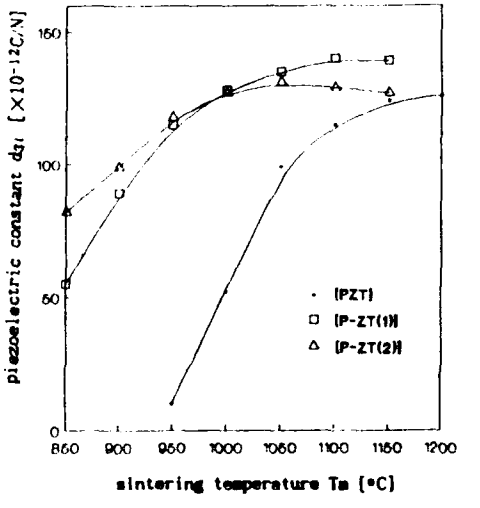


Fig. 8. Piezoelectric constant d_{31} as a function of sintering temperature for three types of samples.

Piezoelectric constants d_{31} for three types of samples are shown in Fig. 8, which is important in actuator application. The results also show the similar sintering temperature dependence as relative permittivity and electromechanical coupling factor.

Remanent polarization from D-E hysteresis loops for samples sintered at four different temperatures using three types of powders is plotted in Fig. 9. It shows that remanent polarization increases with sintering temperature. This temperature dependence again resembles those in relative permittivity and bulk density. From the figure, the saturated values of remanent polarization are 25 ~ 30μm /cm^2. In addition, from Figs. 7 and 9, one can find that remanent polarization is proportional to the planar coupling factor.

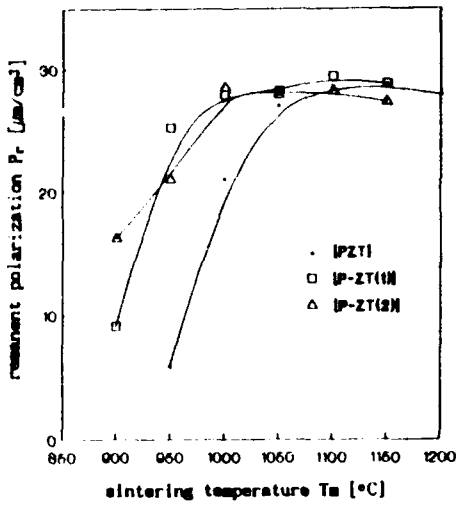


Fig.9. Remanent polarization as a function of sintering temperature.

4. Conclusions

From the results found in this study, it can be concluded that two partial oxalate methods are better techniques to produce fine, homogeneous PZT powder than the mixed oxide method accompanied by ball-milling. Using partial oxalate-derived PZT powders, sintering temperatures can be reduced as low as 950℃ without sacrificing desired dielectric and piezoelectric properties, such as relative permittivity, electromechanical coupling factor, and piezoelectric constant. Two partial oxalate methods yield ceramics with almost the same physical and electrical properties, so that the step of producing ZTO powder does not seem to be necessary.

Acknowledgement

Authors are grateful to Korea Research Foundation for its financial support for this work and Prof. Yamamoto of National Defense Academy, Japan for his helpful comments and supplying many valuable literature and data.

References

1. B.Jaffe, R.S.Roth, and S.Marzullo, "Piezoectric Properties of Lead Zirconate-Lead Titanate Solid Solution Ceramics", J. Appl. Phys. 25, 809-810 (1954).

2. H.Yamamura, S.kuramoto, H.Hanada, A.Watanabe and S.S hirasaki, "Preparation of $Pb(Zr,Ti)O_3$ by Oxalate Method in Ethanol Solution," J. Ceram. Soc. Jpn., 94, 470-74 (1986).

3. S. Tashiro, Y. Tsuji and H. Igarashi: "Sintering of Submicron $Pb(Zn,Nb,Fe,W)O_3$ Powders and Dielectric Properetes of the Ceramics Fabrticated Therefrom", J. Ceram. Soc. Jpn., 96(5), 579-84(1988).

4. A. Watanabe, S.Kyramoto, H.Yamamura, H.Haneda and S. Shirasaki, "Shyntesis of $Pb(Mg_{1/3}Nb_{2/3})O_3$ by Coprecipitation Method", in Proc.25th Meeting Basic Ceram., 3E04, (1987).

5. T. Yamamoto, R. Tanaka, K. Okazaki and T. Ueyama, "Micro- structure of $Pb(Zr_{0.53}Ti_{0.47})O_3$ Ceramics Synthesized by Partial Oxalate Method (Using $Zr_{0.53}Ti_{0.47}O_2$ Hydrothermal Produced Powders as a Core of $Pb(Zr_{0.53}Ti_{0.47})O_3$)," Jpn. J. Appl. Phys., 28[Supplement 28-2] 67-70 (1987)

6. T. Yamamoto, "Optimum Preparation Methods for Piezoelectric Ceramics and Their Evaluation," Ceramic Bulletin, 71(6), 978-985 (1992).

7. Matso, Y., and Sasaki, H. : "Formtion of lead zirconate-lead titanate solid solution", J. Amer. Ceram. Soc., 48, 289-296(1989).

8. S. L. Swartz, T. R. Shrout, W. A. Schulze, and L. E. Cross, "Dieiectric Properties of Lead-Magnesium Niobate Ceramics," J. Am.Ceram. Soc., 67(5), 311-15(1984).

MICROSTRUCTURE AND PROPERTIES OF Cr_2O_3 DOPED LEAD TITANATE PIEZOCERAMICS

Long Wu, Yi-Yeh Lee and Chich-Kow Liang
Department of Electrical Engineering
National Cheng Kung University
Tainan, Taiwan, R.O.C.

Abstract

The chromium addition has been investigated extensively in the PZT type ceramics but seldom mentioned in PT type ceramics. In this study, the effect of Cr_2O_3 additives (0—0.6 wt%) on the microstructure and electrical properties of $Pb_{0.88}Ln_{0.08}(Ti_{0.98}Mn_{0.02})O_3$ ceramics where Ln=Nd, La is discussed. In Nd modified PT ceramics, the chromium ions enter into the lattice of the perovskite structure. They are taken as a grain growth promoter and accelerate densification in microstructure and act as a hardener which favors the higher mechanical quality factor, lower dielectric loss and lower electrical resistivity in electrical properties. However, in the La modified PT ceramics, with increasing Cr_2O_3 additives the tetragonality c/a and the Curie temperature Tc nearly keep no change. Thus, the chromium ions maybe tend to mostly segregate at the grain boundaries and act as grain growth inhibitor and binder responsible for the increase of the porosity, dielectric constant ϵ_{33}^T and electrical resistivity.

Introduction

Much tentative investigations were made to improve the performance of PZT type ceramics after the fundamental studies by Jaffe et al.. Typically three type of additives are classified as softener, hardener and stabilizer. It is believed that most of the additives enter into the lattice to a certain extent and thus change the ceramic properties. The stabilizer like Cr_2O_3, MnO_2 and U_3O_8 on the electrophysical aspect is still a special noted issue. Related studies included Takahashi, Atkin, Roy-Chowdhury et al., Ouchi et al. and Cheon et al.[1-5] Takahashi[1] pointed that the Cr-group impurities have the combined effect of partial donor and partial acceptor on the electromechanical properties and result in a stable temperature and aging characteristics. It is considered to be related to more than one valence state of the transition ion in the lattice.

Lastly, lead titanate ceramics modified by rare earth ions are concentrated on a possibility of the applications on high frequency resonators or filters like surface and bulk acoustic wave devices. Takeuchi.[6] and Ito.[7] et. al. have systematically explored the modified $PbTiO_3$ ceramics having the general formula $Pb_{(1-1.5x)}Ln_x(Ti_{1-y}Mn_y)O_3$, with Ln=La, Nd, Sm, or Gd. Therefore, the two compositions $Pb_{0.88}Nd_{0.08}(Ti_{0.98}Mn_{0.02})O_3$ (PNT) and $Pb_{0.805}La_{0.13}(Ti_{0.98}Mn_{0.02})O_3$ (PLT) are chosen to study the effect of the Cr_2O_3 additives on the variations of the microstructure and electrical properties.

Experimental procedure and measurement

Two types of ceramics with composition (a) $Pb_{0.88}Nd_{0.08}(Ti_{0.98}Mn_{0.02})O_3$+x wt% Cr_2O_3 (b)$Pb_{0.805}La_{0.13}(Ti_{0.98}Mn_{0.02})O_3$ + x wt% Cr_2O_3 (x=0-0.6) were prepared by conventional processing method using mixed oxide powders. After wet milling for 6 hr, the mixture was dried and calcined at 880°C for 2 hr. The green compacts were sintered in a closed alumina crucible for 2hr at 1200°C. The poling condition was 6 KV/mm at 150°C in silicon oil for 10 min.

The mean grain size was obtained by line intercept method from SEM micrographs. The porosity was calculated from the density measurement by using the Archimedes technique. Lattice constant was determined by an X-ray diffractometer using CuKα radiation. The temperature dependence of electrical permittivity ϵ_r of unpoled samples was carried out in the temperature range of 50-400°C. The poled dielectric constant ϵ_{33}^T and dielectric loss tan δ_e were measured at 1 KHz using HP4192 impedance analyzer. The planar coupling factor k_p and mechanical quality factor Qm was determined by the resonance method according to IRE standard. The thickness coupling factor k_t was calculated from the ratio of the overtone frequency to the fundamental frequency of thickness mode using Onoe's table.

Temperature dependence of electrical resistivity was measured by the two-point method using a digital multimeter (Keithley 199) and a applied DC field of 1 V/mm in the temperature range of 25—500°C.

Results and discussion

(A) X-ray measurement and microstructure

The X-ray diffraction patterns of PNT and PLT ceramics without and with 0.6 wt% Cr_2O_3

CH3080-0/92/0000-0529$3.00 ©IEEE

additions are shown in Fig 1 respectively. In contrast to no evident distinction of XRD patterns in PLT ceramics, the (002) and (200) peaks of PNT ceramics doped with 0.6 wt% Cr_2O_3 additives show closer than that without doping. So in PNT ceramics the tetragonality c/a has tendency to decrease with increasing concentrations of Cr_2O_3 additives but c/a keeps nearly the same within this doping range in PLT ceramics as shown in Fig 2. It is concluded that the chromium ions are soluble in the perovskite structure of Nd modified lead titanate ceramics which also can be confirmed by Energy Dispersive Spectrometer (EDS) analysis but maybe tend to mostly segregate at the grain boundaries in PLT ceramics.

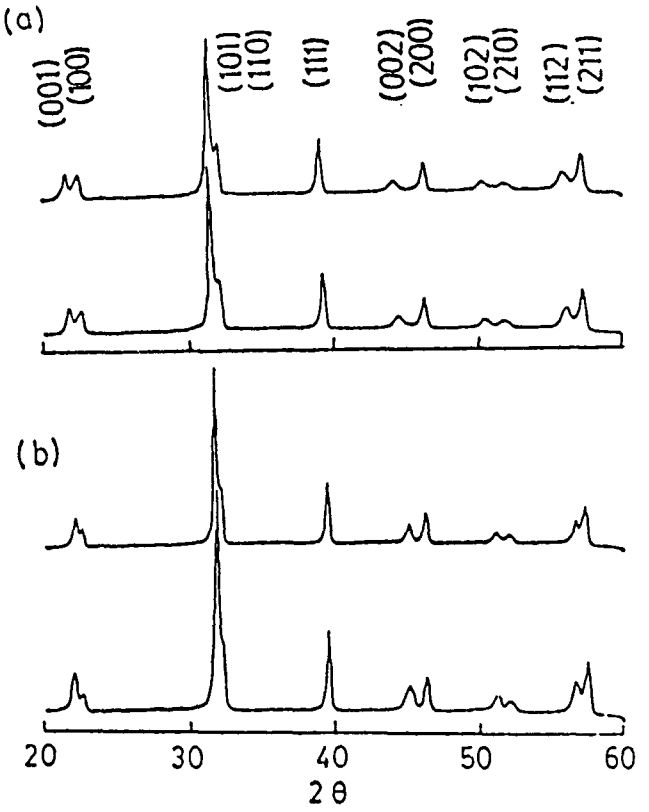


Figure 1 X-ray diffraction patterns of (a) PNT and (b) PLT ceramics without and with 0.6 wt% Cr_2O_3 additives.

The variations of the grain size and porosity as a function of Cr_2O_3 concentrations are shown in Fig 3. Within this doping range, fine grained ceramics are all presented in PNT ceramics; the grain size increases from 0.98 μm to 2.2 μm and the porosity decreases form 2.5% to 1.2%. So, the chromium ions are taken as a grain growth promoter and accelerate densification. In PLT ceramics, a dense and fine-grained microstructure can be reached within 0.4 wt% doping. After that, although the grain size keeps similar, the porosity

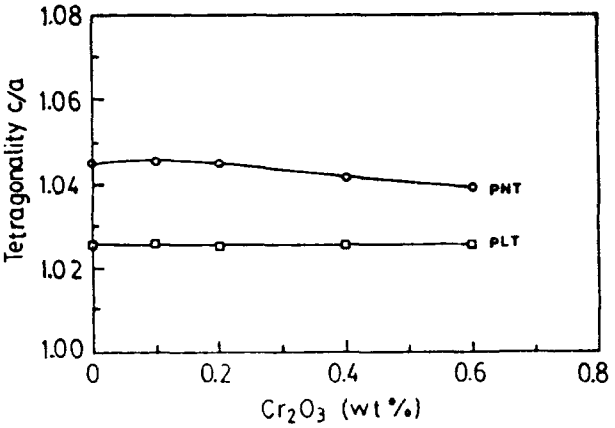


Figure 2 Variation of the tetragonality of PNT and PLT ceramics as a function of Cr_2O_3 concentration.

increases. So, it is suggested that these additives act as grain growth inhibitor and binder.

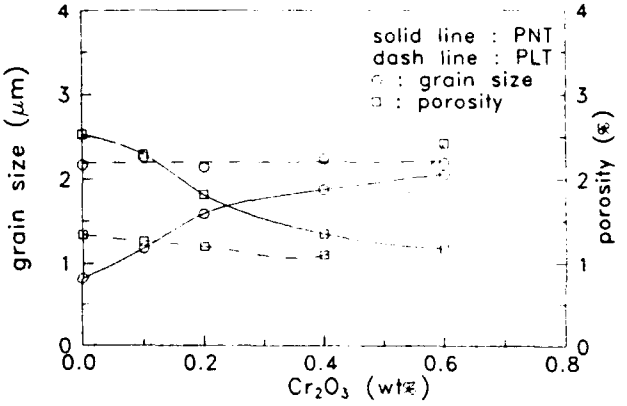


Figure 3 Variation of the average grain size and porosity of PNT and PLT ceramics as a function of Cr_2O_3 concentration.

(B) Electrical properties

(a) PNT ceramics: The Curie temperature Tc and the peak dielectric constant ϵ_{max} at Tc determined from measurements of temperature dependence of dielectric constant in unpoled samples are shown in Fig 4. The Curie temperature Tc is decreased with increasing the concentrations of Cr_2O_3, but ϵ_{max} is increased with the increase of doping.

The poled dielectric constant (ϵ_{33}^T) and dielectric loss (tan δ_e) as a function of Cr_2O_3 additives are shown in Fig 5. The variation of ϵ_{33}^T is nearly comparable to the variation of ϵ_{max}, which results from the ease of domain wall motion in larger grain size.[8] Due to the porosity promoting the inner friction in time of domain boundary movement, thus the dielectric loss decreases with Cr_2O_3 additions.

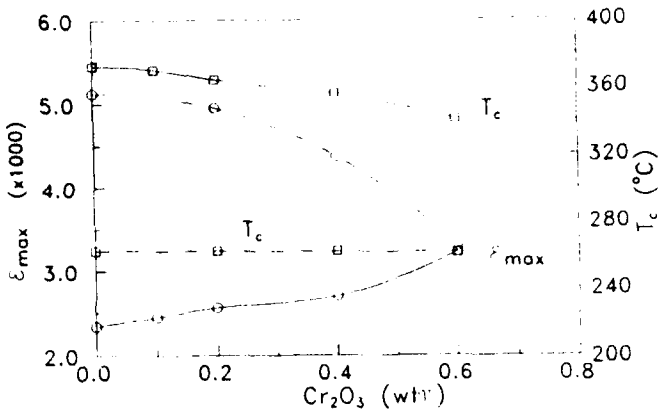


Figure 4 Variation of the Curie temperature Tc and peak dielectric constant ϵ_{max} of PNT and PLT ceramics as a function of Cr_2O_3 concentrationin.

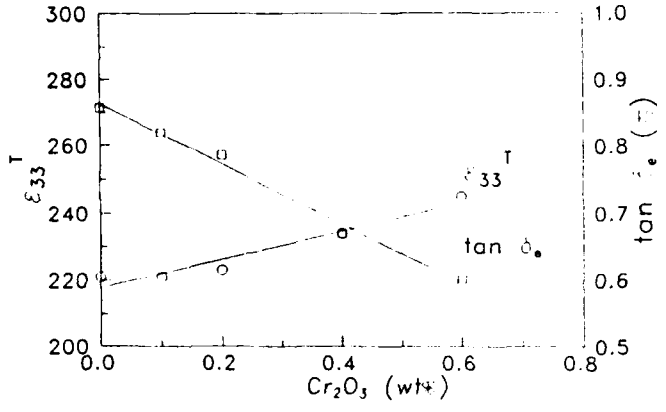


Figure 5 Variation of the ϵ_{33}^T and tan δ_e of PNT ceramics as a function of Cr_2O_3 concentration.

Fig 6 shows the dependence of mechanical quality factor Qm, planar coupling factor k_p and thickness coupling factor k_t on the Cr_2O_3 additions. The mechanical quality factor increased from about 2000 without doping to about 2200 at 0.6 wt% doping. The electric (tan δ_e) and mechanical (1/Qm) loss exist a approximately linear relationship which matches the loss mechanism developed in PZT ceramics.[9] [10] As can be seen, the thickness coupling factor k_t and the planar coupling factor k_p increase slightly, but the increase of k_t is more apparent. The anisotropy k_t/k_p is around 4.5 .

The temperature dependence of electrical resistivity of chromium doped PNT ceramics gives a clear explanation about the variations of microstructures, point defects and electrical properties of PNT ceramics. Jamadar et al.[11] pointed out that in barium and strontium modified lead titanate ceramics the electrical conduction is electronic in nature in the paraelectric state. Because of high volatility of lead oxide, Gerson and Jaffe[12] proposed that the unmodified PZT

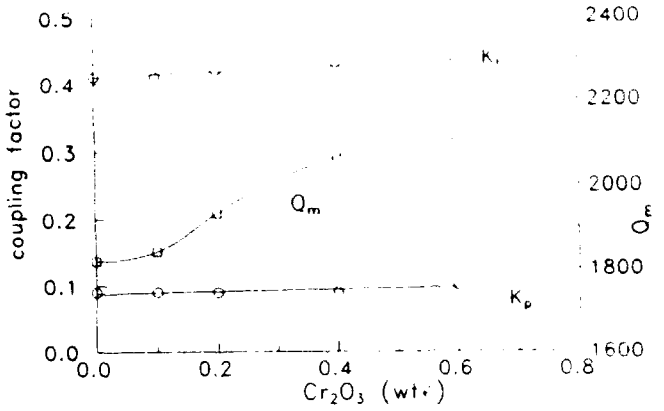


Figure 6 Variation of the k_p, k_t and Qm of PNT ceramics as a function of Cr_2O_3 concentration.

compositions have p-type (hole) conduction, especially prepared by sintering in air. Thus, in the paraelectric phase, the decrease of electrical resistivity with increasing Cr_2O_3 additives means the more hole carriers participate in the conduction process. From the examination previously, the chromium ions enter into the lattice structure of PNT solid solution in all doping rage. So the lower valence state of chromium ion (Cr^{+3}) substituted for the Ti site could be the cause, that is, the chromium ions act as an acceptor in the PNT ceramics and favor the higher mechanical quality factor and lower dielectric loss which are consistent with the *previous results.*

(b) PLT ceramics: As also seen in Fig 4 (dash line), the Curie temperature Tc has no change to be observed like the tetragonality in Fig 2 but the peak dielectric constant ϵ_{max} decreases with the additions of Cr_2O_3. In all measuring curves, sharp peaks of dielectric constant are found. Therefore, the diffuse phase transition does not exist in the PLT ceramics like that in the PNT ceramics.

The dielectric constant (ϵ_{33}^T) and dielectric loss (tan δ_e) as a function of Cr_2O_3 additives are shown in Fig 7. The dielectric constant ϵ_{33}^T increases slowly with increasing the additives. Because most additives segregate at the grain boundaries, the presence of interfacial polarization is suggested as a possible explanation for this increase.[13] The dielectric loss shows smaller at close to 0.4 wt% additions of Cr_2O_3 which is supposed to a dense ceramics to be made. The mechanical quality factor Qm also shows higher values over 2100 within the range of 0.4 wt% doping but possibly because of two combined factors ,which are the accumulation of doping ions between grains and an increase of porosity after 0.4 wt% doping, the inner friction increases leading to a largely deterioration in Qm. The planar coupling factor k_p and thickness coupling factor k_t are also shown in Fig 8, where k_t

increases a little near 0.4 wt% doping and k_p slightly decreases. The anisotropy k_t/k_p in the PLT ceramics is scarcely higher than that in the PNT ceramics.

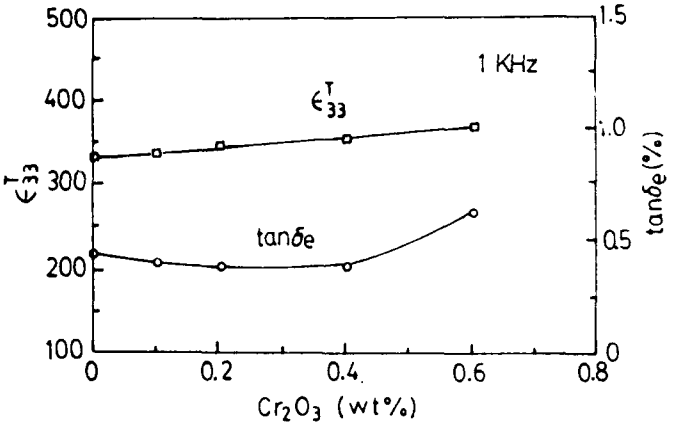


Figure 7 Variation of the ϵ_{33}^T and tan δ_e of PLT ceramics as a function of Cr_2O_3 concentration.

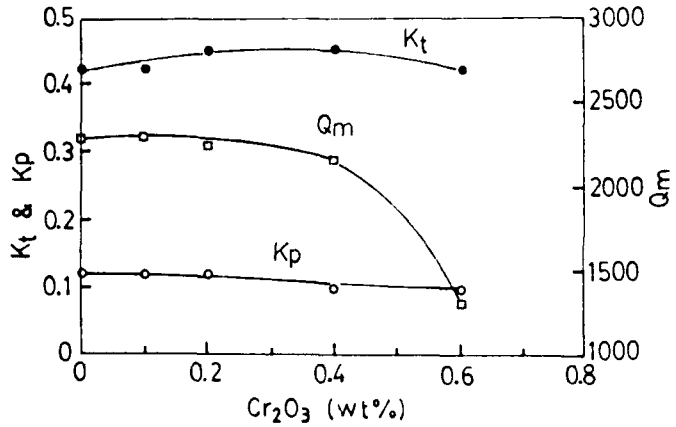


Figure 8 Variation of the k_p, k_t and Qm of PLT ceramics as a function of Cr_2O_3 concentration.

The electrical resistivity of chromium doped PLT ceramics increases with the Cr_2O_3 additives in the paraelectric phase of higher which is perfectly different from that of PNT ceramics in the paraelectric phase. So, the generating effect by Cr_2O_3 doping is sure to be different. The segregation of chromium ions at the grain boundaries as binders is responsible for the increase of the porosity, dielectric constant ϵ_{33}^T and electrical resistivity.

Conclusion

In this study, the chromium doping effect of Nd and La modified lead titanate ceramics on the lattice constant, microstructure, dielectric and piezoelectric properties are investigated. It appears perfectly different doping phenomena, soluble in the former and segregative around grain boundaries in the latter, leading to different electrical behaviors. By measuring the temperature dependence of the electrical resistivity, more insight to the understanding of variations of microstructure, lattice constant, dielectric and piezoelectric properties can be reached.

Acknowledgement

This work was supported by the National Science Council of R.O.C. under the contrast NSC 81-0606-E004-109

References

[1] M. Takahashi, Jpn. J. Appl. Phys., vol. 9, pp.1236, 1982
[2] R. B. Atkin and R. M. Fulrath, J. Am. Ceram. Soc., vol. 54, pp.265, 1971
[3] P. Roy-Chowdhury and S. B. Deshpande, J. Mater. Sci., vol. 22, pp.2209, 1987
[4] H. Ouchi, M. Nishide and S. Hayakawa, J. Am. Ceram. Soc., vol. 49, pp.577, 1966
[5] C. I. Cheon, S.J.Kim and H. G. Kim, Ferroelectrics, vol. 115, pp.35, 1991
[6] H. Takeuchi, S. Jyomura, E. Yamamoto and Y. Ito, J. Acoust. Soc. Am., vol. 72, pp.1114, 1982
[7] Y. Ito, K.Nagatsuma, H. Takeuchi and S. Jyomura, J. Appl. Phys., vol. 52, pp.3223, 1981
[8] T. Yamamoto, H.Igarashi and K. Okazaki, Ceram. Int., vol. 11, pp.7, 1985
[9] P. Gerthern, K. H. Hardtl and N. A. Schmidt, J. Appl. Phys., vol. 51, pp.1131, 1980
[10] G. Arlt and H. Dederichs, Ferroelectrics, vol. 29, pp.47 1982
[11] V. M. Jamadar, T. A. Patil and S. H. Chavan, India. J. Pure & Appl. Phys., vol. 26, pp.527, 1988
[12] R. Gerson and H. Jaffe, J. Phys. Chem. Solids, vol. 24, pp.979, 1963
[13] T. Y. Tien and W. G. Carlson, J. Am. Ceram. Soc., vol. 45, pp.567, 1962

ELABORATION PROCESS AND STUDY OF Nb-Ni SUBSTITUTED PZT CERAMICS WITH HIGH d_{33} AND ε_r COEFFICIENTS

L. Eyraud, P. Eyraud, S. Rey, M. Troccaz
Laboratoire de Génie Electrique et Ferroélectricité
INSA de Lyon, 69621 Villeurbanne cédex, France

Abstract : PZT ceramics with high Nb-Ni substitution (about 40 %) are prepared according to a solid process and a wet chemical process by coprecipitated oxalates. Precipitation conditions were carefully examined because some variations in the properties of sintered ceramics were observed. The best conditions of thermal decomposition, thermal treatment and sintering are determined for the $PbZr_{0.23}Ti_{0.37}(Nb_{2/3}Ni_{1/3})_{0.4}\ O_3$ composition. A notable improvement of texture and dielectric constant is obtained with hot pressing sintering. The main electromechanical coefficients were measured.

INTRODUCTION

Fabrication of multielement arrays used for ultrasonic imaging applications at high frequencies requires the following conditions for ferroelectric ceramics :

* high piezoelectric properties, that is values of d_{33} and k_{33} coefficients as high as possible
* low dielectric losses tanδ (< 2 %)
* low mechanical quality factor Q (< 50)
* Curie temperature T_c close to 200° C
* good homogeneity and lack of porosity in order to get very thin identical elements
* high value of relative permittivity ε_r

This last factor was imposed by users : a very high ε_r is necessary to make impedance matching easier and to reduce interferences between array elements. This requirement eliminated $PbTiO_3$ and $PbNb_2O_6$ type materials, attractive for their low coefficient Q and their weak transverse coupling factor k_{31}, but neglected because of their very low ε_r value.

According to Jaffe [1] there are several possibilities to increase piezoelectric activity of lead zirconate titanates type materials (PZT). Mixture with a complex perovskite $Pb(Nb_{2/3}Ni_{1/3})\ O_3$ was chosen.

Moreover due to very high frequencies measurements (10 to 20 MHz), piezoelectric array elements must be very homogeneous, very thin (up to 100 µm) with identical widths (20 µm). Therefore the other important point to be considered is the ceramics manufacturing process.

CHOICE OF A COMPOSITION

Phase diagram of $PbTiO_3$-$PbZrO_3$-$Pb(Nb_{2/3}Ni_{1/3})\ O_3$ system (Figure 1) given by Banno [2] shows that a morphotropic phase boundary, near which piezoelectric properties would be better, lies in vicinity of 20 moles % $PbZrO_3$ and 40 moles % $Pb(Nb_{2/3}Ni_{1/3})\ O_3$ to maintain T_c abou 200° C.

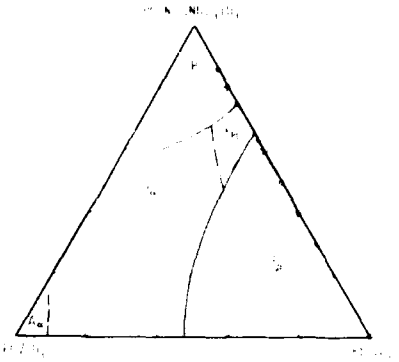


Figure 1
Phase diagram of $PbTiO_3$-$PbZrO_3$-$Pb(Nb_{2/3}Ni_{1/3})O_3$ system

Using the standard mixed oxide method of ceramics preparation (firing 950° C/6 h, sintering under PZT powder 1240° C/6 h) a composition is selected. Figure 2 shows the variations of ε_r, tanδ (measured at 1 KHz, 1 V) and d_{33} (calculated from resonance and antiresonance curves) with zirconium content, keeping the sum (Zr + Ti) equal to 0.6, for a 40 atom % Nb-Ni substitution. It can be seen that a maximum is obtained about 0.23 Zr content whatever the concentration ratio Nb/Ni.

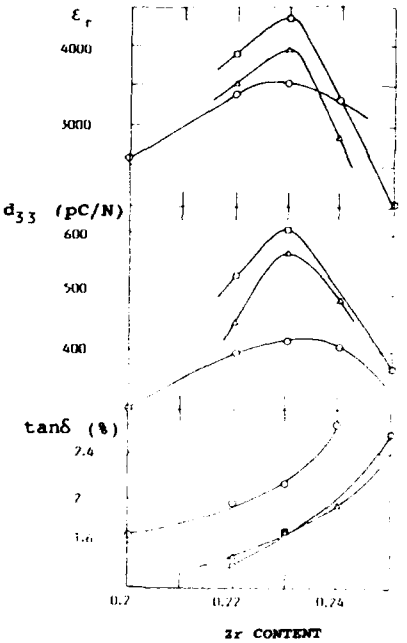


Figure 2
Zr/Ti ratio influence on ceramics characteristics
□ Pb Zr_x $Ti_{0.6-x}$ $(Nb_{2/3}$ $Ni_{1/3})_{0.4}$ O_3
△ Pb Zr_x $Ti_{0.6-x}$ $Nb_{0.26}$ $Ni_{0.14}$ O_3
○ Pb Zr_x $Ti_{0.6-x}$ $Nb_{0.27}$ $Ni_{0.13}$ O_3

CH3080-0-7803-0465-9/92$3.00 ©IEEE

These same piezoelectric coefficients are then plotted in Figure 3 as a function of Nb/Ni values for the 23 atom % Zr previously determined. It can be noted that the best ratio Nb/Ni is 2 corresponding respectively to pentavalent and divalent ionic states.

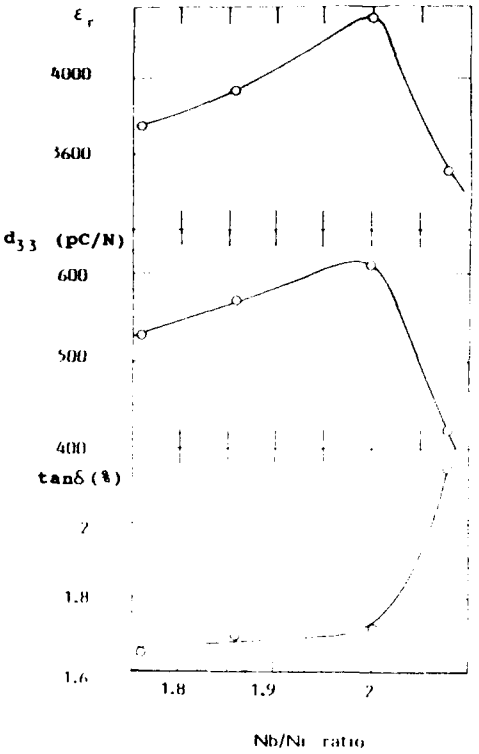


Figure 3 Dependence of $Pb_{0.23}Ti_{0.37}Nb_{0.4-x}Ni_xO_3$ ceramics characteristics on Nb/Ni ratio

Finally the following composition is chosen for further studies :

$$Pb\ Zr_{0.23}Ti_{0.37}(Nb_{2/3}Ni_{1/3})_{0.4}\ O_3 \qquad \text{(PZT NN)}$$

POWDER PREPARATION

Ceramics manufactured following the preceding formula are quite dense, but their microstructure is not very homogeneous, probably due to the bad grain size distribution of powders prepared by the solid process. Hot pressing sintering does not improve significantly ceramic texture because powder grains obtained after the 950° C calcination are not malleable enough, even under an external pressure.

Homogeneity and absence of porosity can be greatly improved by a liquid preparation process coupled with hot pressing. Powders preparation process by multiple oxalates coprecipitation was already described [3][4]. In most cases it allows insoluble multiple oxalates to be obtained. However in PZT NN presence of Ni poses problem because it makes up complexes with ammonia. Therefore this element is introduced separately as oxalate and mixed with the other coprecipitates to form a highly reactive oxalates mixture.

During PZT NN manufacturing some difficulties concerning a good reproduction of piezoelectric constants were encountered. So the part played by various factors along the process was successively examined.

- **Thermal treatment**

Differential thermal analysis of the precipitate shows total oxalates decomposition at 400° C. X Rays analysis performed on powders fired at different temperatures shows in all cases the diffraction pattern of a pyrochlore phase $Pb_2Nb_2TiO_9$ (PTN). The optimum conditions for minimizing this phase are the following : thermal decomposition 600° C/10 h, thermal treatment 900°C/2 h (Figure 4). Note that the pyrochlore phase does not exist in the ceramic material.

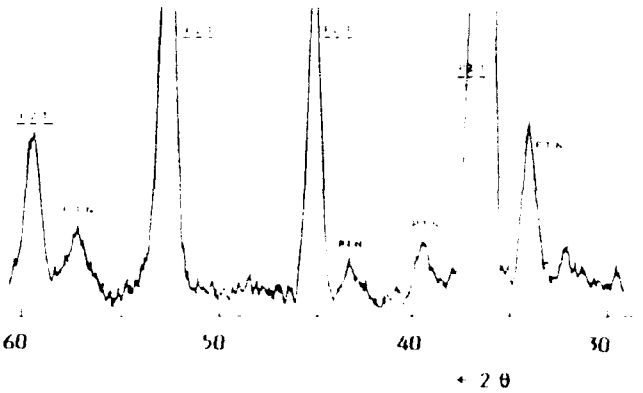


Figure 4 Diffraction pattern of a coprecipitated powder (PTN = pyrochlore phase)

- **PbO excess**

In relation to the general perovskite formula ABO_3, $Pb_2Nb_2TiO_9$ is in deficit on A site. Therefore vaporization of PbO in excess can occur during sintering. Tests carried out on samples with A/B ratios higher than 1 lead to uncertain results (Table I). Moreover some ceramics are not homogeneous.

No conclusion can be obtained from these experiments.

Table I

Influence of PbO excess on electrical characteristics

A/B	ε_r	tanδ (%)	d_{33}
1.00	4050	1.5	500
1.01	3840	1.7	450
1.03	4450	1.6	610
1.04	3650	2.1	140

- **Precipitation pH**

Table II lists ε_r, tanδ and d_{33} coefficients for ceramics prepared from powders coprecipitated at various pH values. A pH around 8.1 seems suitable for correct material manifacturing but some ceramics are not homogeneous.

Table II Variation of electrical characteristics versus precipitation pH

pH	7.6	8.1	8.8	9.3	10
ε_r	2910	4530	3280	3360	3090
d_{33} pC/N	460	660	390	410	330
tanδ (%)	1.6	1.8	1.5	1.6	1.7

- **Chlorides presence**

When niobium is introduced directly as $NbCl_5$ in aqueous solution of oxalic acid a small amount of $PbCl_2$ can be formed which is found again more or less in the precipitate according to the amount of washing water used. As $PbCl_2$ boiling point is 950° C its loss leads to large porosities in ceramics, causes also occurence of Pb vacancies and makes pyrochlore phase more stable.

In order to eliminate Cl^- ions in the coprecipitation medium, niobium was introduced as hydroxide newly prepared by precipitation from niobium chloride. Homogeneous and reproductive results are then achieved.

To conclude, powder preparation of PZT NN is given in Figure 5.

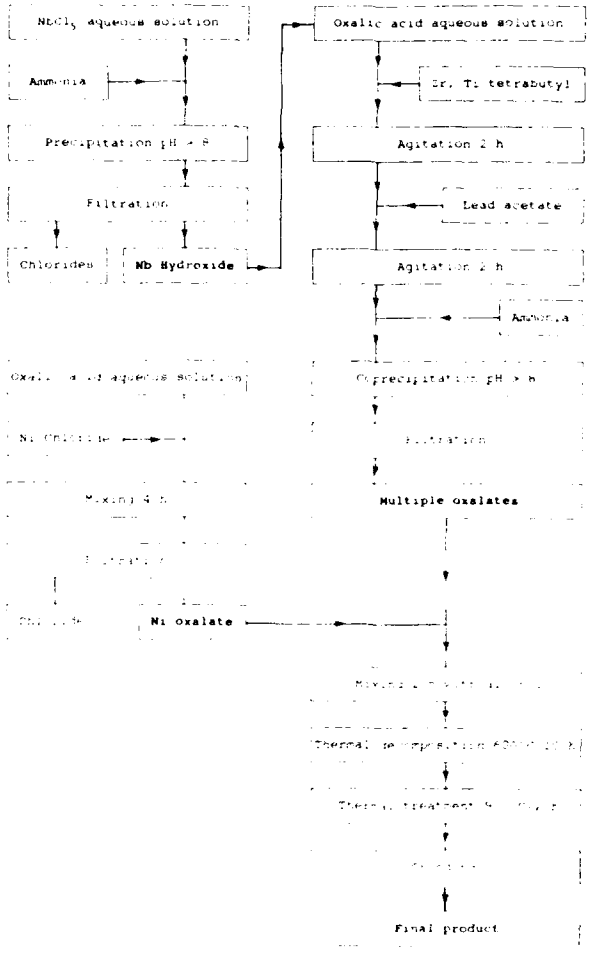


Figure 5 Flow sheet of the preparation of PZT NN

CERAMICS MANUFACTURING CONDITIONS IMPROVEMENT

To improve the microstructure of powder prepared according to the preceding process, influence of coprecipitation pH on the specific area of the final product was studied. The results are compiled in Table III. Study of the thermal treatment temperature influence on the particule size distribution given in Figure 6 shows that the difference between 800 and 900°C is not very large, but 900°C is better for minimizing pyrochlore phase amount before sintering.

Table III Specific area of the final product as a function of precipitation pH

Précipitation pH	7.6	8.1	8.8	9.3	10.0
Specific area m^2/g	0.68	0.84	1.04	1.28	0.91

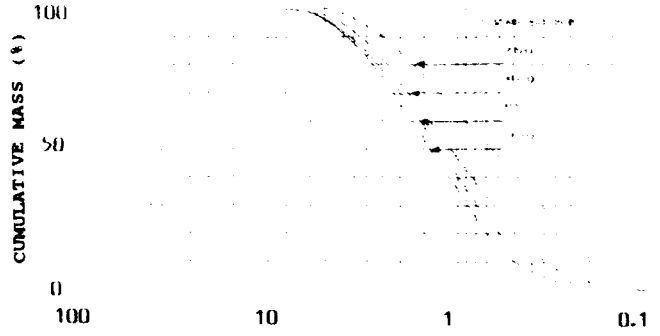


Figure 6 Grain size distribution curves for various thermal treatments

Figure 7 shows the microstructure of two ceramics obtained by natural sintering (1240° C/6 h) of powders prepared by the dry or wet process. It can be noticed that the texture of ceramic prepared by coprecipitation is better with smaller grain size. However it still isn't sufficient for achievement of a low porosity material resisting to thermal and mechanical agents developed during machining. Sintering under uniaxial stress (about 2 MPa) is necessary.

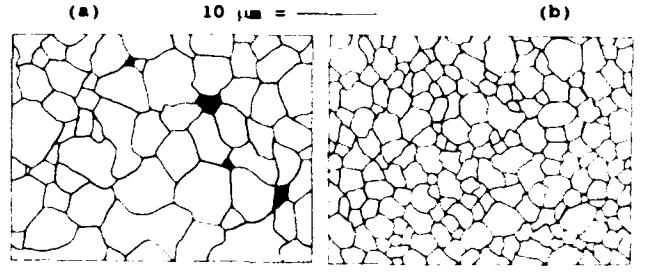


Figure 7

Microstructure of ceramics prepared by a solid (a) or a liquid (b) process and natural sintering

Table IV gives ε_r, $\tan\delta$, d_{33} values according to the manufacturing process. This table shows that hot pressing sintering, essential for mechanical quality of arrays, improves also notably ε_r value, corresponding to user's wishes. Table V summarizes the main characteristics of the ceramic material

$Pb\ Zr_{0.23}Ti_{0.37}(Nb_{2/3}Ni_{1/3})_{0.4}\ O_3$ prepared by coprecipitation and hot pressing sintering.

Table IV Dependence of ceramics characteristics on manufacturing process

VS = solid process, VL = liquid proce s
FN = natural sintering, FC hot pressi g sintering

	VSFN	VSFC	VLFN	VLFC
ε_r	4150	4750	4850	5350
d_{33} pC/N	610	640	640	650
$\tan\delta$ (%)	1.5	1.8	1.7	1.7

Table V

Main coefficients of coprecipitated and hot pressing sintered $PbZr_{0.23}Ti_{0.37}(Nb_{2/3}Ni_{1/3})_{0.4}O_3$ composition

ε_r	tanδ (%)	d_{33} pC/N	k_{33}	k_{31}	E_c kV/mm	P_r μc/cm²	Q	T_c (°C)	ε_r variation between 125 and 25°C (%)
5300	1.7	640	0.73	0.39	1	30	70	180	40

CONCLUSION

Ferroelectric ceramics of the system x $PbZrO_3$-y $PbTiO_3$-z $Pb(Nb_{2/3}Ni_{1/3})O_3$ exhibit the best piezoelectric coefficients for x = 0.23, y = 0.37, z = 0.4 as determined by a solid preparation process. Powder preparation conditions by a coprecipitation method in oxalic medium were examined and a fabrication process is given. Hot pressing sintering still improves electrical and mechanical ceramics quality and allows achievement of material with a large value of ε_r (5300), high d_{33} and k_{33} constants, along with a not very important temperature variation between 25 and 125° C in view of a 180° C Curie temperature. These properties make this material promising for high frequency medical ultrasonic imaging transducers.

ACKNOWLEDGEMENTS

We are grateful to Société Quartz et Silice, 77140, Nemours, France, for having supported this work.

REFERENCES

[1] Jaffe B., Cook W.R., Jaffe H., Piezoelectric Ceramics, London, Academic Press (1971)

[2] Banno H., Tsunooka T., Shimano I., Proc. 1 st meeting Ferro. Mat. and Appl., Kyoto, Ed. Omoto and Kumada (1977)

[3] Eyraud L., Eyraud P., Gonnard P., Troccaz M., Ferroelectrics, 34, p 133 (1981)

[4] Eyraud L., Ind. Ceramique, 761, p 343 (1982)

PIEZOELECTRIC ACTUATORS IN ROTARY OR LINEAR MOTIONS BY EXCITATION OF ASYMMETRIC DISPLACEMENT

Yoshiro Tomikawa, Manabu Aoyagi and Chitaru Kusakabe †

Department of Electrical Engineering and Information Science, Yamagata University,
Yonezawa, Yamagata, Japan 992
† Section of Electricity, Faculty of Education, Yamagata university,
Yamagata, Yamagata, Japan 990.

This paper deals with a new excitation method of a piezoelectric actuator in order to achieve its asymmetric displacement as a function of time elapsed without its residual vibration. The method is to use the rectangular pulse of voltage and is aimed to develop a new type piezoelectric actuator with a function of a double-trip operation.

Analysis on displacement of such actuator driven by the rectangular pulse, and proposal of its application to concrete actuators with its experimental description are reported.

Introduction

A piezoelectric actuator is one of attractive devices in the modern engineering, due to its inherent multi-functions and small construction [1], and then we have investigated it until now[2]. The most important point in the piezoelectric actuator is achievement of its quick response. As for this demand, we proposed some excitation methods[3], in which electrical pulse driving was considered to prevent the mechanical residual vibration of the actuator. However, the investigation until now was for achievement of a symmetrical operation of displacement as a function of time elapsed.

In this paper, we deal with an asymmetric operation without residual vibration of this actuator excited by electrical rectangular pulse. That is, we describe that by electrical pulse driving taking into account the vibrational periodic time of the actuator, an asymmetric displacement in the time process can be made possible, with no accompanying its residual vibration.

The prevention of residual vibration succeeds to a quick response of the actuator.

This asymmetric operation of an actuator can be variously applied, for example, to construct a rotary motor, a linear motor and a part feeder etc.. In these devices, a specific feature is that a double-trip movement can easily been achieved by changing polarity of input pulses or reforming them.

In the first part of this paper are described some responses of a piezoelectric actuator by input voltage wave form of pulse. The second part contains applications of such actuators and experimental results on them.

Input Voltage Wave Form of Pulse and Responses

A Piezoelectric Actuator and Its Equivalent Circuit

A piezoelectric actuator, which is a subject of investigation in this paper, is shown in Fig.1(a) and its equivalent circuit is Fig.1(b). However, it must be remarked that the actuator is not specially fixed to Fig.1(a), but the actuator in Fig.1(a) is only a representative of general piezoelectric actuators. Moreover, the reason why the equivalent circuit of a single resonance shown in Fig.1(b) is used, is that the lowest resonance of vibration is dominant for actuator operations, even if the actuator has many resonances.

Between the actuator in Fig.1(a) and its equivalent circuit in Fig.1(b), obviously, there are such following correspondences that motional current $\dot{q}_m(t)$ and electric charge $q_m(t)$ are equal to a speed of vibration and a displacement, respectively, at a certain point of the actuator (in Fig.1(a), usually, the free end is considered.). Therefore, by analyzing $\dot{q}_m(t)$ and $q_m(t)$ in the equivalent circuit when the input voltage wave form of pulse in Fig.1(b) is supplied, vibrational characteristics of the actuator can be obtained.

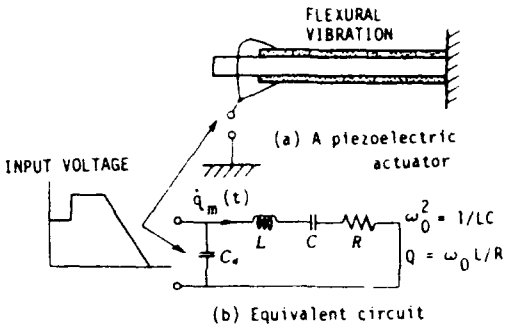


Fig.1: (a) Piezoelectric actuator and (b) its equivalent circuit

Input voltage wave form of pulse

The input voltage wave forms, which are proposed here, to the actuator are shown in Fig.2(a) and (b), that is, in Fig.2(a), in

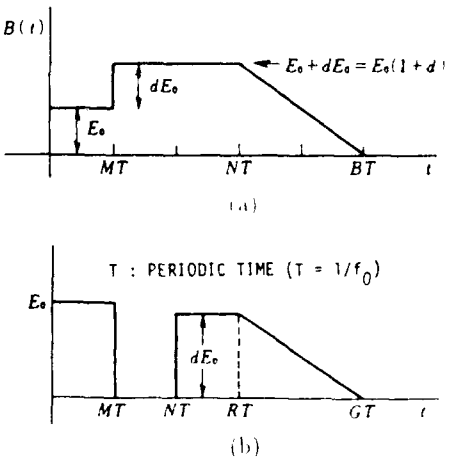


Fig.2: Input voltage wave forms.

CH3080-0-7803-0465-9/92$3.00 ©IEEE

order to achieve a sharp rising-up displacement of the actuator, such rectangular pulse as shown in the figure is first applied and in the next step, after a somewhat interval, the voltage goes down slowly.

By such asymmetric voltage wave form, we expect, the asymmetric operation of an actuator can be made possible. The wave form shown in Fig.2(b) is invented to achieve same operation as by the wave form in Fig.2(a). In Fig.2(b), the applied voltage is discrete to share their own functions; that is, the first pulse raises promptly the displacement and the second pulse controls the raised displacement.

The calculated results of displacement, obtained by applying the voltage wave form shown in Fig.2(a) to the equivalent circuit in Fig.1(b), are shown in (a) and (b) of Figs.3 and 4,

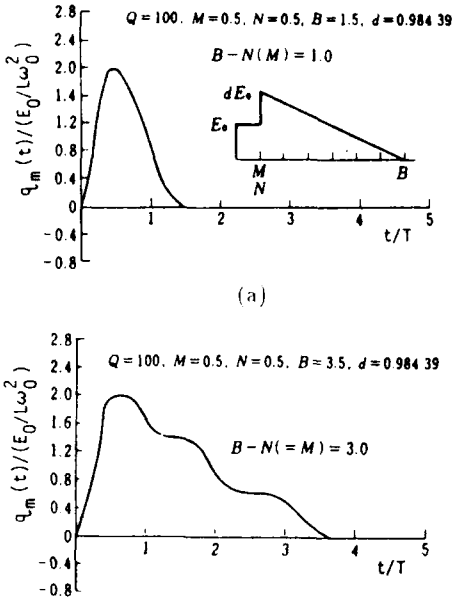


Fig.3: Normalized displacement responses as a function of time elapsed by the voltage wave form in Fig.2(a).

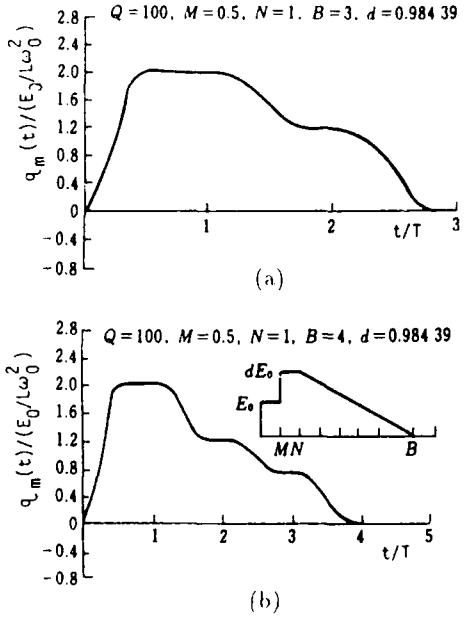


Fig.4: Normalized displacement responses as a function of time elapsed by the voltage wave form in Fig.2(a).

where the longitudinal axis shows the normalized displacement of $q_m/(E_0 L\omega_0^2)$ and the horizontal one, the normalized time of t/T (T: a periodic time). Quality factor Q of the actuator and some conditions to determine the input voltage wave form of pulse are represented in the figures.

From these results, it is found that actuator displacement responses of a sharply rising-up and gently sloping-down characteristic can easily be obtained and the form of characteristic is differently changed by the input voltage wave form. A specific feature of the characteristic appears at the condition $(B - N) \geq 2.0$, that is, one or two plateaus are yielded in the gently sloping-down part.

The characteristic shown in Fig.5 is one example to the wave form shown in Fig.2(b).

We say in addition that the input voltage wave form of pulse shown in Fig.6 can also be utilized to yield the asymmetric displacement response.

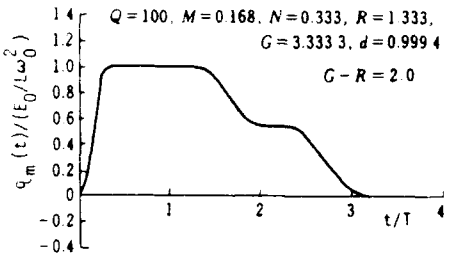


Fig.5: Normalized displacement response by the voltage wave form in Fig.2(b).

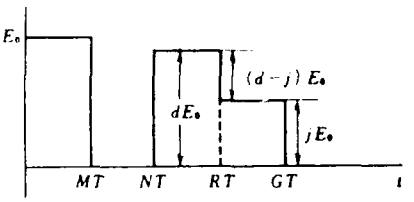


Fig.6: Input voltage wave form for asymmetric displacement response in time elapsed.

Piezoelectric Actuators

Applying the asymmetric displacement responses mentioned above, it is possible to construct some actuators[3] with a function of double-trip operation by only one channel electrical excitation.

Concrete actuators utilizing such characteristics are shown in Figs.7 and 11. The actuator shown in Fig.7 is a kind of rotary motor; that is, the stator disk vibrator is driven by bonded piezoelectric ceramics, for example, in the B_{13} mode (B_{13} means the bending vibration having one nodal circle and three nodal diameters). In this case, 3 projection-teeth are equipped on the nodal diameters as shown in Fig.7(a) and (b). By asymmetric operation of these projection-teeth, the rotor which is pressed down on the stator by a spring, a bearing and a nut, etc., rotates toward a certain direction.

The actuator shown in Fig.11 is to construct a kind of lineai motor. The direction of their motions, in any cases, can be easily changed by the input voltage wave form.

Of course, other constructions of actuator will be possible.

Experimental Results

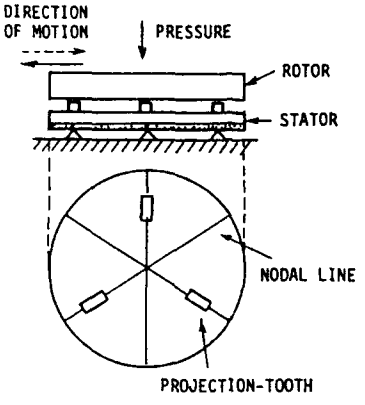
Rotary Motor

A prototype rotary motor is shown in Fig.7(b).

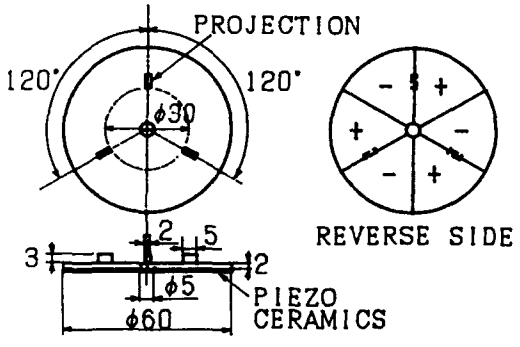
Piezoelectric ceramics are bonded on the reverse side of a stator as shown in Fig.7(b) so as to excite only one B_{13} resonance mode.

When the input voltage wave form in Figs.2(a) or (b) is supplied to such a stator disk, the projection teeth operate promptly as shown in Fig.8(a) in the first stage and in the next stage, they return gently to the state of start according to the asymmetric displacement shown in Figs.3 and 4. By repetition of operation shown in Fig.8, the rotor rotates with a specific feature of a small angular displacement.

Experimental results of this prototype motor are shown in Figs.9 and 10, where the revolution were measured by changing the input voltage wave form; that is, the length of $b(=N-M)$ and $C(=B-N)$ in the wave form shown in Fig.9(a) were changed in Figs.9(c) and 10, respectively. Direction of rotator rotation could easily be changed by the reverse displacement shown in Fig.9(b). In Figs.9 and 10, characteristics presented by signs of O -O and △-△ are ones in a different direction of rotation. It is found that almost same characteristics could be obtained even if the direction of rotation differed. However, we don't understand why the direction of rotation changed, increasing the length of B and C without change of polarity of displacement in Fig.9(b) The specific feature of this motor was found to be that the prototype motor did not radiate unwanted noises, because the stator disk was driven, taking into account no residual mechanical vibration of it.

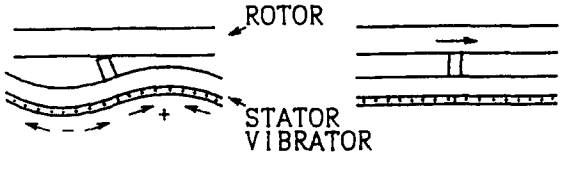


(a)



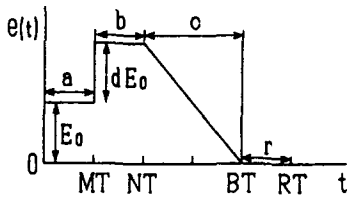
(b)

Fig.7: Application to a rotary movement device (rotary motor).

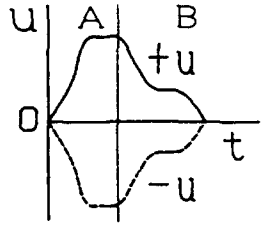


(a) (b)

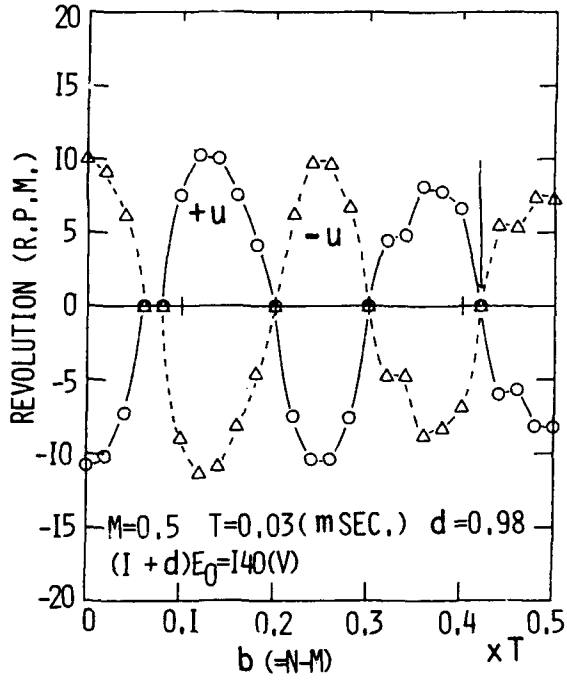
Fig.8: Operation of stator.



(a)Voltage.



(b)Displacement.



(c)

Fig.9: Revolution characteristics.

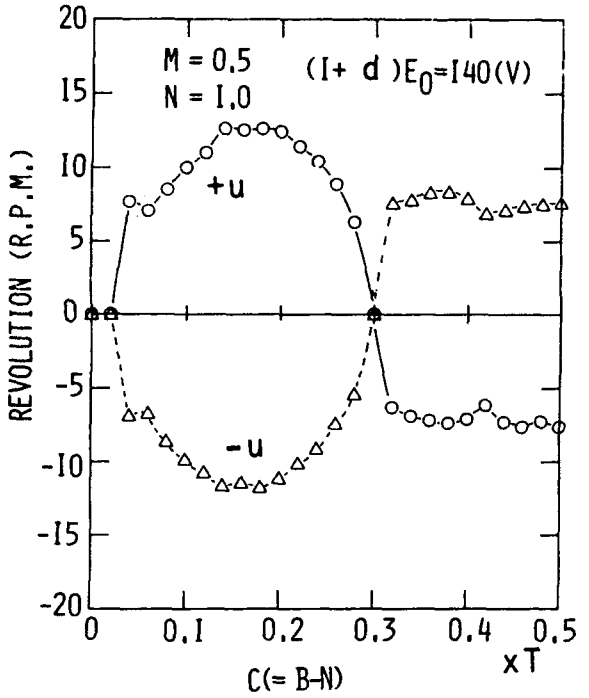


Fig.10: Revolution characteristics.

Linear Motor

The same operation principle as mentioned above was applied to the prototype linear motor shown in Fig.11(b), where the dimensions of the vibrator and projection-tooth were $35.0\times8.0\times1.5(mm^3)$ and $8.0\times2.5\times1.5(mm^3)$. The vibrator was also driven piezoelectrically by the input voltage wave form shown in Fig.9(a), under pressing force to the center nodal line of the vibrator. One example of experimental results are shown in Fig,12. Although the operation in the double-trip were a little different in this case, it is found that the linear motor having a small displacement can be constructed.

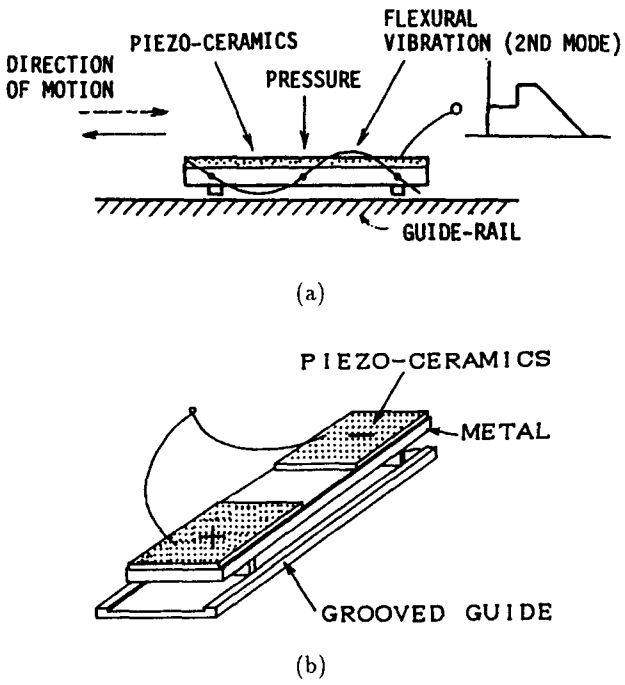


Fig.11: Application to a linear movement device (linear motor).

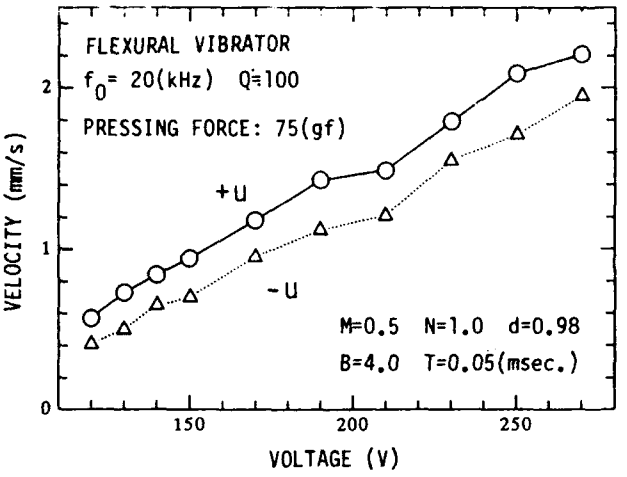


Fig.12: Measured characteristics of the linear motor shown in Fig.11.

Conclusions

We proposed a new excitation method of a piezoelectric vibration without residual displacement to achieve the asymmetric displacement responses as a function of time elapsed, and moreover we presented its application to construct an actuator. That is, the analytical results of such operation of actuator and the experimental results were dealt with in this paper. Hereafter, we want to investigate piezoelectric actuators using such a phenomenon and improve their characteristics further.

Reference

[1] K.Uchino : Piezoelectric/Electrostrictive Actuators, Tokyo, Morikita Shuppan Co. Ltd. (1986) [in Japanese].

[2] C.Kusakabe, Y. Tomikawa and T. Takano : "High-Speed Actuation of a Piezoelectric Actuator by Pulse Driving and Stopping of its Residual Mechanical Vibration", IEEE Trans. on UFFC, Vol.37, No.6 pp.551-557 (1990).

[3] T.Higuchi, Y. Hojjat and M. Watanabe : "Micro Actuators Using Recoils of an Ejected Mass", IEEE, Micro Robot and Teleoperators Work-shop Proceedings, Nov.(1987).

HIGH TORQUE ULTRASONIC MOTOR USING LONGITUDINAL AND TORSIONAL VIBRATIONS

—CHARACTERISTICS OF THE MOTOR WITH A REVOLVING TORSIONAL VIBRATOR USED IN COMMON AS A STATOR AND A ROTOR—

Manabu Aoyagi, Atsushi Satoh and Yoshiro Tomikawa

Department of Electrical Engineering and Information Science, Yamagata University,
Yonezawa, Yamagata, Japan 992.

This paper deals with construction and characteristics of the ultrasonic motor using longitudinal and torsional vibrations: the construction is aimed to achieve a high torque motor. The feature of this motor is that the torsional stator vibrator is used in common as a rotor and revolves about its length axis. Experimental results have revealed that this type motor is suited to construct a high torque ultrasonic motor. In this paper, some detailed data of the prototype motor are described.

Introduction

An ultrasonic motor is investigated actively up to the present. Output power per unit volume of an ultrasonic motor is generally larger than that of electromagnetic motor because mechanical vibration is used in its operation Accordingly, in the same volume, the ultrasonic motor can generate large output torque in comparison with the electromagnetic motor. In other word, the ultrasonic motor is also expected as a powerful device in a small size.

In this paper, the authors deal with the large output torque ultrasonic motor using longitudinal and torsional vibrations. Some ultrasonic motors constructed by combining these vibrations have been reported until now. [1][2][3][4] In them, this motor has such a specific merit that a torsional stator vibrator revolves as a rotor, too.

It is thought that there are two methods in order to elevate the torque of this type motor. One is to increase the frictional force between the rotor and the stator. This method still has such problems that the frictional material used can't bear a very large frictional force and the longitudinal vibration mode is also fairly changed by increasing the rotor pressing force. The other is to increase the diameter of the stator vibrator. Generally, in this case it is not so easy to produce a large diameter stator vibrator using the longitudinal or torsional vibrations. This is the reason that this type ultrasonic motor with a large diameter have not been reported until now. To break through the problems, authors have tried to construct a high torque motor as mentioned below: the diameter of the ultrasonic motor dealt with in this paper is set twice as large as that reported before[3] and the rotor pressing force of it is also made larger than reported before. It is found as the result that the prototype motor could perform the characteristics of the maximum torque of about 10kgf·cm and the optimum efficiency of 15%.

Motor Construction

The construction of the ultrasonic motor made as a trial is shown in Fig.1. The motor is fabricated by two bolt tightening langevin-type vibrators; one is a longitudinal vibrator and the other is a torsional vibrator which is used in common as a rotor. Moreover, radial and thrust bearings, two insulators, and a shaft for supporting them are also used together with a few springs of disk type. In the torsional vibrator, the cylindrical bolt is used

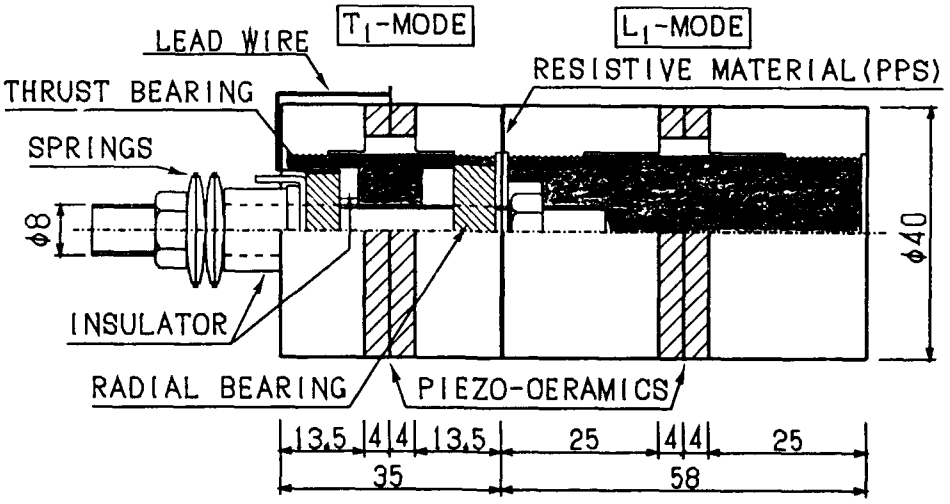


Fig.1: Motor construction of torsional vibrator revolving type.

CH3080-0-7803-0465-9/92$3.00 ©IEEE

in order that the vibrator is pressed by the springs at its inside node point and is supported by the bearings and the shaft. In the motor investigated here, the longitudinal stator vibrator and the torsional one in the first resonance are used for the motor operation. It is ideal that these two vibrations of the first resonance can be excited powerfully at the same driving frequency. This condition of excitation is not always performed in practice. Accordingly, these two resonance frequencies actually need to be close to each other. Considering the condition of excitation, the length of both vibrators made as a trial for the ultrasonic motor were determined as follows: the lengths are 35.0mm and 58.0mm in the torsional vibrator and the longitudinal one, respectively. The ratio of these lengths is near the sound velocity ratio $\sqrt{E/G}$ of the longitudinal and torsional vibration in duralmin, where E is *Young's* modulus and G is shear modulus. The diameter of two vibrators is set as 40.0mm. The thickness of one annular type piezoelectric ceramics is 4.0mm and two plates of such piezoelectric ceramics are used in each vibrator in order to excite the first resonance of both vibrations(L_1 and T_1 modes). The frictional material, which is called PPS(thickness: 0.3mm), is adhered on the surface of the torsional vibrator faced on the longitudinal vibrator. Moreover, the contact surfaces of the torsional vibrator and the longitudinal one are uniformly rubbed with abrasives of #4000(grain size: 3μm). The longitudinal vibration controls the contact between the torsional vibrator and the longitudinal one and when two vibrators keep in contact with each other, the torsional vibrator revolves reactively. Accordingly, the electric power for excitation of the torsional vibrator was supplied through the thrust bearing acting as a slip-ring.

Characteristics of Longitudinal and Torsional Vibrators

The measured equivalent circuit elements of the vibrators made as a trial are shown in Table 1. As the result, the resonance frequency of longitudinal vibration is about 2.3kHz lower than that of torsional one.

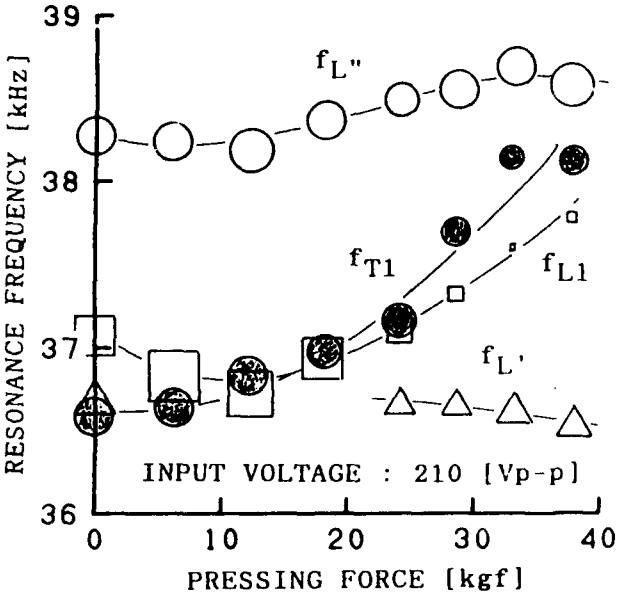
Table 1: Measured values of the equivalent circuit elements of both vibrators.

		L_1-MODE	T_1-MODE
Q		410.88	201.28
f_0	[kHz]	36.40	38.60
Y_{m0}	[mS]	23.56	37.13
R	[Ω]	42.45	26.93
L	[mH]	76.26	22.30
C	[nF]	0.25	0.76
γ		15.46	5.83
K_{vn}	[%]	25.43	41.41

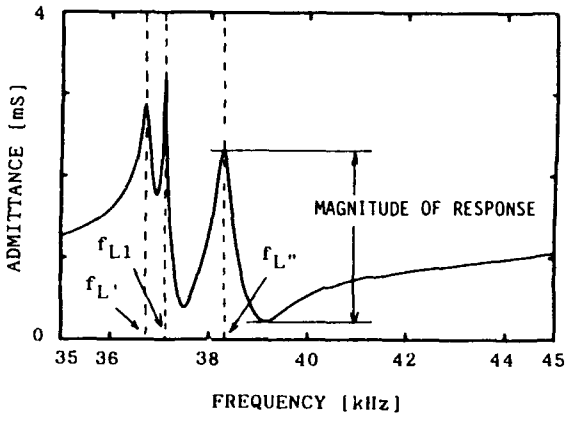
Q : Quality Factor
f_0 : Resonance Frequency
Y_{m0} : Motional Admittance
γ : Capacitance Ratio [C_d/C]
K_{vn} : Electromechnical Coupling Factor

Pressing Force vs. Resonance Frequencies of the Longitudinal and the Torsional Vibrations

The characteristics of the longitudinal and the torsional vibrators, under such condition that two vibrators were pressed against to each other by springs, are different from that of the vibrators measured freely. The relations between the resonance frequency and the pressing force to the torsional vibrator are shown in Figs.2(a) and (b). In Fig.2(a), the plotted mark size shows the magnitude of response, and f_{L1} represents the resonance frequency of the longitudinal vibrator and f_{T1} is one that of the torsional vibrator. As shown in Fig.2(b), it is found that the relativity large responses denoted by its resonance frequencies f'_L and f''_L exist; f'_L is lower than f_{L1}, and f''_L is higher than it. That is, both f_{L1} and f_{T1} go up according to increase of the force. On the contrary, f'_L and f''_L are not so changed by increasing the



(a)



(b)

Fig.2: (a) Resonance frequency vs. pressing force characteristics and (b) Admittance responses of L-mode resonances in the case of no pressing force applied.

pressing force. Moreover, it was found that the response of f_{L1} was small, but the others were not so changed even if the pressing force was increased. The authors think that the vibration modes corresponding to the resonance frequencies f_{L1} and f'_{L1} can be illustrated as shown in Fig.3. Accordingly, it is supposed that the use of f_{L1}-mode is difficult to drive the motor effectively.

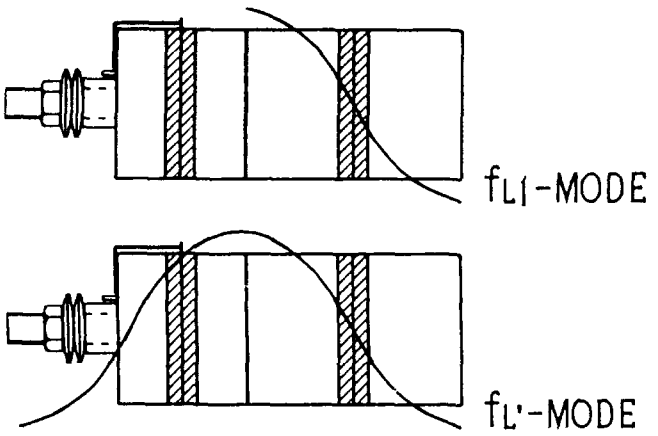


Fig.3: Vibration modes corresponding to the resonance frequencies f_{L1} and $f_{L1'}$.

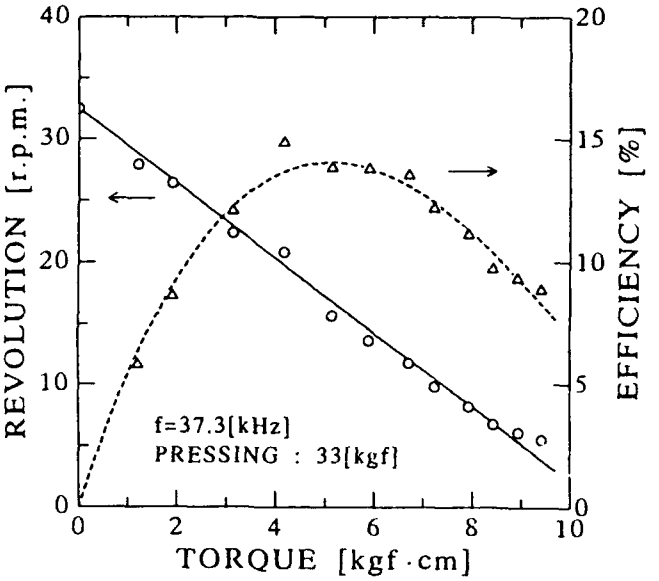


Fig.4: Measured characteristics of the motor shown in Fig. 1 at the optimum input power.

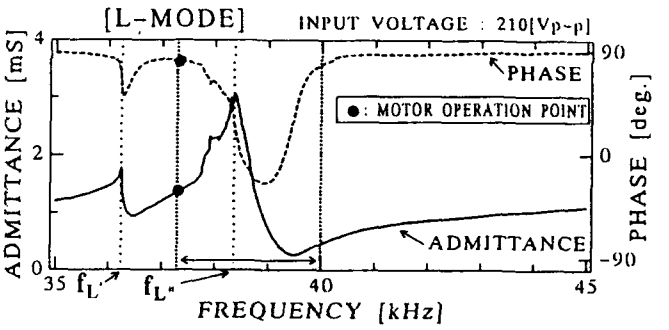
Measured Characteristics of the Motor

Load Characteristics

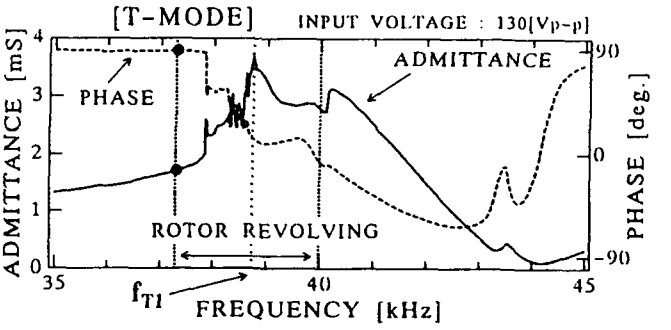
The load characteristics of the motor were measured as shown in Fig.4, where the optimum conditions were such that the driving frequency was 37.3kHz and input power was 6 Watt (2 Watt was for the longitudinal vibration and 15 Watt was for the torsional one). As a result, the maximum torque and the maximum efficiency were 9.4 kgf·cm and 14.8%, respectively, and the rotor revolution at the no load was 33 r.p.m..

Frequency vs. Admittance Characteristics

Figure 5(a) and (b) show measured input admittances of the vibrators versus driving frequency at the condition that the motor operated actually, i.e. the rotor pressing force was 33kgf, the phase difference of input voltages was in phase, and the input voltage were 210Vp-p and 130Vp-p in the longitudinal and torsional vibrators, respectively. In the figures, the arrow marks mean the range of rotor revolving at the measurement; that is, the rotor revolved at the frequency range from 37.3kHz to 40.0kHz and its optimum operation frequency was 37.3kHz as shown by • marks in these figures. This operation point was not the resonance or antiresonance points of the longitudinal and torsional vibrations. The motor could also operate in the neighborhood of the resonance frequency of the longitudinal and the torsional vibrations. However, in these operation points, the torque and efficiency characteristics were not only inferior to the operation at the point marked by •, but at these operation points, it was found that the motor generated much heat.



(a)



(b)

Fig.5: Measured characteristics of the input admittance of the motor in Fig. 4.

Conclusions

From the investigation mentioned above, following conclusions can be drawn:

1) The maximum torque of the motor is improved by making the diameter of the longitudinal and the torsional vibrators large. For example, at the diameter of the vibrator was 20mm, the maximum torque was 1.3kgf·cm[3], but at the diameter of the vibrator was 40mm, the maximum torque was 9.4kgf·cm.

2) The motor didn't operate effectively at the resonance frequencies of the longitudinal and the torsional vibrations.

3) The resonance frequency f_{L1} went up according to increase of the rotor pressing force and the f_{L1}-mode trended toward disappearance of response. Hence it was found that the f_{L1}-mode could not be used at the large rotor pressing force.

4) The resonance frequency f_{T1} also changed as f_{L1} did under the condition that the frictional surface of the torsional and the longitudinal vibrators was treated by fine abrasive, but the response of this mode don't change so.

5) It is expected that the motor characteristics may further be improved by making the resonance frequencies f'_L and f_{T1} be more close to each other than the prototype motor in this paper.

Acknowledgement

The authors wish to express their thanks to Dr. K.Adachi and Mr. T.Ogasawara, who are a lecturer and a technician of Yamagata University, respectively. They supported authors in fabrication of the stator vibrators and in supplying some parts of the motor.

Reference

[1] A.Kumada :"A Piezoelectric Ultrasonic Motor", Jpn. J. Appl. Phys., Vol.24, Suppl. 24-2. pp.739-741(1985).

[2] K.Nakamura, M.Kurosawa and S.Ueha :"Characteristics of hybrid transduser-type ultrasonic motor", IEEE Trans. on UFFC, vol.38, No.3, pp.188-193(1991).

[3] Y.Tomikawa, K.Adachi, M.Aoyagi, T.Sagae and T.Takehiro :"A Rod Type Ultrasonic Motor Using Longitudinal and Torsional Vibration Modes", Proceedings of 1990 IEEE 7th Inter. Sympo. Appli. of Ferroelectrics, pp.229-232(1992).

[4] J.Tsujino and M.Takeuchi :"Ultrasonic Rotary Motor Using a Longitudinal-Torsional Vibration Converter", Jpn. J. Appl. Phys., Vol.31, Suppl. 31-1, pp.245-247(1992).

A STUDY ON THE RELATIONSHIP OF PHASE EQUILIBRIUM AND ELECTROMECHANICAL PROPERTIES IN THE MODIFIED $PbTiO_3$-$BiFeO_3$ SYSTEM

*Peiwen LU, Weiming ZHANG, Dawei SHEN, Wanrong XUE and **Meiyu ZHAO
*Nanjing Institute of Chemical Technology
Nanjing, Jiangsu 210009, P. R. China
**Shanghai Institute of Ceramics
Chinese Acadamy of Science
Shanghai 200050, P. R. China

ABSTRACT In modified $PbTiO_3$-$BiFeO_3$ system, there is a morphotropic phase boundary(MPB) between tetragonal and rhombohedral phases. The electromechanical properties of ceramics with the composition near MPB were examined. When the $BiFeO_3$ content is within 57.5-60mol%, there is mutation of electromechanical properties in the modified $PbTiO_3$ system, which is similar to the $PbTiO_3$-$PbZrO_3$ system. In order to explain the mutation on electromechanical properties, the microstructure, domain structure and electronic diffraction of samples were observed by SEM. It is found that the specical microstructure, domain structure and one dimensional superlattice presented in the samples are possible reasons which result in excellent electromechanical properties for the ceramics.

Introduction

In 1962, Fedulov S. A. etal. fisrt researched the characteristics of pure $PbTiO_3$(PT)-$BiFeO_3$ (BF) system. They found that phase transition temperture of PT-BF solid solution almost increased linearly with $BiFeO_3$ contents increasing. In this system, There is a morphotropic phase boundary between tetragonal and rhombohedral phases. The MPB position is near 70wt% $BiFeO_3$. When $BiFeO_3$ content goes beyond 25wt%, ferroelectric phase and weak ferromagnetic phase coexist in the solid solution below 400°C. They believed that the existence of weak ferromagneticphase destoried the good *piezoelectric properties of* $PbTiO_3$ ceramics. But L. E. Cross etal.[1] developed the piezoelectric application of PT-BF system in 1985. By using proper processing, They have prepared piezoelectric-polymer composites with 0-3 connectivity for transducer application. They believed the spontaneous strain in PT-BF system is among the highest for any piezoelectric material. This anisotropy on the crystallographic axes is the source of the high piezoelectric coefficients exhibited by those compositions. The anisotropy and its temperature dependence are also the sources of strain of PT-BF crystallities. This limits the utility of these compositions in forming dense ceramics.

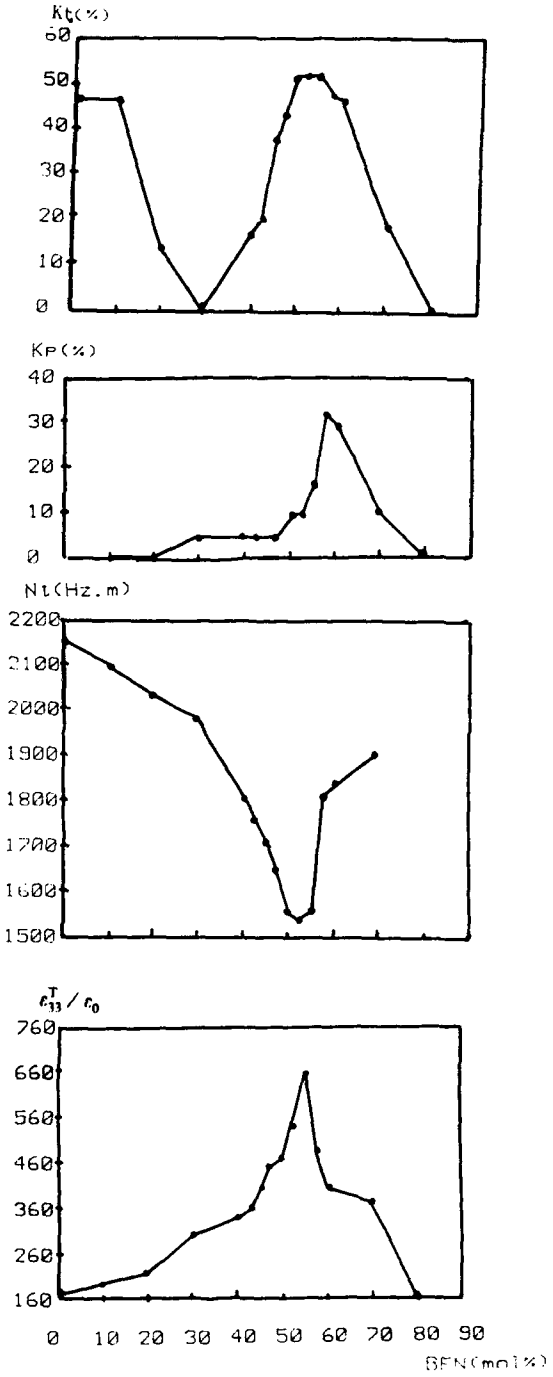
In this study, relations among composition, structure and properties of modified PT-BF system were investigated. The possible reasons why the composition near the MPB show the excellent electromechanical properties were approached.

Materials and Methods

The chemical formula for modified PT-BF system is $[(Pb,Ln)TiO_3]_{1-x}$-$[Bi(Fe_{1-y}Me_y)O_3]_x$, where Ln=La, Pr, Nd, Sm or Gd and Me=Mn, Fe, Nb or W, x=0.2-0.8, y=0-0.2. The main electromechanical properties of the samples were measured by HP-4192A impedance analyser and d33 meter. The microstructure, domainstructure and electronic diffraction were observed through the thin foil specimens with a H-800 SEM.

Results and Discussion

The electromechanical properties of K_t, K_p, N_t, ε, $tg\delta$ and d33 are shown in Fig.1. In each of the properties, there is a mutation when x is in the range of 0.5-0.6.[2] The optimum properties of the sample in the modified PT-BF system are listed in Table 1. This material exhibits excellent electromechanical properties of high K_t and low Q_m.



CH3080-0-7803-0465-9/92$3.00 ©IEEE

Table 1 The optimum electromechanical properties of the sample in the modified PT-BF system

K_t %	K_p %	K_t/K_p	Q_m	ε	tgδ %	$d_{33}\times10^{-12}$ C/N	T_c ℃
53	5	10.6	20	450	1.5	130	350

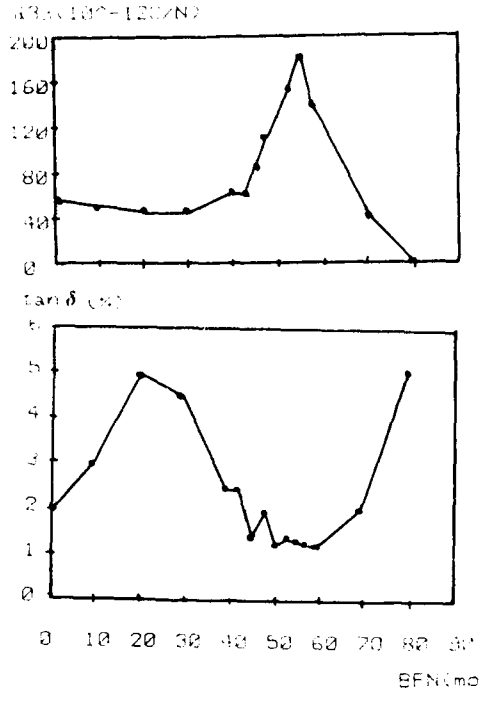


Fig.1 K_t, K_p, N_t, ε, tgδ and d_{33} vs. compositions of modified PT-BF system

The microstructures of the samples with the compositon near MPB are shown in Fig.2. This is a very specical microstructure that most of the grains look like cubic and some of them are rhombohedral.The grains grow well and arrange loosely although there are little pores. This microstructure is different from those of PZT and PT ceramics and this may be a reason for high K_t and low Q_m.

Fig.3 and Fig.4 show the domain structure and electronic diffraction pattern of the thin foil specimens . It is found that domains are more intensive in





Fig.2 SEM micrograph of the sample with the composition near the MPB (A)3000x (B) 5000x

the specimen with composition near MPB than those with other compositions. According to the thermodynamics, a certain amount of domains can form to make free energy of materilas lowest. When the average value of domain wall energy of materials is lower, the amount of domains is more. It can be guessed that domain-wall energy in the MPB composition is lower than those of other compositions and the domain rotation is easier. This is corresponding with the high degree rotation of 90° domain which means high K_t and low Q_m.

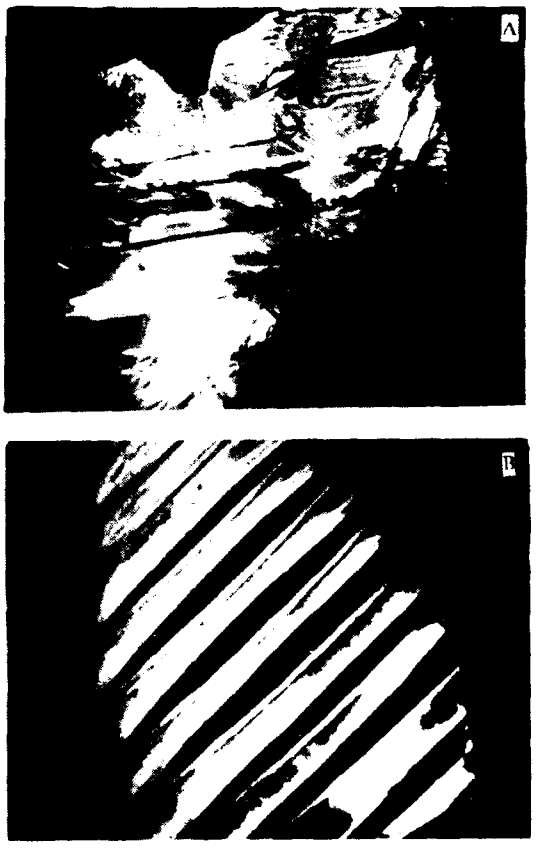
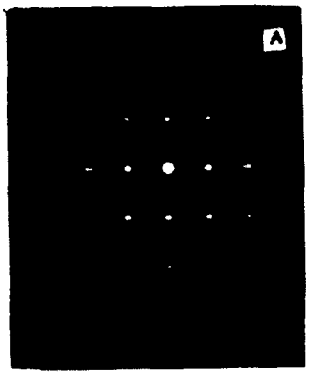


Fig.3 Domain structure of the specimen with the composition near MPB (A)3000x (B) 7500x



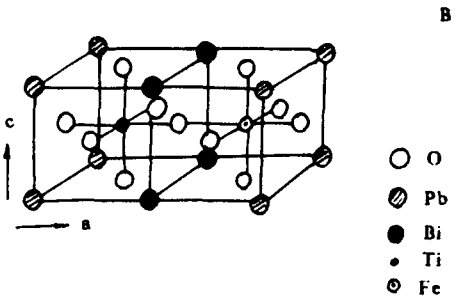


Fig.4 (A) SAD electronic diffraction pattern of (010) zone axis of specimen near MPB composition (B) Scheme for ordered microarea of modified PT-BF ceramics

One dimension superlattice has been observed by electronic diffraction spectrum(Fig.4(A)). The ordered microarea appeares extensively in the spectrum with the composition near MPB. For the crystal structure of the ordered microarea of modified PT-BF ceramics, a scheme has been established. It is imagined that the ordered microarea is a tetragonal structure with volume of $c_0 \times 2a_0 \times 2a_0$ which consists of Pb^{2+}, Bi^{3+} in A site and Ti^{4+} Fe^{3+} in B site of perovskite structure arranging orderly in a ratio of 1:1(Fig.4(B)). Superlattice in ceramics has obvious influences on electromechanical properties.[3] Therefore these ordered microareas might be a structural reason of considerable electromechanical activity of the ceramics with the composition near MPB in the modified PT-BF system. It agrees with the high K_t anf low Q_m.

Conclusion

The ceramics with the composition near MPB in the modified PT-BF system show excellent electromechanical properties of high K_t and low Q_m. A special microstructure , more intensive domains and one dimension superlattice in ceramics may be a reason of remarkable electromechanical activity for the ceramics.

References

[1] Giniewicz etal., United States Patent, 4,624, 796

[2] P. W. Lu etal., "A study on phase constituents of modified $PbTiO_3$-$BiFeO_3$ system," in Proceedings of the 1st International Symposium on the Sciences of Engineering Ceramics, 1991, pp543-547.

[3] J. Chen etal., "Ordering structure and dielectric properties of undoped and La/Na doped $Pb[Mg_{1/3}Nb_{1/3}]O_3$," J. Am. Ceram. Soc., vol.72(4), pp.593-598, 1989.

LARGE ANISOTROPY ON ELECTROMECHANICAL PROPERTIES OF RARE-EARTH AND ALKALINE-EARTH OXIDES COMPLEX MODIFIED $PbTiO_3$ CERAMICS

*H. Wang, W. R. Xue, P. W. Lu, D W. Shen, Q. T. Zhang and **M. Y. Zhao

*Department of Silicate Engineering
Nanjing Institute of Chemical Technology
Nanjing, Jiangsu 210009, P. R. China

**Shanghai Institute of Ceramics
Chinese Academy of Science
Shanghai 200050, P. R. China

The dielectric and piezoelectric properties, the microstructural developments and crystal structures of $(Pb_{0.88-x}Gd_{0.08}Me_x)(Ti_{0.98}Mn_{0.02})O_3 + y(Sb_2O_3 + Nb_2O_5)$wt% (x=0-20mol%, 0<y<1.5, Me=Ca, Ba or Sr) were investigated. The results showed that the alkaline-earth ions content influenced strongly on the electromechanical properties of the samples. When Me=15 mol%, the optimum properties presented: K_t=55%, K_p=0, K_t/K_p=∞, Q_m=60, $\varepsilon^T_{33}/\varepsilon_0$<250, tgδ<1.5% and d_{33}=70x10^{-12} c/N. The effects of the poling electric field on such properties were studied. SEM and XRD revealed that the ceramic microstructure changed obviously and tetragonality (c/a) decreased due to the Me ions doped. It was suggested that both the microstructure and crystal structure are resonsible for such behaviors

Introduction

Modified $PbTiO_3$ ceramics has attracted much attention in view of its excellent electromechanical anisotropy and low dielectric constant. It is expected to be a promising piezoelectric materials in the field of nondestructive testing for metals(NDT) and ultrasonic medical diagnosis. P. Duran[1] and Y.Ito etal.[2] respectively researched on the electromechanical properties of alkaline-earth or rare-earth oxides modified $PbTiO_3$ based piezoelectric ceramics and obtained materials with large anisotropic electromechanical coupling factor(K_t/K_p) and low dielectric constant. Authors[3] of this paper have systematically studied rare-earth oxides Gd_2O_3 and small amounts of transition metal oxides MnO_2 modified $PbTiO_3$ ceramics(Gd-PT). In this study, by adding alkaline-earth oxides in Gd-PT ceramics, the dielectric, piezoelectric, crystallographic properties and the microstructure of rare-earth and alkaline-earth oxides complex modified $PbTiO_3$ ceramics have been investigated.

Experimental Procedure

The following compositions of modified lead titanate ceramics were prepared by conventional piezoelectric ceramics technique: $(Pb_{0.38-x}Gd_{0.08}Me_x)(Ti_{0.98}Mn_{0.02}) + y(Sb_2O_3 + Nb_2O_5)$wt%, where $Me=Ca^{2+}$, Ba^{2+} or Sr^{2+}, x=0-20mol%, 0<y<1.5. Applied with fired silver electrodes, these samples were poled under an electric field of 50 to 60kv/mm in 120°C silicon oil for 15 minutes.

The piezoelectric and dielectric properties of the samples were measured according to IRE standard. Crystal structure was examined with XRD and IR methods. The micrographs of the sample were carried out by SEM.

Results

Fig.1 shows the effects of the alkaline-earth ions Me amount on the dielectric properties of the samples. As can be seen, with the addition of Me content from 0 to 20 mol%, the relative permittivity $\varepsilon^T_{33}/\varepsilon_0$ increases from 145 up to 350. When 10mol% Me is employed to the composition, the dielectric loss factor tgδ presents a special maximum, but other additions of Me will reduce value of tgδ. The dependence of piezoelectric properties d_{33}, K_t and K_p on Me content is shown in Fig.2. With increasing Me amount from 0 to 15mol%, d_{33} increases linearly from 44x10^{-12}c/N to 70x10^{-12}c/N then abruptly falls down to 9x10^{-12}c/N when 20mol% Me was added. The appropriate amounts of doping alkaline-earth ions can pronouncedly enhance the anisotropic electromechanical coupling factor, i.e. increase electromechanical coupling factor for thickness vibration K_t and decrease that for planar vibration K_p. Especially for the sample containing 15mol% Me, K_t increases up to 54% and Kp reduces down to 0. However, further increasing of Me content to 20mol% will greatly lower the piezoelectric properties of the samples.

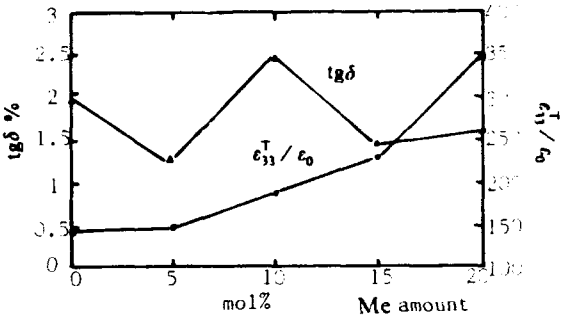


Fig.1 Dielectric properties $\varepsilon^T_{33}/\varepsilon_0$ and tgδ vs. alkaline-earth ions content

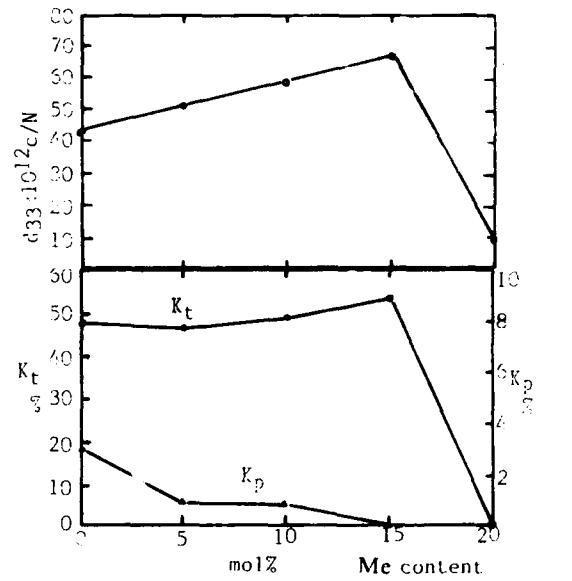


Fig.2 The dependence of d_{33}, K_t and K_p on Me content

Electromechanical properties of the piezoelectric ceramics strongly depend on the poling conditions. In this study, the specimens with 15mol% Me are chosen to examine the effects of the poling electric field on K_t, K_p, d_{33} and Q_m, as shown in Fig.3 and Fig.4. As the poling electric field intensifies, d_{33} and K_t mono-

CH3080-0-7803-0465-9/92$3.00 ©IEEE

onically rise and K_p is zero in the whole poling process. When the poling electric field is 3KV/mm, Q_m reaches to the maximum, and further increase of the poling electric field will result in the gradual decrease of Q_m. As a result, the specimen is obtained with moderate alkaline-earth and rare-earth oxides and appropriate poling electric field, and presents K_t=55%, K_p=0, d_{33}=70x10^{-12}C/N, Q_m=60, $tg\delta$<1.5% and $\varepsilon_{33}^T/\varepsilon_0$<250.

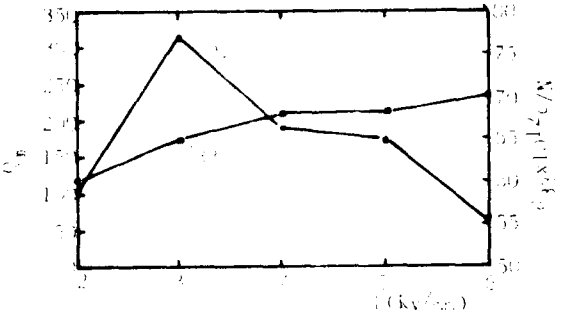


Fig.3 d_{33} and Q_m vs, the poling electric field

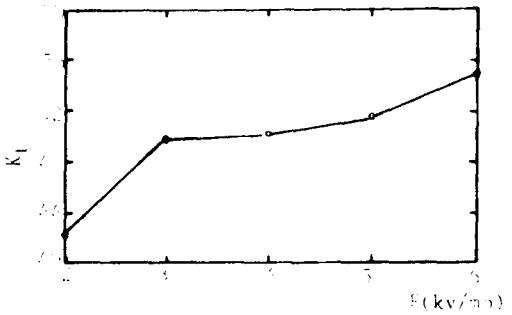


Fig.4 The dependence of K_t on the poling electric field

By analysing XRD patterns and IR spectra of the samples, it is found that the lattice distortion results from the doping alkaline-earth ions. Compare the lattice parameters of the specimen with 15mol% Me with those of Gd-PT ceramics, c decreases from 0.41274 nm to 0.40634nm while a reduces from 0.3899nm to 0.3868nm and c/a ratio also decreases from 1.059 to 1.050. From the IR spectra of the samples, as shown in Fig.5, it is observed that doping alkaline-earth ions can change the stretching vibration of $[TiO_6]$ octahedrons, that is, the absorption peak at 560cm^{-1} moves to 590cm^{-1} and the peak at 760cm^{-1} disappears.

Fig.6 shows the micrographs of the micro structural developments of the specimens with variable Me content. As can be seen, with increasing Me content from 5mol% to 20mol%, the regular polygonous grains with an average grain size of approximate 4μm gradually change into the concavo-concave irregular grains with an average grain size of 2μm. Corresponding to the variation, a wide distribution of grain size is gradually formed. Rather typically, for the sample with 15mol% Me, the microstructural density is smaller than those of the other two compositions. Loosely arranging grains, broad grain boundaries and porosities can be observed in the sample.

Discussion

Spontaneous strain δ as a parameter of crystal structure is taken into account. For the ferroelectric tetragonal phase, δ is related to c/a-1. According to the theory of ferroelectric thermodynamics, a relationship between δ and spontaneous polarization P_S is given by $\delta=kP_S^2$, where k is a constant. After the alkaline-earth oxides are induced, two effects will be caused: (1) If k is constant before and after the doping of Me ions, the reduction of δ which is induced by the $[TiO_6]$ octahedrons compression distortion and the decrease of c/a ratio will decrease P_S value. (2) Pb^{2+} ions being substituted by Me ions with a lower polarizability also makes P_S fall. Devonshire showed that for a tetragonal ferroelectric single crystal, the dependence of permittivity on P_S is

$$\frac{4\pi}{\varepsilon_a} = \frac{4\pi}{\varepsilon_b} = 2A + 12B_1P_S^2 + 15C_1P_S^4,$$

$$\frac{4\pi}{\varepsilon_c} = 2A + 2B_1P_S^2 + 30C_1P_S^4$$

If the effect of the doping Me ions on the coefficient is negligible, the reduction of P_S will raise the permittivity. So it is not difficult to know that the increasing $\varepsilon_{33}^T/\varepsilon_0$ of the polycrystalline samples arise from the same behavior of P_S. However, on the other hand, decreasing c/a ratio also lowers the internal stress induced by 90° domain rotation, and hence the number of 90° domain rotation will rise. This behavior can lead to $\varepsilon_{33}^T/\varepsilon_0$ decrease, but the decrease is not dominant compared with the effect of P_S. The resulting effect is that the relative permittivity $\varepsilon_{33}^T/\varepsilon_0$ rises with increasing Me amount.

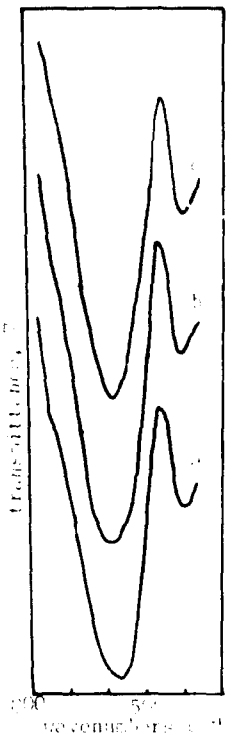


Fig.5 IR spectra of
(a)(Pb,Gd)(Ti,Mn)O_3
(b)(Pb,Gd,Me$_{0.15}$)(Ti,Mn)O_3
(c)(Pb,Gd,Me$_{0.20}$)(Ti,Mn)O_3

According to the ferroelectric thermodynamics, d_{33} for piezoelectric ceramics is given by

$$d_{33}=2Q_{11}P_r$$

where Q_{11} is electrostrictive coefficient and is an approximate

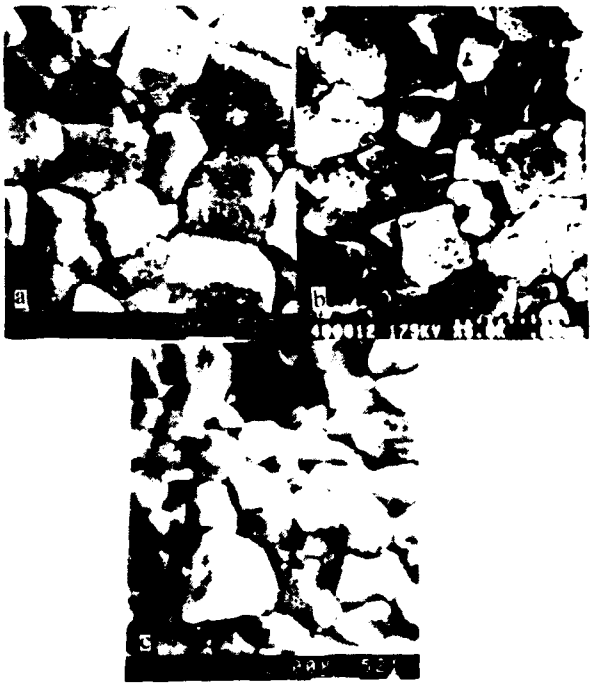


Fig.6 Scanning electron micrographs of the samples (a) doped with 5mol% Me (b) doped with 15mol% Me (c) doped with 20mol% Me.

nstant for perovskite structure, Pr is the remanent larization which is the product of both factors, mely, the number of domains aligned in the direction the electric field and the value of P_S. After the mples are doped with Me ions, inspite of the reducing of P_S, the mber of 90° domain rotation greatly rises, which is e to the decrease of coercive field E_S caused by the a reduction. Finally, P_r is increasing. In particular, e specimen with 15mol% Me presents a microstructure th broad grain boundaries and more porosities, and e microstructure acts as such a smaller pinning effect on the domain wall motion that the number of 90° main rotation will be more. Thus P_r increases and so es ε_{11}^T. As a result of these factors, with the doping ions amount increase, d_{33} rises linearly and shows maximum when the specimen containing 15mol% Me. The dition of excess Me ions causes d_{33} to drop abruptly, obably due to the reduction of P_S being dominant.

Although the mechanism of the electromechanical isotropy for modified $PbTiO_3$ ceramics is not clear, me studies[1] have shown that the large electromechanical anisotropy(K_t/K_p) and K_t value are usually related to a low c/a ratio. The present work also indicates that when 15mol% Me is doped, K_p approaches to zero d K_t reaches to the maximum of 54%. Correspondingly, e c/a ratio is 1.050 and microstructure with wide rain boundaries and more porosities is occurred. The ystal structure and microstructure can give rise to e maximum amount of domains aligned in the direction electric field applied. So the distribution of domains in the direction of electric field is an important factor in improving the electromechanical anisotropy.

The dependence of the electromechanical properties of the samples on the poling electric field is tually that such properties are as a function of the mber of domains aligned in the direction of poling ectric field. With the increasing poling electric eld, the amount of domains paralleled to the poling ectric field increases and the electromechanical properties are improved gradually.

Conclusion

1) A moderate amount of rare-earth and alkaline-earth oxides combined modified $PbTiO_3$ceramics exbit an extremely high anisotropic electromechanical oupling factor.

2) The lower c/a ratio and the microstructure th wide grain boundaries and more porosities can ad to the increase of domains paralleled to the poling lectric field, and hence improve the electromechanical operties.

References

[1] P. Duran etal., "Large electromechanical anisotropic modified lead titanate ceramics," J. Mat. Sci., vol.24, pp447-452, 1989

[2] Y. Ito etal., "Surface acoustic wave and piezoelectric properties of (Pb,Ln)(Ti,Mn) O_3 ceramics (Ln=rare earth)," J. Appl. Phys., vol.52, pp4479-4486, July 1981

[3] H. Wang etal., "A study on Gd_2O_3+MnO_2 modified $PbTiO_3$ piezoelectric ceramics," to be presented at Intl. Conference on Electric components and Materials, Hangzhou, P. R. China, 1992

SOL-GEL PROCESS FOR THE PREPARATION OF ULTRAFINE $PbTiO_3$ POWDERS

*Qitu Zhang, Zhiqi Zhang, Dawei Shen, Wanrong Xue, Hui Wang and **Meiyu Zhao
*Department of Silicate Engineering
Nanjing Institute of Chemical Technology
5 Xinmofan Road, Nanjing
Jiangsu 210009
**Shanghai Institute of Ceramics
Chinese Academy of Science
Shanghai 200050
The People's Republic of China

In this work tetrabutyl titanate and lead acetate are used as the precursors to prepare ultrafine lead titanate powders through sol-gel process. The results indicate that powders with high purity($PbTiO_3$ concentration 99.67wt%), small particle size(average particle size 0.1μm) and narrow size distribution can be obtained via sol-gel process. The sol-gel derived gel highly crystalized after heat treated at 400°C for 2 hours. It is also found that $Pb(CH_3CO_2)_2$ can be effectively dehydrated at 190°C for several hours.

INTRODUCTION

Lead titanate piezoelectric ceramics is a promising material due to its high Curie temperature, large eletromechanical coupling factors and low dielectric constant. However, $PbTiO_3$ prepared via conventional methods exhibits poor sintering behaviors. This owes primarily to the high boundary energy of its grains. Though modified lead titanate ceramics can be produced by doping additives,[1][2] the Curie temperature and some other electromechanical properties are demaged to some degree.

To obtain $PbTiO_3$ ceramics with high performance and good reproducibility, it is important to prepare superpure, ultrafine and narrowly distributed $PbTiO_3$ precursor powders with high chemical activity. There have some reports on preparing $PbTiO_3$ materials through sol-gel process[3][4][5] but few on preparing $PbTiO_3$ precursor powders. As the most effctive method for the preparation of high performance powders, sol-gel technique meets the higher and higher demands for precursor powders of today's high performance ceramics.

In this work the technological procedure of sol-gel process for the preparation of ultrafine $PbTiO_3$ powders, which uses tetrabutyl titanate and lead acetate as the precursors, and the characteristics of the derived powders are investigated.

EXPERIMENTAL PROCEDURES

Raw Materials

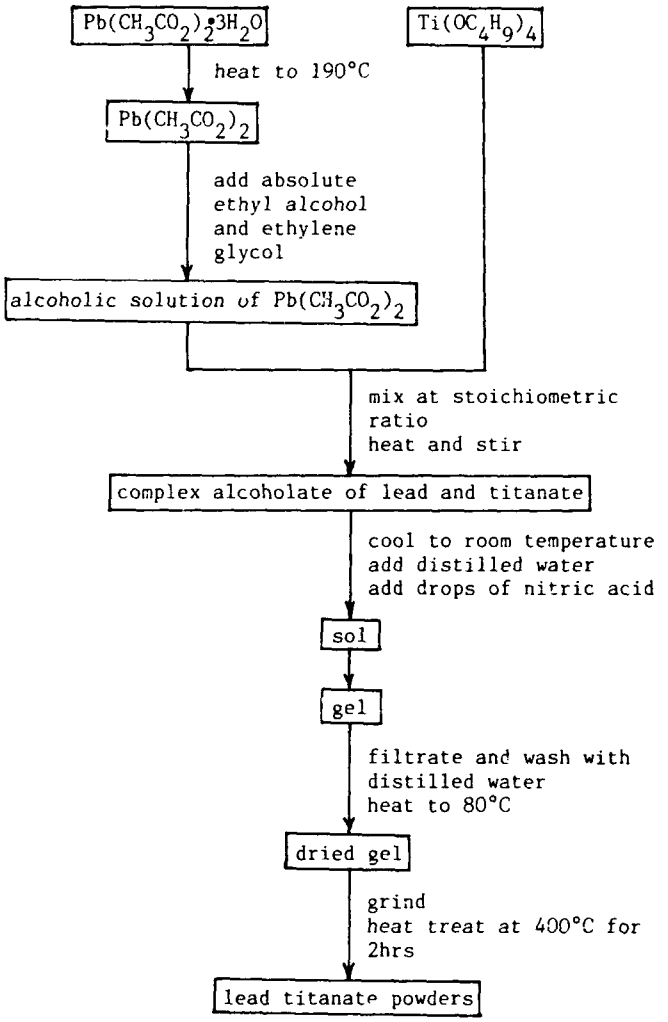
Tetrabutyl titanate($Ti(OC_4H_9)_4$), hydrous lead acetate($Pb(CH_3CO_2)_2 \cdot 3H_2O$), absolute ethyl alcohol and ethylene glycol, used as supplied, are the raw materials in ths study.

Dehydration of Lead Acetate

The hydrous lead acetate is putted in the evaporating dish and simply heated at 190°C for several hours. The anhydrous lead acetate($Pb(CH_3CO_2)_2$) is then derived.

Preparation of Ultrafine Lead Titanate Powders

The preparing procedure is listed as following



The solubility of anhydrous lead acetate in absolute alcohol is increased because of the presence of ethylene glycol. Furthermore, ethylene glycol in the system can reduce the hydrolysis rate of tetrabutyl titanate to match that of lead acetate. The balanced hydrolysis rates are the basis of the homogenity and purity of the obtained gel.

Tests and Analyses

Phase analyses were performed with a D/max-rb X-ray diffractometer on the dehydrated lead acetate and lead titanate powder samples heat treated at different temperatures. Thermal analyzer LCT-II was used to conduct differential thermal analysis and thermalgravimetry on the air-dried $PbTiO_3$ gel. The heating rate in these

* project supported by the Open Research Laboratory of High Performance Ceramics and Superfine Microstructure Studies

CH3080-0-7803-0465-9/92$3.00 ©IEEE

analyses was controlled to be 20°C/min. For the lead titanate powders heat treated at 400°C for 2 hours, the particle size and appearance were observed through a H-800 electron microscope. The purities of anhydrous lead acetate and obtained lead titanate powders were determined by chemical analysis.

RESULTS AND DISCUSSIONS

Dehydration of Lead Titanate

Fig.1 shows the XRD pattern of the hydrous lead acetate dehydrated at 190°C. Only the anhydrous lead acetate diffraction peaks appear in the pattern. Chemical analysis revealed that the concentration of lead acetate in the dehydrated sample is 99.87wt%. The unanimous results of XRD and chemical analysis suggest that hydrous lead acetate can be effectivly dehydrated at 190°C.

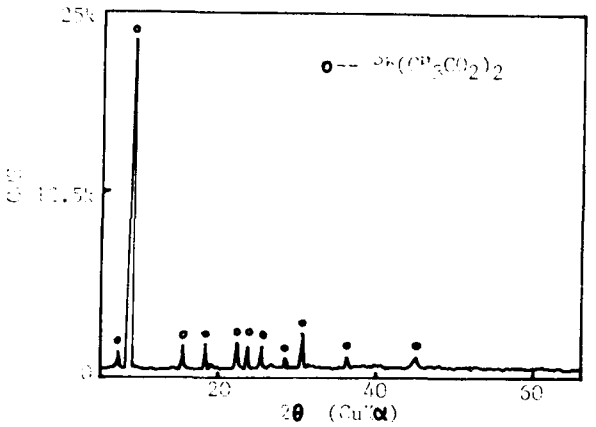


Fig.1 XRD pattern of dehydrated lead acetate

Differential Thermal Analysis and Thermalgravimetry for Dried Lead Titanate Gel

Differential thermal analysis and thermalgravimetry were conducted on the derived gel dried at 80°C. The results are shown in Fig.2. The endothermic peak at 86°C on DTA curve along with 15% weight loss on TG curve owes to the volatilization of enthnol and water in the gel. The buring out of the organic compounds and substituents cause the heat release at 322°C on DTA curve and a 20% weight loss on TG curve. Another heat release peak appears at 396°C on DTA curve accompanied with no significant TG effect. This is caused by the crystallization of $PbTiO_3$ powders at this temperature.

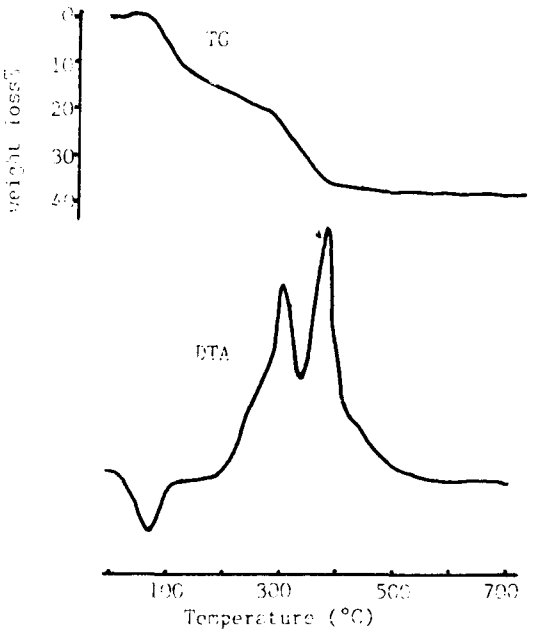


Fig.2 TG-DTA curves of the dried $PbTiO_3$ gel

Phase Analysis by XRD

The XRD pattern for the obtained $PbTiO_3$ powders heat treated at different temperatures are shown in Fig.3. It has been enviced that the sample exists principally in amorphous state after heat treated at 300°C for 2 hours while 400°C heat treat promotes the crystallization significantly. The result shows no difference with TG-DTA analyses. Besides, the concentration of lead titanate in derived ultrafine powders is 99.67wt% according to chemical analysis.

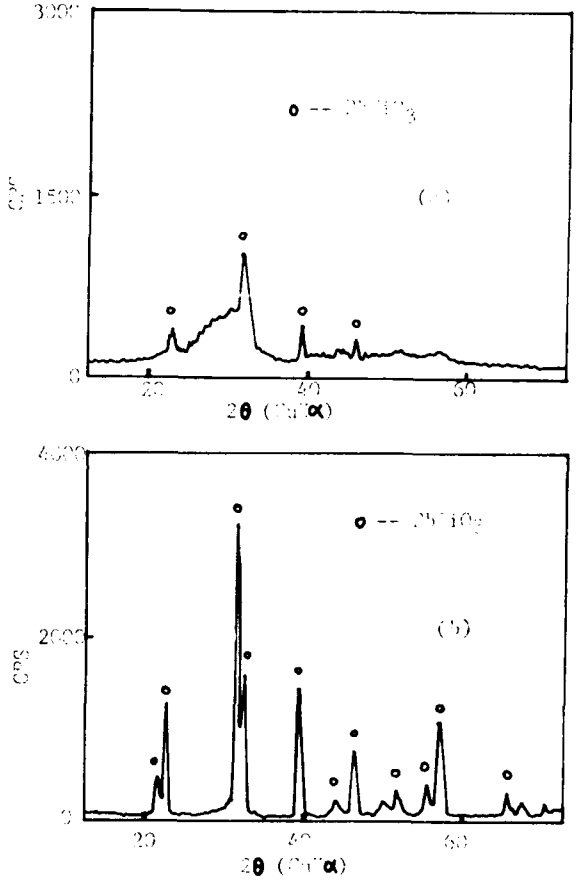


Fig.3 XRD patterns for $PbTiO_3$ powders (a) heat treated at 300°C for 2h (b) heat treated at 400°C for 2h

Particle Size and Appearance Observation through TEM

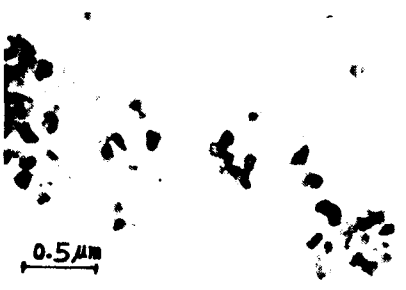


Fig.4 TEM Micrograph of $PbTiO_3$ powders

The particle size and appearance of the ultrafine powder sample heat treated at 400°C for 2 hours were observed through TEM, as shown in Fig.4. According to the micrograph, the average particle size of the sol-gel derived lead titanate powders is 0.1μm. It is also revealed that the powders are narrowly distributed in size and are spherical and polyhedral in appearance.

CONCLUSIONS

1. Lead acetate can be effectively dehydrated at 190°C.

2. Lead titanate precursor powders for ceramics with high purity, small particle size and narrow size distribution can be prepared through sol-gel process.

3. The sol-gel derived lead titanate powders crystallized at a relatively lower temperature.

REFERENCES

[1] P. Duran etal., "Large electromechanical anisotropic modified lead titanate ceramics," J. Mat. Sci., vol.24, pp.447-452, 1989

[2] Y. Ito etal., "Surface acoustic wave and piezoelectric properties of $(Pb,Ln)(Ti,Mn)O_3$ ceramics (Ln=rare earth)," J. Appl. Phys., vol.52, pp.4479-4486, July 1981.

[3] Y. Hayashi etal., "Sol-gel derived $PbTiO_3$," J. Mat. Sci., vol.70[10], pp.2655-2660, 1987

[4] S. K. Dey etal., "Structure of polymeric $PbTiO_3$ gels," J. Am. Ceram. Soc., vol.70[10], pp.C295-C296, 1987

[5] T. V. Dekleva etal., "Sol-gel processing of lead titanate in 2-methoxyethanol: investigations into the nature of the prehydrolyzed solutions," J. Am. Ceram. Soc., vol.71[5], pp.C280-C282, 1988

DEVELOPMENT OF PORTABLE DC VOLTAGE STANDARD USING PZT's

Mohan Lal

Materials Division
National Physical Laboratory, Dr. K.S. Krishnan Road, New Delhi - 110 012 (India)

ABSTRACT

A method has been developed using poled lead zirconium titanate (PZT) ceramic by the application of charge recovery technique. The charge decay is due to compensating charges coming to the PZT surfaces from the atmosphere and/or by electrical loading of the these charges screening the intrinsic PZT charge. In this paper PZT decayed charges ully recovered by the charge reactivation process and found constant voltage on the PZT. Thus overed dc voltage of PZT made use of development of dc voltage standard for intercomparison at constant temperature.

INTRODUCTION

Lead Zirconium Titanate (PZT) is being commonly used in pressure transducers for dynamic applications, such as for producing micro-displacements for laser cavity - adjustments and other transducer applications [1]. There is now considerable interest in the area of ferroelectric materials for use as non-volatile, high speed random access memories (FRAMS) [2]. Among the many types of ferroelectric perovskites, PZT class of ferroelectrics are being used for FRAM type applications. For such applications, PZT's also need to have good resistance to bipolar voltage cycling (fatigue resistance); good retention of polarisation states and resistance of ageing. In this paper we shall be describing a method of use of poled PZT for dc voltage standard applications for inter-comparison (at different countries). The proposed method is based on the electret nature and application of charge activation or recovery technique. The charge reactivation technique is described in detail elsewhere [3].

It is essential and proper to describe here that PZT bars and discs being used for dc voltage standard were giving a self voltage [4] which was varying with time and weather conditions. It is difficult to neutralise or nullify the self voltage would be varying in uncontrollable way. Of course, for dynamic applications, the instant change in the self voltage or in other words, the voltage generated by piezoelectric effect would pass through a capacitor produced in the PZT system and so these above mentioned dynamic applications will not suffer for existence of a varying self voltage.

But the author observed rapid enough charge decay in PZT and proposed a mechanism [5]. A simple and practical method was evolved to successfully revive decayed charge on PZT. Before describing the mechanism of charge decay author noted that since the excess poled charge at and near the surface of PZT is trapped to depth of 1-2 eV and the aligned dipoles are rigidly fixed up at room temperature, the intrinsic PZT charge at room temperature is immobile and so far the charge on PZT to decay, compensating external charge must come to the PZT surface. In the following is suggested how this can happen?

In author's view the compensating charge can come from the floating charge (of both polarities) present in the atmosphere and from electrical resistance across the PZT if any. The electrical load will supply mobile charge carriers which would move to each of the PZT faces (having the opposite intrinsic charge) under the driving voltage of the poled PZT itself and compensate this intrinsic charge, all this resulting in the PZT becoming inoperative.

Basic premise in our thinking is that compensating charge coming to the PZT faces through electrical loading or otherwise screens the intrinsic PZT charge but does not destroy it. Hence the PZT is only apparently decayed its charge but is not really so. The question now arises, can the screening charges be removed, thus reviving the PZT charge or voltage? The answer is fortunately yes as provided by the charge reactivation technique.

EXPERIMENTAL

In our experimental work, either PZT discs of diameters about 22 mm and thickness 3 mm were used or PZT cylinderical bars (originally designed to be used as gas lighters of dimensions 15 mm length 6 mm diameters of top and bottom faces) were used. PZT faces were marked plus (+) or minus (-) corresponding to polarity of voltages applied to the faces for poling (necessary for obtaining the piezoelectric effect for the PZT's). Both the faces of each of the PZT samples were silvered. It was observed and found that positive voltage on the face marked (+) could be apparently as in electrets, the positive electrode would orient towards it the negative charges of PZT or negative electrode would orient the positive charges, even for this effect also there seem to be no clear indication in literature [6] that this would be so. However, our results experimentally observed occasionally (face marked (-) shows positive voltage and vice versa) was equivalent to the hetro-voltage of the PZT operating as an electret. If this so, author forcefully concluded that opposing kind of voltage, i.e. opposite to the hetro-voltage is nothing but homo-charge on the PZT faces. PZT either exhibit a hetro-charge or homo-charge or even almost zero voltage depending upon weather conditions. On our thinking, this fact due to screening of both hetro- and homo- charges independently of each other, the net charge or voltage is also depending on th initial hetro- and homo- charges present before the decay began.

By proper application of charge reactivation technique on the PZT disc or bar, the surface voltage of PZT increased towards the maximum of the hetro-voltage. The voltage accuraately measured with the FET input voltmeter (Keithley Electrometer Amplifier, 610 model) within the accuracy available (+ 10 μv). The fully reactivated d.c. voltage of PZT was found constant enough. Thus, it was seen that measuring the open circuit recovered voltage of PZT on successive days for about one month remained constant within the accuracy mentioned above.

CH3080-0-7803-0465-9/92$3.00 ©IEEE

In this method, of use of poled PZT for d.c. voltage standard, all what one has to do at place of measurement is the application of charge recovery tecnnique to get the maximum open circuit voltage for the PZT concerned and subject it to the relevant measurements afforded by the standards laboratory concerned at a pre-fixed temperature. The constancy of temperature, is of course important because the open circuit voltage of PZT is sensitive function of temperature. It follows that this method for intercomparison of d.c. voltage standard would become all the more feasible and practical if PZT's of decreased temperature sensitivity, than those available at present, were developed.

In principle, the electrets should also serve for voltage standardisation but this was not investigated.

DISCUSSION OF RESULTS

The method is extremely simple in operation of charge activation process and its measurements. Here, it may be stated that, in principle, while measuring d.c. open circuit voltage of PZT, the PZT should be revived fully. A fundamental significance of charge recovery technique and its success shows that almost all the mechanisms suggested for charge decay has been summarized by Sessler et al [7] only for academic interest not applying in practice. Here, the obvious effect of humidity in producing the apparent charge decay may be discussed. The adverse effect of humidity is most probably due to electrical loading of the PZT, the water film, connecting the two opposite surfaces of the PZT, forming are electrical shunting path (of finite electrical resistance) between the two surfaces. This path would polarising charges of opposite polarities to the inherent, intrinsic surface charges of PZT.

The above suggests that for the over all process of charge decay of PZT, the polarising charges can also come from the atmosphere. Since, it contains charges of both polarities [8], the resulting decay of charge of the PZT surface would be due to attraction of opposite charges from the atmosphere and the shunting effect of moisture or any other intended or non-intended electrical load (across the PZT surfaces). The charge reactivation technique merely depolarises the polarised surface due to the fact that, as has been mentioned above, the polarising external charges are as firmly bound to the PZT surfaces than the polarised, inherent surface charges of the PZT faces. In reverse, the success of the charge reactivation techniques also indicates that the PZT charges in the bulk or on the surface are stable enough against the destabilising effect of the internal electric field of the PZT.

The success of this method has one more fundamental aspect in that a way has been found for releasing the polarising but less strongly bound charges present on the insulator surfaces. This fact has also made the matter of using PZT's as portable constant d.c. voltage sources.

Electrical nature of ferro electrics

The success of the charge activation process enabled us to unravel the electret nature of ferroelectrics, both single crystal and poled-ceramic. By carrying out contact reversals, both the kinds exhibited surface voltage and therefore charge. For poled ceramics the analogue with electrets went a step further. The ceramic (PZT) exhibited both homo- and hetro-charge in the process of contact reversals. The homo-charge must be due to charges transferred from the poling electrodes to the ceramic surfaces (in the act of poling) and getting trapped therein.

CONCLUSION

A simple, portable d.c. voltage standard method has been developed, using poled PZT, by the application of charge revival process. It was found that the maximum open circuit voltage of the PZT has been recovered and measured within the accuracy ($\pm$ 10 μv). It was also confirmed by the observations that the PZT d.c. voltage source remained constant on different places.

REFERENCES

[1] M.E. Lines and A.M. Glass, Principle and Applications of Ferroelectrics and Related Materials, Claren don, Oxford, 1977.

[2] R. Ramesh, W.K. Chan, B. Wilkens, T. Sands, J.M. Tarascon, V.G. Keramidas and J.T. Evans JR. "Fatigue and ageing in Ferroelectric $PbZr_{.2}$ $Ti_{.8}$ O_3/YBa_2 Cu_3O_7 Hetrostructures," Jr. of Integrated Ferroelectrics, vol. 1, pp.1-15, 1992.

[3] Mohan Lal and R. Parshad, "A Suggested New Mechanism of Charge Decay of Electrets and its Application to their Charge Recovery," Proceedings 5th International Symposium Electrets, Heidelberg, p. 352, 1985. (Avail from IEEE, NY).

[4] Mohan Lal and R. Parshad, "Generation of surface-voltage by charged crystal defects and applications," Jr. of Radiation Effects and Defects in Solids, pp. 27-8, 1990.

[5] Mohan Lal and R. Parshad, "The New Electret Charge Recovery Technique : A Review," Presented at the IEEE Conference, 6th International Symp. Electrets (ISE6) Oxford, U.K., Sept 1-3, 1988.

[6] B. Jaffe, W.R. Cook and H. Jaffe, "Piezoelectric Ceramics," Academic Press London and New York, 1977.

[7] G.M. Sessler, "In Topics in Applied Physics," vol. 33, Electrets edit by G.M. Sessler, (Springer Ver Lage, Berlin) 1980.

[8] J. Alan Chalmers, "Atmospheric Electricity," Pregamon Press, London, N.Y. 1967.

THE ELECTRICAL PROPERTIES OF ANTIFERROELECTRIC LEAD ZIRCONATE-FERROELECTRIC LEAD ZINC NIOBATE CERAMICS WITH LANTHANUM.

J.S.Yoon, V.S.Srikanth and A.S.Bhalla
Materials Research Laboratory,
Pennsylvania State University, University Park, PA 16802

Abstract

The electrical properties of antiferroelectric lead zirconate(PZ) with relaxor ferroelectric lead zinc niobate(PZN) are studied from an application viewpoint of the field-induced phase transition near the morphotropic phase boundary. According to the addition of lanthanum, the curie point decreased with increasing lanthanum up to 3m/o, whereas for AF-FE boundary it increased with increasing lanthanum, Over 4m/o lanthanum, it can be find paraelectric and antiferroelectric region. The effect of composition of lanthanum and temperature on the dielectric, pyroelectric and P-E hysteresis are reported.

I. Introduction

Most of the antiferroelectric or ferroelectric oxide ceramics with relaxor are important for piezoelectric, pyroelectric device application as actuators[1-3]. Among the vast range of perovskite structure compounds, solid solution compositions of antiferroelectric lead zirconate(PZ) with ferroelectric perovskite give interesting piezoelectric and pyroelectric properties near their antiferroelectric(AF) - ferroelectric(FE) phase transition and morphotropic phase boundary.

Lanthanum-modified lead zirconate titanate(PLZT) ceramics have interesting electrooptic properties. Their electrical and structural properties were initially reported by Heartling and Land[4].

In this study, electrical properties of the antiferroelectric lead zirconate with a relaxor ferroelectric lead zinc niobate with composition of MPB, 0.929$PbZrO_3$-0.071 $Pb(Zn_{1/3}Nb_{2/3})O_3$, were investigated to the dependence of the change of lanthanum, PZZN-Lx (1 x 5).

II. Experimental Procedure.

1. Ceramic preparation.

Ceramics were prepared by conventional sintering technique used by reagent grade oxide powders of PbO, La_2O_3 ZrO_2, ZnO, and Nb_2O_5 as a raw materials. To compensate for the PbO loss during firing, 2w/o excess PbO was added.

After mixing in ball milling with alcohol for 12-14hr, the powders were calcined at 800'C for 1hr. Calcined powders were ground, and mixed with 3w/o of PVA binder, and were pressed into disk 12mm in diameter for cutting for the desired shape, and about1 mm in thickness. The binder was evaporated during a double steps heat treatment at 300'C for 2hr and 500'C for 2hr[5]. Pressed disks were sintered at 1250'C for 1hr in PbO atmosphere with PbO·ZrO2 source powder.

After sintering, ceramics were alternatively cut and polished, and were coated with sputtered gold electrode for electrical measurements.

2. Electrical measurements.

The dielectric constants were measured at frequencies of 100Hz, 1KHz, 10KHz, and 100KHz over a temperature range of -80'C - 240'C by using an automated dielectric measurement system with a multi frequency LCR meter and a desktop computer.

A modified Sawyer-Towe circuit was used to recorded the P-E hysteresis behavior of the samples at a various temperatures[6]. The electric field was measured by the X-axis of the oscilloscope, and polarization of the sample was measured by the Y-axis.

The pyroelectric properties were investigated with the Byer-Roundy method[7]. To measure the pyroelectric properties, one side of the circular sample of thickness over 0.2mm was electroded by gold sputtering. On otherside, a 5mm circular spot electrode was sputtered through a mask.

Specimens for the pyroelectric property were poled by dynamic method in air oven with an electric field 30KV/cm at 185'C.

The pyroelectric and P-E hysteresis measurements were carried out to determine the saturate polarization, remanent polarization, coercive field, the depolarization temperature, and phase transition.

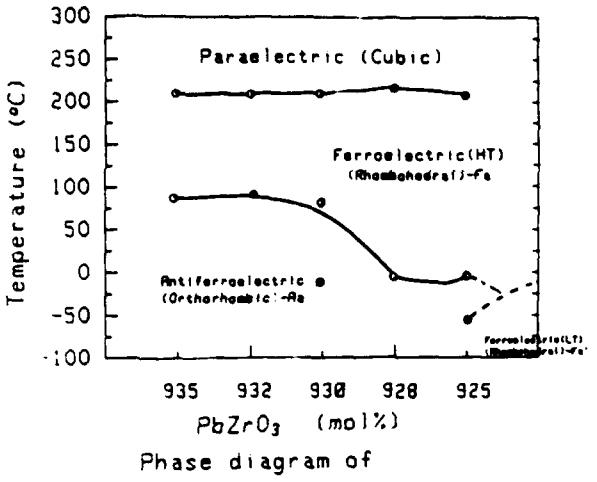
III. Results and Discussion.

Figure 1 is the plot of the phase relations of the PZZN ceramics. It was based on the dielectric measurement, pyroelectric measurement, and P-E hysteresis measurement. According to the these measurements, it can be divided four regions. Those are paraelectric, ferroelectric-HT, ferroelectric-LT, and antiferroelectric region. The phase boundary of high temperature ferroelectric phase-low temperature ferroelectric phase at -60'C was determined by dielectric measurement. The boundary of

CH3080-0-7803-0465-9/92$3.00 ©IEEE

ferroelectric - antiferroelectric for the PZZN 930 - 935 was located at 70'C - 80'C and for the PZZN 925 - 928 was -5'C - -15'C. For the room temperature, it was divided by PZZN 928 - 930 with the large change of the slope. This feature means that it can be switch the phase from an antiferroelectric state to ferroelectric state at the small change of temperature near the PZZN 928 - 930 at the room temperature.

Figure 2 was SEM photographs of PZZN-L0 and PZZN-L3. They show a dense and uniform grain size in the sintered samples. The samples were thermally etched at 1200'C for 30min and the average grain size of PZZN-L0 and PZZN-L3 were 4μm and 2μm, respectively.



Phase diagram of

$PbZrO_3$ -$Pb(Zn_{1/3}Nb_{2/3})O_3$ system.

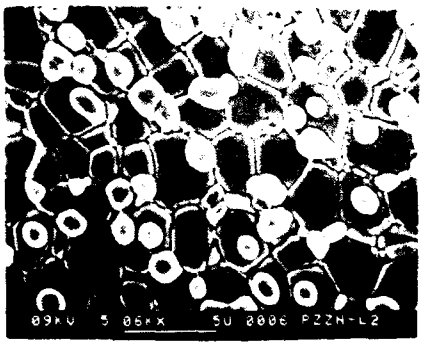
Fig. 1. Phase relations of the PZZN solid solution system at the AF-FE phase boundary.

Figure 3 shows the temperature dependence of the dielectric constants for PZZN-L0 and PZZN-L2 during the cooling. The dielectric constant of PZZN-L0 increased to peak value of 9000 at the transition temperature, Tc=219'C. The dielectric constant of the PZZN-L2 show anomalies behavior at 70'C and Tc was 204'C. This anomalies between the phase boundary between the antiferroelelctrric phase(AF) and the ferroelectric phase(FE). Over the transition temperature, the ferroelectric phases were changed to paraelectric phase.

Figure 4 shows the temperatures dependence of the dielectric constants for PZZN-L series. The transition temperature of PZZN-L3 was 184'C, but Tc was increased with the increasing of the amount of lanthanum[8]. In case of PZZN-L9, Tc was 235'C.

Figure 5 shows the temperature dependence of the pyroelectric coefficient and the remanent polarization of PZZN-L0 and PZZN-L2. The measurements to find the phase boundary

(a)



(b)

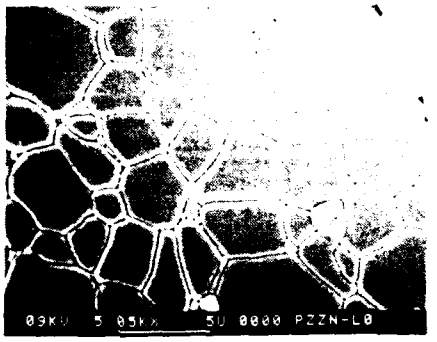
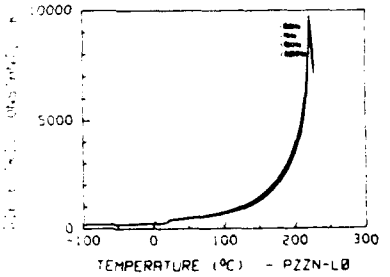
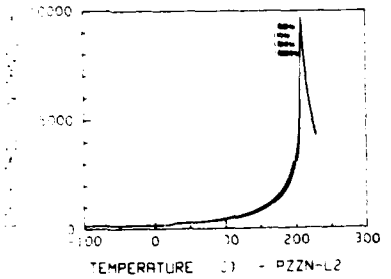


Fig. 2. SEM photograph of the surfaces of the PZZN-L0(a), and PZZN-L 2(b) ceramics. The surfaces were thermally etched at 1200'C for 30min. (bar=1μm)



(a)



(b)

Fig. 3. Temperature dependence of the dielectric constants for PZZN-L0(a) and PZZN-L2(b) showing Tc

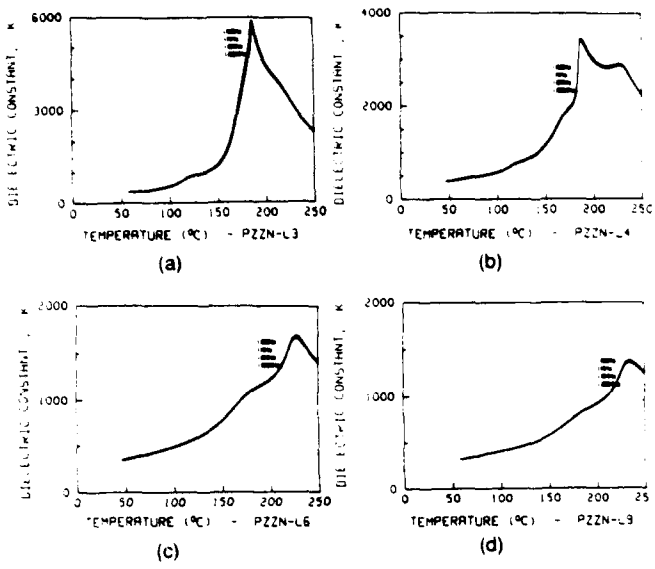


Fig. 4. Temperature dependence of the dielectric constants for PZZN-L3(a), PZZN-L4(b), PZZN-L6(c), and PZZN-L9(d) showing T_c.

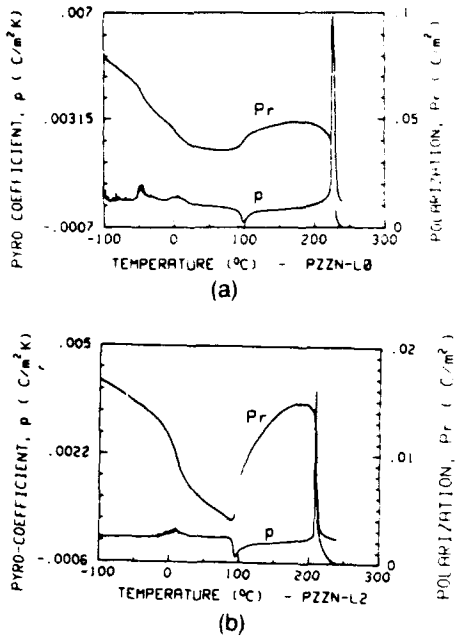


Fig. 5. Temperature dependence of pyroelectric coefficient(p) and polarozation(Pr) of PZZN-L ceramics;
(a) PZZN-L0 (b) PZZN-L2

composition were made during the heating cycle with a typical heating rate of 4'C/min. In the pyroelectric coefficient of the PZZN-L0 and PZZN-L2, two pyroelectric peaks corresponding to orthorhombic-to-rhombohedral and cubic-to-rhombohedral are clearly observed at 80'C and 204'C, respectively.

The hysteresis nature was investigated using a modified Sawyer-Towe circuit applying an ac field of about 30KV/cm. Figure 6 shows the P-E hysteresis loops observed for PZZN-L ceramics at a various temperatures. The samples of the PZZN-L0 shows the ferroelectric behavior and increase the coercive field, Ec, and the remanent polarization,Pr, according to the increasing amount of the lanthanum. The ferroelectric of the PZZN-L system was highly sensitive to composition and temperature. Pr reaches a maximum value of 30μC/cm² at PZZN-L2. In the PZZN-L3, it could find hysteresis loop at 145'C. It meant that an antiferroelectric phase can be forced into a field-induced ferroelectric phase with the remanent polarization and the field-induced ferroelectric state is expected to remain stable even after the electric field is removed. According to the hysteresis, it shows AF-FE boundary is located between PZZN-L0 and PZZN-L2 at 80'C, but between PZZN-L2 and PZZN-L3, boundary is 145'C.

Figure 7 is the plot of the phase relations of the PZZN-L solid solution system. It was based on the dielectric measurement, pyroelectric measurement, and P-E hysteresis measurement. According to the these measurements, it can be divided three regions. Those are paraelectric, ferroelectric, and antiferroelectric region. The phase boundary for PZZN-L0 - PZZN-L2 was located at 80'C and for the PZZN-L3 was 145'C. Over the PZZN-L4, there are antiferroelectric and paraelectric phases.

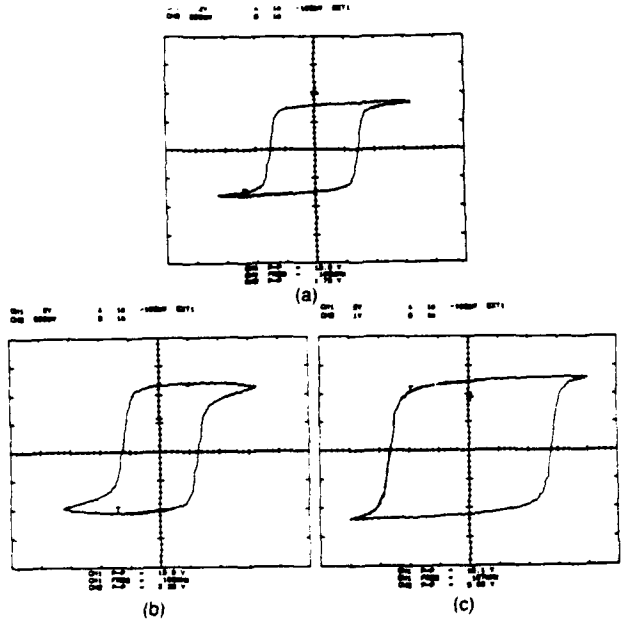


Fig. 6. D-E hysteresis loops of PZZN-L ceramics at various temperature showing ferroelectric.
(a) PZZN-L0, Ec= 15.9 KV/cm, Pr=21.2μC/cm²
(b) PZZN-L1, Ec= 7.3 KV/cm, Pr=24.5μC/cm²
(c) PZZN-L2, Ec= 5.98KV/cm, Pr=30.6μC/cm²

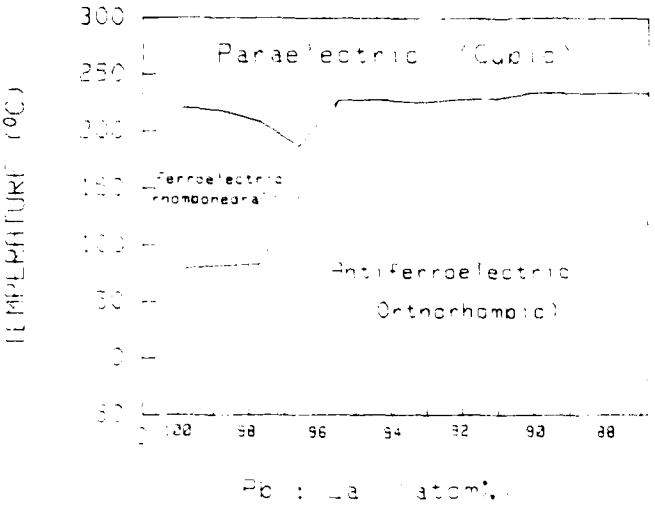


Fig. 7. Phase relations of the PZZN-L solid solution system.

IV. Conclusion

1) It could be divided three regions: paraelectric, ferroelectric, and antiferroelectric region.
2) The curie temperature decreased with increasing lanthanum up to 3m/o, whereas for AF-FE boundary it increased with increasing lanthanum.
3) Over 4m/o lanthanum, it can be find paraelectric and antiferroelectric region.

Reference

1. B.Jaffe, W.R.Cook, Jr., and H.Jaffe, Piezoelectric Ceramics, Academic Press, New York, 1971.
2. H.Jaffe,"Piezoelectric Ceramics", J. Am. Ceram. Soc., **41** [11] 494-498 (1957).
3. E.Sawauguchi,"Ferroelectricity versus Antiferroelectricity in the Solid Solutions of $PbZrO_3$ and $PbTiO_3$", J. Phys. Soc. Jpn., **8** 615-629 (1953).
4. G.H.Heartling and C.E.Land,"Hot-Pressed (Pb,La)(Zr,Ti)O_3 Ferroelectric Ceramics for Electrooptic Applications", J.Am.Ceram.Soc., **54** [1] 1-11 (1971).
5. G.S.Snow,"Improvements in Atmosphere Sintering of Transparent PLZT Ceramics", J.Am.Ceram.Soc., **56** [9] 479-480 (1973).
6. H.Diamurt, K.Drenk, and R.Pepinsky,"Bridge for Actuate Measurement of Ferroelectric Hysteresis", Rev. Sci. Instrum., **28** [1] 30-34 (1957).
7. R.L.Byer and C.B.Roundy,"Pyroelectric Coefficient Direct Measurement Technique and Application to a NSEC Response Time Detector", Ferroelectrics, **3** 333-338 (1972).
8. W.A.Schulze, T.G.Miller, and J.V.Biggers, "Solubility Limit of La in the Lead Zirconate-Titanate System", J.Am.Ceram.Soc., **58** [1-2] 21-23 (1975).

The DC Field Dependence of the Piezoelectric, Elastic and Dielectric Constants For a Lead Zirconate-Based Ceramic.

E.F. Alberta, D.J. Taylor and A.S. Bhalla
Materials Research Laboratory, The Pennsylvania State University, University Park, PA 16802, U.S.A.

T. Takenaka
Faculty of Science and Technology, Science University of Tokyo, Noda, Chiba-Ken, 278 JAPAN.

ABSTRACT

Large pyroelectric figures of merit, F_V and F_D have been found in the solid solution x·$PbZrO_3$ [PZ] - y·$Pb(Zn_{1/3}Nb_{2/3})O_3$ [PZN] - z·$PbTiO_3$ [PT] (PZNT). Previous work within this system has also shown a DC field induced ferroelectric-antiferroelectric transition. This paper will further explore the electrical field dependence of the elastic constant (s_{11}^E), piezoelectric coefficient (d_{31}) and dielectric constant (K_{33}) near this phase transition.

INTRODUCTION

As sensor and transducer technology advances there is an increasing need for smart materials. When evaluating materials for smart applications, the weak field dependence of the dielectric and piezoelectric constants can be effective guides. Earlier studies in solid solution system of the relaxor ferroelectric PMN and the ferroelectric PT have shown strong weak field induced piezoelectric effect. Antiferroelectric materials have also been shown to exhibit this desired non-linear response. It was for this reason that the solid solution of the ferroelectric PT, and antiferroelectric PZ and relaxor PZN has been chosen to be explored for possible use as a smart sensor material under weak DC fields.

Solid solutions containing PZ have be widely studied in the past due to the antiferroelectric [AF] to ferroelectric [FE] phase transition and the existence of morphotropic phase boundaries. The system PZZN combines PZ with PZN. This system has been shown to possess a room temperature orthorhombic AF to rhombohedral FE phase boundary a x ~ 93% PZ. This system looks promising for piezoelectric and pyroelectric applications with F_V = 0.31x10^{-10} C·cm/J and F_D = 0.35x10^{-8} C·cm/J, low coercive fields of 8 to 10 kV/cm, large piezoelectric coupling coefficients such as k_{15}~50% and remanent polarizations on the order of 25 to 30 μC/cm^2.

This paper will explore the dielectric and room temperature piezoelectric properties of PZNT and PZZN compositions near the MPB. Fore the rest of this paper the PZNT(x/z) compositions with z = 0 mol% PT will be referred to as PZZN(x).

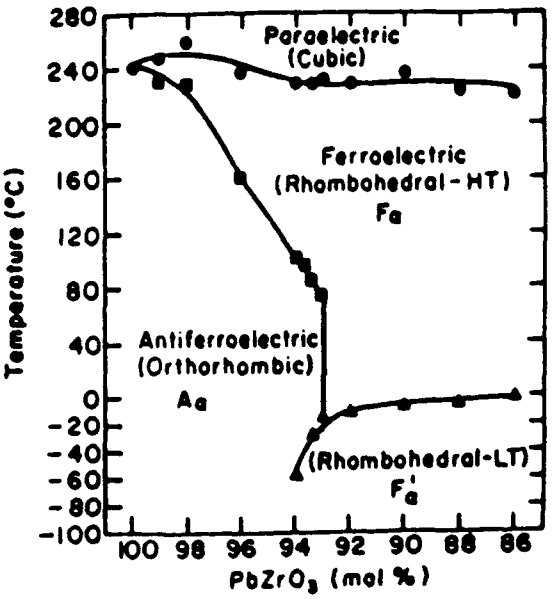


Figure 1: PZZN phase diagram.

EXPERIMENTAL PROCEDURES

Ceramic samples were prepared by the normal ceramic mixed oxide techniques. Samples were then thinned and polished to a 1-μm Diamond finish and gold sputtered electrodes applied. Room temperature polarization versus electric field hysteresis loops were then studied at 10 Hz using a modified Sawyer-Tower circuit. A silicone oil bath was used to prevent electrical breakdown during these experiments.

CH3080-0-7803-0465-9/92$3.00 ©IEEE

The temperature dependence of the dielectric constant was measured at various frequencies in a temperature range from -100°C to 250°C using a computer controlled measurement system consisting of a multifrequency LCR meter (HP4274A, Hewlett Packard Co.), desktop computer (HP 9816) and nitrogen fed furnace. Various DC bias voltages were then applied to the sample by an external power supply.

For resonance measurements the samples were prepared as long, thin bars with typical dimensions of 20 x 2 x 0.2 mm. Specimens were polished thin so as to allow the application of fields between 15 and 20 kV/cm with 600 Volts or less. These bars were then poled at 15 kV/cm for ten minutes at 100°C in a stirred silicone oil bath. All resonance measurements were made using an HP 4192A Impedance Analyzer.

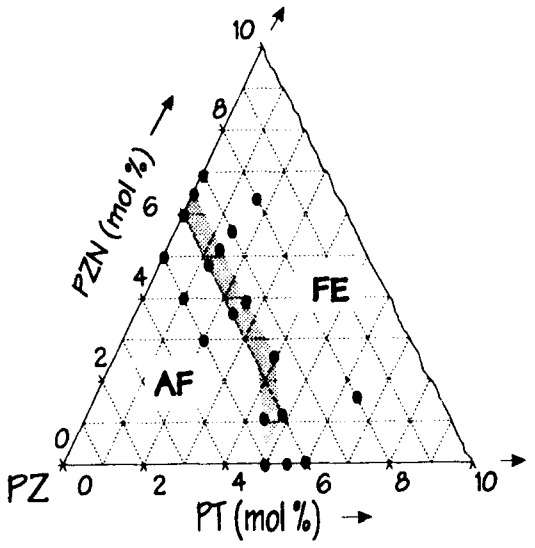


Figure 2: Room Temperature PZNT phase diagram.

The calculation of the real and complex compliance, s_{11}, piezoelectric coefficient, d_{31}, dielectric constant, ε_{33}, and coupling coefficient, k_{31} was made using the equation for the admittance of a bar resonator (1).

$$Y = \frac{j\omega l w}{t}\left(\varepsilon_{33}^{T} - \frac{d_{31}^{2}}{s_{11}^{E}}\right) + \frac{j\,2wd_{31}^{2}}{(\rho s_{11}^{E})^{\frac{1}{2}} s_{11}^{E} t}\tan\frac{1}{2}\omega l\,(\rho s_{11}^{E})^{\frac{1}{2}} \qquad (1)$$

where:

w = width, ρ = density, t = thickness,
ω = frequency and l = length

Since this equation is for an ideal resonator the piezoelectric coefficients are assumed to be complex quantities i.e.:

$$s_{11} = s'_{11} + j\,s''_{11} \qquad (2)$$
$$d_{31} = d'_{33} + j\,d''_{31} \qquad (3)$$
$$\varepsilon_{33} = \varepsilon'_{33} + j\,\varepsilon''_{33} \qquad (4)$$

The complex admittance equation is then solved by the method described by Smits and latter by Damjanovic. This method involves an iterative calculation using an initial guess of the elastic constant and three values of the admittance near resonance.

RESULTS

(1) Hysteresis:

A summary of hysteresis data can be found in figure 3, this shows the room temperature AF - FE transition occurs between compositions (93.2/0) and (92/0). It also shows that the remanent polarization increases with increasing mol% PT, for example the net remanent polarization increases from 0 to 30 to 38 $\mu C/cm^2$ as the composition of PT is increased in the series (93.5/0), (93.5/2.6) to (93.5/3.9). Low coercive fields on the order of 10 kV/cm have also been found in all the compositions measured. It is also interesting to note that increasing the concentration of PZN enhances the "squareness" of the Hysteresis loop (not shown here) which may have several device applications.

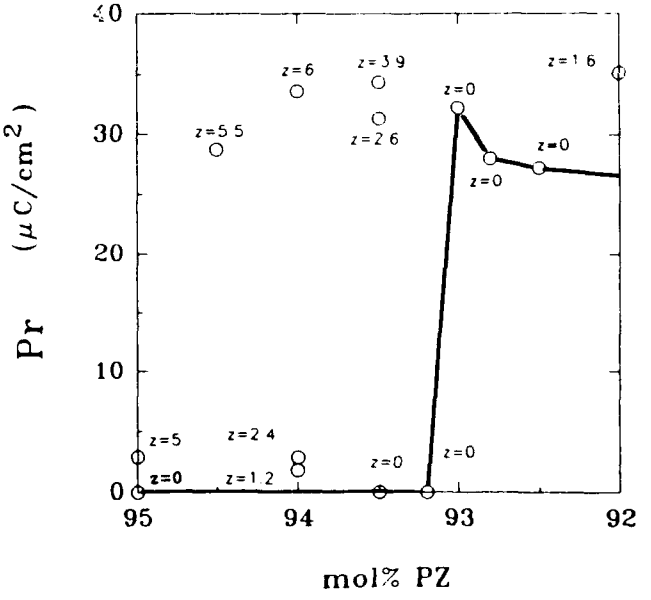


Figure 3: Room temperature remnant polarizaton data plotted versus mol% PZ. The line indicates the room temperature antiferroelectric to ferroelectric phase boundary. (z=mol% PT)

(2) Dielectric Study:

Figure 5 shows the average maximum dielectric constant at the Curie temperature (T_c) from heating and cooling cycles as a function of mol% PZ. Maximum dielectric constant decreases as the concentration of PZN is increased. Also, as expected, increasing the concentration of PT increases the maximum dielectric constant at T_c. The variation in T_c with mol% PZ can be seen in figure 4. This, for example, shows an increase of 10°C between PZNT(93.5/2.6) and PZNT (93.5/3.9) which is an increase in PT of 1.3 mol%.

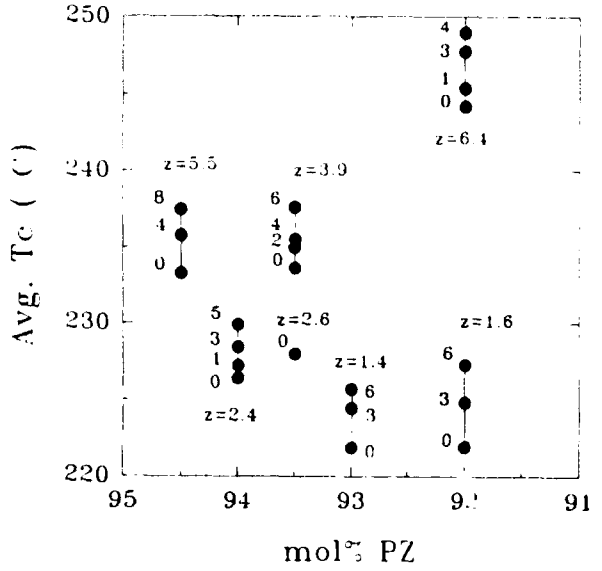


Figure 4: Average T_c at kHz. Superscripts indicate the applied bias in kV/cm. (z=mol%PT)

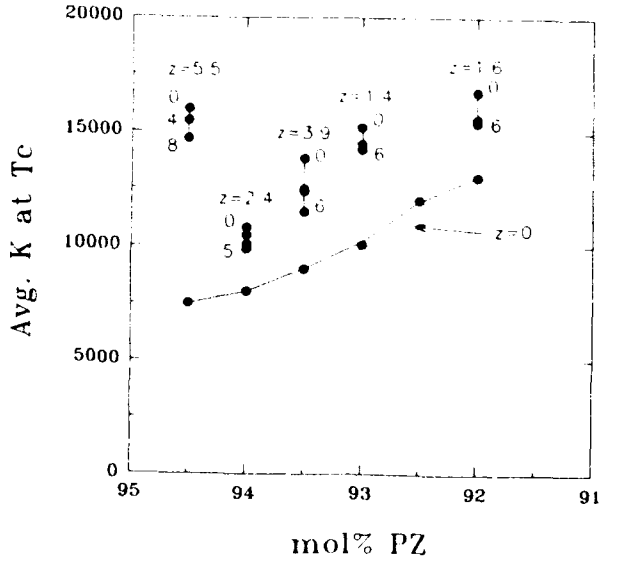


Figure 5: Average maximum dielectric constant at T_c measured a 1 kHz. Superscripts indicate applied bias in kV/cm. (z=mol%PT)

The influence of DC bias is also demonstrated in figures 4 and 5. The average dielectric constant at T_c for PZNT (93.5/2.6) can be seen to increase from 234 at 0 kV/cm to 238 at 6 kV/cm. The bias field also causes a shift in T_c which can be seen in figure 4. This shows the increase in T_c for various compositions in the PZNT as the bias field on each sample is increased.

The dielectric constant has been found to have only a minute dependence on frequency. However, it has a thermal hysteresis when comparing heating and cooling cycles, especially at the lower temperature FE-FE transition (figure 6).

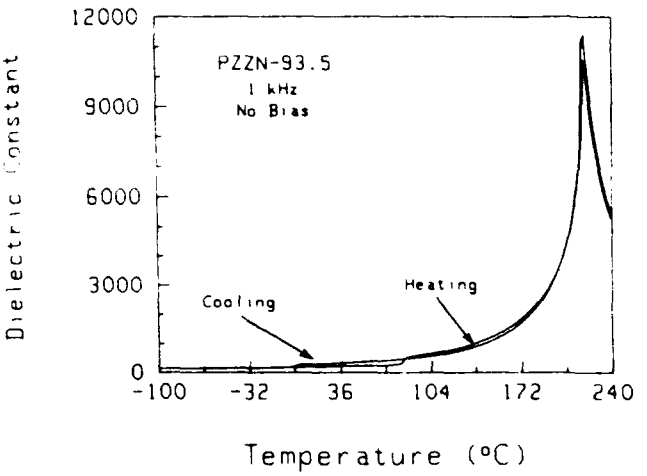


Figure 6: Dielectric constant for PZZN-93.5 measured at 1 kHz with an no applied bias. Note the large thermal hysteresis in the lower temperature AF-FE phase transistion.

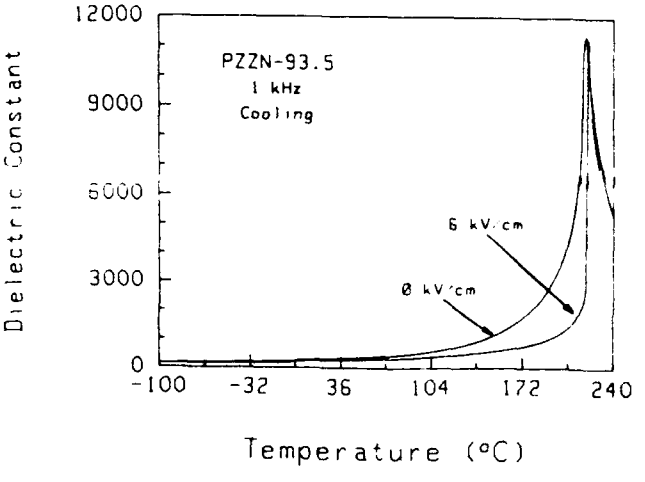


Figure 7: Dielectric constant for PZZN-93.5 measured at 1 kHz with an applied bias of 0 kV/cm and 6 kV/cm.

(3) Piezoelectric Study:

Figures 8 and 9 show the dependence of the room temperature real piezoelectric coefficient, d'_{31}, and elastic coefficient, s'_{11}, on the applied electric field. The zero field d_{33} coefficient was measured using a Berlincourt d_{33} meter and was found to be approximately 50 to 60 pC/N for all samples just after poling. d'_{31} and d''_{31} both show approximately linear behavior even in the room temperature AF compositions. This could be due to a field forced AF-FE transition during the poling process, which was conduced at ~100°C with 15 kV/cm applied for 10 minutes then cooled, with the field still applied, to 25°C. It is interesting to compare figure 4 and figure 8. PZZN(93.5) when poled at room temperature is not FE, as indicated in figure 4. However, when poled at 100°C (figure 8) the sample is FE. This seems to be clear evidence that the FE phase is metastable at room temperature in the antiferroelectric compositions.

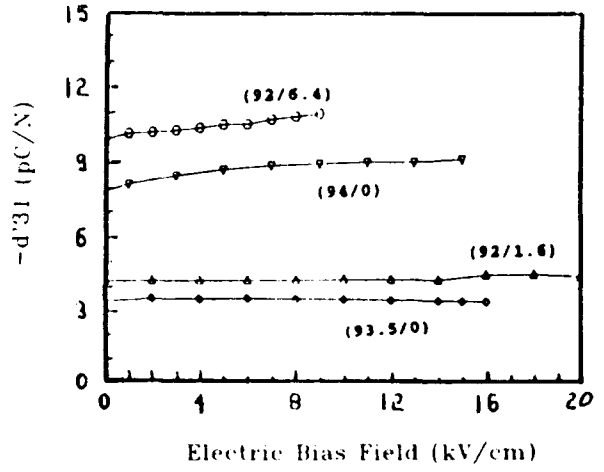


Figure 8: Real piezoelectric coefficient, d'_{31}, as a function of electrical bias field for various PZNT compositions. (All samples poled at 100°C.)

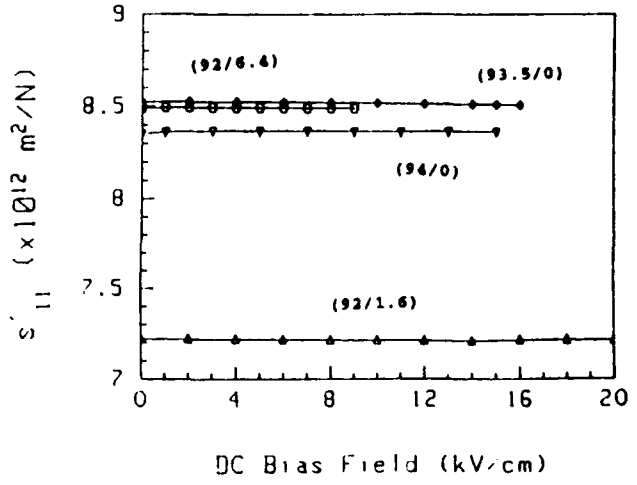


Figure 9: Real elastic coefficient, s'_{11}, as a function of electrical bias field for various PZNT compositions.

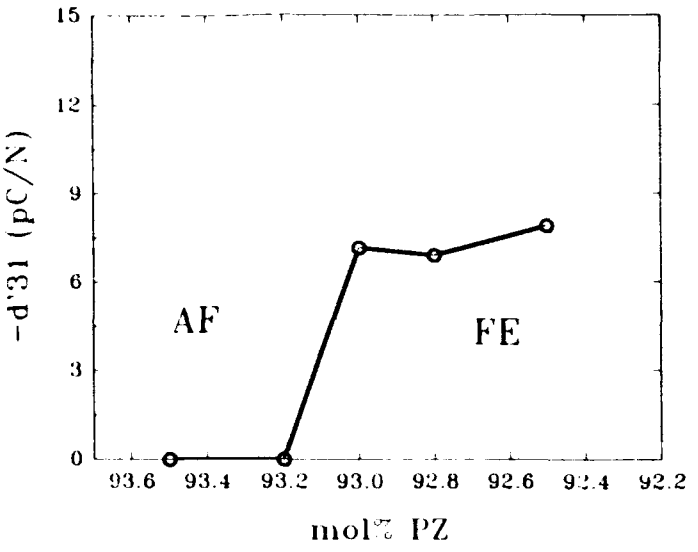


Figure 10: Real piezoelectric coefficient, d'_{31}, as a function of mol% PZ. This indicates the room temperature AF-FE phase boundary is between x=93.0% and x= 93.2% PZ.

To determine the position of the AF-FE boundary above room temperature the samples were thermally depoled and then poled various temperatures. After the samples were poled their resonant behavior was observed, if none was found the process was repeated at a slightly higher temperature. By this method the AF-FE boundary was located.

The coupling coefficient k_{31} shows a slight increase for the compositions studied. The response is still, however, quite linear with values between 2% and 8%. Dielectric and piezoelectric loss were found to be between 2% and 10%. Mechanical loss was independent of field with a value of 0.3% to 0.5%.

Measurements were completed on PZZN compositions of x = 92.5, 92.8, 93.0, 93.2, and 93.5 mol% PZ. From a combination of these data the phase diagram of the PZZN system has been refined. This diagram (figure 11) pinpoints the AF-FE phase transition at room temperature to be between PZZN(93.2) and PZZN(93.0). The paraelectric and ferroelectric low to high temperature phase transition temperature data was obtained from dielectric anomalies and averaged between heating and cooling cycles of 5°C/min. Resonance and hysteresis data was then used to determine the AF-FE boundary.

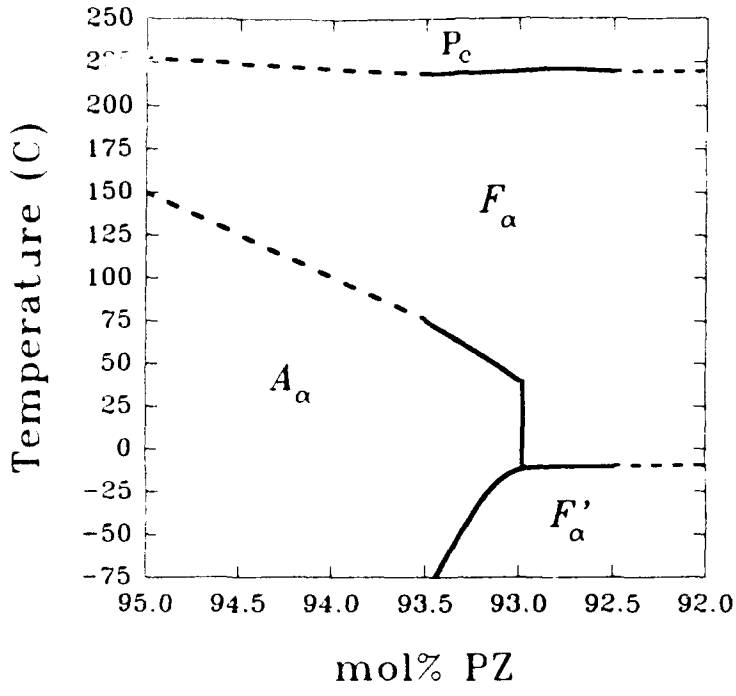


Figure 11: Experimentally determined PZZN phase diagram.

CONCLUSIONS

Various compositions in the PZNT system have been studied to find their weak field piezoelectric and dielectric response at room temperature. Some of the conclusions that have been made are:

(a) Hysteresis results indicate that the location of the AF-FE boundary is between x = 92.8% and x = 93.2% PZ. Large values of P_r (~30 $\mu C/cm^2$) and low values of E_c (~10 kV/cm) for x < 92.8% PZ have been obtained. Also, with decreasing PZ concentrations hysteresis loops become increasingly square in nature.

(b) Room temperature dielectric constants near 250 have been measured and can be altered with suitable compositional adjustments. Large hysteresis in heating and cooling cycles has been displayed, especially in the low to high temperature rhombohedral phase transition. Curie temperatures near 225°C have been found to decrease with both increasing bias field and increasing concentrations of PT.

(c) Piezoelectric coefficient d'_{31} at 25°C was found to be approximately -10 pC/N and linear with electrical bias fields of up to 15 kV/cm. The real elastic coefficient s'_{11} was found to be ~8.5×10^{-10} m^2/N and constant for electric bias fields of up to 20 kV/cm. The piezoelectric coupling coefficient k_{31} was found to be between 2% and 8%.

(d) The PZZN phase diagram has been refined to show the AF-FE boundary at room temperature to be between PZZN(93.2) and PZZN(93.0). Also, after poling at elevated temperature, the ferroelectric phase has been shown to be stable when cooled to room temperature.

REFERENCES

[1] R.E. Newnham, Q.C. Xu, S. Kumar and L.E. Cross, Smart Ceramics from Smart Materials, Structures, and Mathematical Issues, Ed. by C.A. Rogers, Lancaster: Technomic Publishing Co. Inc., 1989.

[2] D.J. Taylor, Ph.D. Thesis, The Pennsylvania State University, 1992.

[3] Takenaka, A.S. Bhalla and L.E. Cross, "Dielectric, Piezoelectric and Pyroelectric Properties of Lead Zirconate-Lead Zinc Niobate Ceramics," J. Am. Ceram. Soc., **72** [6] 1016-23, 1989.

[4] D. Damjanovic, Ph.D. Thesis, The Pennsylvania State University 1987.

[5] E.F. Alberta, D.J. Taylor and A.S. Bhalla, "The DC Field Dependence of the Piezoelectric, Elastic and Dielectric Coefficients of a Lead Zirconate-Based Ceramic," presented at the Amer. Ceram. Soc. 92nd Annual Meeting, Minneapolis, Minn., April 12-16, 1992.

INTERFACES BETWEEN ELECTRODE METALS AND $(Pb,La)(Zr,Ti)O_3$ IN OXIDIZING ATMOSPHERE

S.Sugihara and K.Okazaki
Department of Materials Science and Ceramic Technology
Shonan Institute of Technology, 1-1-25 Tsujido Nishikaigan,
Fujisawa,251, Japan

Abstract

The interfaces between $(Pb,La)(Zr,Ti)O_3$ ceramic and electrode metals such as Ag, Sn, Cu and In were examined by wetting experiments under the atmospheres of air and 100 % oxygen. The wetting experiments were carried out by measurement of a contact angle during rising temperatures. The metals of In and Sn indicated obtuse contact angles every atmosphere. Cu spreaded on PLZT in 100 % and in air resulting in the reaction among Cu,PLZT and quartz plate somehow. Furthermore, the wetting behaviors and the cross sectional interfaces between metals and $(Pb,La)(Zr,Ti)O_3$ were analyzed with an electron probe microanalysis(EPMA) and the bonding mechanisms were discussed as well.

Introduction

The wetting study of an electrode metal with ceramics and their interfaces are important from the view point of an ohmic contact with the electronic packagings, coating materials, brazings and sealings. Especially, In and Sn have been employed as a transparent electrode for $(Pb,La)(Zr,Ti)O_3$ (hereafter, PLZT). The conditions that determine wetting of a molten metal on a solid are not only of basic science but are also of importance in applications described above. Since the oxide ceramic are not generally wetted by metals, a glass is added to a metal to achieve wetting. Many studies have been reported on wettings and reactions in the glass-metal systems.[1),2)] The effects of oxygen on wetting have been reported on the system of Fe-O alloy and alumina substrate by Nakajima et al.,[3)] and the surface tension and the contact angle of liquid iron on the Al_2O_3 substrate were studied over a wide range of oxygen concentration.[4)] Sugihara et al. have studied on the wetting of PLZT in vacuum.[5)] According to the study, Ag showed the tendency of wetting behaviors depending upon a content of Ti in the PLZT. The present work was especially focused on the interfaces and wettings of In and Sn as far as the metal.

Experiment

The wafers of PLZT employed for the wetting experiments were fabricated by Hayashi Chemical Co.Ltd.and their compositions are X=0.095, Y=0.35 in $(Pb_{1-x},La_x)(Zr_{1-y},Ti_y)$. For the comparison, the composition: X=0.12 and Y=0.60 were also used. The size of specimens is 14x14 mm and 0.5 mm in thickness. The surface roughness of the substrate is 0.6 μRa in an average. The electrode metals are Ag,Cu,In and Sn. The purity of every metal was more than 99.9 % and weight was 60-100 mg in a lump. The wetting experiments in the oxidizing atmosphere were carried out in the electric furnace as shown in Fig.1. The atmospheres are air and 100 % O_2 at 10^5 Pa. The system of metal/PLZT is put on the quarts glass plate and the temperature rised up to more than a melting point of each metal. After the wetting experiments, the system was mounted into the resin,then cut for

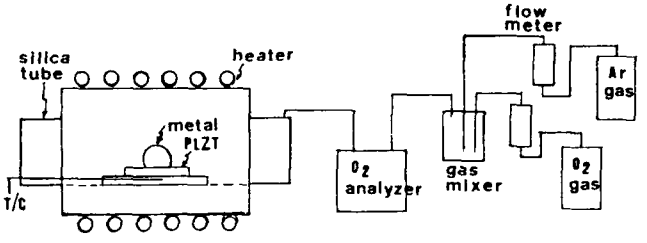


Fig.1 The equipment of wetting study

taking photographs with an optical microscope in order to measure the contact angles, and the cross sectional interfaces of the system were analyzed with a SEM and an EPMA.

Results and discussion

Wetting behaviors

Figure 2 shows the photographs of an opical

CH3080-0-7803-0465-9/92$3.00 ©IEEE

microscope with the vertical cross section for the wetting behaviors for In and Sn on PLZT (9.5/65/35) in 100 % O_2. In started to melt at 158°C (melting point:156.5°C) and showed the contact angles of 147°at 200°C, and Sn started to melt at 250°C (melting point:232°C) resulting in the contact angle of 141° at 280°C. The contact angle for the system of In/PLZT (9.5/65/35) was not much different from the system of In/PLZT (7/65/35) in vacuum indicating the angle of 142°at the same temperature. Sn/PLZT (7/65 /35) in vacuum showed almost the same contact angle of 142°[5] as in the case of 100 % O_2 described above. Figure 3 shows the wetting behaviors for In and Sn on PLZT in air The contact angles for In and Sn were 122° and 141°, respectively.

Generally, wetting property will be affected by the formation of the oxide not only at the surface but also at the interfaces between a molten metal and a solid. The free energy change of formation for an oxidation reaction (1) is presented by the equation (2),

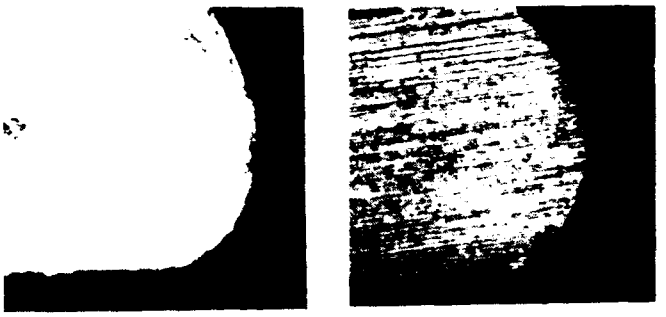
$$2\ In + 3/2\ O_2 = In_2O_3 \qquad (1)$$

$$\Delta G = \Delta G^0 + RT \ln (\alpha [In_2O_3]/[In]^2[O_2]^{3/2}) \qquad (2)$$

In the equation(1), ΔG in the case of 100 % O_2 ambience will be lower than that of air leading to advance oxidation reaction, hence the metal surfaces and the interfaces are covered by the oxides of In resulting in less wettability. This will be also elucidated by the chemical potential at the interfaces between a molten metal and a solid. Providing C is a concentration of In at the interfaces, chemical potential is described by the following equation,

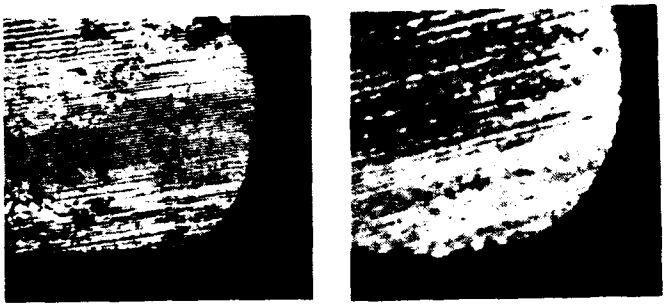
$$\mu = \mu_0 + RT \ln C \qquad (3)$$

If the oxide films of In cover on the surfaces of the metal including the interfaces, the concentration, C will be decreased at the interfaces, then the chemical potential will be decreased leading to less wettability. As described above, Sn showed the same contact angles(141°) in both cases of 100 % oxygen and air. This is suggested that the oxidation potential



In/PLZT(9.5/65/35) Sn/PLZT(9.5/65/35)

Fig.2 Optical microscope photographs after wettings for the systems of In/PLZT(9.5/65/35) and Sn/PLZT(9.5/65/35) in 100 % O_2.



In/PLZT(9.5/65/35) Sn/PLZT(9.5/65/35)

Fig.3 Optical microscope photographs after wettings for the systems of In/PLZT(9.5/65/35) and Sn/PLZT(9.5/65/35) in air.

of Sn is lower than that of In leading to an easier oxidation of Sn even in air as shown in the equation of the free energy change of oxide formation (4) for the chemical reaction (5). Then the oxide covered the metal resulting in the obtuse contact angles.

$$\Delta G = \Delta G^0 + RT \ln (\alpha [SnO]/[Sn][O_2]^{1/2}) \qquad (4)$$

$$Sn + 1/2\ O_2 = SnO \qquad (5)$$



Fig.4 Optical microscope photograph after wetting for the system of In/PLZT(12/40/60) in 100 % O_2.

The system of Cu/PLZT started to melt 1006°C that is lower than the melting point(1083°C), then Cu spreaded on PLZT at the temperature of 1064°C in 100 % O_2, and melting start was 1002 °C, then spreading occurred at 1050°C in air. The causes of spreading were not clear in this moment. As far as In/PLZT(12/40/60), the contact angle was 132° at 200°C, showing the lowest one as compared with the case of PLZT(9.5/65/35) as indicated in Fig.4. The wetting



Ag/PLZT(7/65/35)
Contact angle,115°
at 990°C.



PLZT(9.5/65/35)
Contact angle,113°
at 988°C.



PLZT(12/40/60)
Contact angle,98°
at 988°C.

Fig.5 Changes of contact angles of Ag on PLZT with deifferent compositions in vacuum.

of the system of Ag/PLZT in vacuum were also studied for three kinds of composition of PLZT. The results are shown in Fig.5. The PLZT(12/ 40/60) that is the larger content of Ti showed the least contact angle of 98°. The functions of Ti has been estimated by the oxidation-reduction (redox reaction) at the interfaces: Ag is easily oxidized by the changes of $Ti^{3+} \rightleftarrows Ti^{4+}$, but Ag_2O is decomposed promptly.[6] The oxide formation of metal on the surface of the metal (including interfaces between metal and ceramics) is relating to wettability of the ceramics and metal.

Interfaces between ceramics and metal

The wetting study on $BaTiO_3$+glass-added Ag revealed the diffusion of Ti at the interfaces between $BaTiO_3$ and glass.[6] Furthermore, the diffusions of Ti and Zr into the glass layer were found in the wetting study of Pb(Zr, Ti)O_3 + glass/Ag.[7] From the facts, Ti and/or Zr play an important role for bonding of ceramics with an electrode metal. Figure 6 shows the interfaces between Ag and PLZT(12/40/60). The upper one was analyzed by scanning for Ag and the lower one indicated the result scanned for Pb. Neither migration of an element with metal/PLZT nor reaction layer was found at the interfaces, and Ag was bonded with PLZT without diffusions or reactions. It will be interesting to investigate which atoms in PLZT form

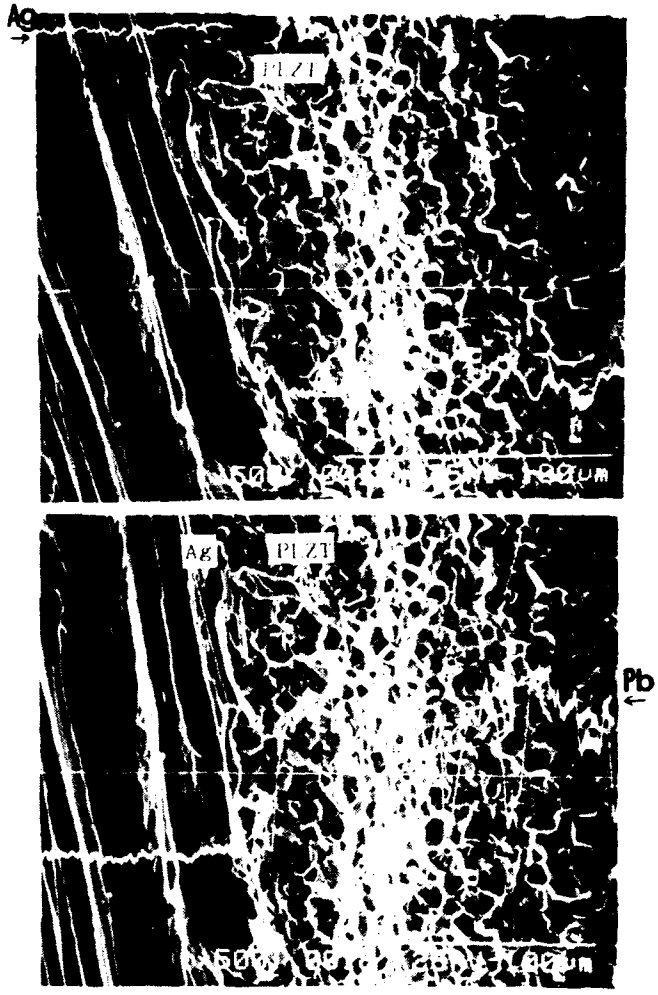


Fig.6 SEM photographs for interface analysises after wetting experiment of Ag/PLZT (12/40/60) systems.
Upper:scanned with Ag, Lower:with Pb.

the bondings with Ag in atomic level. Figure 7 shows the SEM photograph for the interfaces between In and PLZT(9.5/65/35). In did not seem to be bonded with PLZT from the fact that In came off PLZT easily, and the interfaces had fine cracks. Figure 8 shows the interfaces between In and PLZT(9.5/65/35) analyzed with an EPMA. According to this, any elements in

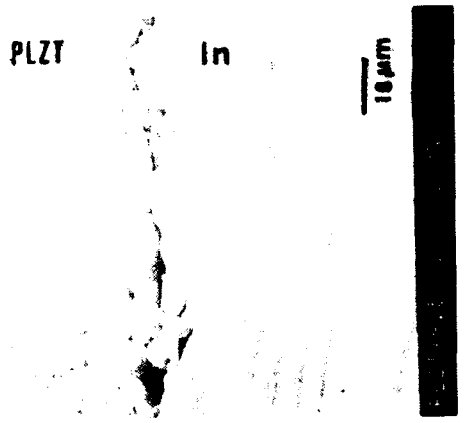


Fig.7 SEM photograph for the interfaces of In/PLZT(9.5/65/35) after wetting experiment in 100 $\%O_2$.

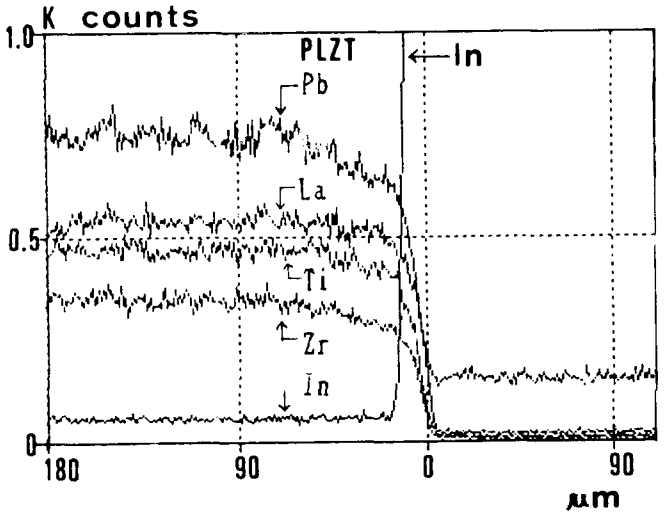


Fig.8 EPMA result for the interfaces of In/PLZT(9.5/65/35) after wetting experiment in 100 $\%O_2$.

PLZT did not diffuse into In, and also In did not seem to react with any elements in PLZT. However, In can form alloys such as, In-Pb and In-Ti as known in a metallurgical phase diagram. Therefore, the interface should be more precisely investigated with transmission electron microscope(TEM).

Conclusion

The interfaces between transparent ceramics, $(Pb,La)(Zr,Ti)O_3$ and electrode metals:Ag,Cu,In and Sn were studied from the view point of wetting properties in an oxidizing atmospheres. The conclusions are as follows;

1)All the metals did not wet on PLZT. In showed less contact angle of 122 in an air than in 100 % O_2 (141°) whereas there were no differences with the contact angles for Sn/PLZT in both atmospheres.

2)Ag indicated dependence of the contact angle on the compositions of $(Pb_{1-x},La_x)(Zr_{1-y},Ti_y)$:PLZT(12/40/60) that contains larger amount of Ti showed the least angle,98°.

3)No EPMA results revealed diffusions or migrations of any elements from metal to PLZT or vis-a-vis. The definite reactions were not found from the analysis of the interfaces except for the Cu/PLZT system.

4)As the next step, more precise analysis with a transmission electron microscope should be necessary in order to investigate the interfaces between ceramics and metal. Furthermor, wetting property and it's improvement should be discussed from the interfacial structures and thermodynamical points.

References

1)V.K.Nagesh,A.P.Tomsia and J.A.Pask, "Wetting and reactions in the lead borosilicate glass -precious metal systems,"J.Mater.Sci.,18,2173 -2180(1983).

2)A.P.Tomsia and J.A.Pask,"Chemical reactions and adherence at glass/metal interfaces: an analysis,"Dent Mater,2,10-16(1986).

3)K.Nakajima,K.Takihira,K.Mori and N.Shinozaki "Wettability of Al2O3 substrateby liquid iron -Effects of Oxygen in liquid iron and purity of Al2O3 substrate." J.Japan Inst. Metals, 55 [11]1199-1206(1991).

4)N.Takiuchi,T.Taniguchi,N.Shinozaki and K.Mukai,"Effects of oxygen on the surface tension of liquid iron and the wettability of aluminum by liquid iron."J.Japan Inst.Metals, 55[1]44-49(1991).

5)S.Sugihara and K.Okazaki, "Interfaces and Wetting Properties between PLZT ceramics and Electrode metals."J.Ceram.Soc.,Japan,in press

6)S.Sugihara and K.Okazaki,"Wetting of ceramic -metal and ceramic-ceramic interfaces." Proc. 1990 IEEE 7th International Symp. on Applications of Ferroelectrics,(1990)pp.432-434.

7)S.Sugihara and K.Okazaki, " Ceramic-Metal-Glass Bonding."Proc.1990 IEEE 7th Internat'l Symp.on Appl.of Ferroelectrics,(1990)pp. 429-431.

THE ELECTROSTRICTIVE AND RELATED PROPERTIES OF $(Pb_{1-x}Ba_x)_{1-3z/2}Bi_z(Zr_{1-y}Ti_y)O_3$ CERAMIC SYSTEM

G. Li and G. Haertling
Department of Ceramic Engineering
Clemson University
Clemson, SC 29634

ABSTRACT

A compositional region was revealed in the $(Pb_{1-x}Ba_x)_{1-3z/2}Bi_z(Zr_{1-y}Ti_y)O_3$ ceramic system where large electrostrictive strains and small hysteresis exist simultaneously. The electrostrictive coefficients, m_{11} (longitudinal) and m_{12} (lateral), are as high as 8.9 and 3.85 $x10^{-16}$ m^2/V^2, respectively, and hysteresis small enough to be negligible depending on the composition involved. It was found that a small amount of Bi_2O_3 additive significantly modified the electrostrictive and dielectric properties of the pure PBZT ceramic system as well as shifting both the F_R–F_T and F_R–P_C boundaries. Hot pressed samples showed higher saturated strains and smaller hysteresis compared with those fabricated by conventional sintering.

INTRODUCTION

In recent years much attention has been paid to ceramic materials with large electrostrictive effects. Electrostriction, which exists in all materials, exhibits many potential applications in electronic and optically controlled system as well as precision machinery. Among the materials available, however, few possess electrostrictive effects large enough to be of practical usefulness. The development of new materials with high electrostrictive coefficients has been a major impetus of much of the research in this area. The $(Pb_{1-x}Ba_x)_{1-3z/2}Bi_z(Zr_{1-y}Ti_y)O_3$ ceramic system appears to be a very promising candidate because the electrostrictive effects of PBZT 27/70/30 (Ba/Zr/Ti) in the system are among the largest discovered today [1].

The main objective of this paper was to investigate the electrostrictive and related properties of the $(Pb_{1-x}Ba_x)_{1-3z/2}Bi_z(Zr_{1-y}Ti_y)O_3$ (PBZT) ceramic system with $0.25 \leq x \leq 0.43$, $0.28 \leq y \leq 0.53$ and $0 \leq z \leq 0.02$. The preparation of samples is described, and measurement results are presented. The characteristics of the PBZT phase diagram on the basis of the results are also provided.

SAMPLE PREPARATION

The compositions of PBZT ceramics chosen to be investigated in this paper are situated along two lines in the $PbZrO_3$–$PbTiO_3$–$BaZrO_3$–$BaTiO_3$ phase diagram which is depicted in Figure 1; i.e., the vertical line along which the Pb/Ba ratio is changed while Zr/Ti is kept constant, and the horizontal line where Pb/Ba is constant and Zr/Ti changed. The two lines intersect at the composition 27/70/30.

All the PBZT samples were prepared via a conventional mixed-oxide method. Reagent grade PbO, ZrO_2, TiO_2, $BaCO_3$ and Bi_2O_3 additive were used as starting raw materials. Weighed components were first wet mixed for 30 minutes, and then calcined at 925 °C for two hours. The calcined powder was milled for 6 hours in distilled water using Al_2O_3 balls. Sample pellets were obtained by pressing the milled powder into plates of about 30x30x4 mm at a pressure of 49 MPa (7000 psi). The samples were sintered at 1250–1280 °C for 4 hours in a closed alumina crucible with a flowing oxygen atmosphere. To avoid the loss of PbO from samples during sintering, a PbO-rich atmosphere was maintained by placing an equalmolar mixture of PbO and ZrO_2 in the crucible. Sintered samples were then lapped to a dimension of 10x10x0.76 mm. The opposite sides of the lapped samples were electroded with electroless nickel.

Some PBZT samples were also fabricated by a hot-pressing technique at a temperature of 1200 °C for 4 hours at a pressure of 14 MPa (2000 psi).

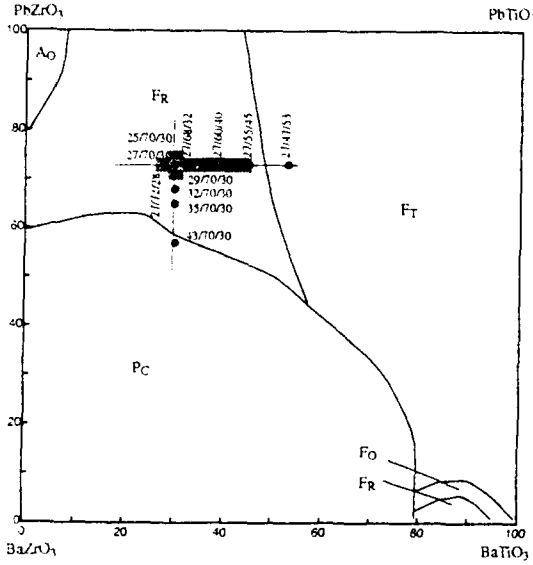


Figure 1. Room temperature phase diagram for the system $PbZrO_3$–$PbTiO_3$–$BaZrO_3$–$BaTiO_3$ (PBZT), where F_R denotes rhombohedral phase, F_T tetragonal phase and P_C paraelectric phase [2].

Table 1. Properties of $(Pb_{1-x}Ba_x)_{1-3z/2}Bi_z(Zr_{1-y}Ti_y)O_3$ ceramics.

z=0.02

Ba/Zr/Ti	Dielectric constant	Loss factor (%)	Density (g/cm^3)	P_{10} ($\mu C/cm^2$)	$S_{1,10}$ x 10^4	$S_{2,10}$ x 10^4	Electrostrictive Coeff.* m_{11}	m_{12}
25/70/30	5830	9.5	7.28	25.6	11.2	4.47	--	--
26/70/30	6110	9.7	7.22	21.4	--	3.46	--	3.85
27/70/30	6400	10.0	7.19	18.0	8.0	3.10	8.5	3.25
29/70/30	7680	12.8	7.07	11.3	2.9	1.20	3.7	1.35
32/70/30	7790	6.6	7.05	9.1	--	0.65	--	0.75
35/70/30	6230	2.3	6.99	6.8	--	0.33	--	--
43/70/30	5940	2.0	6.94	5.3	--	0.33	--	--
27/72/28	6480	10.1	7.18	16.5	8.5	2.57	8.9	3.25
27/68/32	7450	11.1	7.19	16.5	--	2.47	--	2.75
27/64/36	6090	10.8	7.26	18.0	--	2.73	--	--
27/60/40	5230	8.4	7.30	21.5	--	3.75	--	--
27/60/40	5140	8.0	7.36	24.2	--	5.67	--	--
27/55/45	4760	7.8	7.34	24.1	12.5	5.67	--	--
27/47/53	2250	4.0	7.36	--	--	--	--	--

Hot-pressing

26/70/30	6370	9.4	7.49	19.3	--	3.13	--	3.75

z=0.00

27/70/30	3670	5.4	6.88	16.2	--	2.67	--	--
27/60/40	4270	5.4	6.92	21.0	--	3.75	--	--
32/70/30	5780	4.8	6.84	8.9	--	0.95	--	--

* $x10^{16}$ (m^2/V^2)

CH3080-0-7803-0465-9/92$3.00 ©IEEE

SAMPLE MEASUREMENTS

The dielectric properties of samples were determined at 1 kHz with an LCR meter (LEADER, LCR-7450-01). The temperature dependence of dielectric constant and loss factor was obtained by placing samples in an environmental chamber in which samples were first cooled down to -20 °C and then measured at a heating rate of 2 -3 °C/min up to 140 °C. The measurement of relationship between polarization (P) and electric field (E) was carried out using conventional hysteresis loop equipment. The Archimedes displacement method with distilled water was employed to evaluate sample density.

A measurement apparatus using an LVDT as a displacement sensor was made to detect the change of strains with electric field. Electroded samples were placed in line with the movable core of the LVDT. Sample electrodes were parallel or perpendicular to the movable core depending on the measurement of lateral or longitudinal strain. An electric field was applied to the samples continuously between negative and positive maxima. The measured results were recorded on a X-Y plotter.

RESULTS AND DISCUSSION

The important data of the PBZT samples of different compositions obtained in this study are illustrated in Table 1. The values of the dielectric constant at room temperature are in the range from 2250 to 7790 depending on the composition of the samples. The dielectric constant of the compositions with constant Zr/Ti experienced a maximum as the barium content increased across the boundary of rhombohedral and cubic phases, which were plotted in Figure 2 (a). If the maximum in dielectric constant signifies a phase boundary, as is often the case, the boundary was found to occur at a composition somewhere between 29/70/30 and 32/70/30. Figure 2 (b) shows a similar situation occurring among the compositions with constant Pb/Ba, where the maximum in dielectric constant is taken to be indicative of the rhombohedral and tetragonal phase boundary which is located near the composition 27/68/32.

The temperature dependence of dielectric constant and loss factor for a number of selected PBZT compositions was studied. Results are given in Figure 3. All the compositions shown in the figure were characterized by a diffuse phase transition that is manifested as a corresponding broad maximum in the change of dielectric constant with temperature. The temperatures at the maximum dielectric constants were considered to be the temperatures of transition from the rhombohedral or tetragonal ferroelectric phase to the paraelectric phase. The transition temperature for the compositions with constant Zr/Ti decreased, as expected, with increasing barium content.

The relationships between polarization and electric field for the representative samples with constant Zr/Ti are demonstrated in Figure 4. A slim-loop characteristic was found for these samples. Hysteresis became narrow with increasing barium content. At the same time, P_{10} (the polarization at an electric field of 10 kV/cm) decreased monotonically, as shown in Table 1. Nearly linear P-E relationships with negligible hysteresis were obtained at the compositions having barium concentrations larger than 32 mol% indicating that the samples were in the paraelectric cubic phase region. As also clearly illustrated by the P-E curves in Figure 4, the characteristics of the samples with constant Pb/Ba ratio changed from slim-loop phase to tetragonal phase as Zr/Ti ratio decreased. In most cases, polarization became saturated at an electric field around 10 kV/cm.

Both longitudinal and lateral field-induced strains were investigated, however, the curves of lateral strains vs. electric field for selected PBZT compositions are presented in Figures 5. $S_{1,10}$ and $S_{2,10}$ (the magnitudes of longitudinal and lateral strains, respectively, at an electric field strength of 10 kV/cm) were evaluated, and are listed in Table 1. It was found that most compositions exhibited a quadratic strain-electric field relationship with small hysteresis, which is typical of electrostrictive materials. The strains appeared saturated at high electric field due to the saturation of polarization. The butterfly-like S-E curve at the composition 27/47/53 was generated from the tetragonal ferroelectric phase. For the compositions whose strain-electric field hysteresis was small, the strains were plotted against the square of the electric field. The electrostrictive coefficients, m_{11} (longitudinal) and m_{12} (lateral), were then calculated according to the linear part of the S vs. E^2 curves and are displayed in Table 1. The longitudinal electrostrictive coefficients were found to be between 2-3 times as large as the lateral. As seen in Figure 6, the PBZT samples fabricated by hot-pressing showed larger saturated strains and

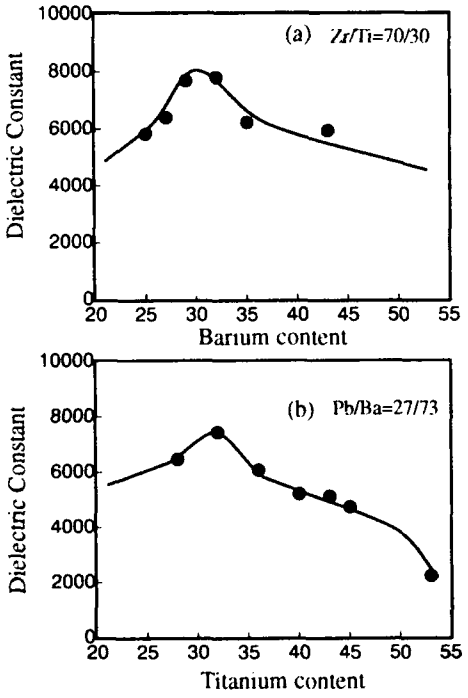


Figure 2. Variation of dielectric constant with PBZT composition.

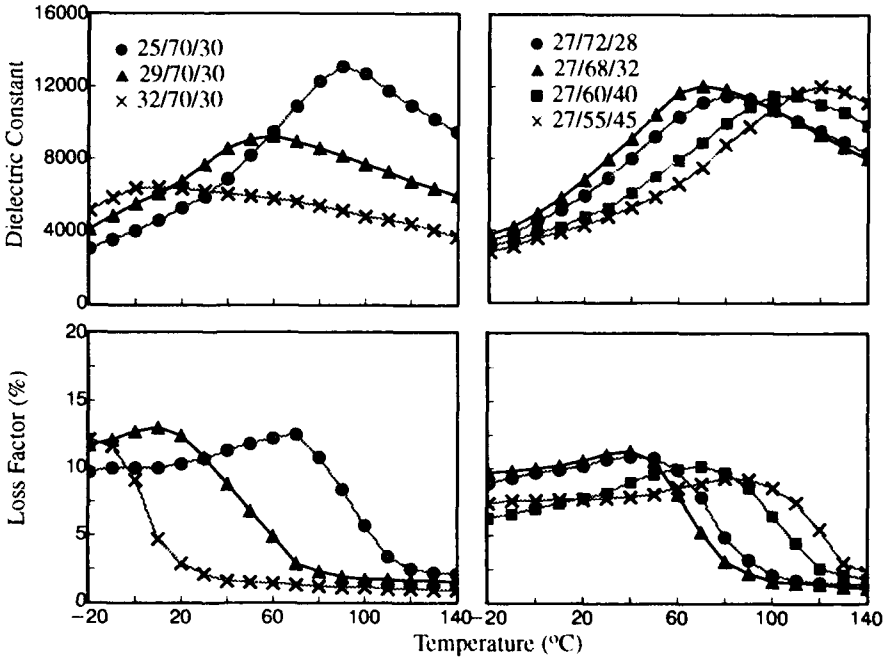


Figure 3. Temperature dependence of dielectric constant and loss factor for the PBZT compositions with constant Zr/Ti (left) and the compositions with constant Pb/Ba (right).

slightly smaller hysteresis compared with those prepared by normal sintering.

The earliest systematic investigation of the pure $PbZrO_3$–$PbTiO_3$–$BaZrO_3$–$BaTiO_3$ system was preformed by Ikeda [2]. The phase diagram shown in Figure 1 was extracted from Ikeda's publication. A significant difference was found between the boundaries for both F_R–F_T and F_R–P_C as given by Ikeda and those based on our results (the composition with a maximum dielectric constant). A reason for this difference is believed to be due to the small amount of dopant (2 atom% Bi_2O_3) added to the pure PBZT system in our investiga-

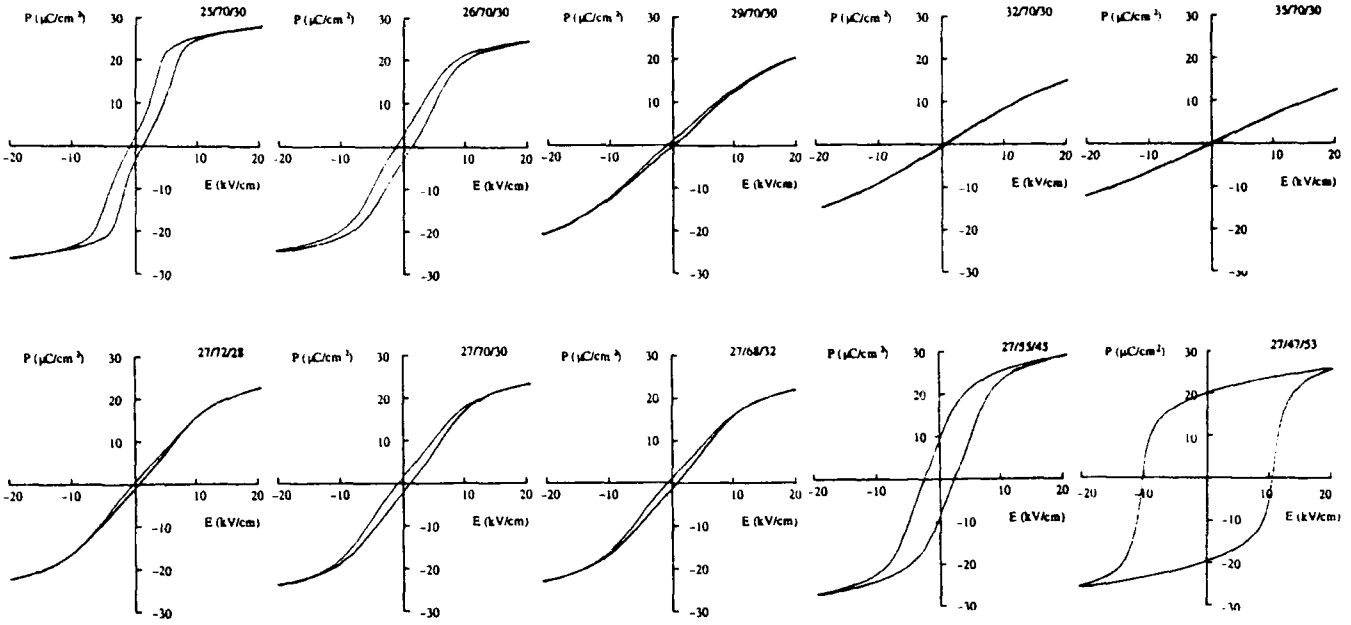


Figure 4. Relationship between polarization and electric field for the PBZT ceramics with constant Zr/Ti ratio (above) and those with constant Pb/Ba ratio (below).

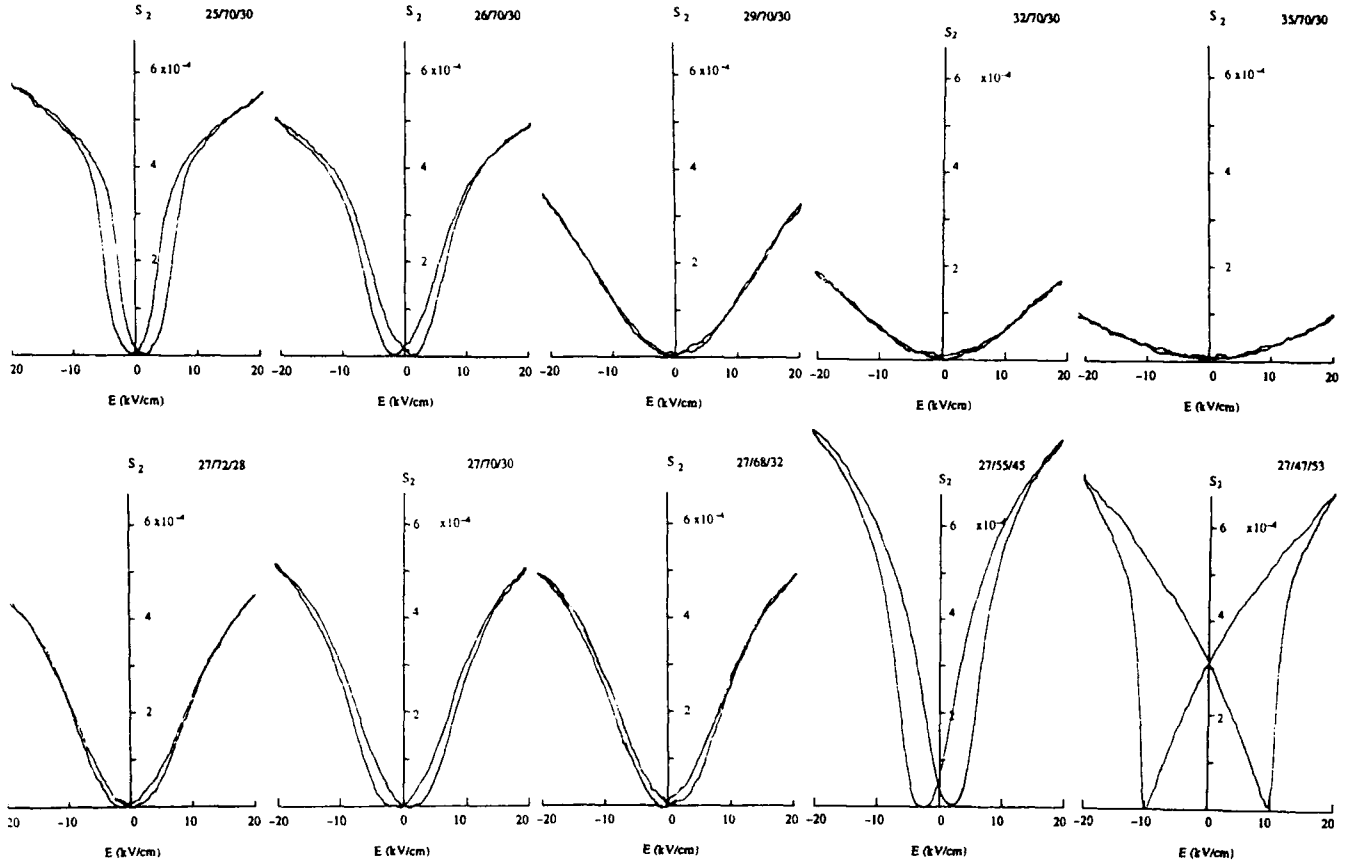


Figure 5. Variation of lateral strain with electric field for the PBZT ceramics with constant Zr/Ti ratio (above) and those with constant Pb/Ba ratio (below).

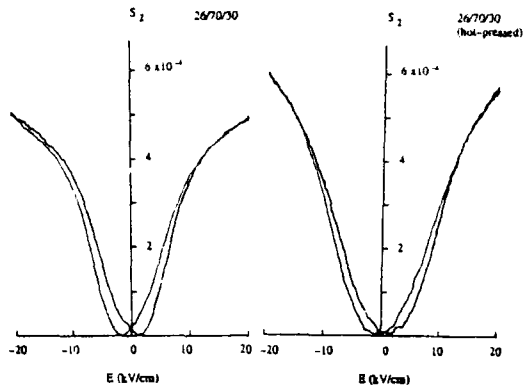


Figure 6. Comparison of the electrostrictive properties of hot-pressed and normal sintered PBZT 26/70/30 ceramics.

tion. The influence of the Bi_2O_3 additive on the properties of several PBZT compositions is demonstrated in Table 1 and Figures 7 and 8. It can be seen in the table and the figures that the additive not only shifted the Curie points to lower temperatures and increased sample density but also enhanced dielectric constant and improved electrostrictive properties. In studying electric field induced strains of PBZT ceramics near the F_R and F_T boundary, Hagimura, et. al., [3] also discovered that a few percent additive of other rare earth elements could remarkably change the strain properties. Further investigation is needed for better understanding of the significant effect of additives on the PBZT ceramic properties.

Based on the data obtained in this investigation, it is believed that there exists a region in the PBZT phase diagram where the rhombohedral phase and diffuse relaxor phase coexist, which is approximately indicated by the shadowed area shown in Figure 1. The large strains with moderate hysteresis found in this compositional region could be explained as resulting from the combined consequence of electrostrictive effects and domain wall motion of rhombohedral phase under electric field.

CONCLUSIONS

A compositional region was identified in the Bi_2O_3–doped PBZT phase diagram where large electrostrictive strains and small hysteresis exist simultaneously. The electrostrictive coefficients, m_{11} (longitudinal) and m_{12} (lateral), are as high as 8.9 and 3.85 $x10^{-16}$ m^2/V^2, respectively, and hysteresis small enough to be negligible depending on the compositions involved. The excellent electrostrictive properties in this compositional region is considered as to be due to the combined consequence of electrostrictive effects and ferroelectric domain wall motion. The Bi_2O_3 additive was observed to play a dominant role in improving the properties of pure PBZT ceramics. A small amount of the additive can significantly enhance the electrostrictive and dielectric properties of the PBZT ceramics. In addition, large displacement in the phase boundaries of both the F_R–F_T and F_R–P_C caused by the Bi_2O_3 additive was discovered.

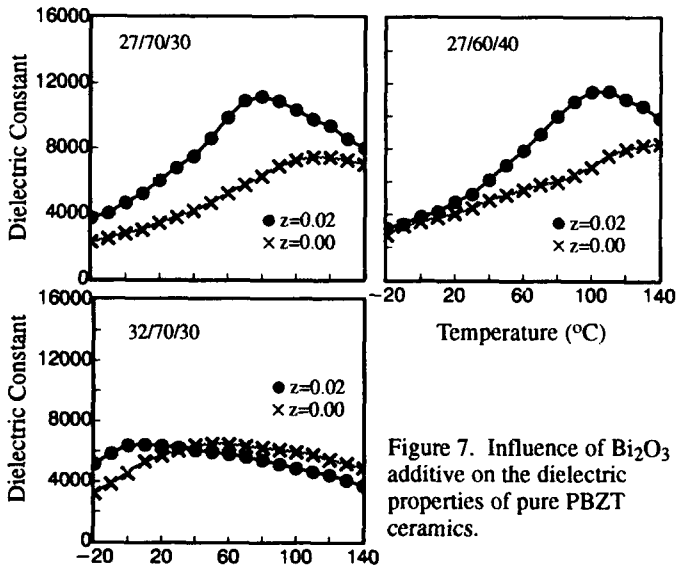


Figure 7. Influence of Bi_2O_3 additive on the dielectric properties of pure PBZT ceramics.

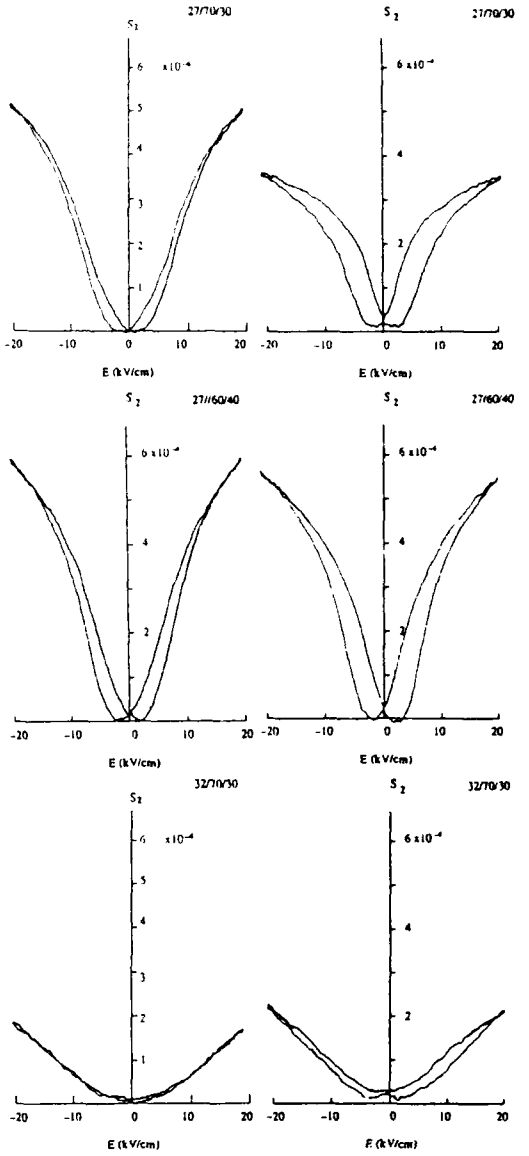


Figure 8. Influence of Bi_2O_3 additive on the electrostrictive properties of pure PBZT ceramics,(left) Bi_2O_3–doped PBZT, (right) pure PBZT.

ACKNOWLEDGMENT

This work was supported by NASA under the contract No. NAG–1–1301.

REFERENCES

[1] K. M. Leung, S. T. Liu and J. Kyonka, Ferroelectrics, vol. 27, pp.41 (1980).

[2] T. Ikeda, J. Phys. Soc. Japan, vol. 14(2), pp. 168 (1959).

[3] A. Hagimura, M. Nakajima, K. Miyata and K. Uchino, IEEE International Symposium on Applications of Ferroelectrics, pp. 185 (1990).

CERAMIC ACTUATOR WITH THREE-DIMENSIONAL ELECTRODE STRUCTURE

Yoshiaki Fuda, Tetsuo Yoshida, and Tomeji Ohno
Tokin Corporation, Tokyo Research Laboratory, Sendai, Japan

Shoko Yoshikawa
Materials Research Laboratory, The Pennsylvania State University
University Park, PA, USA

ABSTRACT

A new type of actuator has been developed by multilayering piezoelectric ceramic green sheets with line electrodes in such a way that electrode lines are parallel and slide one-half a pitch in alternate layers. The large displacements were obtained utilizing multiplication of longitudinal converse piezoelectric effect occurs between nearest electrode lines located a layer below or above.

A long co-fired multilayer actuator with a large displacement can be easily produced, and reliability was improved by eliminating exposure of opposite polarity of electrodes on a same surface of actuator to humidity in the air. For example, a 74mm long actuator with 106 electrode lines on each of 100 layers provided a displacement of 50 μm/350V, with a generative force of 350 kg/cm^2. Also, under the condition of 85°C/90%RH and 180V constant loading, a lifetime of over 1000 hr was demonstrated.

1. INTRODUCTION

With the recent development of electromechanical devices, piezoelectric actuators have been a primary focus of interest owing to their fast response time, large generative forces, high volumetric efficiency, low cost, and relatively simplistic E-field control. Multilayer piezoelectric actuators offer additional performance features such as low driving voltage and large displacements.

In order to avoid delaminations or crack formations, conventional co-fired multilayered actuators which utilize longitudinal piezoelectric effect are limited to a maximum height of approximately 20mm; subsequently, displacement is limited to approximately 15μm. Therefore, when more than 15μm displacement is required, it is necessary to use displacement magnification devices or simply adhere several multilayer actuators in series. The displacement magnification devices, however, often require complicated design. In addition, they also possess the added disadvantage of decreasing the generative force (which is inversely proportional to the displacement). The problems encountered when using the stacked multilayer actuators are inadequate control of total length as well as a loss of response time due to the existence of adhesive layers.

Theoretical analysis and detailed experimental data on piezoelectric resonators with interdigital electrodes on the surface of a rectangular ceramic for both poling and driving purposes are already found in the literatures[1,2]. In addition, we have previously developed torsional actuators by applying interdigital electrode at a 45 degree angle on the outside surface of hollow PZT cylinder[3]. In order to develop a large displacement co-fired actuator, we first investigated the effect of several parameters such as electrode line width, gap, and number of layers on the three dimensional interdigital electrodes (3D-IDE). By optimizing above-mentioned parameters we have developed 74mm long co-fired piezoelectric actuators which provided displacement of a 50μm at 350V.

In addition to the large displacement, the new structure also provides improved reliability by eliminating exposure of internal electrodes on the same surface of actuators to the air as seen in conventional plate-through type actuators. This paper describes the effects of the varying parameters on the three dimensional interdigital electrodes as well as discusses some reliability results in various environments.

2. EXPERIMENTAL PROCEDURES

2-1. SAMPLE PREPARATIONS

Using calcined piezoelectric ceramic powder, $Pb(Ni,Nb)_{0.5}Ti_{0.35}Zr_{0.15}O_3$ (NEPEC-10, TOKIN Corp.), a 70μm thick green sheet was first formed by a slip casting technique. Fine line electrodes were screen-printed on the green sheet using a silver/palladium 70/30 mixture. Two printing patterns were prepared with a half a pitch shift from each other. Table I shows the electrode line width, gap, and number of electrode lines for five different electrode patterns which were tested in the course of this study. The second step was to stack the green sheets 30 to 100 layers thick with alternating half shifts. The stacked multilayers were then heat pressed and fired at 1100°C for two hours in air. External electrodes were applied to the two sides of the fired body where internal electrodes were exposed. After lead wires were soldered onto the actuators, poling was performed by applying a DC voltage at room temperature. A simplified schematic of the procedure is shown in Figure 1. Actual dimensions of each actuator are listed in Table II.

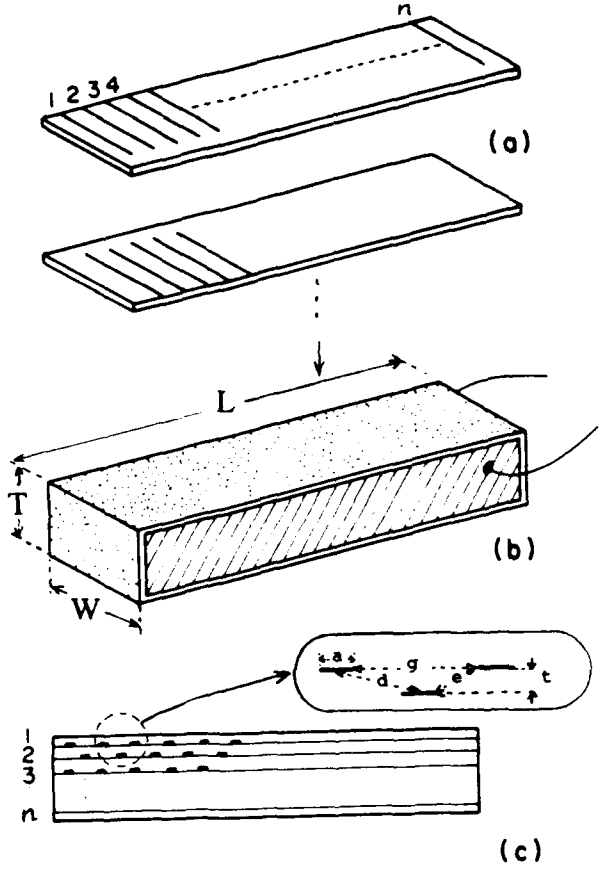


Figure 1. Schematic diagram of 3D-IDE actuators
(a) Green sheets configuration
(b) Fired and electroded sample
(c) Section view of (b)

Table I. Electrode printing pattern in mm

Pattern No.	A	B	C	D	E
Electrode Width (a)	0.15	0.10	0.20	0.15	0.15
Electrode Gap (g)	0.60	0.60	0.60	0.40	0.80
Number of Lines (n)	114	122	106	156	90

Table II. Dimensions of fired actuator in mm

No.	A	B	C	D	E
a	0.13	0.09	0.17	0.13	0.13
g	0.51	0.51	0.51	0.34	0.34
d	0.32	0.30	0.34	0.25	0.41
e	0.05	0.05	0.05	0.05-0.10	0.05-0.10
θ(degree)	8.9	9.5	8.3	11.8-22.6	7.0-13.7
L	74	74	74	74	74
WxT	8x2 for 30 layers, 8x6 for 100 layers				

2-2. DISPLACEMENT AND GENERATIVE FORCE MEASUREMENTS

The voltage induced displacements of each actuator were measured by three different methods: contact (Mitsutoyo micrometer IDA-112M), non-contact (Kienth laser micrometer LD-2500), and strain gage (Minebia SR-4).

Generative force was calculated from the relation between applied uniaxial pressure (using Shimazu compressor) and voltage induced displacement, which was measured using a strain gage. In order to apply a uniform uniaxial pressure to the actuator specimen, a half sphere of zirconia, whose cross sectional area was larger than that of actuator, was placed on top of the actuator.

2-3. RELIABILITY TEST CONDITIONS

Table III lists the reliability test items and their conditions. Samples with electrode pattern C (see Table I) were used for the tests. Conventional plate-through co-fired actuators (size : 5x5x18 mm) with polymer coating were also examined for comparison.

3. RESULTS AND DISCUSSION

3-1. DISPLACEMENTS

Table IV shows the capacitance changes before and after poling for a 30 layer actuator, along with the respective displacement values at 350 V. Each pattern dimension is described in Table II. The actuators were poled at 500V for 30 sec. at room temperature.

Sample #2 whose electrode line width ("a" in Fig. 1) was the smallest value (0.09 mm). Sample #7 whose distance between opposite electrodes was the largest value (0.41 mm) ("d" in Fig. 1), did not function either as a capacitor or an actuator. Also, the comparison between Sample #4 and #5 shows that smaller layer thickness in Fig. 2 gives larger displacements. This indicates that both electric field strength and direction of polarization are important parameters that control the actuator properties. The problem of Sample #2 was analyzed to be a limitation of the conventional screen printing method to form ultrafine uniform lines.

Due to their large capacitance and displacement (see Table IV), electrode patterns C and D were chosen to fabricate 100 layer actuators. Table V shows the data from these samples. Poling was performed at 2.5 kV/mm using the closest distance between opposite electrodes ("e" in Fig. 1). The effective electro-mechanical coupling coefficient, k_{eff}, which was calculated from resonance and antiresonance frequency, are also listed.

The displacement of the piezoelectric ceramic multilayer actuator can be calculated using equation 1.

$$\text{Displacement } \delta = \alpha N d_{33} V \qquad (1)$$

where α is a constant, N is usually the number of layers, but in this case is the number of gaps between the opposite polarity of internal electrodes, d_{33} is piezoelectric strain constant, and V is the applied voltage. Constant α is a correcting coefficient from the weak field d_{33} value to strong field strain constant, and is about 1.5 for conventional plate-through multilayer actuators [4]. In the case of the three dimensional interdigital electrode actuators, N is (2n-1) where n is the number of electrode lines on one layer.

Table III. Reliability Test Conditions

No.	Test Item	Condition
1	Thermal cyclic test	85°C @ 30 min. ↔-25°C @ 30 min. 10 cycle
2	Pulse cycle test	Ambient condition 0-180V, 10Hz
3	DC degradation	
	• Room temp.	25°C/50%RH, 180V constant loading
	• High temp.	85°C, 180V constant loading
	• High temp. & high humidity	85°C/90%RH, 180V constant loading

Table IV. Capacitance and Displacement of Various Actuators

Sample #	1	2	3	4	5	6	7
Pattern #	A	B	C	D		E	
Layer Thickness (mm)	0.05	0.05	0.05	0.05	0.10	0.05	0.10
Cap. Before Poling (nF)	215	---	412	715	416	236	---
Cap. After Poling (nF)	185	---	461	756	403	282	---
Displacement (μm/350V)	20	---	48	50	15	45	---

When calculated using displacement data shown in Table V, α varies between 0.7 and 1.2 which is smaller than the conventional actuator's α at 1.5. This is due to the piezoelectrically inactive areas inside the actuator as well as a non-uniform electric field between the electrodes as expected from the cross-sectioned view in Fig. 1.

3-2. GENERATIVE FORCE

Generative force is defined as a force required to return the voltage induced strain back to its original position while constant voltage is being applied. Figure 2 shows the strain vs. generative force characteristics of two different electrode pattern actuators under an electric drive of 300V. The three dimensional interdigital electrode multilayer actuator with electrode pattern C gave a generative force per unit area of 350 kg/cm^2, which is similar to that of a conventional multilayer configuration actuator using the same piezoelectric ceramic.

The following equation provides generative force of piezoelectric actuator:

$$\text{Stress } P = Y_{33} \frac{\Delta l}{L} \qquad (2)$$

where Y is the elastic constant (5.6 kg/cm^2), Δl is compressive strain (47 μm), and L is the length of the actuator (74 mm). The calculated value was 355 kg/cm^2, which corresponds with experimental data. The elastic constant Y was calculated from resonance frequency at weak electric field as in d_{33} in equation 1. Thus the elastic constant may vary under the application of a large field.

Table V. Capacitance, Displacement, and k_{eff} of 100 Layer-Actuators

Exp.	8	9
Electrode pattern	C	D
Cap. before poling (nF)	1170	1460
Cap. after poling (nF)	1400	1630
Displacement (μm/350V)	55.5	51.4
k_{eff}	0.45	0.31

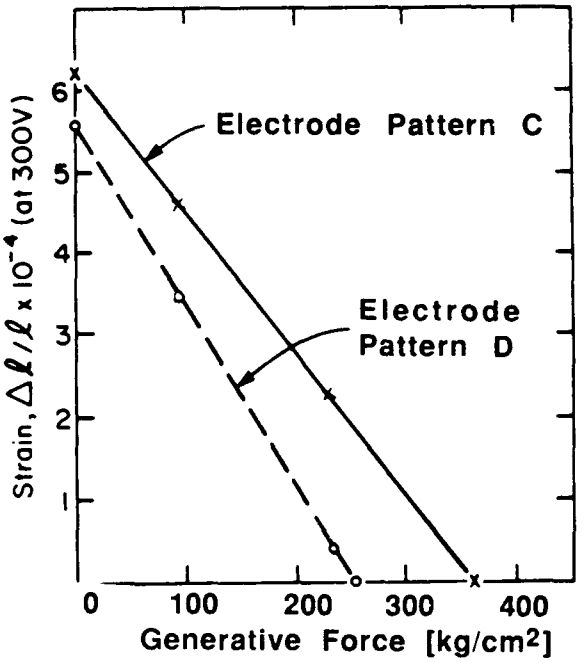


Figure 2. Relationship between generative force and strain of 3D-IDE actuators.

Table VI. Reliability Test Results

No.	Test Items	Results	
		3D-Interdigital MLA[a)]	Conventional MLA
1	Thermal Cycle	OK	OK
2	Pulse Cycle	480 hr. 25% IR[b)] loss	------
3	DC Degradation		
	• Ambient	1000 hr. OK	300 hr. 50% IR loss
	• High temp.	1000 hr. OK	1000 hr. OK
	• High temp. humidity	1000 hr. OK	24 hr. 100% IR loss

a) MLA: multilayer actuator
b) IR: insulation resistance

3-3. Reliability Evaluation

The samples used for reliability tests were the 100-layer actuators with electrode pattern C, which had large displacements and electro-mechanical coupling coefficients. Results of test items listed in Table III are summarized in Table VI. An applied voltage level of 180 V shown in Table III, is equivalent to field strength of 1 kV/mm at the nearest distance "e" in Fig. 1 and is the same as the recommended driving voltage for conventional multilayer actuators.

The 3D-interdigital structure actuator samples tested for reliability did not have any surface treatments such as a polymer coating, so the choice of appropriate coating remains as a future task to perhaps improve reliability further.

Pulse cycle tests of piezoelectric actuators often become self destructive due to the sudden induced tensile and compressive strain. Therefore, all of the pulse cycle tests were performed under constant prestress conditions. With this experimental condition, 25% of the samples tested showed a decrease in IR after 480 hours of testing. Frequency dependence and the degree of prestress are required for further study.

Conventional plate-through type actuators have a weakness in lifetime under humid conditions, and the experiment showed that all of the conventional samples shorted in less than 24 hours in high temperature high humidity conditions. In contrast, the newly designed actuators had a 1000 hour lifetime in the same conditions, proving the improvement of lifetime in high humidity.

4. CONCLUSIONS

1. A long length actuator was developed with a fine line three dimensional electrode structure using longitudinal piezoelectric effect. The displacement direction of this type of actuator is perpendicular to the stacking, unlike a conventional multilayer actuator, in which displacement occurs along the stacking direction.

2. The new structure actuator had a co-fired body length of 74 mm and gave a 50 μm displacement under 350V applied voltage and generative force of 350 kg/cm^2.

3. According to the reliability tests results, the new structure actuators exceeded a 1000 hour lifetime in 85°C/90%RH environment under constant applied field of 1 kV/mm.

ACKNOWLEDGEMENT

One of the authors, Shoko Yoshikawa, would like to thank the Office of Naval Research for its support through Grant No. N00014-92-J-1059.

REFERENCES

1. H. Shimizu, K. Nakamura, S. Oyama, Jpn. J. Appl. Phy. 22, Suppl. 22-2, pp. 163-165 (1983).

2. S. Hirose, T. Yokoyama, H. Shimizu, Jpn. J. Appl. Phy. 22, Suppl. 22-2, pp. 170-172 (1983).

3. Y. Fuda, T. Mashiko, T. Yoshida, JSME the 3rd Electromagnetics Symposium Proceedings, June 12-14, 1991, pp. 154-157.

4. Y. Fuda, M. Murata, Y. Sugita, K. Mitsuhashi, JSME the 24th Symposium Proceedings, July 13-15, 1987, pp. 115-118.

COMPOSITE OF $BaTiO_3$ AND $Pb(Zr,Ti)O_3$ FABRICATED WITH CO_2 LASER

Sunao Sugihara
Department of Materials Science and Ceramic Technology
Shonan Institute of Technology,1-1-25 Tsujido Nishikaigan,
Fujisawa,251,Japan

Abstract

Synthesis of the new composite was carried out by bonding of $Pb(Zr,Ti)O_3$ with $BaTiO_3$ using a CO_2 laser as the preliminary study. $Pb(Zr,Ti)O_3$ was the thick film (0.05 mm in thickness) and $BaTiO_3$ was sintered body fabricated by the conventioal method. The CO_2 laser power was 143 W/cm^2 and the irradiation continued for 50 s. The two starting materials were bonded mutually and $Pb(Zr,Ti)O_3$ was identified with an XRD analysis. The interfaces between two ceramics were discussed with the results electron probe micro analysis (EPMA) and electric properties were referred to as well.

Introduction

Piezoelectric ceramics,$Pb(Zr,Ti)O_3$(hereafter PZT) have been employed for a lot of applications to electronic packagings corresponding to their characteristics as well as $BaTiO_3$ (hereafter BT). And new electronic properties have been achieved by making these ceramics into thin films recently, hence the applications have become wider. In order to make thin film, and coating, laser CVD, PVD,rf-sputtering etc. have been used by many investigators and industries. The purposes of the present study are to bond BT with PZT thick film and to have the composite new electric properties in piezoelectricity and/or ferroelectricity. There could be a variety of combination, such as piezoelectric ceramics/ferroelectric ceramics, piezoelectric/semiconducting, etc. PZT thick films were bonded with BT by CO_2 laser irradiation. After an irradiation, PZT was identified with X-ray diffraction analysis(XRD), and the interfaces between PZT and BT were analyzed with an EPMA and a SEM as well.

Experimental

Fabrication and materials

The BT as a substrate was fabricated by the conventional process; the raw materials of BT (purity 99.9%) and TiO_2(98.5 %) were mixed with a ball-mill for 20 h, then pressed at 1.5 ton/cm^2. The size of a pellet was 10 mm in dia, 0.9 mm in thickness. The sintering was carried out at 1320°C for 1 h after burning out the binders. PZT powder(Hayashi chemical Co. Ltd) was dissolved into an organic solvent with the volume fraction of 50:50 approximately. The mixtures in slurry were blended with a ball-mill for 15 h. The slurry was poured into a doctor blade machine to make PZT thick film (0.05 mm) on a polyethylene film which traveled at the speed of 3.5 mm/s. PZT thick film was dried for a few days in air, and the PZT peeled off a polyethylene film was cut in the size for putting on a BT pellet.

CO_2 laser irradiation

The system of PZT film on a BT was provided for a CO_2 laser irradiation which was shown in Fig.1. The system consists of two parts;

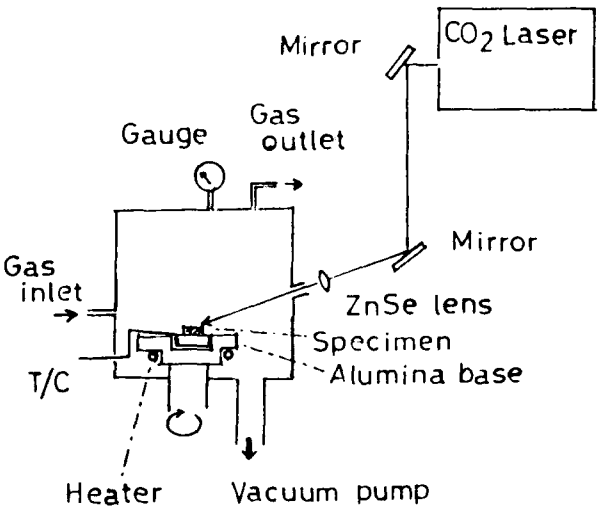


Fig.1 Schematic of a CO_2 laser irradiation system.

CH3080-0-7803-0465-9/92$3.00 ©IEEE

a laser oscillator and a chamber. The focusing distance of CO_2 laser beam (10.6 μmm in wave length) is 38 mm with a continuous mode to give the spot size of 3 mm on the pellet. The chamber was maintained in a mixed gas atmosphere of 20 % O_2 and Ar at 10^5 Pa. The laser power applied to the system was 143 W/cm^2. The specimen holder was heated at 390°C and rotated at 10 rpm. The temperatures were measured by Pt-PtRh(13 %) thermocouples. Figure 2 shows the schematic of specimens both in bulk and thick film of PZT for CO_2 laser/BT irradiation. In the system of bulk PZT, the heat from the laser was absorbed by Al_2O_3 powder and transmitted to PZT by way of Si single crystal plate.

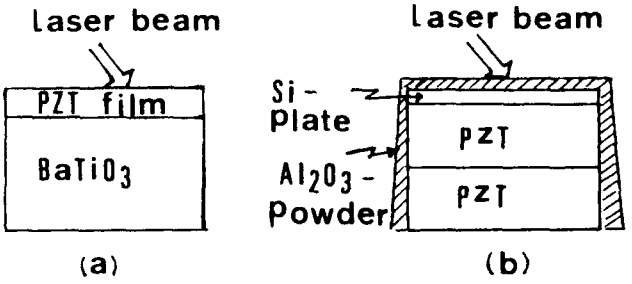


Fig.2 Schematic for specimens with a CO_2 laser irradiaton system.
(a)PZT film/$BaTiO_3$ system
(b)PZT or $BaTiO_3$ system

Results and Discussion

The irradiation with CO_2 laser on a PZT green pellet from PbO, ZrO_2 and TiO_2 powders was reported by Sugihara previously.[1] According to the study, PZT was sintered by the power of 1857 W/cm^2 for 15 min. The XRD analysis revealed the typical PZT patterns as shown in Fig.3. The grain size was 1-2 μm with a large amount of pores, but neckings between grains have developed. The another study for the sintering of BT green pellet using CO_2 laser was reported by Sugihara,[2] which laser power was 1857 W /cm^2. Figure 4 shows the results of the XRD analysis after a CO_2 laser sintering for BT. There are a few studies on the sintering of the oxides, such as ZrO_2-HfO_2 and the ternary system of additioning of Y_2O_3 to the ZrO_2-HfO_2.[3),4)] The CO_2 laser power for the system described above was 2.7 kW/cm^2 that was higher than the sintering of the electronic ceramics. The higher power than 2 kW/cm^2 ,for instances,

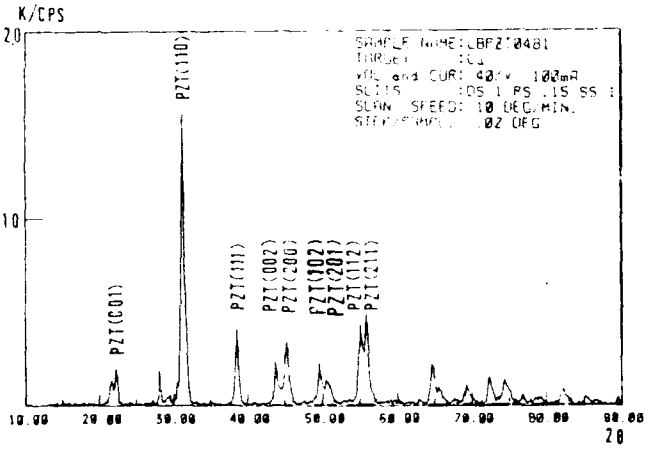


Fig.3 XRD result after CO_2 laser irradiation for PZT bulk (1857 W/cm^2).

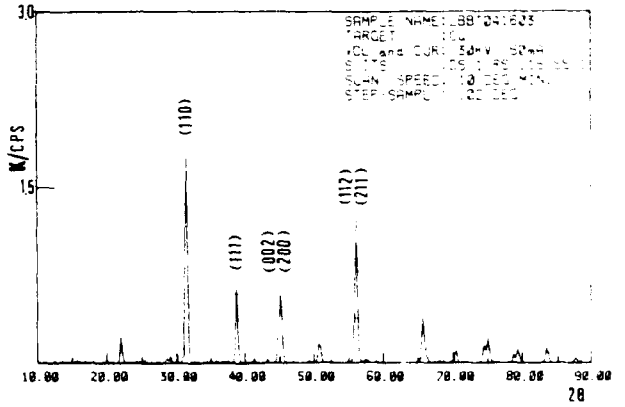


Fig.4 XRD result after CO_2 laser irradiation for BT bulk (1857 W/cm^2).

will make the pellet cracked or broken in the sintering of PZT and BT even though it is covered described in Fig.2. The high powers were not needed for the system of the PZT thick film/BT; that was 143 W/cm^2 for 50 s without any covers for irradiation. After the irradiation, PZT thick film was sintered according to the results of an XRD analysis as shown in Fig.5. The separations of lines on the pattern were not definite as compared with the laser sintering of the PZT bulk at 1857 w/cm^2. The XRD results were similar to the conventional sintering of the system of PZT thick film/BT as shown in Fig.6. Afer CO_2 laser irradiation, the film surface was shown with a scanning electron microscope(SEM) in Fig.7. It revealed the bonding of grains, and pores whereas the developments of necking between particles were much in the CO_2 laser sintering for PZT bulk.[1] It is difficult to achieve the grain growth to 10-20 μm by sintering with a CO_2 laser even at 1857 W/cm^2 for those ceramics in

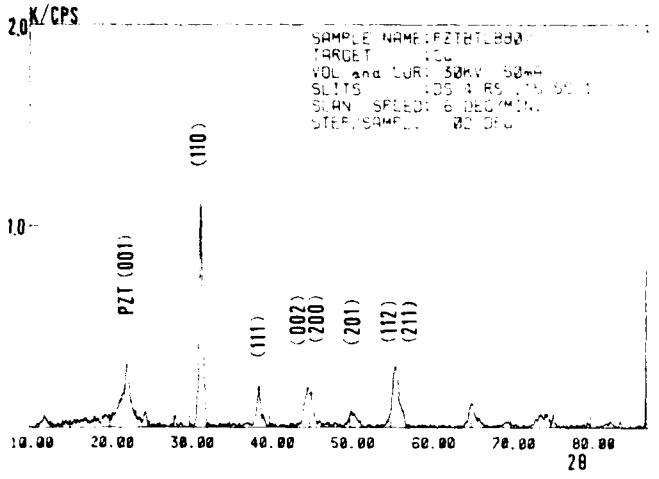


Fig.5 XRD result after CO_2 laser irradiation for PZT thick film/BT (143 W/cm^2).

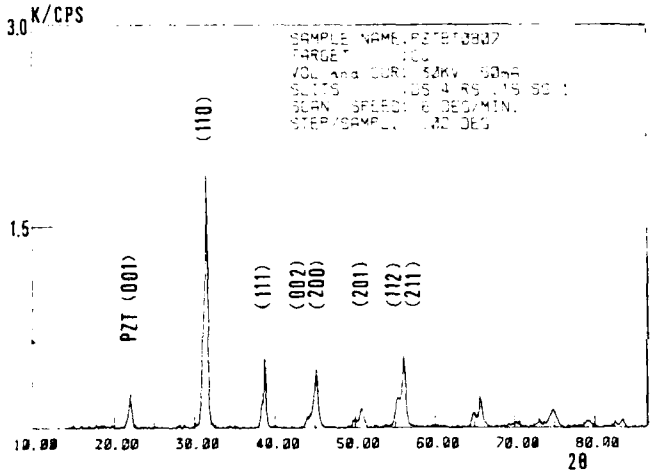


Fig.6 XRD result for PZT thick film/BT by a conventional sintering.

a bulk body. However, the well-developed necks ings for 3-3 composites of PZT will be noteworthy from facts that porous PZT with such structures presented higher piezoelectric voltage coefficient by capsule-free O_2 HIPed process.[5] Figure 8 indicates the interfaces between PZT thick film and BT with an EPMA analysis after the irradiation. There were not any significant diffusion or migration of each element.

The systems were poled at 1 kV/mm for 1 h, then the relative permittivities were measured for the BT and the PZT in a bulk after the laser sinterings, which values were 100 and 200, respectively. As far as PZT thick film/BT system, the permittivity was 144 after poling in the same method.

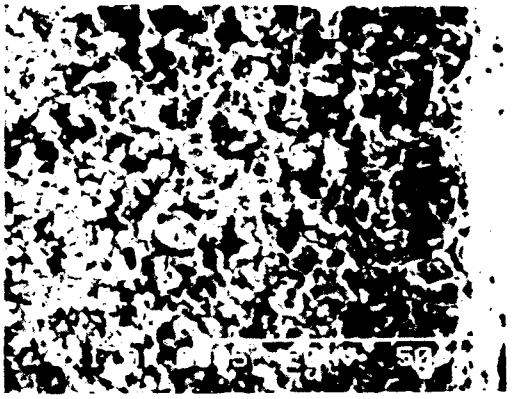


Fig.7 SEM photograph on the surface of PZT thick film/BT system after CO_2 laser irradiation.

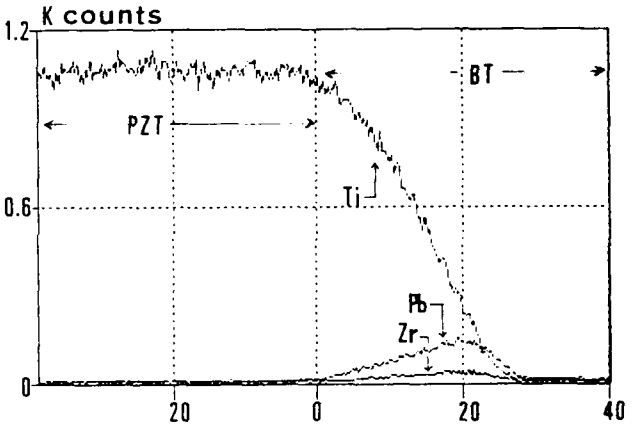


Fig.8 EPMA analysis at the interfaces between PZT thick film/BT after CO_2 laser irradiation.

Conclusion

PZT thick film was bonded with $BaTiO_3$ with a CO_2 laser irradiation at 143 W/cm^2 for 50 s. The PZT film was a porous with some neckings. However, their connectivities of grains and a little more grain growth must be improved. The next step will be aimed at these points and at vapor deposition of PZT thin film on BT by CO_2 laser irradiation.

References

[5] S.Sugibara, "Sintering of Piezoelectric Cera-

mics with CO_2 laser."Jpn.J.App.Phys.in press (1992).

2)S.Sugihara,"Reactions of TiO_2 with $BaCO_3$ by CO_2 laser." presented at Jpn. Powder/Powder Metallurgy Spring Conference, Tokyo, Japan, June 9-11,1992.

3)M.Okutomi,"Sintering of high density oxide ceramics with CO_2 laser." Jpn.High Temp.Vol. 12,pp.109,1986.

4)M.Okutomi,M.Kasamatsu,K.Tsukamoto,S.Shiratori and F.Uchiyama, App.Phys.Lett.Vol.44,pp. 1132-1134,1984.

5)S.Sugihara,T.Hayashi and K.Okazaki,"New processing and Evaluation of Porous PZT with High Connectivity using Capsule-free O_2 HIP. Mat.Res.Proceeding,Vol.251,pp.127-132,1992.

ANOMALOUS MECHANICAL AND PIEZOELECTRIC COEFFICIENTS IN PIEZOCERAMICS USED FOR IGNITION

P. Gonnard, C. Garabédian, H. Ohanessian, L. Eyraud
Laboratoire de Génie Electrique et Ferroélectricité
INSA, 69621 VILLEURBANNE CEDEX, FRANCE

Abstract : An analysis of the impact igniters is developped following the classical electromechanical analogies. From the comparison of the model with the experimental characterization of the converter, unusually high values of s_{33}^E, d_{33}, ε_{33}^T coefficients are shown off. Moreover an important increase of the loss tangent occurs during the dynamic compression. The influence of the applied uniaxial stress, the size of the piezoceramics and their composition are studied.

INTRODUCTION

Piezoelectric spark generators, based on the mechano-electrical energy conversion may be classified into two categories : the squeeze type driven by means of a quasi-static compression and the impact type driven by means of a pulsed stress of a hundred microsecond duration. In both cases the phenomena occuring during the conversion are complex due to the simultaneous occurence of high stresses and high electric fields. The purpose of the present work is to analyse the process of a dynamic igniter and to characterize the electromechanical coefficients during the conversion. The knowledge of these high level coefficients, quite different from the low level ones, is useful with the object of elaborating piezoelectric compositions better suited to those igniters.
The low level coefficients (LL) are measured at 0.5 V according to the IEEE standards [1].

CHARACTERIZATION OF PIEZOCERAMICS UNDER DYNAMIC COMPRESSION

The piezoelectric bar is supposed to be excited only on a longitudinal mode (length ℓ >> diameter $\varnothing$, area A). One face is in contact with the base having an infinite stiffness and the mechanical force F_1 is applied to the other face.
The more classical and simple equivalent circuit of the piezoelectric source is a voltage generator (open circuit voltage V_o) in series with an internal capacitance C [2].

The converter is connected to various external capacitances C_e and the stress pulse is assumed to be sinusoïdal. In such harmonic conditions the external output voltage V is related to the short circuit electrical charges Q_{sc} by the relation :

$$V = \frac{Q_{sc}}{C + C_e} \quad \text{or} \quad \frac{1}{V} = \frac{1}{V_o} + \frac{C_e}{Q_{sc}}$$

with :

$$C = \varepsilon_{33}^T \frac{A}{\ell}, \quad V_o = g_{33} T_M \ell, \quad Q_{sc} = d_{33} T_M A, \quad F_1 = A T_M$$

T_M is the maximum stress.

The $\frac{1}{V} = f(C_e)$ curve is a straight line with a slope $\frac{1}{Q_{sc}}$ and the ordinate at $C_e = 0$ is $\frac{1}{V_o}$ (Figure 1).

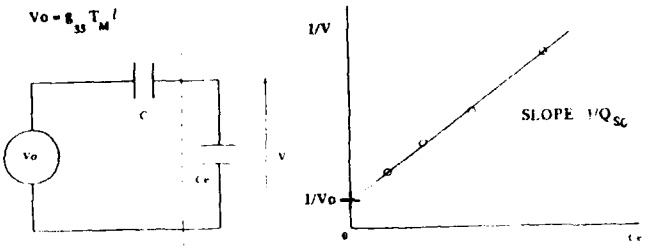


Figure 1 - Classical equivalent circuit of the igniter and determination of V_o, Q_{sc} and C

The maximum energy transfered to the external capacitance is obtained for $C = C_e$. Its value per unit volume of ceramic is :

$$W_e = \frac{1}{8} d_{33} g_{33} T_M^2$$

This method, applied to igniters, leads to anomalously high values of C and Q_{sc}. For example it is found for the sample 4 ($\varnothing$ = 2.7 mm, ℓ = 5 mm) : V_o = 21.000 V, Q_{sc} = ± 0.7 µCb i.e ± 12 µCb/cm² and C = 30 pF whereas C_{LL} = 8 pF, W = $W_e A \ell$ = 2.6 mJ for C_e = 28 pF
Such deviations lead us to find a new method for the characterization of the electromechanical coefficients under high stresses and electric fields.

CH3080-0-7803-0465-9/92$3.00 ©IEEE

DETERMINATION OF THE ELECTROMECHANICAL COEFFICIENTS UNDER HIGH LEVEL FROM AN ANALOG MODEL OF THE WHOLE CONVERTER

This method has been described in Ref. [3] previously. The Mason equivalent circuit of the piezoceramic working as a mechanoelectrical converter is given in part A of Figure 2b. The pulsed stress can be achieved by a spring loaded hammer or a falling steel ball (mass m_1) striking an anvil (mass M) located at the top of the piezoelement (mass m_2, compliance s^E_{33}) (Figure 2a). The equivalent network is given in part B of Figure 2b in which C_M represents the elasticity of the interface ball-anvil. The initial conditions exciting the circuit are given by the velocity v_o of the ball at the impact time. Once the mechanical elements transformed across the electrical side the equivalent circuit is given in Figure 3. R_m represents the lateral clamping of the piezobar owing to the external case and R_o the dielectric losses of the ceramic. The mechanical losses of the ceramic are negligeable with regard to R_m. The virtual rectifiers D_1 and D_2 prevent any tensile force from being applied to both interfaces.

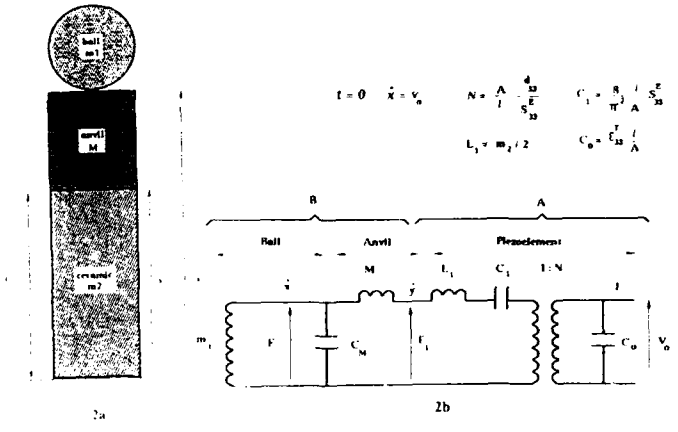


Figure 2 - Equivalent circuit of the spark generator

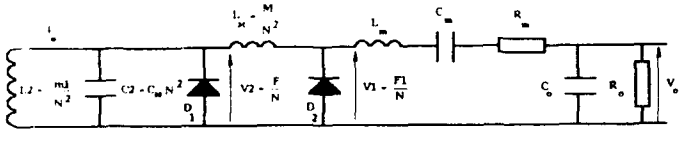


Figure 3 - Electrical equivalent circuit of the whole generator

The resulting frequency of the impact will be the whole system frequency which is generally much lower than the $\lambda/4$ resonance frequency of the piezobar ; the pulsed stress is performed by a 21.6 g ball falling from a height varying from 5 to 33 cm.

The open and short circuit characteristics are recorded (Figure 4, Experimental points) and by adjustement of the network parameters the calculated characteristics (Figure 4, dotted line) can fit the experimental ones very well. From the value of L_m, C_m, C_o, R_o, R_m and N the following high level coefficients are achieved : ε^S_{33}, d_{33}, s^E_{33} as well as the maximum reached stress T_M. Consequently the other electromechanical coefficients are calculated (ε^T_{33}, k_{33}, $g_{33}d_{33}$, tgδ).

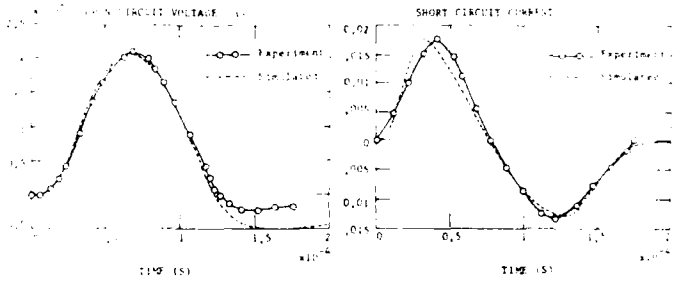


Figure 4 - Experimental and calculated characteristics (sample 4)

VARIATIONS OF THE ELECTROMECHANICAL COEFFICIENTS AS A FUNCTION OF THE APPLIED UNIAXIAL STRESS

This study is made with small sized piezobars ($\varnothing$ = 2.7 mm, ℓ = 5 mm). While increasing the drop h, the incident kinetic energy is increased as well as the uniaxial pressure T_M. After adjustement of network parameters this stress T_M is calculated for each value h. Figure 5 shows that T_M varies as $h^{0.59}$ whereas Marutake [4] found a variation as $h^{0.6}$. We calculated the same function with an exposant 0.66.

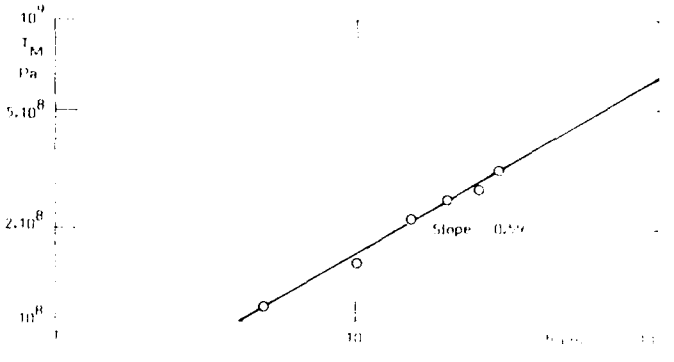


Figure 5 Variations of T_M versus the falling ball height

Figure 6 clearly shows that the ratios of the high level coefficients (HL) above low level coefficients (LL) are strongly dependent on the applied stress. It is well verified that all ratios tend to unity when the stress tends to zero.

At high pressure quite anomalous values of ε^T_{33}, d_{33} and s^E_{33} are found and the figure of merit $d_{33}g_{33}$ is strongly improved.

The electric charges released in short circuit reached $\pm$ 12 $\mu Cb/cm^2$ i.e a third of the remanent polarization. However the open circuit voltage remains limited by the strong increase of both ε^S_{33} (C_o) and the dielectric losses ($R_{oHL} \neq R_{oLL}/30$).

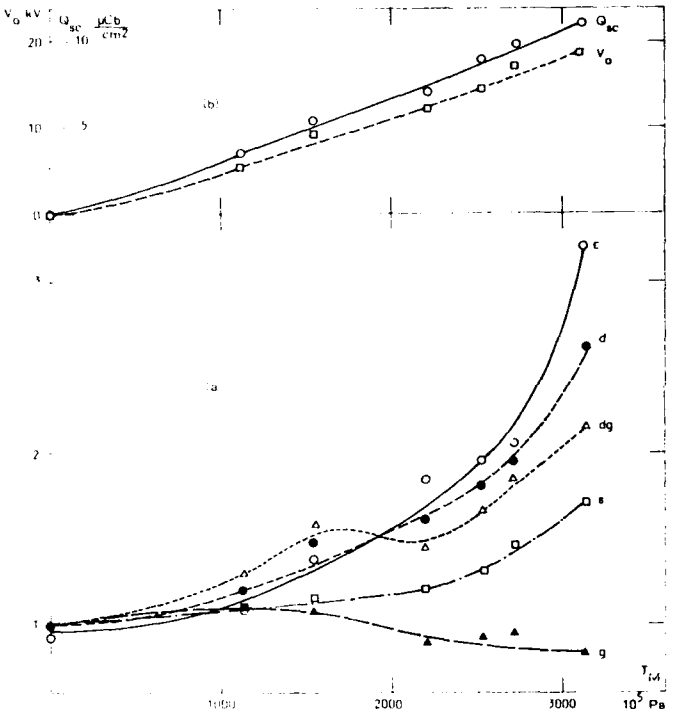


Figure 6

a) Ratios of high level above low level coefficients versus the maximum applied stress (T_M) during the impact

$$\varepsilon = \frac{\varepsilon^T_{33HL}}{\varepsilon^T_{33LL}},\quad d = \frac{d_{33HL}}{d_{33LL}},\quad s = \frac{s^E_{33HL}}{s^E_{33LL}},\quad g = \frac{g_{33HL}}{g_{33LL}},\quad dg = \frac{(d_{33}g_{33})_{HL}}{(d_{33}g_{33})_{LL}}$$

b) Short-circuit electric charges (Q_{sc}) and open circuit voltage (V_o) versus T_M

In industrial small size igniters the piezoceramics are subjected to stresses up to 3.10^8 Nm^{-2} so they are in conditions analog to h = 30 cm. It is surprising that no depolarization effect or cracking occurs under such a stress whereas under static conditions important effects of depolarization appear up to $1.2\ 10^8$ Nm^{-2} for the same composition [5]. It is supposed that the main part of the released electric charges are due to an electronic commutation because of a change of valency in the structure [6]. These reversible fast commutations would not alter the whole dipolar moment and consequently the reversibility is kept on.

Mechanically, the strong lateral clamping of the piezobar due to the case (high value of R_m) protects this element from cracking.

SIZE EFFECTS

For the same drop (h = 33 cm) and the same mechanical environment two elements of P190* material differently sized have been tested. It is shown (Table I, columns 1 and 2) that the same open circuit voltage V_o is almost reached with the small piezoelement which is three times smaller that the standard sized one (Ø 6.35 mm, ℓ 15 mm). Consequently the maximum electric field and stress are three times greater with the small element and it yields to widely enlarged non linearities. The energy W_e per unit volume, transfered to a matched capacitance, varies nearly as $d_{33_{HL}}\, g_{33_{HL}}\, T_M^2$ and is 13 times higher with the small element.

DEPENDENCE OF NON LINEARITIES ON THE MATERIAL COMPOSITION

Two hard compositions having nearly the same low level characteristics are compared in columns 3 and 4 of Table I. It can be observed that the increase of the high level compliance s^E_{33} of sample 4 is related to an important increase of the figure of merit $d_{33}g_{33}$ and a relatively low applied stress T_M. The best energy W_e is obtained with the more non linear material. In sample 3 the high level g_{33} coefficient is particularly low, as a consequence the open circuit voltage V_o is reduced.

A structural analysis by X Rays of various hard compositions shows that the highest non-linearities under high stresses occur for mixed phases situated on the rhombohedral side of the tetragonal-rhombohedral phase transition.

* Quartz et Silice, France

	1	2	3	4
	P 190 6.35 x 15 mm	**P 190** 2.7 x 5 mm	**Sample 3** 2.7 x 5 mm	**Sample 4** 2.7 x 5 mm
$\frac{d_{33HL}}{d_{33LL}}$	$\frac{360}{205} = 1.76$	$\frac{600}{197} = 3.05$	$\frac{410}{245} = 1.67$	$\frac{590}{210} = 2.8$
$\frac{g_{33HL}}{g_{33LL}}$	$\frac{28.9}{32} = 0.9$	$\frac{26.1}{29} = 0.9$	$\frac{19.2}{30} = 0.64$	$\frac{34.5}{33} = 1.05$
$\frac{d_{33}g_{33HL}}{d_{33}g_{33LL}}$	$\frac{10.4}{6.6} = 1.58$	$\frac{15.7}{5.7} = 2.75$	$\frac{7.9}{7.3} = 1.08$	$\frac{20.4}{6.93} = 2.93$
$\frac{\varepsilon_{33rHL}}{\varepsilon_{33rLL}}$	$\frac{1410}{722} = 1.95$	$\frac{2600}{765} = 3.4$	$\frac{2420}{930} = 2.6$	$\frac{1930}{714} = 2.7$
$\frac{s^E_{33HL}}{s^E_{33LL}}$	$\frac{14.9}{14.9} = 1$	$\frac{25.9}{13.7} = 1.9$	$\frac{16.1}{16.1} = 1$	$\frac{29.6}{15.6} = 1.9$
$\frac{k_{33HL}}{k_{33LL}}$	$\frac{0.84}{0.66} = 1.27$	$\frac{0.78}{0.65} = 1.2$	$\frac{0.69}{0.67} = 1.03$	$\frac{0.83}{0.67} = 1.24$
$\frac{\tan\delta_{HL}\ \%}{\tan\delta_{LL}\ \%}$	$\frac{7.8}{0.27} = 28.9$	$\frac{8.15}{0.29} = 28.1$	$\frac{16.6}{0.71} = 23.4$	$\frac{9.47}{0.65} = 14.6$
W_e (mJ/cm^3)	4.8	61	56	91
T ($N/m^2.10^5$)	1061	3080	3615	3094
V_c (kV)	23	19.5	15.7	21
ΔQ_{cc} (μCb)	$\pm$ 0.98	$\pm$ 0.78	$\pm$ 0.69	$\pm$ 0.7
ΔP ($\mu Cb/cm^2$)	$\pm$ 3.1	$\pm$ 13.6	$\pm$ 12	$\pm$ 12.2

Table I

High level characteristics of piezoelements used in dynamic compression :
1 and 2, size effects ;
2, 3 and 4, composition effects
d_{33} in pC/N and g_{33} in 10^{-3}Vm/N,
$d_{33}g_{33}$ and s^E_{33} in $10^{-12}m^2/N$

CONCLUSION

Anomalously high electromechanical coefficients are shown off with the help of an analog model of an impact igniter. When small sized piezoelements are submitted to very high stresses the non-linearities are the highest, but the reversibility is kept on. Further investigations are made in order to determine the relationship between these non-linearities and the composition or the structure of the piezoelectric material.

REFERENCES

[1] IEEE standards on piezoelectricity, ANSI/IEEE std 176 (1978)

[2] H. Ohanessian, Thèse Lyon France, n° 89 ISAL 0020 (1989)

[3] P. Gonnard, C. Garabédian, H. Ohanessian, L. Eyraud, ECAPD2, April 1992 (to be published)

[4] M. Marukake, Chitansan Briumu, Jitsuyoka, Kenkyu, Kai Report, n° XV.83.555 (Sept 1965) (in Japanese)

[5] P. Gonnard, C. Garabédian, C. Richard, D. Audigier, L. Eyraud, Electroceramics III June 1992 (to be published in Sil. Ind. Ceramic Science and Technology)

[6] L. Eyraud, P. Gonnard, B. Claudel, J. Am. Ceram. Soc. 73(7), 1854-56 (1990)

THE MECHANISM OF LOW TEMPERATURE SINTERING PZT CERAMICS WITH ADDITIVES OF Li_2O-Bi_2O_3-CdO

*Xiaoxing Wang, Peiwen Lu, Dawei Shen, Wanrong Xue and **Meiyu Zhao
*Department of Silicate Engineering
Nanjing Institute of Chemical Technology
Nanjing, Jiangsu 210009, P. R. China
**Shanghai Institute of Ceramics
Chinese Academy of Sciences
Shanghai 200050, P.R. China

ABSTRACT The effects of Li_2O, Bi_2O_3, CdO and V_2O_5 on sintering temperature and electromechanical properties were investigated. In order to reduce the sintering temperature further, the complex additives of Li_2O-Bi_2O_3-CdO(LBC) were employed. The rusults show that LBC will melt to form Liquild at low temperature. It was adventageous to promote the densification of ceramics. The mass transport process of solution and reprecipitation made the elements distribution uniform and further densification of ceramics. There was no influences on the electromechanical properties of PZT ceramics because the additives have no harmful impurities in it.

Introduction

The vaporization of PbO in PZT ceramics is of great significance because it influences the electromechanical properties of PZT ceramics and causes the enviromental pollution.[1][2] The additives are always employed to lower sintering temperature.[3][4][5] The amount of vaporization will be reduced remarkably if the sintering temperature can be reduced to 1000°C or below. However, it is very important to choose the additives. In the present paper, The effect of additives and their amounts on sintering temperature and electromechanical properties have been investigated. The mechanism of low temperature sintering was examined.

Materials and methods

As a basic system of PZT ceramics(B-PZT) for low temperature sintering, the composition is $Pb_{1-x}Ba_x(Zr_{0.53}Ti_{0.47})O_3$+ ySb_2O_5 + $zSiO_2$, wher x=0-20 mol%, y=0-2.5wt% and z=0-2.5wt%. If there is no additives in this system, the ceramics should be sintered at 1250°C for 2 hours(see table 2). The additives of $CdCO_3$, Li_2CO_3, Bi_2O_3, V_2O_5 and complex additives of Li_2O-Bi_2O_3-CdO(LBC) were employed to lower the sintering temperature of B-PZT ceramics. The electromechical properties of the samples were measured by HP-4192A impedence analyser and d33 meter. SEM, STEM X-ray energy spectra and TG-DTA methods were used to study the mechanism of low temperature sintering through the observation of the thin foil specimens. The dynamics of low temperature sintering was carried out by determining the linear shrinkage of the cubic samples of LBC-PZT as a function of sintering time at 900°C and 960°C.

Result and Discussion

The effects of various additives on the sintering temperature and electromechanical properties are shown in Table 1. Comparing with $CdCO_3$ Li_2CO_3 and Bi_2O_3, it can be found that V_2O_5 exhibits remarkbale inflence on lowering sintering temperature. The amount of 0.5wt% can reduce sintering temperature about 100°C. However, V_2O_5 shows that it has harmful influences on the electromechanical properties of B-PZT ceramics. The K_p of B-PZT ceramics with 0.5wt% V_2O_5 decreased to 31%. It is only half value of B-PZT ceramics. In this case, V_2O_5 could not be considered as a proper additive.

$CdCO_3$, Li_2CO_3 and Bi_2O_3 show the effects on lowing sintering temperature in a certain degree. The results further indicate that Li_2CO_3 is not only lowing sintering temperature but also increasing the electromechanical properties of B-PZT ceramics. Therefore, it is an ideal additive for B-PZT.

In order to reduce the sintering temperature further, employing complex additives is necessary. Table 2 show the electromechanical properties of the samples with and without additives of LBC sintered at different temperature and remaining time. The results indicate that the optimum sintering temperature has been reduced about 300 C because of the adding of LBC addi-

Table 1 The effects of additives on sintering temperature and electromechnical properties

No.	additives	adding amount wt%	sintering temperature °C	K_p %	ε_r	tgδ %
1			1250	68	2550	1.65
2	$CdCO_3$	1.0	1150	62	2000	1.75
3	$CdCO_3$	2.5	1100	63	2260	1.85
4	$CdCO_3$	5.0	980	58	2250	2.20
5	Li_2CO_3	0.1	1150	69	2250	2.20
6	Li_2CO_3	0.3	1100	68	2570	1.80
7	Bi_2O_3	1.0	1150	58	1850	2.00
8	Bi_2O_3	3.0	1100	46	1600	2.10
9	V_2O_5	0.5	1150	31	1400	1.60
10	V_2O_5	2.0	1050	24	900	1.45

CH3080-0-7803-0465-9/92$3.00 ©IEEE

Table 2 Properties of the samples of LBC-PZT and B-PZT sintered at different temperature and remaining time

	LBC-PZT					B-PZT
time(hrs)	2	4	6	1/3	2	2
sintering temperaure °C	960	960	960	900	900	1250
K_p	67.5	68.0	67.5	57.0	63.0	68.0
$\varepsilon_{33}^T / \varepsilon_0$	2160	2200	2100	1780	1870	2550
$d_{33} \times 10^{12}$ c/N	555	570	565	370	445	610
tgδ %	1.95	1.90	1.90	2.40	2.30	1.40
Q_m	43	44	44			53

tives and there is no significant difference in electro-mechanical properties between B-PZT and LBC-PZT ceramics.

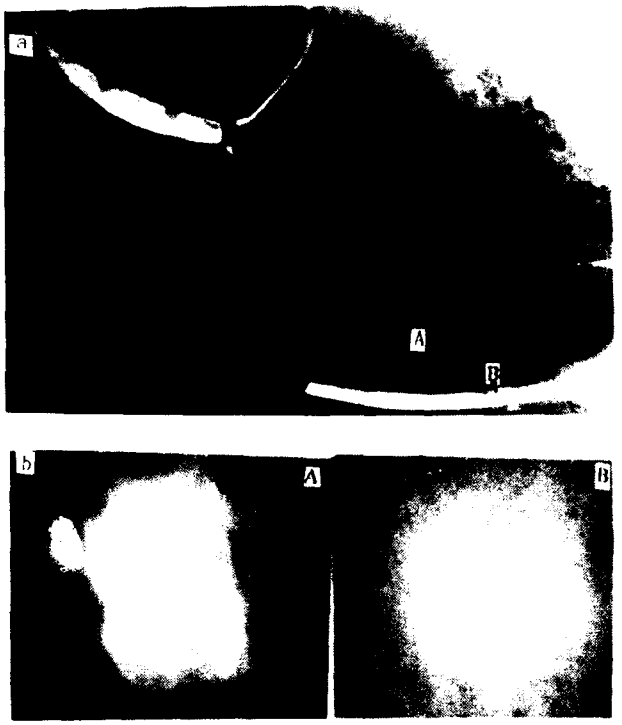


Fig.1 (a) Bright field STEM micrograph of LBC-PZT ceramics quenched from 900°C remaining 10 minutes(40000x) (b) Electron diffraction patterns of microareas A and B

Fig.1 shows the SEM micrograph and electron diffraction patterns of the thin foil specimens. Microareas A and B are located in grain and grain boundary respectively. The results indicate that microarea A is crystalline structure and B is noncrystalline structure.This means that the low temperature sintering of LBC-PZT ceramics is a sintering of presence of liquid. The TG-DTA curves of LBC also indicate that it melt to form liquid at 510°C(Fig.2). The presence of liquid will promote the densification of ceramics. Fig.3 are the STEM, SEM micrograph and the X-ray energy spectrum of sample sintered at 900°C for 10 minutes. It can be found that Bi and Cd content in grain boundary are richer than those in grains. However, the X-ray energy spectrum of the sample sintered at 900°C for 4 hours show that the elements distribution in five microareas from grain boundary to grain has been uniformed(Fig.4).

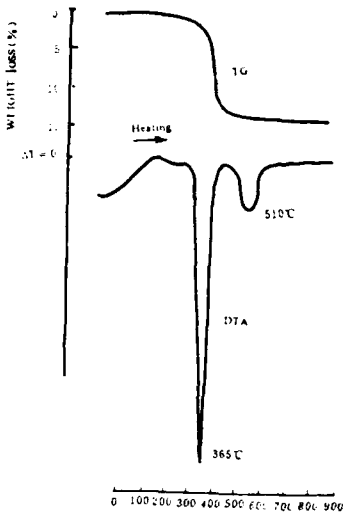


Fig.2 TG-DTA curves of the additives of LBC

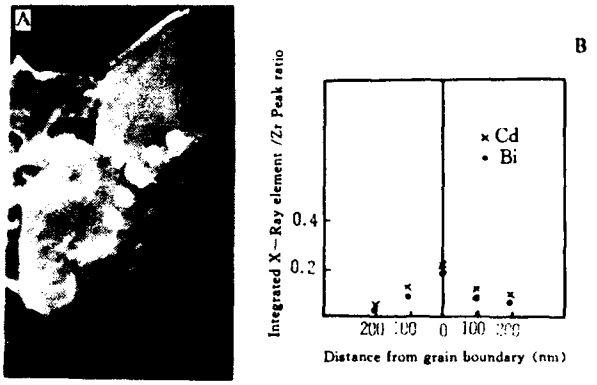


Fig.3 (A) Bright field STEM and SEM micrographs of the sample sintered at 900°C for 10 minutes (B) Cd and Bi content variation from grain boundry to grains.

The result of the experimentof dynamics of low temperature sintering is illustrated in Fig.5. The sinteiring process can be divided into three stages. In the first stage, the relationship between $\Delta L/L$ and t is a line with the slop of 1.04. It corresponds to the rearrange of particles during the initial stage of

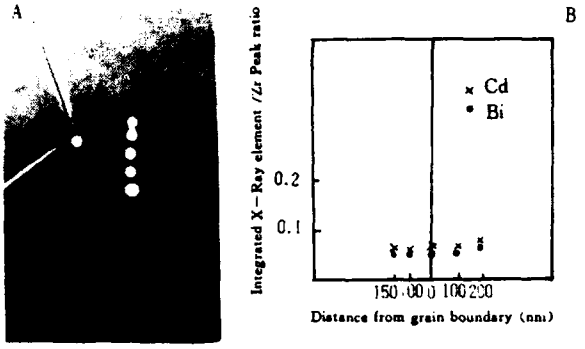


Fig.4 (A) SEM micrograph of sample sintered at 960°C for 4 hrs (B) Cd and Bi content variation from the grain boundary to grains

sintering. The second stage is a line with a slop of 0.3. This means $\Delta L/L \propto t^{1/3}$. It is commensurate with the mass transport process of solution and reprecipitation. The last stage is a line with the slop of 0. This means the end of sintering process because of the seal of the pores remained in the ceramics.

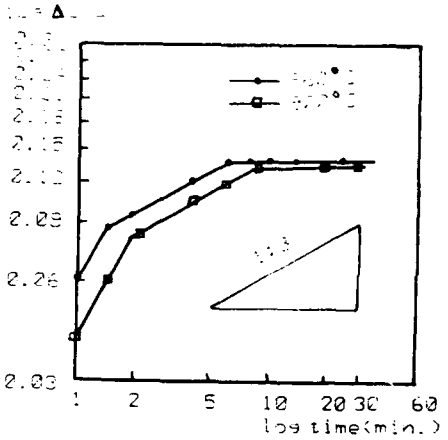


Fig.5 Logarithm of linear shrinkage as a function of logarithm of sintering time for LBC-PZT ceramics

In accordance with these results, the mechanism of low temperature sintering of LBC-PZT ceramics can be derived, that is, the additives melt to form liquid at low temperature and they are rich in grain boundaries. The liquid presented in ceramics promote the densification through the rearranging of particles. After that, the ceramics are densified further by the mass transport process of solution and reprecipitation and the distribution of the elements in the ceramics tends to uniform. At last, the pores remained in ceramics are sealed and the sintering process is to its end. Because there are not any harmful impurities in the additives, the electromechanical properties of LBC-PZT ceramics almost has no change.

Conclusion

A small amount of Li_2O-Bi_2O_3-CdO can be employed as ideal additives for B-PZT ceramics. LBC will melt to form liquid at low temperature and promote the densification of ceramics. A mass transport process of solution and reprecipitation make the elements distribution uniform. Because there are not any harmful impurities in LBC, there is little influence on electromechanical properties.

References

[1] A. H. Webster, "Effect of PbO deficiencyon the piezoelectric properties of lead zirconate-titanate ceramics," J. Am. Ceram. Soc., vol.50, pp.490-491, 1967.

[2] R. L. Holman etal. "Intrinsic nonstoichiometry in single phase $Pb(Zr_{0.5}Ti_{0.5})O_3$," J. Am. Ceram. Soc., vol.72(4), pp.192-195, 1972.

[3] D. E. Wittmer etal., "Low-temperature densification of lead zirconate-titanate with vanadium pentoxide additive," J. Am. Ceram. Soc., vol.64, pp.485-490, 1981.

[4] Gui Zhilun etal., "Low-temperature sintering of lead-based piezoelectric ceramics," J. Am. Ceram. Soc., vol.72, pp.486-491, 1989.

[5] Gui Zhilun etal., "high performance piezoelectric ceramics with low temperature sintering," in Proceedings of International Conference on Electric Components and Materials, Beijing, 1989, pp.30-33.

DIELECTRIC, PYROELECTRIC AND PIEZOELECTRIC PROPERTIES IN THE $Pb(Mg_{1/3}Nb_{2/3})O_3$-$PbTiO_3$-$Pb(Zn_{1/3}Nb_{2/3})O_3$ SYSTEM

S. H. Lee, K.C.Kim, Y. J. Kim, and S. W. Choi
Department of Physics, Dankook University,
29 Anseodong, Cheonan, Chungnam, Korea

Abstract

Dielectric, pyroelectric and piezoelectric properties of ceramics in the PMN-PT-PZN system have been studied as a function of PT and PZN content for compositions near the morphotropic phase boundary(PMN-PT). The dielectric constant and loss of poled ceramic samples were determined. Pyroelectric coefficient and electromechanical coupling factor are observed on various compositions. The transition temperature and peak temperature of the ceramics decreased gradually with the addition of PZN, their rates of decrease are about 5-7℃/mol%. The addition of PZN to the PMN-PT relaxor ferroelectric system resulted in slightly reduced the dielectric constant. Further addition of PZN could be used to shift the Tc downward without significantly changing the electrical behavior.

Introduction

Lead magnesium niobate $Pb(Mg_{1/3}Nb_{2/3})O_3$ (hereafter designed PMN) is a ferroelectric material with a partially disordered perovskite structure. It undergoes a diffuse phase transition near -15℃. In the $Pb(Mg_{1/3}Nb_{2/3})O_3$-$PbTiO_3$ (PMN-PT) system, a morphotropic phase boundary(MPB) exists between the rhombohedral and tetragonal phase, near 35mol% of PT.[1,2] Polycrystalline with compositions near MPB extremely show large dielectric, piezoelectric and pyroelectric coefficient. $Pb(Zn_{1/3}Nb_{2/3})O_3$ (PZN) is also a promising candidate material for electrostricive micropositioners[3].

The present work was undertaken to investigate the dielectric, pyroelectric and piezoelectric properties of ceramics with perovskite structure in the PMN-PT-PZN ternary system.

Experimental procedure

The compositions selected for the present study were of the type (1-x-y)PMN-xPT-yPZN with x varying between 0.05 and 0.35 and y varying from 0.025 to 0.35. Ceramic samples (reagent grade powders) across the PMN-PT-PZN series were prepared by using the columbite precursor method as described by Swartz and Shrout[4]. Completion of the reactions was verified using X-ray diffraction as well as to determine the appropriate structure.

The dielectric properties were measured with an HP multi-frequency LCR meter. The dielectric constant and dissipation factor were measured as a function of temperature at various frequencies between 0.1 and 100kHz at a temperature rate of 4°C/min. The pyroelectric coefficient was measured by the static Byer-Roundy method[5] as the samples were heated, again at rate of 4°C/min, through the phase transition region. Prior to the dielectric, pyroelectric and piezoelectric measurements, the specimens were poled by applying a DC field of about 15 kV/cm while cooling from well above the transition to a temperature well below. Electromechanical coupling factor was measured by using resonance -antiresonance method[6].

Results and discussion

Dielectric properties

Figure 1 shows typical plot of the dielectric constant and the dissipation factor at various frequencies (0.1 to 100 kHz) for composition 0.75PMN-0.20PT-0.05PZN. The transition temperature increases with increasing frequency as shown in Figure 1. Most of the compositions show a diffuse phase transition with a strong frequency dispersion. It is characteristic of relaxor ferroelectric materials.

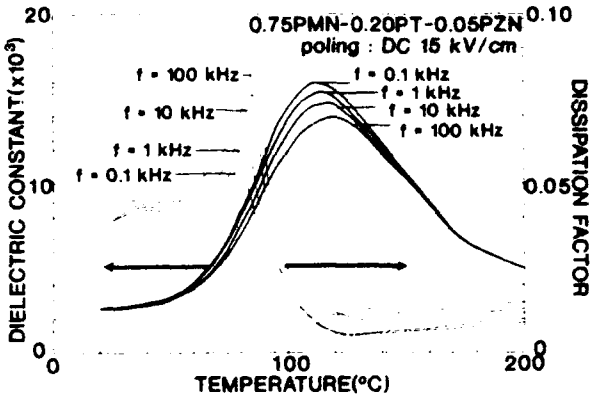


Figure 1. Temperature dependence of the dielectric constant and the dissipation factor as a function of frequency for 0.75PMN-0.20PT-0.05PZN.

The dielectric constant vs. temperature behavior at 1kHz is shown in Figures 2 and 3 for various compositions across the 0.60PMN-(0.40-x)PT-xPZN and 0.75 PMN-(0.25-x)PT-xPZN solid solution series, respectively.

The transition temperature variation of dielectric constant as a function of composition x at 1 kHz is shown in Figure 4. The transition temperature decreases with the amount of PZN.

In the compositions with the same of PZN, the dielectric constant as a function of temperature is shown in Figure 5. As can be seen, the maximum of the dielectric constant increases with rising x until x = 0.225. In the region x > 0.225 the dielectric constant decreases with increasing x. The transition temperature variation of the dielectric constant as a function of mole fraction of PT in the (0.90-x)PMN-xPT-0.10PZN series at 1 kHz is shown in Figure 6. In the compositions with the same percentage of PZN, the transition temperature increases with the amount of PT, their rates of increase are about 5-6°C/mol%.

Pyroelectric and piezoelectric properties

Suitably chosen composition in the (1-x-y)PMN-xPT-

CH3080-0-7803-0465-9/92$3.00 ©IEEE

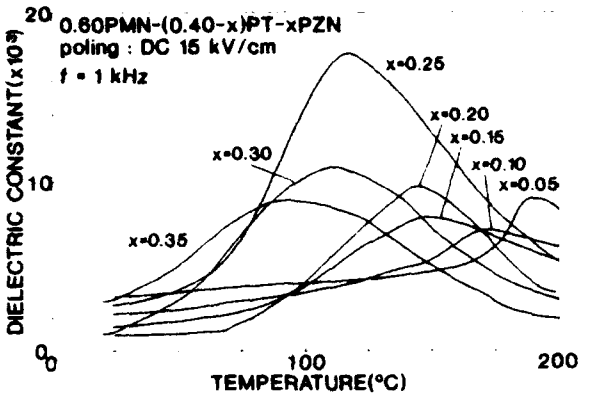


Figure 2. Temperature dependence of the dielectric constant as a function of the mole fraction of PZN for 0.60PMN-(0.40-x)PT-xPZN.

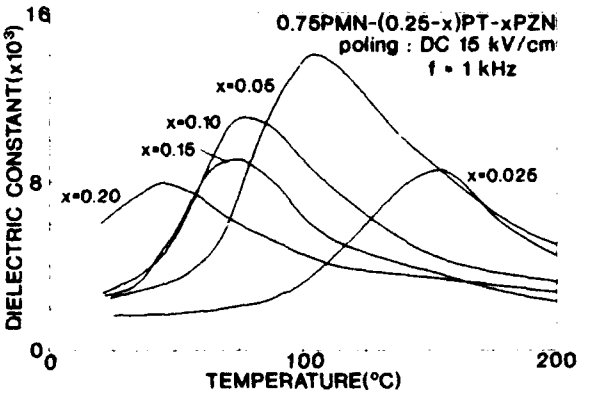


Figure 3. Temperature dependence of the dielectric constant as a function of the mole fraction of PZN for 0.75PMN-(0.25-x)PT-xPZN.

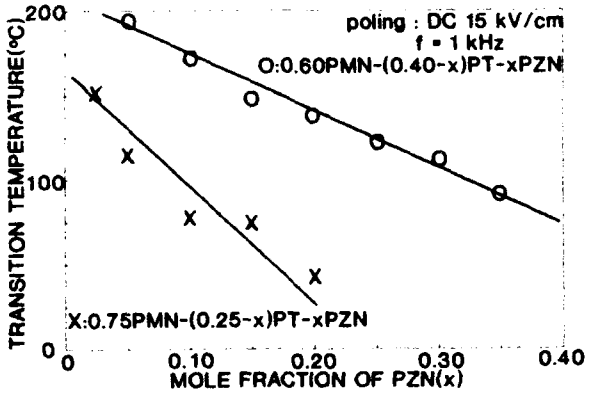


Figure 4. Variation of the transition temperature as a function of the mole fraction of PZN in the PMN-PT-PZN system.

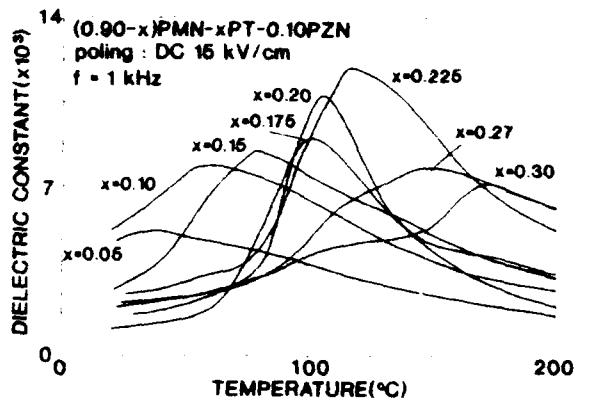


Figure 5. Temperature dependence of the dielectric constant as a function of PT for(0.90-x)PMN-xPT-0.1PZN

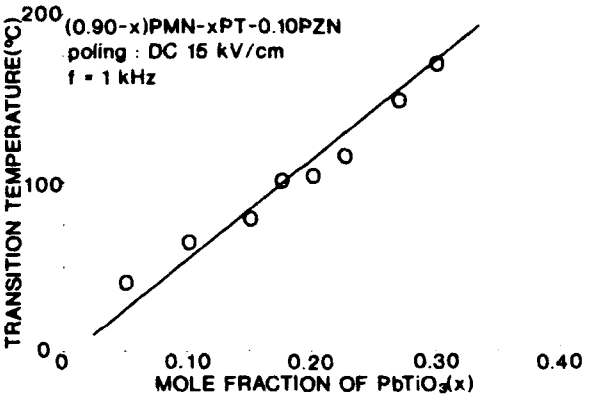


Figure 6. Variation of the transition temperature as a function of the mole fraction of PT in the (0.90-x) PMN-xPT-0.10PZN system.

yPZN solid solution showed sharp anomalies in the temperature dependence of their pyroelectric response near the ferroelectric transition temperature. In the case of pure PMN the transition temperature is below room temperature. With an addition of PT and PZN the transition temperature of the PMN-PT-PZN can be suitably adjusted for the room temperature pyroelectric and piezoelectric applications.

Figures 7 and 8 show the pyroelectric coefficient as a function of temperature for various values of the mole fraction of PZN in the 0.60PMN-(0.40-x)PT-xPZN and 0.75PMN-(0.25-x)PT-x PZN series, respectively. The pyroelectric coefficient increases with decreasing the mol% of PZN. However, the pyroelectric coefficient of two compositions, 0.60PMN-(0.40-x)PT-xPZN and 0.75PMN - (0.25-x) PT-xPZN, decrease for $x < 0.25$ and $x < 0.05$, respectively. The composition with the maximum pyroelectric coefficient might be similar to that observed in the dielectric constant vs. temperature studies. The broadening of the peaks in the pyroelectric coefficient vs. temperature plots may be due to the coexistence of the ferroelectric and paraelectric phases.

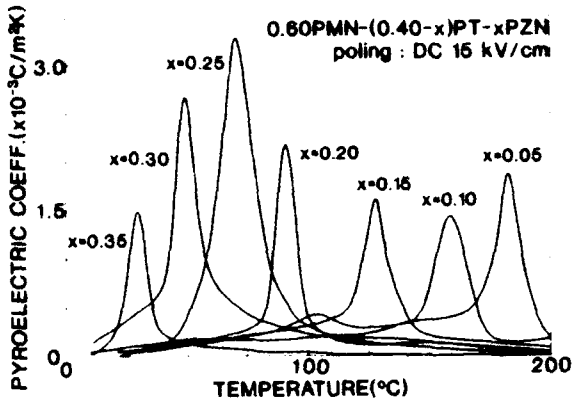


Figure 7. Pyroelectric coefficient for various mole fraction of PZN for 0.60PMN-(0.40-x)PT-xPZN as a function of temperature.

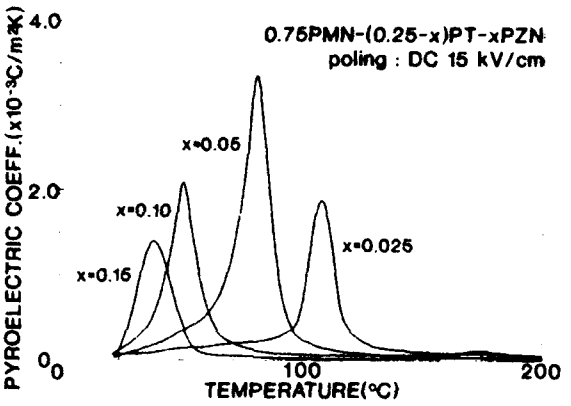


Figure 8. Pyroelectric coefficient for various mole fraction of PZN for 0.75PMN-(0.25-x)PT-xPZN as a function of temperature.

The peak temperature of pyroelectric coefficient with mole fraction of PZN in the 0.60PMN-(0.40-x)PT-xPZN and 0.75PMN-(0.25-x)PT- xPZN is shown in Figure9. The peak temperature decreases almost linearly as the amount of PZN in the composition increases, their rates of decrease are about 5℃/mol%. Figures 10, 11 and 12 show the pyroelectric coefficient as a function of temperature for various values of the mole fraction of PT in the (1-x-y)PMN-xPT-yPZN series. As can be seen, in the compositions with the same mol% of PZN, the peak temperature increases with the amount of PT. In each series the maximum pyroelectric coefficient is observed for the compositions 0.675PMN-0.225PT-0.10 PZN, 0.725PMN-0.125PT-0.15PZN and 0.70PMN-0.10PT-0.20 PZN.

Figure 13 shows the room temperature value of electromechanical coupling factor, Kp, of the compositions 0.60PMN-(0.40-x)PT-xPZN and 0.75PMN-(0.25-x)PT -xPZN series as a function of mole fraction of PZN. A maximum coupling coefficient was found at the compositions 0.60PMN-0.15PT-0.25PZN and 0.75PMN-0.20PT-0.05PZN, respectively. The foregoing compositions are in good agreement with those exhibiting maximums in dielectric constant and pyroelectric coefficient.

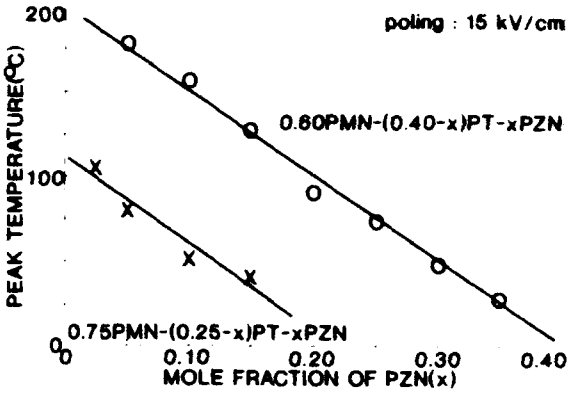


Figure 9. Variation of the peak temperature as a function of the mole fraction of PZN in the PMN-PT-PZN system.

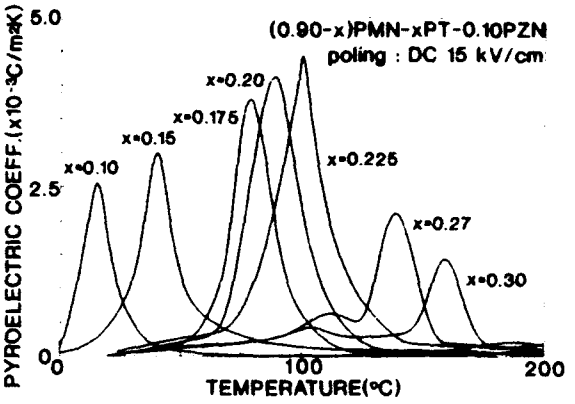


Figure 10. Temperature dependence of the pyroelectric coefficient as a function of the mole fraction of PT for (0.90-x)PMN-xPT-0.10PZN system.

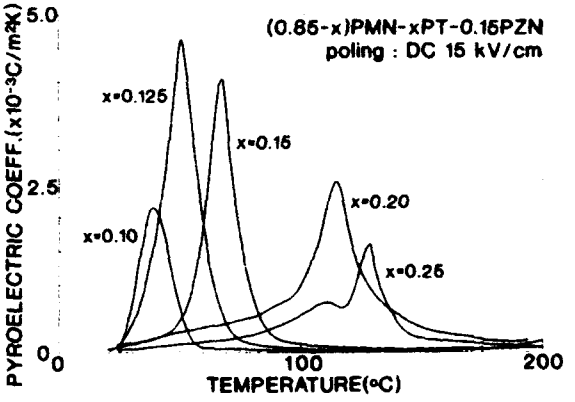


Figure 11. Temperature dependence of the pyroelectric coefficient as a function of the mole fraction of PT for (0.85-x)PMN-xPT-0.15PZN system.

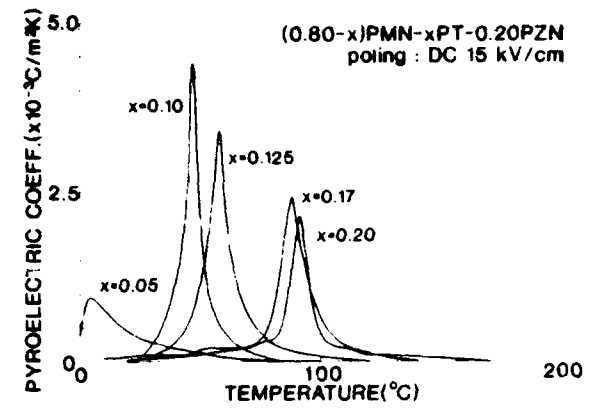


Figure 12. Temperature dependence of the pyroelectric coefficient as a function of the mole fraction of PT for (0.80-x)PMN-xPT-0.20PZN system.

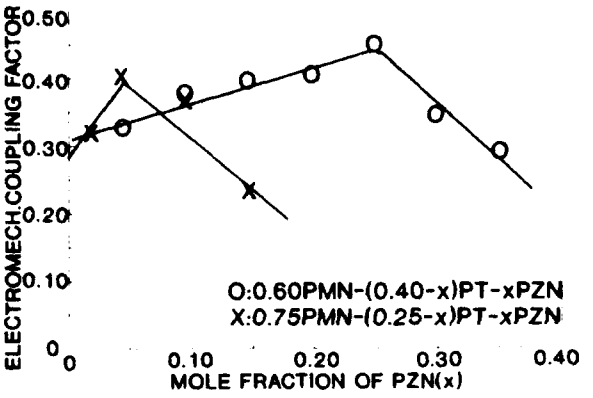


Figure 13. Electromechanical coupling factor as a function of the mole fraction of PZN at the room temperature.

Conclusions

The addition of $Pb(Zn_{1/3}Nb_{2/3})O_3$ to the PMN-PT relaxor ferroelectric system resulted in slightly reduced K and the phase transition temperature decreases with the amount of PZN. Futher additions of PZN could be used to shift the Tc downward without significantly changing the dielectric and pyroelectric behavior. In compositions with the same percentage of PZN, the Tc increase with the amount of PT. The maximum electromechanical coupling factor are obtained in the compositions with the maximum dielectric constant.

Acknowledgement

This work was supported by the Korea Science and Engineering Foundation (KOSEF) through the Science Research Center (SRC) of Excellence Program.

References

(1) S.W.Choi, T.R.Shrout, S.J.Jang and A.S.Bhalla, "Morphotropic Phase Boundary in $Pb(Mg_{1/3}Nb_{2/3})O_3$-Pb TiO_3 System," Materials Letters, vol.8, pp.253-255, July 1989.

(2) S.W.Choi, T.R.Shrout, S.J.Jang and A.S.Bhalla, "Dielectric and Pyroelectric Properties in the Pb $(Mg_{1/3}Nb_{2/3})O_3$-$PbTiO_3$System," Ferroelectrics, vol. 100, pp.29-38, 1989.

(3) S.Nomura and J.Kuwata, S.J.Jang, L.E.Cross and R.E.Newnham, "Electrostriction in $Pb(Zn_{1/3}Nb_{2/3})O_3$," Mater. Res. Bull., vol.14, pp.769-774,1979.

(4) S.L. Swartz and T.R.Shrout, "Fabrication of Perovskite Lead Magnesium Niobate," Mater.Res.Bull., vol.17, pp.1245-1250, 1982.

(5) R.L.Byer and C.B.Roundy, "Pyroelectric Coefficient Direct Measurement Technique and Application to a NSEC Response Time Detector," Ferroelectrics, vol.3, pp. 333-338, 1972.

(6) IRE Standands on Piezoelectric Crystal: Measurement of Piezoelectric Ceramics, Proc. 1961," IRE(Inst. Radio Engrs.) vol. 49 (7), pp.1161-1169, 1961.

Electrooptic, Pyroelectric, Photorefractive

INFLUENCE OF MOISTURE ON PYROELECTRIC PROPERTIES OF BONE

Vadim E. Khutorsky and Sidney B. Lang
Department of Chemical Engineering
Ben-Gurion University of the Negev, Beer Sheva, Israel

Abstract

Pyroelectricity is a universal property of all biological systems, although its source has not yet been determined. In this work, the voltage and time dependencies of the pyroelectric properties of wet and dry bone (turkey femur) were investigated using the dynamic pyroelectric method of Chynoweth. The current generated by the sample had both real and imaginary components. The magnitude of the response was almost the same, regardless of which sample electrode was irradiated with the laser beam, but the signs were opposite. The current increased up to several orders of magnitude when a bias DC field of 1000 V/cm was imposed. When the bias field was switched off, a current in the opposite direction with a decay time of tens of hours was measured. There was also a slow decay of a direct current with a polarity opposite to that of the bias field. In conductivity measurements, the DC varied nonlinearly as the 1.5 power of the voltage. When the samples were stored in vacuum at 100° C for one hour, both the pyroelectric coefficient and the conductivity decreased by several orders of magnitude. We conclude that the pyroelectric properties of bone depend strongly on the moisture content and that the polarization in wet bone is non-uniform. The polarization appears to be due to an internal field at the interfaces of the solid matrix and the fluid within the pores.

Introduction

Electrical polarization in biological systems is determined by their structure. There is much evidence of its importance in physiological processes. The pyroelectric effect, first observed in dried bone and tendon by Lang [1], has been studied in large numbers of biological materials [2]. It results from the alignment of polar organic molecules, usually proteins such as collagen [3]. The measurement of the pyroelectric properties of materials provides a convenient and sensitive means for investigation of the state of polarization. In addition, the pyroelectric effect itself appears to have biological significance [4]. The influence of physiological levels of moisture has not been explicitly considered previously, although some effects have been reported [5-10]. The piezoelectric effect, which is closely related to the pyroelectric effect, plays an important role in processes of bone growth, remodeling and fracture healing. Its different behavioral mechanisms in moist and dried tissues have been extensively studied [11-14].

In these experiments, we investigated the pyroelectric effect in both physiologically moist and dry bone. The effects of bias electric fields were studied and dielectric properties were measured.

Experimental Procedures

The specimens for investigation were cut from turkey femur by a water-cooled saw blade. The samples were about 1 mm in thickness and the specimens were oriented with their major faces either parallel or normal to the long axis of the bones. After cutting, the samples were cleaned and air-dried. Silver paint was used as an electrode material with a thin layer of black ink to increase the absorptivity. The measured absorptivity of the samples for 632-nm radiation was about 96%.

The pyroelectric effect was measured with the dynamic method of Chynoweth [15], in which the sample is heated with a modulated beam of radiation and the generated voltage or current is measured. The apparatus is shown in Fig. 1. The radiation from a 35-mW He-Ne laser was modulated by means of a light chopper. A current amplifier was used for amplification of the pyroelectric current, and the amplifier analog output was input to a lock-in amplifier whose reference voltage was taken from the light chopper. Both real and imaginary components of the current were determined. The measured values are referred to as AC (alternating current) in the discussion below. In some experiments, a DC bias voltage was applied during measurements by means of a high voltage supply. The direct current (referred to as DC below) was measured by a digital electrometer. The dielectric constant and loss tangent of the samples were determined by means of the lock-in amplifier.

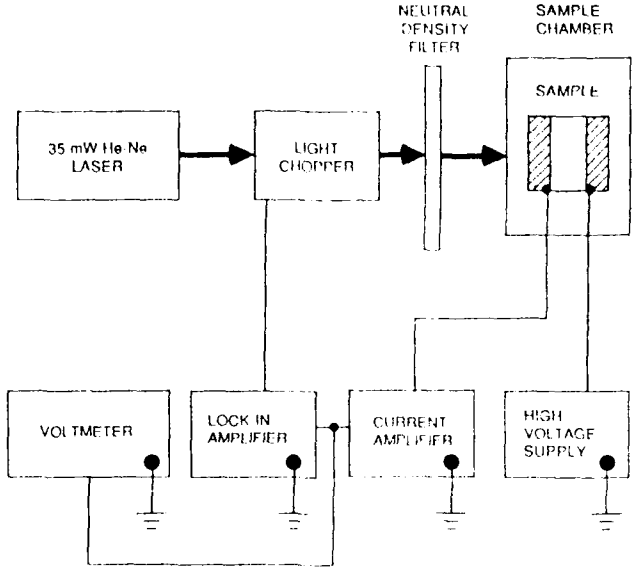


Fig. 1. Experimental apparatus for measurement of pyroelectric properties of bone.

CH3080-0-7803-0465-9/92$3.00 ©IEEE

Dry samples were prepared by placing the physiologically moist samples in a vacuum at 100°C. The samples lost about 10% in weight and the currents measured in the Chynoweth experiment reached steady values after about an hour of drying. The weight and pyroelectric, dielectric and conductivity properties could be restored to approximately their original values by storing the dry samples in deionized water for about 24 hours.

Results and Data Analysis

Both real (in-phase with the laser illumination) and imaginary (out-of-phase) components of an AC were observed for moist bone. The absolute values of the components increased by four to five orders of magnitude for bias fields of about 2000 V/cm as shown in Fig. 2. A bias field of only 1 V/cm was sufficient to develop a magnitude of current equivalent to that of an unbiased sample. A large DC due to conduction was also measured with the imposed bias field, as shown in Fig. 3. The conductivity behavior was nonlinear, with the current varying approximately as the 1.5 power of the voltage. The signs of both AC components were reversed with a reversal of the bias field. The magnitude of the response was almost the same, regardless of which sample electrode was irradiated with the laser beam, but the signs were opposite.

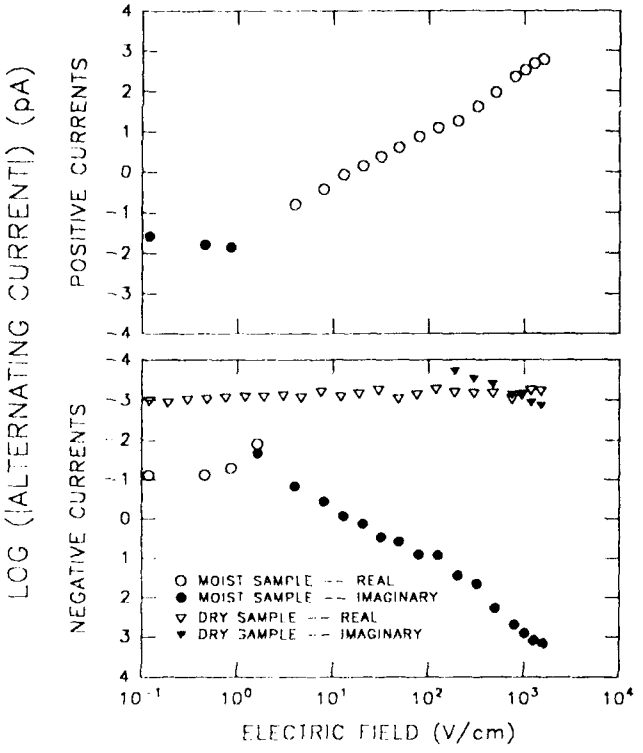


Fig. 2. Dependence on bias field of real and imaginary components of AC generated by moist and dry bone when irradiated by the modulated laser beam. Chopping frequency was 5 Hz.

The observed AC was not solely due to a pyroelectric effect, because it also contained a temperature dependent conduction current. The pyroelectric current of a homogeneous, thermally thick sample having thin electrodes is real and frequency-independent. A thermally-modulated conduction current is imaginary and inversely proportional to frequency. The frequency behavior did not correspond to this model, as shown in Fig. 4. This was due to a phase shift in the current, resulting from two sources: (1) a large electrode thermal mass and (2) a long *pyroelectric* relaxation time. A related *dielectric* relaxation was observed in the frequency dependencies of the dielectric constant and loss tangent, as illustrated in Fig. 5, and also reported previously [16]. The dielectric properties of moist bone appeared to have a Debye-type dispersion with saturation of the dielectric constant below 10 Hz.

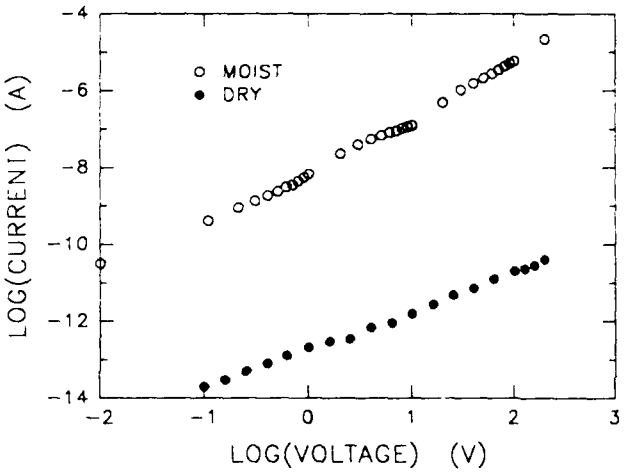


Fig. 3. Current-voltage behavior of moist and dry bone.

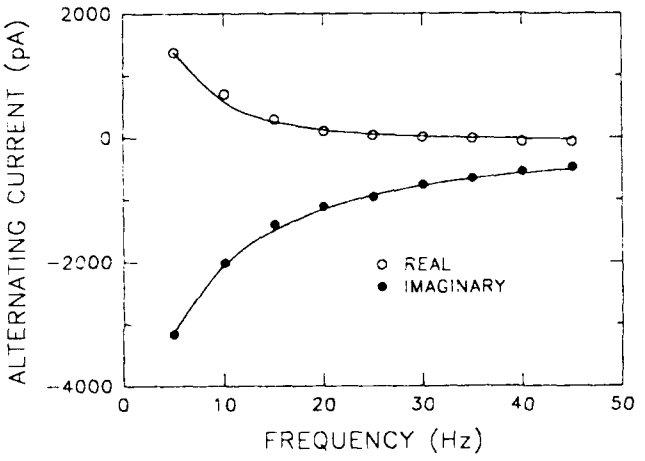


Fig. 4. Dependencies of real and imaginary components of AC on the modulation frequency. Bias electric field was 1600 V/cm.

A theoretical model was developed in order to separate the AC into pyroelectric and thermally modulated conduction current components. The model was based upon the following assumptions: (1) the pyroelectric effect was characterized by a single relaxation time; (2) the conductivity was temperature dependent; (3) the electrodes had a finite thermal mass; and (4) the sample was thermally thick. The model was fitted to the experimental data by a nonlinear least squares technique to determine four parameters: (1) the pyroelectric coefficient; (2) the *pyroelectric* relaxation time; (3) the temperature coefficient of the conductivity; and (4) the thermal mass of the electrodes. The least squares fit was good for all levels of the bias fields. It was less satisfactory for the measurements with no bias field because of nonuniformities in the polarization distribution of the samples [17, 18]. The *pyroelectric* relaxation time was about 0.01 sec, which is of similar magnitude to the relaxation time of the dielectric constant of Fig. 5. However, the latter apparently contains a wide spectrum of relaxation times. The electric field dependence of the calculated pyroelectric coefficient is shown in Fig. 6. The coefficients attain extremely large values for small bias fields, exceeding the pyroelectric coefficients of the best ferroelectric materials by an order of magnitude [19].

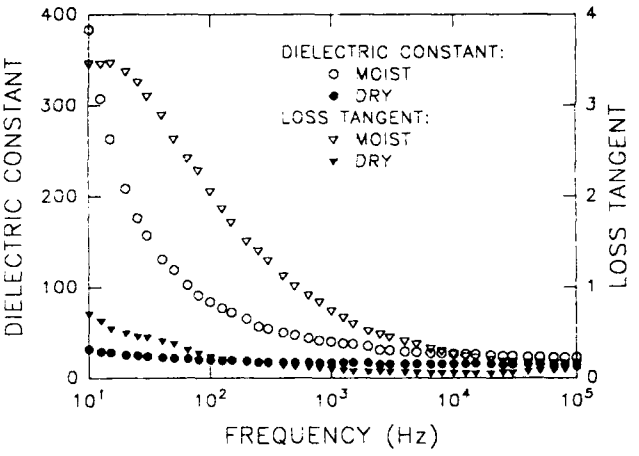


Fig. 5. Frequency dependencic of dielectric constant and loss tangent of moist and dry bone.

After the bias field was turned off, the real and the imaginary AC components and the DC reversed signs and decayed to the non-bias state slowly, requiring about 10-20 hours at ambient temperature. This is illustrated in Fig. 7. The DC component was a discharge current, possibly resulting from electric fields produced at solid-fluid interfaces within the bone [11-13]. The AC consisted of components due to pyroelectricity and to thermal modulation of the DC component. The AC and the DC decayed at the same rate, which indicates that they have a common origin.

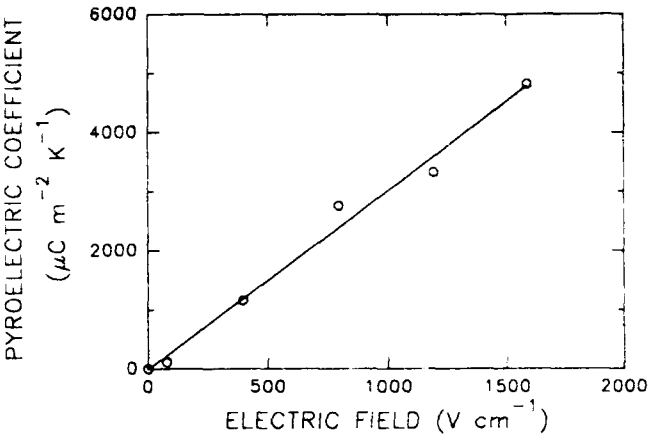


Fig. 6. Dependence of pyroelectric coefficient of moist bone on bias field.

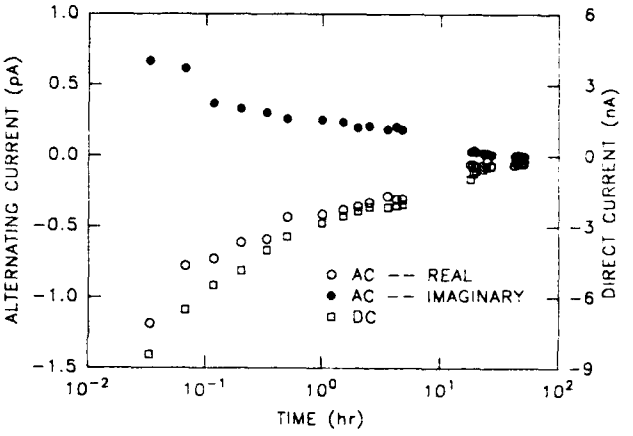


Fig. 7. Decay of AC and DC of moist sample after bias field was switched off and electrodes were short circuited.

This suggests that, when no external bias is applied, an internal bias field produces the much higher pyroelectric coefficient of moist bone as compared to dry bone.

The imaginary component of the AC for dry samples was almost zero, and the real component was essentially independent of bias field, as shown in Fig. 2. Consequently, the real component is almost entirely due to a pyroelectric effect. The induced AC of moist bone at the highest bias field was 6 orders of magnitude greater than that of the dry bone, and the DC conductivity of the wet bone was 4-6 orders of magnitude higher (Fig. 3). The dielectric constant and loss tangent of the dry bone were much smaller, and the frequency dependence weaker than those of the moist bone, as illustrated in Fig. 5.

Discussion

The differences in the behavior of the moist and dry bone depend upon the bonding between the collagen of the bone and water. These bonds are very weak as shown by the ease of evaporation of water from the bone by vacuum at ambient temperature. The strong dependence of the pyroelectric coefficient of moist bone on the bias electric field is caused by the orientational mobility of the water molecules with their large dipole moments. By contrast, the large polar collagen molecules cannot be easily reoriented, and the pyroelectric coefficient of dry bone is field-independent. The dielectric properties show similar effects. The dielectric constant of moist bone is large and shows significant frequency dispersion because of the mobility of the water molecules, but the dried material has a low dielectric constant and little frequency dependence.

The complex heterogeneous structure of bone makes a quantitative interpretation of the results difficult. However, the strong sensitivity of the pyroelectric effect to small bias fields and the presence of many sources of fields in living biological systems suggests that this effect may be of major biological significance.

Acknowledgements

We thank the Israel Ministry of Absorption and the Basic Research Foundation of the Israel Academy of Sciences and Humanities for the support of this research.

References

[1] S. B. Lang, "Pyroelectric effect in bone and tendon," Nature, vol. 212, pp. 704-705, 1966.

[2] S. B. Lang, "Pyroelectricity: Occurrence in biological materials and possible physiological implications," Ferroelectrics, vol. 34, pp. 3-9, 1981.

[3] H. Athenstaedt, "Pyroelectric and piezoelectric properties of vertebrates," Ann. N.Y. Acad. Sci., vol. 238, pp. 68-94, 1972.

[4] H. Athenstaedt, "Epidermis of animals and plants as a pyroelectric detector and transducer," Jpn. J. Appl. Phys. (Suppl.), vol. 24-2, pp. 302-304, 1985.

[5] H. Athenstaedt, "Pyroelectric behaviour of integument structures and of thermo-, photo- and mechanoreceptors," Anat. Entwickl.-Gesch., vol. 136, pp. 249-271, 1972.

[6] H. Athenstaedt, "Pyroelectric polarization in cells, tissues and organs of plants," Z. Pflanzenphysiol., vol. 68, pp. 89-91, 1972.

[7] S. B. Lang and H. Athenstaedt, "Anomalous pyroelectric behavior in the leaves of the palm-like plant *Encephalartos Villosus*," Ferroelectrics, vol. 17, pp. 511-519, 1978.

[8] M. Simhony and H. Athenstaedt, "Measurement of the pyroelectric coefficient and permittivity on rhododendron and encephalartos leaves and on the insect *Periplaneta Americana*," Biophys. J., vol. 29, pp. 331-338, 1980.

[9] H. Athenstaedt and H. Claussen, "Evidence for pyroelectric and piezoelectric sensory mechanisms in the insect integument," Biophys. J., vol. 35, pp. 365-374, 1981.

[10] H. Athenstaedt, H. Claussen and D. Schaper, "Epidermis of human skin: Pyroelectric and piezoelectric sensor layer," Science, vol. 216, pp. 1018-1020, 1982.

[11] D. A. Chakkalakal, "Mechanoelectric transduction in bone," J. Mater. Res., vol. 4, pp. 1034-1046, 1989.

[12] S. Singh and J. L. Katz, "Electromechanical properties of bone: A review," J. Bioelectr., vol. 7, pp. 219-238, 1988-89.

[13] G. W. Hastings and F. A. Mahmud, "Electrical effects in bone," J. Biomed. Eng., vol. 10, pp. 515-521, 1988.

[14] G. W. Hastings and F. A. Mahmud, "The electromechanical properties of fluid-filled bone: A new dimension," J. Mater. Sci.: Mater. Med., vol. 2, pp. 118-124, 1991.

[15] A. G. Chynoweth, "Dynamic method for measuring the pyroelectric effect with special reference to barium titanate," J. Appl. Phys., vol. 27, pp. 78-84, 1956.

[16] J. D. Kosterich, K. R. Foster and S. R. Pollack, "Dielectric permittivity and electrical conductivity of fluid saturated bone," IEEE Trans. Biomed. Eng., vol. BME-30, pp. 81-86, 1983.

[17] N. M. Bezdetny, V. E. Khutorsky and A. K. Zeinally, "Polarization distribution in ferroelectrics calculated by regularization method from pyroelectric measurements," Ferroelectrics, vol. 46, pp. 267-273, 1983.

[18] S. B. Lang, "Laser intensity modulation method (LIMM): Experimental techniques, theory and solution of the integral equations," Ferroelectrics, vol. 118, pp. 343-361, 1991.

[19] M. E. Lines and A. M. Glass, Principles and Applications of ferroelectrics and Related Materials. Oxford: Clarendon Press, 1977.

A PLZT OPTICAL PHASE MODULATOR AND ITS APPLICATIONS

Feiling Wang and Gene H. Haertling
Department of Ceramic Engineering
Clemson University
Clemson, South Carolina 29634-0907

An electrooptic phase modulator was designed and fabricated by using the quadratic electrooptic effect of PLZT ceramic of composition 10/65/35. The modulator can be operated at either the fundamental or double frequency of the AC signal driver. The modulator proved effective as a phase modulation device in a phase-detection measurement of small birefringent shift of thin film materials. The principles for such usage are discussed.

Introduction

Relaxor ceramic materials in the $(Pb,La)(Zr, Ti)O_3$ (PLZT) system are known to possess strong quadratic or slim-looped transverse electrooptic effects[1]. The applications of the materials in optical area have been found in light shutters, spatial light modulators, second harmonic generation as well as waveguide devices such as total internal reflection switches[2,3]. Although single crystal materials that possess linear electrooptic effects such as $LiNbO_3$ and KDP have traditionally been the primary material group for optical phase modulation, polycrystalline PLZT ceramics which possess quadratic electrooptic effects can also be used as optical phase modulation media. In this report, an optical phase modulator made from a hot-pressed PLZT ceramic is presented. The application of the modulator in a phase-detection technique for the measurements of small optical phase retardation in thin film materials is discussed.

Design and Operation

A bulk 10/65/35 PLZT wafer was chosen as the modulating medium. The material was made with a hot pressing process using stoichiometric powder derived from a water-soluble precursor. The material was transparent and showed typical dielectric properties for the material in this composition, i.e. high dielectric constant and very slim hysteresis loop. The electrooptic characterization showed that the dependence of the birefringence shift on the external electric field was primarily quadratic, as presented in Figure 1. The thickness of the PLZT wafer was 0.5 mm (20 mil) with both sides being optically polished. To accommodate the ac driving signal, copper planar electrodes were fabricated on one side of the material by a photolithography technique. The electrode gap width was 50 μm, which allowed a light beam to pass the device without a special focusing effort. An ac electric signal of adjustable amplitude was fed to the electrode pair to drive the modulator. In addition, an adjustable dc bias was also applied to the modulator.

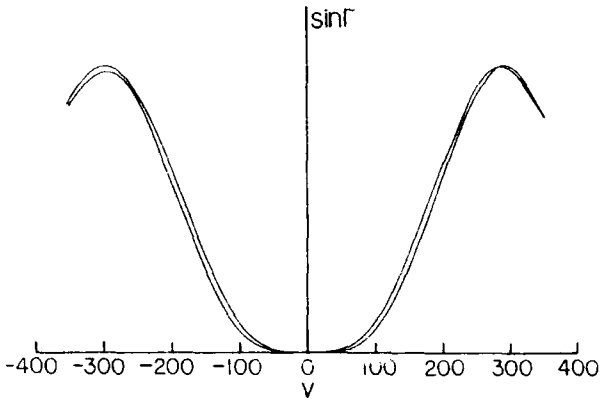


Figure 1 The electrooptic response of a 10/65/35 PLZT ceramic, measured by means of a phase-detection scheme. The Y axis is proportional to sinΓ with Γ being the optical phase shift due to the birefringence of the material.

Under sufficiently small external field, the field-induced birefringent shift of the material can be expressed as a quadratic function of the applied field:

$$\Delta n = \text{constant}\,(E_b + E\sin\Omega t)^2\,, \qquad (1)$$

where E_b is the field strength of the dc bias, Ω is the frequency of the ac driving electric field. It is obvious that under a non-zero bias field, the phase shift generated by the modulator contains both Ω and 2Ω components. By adjusting the bias field E_b, the relative amplitude of Ω and 2Ω components can be altered. The function of the bias field in changing the primary modulating frequency is illustrated in Figure 2 where function $\Gamma(t)$ is the phase retardation produced by the modulator.

To visualize the phase modulating function of the modulator and the interchange of the modulating frequency with the bias electric field, the modulator was sandwiched between two crossed polarizers with the modulation axis, the direction of the applied electric field, being oriented at 45 degree angle with respect to the polarization direction of the polarizer. With such a arrangement the polarization state of the originally linearly polarized light beam was periodically changed due to the phase shift $\Gamma(t)$ imposed by the modulator. The intensity of the light output I(t) is given by:

$$I(t) = B\sin^2[\Gamma(t)/2] = B\sin^2[A(E_b + E\sin\Omega t)^2]\,, \qquad (2)$$

CH3080-0-7803-0465-9/92$3.00 ©IEEE

where A and B are two system constants. The waveform of the light intensity given by Equation (2) is graphically analyzed in Figure 2. As shown by the figure, the modulation is purely 2Ω in frequency at zero bias and gradually becomes dominated by the Ω component with the increase of the bias electric field.

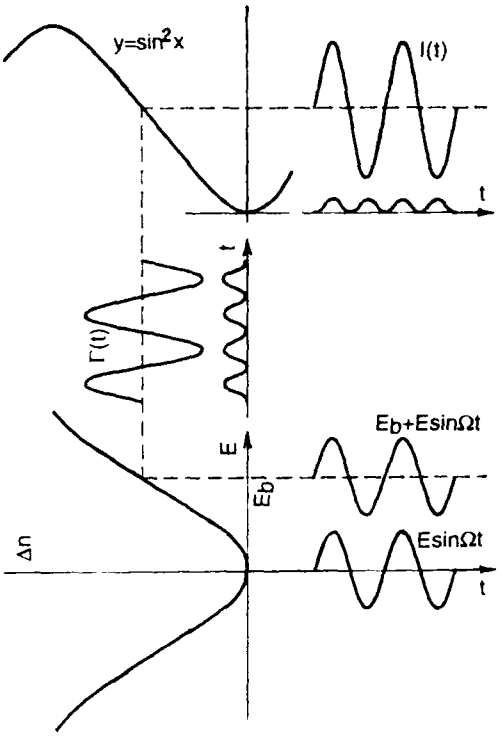


Figure 2 A graphic analysis of the operation modes of the PLZT phase modulator with and without dc bias field.

According to Equation (1), the modulation always contains a 2Ω component although its relative magnitude becomes very small compared to the Ω component when a sufficient bias field is applied. A pure Ω modulation mode can actually be achieved by using the saturation behavior in the electrooptic response of the material. The saturation behavior of the electrooptic response in PLZT materials have been observed[4,5]. In the presence of such saturation, the quadratic relation for the field-induced birefringence is no longer adequate; higher order terms or entirely new functional dependence needs to be used. In the electrooptic response curve that shows saturation behavior, there must be a point where the second derivative of the curve is zero. If a bias electric field is applied to this point, the modulation will be purely Ω in frequency.

In practice, only a fairly low bias field is needed in order for the modulation at 2Ω frequency to become insignificant compared to the Ω component. Figure 3 shows the waveforms of the light output, recorded by an oscilloscope, from the second polarizer with the PLZT modulator driven by a 1kHz ac signal operating under various dc bias voltage. The square waves in the pictures are the trigger signal synchronized with the ac driving voltage. As expected, the modulation was purely 2Ω in frequency under zero bias and eventually became dominated by Ω frequency components under a bias voltage of 150 volts. Components of both frequencies are clearly represented under an intermediate bias, as shown by Figure 3(b). The relative amplitude of modulation at both frequencies as functions of the dc bias was measured by a lock-in amplifier synchronized with the driving function generator. As shown in Figure 4, with the increase of the dc bias voltage, the amplitude of the 2Ω component decreased while the Ω component increased. Under a bias voltage of approximately 120 volts the 2Ω component becomes zero while the Ω component approaches a maximum. Under this bias voltage, the PLZT modulator provides

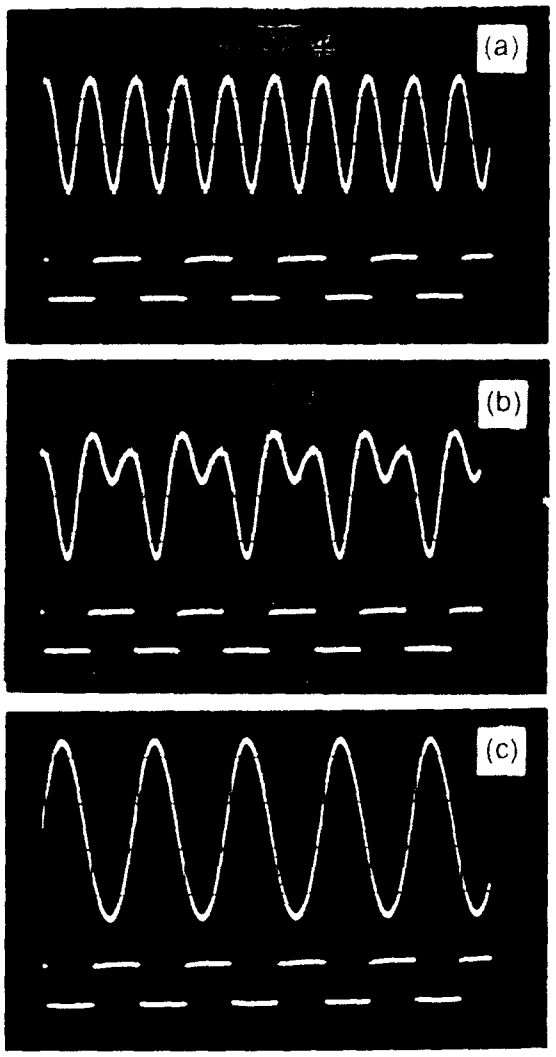


Figure 3 The waveforms of the output light modulated by the PLZT phase modulator operated under (a) bias=0V, (b) bais=20V and (c) bias=150V.

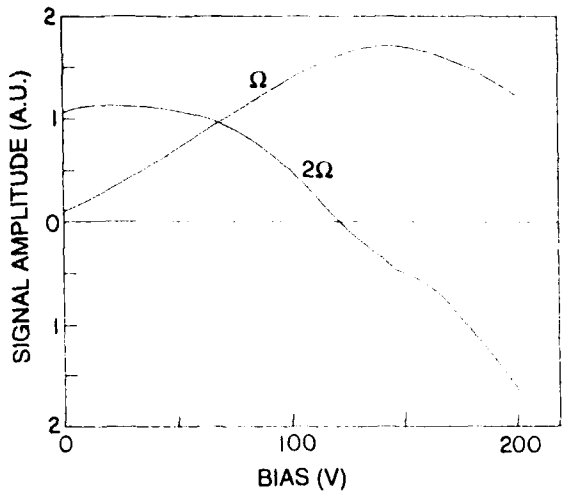


Figure 4 The Ω and 2Ω frequency components in the light modulated by the PLZT phase modulator plotted as functions of the bias voltage.

the same modulation as that from a traditional modulator utilizing the linear electrooptic effect of single crystals, except that there is a constant phase shift. The constant phase shift can be compensated with an optical compensator in applications where it is not desirable. Much lower ac driving voltages are needed to achieve the same phase modulation depth for the PLZT modulator than for traditional modulators because of the strong quadratic electrooptic effect in the PLZT ceramic.

Applications

The PLZT phase modulator has been successfully used as a phase modulation device in a phase-detection scheme for the measurement of small birefringences of thin film materials. The optical arrangement for such application is shown in Figure 5. The PLZT compensator together with an optical compensator and the sample to be measured are sandwiched between two crossed polarizers. The modulating axis of the modulator is oriented 45 degrees with respect to the polarizer but parallel (or perpendicular) to the principle optical axes of the sample determined by the direction of the external electric field. The purpose of the compensator is to compensate the constant phase shift generated by the modulator and to calibrate the system.

With the PLZT phase modulator being driven by an ac signal of frequency Ω under zero bias, the total phase retardation for the light polarized along the modulating axis consists of contributions from all three components, namely, modulator, compensator and sample:

$$\Gamma = \Gamma_{mod.} + \Gamma_{comp.} + \Gamma_{samp.} \qquad (3)$$

As been previously pointed out, the electrooptic effect of PLZT materials exhibits high order field dependence and saturation behavior in some circumstances. The phase modulation produced by the PLZT modulator, therefore, should be expressed by the following Fourier series:

$$\Gamma_{mod.}(t) = \text{constant} + \sum_{m=1}^{\infty} C_m \sin 2m\Omega t\,, \qquad (4)$$

where coefficient C_1 is proportional to the quadratic electrooptic coefficient of the PLZT modulating medium; C_2 is proportional to the quartic electrooptic coefficient, etc. Although in most instances only C_1 needs to be considered, the whole summation in Equation (4) is retained for the strictness of the following discussion.

By adjusting the compensator, the constant in Equation (4) can be eliminated; therefore we have

$$\Gamma(t) = \sum_{m=1}^{\infty} C_m \sin 2m\Omega t + \Gamma_{samp.} \qquad (5)$$

The light intensity detected by the photomultiplier tube (PMT) is therefore given by

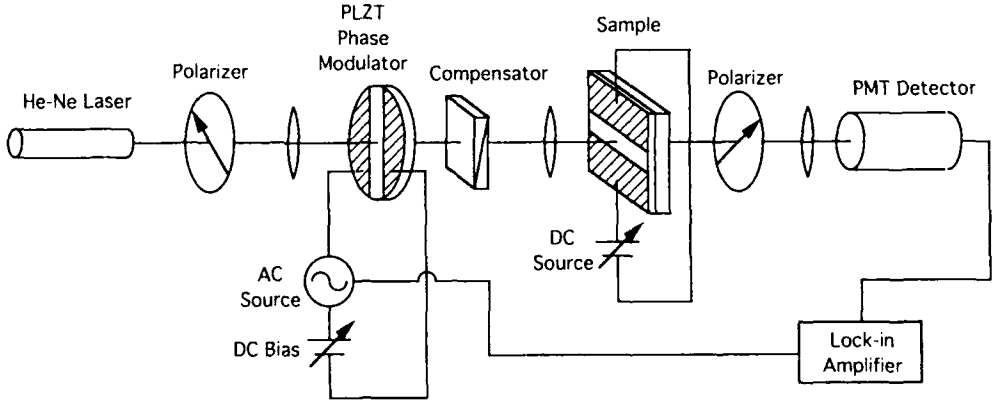


Figure 5 The optical arrangement in a phase-detection scheme using the PLZT modulator as a phase modulating device.

$$I(t) = I_o \sin^2(\Gamma/2)$$

$$= (I_o/2)[1 + \cos(\sum_{m=1}^{\infty} C_m \sin 2m\Omega t + \Gamma_{samp.})]. \quad (6)$$

If the reference signal of the lock-in amplifier is chosen as $\sin 2\Omega t$, the output signal of the lock-in amplifier, S, is proportional to the amplitude of the $\sin 2\Omega t$ term in the Fourier expansion of Equation (6), that is

$$S = D \int_0^t I(t) \sin 2\Omega t \, dt$$

$$= D \int_0^t \cos(\sum_{m=1}^{\infty} C_m \sin 2m\Omega t + \Gamma_{samp.}) \sin 2\Omega t \, dt \quad (7)$$

where D is a system constant. It can be shown that the above integration is approximately given by

$$S = D J_1(C_1) \sin\Gamma_{samp.} \quad (8)$$

where J_1 is the Bessel function of the first order. With a fixed driving signal amplitude, C_1 is a constant; the output signal from the lock-in amplifier therefore is proportional to the phase retardation generated by the sample, namely, $\Gamma_{samp.}$. Moreover, in detecting the electrooptic effect of thin film materials, the phase retardation of the sample is usually very small so that the output from the lock-in amplifier becomes directly proportional $\Gamma_{samp.}$ while the proportional constant can be determined by the compensator.

With the PLZT phase modulator, the above scheme has proven an effective way of detecting very small phase retardations produced by electrooptic effects in thin film materials. As an example, Figure 6 shows the birefringence versus E-field curve of a 2/55/45 thin film of 0.5 μm thick grown on a fused silica substrate, measured with the above phase-detection system under zero-bias mode.

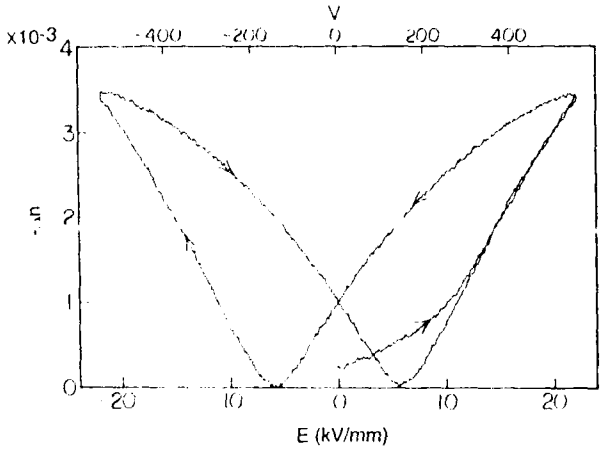


Figure 6 The birefringence versus E-field curve for a 2/55/45 PLZT thin film of 0.5 μm thickness sputter-deposited on a fused silica substrate, measured with the phase-detection scheme using the PLZT phase modulator.

When an appropriate bias field is applied, the modulation becomes predominated by the Ω component. With the reference signal of the lock-in amplifier set at $\sin\Omega t$, the above measuring system functions similarly as in the zero-bias mode.

Conclusions

An optical phase modulator was made by using the quadratic electrooptic effect of a hot-pressed PLZT ceramic. The device can be operated in a zero-bias mode which provides a modulation at double the frequency of the driving signal. When an appropriate bias is applied, the modulator provides a modulation dominated by the component at the frequency of the driving signal. Application of the PLZT modulator has been found in the phase-detection scheme for the measurement of very small birefringence in thin film materials.

References

[1] G.H. Haertling and C.E. Land, "Hot-pressed $(Pb,La)(Zr,Ti)O_3$ Ferroelectric Ceramic for Electronic Applications," J. Am. Ceram. Soc. 54, 1(1971)

[2] G.H. Haertling, "PLZT Electrooptic Materials and Applications-A Review," Ferroelectrics, 75, 25(1987)

[3] H. Higashino, T. Kawaguchi, H. Adachi, T. Makino and O. Yamazaki, "High Speed Optical TIR Switches Using PLZT Thin Film Waveguides in Sapphire," Japan. J. Appl. Phys. 24 suppl., 284(1985)

[4] F. Wang and A.Y. Wu, "Electro-optical and Nonlinear Optical Properties of Thin Film Materials Containing Oxygen-Octahedra under High DC Electric Field," Proc. 7th Intern. Symposium on the Application of Ferroelectrics, pp.131-134, Urbana, IL, June 6-8, 1990.

[5] G.H. Haertling, unpublished results.

MODEL OF ELECTROOPTIC EFFECTS BY GREEN FUNCTION AND SUMMARY REPRESENTATION:APPLICATIONS TO BULK AND THIN FILM PLZT DISPLAYS AND SPATIAL LIGHT MODULATORS

A. Y. Wu,[a] Tom C. C. Chen,[b] and H. Y. Chen[b]

[a]Center for High Technology Materials and
[b]Department of Electrical Engineering and Computer Engeering
University of New Mexico
Albuquerque, New Mexico 87131

Field distributions and electrooptic effects in ceramic bulk and thin film materials have been calculated using summary representation method. The method has been used to treat problems in PLZT bulk and thin film displays/spatial light modulators.

Introduction

For the purpose of understanding the electrooptic effects in electrooptic single crystals or ceramic materials, it is necessary to know the optimum field distribution and the accurate determination of electrooptic parameters including the half-wave voltage applied so that accurate electrooptic coefficients can be obtained. For this purpose, we have used three computational methods: Green function, iteration, and summary representation. The methods of Green function and iteration are familiar to trained researchers, but the method of summary representation is a rather new method and we will explain its fundamental concept and demonstrate its powerful use. The results of our analysis of electrical field distribution and electrooptic effects in PLZT will be presented. The general concept and method can be applied to other dielectric or electrooptic materials.

The Method of Summary Representation

The technique for solving Laplace's equation in finite difference form in a rectangular region known as the method of summary representation allows the numerical values of the potentials along any vertical line in the interior of any material to be immediately written down in terms of simple matrix operations providing the potentials on the boundaries are known. Most finite difference techniques result in a large system of simultaneous equations which must be solved. The technique described here does not require any solution of simultaneous equations which means that the amount of calculation required to obtain numerical solutions to a particular problem is greatly reduced. Furthermore, the technique allows the computation of only selected points on a prescribed topological grid so that complete solution at all the grid points is not required. Polozhii [1] discusses the basic theory of this technique and shows how to apply it to a wide variety of partial differential equations. Basically what Polozhii has done is to reduce the solution of the Poisson's (Laplace's) equation on a prescribed rectangular grid with specified boundary conditions to a unique set of values which are determined in terms of unknown matrices which depend upon the boundary conditions. This is analogous to the classical separation of variables technique in which the solution is known immediately for a given problem in terms of a Fourier expansion of the boundary conditions. The finite difference grid employed in the technique is rectangular as shown in Figure 1. The spacing between horizontal grid lines is ΔY and between vertical grid lines is ΔX. The location of a particular vertical line is given by the value of i and the location of a particular horizontal line is given by the value of k. The i=0 and $i=i_{max}=m+1$ lines are the vertical boundaries and the k=0 and the $k=k_{max}=n+1$ lines are the horizontal boundaries of the region. The boundary conditions used here consist of known potentials along these boundary lines. Polozhii describes boundary conditions which contain partial derivatives of the values along the boundary. The solution at all the interior grid points is expressed in terms of an n-element vector, U(i), along the vertical lines. For all the situations described here, it will be assumed that the boundary conditions on the horizontal lines are zero. This is not a fundamental restriction, but is done to simplify the expressions. The geometry of the grid defines the following terms which appear in the solution. These terms come from the solution of the second order difference equation which describes the specific problem in question:

$$\gamma=\Delta X/\Delta Y;\quad \eta_k=1+\gamma^2(1-\cos[k\pi/(n+1)]);\quad \mu_k=\eta_k+\sqrt{\eta_k^2-1};\quad \nu_k=\eta_k-\sqrt{\eta_k^2-1}. \tag{1}$$

The solution for U(i), in terms of the boundary conditions on the two vertical lines is given by:

$$[U(i)]=[A_1(i)][U(0)]+[B_1(i)][U(m+1)],$$
$$[A_1(i)]=[P][\lambda(i)][P],$$
$$[B_1(i)]=[P][\beta(i)][P],$$
$$\lambda_k(i)=(\mu_k^{m+1-i}-\nu_k^{m+1-i})/(\mu_k^{m+1}-\nu_k^{m+1}) \tag{2}$$
$$\beta_k(i)=(\mu_k^{i}-\nu_k^{i})/(\mu_k^{m+1}-\nu_k^{m+1})$$
$$P(i,k)=\sqrt{2/(n+1)}\sin[ik\pi/(n+1)]$$

The P matrix or P transform operation is an nxn square matrix which is defined in such a way that [P][P]=[I] and $[\lambda(i)]$ and $[\beta(i)]$ are diagonal matrices.

As previously stated, the solutions in (2) are for the Laplace's equation in a region where there are zero field boundary conditions on the horizontal lines. For the Poisson's equation with non-zero horizontal boundary conditions, there should be an additional matrix term in (2).

Homogeneous Interface

We will analyze the case that there is one interface between two regions having the same permittivity. The method can be easily extended to case where there is non-homogeneous interface. In the homogeneous interface case, as shown in Figure 2, the vertical line is labeled as number i in region 1 and number i' in region 2. The interface line is the number m+1 line in region 1 and number 0' line in region 2. Along the interface line, the continuity of the potential between the two regions is assured, but there is an additional requirement, that is, the value along the grid points on the interface must satisfy the Laplace's equation in the finite difference form, with the grid points along the two vertical lines immediately adjacent to the interface lines. Note that these two lines are the number m line in region 1 and the number 1' line in region 2.

The formula of the 5-point finite difference approximation [2] for the Laplace's equation can now be written down explicitly, assuming unequal grid spacings, as follow:

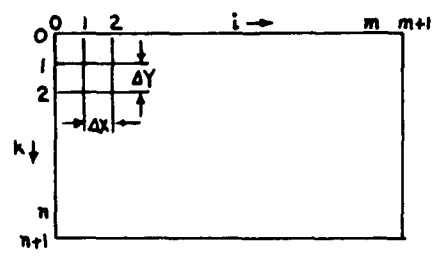


Figure 1

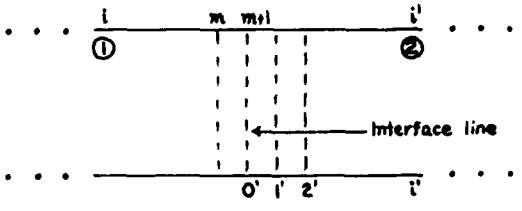
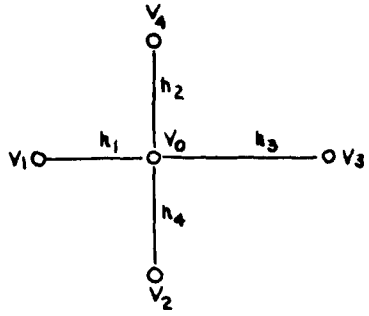


Figure 2

CH3080-0-7803-0465-9/92$3.00 ©IEEE

$$[1/h_1h_3 + 1/h_2h_4]V_0 = V_1/h_1(h_1+h_3) + V_2/h_2(h_2+h_4) + V_3/h_3(h_1+h_3) + V_4/(h_4h_2+h_4) \quad (3)$$

where all variables are defined in Figure 3. For the case considered here, the spacing h_2 and h_4 are equal and is the same as Y defined earlier. By choosing h_1 as ΔX_1 and h_3 as ΔX_2, three values of γ can be defined as



$$\gamma_1 = \Delta X_1/\Delta Y; \quad \gamma_2 = \Delta X_2/\Delta Y; \quad \gamma_3 = \Delta X_1/\Delta X_2.$$

$$V_0 = \frac{\gamma_2}{(\gamma_1+\gamma_2)(1+\gamma_1\gamma_2)}V_1 + \frac{\gamma_1}{(\gamma_1+\gamma_2)(1+\gamma_1\gamma_2)}V_3 + \frac{\gamma_1\gamma_2}{(1+\gamma_1\gamma_2)(\gamma_1+\gamma_2)}(V_2+V_4) \quad (4)$$

for $\gamma_1=\gamma_2=1$, it can be seen that (4) reduces to the standard 5-point stencil expression for the Laplace's equation. Now using the [T] matrix defined by Polozhii, equation (4) can be put into a matrix form relating [U(0')], [U(m)] and [U(1')]:

$$[U(o')] = (r_1r_2/2(1+r_1r_2))[T][U(o')] + (r_2[U(m)] + r_1[U(1')])/(r_1+r_2)(1+r_1r_2)$$

$$[T] = \begin{bmatrix} 0 & 1 & 0 & . & . & . & & & \\ 1 & 0 & 1 & . & . & & & & \\ 0 & 1 & 0 & 1 & . & . & . & & \\ & & & & & & 1 & 0 & 1 \\ & & & & & & 0 & 1 & 0 \end{bmatrix} \quad (5)$$

Note that the [T] matrix provides the coupling to all the elements along the interface line.

Nonhomogeneous interface

The dielectric discontinuity between region 1 and 2 requires $\alpha=\epsilon_1/\epsilon_2$ and the continuity of the normal component of the flux dinsity for $\epsilon\partial U/\partial X$ must be satisfied.

The Boundary Values for Different Interface

We assume that when the boundary potential of a rectangular region is known, the interior potential distribution can be obtained and that once the boundary values are fixed, the interior distribution will be the same despite of the materials inside the boundary. We also assume that any film over-coated on the surface of PLZT wafer, whether the film is PLZT, glass, or any other high permittivity materials, can change the boundary potential completely, provideing that the film is thicker than the thickness of electrodes. Because PLZT wafer is much thicker than the coated film, we will assume that the film can only change the interface potential but contribute very little to the optical retardation.

One Layer Electrodes with Nonhomogeneous Interface

Two cases will be considered:

(1). Electrodes on one side of the wafer, without over-coated film, and
(2). Electrodes on one side of the wafer, with over-coated film but the film is not PLZT.

We now define the symbols shown in Figure 2 in our calculations:

l: the thickness of PLZT.

l': the distance from the interface to the zero potential of the vertical boundary, where $l'=\gamma_3 l$ and $\gamma_3=100$.

$[X_1]$ and $[X_2]$: interfacial potential for the ($[k_{max}-1]$-element vector)

M direction: Calculated from the interface of region 1 and region 2 to another interface from 0 to i_{max}. The vertical line next to the interface $[X_1]$ is indicated by M=1, and the vertical line next to the interface $[X_2]$ is indicated by $M=m=i_{max}-1$.

M' direction: in order to simplify the calculation, we have chosen the point number in the M' direction the same as the number in the M direction from 0 to i_{max}.

k direction: calculated from the top horizontal boundary to the bottom horizontal boundary from 0 to k_{max}.

$[A_1(m)]$: the potential of the vertical line in region 2 next to the interface $[X_1]$ at M'=m.

$[B_1(m)]$: the potential of the vertical line in region 2 next to the interface $[X_1]$ at M=1.

$[A_2(m)]$: the potential of the vertical line in region 2 next to the interface $[X_2]$ at M=m.

$[B_2(1)]$: The potential of the vertical line in region 3 next to the interface $[X_2]$ at M'=m.

It is clear that $[A_1(m)]=[B_1(1)]$ and

$[A_1(1)]=[B_1(m)]$,
$[A_1(m)]=[B_1(m)][X_1]$,
$[B_1(1)]=[A_1(1)][X_1]+[B_1(1)][X_2]=[B_1(m)][X_1]+[B_1(1)][X_2]$,
$[A_2(m)]=[A_1(m)][X_1]+[B_1(m)][X_2]=[B_1(1)][X_1]+[B_1(m)][X_2]$,
$[B_2(1)]=[B_1(m)][X_2]$,
$[X_1]=(\alpha/(\gamma_3+\alpha))[A_1(m)]+(\gamma_3/(\gamma_3+\alpha))[B_1(1)]$,
$[X_2]=(\gamma_3/(\gamma_3+\alpha_1))[A_2(m)]+(\alpha_1/(\gamma_3+\alpha_1))[B_2(1)]$,

where $\alpha=\epsilon_1/\epsilon_2$, and $\alpha_1=\epsilon_3/\epsilon_2$ and ϵ_1 is the permittivity of air or coated film. By choosing $\gamma_3=1$ we have

$[X_2]=(1/(1+\alpha_1))[B_1(1)][X_1]+(1/(1+\alpha_1))[B_1(m)][X_2]+(\alpha_1/(1+\alpha_1))[B_1(m)][X_2]=(1/(1+\alpha_1))[B_1(1)][X_1]+[B_1(m)][X_2]$,
$[X_2]=(1/(1+\alpha_1))([I]-[B_1(m)])^{-1}[B_1(1)][X_1]=[B11][X_1]$,
$[B11]=(1/(1+\alpha))([I]-[B_1(m)])^{-1}[B_1(1)]$,
$[X_1]=(\alpha/(1+\alpha))[B_1(m)][X_1]+(1/(1+\alpha))[B_1(m)][X_1]+(1/(1+\alpha))[B_1(1)][X_2]=[B_1(m)][X_1]+(1/(1+\alpha))[B_1(1)][X_2]=[B_1(m)][X_1]+(1/(1+\alpha))[B_1(1)][B11][X_1]$,
$([I]-[B_1(m)]-(1/(1+\alpha))[B_1(1)][B11])[X_1]=0$.

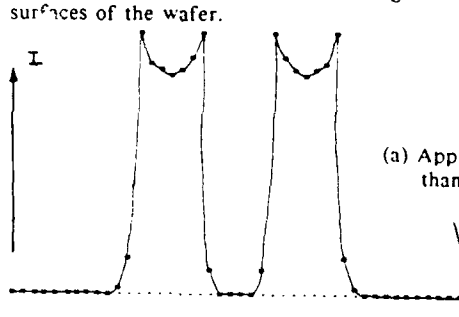
These equations have been programed and solved by using IBM/VSPC system at the University of New Mexico. After $[X_1]$ and $[X_2]$ were obtained, each value on the vertical line inside PLZT wafer can be calculated by the method of summary representation. The methods presented above have been applied to the following cases with more complicated interface structures: **Electrodes on one side of PLZT wafer with over coated PLZT film: Electrodes on Both Wafer Surfaces with Non-homogeneous Interface** (i.e. electrodes on both wafer surfaces without overcoated films, and electrodes on both wafer surfaces with overcoated films but the films are not PLZT); and **Electrodes on both PLZT Wafer Surfaces Over-Coated with PLZT Films**. We will not elaborate all the formalism here but instead present only the final results.

Results

In all the results, except otherwise specified, we have assumed that PLZT has the R coefficient of 1.5×10^{-16} m^2/V^2 and the wavelength of the light is 5000 Å.

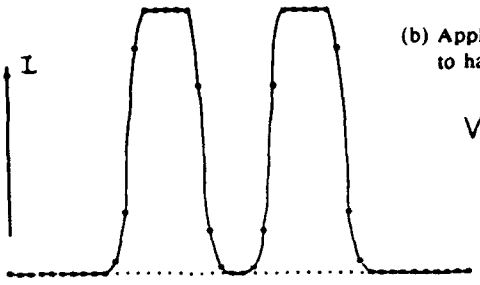
(1) **Transmitted Light Intensity Distribution under crossed polarizers,**

In this case, wafer thickness is 70 μm, electrode width is 50 μm, electrode gap is 50 μm, three interdigital electrodes are on both surfaces of the wafer.



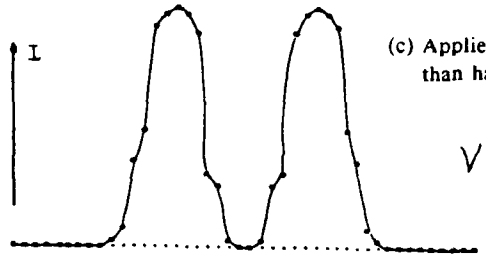
(a) Applied voltage is smaller than half wave voltage.

$V = 132$ Volts $< V_{N2}$



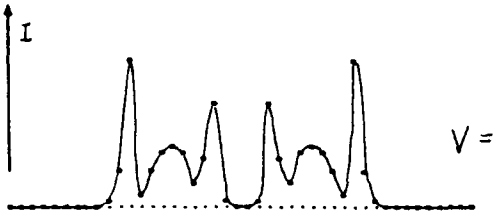
(b) Applied voltage is equal to half wave voltage.

$V = 154$ Volts
$= V_{\lambda/2}$



(c) Applied voltage is larger than half wave voltage.

$V = 170$ Volts



$V = 200$ Volts

(2) **Half Wave Voltages**

In this case, PLZT wafer is 625 μm thick, electrode width is 50 μm and electrode gap is 50 μm. Since l_{max} we chose is only 36 points, the calculated half wave voltages my not be very accurate.

(a) Three electrodes are on one side of wafer.

$V_{\lambda/2} = 259$ Volts

(b) Three electrodes are on both sides of wafer.

$V_{\lambda/2} = 183$ Volts

(c) Three electrodes are on one side of wafer, over-coated with PLZT film.

$V_{\lambda/2} = 174$ Volts

(d) Three electrodes are on both sides of wafer, over coated with PLZT films.

$V_{\lambda/2} = 123$ Volts

(3) **Half Wave Voltage in Thick and Thin Films**

(a) Three electrodes on one side of thin film of 75 μm thick. over-coated with PLZT. The gap is 5 μm and the width is 10 μm.

$V_{\lambda/2} = 53$ Volts

(b) Three electrodes on two sides of thin film of 75 μm thick. not over-coated with PLZT. The gap is 5 μm and the width is 10 μm.

$V_{\lambda/2} = 52$ Volts

(c) Three electrodes on two sides of thin film of 75 μm thick. both sides over-coated with PLZT. The gap is 5 μm and the width is 10 μm.

$V_{\lambda/2} = 37$ Volts

(d) Three electrodes on thin film of 3 μm thick, not over-coated. The gap and width are 10 μm.

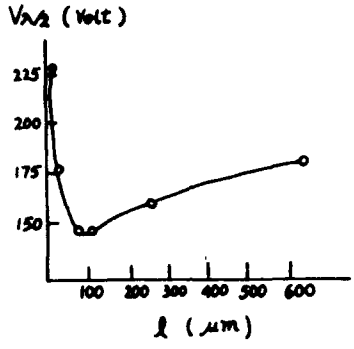
$V_{\lambda/2} = 103$ Volts

(e) Three electrodes on one side of thin film of 10 μm thick, not over-coated. The gap and width are 10 μm.
Three electrodes on thin film of 3 μm thick.

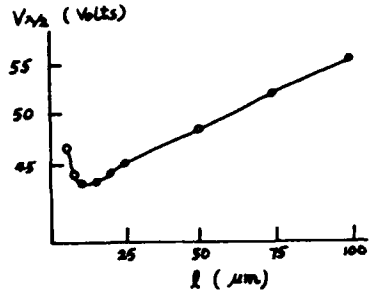
$V_{\lambda/2} = 89$ Volts

(4) **Half Wave Voltage as a Function of PLZT Thickness**

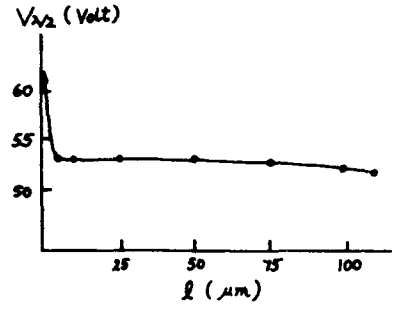
(a) g=w=50 μm, three electrodes on one surfaces.



(b) g=5 μm, w=10 μm, three electrodes on both surfaces.

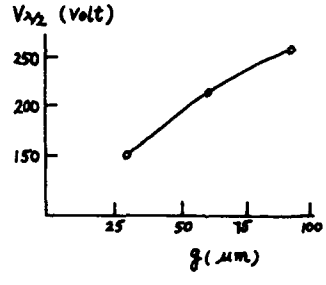


(c) g=5 μm, w=10 μm, three electrodes on one surface, over-coated with PLZT thin film.



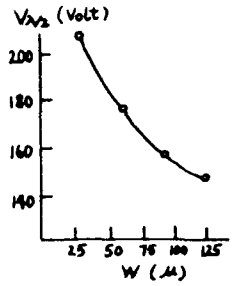
(5) **Half Wave Voltage as a Function of Electrode Gap**

In this case w= 50 μm, l = 625 μm, three electrodes on both surfaces of wafer.



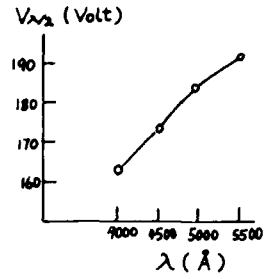
(6) Half Wave Voltage as a Function of Electrode Width

In this case, g=50 μm, l = 625 μm, three electrodes on both surfaces of wafer.



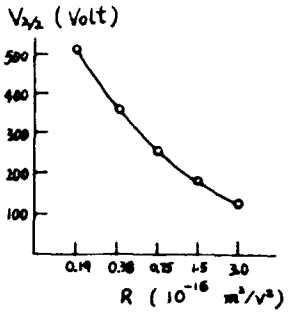
(7) Half Wave Voltage as a Function of wavelength

In this case, g = w = 50 μm, l = 625 μm, three electrodes on both surfaces of wafer.



(8) Half Wave Voltage as a Function of R Coefficient

In this case g = w = 50 μm, l = 625 μm, three electrodes on both surfaces.



CONCLUSION

There are many important and useful results from all the above figures. Most of them are self-evident, for examples: The intensity distribution in the gap is not uniform for different applied voltages; Half wave voltage decreases when there is over-coated film; the half wave voltage does not decrease indefinitely as the gap size decreases, instead, there is a turning point that it will actually increases; etc. Many results are consistent with our experimental observation and some further results will be presented elsewhere.

Acknowledgements

We would like to thank Dr. G. H. Haertling, Dr. M. D. Bradshaw, and Dr. K. Jungling for many helpful discussions. This work was supported in part by Motorola Inc., the University of New Mexico and Air Force Office of Scientific Research.

References

[1] G. N. Polozhii, "The Method of Summary Representation for Numerical Solution of Problems of Mathematical Physics", Pergamon Press, London, 1965.

[2] S. Frankel, "Multiconductor Transmission Lines Analysis", Artech House, Inc., 1977.

FIELD ENHANCEMENT AND REDUCTION AND ELIMINATION OF REMANENT LIGHT FLOW IN ELECTROOPTIC BULK AND THIN FILM DISPLAYS AND SPATIAL LIGHT MODULATORS:THEORY AND PRACTICE

A. Y. Wu

Center for High Technology Materials
University of New Mexico
Albuquerque, NM 87131

Remanent light flow is a very serious problem in electrooptic devices. It can not only degrade the contrast ratio but also shorten the lifetime of the devices. In fact, understanding and solving the remanent light flow problem in an electrooptic device may also help understanding and solving several other problems such as fatique and aging problems in other devices. Efforts have been given to examine the mechanism of the remanent light flow problem in ceramic bulk (such as PLZT) and thin film (such as PLZT, $BaTiO_3$, $LiNbO_3$, SBN, etc.) displays and spatial light modulators and effective methods of reducing and eliminating remanent light flow by using buffer and capping layer on the surface of the devices. Several very effective buffer and capping layers have been tested, they can not only reduce or eliminate the remanent light flow but also can enhance the electrooptic effect by 10 to 30%. The physical origin of the remanent light flow, the method of eliminating it, the physical origin of the electrooptic enhancement effect, and some experimental results will be presented.

Introduction

When an electrical field is applied to a pair of electrodes of an electrooptic device, some unwanted space charge will be built up as a function of time between the electrodes on the surface or inside the electrooptic material. After the applied field is removed, the space charge can creat a residual birefringence. The light intensity detected under crossed polarizers due to this unwanted birefringence is called remanent light flow. The remanent light flow is a very serious problem in electrooptic devices, particularly in ferroelectric ceramic materials, because it can not only degrade the contrast ratio but also shorten the lifetime of the devices (see Figure 1). In this paper, we will report some observations on remanent light flow problem in bulk and thin film PLZT displays or spatial light modulators. The physical origin of the remanent light flow, the method of eliminating it, and the electrooptic enhancement effect will be discussed.

Experimental and Discussion

Several causes of remanent light flow have been identified as follow:

(I) Moisture, Dust, and Surface Containmination are observed to be major causes of surface charges: For example, blowing wet air onto surface of an electrooptic device under an applied electric field can immediately creat serious remanent light flow. Some PLZT 9/65/35 displays with surface planar interdigital electrodes lose their performance quickly under the moisture test, e.g., the

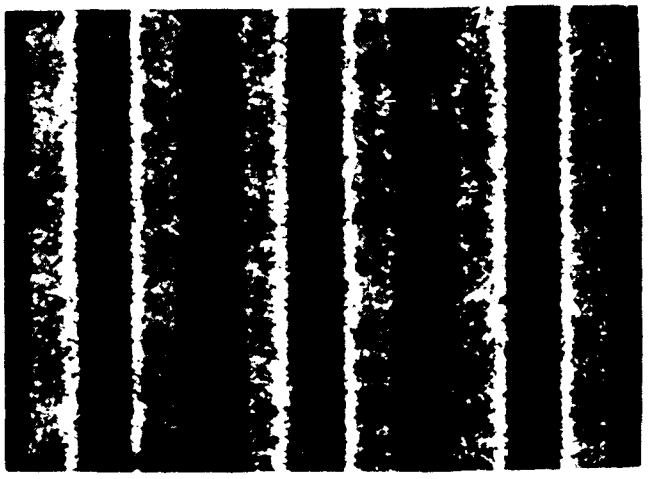


Figure 1(a). Non-uniform surface charge distribution in PLZT 9/65/35 bulk wafer. Gap = 50 μm. This type of space charge can be entirely eliminated using the coating method described in this paper.



Figure 1(b). Remanent light flow in sputtered PLZT 28/0/100 film. Gap = 8 μm.

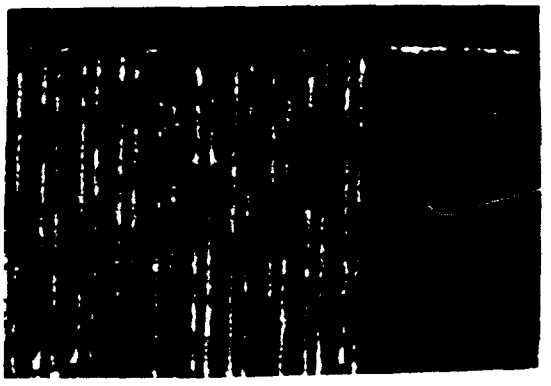


Figure 1(c). Remanent light flow in solution-coated PLZT 9/65/35 film. Gap = 10 μm.

CH3080-0-7803-0465-9/92$3.00 ©IEEE

constrast ratio may drop from 1000 down to less than 200 within a few seconds and the remanent light flow can easily be seen by eyes. The large applied electric field, commonly 1.5 kV/mm or larger, can ionize water droplet, dust and air particles, particularly near electrodes. The ionized droplet or particles can then be attracted to the ceramic surface by the force of the image charge inside the ceramic material and adhere on the surface. Unless the surface is cleaned immediately and constantly, the attracted surface charge may stay on the surface for a long time. Other containmination constantly observed is some residue on the surface from sample processing. For example, if there is a very thin layer of ITO residue on the surface, space charge distribution on the surface (caused by hopping conductivity under applied electric field) can creat non-uniformity in the light intensity under applied electric field and also very likely, remanent light flow (see Figure 1(a)).

(II) Charge injection from electrodes into ceramic material: When the surface is not clean and smooth or the material is porous (particularly, solution-coated thin films), space charge may be injected into and accumulated inside the material near the electrodes. The constrast ratio may deteriorate in only a few hours of operation.

(III) Microcracks: When PLZT devices were operated under large electric field (larger than 1.5 kV/mm), microcracks may appear on the surface, particularly, at the boundaries of ceramic grains (see Figure 2). In severe situations, individual grains on the surface were seen to "pop" out of the ceramic surface and left behind holes of the grains, particularly, near the electrode positions. It is believed that the cracks are due to stress corrosion from electrostriction. These cracks and holes are the places of remanent light flow.

(IV) Chemical Reactions: Edges of chromium electrode were seen to deteriorate fast under normal applied electric field, particularly on the positive chromium electrode. It is believed that electrochemical reaction may take place between PLZT and Cr with the assistance of moisture. One possible route is that Cr becomes chromium oxide and lead oxide is reduced to lead near the positive electrode. The surface of the "pop out' holes mentioned before all became black in color and not transparent any more, indicating some reducing chemical process, particularly in the grain boundaries. When the sample was annealed in air at 500°C, the black coloration disappeared and PLZT restored back to transparency.

(V) Impurity effect: Efforts have been made to dope PLZT 9/65/35 with about 2% of K_2O or 2% of Fe_2O_3 to intentionally increase the space charge problem in the ceramic material. Indeed, space charge problem and remanent light flow problem became even worse than the undoped samples. By appling electric field, one could see slow response of the migration of space charge inside PLZT material. This kind of space charge problem can not be cured by the coating method as will be described below. But from this experiment it is clear that in order to eliminate space charge problem in PLZT, it is necessary to eliminate some impurities such as K and Fe.

(VI) Severe Stress and Strain: Fatique caused by applied voltage larger than 1.5 kV/mm may cause permanent damage in PLZT bulk wafer. Even no microcrack is formed, remanent light flow can still be seen and it is not possible to cure this problem by thin film coating as will be described below.

Once the origin of the space charge is identified, it is possible to cure the remanent light flow problem. Four methods have been used: (1) Draining the surface charge and homogenizing or equalizing the surface potential, (2) Preventing the charge injection from happening, (3) Passivation, (4) Eliminating the space charge on the surface and inside the material by reducing impurities, pores, and other defects in the material, and (5) Avoiding applied field larger than 1.5 kV/mm. We will now describe the first three methods. But before any method is practiced on any sample, *one must be sure that the sample, particularly the sample surface, must be very clean and very well polished right at the first beginning.*

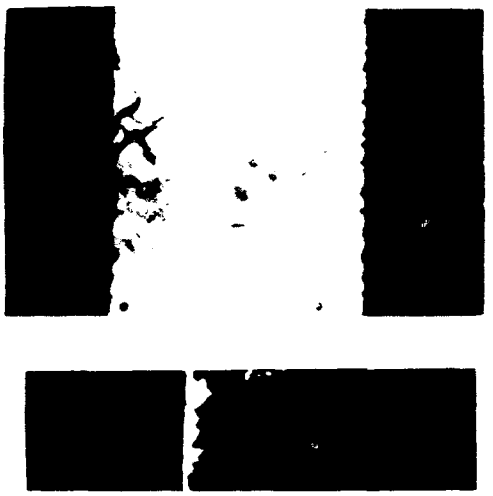


Figure 2. (a) Severe microcracks in PLZT 8.5/65/35 wafer after severe fatigue testing. Gap = 50 μm Note that "blobs" grow out of edges of Cr electrode may be chromium oxide. (b) Remanent light flow at cracked and highly-stressed regions.

Several very effective thin film coatings have been tested. Here we will discuss only five cases (Film thickness is optimized for interdigital electrode gap of 45 μm):

(a) SiO_2 films of 800 to 1000 Å thick were used as buffer layer between interdigital electrodes and PLZT material. This layer was found to be useful for treating problem (1), (2) and (3). Silimar *films were used as an overcoating layer covering the interdigital* electrodes and the PLZT material. This layer was found to be useful for treating problem (1) and (3). The films were deposited using rf magnetron sputtering at 200°C or a solution coating and firing method at 450°C from a precursor solution.

(b) TiO_2 films of 400 to 600 Å thick were used as buffer or overcoating layer. The performance is similarly to (a). The films were deposited using a solution coating and firing method at 450°C from a precursor solution.

(c) Gold films of 100 Å thick were used as overcoating layer. This layer was found to be useful for treating problem (1). The films were deposited using rf magnetron sputtering at room temperature.

(d) PLZT 9/65/35 films of 600 to 1000 Å thick were used as overcoating layer. The films were deposited using a solution coating and firing method at 650°C from a precursor solution. The result is not satisfactory.

(e) ZrO_2 films of 600 to 800 Å thick were used as overcoating layer. The films were deposited using a solution coating and firing method at 450°C from a precursor solution. The result is not satisfactory.

As can be seen, SiO_2 film is an amorphous dielectric insulator, TiO_2 film is a semiconductor with a mixed rutile and amorphous structure, the gold film is a metal, PLZT film is a ferroelectric insulator, and ZrO_2 film is a dielectric insulator with a mixed monoclinic and amorphous structure. The important question now is why some films worked but some do not? After careful testings it was found that the first three film are weakly conducting but the others are not. As can be expected, these weakly conducting films are capable of draining the unwanted surface charge and the oxide buffer layers are thick and strong enough to serve as a charge injection barrier to prevent the space charge from build-up, particularly, near the interface of the

positive electrode and PLZT. [The image of PLZT display coated with TiO_2 film is very "dynamic" as a function of time: At a fixed applied voltage above a *minimum* applied voltage, the intensity distribution is not stable and uniform but migrating and moving around, possibly due to different activation energies required to trigger different semiconducting states in different ceramic grains at different space-time. Also, field enhancement effect occur only above the minimum applied voltage.]

From device passivation viewpoint, a dielectric buffer and overcoating or capping layer is useful to prevent the moisture from attacking the device. But more insight to the remanent light flow is that coating can also provide extra support to prevent microcracks (stress corrosion) from happening and, to reduce the chemical reaction between electrodes and electrooptic material, and most interestingly, to confine and enhance the electric field in the electrooptic material so that half-wave voltage required for operating the device can be reduced. In fact, theoretical calculation from summary representation method showed that when PLZT is coated with a dielectric layer, the half-wave voltage will be reduced [1,2], but if there is a weakly conducting buffer layer between PLZT and electrodes, field line will be drawed in and bend more toward the inside of PLZT material and thus greatly enhance the field in the material and the half-wave voltage will be reduced. When the operating voltage of a device is reduced, the stress and chemical corrosion and thus the remanent light flow will also be reduced. Figure 3 shows that when a PLZT device is overcoated with or has a buffer layer made of a weakly conducting film, the half-wave voltage may be reduced by about 10 to 30%, depending on the electrical and optical properties and the thickness of the film materials. Similar to PLZT devices, observations have been made on several thin films including $BaTiO_3$, $LiNbO_3$, and SBN under high electric field. Remanent light flow in these films is again a serious problem, particularly under high operating field. But the problem can be treated in a similar fashion because physics is similar in all cases. Further results will be presented elsewhere.

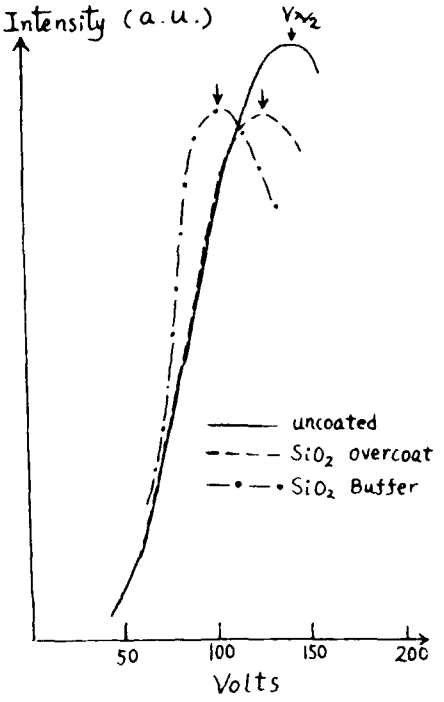


Figure 3(a). Half-wave voltage of PLZT 9/65/35 bulk wafer coated with various films.

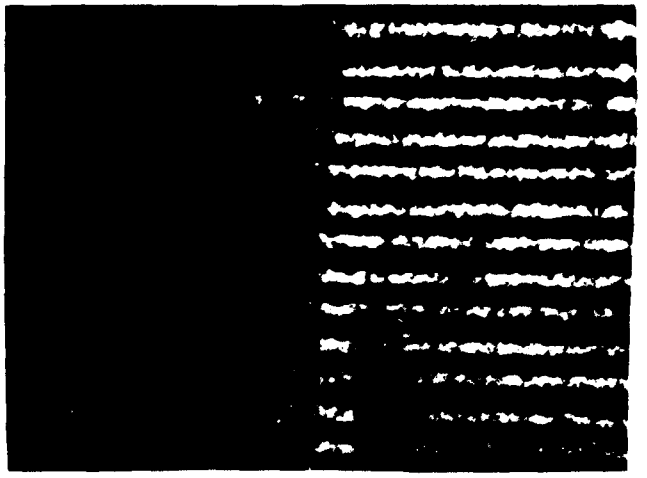


Figure 3(b). Field enhancement and reduction of remanent light flow in PLZT 9/65/35 bulk display. Left side: no coating. Left side: overcoated with SiO_2 film. When applied field was reduced to zero, the coated area showed no remanent light flow (a totally dark image).

Conclusions

Effective methods of reducing and eliminating remanent light flow by using buffer and capping layer on the surface of electrooptic devices are described and experimental results are presented.

Acknowledgement

The auther wishes to thank Dr. G. H. Haerting for many helpful discussions. This work was supported in part by Motorola Inc., DARPA, and AFOSR.

References

[1] A. Y. Wu, Tom C. C. Chen, and H. Y. Chen, "Model of electrooptic effects by Green function and summary representation:applications to bulk and thin film PLZT displays and spatial light modulators", *8th* International Symposium on Applications of Ferroelectrics, Greenville, South Carolina, 1992. This Symposium.

[2] A. Y. Wu, Tom C. C. Chen, and H. Y. Chen. (Unpublished).

THE SELF SECOND HARMONIC GENERATION CRYSTAL NYAB PUMPED BY THE LASER OUTPUT OF $Ti^{3+}:Al_2O_3$

S.W. XIE, W.Y. JIA, P.J. WANG, T. LIOU, Y.L. CHEN

Applied Physics Department, Shanghai Jiao Tong University,
Shanghai 200030, China

Abstract

The paper reports the studies of the self second harmonic generation crystal NYAB pumped by the infrared laser output of $Ti^{3+}:Al_2O_3$. The wavelengths of the pumping laser are from 0.7306μm to 0.8268μm. The size of NYAB crystal is $3\times3\times4\ mm^3$. We adopted type I phase matching self second harmonic generation (self SHG) and got 0.532μm output with NYAB crystal uncoated and not even being put into resonators either. The spot of the green light is 1mm diameter and the diffuse angle is 1.5mrad. In experiment, the threshold of the self SHG of NYAB crystal was measured also.

Keywords: self second harmonic generation,
neodymium yttrium aluminum borate crystal

Introduction

NYAB crystal ($Nd_xY_{1-x}Al_3(BO_3)_4$) is a new multifunctional crystal developed at the end of the 1980's. It belongs to space group R32. NYAB crystal is the laser crystal and also the nonlinear optical crystal. It is promising in the development of miniature green light laser devices pumped by laser diodes, which can be used in optical disc technique, optical fiber communication, underwater detective and display, and other high technology. It has absorbed much attention of the researchers. For the reason of the high cost of high power laser diode at 0.804μm, wide bandwidth infrared laser output of $Ti^{3+}:Al_2O_3$ was used to pump NYAB crystal in experiment. We have got the self SHG green light output, and further have done some research in the use of NYAB crystal.

Experiment

(1) The output of the $Ti^{3+}:Al_2O_3$ laser

The schematic of the experimental setup is shown in Fig. 1.

A commercial Q-switched YAG laser (Model Quantel YG-58) of 1.064μm radiation was the original source. KTP crystal was used to get SHG green laser beam, thereby to pump the $Ti^{3+}:Al_2O_3$ crystal to get the infrared laser output we need. The green laser beam energy can be adjusted by the limiting aperture about 2mJ ~ 20mJ. The $Ti^{3+}:Al_2O_3$ crystal rod was grown by ourselves. Its size is $\phi4.89mm\times25.16mm$. Ti^{3+} ion concentration is 0.3%. In the experimental setup, a 200mm focal length lens L1 was used to concentrate the light energy, therefore to obtain higher energy density. The crystal rod and two mirrors of the resonators were placed near the focal plane, but not in it to avoid damage. The resonators were the flat-flat design and easy for adjustment. Mirror M1 was highly transmitting at 0.532μm and highly reflecting near 0.75μm. Mirror M2 was highly reflecting at 0.532μm and its transmission rate at 0.75μm was 27%. F1,F2,F3 are filters absorbing 1.064μm, 0.532μm and infrared light respectively. In this way, the output of $Ti^{3+}:Al_2O_3$ crystal from 0.7306μm to 0.8268μm was obtained with a duration of 15ns. The maximum pulse energy was 610μJ. We can see the red light with a spot of 1.5mm diameter[1].

(2)The choice of the NYAB crystal

NYAB belongs to the negative uniaxial crystal. Its refractive indices at 1.064μm and 0.532μm[2] are

$n_o^w=1.7553$, $n_e^w=1.6869$, $n_o^{2w}=1.7808$, $n_e^{2w}=1.7050$

According to the following formula:[3]

$$\theta_m^I=\sin^{-1}\left(\frac{(n_o^w)^{-2}-(n_o^{2w})^{-2}}{(n_e^{2w})^{-2}-(n_o^{2w})^{-2}}\right)^{1/2} \quad (1)$$

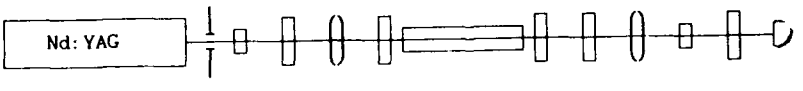
we can obtain the type I phase matching angle easily, which is

$\theta_m^I=34^\circ34'$.

And from formulae (2)--(4)

$$n_e^{2w}(\theta_m^{II})=\frac{1}{2}\left(n_o^w+n_e^w(\theta_m^{II})\right) \quad (2)$$

$$n_e^{2w}(\theta_m^{II})=\left(\frac{\cos^2\theta_m^{II}}{(n_o^{2w})^2}+\frac{\sin^2\theta_m^{II}}{(n_e^{2w})^2}\right)^{-1/2} \quad (3)$$



S KTP F1 L1 M1 $Ti^{3+}:Al_2O_3$ M2 F2 L2 NYAB F3 D

Fig 1. The Schematic of the Experimental Setup

CH3080-0-7803-0465-9/92$3.00 ©IEEE

$$n_e^w(\theta_m^{II}) = \left(\frac{\cos^2\theta_m^{II}}{(n_o^w)^2} + \frac{\sin^2\theta_m^{II}}{(n_e^w)^2} \right)^{-1/2} \quad (4)$$

a simple program needs to be developed to calculate the type II self SHG phase matching angle. The result is

$$\theta_m^{II} = 50^\circ 33'.$$

We know, the azimuthal angle ϕ is selected to make d_{eff} maximum. NYAB crystal belongs to group R32, so its effective nonlinear coefficients are as follows:[4]

$$d_{eff}^I = d_{11}\cos\theta_m^I \cos 3\phi \quad (5)$$

$$d_{eff}^{II} = d_{11}\cos^2\theta_m^{II} \sin 3\phi \quad (6)$$

Thereby, $\phi_m^I = 0^\circ$, $\phi_m^{II} = 30^\circ$. In these directions, the effective nonlinear coefficient expressions are

$$d_{eff}^I(\theta_m^I, \phi_m^I) = 0.823 d_{11} \quad (7)$$

$$d_{eff}^{II}(\theta_m^{II}, \phi_m^{II}) = 0.404 d_{11} \quad (8)$$

We get the conclusion that, the self SHG of NYAB crystal of the type I phase matching is more effective.

In our experiment, the NYAB crystal was cut with type I phase matching angles. Its size was $3\times3\times4mm^3$. It was uncoated and not put into resonators either in order to simplify the experiment.

Experimental Results

A. We got 0.532μm green laser output. Its energy was in μJ order. The light spot was 1mm diameter, and the diffuse angle was 1.5mrad.

B. The self SHG threshold of NYAB crystal pumped by the wide bandwidth infrared laser was about 180μJ.

C. We found the best phase matching angle was $\theta_m^I = 33^\circ 30'$, which was 1° deviation from the theoretical calculation. Comparing the experimental results with calculation, we think, in spite of the deviation in cutting, the main reason is that there are deviations of the Nd ion concentrations of NYAB crystal. Thus, it influenced the crystal indices. There is a slight difference of phase matching angle between the theoretical calculation and the experimental measurement.

D. In experiment, we found the optic principal axial direction of NYAB crystal can be judged by inserting two orthogonal polarizers or observing the polarization of the 0.532μm output. And the polarization of the pumping source had no influence on the output of 0.532μm self SHG light.

In summary, NYAB crystal is a good self SHG laser crystal. It is promising to have a wide use in the future.

References

[1] S.W. Xie et al., Proceeding of the Topical Meeting on Laser Materials and Laser Spectroscopy. World Scientific Press, Singapore (1988).

[2] B.S. Lu et al., J. Appl. Phys., 66(12), 6052, (1989).

[3] A. Yariv, Introduction to Optical Electronics. Holt, Rinehart and Winston Press, New York, U.S.A., (1976).

[4] M.H. Jian, Crystals Physics. Shandong Science & Technology Press, Jinan, China, (1980).

RAMAN SPECTROSCOPY AND NONLINEAR OPTICAL PROPERTIES OF $PbTiO_3$ SUSPENSION

Y. HAN, Q. ZHOU, L. ZHANG, X. YAO

Electronic Materials Research Lab
Xi'an Jiaotong University, Xi'an, China, 710049

ABSTRACT

Ultrafine PT powders are dispersed in different liqiuds to form uniform suspensions of ferro-fluids. Nonlinear optical properties such as second harmonic generation (SHG) and degenerate four wave mixing (DFWM), and Raman spectra were investigated. Changes of optical properties when applying a bias electric field to the samples are shown. Structure and property relationships of fine composites are discussed.

INTRODUCTION

The nonlinear optics of isotropic and anisotropic artficial dielectrics such as 0-3 fine composites has recently been the focus of intense study at visible, infrared, microwave, and millimeter wavelengths.[1,2,3] A number of these composites exhibit nonlinear optical behavior and have been utilized for four-wave mixing and the important application of phase conjugate image reconstruction.[4]

Many shaped-microparticle suspensions such as polystyrene latex microsphere suspensions in aqueous solutions have show an optical-field-induced density modulation of microsphere concentration.[5] Vanadium pentoxide microparticles in a carbon disulfide host medium has show a third-order nonlinear optical susceptibility $X^{(3)}$ $=5*10^{-6}$esu of the particulates.[6] Shaped PTFE microparticles in an aqueous suspension has also caused polarization modulation of probe- laser light.[7]

In this paper, lead titanate (PT) powders in ellipsoidal and needle-like morphorlogies derived from Sol-Gel process and hydrothermal synthesis are suspended in organic solvents. The microstructure of the powders was analysed by Raman spectra. Phase conjugation via DFWM was examined in PT powder suspensions.

EXPERIMENTAL METHOD AND RESULTS

(1) Sample preparation

The spherical and ellipsoidal PT powders were derived from the Sol-Gel process. The size distribution of PT powders can be controlled by changing the reaction conditions of the Sol-Gel process and the successive treatments such as the firing temperature, ultrasonic treatment, etc. Spherical and ellipsoidal PT powders in size ranges 80-160nm and 200-300nm have been used in this experiment. The needle-like PT powders were mainly about 0.5um*0.5um*10um.

PT powders can form stable suspensions in some polar solvents and viscous liquids, but less stable nonpolar solvents such as CCl_4. In general the smaller the PT powders are , then the more stable the suspensions formed. The weight fraction of PT powders in the composites was less than 0.1% to maintain good transparency.

(2) Raman spectroscopy

U-1000 Raman spectroscopy equipment was used with a SP-3000 Ar^+ laser. The laser light was horizontally polarized and focused to a beam 2-5 microns in diameter to generate microscopic Raman spectra. Figs.1 and 2 show the Raman spectra of spherical and ellipsoidal PT powders of different sizes, and Fig.3 was obtained from needle-like PT powders. Most of the main Raman peaks of single domain PT also appear in spherical and ellipsoidal PT powders, but only three of the main peaks E(1TO) mode at 80.997cm^{-1}, second- order Raman line[8] at 150cm^{-1} and A_1(3TO) mode at 624cm^{-1} were observed in needle-like PT powders.

As the sizes of spherical or ellipsoidal PT particle become smaller, the peak intensity of the E(3TO+2LO)+B_1 mode at 288cm^{-1} and A_1(3LO) mode at 723cm^{-1} becomes stronger.

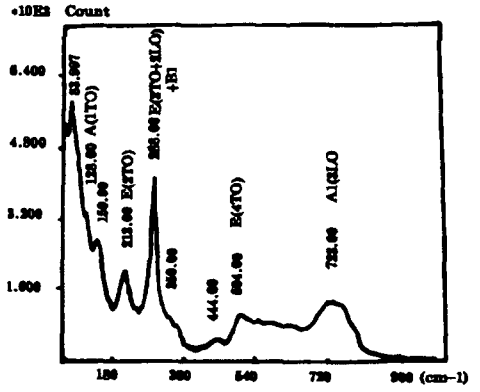


Fig.1 Raman Spectrum of PT Powders (80-160nm)

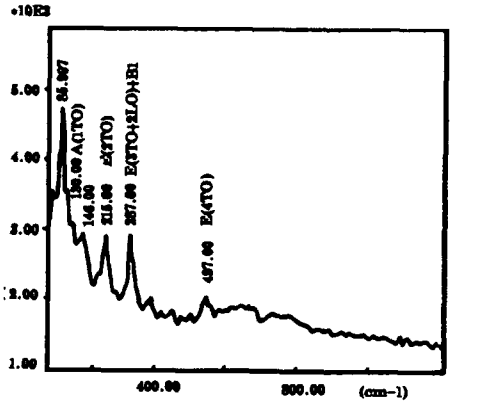


Fig.2 Raman Spectrum of PT Powders (200-400nm)

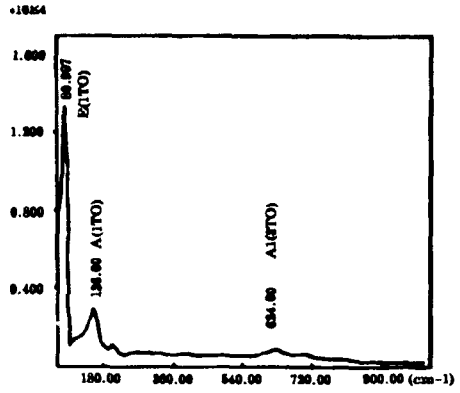


Fig.3 Raman Spectrum of Needle-like PT Powders

In order to see the effect of polarizition on the needle-like PT powders, an AC electric field was applied to the sample in a direction parallel to the light polarization. The electric field was about 216 V/cm with 100Hz sine wave. Figs.4 and 5 show the behavior of needle-like PT powders suspended in CCl_4 with the AC field on and off respectively. Raman peaks of PT powder can be slight distinguished with AC field on.

4

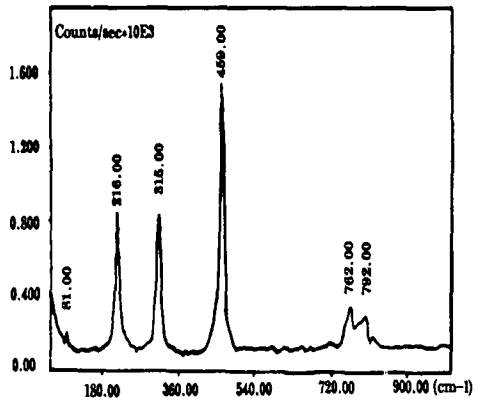


Fig.4 Raman Spectrum of PT/CCl4 Suspension With AC Field (100Hz) on

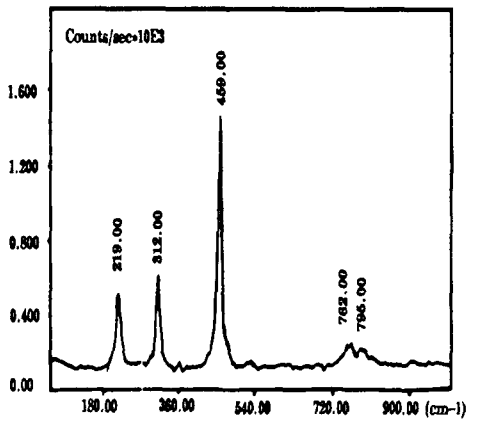


Fig.5 Raman Spectrum of PT/CCl4 Suspension

(3) SHG and DFWM measurement

SHG measurement was carried out with the different PT powders. All PT powders derived from the Sol-Gel process and hydrothermal synthesis in perovskite structure generate obvious SHG signals, with a transverse efficiency measured by powder SHG ranging between 10^{-4}-10^{-7}. SHG signals can also be observed when the PT powders were dispersed in many liquids at high powder densities, which depended on the pulse laser power.

The third order nonlinear optical signals of PT powder suspensions were measured by DFWM[10]. DFWM was performed under different conditions, one was at X=1.06um with 100 mJ pulse energy and 10 ns pulse, the other was at X=0.53um with 50 mJ pulse energy and 15 ns pulses, i.e. the peak power intensities were 10MW and 3.3MW respectively.

DFWM was used to measure the third-order nonlinear optical susceptibility $X^{(3)}$ of the suspensions. $X^{(3)}$ can be calculated by detecting the light density of the conjugate wave. PT powders/CCl_4 suspensions were used, in which the size of the suspension cell was about 5mm*10mm*30mm, and the laser light was transmitted through 5mm sides. The third-order nonlinear optical susceptibility $X^{(3)}$ for small PT powders (<160nm) in suspension was about $3.6*10^{-11}$esu and $2.1*10^{-11}$esu for larger powders (200-400nm), while for the pure liqiuds' $X^{(3)}$ measured by this system was about $0.87*10^{-12}$. All of the above were measured using the double frequency (0.53um) laser, and these results will be shown to be approximately at least 1.5 times larger than that of the suspensions when thc higher power intensity laser at X=1.06um was used.

Needle-like PT powders/CCl_4 suspensions were also measured using the double frequency laser. DC and AC electric fields were applied to the sample perpendicular to the direction of the incident light. Fig.6 shows a diagram of the experimental scheme. The results were as follow:

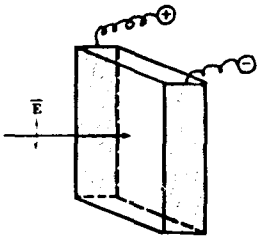


Fig.6 Experimental Scheme

AC field (50Hz)	0	240	360	420	(V/cm)
$X^{(3)}$ ($*10^{-11}$ esu)	1.05	0.83	0.77	0.76	

When the AC electric field was applied, the rise time for the conjugate wave to reach stability at 240V, 360V, 420V are all about 0.8 seconds while the decay time of this signal was about 4 seconds when the AC electric fields were turn off. These phenomena can be repeated very well if the AC electric field has been applied for a short time. With DC electric

field similar observations have been made, but can not be repeated very well because the needlelike PT powders sink quickly after several circles of DC field applicatons. These results agree very well with the previous observations by R.B.Findlay in needlelike PT powder alignment research.

With the smaller ellipsoidal PT powders suspended in CCl_4, only a small vibration in the conjugate wave intensity was observed between the DC electric fields being on and off. The former values were slightly larger than the latter with faster response than was found in the needlelike PT suspensions.

DC field (50Hz) (V/cm)	0	240	360	420
$X^{(3)}$ ($*10^{-11}$ esu)	2.11	2.03	2.05	1.98

In this experiment, the pump beam and the probe beam were used in vertical polarization, i.e. perpendicular to the external electric field.

DISCUSSIONS

According to the Raman spectra of PT powders there were some differences between the different shapes and sizes of PT powders. Most of the main Raman peaks of single domain PT also appear in spherical and ellipsoidal PT powders, but only three of the main peaks E(1TO) mode at 80.997cm^{-1}, second-order Raman line[8] at 150cm^{-1} and A_1(3TO) mode at 624cm^{-1} were observed in needle-like PT powders.

As the sizes of spherical or ellipsoidal PT particles become smaller, the peak intensity of the E(3TO+2LO)+B_1 mode at 288cm^{-1} and A_1(3LO) mode at 723cm^{-1} becomes stronger, i.e. the vibration mode at long wavenumbers are more active in smaller powders, it can be suggested that more vibrations can be stimulated in the PT powders at smaller powder sizes. The ratio of the atoms in the surface to the atoms in the bulk becomes higher as the powder sizes become smaller, so the surface energy states will become more important for many properties. As shown in DFWM measurements, the conjugate signal or $X^{(3)}$ becomes larger as the powder sizes decrease, which may be because there were more vibration modes taking part in the nonlinear optical interactions. In any case, it is seen that the SHG transverse efficiency was also related to the PT powder sizes as controlled by different firing temperatures.

The main crystallographic structure of the nanometer PT powders was still a tetragonal phase with 4mm point group symmetry. According to the Raman spectra a lot of undefine peaks that were different from those of single domain PT appear, which may be caused by the noncrystalline phase near the surface layer of the powder.

In Figs.4 and 5, the Raman peak intensity of some vibration modes of the liquid host (CCl_4) and the PT powders can be modulated by applying external AC electric fields. This may be because the powders were aligned by the electric field and direction of the c- axis of the powder was changed by the incident light.

PT powders can be dealt with as anisotropic particulates because of the large spontaneous polarization. We can also dealt with the ellipsoidal and needle-like powders as cylindrically symmetrical systems. In the small-field limit of the light field, where saturation effects can be ignored, both electrostatatic forces and electrostatic torques can orient the poled PT powders along prefered directions, So that both translational gratings and orientational gratings are created. The orientational gratings are superimposed directly upon the translational ones and thereby share their direction and spacing. Coherent scattering of pump radiation from these two orientational gratings gives rise to the formation of a conjugate wave just as for liqiud suspensions of microspheres.

In the DFWM system a liquid suspension of shaped powders--especially ellipsoidal and needle-like here- -was irradiated by three external laser beams of frequency w: two conterpropagating pump waves and a probe wave. If $E(\vec{r},t)$ denotes the total radiation field, the microparticles will each acquire a dipole moment $\vec{P}_w(\vec{r},t)$, vibrating at w. The field induced dipole can be decomposed into two pieces, arising from the isotropic and the anisotropic components of the polarizability tensor:[9]

$$\vec{P}w(\vec{r},t)=a_s(w)\vec{E}(\vec{r},t)+1/3BK.\vec{E}(\vec{r},t)$$

where K is the orientation matrix, $a_s=(a_p+2a_v)/3$, $B=a_p-a_v$, a_p, a_v are the body-fixed polarizability component parallel to the axis and perpendicular to this axis. In general $a_p>a_v$ and the main term will always the isotropic term because it has nothing to do with the distribution angle, so the differences in some properties between parallel and perpendicular orientations will perhaps not be as big as expected. The changes in $X^{(3)}$ shown in needle-like PT powder suspensions under the external electric field were obvious, but smaller differences were seen for smaller spherical or ellipsoidal PT powders under the same conditions.

Therefore needle-like PT powders are better for the control of alignment in some liquids and the smaller spherical or ellipsoidal PT powders behave better in second order and third order nonlinear optical processes.

CONCLUSIONS:

Shaped PT powders derived from Sol-Gel process and hydrothermal synthesis have shown that the vibration modes are different between different shapes and sizes. More vibraton modes in long wavenuber region are damped in needle-like PT powders with larger sizes. For spherical or ellipsoidal PT powders the peak intensities of E(3TO+2LO)+B_1 mode at 288cm^{-1} and A1(3LO) mode at 723cm^{-1} become stronger with the sizes decrease.

The spontaneous polarized PT powders and PT powders suspensions posses second order and third order nonlinearities. Needle-like PT powders are better for the control of alignment in some liquids and the smaller powders spherical or sllipsoidal PT powders behave better in second order and third order nonlinear optical processes.

In addition, it is also suggested that the larger spherical or ellipsoidal PT powders be aggregated by small powders. Microstrutures and properties of deaggregated PT powders are investigating.

ACKNOWLEDGEMENT

We thank the National Advanced Materials Project of China for financial support, and Dr.R.B.Findlay for helpful discussions.

REFERENCES

[1] R.McGraw, D.Rogovin, W.Ho, B.Bobbs, R. Shih, and H.Fetterman, Phys.Rev. Lett. 61. 943(1988)
[2] R.Pizzoferrato,M.Marinelli,U.Zammit, F.Scadieri,S.Martellucci, and M. Romanagnoli, OPt.Commun.68,231(1988)
[3] R.Shih, H.Fetterman, W.Ho, R.McGraw, and B.Bobbs, Phys. Rev. Lett 65,579(1990)
[4] A.Yariv,IEEE J.Quantum Electron, QE-14, 650(1978)
[5] A.J.Palmer, Opt. Lett., 5,54(1980)
[6] S.O.Sari and D.Rogovin, Opt.Lett. 9, 414 (1984)
[7] D.Rogovin and J.Scholl, R.Pizzoferrato, M.De Spirito, M.Marinelli, and U.Zammit, J.Opt.Soc.Am.B. 8,2370(1991)
[8] Gerald Burns and Bruce A.Scott, Phys.Rev.Lett.,25,1191(1970)
[9] D.Rogovin,Phys.Rev.A, 32,2837(1985)
[10] X.Yao, L.Zhang, Y.Han, Q.Zhou, IEEE Proc. ISE-7, 886(1991), Berlin

AUTOMATIC ELLIPSOMETRY MEASUREMENT FOR ANISOTROPIC MATERIALS

Li Yang, You Boqiang, Zhang Liangying and Yao Xi
Electronic Materials Research Laboratory
Xi'an Jiaotong University, Xi'an, 710049, China

Abstract

A new variable medium and variable angle ellipsometry(VMAE) system which is able to make measurement on anisotropic materials is described in this paper. A rotating analyzer ellipsometer is used to combine with several working mode such as changing medium, changing incident angle of laser beam, changing azimuth of sample etc. Using these methods, it is able to get enough equations for the measurement of anisotropic bulk materials and thin films. The surmount equation group for the calculation of the optical constants of anisotropic materials is able to be solved by a PC type computer combining Powell, Rosenbrock, Palmer direct optimization methods. Software structure is introduced in detail. Experimental results are compared with theoretical values to test the reliability of the system.

Introduction

With the fast development of optoelectronic materials, it is imperative to find an approach to measure the optical parameters of materials, which is undestructive, automatic, rapid and accurate. The reflection ellipsometry is a rapid and simple way to determine the optical parameters and the geometric thickness of materials by analyzing the change of polarization between the incident light and the reflected light from the sample surface. There are mainly two types of working modes, null ellipsometry and photometric ellipsometry. Compared with the traditional optical measuring methods, the ellipsometry measurement is simple and automatic, undestructive and is able todetermine multiple optical parameters simultaneously. However, itspractical application has been limited because of its complicated theoretical calculation. By the end of 70's, with the development of computers, the method been widely used in such domains as the manufacture of semiconductive components, the control of thin optical film growth and surface optical properties improvement of materials[1] , and so on. For optical isotropic materials, many measuring systems have been developed such as RAE[2] (Rotating Analyzer Ellipsometer), RPE[3] (Rotating Polarizer Ellipsometer), VASE [4] (Variable Angle Spectroscopic Ellipsometer) etc. For optical anisotropic materials, the preliminary studying[5-6] using ellipsometry has been discussed, but no comprehensive measuring system has been reported up to now. In our work, a new Variable Medium and Variable Angle Ellipsometer(VMAE) combining RAE with many other methods such as changing medium, changing angle of incidence and changing azimuth of sample is developed. The system is controlled by computer. A package of integrated window software is developed. This system has be used in studying the optical properties of anisotropic materials. Some results are presented.

Fig.1 shows the VMAE measuring system. Based on the RAE system, many other parts are added such as a adjustable quadruple dimensional sample stage, DC servomoter with tachogenerator which rotating the sample stage, high-accuracy servo system to drive the motor and A / D , D / A interface circuit to control the servo system. In the amplifier circuit, multi-function filter as well as high stability low noise power are added.

Sample is placed on sample stage in proper height and kept horizontal constantly during rotating process. He-Ne laser with 632.8 nm wavelength is turned into linear polarized light through polarizer and became elliptic polarized light after reflecting from the sample surface. By rotating analyzer to process photometric Furrier analysis on elliptic polarized light, the ellipsometric parameters (ψ, Δ) can be

CH3080-0-7803-0465-9/92$3.00 ©IEEE

obtained. For isotropic materials, the required optical parameters can be determined by solving the ellipsometric equation directly [7] . As for anisotropic materials, since the number of the unknown parameters increased, it is required to get enough independent equations by measuring in different medium, incident angle and azimuth of sample etc. so as to set up the surmount equation group. The equation group can be solved by a PC type computer combining direct optimization methods to determine the optical parameters of materials.

Theory

For a RAE system, the relative intensity of the beam passed through the analyzer is:

$$I = K_0 + K_1 \cos 2\alpha + K_2 \sin 2\alpha \qquad (1)$$

where α is the analyzing angle, K_0 、 K_1 、 K_2 are Furrier coefficients. If n points are measured at the same interval of angle while α is between 0 degree and 180 degree, then :

$$K_0 = \frac{1}{N} \sum_{i=1}^{n} I_i$$

$$K_1 = \frac{2}{n} \sum_{i=1}^{n} I_i \cos 2\alpha_i$$

$$K_2 = \frac{2}{n} \sum_{i=1}^{n} I_i \sin 2\alpha_i$$

$$\alpha = \frac{i\pi}{n}, \quad i = 1,2,...n. \qquad (2)$$

where I_i is the relative intensity of the beam at α_i The ellipsometric parameters are given by:

$$\psi = \operatorname{arctg} \sqrt{\frac{(K_0 + K_1)}{(K_0 - K_1)}} / \operatorname{ctg} P \ ;$$

$$\Delta = \operatorname{arctg} \sqrt{\frac{K_0^2 - K_1^2 - K_2^2}{K_2^2}} \qquad (3)$$

where p is polarizing angle.

The ellipsometry equation is:

$$\operatorname{tg}\psi e^{i\Delta} = \frac{R_p}{R_s} \qquad (4)$$

where R_p (R_s) are the complex Fresnel reflection coefficients of p light and s light respectively. The light is called p light when it's electrical vector E is paralle to the incident plane, and called s light when perpendicular to.

For anisotropic materials the 4 * 4 ranks matrix method is used, Which is formulated by Billard, Teitler, Henvis and Berreman [8] . After a series of complicated deduction [9] , an equation canbe obtained, which only comprises the incident field and reflective field, that is:

$$\begin{bmatrix} E_{RP} \\ E_{RS} \end{bmatrix} = \begin{bmatrix} -R_{PP} & R_{PS} \\ R_{SP} & R_{SS} \end{bmatrix} \begin{bmatrix} E_{IS} \\ E_{IP} \end{bmatrix} \qquad (5)$$

Refers to equation (4), it can be obtained:

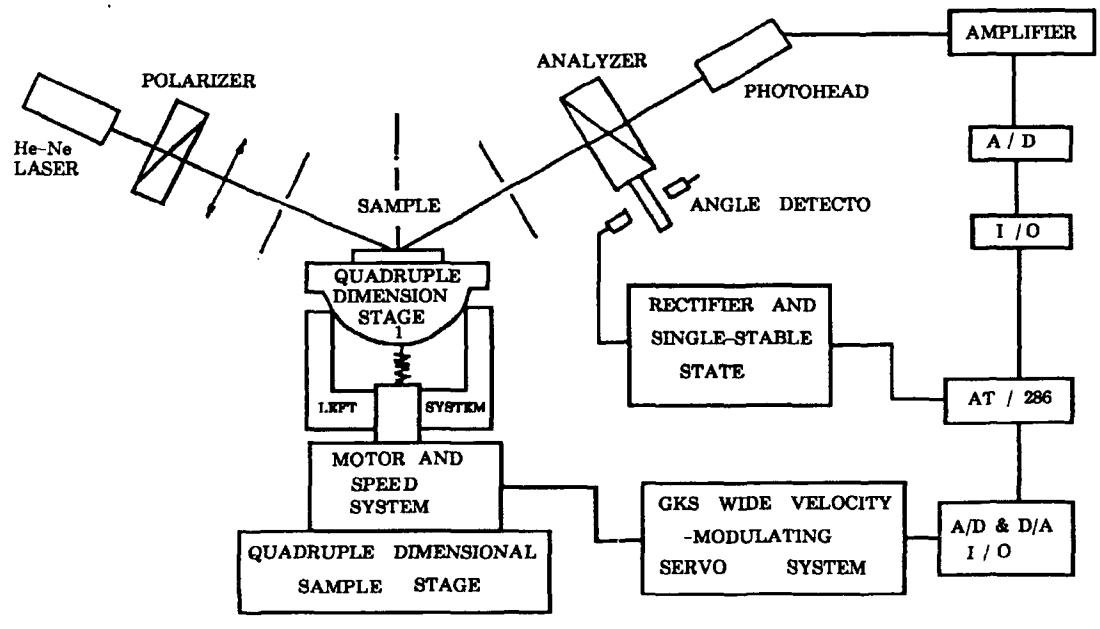


Figure 1 The VMAE measuring system block diagram

$$tg\psi e^{-i\Delta} = \frac{R_P}{R_S} = \frac{E_{RP}}{E_{RS}} = \frac{R_{PP}E_{IP} + R_{PS}E_{IS}}{R_{SP}E_{IP} + R_{SS}E_{IS}}$$

$$= \frac{R_{PP} + R_{PS}\dfrac{E_{IS}}{E_{IP}}}{R_{SP} + R_{SS}\dfrac{E_{IS}}{E_{IP}}} \qquad (6)$$

when polarizing angle is 45 degree, $E_{is} / E_{ip} = 1$, then

$$tg\psi e^{-i\Delta} = \frac{R_{PP} + R_{PS}}{R_{SP} + R_{SS}} \qquad (7)$$

The right side of equation (7) is a complicated implicit function comprising the required optical parameters. For several anisotropic materials (as shown in Fig.2), such as bulk and film materials whose optical axis is parallel or perpendicular to the sample surface.

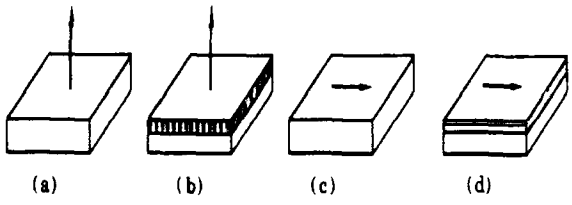


Fig.2 several primary anisotropic materials

In consideration of the most complicated case, equation (7) can be expressed as follows:

$$tg\psi e^{-i\Delta} = F(N_{1O}, N_{1E}, N_{2O}, N_{2E}, N_0, \Phi, \lambda, D, \alpha) \qquad (8)$$

where:

N_{1O} , N_{1E} are the complex refractive index of the film layer;

N_{2O} , N_{2E} are the complex refractive index of the substrate;

N_0 is the refractive index of surroundings medium;

Φ_0 is the incident angle of light;

λ is the wavelength of light;

D is the thickness of film;

α is the angle between the optical axis of uniaxial materials and the incident plane;

In Equ.8, N_0 , Φ_0 , λ, α are all known parameters, the others are to be determined. In order to solve the equation, enough independentequations are needed, which can be obtained as the following approach:

I. replacing the surroundings medium, (changing N_0).

II. altering the incident angle of light, (changing ψ_0).

III. changing the wavelength of light, (changing λ_0).

IV. adjusting the azimuth angle of sample.α_0.

Using the above methods, a group of (ψ, Δ) are obtained to form surmount equation group. The required optical parameters are determined by using direct optimization methods to solve the equation group[10]

Integrated window software

In computer calculation, the following environment need to be set upin software:

(1) attribute of the materials (isotropic or anisotropic);

(2) orientation of the optical axis (parallel, perpendicular to sample surface or arbitraray oriented);

(3) the form of materials(bulk or film materials);

(4) the property of the film layer (absorbent or unabsorbent);

(5) the property of the substrate (isotropic or anisotropic);

(6) the option of optimization methods (Powell, Palmer or Rosenbrock);

(7) the option of measurement methods (multi–medium, multi–angle etc.);

(8) the origin of the data(from the computer or input by keyboard);

And it should be finished to set up system constants, start value of variable, printer etc.. As to such a complicated software architecture, the structural design method is adopted. The whole system is separated into several functional modules, every module fits for its own function, then they are integrated into a multi–window environment by means of standard data structure. Several primary modules are as following:

(1) system initializing module

(2) multi–window menu module

(3) function executing module

(4) testing and controlling module

(5) data collecting module

(6) parameters calculating module

Experimental results

Using the system, the optical properties of several kinds of samples are measured. The results are shown in following tables:

Table 1 LiNbO3(Y cut) anisotropic optical constants (bulk materials)

Times	N_o	N_e	Theory Value
1	2.30+0.30i	2.24+0.26i	
2	2.28+0.35i	2.23+0.40i	$N_o = 2.29$
3	2.30+0.27i	2.25+0.29i	$N_e = 2.21$
4	2.29+0.32i	2.23+0.25i	
5	2.28+0.40i	2.24+0.33i	

Table 2 the results of PLZT sample(8 / 65 / 35)

times	n	k	Theory Value
1	2.45	0.44	
2	2.46	0.40	$n = 2.50$
3	2.46	0.42	
4	2.44	0.42	

Table 3 the results of different MOCVD TiO_2film samples

Sample	n	k	D(nm)
30 / 550℃	1.885	0.400	89.60
35 / 550℃	1.898	0.399	100.2
40 / 550℃	1.909	0.367	108.7
45 / 550℃	1.915	0.359	113.5

As shown in the above tables, experimental results are in goodagreement with previous values measured by other method.

Conclusions

(1) Based on RAE system, a new VMAE system has been built. The system is controlled by a computer and can be used to measure the optical parameters of isotropic as well as anisotropic materials.

(2) A integrated window software based on the advanced structural design has been set up. It is multi-functional, friendly to user and easy to extend.

(3) On the basis of direct optimization, a set of calculation module software for determination of numerical values of optical parameters of anisotropic materials has been set up.

(4) The measurement precision of the system has been investigated.Experimental results are in good agreement with previous values.

Acknowledgment: The research work was supported by Chinese National Natural Science Foundation.

References:

[1] You Boqiang, Zhou Jianhua, Li Yang, Zhang Liangying and Yao Xi, The research report of surface optical properties improvement of LiNbO3 ion-implanted , China (1991)

[2] D.E.Aspnes and A.A.Studna, Appl. Opt. 14, 220-228(1975)

[3] G.E.Jellison, Jr. and F.A.Modine, Appl. Opt. 7, 959(1990)

[4] G.H.Bu-Abbud, N.N.Bashara, and J.A.Woolam, Thin Solid Film 137, 27-41(1986)

[5] Optics Communications, Vol.58, No.5, 303(1986)

[6] Shen Wenjiang, the Journal of instrument and meter, Vol. 6, No.1, (1985) (in chinese)

[7] Li Tonghe, the theme of master's degree, Xian Jiaotong Univ.(1989) (in Chinese)

[8] R.M.A.Azzam, N.M.Bashara, Ellipsometry and Polarized Light, North-Holland Publishing Company, 1977.

[9] Application of Generalized Ellipsometry to Anisotropic Crystals, J. Opt. D. Soc. Amer. N.64, p128(1974)

[10] Li Yang, theme of master's degree, Xian Jiaotong Univ.(1992), (in chinese)

OPTICAL PROPERTIES OF $LiNbO_3$ WITH ION IMPLANTATION AND TITANIUM THERMAL DIFFUSION

YOU Boqiang, ZHANG Liangying and YAO Xi
Electronic Materials Research Laboratory
Xi'an Jiaotong University, Xi'an, 710049, China

ABSTRACT

Optical properties of $LiNbO_3$ single crystal with ion implantation and titanium thermal diffusion are studied. The focus of this paper is to compare the separate and combined effect of the two processes. Titanium film on $LiNbO_3$ was prepared by conventional sputtering technique and CVD method. Thermal diffusion was achieved by annealing in atmosphere under various temperatures. The optical property of Ar implanted sample is close to isotropic. For a Ti film in thickness of 20nm, 5 hours are needed to diffuse in completely. The optical property of Ti diffused sample is still birefringence with N_o increased by 10-12% and N_e by 8-10%. Negative birefringence and small light loss can be achieved on the samples treated by Ti thermal diffusion combined with successive Ar implantation, which is very useful for waveguide applications.

INTRODUCTION

With the development of ion implantation and thermal diffusion technology, more and more optical devices such as optical waveguide, directional couplers, switches, modulators and isolator etc. have been successfully prepared by surface modification of lithium niobate.

Several different techniques, e.g. Li_2O out-diffusion, ion exchange, can be used to prepare optical devices. Among them the Ti in-diffusion and Ti ion implantation process have been receieved the greater attention owing to their advantages. Some devices have been made by the diffusion method for its simplicity, easy and cheap in making; and others are made by the latter method for taking advantages of ion implantation such as the control over implanted ions is easy, is not confined by atomic solubility, scaly diffuse in cross section[1,2,3].

In this paper we will discuss the combination effect of Ti thermal diffusion and Ar ion implantation techniques. The optical properties of separate and combined effect of the two processes will be shown.

EXPERIMENTAL METHOD

X,Y and Z cut optical-grade $LiNbO_3$ single crystal wafers were cleaned with HF acid, sputtered with Ar ion and then washed with $HF:3HNO_3$. Titanium film on the samples were achieved by using conventional sputtering technique ($U_{accelerate}$=1.1KeV; $I_{L\text{-}board}$=0.25A; $I_{R\text{-}board}$=0.1A; $I_{L\text{-}grid}$=40mA; $I_{R\text{-}grid}$=400mA; sputtering for 5, 10, 15, 18, 25, 35min. at Ar atmosphere) and CVD method respectively. Then the samples were implanted with Ar ion at 650keV energy and $2*10^{16}/cm^2$ dose at room temperature. The samples were annealed under a dry oxygen atmosphere at 900°C, 1000°C, and 1050°C for 0.25, 0.5, 1, 2, 3 and 5 hours respectively.

The optical properties of the samples were measured by anisotropic ellipsometry using which is developed by EMRL of Xi'an

CH3080-0-7803-0465-9/92$3.00 ©IEEE

Jiaotong University of China[6].

RESULTS AND DISCUSSION

Relationship of titanium film thickness and sputtering time

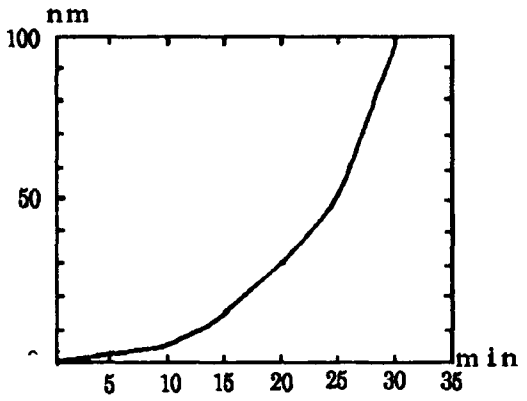


Figure 1 Thickness of Ti film on $LiNbO_3$ Sample with sputtering time

The thickness of Ti film on the $LiNbO_3$ sample changes with the sputtering time as shown in figure 1. The sputtering rate also depend accelerate voltage and working current. The curve is linea before 10min., then with the sputtering time increases, becomes quadratic.

Thermal diffusion effect

As show in table 1 and table 2, when temperature is lower then the Curie point of the crystal, the higher the temperature, the easier the thermal diffusion takes place. For a Ti film thickness of 20nm, at least 5 hours are needed to diffuse in completely. Effect of thermal diffusion is also affected by the heating rate. In our experiment, from fastest heating rate at 12°C/min to slowest 8°C/min effect of thermal diffusion could be changed by 10%.

The ordinary and extra-ordinary refractive indexes N_o and N_e can be increased by 10% and 12% for sputtered sample or 8% and 10% for CVD. The difference of optical

Table 1 Comparison of differemt diffusion times at 1000℃ (thickness=20nm)

Time	Ti film from Sputter method	Ti film from CVD method
1 hr	Ti film still on the sample	sample is dark
2 hr	stage of Ti film is visible	sample become yellowish
3 hr	sample color has some difference	sample color has some difference
4 hr	optical sample	optical sample

Table 2 comparison of differemt diffusion effect at 900℃ and 1000℃

Time	900 ℃	1000℃
2 hr	Ti film still on the sample	stage of Ti film is visible
3 hr	stage of Ti film is visible	sample color has some difference
6 hr	sample color has some difference	optical sample
8 hr	optical sample	optical sample

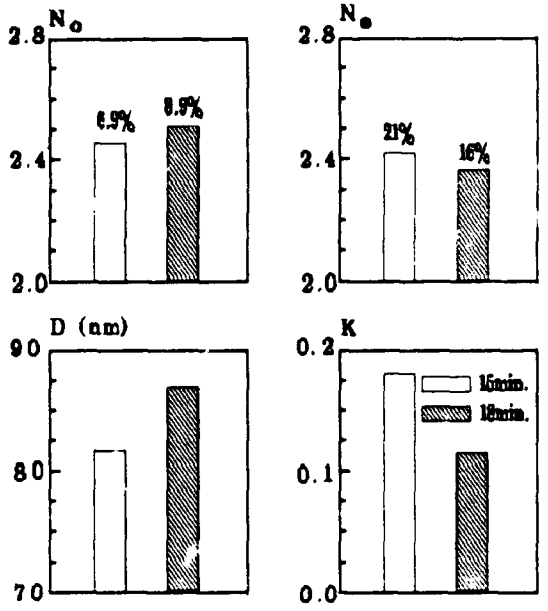


Figure 2 Comparison of Optical Property of the Samples

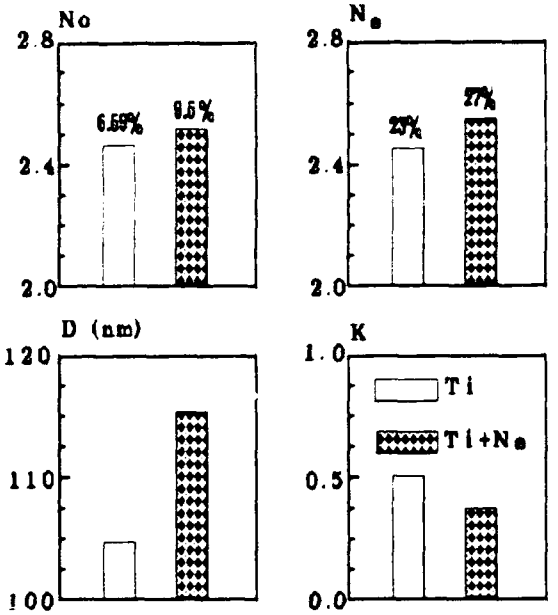


Figure 3 Comparison of Optical Property of Ne Implanted and Ti Diffused Samples.

refractive indexes between them are due to the difference of the Ti film on the samples. The results of refractive indexes N_o and N_e , thickness D and light loss K change with the sputtering time as shown in figure 2. With the sputtering time increases, the sputtered film on the sample becomes smooth and uniform, then the refractive index N_o can be increases by 6.9% to 8.9%; N_e decreased form 21% to 18%; the effective light thickness increases and light loss decreases.

Optical property of Ne ion implantated and Ti diffused samples

The comparison of optical property of Ne ion implantation and Ti diffusion combined with Ne ion implantation is shown in figure 3. Surface amorphous damage can be induced by the Ne ion implantation. The samples become almost isotropic ($N_o = N_e$), the extra ordinary refractive index changes more fast than ordinary refractive index. Then samples N_e greater than N_o can be obtained by combined Ne ion implantation with Ti diffusion.

The similar results can also be obtained for Y-cut and Z-cut samples. The change of refractive indexes of Y-cut samples is more significant after Ne implantation, induced optical anisotropy also occurs (N_o=2.448 < N_e=2.536, optical thickness D=122.4nm, light loss K=0.36).

CONCLUSION

(1) The Ti film on $LiNbO_3$ the sample can be prepare by sputtering method or CVD method. The thickness of sputtering film on the $LiNbO_3$ increases linearly at first then becomes quadratic.

(2) Below the Curie temperature, the higher the diffusion temperature, the faster the thermal diffusion takes place.

(3) At least 5 hours are needed to diffuse in 20nm Ti film on the $LiNbO_3$ completely.

(4) The refractive index of $LiNbO_3$ with Ti diffused-in can be changed from 10%(12%) to 8%(10%) for $N_o(N_e)$.

(5) The thicker the Ti film on the sample, the less the light loss is.

(6) Isotropic refractive index can be obtained for Ne implanted $LiNbO_3$ sample.

(7) Combined Ti thermal diffusion with Ne ion implantation can change the anisotropic of $LiNbO_3$ ($N_o < N_e$), and achieve low light loss.

ACKNOWLEDGMENT

This work was financially supported by the Chinese National Science Foundation.

REFERENCES

[1] M.J. Li, et al.," High Index Low loss Characterization of TiO_2, $LiNb_3O_8$ Waveguide ", *Optics Comm.*, 62 (1987), pp. 17-20

[2] O.Eknoyan, et al., "Characterization of Ti:$LiNbO_3$ deep waveguides diffused in dry and wet oxygen ambient", *Appl. Opt.*, 25, (1986),5, pp. 737-741.

[3] H.Karge, et al., "Radiation Damage and Refractive Index of Ion Implantated $LiNbO_3$", Nuclear Instruments and Methods, North-Holland, (1981), pp. 777-780.

[4] Zhou Jianhua, et al., "Studies on Surface ion Density Distribution of $LiNbO_3$ Implantation", *ADVANCED CERAMICS*, Tianjin Univ. 1991, pp. 88-94 (in chinese).

[5] You Boqiang, et al, "Radiation Damage and Optical Properties of $LiNbO_3$ Implanted by Ti ion", *ICECM'92*, Hangzhou, China, Nov. 1992 (to be published)

[6] You Boqiang, et al, "Ellipsometry Measurement on Anisotropic Film and Crystal", Vacuum Sci. & Tech. (China), Vol.12, 2-3 (1992), pp 115-119

OPTICAL PROPERTIES OF $PbTiO_3$/EPOXY 0-3 FINE COMPOSITES

Q.F.ZHOU, Y.HAN, L.Y.ZHANG and X.YAO
Electronic Materials Research Laboratory
Xian Jiaotong University, Xian, 710049, China

Abstract: Ultrafine $PbTiO_3$(PT) powder has been made using the Sol-Gel process. PT/Epoxy 0-3 composites have been successfully prepared by application of an external DC electric field during solidification of epoxy. The structure and optical properties of the composite materials prepared under various electric fields are carefully analyzed by XRD and optical spectrum technique such as ultraviolet absorption spectroscopy, Raman spectroscopy and photoluminescence spectroscopy. Second harmonic generation (SHG) by the composite has also been observed. The effect of the electric field on the structure and optical properties of the composites is discussed.

Introduction

There has been a significant increase of interest in new and multi-functional nonlinear optic and electro-optic materials to meet very rapid development of electronics and optoelectronics. Fine composites are good candidate materials for solving the problems in single phase materials when optimizing its figure of merit for certain applications. In particular, there are two kinds of size effects for nanometer materials: the thermodynamic size effect and the quantum size effect[1]. It is well known that the properties of nanometer materials are quite different from their bulk properties, so new and better properties might be achieved through sum and product effects in fine composite materials.

During the last few years many high-concentration piezoelectric ceramic-polymer composites with many different connectivity patterns have been successfully designed and fabricated to make an improved hydrostatic pressure sensor[2]. However, almost no work has been reported on the optical properties of PT ultrafine powder/epoxy fine composites with a low PT powder concentration formed under a DC electric field during epoxy solidification. In the present work, changes of XRD peaks and optical properties of the composites are carefully investigated under various conditions.

Experiments

Ultrafine PT powders are successfully prepared by Sol-Gel processing using lead acetate and titanium butoxide as the raw materials. The powders obtained are in soft aggregation, the size of agglomerates being about 200 to 300 nm. Ultrasonic treatment is used to deaggregate PT powders. The number average size of PT powders is in the range 20 to 80 nm[3].

To prepare fine composites, ultrafine PT powders are dispersed in an epoxy matrix according to the desired weight fraction, then mixed with ethanol and ultrasonically dispersed for 30 minutes. The mixture is then heated to 70°C to allow complete solvent volatilization under stirring and placed in a mould; the solid composite forms through a solidification reaction of the epoxy mixture under defined conditions in an applied electric field, samples are cut and polished to ensure parallelism of the two faces. In our experiment, the weight fraction of the ultrafine PT powder in the composite is 1%(Wt) unless noted elsewhere.

The structure of the composite is examined using a Rigaku D/max-IIIA X-ray diffractometer(XRD). Ultraviolet absorption spectra are analyzed using a PELIT UV/VIS analyzer, Raman and photoluminescence spectra are measured by a SPEX-1403 Raman and a Perkin-Elemer LS50.

Results and Discussion

1.Structural Analysis

Fig.1 shows the variation of the XRD patterns of the composite with a PT weight fraction of 5%(Wt) and a solidification field of 0-400V/mm. As shown in Fig.1, the intensity of I(001)/I(100) increases with increasing solidification field. It is calculated from Fig.1 that the I(001)/I(100) ratios under the different fields are about 0.50, 0.77, 0.74 respectively. The results indicate that the PT particles in the composite are oriented along C axis. It can be also seen from Fig.1 that each XRD peak shifts toward lower angle with increasing solidification electric field, the maximum change for (100) peaks is 0.213°, the average change is 0.0295°. C. Muralidhar et.al. have also observed the shifting of the peaks in $BaTiO_3$/polyvinylidene fluoride(PVDF) with changes of composite weight fraction formed under internal stress[4]. However, in our experiment, it is suggested that the shift of peaks are

CH3080-0-7803-0465-9/92$3.00 ©IEEE

attributed to the action of both internal stress and electric field force.

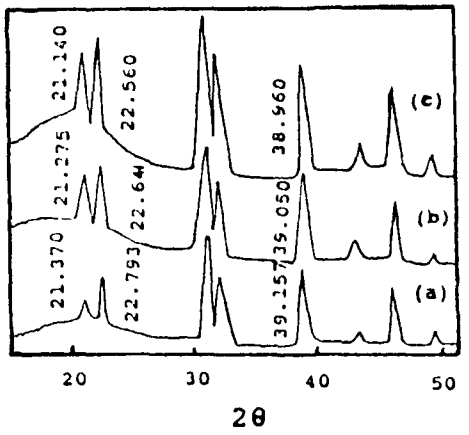


Fig.1. XRD patterns of the composite with electric field during solidification
(a) E=0V/mm (b) E=200V/mm (C) E=400V/mm

2.Optical properties

1) Optical absorption spectra

The optical absorption spectra of various samples(d=0.23mm) under different conditions are shown in Fig.2. The absorption edge of the epoxy is quite different from that of the PT ultrafine powders, meaning that the optical absorption mechanism is quite different. Without applying an electric field during solidification as in Fig.2(b), the optical absorption edge of the composite exhibits characteristics of both materials. In particular, when the external electric field is 400V/mm during solidification, the absorption edge of the composite apparently shifts toward long wavelengths as shown from Fig.2(d). Extrapolating the absorption to zero from Fig.2, the gap energy of the composites changes from 2.95eV to 2.75eV under a moderate DC electric field. However, in our experiment, no shift of the absorption edge of the epoxy has been observed. It is suggested that changes in the absorption edge under an external electric field are due to interactions between the electric field and the PT ultrafine particles. Some works[5] have shown that the absorption edge of semiconductors shifts with application of an external DC electric field. Their physical mechanism will be studied in future work.

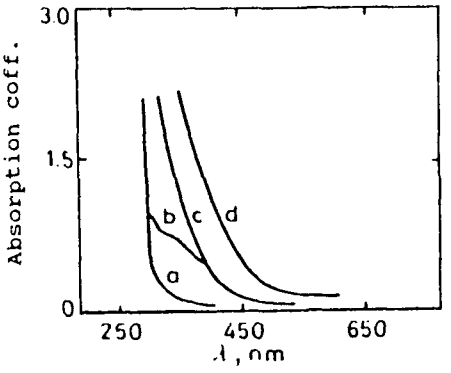


Fig.2 Optical absorption spectra of sample
(a) epoxy (b) composite(0V/mm) (c) PT powders
(d) composite(400V/mm)

2) Raman spectroscopy

Some clues to the bonding in complex systems may be obtained by taking Raman spectra measurements at various conditions, which is an important tool in studying the structure changes of materials. The Raman spectra of the PT fine particles, epoxy,and PT/epoxy are shown in Fig.3. It is observed from Fig.3(a) that the positions of Raman vibration of PT fine particles are in very close agreement with those of the PT bulk ceramic[6]. The Raman vibration of the epoxy is very complex due to the large molecular structure, but structure changes in the materials can be detected by comparing changes of the Raman peaks at different stages. From Fig.3(c) the Raman peaks of PT/epoxy are basically the same as a sum of those peaks from PT particles and epoxy, but there are new peaks appearing, such as those at 332 and 452cm^{-1}. When the DC electric field is 400V/mm, the Raman peaks of the PT/epoxy decreased, some of peaks disappeared such as those at 332cm-1 and 359cm^{-1}, and some of peaks shifted toward a larger wavenumber. It indicates that structure of composites can be changed by two phase fine composites under DC electric field.

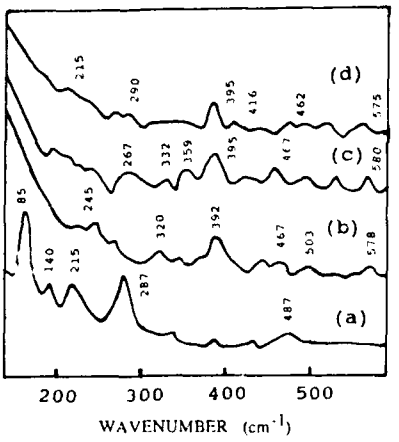


Fig.3 Raman spectra of samples
(a) PT powders (b) epoxy
(c) PT/epoxy(0V/mm)
(d) PT/epoxy(400V/mm)

3) Photoluminescence spectra

Photoluminescence spectra(PS) of epoxy and PT/epoxy fine composites are measured at room temperature. Fig.4(b) is the PS of the matrix, and

the excitation spectra peaks at 400 nm when the emission band is at 434 nm as shown in Fig.4(a), PS peaks are 460,470 nm under 380nm ,400nm excitation, respectively. There is about a 10 nm shift of PS peaks between different emission bands. Fig.5 is the PS of PT/epoxy (20wt%), the excitation spectrum peaks is 378nm when the emission band is at 434nm from Fig.5(a), the PS peaks are 425, 442nm under 370, 380nm excitation, respectively, and intensity of PS peaks on PT/epoxy is much lower than that of the epoxy. Moreover, it is observed that the PS curves show a long tail, suggesting a broad distribution of PT particle sizes dispersed in the epoxy. However, in our experiment, no PS peaks of PT powders have been observed at room temperature. Results indicate that PT particles have a strong effect on the PS when PT is dispersed in the matrix. More work is needed to elucidate this problem.

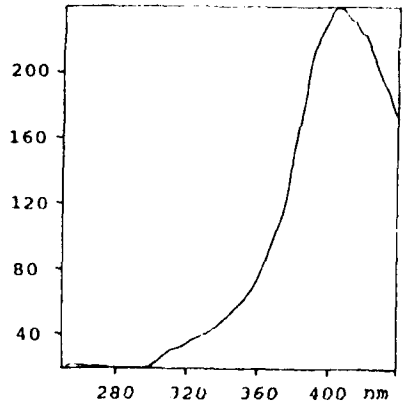


Fig.4(a) Excitation spectrum of epoxy
E_m=434nm

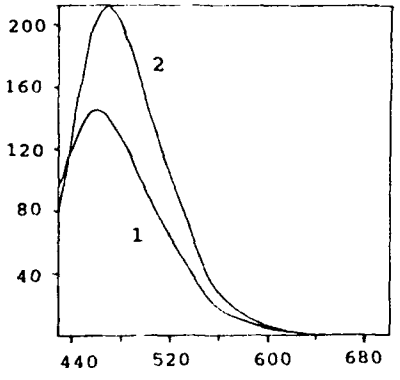


Fig.4(b) Emission spectra of epoxy
1.E_x=380nm
2.E_x=400nm

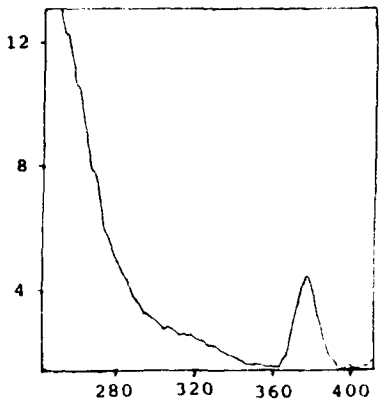


Fig.5(a) Excitation spectrum of PT/epoxy
E_m=434nm

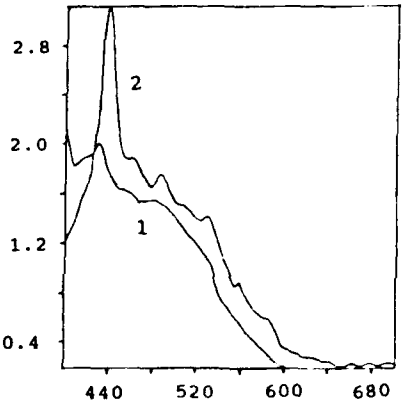


FIG.5(b) Emission spectra of PT/epoxy
1.E_x=370nm
2.E_x=380nm

4) SHG measurement

Second harmonic generation(SHG) by the PT/epoxy fine composites has been observed. The relative intensities of SHG under different longitudinal electric fields are shown in Fig.6. In the experiment, the pump laser is a Nd:YAG pulse laser with a wavelength of 1.06 um, a single pulse energy of 100mJ, a pulse duration of 10ns and a repetition rate of 2 Hz. A dual channel ratio energy meter of R_j-7200 is used to reduce fluctuations of the pulse energy. Experimental results show that the SHG intensity increases with increasing solidification electric field, indicating that the SHG efficiency can be modulated with an external bias field during solidification.

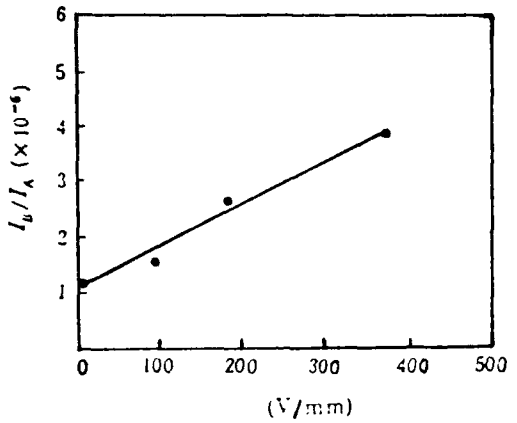


Fig.6 SHG relative intensity of samples under DC bias field

3.Discussion

The changes of the optical properties of PT/epoxy fine composites have been observed due to the application of an electric field during solidification. Results show that applying such a field is very different from applying an electric field to the sample after solidification. According to Furakawa theory[7], the effective field E_{eff} acting on an isolated spherical grain, as a function of the applied electric field E_p is given by

$$\frac{E_{eff}}{E_p} = \frac{3K_1}{[2K_1+K_2+p(K_1-K_2)]}$$

where K_1,K_2,and p are the dielectric constant of the polymer matrix, ceramic filler, and volume fraction of the filler, respectively. In the present work, $K_1=8$, $K_2=200$, $p=0.0015$, so the effective field E_{eff} is 32.9V/mm when the applied electric field E_p is 400V/mm. This is much lower than the coercive field of PT ceramics ($E_c=675$V/mm), so the effects of the electric field on the composite can not been explained by conventional polarization theory. It was observed from TEM that most of the PT ultrafine particles are ellipsoidal ; if macro polarization of each particle is along the long axis of ellipsoid, PT particle is subjected by a force couple from applied electric field. Lee et.al. discovered that most of PT ultrafine particles are mainly single domain when the size of the PT particle is less than 200nm[8]. In this case, the single domain particles are easily oriented along the direction of the poling field while the viscosity of the epoxy is still low before solidification. This result has been observed by XRD experiment of composites. Also, research results indicate that the absorption edge and Raman spectra of the composites all change, and the SHG efficiency can be modulated with an external DC electric field during solidification. It is suggested that these properties may be associated with a coupling effect between nanopowders and the external electric field. Other nonlinear optical properties such as DFWM of the fine composites is being investigated.

Acknowledgment

We would like to thank the National Advanced Material Research Project of China for financial support, and Dr. R. B. Findlay, Mr.Jia Pinpin, Mr.Lu Shengguo for helpful discussions.

References

[1] R.Kubo, J.Phys.Soc.Jap, 17, 975(1962)
[2] R.E.Newnham, et.al., Mat. Res. Bull., 13, 525(1987)
[3] Q.F.Zhou, X.Yao etal., Chinese Kexu Bulletin, 22,1752(1991)
[4] C.Muralidhar, etal., J.Mat.Sci., 23,410(1988)
[5] J.S.Lu etal., semiconductor physics , Xian electronic science and technology university press,1991.
[6] T.Mitsui etal.,L-B handbook , Ferro and Antiferroelectric Substances, New York,1969.
[7] M.Furakawa, Jap. J.Appl. phys., 15, 2119(1976)
[8] M.H.Lee, etal., Ferroelectrics, 87, 71(1988)

MEASUREMENT OF DARK CONDUCTIVITY AT EXTREMELY LOW LIGHT LEVELS USING PHOTOREFRACTIVE TWO WAVE MIXING

by

A. E. Clement, G. C. Gilbreath, R. McKnight, Jr., J. Reintjes+, and J.M.K. Chock
Optical Systems Section
Naval Research Laboratory
Washington, D. C. 20375-5320

ABSTRACT

In this paper, we report dark conductivity measurements for $BaTiO_3$ and Ce: SBN:60 using photorefractive two-wave mixing at intensities of less than 10 mW per cm^2. These are the first such measurements reported at extremely low levels and the first measurements reported for $BaTiO_3$.

I. INTRODUCTION:

There is a growing interest in the study of noise reduction techniques and noise-limited image enhancement using photorefractive two wave mixing [1-4]. Photorefractive Two Wave Mixing (TWM) refers to the exchange of optical energy between two mutually coherent beams.[5] Typically, an intense pump beam, P_O, and a much weaker signal beam, S_O, are recombined in a photorefractive crystal configured such that energy is transferred from the pump to the signal beam. Net photorefractive gain results when the total amount of energy received in the signal path less the total contribution to the noise floor is greater than the energy in the incident signal.

A fundamental limit on the lower bound of photorefractive gain is the dark conductivity, σ_d. Dark conductivity refers to the random, thermally-induced motion of electrons in a given medium. In photorefractive interactions, it serves as an "erasing" mechanism that can impede the formation of desired gratings, thereby contributing to the noise. In most photorefractive TWM experiments, intensities are relatively high (>100 mW/cm^2). Consequently, phenomena such as the formation of competing gratings [6], become the dominant contributors to the noise, overwhelming the contribution from dark conductivity.

As the total intensity used in TWM experiments is decreased, the photocarrier concentration is reduced and the dark conductivity can become a significant contributor to the noise. Dark conductivity measurements for $BaTiO_3$ and Ce:SBN:60 at extremely low light levels were made using photorefractive two wave mixing. We believe that these are the first such measurements reported at these low light levels in these materials. In this paper, we show that dark conductivity must be measured using low intensity data collected near the TWM noise floor, particularly if an understanding of contributions from different sources of noise is pertinent. Dark conductivity computed using low intensity levels in TWM experiments differs from that computed when only high intensity data is included.

II. THEORY:

As previously noted, at the noise floor of a TWM interaction, grating formation can be impeded by the finite dark conductivity. Therefore, for low light level work, it is necessary to determine the bound imposed by this parameter in each type of crystal used. Ewbank, et.al. have shown that σ_d can be determined experimentally from the photorefractive grating formation time, τ_{PR} [7]. This parameter is the time it takes the signal to reach $(1\text{-}e^{-1})$ of its steady-state value during two wave mixing. Dark conductivity has been measured for doped samples of SBN using TWM with incident intensities as low as 100 mW/cm^2 and as high as 14 W/cm^2 [7,8]. For the diffusion-driven case, i.e.: no externally applied field, and in the limit that the grating spacing, Λ_g, is much greater than the diffusion length, L_d, τ_{PR} is given by the inverse of the dielectric relaxation rate and can be defined in mks units as [7]:

$$(\tau_{PR})^{-1} = \frac{1}{\varepsilon}\left\{ \sigma_d + \left(\frac{q\lambda\alpha\mu\tau_R I_o}{hc}\right)\right\} \qquad (1)$$

where ε is the dielectric constant, q is the charge of the photocarrier, λ is the wavelength, α is the absorption coefficient, μ is the carrier mobility, τ_R is the carrier

+ Dr. Reintjes is with the Laser Physics Branch

CH3080-0-7803-0465-9/92$3.00 ©IEEE

relaxation rate, and I_o is the total incident intensity. The value of the dark conductivity for a given crystal can be determined from the y-intercept when $1/\tau_{PR}$ is plotted against total intensity, $I_{Po}+I_{So}$. At $I_o=0$:

$$\sigma_d = \frac{\varepsilon_r \varepsilon_o}{\tau_{PR}} \qquad (2)$$

where ε_r is the relative dielectric constant.

To verify that the experiment was performed under the condition that $\Lambda_g \gg 2\pi L_d$, the diffusion length of the photorefractive charge carrier was calculated from this data as well. This calculation requires that the product of the mobility and the relaxation rate, $\mu\tau_R$, is obtained from the slope of the graph. From this product, L_d is determined as [7]:

$$L_d = \sqrt{\mu\tau_R k_B T/q} \qquad (3)$$

III. EXPERIMENT:

The dark conductivity was measured in Ce:SBN:60 and $BaTiO_3$ over the intensity range from 90 $\mu W/cm^2$ to 0.33 W/cm^2. The upper end of this regime overlaps with the those used by Ewbank [7] and Vazquez [8]. The Ce:SBN:60 was obtained from Rockwell. Its photocarriers were n-type. The $BaTiO_3$ came from MIT and its photocarriers were p-type. Carrier types were determined using the pyroelectric effect.

The bench configuration used in this experiment is shown in Fig. 1. The polarization of the λ=514.5 nm line from an argon ion laser was rotated with a half-wave plate to create extraordinarily polarized light at the crystal. The beam passed through variable attenuators and was spatially filtered and collimated before being split into a strong pump beam and a weaker signal beam. The attenuator in the signal path was used to set the beam ratio, I_{Po}/I_{So}. Mirrors, M1 and M2, directed the 1 mm diameter pump and signal beams to the crystal with an external Bragg angle of θ_{Bo}=14°, creating a grating spacing equal to 1 μm. The signal power was measured with a photodetector, P.D. Data acquisition and control was done with an HP9836 over the IEEE-488 bus.

The total intensity was varied by rotating a variable attenuator in the common path while the ratio I_{Po}/I_{So} was kept constant at approximately 10^4. The minimum intensity level that was used for each material was the lowest level at which the crystal exhibited TWM gain. Two wave mixing response was seen for signal power levels as low as S_{min}=20 pW in the $BaTiO_3$ crystal and S_{min}=35 pW in the Ce:SBN:60 crystal. Total intensities at these lowest light levels for $BaTiO_3$ and Ce:SBN:60 were 9 x 10^{-5} W/cm^2 and 5 x 10^{-4} W/cm^2, respectively.

Typically, when $BaTiO_3$ is used in TWM experiments, the crystal is rotated in the b-c plane by an

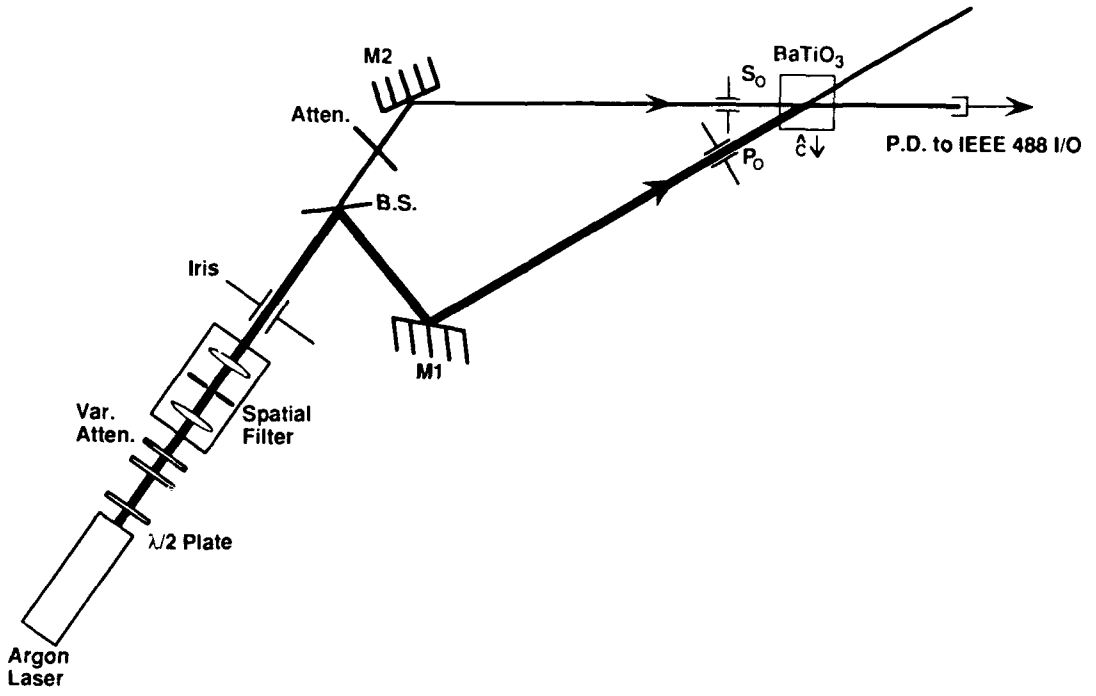


Fig.1 Experimental bench configuration used to measure the photorefractive response time $BaTiO_3$ and Ce:SBN:60.

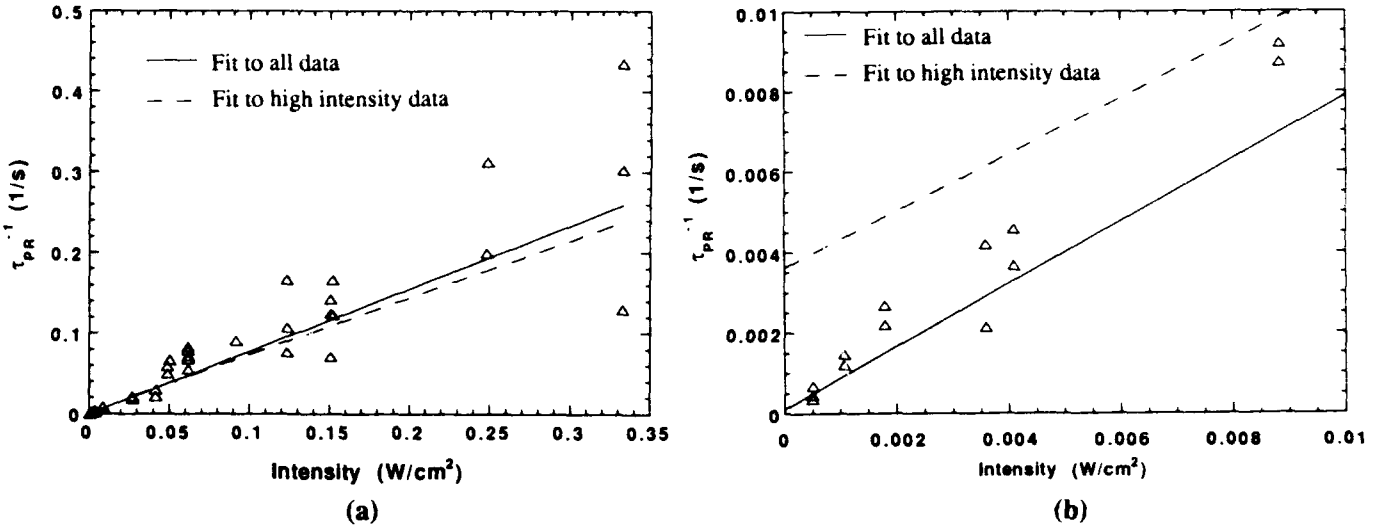


Fig. 2 Photorefractive grating formation rate as a function of total intensity incident on Ce:SBN:60. The solid line is a weighted least squares fit to all data and the dashed line is a similar fit to the high intensity data only. In 2(b) the dashed line has been extended to allow for comparison.

angle β, which is the angle between the grating vector and the c-axis, in order to make use of the high r_{42} coefficient. For the experiments reported here, β was set to 30° because it was the maximum angle of rotation which was possible due to the combination of crystal dimensions and beam diameters. A symmetric geometry was used for the SBN crystal (β=0°) to exploit the high r_{33} coefficient. The $BaTiO_3$ and Ce:SBN:60 had effective interaction lengths of L_{eff}=4.6 mm and L_{eff}=6.0 mm respectively. The corresponding absorption coefficients were α=0.04/mm and α=0.24/mm. Multiple readings were taken at each intensity level to determine error bars and overall repeatability of measurements

IV. RESULTS:

The dark conductivity and the diffusion length were calculated from the plot of τ_{PR}^{-1} vs. total incident intensity as shown in Fig. 2. The considerable scatter in the data points indicates that there is a wide range of variation from one measurement to the next , which is typical of photorefractive interactions. At the highest intensity, the absolute magnitude of the scatter is 100 times greater than at the lowest intensity. Consequently, it is necessary to use a weighted least squares fit which accounts for the error in the scatter as a percentage of the predicted value. From the weighted fit, σ_d was computed using Eqn. (2), and the y-intercept. Similarly, Ld was computed using Eqn. (3) and the slope, as previously described. These results are summarized in Table I.

The value of σ_d for the SBN sample in our experiment is smaller by over an order of magnitude compared to those measured by Ewbank, et al, for similar crystals [7]. That group reported dark conductivity measurements ranging from $\sigma_d=2.0 \times 10^{-11}$ to $\sigma_d=3.0 \times 10^{-11}$ for 3 samples of Ce:SBN:61. We found that if we used only our higher intensity data points for the calculations (I_o>10mW/cm²), our computations for σ_d would fall within their range.

Table I. Experimental Results

	Ce:SBN:60	$BaTiO_3$
σ_d $(\Omega\ cm)^{-1}$	9.2×10^{-13}	5.4×10^{-12}
$\mu\tau_R$ (cm²/V)	6.1×10^{-11}	9.2×10^{-11}
L_d (Å)	126	154

In Figure 2a, the dashed line is a weighted fit to the high intensity data only. The solid line was fit to all of the data. As can be seen from the grapi., the two lines appear to converge at the ordinate axis. However, a closer examination of the y-intercepts is obtained from the graph shown in Fig 2b. The divergence in the y-intercepts translates to a difference of the order of 30 for computed values of σ_d in this work.

Because dark conductivity, by definition, is the conductivity when the intensity goes to zero, we would expect that the more accurate value of σ_d would be obtained from the lower intensity measurements. In lower intensity regimes knowing a noise bound to more accurate levels can be critical. These results indicate that dark conductivity should be computed from measurements taken in the working regime of interest or the contribution from σ_d may be overestimated.

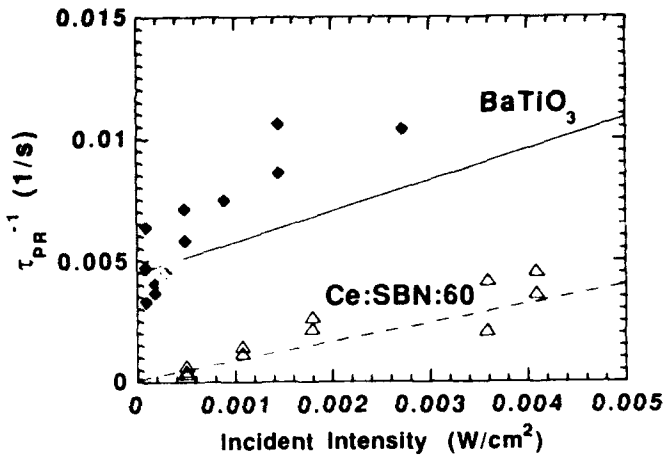


Fig. 3 Photorefractive grating formation rate as a function of total intensity incident on Ce:SBN:60 and $BaTiO_3$ for extremely low light levels.

The slopes of the lines and therefore the diffusion lengths for a given crystal also differ depending on whether the low intensity data was used in their calculation. The implication from the data is that at the lower intensity levels, L_d is greater; hence, the bound on the geometry will be different, which can impact overall bench configurations.

Grating formation rates measured in this experiment are plotted as a function of total incident intensity for $BaTiO_3$ and Ce:SBN:60, in Figure 3. This figure shows the low intensity regime which is of particular interest in the investigation of noise sources. As in Figure 2, the straight lines represent weighted least squares fits to all of the data. The y-intercepts and slopes of these two lines are considerably different because of the differing response times of the two photorefractive crystals. In this case, the $BaTiO_3$ was approximately 6 times faster than the Ce:SBN:60 in the intensity regime of interest. These results are in contrast with those of Ewbank, et.al., who report that the response rate of $BaTiO_3$ was approximately one third the rate of the Ce:SBN:61 crystals under study[7].

V. CONCLUSIONS:

We have shown that the most accurate measurements of dark conductivity are made when the y-intercept is computed using weighted least squares fit including measurements taken near the noise floor for two wave mixing interactions in a specific crystal. Such a bound is important to determine experimentally when seeking to understand noise mechanisms in a given photorefractive medium.

We report σ_d=9.2 x 10^{-13} $(\Omega\ cm)^{-1}$ for Ce:SBN:60 and σ_d=5.4 x 10^{-12} $(\Omega\ cm)^{-1}$ for $BaTiO_3$ when intensities less than 10 mW/cm^2 are included in the calculation. Our results also indicate that diffusion length varies with intensity regime. Therefore, experimental configurations may be impacted as well.

Simple exponential models for thermal heating cannot account for the magnitude of change observed in σ_d. Possible mechanisms to account for this change are the subject of further study.

REFERENCES:

[1] H. Rajbenbach, A. Delboulbe and J.-P. Huignard, "Low-Noise amplification of ultraweak optical wave fronts in photorefractive $Bi_{12}SiO_{20}$," Opt. Lett., vol. 16, p. 1481, 1991.

[2] W.S. Rabinovich, B.J. Feldman, and G.C. Gilbreath, "Suppression of photorefractive beam fanning using achromatic gratings," Opt. Lett., vol. 16, p. 1147, 1991.

[3] H. Rajbenbach, A. Delboulbe, and J.-P. Huignard, "Noise suppression in photorefractive image amplifiers," Opt. Lett., vol. 14, p. 1275, 1989.

[4] J. Khoury, C. L. Woods, and M. Cronin-Golomb, "Noise filtering using adaptive spatial filtering in photorefreacive two-beam coupling," Opt. Lett., vol. 16, p. 747, 1991.

[5] D.L. Staebler and J.J. Amodei, "Coupled-wave analysis of holographic storage in $LiNbO_3$," J. Appl. Phys., vol. 43, p. 1042, 1972.

[6] J. Feinberg and K.R. MacDonald, "Phase-conjugate mirrors and resonators with photorefractive materials", Topics in Applied Physics, vol. 62, p. 180, 1989.

[7] M. D. Ewbank, R. R. Neurogaonkar, W. K. Cory, and J. Feinberg, "Photorefractive properties of strontium-barium niobate," J. Appl. Phys., vol. 62, p. 374, 1987.

[8] R. A. Vazquez, M. D. Ewbank, and R. R. Neurogaonkar, "Photorefractive properties of doped strontium-barium niobate," Opt.Comm., vol. 80, p. 253, 1991.

PHOTOREFRACTIVE IMAGE AMPLIFICATION AT EXTREMELY LOW LIGHT LEVELS

by

G. C. Gilbreath, A. E. Clement, J. Reintjes* and R. McKnight, Jr.
Optical Systems Section
Naval Research Laboratory
Washington, D. C. 20375

ABSTRACT

We report measurements of image amplification at extremely low light levels in $BaTiO_3$ using photorefractive two wave mixing. We observed image amplification for signal levels as low as 20 pW with a Fresnel number of 382. Comparisons of Fourier and direct imaging show that amplification of the Fourier transform of the image provides improved image quality and field-of-view at the lowest light levels.

I. INTRODUCTION

Image amplification using photorefractive Two Wave Mixing (TWM) is well-known.[1,2] In TWM, two mutually coherent beams of light are combined in a photorefractive material in a configuration that enables light to couple from one beam to the other. Typically, one beam (signal) is much weaker than the other (pump) and carries a spatial distribution (the image) to be amplified through coupling with the stronger pump beam. At extremely low light levels, the quality of such an amplified image is affected by scattering from defects in the crystal, such as scratches, cleaves, and embedded scattering centers. These defects can degrade the image directly through obscuration and distortion. In addition, these scattering centers can set up competing TWM gratings that contribute noise to the amplified image by scattering pump light into the solid angle of the amplified image. This effect is known as beam fanning.[3] The competing gratings can also give rise to nonuniform amplification[4], and can reduce signal-to-noise[5], consequently limiting minimum detectable signal levels.

Various techniques for reducing the noise in photorefractive TWM have been reported[6-9]. The lowest signal level reported to date for image amplification is 70 pW in BSO which was achieved using crystal rotation to reduce noise[9]. In this paper, we examine image amplification in $BaTiO_3$ at extremely low light levels. Image amplification was observed down to signal levels of 20 pW. We compare images obtained by amplifying the direct image of an object with images obtained by amplification of the Fourier transform. The results indicate that the gain and image quality are both higher with the Fourier imaging technique than with the direct imaging technique.

Extremely low light image amplification using photorefractive TWM requires that $G_n I_{so} > I_s - N$, where G_n is photorefractive net gain, I_{so} is incident signal intensity, I_s is the total intensity received in the signal path, and N is noise defined as characteristics which degrade the true image. G_n is related to the photorefractive gain, G, by the ratio of I_{so} to the signal propagated through the crystal with no pump present, or $G_n = G I_{s(\text{no P})}/I_{so}$. The photorefractive gain, G, is a function of beam ratio, geometry, electro-optic characteristics, dark conductivity and absorption. It is defined as:

$$G = \frac{1+m}{1+m\exp\{(\alpha-\Gamma)L_{eff}\}} \qquad (1)$$

where $m=I_{po}/I_{so}$, I_{po} is the incident pump intensity, I_{so} is the incident signal intensity, L_{eff} is the effective interaction length, α is the absorption coefficient, and Γ is the exponential gain coefficient defined in terms of material parameters and geometry[10].

The amount of the noise diffracted into the signal from the pump due to beam fanning, can be reduced by decreasing the Fresnel number of the TWM amplifier, such that: $F\#=A/\lambda L_{eff}$, where A is the area of the pump beam, λ is the wavelength, and L_{eff} is the effective interaction length of the amplifier[11]. In imaging systems, a lower limit on the F# is set by the desired image resolution. Consequently, there is a compromise between resolution and reduction of noise level. For resolution that supports standard video imaging, an F# of the order of 400 is suitable.

The noise level in the amplified image can also be affected by the imaging geometry. If the direct image of an object is amplified and then reimaged onto a detector, the noise generated in the crystal will also be imaged into the same area. If the Fourier Transform of the object is amplified and the image of the object is subsequently reconstructed at the detector, the noise generated in the crystal will be transformed at the detector. In this situation, small scale defects in the crystal will not appear directly in the reconstructed image. In addition, the noise generated from beamfanning will be spread over an area corresponding to the spread of spatial frequencies accepted by the TWM amplifier. The area over which the noise appears in the reconstructed image plane can be larger than the area of the re-transformed image, resulting in an increase in the signal-to-noise ratio within the recovered image.

II. EXPERIMENT

The experimental apparatus used in the experiments reported here is shown in Fig. 1. A beam from an argon ion laser was directed through polarizing optics, a variable attenuator, a spatial filter, collimating optics, and an iris to form a 3 mm diameter beam in the shape of an

CH3080-0-7803-0465-9/92$3.00 ©IEEE

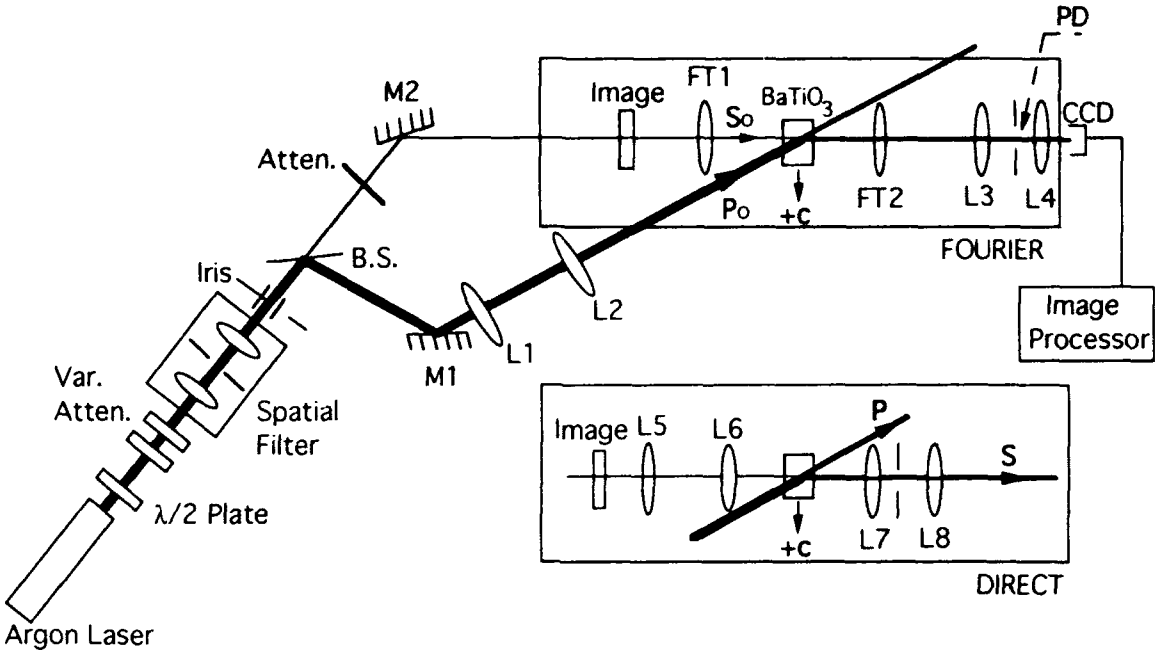


FIG. 1. Experimental interferometer for photorefractive image amplification using two wave mixing. Upper box shows configuration used for Fourier imaging; inset shows optics used in direct imaging.

Airy disk at a wavelength of λ = 514.5 nm. The primary beam was then split into a strong pump beam, $\mathbf{P_0}$, and a weaker signal beam, $\mathbf{S_0}$, with a 10:1 reflecting beam splitter. The pump beam was directed through a reducing telescope consisting of lenses L1 and L2 by mirror M1 to form a 1 mm diameter beam at a $BaTiO_3$ crystal. The signal beam passed through an additional attenuator to set the beam ratio and was then directed to the $BaTiO_3$ crystal by mirror M2.

An image was placed on the signal beam with an Air Force resolution chart. Depending on the measurements being made, either the image of the resolution chart was relayed to the $BaTiO_3$ crystal with lenses L5 and L6, or the Fourier transform of the resolution chart was formed at the crystal by lens FT1. When the direct image was amplified, the diameter of the signal beam was reduced to 1 mm with lenses L5 and L6 to match the pump beam diameter. When the Fourier transform configuration was used, the central disk of the transform was ≈31.6 μm in diameter, corresponding to about 1/30 th of the pump beam diameter. This latter geometry enabled high spatial components containing information about the image structure to be subtended by the pump beam.

The image in the amplified signal beam was detected with a Cohu CCD camera and a computerized image processor. Using the direct method, the amplified image of the chart was transferred to the CCD camera with imaging lenses L7 and L8. When the Fourier transform of the chart was amplified, the image was reconstructed with lens FT2 and was then transferred to the CCD camera with lenses L3 and L4. An aperture between lenses L3 and L4, or lenses L7 and L8 reduced the scattered light transferred to the camera.

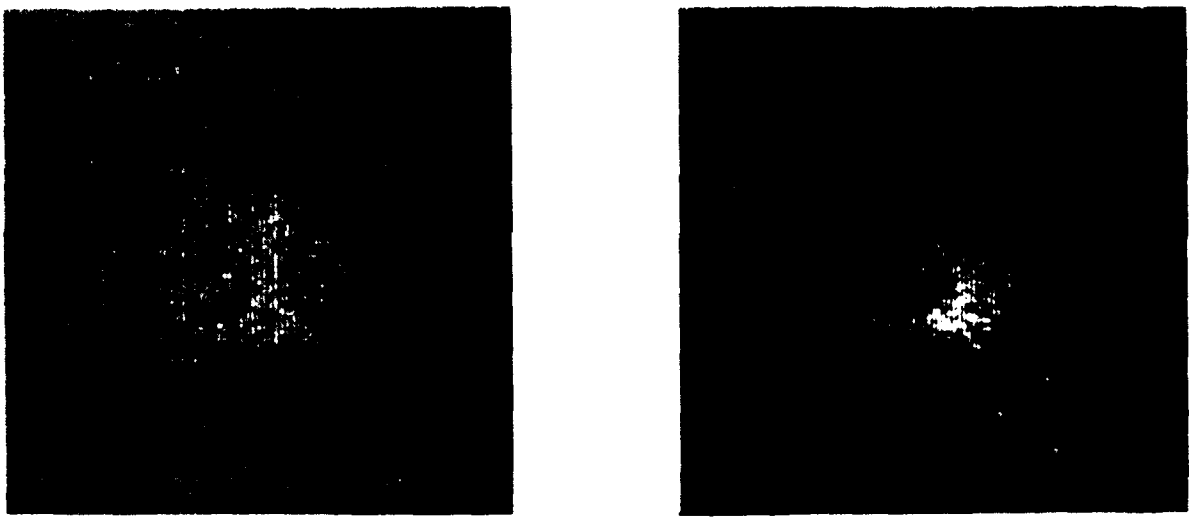
The aperture of the $BaTiO_3$ crystal was 3×5 mm. For this crystal and geometry, the effective interaction length, L_{eff}, was 4 mm, and α=0.04 mm^{-1}. The dark conductivity was 9.2E(-13) per ohm-cm, as determined by the technique of Ewbank, et. al.[12] at the extremely low light levels used in these experiments. The pump and signal beam were extraordinarily polarized with respect to the **c** axis and the external Bragg angle was 14°. The bisector was rotated 30° with respect to the c axis which was the maximum permitted by the crystal dimensions. At this ratio, Γ at saturation was 1.25/mm. The Fresnel number for this geometry was F#=382, corresponding to approximately $(382)^2$ resolvable spots in the image.

Measurements of the photorefractive gain and the amplified images were made for both the Fourier and direct imaging configurations as a function of total power. The incident power was varied over the range from 8.2μW to 0.88μW by adjusting the variable attenuator in the primary beam before the beam splitter. The ratio of powers in the pump and signal beams was signal set to 26000:1 by adjusting the attenuator in the signal beam after the beam splitter. This ratio was kept constant throughout the experiments. The value of m at the crystal was approximately 26000:1 for the direct imaging measurements. For Fourier imaging, m is estimated to be on the order of 35:1 in the central lobe of the transformed image, if it is assumed that the transformed image is comparable to an Airy disk.



(a) (b)

FIG. 2. Photorefractively amplified images at S(no pump)=185 pW. (a) Fourier imaging; (b) direct imaging



(a) (b)

FIG. 3. Photorefractively amplified images at minimum detectable signal levels. (a) Fourier imaging at S(no pump) = 20 pW; (b) direct imaging at S(no pump)=27 pW.

Spatially integrated intensities were measured by inserting a UDT detector (PD) after the iris between lenses L3 and L4 (or L7 and L8 as appropriate) as shown. This detector was calibrated to provide linear response down to 1 pW. The power in the transmitted, unamplified signal beam, $S_{(no\ pump)}$, was measured with the pump beam blocked, the power in the amplified signal beam, $S_{(pump)}$, was measured with the pump present, and the power induced from pump noise diffracted into the signal path, P_N, was measured with the signal beam blocked. Beam fanning out of the signal was not induced in the range of intensity levels examined. These measurements allowed computation of the net photorefractive gain G, where

$$G = \frac{(S_{(pump)} - P_N)}{S_{(no\ pump)}} \qquad (2)$$

III. RESULTS

Examples of photorefractively amplified images using Fourier and direct imaging are shown in Figures 2 and 3. In Figure 2, a comparison may be made between amplified images for an unpumped signal level of 185 pW. In these pictures, image structure of 5 line pairs per mm is shown and is easily resolved. The integrated gains as measured with the photo diode were 35 and 7 for the Fourier and direct methods respectively.

A similar set of pictures is shown in Fig. 3, for Fourier image amplification with S(no pump) = 20 pW (Fig. 3a); and for direct imaging with S(no pump) = 27 pW. These were approximately the lowest incident powers at which viable amplified images could be detected for each technique. Again, the image structure was 5 line pairs per mm. The integrated gain for both methods as measured with the photo diode was about 4.

A comparison of the images obtained by direct and Fourier imaging shows that the Fourier images had a larger field-of-view and could be detected at lower signal intensities than the direct images. The field-of-view for direct imaging is controlled by the diameter of the pump beam, D_p, relative to that of the signal beam, D_S. For these experiments, the pump beam profile was approximately Gaussian and therefore formed an apodizing filter for the image. The diameters were matched 1:1. Effective amplification was observed over the central 470μm of the pump, which coincides approximately with the 1/e diameter (400μm). However, at the higher intensities, structure was evident in the "wings" of the amplified image. As the signal power was changed from 185 pW to 20 pW, the FOV for the direct images decreased from recovering most of the original image to just that subtended by the approximate 1/e diameter.

For the Fourier imaging, D_p does not directly affect the field-of-view. This parameter affects only the maximum number of spatial frequencies that can be retained in the image. As a result ,we would expect this configuration to provide a larger field-of-view, but potentially a reduced resolution. As can be seen by comparing Fourier images in Figs. 2 and 3, there is some reduction in the FOV at the lowest light levels but not nearly to the extent evident when the direct imaging method.

The expected difference in FOV between the two methods can be seen in Figs. 2 and 3. The resolution for each method evident in the two figures appears comparable, indicating that the resolution attainable with the Fourier imaging is not severely limited for these experimental conditions. To acquire an equivalent FOV using direct imaging, the image would have to be demagnified such that $D_S \approx 400\mu m$. Such reductions make the image vulnerable to obscurations, scratches, and other effects impressed directly by the defects and imperfections in the crystal itself.

IV. CONCLUSION

In conclusion, we have shown that Fourier imaging is preferable to direct imaging for extremely low light image amplification using photorefractive energy couplers. The technique inherently filters out noise generated from scatterers; consequently, minimum detectable signal levels can be lower. Image structure is viably recovered with far smaller illuminated volumes using Fourier imaging. Hence, crystals with smaller apertures may be used. Finally, Fourier imaging is readily implementable and does not require complex optical interferometers or mechanical methods which reduce signal power as well as noise.

ACKNOWLEDGMENTS

The authors would like to thank Dr. William Rabinovich for his many helpful suggestions and discussions.

REFERENCES

1. P. Gunter, "Holography, coherent light amplification and optical phase conjugation with photorefractive materials," Physics Reports, vol. 93, p. 199, 1982.

2. Y.Fainman, E. Klancnik, and S. H. Lee, "Optimal coherent image amplification by two-wave coupling in photorefractive BaTiO3," Opt. Eng., vol. 25, p. 228, 1986.

3. J. Feinberg and K. R. MacDonald, "Phase-Conjugate Mirrors and Resonators with Photorefractive Materials," Topics in Applied Physics, vol. 62, p. 180, 1989.

4. G. C. Gilbreath, "Forward Multibeam Mixing in Diffusion-Driven Photorefractive Media," Jnl. of Lightwave Tech., Vol. 9, no. 1, p. 105, 1991.

5. J. Joseph, K. Singh, and P.K.C. Pillai, "Crystal orientation dependence of SNR for signal beam amplification in photorefractive BaTiO3," Opt. & Laser Tech., vol. 23, p. 237, 1991.

6. H. Rajbenbach, A. Delboulbe, and J.-P. Huignard, "Noise suppression in photorefractive image amplifiers," Opt. Lett., vol. 14, p. 1275, 1989.

7. J. Khoury, C. L. Woods, and M. Cronin-Golomb, "Noise filtering using adaptive spatial filtering in photo refractive two-beam coupling," Opt. Lett., vol. 16, p. 747, 1991.

8. W. S. Rabinovich, B. J. Feldman, G. C. Gilbreath, "Suppression of photorefractive beam fanning using achromatic gratings," Opt. Lett., vol. 16, p. 1147, 1991.

9. H. Rajbenbach, A. Delboulbe, and J.-P. Huignard, "Low-noise amplification of ultraweak optical wave fronts in photo refractive $Bi_{12}SiO_{20}$," Opt. Lett., vol. 16, p. 1481, 1991.

10. A. Marrakchi and J. P. Huignard, "Diffraction Efficiency and Energy Transfer in Two-Wave Mixing Experiments with $Bi_{12}SiO_{20}$," Appl.Phys., vol. 24, p. 131, 1981.

11. M. D. Duncan, R. Mahon, L. L. Tankersley, and J. Reintjes, JOSA B (submitted for publication: March, 1992).

12. M. D. Ewbank, R. R. Neurogaonkar, and W. K. Cory, "Photorefractive properties of Strontium Barium Niobate," J. Appl. Phys., vol. 62, p. 374, 1987.

+Dr. Reintjes is with the Laser Physics Branch.

AUTHOR INDEX

Adair, J.H., 89
Adhikari, P., 116
Ahmad, A., 516, 520
Al-Shareef, H.N., 448
Alberta, E.F., 560
Alemany, C. 512
Amin, A., 1
Anderson, M.U . 273
Andriamampianina, V., 364
Aoyagi, M., 537, 541
Armstrong, T.R., 455
Auciello, O., 229, 320, 448
Audaire, L., 27
Audigier, D., 255
Azuma, M., 356

Baidy, E., 281
Bailey, A.E., 152
Ballato, A., 281
Banno, H., 266
Barrett, J., 484
Bauer, F., 27, 273
Bellur, K.R., 448
Bendale, P., 89
Beratan, H.R., 1
Bhalla, A.S., 401, 480, 556, 560
Bhanumathi, A., 144, 209, 500
Birks, E., 134
Birnie, III, D.P., 424, 240
Boulton, J.M., 424
Bowen, L.J., 160
Brooks, K.G., 182, 269
Brown, A.E., 74
Brown, L.F . 277
Buchanan, R.C., 185, 455
Burton, L.C., 94

Canaday, J.D., 516
Cao, W., 107, 252
Carabatos-Nedelec, C., 370
Carter, C.F., 202
Cerro, J. del, 398
Chadney, J.E., 452
Chaminade, J.P., 364
Chan, K.S., 233
Chen, H.Y., 600
Chen, H. T., 353
Chen, J., 111, 182, 313
Chen, T.C.C. 600
Chen, X., 229
Chen, Y .., 31, 607
Chen, Z., 47
Choch, J.M.K., 625
Chodelka, R.E., 89
Choi, S.W., 213, 395, 588
Choi, W.-S., 164
Cl-Harrad, I., 370
Clement, A.E., 625
Clement, A.D., 629
Collier, D.C., 199
Costantino, S.A., 89
Criado, J.M., 398
Cross, L.E., 107, 182, 252, 313, 401, 480

Dausch, D.E., 297
Day, J.E., 74
deFrutos, J., 39
Desu, S.B., 225, 293, 399, 412
Dexter, K.F., 452
Dimza, V., 134
Ding, A.-L., 19, 233
Dmytrow, D . 370
Doripella, C.R., 206
Dougherty, J.P., 55, 70, 492
Drummond, M.A., 374

Eatough, M O., 344
Elissalde, C., 458, 462, 465
Eyraud, L., 255, 533, 581
Eyraud, P., 255, 533

Feng, X.-Q., 43
Fijii, E., 356
Fousek, J., 171
French, K.W., 160
Fuda, Y., 573
Fujimoto, S., 405
Furuta, A., 195
Furuya, M., 66

Gachigi, K.wa, 492
Galloway, K.F., 240, 424
Garabédian, C., 581
Gardiner, R., 340
Garino, T.J., 344
Gaucher, P., 458
Ge, M., 19
Gifford, K.D., 448
Gilbreath, G.C 625, 629
Gonnard, P., 581
Goodnow, D.C., 344
Gotor, F.J., 398
Graham, J.T., 167
Graham, R.A., 273
Greegor, R.B 436
Gupta, S.P., 206
Gururaja, T.R., 259

Hadnagy, T. D., 416
Haertling, G.H., 23, 236, 297, 488, 569, 596
Hagenmuller, P., 123, 360
Hagiwara, M., 103
Hall, D.A., 51, 508
Han, Y., 609, 621
Handerek, J., 370
Hanson, C.M., 1
Harmer, M.P., 111
Hayashi, K , 428
Headley, T.J., 344
Hendricks, W.C., 293
Hu, H., 305, 309, 440
Huang, B., 381
Huang, C.-Y., 401
Huang, C.H.-J., 332
Huang, S.-Y., 123, 360
Huang, Y.-H., 19
Huang, Z.Z., 476
Huebner, W., 148
Hwang, D.M., 301, 392

Ichinose, N., 94
Imai, T., 317

Jang, S.-J., 480
Janna, P., 374
Jaquays, C., 116
Jia, W.Y., 31, 607
Jiang, Q., 107
Jimene, B., 512
Jiménez, B., 39

Kallur, V.A., 374
Kampschöer, G.L.M., 217
Kanai, K., 405
Kanegae, T., 140
Kankul, H., 148
Kano, G., 356
Kasamatsu, T., 47
Katayama, T., 327, 428
Kato, Y., 405
Kazaoui, S., 465
Khan, A.R., 412
Khutorsky, V.E., 592
Kim, J., 185
Kim, J.S., 367
Kim, Y.J., 213, 395, 588
Kim, K.C., 588
Kingon, A.I., 229, 320, 448
Kirlin, P.S., 340
Klee, M., 217
Klein, L.C., 444
Klotins, E., 134
Knauss, L.A., 116
Kneer, E.A., 424
Ko, J.S., 395
Komachi, T.K., 94
Kosinski, J., 281
Krupanidhi, S.B., 305, 309, 340, 440
Kulwicki, B.M., 1
Kumar, U., 55, 70, 148, 492
Kuriakose, A.K., 516
Kurtz, S.K., 269
Kuskbabe, C., 537
Kwok, C.K., 408

Lal, M., 554
Lamppa, D.L., 344
Lang, S.B., 592
Larsen, P.K., 217
Lee, B.I., 488
Lee, H.Y., 94, 524
Lee, J.W., 248
Lee, L.M., 273
Lee, S.C., 240, 424
Lee, S.H., 213, 588
Lee, T.-Y., 529
LeFebvre, H., 273
Leung, M.S., 349
Lewis, K.L., 452
Li, G., 569
Li, K.K., 236
Li, L., 349
Li, L. T., 468
Li, S., 401, 480
Li, Y., 613
Liang, C.-K., 529
Lin, C., 488
Lin, C.T., 349
Lin, H., 332
Liou, T., 607
Lipeles, R.A., 349
Livage, C., 444
López, F., 39
Lu, H.M., 476
Lu, P., 545, 585
Lu, P.W., 548
Lu, S., 385
Luo, W.-G., 19, 233
Lytle, F.W., 436

Mao, Z.Y., 468
Maiwa, H., 103

Mann, L.A., 206
Marsh, P., 148
Massuda, M., 152
Matsubara, S., 285
McKnight, Jr., R.A., 625, 629
McMillian, L.D., 356
Mei, B.Z., 248
Millar, C.E., 59, 512
Ming, N.-B., 35
Mitra, S. N., 416
Miyasaka, Y., 285
Mori, T., 66
Mouli, K.C., 144, 500
Mukherjee, B.K., 167, 520
Mundi, M., 398
Murty, K.L., 209
Murty, K.V.R., 144, 209, 500
Murty, S.N., 144, 209, 500

Nam, H.-D., 524
Nance, J.D., 74
Newman, B.A., 248
Nicolaides, G., 392
Nigli, S., 374

Oakley, C.G., 148
Obhi, J.S., 11
Ochi, A., 66
Ogura, K., 266
Ohanessian, H., 581
Ohki, M., `49
Ohno, T., 573
Okazaki, K., 103, 504, 565
Orr, M.N., 424
Osbond, P.C., 202
Otsuki, T., 356
Ozolinsh, M., 134

Padmavathi, G., 209
Pan, W., 408
Pandey, R.K., 374
Pardo, L., 512
Patel, A., 11
Paz de Araujo, C.A., 356
Peng, C.H., 293
Peng, C.-J., 305
Perez-Maqueda, L., 398
Pilgrim, S.N., 152
Pinto, N.J., 119
Pitzius, P., 76
Polla, D., 127
Prasad, S.E., 516
Preston, K.D. 23
Proddey, J.D., 152

Rabson, T.A., 332
Ravez, J., 123, 360, 364, 458, 462, 465
Real, C., 398
Reed ., R.P, 273
Reintjes, J., 625
Rey, S., 533
Richard, C., 255
Richard, M., 255
Ricote, J., 512
Roberts, T., 356
Roseman, R.D., 185, 455
Rou, S.H., 448
Ryu, Y.I., 367

Safari, A., 281, 420, 444
Satoh, A., 541

Sayer, M., 244
Sayer, M., 289
Scheinbeim, J.I., 248
Schmidt, V.H., 119
Schmitt, H., 76
Schrimpf, R.D., 240, 424
Schwartz, R.W., 344
Scott, J.F., 356
Scott, M.C., 356
Selvaraj, U., 269
Shannon, J., 281
Shebanov, L., 134
Sheen, J., 480
Sheldon, D. J., 416
Shen, D., 63, 545, 551, 585
Shen, D.W., 548
Sherrit, S., 167
Sherrit, S., 520
Shimizu, M., 47, 327, 428
Shin, Y.H., 213, 395
Shiosaki, T., 47, 156, 327, 428
Shiozaki, T., 317
Shorrocks, N.M., 11, 202
Shrout, T.R., 80
Simon, A., 364
Simon, D., 76
Simonne, J.J., 27
Siu, G.G., 233
Skaar, E.C., 484
Smits, J.G., 164
Smyth, D.M., 111
Srikanth, V.S., 556
Sternberg, A., 134
Stringfellow, S.B., 202
Sugihara, S., 103, 565, 577
Sugiyama, M., 327
Sun, H.-T., 189
Sun, P., 432
Sutherland, A.E., 152
Swartz, S.L., 80

Tahan, D.M., 420
Takemura, K., 285
Takenaka, T., 560
Taniguchi, N., 156
Tanimoto, T., 504
Taylor, D.J., 560
Tekenaka, T., 140
Teowee, G., 240, 424
Tomikawa, Y., 537, 541
Tossell, D.A., 10
Toulouse, J., 116, 179
Troccaz, M., 533
Tuttle, B.A., 344

Udayakumar, K.R., 182, 313
Uhlmann, D.R., 240, 424
Ujma, Z., 370
Umakantham, K., 500
Unchino, K., 195

Van Buskirk, P.C., 340
Van Der Mark, M.B. , 217
Van Nice, D.B. , 167
Varanasi, S., 55
Varma, S., 516
Venigalla, S., 89
Vijay, D.P., 408
Voigt, J.A., 344
Von Der Mühll, R., 123, 360, 364
Vugmeister, B.E., 116, 179

Wang, A.Y., 389
Wang, F., 55, 236, 596
Wang, H., 63, 252, 472, 548 551
Wang, H.-F., 185
Wang, H.-W., 51
Wang, L.M., 301, 389
Wang, P.J., 31, 607
Wang, S.F., 70
Wang, S.F., 148
Wang, X., 377, 381, 585
Wang, X.M., 179
Wang, Y. L., 353
Watton, R., 202
Webb, J.S., 349
Whatmore, R.W., 11, 202
Wheat, T.A., 516, 520
Wiederick, H.D., 167
Williams, M.A., 508
Wolny, W.W., 59
Wood, A.K., 508
Wu, A.Y., 301, 389, 392, 436, 600, 604
Wu, D. H., 353
Wu, L., 529
Wu, Z., 244

Xie, S.W., 31, 607
Xu, B., 472
Xue, W., 63, 545, 551, 585
Xue, W.R., 548

Yamaguchi, H., 285
Yamamoto, T., 317
Yang, D., 496
Yao, X., 189, 377, 381, 385, 432, 462,468, 609, 613, 617, 621
Yi, G., 289
Yin, Z.W., 472, 476
Yon, J.S., 556
Yoo, I.K., 225, 408
Yoshida, T., 573
Yoshikawa, S., 269, 573
You, B., 613, 617
You, I. K., 412
Yu, D. W., 353
Yu, I., 367

Zhang, L.-Y., 189, 385, 432, 609, 617, 621
Zhang, Q.-R., 43
Zhang, Q.M., 252, 480
Zhang, Q.T., 63, 548, 551
Zhang. R.-T., 19, 233
Zhang, W., 545
Zhang, Z., 551
Zhao, M.Y., 63, 545, 548, 551, 585
Zhou, Q.F., 607, 621

Attendance Roster

ATTENDEE LIST

ADACHI, Masatoshi
Toyama Prefectural University
Kosugimachi
Toyama, Japan 939-03

ADAIR, James
University of Florida
323 Mae Building
Gainesville, FL 32611

ALBERTA, Edward F.
Penn State University
143 Materials Research Lab
University Park, PA 16802

ALEXANDER, Jane A.
DARPA
3701 N. Fairfax Drive
Arlington, VA 22203

AL-SHAREEF, Sam
North Carolina State University
2603 L Village Court
Raleigh, NC 27607

AMIN, Ahmed
Texas Instruments
34 Forest Street
Attleboro, MA 02703

AOYAGE, Manabu
Yamagata University
4-3-16, Jonan Yonezawa
Yamagata, Japan 992

AUCIELLO, Orlando
MCNC, Center for
Microelectronics
3021 Cornwallis Road
Research Triangle Park, NC
27511

BALLATO, Art
US Army Electronics Technology
& Devices Lab
SLCET - DS
Fort Monmouth, NJ 07703-5601

BANNO, Hisao
NGK Spark Plug Company, Ltd.
14-18, Takatsuj-cho
Mizuho-ku, Nagoya Japan 467

BARLINGAY, C.K.
Arizona State University
Chem Bio and Mat Engrg
Tempe, AZ 85281

BARRETT, James R.
Clemson University
Olin Hall
Clemson, SC 29634-0907

BAUER, Francois
Institut Granco-Allemand (J.S.L.)
5 rue General Cassagnou
Saint-Louis, 68301 France

BEDEKAR, Milind M.
Rutgers University
Department of Ceramics
POB 909
Piscataway, NJ 08855

BELL, Andrew
Ecole Polytechnique Federale
de Lausanne
Lab. de ceramique, MX-Ecublens
1015 Lausanne, Switzerland

BELLUR, Kashyap
Dept/Mat Sci & Engrg, NCSU
Raleigh, NC 27695-7907

BENEDITTO, Joseph
Harry Diamond Labs
2800 Powder Mill Rd.
Adelphi, MD 20783

BENNETT, Kelly W.
Harry Diamond Labs
2800 Powder Mill Rd.
Adelphi, MD 20783

BERNACKI, Steve
Raytheon Company
528 Boston Post Road
Sudbury, MA 01776

BHALLA, A.S.
Penn State University
Materials Research Lab
University Park, PA 16802

BHAWUMATHI, A.
Andhra University
Dept. of Physics
AU, Visakhapatnam, India

BLOOMFIELD, Phillip E.
Drexel University
Biomedical Engineering &
Science Inst.
Philadelphia, PA 19104

BOWEN, Leslie J.
Materials Systems Inc.
53 Hillcrest Road
Concord, MA 01742

BROWN, Lewis F.
South Dakota State University
POB 2220, Harding Hall 201
Brookings, SD 57007

BUCHANAN, Relva C.
University of Illinois
Dept. of Mat Sci/Engrg
105 S. Goodwin Ave.
Urbana, IL 61821

CAO, Wenwu
Penn State
164 Materials Research Lab
University Park, PA 16802

CATALAN, Tony
General Motors Corporation
13 Mile at Chicago Rd.
Research Labs
Warren, MI 48090

CHEN, C.J.
AVX Corporation
2875 Highway 501
Conway, SC 29526

CHEN, Jiayu
Pennsylvania State University
A6, Materials Research Lab
State College, PA 16802

CHEN, Jie
Lehigh University
Whitaker Lab #5
Bethlehem, PA 18015

CHEN, Xiaohua
Dept. Mat. Sci/Engrg, NCSU
Raleigh, NC 27695-7907

CHEN, Z.J.
Dept. of Mat Sci/Engrg
Blacksburg, VA 24060

CHENG, Lap Kin
E.I. DuPont De Nemours & Co.
Experimental Station
PO Box 80306
Wilmington, DE 19880-0306

CHIU
Virginia Tech
213 Holden Hall
Blacksburg, VA 24060

CHODELKA, Robert E.
University of Florida
305 MAE
Gainesville, FL 32611

CLARK, Fred
CeramPhysics, Inc.
921 Eastwind Dr., Suite 110
Westerville, OH 43081

CLEMENT, Anne E.
Naval Research Lab
4555 Overlook Avenue SW
Washington, DC 20375-5320

COLLIER, Donald C.
Norden Systems
Norden Place
Norwalk, CT 06856

COSTANTINO, Steve
Cabot Performance Materials
County Line Road
Boyentown, PA 19512

CROSS, L.E.
Materials Research Lab
Penn State University
University Park, PA 16802

CUTCHEN, J. T. (Tom)
Sandia National Laboratories
Dept. 2506
Albuquerque, NM 87185

DAEMEN, A.
DSM Research
P.O. Box 16
Geleen, Netherlands

DAI, Xunhu
University of Illinois105 S
Goodwin St, Ceram Bldg, Rm 421
Urbana, IL 61801

DAM, Chuong
Caterpillar
Technical Center, Bldg. E
POB 1875
Peoria, IL 61656-1875

DAMJANOVIC, Dragan
Ecole Polytechnique
Federale de Lausanne
Lab. de ceramique, MX-Ecublens
1015 Lausanne, Switzerland

DAUSCH, David
Clemson University
Olin Hall
Clemson, SC 29634-0907

DAY, John
Kemet Electronics
POB 5928
Greenville, SC 29615

DEBASIS, Roy
Penn State University
143 MRL
State College, PA 16801

DeFRUTOS, Jose
Dpts Fisica Aphicada UPMEVIT
Telecomm
Crta Valencia, Km F.28031
Madrid, Spain

DEL CERRO, Jaime
Penn State University, MRL
University Park
State College, PA 16802-4801
(address after conference:
Seville University
P. Box 1065
Seville, Spain)

DE VRIES, Hans
Philips Components
P.O. Box 278
5600 MD Eindhoven,
Netherlands

DEXTER, Kathleen
DRA, Malvern (UK)
St. Andrew's Road
Malvon, Worch., WR1L 10Z
Englund

DIMOS, Duane
Sandia National Laboratories
Department 1845
Albuquerque, NM 87185-5800

DOUGHERTY, Joseph P.
Penn State University
144 Materials Research Lab
University Park, PA 16802

ELISSALDE, C.
Laboratoire de Chimie du Solide
du CNRS
Universite Bordeaux
351, Cours de la Liberation
33405 Talence Cedex, France

ERBIL, Ahmet
Georgia Tech
School of Physics
Atlanta, GA 30332

ESAYAN, Stepan
Rutgers University
Dept. of CerPOB 909
Piscataway, NJ 08855

EVANS, Joseph T.
Radiant Technologies, Inc.
1009 Bradbury Drive, SE
Albuquerque, NM 87106

FADA, Yoshiaki
Tokin Corporation
6 Chome 7-1 Kooriyama
Taihaku-Bu Sendai-City
Miyage-Pref Japan

FOUSEK, Jan
Institute of Physics
Na Slovance 2
18040 Prague 8, Czechoslovakia

FUJIMOTO, Sanji
Fukui Institute of Technology
3-6-1 Gakuen
Fukui 910, Japan

FURMAN, Eugene
350 Baldwin Rd, K-4
Parsippany, NJ 07054

GACHIGI, Kamau Wa
Penn State University
9B Graduate Circle
State College, PA 16801

GAUCHER, Philippe
Thonson CSF/LCR
Orsay, 91190, France

GIFFORD, Kenneth D.
North Carolina State University
1901-202 Eyrie Court
Raleigh, NC 27606

GILBREATH, G. Charmaine
Naval Research Lab
4555 Overlook Avenue SW
Washington, DC 20375

GONNARD, Paul
Institut National des Sci Appli
20, Avenue Albert Einstein
69621 Villeurbanne Cedex,
France

GUO, R.
Penn State University
Materials Research Lab
University Park, PA 16802

GUPTA, Sri P.
Kemet Electronics
P.O. Box 5928
Greenville, SC 29606

GURURATA, Raj
Hewlett Packard
3000 Minuteman Road
Andover, MA 01810

HADNAGY, Domokos
Ramtron
1580 Ramtron Drive
Colorado Springs, CO 80907

HAMMETTER, Bill
Sandia National Laboratories
Department 1845
Albuquerque, NM 87185-5800

HAERTLING, Gene
Clemson University
206 Olin Hall
Clemson, SC 29634-0907

HALL, D.A.
University of Manchester
Grosvenor Street
Manchester, MI 7HS UK

HARRAD, El
Cloes-Supele 2 Rue Edovard
Belin Metz 57070
France

HAUN, Michael J.
Colorado School of Mines
Dept. of Metall & Mat Engrg
Golden, CO 80401

HENDERSON, Jack
Naval Surface Warfare Center
Crane, IN 47522

HENDRICKS, Warren C.
Dept. of Mat Sci/Engrg
Virginia Tech
213 Holden Hall
Blacksburg, VA 24060

HERABUT, Aree
Rutgers University
Dept. of Ceramics Sci. & Engrg.
POB 909
Piscataway, NJ 08855

HIRATANI, Masahiko
SUNY at Buffalo
330 Bonner Hall
Buffalo, NY 14260

HU, Hongxing
Penn State University
A-1 MRL
University Park, PA 16802

HUANG, Charles H.-J.
Rice University
6100 S. Main St.
Houston, TX 77251

ICHINOSE, Noboru
Waseda University
3-4-1 Ohkubo Shinjuku-ku
Tokyo, Japan

JANA, Pradeep
Texas A&M University
Center for Electronic Materials
Electrical Engineering
Department
College Station, TX 77843-3128

JHING-FANG, Chang
Virginia Tech
Dept. of Mat Sci/Engrg
Blacksburg, VA 24061

JOSHI, Pooran C.
Penn State University, Mat Res
Lab
135 R.O.B., M.R.L.
University Park, PA 16802

JULLIEN, Pierre
Lab de Physique du Solide
Bd Gabriel
Dijou 21000 France

KAHN Manfred
NRL DOD
3412 Austin Court
Alexandria, VA 22310

KALLUR, Venugopal A.
Texas A&M University
Center for Electronic Materials
Electrical Engineering
Department
College Station, TX 77843-3128

KATAYAMA, Takuma
Kyoto University
Dept. of Electronics
Yoshida Honmachi, Sakyo-ku
Kyoto, Japan 606

KATO, Yoshinobu
Fukai Institute of Technology
3-6-1 Gakeun
Fukui City, Japan

KHAN, Ashraf
Virginia Tech
Dept. of Materials Engineering
Blacksburg, VA 24061

KINGON, Angus
Dept/Mat Sci & Engrg, NCSU
Raleigh, NC 27695-7919

KLOHN, Kenneth
US Army Electronics
Tech/Devices Lab
SLCET-MA
Ft. Monmouth, NJ 07703

KORIPELLA, Ramesh
Kemet Electronics
POB 5928
Greenville, SC 29606

KULWICKI, Bernard M.
Texas Instruments
34 Forest Street, MS 10-13
Attleboro, MA 02703

KUMAR, Umesh
MRL, Penn State University
University Park, PA 16802

KUPFERBERG, Lenn C.
Raytheon Company
131 Spring Street
Lexington, MA 02173

LAMPE, Donald R.
Westinghouse Electric Corp
POB 1521 - MS 3D12
Baltimore, MD 21203

LANG, Sidney B.
Ben-Gurion Univ of the Negev
Department of ChemEngrg
84105 Beer Sheva, Israel

LEE, Burt
Clemson University-Olin Hall
Clemson, SC 29634-0907

LEE, Hee Young
Yeungnam University
214-1 Dae-dong
Kyongsan 712-749, Korea

LEE, Jai chan
Rutgers University
Dept/Ceramics
POB 909
Piscataway, NJ 08855

LEE, Sungchul
University of Arizona
ECE Department
Tucson, AZ 85721

LI, Chen-Chung G.
Virginia Tech
213 Holden Hall, MSE Dept.
Blacksburg, VA 24061

LI, Guang
Clemson University
Olin Hall
Clemson, SC 29634-0907

LI, Shaoping
Penn State University
214 Materials Research Lab
University Park, PA 16802

LIN, C.
Clemson University
Olin Hall
Clemson, SC 29634-0907

LIN, Chhiu-Tsu
Northern Illinois University
Department of Chemistry
DeKalb, IL 60115-2862

LIN, Donhang
University of Illinois 105 S.
Goodwin
Urbana, IL 61801

LIPELES, Russell
The Aerospace Corporation
POB 92957, MS MZ-244
Los Angeles, CA 90009

LIU, S. T.
Honeywell
12001 State Highway 55
Plymouth, MN 55441

LIVAGE, Carine
Rutgers University
POB 909
Piscataway, NJ 08855-0909

LUO, Wei-Gen
Shanghai Institute of Ceramics
Chinese Academy of Sciences
1295 Ding-X: Rd.
Shanghai 200050 China

MAIER, Roe J.
Phillips Lab
PL/VTET
Kirtland AFB, NM 87117-6008

MANSOUR, Said A.
Purdue University
School of Material Engineering
W. Lafayette, IN 47906

MANTESE, Joseph V.
General Motors
30500 Mound Rd.
Warren, MI 48090-9055

McKEIGHEN, Ron
Advanced Technology Labs
22100 Bothell Hiway SE
Bothell, WA 98041

MECARTNEY, Martha
University of California, Irvine
Dept of Mech & Aero Engrg
Irvine, CA 92717

MEGHERHI, Mohammed
Piezo Kinetics Inc.
POB 756
Bellefonte, PA 16823

MEITZLER, Allen H.
Ford Motor Co.
Scientific Research Lab,
POB 2053, Rm. E-1170
Dearborn, MI 48121

MEIYU, Zhao
Shanghai Institute of Ceramics
1295 Dingxi Road
Shanghai, China 200050

MEYER, Tim
Morgan Matroc
232 Forbes Road
Bedford, OH 44146

MICHELI, Adolph L.
G.M. Research Labs
12 Mile & Mound Rds., Dept. 40
Warren, MI 48090

MILLAR, Caroline
Ferroperm A/S
Hejreskovvej 6
3490 Kvistgard, Denmark

MING, Nai-Ben
Nanjing University
LSSM, Nanjing University,
Nanjing, 210008, China

MIYASAKA, Yoichi
NEC Corporation
4-1-1 Miyazaki
Kawasaki, Japan 216

MOORE. Randall
Harry Diamond Labs
2800 Powder Mill Rd.
Adelphi, MD 20783

MOYNIHAN, Ted
Spectra, Inc.
P.O. Box 68 C
Hanover, NH 03755

MYERS, Ed
National Semiconductor
2900 Semiconductor Dr.,
M/S E-140
Santa Clara, CA 95052

NAM, Hyo-Duk
Yeungnam University
214-1 Dae-dong
Kyongsan 712-749 Korea

NASBY, Robert D.
Sandia National Laboratories
POB 5800, Dept. 1325
Albuquerque, NM 87185-5800

NEAR, Craig
Morgan Matroc
232 Forbes Road
Bedford, OH 44146

OCHI, Atsushi
NEC Corporation
Miyazaki 4-1-1 Miyamae
Kawasaki, Kanagawa 216
Japan

OHKI, Michio
Kyoto University
Dept. of Electronics
Yoshida Honmachi, Sakyo-ku
Kyoto, Japan 606

OKAZAKI, Kiyoshi
Shonan Institute of Technology
1-1-25, Tusujido Nishikaigan
Fujisawa, 251, Japan

ONITSUKA, Katsuhiko
Penn State University
Materials Research Lab.
University Park, PA 16802

PAN, Wei
Virginia Tech
213 Holden Hall
Blacksburg, VA 24061

PANDEY, R. K.
Texas A&M University
Electrical Engineering Dept.
College Station, TX 77843-3128

PANHOLZER, Rudy
Naval Postgraduate School
Monterey, CA 93943

PAPET, Philippe
Quartz & Silice
108 Av Carnob
Nemours, 77140, France

PARADISE, Bill
Clemson University
Olin Hall
Clemson, SC 29634-0907

PARDO, Lorena
Insto. Ciencia De Materiales
(A)CSIC
Serrano, 144
28006-Madrid, Spain

PENG, Cheng-Jien
MRL/ Penn State University
129 MRL/PSU
University Park, PA 16802

PENG, Chien-Hsiung
Virginia Tech
213 Holden Hall
Blacksburg, VA 24061

PHULE, P.P.
University of Pittsburgh
848 Benedum Hall
Pittsburgh, PA 15261

PILGRIM, Steve
Martin Mariette Laboratories
1450 S. Rolling Rd.
Baltimore, MD 21227-3898

PINHO, John
Acoustic Imaging
10027 S. 51st St.
Phoenix, AZ 85226

POHANKA, Robert
Office of Naval Research
800 N. Quincy St.
Arlington, VA 22217

PRESTON, Kimberly
Clemson University
Olin Hall
Clemson, SC 29634-0907

PUGH, Robert D.
USAF Phillips Laboratory
PL/VTET
KAFB, NM 87117-6008

QIU, Chuan
Virginia Tech
Dept. of Mat Sci/Engrg
Blacksburg, VA 24060

QIREU, Zhang
Perfect structures
Suzhou Railway Teacheve
College
Suzhou, China

RAVINDRANATHAN, P.
Penn State University
204 Materials Research Lab.
University Park, PA 16802

RAYMOND, Mark
Lehigh University, MRL
Whitaker Lab #5
Bethlehem, PA 18015

RICHARD, Claude
Institut National des Sciences
Appliquees (INSA)
20, avenue Albert Einstein
69621 Villeurbanne cedex
France

RIECK, Vernon W.
Spectra, Inc.
P.O. Box 68 C
Hanover, NH 03755

RIMAN, Richard E.
Rutgers University
P.O. Box 909
Piscataway, NJ 08855-0909

RITTENMYER, Kurt M.
U.S. Naval Research Laboratory,
P.O. Box 568337
Orlando, FL 32856

ROSEMAN, Rodney D.
University of Illinois
105 S. Goodwin, Ceramics Bldg.
Champaign-Urbana, IL

SAFARI, A.
Rutgers University
PO Box 909
Piscataway, NJ 08855-0909

SAYER, Michael
Dept. Of Physics
Queens University
Kingston, Ontario K7L 3N6
Canada

SCHMIDT, Hugo
Montana State University
Bozeman, MT 59717

SCHMITT, Heinz
Universitat des Soiarlaudes
Fachbereich 10.3 Physik
D-6600 Saarbrucken Germany

SCHUTZING, Norman W.
General Motors Research Labs
30500 Mound Rd.
Warren, MI 48090

SELVARAJ, Raj U.
Penn State University, MRL
State College, PA 16802

SETTER, Nava
Ecole Polytechnique
Federale de Lausanne
Lab. de ceramique, MX-Ecublens
1015 Lausanne, Switzerland

SHERRIT, Stuart
Royal Military College
Kingston, Ontario Canada

SHIH, Wei-Heng
Drexel University
Dept/Mat. Engrg.
Philadelphia, PA 19104

SHIMIZU, Masaru
Kyoto University
Dept. of Electronics
Yoshida Honmachi, Sakyo-ku
Kyoto, Japan 606

SI, Jie
Virginia Tech
213 Holden Hall
Blacksburg, VA 20060

SIDNEY, Ian
Morgan Matroc, Unilator Division
Vauxhall Industrial Estate
Ruabon, CLWYD LL14 6HY UK

SIMONNE, John J.
LAAS-CNRS
7 Avenue Colonel Roche
Toulouse F-37000 France

SINHAROY, Sam
Westinghouse STC
1310 Beulah Road
Pittsburgh, PA 15235

SMITH, Wallace Arden
Office of Naval Research
Materials Division, Code 1131
800 North Quincy Street
Arlington, VA 22217-5666

SMITS, Jan
Boston University
44 Cummington Street
Boston, MA 02215

SRINIVASAN, T. T.
Ferro Corporation
Perry Point Rd, POB 217
Penn Yan, NY 14527

SUGIHARA, Sunao
Shonan Institute of Technology
1-1-25, Tusujido Nishikaigan
Fujisawa, 251, Japan

SUI-YANG, Huang
Laboratoire de Cherie du solide
Unive Bordeaux 1
Talence, France

SUWANNASIRI, Thitima
Rutgers University
BPO 29886 POB 1119
Piscataway, NJ 08855

TAHAN, Danielle
Rutgers University
POB 1119
Piscataway, NJ 08855

TAKADA, Takahiro
Sumitoyo Metal Industries Ltd.
3603 Plaza Drive
State College, PA 16801

TAKENAKA, Tadashi
Science University of Tokyo
Noda, Chiba-ken, 278 Japan

TAKEUCHI, Hiroshi
Hitachi, Ltd.
Minami Oi, Shinagawa-ku
Tokyo, Japan

TANCRELL, Roger
Raytheon Research Division
131 Spring St.
Lexington, MA 02173

TANIMOTO, Toshio
Shonan Institute of Technology
1-1-25, Tusujido Nishikaigan
Fujisawa, 251, Japan

TANTIGATE, Chutima
Rutgers University
Dept of Ceramic Science/Engrg
POB 909
Piscataway, NJ 08855

TEOWEE, Gintong
University of Arizona
4715 E. Ft. Lowell Rd.
Tucson, AZ 85718

THAKOOR, Sarita
Jet Propulsion Laboratory
4800 Oak Grove Drive
Pasadena, CA 91109

TOMIKAWA, Y.
Yanagata University
4-3-16 Johnan
Yonezawa 992 Japan

TOULOUSE, Jean
Lehigh University
Physics Building
Bethlehem, PA 18015

TRAYNOR, Steven
Ramtron Corporation
1850 Ramtron Drive
Colorado Springs, CO 80918

TUTTLE, Bruce
Sandia National Laboratories
Division 1845
Albuquerque, NM 87185

TZE-CHIUN, C. Chen
Virginia Tech
Dept. of Mat Sci/Engrg
Blacksburg, VA 24061

UCHINO, Kenji
The Pennsylvania State Univ
134 Materials Research Lab
University Park, PA 16802

UDAYAKUMAR, K.R.
Penn State University
Room A4, Mat Res Lab
University Park, PA 16802-4801

VAN BUSKIRK, Peter
ATM
7 Commerce Dr.
Danbury, CT

van der KLINK, J. J.
EPFL
Institut de Physique
Experimentale
Lausanne, CH-1015 Switzerland

VAUDIN, Mark
NIST
Ceramics Division
Gaithersburg, MD 20874

VIJAY, Dilip P.
Virginia Tech
Blacksburg, VA 24061

VOLK, Eve
SEACOR Piezo Ceramics
8 Huntington Street, Suite 300
Huntington, CT 06484

VUGMEISTER, Boris
Lehigh University
Department of Physics
Bethlehem, PA 18015

WALLER, Dave
Hewlett Packard
3000 Minuteman Rd.
Andover, MA 01810

WALLIS, Jeremy
Mattek, CSIR
Meiring Naude Road, Brummeria
Pretoria, South Africa 0184

WANG, Feiling
Clemson University
Olin Hall
Clemson, SC 29634-0907

WANG, Sea-Fue
Materials Research Lab
Penn State University
University Park, PA 16802

WANG, Yong Ling
Shanghai Institute of Ceramics
1295 Ding-xi Road
Shanghai, China 200050

WASILIK, John H.
Wasilik Associates
1304 Sarah Drive
Silver Spring, MD 20904

WECHSLER, Barry
Hughes Research Laboratory
3011 Malibu Canyon Rd.
Malibu, CA 90265

WHATMORE, Roger W.
Gec-Marconi Materials Technical
Caswell, Towcester
Northants NN 12 8EQ

WILLIAMS, Martin
Manchester University
Manchester Mat Sci Ctrr
Grosvenor St
Manchester MI 7HS England

WOLNY, Wanda W.
Ferroperm A/S
Hejreskovvej 6
3490 Lavistgard
Denmark

WON CHOI, Seong
Dankook University
24 Anseodong, Chungnam,
Seoul, Korea

WOOD, Steven
Memory Development
Bell-Northern Research Ltd.
POB 3511, Station C
Ottawa, Ontario K1Y4H7
Canada

WOUTERS, Dirk
IMEC
Kapeldreef 7S
3001 Leuven Belgium

WU, Richard
Cabot Corporation
County Line Road
Boyertown, PA 19460

WU, Shu-Yau (Jim)
McDonnell Douglas Electronic
Systems Co.
1801 E. St. Andrew Pl.
Santa Ana, CA 92705

WU, Zheng
Queens University
Kingston, Ontario, K7L 3N6
CANADA

XIE, Sheng-wu
Shanghai Jiao Tong University
1954 Hua Shan Road
Shanghai 200050 China

YAMAGUCHI, Hiromu
NEC Corporation
4-1-1 Miyazaki
Kawasaki, Japan 216

YAMAMOTO, Takashi
National Defense Academy
Yokosuka, Japan

YAMASHITA, Yohachi
Toshiba Corporation
70 Yanaol-Cho Saiwai-ku
Kawasaki 210 Japan

YAO, Si
Aian Jiaotong University
Department of Electronic
Engineering
Xian 710049 China

YOO, In K.
Virginia Tech
Blacksburg, VA 24060

YOON, Soon-Gil
Rutgers University
Dept. of Ceramics
POB 909
Piscataway, NJ 08855

YOSHIKAWA, Shoko
The Pennsylvania State
University MRL
University Park, PA 16802

YOUNG, Ho Shin
Chenan National Junior Tech
College
275-1 Budaedong, Chenan
Chunnam, Korea

YU, Insuk
Seoul National University
Sinrim-dong
Seoul, 151-742 Korea

YU, Suolong
Fuyang
Hangzhou Ahejiang 311400
China

ZHANG, Qiming
Penn State
Materials Research Lab.
University Park, PA 16802

ZHONGANG, Huang
Shanghai Institute of Ceramics
1295 Dingxi Road
Shanghai, 200050 China

ZU-YOU, Mao
Low Firing High Properties MLC
Hong-Ming Electronic
Component Factory
Chengdu, Sichuan 610058
China